

Proceedings of the Tenth International Conference on Permafrost

Salekhard, Yamal-Nenets Autonomous District, Russia
June 25–29, 2012

**TENTH
INTERNATIONAL
CONFERENCE
ON PERMAFROST**



**VOLUME I:
INTERNATIONAL
CONTRIBUTIONS**

Edited by Kenneth M. Hinkel

Salekhard
2012

Organizers



General-partner



Partners



Tenth International Conference on Permafrost

Proceedings of the Tenth International Conference on Permafrost
Salekhard, Yamal-Nenets Autonomous District, Russia
June 25–29, 2012

**Tenth International
Conference on Permafrost**

Volume 1: International Contributions

Edited by Kenneth M. Hinkel

**The Northern Publisher
Salekhard
2012**

Tenth International Conference on Permafrost
Volume 1: International Contributions
Edited by Kenneth M. Hinkel

© 2012

The State Enterprise of the Yamal-Nenets Autonomous District
The Northern Publisher (Severnoye Izdatelstvo)
All rights reserved.

Printed in Russia

Elmer E. Rasmuson Library Cataloging in Publication Data

International Conference on Permafrost (10th : 2012 :

Salekhard, Yamal-Nenets Autonomous District, Russia)

Tenth International Conference on Permafrost :

Resources and Risks of Permafrost Areas in a Changing World /

edited by Kenneth M. Hinkel [v.1], Vladimir P. Melnikov [v.2, 3].

Salekhard, Russia: The Northern Publisher; Tyumen, Russia: Pechatnik; Ekaterinburg,

Russia: Fort Dialog-Iset, 2012, 5 v. : ill., maps, cm.

Includes bibliographical references and index.

June 25-29, 2012.

Contents: vol.1. International contributions - vol.2. Translations of Russian contribution - vol.3. Russian contribution - vol.4. Extended Abstracts - vol.5. Extended Abstracts in Russian.

1. Permafrost-Congresses. 2. Frozen ground-Congresses.

I. Title. II. Hinkel, Kenneth M. III. Melnikov, Vladimir P.

Cover Design: The Northern Publisher

GB641.I6.2012

УДК 551.34; 502.3; 624.139

ББК 26.3

Д 37

ISBN 978-5-905911-01-9 (v.1)

ISBN 978-5-905911-02-6 (v.2)

ISBN 978-5-9961-0510-6 (v.3,5)

ISBN 978-5-91128-050-5 (v.4/1)

ISBN 978-5-91128-052-9 (v.4/2)

Production Editor: Thomas Alton (Fairbanks, Alaska)

Hinkel, K.M. (ed.). 2012. *Tenth International Conference on Permafrost. Vol. 1: International Contributions*. The Northern Publisher, Salekhard, Russia, 504 pp.

Contents

| | |
|--|------------|
| Preface | x |
| Acknowledgments | x |
| Associate Editors and Reviewers | xi |
| | |
| Fifty Years of Permafrost Collaboration with the Soviet Union and Russia | 1 |
| J. Brown | |
| Airborne Electromagnetic Mapping of the 3-D Distribution of Permafrost in the Yukon Basin, Alaska | 15 |
| J. D. Abraham, B.J. Minsley, B.D. Smith, L.B. Ball, L. Anderson, M.A. Walvoord, J.C. Cannia, C.I. Voss, B.K. Wylie | |
| Improvement of Pulse-NMR Technology for Determining the Unfrozen Water Content in Frozen Soils | 21 |
| S. Akagawa, G. Iwahana, K. Watanabe, E.M. Chuvilin, V.A. Istomin | |
| Geochemically-Induced Unfrozen Water Effects on CCR Surveys of Massive Ground Ice, Western Canadian Arctic | 27 |
| M. Angelopoulos, D. Fox, W.H. Pollard | |
| Soil Moisture from Metop ASCAT Data at High Latitudes | 33 |
| A. Bartsch, T. Melzer, K. Elger, B. Heim | |
| A New Permafrost Research Tunnel: Methodology, Design, and Excavation | 39 |
| K. Bjella, M. Sturm | |
| The Measurement of Compressional and Shear Wave Velocities in Permafrost: A Comparison of Three Seismic Methods | 45 |
| W. Black, E. Bashaw, J. Drage, R. Kmack | |
| Quantifying Rock Glacier Creep Using Airborne Laser Scanning: A Case Study from Two Rock Glaciers in the Austrian Alps | 49 |
| E. Bollmann, C. Klug, R. Sailer, J. Stötter, J. Abermann | |
| Effects of Rising Temperature on Shear Strength of Slopes in Alpine Permafrost | 55 |
| C. Bommer | |
| An Integrated Assessment of the Influences of Upland Thermal-Erosional Features on Landscape Structure and Function in the Foothills of the Brooks Range, Alaska | 61 |
| W.B. Bowden, J.R. Larouche, A.R. Pearce, B.T. Crosby, K. Krieger, M.B. Flinn, J. Kampman, M.N. Gooseff, S.E. Godsey, J.B. Jones, B.W. Abbott, M.T. Jorgenson, G.W. Kling, M. Mack, E.A.G. Schuur, A.F. Baron, E.B. Rastetter | |
| Influence of Physical Properties on Frozen Soil Creep Parameters and Foundation Design | 67 |
| P. Cavanagh, K. Spencer, A. Tchekhovski, V. Aksenov | |
| The Significance of the Permafrost Tunnel (Fox, Alaska) | 73 |
| M. Cysewski, M. Sturm, K. Bjella | |
| Annual Frost Heave Distribution in a Non-Sorted Circle System Measured with a Terrestrial Laser Scanner | 79 |
| R.P. Daanen | |
| Using Ground Data from the Global Terrestrial Network of Permafrost (GTN-P) for the Evaluation of the ESA DUE Permafrost Remote Sensing Derived Products Land Surface Temperature and ASCAT Surface State Flag | 85 |
| K. Elger, B. Heim, A. Bartsch, C. Paulik, C. Duguay, S. Hachem, A. Soliman, H. Lantuit, J. Boike, F-M. Seifert | |
| Investigating the Effects of Lateral Water Flow on the Spatial Patterns of Thaw Depth | 91 |
| S. Endrizzi, S. Gruber | |
| Sustainable Arctic Marine and Coastal Technology | 97 |
| J. Finseth, A. Instanes | |
| Soil and Water Chemistry Characteristics of Thermo-Erosional Features in the Western Noatak River Basin, Alaska, USA | 101 |
| M.B. Flinn, W. Bowden, A.W. Balsler, J.B. Jones, M.N. Gooseff | |

| | |
|--|-----|
| Cryostructures of Basal Glacier Ice as an Object of Permafrost Study: Observations from the Matanuska Glacier, Alaska | 107 |
| D. Fortier, M. Kanevskiy, Y. Shur, E. Stephani, M. Dillon, M.T. Jorgenson | |
| PSInSAR Monitoring of Ground Movement at Salluit, Quebec (Canada), Due to Freeze-Thaw Cycles, Active Layer Thickening, and Permafrost Warming | 113 |
| R. Fortier, A-M. LeBlanc, G. Falorni, R. Therrien | |
| Linkages between Patterned Ground, Alder Shrubland Development, and Active Layer Temperature in the Northwest Siberian Low Arctic | 119 |
| G.V. Frost, H.E. Epstein, D.A. Walker, G. Matyshak, K. Ermokhina | |
| Fine-Scale Spatio-Temporal Monitoring of Multiple Thermo-Erosion Gully Development on Bylot Island, Eastern Canadian Archipelago | 125 |
| E. Godin, D. Fortier | |
| A Global View on Permafrost in Steep Bedrock | 131 |
| S. Gruber | |
| Thermo-Erosion along the Yedoma Coast of the Buor Khaya Peninsula, Laptev Sea, East Siberia | 137 |
| F. Günther, P.P. Overduin, A.V. Sandakov, G. Grosse, M.N. Grigoriev | |
| Shear Strength of Rock Joints Filled with Frozen Sand | 143 |
| F.K. Günzel | |
| Tessellons and “Sand Wedges” on the Qinghai-Tibet Plateau and Their Palaeoenvironmental Implications | 149 |
| S.A. Harris, H. Jin | |
| Estimating Snowdrift Depth Using Differential GPS and a High-Resolution Digital Surface Model | 155 |
| K.M. Hinkel, J.K. Hurd, Jr. | |
| Recent Hydrological and Ecological Changes in Relation to Permafrost Degradation under Increased Precipitation in an Eastern Siberian Boreal Forest | 161 |
| Y. Iijima, A.N. Fedorov, T. Ohta, A. Kotani, T.C. Maximov | |
| Engineering Design Utilizing Climate Change Information – Permafrost Application | 167 |
| A. Instanes | |
| Thermal State of Mongolian Permafrost | 173 |
| M. Ishikawa, N. Sharkhuu, Y. Jambaljav, G. Davaa, K. Yoshikawa, T. Ohata | |
| Thermokarst Lake and Shore Fen Development in Boreal Alaska | 179 |
| M.T. Jorgenson, M. Kanevskiy, Y. Shur, T. Osterkamp, D. Fortier, T. Cater, P. Miller | |
| Investigating Hydrologic Storage in Catchments Underlain by Continuous Permafrost | 185 |
| D.L. Kane, E.K. Youcha, R.E. Gieck | |
| Study of Ice-Rich Syngenetic Permafrost for Road Design (Interior Alaska) | 191 |
| M. Kanevskiy, Y. Shur, B. Connor, M. Dillon, E. Stephani, J. O’Donnell | |
| Two-Dimensional Frost Heave Simulation Based on Takashi’s Equation | 197 |
| S. Kanie, H. Zheng, S. Akagawa | |
| Regional and Local Variability of Modern Natural Changes in Permafrost Temperature in the Yakutia Coastal Lowlands, Northeastern Siberia | 203 |
| A. Kholodov, D. Gilichinsky, V. Ostroumov, V. Sorokovikov, A. Abramov, S. Davydov, V. Romanovsky | |
| Modeling Permafrost Response of the Last Glacial Termination: First Results of the VAMPER Model | 209 |
| D.C. Kitover, H. Renssen, R.T. Van Balen, J. Vandenberghe | |
| Monitoring of Permafrost Creep on Two Rock Glaciers in the Austrian Eastern Alps: Combination of Aerophotogrammetry and Airborne Laser Scanning | 215 |
| C. Klug, E. Bollmann, R. Sailer, J. Stötter, K. Krainer, A. Käab | |
| Active Layer Processes in the McMurdo Dry Valleys, Antarctica: Decadal Trends and Experimental Responses to Changes in Soil Moisture | 221 |
| J. Levy, A. Fountain, M. Gooseff, J. Barrett, D. Wall, U. Nielson, B. Adams, W.B. Lyons | |

| | |
|---|------------|
| Thermal Conductivity and Freezing Temperature of Oil-Contaminated Foundation Soils Surrounding the China-Russia Crude Oil Pipeline | 227 |
| G. Li, W. Ma, W. Feng, Y. Mu, X. Li | |
| Ice-Wedge Polygon Type Controls Low-Gradient Watershed-Scale Hydrology | 231 |
| A.K. Liljedahl, L.D. Hinzman, J. Schulla | |
| Compression Test and Pore-Water Pressure Measurement for Warm and Ice-Rich Frozen Soil..... | 237 |
| S. Liu, J. Zhang, H. Zhang, B. Zheng | |
| Distribution of Permafrost in the Source Area of the Yellow River on the Northeastern Qinghai-Tibet Plateau, China | 243 |
| D. Luo, H. Jin, L. Lin | |
| Progress in Frozen Soil Mechanics Research in China: A Review | 249 |
| W. Ma, D. Wang, Z. Wen | |
| Reassessment of Lakes and Ponds in an Arctic River Delta Using Modern Spatial Technology | 255 |
| M. McGraw, H.J. Walker | |
| Thermal Performance of the Permafrost Protection Techniques at Beaver Creek Experimental Road Site, Yukon, Canada | 261 |
| J. M-Lepage, G. Doré, D. Fortier, P. Murchison | |
| Monitoring Instruments for Freeze-Thaw Depth | 267 |
| J. Mori, T. Sone | |
| Evaluation of the ERA-Interim Reanalysis for Modeling Permafrost on the North Slope of Alaska..... | 271 |
| R.I. Mugford, P. Christoffersen, J.A. Dowdeswell, A. Consonni | |
| Multi-Satellite-Derived Changes in Energy and Mass of Russian Permafrost Regions..... | 277 |
| R.R. Muskett, V.E. Romanovsky | |
| “The Worst Thing We Had To Contend With”: Permafrost and Construction of the Alcan Highway..... | 283 |
| F.E. Nelson | |
| Thermal Status of Traditional Roadbed and Roadbed with Slopes Covered by Crushed Rocks along the Qinghai-Tibet Railway | 289 |
| F. Niu, Z. Lin, H. Liu, J. Lu, Z. Liu | |
| Effect of Vegetation on Soil-Surface Temperatures in Northern Alaska | 295 |
| K.E. Nyland, N.I. Shiklomanov, D.A. Streletskiy, A.E. Klene, F.E. Nelson | |
| Preliminary Development of a Field Tool to Assess the Load Capacity of Frozen Muskeg..... | 301 |
| J.M. Oswell, R. Coutts, R. Stancliffe | |
| Ground Ice Conditions in University Valley, McMurdo Dry Valleys, Antarctica | 305 |
| W.H. Pollard, D. Lacelle, A.F. Davila, D. Andersen, C.P. McKay, M. Marinova, J. Heldmann | |
| Numerical Estimation for Settlement of Roadway Embankment in Permafrost Regions..... | 311 |
| J. Qi, S. Wang, F. Yu | |
| Estimation of the Mean Annual Surface Temperature and Surface Frost Number Using the MODIS Land Surface Temperature Products for Mapping Permafrost in China | 317 |
| Y. Ran, X. Li, R. Jin | |
| Encounters with Relict Permafrost in the Anchorage, Alaska, Area | 323 |
| C.H. Riddle, J.W. Rooney | |
| Vegetation Cover on Alpine Rock Glaciers in Relation to Surface Velocity and Substrate..... | 329 |
| L. Rieg, R. Sailer, J. Stötter, D. Burger | |
| Simplified Climate Statistics for Permafrost Modeling: Yellowknife Case Study | 335 |
| D. Riseborough, S. Wolfe, C. Duchesne | |
| Foundation Engineering in Svalbard, 1950–2012 | 341 |
| J.L. Rongved, A. Instanes | |

| | |
|---|-----|
| City of Kotzebue's Vortac Earthen Dam: A Review of the Naturally Frozen Back Embankment and Reservoir Slopes | 347 |
| J.W. Rooney, C.H. Riddle | |
| Warming Permafrost Temperatures at Two Mine Sites in the North Slave Region, Northwest Territories, Canada | 353 |
| V.E. Roujanski, B. Horne, G. Zhang, S. McCuaig, M. Blade, M. Regular | |
| Thermo-Mechanical Modeling of a Glacier-Permafrost System in Spitsbergen: Implications for Subglacial Hydrology | 359 |
| N. Roux, C. Grenier, C. Marlin, E. Delangle, A. Saintenoy, J-M. Friedt, M. Griselin | |
| Mountain Permafrost Distribution in the Andes of Chubut (Argentina) Based on a Statistical Model | 365 |
| L. Ruiz, D. Trombotto Liaudat | |
| Perennial Frost Mounds in Mongolia | 371 |
| N. Sharkhuu, K. Yoshikawa, S. Anarmaa | |
| Northern Hemisphere Component of the Global Circumpolar Active Layer Monitoring (CALM) Program | 377 |
| N.I. Shiklomanov, D.A. Streletskiy, F.E. Nelson | |
| Permafrost Degradation and Thaw Settlement under Lakes in Yedoma Environment | 383 |
| Y. Shur, M. Kanevskiy, M.T. Jorgenson, M. Dillon, E. Stephani, M. Bray, D. Fortier | |
| Vegetation Patterns of Retrogressive Thaw Slumps, Herschel Island, Southern Beaufort Sea, Yukon Territory, Canada | 389 |
| H.A. Sloan, W.H. Pollard | |
| A Community-Based Permafrost/Active Layer Monitoring Program | 395 |
| E. Sparrow, K. Yoshikawa | |
| High-Resolution Permafrost Simulations in Western Greenland and an Assessment of Permafrost Degradation Risk | 401 |
| M. Stendel, J.H. Christensen, S. Marchenko, R.P. Daanen, V.E. Romanovsky | |
| Infrastructure and a Changing Climate in the Russian Arctic: A Geographic Impact Assessment | 407 |
| D. Streletskiy, N. Shiklomanov, E. Hatleberg | |
| Feasibility Study of Using Active Microwave Data for Examination of Thaw Lake Drainage Patterns over the Yamal Peninsula | 413 |
| A.M. Trofaier, W.G. Rees, A. Bartsch, D. Sabel, S. Schlaffer | |
| Inventory and Monitoring of Rock Glaciers and Cryogenic Processes in the Central Andes of Mendoza, Argentina: Birth and Extinction of a Periglacial Lake | 419 |
| D. Trombotto Liaudat, M. Gabriela Lenzano, M. Castro | |
| Spatial and Temporal Dynamics of Erosion along the Elson Lagoon Coastline near Barrow, Alaska (2002–2011) | 425 |
| C.E. Tweedie, A. Aguirre, R. Cody, S. Vargas, J. Brown | |
| Controls on Patterned Ground Variability at a Continuous Permafrost Site, Central Spitsbergen | 431 |
| T. Watanabe, N. Matsuoka, H.H. Christiansen | |
| Design of a Measurement Assembly to Study In Situ Rock Damage Driven by Freezing | 437 |
| S. Weber, S. Gruber, L. Girard, J. Beutel | |
| Model Test Study of the Impact of Rainfall on Thermal-Moisture Dynamics of the Active Layer | 443 |
| Z. Wen, W. Ma, Y. Sheng, Q. Wu, D. Wang, W. Feng | |
| Application of the Fill-and-Spill Concept in Permafrost Hydrology | 449 |
| M. Woo | |
| Atmospheric Methane in the High Northern Hemisphere and its Relationship with Permafrost | 455 |
| X. Xiong, T. Zhang, E. Maddy, Q. Zhuang, C. Barnet | |
| Stress Path Tests on Artificially Frozen Soil Samples | 461 |
| Y. Yamamoto, S.M. Springman | |
| The Effect of Freeze-Thaw Action on the Dry Density and Water Content of Soil | 467 |
| C. Yang, H. Ping, G. Cheng | |

| | |
|--|------------|
| Stable Isotope Composition of Ice Cores in Open- and Closed-System Pingos | 473 |
| K. Yoshikawa, D. Lawson, S. Natsagdorj | |
| Thermal Evidence of Recent Talik Formation in Ritigraben Rock Glacier: Swiss Alps | 479 |
| E. Zenklusen Mutter, M. Phillips | |
| Variability of Soil Organic Carbon Stocks of Different Permafrost-Affected Soils: | |
| Initial Results from a North-South Transect in Siberia | 485 |
| S. Zubrzycki, L. Kutzbach, E-M. Pfeiffer, P. Vakhrameeva | |
| Author Index | 491 |

Preface

Since the Second International Conference on Permafrost held in 1973 in Yakutsk, permafrost science and engineering has witnessed the ever-increasing need for new knowledge and understanding, within Russia and the Former Soviet Union and throughout the international cold regions communities. The Tenth International Conference on Permafrost, held in Salekhard, provides the venue for the exchange of current information and knowledge concerning the dynamics of permafrost regions, their roles in global change, and challenges for development and environmental protection.

At its June 2010 meeting, the Council of the International Permafrost Association approved the preparation of proceedings of peer-reviewed papers for the Tenth International Conference on Permafrost. The two proceedings volumes are the results of a collaborative effort between the U.S. Permafrost Association and the Russian Organizing Committees. Many of the review and production procedures and software that were developed

for the Ninth International Conference on Permafrost were utilized. Volume 1 contains the English-language papers submitted electronically in autumn 2011. Reviews of the English-language papers were assisted by a team of 17 Associate Editors who in turn recruited two reviewers for each paper, resulting in a total of 113 reviewers. Final camera-ready copy of both volumes was prepared in Fairbanks by Tom Alton, copy editor, using Adobe InDesign. Papers are presented in a standard format; however, the completeness and accuracy of the references cited are solely the authors' responsibility. A total of 82 papers from 13 countries are presented in Volume 1. Volume 2 contains 106 Russian papers that were reviewed and translated in Russia, and subsequently read and edited in North America. A companion volume of approximately 370, two-page, Extended Abstracts from 15 countries was prepared by the Russian organizers.

Acknowledgments

The International Permafrost Association and the Russian organizers of the Tenth International Conference on Permafrost express their appreciation to the many individuals and sponsoring organizations that made the production of these proceedings volumes possible. The Governor of Yamal-Nenets Autonomous District, Dmitry N. Kobylking, and Vice-governor Aleksander V. Mazharov, as co-chairs of the local TICOP Committee, provided support and advice throughout the conference organizational process. They were ably assisted by staff members Aleksey Titovskiy and Irina Voronov. Dmitry Drozdov and members of the Earth Cryosphere Institute, Siberian Branch of the Russian Academy of Science (SB RAS) and Anna Kurchatova and Sergey Turenko of Tyumen State Oil and Gas University provided guidance in the preparation and publication processes.

The resources of the U.S. Permafrost Association based

in Fairbanks, Alaska, were provided through GW Scientific and the expertise of Engineering and Environmental Internet Solutions (EEI), and particularly Gary Whitton. The International Arctic Research Center, University of Alaska Fairbanks (UAF), provided logistical support for copy editor Tom Alton. Two major sponsors helped defer U.S. costs for the preparation of the proceedings: BP and Arctic Foundations, Anchorage. Printing costs were provided by the government of the Yamal-Nenets Autonomous District.

Finally, as has often been the case with previous proceedings, Jerry Brown stimulated and guided the overall review and production effort.

—Kenneth M. Hinkel, Editor,
University of Cincinnati

Reviewers of Volume 1 Papers

Associate Editors

Hanne Christiansen, Univ. Centre in Svalbard, NO
 Claude Duguay, University of Waterloo, CA
 Hugh French, University of Ottawa, CA
 Jen Harden, U.S. Geological Survey, US
 Don Hayley, EBA Engineering Consultants Ltd., CA
 Ole Humlum, University of Oslo, NO
 Torre Jorgenson, Alaska Ecoscience, US
 Doug Kane, University of Alaska Fairbanks, US
 Anna Klene, University of Montana, US

Hugues Lantuit, Alfred Wegener Institute, DE
 Marcia Phillips, WSL Inst. for Snow & Avalanche Research
 SLF, CH
 Vladimir Romanovsky Univ. of Alaska Fairbanks, US
 Jim Rooney, J&F Rooney, LLC, US
 Sharon Smith, Geological Survey of Canada, CA
 Bucky Tart, Golder & Associates, US
 Ted Vinson, Oregon State University, US
 Tingjun Zhang, University of Colorado, US

Reviewers

Steve Anderson, Golder Associates Inc., US
 Lukas Arenson, BGC Engineering, CA
 Megan Balks, University of Waikato, NZ
 Kais Ben Khadhra, University of Waterloo, CA
 Ivar Berthling, Norwegian Univ. of Sci. & Technology, NO
 Lorenz Böckli, University of Zurich, CH
 Julia Boike, Alfred Wegener Institute, DE
 Robert Bolton, University of Alaska Fairbanks, US
 Phillip Bousquet, Lab. des Sciences du Climat et de
 l'Environnement, FR
 Alexander Brenning, University of Waterloo, CA
 Brian Brisco, Natural Resources Canada, CA
 Jerry Brown, Woods Hole. MA, US
 Laura Brown, University of Waterloo, CA
 Yves Bühler, WSL Inst. for Snow & Avalanche Research
 SLF, CH
 Chris Burn, Carleton University, CA
 Sean Carey, McMaster University, CA
 Hanne Christiansen, Univ. Centre in Svalbard, NO
 Francois Costard, Université Paris Sud, FR
 Ronald Daanen, University of Alaska Fairbanks, US
 Mark Demitroff, University of Delaware, US
 Guy Doré, University Laval, CA
 Bob Dugan, Golder Associates Inc, US
 Claude Duguay, University of Waterloo, CA
 Wendy Eisner, University of Cincinnati, US
 Bernd Etzelmuller, University of Oslo, NO
 Regula Frauenfelder, Norwegian Geotechnical Institute, NO
 Hugh French, University of Ottawa, CA
 Isabelle Gärtner Roer, University of Zurich, CH
 Guido Grosse, University of Alaska Fairbanks, US
 Mauro Guglielmin, University of Insubria, IT
 Frank Günther, Alfred Wegener Institute, DE
 Sonia Hachem, University of Waterloo, CA
 Wilfried Haerberli, University of Zurich, CH
 Jen Harden, U.S. Geological Survey, US
 Don Hayley, EBA Engineering Consultants Ltd., CA
 Ken Hinkel, University of Cincinnati, US
 Larry Hinzman, University of Alaska Fairbanks, US
 Martin Hoelzle, University of Fribourg, CH

Ed Hoeve, EBA Engineering Consultants Ltd., CA
 Bill Horne, EBA Engineering Consultants Ltd., CA
 Hans-W. Hubberten, Alfred Wegener Institute, DE
 Gustaf Hugelius, Stockholm University, SW
 Ole Humlum, University of Oslo, NO
 Charles Hunt, EBA Engineering, CA
 Arne Instanes, INSTANES POLAR AS, NO
 Ketil Isaksen, Norwegian Meteorological Inst., NO
 Benjamin Jones, USGS Alaska Science Center / Univ. of
 Alaska Fairbanks, US
 Kevin Jones, EBA Engineering, CA
 Janet Jorgenson, U.S. Fish and Wildlife Service, US
 Torre Jorgenson, ABR Inc., US
 Douglas Kane, University of Alaska Fairbanks, US
 Julian Kanigan, Aboriginal Affairs & Northern Development
 Canada, CA
 Robert Kenner, WSL Inst. for Snow and Avalanche Research
 SLF, CH
 Homa Kheyrollah Pour, University of Waterloo, CA
 Joshua King, University of Waterloo, CA
 Anna Klene, University of Montana, US
 Michael Krautblatter, University of Bonn, D
 Keith Kvenvolden, U.S. Geological Survey, US
 Hugues Lantuit, Alfred Wegener Institute, DE
 David Leverington, Texas Tech University, US
 Anna Liljedahl, University of Alaska Fairbanks, US
 Jacek Majorowicz, Northern Geothermal Consult. CA
 Gavin Manson, Geological Survey of Canada, CA
 Sergei Marchenko, Univ. of Alaska Fairbanks, US
 Robyn McGregor, EBA Engineering, CA
 Heather McNairn, Agric. and Agri-Food Canada, CA
 James McNamara, Boise State University, US
 Harold Morowitz, George Mason University, US
 Frederick Nelson, University of Delaware, US
 Derick Nixon, Nixon Geotech, CA
 Jonathan O'Donnell, U.S. Geological Survey, US
 Jason Oldham, University of Waterloo, CA
 Jim Oswell, Naviq Consulting, CA
 Samuel Outcalt, University of Michigan, US
 Kim Peterson, University of Alaska Anchorage, US

Marcia Phillips, WSL Inst. for Snow and Avalanche Research
SLF, CH
Frédérique Pivot, Athabasca University, CA
Wayne Pollard, McGill University, CA
Jaakko Putkonen, University of North Dakota, US
Charles Racine, U.S. Army CRREL, Retired, US
Dhananjay Regmi, Tribhuvan University, Nepal
Daniel Riseborough, Geol. Survey of Canada, CA
Vladimir Romanovsky, Univ. of Alaska Fairbanks, US
Jim Rooney, J&F Rooney, LLC, US
Vlad Roujanski, EBA Engineering, CA
Bill Ryan, Arctic Eng Consultant, US
Kazuyuki Saito, JAMSTEC, Japan
Jack Seto, BGC Engineering, CA
Natalia Shakhova, Int'l. Arctic Research Center, US
Andrew Slater, CIRES, University of Colorado, US
Bruce Smith, Thurber Consultants, CA
Larry Smith, University of California – LA, US
Sharon Smith, Geological Survey of Canada, CA
Aiman Soliman, University of Waterloo, CA

S. Adam Soule, Woods Hole Ocean. Institution, US
Christopher Stevens, Geol. Survey of Canada, CA
Veronika Stöckli, WSL Inst. for Snow & Avalanche Research
SLF, CH
Dmitry Streletskiy, George Washington Univ., US
Tazio Strozzi, Gamma Remote Sensing, CH
Svetlana Stuefer, University of Alaska-Fairbanks, US
Nicolas Svacina, University of Waterloo, CA
Dave Swanson, National Park Service, US
Bucky Tart, Golder & Associates, US
Allan Taylor, ASL Environmental Sciences Inc., CA
Craig Tweedie, University of Texas – El Paso, US
Gonçalo Vieira, University of Lisbon, PT
Ted Vinson, Oregon State University, US
Ming-ko Woo, McMaster University, CA
Ed Yarmak, Arctic Foundations, US
Kenji Yoshikawa, Univ. of Alaska Fairbanks, US
Gordon Zhang, EBA Engineering, CA
Tingjun Zhang, University of Colorado, US
John Zufelt, US Army CRREL, US

Plenary Paper

Fifty Years of Permafrost Collaboration with the Soviet Union and Russia

Jerry Brown
Past President (2003–2008), International Permafrost Association
Woods Hole, MA, USA

Abstract

Prior to the 1980s, major contacts with the Soviet permafrost community were through traditional conferences, bilateral agreements, and limited personal exchanges. In 1963 Soviet permafrost specialists participated in the First International Conference on Permafrost (ICOP). Major international field conferences were held in Siberia in 1969, 1973, and 1989. The formal organization of the International Permafrost Association in 1983 provided opportunities to initiate non-governmental, multi-national activities. With the dissolution of the Soviet Union in 1991, a new era of institutional and individual cooperation emerged. This paper chronicles, by decade starting in the 1960s, many of the international activities with Soviet/Russian organizations and individuals in the fields of permafrost science and engineering.

Keywords: active layer; bilateral agreements; history; permafrost; Russia; Soviet Union; USSR.

Introduction

In the midst of the Cold War, cooperation on international permafrost science and engineering showed signs of warming. In 1963, several Soviet permafrost specialists attended the First International Conference on Permafrost (ICOP). Two major international conferences were held in Yakutsk, Siberia, in 1969 and 1973. Prior to the 1980s, major contacts were through these traditional conferences, bilateral agreements, and limited personal exchanges. The formal organization of the International Permafrost Association (IPA) in 1983 provided opportunities for increased non-governmental, multi-national activities. By the early 1990s, a new era of institutional and individual cooperation emerged and has continued to flourish over the past two decades.

In June 2009, the U.S. National Academies and the Russian Academy of Sciences celebrated the 50th anniversary of the signing of the first cooperation between the two academies (Schweitzer 2009). In his *Science* editorial, Schweitzer briefly reviews the decadal accomplishments between the two countries and the challenges for the next 50 years, including those related to climate change. For our U.S. and Soviet permafrost communities, these activities officially started in 1963 and were pursued under various bilateral and organizational initiatives. Many of these activities involved the early and sustained leadership of Academician Pavel I. Melnikov. Academician Melnikov made numerous visits to North America, with at least eight visits to the U.S. On most occasions he was accompanied by either Nikolai Grave or Feliks Are. Many of the U.S. visits were facilitated by federal agencies (USGS, CRREL, FWS, EPA, and others) and the U.S. National Academy of Sciences and its Polar Research Board.

This paper reports on many of the activities that fostered the cooperation between Soviet/Russian and Western and Asian researchers in the fields of permafrost science and engineering, including cryopedology. The paper is based largely on the author's personal involvements and other readily accessible information.

The Formative Period: 1960s

The development of Soviet knowledge and engineering practices related to perennially frozen ground (permafrost) is well documented in several English-language books and papers (French & Nelson 2008, Muller 1947, Shiklomanov 2005). Personal contacts were limited, in part due to restrictions on travel and communications. Early exceptions, such as with Armstrong (1965), provided unique and personal insights into northern developments in the Soviet Union. It was Muller, a university professor in the United States during World War II, who coined the term “permafrost” and is considered the “father of permafrost” in North America. During the International Geophysical Year (1957–1958), Soviet, U.S., and other researchers conducted permafrost and periglacial studies in the Antarctic, with Zotikov developing the basis for a map of the continent that illustrated likely occurrences of permafrost (Kotlyakov 1997).

The initial post-World War II contact was highlighted in 1963 by Soviet participation in the First International Conference on Permafrost (First ICOP) held at Purdue University (Woods & Leonard 1964). This participation was based on the formal 1962 letter of invitation by President Seitz of the U.S. National Academy of Sciences-National Research Council to President Keldysh of the Academy of Sciences of the USSR. Prominent permafrost participants included P.I. Melnikov, S.S. Vyalov, and N.A. Tsytoivitch. The conference proceedings included papers by additional well-known Soviet authors who did not attend, including Baronov, Kudravtsev, Dostovalov, Nersesova, Popov, Shumskiy, and Vtyurin. Also in September 1963, Shumskiy attended a conference in Montreal and was reportedly the first Soviet scientist to visit the Canadian High Arctic (see Soviet Union Today 1964).

Prior to the First ICOP, contact with Soviet permafrost specialists (geocryologists) was principally through translations of the published literature by Russian-reading researchers and professional translators in Canada and the United States. These included the translation series in the United States by CRREL and its predecessor SIPRE, and in Canada by its National

Research Council. More recent scholarly translations, such as the one by Barr (2009), provided added insight into early twentieth century Soviet permafrost discovery. Much of the early Soviet literature and many citations can be found in the Cold Regions Bibliography (<http://www.coldregions.org/>) and a link to the Arctic Bibliography. Starting in the early 1950s, Russian-language literature was regularly obtained and accessioned by the U.S. Library of Congress and most recently by the American Geological Institute (AGI). During the decades of the 1960s through 2010, more than 13,500 Russian-language citations and documents were accessioned. The peak period for Russian publications was 1970–1990, with more than 4,400 documents in each of those two decades (pers. comm. Sharon Tahirkheli, AGI, September 2011).

In addition to the First ICOP, the 1960s provided several other openings between the Soviets and the West. In summer 1966, Canadian colleagues Roger J.E. Brown and G. “Hank” Johnston spent six weeks visiting eastern Siberia and subsequently provided the first insight into the activities of the Yakutsk-based Permafrost Institute under the directorship of Academician P.I. Melnikov. This landmark visit was the first extended and substantive contact with Soviet permafrost researchers at their home institutions.

Following the Periglacial Commission conference of the International Geographical Union (IGU) in Poland in summer 1967, a follow-up Commission conference was held in Yakutsk in summer 1969. This conference, attended by 50 foreign scientists, was considered the first official multinational visit to Siberia and a major breakthrough in travel restrictions to this politically sensitive region. In addition to technical sessions in Yakutsk, the conference included a memorable field excursion on the Lena and Aldan rivers and the viewing by Western scientists of the expansive ice-rich and loess-like Yedoma deposits. Included in the conference were visits to the Shergin Shaft and the Permafrost Institute’s extensive underground research facility (multi-layered tunnel). The conference and arrangements for permission of such a large group of “foreigners” was under the leadership of Academician P.I. Melnikov and was considered the “dress-rehearsal or dry-run” for the more complex Second ICOP to take place in Yakutsk in 1973.

Conferences and Bilateral Exchanges: 1970s

The Second International Conference on Permafrost and field excursions took place in Yakutsk, Siberia, on July 11–27, 1973. More than 100 foreign participants from 14 countries joined 300 Soviet geocryologists in this monumental and memorable conference organized, once again, under the direction of Academician P.I. Melnikov. The U.S. Academy of Sciences, assisted by Canadians, produced a North American publication, followed by a translated volume of Russian papers (Brown et al. 2008). These two proceedings volumes, and particularly the Russian translations, represented the current status of permafrost investigations at that time. The concluding joint Canadian, Soviet, and U.S. conference resolution outlined a series of urgent problems, including

international research on environmental protection, the need for rapid exchange of information, and the recommendation that the Third ICOP be held in Canada. The Yakutsk conference was preceded by a three-week spring visit to the United States by Melnikov, accompanied by Feliks Are and Andrei Kapitsa. As part of that visit, a joint U.S.-USSR-Canada seminar was convened at CRREL in Hanover, NH, and was attended by some 45 researchers. Melnikov had also visited Canada in November 1972.

The first major and formal step in U.S.-Soviet permafrost cooperation was initiated on May 23, 1972, when U.S. President Nixon and USSR Chairman Podgorny signed the Agreement on Cooperation in the Field of Environmental Protection. Documentation of the agreement’s early activities and accomplishments were reported by Robinson (1988) and Scriabine (1978). The agreement included the program Area X: Arctic and Sub-Arctic Ecological Systems. However, due to political considerations during the Cold War, many related activities took place within program Area V: Protection of the Nature and the Organization of Reserves under the organizational leadership of Stephen Kohl, U.S. Fish and Wildlife Service. The Area V project *Protection of Northern Ecosystems* resulted in several permafrost activities, including those related to pipelines. Annual joint meetings of the agreement participants alternated between the USSR and United States, and these provided the opportunity to meet counterparts, plan activities, and review progress.

From the 1970s and continuing into the 1990s, a number of bilateral visits of delegations and individuals took place between Siberia and Alaska. Among the initial activities was an Area V visit in August 1974 by a five-person U.S. delegation to Norilsk, Yakutsk, and Magadan. This momentous visit represented the first visit of non-Soviets, or at least Americans, to that part of the Far East since the airlift from Alaska in World War II (Jorgenson 1974). The visit set the stage for a series of permafrost-related projects, including one on environmental problems posed by the construction and operation of pipelines, roads, and other engineering projects. Other exchanges included a series on ecological and hydrological activities under the leadership of V. Kontrimavichus, Director, RAS Institute of Biological Problems of the North (IBPN), in Magadan. Numerous agreements and exchange visits with IBPN researchers took place over the subsequent years. Also in summer 1974, the 10th International World Congress of Soil Science took place in Moscow, and that event gave the author the opportunity to meet a number of polar soil scientists.

In the course of the many environmental exchanges, we learned of the Soviet’s increasing interests in environmental protection in regions undergoing economic development. The first All Union Conference on the topic, held in October 1975 in Moscow, provided additional interest for further collaboration.

Starting in the early 1970s, implementation of the Tundra Biome program of the International Biological Program (IBP) provided an opportunity for cooperation with Soviet researchers that included studies on seasonal variations of the active layer and its soil properties. The Tundra Biome program involved 10 countries and 23 sites. Following international

workshops in Norway (1968) and Finland (1970), the Soviets hosted the Tundra Biome working meeting with more than 100 participants in October 1971 in Leningrad. The workshop was under the leadership of B.A. Tikhomirov and N.V. Matveyeva from the Komarov Botanical Institute (Wielgolaski & Rosswall 1972). Four Tundra Biome sites were located on the Taimyr Peninsula that included the continuation of long-term observations of soil and active layer dynamics. The Tundra Biome program provided exceptional opportunities to visit sites, exchange data, and establish long-lasting scientific cooperation with many Soviet colleagues. Some of the cooperation carried over into the UNESCO Man and the Biosphere (MAB) program and its Northern Science Network (NSN), and later into the International Tundra Experiment.

Following the 1971 Tundra Biome workshop, the author had an opportunity to discuss in Moscow with Nikolai Grave and Sergei Vyalov the forthcoming Second ICOP planned for 1973 in Yakutsk. Over the decades, Grave and the author developed a close working relationship on problems of environmental protection of permafrost terrains (Brown & Grave 1979).

During the XXIII International Geographical Congress held in July 1976, a special symposium was organized in Leningrad and hosted by Academician A.F. Treshnikov, Director, Arctic and Antarctic Research Institute. A delegation from the United States participated in the Symposium on Geography of Polar Countries, which consisted of 83 papers, many of which dealt with permafrost-related and environmental problems (Brown 1977). Following the Leningrad Congress, a two-person delegation visited Magadan and the Kolyma Water Balance Station (Stokovaya) to develop cooperative hydrometeorological observations (Slaughter & Bilello 1977). Also in summer 1976, ecologists visited the Taimyr Peninsula to conduct plant and caribou investigations (Webber & Klein 1977). Subsequently, Webber and several soil entomologists also visited the IBPN Chaun Bay and Aborigin field stations in Chukotka (Hodkinson & MacLean 1980).

Based on a formal agreement between CRREL and the Permafrost Institute, a two-person team from CRREL spent two months in summer 1976 in the USSR investigating the design and performance of embankment dams on permafrost (Johnson & Sayles 1980). A visit to CRREL in June 1976 by P.I. Melnikov and F.E. Are preceded the visit. Other Environmental Agreement exchanges included a five-member Soviet pipeline delegation to Alaska in October 1978 and reciprocal visits to Siberia under the leadership of Oscar Ferrians (USGS) and Fred Crory (CRREL).

The Third ICOP, held in Edmonton in July 1978, was well attended by a large delegation of Soviets led by Academician Melnikov. It included 132 Russian papers and reports. Plans were put in motion for the development of an international permafrost organization, in part based on the earlier vision of Melnikov. Later in that year, Melnikov and Grave traveled to the United States and visited the USGS in Menlo Park, CA.

In 1979, the XIV Pacific Science Congress in Khabarovsk offered the opportunity for a number of Alaskans and other foreign scientists to establish additional working contacts with counterparts in the Far East. As part of the Congress, Andrei

Sher organized the first international field excursion to the main Kolyma River to view Yedomas exposures. His book on Pleistocene mammals and stratigraphy of the Far Northeast USSR and North America was published in the United States in 1974.

Canada, continuing its long history of joint scientific and technical cooperation with the Soviet Union and Russia in the North, concluded agreements in October 1971 and February 1987 that included arctic petroleum, gas hydrates, northern environments, construction, and related topics (for more information, see Canadian Arctic Resources Committee 1991). A 1973 visit by Nikolai Grave to Canada advanced interest in environmental protection. In 1978, a four-person delegation led by G. Hank Johnston visited the western end of the Baikal-Amur Mainline Railway to observe earthwork construction. J. Ross Mackay, University of British Columbia, visited Moscow State University as an invited lecturer and was inducted into the Geographical Society of the Soviet Union in 1980.

During the mid-1970s, considerable attention in North America was devoted to the potential exploration of the outer continental shelves. Based on his Soviet experience and knowledge of the extensive literature, Michael Vigdorichik, a Soviet expatriate residing in the United States, produced a series of reports and a book on submarine permafrost of the Eurasian and North American shelves (Vigdorichik 1980).

IPA, Conferences, and the Opening of the Soviet Arctic: 1980s

The early 1980s was devoted to preparation of the Fourth ICOP (FICOP), Soviet involvement in the conference, and the formal organization of the International Permafrost Association (IPA), which took place in Fairbanks in July 1983 during FICOP (Brown et al. 2008). Academician P.I. Melnikov was elected the first President of IPA, partly in recognition of his leadership both within the USSR and his working relationships with Western nations. During the 1980s, the IPA organized multi-national activities and initiated publications through its Working Groups related to climate change, data, terminology, foundations, mountain permafrost, and periglacial activities (Brown et al. 2008). During this formative organizational period of the 1980s, the IPA Executive Committee and its Presidents Melnikov and Péwé and Secretary General Mackay led the development of the IPA, and it became an Affiliated Member of the International Union of Geological Sciences. The Fifth ICOP was held in Trondheim, Norway, in 1988, again with active participation of Soviets. A workshop on data held during the conference ultimately led to development of the IPA Global Geocryological Database, which subsequently involved active Russian participation. In the following years, other Russians served as IPA Vice Presidents and members of the Executive Committee. These included V.P. Melnikov (1988), N.N. Romanovskii (1993), F.E. Are (1998), and G. Perlshtein (2003).

The Geneva Summit between President Reagan and Soviet leader Gorbachev (November 19, 1985) resulted in the signing

of a new Environmental Agreement and the subsequent formal initiation of permafrost projects. During the February 1–4, 1988, Joint Committee Meeting in Moscow, Project X of the Environmental Agreement (Arctic and Subarctic Ecology) was activated as a formal area of study. Jerry Brown and James Devine (USGS) were designated as co-chairs on the U.S. side, and Yuri Chernov and N.P. Morozov co-chairs on the Soviet side. Among other science memoranda was the NSF-USSR Academy of Science on Cooperation in the Field of Basic Scientific Research.

During 1987, a Chinese delegation led by Professor Zhou Youwu visited the Former Soviet Union, followed by subsequent return visits to China by Russian geocryologists. Madame Zhou and her colleague Tong Boliang had graduated in 1959 from Moscow State University under the supervision of Professor Kudryavtsev (Zhang 2001).

In October 1987 in Murmansk, Mikhail Gorbachev presented a speech that focused on expansion of international cooperation in the North and Arctic (Scrivener 1989). The conference on arctic research held in St. Petersburg in December 1988 was a follow-up to the 1987 Gorbachev doctrine. The conference identified future international research (Kotlyakov & Sokolov 1990).

In a letter dated June 15, 1988, Academician Melnikov announced that in connection with “Perestroika” (restructuring), the Soviet permafrost community was ready to conduct joint research, including research by contract. In April 1989, as part of the Environmental Agreement Project X, V.P. Melnikov attended a permafrost workshop at the U.S. Geological Survey in Menlo Park, California, organized by Bruce Molnia and chaired by Art Lachenbruch.

Following these statements and events, the International Symposium on Geocryological Studies in the Arctic Regions was held August 1–10, 1989, in Yamburg, northern West Siberia. The symposium was organized by the USSR Academy of Sciences under the auspices of its National Committee on Permafrost and the Scientific Council on Earth Cryology. V.P. Melnikov was the presiding officer. In addition to the approximately 65 Soviet participants at the Yamburg symposium, there were 25 invited foreign participants representing Canada (9), China (3), Denmark (1), Finland (1), Japan (1), Norway (1), and the United States (9). The symposium was unique in a number of ways. The two days of helicopter tours provided unprecedented access to the gas developments and site visits to the massive ice-rich terrain exposures of northern West Siberia. The informal recommendations made in Yamburg provided direction for future cooperation and included the need for networks of polar monitoring stations, an international mapping project, and environmental protection to minimize terrain disturbance. Many long-term friendships were renewed and/or established between Soviet and foreign colleagues. In our meetings with Evgeny Melnikov, we formed lasting friendships and established the base for development of the circumarctic permafrost map and cooperative monitoring programs.

Academician P.I. Melnikov was an active participant in both the First and Second IPCC Assessment and co-chaired the

Working Group II chapter on snow, ice, and permafrost (cryosphere) with R. Street of Canada. Several working meetings in Canada in 1989 included Oleg Anisimov and Maria Gavrilova. Anisimov’s initial involvement with the permafrost community was through a U.S. NSF grant with Frederick Nelson in 1988, which subsequently led to a series of hemispheric-scale maps of permafrost and active layer thickness (Anisimov & Nelson 1996). Anisimov continued his IPCC contributions as Coordinating Lead Author in the 2001 and 2007 assessments.

As the decade came to a close, scientific and commercial ties between Alaska and the Soviet Far East began to flourish, with resulting scheduled airline flights across the Bering Sea. This began with the Alaska-Siberia Friendship Flight in March 1989 to Anadyr. In September of that year, the “All-Union conference on engineering-geological investigations in the permafrost zone” was held in Magadan and was attended by Alaskan engineers Jim Rooney, Ray Krieg, and Duane Miller. Among participants in Magadan were Ninel F. Krivonogova, Head, Laboratory of Engineering Geology and Permafrost Studies (VNIIG); Valentin Kondratiev, Chita State Technical University; and Edward Ershov, Vladimir Romanovsky, and Vladislav Roujanski as the co-sponsors from Moscow State University. The following year, Rooney attended meetings in St. Petersburg in the All-Union Research Institute of Hydraulic Engineering (VNIIG).

The Golden Decade of Cooperation: 1990s

The International Permafrost Association played an important role in this new era of cooperation. Starting in 1989 and continuing to the present, many permafrost activities in Russia are reported and archived in the IPA News Bulletin *Frozen Ground* (<http://ipa.arcticportal.org/publications/frozen-ground>). These bulletins contain details of conference and national member reports, and bilateral and international programs.

As a result of “Perestroika” and the resulting policy of openness (Glasnost), the 1990s marked the beginning of intense international collaboration with Russia and the establishment of numerous joint programs. The early years of the decade witnessed a major change in our relationships with Russian science and geocryology. Due to the austerity conditions at their home institutions and increased openness, many Russians sought collaboration and financial opportunities outside Russia. In some cases, both senior and junior researchers emigrated to the West. The net result was an enhancement in the exchange of information and experience for many non-Russian institutions and nations. Other benefits included additional resources within Russia for collaborative international research, and access to remote regions of Russia. The Russian Fund for Basic Research, the George Soros International Science Foundation and, starting in 1993, the International Association for the promotion of cooperation with scientists from the independent states of the former Soviet Union (INTAS) provided much needed support. In many instances, these seed grants helped to increase collaboration with non-Russian researchers.

The Institute of Earth Cryosphere (IEC) of the Siberian Branch of the Russian Academy of Sciences was created in 1991 to develop basic studies of cryogenesis in the evolution of the geospheres and to develop the research basis for the use of natural resources in the North. Many international collaborations developed with IEC members located in its Moscow branch, its field stations, and later in Tyumen under the direction of Academician Vladimir P. Melnikov. The journal *Earth Cryosphere* started publication in 1997 with four issues per year. It provided ready access to results of new Russian investigations and offered the possibility for non-Russian papers.

The Fifth Canadian Permafrost Conference was held June 5–8, 1990, at Laval University in Quebec City, and among the 146 participants were 22 members from the USSR, representing the largest Soviet delegation to ever visit North America. During the conference, the IPA Council passed a resolution calling for the production of a circumpolar map depicting the current knowledge of permafrost distribution and boundaries in the Northern Hemisphere. Under the coordination of the IPA Editorial Committee and chaired by the author, Canada, Russia, and the United States took the lead in organizing the mapping effort. Numerous subsequent meetings took place, mostly in North America. Principals involved were Evgeny Melnikov, All-Union Research Institute of Hydrology and Engineering Geology (VSEGINGEO); Alan Heginbottom, Geological Survey of Canada (GSC); Oscar Ferrians, U.S. Geological Survey (USGS); and Jerry Brown, IPA. The USGS agreed to prepare the final edited map and published it as part of the Circum-Pacific Map Project (Brown et al. 1997). The Russian portion of the map was based on existing and updated maps by several government institutions and the newly published geocryological map of the USSR (Zaitsev et al. 1998). All relevant Russian institutions approved the final version of the newly compiled IPA map. Without this new Russian cooperation and openness, and the leadership of Evgeny Melnikov, this mapping effort would not have been possible. Melnikov and his colleague from VSEGINGEO, Stanislav Grechishchev, received several grants in 1993 from the U.S. Department of State MAB program for global change prognosis and geocryological mapping.

Other IPA international initiatives included the Russian contributions by Nikolai N. Romanovskii and V.V. Konishchev to the twelve-language glossary (van Everdingen 1998), and the initiation of Russian data compilation aided by Marina Leibman and Irina Streletskaya. The Circumpolar Active-Layer Permafrost System CD-Rom contained many Russian datasets for boreholes and soil temperatures (IPA 1998).

In a research note, Melnikov et al. (1993) described Russian programs to monitor the response of permafrost conditions and engineered structures to the observed late twentieth century warming. They discussed the use of Canadian and Japanese data recorders in Russian boreholes, and anticipated the development of “a unified circumpolar permafrost-monitoring network” with long-term sites in Alaska, Canada, and Russia. A summary of permafrost monitoring was later published by Oberman (2006).

During the 1990s three international, ground-based cooperative networks were initiated and remain active to present with multiple Russian sites, institutions, and individuals involved. The networks are Circumpolar Active Layer Monitoring (CALM), Arctic Coastal Dynamics (ACD), and Global Terrestrial Network-Permafrost (GTN-P) (Burgess et al. 2000). A fourth network, the International Tundra Experiment (ITEX) (Arft et al. 1999) with its origins in the late 1980s (pers. comm. P.W. Webber, January 2012), provided valuable interface with ecologists and resulted in the early establishment of CALM protocols for active layer and soil temperature observations (Brown et al. 2000).

The first reporting Russian CALM sites, starting in 1992, were from the Gydan Peninsula and Anadyr. The number of Russian CALM sites increased rapidly with support provided by the U.S. NSF to Kaye Everett at Ohio State University and subsequent grants to the University of Cincinnati (K.M. Hinkel), the State University of New York and the University of Delaware (F.E. Nelson), and George Washington University (N.I. Shiklomanov). Building on these early efforts, there were, by the end of the 1990s, 20 Russian sites, which increased to the current total of 33 reporting sites across the European North, Siberia, and the Far East. Russian collaborators participated in several international CALM workshops in Lewes, Delaware (2002), and Fairbanks (2008).

Several hundred Russian boreholes, including those located on the network of permafrost stations (Pavlov & Malkova 2005), were identified as potential GTN-P sites for the long-term monitoring of permafrost temperatures (www.gtnp.org). A related effort was initiated by David Gilichinsky to recover historical soil temperature data from the hundreds of meteorological stations located in the permafrost zones of Russia (NSIDC <http://nsidc.org/data/arcss078.html>).

Permafrost research along the Russian Arctic coast and its coastal stations was greatly enhanced by the Arctic Coastal Dynamics (ACD) project. Initial planning for the ACD took place in the late 1990s with a workshop in 1999 at Woods Hole in the United States. Fifteen Russians attended and represented key institutions and sites (Brown & Solomon 2000). The field and synthesis activities of ACD, building on existing sites, were formally conducted in the following decade. Meetings and annual workshops took place in Potsdam (2000, 2001), Oslo (2002), St. Petersburg (2003), Montreal (2004), and Groningen (2006). The ACD database includes information for a total of 70,000 km of Russian arctic coastline (Lantuit et al. 2011).

One of the first exchange visits to the United States under the newly activated Environmental Agreement Project X was a June 1990 five-person Soviet delegation from the Ministry of Oil and Gas Construction to Washington DC and Alaska. The visit also included Canada and was in reciprocity for several visits in 1989 to the Yamal Peninsula.

In August 1991, a major international permafrost meeting took place in Anadyr, Chukotka, with U.S. and Japanese researchers attending the “Conference on Ground Ice and Cryomorphogenesis.” It was organized by Edward Ershov, Nina Trush, and Vladislav Roujanski, Department of

Geocryology, Moscow State University, and the Far East Branch of the USSR Academy of Sciences. Field excursions led by Michael Tishin, Director of the Anadyr Permafrost Station, included visits to experimental field sites and coastal exposures of ice-rich permafrost. The conference took place during the August 1991 coup (see details in *Frozen Ground No. 10*).

The Anadyr conference was preceded by the USSR-US Shared Beringia Heritage meeting in Provideniya with extensive helicopter flights over northeast Chukotka. David Hopkins and Julie Brigham-Grette began a multi-year program in Chukotka to reconstruct the late Quaternary history of Beringia.

Following the Anadyr conference, the author met Evgeny Melnikov and Vladimir Solomatin in Magadan and we flew to Alaska for an extensive field trip with Kaye Everett along the Trans-Alaska pipeline and Prudhoe Bay. Also in 1991, Donald (Skip) Walker and Kaye Everett attended a conference in Syktyvkar on development of the North and problems of restoration. They visited Vorkuta, Nadyrn, and Bovanenkovo and associated oil and gas fields (BPRC 1994). Everett participated in the follow-up conference in Syktyvkar in April 1994.

In the early 1990s, Valentin Kondratiev and Edward Ershov invited the U.S. consultants involved in the earlier Magadan and Anadyr conferences to participate in a technical review of the Baikal-Amur-Mainline Rail System (BAM) and permafrost issues along the project route. Also, Rooney participated in May 1992 with his Russian counterparts in the review of major ground thawing and adverse drainage impacts that had since occurred along the BAM. Valentin Kondratiev and some of the BAM representatives were subsequently hosted in a review of Alaskan projects dealing with similar issues. During the early 1990s, Ershov, on behalf of MSU, established agreements with U.S. and Canadian universities, including Oregon State, Illinois, SUNY Buffalo, and Carleton.

In April 1990, the Canadians released a publication entitled *Building international relations in the Arctic: 25 years of Canada-USSR cooperation*. Permafrost cooperation was one of the earliest activities. The Canada-USSR Cooperative Arctic Geosciences Research Agreement began with a planning meeting in 1990 organized by the Geological Survey of Canada (GSC). This was followed in 1991 by field investigations on the Gydan and Yamal peninsulas. Focus was on the geocryological conditions of petroleum-bearing regions in both the USSR and Canada. The lead Soviet institution was VSEGINGEO, with Evgeny Melnikov and Pavel Kurfurst (GSC) the principal organizers. Scott Dallimore (GSC) and Evgeny Chuvilin (MSU) collaborated on gas hydrates. On June 19, 1992, in Ottawa, Canadian Prime Minister Mulroney and President of the Russian Federation Yeltsin signed an agreement on the Arctic and the North.

The First International Conference on Cryopedology (Cryosols: Effects of Cryogenesis on the Processes and Peculiarities of Soil Formation) was held in Pushchino in November 1992. It was immediately followed by the joint Russian-American seminar and attended by 18 U.S. participants. Chien Lu Ping from the University of Alaska

and David Gilichinsky of the Institute of Soil Science and Photosynthesis (ISSP) organized the seminar, which was funded by the U.S. NSF. It resulted in the planning of joint research projects that subsequently received support for both U.S. and Russian researchers. Main topics included gas exchange, soil climate, organic matter, mapping, microbial activity, geochemical cycling, and agricultural land use. Ping and Russian colleagues organized three expeditions to the Kolyma River region to investigate soils and the ice-rich Yedomas sediments. The third one was part of a National Geographic Society project led by Wendy Eisner. Prior to this, in 1990, Gilichinsky and Chris McKay, NASA Ames Research, undertook a drilling program in the Kolyma lowlands in support of astrobiology and planetary exploration.

The Russian Academy of Sciences campus at Pushchino provided an extraordinary venue for international exchanges, workshops, and roundtables, with Gilichinsky and the staffs of ISSP providing leadership and logistical planning. Between 1992 and 2010, a total of 12 annual conferences were convened in Pushchino. These also included the annual meetings of the Scientific Council on Earth Cryology under the chairmanship of Vladimir P. Melnikov. During this period, four additional annual conferences were held in Tyumen at the Tyumen State Oil and Gas University and in Salekhard; these venues provided opportunities to visit oil and gas developments in permafrost regions of West Siberia. Proceedings containing extended abstracts in English are available for all conferences.

During the period 1990–1994, Andrei Sher and David Gilichinsky organized the International Paleocological Expedition “Beringia” to the Kolyma lowland, which provided the opportunity for many scientists from Canada, Germany, the UK, and the United States to work in this area and compare permafrost conditions with those in North America. The Alaskan field program and international seminar for the same group was organized in 1991 by Dale Guthrie and Mary Edwards (Edwards et al. 1997).

Starting in 1997, International Conferences on Cryopedology organized under the auspices of the Cryosol Working Groups of the IPA and the International Union of Soil Science (IUSS), took place in Syktyvkar (August 1997), Arkhangelsk (August 2005), Ulan-Ude (August 2009), and a fourth in Copenhagen (August 2001). Sergei Goryachkin, RAS Institute of Geography, and Galina Mazhitova, RAS Institute of Biology, helped to facilitate these and other meetings of the Cryosol Working Group in Russia.

In November 1998, a major international conference under NATO’s Advanced Research Workshop program was convened in Novosibirsk under the leadership of V.P. Melnikov, Siberian Branch of the Russian Academy of Sciences, and Roland Paepe of Belgium. The workshop focused on permafrost responses to economic development and environmental security (Paepe & Melnikov 2001). Twenty-five senior Russians representing major engineering and environmental institutions and disciplines were among the 51 participants. Substantial discussions were held and recommendations made related to infrastructure, data exchange, and monitoring. An earlier NATO workshop on disturbance and recovery of

terrestrial ecosystems was held in Rovaniemi in 1995 and was well attended by Russians (Crawford 1997).

During the mid-1990s, there were several international efforts to develop research with Russian colleagues and institutions in the region of the continental shelves. The U.S. NSF sponsored three workshops in the United States and St. Petersburg to define research priorities on the Russian Arctic Land-Shelf Systems in a program that became known as RAISE (Russian-American Initiative on Shelf Environments in the Arctic) (Forman & Johnson 1998). A second program, developed at a Russian workshop in Moscow in September 1996 at the request of the International Arctic Science Committee, was the Land-Ocean Interactions in Russian Arctic-LOIRA (IASC 2000). Both programs proposed and supported permafrost-related projects and helped to promote additional collaboration with Russian scientists. For example, Forman and Russian colleagues investigated stratigraphy and ice sheet limits and retreat in the regions of the Yamal Peninsula and Franz Josef Land (Forman et al. 1999).

Following the dissolution of the Soviet Union, access to data and sites in Kazakhstan increased. In August 1996, members of the IPA Executive Committee visited the Institute of Geography in Almaty and the nearby alpine geocryological station. The station was formally part of the Permafrost Institute in Yakutsk. Although not an FSU Republic, cooperation with Mongolia developed in the mid-1990s with data becoming available from boreholes drilled by the Soviets. Both Kazakhstan and Mongolia became active in the CALM and thermal borehole networks.

On June 23, 1994, Vice President Gore and Prime Minister Chernomyrdin signed the agreement between the governments of the United States of America and the Russian Federation on Cooperation in the Field of Protection of the Environment and Natural Resources. It included the protection of the environment and natural resources within arctic and subarctic areas, and superseded the 1972 Agreement on Cooperation in the Field of Environmental Protection. Also, on December 16, 1994, in Moscow, a second agreement was signed on the prevention of pollution in the Arctic. Neither agreement specifically addressed permafrost activities, although a major, high-level conference on technologies of arctic oil and gas operations was held in Anchorage in August 1995.

Japanese-Russian collaboration started with exchange visits of Masami Fukuda and Rostislav M. Kamensky and others in 1990 and 1991 between the Permafrost Institute and the Institute of Low Temperature Science. Field studies began in Siberia in 1992. Many of these joint studies continue to the present and initially included those on permafrost response to climate, water and heat-energy studies, and greenhouse gases. Annual reports contain details (e.g., Fukuda 1993).

The Russian-German scientific cooperation is performed under the umbrella agreement of the German Federal Ministry of Education and Research (BMBF) and the Russian Ministry of Science and Education. Initial Joint Russian-German cooperation started in the early 1990s with cruises in the Laptev Sea, land expeditions on the Taimyr Peninsula, and studies of late Quaternary history. The Arctic and Antarctic Research

Institute was the main scientific point of contact along with the several German institutes from Potsdam, Bremenhaven, and Keil. Results of these annual expeditions to the Laptev Sea are reported in Kassen et al. (1999) and in the journal *Reports of Polar Research* of the Alfred Wegener Institute for Polar and Marine Research (AWI). Annual visits of Nikolai Romanovskii to Potsdam and by Feliks Are and Erk Reimnitz (USGS) to Keil with Heidi Kassens (GEOMAR) took place to discuss subsea permafrost and related coastal and shelf processes. Permafrost research in the terrestrial Arctic was mainly undertaken by the AWI in Potsdam with the main study areas in southeast Taimyr Peninsula (1993–1997), Central Yakutia (1997–1998), and the Lena Delta (Laptev Sea Project, 1997–2011). The latter involved 15 Russians and 15 Germans and included establishing sites at the Samoylov Island research station, and studies of Lena Delta sedimentation and ice complexes (Hubberten et al. 2003). Many of these activities were under the direction of Hans-W. Hubberten, AWI.

In summer 1994, Sweden conducted a multi-national ecological expedition along the Russian Arctic coast aboard the icebreaker *Oden*. Teams of researchers, including upwards of 60 Russians, visited many permafrost-dominated sites (Gronlund & Melander 1995).

Starting in 1991 and continuing to the present, Bruce Forbes, Arctic Centre, Rovaniemi, Finland, has collaborated with numerous Russian researchers on field investigations related to the effects of Siberian oil and gas development and climate change on northern ecosystems, including the impact on reindeer economies. His first year of study on the Yamal Peninsula was at the invitation of V.P. Melnikov. Recent research has been supported by the Academy of Finland through the joint ‘Russia in Flux’ program with the Russian Academy of Sciences and NASA in collaboration with D.A. Walker.

Norway, although not directly involved in permafrost exchanges, provided a common meeting ground for “East and West” workshops, conferences, and negotiations. Norway and the USSR had an agreement concerning technical and scientific cooperation in the Arctic and northern areas. Early efforts by Norway to launch a joint subsea geosciences program in the Kara Sea met with Russian concerns about access. Odd Rogne and the International Arctic Science Committee Secretariat in Oslo played an important role in developing plans and programs with Russia.

Throughout the 1990s, Russian institutions, ministries, and individuals were engaged in bilateral programs that provided access for national programs, and numerous individual permafrost-related field expeditions and projects were undertaken. One example is the Chersky station situated on the Kolyma River, where cooperation on long-term ecological and trace gas research began in 1992 between Sergei Zimov and Terry Chapin and their colleagues. That collaboration was initiated with Soros Foundation funding and continued with Civilian Research and Development Foundation (CRDF) and NSF grants, (Zimov et al. 1993). The Chersky station continues to support a wide range of international permafrost-related research and educational programs.

Other forms of collaboration included commercial ventures with North American geotechnical firms offering technical assistance. For example, the EBA of Canada provided multi-decadal services for oil, gas field, and pipeline developments in West Siberia, and mining activities in the Far East.

Arranging field logistics with the capable assistance of Russian institutes and colleagues had its challenges, but few experienced serious difficulties once in the field. One exception was the unfortunate incident in spring 1997, when University of Alaska researchers Larry Hinzman and Vladimir Romanovsky had their GPS equipment, computer, and field books confiscated by security officials. They had been working at the joint Russian-Japanese site at Tiksi. Some details were reported in *Science* (Mervis 1997).

The New Century: 2000s

Many of the joint activities of the 1990s continued throughout the first decade of the twenty-first century. The Eighth and Ninth International Conferences on Permafrost, held respectively in Zurich and Fairbanks, were attended by large numbers of both young and senior Russian researchers. Much of the decade was devoted to planning and implementing cooperative efforts within the framework of the International Polar Year (Brown 2010). A major emphasis was on the measurements of the thermal state of permafrost (TSP) (Romanovsky et al. 2010) and active layer thickness (CALM) (Brown & Christiansen 2011). Measurements of some 150 Russian boreholes, temperature sites, and 33 active layer sites under CALM were available by the end of the decade. Many of these sites benefited from support of U.S. NSF grants under the program Arctic Observing Network to V.E. Romanovsky at the University of Alaska, F.E. Nelson of the University of Delaware, and Nikolai Shiklomanov of George Washington University.

New international permafrost initiatives in astrobiology, microbiology, and life at extreme low temperature developed in part under the leadership of David Gilichinsky and in cooperation with U.S. researchers Imre E. Friedmann, James M. Tiedje, and Christopher P. McKay. On the basis of this collaboration, permafrost drilling for microbial and astrobiology studies moved to Antarctica (Gilichinsky et al. 2007). With NASA funding, the US-Russian Astrobiology Expedition to volcanic permafrost on the Kamchatka peninsula was organized by Andrei Abramov in 2006. During the IPY (2007–2009), the Russian Antarctic Expedition implemented in the vicinity of its ice-free coastal stations a network of boreholes equipped with dataloggers for year-round temperature monitoring (Viera et al. 2010).

Although initially visited in 1998, more intensive investigations started in 2000 on the Lake Elgytgyn crater in north-east Chukotka. The program was undertaken by a team of Russian, German (AWI), and U.S. researchers to reconstruct the region's paleoclimate and permafrost environments. The lake sediments are thought to contain a high-resolution, 3.6-million-year paleoclimate record. During 2008–2009, following a multi-year program of geophysical and climate investigations, a 141-m sediment core, which penetrated into the permafrost

zone beneath the lake talik, was obtained. Permafrost temperatures are being measured in the lake borehole and in a shallow borehole on the adjacent uplands by AWI.

Other German-Russian collaboration continued throughout the decade with annual, multi-institutional expeditions, including the 2002 trips to the Lena Delta, New Siberian Islands, and Verkhoyansk Mountains. A joint study of onshore and offshore permafrost dynamics was started in 2003 in the Cape Mamontov Klyk, Western Laptev Sea, and followed in 2005 with a subsea drilling program logistically organized by Mikhail Grigoriev of the Permafrost Institute (Rachold et al. 2007). In all, there have been 14 expeditions to the Lena River Delta by the AWI Potsdam group. A highlight of this cooperation was a visit by Prime Minister Vladimir Putin to the Samoylov Station on August 23, 2010. A recent publication by Schirrmeister et al. (2011) on fossil organic matter in Northeast Siberia is just one illustration of the benefits of long-term collaboration between the two countries. As part of the implementation of ACD, Georgy Cherkashov, Institute for Geology and Mineral Resources of the Ocean, St. Petersburg (VNIIOkeangeologia), organized several international shipborne field programs on the Siberian shelf. E-M. Pfeiffer at Hamburg University, in addition to her collaborative research on soil microbiology in Siberia, developed joint field courses for German and Russian university students.

International collaboration in Russia became even more urgent with the increasing concerns over the fate and potential release of carbon from the cold soils and the underlying permafrost (Grosse et al. 2011). The IPA-IUSS Working Group on Cryosols led the project Carbon Pools and Permafrost (CAPP), co-chaired by Russian colleagues. There were renewed interests in methane emissions from degrading permafrost and the Russian ice complexes (Zimov et al. 2006).

The Circumpolar Arctic Vegetation Map (Walker et al. 2005), involving 14 Russian collaborators, was completed following a workshop in Moscow in 2001. A new collaboration between Russian and U.S. researchers involved the project "Greening of the Arctic" led by D.A. Walker. Over a five-year period, field sites were visited and instrumented for active layer measurements along a transect from Nadym northward including the northern coast of Yamal, Franz Josef Land, and the Polar Urals. This project was preceded by an expedition in 2002 to the Kolyma River region.

On October 30, 2002, NASA and the RAS formally agreed to jointly develop a plan for the Northern Eurasia Earth Science Partnership Initiative (NEESPI) and to invite the international scientific community to jointly develop a plan of research beneficial to the community. NEESPI was designed to establish an international large-scale, interdisciplinary program aimed at developing a better understanding of the interactions between the terrestrial ecosystem, the atmosphere, and human dynamics in Northern Eurasia. Modeling of permafrost distribution and landscape response to climate were important components of the program.

In 2002, the U.S. NSF PARTNERS Project (Pan-Arctic River Transport of Nutrients, Organic Matter, and Suspended Sediments) was formally initiated as a coordinated,

international effort to collect and analyze a time series of biogeochemical samples from the six largest arctic rivers—the Ob', Yenisey, Lena, Kolyma Siberia, Yukon, and Mackenzie. In 2008, the PARTNERS Project was revised as the Arctic Great Rivers Observatory (Arctic-GRO, a component of NSF's Arctic Observing Network [AON]).

Japanese-Russian research was undertaken on the thermal impact of fire in the boreal forest of Eastern Siberia along the Lena River, joint research in the Russian Altai, and on rock glaciers in Central Kamchatka. In 2009, JAMSTEC and the Permafrost Institute started to upgrade the soil and temperature-monitoring program around Yakutsk.

The Swedish Polar Research Secretariat organized a research expedition to the Beringia region in the summer of 2005 using once again the icebreaker *Oden* as its platform. Swedish, Russian, and U.S. organizations participated. Peter Kuhry at the University of Stockholm continued his Finnish-initiated, GIS-based project in the Usa Basin in Northeast Russia to evaluate regional soil carbon distribution. In 2007, the EU-funded CARBO-North project undertook studies of soil organic matter.

French researchers, in collaboration with colleagues from Moscow State University and the Melnikov Permafrost Institute, continued their modeling and long-term studies of erosional processes along the Lena River.

Since 2003, the Dutch have maintained a station at Chocurdagh (Kytalyk) in Yakutia to measure trace gas fluxes and energy balance, and more recently plant ecological experiments and active layer measurements. It was the result of cooperation between Vrije Universiteit in Amsterdam and the RAS Institute for Biological Problems of the Cryolithozone in Yakutsk. The station was started as part of the EU Terrestrial Carbon Observation System project and, more recently, was supported by Dutch research grants. The research station is part of the new PAGE21 project.

A significant basis for cooperation and communication within Russia and between Russian and Western researchers and students was facilitated with the organization of the Permafrost Young Researchers Network (PYRN). PYRN was formed to foster innovative collaboration and to recruit, retain, and promote future generations of permafrost researchers (<http://pyn.org/>). It currently has more than 1000 members, of whom approximately 170 are from Russia. PYRN, as an international organization, was established under the patronage of the IPA and was acknowledged by IPY as an official activity. Activities in Russia have included field courses, workshops, and drilling of boreholes for temperature measurements. A series of Russian-based PYRN meetings started in Salekhard in 2007 and was highlighted there by a poster competition. Fifty young researchers from 13 countries met in December 2007 in the Otto Schmidt Laboratory for Polar and Marine Sciences at the Arctic and Antarctic Research Institute, St. Petersburg. The latest methods used in permafrost research and engineering, and future plans to address climate change issues in permafrost areas, were discussed. Another workshop was held in Pushchino in October 2009. The Forum for Young Permafrost Scientists—The Past, Present and Future of Geocryology was

held in Yakutsk as part of the 50th anniversary of the institute. These meetings brought together young Russian scientists and provided opportunities for non-Russians to meet their counterparts under their host's working environments. Such interactions will provide new opportunities for collaboration and professional careers.

The U.S. NSF *Polaris* Project is a joint initiative that offers research opportunities for college students from the United States and Russia to work with scientists and conduct their own field research on changes in permafrost. The Chersky Northeast Science Station is the home base for the *Polaris* Project. Other continuing research activities here involve measurements of land-atmosphere exchanges using towers installed in 2001 as part of a RAISE project.

The International Polar Year (IPY) conference in June 2010 in Oslo offered the opportunity for Russians and PYRN members to present oral reports and posters in the special IPA sessions on permafrost on a warming planet. Similar opportunities were planned for the Montreal IPY conference in April 2012 and for TICOP.

The Geographical Society of Russia hosted the First International Arctic Forum, entitled "The Arctic: Territory of Dialogue," on September 22–23, 2010, in Moscow. In his closing remarks, Russian Prime Minister Vladimir Putin, who heads the Society's Board of Trustees, reminded the audience of his visit to the Lena Delta and the joint German-Russian research. The Second Forum took place in Arkhangelsk in September 2011 and focused on arctic navigation and environment.

At the close of the decade, on December 9, 2010, RAS Academician Vladimir Fortov co-chaired in Moscow a working group meeting of the U.S.-Russia Presidential Commission on Clean Energy Technology. Included in this program is an area of cooperation "Arctic permafrost" led on the Russian side by Academician V.P. Melnikov.

In 2011, the 7th Framework Program of the European Union initiated a new four-year project "Changing Permafrost in the Arctic and its Global Effects in the 21st Century." PAGE21 includes Russian collaborators from the Institute for Biological Problems of Cryolithozone and Moscow State University and six field sites in Russia. The project is under the direction of the Potsdam Research Unit of the Alfred Wegener Institute for Polar and Marine Research.

The booklet commemorating the 50th anniversary in 2010 of the Melnikov Permafrost Anniversary contains a summary of its past and on-going international activities including conferences (Shepelev 2010). At the present time, and under the directorship of Rudolf Zhang, the Institute, with a staff numbering 277, has cooperative agreements with 11 institutes and universities from China, France, Germany, Japan, Mongolia, and the United States. Included in this cooperation is the co-convening with China of nine meetings of the "International Symposium on Permafrost Engineering." For those of us who started our visits to the Soviet Union in 1969 in Yakutsk, we are pleased to know that the Melnikov Permafrost Institute is performing under its pioneering and well-established heritage.



1963: logo for First International Conference on Permafrost (ICOP)



1966: Canadian visit to Siberia, from left, G.F. Biyanov, S.E. Grechishev, G.H. Johnston, R.J.E. Brown



1969 and 1973: symbol for Yakutsk Permafrost Institute



1969: P.I. Melnikov opens IGU conference



1969: Lena-Aldan rivers excursions



1974: Magadan gold mining



1983: N.A. Grave and P.I. Melnikov at Fourth ICOP, Fairbanks



1989: P.I. Melnikov and V.P. Melnikov welcoming for Yamburg conference



1989: Yamal Peninsula ground ice exposures



1991: Norilsk nickel and copper mine visit



David Gilichinsky, 1948-2012



1992: First Pushchino conference



1998: Novosibirsk NATO conference



2006: Tyumen conference



2007: Salekhard conference



2010: Putin visit to Samoylov Station, Lena River Delta



Russian members of IPA Executive Committee, from left: P.I. Melnikov, 1983–1988; V.P. Melnikov, 1988–1993; N.N. Romanovskii, 1993–1998; Feliks Are, 1998–2003; Georgy Perlshtein, 2003–2008; Dmitry Drodzov, 2008–2012

Epilogue

Over the past fifty years, cooperation and communications between the FSU/Russia and Western countries have evolved from formal conferences and bilateral agreements to extensive collaboration between individuals and teams of researchers. In recent decades, the mobility for Russian scientists to collaborate with individuals, universities, and organizations outside of Russia has facilitated our mutual understanding of each other's approaches in geocryology. Increased access to the vast reaches of the permafrost-dominated Russian territories allows for improved understanding on a circumpolar basis of permafrost properties, formation, and dynamics. In turn, this understanding provides new insights into the response of permafrost regions to past, present, and future climate changes. Russian researchers have contributed and continue to contribute to international permafrost monitoring networks, to international mapping and modeling efforts, and to the operation of stations and sites required for climate change research. The new generation of international researchers is benefiting from renewed access to more traditional Russian approaches including the benefits of long-term observations and site investigations. These collective results will advance our communities' knowledge of terrestrial and planetary permafrost and processes.

Finally, as we continue into a future of sustained cooperation with Russian colleagues, let us remember some of those in the FSU and Russia who provided the foundations for this cumulative knowledge and cooperation, many of whom the author had the privilege to know:

Pre-1990 (year deceased)

Boris N. Dostovalov (1977) Igor A. Nekrasov (1989)
Vladimir A. Kudryavtsev (1982) Petr A. Shumskiy (1988)

1990s

Leonid Chistotinov (1997) Aleksandr I. Popov (1993)
Igor D. Danilov (1999) Lev Semenov (1994)
E.M. Katasonov (1998) P.F. Shvetsov (1992)
Oleg V. Makeev (1999) Sergei S. Vyalov (1998)
Pavel I. Melnikov (1994)

21st century

Alexei Arkhangelov (2002) Rostislav M. Kamensky (2007)
Nina Anisimova (2011) Anatoly N. Kotov (2006)
Veniamin Balobaev (2011) Galina G. Mazhitova (2009)
Grigoriy I. Dubikov (2001) Evgeny S. Melnikov (2006)
Adrian I. Efimov (2000) Irina Protas'eva (2000)
Edward D. Ershov (2009) Andrey Sadovsky (2006)
Petr P. Gavriliev (2009) Andrei V. Sher (2010)
David A. Gilichinsky (2012) Il'ya A. Sokolov (2006)
Nikolai A. Grave (2002) Petr Soloviev (2002)
Stanislav E. Grechishev (2010) Vera D. Vasilievskaya (2010)
Nikolai F. Grigoriev (2005) Kirill Voytkovskiy (2006)
Anatoly D. Frolov (2006) Igor A. Zotikov (2010)
Igor V. Ignatenko (2003)

Acknowledgments

Over the span of 50 years, many U.S. organizations and individuals have supported the author's activities. Foremost for their direct financial and/or operational support are the U.S. Army Cold Regions Research and Engineering Laboratory, the U.S. Geological Survey, and the U.S. National Science Foundation, the latter for grants to many investigators and institutions. The Environmental Protection Agency and the U.S. Fish and Wildlife Service provided administrative support for many projects under the Environmental Agreement with the continuing support of Gary Waxmonsky and Stephen Kohl, respectively. During the 1990s, many of the author's IPA activities and related conferences, meetings, and workshops were supported by an NSF grant to the American Geophysical Union. Also during the 1990s, Melissa Stone and the staff of Kompas Resources International (KRI) facilitated communication and numerous visits of Russian colleagues. The Civilian Research and Development Foundation (CRDF), Gerson Sher (formerly CRDF), and Marianna Voevodskaya (Moscow office) facilitated projects and activities in Russia. The U.S. National Academy of Sciences and its Polar Research Board promoted exchanges and provided administrative support for several international permafrost conferences that involved many Russian colleagues. I appreciate the assistance and constructive comments of Feliks Are, David Gilichinsky, Guido Grosse, Ken Hinkel, Hans-W. Hubberten, Frederick Nelson, Vladimir Romanovsky, James Rooney, Yuri Shur, Dmitry Streletskiy, and Patrick Webber during the preparation of this paper. Omissions and inaccurate historical recollections are solely the responsibility of the author.

References

- Anisimov, O.A. & Nelson, F.E. 1996. Permafrost distribution in the Northern Hemisphere under scenarios of climatic change. *Global and Planetary Change* 14: 59-72, doi:10.1016/0921-8181(96)00002-1.
- Arft A.M. et al. 1999. Responses of tundra plants to experimental warming: meta-analysis of the international tundra experiment. *Ecological Monographs* 69: 491-511.
- Armstrong, T. 1965. *Russian Settlement in the North*. Cambridge University Press, 223 pp.
- Barr, W. 2009. *Arctic scientist. Gulag survivor. The biography of Mikhail Mikhailovich Ermolaev 1905-1991*. Arctic Institute of North America and University of Calgary Press, 591 pp.
- BPRC 1994. *Extended abstracts for an international conference on "The Development of the North and Problems of Recultivation", July 8-14, 1991, Syktyvkar, Russia*. Byrd Polar Research Center Miscellaneous Series M-334, The Ohio State University, Columbus, Ohio, 151 pp.
- Brown, J. (ed.). 1977. Selected papers and summaries, Symposium: Geography of Polar Countries, XXIII International Geographical Congress, Leningrad, USSR, 22-26 July 1976. *US Army CRREL Special Report 77-6*, 61 pp.

- Brown, J. 2010. Report from the International Permafrost Association: The IPY Permafrost Legacy. *Permafrost and Periglacial Processes* 21: 215-218.
- Brown, J. & Grave, N. 1979. Physical and thermal disturbance and protection of permafrost. In *Proceedings, Third International Permafrost Conference, Edmonton, Alberta, Canada 10-13 July 1978*, 2: 51-92 (also published in Russian, 1981, and *CRREL Special Report* 79-5).
- Brown, J. & Christiansen, H.H. 2011. Permafrost observatory project: A contribution to the Thermal State of Permafrost (TSP, IPY no. 50). In *Understanding Earth's Polar Challenges: International Polar Year 2007-2008, Summary by the Joint Committee* (I. Krupnik et al., eds.), WMO-ICSU, pp. 259-261, plus references, pp. 266-271.
- Brown, J., Ferrians, O.J., Jr., Heginbottom, J.A., & Melnikov, E.S. 1997. Circum-Arctic map of permafrost and ground-ice conditions, *U.S. Geological Survey Circum-Pacific Map CP-45*, 1:10,000,000, Reston, Virginia.
- Brown, J., Hinkel, K.M. & Nelson, F.E. 2000. The Circumpolar Active Layer Monitoring (CALM) Program: Research Designs and Initial Results. *Polar Geography* 24 (3) 165-258 (published in 2002).
- Brown, J. & Solomon, S. 2000. Arctic Coastal Dynamics: Report of an International Workshop, Woods Hole, MA, November 2-4, 1999, *Geological Survey of Canada Open File* 3929, 28 pp. plus appendices.
- Brown, J., French, H., & Guodong, Cheng. 2008. The International Permafrost Association: 1983-2008. In *NICOP 2008: Proceedings of the Ninth International Conference on Permafrost*. June 29-July 3, 2008, Fairbanks, Alaska. D.L. Kane, K.M. Hinkel (eds.). Institute of Northern Engineering, University of Alaska Fairbanks, 1: 199-204.
- Burgess, M.M., Smith, S.L., Brown, J., Romanovsky, V., & Hinkel, K. 2000. Global Terrestrial Network For Permafrost (GTNet-P): permafrost monitoring contributing to global climate observations, Geological Survey of Canada, Current Research 2000 E-14, 8 pp.
- Canadian Arctic Resources Committee. 1991. *The Arctic environment and Canada's international relations*. Ottawa, 83 pp, plus appendix.
- Crawford, R.M.M. (ed.). 1997. *Disturbance and recovery of Arctic terrestrial ecosystems*. Proceedings, September 24-30, 1995, Rovaniemi, NATO ASI Series, 2. Environment, Vol. 26, Kluwer Academic Press, 623 pp.
- Edwards, M.E., Sher, A.V., & Guthrie, R.D. (eds.). 1997. *Terrestrial paleoenvironmental studies in Beringia*. Alaska Quaternary Center, Fairbanks.
- Forman, S.L. & Johnson, G.L. 1998. *Prospectus for the Russian-American Initiative in the Arctic (RAISE)*. Arctic Research Consortium of the United States, Fairbanks, Alaska, 59 pp.
- Forman, S.L., Ingolfsson, O., Manley, W.F., & Lokrantz, H. 1999. Late Quaternary stratigraphy of Marresale, Yamal Peninsula, Russia: New constraints on the configuration of the Eurasian ice sheet. *Geology* 27: 807- 810.
- French, H.M. & Nelson, F.E. 2008. In *Frozen in time: Permafrost and engineering problems*. Edited by S.W. Muller. Reston, VA: American Society of Civil Engineers, 280 pp.
- Fukuda, M. (ed.). 1993. *Proceedings of First Symposium on Joint Siberian Permafrost Studies between Japan and Russia in 1992*. Institute of Low Temperature Science. Hokkaido University, Sapporo, 112 pp.
- Gilichinsky, D.A. et al. 2007. Microbial populations in Antarctic permafrost: Biodiversity, state, age, and implication for astrobiology. *Astrobiology* 7(2): 275-311. doi:10.1089/ast.2006.0012.
- Gronlund, E. & Melander, O. (eds.). 1995. *Swedish-Russian Tundra Ecology-Expedition-94, Tundra Ecology-94, A Cruise Report*. Swedish Polar Research Secretariat, Stockholm, 462 pp.
- Grosse, G., Romanovsky, V., Jorgenson, T., Walter Anthony, K., Brown, J., & Overduin, P.P. 2011. Vulnerability and feedbacks of permafrost to climate change. *Eos*, Vol. 92, No. 9, pp.73-74.
- Hodkinson, I.D. & MacLean, S.F. Jr. 1980. The Psyllids (Homoptera: Psylloidea) of Chukotka, Northeast USSR. *Arctic and Alpine Research* 12: 377-380.
- Hubberten, H-W., Wagner, D., Pfeiffer, E-M., Boike, J., & Gukov, A.Y. 2003. *Polarforschung* 73 (2/3): 111-116.
- International Arctic Science Committee 2000. *LOIRA: Land-ocean Interactions in Russian Arctic: Implementation Plan*. Moscow/Oslo, 43 pp.
- International Permafrost Association, Data and Information Working Group, comp. 1998. *Circumpolar Active-Layer Permafrost System (CAPS), version 1.0*. CD-ROM available from National Snow and Ice Data Center, nsidc@kryos.colorado.edu. Boulder, Colorado: NSIDC, University of Colorado at Boulder.
- Johnson, T.C. & Sayles, F.H. 1980. Embankment dams on permafrost in the USSR. *US Army Cold Regions Research and Engineering Laboratory CRREL Special Report* 80-41, 59 pp.
- Jorgenson, H.T. 1974. "Siberia and Alaska 1974" *A report on technical exchanges of the Environmental Workgroups of USA and USSR for cooperative protection of northern Ecosystems; Area V-Nature and Preserves; Project 2-Protection of Northern Ecosystems*. Bureau of Land Management, Washington DC, 89 pp.
- Kassens, H. et al. (eds.). 1999. *Land-Ocean System in the Siberian Arctic: Dynamics and History*. Springer-Verlag Berlin Heidelberg, 711 pp.
- Kotlyakov, V. (ed.). 1997. *World atlas of snow and ice resources*. Moscow, Nauka (in Russian), map 588.
- Kotlyakov, V.M. & Sokolov, V.E. (eds.). 1990. *Arctic research: advances and prospects; Proceedings of the conference on Arctic and Nordic countries on coordination of research in the Arctic, December 12-15, 1988, Leningrad*, Part 1, 366 pp., Part 2, 447 pp.
- Lantuit, H. et al. 2011. The Arctic Coastal Dynamics Database: A new classification scheme and statistics on arctic permafrost coastlines. *Estuaries and Coasts*. DOI 10.1007/s12237-010-9362-6.

- Melnikov, P.I., Kamenskii, R.M., & Pavlov, A.V. 1993. From the Researcher's Notebook: Permafrost-zone monitoring. *Herald of the Russian Academy of Sciences* 63: 1090-1095.
- Mervis, J. 1997. Cold wind blow through arctic climate project. *Science* 276: 1965.
- Muller, S.W. 1947. *Permafrost or permanently frozen ground and related engineering problems*. J.W. Edwards, Inc., Michigan, 231 pp.
- NSIDC. *Russian Historical Soil Temperature Data*. National Snow and Ice Data Center, Boulder, Colorado, <http://nsidc.org/data/arcss078.html>
- Oberman, N.G. 2006. Permafrost Monitoring. In *Geology and Ecosystems*. Edited by I.S Zektser et al. Springer. Chapter 28, pp 341-354.
- Overduin, P.P., Grigoriev, M.N., Junker, R., Rachold, V., Kunitsky, V.V., Bolshiyarov, D.Y., & Schirmeister, L. 2007. Subsea permafrost studies in the near-shore zone of the Laptev Sea. The expedition COAST I. *Reports on Polar and Marine Research* 550: 1-40.
- Pavlov, A.V. & Malkova, G.V. 2005. *Contemporary Changes of Climate in Northern Russia: Album of Small-scale Maps*. Academic Publishing House Geo, Novosibirsk, 54 pp.
- Paepe, R. & Melnikov, V. (eds.). 2001. *Permafrost response on economic development, environmental security and natural resources*. November 12-16, 1998. Novosibirsk. NATO Science Series, 2. Vol. 76, Environmental Security, Kluwer Academic Publishers, 636 pp.
- Rachold, V. et al. 2007. Nearshore Arctic Subsea Permafrost in Transition. *Eos Trans. AGU*, 88(13), doi:10.1029/2007EO130001.
- Robinson, N.A. 1988. *The US-USSR Agreement to Protect the Environment: 15 Years of Cooperation*. Pace Law Faculty Publications. Paper 384.
- Romanovsky, V.E. et al. 2010. Thermal state of permafrost in Russia. *Permafrost and Periglacial Processes* 21: 136-155.
- Scriabine, R.A. 1978. US-Soviet program on the protection of northern ecosystems: A Commentary. *Arctic and Alpine Research* 10: 553-557.
- Schirmeister, L., Grosse, G., Wetterich, S., Overduin, P.P., Strauss, J., Schuur, E.A.G., & Hubberten, H-W. 2011. Fossil organic matter characteristics in permafrost deposits of the northeast Siberian Arctic, *Journal of Geophysical Research* 116, G00M02, doi:10.1029/2011JG001647.
- Schriener, D. 1989. *Gorbachev's Murmansk speech: The Soviet initiative and Western response*. The Norwegian Atlantic Committee, Oslo, 75 pp.
- Shepelev, V.V. (ed.). 2010. *Melnikov Permafrost Institute*. Yakutsk, Permafrost Institute Press, 55 pp.
- Sher, A.V. 1974. Pleistocene mammals and stratigraphy of the Far Northeast USSR and North America, *International Geology Review* 16 (7-10), American Geological Institute, Falls Church, pp. 1-284.
- Shiklomanov, N.I. 2005. From exploration to systematic investigation: Development of geocryology in 19th-and early-20th-century Russia. *Physical Geography* 26: 249-263.
- Slaughter, C.W. & Bilello, M.A. 1977. *Kolyma water balance station, Magadan Oblast, Northeast USSR, United States-Soviet scientific exchange visit*, CRREL Special Report 77-15, 66 pp.
- Soviet Union Today 1964. Commentary: A Soviet Scientist on the Canadian North. *Arctic* 17: 67-68.
- Schweitzer, G. 2009. Reset cooperation with Russia. *Science* 324, 12 June 2009 (10.1126/science1175097).
- van Everdingen, R.O. 1998. *Multi-language glossary of permafrost and related ground-ice terms*. Arctic Institute of North America, Calgary.
- Vigdorichik, M. 1980. *Arctic Pleistocene history and the development of submarine permafrost*. Westview Press, Boulder, Colorado, 286 pp.
- Walker, D.A. et al. 2005. The Circumpolar Arctic vegetation map. *Journal of Vegetation Science* 16, 267-282.
- Webber, P.J. & Klein, D.R. 1977. Geobotanical and ecological observations at two locations in the West Central Siberian Arctic. *Arctic and Alpine Research* 9: 305-315.
- Wielgolaski, F.E. & Rosswall, Th. (eds.). 1972. *Tundra Biome, Proceedings, IV International Meeting of the Biological Productivity of Tundra*, Leningrad, USSR, October 1971, 320 pp.
- Woods, K.B. & Leonard, G.A. 1964. Permafrost. *Science* 143: 1060-1061.
- Vieira, G.J. et al. 2010. Thermal state of permafrost and active-layer monitoring in the Antarctic: Advances during the International Polar Year 2007-2009. *Permafrost and Periglacial Processes* 21(2):182-197.
- Zaitsev, V.N., Ershov, E.D., & Kondratieva, K.A. 1998. Geocryological map of the USSR at a scale of 1:2,500,000. In *Permafrost, Seventh International Conference, Proceedings*. Centres d'études nordique, Université Laval, Quebec, Collection Nordica no. 57, 1201-1205.
- Zhang, T. 2001. Geocryology in China. Zhou Youwu, Guo Dongxin, Qiu Guoqing, Cheng Guodong, & Le Shude 2001. Book Reviews. *Permafrost and Periglacial Processes* 12:315-322.
- Zimov, S. et al. 1993. Wintertime CO₂ emission from soils of northeastern Siberia. *Arctic* 46: 197-204.
- Zimov, S. et al. 2006. Permafrost carbon: Stock and decomposability of a globally significant carbon pool, *Geophysical Research Letters* 33, L20502, doi:10.1029/2006GL027484.

Airborne Electromagnetic Mapping of the 3-D Distribution of Permafrost in the Yukon Basin, Alaska

Jared D. Abraham, Burke J. Minsley, Bruce D. Smith, Lyndsay B. Ball, Lesleigh Anderson, Michelle A. Walvoord
United States Geological Survey, Denver, Colorado, USA

James C. Cannia
United States Geological Survey, Mitchell, Nebraska, USA

Clifford I. Voss
United States Geological Survey, Menlo Park, California, USA

Bruce K. Wylie
United States Geological Survey, Sioux Falls, South Dakota, USA

Abstract

The distribution of permafrost in the earth's subsurface has profound impacts on arctic ecosystems, climate feedbacks, and hydrologic processes, and it is pertinent to the stewardship of arctic environments. Despite this, knowledge about the arrangement of permafrost at depth is lacking due to the difficulty of densely probing the subsurface over large spatial areas. Airborne electromagnetic surveys provide information on the subsurface distribution of electrical resistivity. Numerical inversion of the data produces a resistivity depth 3-D image, which can provide insight to permafrost distribution. Here we present the results of a large airborne electromagnetic survey near Fort Yukon, Alaska. The survey provides unprecedented 3-D images of subsurface electrical properties that reveal changes in lithology and the presence or absence of permafrost. Permafrost distributions derived in this study will be used to inform models generated to evaluate potential consequences of permafrost thaw, and they will serve as a critical baseline for future permafrost investigations.

Keywords: Alaska; geophysics; permafrost; survey; talik; Yukon.

Introduction

Permafrost—defined as ground that remains at or below 0°C for at least two consecutive years—is present throughout much of the Arctic and in alpine environments, and it underlies approximately 24% of the land area in North America. The distribution of permafrost in the earth's subsurface is highly relevant to hydrogeologic processes, climate feedbacks, and arctic ecology. Mapping permafrost at depth is critical to the understanding of these natural phenomena and provides guidance for management decisions regarding resources and infrastructure. Despite the significance of permafrost regions, detailed information about the spatial distribution of permafrost in the subsurface is lacking. Here we present the results of an airborne electromagnetic (AEM) survey that provides three-dimensional views of discontinuous permafrost near Fort Yukon, Alaska.

Physiographic Setting of the Yukon Flats Study Area

The Yukon River Basin, with an area of more than 856,000 km², is the fourth largest watershed in North America. It covers a large region of central Alaska as well as portions of the Yukon Territory and British Columbia in Canada. The AEM geophysical survey was conducted near Fort Yukon, Alaska, USA, and the confluence of the Yukon, Porcupine, Black, Chandalar, and Sheenjek rivers, approximately 225 km northeast of Fairbanks (Fig. 1). This region of the basin is known as the Yukon Flats, an area of low topographic relief

with numerous streams and lakes where the Yukon River is characterized by braided and meandering channels. Permafrost in the Yukon Flats is discontinuous; it is thought to be present in most areas but may be absent beneath persistent lakes and rivers (Ferrians 1965).

Methods

Previous investigators have determined that resistivity in earth materials and ice decreases with temperature (Olhoeft 1978, Petrenko 1994, Scott & Kay 1988). These variations in resistivity can then be mapped using electromagnetic (EM) techniques (Hoekstra & McNeill 1973, Hoekstra et al. 1975, Scott, et al. 1990, Vonder et al. 2002). Airborne electromagnetic surveys have been used recently to provide subsurface information for hydrogeological characterization (Siemon et al. 2009). A unique value to these surveys is that data can be quickly collected over large areas without disturbing local activities or delicate environments (e.g., arctic tundra). These electromagnetic (EM) datasets are then processed, inverted, and interpreted to provide information on the structure of the geological and hydrogeological environment.

The AEM data were acquired with the Fugro Resolve system from June 3 to 10, 2010 (Ball et al. 2011), and the results of this survey are described in Minsley et al. (2012). The survey was flown in June due to aircraft scheduling constraints. Optimal survey time would have been in late August at the maximum development of active layer depth. However, we believe this did not negatively impact the survey results.

AEM data were acquired in two different acquisition

methods (Fig. 1). First, a block of closely spaced survey lines covers approximately 300 km² in the vicinity of Fort Yukon for the purpose of mapping subsurface features in three dimensions with high spatial resolution. Second, a number of widely spaced 'reconnaissance' lines, totaling nearly 900 km in length, were flown over a much larger area in order to sample a variety of hydrogeologic settings in the region and provide a broader context for the study.

The Resolve system is a multi-frequency electro-magnetic induction surveying tool that operates with six transmitter-receiver coil pairs. The transmitter and receiver coils are separated by approximately 8 m, and operate between 0.4 and 140 kHz. The system is towed approximately 30 m beneath a helicopter at average survey speeds of 30 m/s and ground clearance of 30 m. Oscillating electrical currents in the transmitter coils induce secondary currents in the earth that are influenced by the subsurface electrical resistivity structure, where lower frequencies are sensitive to greater depths. The system of induced currents generates secondary magnetic fields that are picked up by the receiver coils, providing measurements of the in-phase and quadrature components of the secondary field reported in parts-per-million of the primary field. At typical survey speeds, one sample of all six frequencies is output approximately every 3 m along the flight line. The lateral footprint of the system is about 20–100 m but varies with frequency, survey altitude, and resistivity (Beamish 2003).

Each sounding is converted to a one-dimensional profile of subsurface resistivity using a regularized least-squares inversion algorithm (Farquharson et al. 2003) (Fig. 2). Use of a one-dimensional algorithm is an approximation when structures are laterally heterogeneous over the footprint of the system, but is reasonable for this study area where features of interest have a long spatial wavelength. Each inversion was run with three different reference models to assess the depth of investigation at each sounding (Oldenburg & Li 1999). Transparency shading is used at the bottom of the sections and indicates this depth, beyond which resistivity values are no longer constrained by the data.

Because electrical resistivity is an indirect measure of subsurface physical properties, it is necessary to incorporate site-specific knowledge about how resistivity is related to the properties of interest. The only available ground truth data in this remote study area come from the 1954 water well near Fort Yukon and the nearby 1994 borehole, which was re-drilled in 2004 (Fig. 1) (Clark et al. 2009).

Resistivity values of 100–200 ohm-m are observed in the uppermost unfrozen eolian silt and sand. Resistivity rapidly increases to greater than 1000 ohm-m in the upper fluvial gravel unit, which was entirely frozen except for the top 2–3 m (in 2005). A transition to lower resistivity values near or less than 100 ohm-m is observed at depth where frozen lacustrine silt and clay are present. Decreased resistivity in the unfrozen upper 5–10 m, and the trend toward lower resistivity values

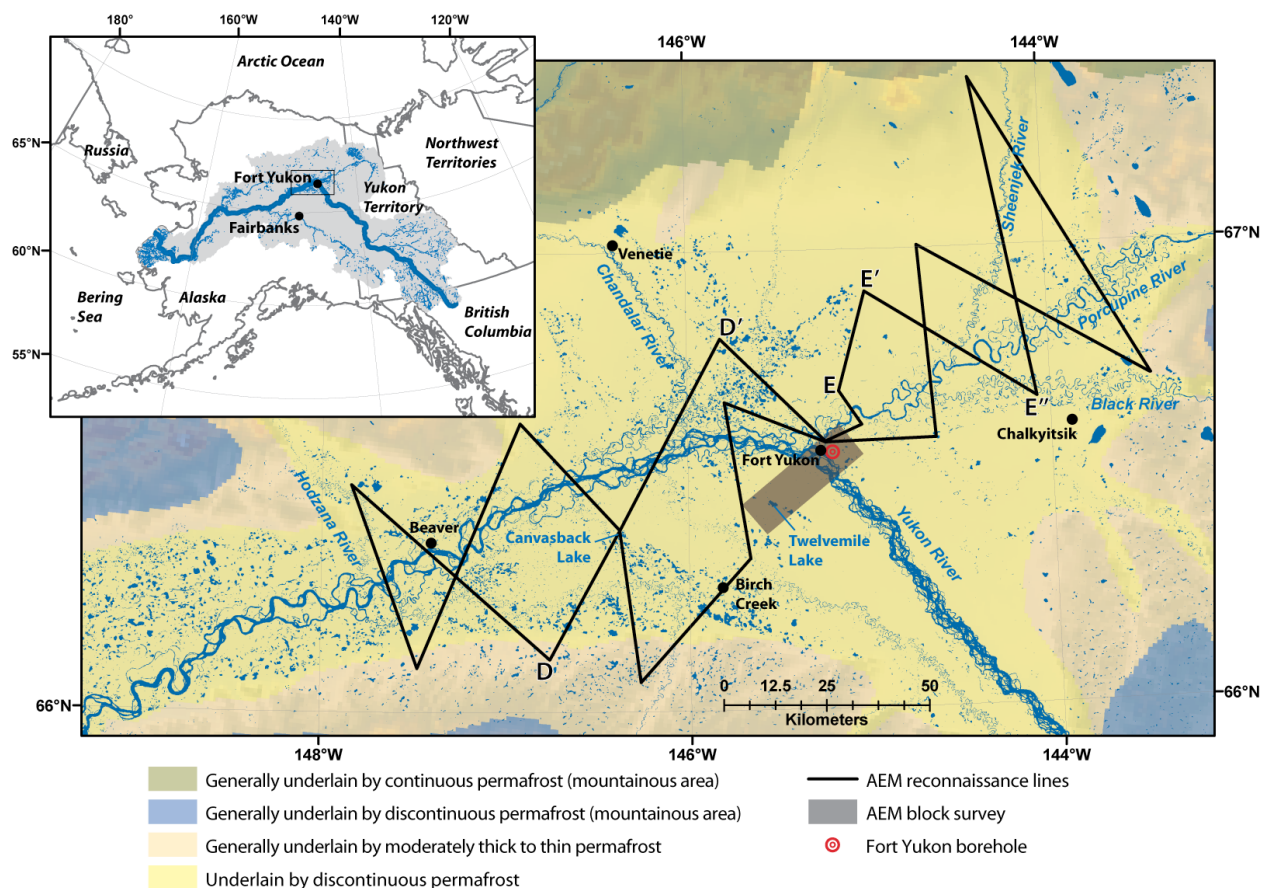


Figure 1. Yukon River Basin location (inset) and geophysical study area with surface water features (Rover et al. 2010) and background shading indicating permafrost characteristics (Ferrians 1965) (modified from Minsley et al. 2012).

below the depth of permafrost at ~90 m, are consistent with the fact that frozen materials are more resistive than their unfrozen counterparts (Yoshikawa et al. 2006).

An interpretive framework is defined based on the well and borehole data, additional knowledge about the

depositional environment, and existing information about typical resistivity values of various earth materials. Each material can occupy a relatively wide range of resistivity values due to variability in porosity, saturation, and mixing of different lithofacies. Resistivity values rapidly increase

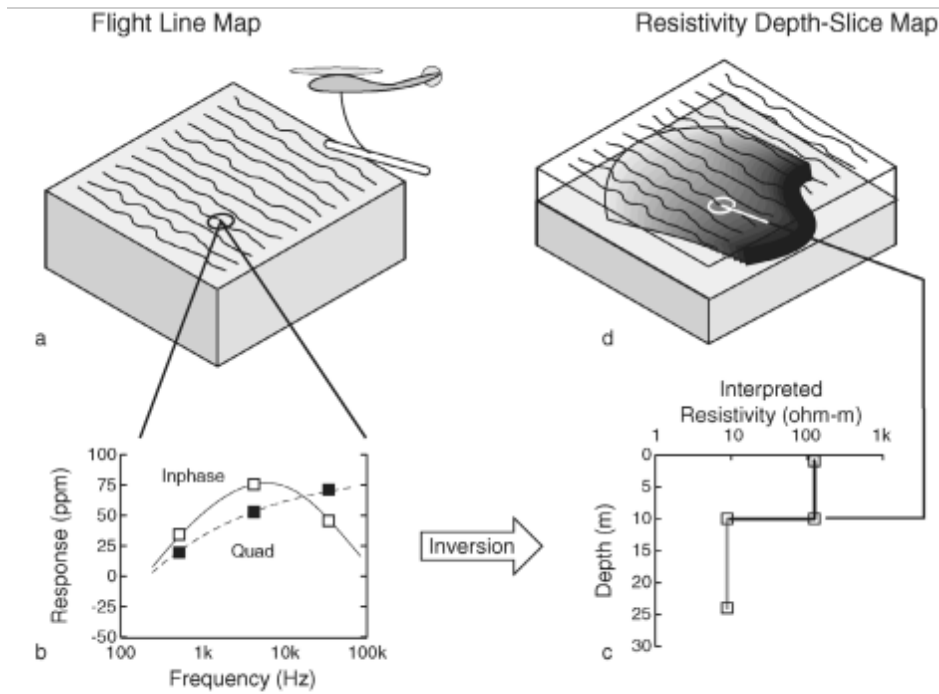


Figure 2. Schematic of HEM data collection and interpretation. a) Parallel lines are flown 400 m apart. b) In-phase and quadrature electromagnetic response are measured at several frequencies. c) Inversion is used to determine the resistivity-depth image. d) Resistivity-depth images are combined to produce an interpreted depth-slice map (modified from Fitterman & Deszcz-Pan 1998).

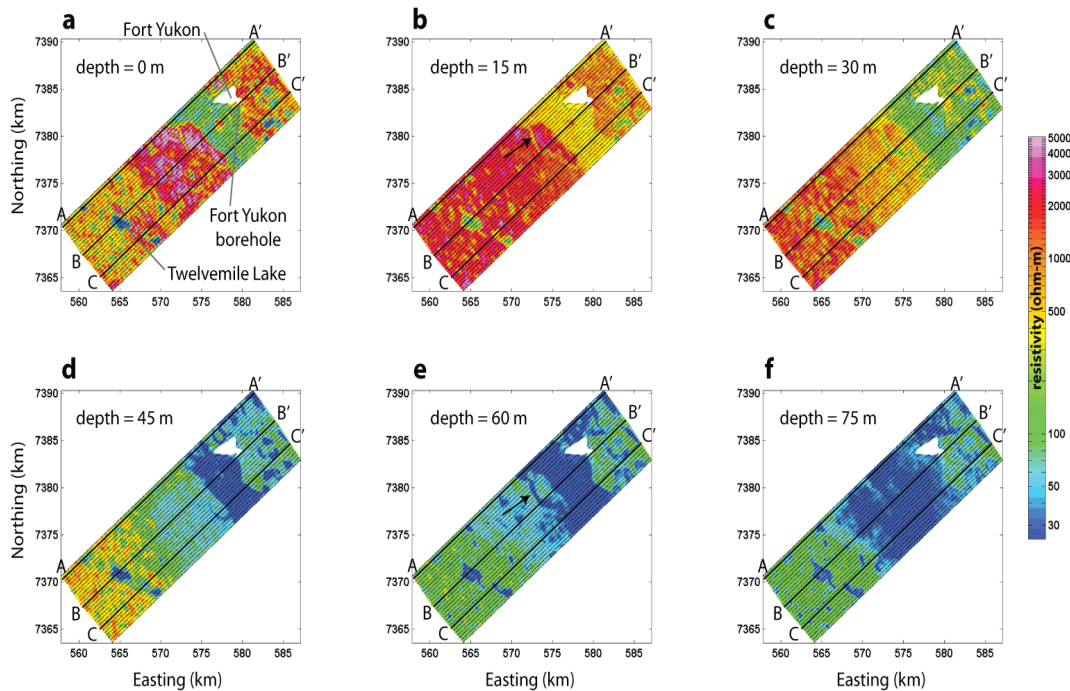


Figure 3. Plan-view slices at depth increments of 15 m through the inverted resistivity models within the AEM survey block. Thin black lines indicate the actual flight path during the survey. Transects denoted A-A', B-B', and C-C' indicate the locations of selected cross-sections illustrated in Figure 4. The black arrows in (b) and (e) highlight the location of a sinuous side-channel of the Yukon River that is also shown in Figure 4 (Minsley et al. 2012).

as temperatures drop below 0°C, although similar increases in resistivity can also be observed in unfrozen materials at very low saturation. The range of resistivity values for surface waters, which is primarily a function of salinity, is defined empirically from this survey where data were acquired over known water bodies. Typical water resistivity values are on the order of tens of ohm-m, though several locations as low as 2–3 ohm-m were observed. Loess on the marginal uplands, which can occupy a wide range of resistivity values, is observed only over very limited portions of the reconnaissance survey lines at higher elevations and is therefore easily identified.

Lithologic and Permafrost Inferences from AEM Data

Plan-view slices at 15 m depth intervals from the surface to 75 m show the distribution of electrical resistivity over the block portion of the survey (Fig. 3). There are a number of notable features in these images: (1) surface water features consistently appear as regions of low-resistivity (blue) in the near-surface, several of which extend throughout the entire depth-extent of the model; (2) very high resistivity values greater than 1000 ohm-m (orange-pink) are observed throughout the upper 15–30 m in the northeast and up to 45 m in the southwest portions of the survey area, and overlie decreased resistivity (blue-green) regions at depth; and (3) the Yukon River is characterized by a broad, relatively low-resistivity zone that widens to the southwest with depth. Two-

and three-dimensional views of parts of the block section are also presented (Figs. 4, 5).

Conclusions and Future Directions

Airborne geophysical data have provided extraordinary new insights into subsurface lithologic variability and discontinuous permafrost distributions in the Yukon Flats area. The geophysical observations are consistent with the known depositional history of the region, and with thermal features associated with surface water and groundwater. We have shown that sensitivity of the resistivity models to the presence or absence of permafrost can be used to make inferences about the recent (~1000 year) chronology of the Yukon River migration, and has implications for studying the development and re-freezing of taliks as they undergo variable thermal forcing.

These data represent the foundation upon which numerous interdisciplinary studies will be focused. Future work will integrate remote sensing data, targeted ground-based geophysics, shallow probing to assess the top of permafrost, geochemical analyses of lake and river samples, and thermally coupled flow modeling to better understand dynamic permafrost-related processes in the Yukon Flats over multiple scales (Jepsen et al. 2011, Pastick et al. 2011, Walvoord et al. 2011). This interdisciplinary approach aims to explore the connections between hydrogeologic, climatic, and ecological processes. It has significant implications for the future stewardship of arctic environments.

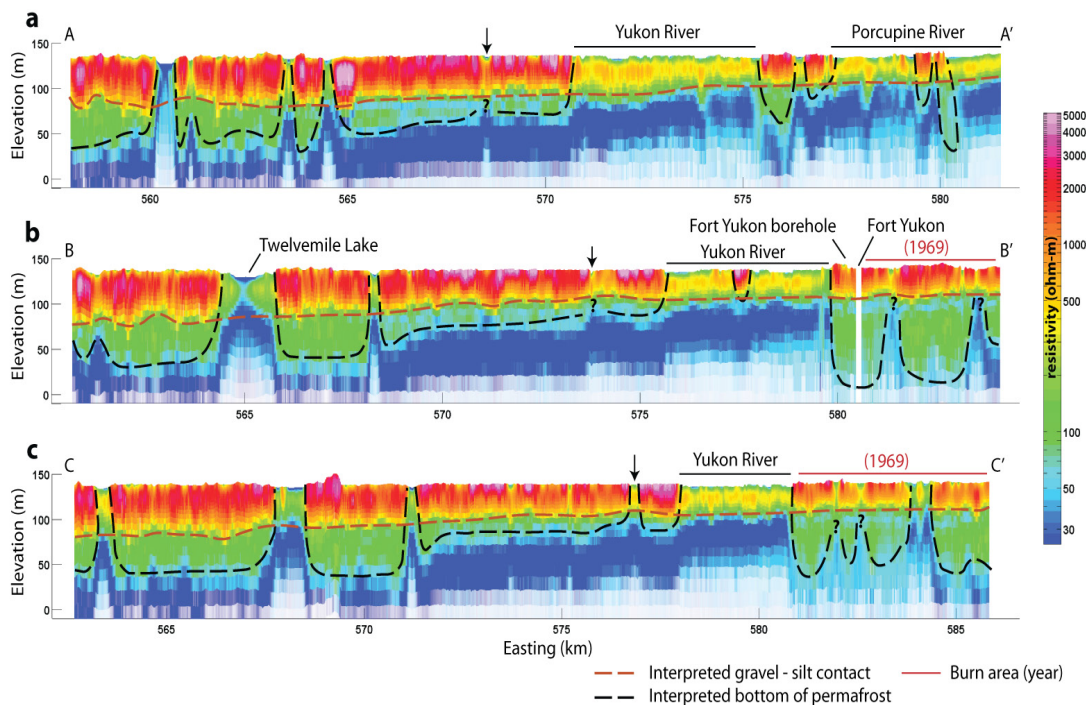


Figure 4. Resistivity cross-sections along the three transects highlighted in Figure 3 with relevant surface features and recent burn areas annotated. The downward-pointing arrows indicate the location of a sinuous side-channel of the Yukon River that is also evident as a shallow low-resistivity zone (Fig. 3 b and e). Interpreted lithologic and permafrost boundaries are superimposed as dashed lines. Vertical exaggeration is approximately 25:1.

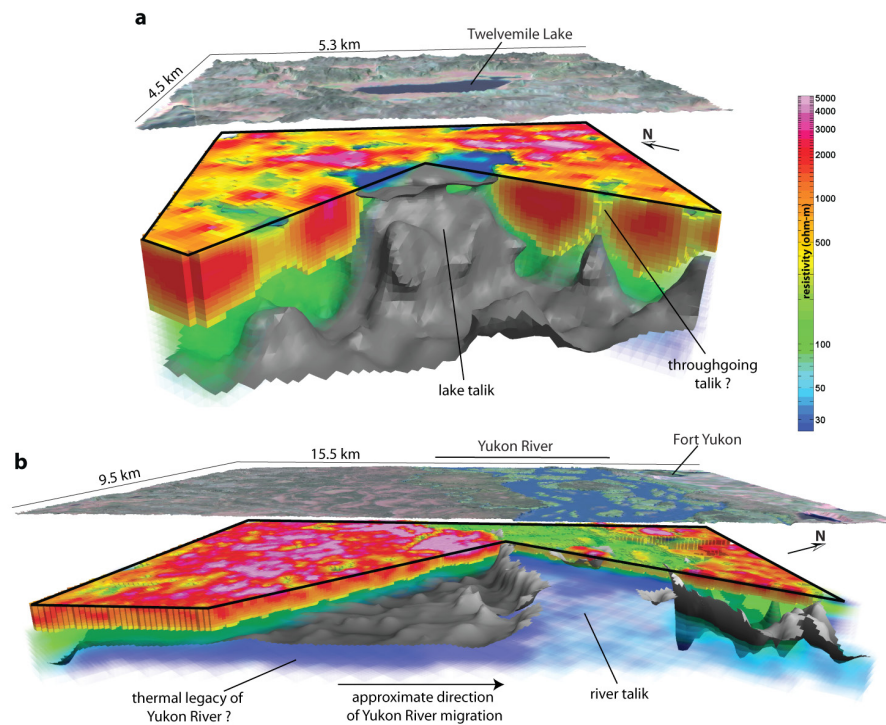


Figure 5. Three-dimensional cutout view of the resistivity model in the vicinity of (a) Twelvemile Lake and (b) the Yukon River. The grey isosurfaces are interpreted to indicate the base of permafrost in the subsurface. The upper image in each figure is a Landsat view of the region displayed below. Vertical exaggeration is 12:1 (Minsley et al. 2012).

Acknowledgments

This research was funded by the U.S. Geological Survey Climate Effects Network project and the U.S. Geological Survey Minerals Program. The authors would like to also thank the many people who have contributed to this project including Torre Jorgenson, Maryla Deszcz-Pan, Thomas Ager, Tristan Wellman, Joshua Rose, and Steven Jepsen.

References

- Abraham, J.D., Ball, L.B., Cannia, J.C., Jorgenson, T., Minsley, B.J., Smith, B.D., Walvoord, M.A., Wylie, B.K. & Voss, C.I. 2011. Airborne electromagnetic mapping of subsurface permafrost: quantifiable characterization for now and in the future. *Abstracts from the 6th International Conference on Arctic Margins*, Fairbanks Alaska, May 30-June 3, 2011
- Ball, L., Smith, B., Minsley, D., Abraham, J., Voss, C.I., Deszcz-Pan, M., & Cannia, J.C. 2011. *Airborne Electromagnetic and Magnetic Geophysical Survey Data of the Yukon Flats and Ft. Wainwright areas, central Alaska, June 2010*. U.S. Geological Survey Open File Report 2011-1304, 28 pp.
- Beamish, D. 2003. Airborne EM footprints. *Geophysical Prospecting* 51: 49-60.
- Brown, J., Ferrians, O.J., Heginbottom, J.A., & Melnikov, E.S. 1998, revised February 2001. *Circum-Arctic map of permafrost and ground ice conditions*. Boulder, CO: National Snow and Ice Data Center/World Data Center for Glaciology. [http://nsidc.org/data/docs/fgdc/ggd318_map_circumarctic/index.html] Accessed June 29, 2011.
- Clark, A., Barker, C.E., & Weeks, E.P. 2009. *Drilling and testing the DOI-04-1A coalbed methane well, Fort Yukon, Alaska*. U.S. Geological Survey Open-File Report 2009-1064, 69 pp.
- Farquharson, C.G., Oldenburg, D.W., & Routh, P.S. 2003. Simultaneous 1D inversion of loop-loop electromagnetic data for magnetic susceptibility and electrical conductivity. *Geophysics* 68: 1857-1869.
- Ferrians, O.J. 1965. *Permafrost map of Alaska*. Boulder, CO: National Snow and Ice Data Center/World Data Center for Glaciology. <http://nsidc.org/data/ggd320.html>. Accessed July 25, 2011.
- Fitterman, D.V. & Deszcz-Pan, M. 1998. Helicopter EM mapping of saltwater intrusion in Everglades National Park, Florida: *Exploration Geophysics* 29: 240-243.
- Hoekstra, P. & McNeill, D. 1973. Electromagnetic probing of permafrost: Proceedings of the 2nd International Conference on Permafrost, National Academy of Science: 517-526.
- Hoekstra, P., Sellmann, P.V., & Delaney, A. 1975. Ground and airborne resistivity surveys of permafrost near Fairbanks, Alaska. *Geophysics* 40: 641-656.

- Jepsen, S.M., Voss C.I., Walvoord, M.A., Minsley, B.J., Rose, J., & Smith, B.D. 2011. Disappearing Twelvemile Lake in Alaska's discontinuous permafrost: Scoping analysis of water budget. *Abstracts from the 2011 Fall Meeting of the American Geophysical Union* San Francisco, California, December 4 – 9, 2011.
- Kellett, R., Hinnell, A., Gamey, J., & Hodges, G. 2000. Mapping discontinuous permafrost in the Canadian Sub-Arctic using a combination of airborne and surface geophysical surveys. *SEG Conference 2000 Expanded Abstracts*, Calgary, Alberta
- Minsley, B.J., Abraham, J.D., Smith B.D., Cannia, J.C., Voss, C.I., Jorgenson, M.T., Walvoord, M.A., Wylie, B.K., Anderson, L., Ball, L.B., Deszcz-Pan, M., Wellman, T.P., & Ager T.A. 2012. Airborne electromagnetic imaging of discontinuous permafrost. *Geophysical Research Letters* 39, L02503, doi:10.1029/2011GL050079.
- Oldenburg, D.W. & Li, Y. 1999. Estimating depth of investigation in DC resistivity and IP surveys: *Geophysics* 64: 403-416.
- Olhoeft, G.R. 1978. Electrical properties of permafrost. Proceedings 3rd International Conference on Permafrost, Natural Resources Counsel of Canada: 127-131.
- Pastick, N., Wylie, B.K., Minsley, B.J., Jorgenson, T.T., Ji, Lei, Walvoord, M.A., Smith, B.D., Abraham, J.D., & Rose, J. 2011. Using remote sensing and ancillary data to extend airborne electromagnetic resistivity surveys for regional permafrost interpretation. *Abstracts from the 2011 Fall Meeting of the American Geophysical Union* San Francisco, California, December 4 – 9, 2011.
- Petrenko, V.F., 1994. *Electrical Properties of Ice*. Special Report #93-20. Hanover, NH:US Army Corps of Engineers, Cold Regions Research & Engineering Laboratory, 81 pp.
- Rover, J., Lei, J., Wylie, B., & Tieszen, L. 2010. Surface Water extent trends in interior Alaska (1979-2009). *Abstracts from the 2010 Fall Meeting of the American Geophysical Union* San Francisco, California, December 12 – 17, 2010.
- Scott, W.J. & Kay, A.E. 1988. Earth resistivities of Canadian soils. Montreal, Canada: Canadian Electrical Association Vol. 1.
- Scott, W.J, Sellmann, P.V., & Hunters, J.A. 1990. Geophysics in the study of permafrost. In: S.H. Ward (ed.) *Investigations in Geophysics—Review and Tutorial*, Vol. 5. Tulsa, OK : Society of Exploration Geophysicists, 355-384.
- Siemon, B., Christiansen, A.V., & Auken, E. 2009. A review of helicopterborne electromagnetic methods for groundwater exploration: *Near-Surface Geophysics* 7: 629-646.
- Vonder Mühlla, D., Haucka, C., & Gubler, H. 2002. Mapping of mountain permafrost using geophysical methods. *Progress in Physical Geography* 26: 643-660.
- Walvoord, M.A., Voss, C.I., & Wellman, T.P. 2011. Influence of permafrost distribution on regional groundwater flow in the Yukon Flats Basin, Alaska *Abstracts from the 2011 Fall Meeting of the American Geophysical Union* San Francisco, California, December 4 – 9, 2011.
- Yoshikawa, K., Leuschen, C., Ikeda, A., Harada, K., Gogineni, P., Hoekstra, P., Hinzman, L., Sawada, Y., & Matsuoka, N. 2006. Comparison of geophysical investigations for detection of massive ground ice (pingo ice). *Journal of Geophysical Research* 111: 10 pp.

Improvement of Pulse-NMR Technology for Determining the Unfrozen Water Content in Frozen Soils

Satoshi Akagawa

Cryosphere Engineering Laboratory, Hachioji, Tokyo, Japan

Go Iwahana

University of Alaska Fairbanks, USA

Kunio Watanabe

Mie University, Mie, Japan

Evgeny M. Chuvilin

Moscow State University, Moscow, Russia

Vladimir A. Istomin

GAZPROM VNIIGAZ LLC, Moscow, Russia

Abstract

Several methods are used to observe unfrozen water content in frozen soil. These include pulse-NMR (P-NMR), time domain reflectometry (TDR), differential scanning calorimetry (DSC), and the contact method. However, a preliminary study by the authors reveals that test results depend on the method. This disagreement may be caused by improper treatment of data in P-NMR analysis. In this paper, free induction decay (FID) followed by a 90° pulse of P-NMR has been reexamined with four different soils in order to confirm the validity of the analytical method. In the discussion, two different methods used to determine the appropriate time for choosing signal intensity of each specific FID, are discussed. After the appropriate method to determine the rational time for the signal intensity of FID is clarified, the effect of cooling and warming runs (hysteresis) is discussed.

Keywords: unfrozen water content; P-NMR; 90° pulse; FID, hysteresis.

Introduction

The behavior of water molecules in the liquid phase in frozen soil has drawn attention for a long time. In this paper, the liquid phase H₂O in frozen soil is defined as “unfrozen water.” Several methods are used to measure the quantity of unfrozen water, such as pulse nuclear magnetic resonance (P-NMR) (Tice et al. 1978, Tice et al. 1981), time domain reflectometry (TDR) (Smith & Tice 1988, Hivon & Segó 1990), differential scanning calorimetry (DSC) (Smith & Tice 1988, Hivon & Segó 1990, Kozłowski 2002), and the contact method (Ershov et al. 1979, Chuvilin et al. 2008). However, results produced from these various methods are rarely identical. In order to improve consistency among these methods, the authors re-examined the data analysis procedure for the P-NMR method as an initial step. We give special attention to the free induction decay (FID) signal after a 90° pulse; in the P-NMR method, the FID signal intensity is directly proportional to water content.

P-NMR Method

Conventional P-NMR method

Since the main objective of this paper is the technological improvement of the P-NMR method, the theory of P-NMR (e.g., Hornek <http://www.cis.rit.edu/htbooks/nmr/>) is not discussed. The conventional data analysis procedure is summarized in Figure 1. The P-NMR method utilizes free induction decay (FID) followed by a 90° pulse (Fig. 1A). During and after the 90° pulse, the receiver that monitors FID

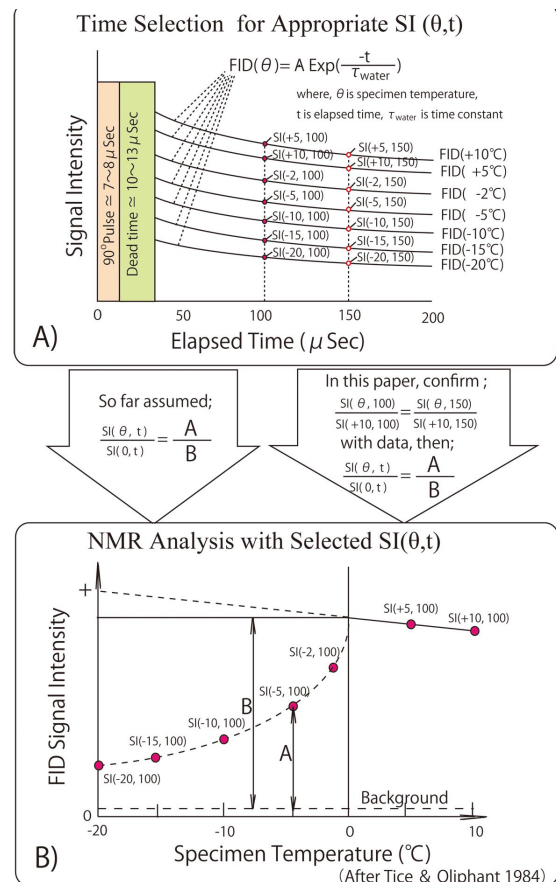


Figure 1. Data analysis procedure of P-NMR.

is turned off for a certain period to protect the receiver from the strong pulse.

This period is called “dead time” and masks the early portion of FID. Generally speaking, the length of the dead time is chosen to mask the FID of the solid phase.

According to the pioneering work by Tice and Oliphant (1984), the basis of P-NMR is that the FID signal intensity is directly proportional to the amount of unfrozen water in the frozen soil sample. This means that we can calculate the unfrozen water content of the soil shown in Figure 1B if we compare the signal intensity at a positive temperature to the water content of the soil. In other words:

$$SI(0,t):w(0) = SI(\theta,t):w_n(\theta) \quad (1)$$

where $SI(0,t)$ is the signal intensity at 0°C and time t , $w(0)$ is water content of the soil, $SI(\theta,t)$ is the signal intensity at the negative temperature $\theta^\circ\text{C}$, and $w_n(\theta)$ is the unfrozen water content by weight (i.e., weight of unfrozen water / weight of soil particles, in percent) at the negative temperature $\theta^\circ\text{C}$. Based on the principle demonstrated by Tice and Oliphant (1984), equation 1 is valid.

A question on the conventional P-NMR method

The validity of equation 1 requires the following FID relationship, as depicted in Figure 1A:

$$R(\theta,t) = \frac{SI(\theta,t)}{SI(0,t)} \quad (2)$$

$$R(\theta,t) = \text{Const}(\theta) \quad (3)$$

where $R(\theta,t)$ is a ratio at the temperature θ and the time t . The relationships shown in equations 2 and 3 suggest that the FID curves shown in Figure 1A should be converted into horizontally parallel lines. This conversion is necessary in order to apply equation 1. We examined the FIDs of four different soils using this procedure.

P-NMR system used

The P-NMR system we used (see Fig. 2) consists of a P-NMR machine (MARAN Ultra) and a temperature bath housed within a walk-in type cold room held at a temperature of $+1^\circ\text{C}$. The operating frequency of the P-NMR is 23MHz. The 90° pulse length is $7.6 \mu\text{Sec}$ followed by a dead time of $10 \mu\text{Sec}$. For one FID measurement, 90° pulses are applied 10 times so as to improve the signal-to-noise ratio.

The temperature of the samples is controlled within the temperature bath. The temperature control function of the P-NMR probe is not used so as to avoid shifts in resonant frequency due to changing temperature. Instead, for a reading, the temperature controlled soil samples are moved into the P-NMR probe, in which the temperature is maintained at about $+1^\circ\text{C}$ by the temperature of the cold room.

Since the time required for a P-NMR measurement is less than 30 seconds, the effect of sample temperature on the probe temperature is negligible and vice versa.



Figure 2. P-NMR System (MARAN Ultra with temperature bath).

Soil samples tested

The properties of the FID signal acquired from a soil and water mixture is not completely understood. In order to generalize the result of this study, we selected four different soils. MZ Kaolin is a typical clay sample, predominantly consisting of the clay mineral Kaolinite. NSF Clay is unique clay with Pyrophyllite as the predominant mineral. We examined a volcanic ash that contains no clay minerals but instead consists primarily of quartz and plagioclase. Finally, we tested the soft mudstone called Dotan in Japan. This soil is caked Diluvium silt and the predominant clay minerals are illite and chlorite.

Some physical properties of these soils are listed in Table 1. All of the specimens were saturated with water and then consolidated with an oedometer. The water content and wet density reported in Table 1 were measured after the specimens were consolidated.

Measurement

Soil sample freezing

The focus of this experiment is the measurement method of unfrozen water content. If ice lenses form in the specimen while it is freezing, the unfrozen water content may decrease. In order to inhibit ice lens formation, samples were frozen rapidly with liquid nitrogen. Then frozen samples were placed into the bottom of the sample holder, which was made of a non-magnetic material such as Teflon.

Test temperatures and measurement

The sample holders were inserted into the temperature bath, set at -20°C , and brought to thermal equilibrium. For the first measurement following thermal equilibration, the sample holders were sequentially removed from the bath, wiped dry, measured in the P-NMR analyzer, and then reinserted into the bath. After all samples were measured, the bath temperature was adjusted to the next measurement temperature. In our

Table 1. Soil physical properties.

| | MZ Kaolin | NSF Clay | Volcanic Ash | Soft Mudstone |
|---|-----------|----------|--------------|---------------|
| Soil particle density(g/cm ³) | 2.64 | 2.75 | 2.65 | 2.60 |
| Dry density (g/cm ³) | 1.02 | 1.08 | 1.48 | 1,26 |
| Wet density(g/cm ³) | 1.63 | 1.65 | 1.78 | 1.76 |
| Water content (%) | 60.1 | 53.2 | 20.3 | 39.2 |
| Liquid limit(%) | 70.2 | 55.0 | 28.6 | 62.3 |
| Plastic limit (%) | 35.3 | 29.0 | 17.7 | 41.9 |
| Plasticity index (-) | 34.9 | 26.0 | 10.9 | 20.4 |

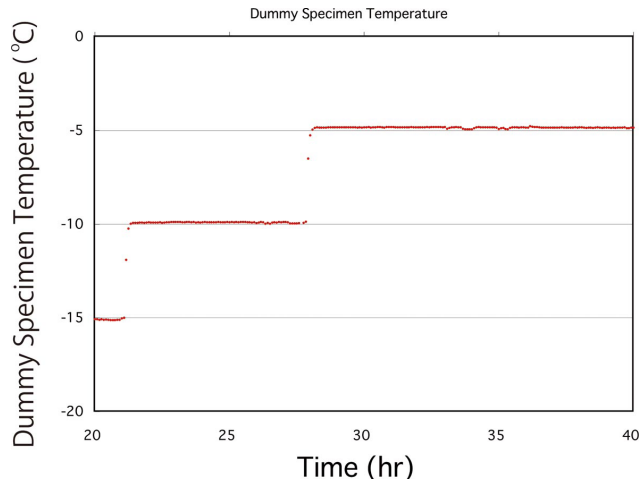


Figure 3. Temperature response in the dummy specimen.

case, the suite of measurement temperatures were -20, -15, -10, -5, -2, -1, -0.5, -0.2, -0.1 -0.2, -0.5, -1, -2, -5, -15, -20, +5, and +10°C. The time between measurements at two different temperatures was set for at least three hours to ensure thermal equilibrium. The monitored temperature in a dummy sample is shown in Figure 3. Thermal equilibrium is reached well within the three-hour period. Using this suite of temperature measurements, we also investigated hysteresis between cooling and warming runs.

Analysis method

1) Misgivings with the analysis

The main assumption of the P-NMR method is that the FID signal intensity is directly proportional to the water content (or unfrozen water content of a frozen soil sample) as shown in equation 1. Another assumption is that the signal from the water phase in a soil sample follows the exponential curve. The FID curves acquired from MZ Kaolin (shown in Fig. 4), however, appear to demonstrate characteristics that differ from these assumptions.

The important point is that the signal intensity ratio between any two FID curves at any time should be constant, as indicated by equation 2 and equation 3. In the following, two different methods will be demonstrated and verified with FID data.

2) Method A

Equation 2 and equation 3 are the necessary conditions to satisfy equation 1. Thus the rationale behind the use of equation 2 and equation 3 should be first verified.

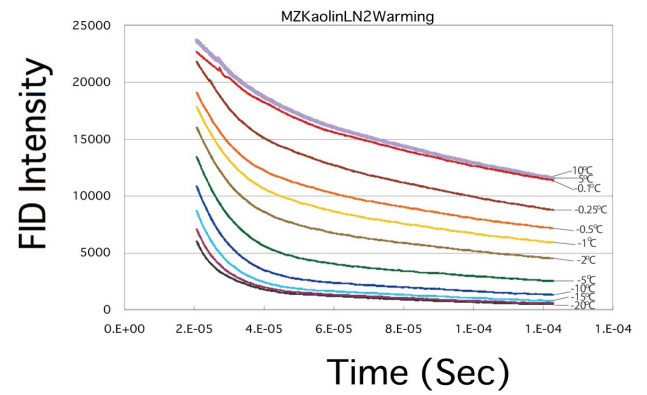


Figure 4. Typical FID curves after 90° pulse.

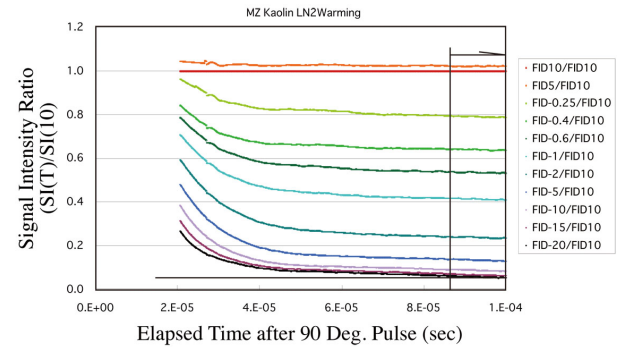


Figure 5. Normalized FID curves with SI(10).

As is shown in equation 2, $R(\theta, t)$ is calculated using FID data. In other words, all the FID curves were compared with the FID acquired at the sample temperature of +10°C by taking the fraction of each FID over the FID of +10°C. The results are shown in Figure 5.

If all the lines in Figure 5 are horizontally parallel, as is restricted by equation 3, the assumption is applicable at any specific time during the acquisition of the FIDs. However, the horizontally parallel section becomes shorter as the sample temperature becomes lower. The time for which the assumption is true is later than 80 μ Sec in this case, as indicated by the vertical line in Figure 5.

By completing this procedure, one can determine the time range that will satisfy the assumption. Therefore, by selecting the suitable time after the 90° pulse for unfrozen water content analysis, equation 1 is applicable as the conventional data analysis procedure.

3) Method B

Generally speaking, water and ice in soil have longer FIDs (Quinn et al. 1991), with the FID of water longer than that of ice. From this it follows that the dead time after the 90° pulse in the conventional method is not long enough to mask the FID from the ice. Assuming that the disorder that is seen in the early part of the FID curves in Figure 5 is due to the overlapping of FIDs of unfrozen water and ice:

$$FID(\text{measured}) = FID(\text{water}) + FID(\text{ice}) \quad (4)$$

$$FID(water) = A \cdot \text{Exp}\left(\frac{-t}{T_{water}}\right) \tag{5}$$

$$FID(ice) = B \cdot \text{Exp}\left(\frac{-t^2}{T_{ice}}\right) \tag{6}$$

where, A, B, T_{water} , and T_{ice} are constants. The measured FID was discriminated into FID(water) and FID(ice) with the SOLVER function in Excel.

The typical result is shown in Figure 6. As is seen in the figure, FID(water) and FID(ice) are well discriminated using SOLVER. The FID(water)s of MZ Kaolin are shown in Figure 7. If these straight lines satisfy equation 2 and equation 3, then equation 1 is applicable.

T_{water} is the time constant of the decay function of equation 5, and the values of T_{water} of the each FID(water) acquired from FIDs at different temperatures are shown in Figure 8. The shape of the FID curves of each soil sample indicates that the T_{water} of the four soils tested has temperature dependence.

Mathematically, a condition required by equation 3 is that T_{water} is constant over the specimen temperature range. Therefore, it will be difficult to determine the appropriate time t which fulfills the requirement. However, Method B is applicable for the soils in cases where the temperature dependence of T_{water} is negligible.

4) Comparison of Method A and Method B

Method A and Method B were applied to the soils summarized in Table 1, and the results are shown in Figures 9-1 to 9-4.

For Method A, 100 μ Sec was selected as the time t required to fulfill equation 3. For Method B, T_{water} in equation 5 of different FIDs were assumed to be equal. With this assumption, the requirement is fulfilled at any time t . So $t=0$ was chosen for equation 5, resulting in $SI(\theta,0)=A$.

As shown in Figure 9, Method A and Method B provide the same trends in unfrozen water content versus temperature (i.e., unfrozen water content decreases with temperature). However, the difference between the two methods increases as temperature decreases. The differences between Method A and Method B in the low temperature range, such as below -1°C , in the four soil samples are considerably large.

According to the data shown in Figure 5, Method A fulfills the requirement to choose the appropriate time t for FID signal intensity analysis. The data shown in Figure 9 indicates that Method B consistently provides higher unfrozen water content per soil sample. Therefore, the authors recommend Method A for finding the appropriate time t for the unfrozen water content analysis using FID signal intensity data.

Hysteresis

Unfrozen water content curves of warming and cooling temperature runs are shown in Figure 9. Hysteresis is clearly visible in each of these figures. All of the cooling curves demonstrate higher unfrozen water content than warming curves. It is noteworthy that the predominant temperature

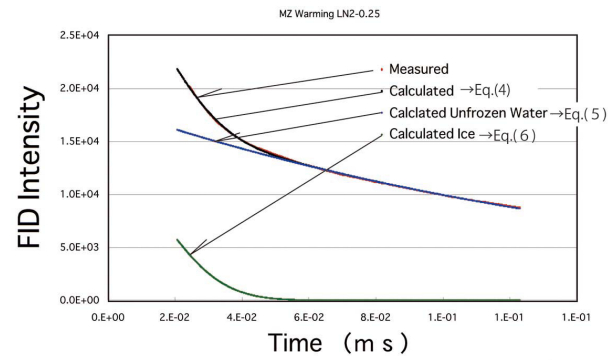


Figure 6. Discriminated FID(water) and FID(ice).

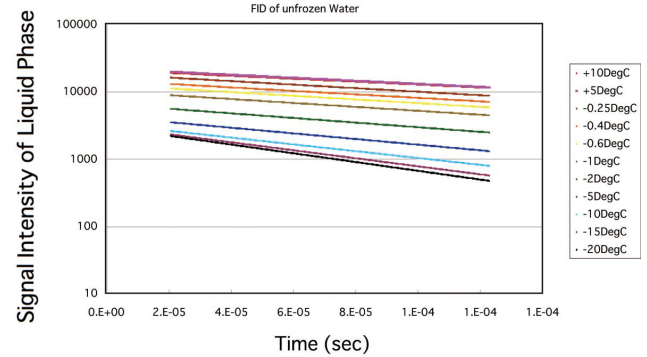


Figure 7. Typical FID(water)s at different temperatures.

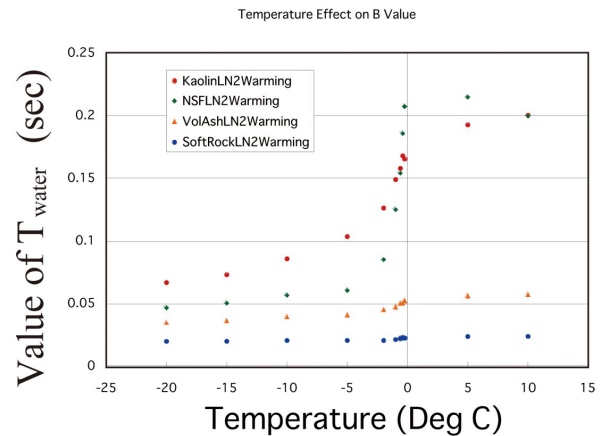
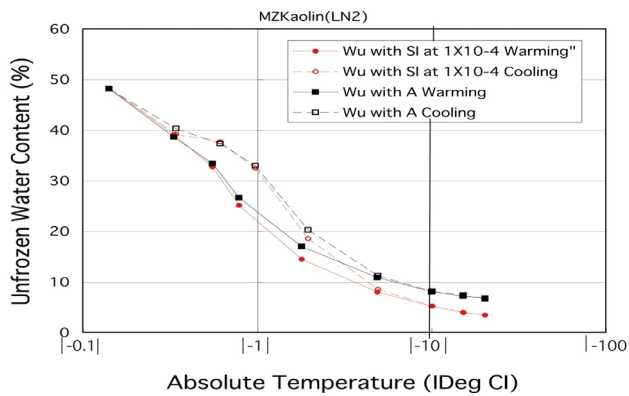


Figure 8. Temperature dependence of T_{water} .

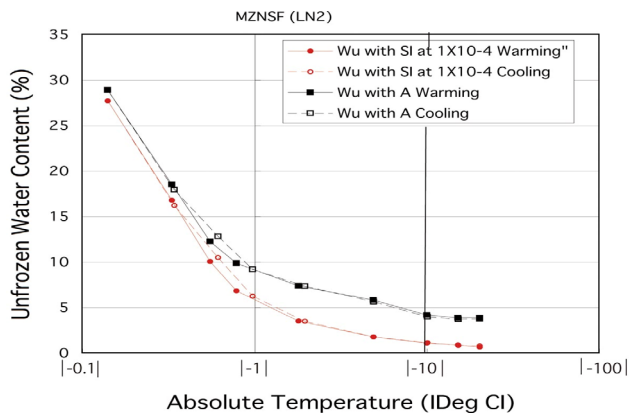
range of the hysteresis depends on soil type. Therefore, it is important to indicate which process (either the cooling or warming process) is used when discussing unfrozen water content curves.

Conclusions

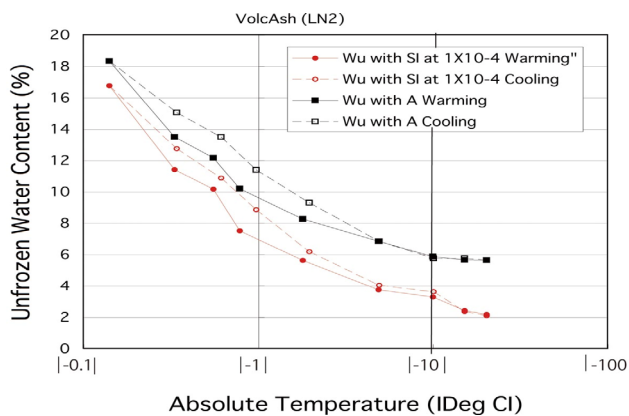
- 1) None of the FID curves that were acquired from the four different soils follow a simple exponential curve.
- 2) The early part of the FID curves especially demonstrate the tendency mentioned in conclusion 1.
- 3) Therefore, it is important to choose the appropriate time “ t ” for the analysis of unfrozen water content.
- 4) Method A is a simple and effective technique.



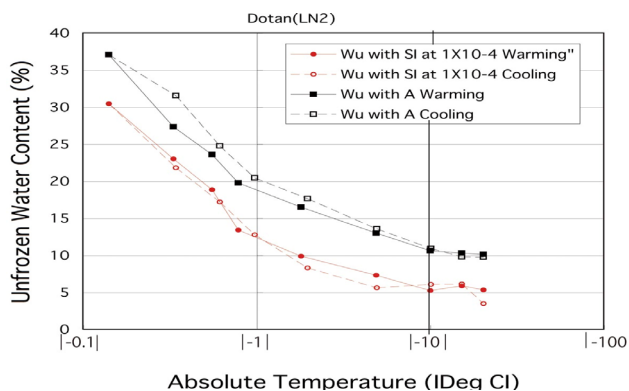
1) Comparison of Method A and Method B with MZ Kaolin frozen by LN2



2) Comparison of Method A and Method B with NSF Clay frozen by LN2



3) Comparison of Method A and Method B with volcanic ash frozen by LN2



4) Comparison of Method A and Method B with Dotan frozen by LN2

Figure 9. Comparison of Method A and Method B for different soils (data also show hysteresis).

- 5) Method B may discriminate between the FIDs from ice and water, assuming equation 5 and equation 6 are applicable.
- 6) Since the time constant, T_{water} , of four soils demonstrates temperature dependency, equation 2 and equation 3 may not be satisfied.
- 7) Therefore, Method B may not be the universal technique for the unfrozen water analysis.
- 8) The predominant temperature range of hysteresis depends on soil type. The description of cooling or warming processes is important when discussing unfrozen water curves.
- 9) An appropriate data analysis procedure for the P-NMR method is demonstrated in this paper. The consistency of the P-NMR method with other methods such as TDR, DSC, the contact method, and so forth can now be studied further.

Acknowledgments

The authors would like to express their appreciation to Dr. M.M. Darrow of the University of Alaska Fairbanks for her useful advice in preparing this manuscript.

References

- Chuvilin, E., Guryeva, O., Istomin, V., & Safonov, S. 2008. Experimental method for determination of the residual equilibrium water content in hydrate-saturated natural sediments, *Proc. of the Sixth Inter. Conf. on Gas Hydrates (ICGH 2008)*: 8.
- Ershov, E.D., Akimov, Y.P., Cheverev, V.G., & Kuchukov, E.Z. 1979. *Water phase composition in frozen soils*. Moscow: MSU, 192 (in Russian).
- Hivon, E. & Sego, D.C. 1990. Determination of the unfrozen water content of saline permafrost using time-domain reflectometry (TDR). *Proc. of the Fifth Canadian Permafrost Conference*: 257-262.
- Hornek, J.P. The basics of NMR. <http://www.cis.rit.edu/htbooks/nmr/>.
- Kozłowski, T. 2002. A comprehensive method of determining the soil unfrozen water curves 1. Application of the term convolution. *Cold Regions Science and Technology* 36: 71-79.
- Quinn, F.X., Weldon, V.L., McBrierty, V.J., Kruijzen, A.A.T.J.J.M., & Unsworth, J.F. 1991. Cryogenic properties of soils and rocks 1. Anomalous behaviour of water. *Geotechnique* 41-No.2: 195-209.
- Smith, M.W. & Tice, A.R. 1988. Measurement of the unfrozen water content of soils: A comparison of NMR and TDR method. *Proc. Of the Fifth Inter. Conf. on Permafrost*: 473-477.
- Tice, A.R., Burrous, C.M., & Anderson, D.M. 1978. Determination of unfrozen water in frozen soil by using nuclear magnetic resonance. *Third Int. Conf. on Permafrost*: 149-155.

- Tice, A.R., Anderson, D.M., & Sterrett, K.F. 1981. Unfrozen water contents of submarine permafrost determined by nuclear magnetic resonance. *Engineering Geology* 18: 135-146.
- Tice, A.R. & Oliphant, J.L. 1984. The effect of magnetic particles on the unfrozen water content of frozen soils determined by nuclear magnetic resonance. *Soil Science* 138-No.1: 63-73.

Geochemically-Induced Unfrozen Water Effects on CCR Surveys of Massive Ground Ice, Western Canadian Arctic

Michael Angelopoulos, David Fox, Wayne H. Pollard
Department of Geography, McGill University, Montreal, QC, Canada

Abstract

Capacitively-coupled resistivity (CCR) surveys were performed at two ice-rich sites in the Western Canadian Arctic, each with fundamentally different geochemical properties. On Herschel Island, a CCR profile was carried out above and parallel to the headwall of a retrogressive thaw slump. At Parsons Lake, a CCR survey intersecting three boreholes shown to contain massive ice was conducted. Vertical sampling transects were performed at massive ground ice exposures to measure electrical conductivity and cation concentrations. The average conductivity of melted massive ice samples on Herschel Island was 5.6 times greater than Parsons Lake. In addition, an electrical contrast of similar magnitude was found for CCR surveys. In combination with observations of relatively high Na cations, CCR profiles suggest that brine films containing significant unfrozen water content exist on Herschel Island. Hence this research illustrates geophysical heterogeneity for similar massive ice volumes.

Keywords: permafrost; massive ground ice; Western Canadian Arctic; capacitively-coupled resistivity; geochemistry; geophysics.

Introduction

Acquiring subsurface information about ground ice and stratigraphy is an important starting point for most development activities in the North. The labor and costs associated with excavation or drilling are a drawback compared to most shallow geophysical surveys, and although exposed sections provide 2D stratigraphic data, their presence is not guaranteed. Capacitively-coupled resistivity (CCR) is a relatively new technique with operational advantages in permafrost terrain. Direct current resistivity (DCR) places electrodes in the ground to pass an electric current, but with CCR, no galvanic contact with the ground is required. Hence CCR overcomes problems associated with impenetrable surfaces, which were first reported in Muller (1947) as well as Scott and Mackay (1976).

Although previous CCR investigations in permafrost areas (e.g., de Pascale et al. 2008, Calvert et al. 2001) have demonstrated the tool's utility to detect massive ground ice, they do not show how geophysical outputs for massive ground ice can vary as a function of its geochemical properties, which could affect unfrozen water content. The goal of this paper is to explore how changing concentrations of salt in massive ground ice bodies affect CCR results. Since ground ice is a critical factor affecting disturbance patterns associated with thermokarst, exploring electrical heterogeneity for similar massive ground ice volumes is imperative for accurate subsurface mapping products. This is particularly true if ground-truth calibrated resistivity data are used as a baseline to interpret CCR profiles from other locations with different ice geochemistry. This study compares the results of CCR surveys with geochemical analyses of ice samples at two sites in the western Canadian Arctic, each with fundamentally contrasting geochemical properties related to salinity.

Background

For CCR surveys, one or multiple receivers are used to detect an electric field and measure the potential difference (voltage) of the materials through which a current has passed. Electrical resistivity is controlled by water and ice volumes, geochemistry, temperature, grain size, as well as the porosity and degree of saturation of soil (McNeill 1980). The effects of these variables are not always independent because each contributes to the amount of unfrozen water present. Unfrozen water content is a key variable responsible for resistivity changes (Hauck 2002), and a large increase in resistivity occurs at the freezing point when most of the available moisture turns to ice (e.g., Hauck et al. 2003). In interstitial ice, the unfrozen water films are continuous in pores and interconnected passages; thus, resistivity is less compared to stratified cryostructures (Fortier et al. 1994).

In terms of geochemistry, increasing the concentration of dissolved solids like salt decreases resistivity by 1) increasing the conductivity of pore water, and 2) increasing the amount of unfrozen water by depressing the freezing point (e.g., Kneisel et al. 2008, Scott et al. 1990).

Study Areas

Two ice-rich sites in the western Canadian Arctic were studied (Fig. 1). Herschel Island (69°36'N, 139°04'W) is located 3 km off the mainland of the Yukon Coast in the Canadian Beaufort Sea. The island is part of a push moraine made up of highly deformed marine sediments that were excavated and pushed into place by advancing ice sheets during the last glacial period (Rampton 1982, Mackay 1959). Covering an area of 108 km², it is characterized by a gently rolling landscape with a maximum elevation of 182 m a.s.l. Mean annual temperature on the island is -11°C (Pollard 1990). Permafrost in this area is continuous and can reach depths of 300 m (Smith & Burgess

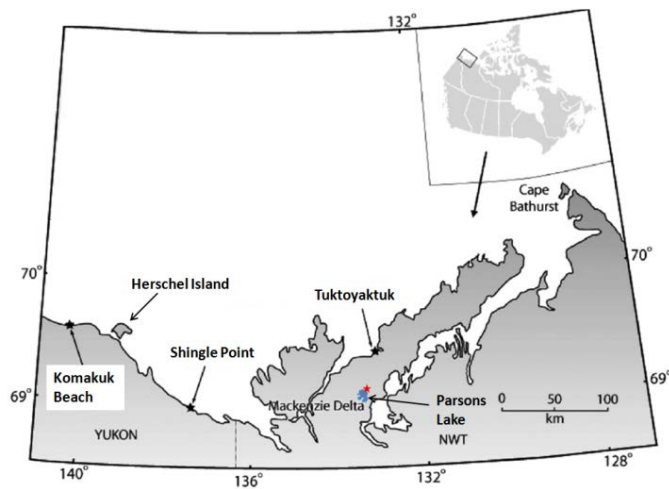


Figure 1. The locations of Herschel Island and Parsons Lake in the western Canadian Arctic (modified from Lantuit and Pollard 2008). Herschel Island is a push moraine made up of highly deformed marine sediments and is 3 km off the mainland of the Yukon Coast. The Parsons Lake area has been identified as a possible staging site for future hydrocarbon development.

2000). The surficial geology of Herschel Island is ice-rich with extensive massive ground ice characterized by large bodies of nearly pure ice, often several meters thick and extending for hundreds of meters (Fritz et al. 2011, Moorman et al. 1996, Pollard 1990, Bouchard 1974). These bodies of ice are largely exposed by retrogressive thaw slumps (Lantuit & Pollard 2008).

Parsons Lake (68°59'N, 133°33'W) is located above the tree line approximately 55 km southwest of Tuktoyaktuk. It has a mean annual air temperature of -8.8°C and mean annual precipitation of 248.6 mm (Environment Canada). Massive ground ice origins in this area are complex and can be both intrasedimental and glacial in nature (French & Harry 1990). Since the site has potential for the development of natural gas, extensive site assessment has been undertaken including the collection of numerous cores by ConocoPhillips Canada in 2004. Many of the cores confirm the presence of massive ground ice several meters thick. Materials overlying the massive ice are fine-grained glacial diamicton containing segregated ice, while the underlying sediments tend to be glacial fluvial sand. This stratigraphic sequence is a typical pattern observed in the Pleistocene Mackenzie Delta (e.g., Mackay & Dallimore 1992). When coupled with stable isotope studies carried out at a nearby retrogressive thaw slump (Fox 2011), the massive ice at Parsons Lake could conform to the segregation model for the Western Arctic (Rampton 1988). Irrespective of ice genesis, the surficial geology is made up of non-marine sediments and is therefore less salty compared to Herschel Island.

Methods

The TR1 capacitively-coupled resistivity system designed by Ohmmapper Geometrics was used for all surveys. The

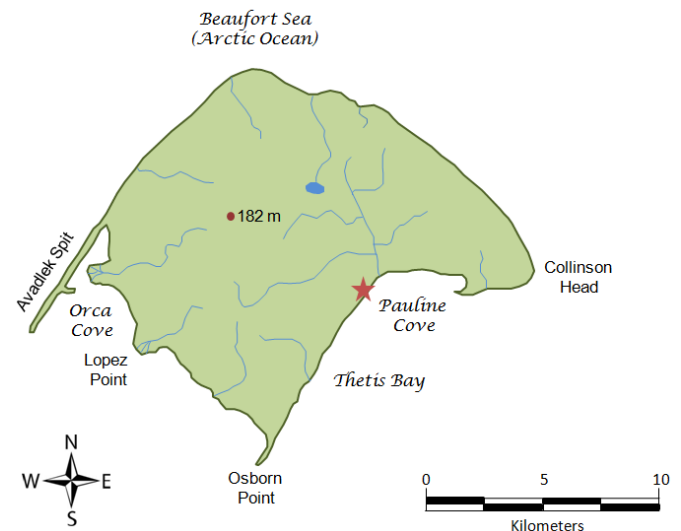


Figure 2. The location of Hawk's retrogressive thaw slump (star) on Herschel Island.

instrument is deployed in dipole-dipole configuration where the transmitter and receiver are placed in a line and separated by a user-defined distance. The system has a relatively high lateral resolution and relatively poor vertical resolution compared to alternative array types (Loke 2010). Pseudosections generated with Mapmap2000 were inverted using RES2DINV. Since there were no obvious outliers in the datasets, the smoothness-constrained inversion method was selected to compute the misfit between the logarithms of the measured and calculated apparent resistivity values. For a review of inversion techniques, the reader is referred to Loke et al. (2003). The data quality of the CCR surveys was analyzed through depth of investigation (DOI) tests introduced by Oldenburg and Li (1999). This is an empirical method that compares two inversions of the dataset using different reference resistivities for the model cells. The DOI approaches a value of zero where the two inversions generate similar values. In these zones, the cell resistivity is well constrained by the data. In areas where the model cells contain minimal information about the cell resistivity, the DOI approaches a value of 1. It is suggested that a reasonably cautious cut-off value is 0.1.

On Herschel Island, a 130-m CCR survey was conducted above and parallel to the headwall of a retrogressive thaw slump 20 m high near Thetis Bay (Fig. 2). The survey revealed alternating zones of ice-poor permafrost and massive ice with ice wedges throughout. The stratigraphy of the slump headwall was mapped and sampled along a vertical profile through an area characterized by massive ice (Fig. 3). Samples were subsequently analyzed for a range of geochemical and sedimentological characteristics at the G.G. Hatch Laboratory at the University of Ottawa, Canada.

At Parsons Lake, a 250-m CCR survey intersecting three boreholes was carried out. The core logs show silty clay in the upper 2–3 m of the subsurface underlain by massive ice 7.5–14.2 m thick. In addition, a vertical sampling transect was conducted at a nearby retrogressive thaw slump (Fig. 4).



Figure 3. In order to correspond to CCR's depth of investigation, only sampling results from the upper 8 m of the subsurface are discussed in this paper (unit 3 and part of unit 4). Unit 3 is classified as ice-poor silty clay (2.5–4.0 m) and massive ice is represented in unit 4 (4.0–13.5 m).

Results

There are clearly resistive and conductive bodies exposed at the thaw slump on Herschel Island (Fig. 5). From 10 to 50 m, resistivity predominantly fluctuates between 5000 and 6000 ohm-m. This structure represents the massive ice just to the left of thick ice-poor permafrost. Within this structure, there are a few zones of relatively high resistivity values (>9000 ohm-m). Between 50 and 65 m, resistivities above the 0.1 depth of investigation (DOI) contour are relatively low (250–2000 ohm-m). This region is associated with ice-poor clayey permafrost and, as a consequence, greater unfrozen water content capacity. Due to enhanced signal attenuation, the 0.1 DOI contour is closer to the surface compared to the rest of the profile. On the right side of the thick ice-poor permafrost is a large ice wedge. As a consequence, relatively high resistivity values (>10,000 ohm-m) are recorded. Between 76 and 89 m, another massive ice unit is observed with resistivities gradually increasing from the structure's perimeter (≈ 5000 ohm-m) to the middle portion of the upper layer (just over 10,000 ohm-m). At 89 m, there is an abrupt near-surface transition from massive ice to ice-poor permafrost; as a result, resistivities primarily oscillate between 3000 and 4000 ohm-m.

At Parsons Lake, CCR shows more resistive signatures for

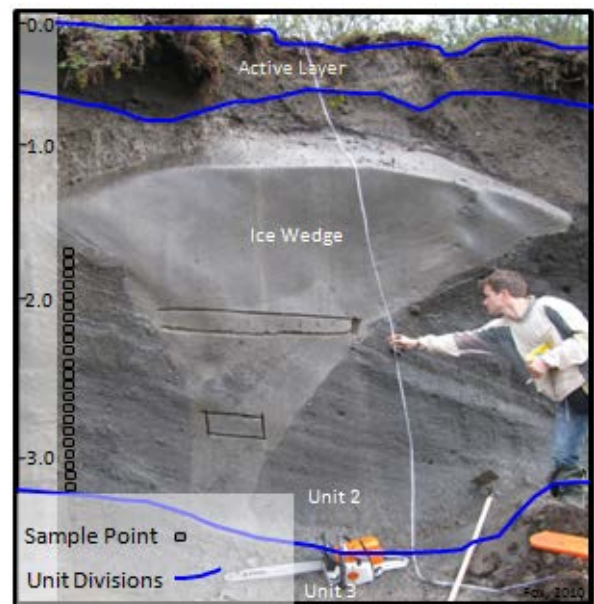


Figure 4. Vertical sampling transect of intrasedimental massive ice at a retrogressive thaw slump near Parsons Lake.

massive ice bodies (Fig. 6). Between 50 and 85 m, as well as between 165 and 240 m, resistivity fluctuates between 25,000 and 40,000 ohm-m. Furthermore, the DOI tests suggest that these results are reliable. In the middle of the cross-section (88–145 m), there is a more conductive zone, which is interpreted as icy sediments. Here, resistivities range from 2800 to 6200 ohm-m. According to the borehole logs for P6, P7, and P8, the depths to the top of massive ground ice range from 1.8 to 2.4 m. Resistivity, however, does not begin to plateau until a depth of 5 m for the massive ground ice. This demonstrates the relatively poor vertical resolution of a dipole-dipole configured CCR system. At Herschel Island, the resolution is noticeably better because a smaller interval between changing transmitter-receiver separations was employed.

Out of the seven massive ice samples on Herschel Island, the average conductivity is 5348 $\mu\text{s}/\text{cm}$ and the standard deviation is 1256 $\mu\text{s}/\text{cm}$ (Fig. 7). At Parsons Lake, the conductivities range from 1360 to 2018 $\mu\text{s}/\text{cm}$ in the shallow subsurface (1.8–2.1 m). Conversely, conductivities fluctuate between 675 and 960 $\mu\text{s}/\text{cm}$ from 2.2 to 4.7 m depths. Out of all 20 samples, the massive ice has an average conductivity of 907 $\mu\text{s}/\text{cm}$ and a standard deviation of 306 $\mu\text{s}/\text{cm}$.

Discussion

Laboratory analyses show that the average conductivity of the massive ice from Herschel Island is 5.6 times greater than Parsons Lake. The higher levels of dissolved solids for the Herschel Island ground ice are interpreted as a result of source water interaction with marine sediments as compared to Parsons Lake, where the water prior to freezing interacted with non-marine sediments. As shown in Figure 8, the mean concentration of cations in the massive ice on Herschel Island is 1120.1 ppm compared to 177.2 ppm for Parsons Lake. In

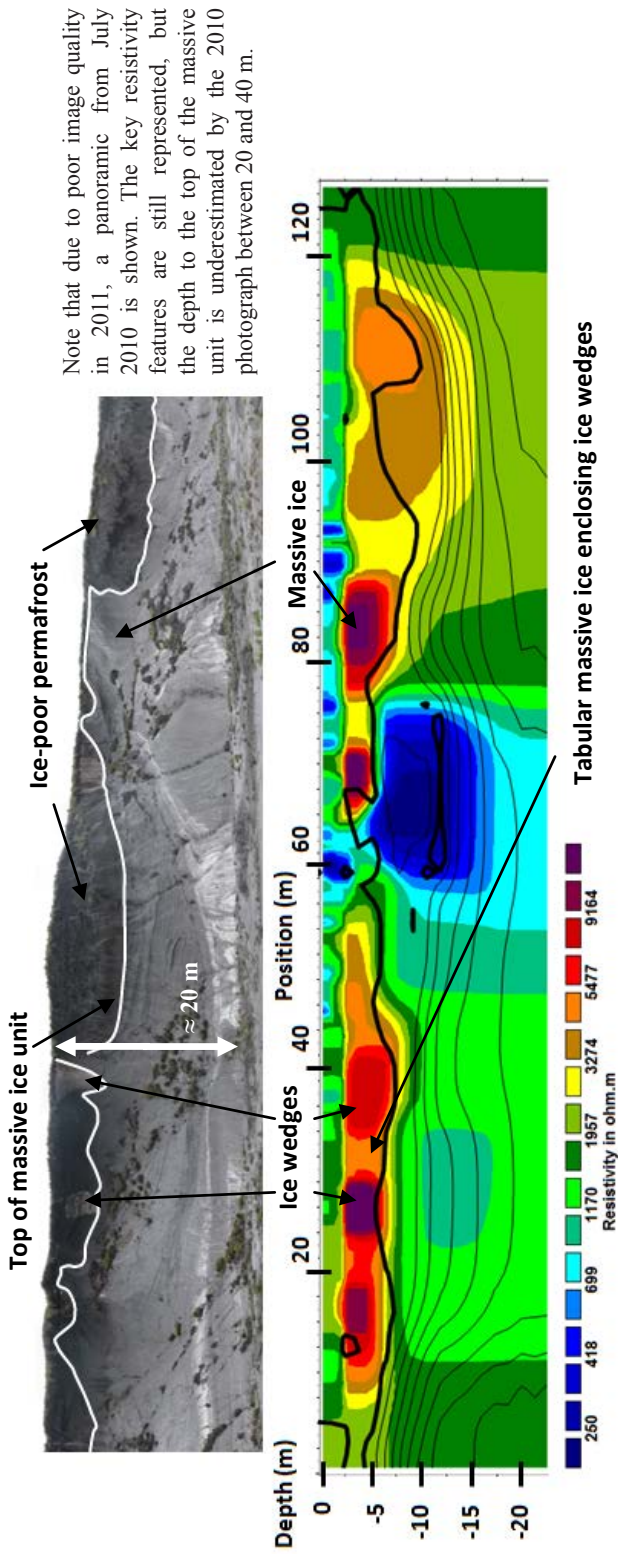


Figure 5. DOI tests are superimposed upon the Herschel Island CCR data collected in July 2011. The DOI contour interval is 0.1 with smaller values being closer to the surface. All model cells above the 0.1 DOI contour (thick black line) are considered reliable, whereas model cells below the 0.1 contour are not. Resistivity for massive ice usually ranges between 5000 and 6000 ohm-m but can reach values close to 9000 ohm-m for ice wedges. For ice-poor permafrost, particularly the middle section, resistivity can range from 250 to 2000 ohm-m.

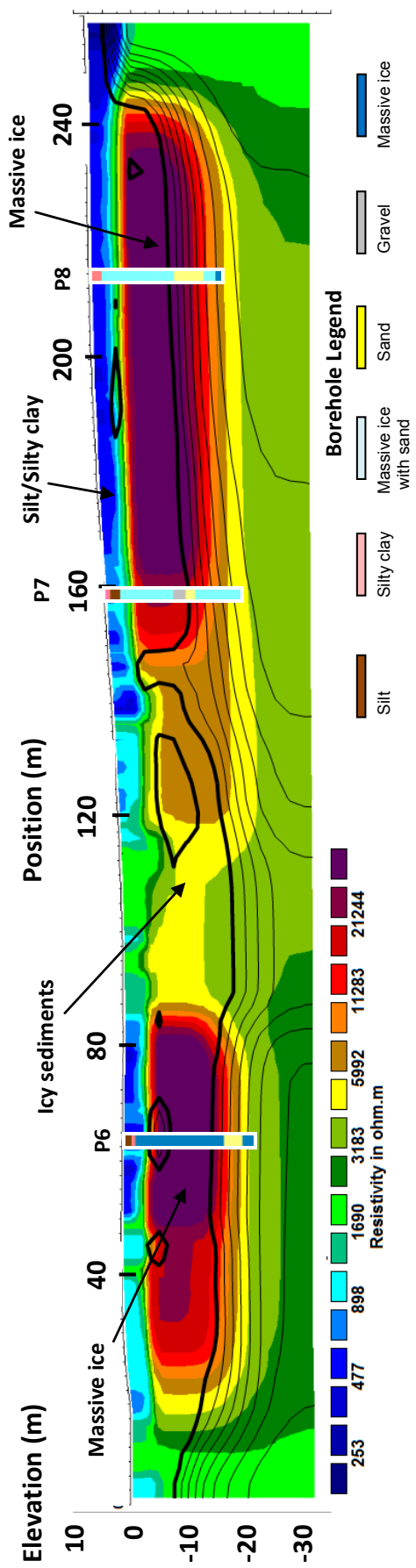


Figure 6. DOI tests are superimposed upon the Parsons Lake CCR data collected in July 2010. The DOI contour interval is 0.1 with smaller values being closer to the surface. All model cells above the 0.1 DOI contour (thick black line) are considered reliable, whereas model cells below the 0.1 contour are not. Resistivity for massive ice ranges from 25,000 to 40,000 ohm-m, while it oscillates between 2800 and 6200 ohm-m for icy sediments.

addition, salt (i.e., Na) occupies a much larger proportion of the total concentration of ions on Herschel Island. If all the samples are grouped together, Na represents 72.4% of dissolved ions on Herschel Island compared to 17.4% at Parsons Lake.

Comparisons between CCR surveys at the two sites illustrate that the contrast in electrical properties is still observable under frozen conditions. Hence concentrations of dissolved solids (Na in particular) likely occur as brine films. If so, the depression of the freezing point could result in continuous unfrozen water films and, thus, pathways for electric currents. This might explain why the resistivity observed for massive ice at Herschel Island is substantially lower than that of Parsons Lake. The pattern of inter-crystalline brine films will be related to ice fabrics dominated by vertically oriented ice crystals (Pollard 1990). Hence there is potentially a directional bias for intrasedimentally formed ice crystals and, thus, a preferred connectivity for the entrapped brine.

The relatively high resistivity zones in the massive bodies on Herschel Island could be a result of ice wedges embedded throughout the profile. Note that there could also be ice wedges adjacent to the headwall that are not yet exposed but still close enough to the survey line to impact the results. Since the water for ice wedges originates from an atmospheric source, these structures are characterized by relatively low concentrations

of dissolved ions. Hence no significant depression of the freezing front is expected and, thus, unfrozen water content is negligible. As a result, one might suspect that the resistivities of the ice wedges at Herschel Island should be similar to the massive ice at Parsons Lake. This is not the case because when the CCR detects an ice wedge, the output is a combination of the latter and the enclosing material.

Conclusion

This study demonstrates that capacitively-coupled resistivity surveys can generate drastically different outputs for similar massive ice volumes. Since Herschel Island is largely made up of highly deformed marine sediments, there exists a large concentration of dissolved ions (1120.1 ppm), and Na represents 72.4% of them. On the other hand, Parsons Lake showed a relatively low number of dissolved ions (177.2 ppm), 17.4% of which were Na. As a consequence, the average conductivity of melted massive ice samples was 5.6 times greater at Herschel Island compared to Parsons Lake. An electrical contrast of similar magnitude was observed during frozen conditions using CCR. As a result, the key findings of this research are as follows:

- CCR can effectively distinguish ice-poor permafrost from massive tabular ground ice, as well as ice wedges.
- Resistive signatures for nearly sediment-free massive ice bodies are non-unique and are largely a function of geochemical properties.
- The low resistivity values observed for massive ice on Herschel Island are likely because of brine films that depress the freezing point and hold significant quantities of unfrozen water.

Understanding the heterogeneity of geophysical responses for massive ice as a function of geochemically-induced unfrozen water content is critical for developing accurate subsurface mapping products. Improving the use of CCR to detect the nature and extent of ground ice bodies should enable scientists to estimate the thermokarst risk of an area with a greater degree of confidence in the future.

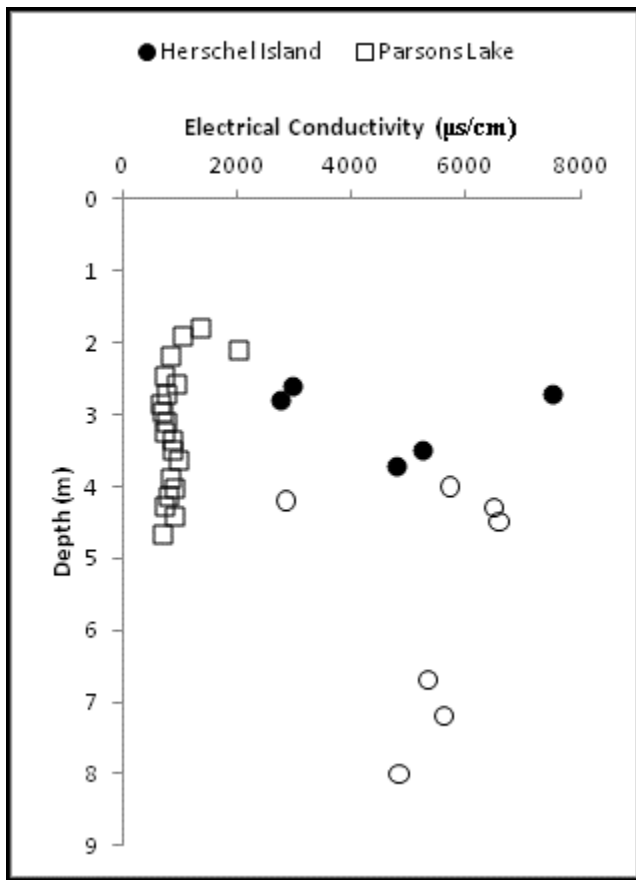


Figure 7. Electrical conductivity is plotted as a function of depth, where massive ice samples are the non-filled shapes. For massive ice, the conductivity on Herschel Island is 5.6 times greater than Parsons Lake.

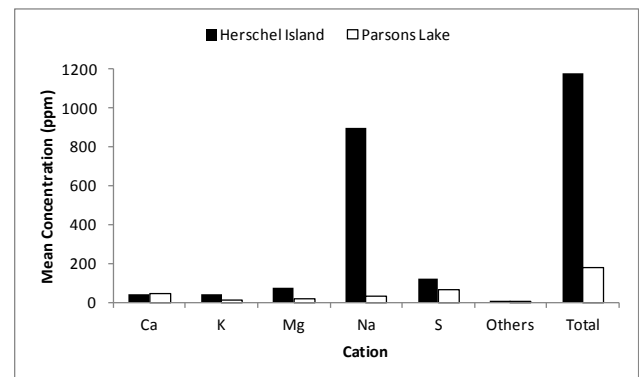


Figure 8. Cation concentrations in massive ground ice on Herschel Island (3 samples) and at Parsons Lake (6 samples).

References

- Bouchard, M. 1974. Geologie de depots de L'île Herschel, Territoire du Yukon, thèse M.Sc. non publiée Université de Montréal, Montréal.
- Calvert, H.T., Dallimore, S.R., & Hunter, J.A. 2001. Application of geophysical techniques for mapping ice-bearing sediments, Mackenzie Delta, Western Arctic, Canada. Conference on the Geophysical Detection of Subsurface Water on Mars, Abstract 7041.
- De Pascale, G.P., Pollard, W.H., & Williams, K.K. 2008. Geophysical mapping of ground ice using a combination of capacitive coupled resistivity and ground-penetrating radar, NWT, Canada. *Journal of Geophysical Research* 113, F02S90.
- Environment Canada. National Climate Data and Information Archive.
- Fortier, R., Allard, M., & Seguin, M.K. 1994. Effect of physical properties of frozen ground on electrical resistivity logging. *Cold Regions Science and Technology* 22: 361-384.
- Fox, D. 2011. Observations of massive ground ice, Herschel island, Yukon. MSc thesis, McGill University, Montreal, Canada.
- French, H.M. & Harry, D.G. 1990. Observations of buried glacier ice and massive segregated ice, Western Arctic coast, Canada. *Permafrost and Periglacial Processes* 1: 31-43.
- Fritz, M., Wetterich, S., Meyer, H., Schirrmeister, L., Lantuit, H., & Pollard, W.H. 2011. Origin and characteristics of massive ground ice on Herschel Island (western Canadian Arctic) as revealed by stable water isotope and Hydrochemical signatures. *Permafrost and Periglacial Processes* 22(1): 26-38.
- Hauck, C., Vonder Muhll, D., & Maurer, H. 2003. Using DC resistivity tomography to detect and characterize mountain permafrost. *Geophysical Prospecting* 51: 273-284.
- Hauck, C.H. 2002. Frozen ground monitoring using DC resistivity tomography. *Geophysical Research Letters* 29(21), 2016, doi:10.1029/2002GL014995, 2002.
- Kneisel, C., Hauck, C., Fortier, R., & Moorman, B. 2008. Advances in geophysical methods for permafrost investigations. *Permafrost and Periglacial Processes* 19: 157-17.
- Lantuit, H. & Pollard, W.H. 2008. Fifty years of coastal erosion and retrogressive thaw slump activity on Herschel Island, southern Beaufort Sea, Yukon Territory, Canada. *Geomorphology* 85(1-2): 84-102.
- Loke, M.H. 2010. Tutorial: 2D and 3D electrical imaging surveys.
- Loke, M.H., Acworth, I., & Dahlin, T. 2003. A comparison of smooth and blocky inversion methods in 2D electrical imaging surveys. *Exploration Geophysicists* 34: 182-187.
- Mackay, J.R. & Dallimore, S.R. 1992. Massive ice of the Tuktoyaktuk area, western Arctic coast, Canada. *Canadian Journal of Earth Sciences* 29(66): 1235-1249.
- Mackay, J.R. 1959. Glacier ice-thrust features of the Yukon coast; Geographical Bulletin, no. 13, 5-21.
- McNeill, J.D. 1980. Electrical conductivity of soils and rocks. Geonics Letd., Technical Note TN-5.
- Moorman, B.J., Michel, F.A., & Wilson, A. 1996. ¹⁴C dating of trapped gases in massive ground ice, Western Canadian Arctic. *Permafrost and Periglacial Processes* 7(3): 257-266.
- Muller, S.W. 1947. *Permafrost or permanently frozen ground and related engineering problems*. L.J.W. Edwards, Ann Arbor.
- Oldenburg, D.W. & Li, Y. 1999. Estimating depth of investigation in dc resistivity and IP surveys. *Geophysics* 64(2): 403-416.
- Pollard, W.H. 1990. The nature and origin of ground ice in the Herschel Island area, Yukon Territory. In *Proceedings, Fifth Canadian Permafrost Conference*, Quebec, Canada. 23-30.
- Rampton, V.N. 1988. Origin of massive ground ice on Tuktoyaktuk Peninsula, Northwest Territories, Canada: A review of stratigraphic and geomorphic evidence. 5th International Conference on Permafrost, Trondheim, Norway: 850-855.
- Rampton, V.N. 1982. Quaternary geology of the Yukon Coastal Plain. Geological Survey of Canada, Bulletin, 317.
- Scott, W., Sellman, P., & Hunter, J. 1990. Geophysics in the study of permafrost. In *Geotechnical and Environmental Geophysics*, S. Ward (Ed.), Society of Exploration Geophysicists, Tulsa: 355-384.
- Scott, W.J. & Mackay, J.R. 1977. Reliability of permafrost thickness determination by DC resistivity sounding. National Research Council, Technical Mem. 119: 25-38.
- Smith, S. & Burgess, M. 2000. Ground temperature database for northern Canada. Geological Survey of Canada Open File 3954.

Soil Moisture from Metop ASCAT Data at High Latitudes

Annett Bartsch, Thomas Melzer

Institute of Photogrammetry and Remote Sensing, Vienna University of Technology, Austria

Kirsten Elger, Birgit Heim

Alfred Wegener Institute for Polar and Marine Research, Potsdam, Germany

Abstract

Several global satellite-derived soil moisture datasets exist to date. They are based on analyses of passive or active microwave data. Resolution is coarse at 25 km, but temporal sampling is very high. A monitoring service for applications at high latitudes is implemented within the European Space Agency (ESA) data User Element (DUE) initiative ‘Permafrost.’ Measurements are based on Metop ASCAT, a European active microwave instrument (scatterometer, C-band). This study discusses comparisons between these data and in situ measurements from Alaska. Weekly averaged values have been compared to soil moisture records at several USDA stations. Results show that in situ soil moisture measurements at shallow depths reflect variations of satellite-derived relative near-surface soil moisture although the used sensor provides data at only 25 km resolution. There are indications that this relationship is impacted by micro-topography and temporal offsets related to snowmelt and active layer dynamics.

Keywords: remote sensing; active microwave; tundra; time series; soil moisture.

Introduction

Monitoring of soil moisture is valuable at high latitudes, especially in the context of climate change. Large areas at high latitudes are underlain by permafrost. Variations in parameters that impact heat conductivity play a role in the reaction of the subsurface frozen ground to changes in the atmosphere. Soil moisture information is one of the key parameters for modeling of permafrost extent (Marchenko et al. 2008). The moisture regime is important for active layer development (Shiklomanov et al. 2010). Soil moisture, together with temperature, is also a limiting factor for heterotrophic soil respiration. It is therefore important for estimation of carbon exchange (Kimball et al. 2009).

A range of satellite-derived global soil moisture datasets are currently available. They are derived using passive as well as active microwave sensors. Recently launched satellites (Metop ASCAT, SMOS) allow for continuity in monitoring at the global scale. ScanSAR technology enables the step from coarse (approximately 25 km) to medium (~1 km) resolution (Wagner et al. 2008, Bartsch et al. 2009a, Pathe et al. 2009). However, the majority of validation and application activities of such datasets are largely restricted to the mid- to low latitudes.

Challenges for the derivation of soil moisture in high latitudes include the following (Bartsch et al. 2011):

- frozen/snow-covered ground conditions,
- landscape heterogeneity,
- seasonal variation in landcover type (water-nonwater),
- micro-topographic patterning,
- scarcity of ground data,
- issues related to the surface vegetation such as the moss cover,
- large difference in scale between satellite and ground data.

These issues are addressed within the ESA DUE Permafrost (www.ipf.tuwien.ac.at/permafrost) and STSE ALANIS (www.alanis-methane.info) projects focusing on time series analysis using C-Band active microwave data from scatterometer (ASCAT) and Advanced Synthetic Aperture Radar (ENVISAT ASAR).

This paper details the comparison of the DUE Permafrost pan-Arctic satellite data-based near-surface soil moisture monitoring service with in situ soil moisture measurements in northern Alaska.

Data and Methods

Satellite products

Metop ASCAT is a scatterometer, which is an active microwave sensor operating in the C-band (~5.6 cm). Backscatter is recorded regularly with 25-km resolution, and the entire globe is covered within 2–3 days. Microwave backscatter during freeze/snow-free conditions increases with increasing soil moisture (Ulaby et al. 1982). The applicability for soil moisture retrieval has been demonstrated for C-band scatterometer in the past (e.g., Wagner et al. 1999a, 1999b, Zhribi et al. 2008). The relative surface soil moisture (%) can be derived by time series analyses. The minimum (dry reference) and maximum (wet reference) values are site (pixel) specific. Once they have been determined from a sufficiently long record, the measurements can be scaled between those boundary values and a relative near-surface soil moisture content (Wagner et al. 1999a, 1999b). Metop ASCAT measurements are available since 2007. Its predecessors, the scatterometer onboard the ERS1 and ERS2 satellites, allow a long-term (since 1991) estimate of the reference values (Naeimi et al. 2009).

Moisture can be derived only for unfrozen and snow-free conditions and, thus, high-latitude application requires

masking. An algorithm for the detection of the surface status has therefore been implemented using an empirical threshold-analysis algorithm also based on Metop ASCAT (Naeimi et al. 2012).

Measurements are not available daily or at regular intervals (every two to three days). To provide a value for each day and to compensate for missing data, weekly averages have been derived for each single day. All available measurements from the day of interest and the preceding six days are used as input for the averaging at each grid point. At the same time, data are projected from orbit format onto a regular grid (Naeimi et al. 2009). The final projection is the EASE Grid (polar stereographic). The data represent the relative near-surface soil moisture content in % (saturation). Records for the years 2007–2009 have been analyzed.

In situ data

The in situ soil moisture measurements are available through the United States Department of Agriculture- Natural Resources Conservation Service (USDA-NRCS). Seven sites from Arctic Alaska have been chosen; their locations are shown in Figure 1. The instrumentation differs, especially regarding the minimum depth of probes (Table 1). Stations Barrow 1, Betty Pingo, Atqasuk, Sagwon 1 & 2, and Toolik were selected. These sites have been investigated in many permafrost studies in the past (Hinkel & Nelson 2003). West Dock was not used due to its proximity to the coast. Barrow

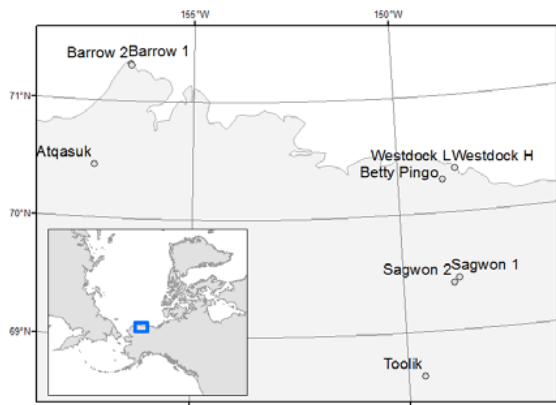


Figure 1. Location of arctic USDA stations.

is also close to the sea, but the lowest probe depth (5 cm) is available from this site. This location has also been the focus of several soil moisture and permafrost-related studies in the past (e.g., Hinkel et al. 1996, Engstrom et al. 2008, Shiklomanov et al. 2010). Measurements at Betty Pingo provide detail on the differences between the center, rim, and trough of a high-centered ice-wedge polygon.

Both in situ and satellite data relate to the dielectric properties of the soil. In situ measurements shown in the comparison were not masked when frozen. This allowed comparison of time periods in spring and autumn when the ground was not completely unfrozen.

Comparison

Time series for the three years are plotted for all selected stations in Figures 2 and 3. In all cases, the minimum probe depth has been chosen. Other depths are displayed in the case of Toolik and Sagwon 1. The Pearson correlation coefficient and corresponding soil depths are shown in Figure 4.

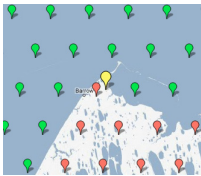
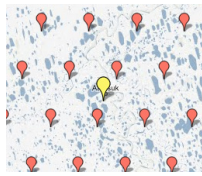

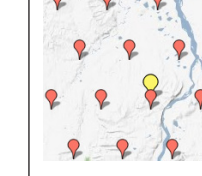
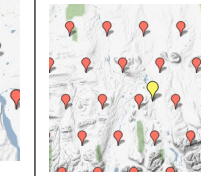
The satellite data show, in all cases, the characteristically high moisture after snowmelt and the gradual drying afterward. This is not reflected in all the in situ records (such as Atqasuk). The minimum depth of measurement at this site is comparably deep at 15 cm, and soil moisture values are rather stable all summer. However, the magnitude of change in the ASCAT data at Atqasuk was also lower than at the other sites.

Inter-annual dynamics

The spring peak always occurs earlier in the satellite data than is visible in the field probe measurements because the satellite data characterize the near surface. The timing difference is small for Barrow 1 in 2007 and 2008 as the probe is at a shallow depth.

Periods of increasing moisture occasionally occurred during the summer (Fig. 2). The level exceeded the spring maximum in the in situ measurements in a few instances. This is not the case for the ASCAT surface soil moisture, although variations are visible. An exception is the Barrow site, where variations are well reflected in magnitude and timing. The ASCAT footprint also includes numerous water bodies for this location (Table 1), which may introduce errors. If the distribution of

Table 1. Location of in situ soil moisture measurements sites (USDA) related to the ASCAT grid (satellite orbit oriented- <http://www.ipf.tuwien.ac.at/radar/dv/dgg/>) and available minimum depth of soil moisture probes.

| Station name | Barrow 1, 4 sub-sites | Atqasuk | Betty Pingo, polygon sub-sites | Sagwon 1/2 | Toolik |
|---|---|--|---|---|---|
| Distance (km) to closest ASCAT grid point | 3.77  | 6.6  | 2.73  | 2.27/8.11  | 5.56  |
| Minimum in situ depth (cm) | 5 | 15 | 10 | 10 | 9 |

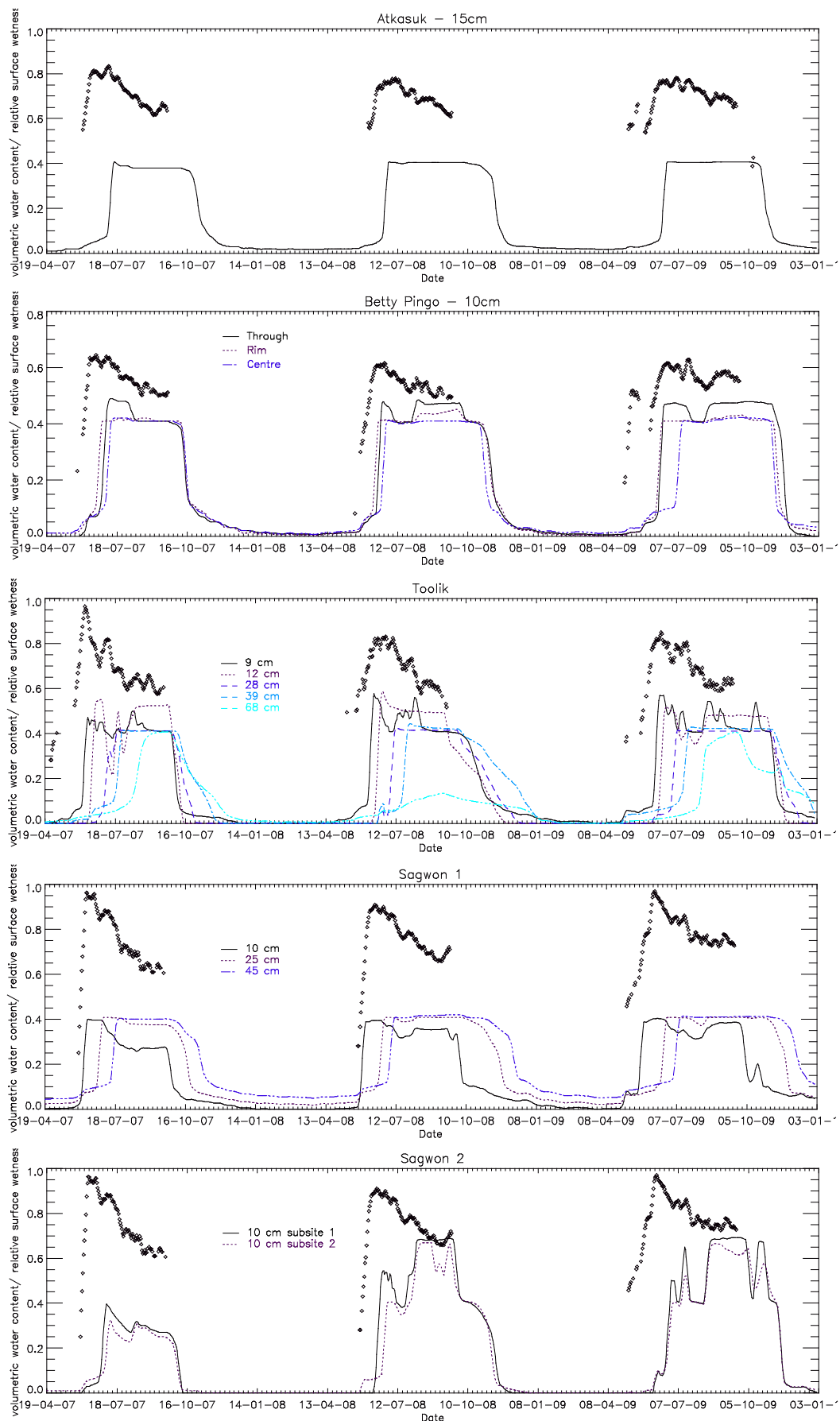


Figure 2. Comparison of Metop ASCAT relative surface soil moisture (diamonds) and USDA soil moisture measurements at various depths (lines) and locations.

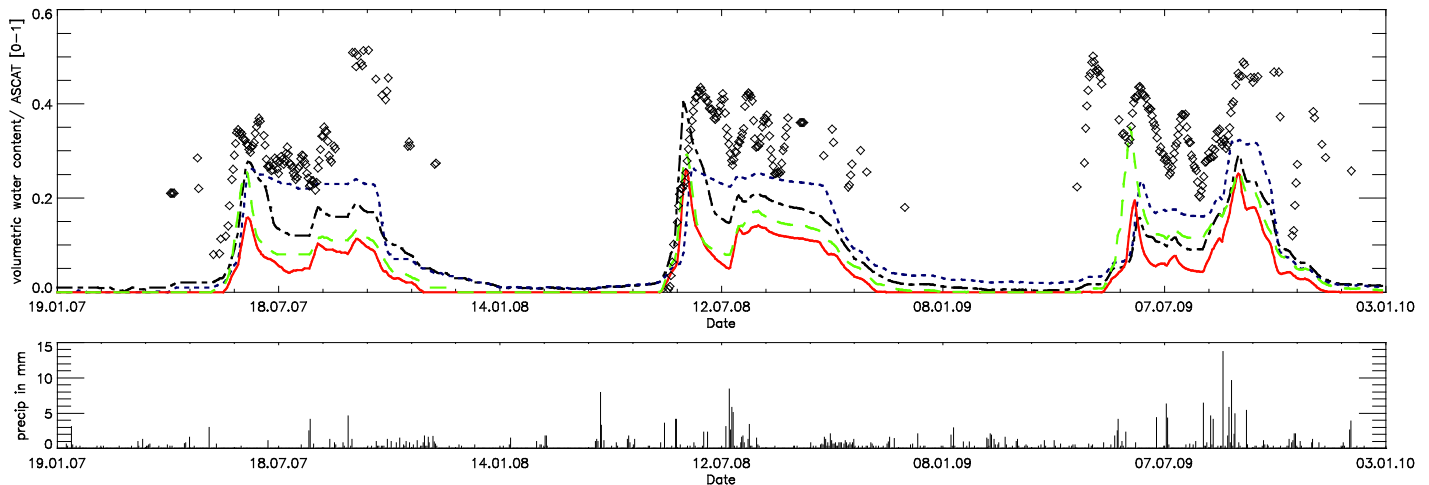


Figure 3. Comparison of Metop ASCAT surface wetness and USDA soil moisture measurements (5 cm depth) at site Barrow 1 (subsites : 1 – black, 2 –blue, 3-red, 4-green). Top: time series plot of weekly averages for ASCAT relative soil moisture scaled between 0 and 1 (diamonds), volumetric soil moisture values at USDA sub-sites (lines); Bottom: total daily precipitation in mm (WMO 512 dataset).

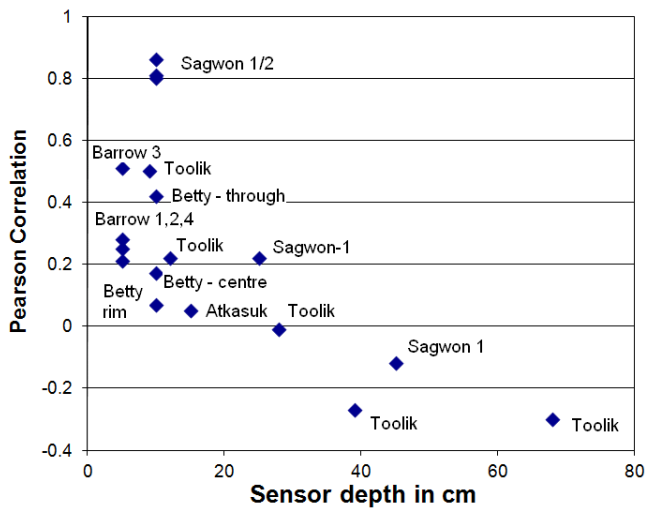


Figure 4. In situ volumetric and ASCAT relative near-surface soil moisture ($p < 0.05$ for sites with $R > 0.2$).

water is stable within the footprint, variations over time can nevertheless be attributed to soil moisture changes. The agreement is best at Sagwon 1 (10 cm), Sagwon 2 (10 cm), and Barrow (sub-site 3, 5 cm) (Fig. 4).

Variations in mid- to late summer coincide with rain events at Barrow (Fig. 3). The mid-summer surface increase in wetness is often initialized earlier in the soil than is seen from the satellite data at other stations. This can be observed in 2009 at Betty Pingo, 2008 at Toolik, and 2007–2008 at Barrow.

Seasonal variations show better agreement with near-surface probes (<12 cm depth) compared to deeper probes (25 cm). Especially interesting is that the measurements for the polygon trough at Betty Pingo compare better with the ASCAT measurements than the polygonal rim and center.

Intra-annual dynamics

The difference of mid-summer surface soil moisture levels between the years can be inferred from ASCAT. For example,

at Sagwon 2, soil moisture values are higher in 2008 and 2009 than in 2007. This is similar for Sagwon 1 and the polygon through measurements of Betty Pingo.

Discussion

The results from the Betty Pingo polygon measurements differ from a previous study on Samoylov in the Lena Delta (Heim et al. 2010, 2011). The Samoylov polygons are low-centered. The agreement was highest for the polygon center compared to slope measurements, whereas records at Betty Pingo indicate that satellite measurements corresponded better to the variations in the polygon trough. This can be explained by the impact of micro-topography; both polygon (low) centers and polygon troughs represent the topographically lower and wetter parts. The localized drying of the higher parts of the features seems to be uncoupled from the general moisture conditions in the surroundings, which are captured by the satellite data. Persistent saturation at low-lying sites may contribute in general to the observed differences. Variation is locally lower than what might be characteristic for the surrounding.

In some cases there are seasonally differing offsets between the satellite and in situ measurements. The advance of the soil moisture peak in spring reflects the earlier snowmelt and soil thaw at the surface. The summer lag may relate to the gradual increase of active-layer depth and increased availability of liquid water.

The possibility of capturing intra-annual variations also allows for studies of natural hazards. The ERS1/2 scatterometer historical data of ASCAT (Naeimi et al. 2009) allows derivation of long-term averages and anomalies. For example, dry anomalies can be related to fire events (Bartsch et al. 2009b). However, intra-annual variation observed at the tundra sites analyzed in this study are rather large compared to inter-annual variations that should be taken into consideration.

Many previous studies have investigated the possibility of

satellite-derived soil moisture validation with in situ data. In general, very shallow measurements correspond best to the satellite records. This has also been demonstrated in this paper. Greater moisture depth measurements are, however, required for many applications. These profile values of soil moisture can be modeled by temporal filtering which reflects percolation (e.g., SWI, Wagner et al. 1999). This cannot be directly applied, since the actual depth of the active layer would need to be taken into account in the case of permafrost. A previous study suggested that near-surface soil moisture (upper 7 cm) relates to greenness (NDVI) of vegetation of the North Slope in Alaska (Engstrom et al. 2008). C-band-derived soil moisture represents depths of up to 5 cm. There is, however, a significant scale difference in the satellite datasets investigated in this and the NDVI study, and this difference needs to be investigated in the future. Tools for downscaling may provide SAR (Synthetic Aperture Radar, <1 km spatial resolution) with measurements (Wagner et al. 2008, Pathe et al. 2009).

Conclusions

In situ soil moisture measurements at shallow depths reflect variations of satellite-derived relative near-surface soil moisture, although the sensor used provides data at 25-km resolution. There are indications that this relationship is impacted by micro-topography and temporal offsets related to snowmelt and active layer dynamics. These issues, and relationships to other environmental parameters such as vegetation, need to be further investigated.

Acknowledgments

This study has been carried out in the framework of the ESA initiatives DUE Permafrost (ESRIN Contr. No. 22185/09/1-OL). A. Bartsch has been the recipient of a research fellowship by the Austrian Science fund (FWF Elise Richter Program, V150- N21) during the course of the study.

References

- Bartsch, A., Doubkova, M., & Wagner, W. 2009a. ENVISAT ASAR GM soil moisture for applications in Africa and Australia. *Proceedings of The Earth Observation and Water Cycle Scieny Conference*, Frascati, November 2009.
- Bartsch A., Balzter H., & George, C. 2009b. Influence of regional surface soil moisture anomalies on forest fires in Siberia observed from satellites. *Environmental Research Letters* 4: 045021.
- Bartsch, A., Sabel, D., Wagner, W., & Park, S.E. 2011. Considerations for derivation and use of soil moisture data from active microwave satellites at high latitudes. *Proceedings IGARSS* 2011.
- Engstrom, R., Hope, A., Kwon, H., & Stow, D. 2008. The relationship between soil moisture and NDVI near Barrow, Alaska. *Physical Geography* 29: 38-53.
- Heim, B., Boike, J., Langer, M., Muster, S., Sobiech, J., Piel, K., & Bartsch, A. 2010. The Lena River Delta, Arctic Siberia: An arctic ground data observatory of the DUE Permafrost project. *Proceedings of the ESA Living Planet Symposium*, Bergen, 2010.
- Heim, B., Bartsch, A., Elger, K., Lantuit, H., Boike, J. Muster, S., Langer, M., Duguay, C., Hachem, S., Soliman, A., Paulik, Chr., Strozzi, T., & Seifert, F.-M. 2011. ESA DUE Permafrost: an Earth Observation (eo) Permafrost Monitoring System. *EARSeL eProceedings* 10: 73-82.
- Hinkel, K.M. & Nelson, F.E. 2003. Spatial and temporal patterns of active layer thickness at Circumpolar Active Layer Monitoring (CALM) sites in northern Alaska, 1995–2000. *Journal of Geophysical Research* 108: D2, 8168.
- Kimball, J.S., Jones, L.A., Zhang, K., Heisch, F.A., McDonald, K.C., & Oechel, W.C. 2009. A satellite approach to estimate land-atmosphere CO₂ exchange for boreal and arctic biomes using MODIS and AMSR-E. *IEEE Transactions on Geoscience and Remote Sensing* 47: 569–587.
- Marchenko, S., Romanovsky, V., & Tipenko, G. 2008. Numerical modeling of spatial permafrost dynamics in Alaska. *Proceedings of the Ninth International Conference on Permafrost*. D.L. Kane, K.M. Hinkel (eds.). Institute of Northern Engineering, University of Alaska Fairbanks, 1125–1130.
- Naeimi, V., Scipal, K., Bartalis, Z., Hasenauer, S., & Wagner, W. 2009. An improved soil moisture retrieval algorithm for ERS and METOP scatterometer observations. *IEEE Transactions on Geoscience and Remote Sensing* 47 (7): 1999–2013.
- Naeimi, V., Paulik, C., Bartsch, A., Wagner, W., Kidd, R., & Boike, J. 2012. Extracting information on surface freeze/thaw conditions from backscatter data using an empirical threshold-analysis algorithm. *IEEE Transactions on Geoscience and Remote Sensing* 99, 1-17.
- Pathe, C., Wagner, W., Sabel, D., Doubkova, M., Basara, J.B. 2009. Using ENVISAT ASAR Global Mode Data for Surface Soil Moisture Retrieval Over Oklahoma, USA. *IEEE Transactions on Geoscience and Remote Sensing* 47: 468-480.
- Shiklomanov, N.I., Streletskiy, D.A., Nelson, F.E., Hollister, R.D., Romanovsky, V.E., Tweedie, G.E., Bockheim, J.G., & Brown, J. 2010. Decadal variations of active layer thickness in moisture controlled landscapes, Barrow, Alaska. *Journal of Geophysical Research* 115: G00I04.
- Ulaby, F.T., Moore, R.K., & Fung, A.K. 1982. *Microwave Remote Sensing—Active and Passive*, vol. II. Artech House, Norwood, Mass.
- Wagner, W., Pathe, C., Doubkova, M., Sabel, D., Bartsch, A., Hasenauer, S., Blöschl, G., Scipal, K., Martýnez-Fernández, J., & Löw, A. 2008. Temporal stability of soil moisture and radar backscatter observed by the advanced synthetic aperture radar (ASAR). *Sensors*. 8: 1174–1197.
- Wagner, W., Lemoine, G., Borgeaud, M., & Rott, H. 1999a. A study of vegetation cover effects on ERS scatterometer Data. *IEEE Transactions on Geoscience and Remote Sensing* 37(2): 938–948.

- Wagner, W., Noll, J., Borgeaud, M., & Rott, H. 1999b. Monitoring soil moisture over the Canadian prairies with the ERS scatterometer. *IEEE Transactions on Geoscience and Remote Sensing* 37: 206–216.
- Zhribi, M., André, C., & Decharme, B. 2008. A method for soil moisture estimation in Western Africa based on the ERS scatterometer. *IEEE Transactions on Geoscience and Remote Sensing* 46 (2): 438–448.

A New Permafrost Research Tunnel: Methodology, Design, and Excavation

Kevin Bjella, Matthew Sturm

U.S. Army Cold Regions Research and Engineering Laboratory, Fairbanks, Alaska, USA

Abstract

During March and April of 2011, the first phase of excavation of a new underground permafrost research facility was completed at the Cold Regions Research and Engineering Laboratory's Alaska Permafrost Research Center at Fox, Alaska. The New Tunnel, 28.5 m long, was excavated adjacent to the existing 110-m-long permafrost tunnel. The New Tunnel was excavated using a rotary cutter mounted on an excavator. When completed, the New Tunnel will eventually expose over 300 m of warm, fine-grained, syngenetic permafrost. The Phase I excavation penetrated through one composite wedge, one large ice wedge, a range of cryostructures, and numerous paleosols that promise to provide a wealth of paleo-climate information. When completed, the New Tunnel facility will provide a three-dimensional block of permafrost bounded on four sides by passageways, allowing for many types of engineering, geophysical, and paleo-climatic studies.

Keywords: loess; massive ice; permafrost; syngenetic; tunnel; yedoma.

Introduction

The Cold Regions Research and Engineering Laboratory (CRREL) in Fairbanks, Alaska, has completed the first phase of excavation and construction of a new underground permafrost research facility. This new excavation is adjacent to the existing CRREL Permafrost Tunnel located in Fox, Alaska. When completed, the new excavation will expand the underground passageways available for research nearly threefold. Combined, these facilities (plus a new building with lab space, cold rooms, and offices) will constitute the Alaska Permafrost Research Center (APRC).

Background

Setting

The CRREL Permafrost Tunnel is located 15 km north of Fairbanks, Alaska, in hills that are part of the Yukon-Tanana uplands. Specifically, it is located in Goldstream Creek valley, which drains the watershed directly north of Fairbanks. During the more rigorous climate of the Late Pleistocene, this valley became blanketed with windblown glacial silt (loess) that was transported north from the rivers draining the Alaska Range. Pewe (1975) identifies two silt units of interest in the area. The near-surface unit is the Ready Bullion Formation of Holocene age. It is composed of reworked silt and colluvium; the reworking has resulted in thicker sections in the valley bottoms than on the upper hill slopes. The lower unit is the Goldstream Formation of Wisconsin age and is composed of homogenous windblown loess with some reworking. Sellmann (1967) identified two sections within the Goldstream Formation in the tunnel stratigraphy. They are differentiated by their ice wedge development. Ice wedge tops in the lower section are just visible in the walls of the Old Tunnel, while the bottoms of an upper tier of ice wedges are visible near the ceiling of the Old Tunnel. The two sections are separated by a thaw unconformity (Hamilton 1988). The upper and lower

silt formations lie unconformably over an auriferous alluvial unit, the Fox Gravels, of late Pliocene to middle Pleistocene age. This, in turn, lies unconformably on the weathered pre-Cambrian schist bedrock.

Permafrost in the Goldstream Creek area is discontinuous, existing primarily in wet valley bottoms and on lower northerly exposed hill slopes. The permafrost was created syngenetically during the loess deposition. A temporally continuous frozen sequence beginning at approximately 40 kya and extending to the present exists and can be found in a complete vertical loess sequence in the tunnel. The temperature of this permafrost at the depth of zero annual amplitude is approximately -0.8°C (Bjella 2008). The permafrost extends approximately 30 m to 50 m below the surface but can exceed a thickness of 100 m in places (Pewe 1975). Due to the mode of permafrost development, the cryostructures contained within the permafrost are very diverse (Bray et al. 2006, Kanevisky et al. 2008, Shur et al. 2004). Segregated ice, massive ice (ice wedge polygons), paleosols, lacustrine cave ice, and erosional and climate change induced boundaries are all found in the loess sequences.

The Old Tunnel

The original excavation was completed by the U.S. Army Corps of Engineers using continuous mining methods in the winters of 1963–64, 1964–65, and 1965–66 (Sellmann 1967). This resulted in an adit (a horizontal mine passage) with a length of 110 m (Fig. 1). The goal of the excavation was to understand the challenges involved in the expedient placement of men and equipment underground in permafrost areas. A winze (an inclined adit) was driven by the U.S. Bureau of Mines (USBM) in 1968 and 1969 using drill and blast, thermal relaxation, and hydraulic relaxation methods (Chester and Frank 1969). The winze drops obliquely at an incline of 14% for 45 m, passing into the Fox Gravels and ultimately into the weathered bedrock. The goal of the winze excavation was to better understand the issues associated with drilling and blasting ice-bonded, shock

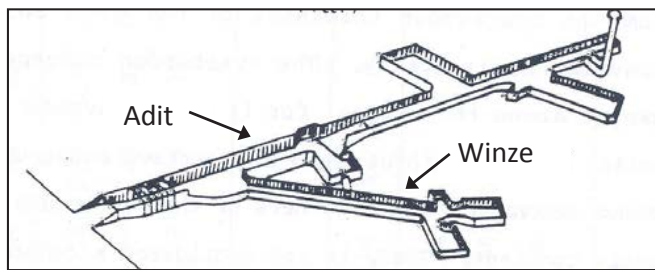


Figure 1. Old Tunnel isometric view.

absorbing earth materials. The adit begins at a silt escarpment created during placer gold mining operations in the 1930s, which produced dredge tailing piles adjacent to the escarpment. These piles were leveled to create the base elevation for the portal and the beginning of the adit. The escarpment is 10 m high at the portal, and the surface above the tunnel rises gently along the axis of the adit, leaving approximately 7 m of overburden at the portal, approximately 14 m of overburden at the rear of the adit, and 18 m of overburden over the Gravel Room. The average geometry of the Old Tunnel is 4.0 m in width by 2.5 to 3.0 m in height.

The Old Tunnel has proved to be an extremely valuable all-weather, all-season permafrost research facility. To date more than 70 peer-reviewed publications have been produced on topics including geocryology, paleoscience, geochemistry, permafrost engineering, planetary permafrost, and mining engineering, to name but a few. These studies have been performed generally within the confines of the original excavation geometry, with some exceptions being small- to medium-sized side rooms that were created for specific investigations.

Preliminary Work

Purpose

One of the long-term goals in excavating the New Tunnel is to create a large underground facility that allows access to a larger volume of permafrost than is currently available in the Old Tunnel. Another objective is to expose fresh geologic materials from which samples can be taken for dating, paleo-ecological reconstruction, and DNA analyses using the latest techniques and methods. It is envisioned that the new and old tunnels combined will allow us to delineate a three-dimensional block of permafrost more than 100 m on a side, where all features can be mapped, including wedge ice, segregated ice, and cryostructures. This block of permafrost, mapped in more detail than any other known permafrost section, is expected to function as a test bed for surface and stand-off geophysical methods for characterizing permafrost and its thermo-physical state. In addition, the engineering and excavation methods used in creating the tunnel have already provided useful information related to permafrost engineering and infrastructure, and they are expected to continue to do so.

Site location

The New Tunnel could have been excavated in several different sites near Fairbanks, but its location adjacent to

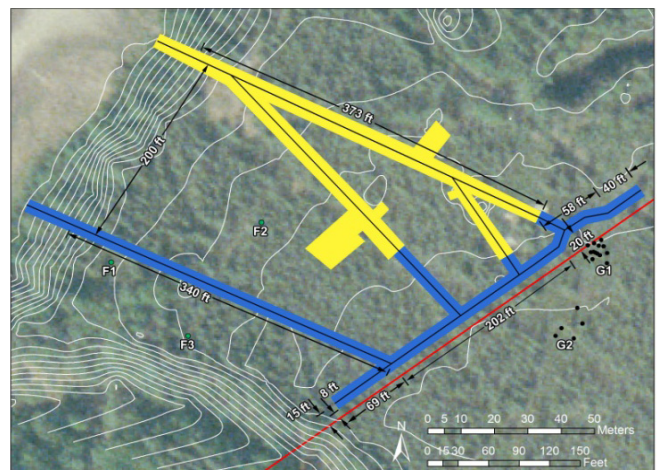


Figure 2. Old Tunnel (yellow) and New Tunnel (blue) plan view.

the Old Tunnel will make spatial and temporal correlations between the old and new tunnels possible. Furthermore, critical infrastructure, such as three-phase electric power and all-weather road access, already existed at the Old Tunnel. Most importantly, the stratigraphy and permafrost features exposed in the Old Tunnel provided assurance that the New Tunnel would intersect scientifically interesting features, while lessons learned during the excavation of the Old Tunnel could be applied to ensure the best possible construction practices. Because of property boundaries and terrain features, specifically two deep erosional gullies and a small lake, the location of the New Tunnel was constrained to a 150-m-long reach of the existing silt escarpment. The Old Tunnel bisects this reach, so it was determined to locate the New Tunnel on the southwest side of the Old Tunnel (Fig. 2).

Borehole drilling

To further constrain the New Tunnel location, nine borings (Fig. 2) were completed in late March 2010 using a combination of direct push technology (DPT) and air rotary drill tools. The DPT was capable of providing a 1.5 m x 8.25 cm (length x diameter) continuous core entirely through the sequence of silt, averaging 27 m in thickness. Two borings were done upslope of the CRREL property (by permit) to determine if Illinoian-aged silt (the Gold Hill Loess) was present (Pewe 1975); preliminary analysis indicates it is not. Three of the borings were driven to the top of the gravel, four of the borings were drilled through the gravel and into the bedrock, and two borings were relatively shallow and used as confirmation borings. The deepest boring was 36 m and penetrated partially weathered schist bedrock and was frozen throughout the hole. The borings indicated that the bedrock slopes upwards at a steeper gradient than the silt surface in the tunnel area. However, this is not steep enough within the CRREL property to intersect the New Tunnel driven at the same elevation as the existing tunnel.

Excavation methods

The original tunnel was excavated using the Alkirk Miner (Swinow 1970), which used two side-by-side, transverse

mounted disks with cutting teeth (picks). We considered using it again for the New Tunnel, but the unit was a prototype and was plagued with many deficiencies that prevented continuous high excavation rates (Swinzow 1970). Also, its current location and serviceability were unknown. Two other more reliable alternatives were considered: rotary milling and drill and blast. Although drill and blast would create larger blocks of material favorable for preservation of scientific specimens (plant material, ashbeds, mega fauna bone remains, etc.), the use of explosives was rejected due to the hazard and higher cost.

In the last two decades, various new configurations of rock/soil rotary milling equipment have been manufactured. Some of this equipment is purpose-built and in addition to excavating, it also continuously mucks (removes) the milled material. Included in this class of machines are tunnel boring machines, continuous miners, and roadheaders. Tunnel boring machines (TBM) tend to be complex and massive, have poor maneuverability, and require high capital investment. Continuous miners are less complex, less massive, and more moderate in cost. However, they are generally designed for forward advancement in relatively thin coal seams. Roadheaders are even less complex, less massive, and designed to excavate varying geometries. Their cost is also relatively modest. All of the purpose-built machines can be electrically powered, which is attractive when excavating in a thaw-sensitive environment and in a tunnel where ventilation is required if an internal combustion powered machine is used.

Other milling equipment has been designed as tools that can be mounted on any suitable excavator, skid steer loader, or other prime mover. This class is the simplest of milling machines and the least expensive because they can be mounted on conventional equipment that can be leased. Unlike the purpose-built machines, these milling tools do not allow for continuous mining, so additional time and equipment are required for mucking. Examples are rotary cutters and planers. Rotary cutters are either axially or transverse mounted drum assemblies. They are not complex, are of only moderate cost, and are very maneuverable. Planers are generally the same as rotary cutters but designed for milling of horizontal surfaces such as asphalt, so this type of unit requires further fabrication for mounting on an excavator or other prime mover.

Excavation test

Given a limited budget, we decided that we were best served leasing an excavator and purchasing a cutter that could be mounted on the excavator. We purchased an Eco-Cutter EC-25, a drum-style rotary cutter 62 cm in width. The drums are 45 cm in diameter and the entire assembly weighs 450 kg. The EC-25 was mounted on a John Deere 135C reduced tail swing excavator. This machine has a weight of 13 t and is powered with a 65 kW engine (Fig. 3). For the test, the cutter was mounted at the end of the stick, or the second section of the excavation arm. Removal of material (mucking) was to be conducted with a John Deere 333D rubber tired skid loader.

It has been shown that the cutting of frozen fine-grain soil is better accomplished utilizing a tool that shaves the



Figure 3. EC-25 mounted on the boom of a 13-t excavator for the Phase I excavation.



Figure 4. One drum of the EC-25 installed with chisel type picks



Figure 5. Chisel pick (left), conical pick (right).

ice-rich material, rather than impacting and causing fracture disaggregation (Sellmann and Mellor 1986). However, chisel type picks are not robust when excavating frozen coarse-grained materials. The carbide blades that are attached to the pick do not withstand the high impact forces. Conical picks, however, have proved to be very durable when excavating coarse-grained material. Because both frozen fine-grained and frozen coarse-grained material would be encountered in digging the tunnel, we purchased pick holders (pick blocks or sockets) that would allow for interchangeability of the two

types of picks: chisel type for frozen silt and massive ice, and conical type for frozen gravel (Fig. 4 and Fig. 5).

Only one chisel pick was offered from the manufacturer while nearly 20 conical type picks were available. The many conical styles differ in the shape and embedded length of the carbide tip and in the shape and diameter of the softer steel surrounding the carbide. Conical picks are allowed to rotate within the block to even the wear, while chisel picks are fixed from rotating to maintain attack angle.

We felt that it was crucial to test our ability to mill permafrost before beginning the tunnel; therefore, a test excavation was conducted 100 m to the northeast of the existing tunnel. The test was conducted December 14 to 17, 2010, at temperatures ranging from -30°C to -35°C . The John Deere 135C and the rotary cutter required 1.5 hours of heating with auxiliary oil heaters each morning before excavation and mucking could begin; however, no problems were encountered once the pre-heat was complete. The excavation proceeded in a cycle of approximately 45 minutes of milling followed by 15 minutes of mucking.

Because the equipment we were using did not allow for continuous mining, the muck pile quickly hindered the operator's ability to see lower-level grinding. We developed a technique in which we first milled the floor elevation to maintain grade, then milled upward allowing the muck to pile where the floor grinding had just occurred. Approximately eight hours were required to gain operator proficiency with this equipment. Also, it required five to six grinding cycles before we penetrated through the brittle, cold-soaked outer permafrost and into the more plastic, warmer permafrost at -1.0°C . Higher temperatures resulted in smaller size of the muck material and less bouncy operation of the cutter. Combined, these resulted in much higher penetration rates in warm permafrost.

Two full days of the tests were conducted on the frozen silt using chisel type picks. Dust generation utilizing this type of pick was negligible, and the picks showed no noticeable wear. The rate for the first day of testing was $2.8\text{ m}^3/\text{hr}$, and the swell factor (excavated volume/in situ volume) for the muck was 2.4. In the second full day of testing, the rate increased to $4.1\text{ m}^3/\text{hr}$, and the swell decreased to 1.5. The next two days we tested the excavation of frozen gravel and pure ice. Plastic lined wooden forms 2.5 m on a side and 1.2 m in height were constructed. One form was filled with water only, and the other was filled with dredge tailings from a local pit and saturated with water. These were allowed to sit for five weeks prior to the testing to insure complete freezing. The chisel type picks survived less than 10 minutes of milling on the frozen gravel where the attached carbide blades were prone to breaking off immediately, and in some instances, the shank of the pick fractured at the level of the block. The conical picks were then engaged on the frozen gravel, and they performed very well for more than 30 minutes without any breakage. Overall operation on the gravel was not pleasant, as the excavator was bucked about violently, the rotary drum stalled when it caught on the gravel, and the noise level was extreme. The chisel picks and conical picks performed well on the massive ice, both at a comparable rate.

In an effort to increase maneuverability, a John Deere 85D excavator (smaller than the John Deere 135C) with an offset boom was tested on February 12 and 13, 2011, with the EC-25. The 85D weighs 8.5 t with a 40 kW engine. Although the hydraulic flow and pressure met the specifications for the EC-25, the rpm of the cutter was significantly decreased, drastically affecting the excavation rate, with constant stalling of the drum. It was determined there was no easy alteration that would increase the hydraulic flow, so the 85D test was ended.

Layout

The new adit (south adit) was placed parallel to and 60 m southwest of the existing adit (north adit). We had concerns that this might be too close to the deep gully on the southwest margin of the property, but temperature measurements in borehole F3 (located between the south adit and the bluff [Fig. 2]) indicated no thermal impact from the exposed face. Taking full advantage of the available property, it was then determined to drive the south adit across the full width of the property to within 6 m of the southeast boundary line, where a T-intersection would be constructed. The east adit would be driven to the southwest to within 7 m of the bluff and also driven northeast along the southeastern property boundary line. The new adits would be connected to the Old Tunnel through the Gravel Room, north adit, and in several other places (Fig. 2).

Geometry

For scientific purposes, a narrow but tall adit maximizes geologic exposures and provides a greater geological time sequence. The new adit geometry was guided by this concept but was also determined by the type of equipment to be used to excavate the tunnel. Additionally, nowhere could the adit be close to the surface. Although overburden stress is decreased the closer the excavation lies to the surface, the bearing capacity at the surface is decreased, raising concerns about vehicle and other surface traffic. With the use of a 135C and the EC-25, the final cross-section of the adit was $4.25\text{ m} \times 4.25\text{ m}$ (H x W). This allowed the 135C to sit in the middle of the adit and excavate fully from side to side without requiring repositioning. Also, the 4.25-m height is reachable with this machine and sufficient for research purposes. The 135C can also fit through a standard 3 m x 3 m panel garage door which was planned as the portal access that would be installed after Phase I excavation was complete.

Excavation

Portal excavation

The new construction had to be done while there was still low-temperature winter air available for cooling. All construction needed to be complete, and the adit closed with an insulated portal, by the end of March. Excavation began on February 17, 2011. The portal structure physically required a horizontal depth of 8 m, a horizontal width of 9 m, and a vertical height of 5 m. This was accommodated by excavating

to those required dimensions starting at the toe of the existing slope. The portal area excavation was done using a Hitachi EX450, with a weight of 45 t and engine power of 260 kW. This machine was outfitted with 'frost teeth' and had little problem excavating the frozen active layer and underlying permafrost. This preparation work also provided a vertical face for adit initiation. Once this wedge of material was removed, the adit excavation could begin (Fig. 3). Although the final adit height would be 4.25 m, it was determined to initiate the adit height at 3.25 m and gradually increase to full height after 6 m of penetration in order to maintain structural integrity over the initial opening. The initial cut then provided 1 m of syngenetic permafrost over the ceiling (back), with an additional 1.5 m of active layer above the permafrost (Fig. 3).

Phase I

On February 23, 2011, Phase I adit excavation commenced using the JD135C equipped with the EC-25. It ended on March 11. A critical design change on the excavator for Phase I was mounting the EC-25 at the end of the boom, rather than the stick. This improved the machine geometry, which allowed maximum cutting height while maintaining as small a distance as possible between the operator and the cutter. The cutter was outfitted with conical picks, and mucking was performed using a John Deere 326D rubber tired skid loader. Once the excavator had advanced into the adit to the point where the exhaust system was fully in the excavation, subfreezing ambient air was delivered to the face via a 22 kW, 60-cm-diameter axial mounted fan system and collapsible ventilation bag hung from the ceiling. The cold ambient air maintained an average temperature in and around the excavator at -3°C . Additionally, the fan provided needed ventilation to remove diesel particulate matter, which was used in conjunction with an exhaust pipe mounted particulate scrubber. The permafrost temperature ranged from -4°C to -2°C , morning to afternoon.

Typical mill-muck cycle

The typical excavation cycle took this form:

1. The 135C would cut into the working face at the finish floor elevation, milling across the full width of the face. This was termed 'digging the gutter.'
2. The 135C would excavate the right half of the face (because the cab of the 135C was offset left of the boom). Grinding would commence from the gutter upwards to the ceiling and forward ~ 50 cm toward the face.
3. The 135C would withdraw and the skid steer would muck out the material lying at the foot of the right face.
4. The 135C would mill the left half face to the same horizontal depth as the right, and withdraw.
5. The skid steer would muck out the left side, and the adit floor would be scraped smooth.
6. Survey control would take place while other personnel were taking soil and vegetation samples and photographing the face. The floor and ceiling grade and the lateral alignments were maintained utilizing an optical total station located 30 m from the portal and set on the centerline of the adit alignment.



Figure 6. View of the New Tunnel. At the time of this photo, the face was at a horizontal depth of 26.3 m.

Excavation rate

At the beginning of Phase I, 45 minutes was required to excavate the full face, with mucking and surveying requiring an additional 30 minutes. The overall advance rate was $5.8 \text{ m}^3/\text{hr}$ over a 6-hour operating day. By the end of Phase I, an average of 40 minutes was required to excavate each half of the face, with the mucking requiring 25 minutes per half face. Surveying required an additional 15 minutes each cycle. The overall rate at the end of Phase I was $7.7 \text{ m}^3/\text{hr}$ over an 8-hour operating day. The best one-day horizontal advance was 3.4 m (for a 4.25-m x 4.25-m cross-section) in 8 hours.

The excavation rate was quite high in comparison to the size of the cutting unit, particularly when excavating pure ice. The frozen silt and ice shattered into pieces usually less than 7 cm in length although chunks over 15 cm were not uncommon. No adverse heating was noted on the rotary cutter that could cause buildup hindering the operation. Dust was minimal and did not obscure the operator's view or require excessive filtering. The conical picks used for the excavation test and the first half of Phase I experienced 'washing' of the steel surrounding the carbide insert. When this occurred, the picks would 'keel' preventing rotation and even wear. The conical picks were changed to another style manufactured with a beveled head carbide insert which effectively created an umbrella over the steel surrounding the insert. This prevented further washing, and pick rotation was assured. After the change, further wear on the picks was minimal.

Discussion

The final adit length was 28.4 m, well exceeding our target of 15 m (Fig. 6). The advance rate (all phases of milling, mucking, and surveying) increased by 25% during the life of the 13-day excavation, despite longer haulage as the adit advanced. This increase was primarily due to increasing operator experience. Using the equipment and methods described above, it would

be feasible to excavate 300 m of tunnel during a three-month winter period. By changing the mucking system or using a larger loading unit, and providing passing rooms along the adit, even this 300-m mark could be exceeded. Far faster advance rates could be achieved using a roadheader or other continuous mining machine but at additional cost and loss of maneuverability. In addition, these faster rates would require increased scrutiny to insure scientific interests are not compromised.

Refreezing of disaggregated silt onto the cutter picks never occurred, even on the warmest days of operation. In fact, the permafrost tended to mill better the warmer the air and soil. One deficiency noted is with the geometry of the excavator mounted rotary cutter, where a scalloped surface remained in the walls and ceiling after cutting. Finish milling will be required to obtain a science-quality surface.

Cryological features

The new excavation was entirely in syngenetic permafrost, which was gray in color after being excavated but within hours had oxidized to a tan buff color. The two distinct ice wedge units from the Old Tunnel were uncovered in the New Tunnel, at approximately the same elevation and polygonal diameter. A very large ice wedge encountered at the 18-m mark extends from the floor to the ceiling and is nearly 3 m in width. Varying cryostructures were encountered ranging from micro-lenticular to reticulate chaotic.

The reworked zone in the Old Tunnel near the portal is the location of mega fauna remains. Woody fragments and other organic material were not encountered in the New Tunnel. The only remains were two bison horns (*Bison priscus*) found in the syngenetic permafrost at the base of the new portal.

Conclusions

A new underground excavation has been started at the existing CRREL Permafrost Tunnel. The Phase I excavation achieved 28 m of the 300-m proposed length for the new facility. When completed, an approximate three-dimensional block of warm, fine-grained permafrost will be available for all aspects of permafrost research.

References

- Bjella, K. 2008. The effect of near-freezing temperatures on the stability of an underground excavation in permafrost. In *NICOP 2008: Proceedings of the Ninth International Conference on Permafrost*. Edited by Douglas L. Kane and Kenneth M. Hinkel. University of Alaska Fairbanks, June 29–July 3, 2008, 1: 119–124.
- Bray, M.T., French, H.M., & Shur, Y. 2006. Further cryostratigraphic observations in the CRREL Permafrost Tunnel, Fox, Alaska. *Permafrost and Periglacial Processes* 17: 233–243.
- Chester, J.W. & Frank, J.N. 1969. *Fairbanks placers fragmentation research final report*. Minneapolis: Twin Cities Mining Research Center, U.S. Bureau of Mines, Heavy Metals Program, 52 pp.
- Hamilton, T.D., Craig, J.L., & Sellmann, P.V. 1988. *The Fox permafrost tunnel: A late Quaternary Geologic record in central Alaska*. GSA Bulletin; June 1988; v. 100; no.6: 948–969.
- Kanevskiy, M., Fortier, D., Shur, Y., Bray, M., & Jorgenson, T. 2008. Detailed cryostratigraphic studies of syngenetic permafrost in the winze of the CRREL permafrost tunnel, Fox, Alaska. In *NICOP 2008: Proceedings of the Ninth International Conference on Permafrost*. Edited by Douglas L. Kane and Kenneth M. Hinkel. University of Alaska Fairbanks, June 29–July 3, 2008, 1: 889–894. .
- Pewe, T.L. 1975. *Geologic hazards of the Fairbanks area, Alaska*. Special Report 15, State of Alaska Division of Geological and Geophysical Surveys.
- Sellmann, P.V. & Mellor, M. 1986. *Drill bits for frozen fine-grained soils*. Special Report SR 86-27. Hanover, NH: Cold Regions Research and Engineering Laboratory.
- Sellmann, P.V. 1967. *Geology of the USA CRREL Permafrost Tunnel in Fairbanks, Alaska*. Technical Report 199. Hanover, NH: Cold Regions Research and Engineering Laboratory.
- Shur, Y., French, H.M., & Bray, M.T. 2004. Syngenetic permafrost growth: Cryostratigraphic observations from the CRREL Tunnel near Fairbanks, Alaska. *Permafrost and Periglacial Processes* 15: 339–347.
- Swinzow, G.K. 1970. *Permafrost tunneling by a continuous mechanical method*. Technical Report 221. Hanover, NH: Cold Regions Research and Engineering Laboratory.

The Measurement of Compressional and Shear Wave Velocities in Permafrost: A Comparison of Three Seismic Methods

William Black

NORCAL Geophysical Consultants, Inc., Cotati, CA

Erin Bashaw, Jeremiah Drage
Golder Associates, Anchorage, AK

Richie Kmack
ExxonMobil Development Company, Houston, TX

Abstract

Seismic compressional (P) and shear (S) wave velocities were measured in permafrost at a proposed facility foundation site located on the North Slope of Alaska. The general soil profile at the site included layers of sand and gravel with varying amounts of fines, a layer of organic silt, and massive ice at a depth of approximately 4.6 to 7.6 m. The soils were fully frozen and well bonded throughout the 11-m depth range of the survey. The velocity data were used to produce stiffness and damping parameters for further structural analysis of the proposed facility. The seismic velocities were measured using the crosshole, downhole, and surface wave methods. The velocities measured using the three seismic methods were comparable. On average, the P-wave velocities ranged from 4,100 m/sec at the surface to 4,850 m/sec at the maximum borehole depth of 11 m. The S-wave velocities ranged from 1,800 m/sec at the surface to 2,200 m/sec at depth.

Keywords: Seismic velocity; compressional wave; shear wave; crosshole; downhole; surface wave.

Introduction

The static and dynamic design and analysis of block foundations require information on damping coefficients and soil parameters that includes, but is not limited to, Poisson's ratio, the shear modulus, and Young's modulus (Bowels 1988). These dynamic properties can be determined by measuring the shear wave velocity (V_s) and the compressional wave velocity (V_p) of foundation soils (Cunning et al. 1995). The seismic velocities can be measured in situ using a wide variety of techniques including seismic refraction (MacAulay and Hunter 1982), seismic reflection (Johansen et al. 2003, Miller et al. 2000), seismic cone penetrometer tests (Schneider et al. 2001, Leblanc et al. 2004), downhole and crosshole seismic testing (Auld 1977, Hoar and Stokoe 1978, Hunter et al. 2002), and spectral analysis of surface waves (Stokoe 1994, Park et al. 1998). A number of seismic studies have been conducted to measure V_p and V_s in permafrost, but most of these studies have been conducted in the Canadian Arctic (McAulay & Hunter 1982, Nieto & Stewart 2003, Leblanc et al. 2004). Our literature research has uncovered only a small number of studies in Alaska (Barnes 1963, Miller 1984).

This paper presents the results of a seismic study conducted at a proposed facility in the North Slope area of Alaska. Three different seismic techniques were used to measure V_p and V_s in permafrost underlying the footprint of a proposed facility. These techniques consisted of crosshole seismic testing, downhole seismic testing, and multichannel analysis of surface waves. The seismic velocity data will be used by others, along with other subsurface information, to produce stiffness and damping parameters to augment a structural analysis of the proposed facility.

Site Description

The footprint of the proposed structure measures approximately 27 m north-south by 49 m east-west. At the time of the geophysical investigation, the study area had been cleared of snow and was surrounded on the south, west, and north by snow banks. The ground surface was flat and open with a thin veneer of snow and ice over frozen tundra. The air temperature ranged from approximately -21° to -7°C with minimal wind and no cloud cover. The study area is underlain to a depth of 11 m by frozen soils consisting of 4.6 m of poorly graded gravel with silt and sand, 1.2 m of organic silt, 1 m of massive ice, another 1 m of organic silt, and 3.1 m of silty sand with gravel.

Seismic velocities were measured in two suites of boreholes designated Suite A and Suite B, as shown in Figure 1. Each suite consisted of three boreholes distributed at 7.6-m intervals in a collinear array. Suite A was oriented east-west and Suite B

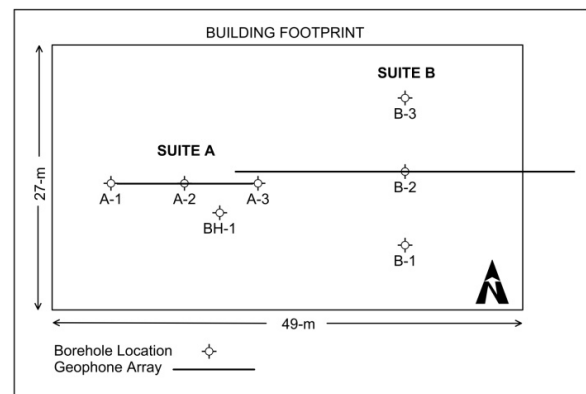


Figure 1. Borehole suites.

was oriented north-south. The boreholes that composed each suite were completed to a depth of 12 m with 10-cm i.d. PVC casing that was frozen in place. Two borehole suites were used instead of one in order to provide a more representative sample of the subsurface conditions. In addition, the boreholes were oriented perpendicular to each other in order to determine if the subsurface is seismically anisotropic. East-west trending arrays (spreads) of surface geophones were centered over the central borehole of each suite for the surface wave survey.

Seismic Surveys

The crosshole survey consisted of measuring the time required for P- and S-waves to travel from a seismic source placed in one borehole to receivers placed at the same depth in adjacent boreholes. The survey was conducted according to ASTM Standard D4428/D 4428M-00 (ASTM 2009). The crosshole velocity measurements were conducted at 0.76-m intervals in both borehole suites starting at a depth of 0.76 m and concluding at a depth of 10.7 m.

The downhole seismic velocity survey consisted of measuring the time required for seismic waves generated on the surface to travel to a receiver placed inside a borehole. The survey was conducted according to ASTM Standard D7400-08 (ASTM 2009). The downhole velocity measurements were conducted using the center borehole of each borehole suite. The measurements were conducted at 0.76-m intervals starting at a depth of 0.76 m and concluding at a depth of 10.7 m.

The surface wave technique is a non-invasive geophysical method that is used to measure subsurface V_p and V_s . The method consists of measuring the variation of surface wave velocity versus frequency. The resulting data can be inverted to provide an indication of P-wave and S-wave velocity versus depth (Park et al. 1998). We conducted one surface wave sounding at each of the two borehole suites according to the procedures described by Park et al. (1999). Each sounding consisted of generating seismic energy on the surface and detecting the resulting surface waves using 24-geophones distributed in a collinear array (spread). At each borehole suite the geophone spread was oriented east-west and centered over the center borehole of the suite. Seismic energy was produced at both ends of each spread. At Suite A the geophones were distributed at 0.6-m intervals for a total spread length of 14 m, as shown in Figure 1. At Suite B the geophones were distributed at 1.5-m intervals for a total spread length of 35 m (Fig.1).

Seismic Velocities

Most of the studies that appear in the literature involving the seismic velocity of permafrost present only P-wave velocities (King et al. 1982, Johansen et al. 2003, Ramachandran et al. 2008). These studies, and others, indicate V_p in permafrost ranging from 1,800 to 4,300 m/sec. King et al. (1982) presented data indicating that the V_p of permafrost is directly proportional to grain size and inversely proportional to temperature. That is, coarse materials like sand have significantly higher

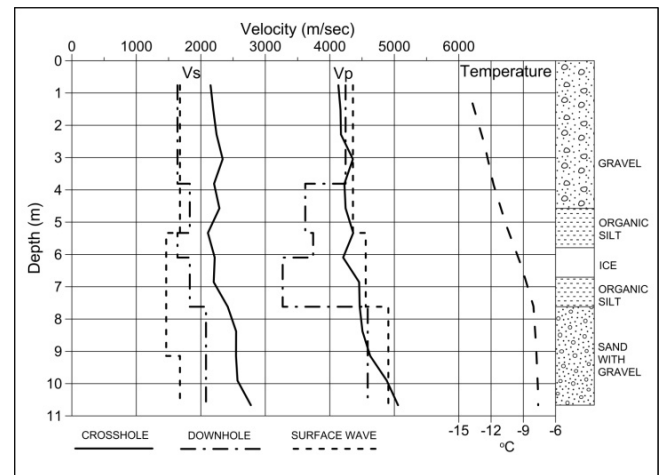


Figure 2. Velocity vs. depth.

velocities than silts, which have higher velocities than clays. In addition, the velocities of these materials increase with decreasing temperatures. A couple of studies (Nieto & Stewart 2003, Leblanc et al. 2004) also presented S-wave velocities and indicated values ranging from 900 to 2,030 m/sec.

The P-wave and S-wave velocities that we measured using the crosshole, downhole, and surface wave techniques are illustrated by the velocity versus depth graph shown in Figure 2. The seismic velocities illustrated on this graph are an average of those measured in the two borehole suites shown in Figure 1.

The velocity versus depth graph shows that the downhole V_s is lower than the V_s measured using the crosshole method. This is probably because the crosshole method measures the velocity of seismic waves traveling horizontally, parallel to stratigraphic boundaries, whereas the downhole method measures the velocity of seismic waves that are traveling vertically, across those boundaries. The V_s measured using the surface wave method, which is sensitive to both horizontal and vertical velocity variations, falls right in between the crosshole and downhole velocities. The V_p measured using all three methods are very similar, except within the organic silt and ice layer where the downhole velocities are much lower than the crosshole and surface wave velocities. Given the V_p versus grain size relationship reported by King et al. (1982), we would expect the organic silt to have lower V_p than the sands and gravels, as is the case. Crosshole velocities do not decrease within the organic silt and ice layer probably because the crosshole measurements are affected by refracted arrivals from the higher velocity gravels and sands above and below the silt and ice. However, we cannot explain why the surface wave measurements did not resolve the low V_p within the silt and ice layer, or why the V_s show only a minimal affect from the fine grained material.

The overall average P- and S-wave velocities measured using the crosshole, downhole, and surface wave methods are illustrated by the velocity versus depth graph shown in Figure 3. This graph indicates a gradual increase in both V_p and V_s with depth. V_p ranges from 4,100 to 4,850 m/sec, and V_s

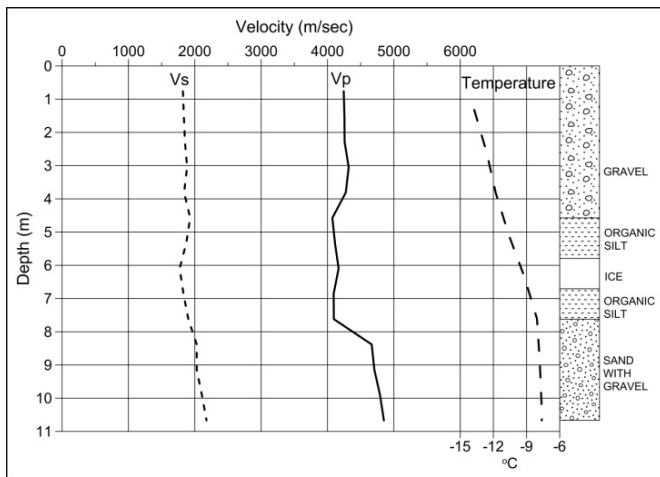


Figure 3. Overall velocity vs. depth.

ranges from 1,800 to 2,200 m/sec. These velocities are at the high end of those reported in the literature (King et al. 1982, Johansen et al. 2003, Nieto & Stewart 2003, Leblanc et al. 2004, Ramachandran et al. 2008) but are consistent with the seismic velocities we measured at another site in the North Slope area. It is interesting to note that the overall average Vp and Vs do decrease slightly within the organic silt and ice layer, but not as much as the downhole Vp alone. Figures 2 and 3 show that the temperature increases with depth. This phenomenon is caused by the residual effect of the cold surface temperatures during the winter (the temperature and velocity measurements were conducted in April of 2010). The fact that the velocity also increases with depth runs contrary to the velocity versus temperature relationship reported by King et al. (1982) where velocity increases with decreasing temperature. However, our findings merely suggest that temperature has a much smaller effect than compaction and grain size.

Elastic Moduli

The overall average seismic velocities shown in Figure 3 were used to compute the elastic moduli of the frozen soils. These consisted of Poisson's Ratio (σ), the shear modulus (G), and Young's Modulus (E). The values were computed using the following equations after Christiansen (1996):

$$\sigma = (Vp^2 - Vs^2)/2(Vp^2 - Vs^2) \quad (1)$$

$$G = \rho Vs^2 \quad (2)$$

$$E = \rho Vs^2(3Vp^2 - 4Vs^2)/(Vp^2 - Vs^2) \quad (3)$$

where ρ represents the density of samples that were collected in borehole BH-1 (Fig. 1).

The computed elastic moduli are illustrated in Figure 4. The soil density ranged from as low as 900 kg/m³ in massive ice at a depth of 6 m to as high as 2,320 kg/m³ in silty sand with gravel below 8.5 m. The computed Poisson's Ratio ranged from a low of .325 in silty sand with gravel at a depth of 8.5

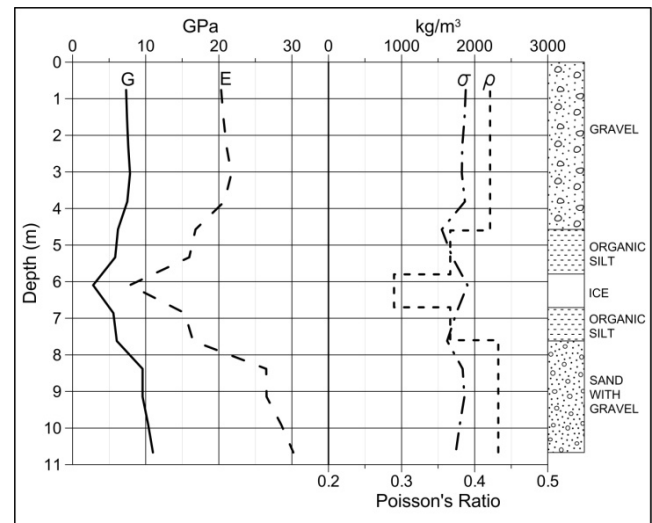


Figure 4. Elastic moduli.

m to a high of .373 in poorly graded gravel with silt and sand at a depth of 1.5 m. The computed shear modulus ranged from a low of 2.8 Giga Pascals (GPa) in the massive ice unit to 11.0 GPa at the maximum measurement depth of 10.7 m (in silty sand with gravel). Finally, Young's modulus ranged from a low of 7.8 GPa in the massive ice unit to 30.2 GPa at a depth of 10.7 m in the silty sand with gravel. The marked decrease in both G and E at a depth of 6 m in the massive ice unit is more a reflection of the low density of the ice (Fig. 4) than its low velocity (Fig. 3).

Summary

The crosshole, downhole, and surface wave seismic techniques produced similar results except with regard to the organic silt and ice layer. The low seismic velocities of this layer were well defined by the downhole P-wave velocities, but only barely evident in the crosshole and surface wave P-wave velocities or the S-wave velocities measured with all three methods. The crosshole S-wave velocities tended to be higher than those measured using the downhole and surface wave techniques. This is probably because the crosshole method measures the velocity of seismic waves propagating parallel to stratigraphic boundaries rather than across them (downhole method). Variation in temperature seemed to have little effect on the measured seismic velocities. We assume that this is because grain size (silt versus sands and gravels) and increased compaction with depth probably have a much larger effect.

Conclusions

Of the three seismic methods tested in this study, the surface wave method is the least expensive and least invasive because it does not require the installation of boreholes. Its vertical resolution is not as good as the crosshole and downhole methods, but the velocities it measured are generally

consistent with the crosshole and downhole velocities. The downhole method appears to have been far superior to the crosshole and surface wave methods at delineating the low (P-wave) velocity zone associated with the organic silt and ice layer. This is partly attributable to the fact that the crosshole measurements were probably affected by refracted arrivals from the higher velocity gravel and sand layers above and below the silt layer. Whichever seismic method is employed, the measured velocities can be used, in conjunction with density information, to compute elastic moduli such as Poisson's ratio, shear modulus, and Young's modulus.

References

- Auld, B. 1977. Cross-Hole and Down-Hole VS by Mechanical Impulse. *Journal of the Geotechnical Engineering Division ASCE*, Vol. 103, No. GT12, pp. 1381–1398.
- ASTM Standard D 4428/D 4428M-00, 2009. Standard Test Methods for Crosshole Seismic Testing, ASTM International, West Conshohocken, PA.
- ASTM Standard D 7400-08, 2009. Standard Test Methods for Downhole Seismic Testing, ASTM International, West Conshohocken, PA.
- Barnes, D.F. 1963. Geophysical Methods for Delineating Permafrost. *Proceedings of the 1st International Conference on Permafrost*, Lafayette, Ind. NAS-NRC Publ. 1287:349-355.
- Bowels, J.E. 1988. *Foundation Analysis and Design*, 4th Edition, McGraw Hill.
- Christensen, N.I. 1996. Poisson's Ratio and Crustal Seismology, *Jour. of Geophys. Research* 101, 3139-3156.
- Cunning, J.C., Robertson, P.K., & Sego, D.C. 1995. Shear Wave Velocity to Evaluate In Situ State of Cohesionless Soils. *Canadian Geotechnical Journal* 32, 848-858.
- Hoar, R.J. & Stokoe, K.H. II. 1978. Generation and Measurement of Shear Waves In Situ. *Dynamic Geotechnical Testing, ASTM STP 654*, ASTM International, West Conshohocken, PA, pp. 3–29.
- Hunter, J.A., Benjumea, B., Harris, J.B., Miller, R.D., Pullan, S.E., Burns, R.A., & Good, R.L. 2002. Surface and Downhole Shear Wave Seismic Methods for Thick Soil Site Investigations. *Soil Dynamics and Earthquake Engineering* Vol. 22, pp. 931–941.
- Johansen, T.A., Digranes, P., van Schaack, M., & Lonne, I. 2003. Seismic mapping and modeling of near-surface sediments in polar areas. *Geophysics*, vol. 68, No. 2, 566-573.
- LeBlanc, A-M, Fortier, R., Allard, M., & Cosma, C.G. 2004. Seismic cone penetration test and seismic tomography in permafrost. *Canadian Geotechnical Journal* 41: 796-813 Abstract, ISI.
- King, M.S., Pandit, B.I., Hunter, J.A., & Gajtani, M. 1982. Some seismic, electrical and thermal properties of sub-seabottom permafrost samples from the Beaufort Sea. *Proc. 4th Canadian Permafrost Conference*, Calgary, Alberta, 1981, National Resources Council, Ottawa, pp. 268-273.
- MacAulay, H.A. & Hunter, J.A. 1982. Detailed seismic refraction analysis of ice-bonded permafrost layering in the Canadian Beaufort Sea, *Proceedings, 4th Canadian Permafrost Conference*.
- Miller, R. 1984. Shallow Geophysical Borehole Logging in Permafrost: A Case History, Abstract from Workshop on Permafrost Geophysics, Golden, Colorado, October 23-24, 1984, U.S. Army Cold Regions Research and Engineering Laboratory Special Report 85-5, pp. 51-52.
- Miller, R.D., Hunter, J.A., Doll, W.E., Carr B.J., Burns, R.A., Good, R.L., Lafren, D.R., & Douma, M. 2000. Imaging permafrost with shallow P- and S-wave reflection, *7th Ann. Internat. Mtg., Soc. of Expl. Geophys.* Expanded Abstracts, Calgary, Canada, 1339-1342.
- Nieto, C.E. & Stewart, R.R. 2003. Ultra high-resolution seismic and GPR imaging of permafrost, Devon Island, Nunavut, CREWS Conference, University of Calgary.
- Park, C.B., Xia, J., & Miller, R.D., 1998a. Ground roll as a tool to image near-surface anomaly: *68th Ann. Internat. Mtg., Soc. Expl. Geophys.*, Expanded Abstracts, 874–877.
- Ramachandran, K., Brent, T., Bellefleur, G., & Dallimore, S. 2008. Imaging Permafrost Velocity Structure Using High Resolution 3D Seismic Tomography, Expanded Abstract, Soc. of Expl. Geophys., Annual Meeting, Las Vegas, NV.
- Schneider, J.A., Mayne, P.W., & Rix, G.J., 2001. Geotechnical Site Characterization in the Greater Memphis Area Using Cone Penetration Tests. *Engineering Geology* Vol. 62, 169–184.
- Stokoe, K.H. II, Wright, G.W., James, A.B., & Jose, M.R. 1994. Characterization of geotechnical sites by SASW method, in Geophysical characterization of sites, ISSMFE Technical Committee #10, edited by R. D. Woods, Oxford Publishers, New Delhi.

Quantifying Rock Glacier Creep Using Airborne Laser Scanning: A Case Study from Two Rock Glaciers in the Austrian Alps

Erik Bollmann, Christoph Klug, Rudolf Sailer, Johann Stötter
Institute of Geography, Innsbruck University, Innsbruck, Austria

Jakob Abermann
Institute of Meteorology and Geophysics, Innsbruck University, Innsbruck, Austria

Abstract

Horizontal displacement rates as well as surface elevation changes of two rock glaciers in the Eastern Austrian Alps are calculated over different time spans between 2006 and 2010 using airborne laser scanning (ALS) data and the image correlation software Imcorr. By comparing the ALS-based horizontal displacement rates with results from global navigation satellite system data (dGNSS), an average absolute deviation of 0.22 m (STD 0.30 m) is determined for the time period 2009–2010 and 0.34 m (STD 0.5 m) for 2006–2010. For the Äußere Hochebenkar rock glacier (AHK), a gradual increase of flow velocity from about 0.1 m a^{-1} at the root zone to $> 2 \text{ m a}^{-1}$ at the lower part is calculated for the period 2006–2010. Over the period 2009–2010, the velocity of AHK generally increased compared to 2006–2009. At the Kaiserberg rock glacier (KBR), two distinct flow velocity fields are detected. In contrast to AHK, the Kaiserberg rock glacier shows significant surface lowering caused by ice melt.

Keywords: accuracy; airborne laser scanning; creep; monitoring; permafrost; rock glacier; velocity.

Introduction

Active rock glaciers are morphological features composed of a mixture of ice and debris that slowly creep downslope by the force of gravity. As a consequence of the downslope movement, they show a typical surface topography with transverse and longitudinal ridges and furrows, a steep front, and lateral sides (Barsch 1996). The surface topography is the result of an interaction between mass advection, advection of topography by creep, 3-dimensional strain, and local mass changes (Barsch 1996, Kääb et al. 2003), and it cumulatively reflects the dynamic history and thus the past and present internal conditions of the rock glacier (Kääb & Weber 2004).

Active rock glaciers creep with surface velocities ranging from a few centimeters to several meters per year. The majority of them show surface velocities around one meter per year or below (Haerberli 1985, Whalley & Martin 1992, Barsch 1996, Kaufmann & Landstädter 2003, Haerberli et al. 2006, Kääb 2007, Kääb et al. 2003). There are clear indications that differences in thickness, temperature, and internal composition play a major role in the deformation rate of rock glaciers. However, it is suggested that these factors do not sufficiently explain differences in velocity fields on individual rock glaciers (Kääb et al. 2003).

Within the last decade, an increasing number of studies monitored and quantified the creep of active rock glaciers. The main focus of recent research has been on either a better understanding of rock glacier evolution and kinetics (Kääb et al. 2003, Kääb & Weber 2004, Kääb & Reichmuth 2005, Roer et al. 2005), on an interpretation of surface velocity fields in relation to climatic and paleoclimatic conditions, or on rock glacier age estimations (Schneider & Schneider 2001, Kääb et al. 2002, Kääb et al. 2007).

To quantify 2- and 3-dimensional creep, various monitoring

techniques have been applied. The potential of airborne laser scanning (ALS) for rock glacier studies, especially for volume change calculations, has already been mentioned by Harris et al. (2009). However, the volume change of a rock glacier, as it can be derived from multi-temporal Digital Terrain Model (DTM) differencing, only represents the results of an interaction between mass advection, advection of topography by creep, 3-dimensional straining, and local mass changes. To get a more detailed understanding of the processes involved in rock glacier creep, it is of fundamental interest to determine 3-dimensional surface displacement rates (Kääb & Weber 2004, Kääb & Reichmuth 2005).

In this contribution, horizontal displacement rates and vertical changes of two rock glaciers are calculated using multi-temporal ALS data. The accuracy of the results is assessed using differential global navigation satellite systems (dGNSS) data, and we discuss the potential of ALS for rock glacier analysis.

Monitoring Techniques

Established techniques for rock glacier monitoring

Today, a variety of methods to quantify rock glacier creep rates is available. Terrestrial survey techniques such as dGNSS are widely used. They provide highly accurate measurements over relatively long time series and high temporal resolution (Schneider & Schneider 2001, Krainer & Mostler 2006). Recently, terrestrial laser scanning grew in importance because it produces very high resolution digital terrain models and it can be applied over relatively large areas of a rock glacier (Bauer et al. 2003). The main disadvantage of the terrestrial surveys is the lack of area-wide data coverage. For area-wide data acquisition, airborne and space-borne monitoring techniques are more appropriate. Using photogrammetry on repeated

airborne optical data, highly accurate horizontal velocity fields and their spatio-temporal changes have been measured over entire rock glaciers (Kääb et al. 1997, Kaufmann & Landstädter 2003, Kääb et al., 2003, Kääb & Weber 2004, Roer et al. 2005). Space-borne radar interferometry has been successfully applied to detect and quantify surface deformation over large areas on rock glaciers (Kenny & Kaufmann 2003, Strozzi et al. 2004).

Airborne laser scanning (ALS)

ALS is an active remote-sensing technique, using a laser beam as the sensing carrier, for the acquisition of 3-dimensional point data that geometrically represent the earth surface or objects on it. In contrast to optical remote sensing raster data, the raw product of an ALS data acquisition campaign is a so-called point cloud consisting of points with x,y,z coordinates (Baltsavias 1999). Over the last 15 years, airborne laser scanning has become a standard method for the acquisition of high-resolution and high-accuracy topographic data. The accuracy of ALS-derived DTMs has been determined in several studies, and an absolute vertical accuracy in the order of one decimeter is given for areas less inclined than 30° (Baltsavias 1999, Hodgson & Bresnahan 2004, Bollmann et al. 2010).

Study Area and Data

Äußerer Hochebenkar rock glacier (AHK)

The Äußere Hochebenkar rock glacier is a tongue-shaped, talus-derived rock glacier in the Ötztal Alps, Austria. It expands from about 2830 m a.s.l. down to about 2365 m a.s.l. and reaches a length of 1.6 km. The surface layer is characterized by large boulders with an average diameter of about 1 m (Vietoris 1972, Haeberli & Patzelt 1982).

Systematic investigations on surface flow velocities, front advance rates, and surface elevation changes of AHK started in 1938 and have been carried out on at least an annual scale since then (Schneider & Schneider 2001). AHK is characterized by very high surface velocities of up to several meters per year in its lower part, especially below a terrain edge at about 2570 m. At the cross profile L1 (see Fig. 2), mean displacement rates of 3.9 ma⁻¹ and maximum values of 6.6 ma⁻¹ were recorded in the 1950s and 1960s (Schneider & Schneider 2001). These high values most likely resulted from sliding processes of the creeping permafrost body on the underlying bedrock (Haeberli & Patzelt 1982, Schneider & Schneider 2001).

Kaiserberg rock glacier (KBR)

The Kaiserberg rock glacier is a lobate rock glacier in the Ötztal Alps with a maximum width of about 550 m and a length of 350–400 m. The highest point at the rock glacier head is at 2710 m a.s.l. Following Krainer & Mostler (2006), the lowermost part of the rock glacier is active and ends with a steep front at an altitude of 2585 m a.s.l. KBR consists of a coarse-grained surface layer with blocks of several meters in length. However, most are several decimeters in diameter. The surface topography is characterized by well-developed transverse and longitudinal ridges and furrows.

Table 1. Overview of data acquisition dates.

| Data acquisition dates | | 2006 | 2009 | 2010 |
|------------------------|-----|--------|--------|--------|
| ALS | AHK | 23.08. | 30.09. | 07.10. |
| | KBR | 02.09. | --- | 07.10. |
| dGNSS | AHK | 22.09. | 06.08. | 08.09. |
| | KBR | --- | --- | --- |

ALS data

ALS data acquisition campaigns at AHK were carried out in 2006, 2009, and 2010, whereas for KBR only data from 2006 and 2010 are available. The 2006 and 2010 ALS data of both rock glaciers result from the same data acquisition campaigns (see Table 1). The average ALS point density of the individual ALS campaigns varies between 2.7 and 4.8 points per m².

Reference data: dGNSS

Differential global navigation satellite system (dGNSS) data are used to validate the vertical accuracy of the ALS-based DTMs as well as the calculated horizontal displacement rates. The dGNSS measurements were acquired in a well-established monitoring network (Schneider & Schneider 2001) of which four cross profiles at AHK and eleven fix points outside the rock glacier were included in our analysis. The locations of the dGNSS measurements (four cross profiles: L0 to L3 and the fix points) are given in Figure 1 and Figure 2.

Methods

Calculation of horizontal surface displacement

The image correlation software Imcorr is used to calculate horizontal surface displacements (Scambos et al. 1992). Imcorr has been widely applied to calculate flow velocities of glaciers using a variety of input data (Dowdeswell & Benham 2003, Giles et al. 2009). The software calculates displacement rates as a function of systematic changes in image digital numbers (DNs). The algorithm normalizes a reference chip and a larger search chip to a DN mean of zero and unity standard deviation prior to correlating the two chips (Scambos et al. 1992). The software uses raster images of two different dates as input and produces an output file consisting of the x- and y-coordinates (center pixel) of the moved reference chip, the displacement rates in x- and y-directions, as well as a correlation strength parameter.

As Imcorr uses raster images as input, the original ALS point clouds of 2006, 2009, and 2010 are interpolated to DTMs with 0.5 m raster resolution in a first step. Each raster cell is populated with the average value of all z-coordinates (height value) that spatially lie within that cell. As the horizontal ALS point spacing is very regular, more than 76% of all raster cells are populated without interpolating from neighboring cells; the remaining 24% are filled using a nearest-neighbor function. For each DTM, a shaded relief raster is calculated (azimuth

North-West, altitude 45°), which is then used as input for the image correlation. Imcorr was run with a reference chip of 16 x 16 cells, a search chip of 64 x 64 cells, and a moving window spacing of 1 cell.

Accuracy assessment

The accuracy of the calculated horizontal displacement rates is evaluated using dGNSS data. As the dGNSS measurements and ALS data acquisitions have not been carried out at the same dates (Table 1), the ALS-based displacement rates are adjusted to the time span between the dGNSS data acquisitions using

$$\overline{dALS}_{t1,t2} = ALS_{t1,t2} / \Delta t ALS_{t1,t2} * \Delta t dGNSS_{t1,t2} \quad (1)$$

where $\overline{dALS}_{t1,t2}$ is the adjusted displacement rate [ma^{-1}] of the Imcorr results, $ALS_{t1,t2}$ is the displacement rate of the original Imcorr results, $\Delta t ALS_{t1,t2}$ is the number of days between the ALS flight campaigns and $\Delta t dGNSS_{t1,t2}$ is the number of days between the dGNSS measurements. The time-adjusted Imcorr output point file and the interpolated displacement raster values are compared to the dGNSS displacement rates. For the generation of displacement rates, a trimmed mean interpolation function (search radius 2 m) was used. This allowed the removal of erroneous measurements (outliers).

For the 2009–2010 time period, 39 dGNSS measurements from the cross profiles L0 to L3 are used for validation. For the period 2006–2010, dGNSS data from L1 are not available and therefore only 28 reference measurements could be used. The vertical accuracy of the generated DTMs at AHK is determined using eleven dGNSS measurement sites (see Fig. 1). The eleven fix points are not influenced by any topographic changes.

Results and Discussion

Vertical accuracy of the DTMs

A comparison between the generated DTMs of AHK and the dGNSS heights at 11 fix points shows mean deviations of -0.02 m (std 0.15 m) for the 2006 DTM, 0.04 m (std 0.09 m) for 2009 DTM, and 0.09 m (std 0.09 m) for 2010 DTM. Thus, using the standard deviation as an accuracy measure, the vertical accuracy of all DTM heights is better than 0.15 m.

Accuracy of horizontal displacement rates

The mean deviations between the ALS-based displacement rates and the dGNSS results range between -0.10 m and 0.08 m and are relatively small. These values near zero indicate that no systematic respective over- underestimation of the velocity occurs. However, the standard deviations between 0.30 m and 0.51 m, as well as the average absolute deviation between 0.22 m and 0.39 m, are more appropriate to define the accuracy of the ALS-based displacement rates. In this study we use the standard deviation as the level of significance. Thus, for the one-year time period 2009–2010, displacement rates > 0.30 m exceed the level of significance. For the four-year time period 2006–2010, the level of significance is 0.50 m.

Table 2. Comparison between adjusted horizontal displacement rates from Imcorr (equation 1) and dGNSS (Imcorr – dGNSS).

| Imcorr - dGNSS | Mean [m] | Amean [m] | Std [m] | Max [m] | Min [m] | RMS [m] | R ² |
|----------------|----------|-----------|---------|---------|---------|---------|----------------|
| Pts. 09/10 | -0.10 | 0.25 | 0.36 | 0.96 | -1.28 | 0.37 | 0.92 |
| Raster 09/10 | -0.08 | 0.22 | 0.30 | 0.52 | -0.91 | 0.30 | 0.94 |
| Pts. 06/10 | -0.19 | 0.39 | 0.51 | 1.09 | -1.11 | 0.54 | 0.97 |
| Raster 06/10 | -0.12 | 0.34 | 0.50 | 1.27 | -1.15 | 0.50 | 0.98 |

Mean: Mean deviation between dGNSS and Imcorr; Amean: average absolute deviation; Std: Standard deviation; Max/Min: Maximum/Minimum deviation; RMS: root mean square error; R²: Coefficient of determination. In columns with “Pts.” the adjusted Imcorr output points (equation 1) are compared to dGNSS; 2009-10 n=39, 2006-10 n=28.

All accuracy measures in Table 2 indicate that the accuracy of the 2009–2010 displacements is generally better than the accuracy for 2006–2010. Furthermore, it becomes obvious that the interpolation of the original Imcorr output point files to the raster maps improved the accuracy. This is due to the fact that outliers (e.g., local maxima and minima) are removed by the trimmed mean interpolation algorithm, and also due to averaging all values found in the search radius of 2 m to populate each raster cell.

As dGNSS data are only available for AHK, we also use the level of significance determined at AHK for the KBR data.

Surface elevation change of AHK

Surface elevation change rates > 0.5 m are identified in several areas of AHK. At the orographic right margin of the rock glacier, values > 0.5 m are caused by creep processes that resulted in a downward transport of mass and expansion of AHK between 2006 and 2010 (Figs. 1 and 2). Distinct elongate-shaped alterations of positive and negative values occur on the main part of the rock glacier, especially between 2730 m and 2820 m at the orographic right side. They clearly result from advancing ridges and furrows. Between L0 and L1, at about 2500 m at the middle part of AHK, a sharp transition from areas with high surface elevation decrease and gain is evident. These areas correspond well with the area described by Haerberli & Patzelt (1982) and Schneider & Schneider (2001), where deep cross cracks occur as a consequence of local sliding of the rock glacier on the bedrock and increased tension in the permafrost body.

In general, the detected local surface elevation changes of AHK are caused by horizontal displacements of the creeping rock glacier. Regarding the entire rock glacier, an area-averaged mass loss is not detected. Therefore, the ice content of AHK seems to be well protected from surface energy input, and significant ice melt did not occur between 2006 and 2010.

Surface velocity of AHK

Individual surface velocity fields are detected for the time period 2006 to 2010 (Fig. 2). In general, the mean annual

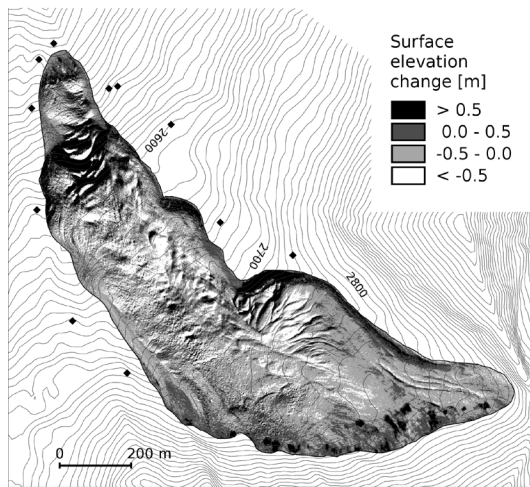


Figure 1. Surface elevation change of AHK between 2006 and 2010. Results based on DTM differencing with 0.5 m resolution. Black rhombus shows location of dGNSS fix points.

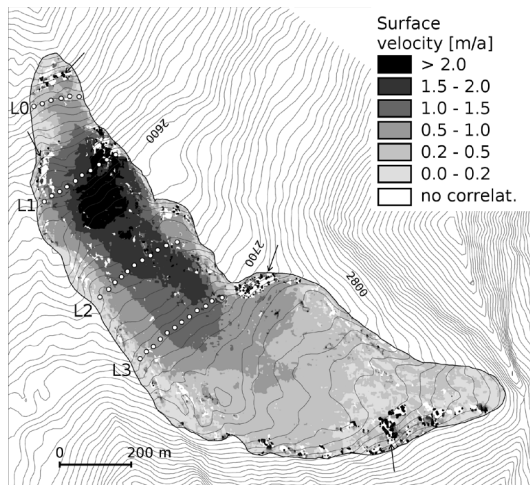


Figure 2. Mean annual surface velocity of AHK between 2006 and 2010. Results interpolated from Imcorr output. L0 to L3 (white circles) indicate location of dGNSS measurement points along 4 cross profiles. Arrows indicate areas with artifacts.

velocity increases gradually from $< 0.2 \text{ ma}^{-1}$ at the root zone to a maximum of $> 2 \text{ ma}^{-1}$ in the middle part of the rock glacier and at its orographic right side at about 2600 m. Maximum velocities correspond well with an increase of terrain steepness below 2640 m. Below 2560 m, the surface velocity decreases again, even though the terrain is still steep. A complete decoupling of the upper and lower part of AHK, as has been assumed by Haerberli & Patzelt (1982), cannot be found in the analysis of the 2006–2010 velocity fields. The velocity decrease between L1 and L0 is gradual rather than abrupt. However, the lowest part of AHK (around L0) is clearly influenced by other creep characteristics than the part above 2560 m (Figs. 1 and 2).

For some areas, no creep rates could be calculated because no correlations between the two input images are made by Imcorr. These areas occur either at steep lateral sides or in

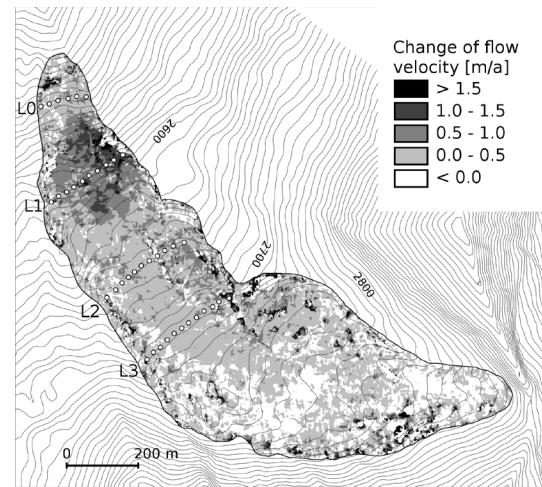


Figure 3. Changes in mean annual flow velocity between the time period 2006-2009 and 2009-2010.

fast creep steep areas. In these areas, the surface topography changes strongly due to rotation of boulders and surface instabilities. Several velocity artifacts occur (arrows in Fig. 2) that result from miss-matching of the two Imcorr input images. In most cases, they are spatially connected to areas where no correlation of the two images could be made. Such areas have to be excluded from interpretation.

Flow velocity changes of AHK

Between the 2006–2009 period and 2009–2010, a general velocity increase is detected. Comparing Figure 2 and Figure 3 shows that the absolute increase of surface velocity is highest for areas that initially show high mean annual velocities. The most significant acceleration on the order of $1.0\text{--}1.5 \text{ ma}^{-1}$ occurs in the steep part of the rock glacier at the cross profile line L1. Velocity changes in that area have been discussed by Haerberli & Patzelt (1982) and Schneider & Schneider (2001). Most likely they do not present variations in internal creep characteristics but are a result of sliding at the base of the creeping permafrost body on the bedrock. Over large parts of the rock glacier, a velocity increase on the order of $0.0\text{--}0.5 \text{ ma}^{-1}$ is observed, whereas toward the root zone slightly negative values are calculated. These values are near or below the level of significance of 0.3 m (cf. Table 2, Std Raster 09/10). Thus, considering the accuracy of the data and method, it cannot be stated that the velocity really decreased in the root zone of AHK.

Surface elevation change of KBR

DTM differencing of the KBR rock glacier indicates a mean surface lowering of -0.21 m between 2006 and 2010 (Fig. 4). Positive values, indicating an increase of surface elevation, are found at the margins of the rock glacier and result from the advance of the rock glacier lobe. Surface elevation increase $> 0.6 \text{ m}$ occurs at the front of the eastern lobe. Further positive values, between 0.0 m and 0.6 m, are identified in the areas of well-defined ridges as a result of the creep process and in the root zone. Surface elevation increase in the root zone might

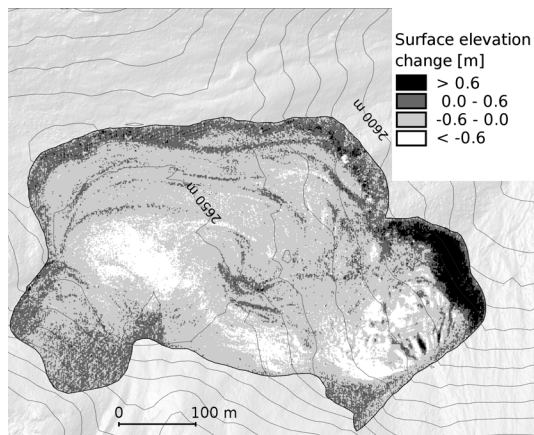


Figure 4. Surface elevation change of KBR between 2006 and 2010. Results based on DTM differencing with 0.5 m resolution.

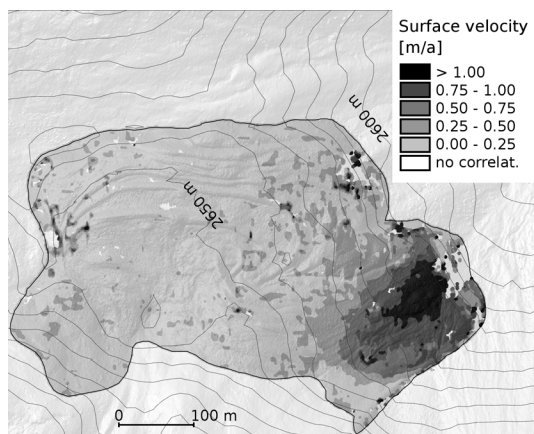


Figure 5. Mean annual surface velocity of KBR between 2006 and 2010. Results interpolated from Imcorr output.

result from debris input from the headwall area. The largest part of KBR shows surface elevation lowering in the order of 0.0 to -0.6 m, whereas surface lowering < -0.6 m is found at the fast creeping body and the central part of the western lobe.

Due to the fact that surface elevation losses are not balanced out by surface elevation gain, it can be concluded that KBR is in a degrading stage where ice melt occurs.

Surface velocity of KBR

The mean annual surface velocity between 2006 and 2010 of KBR ranges from areas with 0.00 – 0.25 ma^{-1} to areas with > 1.00 ma^{-1} (Fig. 5). A clear distinction in creep dynamics between a larger, slow-creeping western part and a smaller, faster-creeping eastern part is evident. Maximum velocities of > 1.00 ma^{-1} occur in the central part of the fast-creeping body and can be explained by a rather steep slope gradient of 15° compared to the flatter western part of KBR. Velocities gradually decline toward the orographic right margin and toward the main body orographic left.

Conclusion and Outlook

Horizontal displacements of the Hochebenkar and Kaiserberg rock glaciers could be calculated from multi-temporal ALS data. Comparisons between the ALS-based surface displacement raster and dGNSS data indicate an accuracy (standard deviation) of the calculated displacement rates of 0.3 m for the period 2009–2010 and 0.5 m (0.13 for an annual scale) for the period 2006–2010. As AHK is a very fast-creeping rock glacier, the data and method used are sufficient to achieve significant results for almost all parts of the rock glacier. However, a time span smaller than five years between the ALS data acquisition dates and raster resolution of 0.5 m might not be long enough to obtain significant results for slow-creeping rock glaciers.

For the AHK, a gradual increase of mean annual surface velocity from < 0.1 ma^{-1} at the root zone to > 2 ma^{-1} at the lower part (around 2600 m) was calculated over the period 2006–2010. Beside the class 0.0 – 0.2 m a^{-1} , all other velocity classes exceed the level of significance of 0.13 m for an annual scale. From 2600 m downward, the mean annual velocity gradually declined again. Comparing the period 2006–2009 with the period 2009–2010, a general increase of flow velocity is evident. Over large parts of AHK, the velocity increase is > 0.5 ma^{-1} , but increases of > 1.5 ma^{-1} also occur in areas with high initial flow velocities.

The KBR rock glacier showed two spatially distinct flow velocity patterns; a fast-creeping orographic right part (up to > 1 ma^{-1}) and a relatively slow-creeping left part (< 0.25 ma^{-1}).

In the case of AHK, permafrost creep is the most important factor governing local surface elevation changes. Conversely, the detected area-averaged surface lowering of KBR of -0.21 m is attributed to ice melt.

Future applications of ALS in rock glacier monitoring should focus on (1) the method's capability to quantify very slow-creeping permafrost, (2) the performance on rock glaciers with small changes of local surface topography (smooth surface), (3) the calculation of 3D displacements, and (4) area-wide quantification of rock glacier creep.

Acknowledgments

We thank the Tyrolean Government, the Austrian Climate and Energy Funds (C4AUSTRIA project, ACRP-A963633), and alpS – Centre of climate change adaption strategies (MUSICALS project) for the funding and provision of the ALS data. Furthermore, we thank H. Schneider, who provided the dGNSS data. The constructive comments of the two reviewers, Y. Buhler and R. Kenner, are much appreciated.

References

- Baltsavias, E. 1999. Airborne laser scanning: basic relations and formulas. *ISPRS Journal of photogrammetry and remote sensing* 54: 199-214.
- Barsch, D. 1996. *Rockglaciers. Indicators for the present and former geoecology in high mountain environments*. Springer-Verlag, Berlin.

- Bauer, A., Paar, G., & Kaufmann, V. 2003. Terrestrial laser scanning for rockglacier monitoring. In: Phillips, M., Springman, S.M., Arenson, L.U. (Eds.), *Proceedings of the 8th international conference on permafrost*. Swets and Zeitlinger, Lisse, 1: 55-60.
- Bollmann, E., Sailer, R., Briese, Ch., Stötter, J., & Fritzmann, P. 2010. Potential of airborne laser scanning for geomorphologic feature and process detection and quantification in high alpine mountains. *Zeitschrift für Geomorphologie* 55(Suppl. 2): 83-104.
- Dowdeswell, J.A. & Benham, T.J. 2003. A surge of Perseibreen, Svalbard, examined using aerial photography and ASTER high resolution satellite imagery. *Polar research* 22(2): 373-383.
- Giles, A.B., Massom, R.A., & Warner, R.C. 2009. A method for sub-pixel scale feature-tracking using Radarsat images applied to the Mertz glacier tongue, East Antarctica. *Remote sensing of environment* 113: 1691-1699.
- Haerberli, W. 1982. Creep of mountain permafrost: Internal structure and flow of alpine rock glaciers. *Mitteilungen der Versuchsanstalt für Wasserbau, Hydrologie und Glaziologie ETH Zürich* 77: 1-142.
- Haerberli, W. & Patzelt, G. 1982. Permafrostkartierung im Gebiet der Hochebenkar-Blockgletscher, Obergurgl, Ötztal Alpen. *Zeitschrift für Gletscherkunde und Glazialgeologie* 18 (2): 127-150.
- Haerberli, W., Hallet, B., Arenson, L., Elconin, R., Humlum, O., Käab, A., Kaufmann, V., Ladanyi, B., Matsuoka, N., & Vonder Mühl, D. 2006. Permafrost creep and rock glacier dynamics. *Permafrost and periglacial processes* 17 (3): 189-214.
- Harris, C., Arenson, L., Christiansen, H., Etzelmüller, B., Frauenfelder, R., et al. 2009. Permafrost and climate in Europe: Monitoring and modelling thermal, geomorphological and geotechnical responses. *Earth-science reviews* 92: 117-171.
- Hodgson, M. & Bresnahan, P. 2004. Accuracy of airborne Lidar-derived elevation: Empirical assessment and error budget. *Photogrammetric engineering and remote sensing* 70(3): 331-339.
- Kaufmann, V & Landstädter, R. 2002. Spatial-temporal analysis of the dynamic behaviour of the Hochebenkar rock glacier (Ötztal Alps, Austria) by means of digital photogrammetric methods. *Grazer Schriften der Geographie und Raumforschung* 37: 119-140.
- Kaufmann, V & Landstädter, R. 2003. Quantitative analysis of rock glacier creep by means of digital photogrammetry using multi-temporal aerial photographs: two case studies in the Austrian Alps. In: Phillips, M., Springman, S.M., Arenson, L.U. (Eds.), *Proceedings of the 8th international conference on permafrost*. Swets and Zeitlinger, Lisse, 1: 525-530.
- Käab, A. & Weber, M. 2004. Development of transverse ridges on rock glaciers: Field measurements and laboratory experiments. *Permafrost and periglacial processes* 15: 379-391.
- Käab, A., Frauenfelder, R., & Roer, I. 2007. On the reaction of rockglacier creep to surface temperature variations. *Global and planetary change* 56: 172-187.
- Käab, A., Haerberli, W., & Gudmundsson, H. 1997. Analysing the creep of mountain permafrost using high precision aerial photogrammetry: 25 years of monitoring Gruben rock glacier, Swiss Alps. *Permafrost and periglacial processes* 8: 409-426.
- Käab, A., Kaufmann, V., Landstädter, R., & Eiken, T. 2003. Rock glacier dynamics: implications from high-resolution measurements of surface velocity fields. In: Phillips, M., Springman, S.M., Arenson, L.U. (Eds.), *Proceedings of the 8th international conference on permafrost*. Swets and Zeitlinger, Lisse, 1: 501-506.
- Käab, A., Isaksen, K., Eiken, T., & Farbot, H. 2002. Geometry and dynamics of two lobe-shaped rock glaciers in the permafrost of Svalbard. *Norsk geografisk tidsskrift* 56: 152-160.
- Kenny, L.W. & Kaufmann, V. 2003. Estimation of rock glacier surface deformation using SAR interferometry data. *Geoscience and remote sensing* 41(6): 1512-1515.
- Krainer, K. & Mostler, W. 2006. Flow velocities of active rock glaciers in the Austrian Alps. *Geografiska Annaler* 88 A (4): 267-280.
- Roer, I., Käab, A., & Dikau, R. 2005. Rockglacier kinematics derived from small-scale aerial photography and digital airborne pushbroom imagery. *Zeitschrift für Geomorphologie* 49(1): 73-87.
- Scambos, T.A., Dutkiewitz, M.J., Wilson, J.C., & Bindschadler, R.A. 1992. Application of image cross-correlation software to the measurement of glacier velocity using satellite data. *Remote sensing of environment* 42: 177-186.
- Schneider, B. & Schneider, H. 2001. Zur 60jährigen Messreihe der kurzfristigen Geschwindigkeitsschwankungen am Blockgletscher im Äußeren Hochebenkar. *Zeitschrift für Gletscherkunde und Glazialgeologie* 37: 1-33.
- Strozzi, T., Käab, A., & Frauenfelder, R. 2004. Detecting and quantifying mountain permafrost creep from in-situ, airborne and spaceborn remote sensing methods. *International journal of remote sensing* 25(15): 2919-2931.
- Vietoris, L. 1972. Über den Blockgletscher des Äußeren Hochebenkars. *Zeitschrift für Gletscherkunde und Glazialgeologie* 8 (1-2): 169-188.
- Whalley, W.B. & Martin, H.E. 1992. Rock glaciers: II models and mechanics. *Progress in physical geography* 16: 127-186.

Effects of Rising Temperature on Shear Strength of Slopes in Alpine Permafrost

Christian Bommer

HSR - University of Applied Sciences, Department of Geotechnics, Rapperswil, Switzerland

Abstract

Focus is placed on the effect of climate on shear strength in mountain permafrost. The change in shear strength of soils, primarily caused by an increase in the mean annual air temperature, is analyzed with an effective stress theory using an infinite slope model. It is assumed that the volumetric friction angle is approximately constant. Ice and unfrozen water coexist in soils at temperatures close to the melting point. Hence water menisci are formed between adjacent grains producing an apparent cohesion, which is an additional shear strength component in thawing soils. The shear strength equation of thawing soils is therefore dependent on two components, the effective stress and the apparent cohesion. The apparent cohesion exists as long as water menisci between grains can be formed. A quantification of the effect of temperature on shear strength on a slope in mountain permafrost is illustrated with a case study.

Keywords: apparent cohesion; effective stresses; ice cohesion; mountain permafrost; shear strength; rising temperature.

Introduction

Slope instabilities occur when shear stresses on a potential slip surface exceed the shear resistance. The shear resistance of frozen soils is controlled by its composition, consisting of a four-phase system with solid particles, ice, unfrozen water, and gas or air (Fig. 1). The ice can be uniformly distributed, as in talus slopes with coarse debris, or accumulated in thin ice layers found in fine-grained soils as a result of ice segregation. Different ice contents are possible in soils. Ice in saturated soils has two effects on shear strength: 1) development of pore pressure (i.e., ice pressure which results in a decrease of the effective stress) and 2) strengthening effect due to bonding of the solid particles. These two effects are altered when the ice matrix is continuously transformed to water due to, for example, increasing air temperature or changing confining pressure. Therefore, the shear resistance can vary considerably

depending on environmental influences. Ice in unsaturated soil also has a strengthening effect due to ice bonding and can lead to an increase of the effective stresses (Nixon & Morgenstern 1973b, Bommer et al. 2012). This increase is due to negative pore pressures on freezing.

Different authors have developed theories for slope stability calculations in permanently frozen soils (Lambe & Whitman 1969, Hutchinson 1974, McRoberts & Morgenstern 1974a, Rist 2007). Most theories are based on the infinite slope model (Lambe & Whitman 1969) and on total stresses (Nishimura et al. 2009). Within this present study of permafrost in alpine regions, an effective stress theory is applied on an infinite slope. Special attention is given to the effect of rising temperatures (air and ground). A case study quantifies the influence of temperature on the shear strength of a talus mantled slope in alpine permafrost in Switzerland.

Effects of Rising Temperatures on Shear Strength of a Slope

Theory: effective stress equation

An increase in the mean annual air temperature can induce a phase change of ice to water depending on the soil-water bondage (e.g., Anderson & Morgenstern 1973) and occurs over a range of temperatures below 0°C. Accordingly, in a soil with temperatures close to the melting point, ice and unfrozen water coexist. The unfrozen water forms menisci between adjacent grains causing apparent cohesion (Fig. 1). These considerations lead to a generalized form of the shear strength equation of frozen and thawed soils depending on two strength components, σ' effective stress [kPa] and c_{app} apparent [kPa] cohesion or c_i ice cohesion [kPa] respectively:

$$\tau = \underbrace{\sigma'(u_w, u_i) \tan \varphi'}_{\text{interparticle friction}} + \underbrace{c_{app}(s, \tan \varphi')}_{\text{cohesion due to suction}} + \underbrace{c_i(t, T, \sigma_{c,i}, \varepsilon)}_{\text{ice cohesion}} \quad (1)$$

where τ = shear strength [kPa], $\sigma' = \sigma - \max(u_w, u_i)$ = effective stress [kPa], σ = total stress [kPa], u_w and u_i excess pore-water and -ice pressure [kPa], respectively, φ' = effective internal

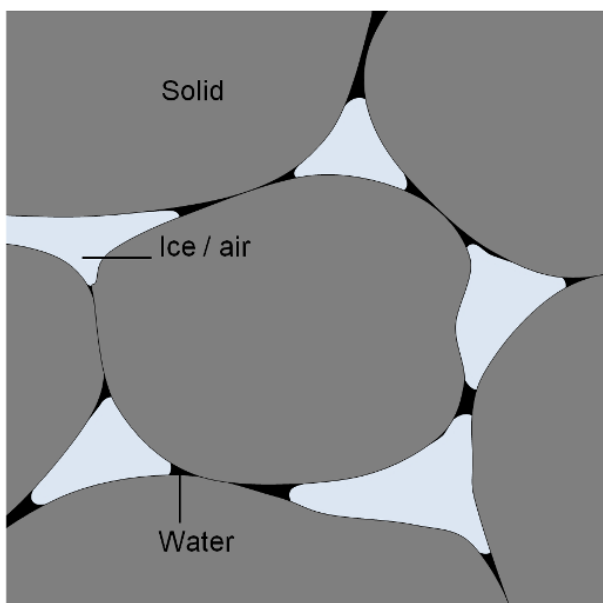


Figure 1. Schematic arrangement of solid phase, unfrozen water (menisci), ice, and/or air interfaces in a frozen soil.

friction angle [°], c_{app} = apparent cohesion or friction due to suction [kPa], s = suction [kPa], c_i = ice cohesion [kPa], t = time [s], T = temperature [K], σ_{ci} = confining pressure of the ice [kPa] which is equal to the ice pressure u_i , and $\dot{\epsilon}$ = strain rate [s^{-1}].

Equation 1 is based on effective stresses and the generalized form adapted from the unsaturated soil mechanics (Alonso et al. 1990, Fredlund 2000). Historically, most studies on shear strength of frozen soils are based on total stresses, as pointed out by Nishimura et al. (2009). For example, Arenson and Springman (2005) presented a Mohr-Coulomb failure criterion based on total stresses, in which the friction angle varies with changing ice content. This approach was extended and generalized by Nater et al. (2008) for well-drained soils. Using the effective stress approach, the volumetric friction angle (at constant volume) is assumed to be approximately constant, irrespective of normal stresses (as long as no grain crushing occurs) and whether it is dry or wet (Mitchell & Soga 2005). Therefore, only effective stresses are changing with altering ice content.

Cohesion based second strength components

The two types of cohesion in equation 1 are based on the second strength components, the apparent cohesion, and the ice cohesion, respectively ($c_{app}(s, \tan \varphi') + c_i(t, T, s_{c,i})$). These components change as soon as the volumetric ice content θ_p , together with the volumetric unfrozen water content θ_{uw} , exceeds the natural porosity n ($\theta_i + \theta_{uw} \geq n$) and the grains lose their contacts with adjacent grain particles. As long as grain contacts exist and water menisci can form, the matric suction can be used as a second strength component (Nishimura et al. 2009). The matric suction between the ice and the unfrozen water can be calculated with the Clapeyron equation, valid only for soils without an air phase (e.g., Black 1995, Henry 2000):

$$s_{iw}(u_w) = u_i - u_w = -u_w + \frac{\rho_i}{\rho_w} u_w - \rho_i L_f \ln \left(\frac{T}{T_0} \right) \quad (2)$$

where ρ_i [kg/m^3] and ρ_w [kg/m^3] are the densities of ice and water respectively, L_f the specific latent heat of fusion [J/kg], T the temperature of the soil [K] and T_0 the reference temperature (273.15 K).

The second strength component needs to be modified from the matric suction into the ice cohesion, as soon as the solid particles lose their contacts and the menisci are broken. This occurs, for example, when porosity increases due to the volume increase of freezing water or due to ice segregation and the ice-phase becomes continuous. In this case, the pore-water pressure of the unfrozen water and the ice pressure become equal (i.e., no suction exists) and turn into the new strength component—the ice cohesion. Up to the present, neither such a distinction of the second strength components nor a constitutive relationship for the shear strength depending on suction was considered.

Samples of frozen soil are often tested ice saturated. Therefore, the pore-ice pressure has to be inserted as a stress component with the corresponding constitutive relationship for the

ice cohesion. In addition, the ice cohesion depends on pressure, on temperature, strain rate, and total strain (Andersland & Ladanyi 2004). According to Arenson & Springman (2005) and Nater et al. (2008), the ice cohesion can be extremely high even with a low ice content and temperatures close to 0°C. Therefore, no shear strength failures are to be expected in a frozen soil. Of course, frozen talus slopes are prone to slow movement because of the creeping behavior of the ice matrix.

It is more likely that instabilities occur in the active layer due to deepening of the permafrost table as a result of an increase in the mean annual air temperature. Thawing of the ice matrix in frozen soil reduces the ice cohesion as well as the apparent cohesion. In addition, rapid thawing rates can develop excess pore-water pressures, which decrease the effective stress and result in a reduction of the frictional shear strength. This is true in fine-grained soils, with corresponding high ice contents. Conversely, Bommer et al. (2012) showed for a coarse scree slope in mountain permafrost that the influence of excess pore-water pressure due to thaw consolidation is small.

Case Study

Site characterization

In this section, the effect of rising temperature on shear strength is applied to a scree slope located above the village of Pontresina in the Upper Engadin valley (canton Grison), Eastern Swiss Alps. The slope lies at an altitude between 2,930 and 2,980 m a.s.l., and its inclination consists of an average angle of about 37°. Several investigations have been performed on the site. The geology, stratigraphy, and grain size distribution, the ice content as well as the hydrothermal processes in the permafrost and the active layer above are well documented (Phillips 2000, Arnold et al. 2005, Rist 2007). Unfortunately, no pore pressures have been measured. Figure 2 shows the typical stratigraphy of the site, consisting of the active layer (coarse talus material) on top. Under the active layer, permafrost was found consisting of finer material such as clay and silt, as well as larger stones. The two layers described superpose the bedrock, which is weathered on the top meter.

Assessment of shear strengths

For the calculation of the effect of rising temperatures on shear strength, Nixon and Morgenstern's (1973b, 1973a) general theory of thaw rate, developed from the thaw consolidation theory, is incorporated in the form of:

$$X(t) = Bt^n \quad (3)$$

where B [m/s] and n [-] are thaw-penetration parameters; the influence of nonlinear stress strain relation and the measurement and implication of the residual effective stress. Further, an infinite slope analysis is adapted. This is appropriate as slope failures in thawing permafrost tend to be long and shallow (McRoberts & Morgenstern 1974b, Harris & Lewkowicz 2000). Therefore, the shear strength can be obtained with:

$$\tau = c' + ((\gamma_1 H_1 + \gamma_{sat} X(t)) \cos \beta - u_w) \tan \varphi' \quad (4)$$

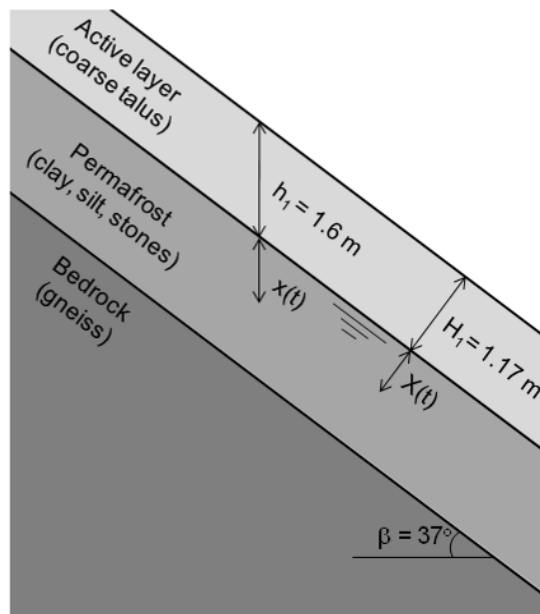


Figure 2. Simplified schematic stratigraphy of the steep test site in Pontresina (canton Grison), Eastern Swiss Alps, based on bore-hole cores (Phillips 2000).

where c' is the effective cohesion [kPa] depending on the strength component (apparent cohesion) of equation 1. Due to the restricted validity of equation 2, a fully ice-saturated soil is analyzed in this case study. The excess pore-water pressure u_w [IPa] in equation 4 is calculated after Morgenstern and Nixon (1971):

$$u_w = \frac{\gamma' X(t) \cos \beta}{1 + \frac{1}{2R^2}} \quad (5)$$

where γ' is the buoyant unit weight [kN/m³] of the soil and R the thaw consolidation ratio [-]. The hydrostatic pore-water pressures are negligible due to the sloping conditions.

In Table 1 the parameters and the soil properties used for the shear strength analysis are summarized. The soil temperature was varied to show the sensitivity of that parameter.

For the calculation, a mean annual thaw rate $X(t) = 0.6$ m normal to the slope was assumed. This assumption is based on a soil temperature time series of the active layer depth between 2001 and 2005 in borehole B2 on the site above Pontresina (Fig. 3). The depths in Figure 3 are shown in vertical direction and not perpendicular to the slope surface. The temperature of the frozen soil in the considered depth oscillates between +2°C (275.15°K) and around -2°C (271.15°K) (Zenklusen et al. 2010).

Results

The effect of warming temperature on shear strength in ice-saturated conditions for the assumed mean thaw rate $X(t) = 0.6$ m is shown in Figure 4. The increasing shear strength of the soil with decreasing soil temperature can be subdivided into the strength components discussed above; effective stresses σ' , ice suction s_{iw} (apparent cohesion) and ice cohesion c_i . For a certain depth and soil temperatures $\geq 0^\circ\text{C}$, the effective stress-

Table 1. Used parameters and soil properties for the shear strength analysis at the test site.

| Parameter / Property | Value |
|---|---------|
| Active layer (coarse talus) | |
| Degree of saturation, S_r [%] | 30 |
| Porosity, n [-] | 0.3 |
| Unit weight soil, γ_s [kN/m ³] | 19.5 |
| Permafrost layer (clay, silt, stones, ice) | |
| Degree of saturation, S_r [%] | 100 |
| Porosity, n [-] | 0.3 |
| Unit weight saturated soil, γ_{sat} [kN/m ³] | 21.6 |
| Internal friction angle, ϕ' [°] | 43 |
| Cohesion, c' [kPa] | 0 |
| Thaw penetration normal to the slope | |
| Soil temperature, T [°K] | 267–275 |
| Specific latent heat of fusion, L_f [J/kg] | 333.7 |
| Density of water, ρ_w [kg/m ³] | 1,000 |
| Density of ice, ρ_i [kg/m ³] | 918 |
| Thaw consolidation ratio, R [-] | 0.12 |
| Assumed mean thaw rate, $X(t)$ [m] | 0.60 |

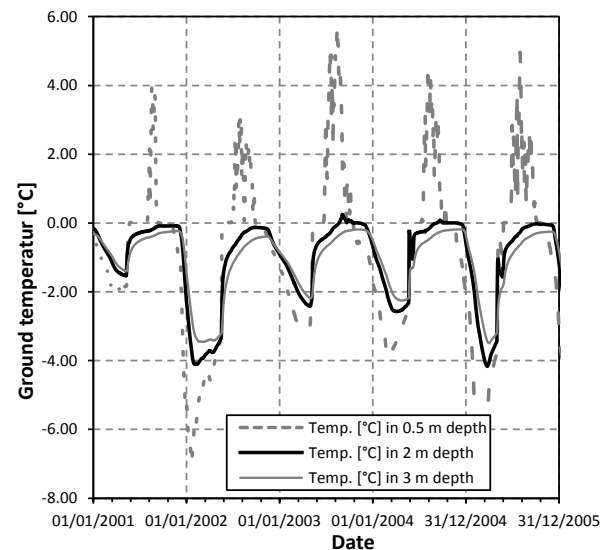


Figure 3. Temperature time series between 2001 and 2005 in borehole B2 (data from WSL/SLF, Davos).

es and therefore the shear strength are constant due to constant overburden and pore-water pressure. When ice and unfrozen water together with interconnected grains coexist and the soil temperature ranges between $\leq 0^\circ\text{C}$ and $\geq -3^\circ\text{C}$, matric suction or ice suction can develop due to the negative pore pressure. In the present case study, the calculated negative pore pressure with equation 2 leads to an increase in shear strength of about 4 kPa with respect to the effective stresses. A further decrease of the soil temperature, $\leq -3^\circ\text{C}$, turns most of the unfrozen water into ice, and ice cohesion (bonding) can develop. This leads to the evident increase in shear strength, shown in Figure

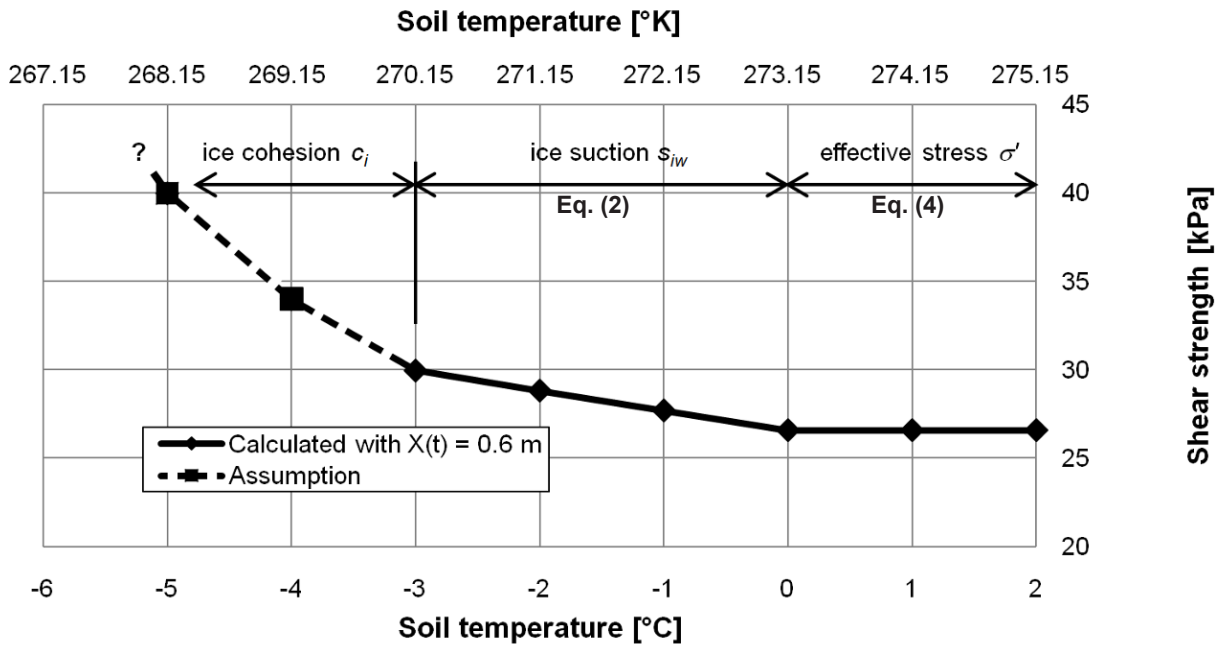


Figure 4. Shear strength increase of the soil with decreasing temperature and a constant thaw rate $X(t)$ of 0.6 m for an ice-saturated case.

4 (dashed line). The plotted increase in shear strength is not calculated for this case study, but the assumption reverts to tested frozen soil samples (e.g., Arenson & Springman 2005).

Discussion

The temperature-dependent shear strength results shown in Figure 4 are based on the assumption of ice-saturation of the frozen soil. The temperature thresholds of the different strength components are dependent on the soil composition and overburden pressure. For this case study within alpine permafrost, the following thresholds have been chosen: if the soil temperature is $\geq 0^\circ\text{C}$, the strength component depends on effective stresses only (saturated soil mechanics); if the soil temperature is between $\leq -0^\circ\text{C}$ and $\geq -3^\circ\text{C}$, the strength component depends on ice suction; and if the soil temperature is $\leq -3^\circ\text{C}$, the strength component depends on ice cohesion only. These assumed thresholds are based on the perception that in mountain permafrost, most water below -3°C is frozen (Arenson et al. 2009) due to the grain size distribution and the low salt content of the soils found in alpine permafrost.

Within the observed soil temperature range in Figure 3, seasonal thawing and freezing can be expected. Unfrozen water and ice in the saturated pores coexist. Therefore, shear strength depends on the temperature of the first strength component σ' effective stresses only, or on the first and the strength components c_{app} apparent cohesion due to ice suction.

For a soil temperature below the observed range ($\leq -3^\circ\text{C}$), a new constitutive relationship for the distinct increase of shear strength due to ice cohesion needs to be developed. One approach could be based on triaxial shear strength tests on frozen specimens. To determine the effective stresses, the ice-pres-

sure would have to be measured. So far, only total stress tests have been performed (Andersland & Ladanyi 2004, Arenson & Springman 2005).

To calculate the temperature-dependent shear strength for unsaturated conditions, a soil freezing characteristic curve (SFCC) for the temperature range $\leq 0^\circ\text{C}$, and a soil water characteristic curve (SWCC) for temperature $\geq 0^\circ\text{C}$ need to be determined in the laboratory. With the SFCC and the SWCC, the temperature and water content-dependent apparent cohesion due to suction can be calculated within the temperature thresholds discussed above and the shear strength can be defined.

The calculation of the excess pore-water pressure due to thaw consolidation (equation 5) showed only a minor influence on the shear strength for this case study. This is due to the high hydraulic conductivity of the coarse-grained soil and the steep slope on the site. This leads to a small thaw consolidation ratio, and a negligible value of excess pore-water pressure due to thaw consolidation. These findings are similar to those of an earlier study about thaw consolidation effects on slope stability (Bommer et al. 2012).

Conclusion

The shear strength of frozen soils is controlled by its grain size distribution, ice content, thermal state, and strain rate. On thawing, caused for example by an increase in the mean annual air temperature, two cases need to be considered to assess the shear strength of a soil. Case one consists of an ice-saturated soil, where a distinction between the ice cohesion and apparent cohesion should be incorporated in the analysis. Ice cohesion will be developed only if most of the water in the soil is frozen and has two effects on shear strength: 1) ice

pressure which results in a decrease of the effective stress and 2) strengthening effect due to bonding of the solid particles. With a further temperature increase, the ice matrix continuously transforms into water, and the ice cohesion is altered into apparent cohesion, that is, the matric suction between the ice or grains and the unfrozen water, respectively. Therefore, the shear strength of thawing soils varies considerably with changing temperature.

Case two consists of thawing ice in an unsaturated soil. Within this condition, a strengthening effect, due to ice bonding (ice cohesion), can lead to an increase in the effective stresses. To quantify the shear strength, if the ice bonding is lost through a temperature increase, a soil freezing characteristic curve for temperature $\leq 0^\circ\text{C}$ and a soil water characteristic curve for temperature $\geq 0^\circ\text{C}$ for the soil must be determined. With these two characteristic curves, the temperature and water content-dependent apparent cohesion due to suction can be defined and the shear strength can be quantified.

In a talus consisting of coarse ice, unsaturated or saturated soil, the excess pore-water pressure due to thaw consolidation can be neglected. This is due to the high hydraulic conductivity of the coarse-grained soil and gravitation drainage of the melting water on a slope.

Acknowledgments

This work was supported by the HSR (University of Applied Sciences, Rapperswil, Switzerland). The author is thankful to M. Phillips (WSL Institute for Snow and Avalanche Research SLF Davos) for providing this study with climate and borehole temperature data, and an anonymous reviewer for helpful comments and suggestions.

References

- Alonso, E.E., Gens, A. & Josa, A. 1990. A Constitutive Model for Partially Saturated Soils. *Geotechnique* 40(3): 405-430.
- Andersland, O.B. & Ladanyi, B. 2004. *Frozen ground engineering*. Hoboken, N.J., Wiley; American Society of Civil Engineers.
- Anderson, D.M. & Morgenstern, N.R. 1973. Physics, chemistry, and mechanics of frozen ground: A review. *North Am. Contrib. 2nd Int. Conf. on Permafrost*. Yakutsk, USSR, Washington, D.C.: National Academy of Sciences: 257-288.
- Arenson, L., Phillips, M. & Springman, S.M. 2009. *Geotechnical Considerations and Technical Solutions for Infrastructure in Mountain Permafrost*. New Permafrost and Glacier Research. M. I. Krugger and H. P. Stern.
- Arenson, L. & Springman, S. 2005. Mathematical descriptions for the behaviour of ice-rich frozen soils at temperatures close to 0 C. *Canadian Geotechnical Journal* 42(2): 431-442.
- Arnold, A., Thielen, A & Springman, S.M. 2005. On the stability of active layers in alpine permafrost. *Landslides and Avalanches: ICFL 2005 Norway*: 19-25.
- Black, P.B. 1995. *Applications of the Clapeyron equation to water and ice in porous media*. Hanover, N.H.; Springfield, Va., US Army Corps of Engineers, Available from NTIS.
- Bommer, C., Fitze, P. & Schneider, H.R. 2012. Thaw consolidation effects on the stability of alpine talus slopes in permafrost. Submitted for possible publication in *Permafrost and Periglac. Process*.
- Fredlund, D.G. 2000. The 1999 R.M. Hardy Lecture: The implementation of unsaturated soil mechanics into geotechnical engineering. *Canadian Geotechnical Journal* 37(5): 963-986.
- Harris, C. & Lewkowicz, A.G. 2000. An analysis of the stability of thawing slopes, Ellesmere Island, Nunavut, Canada. *Canadian Geotechnical Journal* 37(2): 449-462.
- Henry, K.S. 2000. A review of the thermodynamics of frost heave. Hanover, N.H., US Army Corps of Engineers Engineer Research and Development Center.
- Hutchinson, J.N. 1974. Periglacial solifluxion: an approximate mechanism for clayey soils. *Géotechnique* 24(3): 438-443.
- Lambe, T.W. & Whitman, R.V. 1969. *Soil mechanics*. New York, Wiley.
- McRoberts, E.C. & Morgenstern, N.R. 1974a. Stability of slopes in frozen soil, Mackenzie Valley. *Canadian Geotechnical Journal* 11(4): 554-573.
- McRoberts, E.C. & Morgenstern, N.R.. 1974b. The stability of thawing slopes. *Canadian Geotechnical Journal* 11(4): 447-469.
- Mitchell, J.K. & Soga, K.i. 2005. *Fundamentals of soil behavior*. Hoboken, N.J., John Wiley & Sons.
- Morgenstern, N.R. & Nixon, J.F. 1971. One-dimensional consolidation of thawing soils. *Canadian Geotechnical Journal* 8(4): 558-565.
- Nater, P., Arenson, L. & Springman, S. 2008. Choosing geotechnical parameters for slope stability assessments in Alpine permafrost soils. In *NICOP 2008: Proceedings of the Ninth International Conference on Permafrost*. D.L. Kane, K.M. Hinkel (eds.). Institute of Northern Engineering, University of Alaska Fairbanks, 1: 1261-1266.
- Nishimura, S., Gens, A., Olivella, S., & Jardine, R.J. 2009. THM-coupled finite element analysis of frozen soil: formulation and application. *Geotechnique* 59(3): 159-171.
- Nixon, J.F. & Morgenstern, N.R. 1973a. Practical Extensions to a Theory of Consolidation for Thawing Soils. *North Am. Contrib., 2nd Int. conf. on Permafrost*. Yakutsk, USSR, Washington, D.C.: National Academy of Sciences: 369-377.
- Nixon, J.F. & Morgenstern, N.R. 1973b. The residual stress in thawing soils. *Canadian Geotechnical Journal* 10: 571-580.
- Phillips, M. 2000. Influences of snow supporting structures on the thermal regime of the ground in alpine permafrost terrain. Davos, Swiss Federal Institute for Snow and Avalanche Research SLF: 146.
- Rist, A. 2007. Hydrothermal processes within the active layer above alpine permafrost in steep scree slopes and their influence on slope stability (PhD thesis). Permafrost and Snow Climatology SLF; Department of Geography, Swiss Federal Institute for Snow and Avalanche Research SLF; University of Zurich.: 201.

Zenklusen, M.E., Blanchet, J., & Phillips, M. 2010. Analysis of ground temperature trends in Alpine permafrost using generalized least squares. WSL Institute for Snow and Avalanche Research SLF, Davos Dorf, Switzerland.

An Integrated Assessment of the Influences of Upland Thermal-Erosional Features on Landscape Structure and Function in the Foothills of the Brooks Range, Alaska

W.B. Bowden, J.R. Larouche, A.R. Pearce

The Rubenstein School of Environment and Natural Resources, University of Vermont, USA

B.T. Crosby, K. Krieger

Department of Geosciences, Idaho State University, USA

M.B. Flinn, J. Kampman

Department of Biological Sciences, Murray State University, KY, USA

M.N. Gooseff, S.E. Godsey

Department of Civil & Environmental Engineering, Pennsylvania State University, USA

J.B. Jones, B.W. Abbott, M.T. Jorgenson

Institute of Arctic Biology, University of Alaska Fairbanks, USA

G.W. Kling

Department of Ecology & Evolutionary Biology, University of Michigan, USA

M. Mack, E.A.G. Schuur, A.F. Baron

Department of Botany, University of Florida, USA

E.B. Rastetter

The Ecosystems Center, Marine Biological Laboratory, Woods Hole, MA

Abstract

We established the Arctic System Science/Thermokarst (ARCSS/TK) project in 2008 with the intent to use a systems approach to address hypotheses about how upland thermo-erosional features influence the structure and function of the foothill and mountainous landscape in the vicinity of the Brooks Range in arctic Alaska. We found that the common thermo-erosional features in this region are thaw slumps, thermo-erosional gullies, and active layer detachment slides. These features significantly redistribute and reduce soil carbon and nutrients. Sediments and nutrients are exported from thermo-erosional features and may impact streams and lakes. In general, productivity was greater in streams and lakes influenced by thermokarst inputs; that is, nutrient stimulation outweighed sediment interference. In either case, however, these effects are transitory on the timescale over which these thermo-erosional features form, stabilize, and revegetate. Our estimate of the rates at which carbon and nutrients accumulate after these thermo-erosional features stabilize is much faster based on field measurements than our estimates based on model predictions, suggesting that alternative sources of C and nutrients must be available. These features are numerous in the current landscape ($\sim 4/\text{km}^2$ in the area of this study) and are likely to be important as agents of nutrient redistribution across the arctic landscape.

Keywords: lakes; permafrost; thermo-erosion; slope processes; thermokarst; soil nutrients; streams; vegetation.

Introduction

A substantial portion of the permafrost in the arctic region may thaw in coming decades (e.g., Grosse et al. 2011, Hugelius et al. 2011). When ice-rich permafrost thaws, thermo-erosional features, or thermokarst terrain, often form. The threats of thermal erosion to civil infrastructure are reasonably well recognized if not quantified (e.g., Nelson et al. 2002). More recently, attention has turned to the impacts that thermal erosion might have on undeveloped systems (e.g., Jorgenson et al. 2001).

The dynamics of permafrost degradation and thermo-erosion in foothill and mountain terrain are less well known than similar dynamics on coastal plains and peat plateaus in the Arctic. These dynamics might differ by region on the basis of fundamental differences in topography, precipitation regimes, and runoff characteristics. The ARCSS/TK project was designed to address a set of interacting questions: What

physical factors predispose hillslopes to fail when permafrost thaws? How do soil and water chemical characteristics change when thermo-erosional features form? How do the fluxes of carbon, nutrients and sediment change? What are the short-term and long-term trajectories of carbon and nutrient accumulation, including vegetation regrowth? What are the implications of past and future landscape change? In this paper, we provide results regarding the internal dynamics of C and N within selected thermo-erosional features and the impacts of these features on local streams and lakes.

Site Description

For this paper, we have focused on a limited set of upland thermo-erosional features that include thaw slumps (TS), thermo-erosional gullies (TEG), and active layer detachment slides (ALDS).

This research was conducted in the vicinity of the Toolik Field Station (TFS) (68°38'N, 149°36'W), approximately 255 km north of the Arctic Circle at an average elevation of 720 m a.s.l. in the foothills of the Brooks Range. The glacial history of the TFS region is described by Hamilton (2003), who concluded that the complex deposits in this area are the product of drift from at least four separate glacial intervals whose northward advance from the Brooks Range progressively decreased with each advance. This created four distinct landscape ages ranging from late Tertiary and early Pleistocene glacial advances to the more recent late Wisconsin advances of North America.

The mean annual temperature ranges from -6 to -11°C with summer highs of 10 to 18°C and winter lows of -30 to -40°C. Mean annual precipitation ranges from 250 to 407 mm with 30-40% falling as snow between September and May. According to Walker et al. (2002), the study area is in the warmest of the arctic subzones (Subzone E), defined by shrubs including dwarf birch (*Betula nana*) and several species of willows (*Salix* spp.). The dominant vegetation community is tussock tundra, defined by the tussock-forming grass *Eriophorum vaginatum*. Vegetation and soils in the study area have developed in response to interactions among the glacial legacy described above, topography, and climate. The plant and soil associations can be broadly divided into acidic and non-acidic tundra landscapes based on differences in organic matter accumulation and weathering processes (van der Welle et al. 2003).

Methods

We sampled 11 sites (7 TEG and 4 TS). Each site was classified into several patch types: exposed (unvegetated), revegetated (formerly exposed but newly vegetated), rafts (detached clumps of original vegetation displaced downslope), margins (edges of sites but not subsided), and drapes (edges of sites that had subsided).

We calculated soil respiration using a closed, recirculating chamber in which we measured the accumulation of CO₂ with a LICOR Li-8100 automated soil respiration monitoring system. Respiration was measured at 10–20 locations within each patch type at each site. Most sites were visited monthly (3 times) during the summer of 2010. For this paper, the results from all visits to a specific site were summarized into a seasonal mean value. At each respiration sampling point we also measured the soil temperature at 10 cm depth and integrated soil moisture between the soil surface and 15 cm depth, and summarized this data as for respiration. We estimated organic and mineral carbon (C) and nitrogen (N) pools on the basis of bulk density and element concentrations measured on 6 soil monoliths randomly located in the patch types at each site, and scaled via organic layer depth measured at 20 additional representative points.

At several of our sites we could identify disturbance events (lobes) that clearly occurred at different times. We used two independent approaches to estimate the ages of these lobes: the population age structure of tall shrub species that establish

after disturbance (primarily *Salix alexensis*), and radiocarbon dating of moss litter at the base of the organic layer.

To explore different scenarios for soil and vegetation C accumulation over time since disturbance, we calibrated the Multiple Element Limitation (MEL; Rastetter et al. 2005) model to data from the Toolik Lake, Arctic LTER database (<http://ecosystems.mbl.edu/arc/datacatalog.html>). MEL simulates interactions of the C, N, P, and water cycles at a plot scale on a daily time step. The model uses an allocation scheme that continually redistributes resource uptake effort within plants to maintain a stoichiometric balance and maximize growth. Analogous processes are represented for microbial metabolism in soils, but microbial biomass is implicitly represented as part of the soil organic matter. In this paper, we focus primarily on the predictions for C accumulation by the MEL model.

To detect differences in reference and thermokarst-impacted streams, we established monitoring sites above and below the point of impact of TEGs on two streams: the Toolik River and Iminus2 stream. We used YSI Model 600 OMS data sondes with ROX optical dissolved oxygen sensors, thermistors, and electrical conductivity sensors to measure whole-stream metabolism using standard, single-station methods (Bott 2004). Sensors were placed at the end of representative reference (upstream of impact) and impacted (downstream of impact) reaches in both streams. A standard light-dark incubation approach was used to measure metabolism in lake NE-14 sediments, a typical thermokarst lake that has been affected by multiple TS events over time.

In 2010 we quantified the impact of sediment inputs on benthic macroinvertebrate community characteristics (i.e., diversity, richness, abundance, overall biomass, functional feeding groups) in downstream impacted reaches of the Toolik River and Iminus2 stream, relative to upstream reference reaches. Benthic macroinvertebrates were sampled at 5 sites within each reference and impacted reaches, and identified to lowest taxonomic level. Samples were collected once per month over the summer 2010 season to assess seasonal shifts within the community. Macro-invertebrate data were then compared to sedimentation data to assess correlations between community characteristics and sediment inputs throughout the season.

To estimate the density of thermo-erosional features on our study landscape, we utilized Light Detection and Ranging Radar (LiDAR) data provided to us by the Alaska State Department of Transportation (ADOT). LiDAR data provide a level of spatial resolution (1 m horizontal and 0.15 m vertical) that far exceeds what can be obtained by most satellite-based remote sensing products (10s to 100s m) and are better suited to detect the fine detail of small thermo-erosional features. In 2009, the ADOT acquired LiDAR data for a proposed road corridor on the western boundary of the area in which we conducted this research. The corridor is about 170 km long and 5–15.5 km wide, and it covers landscape forms similar to those that we studied. We reprocessed this data and visually inspected the entire scene searching for features that matched the expected morphologies for TS, TEG, and ALDS.

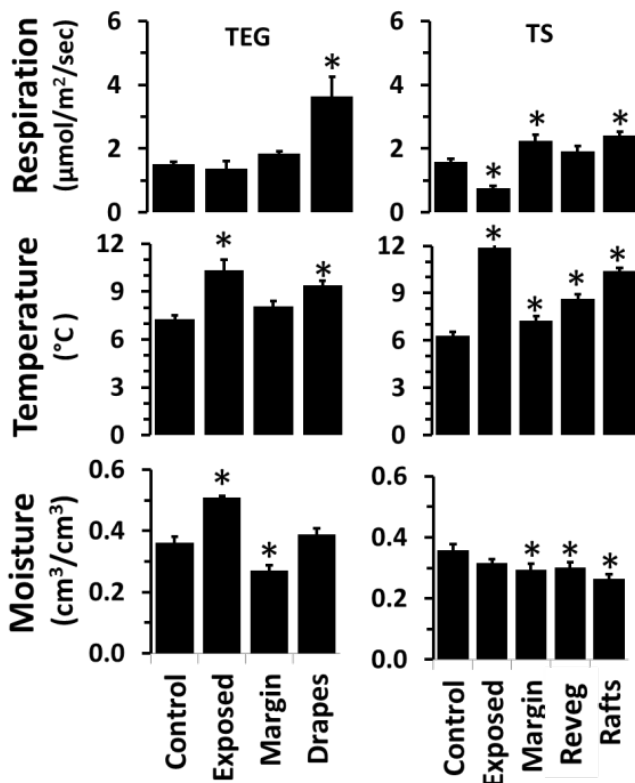


Figure 1. Respiration, soil temperature (at 10 cm depth), and soil moisture (in top 15 cm of soil) in patch types within 7 TEG and 4 TS during the summer (June, July and August) of 2010. Significant differences ($P > 0.05$) from measurements in control patches are noted with an asterisk (*).

Results

Local impacts

Soil moisture in TEG was higher in exposed soils and lower in margin patch types compared to control patches, but did not differ in drapes (Fig. 1). In thaw slumps, soil moisture was lower in all patch types except exposed soils. Soil temperature in TEG was higher in exposed soils and drapes compared to control patches, but did not differ in margins. In thaw slumps, soil temperature was higher in all patch types than in the control patches. The effect of soil warming could be detected to at least 80 cm below the surface (data not shown).

We measured significantly higher respiration in the moderately disturbed drape patch types of TEG. Respiration in exposed patch types of thaw slumps was lower than the control patch or any other impacted patch types. Respiration in the margin and raft patch types of thaw slumps was similar and higher than respiration in the control patches. A similar difference was observed in re-vegetated patch types, but this difference was not significant.

We concluded that the NE-14 site (a TS) had three shoreline lobes with ages of 5, 42, and 46 years based on shrub ages and radiocarbon dating of moss litter. Analyses of soil C and N pools in these lobes suggest that in the initial years of thermokarst activity there is a rapid decrease in the organic soil C and N pool as it breaks up and moves down slope, in many cases

Table 1. Soil C and N. The organic soil pool is shown as the total accumulation per site to a variable depth, whereas the mineral soil is standardized using the top 10 cm of that horizon. Values in parentheses are standard errors of the means.

| Site | C pools (KgC*m ²) | | N pools (KgN*m ²) | |
|-----------------------|-------------------------------|---------|-------------------------------|---------|
| | Organic | Mineral | Organic | Mineral |
| Undisturbed | 23.8 | 3.5 | 1.4 | 0.22 |
| Tundra | (0.9) | (1.2) | (0.11) | (0.07) |
| Lobe 1 (active) | 12.8 | 1.4 | 0.8 | 0.11 |
| | (1.8) | (0.25) | (0.09) | (0.02) |
| Lobe 2 (~42 years) | 21.6 | 2.6 | 1.4 | 0.17 |
| | (5.8) | (0.49) | (0.44) | (0.03) |
| Lobe 3 (~46 years) | 19.8 | 4.5 | 1.3 | 0.29 |
| | (2.9) | (0.32) | (0.14) | (0.02) |

tumbling and mixing with mineral soil and sediments. At NE-14, organic soil C stocks were reduced by about 50% between the undisturbed tundra and the center of lobe 1, the active thermokarst feature (Table 1). Carbon pools in the top 10 cm of mineral soil C pools were similarly reduced by 60% relative to the undisturbed tundra. Thus in the organic layer and top 10 cm of mineral soil, about 13 kg C/m² were not accounted for in the active layer of the thaw slump. This C may have been lost to the atmosphere via rapid decomposition, to the lake via hydrologic export, to deeper soil strata that are now frozen, or were not adequately characterized in our sampling. Assuming this loss is real and not due to sampling error, this is a substantial loss of soil C from the younger lobe.

However, we also found that the older Lobes #2 and #3 of NE-14 had as much C in the organic and thawed mineral soil layers as did the undisturbed tundra. If the thermokarst lobes and undisturbed tundra sites represent an adequate temporal sequence since disturbance, then this suggests that soil C stocks recover to pre-disturbance levels within as little as 42 years. This accumulation rate would require sequestration of about 300 g C/m² in the vertically aggrading organic soil layer, which is within the range of annual vascular plant and moss litter production in shrub tundra (Shaver and Chapin 1991, DeMarco et al. 2011).

We used the MEL model to simulate tundra regrowth following a thermal erosion disturbance in which 90% of the plant biomass was removed. An equal proportion of C, N, and P was removed or added to the soil organic matter (SOM). The SOM remaining within a plot might increase or decrease as a result of thermal erosion, depending upon location within the scar. We therefore simulated regrowth with initial SOM ranging from 25% to 125% of the original SOM in the undisturbed site (Fig. 2).

Because the SOM serves as the nutrient reserve that supports the regrowth of plants, the amount of SOM remaining after

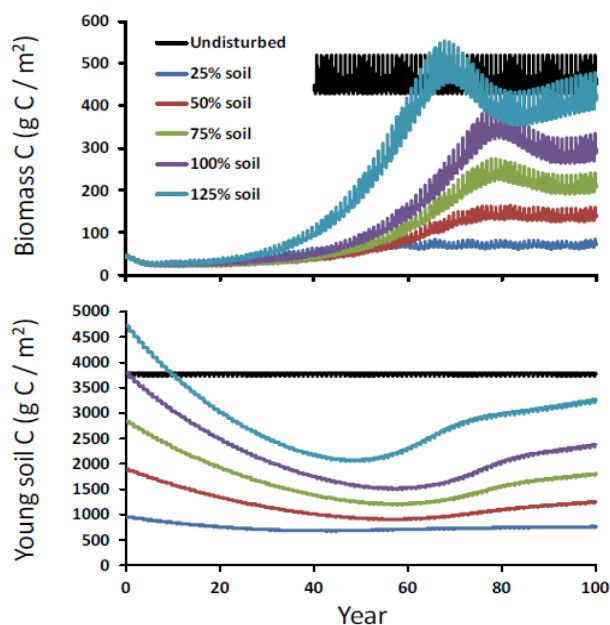


Figure 2. MEL model results.

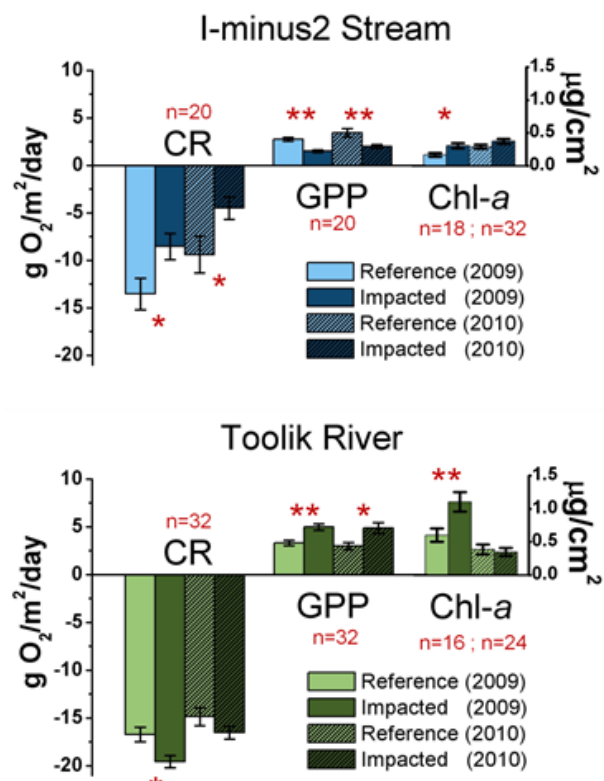
disturbance has a major effect on plant regrowth. Simulated plant biomass recovered faster and by an initially greater amount with a larger starting SOM pool. Regardless of initial SOM, all simulations eventually converged on the undisturbed state but required thousands of years to entrain the necessary nutrients to support this high biomass.

In all simulations, there is a net loss of carbon and nutrients from the ecosystem during the first 40 years of recovery. During this time, plant nutrient uptake lagged mineralization, and low litter input limited microbial access to the fresh, labile carbon that supports nutrient immobilization. Absolute losses increased with the amount of initial SOM in the simulation. Even beginning with 125% of the undisturbed SOM, the ecosystem lost carbon and nutrients over the 100 years of the simulation. The simulations follow the general pattern observed in the field samples (Table 1) but not the timing; nutrients and biomass appear to accumulate faster in the field than in the model.

Distal impacts

The impacts of thermo-erosional features are not restricted to local influences on C, N, and P in soils and vegetation. These features sometimes form in close proximity to streams and lakes and can influence the nutrient and sediment loading to these water bodies (Kokelj et al. 2005, Bowden et al. 2009). In general, we expect increased nutrient loading to increase gross primary production (GPP) and community respiration (CR) and to promote diversity in benthic invertebrate community composition. We expect increased sediment loading to have opposite effects.

During 2009 and 2010, we intensively monitored nutrient and sediment concentrations and loads in Toolik River and Iminus2. In general, we observed that concentrations of sediment, dissolved organic C, and ammonium were higher

Figure 3. Whole-stream metabolism and chlorophyll-*a*.

below the thermal erosion impact points than above them. However, concentrations of nitrate and phosphorus were not significantly different (data not shown).

Our estimates of community respiration (CR), gross primary productivity (GPP), and chlorophyll-*a* (Chl-*a*) in Iminus2 and Toolik River differed in response to sediment and nutrient loading and by year (Fig. 3). Rates of CR and GPP in the impacted reach of Iminus2 were significantly lower than in the reference reach, despite having higher chlorophyll-*a*. Conversely, CR and GPP in the impacted reach of the Toolik River were significantly higher in 2009 but not in 2010. In 2010 there were only moderate differences in GPP alone. Chlorophyll-*a* in the impacted reach of the Toolik River was higher compared to the reference reach in 2009 only.

In the impacted reach of Iminus2, early in the season as sedimentation rates increased, macroinvertebrate diversity decreased ($p < 0.10$) while abundance ($p < 0.05$) and biomass ($p < 0.10$) both increased. However, nutrients added from thermal erosion increased biofilm density and food availability in the impacted reaches during the early season. The quality of this additional food source may have been compromised as the season progressed due to increased deposition of inorganic sediment, which decreased food quality for benthic macroinvertebrates. There was a decrease in the functional group of macroinvertebrates that preferentially use this food resource later in the season (data not shown). The patterns observed in Toolik River were more variable, with no significant shift in any macroinvertebrate community parameters.

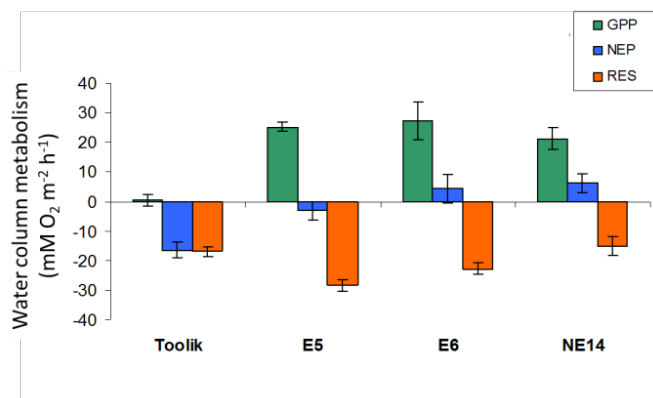


Figure 4. Gross primary production (GPP), net primary production (NEP), and respiration (CR) in the sediments of Toolik Lake and three smaller lakes near it. NE-14 has a large active thaw slump and has been affected by other thaw slumps in the past.

Metabolism in lake NE-14 also appeared to be stimulated by inputs from the TS (Fig. 4). Rates of gross primary production (GPP), respiration (RES), and the resulting net ecosystem productivity (NEP) were much higher than in a nearby reference lake (Toolik Lake). These rates were similar to measured values in two lakes that had been experimentally fertilized with N and P in earlier experiments (E5 and E6, Fig. 4, A. Giblin & T. Coolidge, unpublished data).

We found that thermo-erosional features such as those studied for this project are common in the foothills region around Toolik Lake. In the LiDAR scene we obtained from the ADOT, we identified nearly 7000 features (Fig. 5), an average density of roughly 4 features per km². In total, the identified features occupied nearly 2% of the 1698 km² scene.

Discussion

It is difficult to identify the age (time since original disturbance) for individual features. Remote sensing data provide a limited answer. The only data product with a sufficiently long temporal record is LANDSAT imagery. However, the spatial resolution of this imagery is not sufficient to reliably identify smaller thaw slumps and ALDS, which tend to be long and narrow. Bowden et al. (2009) used high-resolution aerial imagery from the early 1980s and newly acquired imagery from 2006 to conduct a roughly 25-year change analysis. However, most features are much older than this.

Our detailed analysis of the NE-14 feature suggests that the most mature thaw features may only be ~50 years old, which is somewhat younger than we expected. We found that, as expected, thermo-erosional features mix and disperse soil C, N, and P downslope. We were surprised at how quickly C and N seem to accumulate as these features stabilize. Some of the rapid C accumulation is apparently due to rapid colonization by shrub species, notably the willow *Salix alexandris*. However, the mechanisms of nutrient accumulation to support this C accumulation are not entirely clear. The current state of our modeling captures the correct pattern of C accumulation but

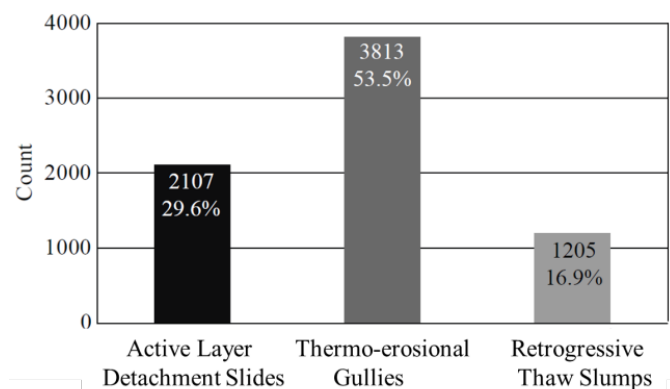


Figure 5. Number of thermo-erosional features by type.

suggests that the C and nutrient accumulation rates should be slower than we have observed. This is an important discrepancy that bears further consideration.

The impacts of thermo-erosional features in hilly landscapes are not restricted to the local disturbance. Topography and gravity redistribute displaced soils and soil nutrients downslope, often to streams and lakes. However, the influences of sediment and nutrient inputs from thermokarst terrain to streams and lakes are not well known. Kokelj et al. (2005) have shown that sediment inputs from thaw slumps on thermokarst lakes in the McKenzie River delta in the Canadian Arctic can have profound impacts on the color (DOC content) and clarity of these lakes. However, there is no comparable information for streams and lakes in foothill and mountain landscapes, and relatively little information anywhere about how thermo-erosional features affect higher-order ecological processes like photosynthesis and respiration.

During the period 2009 to 2010, the weather patterns in the Toolik Lake region were relatively quiet, with few large storm events to mobilize sediment and nutrients from thermo-erosional features. Nevertheless, we did observe significantly higher sediment concentrations and slightly higher concentrations of some nutrients (ammonium) in thermokarst-impacted versus reference reaches of the streams we monitored intensively.

Despite these somewhat subtle impacts, we observed significant changes to benthic characteristics (total C and N, chlorophyll-*a*) and to important ecosystem processes like GPP and CR. There appear, however, to be interactions between these effects and the stream type. The Iminus2 stream has a steeper gradient than the Toolik River and has a step-riffle morphology with large cobble substrate. The Toolik River is a beaded stream with a lower gradient and a greater influence of silty substrate, especially in pools. These geomorphic characteristics may have had some influence on the responses of these streams to sediment and nutrient inputs. In particular, GPP and CR in the Iminus2 stream were impaired by these inputs, while GPP and CR in the Toolik River were stimulated. This may be a consequence of different communities in these two streams, with different sensitivities to sediment and nutrient inputs. It appears, for example, that the alluvial Iminus2 stream may be more sensitive to sediment inputs

while the Toolik River community may be less sensitive. It is notable that Chl-a in the Toolik River increased significantly in the slightly wetter 2009 field year, and that the benthic macroinvertebrate community did not decrease noticeably. We conclude that while sediment has the potential to interfere with primary and secondary production and nutrients have the potential to increase production, in the long-term these stream communities can tolerate these effects. Nutrient loading would have to be higher and more persistent to fundamentally alter stream ecosystems in the ways reported by Slavik et al. (2004) for the Kuparuk River long-term phosphorus fertilization experiment. The effects on lakes may be similar. We observed that GPP was significantly higher in NE-14 than in the reference Toolik Lake, although CR was similar. It is not clear, however, whether the nutrient enrichment or its effect will persist.

Our analysis of the LiDAR imagery suggests that these thermo-erosional features are a common component of the landscape around Toolik Lake. Our earlier analysis (Bowden et al. 2009) concluded that the density of these features had probably increased in recent decades. However, these are natural features whose frequency almost certainly waxes and wanes as the climate moves from warmer to cooler periods. On the basis of the work presented here, we conclude that these features may have local and temporary impacts on stream and lake ecosystems. But these effects are likely to be ephemeral. The longer-term impacts of thermo-erosional features are to shape the landscape and, in so doing, to redistribute C and nutrients.

Acknowledgments

The material presented here is based on work supported by the U.S. National Science Foundation under collaborative grants ARC-0806394, ARC-0806399, ARC-0806329, ARC-0806254, ARC-0806465, ARC-0806451, ARC-0806341, ARC-0806271, and DEB-1026843. Any opinions, findings, conclusions, or recommendations expressed in this material are those of the authors and do not necessarily reflect the views of the National Science Foundation. We thank the staff of the Toolik Field Station and CH2M-Hill Polar Services for logistical support.

References

- Bowden, W.B., Gooseff, M.N., Balsler, A., Green, A., Peterson, B.J., & Bradford, J. 2008. Sediment and nutrient delivery from thermokarst features in the foothills of the North Slope, Alaska: Potential impacts on headwater stream ecosystems. *Journal of Geophysical Research* 113, G02026, doi:10.1029/2007JG000470.
- Bott, T.L. 2004. Primary Productivity and Community Respiration. 2006. Chapter 28 in R. Hauer and G. Lamberti, *Methods in Stream Ecology*. Boston: Academic Press.
- DeMarco, J., Mack, M.C., & Bret-Harte, M.S.. 2011. The Effects of Snow, Soil Microenvironment, and Soil Organic Matter Quality on N Availability in Three Alaskan Arctic Plant Communities. *Ecosystems* 14(5): 804-817, DOI: 10.1007/s10021-011-9447-5.
- Grosse, G., Harden, J., Turetsky, M., McGuire, D., Camill, P., Tarnocai C., Frolking S., Schuur, E.A.G., Jorgenson, T., Marchenko, S., Romanovsky V., Wickland, K.P., French N., Waldrop, M., Bourgeau-Chavez, L., & Striegl, R.G. 2011. Vulnerability of High-Latitude Soil Organic Carbon in North America to Disturbance. *Journal of Geophysical Research* 116, G00K06, doi:10.1029/2010JG001507.
- Hamilton, T.D. Glacial geology of the Toolik Lake and Upper Kuparuk River region, University of Alaska Fairbanks, Institute of Arctic Biology, Biological Papers of the University of Alaska, Fairbanks, Alaska, 2003.
- Hobbie, J.E., Peterson, B.J., Bettez, N., Deegan, L., O'Brien, W.J., Kling, G.W., Kipphut, G.W., Bowden, W.B., & Hershey, A.E. 1999. Impact of global change on the biogeochemistry and ecology of an Arctic freshwater system. *Polar Research* 18, 207-214.
- Hugelius, G., Virtanen, T., Kaverin, D., Pastukhov, A., Rivkin, F., Marchenko, S., Romanovsky, V., & Kuhry, P. 2011. High-Resolution Mapping of Ecosystem Carbon Storage and Potential Effects of Permafrost Thaw in Periglacial Terrain, European Russian Arctic. *Journal of Geophysical Research* 116, G03024, doi:10.1029/2010JG001606.
- Jorgenson, M.T., Racine, C.H., Walters, J.C., & Osterkamp, T.E. 2001. Permafrost degradation and ecological changes associated with a warming climate in central Alaska. *Climatic Change* 48, 551-579.
- Kokelj, S.V., Jenkins, R.E., Milburn, D., Burn, C.R., & Snow, N. 2005. The influence of thermokarst disturbance on the water quality of small upland lakes, Mackenzie Delta Region, Northwest Territories, Canada. *Permafrost and Periglacial Processes* 16, 343-353.
- Nelson, F.E., Anisimov, O.A., & Shiklomanov, N.I. 2002. Climate change and hazard zonation in the circum-Arctic permafrost regions. *Natural Hazards* 26, 203-225.
- Rastetter, E.B., Perakis, S.S., Shaver, G.R., & Ågren, G.I.. 2005. Carbon Sequestration in Terrestrial Ecosystems Under Elevated CO₂ and Temperature: Role of Dissolved Organic N Loss. *Ecological Applications* 15:71-86.
- Rouse, W.R., Douglas, M., Hecky, R.E., Hershey, A., Kling, G.W., Lesack, L., Marsh, P., McDonald, M., Nicholson, B., Roulet, N., & Smol, J. 1997. Effects of climate change on the fresh waters of arctic and subarctic North America. *Hydrological Processes* 11, 873-902, 1997.
- Shaver, G.R. & Chapin, F.S. III. 1991. Production:biomass relationships and element cycling in contrasting arctic vegetation types. *Ecological Monographs* 61:1-31.
- Slavik, K., Peterson, B.J., Deegan, L.A., Bowden, W.B., Hershey, A.E., & Hobbie, J.E. 2004. Long-term response of the Kuparuk River ecosystem to phosphorus fertilization. *Ecology* 85, 939-954.
- van der Welle, M.E.W., Vermeulen, P.J., Shaver, G.R., & Berendse, F. 2003. Factors determining plant species richness in Alaskan arctic tundra. *Journal of Vegetation Science* 14, 711-720.
- Walker, D.A., Gould, W.A., Maier, H.A., & Reynolds, M.K. 2002. The Circumpolar Arctic Vegetation Map: AVHRR-derived base maps, environmental controls, and integrated mapping procedures. *International Journal of Remote Sensing* 23, 4551-4570.

Influence of Physical Properties on Frozen Soil Creep Parameters and Foundation Design

Paul Cavanagh, Kevin Spencer, Alexandre Tchekhovski
AMEC Environment and Infrastructure, Calgary, Canada

Victor Aksenov
Fundament Project, Moscow, Russia

Abstract

Unconfined compressive tests were carried out for frozen sand, silt, and clay at various temperatures and salinity. Plots of strain rate versus applied load during secondary creep were used to calculate “B” and “n” creep parameters used for designing adfreeze piles. Results of calculations show that the “B” parameter functions for sand, silt, and clay are different in shape, reflecting the complexity of the freezing process in saline soils. It was also found that the “n” parameter value is unique for each soil at a given temperature and salinity. As a practical application, this paper provides a methodology to estimate the allowable stress that will satisfy given settlement criteria.

Keywords: creep; design; foundation; frozen; soil; strength.

Introduction

Frozen soil under applied loading will deform, or creep, over time. Generally, the creep phenomenon is divided into three categories known as primary, secondary, and tertiary creep, which develop in response to specific conditions of applied stress, soil temperature, soil salinity, and soil composition (i.e., ice content). Figure 1 illustrates the three types of soil creep and shows that the creep rate for a frozen soil sample under load is dependent on time. The creep rate decreases continuously to a near-zero value during primary creep, remains constant during secondary creep, and continuously increases to the point of sample failure during tertiary creep. Typically, frozen samples under high applied loading undergo all three types of creep (Fig. 1). Frozen soils under low applied loading usually exhibit either primary creep only, or a short interval of primary creep followed by secondary creep (Andersland & Ladanyi 2004). The literature (Valyov 1958, Hult 1966, McRoberts 1975) documents that the behavior of ice-poor soils under low applied loading is dominated by primary creep between soil particles. At higher soil ice contents, secondary creep increasingly influences soil deformation under loading because there is less contact between soil particles, and soil behavior is primarily determined by creep within the ice.

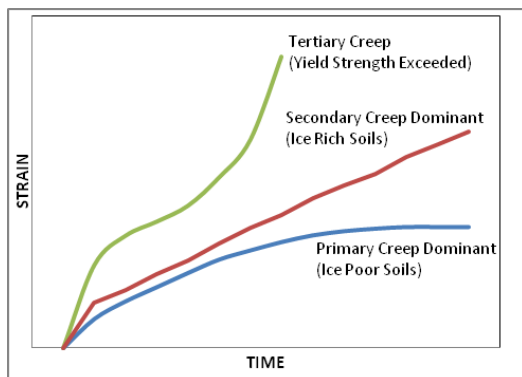


Figure 1. Typical Creep Curves for Frozen Soils.

Predicting settlement of frozen soil under loading must consider that the total settlement is the sum of short-term settlement plus creep settlement (equation 1).

$$S_{tot} = S_{short} + S_{long} \quad (1)$$

The short-term settlement (S_{short}) consists of elastic settlement, and potentially some plastic settlement, together with the settlement due to primary creep. Normally in pile design practice, if no actual data are available on primary creep, the short-term settlement may be calculated using the shear modulus of the frozen soil. The long-term settlement (S_{long}) is predicted from the strain rate for the secondary creep over the design life of the structure. Equation 1 can also be expressed as follows:

$$S_{tot} = S_{short} + \dot{\epsilon}t \quad (2)$$

where $\dot{\epsilon}$ = strain rate during secondary creep and t = time.

Equation 3, describing creep flow in polycrystalline ice, is most commonly used to characterize secondary creep settlement, where “ σ ” is the applied shear stress (Odqvist 1966).

$$\dot{\epsilon} = B\sigma^n \quad (3)$$

The “B” parameter is a function of soil composition (type and ice content), porewater salinity, and soil temperature. The “n” parameter has documented values of 3 for polycrystalline ice and between 1 and 7 for ice-rich soils, depending on individual soil properties.

Modifying equation 3, Nixon and McRoberts (1976) derived the following equation to predict the secondary creep rate for friction piles in ice rich frozen soils:

$$\dot{\epsilon}_{pile} = \frac{a^3 \cdot 0.5(n+1)}{n-1} B \sigma^n \quad (4)$$

where $\dot{\epsilon}_{pile}$ = pile strain rate, m/year and a = pile radius, m.

Equation 4 is used to calculate the steady state pile

displacement rate (due to secondary creep) resulting from an applied shaft shear stress for a given pile radius and for a variety of ice-rich frozen soil types and salinity contents as included in the “B” and “n” creep parameters. Calculations performed using equation 4 assume a constant frozen soil temperature along the pile shaft.

Although straightforward, the use of equation 4 to calculate allowable shaft shear stress for an acceptable pile strain rate has limited application due to scarcity of data on the creep parameters of frozen soils.

This paper provides additional information related to the “B” and “n” creep parameters for frozen sand, silt, and clay soils with a range of ice contents, temperatures, and salinity.

The laboratory test program, consisting of an extensive suite of unconfined compressive strength tests, was carried out by V. Aksenov and A. Tchekhovski in the mid-1990s in PNIIS (Moscow) laboratories.

Laboratory Testing Methodology

Table 1 provides general information on the physical parameters of the test samples and on the number of tests that were acceptable for determination of creep parameters. The test soil moisture contents were selected to provide the presence of some excess ice, as is commonly encountered in ice-rich soils.

Sample preparation

Test specimens consisted of field samples of sand, silt, and clay soil of marine and fluvial origin. The specimens were derived from arctic regions of Western Siberia and reconstituted in the laboratory. For silt and clay samples, the dry clay or silt was mixed with a solution of known salinity and prepared based on the natural salinity and dry weight of the samples. The volume of solution added to the samples was sufficient to obtain specimens with moisture contents above the liquid limit for the soil. Prior to freezing, each specimen was kept in a sealed bowl and held at room temperature for 24 to 48 hours to obtain uniform moisture content throughout the sample. A detailed description of the methodology used for specimen preparation is outlined in Aksenov (2008). Test specimens then were placed in a freezer at a temperature range of -3°C to -5°C. After cooling to the freezing point for the prepared salinity, the specimens were pounded into frozen particles less than 2 mm in size and then left at room temperature for 2 to 4 hours to provide paste-like specimens with a high degree of the moisture content uniformity. The paste specimens then were packed into refrigerated metal casings with paper filters and perforated pistons at both ends of the casing; the pistons were used to apply load to the samples. The individual specimens were then frozen to the test temperature for the specimen under an axial load of 50 kPa.

Sand specimens were packed into the refrigerated metal casing and saturated over a period of 7 to 20 minutes. After saturation, the specimens in the casings were frozen at a temperature of -20°C to obtain a uniform distribution of ice within the specimens. The individual frozen specimen was later held at the test temperature for the specimen for about 24 hours prior starting the test.

Table 1. Physical properties of tested soils.

| | Sand | Silt | Clay | |
|--------------------------------------|--------------|--------------|--------------|----|
| Bulk Density kN/m³ | 18.0 to 19.4 | 18.4 to 19.0 | 16.7 to 18.1 | |
| Moisture Content % | 21 to 29 | 30 | 40 | |
| Average Fraction Content % | Sand | 85 | 14 | 1 |
| | Silt | 13 | 82 | 5 |
| | Clay | 12 | 40 | 48 |
| Number of Tests | 46 | 68 | 29 | |

Table 2. Test specimen temperature deviation standards.

| Test Temperature °C | Deviation °C |
|---------------------|--------------|
| -1 | ±0.1 |
| -2 to -4 | ±0.2 |
| -6 | ±0.5 |

Overview of testing details

Two types of load-controlled uniaxial tests were used for the study: tests under constant loading (multiple samples of the same soil type, salinity, temperature, etc. and different loads) and tests under step-increased loading (single sample). The loads for the constant load tests and the load increments for the step-load tests were selected based primarily on pore water salinity. The equations below were applied to calculate the constant loads or load increments.

$$\sigma_i = \sigma_{\text{short}} (1 - n_i/20) \text{ for salinity less than 5 ppt} \quad (5)$$

$$\sigma_i = \sigma_{\text{short}} (1 - n_i/100) \text{ for salinity more than 5 ppt} \quad (6)$$

where σ_i – test load; σ_{short} - short term strength of frozen soil; and n_i - test number. Thus, for high salinity content, the increments between test loads were about five times smaller than for lower salinity content samples.

The short-term strength of the frozen soil for a given salinity and temperature was selected based on available existing data, or was estimated based on engineering judgment and previous experience with similar soil. From a practical standpoint, in order to determine the strain rate for secondary creep, the constant loads or load increments were at an interval from $0.2\sigma_{\text{short}}$ to $0.05\sigma_{\text{short}}$ for salinity contents less than 5 ppt, and from $0.025\sigma_{\text{short}}$ to $0.01\sigma_{\text{short}}$ for salinity contents greater than 5 ppt.

During the creep tests, the specimen temperature and temperature in the freezing room was maintained constantly within the deviation standards summarized in Table 2.

Constant load tests were usually conducted over a period of 10 to 20 days. However, when applied loads were close to the short-term strength of the sample, specimens often reached 20% strain or failed in a shorter time period. At smaller applied loads, a steady secondary creep strain rate was usually achieved after 2 to 3 days of testing.

The time interval for each load increment (step-load tests) was up to 72 hours, or until specimen deformation did not exceed 0.01 mm over 12 hours. Addition of incremental loads continued until the specimen strain exceeded 20% of the initial specimen height.

The creep parameters were determined using those constant load tests or step-load tests where a constant secondary creep strain rate was clearly achieved based on review of strain-time plots. The results from tests where the strain rate continuously decreased, or where a constant strain rate did not develop, were excluded from the data used to calculate “B” and “n” creep parameters.

Discussion of Results

Constant secondary creep strain rates were achieved for a total of 143 tests, and these tests were used to calculate “B” and “n” parameters. Table 3 provides a summary of the ranges of test temperatures, soil salinity, and applied loads for the tests used to calculate “B” and “n” parameters. A review of Table 3 indicates that for the variety of tests conducted, constant secondary creep strain rates developed for sand at a minimum applied load of 60 kPa (-2°C, salinity 6 ppt), for silt at a minimum applied load of 20 kPa (-4°C, salinity 28 ppt), and for clay at a minimum applied load of 70 kPa (-6°C, salinity 19.5 ppt). Table 3 also indicates that for some specimens, a constant secondary creep strain rate was maintained at very high applied loads: for sand 1400 kPa (individual test data indicated -2°C, salinity 3.6 ppt), for silt 990 kPa (individual test data indicated -4°C, salinity 7.4 to 8 ppt), and for clay 810 kPa (individual test data temperature -6°C, salinity 16.7 ppt).

For each test listed in Table 3, plots were produced showing the strain rate versus time. The minimum strain rate corresponds to the secondary creep rate, as illustrated in Figure 1. As an example, Figure 2 provides the strain rate versus time for a silt specimen tested at a temperature of -2°C and salinity content of 6.5 ppt. Horizontal intervals on the strain rate-time plot correspond to the secondary creep phase, and were used for calculation of “B” and “n” creep parameters. Identification of the horizontal intervals was carried out for each of the tests shown in Table 3. The tests revealed that the secondary creep phase normally develops if the applied load is more than about 90% of the yield strength of the frozen soil. If the applied loading was less than 90% of the yield strength, then the creep strain rate tended to decrease with time and approach zero.

Results of tests where the secondary creep phase was identified were used for calculation of creep parameters (“B” and “n”) for sand, silt, and clay at various temperatures (Table 3) and for the following ranges of salinity content: less than 5 ppt, 5–10 ppt, 10–20 ppt, and greater than 20 ppt. Initially, the data for each soil type were plotted separately as natural logarithm strain rate versus natural logarithm load for a given temperature and range of salinity. A sloped line was then drawn as the best fit to the data points and crossed both of the plot axes (logarithm strain rate: vertical axis; and logarithm load: horizontal axis). Examples of sloped line plots obtained for sand, silt, and clay are presented as Figures 3 through 5, respectively.

It can be seen that the sloped line for the tested soil specimens crosses the vertical axis at about -18.5 for sand (-1°C, salinity < 5 ppt), at about -25.5 for silt (-2°C, salinity 5 to 10 ppt), and at about -28.5 for clay (-6°C, salinity 10 to 20

Table 3. Information summary for unconfined compression tests used to calculate “B” and “n” parameters.

| Soil Type | Number of Samples Tested | Range of Test Temp. °C | Range of Test Salinity ppt | Range of Applied Test Loads kPa |
|-----------|--------------------------|------------------------|----------------------------|---------------------------------|
| Sand | 46 | -1 to -4 | 1.1 to 9.4 | 60 to 1400 |
| Silt | 68 | -1 to -4 | 2.9 to 29.0 | 20 to 990 |
| Clay | 29 | -3 to -6 | 0.5 to 19.5 | 70 to 810 |

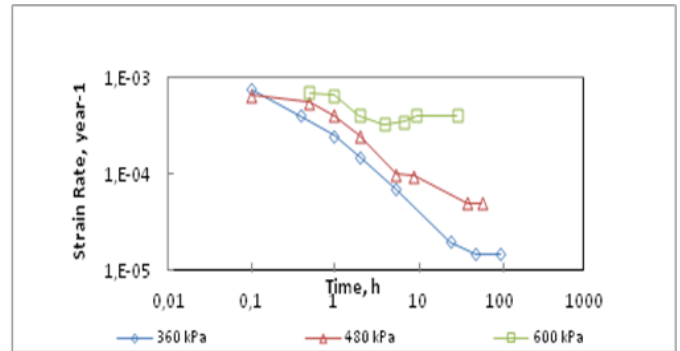


Figure 2. Strain rate vs. time for silt (-2°C, salinity 6.5 ppt).

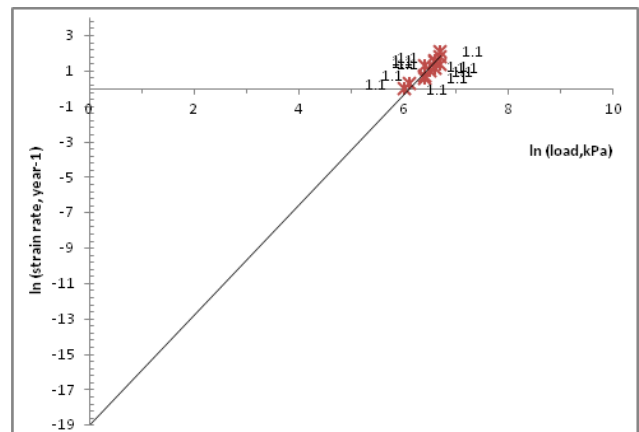


Figure 3. Slope line for sand (-1°C, salinity <5 ppt).

ppt). Inspection of the ln-ln plots indicated that irrespective of the soil type, temperature, and salinity, the sloped line crossed the horizontal axis at about 6, with some variation. However, the location of the intersection of the sloped line and the vertical axis exhibits substantially more variation than the intersection with the horizontal axis. This variability indicates that there is no functional dependence between the “B” and “n” parameters, although both depend on the same soil properties, such as temperature and salinity.

“B” and “n” calculation and analysis

Plots of the sloped lines were used to calculate the “B” and “n” creep parameters. The “B” parameter was calculated as

$$B = e^{\ln(\text{strain rate})}$$

where the value of the strain rate logarithm is equal to the value at the intersection of the sloped line and the vertical axis. The

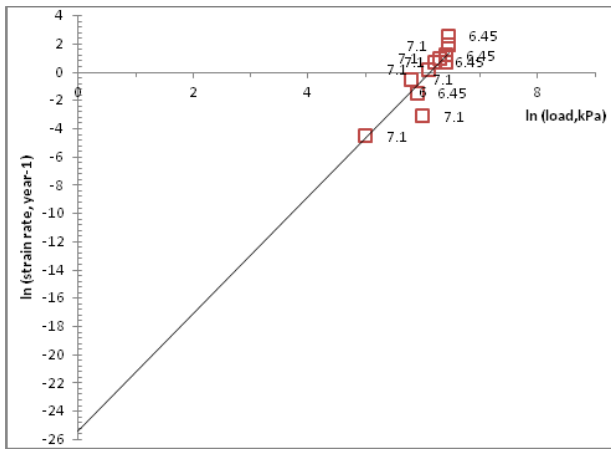


Figure 4. Slope line for silt (-2°C, salinity 5-10 ppt).

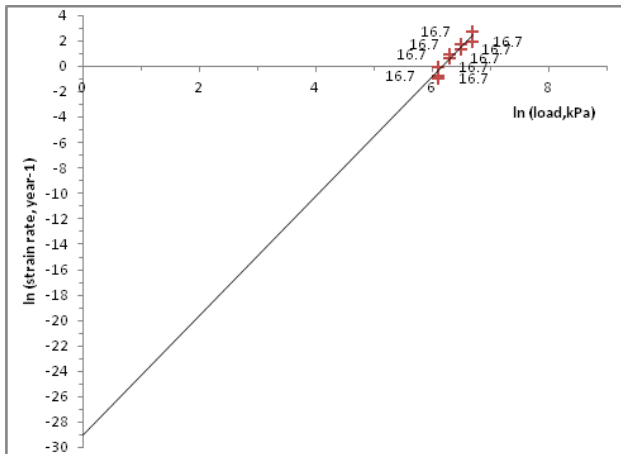


Figure 5. Slope line for clay (-6°C, salinity 10-20 ppt).

“n” parameter is the slope of the line, calculated as $\ln(\text{strain rate})/\ln(\text{load})$. Figure 6 presents a plot showing the “B” parameter as a function of temperature and salinity for sand.

The “n” parameters for each dataset were also calculated and are provided in Table 4.

For frozen sand, a linear relationship is evident between the salinity content and the “B” parameter. For sand temperatures of -1°C to -2°C, and salinity contents from less than 5 ppt to 20 ppt, the value of the “B” parameter ranged from 10^{-9} to 10^{-6} kPa⁻ⁿ/year (Fig. 6), and the “n” parameter varied from 2.7 to 3.0. The “B” parameter for a temperature of -4°C was considerably lower, ranging from 10^{-12} to 10^{-10} kPa⁻ⁿ/year; however, the “n” parameter was considerably higher, being in the order of 4.

Figure 7 presents a plot showing the “B” parameter for silt as a function of salinity content and temperature. Values of the “n” parameter calculated for silt are shown in Table 5.

It was surprising to find that the pattern of variation in the “B” parameter with salinity was dramatically different for silt (Fig. 7) than for sand (Fig. 6). The plot of the “B” parameter for silt has a shallow bench between the salinity ranges of 5–10 ppt and 10–20 ppt (Fig. 7). The “B” parameter decreases approximately 1.5 to 3 times within a salinity content range of 10–20 ppt, whereas the “B” parameter decreased in the order of 40 times where soil salinity content ranged from <5 ppt to

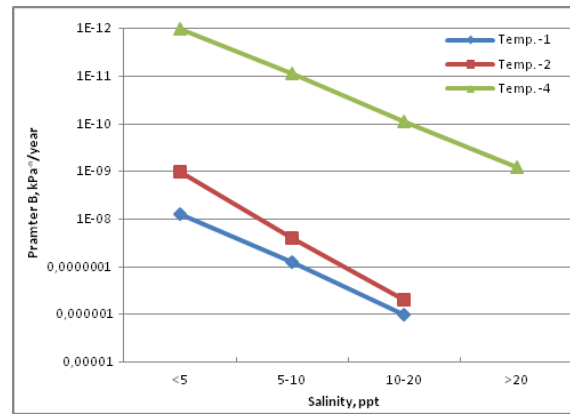


Figure 6. Creep parameter “B” for sand.

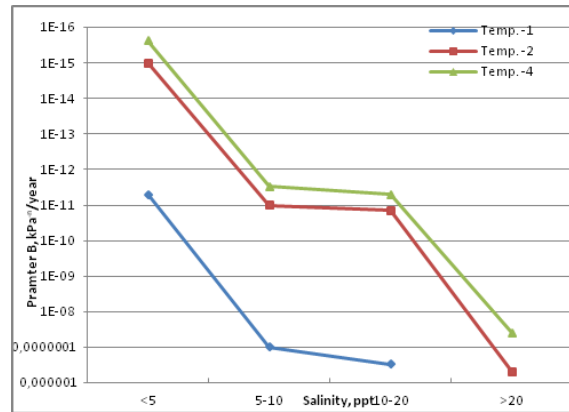


Figure 7. Creep parameter “B” for silt.

Table 4. Creep parameter “n” for sand.

| Salinity ppt | Temperature °C | | |
|--------------|----------------|-----|-----|
| | -1 | -2 | -4 |
| <5 | 3.0 | 2.8 | 4.0 |
| 5 to 10 | 2.7 | 3.0 | 3.9 |
| 10 to 20 | 2.7 | 2.8 | 4.0 |
| >20 | n/a | n/a | 4.0 |

Table 5. Parameter “n” for silt.

| Salinity ppt | Temperature °C | | |
|--------------|----------------|-----|-----|
| | -1 | -2 | -4 |
| <5 | 4.0 | 5.5 | 5.1 |
| 5 to 10 | 2.9 | 4.0 | 4.0 |
| 10 to 20 | 2.4 | 4.5 | 4.1 |
| >20 | n/a | 3.0 | 4.0 |

5–10 ppt, and from 10–20 ppt to >20 ppt. A high “n” parameter was obtained for sand at a temperature of -4°C, and the silt has a high “n” parameter value at a temperature of -2°C. Analysis of the “B” and “n” parameters for silt suggests that from a physical (and likely chemical) point of view, silt is a more complex medium than sand, and freezing results in a relatively slow increase in soil strength within salinity ranges between 5–10 ppt and 10–20 ppt.

Table 6. Creep parameter “n” for clay.

| Salinity ppt | Temperature °C | | |
|--------------|----------------|-----|-----|
| | -3 | -4 | -6 |
| <5 | 1.7 | 2.0 | 2.0 |
| 5 to 10 | 1.6 | 2.3 | 2.6 |
| 10 to 20 | 2.0 | 4.5 | 4.6 |

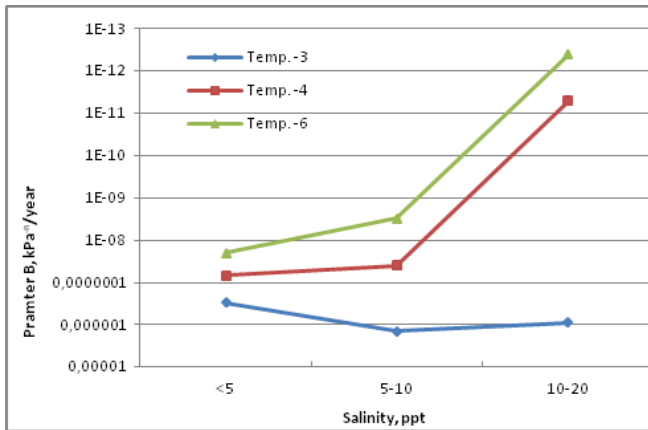


Figure 8. Creep parameter “B” for clay.

In general, test results for clay specimens provided considerably smaller “n” parameters than for sand or silt, as summarized in Table 6.

An increase of the “n” parameter value with increasing salinity was obtained for all test temperatures. The most noticeable increase of the “n” parameter occurred for test temperatures of -4°C and -6°C while for a test temperature of -3°C, the “n” parameter increased only marginally with increasing salinity. The described particularities of “n” parameters resulted in the opposite uniformity of the “B” parameter dependence of salinity (Fig. 8).

In Figure 8, the “B” parameter for temperatures of -4°C and -6°C increased sharply by approximately 40 times when salinity was decreased from 10–20 ppt to 5–10 ppt. The “n” parameter in this range of salinity decreased from 4.5–4.6 to 2.3–2.6. Only a marginal increase of the “B” parameter occurred with increasing salinity for clay at a temperature of -3°C, likely due to the relatively small decrease of the “n” parameter from 2.0 to 1.6 over the same range of salinity.

Application

The “B” and “n” parameters provided in the present paper can be used for prediction of long-term settlement of adfreeze piles in ice-rich permafrost as required by the Canadian Building Codes for the Limit State Design (Canadian Foundation Engineering Manual 2006). Discussions on the ultimate capacity of adfreeze piles in detail are provided in Weaver and Morgenstern (1981). For predicting the allowable adfreeze shear stress, equation 4 may be expressed as follows:

$$\sigma = \left[\frac{(n-1) \dot{\epsilon}_{pile}}{3^{0.5(n+1)} \cdot aB} \right]^{\frac{1}{n}} \tag{7}$$

If creep parameters have not been determined for a given site, then the “B” and “n” parameters from the current paper can be used for preliminary assessment of allowable shear stress. Three typical scenarios for the adfreeze pile design may be considered: 1) a pile installed in low salinity frozen soils (less than 5 ppt) with the use of sand slurry; 2) a pile installed in moderate to high salinity frozen soils (more than 5 ppt) with the use of sand slurry; and 3) a pile installed in frozen soils of any salinity with the use of grout slurry.

Scenario 1: The allowable shear stress is calculated by equation 7 for the given pile radius, applying values of “B” and “n” parameters for low salinity (less than 5 ppt). A reduction coefficient of 0.7 should be applied to the calculated allowable stress to account for smooth surface of steel piles together with a factor of safety of 1.5 on the calculated stress.

Scenario 2: Step 1, the allowable stress is calculated in accordance with recommendations for Scenario 1 above. Step 2, the allowable stress is calculated by Equation 7 for the given hole diameter, applying “B” and “n” parameters corresponding to the salinity that matches the actual in-place soil salinity. A factor of safety of 1.5 should be applied to the calculated allowable stress. The lesser calculated allowable stress, resulting from calculations for Step 1 and Step 2, is recommended to be used for prediction.

As an example, calculation of the allowable shear stress for a pile 0.5 m in diameter, embedded in ice-rich sand at a temperature of -4°C and salinity of 10–20 ppt, is provided below. It was assumed in the calculations that the tolerant strain rate of the pile is 0.001 m/year.

In Step 1, the allowable shear stress was calculated at the pile-slurry interface using “B” and “n” parameters from Figure 8 and Table 6 for salinity less than 5 ppt. Applying the reduction coefficient of 0.7 and factor of safety of 1.5, the allowable shear stress at the pile-slurry interface is calculated to be 75 kPa. In Step 2, the allowable shear stress was calculated at the hole-slurry interface with a hole diameter of 0.55 m, using “B” and “n” parameters for salinity of 10–20 ppt. Applying the factor of safety of 1.5, the allowable shear stress at the hole-slurry interface is calculated to be 35 kPa. The lesser of the allowable shear stresses should be used for pile design.

Scenario 3: The allowable stress is calculated by equation 7 for the given hole diameter applying “B” and “n” parameters corresponding to salinity contents that match the actual existing soil salinity. A factor of safety should be applied to the result.

Conclusions

The results of numerous unconfined compressive tests for various saline soils, and calculations of “B” and “n” parameters, have demonstrated that the functions that describe the secondary creep behavior of ice-rich soils are complex. Creep behavior of ice-rich soils depends on the mutual

influence of three main factors: soil composition, soil salinity, and soil temperature. The creep behavior is more complex for clay and silt soils compared with creep in sand. This is evident in Figures 6, 7, and 8, where the “B” parameter for sand can be described by a simple linear function versus salinity and temperature; the functions required to relate the “B” parameter to soil salinity and temperature are more complicated for silt and clay. A similar conclusion can be made based on analysis of Tables 4, 5, and 6. The “n” parameter for a given temperature is more stable, with a minimum fluctuation, for sand in comparison to silt and clay. With the limited data available to undertake the current study, it was not possible to find a single equation that would reasonably characterize the secondary creep behavior of frozen soil (strain rate) based on primary soil properties such as soil composition, salinity, and temperature. Analysis of additional laboratory test data may provide the basis for such a single function, or alternatively may demonstrate a requirement for separate functions to predict secondary creep behavior depending on soil type.

References

- Aksenov, V.I. 2008. Saline frozen soils of Arctic shore as structure base. Moscow: Publishing house "World of Build" (in Russian).
- Andersland, Orlando B. & Ludanyi, Branko. 2004. *Frozen Ground Engineering*, 2nd ed. John Wiley & Sons, Inc., 363 pp.
- Canadian Foundation Engineering Manual, 4th ed. 2006.
- Hult, J.A.H. 1966. *Creep in Engineering Structures*. Walktham, Mass: Blaisdel.
- McRoberts, E.C. 1975. Some Aspects of a Simple Secondary Creep Model for Deformations in Permafrost Slopes. *Canadian Geotechnical Journal* 12(1): 98-105.
- Nixon, J.F. & McRoberts. 1976. A Design Approach for Pile Foundations in Permafrost. *Canadian Geotechnical Journal* 13(1): 40-57.
- Odqvist, F.K.G. 1966. *Mathematical Theory of Creep and Creep Rupture*. Oxford Mathematical Monographs, Oxford: Clarendon Press.
- Vylov, S.S. 1959. Rheological Properties and Bearing Capacity of Frozen Soils, Russian, translated in 1965, by US Army Corps of Engineers, Cold Regions Research and Engineering Laboratory, Army Translation No. 76, Hanover, NH, 301.
- Weaver, J.S. & Morgenstern, N.R. 1981. Pile Design in Permafrost. *Canadian Geotechnical Journal* 18: 357-370.

The Significance of the Permafrost Tunnel (Fox, Alaska)

Margaret Cysewski, Matthew Sturm, Kevin Bjella

U.S. Army Cold Regions Research and Engineering Laboratory, Fairbanks, AK, USA

Abstract

The Permafrost Tunnel near Fox, Alaska, will be 50 years old in 2013. More than 70 technical papers have been written under the topics of mining engineering, civil engineering, cryostratigraphy, and geology based on research in the tunnel. This paper highlights the key, unique, and large research projects performed in the tunnel, along with their significant findings. The tunnel's syngenetic permafrost is representative of permafrost found across the interior of Alaska, including rich climate history data dating to 43,000 years BP and permafrost features of cryostructures, ice contents, and properties. The tunnel's close proximity to the city of Fairbanks makes it accessible to the local population, including the University of Alaska Fairbanks, visiting researchers, and leaders. Education and outreach are important functions, with tours given to thousands of people and college classes that collect samples; six graduate student research projects have been conducted in the tunnel.

Keywords: tunnel; mining; engineering; cryostructure; climate; CRREL.

Introduction

The Permafrost Tunnel near Fox, Alaska, will have its 50th anniversary in 2013. More than 70 technical papers have resulted from research conducted within the tunnel and surrounding property. The tunnel is located 17 kilometers from Fairbanks, Alaska (Fig. 1). It comprises two sections: the horizontal 110-meter adit and the inclined 45-meter winze (Fig. 2). Currently, it is jointly operated by the U.S. Army Cold Regions Research and Engineering Laboratory (CRREL) and

the Institute of Northern Engineering (INE) of the University of Alaska Fairbanks (UAF). In February 2011, CRREL started to excavate a new adit located 60 meters from the existing adit.

Evolution

The initial tunnel excavation, which created the adit, was essentially related to mining and engineering, although it was slated for military uses. Shortly after its excavation by CRREL, the U.S. Bureau of Mines was allowed to conduct its own excavation experiments, creating the winze. The tunnel then became a working natural laboratory. Mining engineering research continued along with civil engineering research, including studies in underground stability and strength properties. Around the late 1980s, some of the research focus turned to the geology and climate record captured in the tunnel's frozen sediments. A notable paper by Thomas Hamilton, John Craig, and Paul Sellmann (1988) provided a detailed overview of the tunnel's geology and paleontology. Currently, the topics investigated in the tunnel are even broader, encompassing paleoclimatology, biology, and Mars permafrost. Most recently, a team led by Dr. Yuri Shur from UAF has begun studying the cryostructures and mapping the cryostratigraphy in the tunnel (Shur et al. 2004, Bray et al. 2006, Kanevskiy et al. 2008).

Mining Engineering

Adit excavation

The adit excavation, from 1963 to 1968, was performed by CRREL for military purposes, but it was essentially mining-related. The primary purpose was to study continuous mechanical tunneling in permafrost. The secondary purpose was to study the utilization of permafrost tunnels as military shelters and storage facilities. It was thought that the plastic nature of permafrost could absorb explosive shocks without shattering, making rooms within tunnels relatively stable if under attack. Arctic and subarctic permafrost tunnels, while still below freezing, would be warmer than the outside air temperature

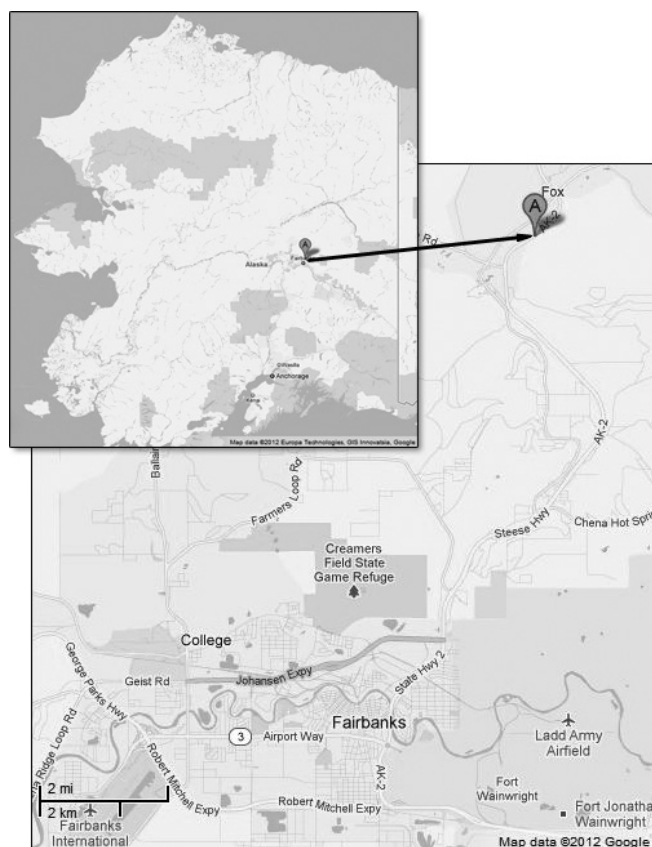


Figure 1. Location of Permafrost Tunnel (Pin A).

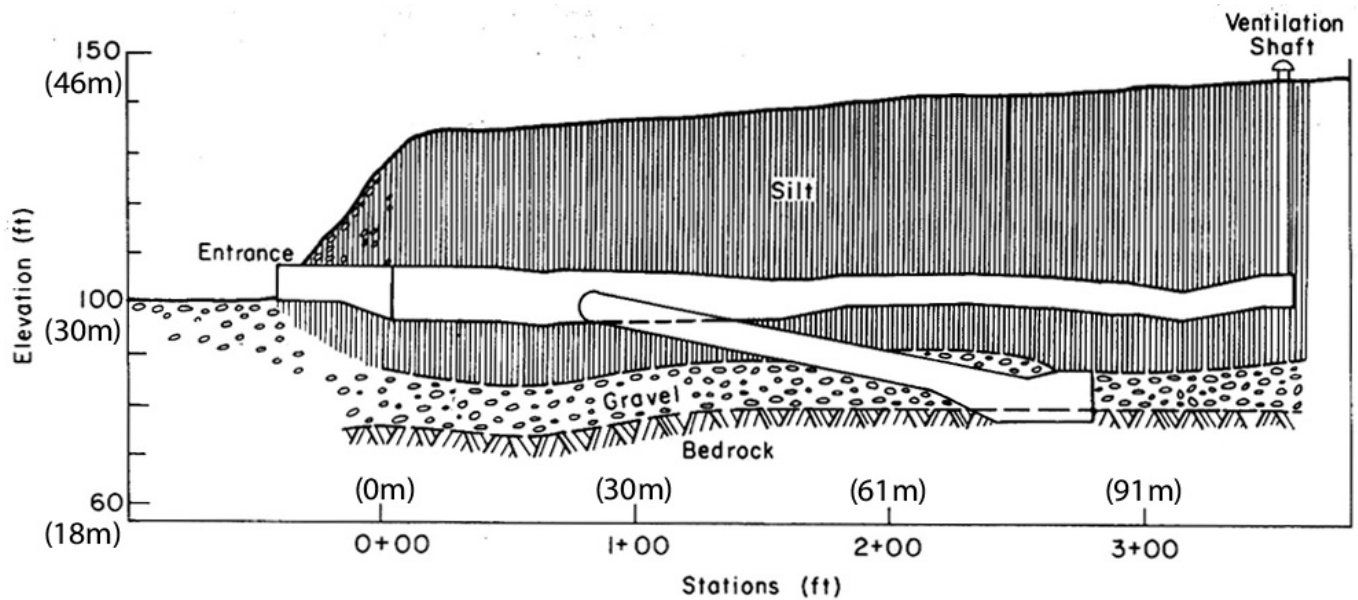


Figure 2. Profile of the Permafrost Tunnel (adapted from U.S. Army 1981).

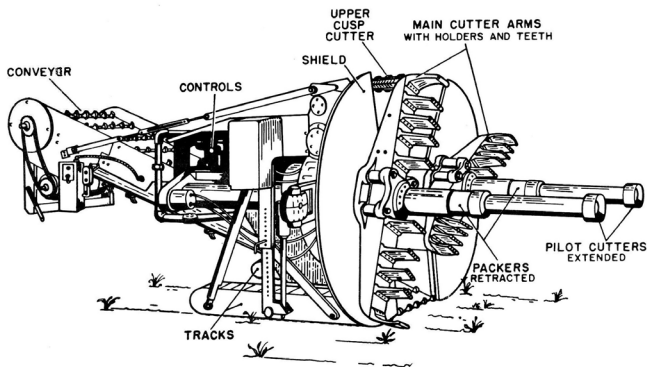


Figure 3. Diagram of Alkirk Miner (Swinzow 1970).



Figure 4. Photo of cutting face from Alkirk Miner.

and also protect against wind. While the bulk of the initial tunnel research was on the excavation, some effort was invested in studying ventilation, roof deformation, and the response of the thermal regime to human activity (Swinzow 1970).

The bulk of the adit was excavated with the Alkirk Continuous Miner (Fig. 3). It was a first-generation machine, and its revolutionary pilot-pull principle made it light in weight and highly mobile. For military operations, mobility and speed are higher priorities than cost. The lightness of the machine comes from the fact that it pulls itself into the face instead of pushing with its own weight or hydraulic rams. Frequent problems with the Alkirk stemmed from the fact that it was a prototype and an untested machine. Learning to repair it was a complex process because there was no specialized training for its very complex hydraulic system. Steering was limited by peculiarities of the track and the pilot cutter design.

Another major problem was insufficient cooling. This was especially true with the pilot cutters, which would thaw the ice-rich permafrost, making the rubber packers unable to grip the pilot hole walls enough to pull into the cutting face. Overall, the Alkirk advanced the 3.8-meter by 2.1-meter oval tunnel (Fig. 4) at an average of 3 meters per hour (Swinzow 1970).

Before the Permafrost Tunnel near Fox, Alaska, was built, two other tunnels were constructed at Camp Tuto near Thule, Greenland. The U.S. Army Snow, Ice and Permafrost Research Establishment (SIPRE) was in Greenland to conduct research and to serve as technical consultant for the U.S. Army and its projects in Greenland, including Camp Century. SIPRE became part of CRREL in 1961 (Clark 1965). From 1955 to 1959, a 335-meter tunnel with five cross drifts was tunneled in the Greenland Ice Cap with a continuous miner. Heated prefabricated buildings were placed inside the tunnels with everything necessary to keep a 25-man camp functioning for a couple months (Rausch 1958, Russell 1961). In 1959–1960, SIPRE excavated a 185-meter tunnel with three rooms in frozen glacial till at Camp Tuto using adapted hard-rock conventional mining methods (Swinzow 1964). Shortly after the excavation and initial research, the Greenland tunnels were filled with ice caused by glacial run-off. The Permafrost Tunnel near Fox was excavated with similar purposes and ideas, but in ice-rich silt permafrost.

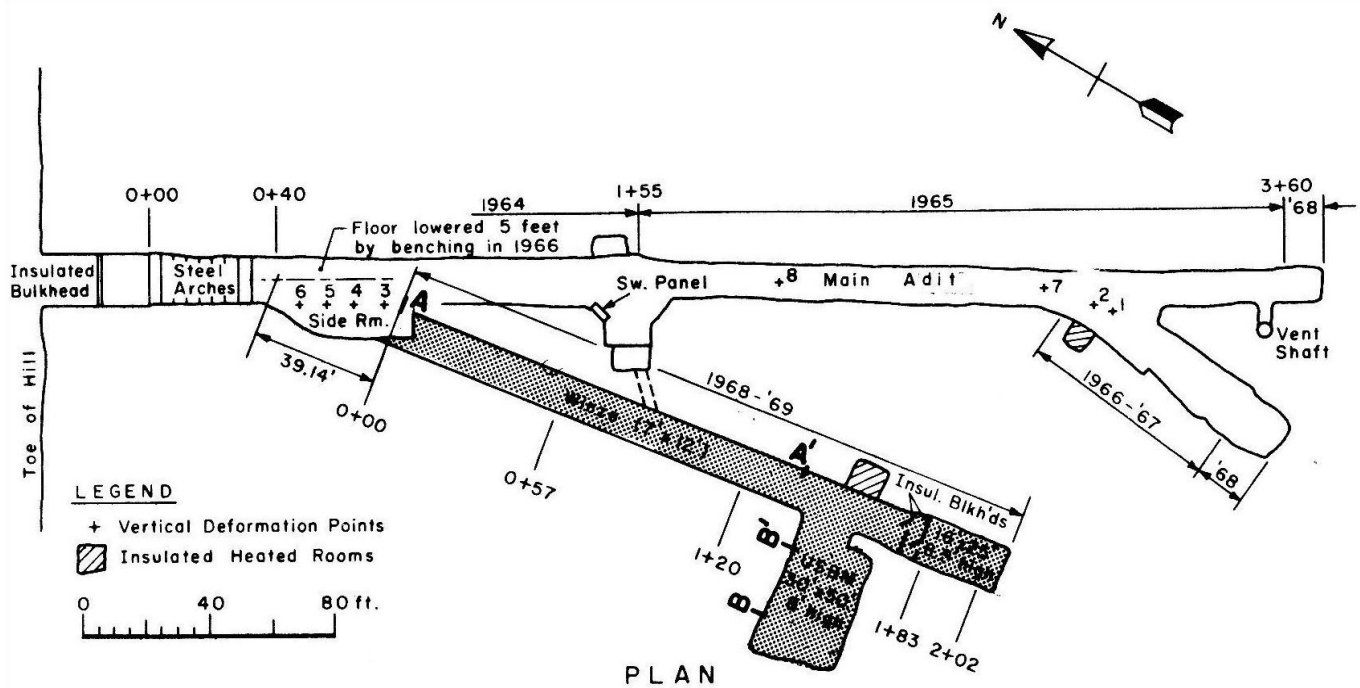


Figure 5. Plan view of the Permafrost Tunnel (Sellmann 1972).

Winze excavation

The winze was excavated in 1968–1969 by the U.S. Bureau of Mines, specifically to study mining methods in frozen gravels. The project was part of a larger program “to increase the supply of gold to the United States” (Chester & Frank 1969, 1). In central Alaska, gold is found in a gravel layer that overlies bedrock and underlies a thick layer of silt; the adit was excavated within that underlying silt. Conventional and unconventional mining techniques were tested within the frozen gravels, and results were used to estimate mining costs and ease of hauling (Chester & Frank 1969).

To reach the frozen gravels, the U.S. Bureau of Mines excavated a 3.7-meter by 2.1-meter tunnel, approximately 43 meters long at a 12% decline, through the silt with conventional mining techniques (Dick 1970). The conventional mining techniques were drilling and blasting with different drilling machines and bits. The shot patterns were adjusted by varying the number of holes, length, angle, and powder factor (Dick 1970, Chester & Frank 1969). The unconventional mining methods included thawing the frozen gravels with infrared heating units at the tunneling face and injecting steam into the face and pressurized water jets against the face. Conventional mining techniques created large ice-cemented gravel blocks, while the thawing techniques made the gravels easier to load and haul. The conclusion was that steam thawing was the cheapest method (Chester & Frank 1969).

Stability of the Permafrost Tunnel

A room was excavated in the gravels at the bottom of the winze by the U.S. Bureau of Mines in 1968 (Fig 5). Researchers with the U.S. Bureau of Mines studied the stability of the room’s roof for the first three years after excavation

(Pettibone 1973). The room was also studied in the early 1980s by researchers from UAF. Both studies concluded that the gravel roof separated as a unit from the silt layer above. As the room was heated to thawing, the deformation and parting from the silt above reacted exponentially (Pettibone 1973, Garbeil 1983, Huang & Garbeil 1983). The UAF researchers also studied the main portions of the tunnel within the silt unit and found that the silt deformed approximately 0.05 mm/day versus 0.025 mm/day in the gravels (Huang & Garbeil 1983). In addition, UAF researchers found that the wider the opening span and the thicker the overburden, the more rapidly the tunnel deformed vertically (Wu 1985, Huang et al. 1986).

Civil Engineering

Creep and long-term strength experiments

In addition to the deformation studies mentioned above, a comprehensive study was conducted on remolded samples of silt obtained from the tunnel (Zhu & Carbee 1987). A creep settlement study of a strip footing was also conducted within the tunnel. The results were compared with analytical calculation methods (Sayles 1985).

A more recent study was performed on undisturbed samples to determine the importance of cryostructure. Samples included micro-lenticular, reticulate-chaotic, and massive cryostructure with wedge ice, in addition to remolded-massive cryostructure samples. In comparison, the undisturbed samples were three to four times lower in long-term strength than the remolded-massive cryostructure samples, with micro-lenticular being the lowest. Remolded samples of previous studies are comparable to remolded-massive cryostructure samples, and are therefore non-conservative (Bray 2008a, 2008b).

Geophysical experiments

Testing the distance of ground-penetrating radar (GPR) pulse transmissions through frozen soil was conducted in the tunnel with VHF-band radiowave short pulses (Arcone 1984). A later cross-borehole study on the tunnel's surrounding property used the same GPR as the 1984 study and compared the results with other study sites. Contrasts were found between the ice-rich silt and an ice wedge. But compared to similar sites, it was noted that cross-borehole GPR would only indicate stratigraphic changes, including massive ice (Arcone and Delaney 1989).

Permafrost Features

The tunnel is located within syngenetic permafrost that contains numerous intact cryostructures. The structures related to syngenetic growth are layered, lenticular, and micro-lenticular cryostructures. The massive ice features include ice wedges and thermokarst-cave ice (Shur et al. 2004, Bray et al. 2006), where 19 out of the 20 ice wedges contain thermokarst-cave ice (Fortier et al. 2008). Associated with the thermokarst-cave ice are the reticulate-chaotic structures (Shur et al. 2004, Bray et al. 2006, Fortier 2008). The main texture seen in the tunnel's walls is layered cryostructure with the micro-lenticular in between, and has an average gravimetric moisture content of 130% (Bray et al. 2006). In addition to thermokarst-cave ice, soil pseudomorphs are an example of past underground-erosion and include gravel and massive cryostructure (Shur et al. 2004, Bray et al. 2006). The ice contents in the silt range from 50% to 180% in gravimetric moisture content, excluding the massive ice.

Geological Research

The silt unit has been the main focus of the geological research conducted within the tunnel over the bedrock, gravel layer, and debris-fan at the front of the tunnel. The silt unit dates back to approximately 43,000 BP (Long and Péwé 1996) and is composed of wind-blown loess from the Tanana River floodplain, a glacier-fed river originating in the Alaska Range (Beget 1988).

Several studies focus on a set of large ice wedges that all truncate near the same elevation and contain thermokarst-cave ice near their tops. The initial analysis interpreted the thermokarst-cave ice as buried ponds and theorized that a regional thaw event truncated these ice wedges (Sellmann 1972, Hamilton et al. 1988, Beget 1990). The recent studies reinterpreted the buried ponds as thermokarst-cave ice, which would have been placed by underground tunnels eroded by flowing water. The erosion could have stemmed from an isolated event, and therefore does not have regional climatic significance (Shur et al. 2004, Bray et al. 2006, Kanevskiy 2008). A magnetic susceptibility study, done beside one of these thermokarst-cave ice features, shows a period of lower magnetic susceptibility which is evidence of lower wind intensity (Beget 1990). The dates around the thermal event vary from 30,000 to 35,000 years ago (Hamilton et al. 1988,

Beget 1990, Kanevskiy et al. 2008). These dates have been correlated with other proxy evidence globally (Hamilton et al. 1988, Beget 1990).

Significance

The Permafrost Tunnel is a natural laboratory for studying permafrost and geology and conducting experiments in mining and civil engineering. The tunnel's cryostructures, ice contents, and properties are representative of those in the interior of Alaska, and offer an effective means to research the region's engineering problems and geological reconstructions. The tunnel is refrigerated during the summer, preserving the exposed permafrost within. This allows researchers the opportunity for repeat sampling from the same locations on a year-round basis. The tunnel is easily accessible for the local population and visiting researchers because it is only a 15-minute drive from Fairbanks, which is home to both an international airport and the UAF.

For mining significance, underground placer mining in frozen soils was almost exclusively used in the early 1900s during the Fairbanks Gold Rush. Dredging became the dominant method of gold mining in Alaska in the 1920s but began to fade out after World War II (Boswell 1979). Underground placer mining in frozen soils is active in Alaska today, but it makes up only a small portion of the industry.

The permafrost tunnel has provided numerous samples for strength properties research. It has also provided large, cold work areas for long-term experiments such as strip footing creep experiments (Sayles 1985). While the tunnel's properties are representative of those in the interior of Alaska, the tunnel is maintained at a lower soil temperature (approximately -5°C versus -1°C), rendering some on-site testing slightly inaccurate. CRREL and outside researchers have continued to conduct geophysical experiments within and above the tunnel (Hunter et al. 2003, Dinwiddie et al. 2009). The stability of the Permafrost Tunnel has been a continual concern for both research and operation. A recent set of measurements (from 2006 to 2012) was done to assess the tunnel's deformation; no indication of instability was found (Bjella 2008, Bjella et al. 2008).

Preservation of the tunnel is key for permafrost and geological research because field sites typically either thaw or fall into disrepair without maintenance (Shur et al. 2004). Today, the study of past climates is important to provide context for work in contemporary climate change. The syngenetic nature of the permafrost in the tunnel has preserved paleosols and their associated climate data. Only one climatic event has been discussed in this paper, but there is evidence of other events that warrant further research (Hamilton 1988, Kanevskiy et al. 2008).

Over the past five decades, thousands of people, including high school, undergraduate, and graduate students, Presidents, Cabinet members, Congressmen, and the general public, have toured the tunnel to learn about permafrost firsthand. Three undergraduate and graduate-level classes are taken to the tunnel annually to observe permafrost features and take

samples for laboratory analysis. Six graduate-level research projects have been conducted within the tunnel (Bray 2008b, Garbeil 1983, Law 1987, Mukesh 1985, Weerdenburg 1982, Wu 1985). Education and outreach is carried out by researchers from both CRREL and UAF.

The Future

The Permafrost Tunnel still has not exhausted its research potential, and several projects are currently being conducted. CRREL wants to insure the tunnel's legacy by expanding it. The project plans to add 300 meters of tunnel, with a second entrance 60 meters away from the existing entrance. The new portal entrance will allow for heavy equipment access for periodic maintenance, including upgrades to the existing tunnel to facilitate new projects. Excavation of the new adit started in February of 2011. By April 2011, 30 meters were excavated and the portal structure and refrigeration were installed. For more information on the details of the tunnel expansion and the new adit excavation, see Bjella et al. (2012) in these Proceedings.

Conclusions

Over the past five decades, permafrost-related research within the tunnel has ranged broadly from engineering to natural sciences. It includes mining engineering research from excavation experiments and stability studies, and civil engineering research from strength and creep studies and geophysical experiments. The permafrost features and their interpretations offer geologic reconstruction of past climates. This natural laboratory has and will continue to provide research possibilities and educational opportunities.

Acknowledgments

I would like to thank Richard Hughes, mining expert, for expanding my understanding of recent underground placer mining in Alaska.

References

- Arcone, S.A. 1984. CRREL report 84-17: *Pulse transmission through frozen silt*. Hanover, NH: Cold Regions Research and Engineering Laboratory, 9 pp.
- Arcone, S.A. & Delaney, A.J. 1989. CRREL Report 89-4: *Investigations of dielectric properties of some frozen materials using cross-borehole radiowave pulse transmissions*. Hanover, NH: Cold Regions Research and Engineering Laboratory, 18 pp.
- Begét, J. 1990. Middle Wisconsinan climate fluctuations recorded in central Alaskan loess. *Géographie physique et Quaternaire* 44(1): 3-13.
- Beget, J.E. 1988. Tephros and Sedimentology of Frozen Alaska Loess. *Proceedings of Fifth International Conference on Permafrost*, Trondheim, Norway, August 2-5, 1988: 672-677.
- Bjella, K. 2008. The effect of near-freezing temperatures on the stability of an underground excavation in permafrost. *Proceedings of the Ninth International Conference on Permafrost*: University of Alaska Fairbanks, June 29-July 3, 2008: 119-124.
- Bjella, K., Tantillo, T., Weale, J., & Lever, J. 2008. Technical Report 08-11: *Evaluation of the CRREL Permafrost Tunnel*. Hanover, NH: Engineer Research and Development Center/Cold Regions Research and Engineering Laboratory, 57 pp.
- Boswell, J.C. 1979. *History of Alaskan Operations of United States Smelting, Refining and Mining Company*. Fairbanks, AK: Mineral Industries Research Laboratory, University of Alaska, 125 pp.
- Bray, M.T. 2008a. Effects of soil cryostructure on the long-term strength of ice-rich permafrost near melting temperatures. *Proceedings of the Ninth International Conference on Permafrost*: University of Alaska Fairbanks, June 29-July 3, 2008: 183-188.
- Bray, M.T. 2008b. *The influence of soil cryostructure on the creep and long term strength properties of frozen soils*. Ph. D. Thesis, University of Alaska Fairbanks, 232 pp.
- Bray, M.T., French, H.M., & Shur, Y. 2006. Further cryostratigraphic observations in the CRREL Permafrost Tunnel, Fox, Alaska. *Permafrost and Periglacial Processes* 17(3): 233-243.
- Chester, J.W. & Frank, J.N. 1969. *Fairbanks placers fragmentation research final report*. Minneapolis: Twin Cities Mining Research Center, U.S. Bureau of Mines, Heavy Metals Program, 52 p. Auth. No. 9-1115-33.
- Clark, E.F. 1965. Technical Report 174: *Camp Century Evolution of Concept and History of Design and Performance*. Hanover, NH: Cold Regions Research and Engineering Laboratory, 60 pp.
- Dick, R.A. 1970. *Effects of Type of Cut, Delay, and Explosive on Underground Blasting in Frozen Gravel*. Washington: U.S. Dept. of Interior, Bureau of Mines, 17 pp.
- Dinwiddie, C.L., McGinnis, R.N., Stillman, D., Grimm, R.E., Hooper, D.M., & Bjella, K. 2009. Integrated Geophysical Examination of CRREL Permafrost Tunnel's Fairbanks Silt Units, Fox, Alaska. *American Geophysical Union, Fall Meeting 2009*, abstract #C41A-0429.
- Fortier, D., Kanevskiy, M., & Shur, Y. 2008. Genesis of Reticulate-Chaotic Cryostructure in Permafrost. In *NICOP 2008: Proceedings of the Ninth International Conference on Permafrost*: D.L. Kane, K.M. Hinkel (eds.). Institute of Northern Engineering, University of Alaska Fairbanks, 1: 451-456.
- Garbeil, H.M. 1983. *Temperature and time effects upon the closure of a gravel room in permafrost*. M.S. Thesis, University of Alaska Fairbanks, 134 pp.
- Hamilton, T.D., Craig, J.L., & Sellmann, P.V. 1988. The Fox permafrost tunnel: A late Quaternary geologic record in central Alaska. *Geological Society of America Bulletin* 100(6): 948-969.

- Huang, S.L., Aughenbaugh, N.B., & Wu, M.-C. 1986. Stability study of CRREL permafrost tunnel. *Journal of Geotechnical Engineering* 112(8): 777-790.
- Huang, S.L. & Garbeil, H. 1983. In-situ displacement analysis of underground opening in permafrost regions. *Proceedings of First Annual Workshop: Generic Mineral Technology Center; Mine Systems and Design and Ground Control*, Blacksburg, Virginia, November 28-29, 1983: 67-82.
- Hunter, Lewis E., Delaney, Allan J., Lawson, Daniel E., & Davis, Les. 2003. Downhole GPR for high-resolution analysis of material properties near Fairbanks, Alaska. *Ground Penetrating Radar in Sediments*: Geological Society, London, Special Publications 211: 275-285.
- Kanevskiy, M., Fortier, D., Shur, Y., Bray, M., & Jorgenson, T. 2008. Detailed cryostratigraphic studies of syngenetic permafrost in the winze of the CRREL permafrost tunnel, Fox, Alaska. In *NICOP 2008: Proceedings of the Ninth International Conference on Permafrost*: D.L. Kane, K.M. Hinkel (eds.). Institute of Northern Engineering, University of Alaska Fairbanks, 1: 889-894.
- Law, K.K. H. 1987. *Time-dependent bearing capacity of frozen ground*. M.S. Thesis, University of Alaska Fairbanks, 129 pp.
- Long, A. & Pewe, T.L. 1996. Radiocarbon dating by high-sensitivity liquid scintillation counting of wood from the Fox permafrost tunnel near Fairbanks, Alaska. *Permafrost and Periglacial Processes* 7(3): 281-285.
- Mukesh, K. 1985. *Design of a Pillar in Time Dependent Materials*. M.S. Thesis, University of Alaska Fairbanks, 148 pp.
- Pettibone, H.C. 1973. Stability of an underground room in frozen gravel. *North American Contribution to Permafrost: Second International Conference, Yakutsk, U.S.S.R., 13-28 July 1973*: 699-706.
- Rausch, D.O. 1958. SIPRE Technical Report 44: *Ice Tunnel, Tuto Area, Greenland, 1956*. Wilmette, IL: U.S. Army Snow Ice and Permafrost Research Establishment, 34 pp.
- Russell, F. 1961. Special Report 44: *An Under-Ice Camp in the Arctic*. Hanover, NH: Cold Regions Research and Engineering Laboratory, 14 pp.
- Sayles, F.H. 1985. Creep of a strip footing on ice-rich permafrost. *Foundations in Permafrost and Seasonal Frost*; Proceedings of a session of the ASCE Convention in Denver, Colorado, April 29, 1985: 29-51.
- Sellmann, P.V. 1972. Special Report 177: *Geology and properties of materials exposed in the USACRREL permafrost tunnel*. Hanover, NH: Cold Regions Research and Engineering Laboratory, 16 pp.
- Shur, Y., French, H.M., Bray, M.T., & Anderson, D.A. 2004. Syngenetic permafrost growth: cryostratigraphic observations from the CRREL tunnel near Fairbanks, Alaska. *Permafrost and Periglacial Processes* 15(4): 339-347.
- Swinzow, G.K. 1964. Technical Report 91: *Tunneling in Permafrost, II*. Hanover, NH: Cold Regions Research and Engineering Laboratory.
- Swinzow, G.K. 1970. Technical Report 221: *Permafrost tunneling by a continuous mechanical method*. Hanover, NH: Cold Regions Research and Engineering Laboratory, 37 pp.
- U.S. Army Corps of Engineers Cold Regions Research and Engineering Laboratory. 1981. CRREL permafrost tunnel. *CRREL Benchnotes* 17. Hanover, NH: Cold Regions Research and Engineering Laboratory, 1-7.
- Weerdenburg, P.C. 1982. *Analytical study of time-dependent deformation in permafrost*. M.S. Thesis, University of Alberta, 450 pp.
- Wu, M.-C. 1985. *The temperature and geometry influences on an underground opening in the frozen ground*. M.S. Thesis, University of Alaska Fairbanks, 186 pp.
- Zhu Y. & Carbee, D.L. 1987. CRREL Report 87-10: *Creep and strength behavior of frozen silt in uniaxial compression*. Hanover, NH: Cold Regions Research and Engineering Laboratory, 67 pp.

Annual Frost Heave Distribution in a Non-Sorted Circle System Measured with a Terrestrial Laser Scanner

Ronald P. Daanen

Institute of Northern Engineering, University of Alaska Fairbanks, USA

Abstract

We measured two digital elevation models at very high resolution in a non-sorted circle system using a Terrestrial Laser Scanner in order to understand the frost heave pattern of these systems. The data show large variability in annual frost heave. The variability is strongest on and off the center of the non-sorted circles. The vegetation pattern observed with the data is strongly related to the pattern of frost heave. The total amount of heave for the research grid is on average 8.8 cm but varied from 1 to 15 cm. The total amount of water in the grid does not justify the total amount of heave observed by simply calculating the volume change from liquid water to ice. Other potential reasons for frost heave, suggested here, are water migration from organic layers containing more liquid water, cracks forming in the active layer as it freezes, and drying of the soil ahead of the freezing front.

Keywords: non-sorted circles; frost heave; freezing soil; terrestrial laser scanner; Northern Alaska.

Introduction

Very high resolution surface elevation models are increasingly crucial for development of the understanding of ecosystems. Small-scale elevation differences drive micro climate and soil thermal and moisture conditions. The physical environment near the ground surface promotes or limits vegetation development in non-sorted circle systems (Walker et al. 2004, Kade et al. 2005, Kade et al. 2006, Daanen et al. 2008a, Kade & Walker 2008, Vonlanthen et al. 2008, Walker et al. 2008a, 2008b). In this paper, we discuss the spatial frost heave observations in a non-sorted circles environment near Franklin Bluffs, Alaska. In particular, we discuss differential frost heave, which was identified as the main driving force to non-sorted circles system development and maintenance (Walker et al. 2008a). The area was previously surveyed using a theodolite at a resolution of 25 cm (Daanen et al. 2008b). The dataset discussed in this paper reveals greater details of the shape, location, and size of the non-sorted circles. In particular, we are interested in the size and volume of the heaving versus non-heaving surface area.

Methods

The study area is located in the continuous permafrost zone on the North Slope of Alaska (69.674504°N, 148.720508°W) (Fig. 1). Non-sorted circles are common in this region dominated with non-acidic, erect, dwarf shrubs, cotton grass, and sedge tundra (Kade et al. 2005). In this region, the non-sorted circles are 1–3 meters in diameter. Tundra conditions vary from wet to dry. The grid is located in a zonal site, which allows for a better comparison between various climate factors between grids along a climate gradient. The soil is a loam with more sand and silt than clay, but all parts comprise less than 50% of the total (Michaelson et al. 2008).

Frost cracks have been observed in the soils, both in frozen cores and as micro structures in the soil profile. Typical lenticular structure allows easy horizontal water movement, and vertical

cracks are considered instrumental in transportation of organic matter to greater depths. Active layer depths were measured in late August and varied from 60 cm (vegetated) to 100 cm (bare ground) with an average near 80 cm.

The 10 x 10 meter survey area was one of the main study areas for bio-climatic subzone D in the NSF study “Frost boils along a North American Arctic Transect (NAAT).” The grid is mesic (moist) and can be considered zonal for vegetation purposes. The Arctic has 5 bio-climate subzones; A is the coldest in the high Arctic and E is the warmest in the low Arctic. Each zone is characterized by the occurrence of particular plant species and growth forms (Walker et al. 2002). The region has a mean annual air temperature of approximately -12°C, whereas the mean annual surface temperature is approximately -4°C (Romanovsky et al. 2008).

For this study, two digital elevation models were developed

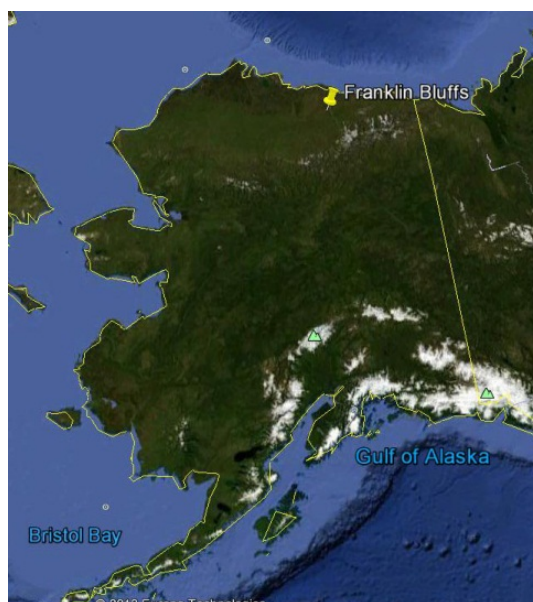


Figure 1. Location of Franklin Bluffs research site in Northern Alaska, USA.

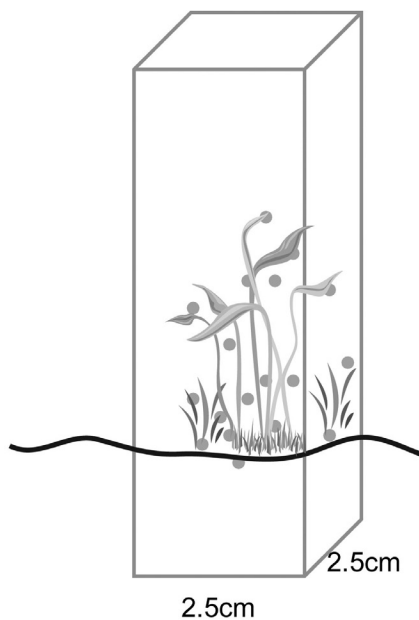


Figure 2. Typical scan distribution for a vegetated surface. Dots represent laser reflection points in the point cloud. Plant canopy density is calculated as the elevation of the points more than 1 cm above the lowest measured point divided by the total number of points within the grid node.

at a resolution of 2.5 centimeters. One dataset was collected during spring at the maximum heave position and the other in the autumn during maximum thaw depth. A Leica (Scanstation 2) Terrestrial Laser Scanner (TLS) was used to scan an area of 100 square meters of tundra near Franklin Bluffs, each containing ~20 million points.

The two datasets consist of TLS measurements from each cardinal direction of the grid. Fixed reference corner points were used between scans to integrate the individual scans. The Cyclone software from Leica used to drive the scanner was employed in this step of the data processing. This software package also converts the data from all scans into a xyz data cloud. This point cloud data from the scans was cut, using a Fortran code, to exclude points that were not inside the 10 x 10 m grid area. The grid was divided in 2.5 centimeter squares, grid nodes, to analyze the point cloud distribution within. The lowest point in each grid node was used as the soil surface elevation. Some cleaning of the data may be required at this point to eliminate erroneous data points. Other points within the grid node with a higher elevation were processed to derive vegetation related data (Fig. 2).

Using the Fortran code, the two elevation data sets (2.5 x 2.5 cm and elevation) were compared after rotating and shifting them to match independent markers in the scan domain. These markers were individual tussocks that were identified in both datasets. Due to the lack of a proper reference elevation of the corners of the grid, the elevation between non-sorted circles was used as a relative reference elevation for both datasets. Only a few grid nodes seemed to be similar in elevation between datasets. This assumption reduces the total potential

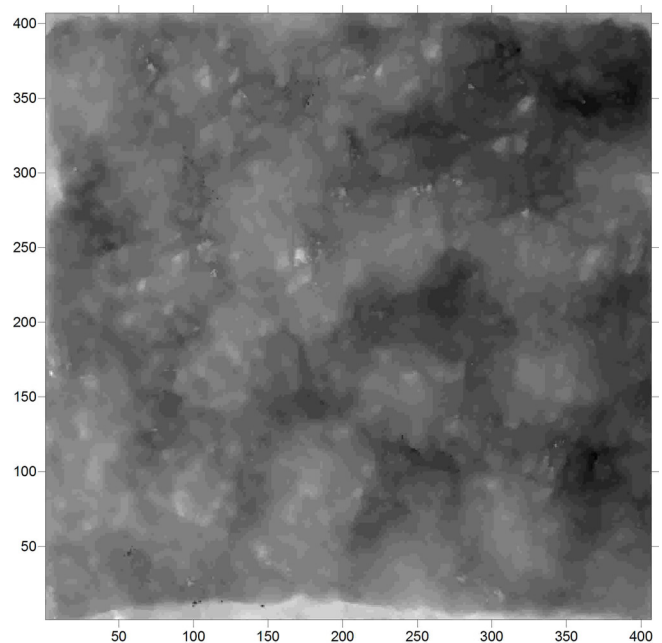


Figure 3. Digital elevation model of a 10 x 10 meter grid near Franklin Bluffs, Alaska, in April 2009. The axes are in multiples of 2.5 cm, and the elevation scale is relative.

heave of the grid, and this dataset is therefore considered a conservative measure of frost heave potential of a non-sorted circle system in bioclimatic subzone D.

Vegetation differences between summer and winter are a potential influence on the calculation of soil surface DEMs. The large numbers of observations of points in the cloud, from four cardinal directions, are to prevent errors due to vegetation obstruction. Some grid nodes had more the 1000 observation points; the more points, the greater the chance that the soil surface was scanned at least once.

Results

The objective of this study was to measure heave distribution accurately and at a high resolution. The results of the TLS survey consist of two digital elevation maps, the subtraction of the two maps, and a vegetation analysis. The first map, presented in Figure 3, is the digital elevation map of spring 2009. The second map, which is based on the August 2009 measurements, is illustrated in Figure 4.

The structure that is visible in these two figures can be attributed to tussocks and soil elevation. The April scan shows greater variability, but non-sorted circles are still difficult to recognize.

These two digital elevation models are then subtracted to find the distribution and amount of frost heave. Data points with singular negative values were considered erroneous and eliminated from the dataset; these were largely grid points with tall dense vegetation that blocked the TLS from penetrating to the ground at that node, and therefore higher in elevation during summer compared to winter. Also, grid nodes that had no points were excluded from the plot. The result of the combined Figures 3 and 4 is given in Figure 5.

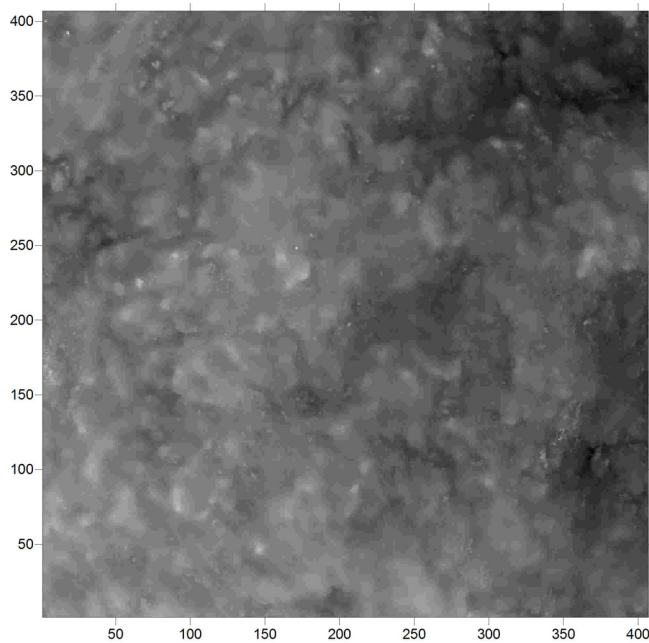


Figure 4. Digital elevation model of a 10 x 10 meter grid near Franklin Bluffs, Alaska in August 2009. The axes are in multiples of 2.5 cm and the elevation scale is relative and the same as Figure 3.

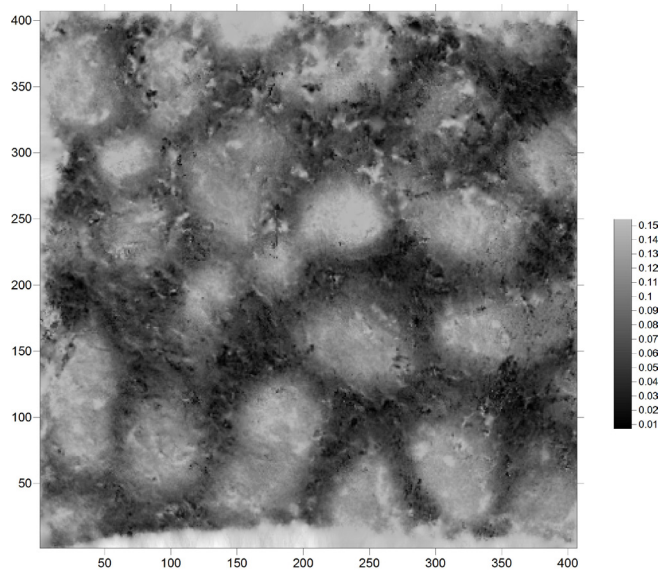


Figure 5. Spatial frost heave distribution in a non-sorted circle ecosystem. The axes are the same as in the previous figures. The scale of the heave is in meters.

In this figure, non-sorted circles can be recognized as the regions that heave most. The average heave in the grid is 8.8 cm, the maximum heave observed in this grid is 15 cm, and the minimum is 1 cm. The area of six heave classes can be found in Figure 6; the total area of the grid is 100 square meters. The total volume of heave for the grid is 8.1 m³. The area of heave below 7.5 cm is similar to the area of heave above 10 cm (see Fig. 6).

Additional information about the vegetation can be derived from the TLS data. The vegetation canopy density is a relative measure of the canopy's ability to reflect the laser from the perspective of the scanner. This value is calculated by counting

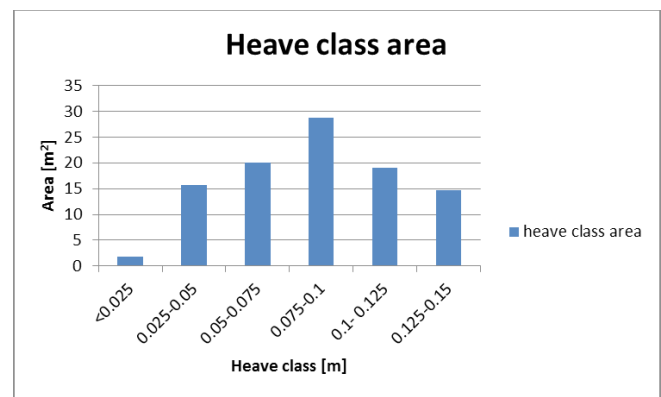


Figure 6. Heave class area distribution.

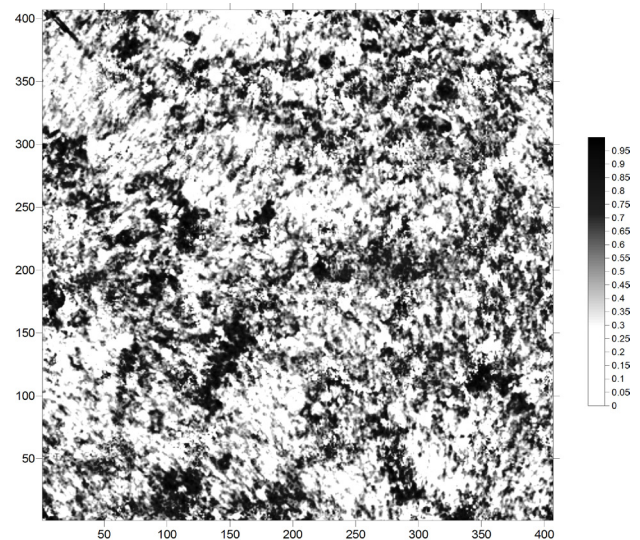


Figure 7. Vegetation canopy density. The number in the legend is the fraction of the total number of points above the lowest 1 cm in a grid node of 2.5 x 2.5 cm.

the number of points in a grid node that did not reach the lowest 1 cm, divided by the total number of observation points in the grid node. Dense vegetation collects many more reflections at a higher elevation above the lowest centimeter above the soil surface, as compared with thin and short vegetation. The values for the canopy density are given in Figure 7.

At the distance of scanning in this project, it was possible to identify individual flag pins, but anything smaller in size would not be distinguishable from random noise in the data. If the laser was more accurate, it would also create more random measurements (e.g., mosquitos, rain, snow, and dust in the air). In this dataset, the focus was not on mosses, but a more detailed study on individual species of plants (and in particular mosses) may be able to capture the abundance or even thickness of moss. Vegetation height can also be measured using the highest elevation recorded in the grid node, but here caution is required because of flying insects and rain in the summer and blowing snow in winter. During spring, these data are more scarce due to the lack of leaves on the shrubs, which in summer may prevent the laser beam from reaching the soil surface. In the current dataset there are multiple empty nodes related to dense leaves, tussocks, or surface water. Smaller

objects are also difficult to capture due to movement in the wind.

In this study, data used from the scanner were limited to the point cloud geometry. However, more information may also be gained from the laser scanner in the form of reflectance strength. One example where the laser showed very weak or no reflectance was in the case of standing water. Comparing vegetation to bare ground, a stronger reflectance was recorded from bare ground in most cases.

The vegetation canopy densities show that vegetation is dense between the non-sorted circles, whereas on the features there is a reduced vegetation density.

Discussion

The maximum frost heave observed in a non-sorted circle system in a previous study near Franklin Bluffs was up to 17 cm using a heavometer (Romanovsky et al. 2008). The device measures frost heave relative to a bench mark fixed in the permafrost. To reach this amount of frost heave in a two dimension model, it was necessary to introduce water from an exterior source (Nicolosky et al. 2008). Near Galbraith Lake, plug circles were evaluated for frost heave and 12 cm of differential heave was observed (Overduin & Kane 2006). The same grid as the current study was previously evaluated using a theodolite system, and a maximum frost heave of 28 cm was found (Daanen et al. 2008b). The current dataset presented in this paper shows a maximum differential frost heave of up to 15 cm.

Moisture availability is important to create frost heave, and multiple dry years on the North Slope of Alaska have likely reduced the amount of frost heave presently measured. It is now observed that more non-sorted circles near Franklin Bluffs have become vegetated, which may be the direct result of reduced frost heave (Daanen et al. 2007, Daanen et al. 2008a).

Frost heave is greatest on the non-sorted circles and is minimal between the circles. The area between circles heaves about 1 cm, so the difference on and off the circles is up to 14 cm in the dataset. Annual frost heave is caused by ice lens formation in the active layer (Miller 1980). The theoretical amount of primary frost heave in the active layer depends on the depth and moisture availability. Assuming an average active-layer depth of 0.75 m, a moisture content of approximately 50% by volume, no moisture movement, and a 10% volumetric expansion of water to ice, there would be only 3.8 cm of frost heave. It is not likely that ground water flow will introduced additional water to the grid due to a lack of topography that would drive this water movement.

The heave for the entire grid can be partially explained by the approximate 90% volumetric moisture content in the organic layer. The organic layer thickness is typically 15 cm between the non-sorted circles. In this grid, with an area of about 50 m² and 90% liquid filled, is a volume of 6.75 m³ of water in the organic layer alone. This amount of liquid water from the organic soils needs to be transported to the mineral soil in the non-sorted circles to account for the heave observed there. A

mechanism for this transport is temperature-gradient driven cryostatic suction and resulting flow (Miller 1980, Fowler & Krantz 1994, Daanen et al. 2007, Daanen et al. 2008a, Nicolosky et al. 2008). The temperature gradients develop during freezing due to better insulation in the vegetated areas, and the heaving causes the non-sorted circles to accumulate less snow on the surface.

The total heave in the grid is 8.8 m³. This heave is likely caused in part by the expansion of liquid pore water to ice, movement of liquid water from the organic layer to the mineral non-sorted circles, and possibly due to cracks created from soil deformation during freezing. Drying of the mineral soil between the ice lenses is also a potential source of water in unsaturated mineral soils, which becomes more likely when cracks in the frozen ground transport air below the freezing front to fill pore voids. Differential heave is also aided by the difference in active layer depth beneath and between non-sorted circles. This difference can be as great as 10 cm. This difference is mainly caused by the lack of heat transport through the soil surface and through the organic layer in summer. The shallower depth between the non-sorted circles allows less of the soil column to actively freeze.

The dataset created for this study seems to capture the frost heave well. The effect of the vegetation density on the measurements of the soil surface is a concern that is overcome with high-resolution scanning from four different cardinal directions. The smooth contours visible in the heave distribution in Figure 5 are evidence of little disturbance by the generally sparse vegetation at this site.

Conclusions

This paper shows measured distributed annual frost heave in a non-sorted circle system using high-resolution TLS. The measurements show large amounts of frost heave over half of the scanned grid. A regular distribution of differential heave is the result of the non-sorted circle distribution. The laser scanning data provided highly accurate and high-density data points for soil surface elevation as well as vegetation canopy density. The data show that the heaved areas are associated with areas of reduced vegetation. These measurements suggest that vegetation is an important factor controlling heave in these systems.

Total heave in the scanned grid is about twice the amount of heave explained by the expansion of liquid pore water to pore ice, assuming an average active layer depth and average volumetric moisture content. Water that could enhance frost heave is available in the organic layer. This water can reach the non-sorted circles, where most of the frost heave is measured, through frost cracks and previous ice lens structures in the unfrozen soil. Another potential explanation for the large amount of frost heave is drying of the soil ahead of the freezing front during ice lens formation.

Acknowledgments

I would like to acknowledge the permafrost laboratory and Dr. V.E. Romanovsky for covering the rental costs of the TLS and time spent on this project. Also I would like to thank Dr. D.A. Walker for many inspiring conversations and help with the vegetation canopy density. I appreciate the reviewer's comments, which improved this paper significantly. This research was partially funded by the Polar Earth Science Program, Office of Polar Programs, National Science Foundation Grant No. ARC-0612533, OPP-0120736 ARC-0632400, and ARC-0520578.

References

- Daanen, R.P., Misra, D., & Epstein, H. 2007. Active-layer hydrology in nonsorted circle ecosystems of the arctic tundra. *Vadose Zone Journal* 6, 694-704, Doi 10.2136/Vzj2006.0173.
- Daanen, R.P., Misra, D., Epstein, H., Walker, D., & Romanovsky, V. 2008a. Simulating nonsorted circle development in arctic tundra ecosystems. *J Geophys Res-Bioge* 113, G03S06, DOI: 10.1029/2008jg000682.
- Daanen, R.P., Romanovsky, V.E., Walker, D.A., & LaDouceur, M. 2008b. High-Resolution Surface and Subsurface Survey of a Non-Sorted Circle System. In *NICOP 2008: Proceedings of the Ninth International Conference on Permafrost*. D.L. Kane, K.M. Hinkel (eds.). Institute of Northern Engineering, University of Alaska Fairbanks, 1: 321-326.
- Fowler, A.C. & Krantz, W.B. 1994. A Generalized Secondary Frost Heave Model. *Siam Journal on Applied Mathematics* 54, 1650-1675.
- Kade, A., Walker, D.A., & Reynolds, M.K. 2005. Plant communities and soils in cryoturbated tundra along a bioclimate gradient in the Low Arctic. *Alaska, Phytocoenologia* 35, 761-820, Doi 10.1127/0340-269x/2005/0035-0761.
- Kade, A., Romanovsky, V.E., & Walker, D.A. 2006. The N-factor of nonsorted circles along a climate gradient in Arctic Alaska. *Permafrost and Periglacial Processes* 17, 279-289.
- Kade, A. & Walker, D.A. 2008. Experimental alteration of vegetation on nonsorted circles: Effects on cryogenic activity and implications for climate change in the arctic. *Arctic Antarctic and Alpine Research* 40, 96-103.
- Michaelson, G.J., Ping, C.L., Epstein, H.E., Kimble, J.M., & Walker, D.A. 2008. Soils and frost boil ecosystems across the North American Arctic Transect. *J Geophys Res-Bioge* 113, doi:10.1029/2007JG000672.
- Miller, R.D. 1980. Freezing phenomena in soil. *Applications of Soil Physics*, edited by: Hillel, D., Academic Press, New York, 254-299 pp.
- Nicolson, D.J., Romanovsky, V.E., Tipenko, G.S., & Walker, D.A. 2008. Modeling Observed Differential Frost Heave Within Non-Sorted Circles in Alaska. In *NICOP 2008: Proceedings of the Ninth International Conference on Permafrost*. D.L. Kane, K.M. Hinkel (eds.). Institute of Northern Engineering, University of Alaska Fairbanks, 2: 1281.
- Overduin, P.P. & Kane, D.L. 2006. Frost boils and soil ice content: Field observations. *Permafrost and Periglacial Processes* 17, 291-307, Doi 10.1002/Ppp.567.
- Romanovsky, V.E., Marchenko, S., Daanen, R.P., Sergeev, D.O., & Walker, D.A. 2008. Soil climate and frost heave along the Permafrost/Ecological North American Arctic Transect, *Proceedings of the Ninth International Conference On Permafrost* Fairbanks, 1519-1525.
- Vonlanthen, C.M., Walker, D.A., Reynolds, M.K., Kade, A., Kuss, P., Daniels, F.J.A., & Matveyeva, N.V. 2008. Patterned-ground plant communities along a bioclimate gradient in the High Arctic, Canada. *Phytocoenologia* 38, 23-63, Doi 10.1127/0340-269x/2008/0039-0023.
- Walker, D.A., Gould, W.A., Maier, H.A., & Reynolds, M.K. 2002. The Circumpolar Arctic Vegetation Map: AVHRR-derived base maps, environmental controls, and integrated mapping procedures. *Int J Remote Sens* 23, 4551-4570, Doi 10.1080/01431160110113854.
- Walker, D.A., Epstein, H.E., Gould, W.A., Kelley, A.M., Kade, A.N., Knudson, J.A., Krantz, W.B., Michaelson, G., Peterson, R.A., Ping, C.L., Reynolds, M.A., Romanovsky, V.E., & Shur, Y. 2004. Frost-boil ecosystems: complex interactions between landforms, soils, vegetation, and climate. *Permafrost and Periglacial Processes* 15, 171-188.
- Walker, D.A., Epstein, H.E., Romanovsky, V.E., Ping, C.L., Michaelson, G.J., Daanen, R.P., Shur, Y., Peterson, R.A., Krantz, W.B., Reynolds, M.K., Gould, W.A., Gonzalez, G., Nicolsky, D.J., Vonlanthen, C.M., Kade, A.N., Kuss, P., Kelley, A.M., Munger, C.A., Tamocai, C.T., Matveyeva, N.V., & Daniels, F.J.A. 2008a. Arctic patterned-ground ecosystems: A synthesis of field studies and models along a North American Arctic Transect. *J Geophys Res-Bioge* 113, Artn G03s01, Doi 10.1029/2007jg000504.
- Walker, D.A., Epstein, H.E., & Welker, J.M. 2008b. Introduction to special section on Biocomplexity of Arctic Tundra Ecosystems. *J Geophys Res-Bioge* 113, Artn G03s00, Doi 10.1029/2008jg000740.

Using Ground Data from the Global Terrestrial Network of Permafrost (GTN-P) for the Evaluation of the ESA DUE Permafrost Remote Sensing Derived Products Land Surface Temperature and ASCAT Surface State Flag

Kirsten Elger, Birgit Heim

Alfred Wegener Institute for Polar and Marine Research, Potsdam, Germany

Annett Bartsch, Christoph Paulik

Institute of Photogrammetry and Remote Sensing, Vienna University of Technology, Vienna, Austria

Claude Duguay, Sonia Hachem, Aiman Soliman,

University of Waterloo, Interdisciplinary Centre of Climate Change, Canada

Hugues Lantuit, Julia Boike

Alfred Wegener Institute for Polar and Marine Research, Potsdam, Germany

Frank-Martin Seifert

European Space Agency ESA, Frascati, Italy

Abstract

The ESA Data User Element (DUE) Permafrost project provides a mid-to-long-term Earth observation service for permafrost remote sensing derived applications for northern high-latitude permafrost areas. The DUE Permafrost remote sensing products are land surface temperature, surface soil moisture, frozen/thawed surface status, elevation, land cover, and surface waters. A major component is the evaluation of the DUE Permafrost products to test their scientific validity for high-latitude permafrost landscapes. These case studies evaluate two DUE Permafrost products (MODIS Land Surface Temperature and ASCAT Surface State Flag) by comparing the results with field-based data obtained by the Global Terrestrial Network of Permafrost (GTN-P). First results showed good correlation, which suggests that the DUE Permafrost approach is a promising one for long-term monitoring of permafrost surface conditions. Furthermore, it demonstrates the great benefit of freely available ground truth databases for the evaluation of remote sensing derived products.

Keywords: ESA DUE Permafrost; GTN-P; evaluation of remote sensing products; MODIS LST; ASCAT Surface State flag; Circum-Arctic.

Introduction

Permafrost, or perennially frozen ground, is an important component of the cryosphere and the arctic system. Fieldwork in the Arctic and Subarctic involve challenging logistics; observational sites are scattered, sparse, and mostly located along coastal areas. Satellite sensors (optical, thermal, microwave) provide a spatially and temporally consistent coverage of key parameters for climate and hydrological and permafrost research.

Several medium- to coarse-scale resolution satellite missions operate on a daily basis and deliver data for large areas. Remote-sensing applications to derive land surface temperature and surface moisture from satellite data are operationally established. However, are remote sensing products that have been developed and tested in agricultural, semi-arid to forest landscapes of low to mid-latitudes also valid for high-latitude permafrost landscapes? Permafrost landscapes pose a challenge for qualitative and quantitative remote sensing. The land surface is characterized by high heterogeneity, patterned ground, disturbances, abundance of small-sized water bodies, and sharp moisture gradients in the near-subsurface (i.e., active layer/permafrost boundary). High spatial resolution remote sensing data are not publicly available but can be acquired, mostly from commercial companies at usually high costs.

In this sense, a service based on publicly available medium- to coarse-scale satellite products is of high value for permafrost-related applications.

ESA DUE Permafrost – a Remote Sensing Permafrost Monitoring System

The ESA Data User Element (DUE) Permafrost project (<http://www.ipf.tuwien.ac.at/permafrost>) provides a mid- to long-term Earth observation service for permafrost remote sensing derived applications for Northern high-latitude permafrost areas (north of 50°N) (e.g., Bartsch et al. 2010, Heim et al. 2011). From the beginning, scientific stakeholders and the International Permafrost Association (IPA) were actively involved in the project. The DUE Permafrost remote sensing derived products are key parameters for permafrost research: land surface temperature, surface soil moisture, frozen/thawed surface status, elevation, land cover, and surface waters.

The DUE Permafrost consortium consists of five project partners. Each is responsible for the development and the evaluation of one or more DUE Permafrost products. The project leader is the Vienna University of Technology (Austria): project coordination and microwave remote-sensing (frozen/ thawed surface status, surface soil moisture, surface waters). Project partners are the University of Waterloo

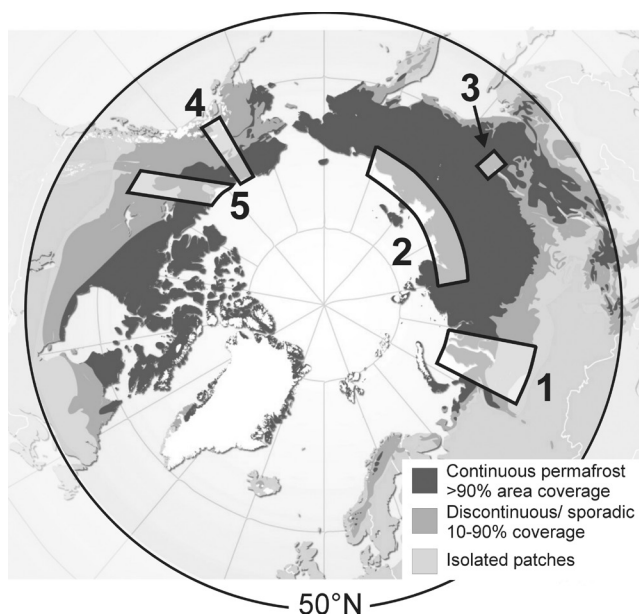


Figure 1. Coverage of DUE Permafrost Circum-Arctic products ($>50^{\circ}$ N) with five test regions (boxes) and permafrost zones of the Northern Hemisphere (modified after Permafrost Extent in the Northern Hemisphere, 2007).

(Canada): land surface temperature; Friedrich Schiller University Jena (Germany): land cover, surface waters; Gamma Remote Sensing (Switzerland): elevation; and Alfred Wegener Institute for Polar and Marine Research (Germany): ground data management, interaction between the permafrost scientific community and remote sensing experts.

The DUE Permafrost products are provided for the entire permafrost area north of 50° N. Circum-Arctic land surface temperature, frozen/thawed surface status, and surface soil moisture are provided with weekly and monthly averages from 2007–2010 with 25-km pixel resolution. The global land cover has a spatial resolution of 350 m. The new Circum-Arctic DEM dataset north of 55° N has a 100-m pixel resolution. In addition, five case study regions were defined, for which products with higher spatial resolution (pixels ranging from 150 m to 1 km) than the Circum-Arctic products were developed (Fig. 1).

The tests regions are (1) the Russian Laptev Sea and Eastern Siberian Sea Region (continuous very cold permafrost/tundra), (2) the Yakutsk Region, Russia (continuous cold permafrost/taiga), (3) the Western Siberian transect including Yamal Peninsula and Ob Region, Russia (continuous to discontinuous permafrost/taiga-tundra), (4) the Alaskan Highway Transect, USA (continuous to discontinuous permafrost/taiga-tundra), and (5) the Mackenzie Delta and Valley, Canada (continuous to discontinuous permafrost/taiga-tundra). All DUE Permafrost products will be freely available via the worldwide web in 2012.

The studies described here show the evaluation of two DUE Permafrost products by comparing the satellite data with in situ measurements derived from the Global Terrestrial Network of Permafrost. The products are MODIS land surface temperature and Metop ASCAT Surface State Flag (SSF) for frozen and thawed surface state.

The Global Terrestrial Network of Permafrost (GTN-P)

The Global Terrestrial Network for Permafrost (GTN-P) was initiated by the International Permafrost Association (IPA) to organize and manage a global network of permafrost observatories for detecting, monitoring, and predicting climate change. The network, authorized under the Global Climate Observing System (GCOS) and its associated organizations, consists of two observational components: the Circumpolar Active Layer Monitoring (CALM) and the Thermal State of Permafrost (TSP) (IPA 2011).

Both have been thoroughly overhauled during the fourth International Polar Year (IPY 2007–2009) and extended their coverage to provide a true circumpolar network, which is the most important source of ground truth data for the evaluation of DUE Permafrost products. A major part of the DUE Permafrost core user group is contributing to GTN-P. All GTN-P data are freely accessible via the worldwide web.

Circumpolar Active Layer Monitoring (CALM)

In the arctic and subarctic lowland of the Northern Hemisphere, active-layer depth was measured with a metal rod in regular grids (1 ha to 1 km²), in thaw tubes, or points at ~125 sites in 15 countries in different permafrost zones (Brown 2010). The active layer thickness was measured at least once a year (in late summer) for at least the last 12 years. Many sites recorded data from the beginning of the 1990s onward. In addition to the active layer depth, detailed descriptions of vegetation and landform, as well as occasionally temperature and soil moisture measurements, are available via the CALM website (<http://www.udel.edu/Geography/calm>).

Thermal State of Permafrost (TSP)

Within the polar region of the Northern Hemisphere, ground temperatures are now measured in ~575 boreholes throughout Russia, North America, and the Nordic countries (Romanovsky et al. 2010b). The existing permafrost database was greatly enhanced during the IPY years 2007–2009. This included the establishment of new boreholes (more than half of the Northern Hemisphere boreholes were drilled during the IPY), the integration of existing permafrost observatory sites, and the collection of historical data. The main focus for the establishment of new sites was to close geographical gaps in the monitoring network. Air, surface, and ground temperatures are measured in boreholes ranging from a few meters to depths greater than 125 m (Brown 2010, Romanovsky et al. 2010a, http://www.gi.alaska.edu/snowice/Permafrost-lab/projects/projects_active/proj_tsp.html).

Evaluation, Ground Data, and Satellite Products

Evaluation concepts

A major component of the project is the evaluation of the DUE Permafrost products using in situ data, ERA interim reanalysis data, and cross-validation studies with other remote

sensing products. These evaluation studies were performed by the project partners who are responsible for the realization of the products. Case studies are described in Hachem et al. (2012), Naeimi et al. (2012), and Park et al. (2011).

This study shows the comparison of two DUE Permafrost products with field-based GTN-P data. The DUE Permafrost project largely benefits from the extensive and freely available ground data acquired within the GTN-P program. In addition to using GTN-P data, user groups were directly involved in providing ground data and evaluating the products (e.g., Helmholtz University Young Investigators Group HGF-Sensitivity of Permafrost in the ARctic [SPARC] at AWI, and the Land Use Land Cover Change programme LCLUC Yamal [NASA]).

For the evaluation of MODIS land surface temperature (LST) and ASCAT surface state flag (SSF), we used air, surface or upper soil temperature time series for the years 2007–2010. Ideal for the evaluation is ground data with high temporal resolution (i.e., time series of at least daily averages).

Satellite products: ASCAT Surface State Flag

Information on the soil surface state is very valuable for the monitoring of permafrost regions. Variation in the state or amount of water in the soil results in significant alteration of dielectric properties that can be observed in the backscattered signal. The ASCAT scatterometer onboard Metop satellite is an active microwave sensor. Long-wave C-band scatterometer data have been identified as a good indicator for the surface frozen or thawed state (Naeimi et al. 2012). The surface state flag (SSF) is the output product of a threshold analysis representing the frozen/ thawed surface status. Within the DUE Permafrost project, SSF is one of two products for the frozen/thawed surface status. SSF is derived from the ASCAT Circum-Arctic product (with 25-km pixel resolution). For regional frozen/thawed surface status products, synthetic aperture radar data from the ASAR sensor are used.

Naeimi et al. (2012) compared ASCAT SSF data with air temperature time series from global climate stations and with air, surface and ground temperature time series from GTN-P permafrost observation sites.

Satellite products: Land Surface Temperature

The current operational satellite sensors operating in the thermal infrared part of the electromagnetic spectrum offer the potential to retrieve land surface skin temperatures on a daily basis over large areas at the 1-km² horizontal resolution. Measurements are at-satellite temperatures that are calculated to land surface temperature (LST) using an operational atmospheric correction. NASA offers atmospherically corrected LST from two Moderate Resolution Imaging Spectroradiometer (MODIS) satellite missions (Aqua and Terra) with day and night acquisitions.

The quality assessments for the DUE Permafrost Product MODIS LST were done by matching the MODIS Aqua and Terra LST against high temporal-resolution air temperature datasets (hourly measurements to daily averages) from climate and GTN-P permafrost monitoring stations.

GTN-P in situ data used for the evaluation

The evaluation of regional LST and SSF products with in situ data from the GTN-P network was performed for sites in Alaska and Western Siberia. Figure 2 gives an overview of the location of all GTN-P sites with near-surface temperature time series (small circles) and those for which data are shown in this paper (larger circles). The Alaskan north-south transect covers continuous to discontinuous permafrost zones of the tundra and taiga (Fig. 2 left). Seventeen GTN-P sites have soil temperatures measured within the first meter below the ground. Available data are time series for daily averaged temperature data for 2006–2010. The Western Siberian test region stretches from Novaya Zemlya in the West, across the Yamal Peninsula, to the western half of the Gydan Peninsula

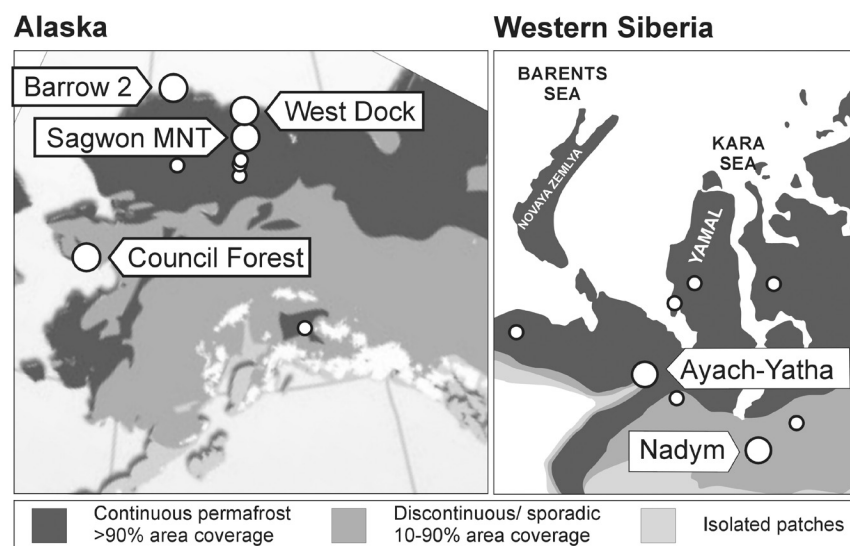


Figure 2. Location of GTN-P sites (circles) in Alaska and Western Siberia and within permafrost zones. Larger circles represent sites for which data are presented in this paper. The Alaskan map shows only GTN-P sites with air and soil temperature for the first meter. “MNT” = moist non-acidic tundra.

in the East, and reaches ~150 km southward (Fig. 2 right). The eight West Siberian GTN-P sites are located in different permafrost zones.

The temperatures used for the evaluation are mostly daily-averaged time series. In addition, for some sites, data with hourly resolution are available (i.e., more than six values daily and the information on the measuring hour). These time series are the ideal database for the evaluation of the LST products because the database allows the selection of temperature data measured within only a couple of hours of the satellite overflight.

Results

Time series of daily averaged GTN-P temperature data (T_{air} , T_{surface}) were used to validate the DUE Permafrost SSF product. For the evaluation of weekly LST, we benefited from GTN-P air and surface temperature data with hourly and daily resolution. The following subsections show examples of the comparison of remote sensing products with GTN-P ground truth data.

ASCAT Surface State Flag (SSF)

For GTN-P sites Nadym and Mare Sale (Western Siberia, Fig. 3 right), the comparison of ASCAT SSF for the period August 2007 to August 2008 shows a good agreement with temperature data provided by the GTN-P program.

The SSF generally shows frozen surface during negative

temperatures and unfrozen surface when temperatures are positive. Between September and the beginning of November 2007, the fluctuations of temperature are in general fairly reflected in SSF time series. For Nadym, the agreement of the SSF with the parameter air temperature is 90.36%, with surface temperature 91.79%. For Mare Sale, soil temperatures at 0.02 m depth have 82.75% and at 0.5 m have 80.13% agreement with SSF (Fig. 3 right).

This good agreement between the SSF and in situ GTN-P temperature data, with mostly well over 80% agreement, is also visible at GTN-P sites in Alaska (Fig. 3 left). Generally, the accuracy is highest in summer and winter and lowest during transitional periods (see also Naeimi et al. 2012). The deeper a ground temperature was measured, the smaller is the agreement with the SSF since the microwaves emitted by ASCAT penetrate only the uppermost centimeters of the surface. The fluctuation of air temperature agrees slightly more with SSF than surface or soil temperature. However, especially during the freezing period, surface or uppermost ground temperatures reflect the delayed change in the SSF better than air temperatures because the snow layer acts as a buffer (e.g., Barrow 2 and Council Forest in May 2007, see Fig. 3 left). SagwonMNT shows the overall highest percental agreement between SSF and in situ data.

Land Surface Temperature (LST)

Comparison of MODIS LST measurements with GTN-P temperatures (with hourly resolution) for two sites in Western

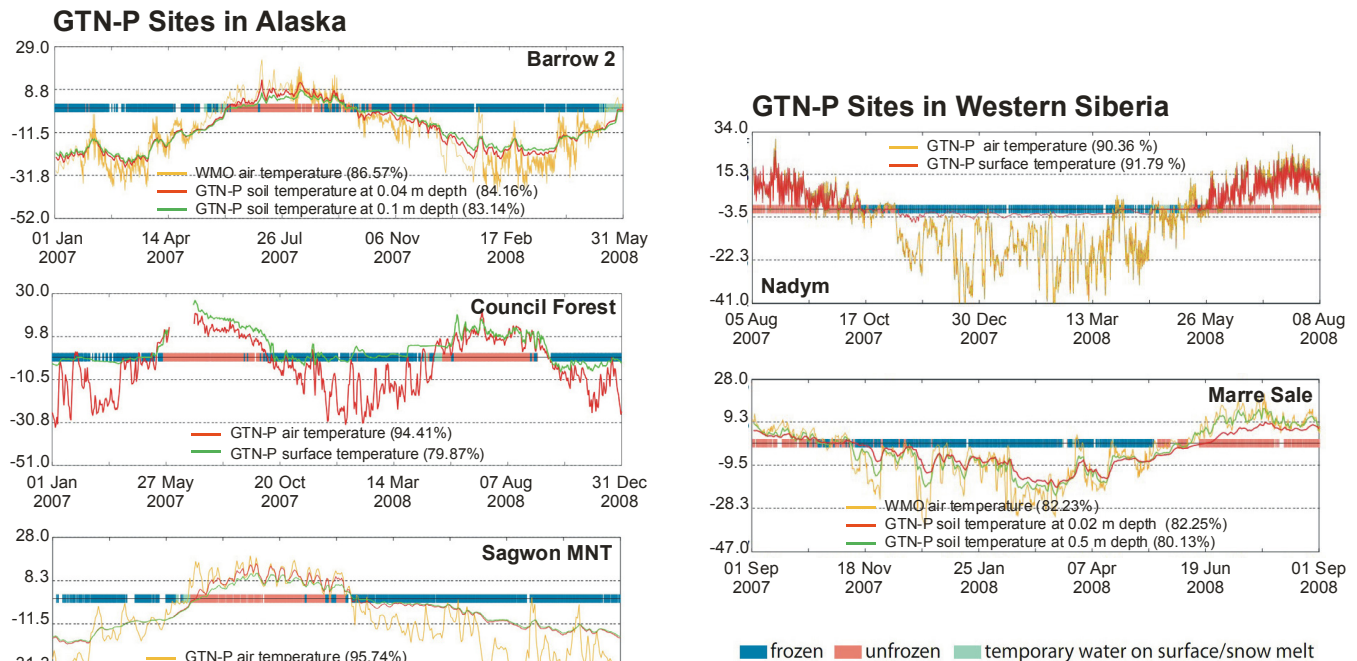


Figure 3. Time series of SSF and temperature data (2007–2008) for GTN-P sites in Alaska (Barrow 2, Council Forest, SagwonMNT) and Western Siberia (Nadym and Mare Sale). Color-coded in the middle of each plot is the satellite-derived Surface State Flag (SSF). Each vertical line represents one day. Blue indicates frozen surface, red unfrozen, and green temporary water on surface/snow melt. The graphs represent measured air and soil temperatures (at different depths) derived from GTN-P permafrost monitoring and WMO Climate stations. The quality of the correlation is given in % agreement for each graph.

Siberia (Nadym, Ayach-Yatha-Vorkuta, Fig. 4) shows a good correlation between ground and satellite data. The selected match-up set of air temperature data is within two hours of MODIS LST. Due to abundant cloud coverage, the total number of MODIS LST measurements is $n = 209$ at Nadym (from Aug. 8, 2009 to Aug. 3, 2010) and $n = 150$ at Ayach-Yatha-Vorkuta (from Jan. 3 to Sept. 24, 2007).

The right graphs of Figure 4 show that the agreement between air temperature and MODIS LST is very good for Nadym ($R^2 = 0.9686$). For Ayach-Yatha-Vorkuta the correlation coefficient is smaller ($R^2 = 0.6222$) and there is more scatter in the data with the largest errors during the summer months. We assume that disagreement is caused by erroneous MODIS LST values due to incorrect cloud masking. Erroneous LST measurements due to undetected clouds have also been described by Langer et al. (2010) and Westermann et al. (2011) for the Lena River Delta (Siberia) and Spitsbergen.

For Alaska, Hachem et al. (2012) investigated the correlation between air and soil temperature and MODIS LST at various sites in Alaska and Canada. For the West Dock case study, which is described in detail in Hachem et al. (2012), the comparison was made for the mean daily LST (combined day

and night data of both Terra and Aqua satellites) and mean daily average air temperature from May 2005 to November 2008 (Fig. 5). The correlation coefficient for the period of almost four years is high ($R^2 = 0.98$), and there is no scatter in the data (Fig. 5 right). This shows that it is also possible to evaluate LST products with time series of daily average air temperatures, which are available for many more sites than data with hourly resolution.

Conclusions and Outlook

In this paper, we showed results from the comparison of field-based data from the Global Terrestrial Network of Permafrost (GTN-P) with the remote sensing derived products ASCAT SSF and MODIS LST for selected sites in Western Siberia and Alaska. The field-based and remotely sensed data showed good correlation, which suggests that the DUE approach is a promising one for long-term monitoring of permafrost surface conditions.

The evaluation of remote sensing products shown here requires ground data with high temporal resolution (time series of daily or hourly averages). For both products, temperature

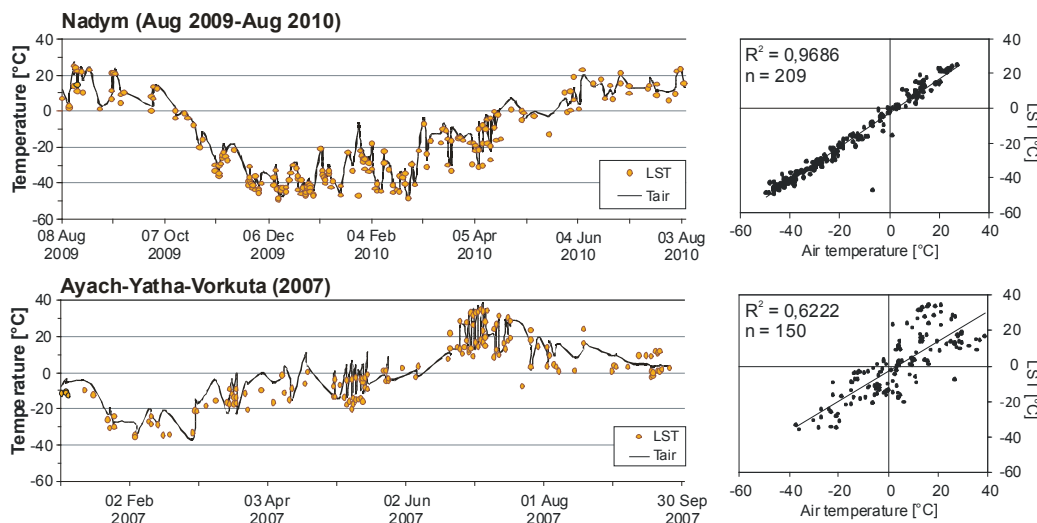


Figure 4. Comparison between LST and air temperature at Western Siberian GTN-P Sites Nadym and Ayach-Yatha/Vorkuta. To the left: LST overlaid on the air temperature graph. To the right: relation between air temperature and LST. Only air temperatures within two hours of satellite flyover were considered for the calculation.

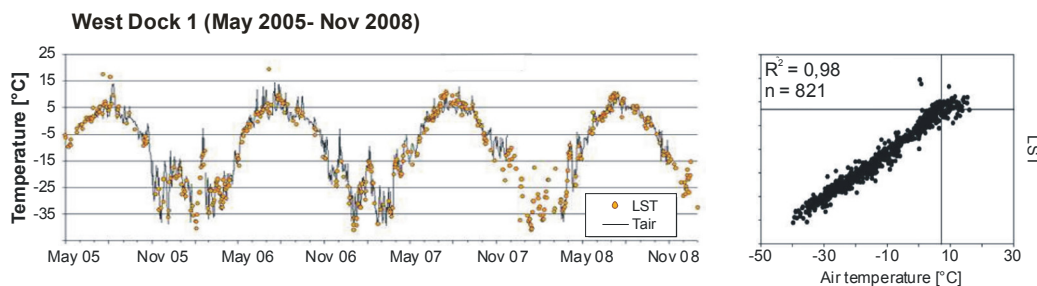


Figure 5. Comparison between the mean daily LST and mean daily air temperature at GTN-P site West Dock (Alaska). To the left: LST overlaid on in situ air temperature (daily averages). On the right: relation between the two sets of measurements (modified after Hachem et al. 2012).

was the validating ground parameter. Ground data from the GTN-P network, with more than 800 sites in the Circum-Arctic, provide an extensive and very valuable database for the evaluation of remote sensing derived products LST and SSF, even for satellite data with coarse resolution (1-km and 25-km pixel size).

The evaluation of the DUE Permafrost surface soil moisture product with in situ data is presented in Bartsch et al. (this volume). The final DUE Permafrost remote sensing products will be released and freely available in 2012. The FP7 project PAGE21 “Changing Permafrost in the Arctic and its Global Effects in the 21st Century” will make use of the DUE Permafrost database.

Acknowledgments

The ESA DUE Permafrost project is an initiative of the European Space Agency (ESA ESRIN 22185/09/I-OL). The DUE Permafrost project gratefully acknowledges the support by the International Permafrost Association (IPA). Alaskan MRC field data (GTN-P) from the University of Alaska Fairbanks (UAF) were derived from the Network of Permafrost Observatories in North America and Russia via the Cadis gateway. Western Siberian field-based data were derived via the CALM website. We also thank the reviewers for their fruitful comments.

References

- Bartsch, A., Wiesmann, A., Strozzi, T. Schmillius, C., Hese, S., Duguay, C., Heim, B., & Seifert, F.M. 2010. Implementation of a satellite data based permafrost information system – The DUE Permafrost Project. *Proceedings of the ESA Living Planet Symposium*, Bergen 2010.
- Brown, J. 2010. Report from the International Permafrost Association: The IPY Permafrost Legacy. *Permafrost and Periglacial Processes* 21: 215-218.
- Hachem, S., Duguay, C.R., & Allard, M. 2012. Comparison of MODIS-derived land surface temperatures with near-surface soil and air temperature measurements in continuous permafrost terrain. *The Cryosphere* 6, 51-69, 2012. doi: 10.5194/tc-6-51-2012.
- Heim, B., Bartsch, A., Elger, K., Lantuit, H., Boike, J. Muster, S., Langer, M., Duguay, C., Hachem, S., Soliman, A., Paulik, Chr., Strozzi, T., & Seifert, F.-M. 2011. ESA DUE Permafrost: an Earth Observation (eo) Permafrost Monitoring System. *EARSeL eProceedings* 10, 2/2011, pp. 73-82.
- IPA (International Permafrost Association). 2011. The Global Terrestrial Network of Permafrost (GTN-P). In: The International Permafrost Association website. Retrieved September 15, 2011, from <http://ipa.arcticportal.org/activities/gtn-p.html>.
- Langer, M., Westermann, S., & Boike, J. 2010. Spatial and temporal variations of summer surface temperatures of wet polygonal tundra in Siberia – implications for MODIS LST based Permafrost monitoring. *Remote Sensing of Environment* 114(9): 2059-2069.
- Naeimi, V., Paulik, Chr., Bartsch, A., Wagner, W., Kidd, R., Park, S-E., Elger, K., & Boike, J. 2012. ASCAT Surface State Flag (SSF): Extracting Information on Surface Freeze/Thaw Conditions From Backscatter Data Using an Empirical Threshold-Analysis Algorithm. *IEEE Transactions on Geoscience and Remote Sensing* (accepted).
- Park, S.-E., Bartsch, A., Sabel, D., Wagner, W. Naeimi, V., & Yamaguchi, Y. 2011. Monitoring freeze/ thaw cycles using ENVISAT ASAR Global Mode. *Remote Sensing of Environment* 115, 12, p. 3457-3467.
- Permafrost extent in the Northern Hemisphere. 2007. In UNEP/GRID-Arendal Maps and Graphics Library. Retrieved 12:47, August 17, 2011 from <http://maps.grida.no/go/graphic/permafrost-extent-in-the-northern-hemisphere>.
- Romanovsky, V.E., Drozdov, D.S., Oberman, N.G., Malkova, G.V., Kholodov, A.L., Marchenko, S.S., Moskalenko, N.G., Sergeev, D.O., Ukraintseva, N.G., Abramov, A.A., Gilichinsky, D.A., & Vasiliev, A.A. 2010a. Thermal State of Permafrost in Russia. *Permafrost and Periglacial Processes* 21: 136-155.
- Romanovsky, V.E., Smith, S.L., and Christiansen, H. 2010b. Permafrost Thermal State in the Polar Northern Hemisphere during the International Polar Year 2007-2009: a Synthesis. *Permafrost and Periglacial Processes* 21: 106-116.
- Westermann S, Langer, M., & Boike, J. 2011. Spatial and temporal variations of summer surface temperatures of high-arctic tundra on Svalbard – Implications for MODIS LST based Permafrost monitoring. *Remote Sensing of Environment* 115(3): 908-922.

Investigating the Effects of Lateral Water Flow on the Spatial Patterns of Thaw Depth

Stefano Endrizzi, Stephan Gruber
Department of Physical Geography, University of Zurich, Switzerland

Abstract

The effects of lateral water flow on the spatial distribution of the thaw depth in permafrost terrain have rarely been investigated with models. The GEOTop model, which solves the soil energy and water budgets in a coupled way and accounts for phase change, has been used to better understand how soil moisture spatial differences in the unfrozen upper part of the ground affect the thawing soil energy balance in idealized hillslope topography. Results show that, in terrains with thermal conductivity highly variable with soil moisture such as organic soils, wetter areas exhibit deeper thaw than drier areas. Conversely, if thermal conductivity depends less on soil moisture, as in mineral soils, the result is the opposite since the effect of the higher thermal capacity resulting from higher soil moisture prevails.

Keywords: thaw depth; GEOTop; permafrost modeling; spatial variability.

Introduction

In the thawed portion of seasonally frozen or permafrost terrain, lateral drainage flow of soil water often occurs and is a significant hydrological process in both high-latitude (e.g., Quinton & Marsh 1999) and high-altitude environments (e.g., Krainer & Mostler 2002). In the complex heterogeneity of soil properties, the spatial variability of soil moisture can also lead to different behaviors with respect to freeze and thaw processes. For example, Kane et al. (2001) observed that in the Alaskan arctic tundra, thawing is enhanced in water tracks and areas of high soil moisture. In a similar arctic environment, Wright et al. (2009) also observed that wetter areas are normally associated with deeper summer thaw.

Most permafrost models are one-dimensional (e.g., Hinzman et al. 1998, Lawrence & Slater 2005, Marchenko et al. 2008) and applied at large scales. As a result, the impact of soil moisture redistribution due to lateral drainage flow on permafrost evolution has rarely been investigated with models. Endrizzi et al. (2010) simulated with the GEOTop model (Rigon et al. 2006, Endrizzi 2009, Dall'Amico et al. 2011) the spatial variability of the thaw depth in a peat-covered small catchment in the Canadian arctic tundra, and found that the end-of-summer thaw depth is significantly greater where the water table is shallower.

The purpose of this work is to qualitatively assess how the spatial variability of soil moisture due to lateral water drainage redistribution in the unfrozen part of the soil affects the spatial variability of the thaw depth. This study will be theoretical and will be carried out in an idealized topography. There is no pretense of finding general results. The purpose is only to have an idea of the spatial variability of the end-of-summer thaw depth in different soil types and to understand controlling processes.

Methodology

This study will be conducted with a model using a very simple planar topography. As various soil types are thought to respond differently to hydraulic gradients and thermal

forcing, three characteristic soil types are considered: 1) loam, representing a soil type with relatively low hydraulic conductivity and high thermal conductivity; 2) sand, a soil type with high hydraulic conductivity and thermal conductivity; and 3) peat, characterized by high hydraulic conductivity and low thermal conductivity.

We use the GEOTop distributed model (Rigon et al. 2006, Endrizzi 2009, Dall'Amico et al. 2011). This model is particularly appropriate for the present study because it couples the equations describing the three-dimensional water flow in the soil (Richards equation in variably saturated conditions for subsurface flow and De-Saint-Venant equation for the surface flow) with a one-dimensional form (normal to the surface) of heat equation accounting for soil freezing and thawing processes. Mass and energy exchanges with the atmosphere constitute the boundary conditions and include a dynamic multi-layer snow cover. Input data to the model are given by the digital elevation model and meteorological data consisting of distributed precipitation, air temperature, relative humidity, wind speed, and incoming longwave and shortwave radiation.

The model has been run for a 200-m-long planar hillslope, with a 20-degree slope angle and south aspect. The hillslope is described with a virtual DEM composed of 40 lines and 1 single column, where the column represents the slope direction and the rows the direction normal to the slope direction. Gradients are different from zero only in the slope direction. The model is forced with the meteorological data measured at the Corvatsch Meteoswiss station, located at 3305 m a.s.l. in the southeastern Swiss Alps (46.42°N, 9.82°E), at the summit of Piz Corvatsch mountain.

Modeling Assumptions

The modeled domain is given by the first 10 m of soil, discretized with 25 layers of variable thicknesses that increase with depth from the surface, since temperature gradients normally decline with depth. The lower boundary of the deepest layer is considered impermeable to water flux, which is reasonable since at this depth the soil generally remains

Table 1. Soil parameters used in the simulation (including the Van Genuchten parameters).

| Parameter | loam | sand | peat |
|--|-------|-------|-------|
| Hydraulic conductivity [mm/s] | 0.005 | 0.080 | 0.100 |
| Residual water content [-] | 0.057 | 0.055 | 0.150 |
| Saturated water content [-] | 0.487 | 0.374 | 0.900 |
| α [mm ⁻¹] | 0.001 | 0.003 | 0.016 |
| n [-] | 1.6 | 2.0 | 1.6 |
| Thermal conductivity of the soil solids [W/mK] | 2.5 | 2.5 | 0.21 |

frozen. On the lower lateral border of the hillslope, a boundary condition of free drainage has been imposed. This condition provides sufficient drainage so that water does not accumulate on the hillslope, and the longitudinal profile of soil moisture is affected by the boundary condition only in a small region near the lower lateral boundary.

Soil parameters, namely Van Genuchten parameters and hydraulic conductivity, were taken from Twarakavi et al. (2010) for loam and sand. Van Genuchten parameters for peat were taken from Carey et al. (2007). Peat hydraulic conductivity normally varies with depth as a result of the stratification of the decomposition process. However, since most variability occurs in the first 15–20 cm from the surface (Quinton et al. 2008), for simplicity we have used a common value measured at a 15 cm depth as representative of the hydraulic conductivity of the peat soil type. Table 1 reports in detail the value of the parameters used in this study.

The soil thermal conductivity is determined in GEOTop with the formula of Cosenza et al. (2003), which combines the thermal conductivities of the soil constituents (liquid water, ice, air, and soil solids) following the quadratic parallel mixing law, in analogy with the behavior of dielectric permittivity in electrical lattices. Thermal conductivities of the mineral and organic soil solids were derived from Farouki (1986). Despite its formal simplicity, the formula of Cosenza et al. (2003) gives values of thermal conductivity that are very similar to other formulations formally more complex and with more parameters.

The heat fluxes at the upper and lower boundaries of the modeled 10-m-deep soil domain are given, respectively, by the ground heat flux and geothermal heat flux. If the ground surface is snow free, the former is given by the surface heat flux (algebraic sum of net radiation and turbulent fluxes), which, in turn, depends on the temperature of the surface, an unknown in the system. If a snow cover is present, the ground heat flux is given by the soil-snow conductive heat flux, which constitutes the exchange coupling term between the heat equations for soil and snow. The geothermal heat flux is the heat flux that maintains an approximately constant temperature geothermal gradient below the zero-amplitude annual soil

temperature depth, normally at 10–15 m in the Alps (Gruber et al. 2004), which is comparable with the depth of the modeled soil. A common value of the geothermal heat flux is 0.08 W/m² (Medici & Rybach 1995).

Model Initialization

The model results should ideally be completely independent of the initial conditions, which always have a certain degree of arbitrariness. In order to accommodate this, we proceeded in the following way. The initial conditions of soil water content and temperature over the domain have simply been guessed and, for simplicity, considered uniform over the hillslope. They are given by the absence of snow cover, soil temperature equal to -5°C at all depths, and soil saturated below a depth of 30 cm. We selected a particular one-year set of meteorological data (from July 2002 to July 2003), and we repeated it several times. Therefore, if the model is forced with periodical meteorological data, it is expected that the state variables also eventually become periodical. When it is determined that the temporal evolution of both soil temperature and moisture has become a periodical function within a reasonable approximation, the results can be considered acceptably independent from the initial condition.

Figure 1 shows the time evolution of the soil temperature at the 10-m depth. While at the surface the effect of the initial condition is immediately lost, at the lowest depth, where there is greater thermal inertia, the effect is felt for approximately 7–8 years, after which the temperature evolution reaches a periodic state. Therefore, if we examine the results after 10 years, we can state that the results are reasonably independent from the initial condition in the whole domain. This is true for the three soils types studied here.

Spatial Variability of the End-of-Summer Thaw Depth

The thaw depth (Fig. 2 upper part) has been defined here as the lowest interface separating a frozen (below) and unfrozen (above) soil layer. This variable reaches the maximum value near the end of September for each soil type. Maximum values are around 1.35 m for sand, 0.9 m for loam, and 0.3 m for peat. In the sandy soil, the thaw depth is the largest since the porosity is relatively low and, consequently, there is less ice to melt. Conversely, the peat yields the shallowest thaw as a result of its high porosity (and therefore there is more ice to melt) and very low thermal conductivity.

Another variable related to the thaw depth is the depth of the saturation front (Fig. 2 lower part), which is defined as the lowest interface between saturated (below) and unsaturated (above) soil layers, no matter if the soil is saturated with frozen or unfrozen water. In this application, the depth of the saturation front is normally just a little deeper than the correspondent maximum thaw depth, although it rises at times during summer. This demonstrates that, due to the relatively steep slope, the thawed part of the hillslope is in general well drained.

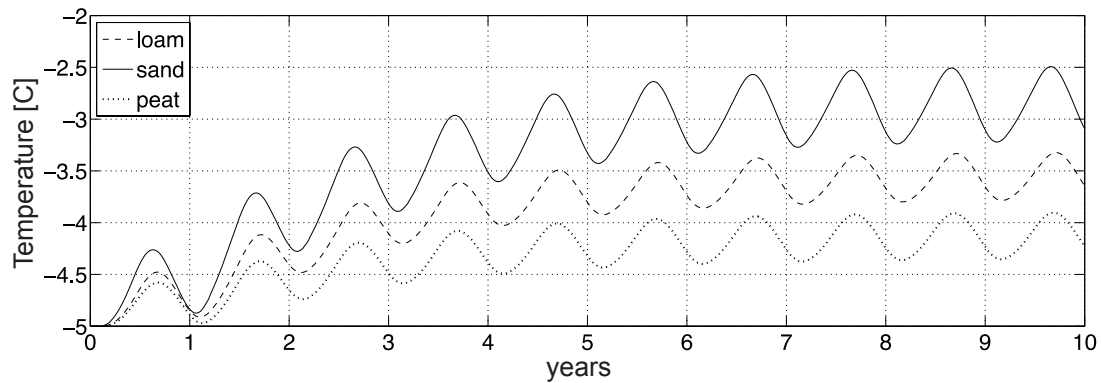


Figure 1. Ground temperatures at the 10-m depth for a point in the middle of the hillslope.

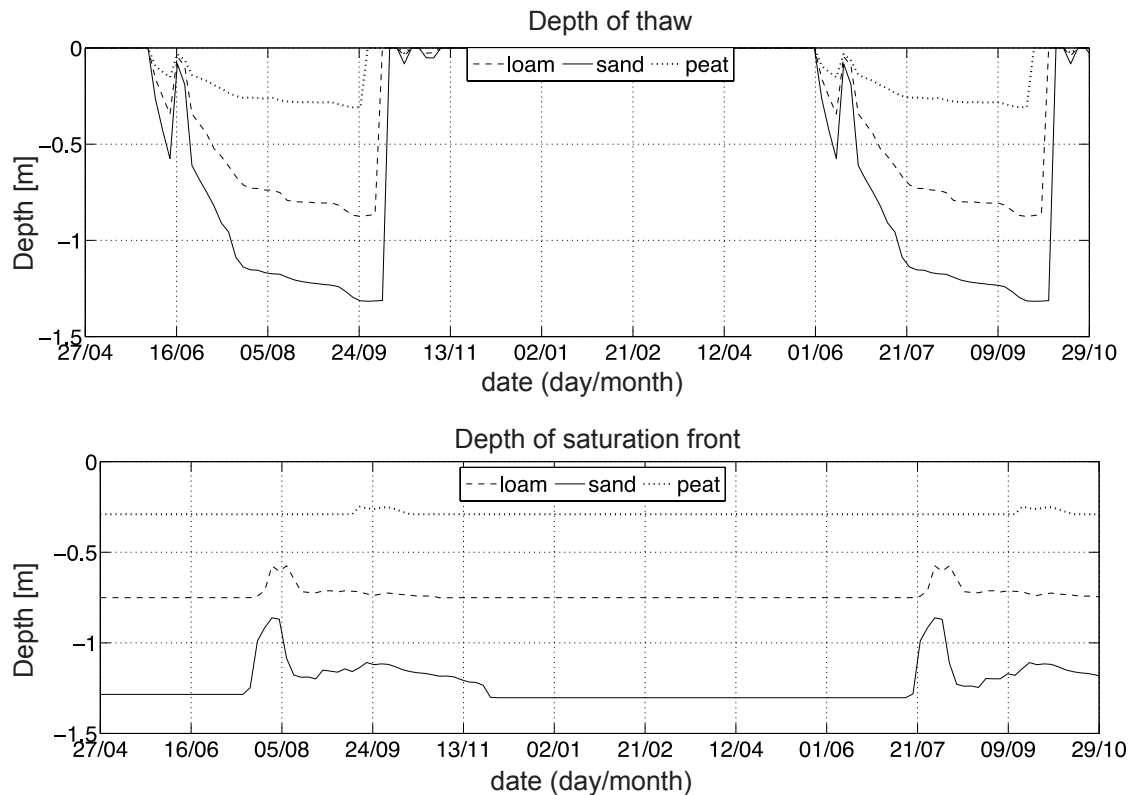


Figure 2. Time evolution (in two following summers) of the thaw depth and saturation front for a point in the middle of the hillslope.

After initializing the model as previously described, the longitudinal profiles of the thaw depth and saturation front at the end of the summer are well correlated in the sandy and loamy soils (Fig. 3). Drainage flow determines the longitudinal profile of the saturation front, which is relatively deep in the upper part of the hillslope since water balance is here negative and downward drainage is not compensated by drainage from upward regions. As we move downslope, the saturation front rises and approaches a state of almost zero longitudinal derivatives. Then it sharply sinks in close proximity to the lateral lower boundary of the hillslope as a consequence of the boundary condition. Therefore, the longitudinal profile of the hillslope can be roughly partitioned in three regions: a relatively dry portion at the top (hereafter referred to as top portion), a relatively wet region in the center

(mid portion) where infinite slope conditions are approached, and a small dry region at the bottom (bottom portion) which directly feels the effect of the boundary condition. The depth of the saturation front at the end of the summer ranges from 0.73 m in the mid portion to 0.86 m in the top portion for loam, and from 1.1 m to 1.4 m for sand. The larger values for sand are explained by the higher hydraulic conductivity and enhanced drainage. The end-of-summer thaw depth is always larger where the saturation front is deeper. This means that relatively dry (wet) regions always experience relatively deep (shallow) thaw. The three portions in which the hillslope can be subdivided according to the profile of the saturation depth can be clearly recognized also in the profile of the end-of-summer thaw depth, which varies from 0.87 m in the mid portion to 0.91 m in the top portion in loam, and from 1.30 m

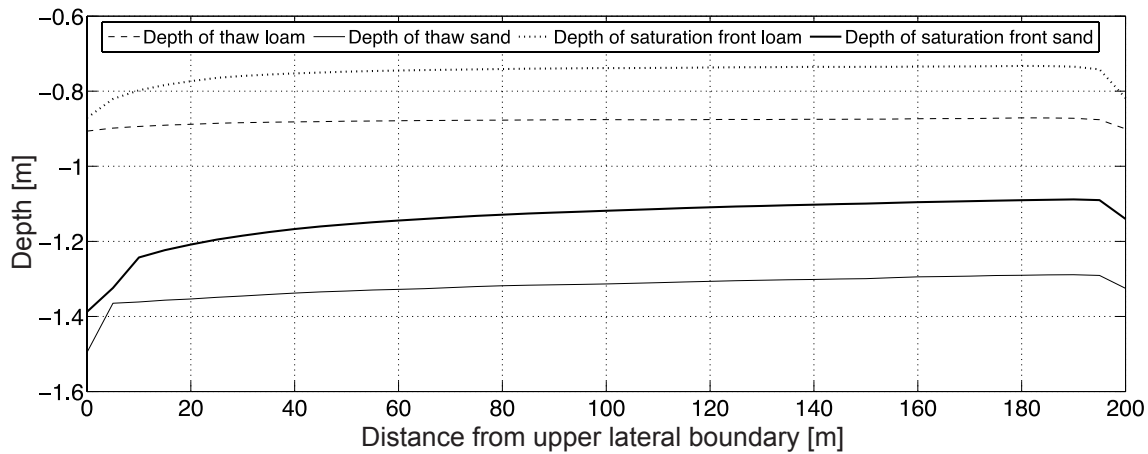


Figure 3. Longitudinal profile of the thaw depth and saturation front for sandy and loamy soil types.

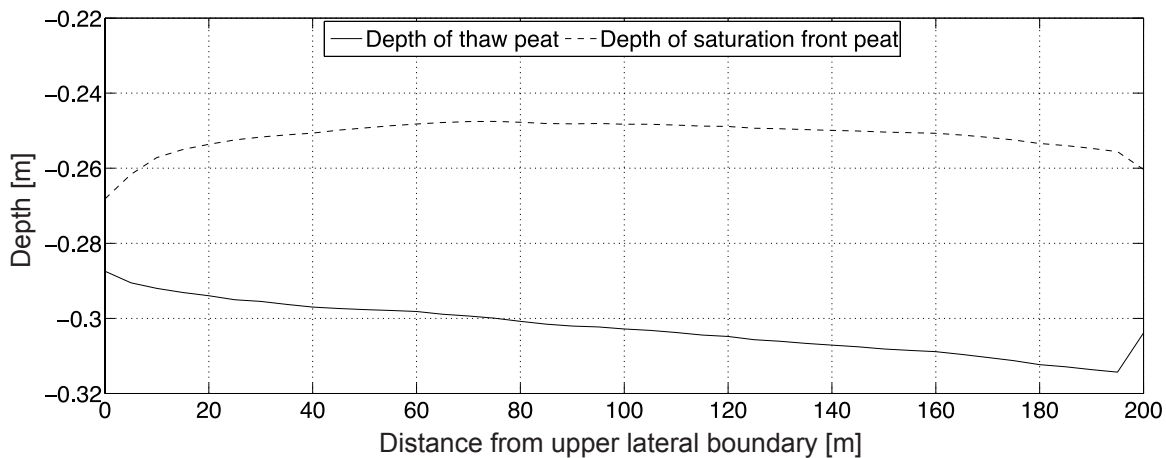


Figure 4. Longitudinal profile of the thaw depth and saturation front for peat.

in the mid portion to 1.50 m in the top portion in sand. The higher values in sand are also a consequence of enhanced soil moisture spatial variability, and this pattern is also reflected in the thaw depth.

The longitudinal profile of the saturation front depth in peat (Fig. 3) is similar to the corresponding variable for sand and clay, even if the distinction between top, mid, and bottom portions is not so clear as in the other soil types, and the state of almost zero longitudinal derivatives, resembling infinite slope conditions, is never reached. The range of variability is limited, with typical values from 0.25 m to 0.27 m. Conversely, the longitudinal profile of the thaw depth in peat (Fig. 4) is significantly different from the correspondent profiles for the sandy and loamy soils. The end-of-summer thaw depth increases almost linearly with distance from the hillslope upper boundary (from 0.29 m to 0.31 m), though with a limited range of variability. Then it sharply decreases in correspondence to the hillslope bottom boundary. In general, unlike the sandy and loamy soils, wetter portions are those that undergo deeper summer thaw. However, this relation is not straightforward since the region with the shallowest saturation front does not exactly correspond to the deepest thaw depth.

Patterns of Soil Temperature and Soil Moisture

In loam and sand, the longitudinal profile of the annual averaged soil temperature (Fig. 5) at all depths is well correlated with the longitudinal profile of the thaw depth at the end of the summer, which means that the regions with deeper thaw are also warmer. The annual averaged soil temperature varies by about 0.10–0.25°C, with higher variability at the surface. Conversely, the opposite pattern is observed in the peat; regions with deeper thaw are colder.

The longitudinal profiles of the annual averaged total soil moisture (Fig. 6) are also well correlated with the longitudinal profile of the depth of the saturation front for sandy and loamy soils. In peat, the longitudinal profile of annual averaged soil moisture is not so clearly correlated with the depth of the saturation front, but shows instead a clear correlation with the thaw depth in the sense that where soil moisture is higher, thaw is deeper. Comparing the spatial variability of the annual averaged soil moisture and temperature at the surface, we observe that higher soil moisture is always correlated with colder temperatures.

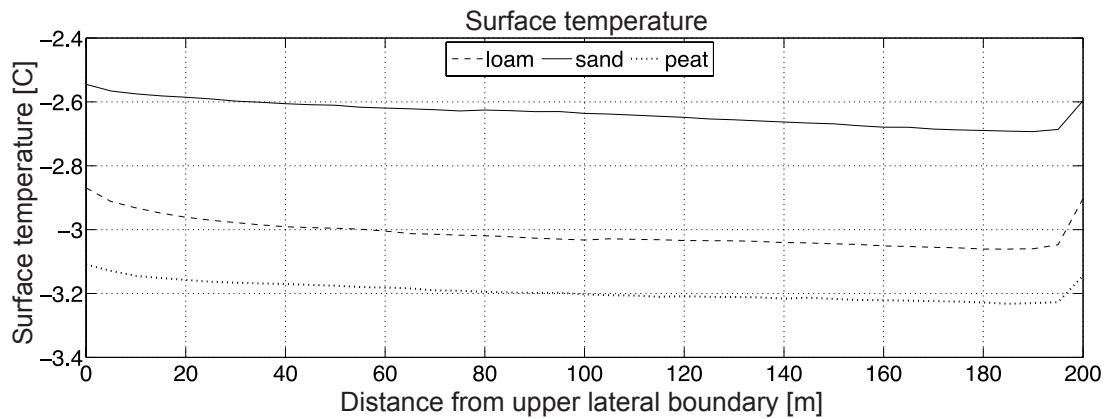


Figure 5. Longitudinal profile of the annual averaged surface temperature.

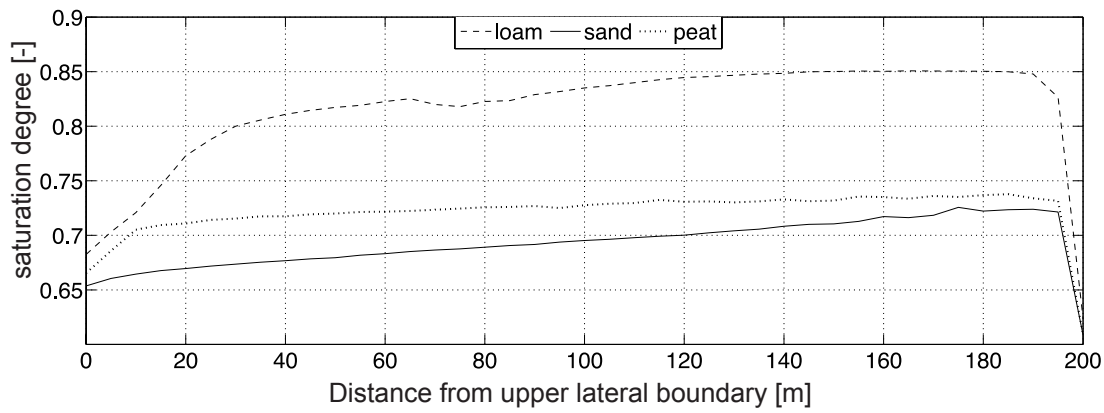


Figure 6. Longitudinal profile of the annual averaged saturation degree, defined as the ratio of total soil moisture (frozen and unfrozen) to saturated water content.

Discussion

The study has shown that higher soil moisture leads to shallower thaw in certain types of soils, and to deeper thaw in others. There are two important processes that affect the spatial variability of the thaw depth in the presence of significant soil moisture spatial differences:

- 1) Where soil moisture is higher, the soil thermal conductivity is also higher, and this is particularly true for peat. This contributes to the positive heat flux exchanged with the atmosphere during the summer that penetrates more deeply into the soil.
- 2) Soil thermal capacity is also higher where soil moisture is higher. Thermal capacity has a “real” component, given by the fact that wetter soils require more heat than drier soils to increase their temperature, and also an “apparent” component, since wetter soils normally have larger ice content to thaw. In addition, wetter soils lose more energy by evaporation than drier soils. This second process obviously causes deeper thaw in drier soils.

In peat, the first process prevails, even if the thermal capacity of the peat soil also varies significantly with water content.

Conversely, in sand and loam the second process prevails since the thermal conductivity does not depend so strongly on soil moisture as does peat.

The quantitative results presented here are not to be generalized to other more complex cases. They are relative only to the simulated case. Other numerical experiments in more complex topographies must be carried out in order to extend these results.

Conclusion

In this study, the spatial variability of the thaw depth in a simple 20-degree sloped ideal planar topography has been investigated using the GEOTop model. The purpose is to have a qualitative idea of how soil moisture redistribution due to lateral drainage can affect the end-of-summer thaw depth. This effect has been investigated in three different soil types: loam, sand, and peat.

The spatial variability of the thaw depth has been found relatively limited, reaching approximately 20 cm when the thaw depth is around 1.5 m. However, this cannot be generalized to other cases. It is remarkable to note that in

loam and sand, deeper thaw has been observed where soil moisture is lower, but in peat, deeper thaw occurs where soil moisture is higher. Wetter soils actually have higher thermal conductivity but also higher thermal capacity. The former allows deeper penetration of the summer thaw, while the latter reduces the thaw rate as more energy is required to increase soil temperature. In peat, as a result of the very high difference between thermal conductivity in drier and wetter portions, the former process prevails. On the other hand, in sand and loam, where the thermal conductivity is only moderately dependent on soil moisture, the effect of thermal capacity is prevalent.

Acknowledgments

This project has been supported by the project X-sense, funded through www.nano-tera.ch. Ronald Daanen and an anonymous reviewer provided helpful comments on the manuscript.

References

- Carey, S.K., Quinton, W.L., & Goeller, N.T. 2007. Field and laboratory estimates of pore size properties and hydraulic characteristics for subarctic organic soils. *Hydrological Processes* 21: 2560–2571.
- Cosenza, P., Guerin, R., & Tabbagh, A. 2003. Relationship between thermal conductivity and water content of soils using numerical modelling, *European Journal of Soil Sciences* 54: 581–587.
- Dall'Amico, M., Endrizzi, S., Gruber, S., & Rigon, R. 2011. A robust and energy-conserving model of freezing variably-saturated soil. *The Cryosphere* 5: 469–484.
- Endrizzi, S. 2009. Snow Cover Modelling at a Local and Distributed Scale over Complex Terrain. Monographs of the Doctoral School in Environmental Engineering 15, Department of Civil and Environmental Engineering, University of Trento, Italy.
- Endrizzi, S., Quinton, W.L., & Marsh, P. 2011. Modelling the spatial pattern of ground thaw in a small basin in the arctic tundra. *The Cryosphere Discussion* 5: 307–338.
- Farouki, O.T. 1986. *Thermal Properties of Soils*. Series on Rock and Soil Mechanics 11, Trans Tech, 136 pp.
- Gruber, S., King, L., Kohl, T., Herz, T., Haeberli, W., & Hoelzle, M. 2004. Interpretation of geothermal profiles perturbed by topography: the Alpine permafrost boreholes at Stockhorn Plateau, Switzerland. *Permafrost and Periglacial Processes* 15(4): 349–357.
- Hinzman, L.D., Goering, D.J., & Kane, D.L. 1998. A distributed thermal model for calculating soil temperature profiles and depth of thaw in permafrost regions. *Journal of Geophysical Research* 103(28): 975–991.
- Kane, D.L., Hinkel, K.M., Goering, D.J., Hinzman, L.D., & Outcalt, S.I. 2001. Non-conductive Heat Transfer Associated with Frozen Soils. *Global Planetary Change* 29: 275–292.
- Krainer, K. & Mostler, W. 2002. Hydrology of Active Rock Glaciers: Examples from the Austrian Alps. *Arctic, Antarctic, and Alpine Research* 34 (2): 142–149.
- Lawrence, D.M. & Slater, A.G. 2005. A projection of severe near-surface permafrost degradation during the 21st century. *Geophysical Research Letters* 32, L24401.
- Marchenko, S., Romanovsky, V., & Tipenko, G. 2008. Numerical Modeling of Spatial Permafrost Dynamics in Alaska. In *NICOP 2008: Proceedings of the Ninth International Conference on Permafrost*. D.L. Kane, K.M. Hinkel (eds.). Institute of Northern Engineering, University of Alaska Fairbanks, 2: 1125–1130.
- Medici, F. & Rybach, L. 1995. Geothermal map of Switzerland. *Géophysique* 30, Schweizerische Geophysikalische Kommission.
- Quinton, W.L. & Marsh, P. 1999. A Conceptual Framework for Runoff Generation in a Permafrost Environment. *Hydrological Processes* 13: 2563–2581.
- Quinton, W.L., Hayashi, M., & Carey, S.K. 2008. Peat Hydraulic Conductivity in Cold Regions and its Relation to Pore Size and Geometry. *Hydrological Processes* 22: 2829–2837.
- Rigon, R., Bertoldi, G., & Over, T.M. 2006. GEOTop: a distributed hydrological model with coupled water and energy budgets. *Journal Hydrometeorology* 7: 371–388.
- Twarakavi, N.K.C., Simunek, J., & Schaap, M.G. 2010. Can texture-based classification optimally classify soils with respect to soil hydraulics? *Water Resources Research* 46, W01501.
- Wright, N., Hayashi, M., & Quinton, W.L. 2009. Spatial and temporal variations in active layer thawing and their implication on runoff generation in peat-covered permafrost terrain. *Water Resources Research* 45, W05414.

Sustainable Arctic Marine and Coastal Technology

Jomar Finseth

SINTEF Building and Infrastructure, Trondheim, Norway

Arne Instanes

Instanes Polar AS, Bergen, Norway

Abstract

This paper presents research plans and results from an ongoing research project that includes arctic coastal engineering in one of the work packages (WP6). Climate change and man-made interaction with arctic coastal areas may affect the temperature regime within permafrost soils. This may result in both increased erosion and instability, thus influencing coastlines, estuaries, and man-made infrastructures. The research project aims at developing improved guidelines, recommendations, and new technology for coastal structures in the Arctic.

Keywords: arctic coastal erosion; engineering; new technology.

Introduction

Sustainable Arctic Marine and Coastal Technology (SAMCoT) is an innovation-based research program covering 5 to 8 years beginning in 2011, funded partly by industrial partners and partly by the Norwegian Research Council. The main research partners in the project are the Norwegian University of Technology and Science (NTNU), the University Centre in Svalbard (UNIS), and SINTEF. SINTEF is responsible for permafrost and arctic coastal research in one of the six work packages. SINTEF is the largest independent research organization in Scandinavia. We perform research and support innovation and develop technological solutions for practical application. SAMCoT aims at becoming the leading national and international center for the development of robust technology needed by the industry for sustainable exploration and exploitation of the valuable and vulnerable Arctic. The project will meet the challenges imposed by ice, permafrost, and changing climate for the benefit of the energy sector and society.

The combined action of ice and waves on coastal permafrost will have a significant influence on the placement and design of structures such as pipeline landfalls, harbor facilities, and breakwaters in the coastal zone. Both climate change and man-made interaction with arctic coastal areas can affect the temperature regime within permafrost soils, resulting in increased erosion and instability, thus influencing coastlines, estuaries, and man-made infrastructure. In addition, arctic coastal areas, particularly those in northwest Russia, are geologically characterized by fine-grained sediments and a lack of hard rock outcrops and coarse materials. These conditions call for new and innovative solutions regarding construction materials, erosion protection, and landfall technology.

The research methods will be a combination of field and laboratory studies, theoretical and numerical investigations, and engineering evaluation of technical solutions and concepts. The field studies are an especially important part of SAMCoT as field data are necessary background for all technical development related to the Arctic. Both NTNU and SINTEF have a long tradition of working in Svalbard

in cooperation with UNIS, located in Longyearbyen. UNIS has easy access to locations that are suitable for the project. Existing infrastructure around the Svalbard settlements provides unique opportunities for continuous monitoring of frozen soil characteristics and environmental loads on coastal zones and industrial objects, as well as in situ studies of ice and soil properties.

The Van Mijen fjord and similar places at Spitsbergen represent unique field laboratories that provide for integrated experiments and modeling activities that will generate results applicable to other arctic regions. Geologically, coastal areas of Svalbard and northwest Russia can be very different, particularly with respect to soil and rock conditions. To



Figure 1. Location map. A – Fredheim, B- Hiorthhamn and Vestpynten (between Longyearbyen and Bjørndalen), C-Svea and van Mijenfjorden.

present general recommendations and guidelines, the research has to be carried out in different soils and sites to study site-specific challenges. In the plans of SAMCoT, a number of research sites in northwest Russia will be included; some are instrumented and some are for observation purposes only.

Research Tasks

The development of sustainable coastal structures and pipeline landfalls in the Arctic depends on structures and shore protection techniques that will function under changing environmental and climatic conditions. Monitoring existing coastal structures and developing test field sites for experimental research on new techniques for shoreline protection will be the basis of the work package connected to permafrost and coastal challenges.

Work package 1: Site-specific erosion rates

The objective of this work package is to monitor erosion rates, the extent of coastal permafrost, and ice conditions at selected coastal locations and structures in Svalbard (van Mijenfjorden and close to Longyearbyen, see Figure 1) and northwest Russia. The roles of ice, waves and melting permafrost in the coastal erosion process will be quantified and modeled. Site-specific permafrost degradation in the coastal zone due to present and future climatic conditions will be modeled using historical observations and results from a downscaled global climate model.

Work package 2: Improved design of coastal structures, harbors, and shoreline protections subjected to ice loads, wave erosion, and unstable permafrost soils

In this work package, an evaluation of the use of local materials in combination with advanced imported materials (geotextiles or soil improvement techniques) will be carried out. Transportation costs will be reduced if more local materials are used in the construction. Laboratory investigations and full-scale field tests of environmental protection measures are planned. The tests will be based on ongoing research at Svea on Svalbard (Fig. 1). Study sites in northwest Russia will also be included. Methods for evaluating and designing site-specific erosion protection measures based on the dominating environmental forcing agents working on the site will then be developed. For ice loads and wave action, geotextiles, gabions, sandbags, and concrete mats will be evaluated. For permafrost degradation, the focus will be on geotextiles, insulation materials, convective embankments, and techniques of artificial cooling.

Work package 3: Landfall areas and areas along rivers

In this work package, the physical, thermal, and mechanical properties of permafrost soils in the coastal zone during climate warming scenarios will be evaluated. The impact of the change in soil parameters may increase the risk for soil instability and risk to structural integrity.

Svalbard is used as a research platform due to the long history of cold regions engineering research in the area, and



Figure 2. Coastal erosion, Svea.

because Svalbard is easily accessible with daily flights from Tromsø, Norway. The technologies developed are intended to assist in environmentally sound and cost-effective construction of coastal facilities in Svalbard and in the northwestern part of Russia. It is, therefore, of interest to instrument selected sites in northwestern Russia. Research results from Svalbard will be correlated with sites that have different soil composition, coastal geometry, permafrost temperatures, and environmental loads such as wind, currents, precipitation, and ice loads.

Sites

For the successful outcome of the project, it is important that the site-specific results can be used in more general models to understand the behavior of the coastal zone under changing environmental loads and man-made interactions. During the summer of 2011, a number of field sites in Russia and Svalbard were evaluated for coastal erosion. The locations of the sites in Svalbard are shown in Figure 1. A two-month project was carried out to measure and study coastal zones in the following areas in Svalbard:

- Hiorthhamn
- Fredheim
- Vestpynten and Hotelneset between Longyearbyen and Bjørndalen
- Svea

For the study on Svalbard, three transects at three different locations will be fully instrumented with thermistor-strings and dataloggers. In addition, meteorological and oceanographic data will be collected, and soil sampling and laboratory analysis will be carried out to investigate the thermo-mechanical properties of the permafrost soils. Surveying by differential global positioning system (DGPS) and laser scanning will also be performed. In this manner, site-specific erosion processes and rates can be quantified and related to variation in metrological data, ice and wave loads, soil conditions, and permafrost properties. Table 1 shows a summary of the planned monitoring system.

Table 1. Planned monitoring system.

| | |
|--|---|
| Investigation | Methodology |
| Erosion rates | Differential global positioning system (DGPS) Laser scanning Satellite images Aerial photography |
| Air temperature Wind Precipitation | Meteorological station |
| Ground temperature | Thermistor strings |
| Soil parameters - Mechanical - Thermal | Soil sampling and geotechnical laboratory testing |
| Wave height Wave period Wave direction | Wave sensors in seabed Hind casting based on wind data |
| Ice conditions | Field observations Stress sensors |

Table 2. Erosion rates at Fredheim, Svalbard.

| Year | Erosion rate (cm/year) | | |
|-----------|------------------------|------------|------------|
| | Outhouse | Main house | “Danielbu” |
| 2010-2011 | 12 | 57 | 37 |
| 1998-2010 | 11 | 51 | 21 |
| 1987-1998 | 30 | 21 | 17 |

In Russia, the following sites have been evaluated in collaboration with Russian scientific partner Moscow State University (MSU):

- Yamal Peninsula, in the vicinity of Baydaratskaya Bay
- Coast of Varandey, Nenets
- Embankments of Ob (to be evaluated)

Results from Summer 2011

Historical data regarding erosion exist from only two of the observed sites in Svalbard: Hiorthhamn and Fredheim. Fredheim is situated in Tempelfjorden and Hiorthhamn in Adventfjorden, both in the central part of Spitsbergen. In both sites, severe coastal erosion threatens cultural heritage. Measurements from Fredheim yield the erosion rates shown in Table 2.

Erosion rates in 2010–11 were measured with a differential global positioning system (DGPS), and other measurements were collected using manual surveying. Similar or higher erosion rates were detected in Hiorthhamn between 2010 and 2011 (no data series before 2010) and show rates varying from 0.5 to 1.5 m over one year. Results from the measurements using DGPS in Hiorthhamn are shown in Figure 3.

Soil composition and sea properties vary between these two sites. Fredheim has direct action from ocean waves at an angle

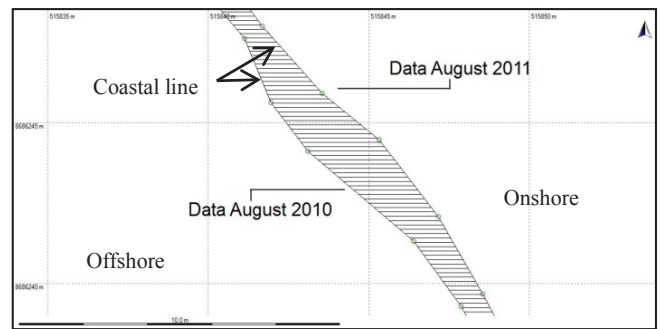


Figure 3. Coastal erosion at Hiorthhamn, DGPS 2010 and 2011, shows approximately 1.5 m of erosion.

Table 3. Soil composition.

| Location | Soil classification | $C_u = d_{60}/d_{10}$ | $d < 0.074 \text{ mm}$ (%) |
|------------|---------------------|-----------------------|----------------------------|
| Vestpynten | Sand | 16.5 | 5.5 |
| | Sand | 22 | 8.8 |
| | Sand | 37.5 | 11.3 |
| | Sand | 17.6 | 6.7 |
| Hiorthhamn | Sand | 50.9 | 8.2 |
| Fredheim | Gravel | 23.6 | 3.5 |
| Svea | Sand, silty | 16.5 | 17.7 |

of almost 90 degrees to the beach; Hiorthhamn has main wave action along the beach. Soil data from the different sites on Svalbard are shown in Table 3. It can be observed from the table that the soils contain relatively limited amounts of fines (grain size $< 0.074 \text{ mm}$). The grain size distribution tests show a coarse soil for Fredheim (clean gravel) and finer sediments for Hiorthhamn (well graded sand). For Vestpynten and Svea, there are no previous studies related to coastal erosion.

Data on soil composition, accessibility for drilling equipment, and varying meteorological and oceanographic conditions make these sites promising for studying coastal erosion processes.

Coastal Structures

In the study, the partners aim at investigating former techniques and building materials and then using the data to build sustainable arctic infrastructure in coastal zones. The ultimate goal is to develop guidelines for future construction of infrastructure. We, therefore, see the need to study arctic coastal structures built and operated under different conditions and challenges. The challenges are very much connected to permafrost-related problems where capacity and stability of soils is related to the temperature regime as influenced by air and sea temperature. The SAMCoT project will select a number of coastal structures and study their sustainability in an arctic environment. SAMCoT partners have already been involved in a coal quay at Kapp Amsterdam, Svea, Spitsbergen, where Store Norske Spitsbergen Kullkompani (SNSK) is the owner (Fig. 4).



Figure 4. Coal quay at Kapp Amsterdam, Svea.



Figure 5. Erosion protection; Kapp Amsterdam, Svea.

The coal quay was built partly on soft soil sediments, marine transported sediments, and glacial moraine deposits. The construction is based on both steel piles and sheet pile walls. One of the main challenges in the quay area is coastal erosion. SINTEF has been involved in three projects where a combination of geotextiles and bags filled with local soils were used (Fig. 5).

The aim has been to develop sustainable erosion protection using local soil materials.

Figure 6 shows the condition of the erosion protection after two years. It can be seen from the figure that the area closest to the sea, rows 6 and 7, sustains more damage than the higher-lying bags toward the beach on rows 1 to 5. The bags are subjected to the combined effects of ice scour in the winter and drifting timber from Siberia in the summer. The damage to the bag on row 3 is probably caused by direct impact from drifting timber.

Since the first erosion protection was established in 2008, all three projects have been through yearly evaluations in order to determine the sustainability of the methods.

In the autumn of 2011, a project connected to the durability of Svalbard quays was carried out, mainly financed by the Svalbard Environmental Protection Fund. The goal was to study historical coastal building techniques and determine if older construction techniques can be used in construction of future coastal infrastructure. The findings from this study will be presented in a report in November 2011

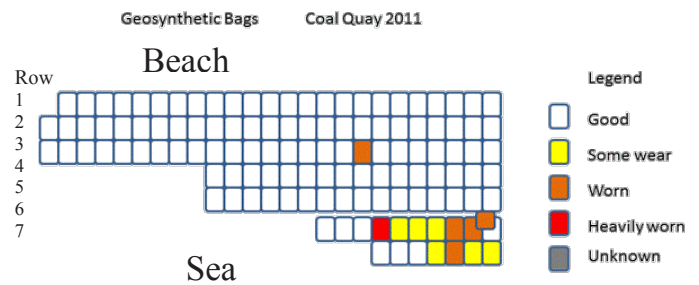


Figure 6. Erosion protection, Svea; condition after two years.

Summary

The research project Sustainable Arctic Marine and Coastal Technology (SAMCoT) is an innovation-based research program covering 5 to 8 years beginning in 2011. It is partly funded by industrial partners and partly by the Norwegian Research Council. The main partners are the Norwegian University of Technology and Science (NTNU), the University Centre in Svalbard (UNIS), and SINTEF. SINTEF is responsible for permafrost and arctic coastal research.

This paper has given an introduction to the research objectives and has reported some initial results from coastal erosion projects carried out in Svalbard. The project will continue to introduce research sites in northwest Russia and fully instrumented sites on Svalbard.

Acknowledgments

The authors would like to acknowledge the support of the SAMCoT CRI through the Research Council of Norway and all the SAMCoT partners.

Soil and Water Chemistry Characteristics of Thermo-Erosional Features in the Western Noatak River Basin, Alaska, USA

Michael B. Flinn

Murray State University, Murray, KY, USA

William “Breck” Bowden

University of Vermont, Burlington, VT, USA

Andrew W. Balsler, Jeremy B. Jones

University of Alaska Fairbanks, USA

Michael N. Gooseff

Pennsylvania State University, University Park, PA, USA

Abstract

In 2007, 24 thermal-erosion and permafrost degradation features (hereafter “thermokarst”) were characterized in northwest Alaska, USA. Geomorphic assessments showed that active-layer detachments and thaw slumps had characteristic morphologies with permafrost thaw depths significantly deeper within these features (106 cm) than surrounding hillslopes and water tracks (86 cm). Characterization of soils and water associated with these features showed that reference transects above each feature were significantly different from feature transects (headwall, active surface, run-out). Water collected within the features showed significantly higher concentrations of nutrients (ammonium, nitrite), total dissolved nitrogen, dissolved organic and inorganic carbon, and anions (chloride and bromide) compared to the reference transect. Water samples from reference transects had higher soil electrical conductivity, calcium, and ratio of DOC:DON. Though thermokarst failures are a relatively rare spatial and temporal feature of the arctic landscape, they play an important role in the biogeochemical processing of terrestrial and aquatic resources of the Arctic.

Keywords: active-layer detachment slide; biogeochemistry; permafrost degradation; thermal-erosion; thermokarst; retrogressive thaw-slump.

Introduction

Recent studies in the Arctic have shown increased temperatures in both air (Serreze et al. 2000, IPCC 2001, Hinzman et al. 2005) and permafrost (Pollack et al. 2003, Zhang et al 2006, Romanovsky et al. 2007). With increased temperatures, myriad effects have been documented for both terrestrial and aquatic ecosystems. These include changes in plant communities (Chapin et al. 2005, Tape et al. 2006), rates of nutrient cycling (Rastetter et al. 2004), solute and sediment fluxes in freshwaters (Hobbie et al. 1999, Bowden et al. 2008), and changes in fire regimes (Mack et al. 2011). The relationship between permafrost degradation and the initiation of thermokarst terrain has received increased attention over the last decade. Several studies have documented extensive changes across arctic landscapes in boreal forests and tundra (Osterkamp et al. 2000, U.S. Arctic Research Commission 2003, Jorgenson and Osterkamp 2005, Lewkowicz 2007, Bowden et al. 2008). Thermokarst features are a natural phenomenon of the Arctic. However, little is known about the rate and extent of their formation, the prevalence of different modes of failure, the frequency of their initiation, or their active longevity (Gooseff et al. 2009).

The objective of this study was to characterize thermokarst features of the western Noatak Basin in an effort to understand their influence on biogeochemical processing, thaw depth variability, soil characteristics, and influence on water chemistry.

Methods

Study sites

The Noatak River in northwest Alaska flows westerly at approximately 67.5°N latitude. The majority of the ~30,000 km² watershed is protected by a national park and preserve and is recognized as a UNESCO Biosphere Reserve. The area is underlain by continuous permafrost with land cover spanning a suite of arctic and alpine tundra types in headwaters areas. Ecotonal boreal forest cover appears at low elevations in the lower half of the Noatak Basin and coastal marshes at the mouth (Young 1974, Viereck et al. 1992, Jorgenson et al. 2010b). In late July and early August of 2007, we visited 24 thermokarst features located in the uplands of the Baird Mountains and in the adjacent upstream reaches of the Mission Lowlands in the western Noatak River Basin, approximately 100 km north of Kotzebue, AK (Fig.1).

Geomorphic, soils, and water chemistry assessments

Basic geomorphic measurements were calculated for 24 failure features that were selected from a conservative estimate of over 200 hillslope thermokarst features. Only six of the 200 features, and none of the 24 surveyed, occurred within historic fire perimeters in the Alaska Fire Service GIS database (2010). Survey outlines were obtained by walking the perimeter of each feature using a Trimble GeoXH GPS. Roving survey data were recorded using Terrasync software logging at 1-second intervals. Due to topographic constraints, Wide Area

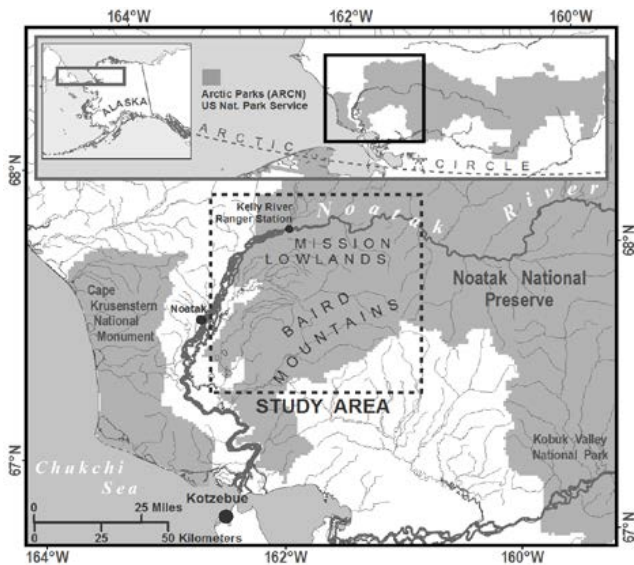


Figure 1. Study area of western Noatak River Basin.

Augmentation System (WAAS) correction was only available in some locations, resulting in sub-meter positional accuracy for most locations and 3-5 meter accuracy without. Data were imported in ArcGIS 9.2 and used to estimate feature length, width, area, aspect, and elevation.

At each site, we established transects that were oriented perpendicular to the failure axis. One reference transect was established approximately 10-m upslope from the disturbed tundra. Transects on the active surface included the base of the headwall, across the middle of the active surface, and across the run-out (Fig. 2). The headwall transects were located just below the vertical face of the actively eroding feature. The active surface transects included areas of the feature that were void of organic horizons and were still actively eroding and transporting soil on the down slope. The run-out transect crossed the bottom of the feature where an accumulation of material from upslope had been deposited. On each transect, thaw depths were measured using an Active Layer Probe (ALP) that was manually pushed into the ground until progress was stopped by frozen ground or rocks. If rocks were encountered, the vicinity of the point was probed several times until frozen ground was reached. If thaw depths were greater than the length of the ALP, the total length of the ALP (132 cm) was used as the minimum thaw depth. We attempted to probe an equal number of points inside and outside of the feature on each transect, and relative elevations were obtained using an XYZ laser range finder for each regularly spaced point.

Soil samples

On each transect, soil samples were collected using a 2-cm diameter soil core. Organic and inorganic horizons were separated within each core and composited into a grand sample (1 organic and 1 inorganic for each transect). Samples were collected in close proximity to the same transects described above (Fig. 2). The headwall samples were collected directly from the vertical face at the headwall of the feature.

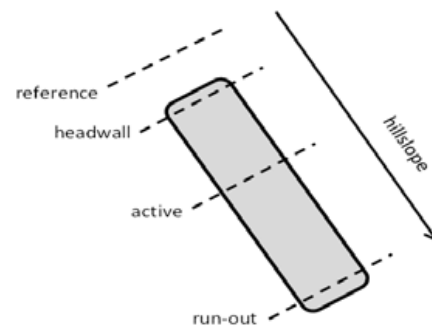


Figure 2. Thermokarst sampling transect classifications.

All soil samples were analyzed at Colorado State University Soil, Water, and Plant Testing Laboratory, Fort Collins, CO, USA, and the Colorado Plateau Stable Isotope Laboratory at Northern Arizona University, Flagstaff, AZ, USA. Analyses included AB-DTBA and Hydro-fluoric acid (HF) extractions with inductively coupled plasma-atomic emission spectroscopy (ICP-AES) to determine metals, minerals, cations, nutrients, and stable isotopes for carbon and nitrogen.

Water samples

Water samples were collected from water tracks above (reference) and from rivulets flowing near the transects within each feature (Table 1). Water temperature, pH, dissolved oxygen (DO), and electrical conductivity were measured in the field using a handheld WTW 3400i multimeter. Each sample was filtered through a 4 μm glass fiber filter with a handheld suction pump. In the lab, dissolved major ions were analyzed on a Dionex DX-320 Ion Chromatograph. Total dissolved nitrogen (TDN) and dissolved organic carbon (DOC) were determined using a Shimadzu TOC-500 analyzer connected to an Antek 7050 nitric oxide chemoluminescent detector. Dissolved organic nitrogen (DON) was calculated as the difference between TDN and ammonium + nitrate. Total dissolved phosphate (TDP) was measured colorimetrically following a persulfate digestion. All water samples were analyzed at the University of Alaska Fairbanks, Fairbanks, AK, USA, using methods described in Clilverd et al. (2007).

Statistical analyses-NMDS

Only sample locations that had both soil and water data were used for the statistical analyses. An ordination using non-metric multidimensional scaling analysis (NMDS) was run using 36 soil variables (Table 2) grouped by transect type (reference, head-wall, active, or run-out) using the Bray-Curtis dissimilarity index. All similar transect types were treated as replicates for analysis in the ordination. An analysis of similarity (ANOSIM) was used to determine differences in transect type using the Gower metric. A vector analysis was used to show the correlation of physical and chemical properties of soil and water chemistry to each grouping (length and direction indicate increases in the attribute, Tables 1, 2). All soil variables were used as drivers for the ordination except pH, electrical conductivity, and percent sand, silt, and clay, which were used

as vectors to help identify potential field-based indicators of disturbance and for comparison to existing data from remote locations. All ordination analyses were run using DECODA statistical software (Minchin 1987, Clarke 1993).

Results

Basic Distribution

Of the 200 thermokarst features we observed in the western Noatak Basin, we present analyses of 20 active layer detachments (ALDs) and four retrogressive thaw slumps. ALDs were located on planar portions of gentle, open slopes (3.5° – 6°) on non-acidic tundra (primarily wet sedge meadow watertracks within open, low birch/willow shrub-graminoid tundra). Retrogressive thaw slumps occurred primarily on convex slopes along lakeshores and riverbanks, and occasionally as secondary features developing from ALDs on open slopes.

Geomorphic assessment

All thaw slumps had a northeast aspect and were located along lakes at approximately 150 m HAE. These thaw slumps were relatively small with L/W ratios of 2.5 or less and areas less than 0.5 ha. In contrast, 15 of 20 ALDs had south-facing aspects, were found at ≥ 500 m HAE, and ranged from older stabilizing features to those that likely occurred during the summer of our study or one year prior. The size of the ALD features ranged from 0.1 ha to over 3.3 ha. The ALDs had high length/width (L/W) ratios (average 7.9) compared to thaw slumps, and the L/W ratios were positively related with areas of ALDs. Site revisits in 2010 demonstrated that, in many cases, ALDs express significant inter-annual, uphill growth primarily at the headwall, which is consistent with the correlation between ALD L/W ratio and area.

Thaw depths transects (>10 points per transect) were recorded on 9 ALDs and one thaw slump. Thaw depth in the wet sedge meadow water tracks above the features (86 cm) averaged 2 cm deeper than surrounding hillslopes (84 cm). Thaw depth inside of thermokarst features averaged 22 cm deeper than similar points outside of features (108 cm deep compared to 86 cm deep, respectively).

Soils and water

All features were located on complex sedimentary lithology according to state soil maps (Beikman 1980, Jorgenson et al. 2006, Jorgenson et al. 2010b), and upslope samples of exposed parent material always included decomposing grey/black micaceous shale, and frequently included fine-grained sandstone, or interbedded shale and sandstone with veins of quartzite. Permafrost soils associated with ALD features typically contained high proportions of silt ($\sim 55\%$ – 70% , as aeolian and colluvially retransported loess, and as weathered shale), smaller proportions of gravel ($\sim 30\%$ – 45%) and reticulate and ataxitic cryostructures indicative of syngenetic permafrost development (French and Shur 2010) throughout the vertical permafrost profile. Permafrost characteristics associated with thaw slumps had greater variability and complexity, and derive from glaciolacustrine, glacial drift

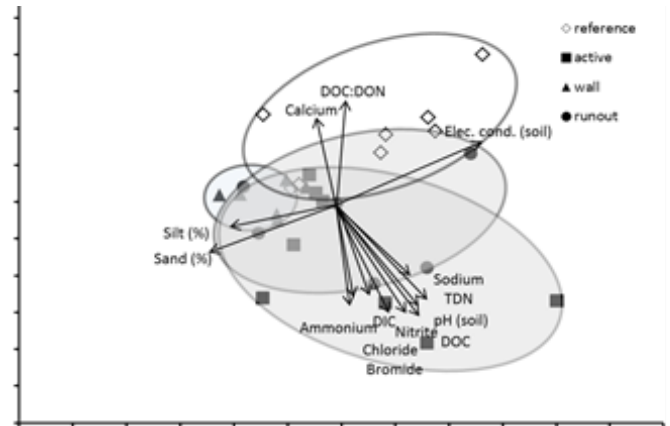


Figure 3. NMDS of thermokarst features from the western Noatak River Basin, AK, USA. Ellipses represent soil characteristics grouped by transects above (reference, \circ) and within (wall, \bullet ; active, \blacksquare ; and run-out, \blacktriangle) failure features.

and aeolian deposits, with abundant epigenetic (wedge, bedded) and syngenetic (atactic, reticulate, lenticular-layered) cryostructures.

Several soil characteristics differed significantly between reference transects and those from within the features (Fig. 3, Tables 1, 2). The NMDS analysis resulted in discrete structuring of the data based on transect groupings (Minimum stress = 0.13 for 2 dimensions, 200 iterations). The ANOSIM analysis resulted in significant differences in overall transect groupings ($R=0.2$, $p<0.005$), and significant differences between the reference transect and all other groups ($R>0.2$, $p<0.02$). Further, the headwall transects were significantly different from the run-out transects ($R=0.3$, $p<0.02$). Overall, the vector analysis yielded 14 variables that were significantly correlated to the NMDS plot (Fig. 3). The active surface transects had the highest concentrations of the nutrients ammonium and nitrite, the anions bromide and chloride, and the highest concentrations of DIC, DOC, TDN, and soil pH (Tables 1, 2, Fig. 3). The reference transects had significant vectors that indicated increased calcium and DOC:DON in water chemistry. All vectors included in the results were highly significant ($p<0.003$).

Discussion

Geomorphic assessment

Without direct observation of the initiation, it is difficult to precisely age thermal-erosion features. Re-establishment of vegetation on the mineral soil may provide some indication of age, but inter-annual cycles of active headwall migration and rafting of material downslope can confound interpretation of feature histories. Shrubs that were present in 'rafted' chunks of tundra may provide evidence of maximum age. The use of high-resolution aerial photography can provide relative age through repeat observations (Gooseff et al. 2009). Bowden et al. (2008) identified failure features in the foothills of the Brooks Range, AK, and a comparison of imagery from 1999–2006 revealed that 23 of the 34 features were new since ~ 1980 . This pattern suggests that there are recent increases in hillslope thermokarst formation.

There were consistent patterns in the general morphology

Table 1. Water chemistry from water tracks above (reference) and rivulets within thermokarst features of the Noatak River Basin, USA. All variables used as vectors in NMDS analysis.

| Sample Variable | Reference \pm std. error | Wall \pm std. error | Active \pm std. error | Run-out \pm std. error |
|--|----------------------------|-----------------------|-------------------------|--------------------------|
| Water chemistry (μM) | n=8 | n=6 | n=8 | n=8 |
| Chloride | 2.1 ± 0.5 | 8.8 ± 0.1 | 58.5 ± 27.5 | 92.30 ± 44.5 |
| Nitrite | 0.09 ± 0.03 | 0.2 ± 0.1 | 0.2 ± 0.1 | 0.3 ± 0.1 |
| Bromide | 0.02 ± 0.01 | 0.3 ± 0.1 | 0.7 ± 0.2 | 0.8 ± 0.3 |
| Nitrate | 0.05 ± 0.00 | 3.2 ± 0.9 | 33.2 ± 13.5 | 41.0 ± 20.9 |
| Sulfate | 223.7 ± 31.3 | 289.3 ± 82.5 | 359.1 ± 137.7 | 685.4 ± 165.4 |
| Sodium | 48.9 ± 6.8 | 139.5 ± 18.7 | 80.0 ± 22.6 | 302.4 ± 57.5 |
| Ammonium | 0.9 ± 0.5 | 6.7 ± 3.1 | 38.5 ± 22.6 | 5.8 ± 2.5 |
| Magnesium | 1892 ± 205 | 1380 ± 99 | 1129 ± 285 | 1587 ± 87 |
| Potassium | 0.2 ± 0.1 | 0.9 ± 0.4 | 2.4 ± 1.3 | 6.5 ± 3.5 |
| Calcium | 1140 ± 102 | 847 ± 93 | 814 ± 140 | 1197 ± 149 |
| DIC | 2197 ± 215 | 1922 ± 124 | 1749 ± 265 | 1901 ± 138 |
| Silica | 30.7 ± 3.0 | 33.5 ± 1.9 | 63.2 ± 9.2 | 58.7 ± 10.5 |
| TDP | 1.9 ± 1.1 | 0.1 ± 0.0 | 0.7 ± 0.2 | 2.1 ± 0.7 |
| Temperature ($^{\circ}\text{C}$) | 12.4 ± 0.4 | 11.4 ± 0.4 | 11.9 ± 1.1 | 13.2 ± 0.3 |
| Conductivity ($\mu\text{S}/\text{cm}$) | 459.3 ± 19.9 | 333.8 ± 30.1 | 328.7 ± 53.0 | 420.2 ± 53.7 |
| Dissolved Oxygen (mg/L) | 9.4 ± 0.1 | 8.3 ± 0.3 | 8.8 ± 0.2 | 10.1 ± 0.4 |
| pH | 8.2 ± 0.1 | 8.1 ± 0.0 | 7.7 ± 0.2 | 8.2 ± 0.0 |
| DOC | 375 ± 44 | 455 ± 34 | 1433 ± 366 | 1085 ± 265 |
| TDN | 13.5 ± 1.3 | 28.0 ± 5.1 | 115.2 ± 36.8 | 84.2 ± 29.0 |
| DON | 13.9 ± 1.5 | 24.8 ± 4.6 | 82.1 ± 31.2 | 43.2 ± 8.7 |
| DOC:DON (ratio) | 27.3 ± 1.0 | 20.9 ± 2.4 | 22.2 ± 31.2 | 24.8 ± 1.9 |
| DOC:TDN (ratio) | 27.5 ± 0.9 | 18.6 ± 2.4 | 18.3 ± 3.0 | 16.6 ± 2.1 |
| DON:TDN (ratio) | 99.6 ± 0.1 | 88.9 ± 3.6 | 78.5 ± 10.6 | 69.5 ± 9.4 |
| % Nitrate:DON (ratio) | 0.0 ± 0.0 | 0.1 ± 0.1 | 2.6 ± 2.3 | 0.7 ± 0.3 |
| (SUVA) L/mg/m | 3.1 ± 0.3 | 3.3 ± 0.4 | 4.0 ± 0.5 | 3.1 ± 0.4 |
| HCO_3^- ($\mu\text{Eq}/\text{L}$) | 1894 ± 199 | 1827 ± 116 | 1587 ± 267 | 1797 ± 131 |

of ALD's and their growth. This suggests that ALD susceptibility on hillslopes is constrained laterally but not longitudinally, and is correlated with vegetation, organic deposits, cryostratigraphy, and hydrology (French and Shur 2010, Jorgenson et al. 2010a).

Studies comparing thaw depth below water tracks versus nearby hillslopes reveal that thaw is deeper below running water (Jorgenson & Osterkamp 2005). Our results show that the thaw depth in all transects within active features was generally an order of magnitude greater compared to the influence of water tracks alone (2 cm versus 20 cm), revealing that thermal erosion features substantially alter thaw depths and likely the permafrost table also. Variability of thaw depths was also typically greater within active thermokarst features compared with thaw depths outside of features. This sharp thaw gradient increases the surface area of permafrost ice, which may result in increased thaw and a continued evolution of permafrost failure.

Soils and water

Our results indicate that the physical and chemical properties of soils and associated water from thermokarst

failures undergo significant shifts compared to undisturbed tundra. The disturbance process mixes organic horizons, which displaces mineral materials and exposes previously frozen mineral soils. It is perhaps not surprising then that soils in the disturbed zones tend to have lower organic carbon and nitrogen contents. However, the water draining these features tends to be enriched with nutrients (ammonium and nitrite), dissolved organic matter (DOC and DON), and indicators of mineral soil exposure (chloride and bromide). Furthermore, the ratio of DOC:DON is lower in water draining disturbed areas. This suggests that not only is the water enriched in nutrients and organic matter, but the quality of this organic matter has a lower C:N ratio and thus is potentially better suited to microbial degradation.

We have previously shown that small amounts of added nutrients can have dramatic effects on the structure and function of biotic communities in arctic streams (e.g., Slavik et al. 2004) and that these changes can be long lasting. With greater nutrient availability and quality, and the potential for long-lasting bottom-up effects, increased rates of thermokarst failures would likely influence terrestrial and aquatic ecosystems beyond their local extent.

Table 2. Physical and chemical characteristics of soils from transects collected above (reference) and within thermal-erosion features of the western Noatak River Basin, AK, USA.

| Sample Variable | Reference \pm stderr | Wall \pm stderr | Active \pm stderr | Run-out \pm stderr | NMDS role |
|--------------------------------|------------------------|-------------------|---------------------|----------------------|-----------|
| | n=8 | n=6 | n=8 | n=6 | |
| pH | 7.1 \pm 0.2 | 7.4 \pm 0.1 | 6.6 \pm 0.2 | 7.3 \pm 0.3 | Vector |
| Electrical cond. (μ S/cm) | 70 \pm 10 | 250 \pm 150 | 100 \pm 30 | 80 \pm 10 | Vector |
| Organic matter % | 33.2 \pm 8.9 | 3.0 \pm 0.8 | 10.7 \pm 6.4 | 12.9 \pm 5.6 | Driver |
| Soils (AB-DTPA digest) | | | | | |
| NO ₃ -N (ppm) | 3.5 \pm 1.0 | 1.0 \pm 0.1 | 7.2 \pm 4.33 | 4.5 \pm 0.9 | Driver |
| Phosphorus (P) (ppm) | 10.2 \pm 2.2 | 2.2 \pm 0.4 | 4.3 \pm 0.9 | 5.4 \pm 1.7 | Driver |
| Potassium (K) (ppm) | 188.6 \pm 61.4 | 21.7 \pm 2.5 | 30.0 \pm 5.7 | 63.5 \pm 25.5 | Driver |
| Zinc (Zn) (ppm) | 16.5 \pm 6.10 | 0.5 \pm 0.1 | 4.4 \pm 3.3 | 6.8 \pm 4.2 | Driver |
| Iron (Fe) (ppm) | 184.3 \pm 106.1 | 791.6 \pm 700.3 | 345.8 \pm 168.0 | 182.1 \pm 51.5 | Driver |
| Manganese (Mn) (ppm) | 43.4 \pm 9.7 | 11.2 \pm 5.7 | 37.2 \pm 18.8 | 31.8 \pm 9.2 | Driver |
| Copper (Cu) (ppm) | 11.4 \pm 2.0 | 6.9 \pm 0.8 | 21.5 \pm 10.9 | 9.77 \pm 1.23 | Driver |
| CaCO ₃ (equiv. %)* | 2.1 \pm 1.0 | 1.2 \pm 0.2 | 1.2 \pm 0.7 | 11.5 \pm 9.3 | Driver |
| SO ₄ S (ppm) | 46.4 \pm 9.3 | 16.4 \pm 2.3 | 43.7 \pm 4.9 | 38.6 \pm 9.2 | Driver |
| Silica (%) | 21.8 \pm 4.0 | 37.9 \pm 0.9 | 30.9 \pm 3.5 | 27.4 \pm 4.6 | Driver |
| Soils (HF digest) (%) | | | | | |
| Calcium (Ca) | 1.1 \pm 0.2 | 0.2 \pm 0.0 | 0.9 \pm 0.3 | 0.8 \pm 0.2 | Driver |
| Magnesium (Mg) | 0.6 \pm 0.1 | 0.5 \pm 0.1 | 0.7 \pm 0.2 | 0.7 \pm 0.1 | Driver |
| Sodium (Na) | 0.2 \pm 0.0 | 0.3 \pm 0.0 | 0.2 \pm 0.0 | 0.2 \pm 0.1 | Driver |
| Potassium (K) | 0.9 \pm 0.0 | 1.2 \pm 0.1 | 1.1 \pm 0.1 | 1.1 \pm 0.1 | Driver |
| Phosphorus (P) | 0.1 \pm 0.0 | 0.1 \pm 0.0 | 0.1 \pm 0.0 | 0.1 \pm 0.0 | Driver |
| Aluminum (Al) | 2.9 \pm 0.3 | 3.4 \pm 0.5 | 4.4 \pm 0.4 | 3.6 \pm 0.6 | Driver |
| Iron (Fe) | 2.6 \pm 0.5 | 3.6 \pm 0.5 | 4.1 \pm 0.2 | 3.00 \pm 0.4 | Driver |
| Manganese (Mn) | 0.1 \pm 0.0 | 0.1 \pm 0.0 | 0.1 \pm 0.0 | 0.1 \pm 0.0 | Driver |
| Titanium (Ti) | 0.01 \pm 0.0 | 0.0 \pm 0.0 | 0.0 \pm 0.0 | 0.0 \pm 0.0 | Driver |
| Copper (Cu) (mg/kg) | 31.6 \pm 3.3 | 29.4 \pm 1.8 | 39.9 \pm 7.5 | 29.8 \pm 2.5 | Driver |
| Zinc (Zn) (mg/kg) | 8.8 \pm 0.7 | 10.5 \pm 0.8 | 11.8 \pm 1.2 | 11.1 \pm 0.8 | Driver |
| Nickel (Ni) (mg/kg) | 28.5 \pm 2.8 | 43.5 \pm 2.4 | 42.9 \pm 5.0 | 34.0 \pm 3.1 | Driver |
| Molybdenum (Mo) (mg/kg) | 0.3 \pm 0.0 | 0.3 \pm 0.0 | 0.3 \pm 0.0 | 0.3 \pm 0.0 | Driver |
| Cadmium (Cd) (mg/kg) | 2.3 \pm 0.5 | 3.4 \pm 0.6 | 4.5 \pm 0.7 | 2.9 \pm 0.5 | Driver |
| Chromium (Cr) (mg/kg) | 13.7 \pm 2.5 | 25.0 \pm 9.1 | 21.3 \pm 4.0 | 21.0 \pm 5.9 | Driver |
| Strontium (Sr) (mg/kg) | 63.1 \pm 6.0 | 44.2 \pm 2.2 | 64.8 \pm 5.1 | 54.6 \pm 4.9 | Driver |
| Barium (Ba) (mg/kg) | 180.0 \pm 26.9 | 157.1 \pm 47.2 | 443.4 \pm 76.5 | 386.0 \pm 129.8 | Driver |
| Beryllium (Be) (mg/kg) | 0.1 \pm 0.0 | 0.19 \pm 0.03 | 0.16 \pm 0.02 | 0.15 \pm 0.03 | Driver |
| Lead (Pb) (mg/kg)* | 0.6 \pm 0.3 | 1.02 \pm 0.62 | 1.05 \pm 0.39 | 0.39 \pm 0.18 | Driver |
| Sulfur (S) (%) | 0.0 \pm 0.0 | 0.0 \pm 0.0 | 0.0 \pm 0.0 | 0.0 \pm 0.0 | Driver |
| Total soil analysis | | | | | |
| Nitrogen (N) (%) | 1.02 \pm 0.25 | 0.11 \pm 0.01 | 0.40 \pm 0.19 | 0.4 \pm 0.1 | Driver |
| Carbon (C) (%) | 17.7 \pm 5.0 | 0.6 \pm 0.2 | 5.51 \pm 3.42 | 7.1 \pm 3.1 | Driver |
| Carbon/Nitrogen | 13.5 \pm 2.1 | 5.1 \pm 2.1 | 10.3 \pm 1.1 | 11.2 \pm 2.9 | Driver |
| Sand (%) | 75.5 \pm 3.6 | 62.2 \pm 1.0 | 67.1 \pm 3.0 | 67.3 \pm 3.9 | Vector |
| Silt (%) | 13.9 \pm 2.7 | 21.2 \pm 1.2 | 21.6 \pm 3.0 | 19.2 \pm 4.0 | Vector |
| Clay (%) | 10.6 \pm 1.7 | 16.7 \pm 0.5 | 11.3 \pm 0.96 | 13.5 \pm 0.4 | Vector |
| Isotope Data (soils) | | | | | |
| $\delta^{13}\text{C}$ (‰) | -25.7 \pm 0.4 | -24.6 \pm 0.8 | -25.1 \pm 0.8 | -25.9 \pm 0.4 | Driver |
| $\delta^{15}\text{N}$ (‰) | 0.7 \pm 0.3 | 1.2 \pm 0.1 | 1.7 \pm 0.2 | 1.2 \pm 0.3 | Driver |

*samples at/below detection limit - substituted with 0.5 x detection limit

Acknowledgments

This research was supported by the Arctic Network Inventory and Monitoring Program of the U.S. National Park Service. We thank Diane Sanzone and Jim Lawler for their support of this project. We thank Aurora Boucher, Amanda Reinhart, and Tara Whitesell for field assistance and Stan Hermens for helicopter support. The conclusions and opinions expressed within this document are those of the authors and not the U.S. National Park Service.

References

- ACIA. 2005. Impacts of a Warming Climate: Arctic Climate Impact Assessment. Cambridge University Press. Available at <http://www.uaf.edu/acia/>.
- Beikman, H.M. 1980. Geologic Map of Alaska: scale 1:2,500,000. U. S. Geological Survey, Reston, VA.
- Bowden, W.B., Gooseff, M.N., Balsler, A. et al. 2008. Sediment and nutrient delivery from thermokarst features in the foothills of the North Slope, Alaska: Potential impacts on headwater stream ecosystems. *Journal of Geophysical Research* 113, G02026, doi:10.1029/2007JG00470.
- Clarke, K.R. 1993. Non-parametric multivariate analysis of changes in community structure. *Australian Journal of Ecology* 18, 117-143.
- Chapin, F.S. III, Sturm, M., Serreze, M.C. et al. 2005. Role of landsurface change in arctic summer warming. *Science* 310:657-660.
- Clilverd, H.M., Jones, J.B., & Kielland, K. 2008. Nitrogen retention in the hyporheic zone of a glacial river in interior Alaska. *Biogeochemistry* 88:31-46. DOI 10.1007/s10533-008-9192-9.
- French, H. & Shur, Y. 2010. The principles of cryo-stratigraphy. *Earth-Science Reviews* 101:190-206.
- Forest Research-Revue Canadienne De Recherche Forestiere 40:1219-1236.
- Gooseff, M.N., Balsler, A., Bowden W.B., & Jones, J.B. 2009. Effects of hillslope thermokarst in northern Alaska. *Eos, Transactions of the American Geophysical Union* 90: 29-31.
- Hinzman, L., Bettez, N., Chapin, F.S. et al. 2005. Evidence and Implications of Recent Climate Change in Terrestrial Regions of the Arctic. *Climate Change* 72:251-298.
- Hobbie, J.E., Peterson, B.J., Bettez, N. et al. 1999. Impact of global change on the biogeochemistry and ecology of an Arctic freshwater system. *Polar Research* 18:207-214.
- Jorgenson, M.T. & Osterkamp, T.E. 2005. Response of boreal ecosystems to varying modes of permafrost degradation. *Canadian Journal of Forest Research* 35:2100-2111.
- Jorgenson, M.T., Loomis, J.E., Roth, T.F., & Duffy, M. 2006. Ecological land classification and landcover mapping for the Arctic Network of National Parks. Annual Report prepared for National Park Service, Fairbanks, AK, by ABR, Inc., Fairbanks, AK, 20 pp.
- Jorgenson, M.T., Romanovsky, V., Harden, J. et al. 2010a. Resilience and vulnerability of permafrost to climate change. *Canadian Journal of Forestry Research* 40:1219-1236.
- Jorgenson, M.T., Roth, J.E., Miller, P.F. et al. 2010b. An ecological land survey and landcover map of the Arctic Network. Natural Resource Technical Report NPS/ARC/NRTR—2009/270. National Park Service, Fort Collins, Colorado.
- Lewkowicz, A.G. 2007. Dynamics of Active-layer Detachment Failures, Fosheim Peninsula, Ellesmere Island, Nunavut, Canada. *Permafrost and Periglacial Processes* 18:89-103.
- Mack, M.C., Bret-Harte, M.S., Hollingsworth, T.N. et al. 2011. *Nature* 475:489-492.
- Minchin, P.R. 1987. An evaluation of the relative robustness of techniques for ecological ordination. *Vegetatio* 96:89-108.
- Osterkamp, T.E. & Romanovsky, V.E. 1999. Evidence for warming and thawing of discontinuous permafrost in Alaska. *Permafrost and Periglacial Processes* 10:17-37.
- Osterkamp, T.E., Viereck, L., Shur, Y. et al. 2000. Observations of thermokarst and its impact on boreal forests in Alaska, USA. *Arctic Antarctic and Alpine Research* 32:303-315.
- Pollack, H.N., Demezhko, D.Y., Duchkov, A.D. et al. 2003. Surface temperature trends in Russia over the past five centuries reconstructed from borehole temperatures. *Journal of Geophysical Research-Solid Earth* 108.
- Rastetter, E.B., Kwiatkowski, B.L., Le Dizes, S., & Hobbie, J.E. 2004. The role of down-slope water and nutrient fluxes in the response of arctic hill slopes to climate change. *Biogeochemistry* 69:37-62.
- Serreze, M.C., Walsh, J.E., Chapin, F.S. III et al. 2000. Observational evidence of recent change in the northern high-latitude environment. *Climate Change* 46:159-207.
- Slavik, K., Peterson, B.J., Deegan, L.A. et al. 2004. Longterm responses of the Kuparuk River to phosphorus fertilization. *Ecology* 85:939-954.
- Tape, K., Sturm, M. & Racine, C. 2006. The evidence for shrub expansion in Northern Alaska and the Pan-Arctic. *Global Change Biology* 12:686-702.
- U.S. Arctic Research Commission. 2003. Climate change, permafrost, and impacts on civil infrastructure. U.S. Arctic Research Commission. Permafrost Task Force. Special Report 01-03. Arlington, Virginia.
- Viereck, L.A., Dyrness, C.T., Batten, A.R., & Wenzlick, K.J. 1992. The Alaska Vegetation Classification. Page 278 in U.S.D.o.A.F. Service, editor. Gen. Tech. Rep. PNW-GTR-286, Portland, OR.
- Young, S.B. 1974. *The environment of the Noatak River basin, Alaska*. Contributions of the Center for Northern Studies, Wolcott, VT.

Cryostructures of Basal Glacier Ice as an Object of Permafrost Study: Observations from the Matanuska Glacier, Alaska

Daniel Fortier

Geography Department, University of Montreal, Montreal, Qc, Canada

Mikhail Kanevskiy, Yuri Shur, Eva Stephani, Matthew Dillon
University of Alaska Fairbanks, Fairbanks, AK, USA

M. Torre Jorgenson

Alaska Ecoscience, Fairbanks, AK, USA

Abstract

In permafrost areas, the extent of former glaciations can be inferred from the occurrence of glacier ice buried in the permafrost. The presence of buried glacier ice has therefore considerable implications for the reconstructions of paleoenvironments and paleoclimates. Buried basal ice of glaciers and ice sheets can be distinguished from other types of massive ice only if the properties and structure of contemporary basal ice are well known. We conducted fieldwork at the Matanuska Glacier, Alaska (61°46'N, 147°44'W), and described, logged, and took detailed photographs of basal ice exposures. We described basal ice in terms of cryostructures, a method widely used by the permafrost community. Microcomputed tomodensitometry of basal ice cores was used to image cryostructures and to quantify their volumetric ice and sediment contents. Particle-size distribution analysis was used to characterize basal ice sediments. We provide in this paper high-resolution imagery of basal ice cryostructures quantitative volumetric ice content and basal ice sediment characteristics.

Keywords: basal glacier ice; permafrost; cryostructure; massive ground ice; Matanuska Glacier.

Introduction

Buried basal glacier ice and paleoenvironments

In permafrost areas, the extent of former glaciations can be inferred by the spatial distribution of erratics and glacial landforms such as moraines, flutes, drumlins, and glacio-tectonically deformed frozen ground. Remnants of glaciers and ice sheets buried in permafrost can also be used to reconstruct paleoenvironments and paleoclimates (Murton (2005, Murton et al. 2005). However, distinguishing the debris-rich basal layer of glaciers and ice sheets buried in the permafrost from other types of massive icy sediments remains a challenge. For instance, scientists have debated for over 50 years about the extension of Pleistocene glaciations in the Russian Arctic (see Astakhov 2001), because massive icy sediments have either

been interpreted as massive segregated ice, injection ice, or buried basal ice. Buried basal ice of former glaciers and ice sheets can be distinguished from other types of massive ice only if the properties and structure of contemporary basal ice are well-known (French 1990, Murton et al. 2005). Several classifications of basal ice have been developed based on geological facies analysis (Lawson 1979, Knight 1994, Hubbard & Sharp 1995). However, none of them have addressed basal ice descriptions in terms of cryostructures, a method widely used by the permafrost community (Murton & French 1994, French & Shur 2010). The objective of this paper is to provide detailed structural descriptions of basal ice cryostructures for permafrost field studies of buried massive icy sediments.

Study Site

We conducted fieldwork at the Matanuska Glacier, Alaska (61°46'11"N, 147°44'3"W). This polythermal glacier is located in the Chugach Range in southcentral Alaska. It is approximately 39 km long and 6 km wide at the glacier terminus. Ice-cored moraines and glacier-derived permafrost are observed close to the margins of the glacier terminus. Excellent exposures of basal ice were observed in several locations of the western glacier front in 2005, 2006, 2007, and 2011 (Fig. 1). The basal ice of the Matanuska Glacier has been extensively studied during the last decades (Lawson 1979, Strasser et al. 1996, Knight 1997, Alley et al. 1998, Lawson et al. 1998, Evenson et al. 1999). These studies demonstrated that the basal ice was formed by several processes such as regelation, glaciohydrologic supercooling accretion, basal

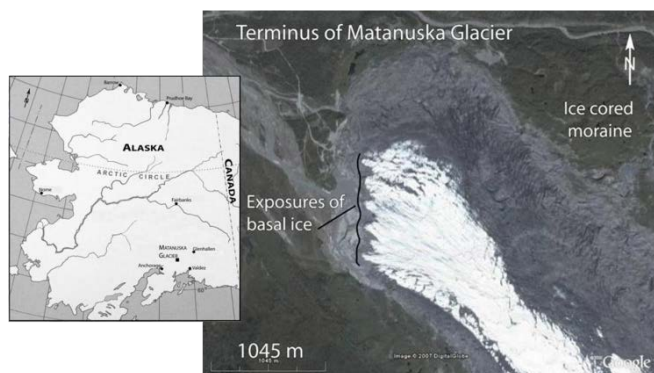


Figure 1. Study site in the Chugach Range, southcentral Alaska (left). Terminus of Matanuska Glacier with localization of basal ice exposures and ice-cored moraine colonized by vegetation (right). Note the extensive debris cover on the northeastern side.

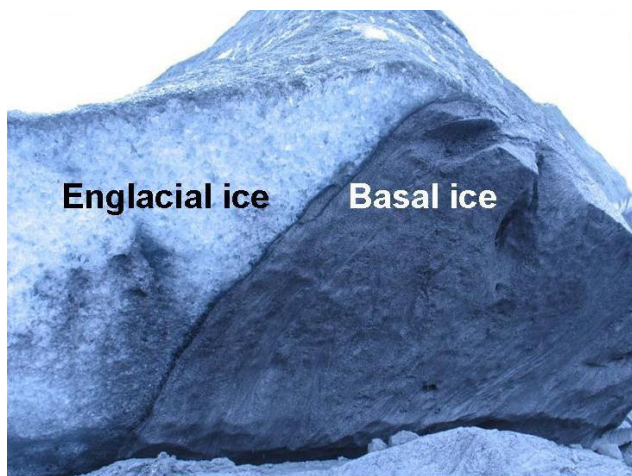


Figure 2. Typical basal ice exposure at the Matanuska Glacier terminus.

freeze-on, entrainment and incorporation of ice and sediments by overriding ice, glacio-tectonics, ice lens segregation, and downward propagation of cold temperature in the sediment at the glacier bed (congelation).

The burial of basal ice can result from a proximal sedimentary source such as glacio-fluvial sand, proglacial lake sediment, marine transgression over glacier ice, or mass movement (French & Harry 1988, Moorman & Michel 2000, Henriksen et al. 2003). The process of burial can also result from supraglacial debris accumulation and in situ melting of debris-rich basal ice forming a protective cover over itself (Østrem 1964, Haeberli & Epifani 1986, Johnson Everest & Bradwell 2003, Kowalewski et al. 2006). Colonization of the sediment covering the ice by vegetation creates, over time, an insulated layer that reduces or prevents melting of the ice and allows for the preservation of the massive ice in the permafrost.

Methods

We described, logged, and took detailed photographs of freshly excavated basal ice exposures at various sites along the western side of the glacier front. Basal ice was described according to the principles of cryostratigraphy (French & Shur 2010).

Cores were extracted from the exposures using a portable core-drill for ice content and particle-size distribution analyses (ASTM-D422 2007). Other cores were extracted, wrapped in plastic film to avoid sublimation, and brought back frozen to the laboratory for micro-computed tomography (CT-scan) analysis. Scans were performed in a cold room to avoid thawing of the samples. The scan images were processed in MATLAB software using a thresholding technique based on the density of basal ice components. These values were used to determine the volumetric content of each component (ice, sediment, gas). The main advantage of this method is to obtain, in a non-destructive manner, precise average ice and sediment contents for a given volume of a particular cryostructure. We have used micro-tomographic scans of basal ice samples to

Table 1: Basal ice cryostructures observed at the Matanuska Glacier, Alaska.

| Cryostructure | Description |
|----------------|--|
| Suspended | Single particles and sediment aggregates suspended in clear ice |
| | <i>Suspended dispersed</i> : sparsely dispersed single grains or micro-aggregates in clear to blue ice (Fig. 3). |
| | <i>Micro-suspended</i> : high density distribution of sub-mm sediment aggregates in ice (Fig. 4) |
| | <i>Macro-suspended</i> : variable, but generally high, density of mm to cm size sediment aggregates in clear ice (Fig. 5) |
| | <i>Intergranular-suspended</i> : Fine to coarse grained sediments trapped in between grains or ice crystals aggregates (ice plates) (Fig. 6) |
| Lenticular | Ice lens mm to cm thick |
| Ice layer | Ice layers dm to m wide and cm to m thick. Ice may contain some suspended fine sediment and gravel to pebble inclusions. |
| Porous visible | Pore ice visible to the unaided eye. |
| Crustal | Partial to complete mm to cm-thick coating of ice around rock fragments. |

produce two-dimensional micro-facies models, similar to fine-scale observations of natural basal ice exposures. The analysis of an isolated component is thus simplified. These models allowed for a detailed visualization of cryostructures, which helps to better describe their spatial arrangement and to study geometric relationships between ice and sediments. The technical details of these operations have been presented by Dillon et al. (2008).

Cryostructures of Matanuska Glacier Basal Ice

The Matanuska Glacier basal ice was characterized by eight typical cryostructures (Table 1). Other types of cryostructures were also observed, but we report here only the most common.

The *suspended-dispersed cryostructure* was usually, although not always, located at the contact between englacial ice and debris-rich basal ice (Fig. 2). The ice had very low sediment content with sparsely distributed millimeter-size particles and aggregates suspended in clear to blue ice (Fig. 3, Table 1). The volumetric ice content of this cryostructure was usually >95% and often close to 100%. Ice sometimes contained flattened air bubbles.

The *porous visible cryostructure* was widely distributed along the glacier terminus and was present wherever the debris content of basal ice was high (Fig. 4). The sediments were massive to stratified and often contain gravel and cobble-to-boulder size clasts. These clasts were usually covered by millimeter-thick coating of ice or sometimes enclosed in a complete ice crust (*crustal cryostructure*). The volumetric ice content of porous visible cryostructures was lower than other cryostructures (30–65%).

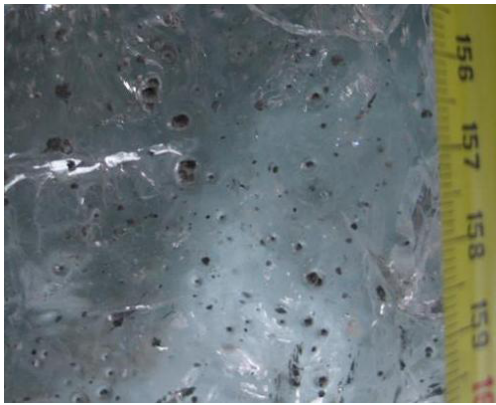


Figure 3. Suspended-dispersed cryostructure. Single grain to mm-size aggregates in clear to blue ice. Scale in cm.

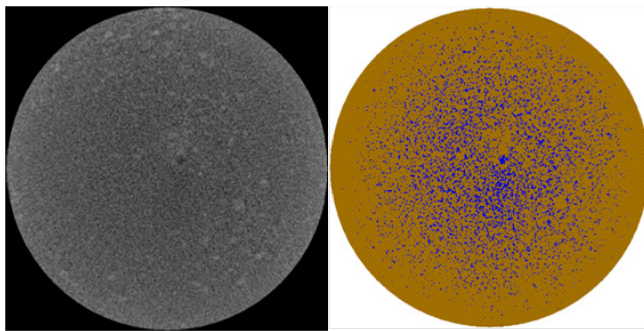


Figure 4. Porous visible cryostructure. Core diameter: 2.55 cm, pixel size: 34.46 microns. Unprocessed scan (left) and processed image (right) with ice in blue and sediment in brown.

The *micro-suspended* and *macro-suspended cryo-structures* were characterized by sediment aggregates suspended in clear ice (Figs. 5, 6, 7). The aggregates were characterized by mm to cm size distribution modes. Together, these cryostructures represented a large portion of exposed basal ice. The aggregates were sometimes randomly distributed in the ice, but most often the cryostructures were layered, which reflects sliding-induced shearing and deformation of overpressured sediment. The suspended aggregates in these layers were often broken and rotated (Fig. 6). Micro-suspended and macro-suspended layers were often separated by wavy sediment-rich bands in which pinch-and-swell and boudinage structures were observed (Fig. 5). The assemblage of mm to cm thick layers often pinched-out or merged together.

The *Intergranular-suspended cryostructure* was characterized by entrapment of silt, sand, and small gravel between rounded ice particles and ice plates (Fig. 7). The volumetric ice content of the micro, macro, and intergranular cryostructures varied between 64 and 96% and was usually between 75 and 90%.

The *lenticular cryostructure* was characterized by clear bubble-poor ice lenses within other types of cryostructures (e.g., macro-suspended, porous visible). The ice lenses themselves were usually a few millimeters thick and separated by closely spaced, debris-rich to ice-rich, cryostructures or sediment bands. This successive assemblage of layers was a

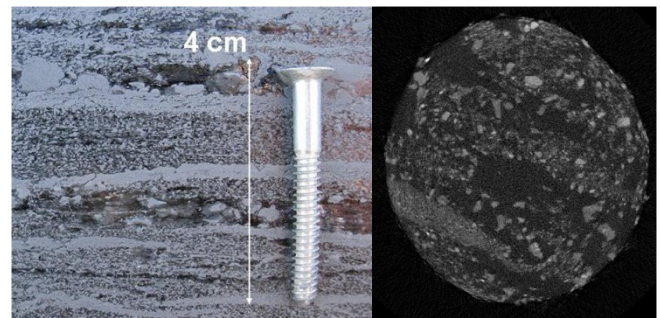


Figure 5. Micro-suspended cryostructure. Field exposure (left) and unprocessed scan images with ice in black and sediments in gray. Cores 4.39 cm in diameter. Cross section pixel size: 34.46 microns.

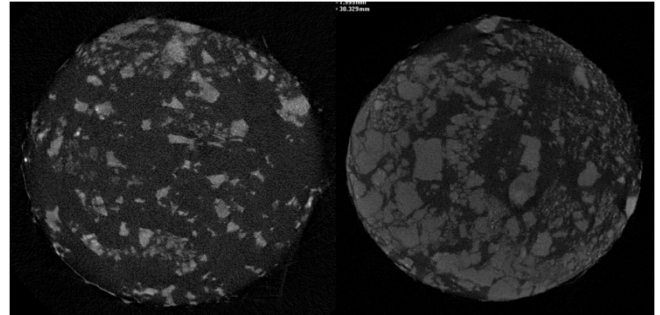


Figure 6. Macro-suspended cryostructure. Unprocessed scan images from two different samples with ice in black and sediment in gray. Cores ~4.4 cm in diameter. Cross section pixel size: 34.46 microns.

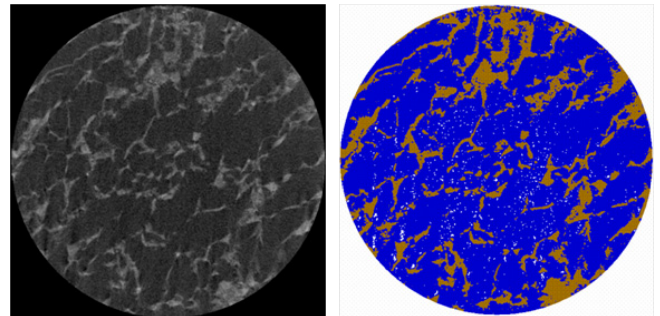


Figure 7. Suspended intergranular cryostructure. Cores 2.55 cm in diameter. Unprocessed scan (left) and processed image (right) with ice in blue, sediment in brown and gas in white. Cross section pixel size: 34.46 microns.

few cm to dm thick and formed the lenticular cryofacies. The volumetric ice content of lenticular cryostructures was close to 100%, whereas the lenticular cryofacies, which included the enclosing sediments, was usually between 80 and 90% but varied between 74 and 99%. The lenticular cryofacies likely reflected refreezing of thin water film and concurrent debris inclusion (regelation processes) in basal ice. The original shape of the ice lenses was often deformed. The ice lenses were often stretched, compressed, bended, contorted, or folded by glacier flow. Boulders were often cutting across the laminations and deforming the ice lenses.

Several ice layers were observed within debris-rich basal ice (Fig. 8). These layers were a few decimeters to a few meters wide in the exposures. Ice layers were often interbedded within sediment-rich or ice-rich layers. The ice was clear and bubble-poor. Very fine silt and clay forming smoke-like

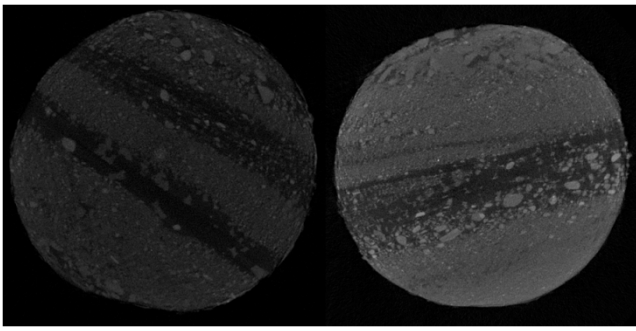


Figure 8. Lenticular cryostructure in debris-rich basal ice. Unprocessed scan images from two different samples 4.58 cm (left) and 4.48 cm (right) in diameter. Ice is black and sediments gray. Cross section pixel size: 34.46 microns.

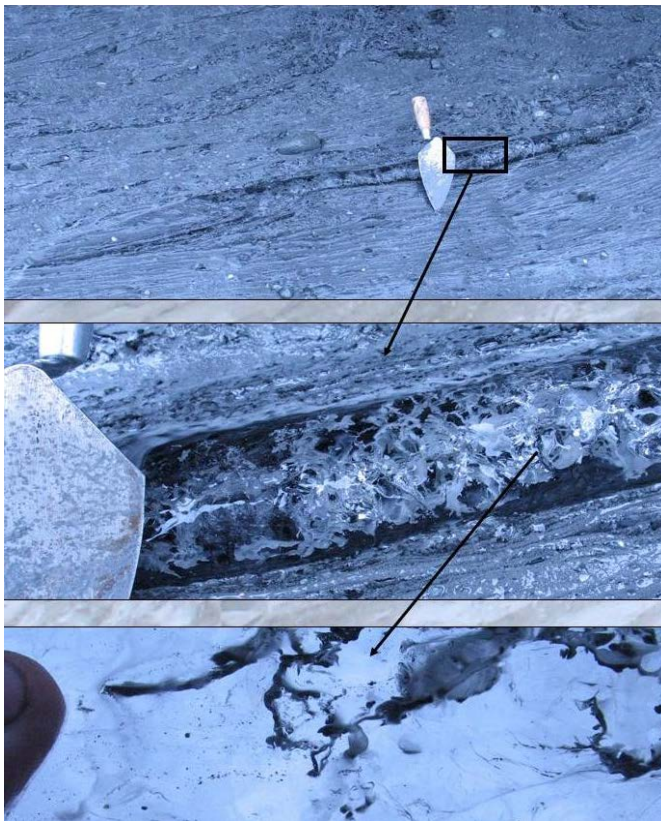


Figure 9. Ice layer with suspended fine-grained sediments in debris-rich basal ice. Trowel for scale is 15 cm long.

suspension were sometimes observed in the ice layers (Fig. 9). Gravel and pebbles were also observed encrusted in the ice and at the contact with the enclosing sediments. The ice layers had planar to undulating shape but were often deformed by bending, which reflects drag folding following movement of the ice along shear planes in the basal ice. The volumetric ice content of these layers is usually over 95%.

Sediments of Matanuska Glacier Basal Ice

The Matanuska Glacier basal ice sediments covered a wide range of particle-size distribution (Fig. 10). They were all polymodal, which is typical of sub-glacial sediments.

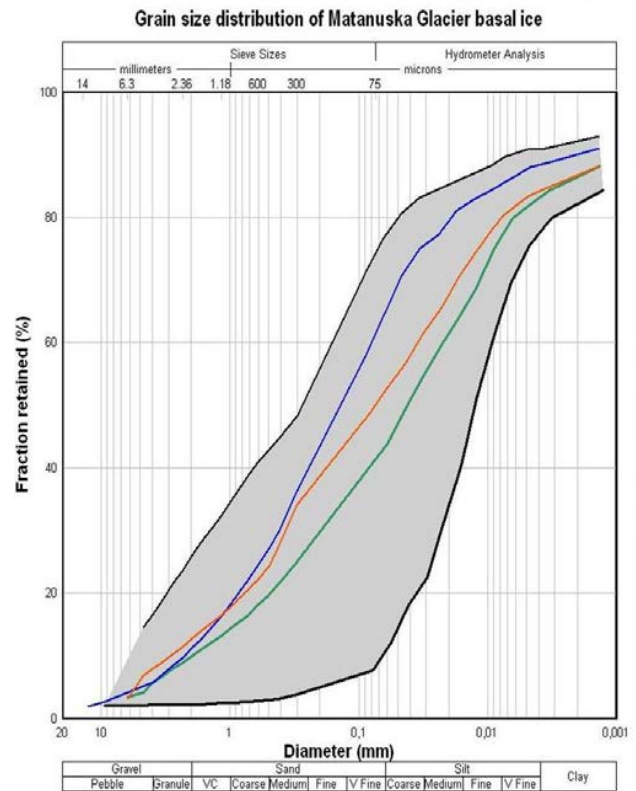


Figure 10. Particle size distribution of Matanuska Glacier basal ice. Note the large envelope curve (n= 41 samples).

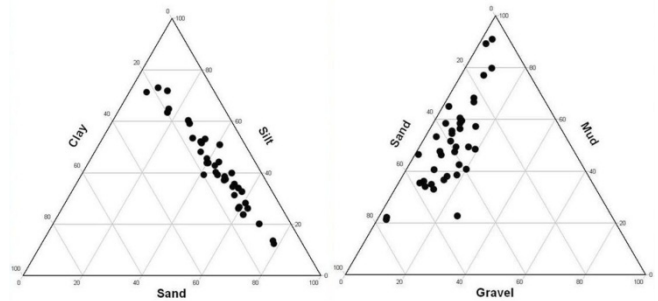


Figure 11. Basal ice sediment clay-silt-sand fractions only (left) and mud-sand-gravel fractions (right).

Sediment texture varied from gravelly silt to gravelly sandy silt diamictons (Fig. 11). The sediments were extremely to very poorly sorted and contained a significant fraction of fines (fine sand to clay) with gravel and cobble-to-pebble size rock fragments (Fig. 12). Frost-susceptible fine-grained sediments (fine sand to clay) are easily transported in the sub-glacial environment and were abundant in most basal ice cryostructures.

An analysis was made to evaluate the relationship between particle-size distribution and a given type of cryostructure observed in basal ice exposures at the study site. These cryostructures always contained a gravel fraction but were dominated by sand or mud.

Figure 13 shows typical sedimentary fractions for the *porous visible cryostructure*. Overall, the sediments are dominated

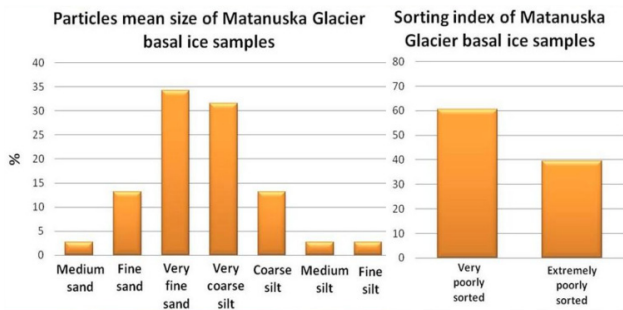


Figure 12. Particle mean size (left) and sorting index (right) of basal ice sediment.

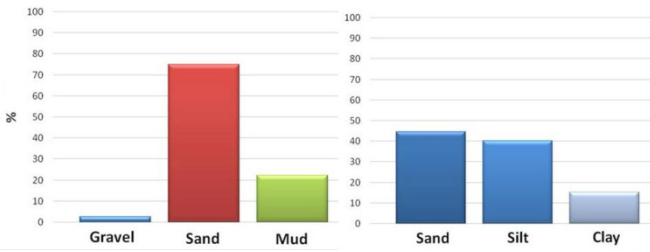


Figure 13. Porous visible cryostructure sedimentary fractions. Basal ice sediment with gravel inclusions (left) and sand to clay fractions only (right).

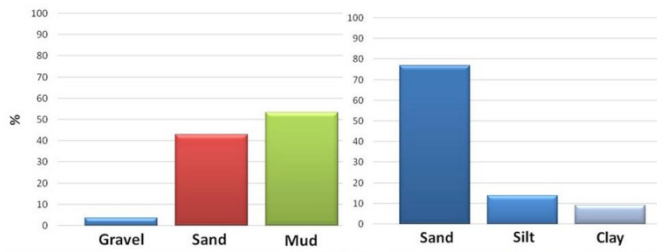


Figure 14. Micro-suspended and macro-suspended cryostructures sedimentary fractions. Basal ice sediment with gravel inclusions (left) and sand to clay fractions only (right).

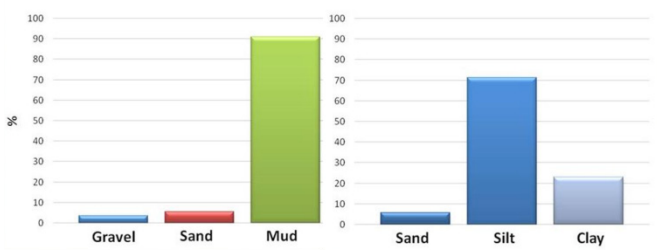


Figure 15. Suspended-intergranular sedimentary fractions. Basal ice sediment with gravel inclusions (left) and sand to clay fractions only (right).

by sand but contain a significant fine-grained component which likely promoted ice segregation and probably explains volumetric ice content in excess of the porosity.

The *micro-suspended* and *macro-suspended* cryostructures were mostly composed of mud. Figure 14 shows a representative distribution of sedimentary fractions within these cryostructures. Interestingly, sand dominated the sand to clay fraction for both types. Even if the silty-clay fraction of the micro-suspended and macro-suspended cryostructures was

lower than the porous visible cryostructure, their volumetric ice content was higher.

The *suspended-intergranular cryostructure* was clearly dominated by mud and contained a significant silt-clay fraction (Fig. 15). This type of sediment is easily transported in suspension in sub-glacial water which could suggest suspension freezing processes at the time of cryostructure development.

The *suspended-dispersed cryostructure* comprised single grains of sand or micro-aggregates of clayey silt.

The *lenticular cryostructure* comprised all types of sediments, often at the interface between bands of other cryostructures (Fig. 8).

Sediments in *ice layers* were of two size modes: very fine suspended clayey silt in ice, and gravel on the side or at the bottom of ice layers.

The *crustal cryostructure* was restricted to coarse gravel to boulder rock clasts included in basal ice layers comprising various types of other cryostructures. It was most common within the porous visible cryostructure layers.

Conclusion

The Matanuska Glacier basal ice was characterized by eight typical cryostructures: porous visible, suspended-dispersed, micro-suspended, macro-suspended, intergranular-suspended, lenticular, crustal, and ice layers. These cryostructures can easily be identified in field exposures of basal ice. Micro-computed tomography was used to image the geometrical patterns of these cryostructures. This technique, along with laboratory measurement, was also used to quantify the volumetric ice content of each cryostructure. Sedimentological analysis of basal ice sediments allowed for the characterization of typical sediment fractions forming specific cryostructures.

The study of structure, formation, and burial of basal ice is very significant for permafrost research. More work remains to be done to evaluate similarities between basal ice cryostructures of glaciers (this study) and ice sheets.

Acknowledgments

The research was supported by grants ARC-0454985 and ARC-0454939 from the USA National Science Foundation and the National Science and Engineering Research Council of Canada. The paper represents the findings of the authors and not necessarily the opinions of funding agencies. Special thanks to Wilfried Haerberli, whose comments greatly contributed to improve the quality of the paper.

References

- Alley, R.B., Lawson, D.E., Evenson, E.B., Strasser, J.C., & Larson, G.J. 1998. Glaciohydraulic supercooling: a freeze-on mechanism to create stratified, debris-rich basal ice. 2. Theory. *Journal of Glaciology* 44: 563-569.
- American Society for Testing and Materials. 2007. Standard test methods for particle-size analysis of soils. ASTM D422-63.

- Astakhov, V. 2001. The stratigraphic framework for the Upper Pleistocene of the glaciated Russian Arctic: changing paradigms. *Global and Planetary Change* 31: 283-295.
- Dillon, M., Fortier, D., Kanevskiy, M., & Shur, Y. 2008. Tomodensitometric Analysis of Basal Ice. *Proceedings, Ninth International Conference on Permafrost*, Fairbanks, U.S.A.: 361-366.
- Evenson, E.B., Lawson, D.E., Strasser, J.C., Larson, G.J., Alley, R.B., & Ensminger, S.L. 1999. Field evidence for the recognition of glaciohydraulic supercooling and basal ice accretion. In *Special Papers* Mickleson, D.M., Attig, J.W. (eds). Geological Society of America 337: 23-36.
- Everest, J. & Bradwell, T. 2003. Buried glacier ice in southern Iceland and its wider significance. *Geomorphology* 52: 347-358.
- French, H.M. 1990. Observations on buried glacier ice and massive segregated ice, western Arctic Coast, Canada. *Permafrost and Periglacial Processes* 1: 31-43.
- French H.M. & Harry, D.G. 1988. Nature and origin of ground ice, Sandhills Moraine, southwest Banks Island, western Canadian Arctic. *Journal of Quaternary Science* 3: 19-30.
- French, H. & Shur, Y. 2010. The principles of cryostratigraphy. *Earth-Science Reviews* 101: 190-206.
- Haeberli, W. & Epifani, F. 1986. Mapping the distribution of buried glacier ice – an example from Lago Delle Locce, Monta Rosa, Italian Alps. *Annals of Glaciology* 8: 78-81.
- Hambre, J. 1984. Sedimentary processes and buried ice phenomena in the pro-glacial areas of Spitsbergen glaciers. *Journal of Glaciology* 30: 116-119.
- Henriksen, M., Mangerud, J., Matiouchkov, A., Paus, A. & Svendsen, J.I. 2003. Lake stratigraphy implies an 80,000 yr delayed melting of buried dead ice in northern Russia. *Journal of Quaternary Science* 18: 663-679.
- Hubbard, B. & Sharp, M. 1995. Basal ice facies and their formation in the Western Alps. *Arctic and Alpine Research* 27: 301-310.
- Knight, P.G. 1994. Two-facies interpretation of the basal layer of the Greenland ice sheet contributes to a unified model of basal ice formation. *Geology* 22: 971-974.
- Knight, P.G. 1997. The basal ice layer of glaciers and ice sheets. *Quaternary Science Reviews* 16: 975-997.
- Kowalewski, D.E., Marchant, D.R., Levy, J.S., & Head, J.W. 2006. Quantifying low rates of summertime sublimation for buried glacier ice in Beacon Valley, Antarctica. *Antarctic Science* 18: 421-428.
- Lawson, D.E. 1979. Sedimentological analysis of the western terminus region of the Matanuska Glacier, Alaska. Hanover, Cold Regions Engineering and Research Laboratory, Report 79-9, 112 pp.
- Lawson, D.E., Strasser, J.C., Evenson, E.B., Alley, R.B., Larson, G.J., & Arcone, S.A. 1998. Glaciohydraulic supercooling: a mechanism to create stratified, debris-rich basal ice. 1. field evidence and conceptual model. *Journal of Glaciology* 44: 547-562.
- Moorman, B.J. & Michel, F.A. 2000. The burial of ice in the periglacial environment on Bylot Island, Arctic Canada. *Permafrost and Periglacial Processes* 11: 161-175.
- Moorman, B.J., Michel, F.A., Murton, J.B., & French, H.M. 1994. Cryostructures in permafrost, Tuktoyaktuk coastlands, western Arctic Canada. *Canadian Journal of Earth Sciences* 31: 737-747.
- Murton, J.B., 2005. Ground-ice stratigraphy and formation at North Head, Tuktoyaktuk Coastlands, western Arctic Canada: a product of glacier-permafrost interactions. *Permafrost and Periglacial Processes* 16: 31-50.
- Murton, J.B., Whiteman, C.A., Waller, R.I., Pollard, W.H., Clark, I.D., & Dallimore, S.R. 2005. Basal ice facies and supraglacial melt-out till of the Laurentide Ice Sheet, Tuktoyaktuk Coastlands, western Arctic Canada. *Quaternary Science Reviews* 24: 681-708.
- Østrem, G. 1964. Ice-cored moraines in Scandinavia. *Geografiska Annaler* 46: 282-337.
- Strasser, J.C., Lawson, D.E., Larson, G.J., Evenson, E.B., & Alley, R.B. 1996. Preliminary results of tritium analyses in basal ice, Matanuska Glacier, Alaska, U.S.A.: evidence for subglacial ice accretion. *Annals of Glaciology* 22: 126-133.
- Vaikmae, R., Michel, F.A., & Solomatin, V.I. 1993. Morphology, stratigraphy and oxygen isotope composition of fossil glacier ice at Ledyanaya Gora, Northwest Siberia, Russia. *Boreas* 22: 205-213.

PSInSAR Monitoring of Ground Movement at Salluit, Quebec (Canada), Due to Freeze-Thaw Cycles, Active Layer Thickening, and Permafrost Warming

Richard Fortier

Centre d'études nordiques, Université Laval, Québec, Canada

Anne-Marie LeBlanc

Geological Survey of Canada, Ottawa, Canada

Giacomo Falorni

TRE Canada inc., Vancouver, Canada

René Therrien

Département de géologie et de génie géologique, Université Laval, Québec, Canada

Abstract

Radar images of Salluit in Northern Quebec, Canada, taken by the ERS-1 and ERS-2 satellites from 1992 to 2000 were analyzed using a permanent scatterer interferometric synthetic aperture radar (PSInSAR) technique to monitor ground movement. Time series of PS targets on rock outcrops show that postglacial uplift generates ground motion toward the satellite at velocities of about 1 mm/year. Other PS targets on ice-poor saline permafrost indicate ground motion away from the satellite at velocities in excess of 7 mm/year with superposed annual variations of 8 mm in amplitude. Numerical simulations of the impacts on the thermal regime of permafrost with an increase in air temperature of about 2°C, as observed in Northeastern Canada over the study period, suggest that the subsidence is due to the active layer thickening and permafrost warming while the annual variations are caused by the freeze-thaw cycles in the active layer.

Keywords: interferometric synthetic aperture radar (InSAR); permanent scatterer (PS); ground movement; freeze-thaw cycles; active layer thickening; permafrost warming.

Introduction

Meteorological records from Environment Canada (Figs. 1 and 2) show that the climate along the shores of Hudson Bay and Hudson Strait was affected by a cooling trend of a few hundredths of degrees Celsius per year from 1945 to 1992. However, since 1992, one of the coldest years ever recorded, the air temperature has increased by about 2°C relative to the 1961–1990 reference period. Among the several types of permafrost degradation resulting from an increase in air temperature, thaw subsidence can have major impacts on the performance of man-made infrastructure. For example, buildings, roads, and airfields built on ice-rich permafrost in the Northern Hemisphere are already affected by thaw subsidence, leading to increased maintenance costs and decreased useful life span (Couture et al. 2003, Fortier et al. 2011, Romanovsky et al. 2001). According to Nelson et al. (2001), vulnerability to thaw subsidence is widespread in the Northern Hemisphere.

Usual detection and monitoring methods for thaw subsidence, such as damage observation on infrastructure and ground surveying, could be improved if combined with remote sensing methods for assessing the spatial variability of ground movement. A case study for the Inuit community of Salluit in Northern Quebec, Canada, is presented here to illustrate that interferometric analysis of radar images allows monitoring of millimetric ground movement over a period of a few months or years due to postglacial uplift, active layer thickening, permafrost warming, and freeze-thaw cycles in the active layer.



Figure 1. Map of Northeastern Canada.

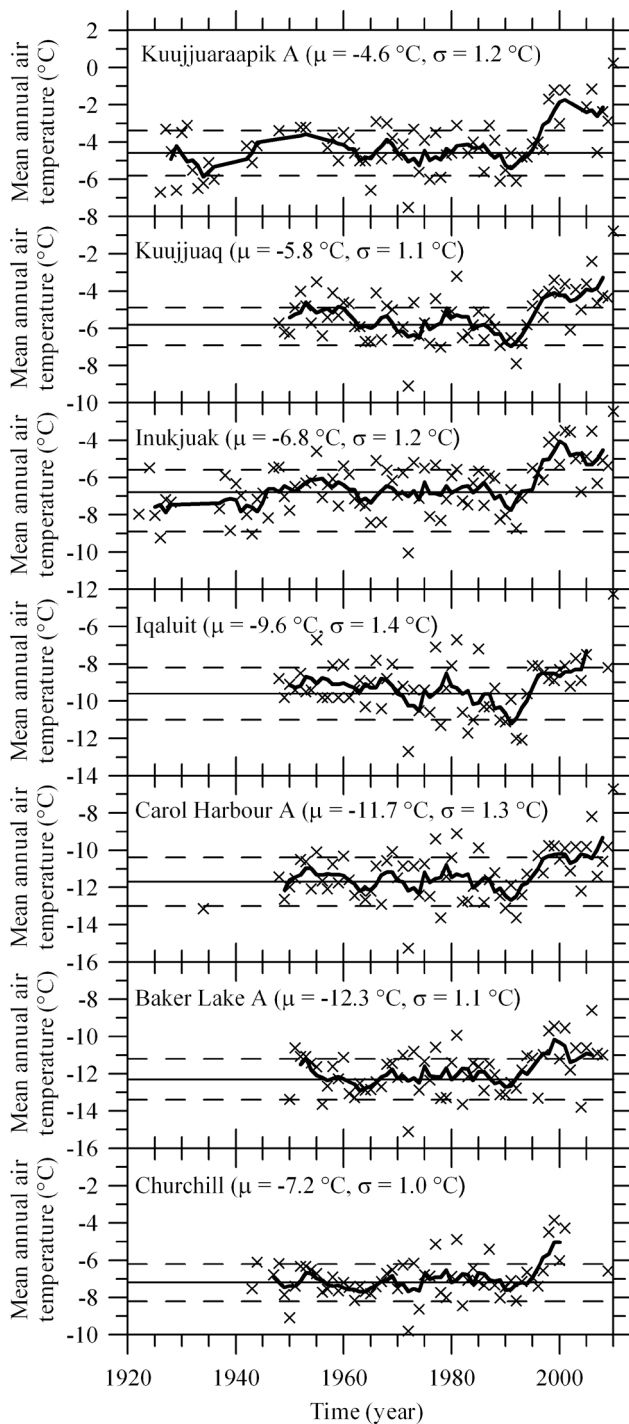


Figure 2. Climate change observed in Inuit communities along the shores of Hudson Bay and Hudson Strait, Canada (see Fig. 1 for the location). Meteorological data from Environment Canada (available from <http://climate.weatheroffice.gc.ca/index.html>; accessed September 20, 2011). The thick solid curves correspond to 5-year running averages to decrease the temperature variability and show the long-term trend. Solid and dotted horizontal lines are the average and \pm standard deviation (values in parentheses), respectively, over the 1961–1990 reference period.

PSInSAR

The use of interferometric synthetic aperture radar (InSAR) methods has increased rapidly over the last decade to measure ground movement such as land subsidence induced by groundwater pumping (Bell et al. 2008), landslides (Ferretti et al. 2005), and thaw subsidence in permafrost environment (Liu et al. 2010). SAR interferometry is based on the analysis of the phase shift of active microwave radar signals generated by a SAR satellite that are sent to and received from objects on the Earth from two images taken at different times. Ground movement can be extracted from the phase shift in the interferogram produced from the image analysis. The phase shift between two SAR images allows measurement of displacements as small as a few millimeters, but this accuracy can be severely decreased by atmospheric distortions. The permanent scatterer interferometric synthetic aperture radar (PSInSAR™) technique, which is a multi-interferogram approach, has been developed by Tele-Rilevamento Europa (TRE) to identify, quantify, and mitigate these distortions (Ferretti et al. 2001). This technique uses the identification and exploitation of individual signal reflectors, or permanent scatterer (PS) targets, remaining coherent on images over long time intervals to develop displacement time series. Time series of accurate phase shift for each PS target can be derived from a multi-interferogram incorporating a minimum of 15 images acquired by a satellite on the same orbit over time (Ferretti et al. 2005). The PS targets are most commonly natural objects, such as rock outcrops free of snow or heating and ventilation structures on building roofs. According to Ferretti et al. (2007), ground movement estimation with sub-millimetric accuracy can be achieved with InSAR time series. To our knowledge, the PSInSAR technique has not yet been applied for monitoring ground movement in permafrost environment.

Application of the PSInSAR Technique in Permafrost Environment

Inuit community of Salluit, Northern Quebec (Canada)

The village of Salluit is located in the continuous permafrost zone along the southern shore of Hudson Strait in Northern Quebec, Canada (Fig. 1). It is a fast-growing community of about 1100 people where 60% of the population is under the age of 25. The village lies at the bottom of a narrow valley and most structures are built on saline ice-poor and ice-rich permafrost, which provides problematic ground conditions. Favorable ground conditions for stable foundations are scarce in the valley. To plan the growth of the village, quaternary deposits (Fig. 3) and permafrost conditions were mapped in detail in the summers of 2002 and 2003, and areas where the ground was stable and suited for construction were delineated (Allard et al. 2004).

According to Gray et al. (1993), the region of Salluit was deglaciated by 8600–8700 BP. The d'Iberville Sea inundated the land at elevations below the current marine limit located at 150 m, leading to the deposition of marine sediments. The present-day rate of land emergence is about 2 to 4 mm/year (Gray et al. 1993). Saline ice-poor and ice-rich permafrost

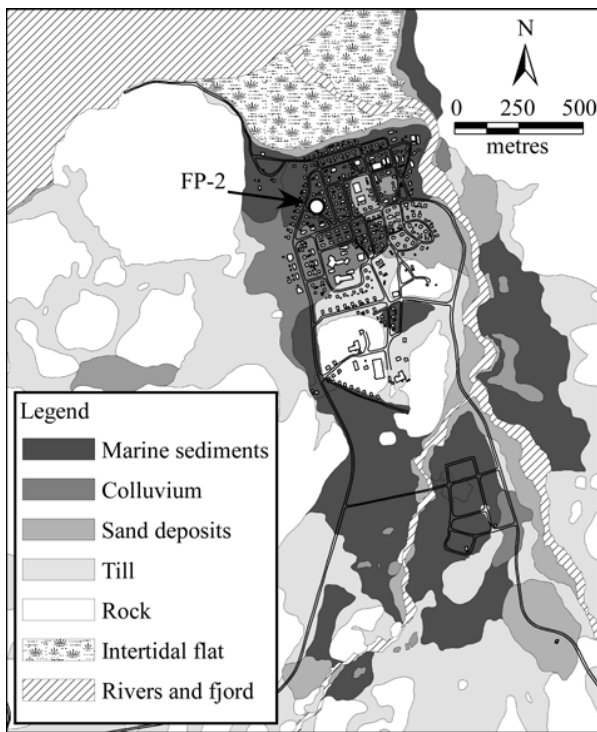


Figure 3. Map of quaternary deposits in the valley of Salluit (modified from Allard et al. 2004).

formed in the marine sediments. Till, glacio-fluvial sand and gravel, deltaic sand, and colluvium were also deposited and form a complex mosaic of quaternary deposits in the valley (Fig. 3). Due to the recent increase in air temperature (Fig. 2), infrastructure is already affected by thaw subsidence. Damages are recorded, but thaw subsidence is currently not monitored. However, the impacts of climate warming on the thermal regime of permafrost have been assessed through numerical modeling (LeBlanc, in prep.).

SAR images and PSInSAR analysis

The PSInSAR analysis used a series of 57 radar images of the Salluit area taken by the European Remote Sensing ERS-1 and ERS-2 satellites from May 1992 to November 2000. Based on extensive statistical analysis of signal phase and amplitude of each radar image, the pixels behaving as permanent scatterer (PS) targets were identified (Fig. 4). The ERS-2 radar image taken on July 9, 1997, was selected as the master image for geometric and temporal reference and the others images as slaves. All displacements were computed with respect to a reference PS target assumed to be motionless on bedrock close to the study area (Fig. 4).

Differential interferograms were then produced by comparing the slave and master images and accounting for topographic and atmospheric distortions. Displacements along the line-of-sight (LOS) of the satellite were calculated for each PS target on each interferogram and the average velocity was assessed considering the set of differential interferograms over the study period from 1992 to 2000 (Fig. 4). Positive velocities correspond to motion toward the satellite while negative values correspond to motion away from the satellite.

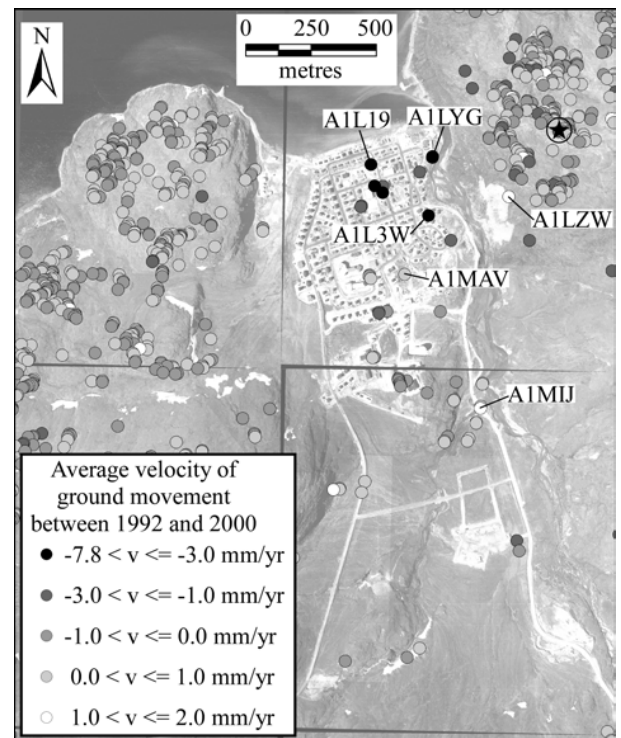


Figure 4. Location of PS targets in the valley of Salluit and its surroundings. The location of the reference PS target assumed to be motionless is identified by a star symbol. The average velocity of each PS target over the study period from 1992 to 2000 is also given by the grey color code. (Mosaic of aerial photographs taken in 2003: © Gouvernement du Québec.)

Time series of LOS displacement of selected PS targets are shown in Figure 5. Simple linear regression and sinusoidal function were fitted on each time series according to the following equation:

$$\Delta d_{\text{LOS}}(t) = V(t - 1992) + \Delta d_{1992} + A \sin\left(\frac{2\pi}{T}t - \phi\right) \quad (1)$$

where Δd_{LOS} is the LOS displacement in mm,
 t is the time in years,
 V is the velocity in mm/year,
 Δd_{1992} is the LOS displacement in 1992 in mm,
 A is the sinusoidal amplitude in mm,
 $T = 1$ is the period in years, and
 ϕ is the phase shift in radians.

Fitted values of the parameters in equation 1, the phase shift of the sinusoidal function in both radian and days, and the coefficient of determination R^2 of the linear regression are given in Table 1. According to the analysis of variance and an F-test with a significance level of 5%, the slope of the linear regression, the velocity, is different from zero for all time series. The sinusoidal function fitted to the time series has a period of one year.

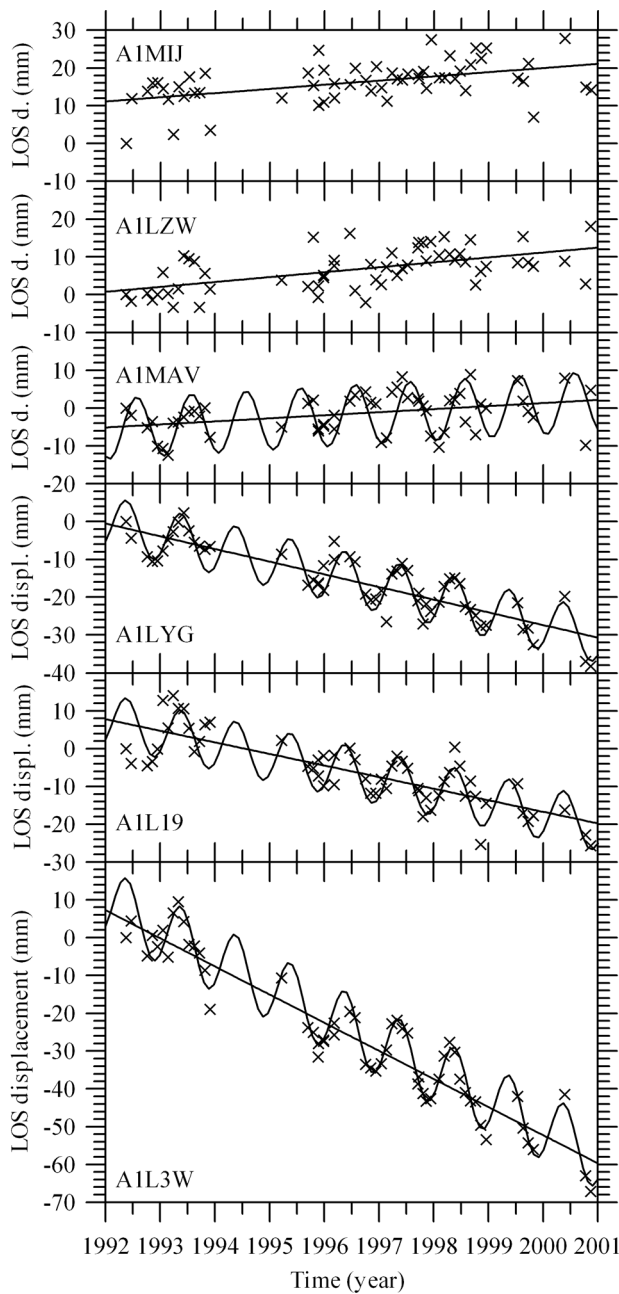


Figure 5. Time series of line-of-sight (LOS) displacement of selected PS targets (see Figure 4 for the location) from 1992 to 2000. Simple linear regression and sinusoidal function were fitted on each time series (Table 1).

Numerical Modeling of the Thermal Regime of Permafrost

The thermal regime of permafrost in the valley of Salluit was simulated to assess the impacts of the increase in air temperature recently observed in Nunavik (Fig. 2; LeBlanc in prep.). The governing differential equations for groundwater flow and heat transfer by conduction have similar forms, and the numerical code HydroGeoSphere (Therrien et al. 2008), which simulates 3D groundwater flow in fractured and porous media, was therefore modified to solve transient heat transfer by conduction in permafrost. Groundwater flow due to melting

Table 1. Parameters of the linear regression analysis and sinusoidal function fitted to the time series of LOS displacement of selected PS targets (Fig. 5).

| PS target | V (mm/year) | Δd_{1992} (mm) | R ² | A (mm) | ϕ (radian) (days) |
|-----------|-------------|------------------------|----------------|--------|------------------------|
| A1MIJ | 1.1 | 11.2 | 0.2 | - | - |
| A1LZW | 1.3 | 0.9 | 0.3 | - | - |
| A1MAV | 0.8 | -5.0 | 0.1 | 8.0 | 2 116.2 |
| A1LYG | -3.4 | -0.6 | 0.7 | 7.0 | 0.8 46.5 |
| A1L19 | -3.1 | 7.9 | 0.6 | 7.0 | 0.8 46.5 |
| A1L3W | -7.4 | 7.2 | 0.9 | 9.0 | 0.8 45.5 |

water and ground ice formation was not simulated. Thaw consolidation and frost heaving were also not considered. However, the permafrost model was based on observations of cryostructures made during the drilling of a deep borehole FP-2 (see the location in Figure 3; LeBlanc in prep., Allard et al. 2004). The phase change affecting the thermal properties was taken into account, a geothermal heat flow was applied at the bottom boundary, and mean monthly thawing and freezing n-factor characteristics of the surface conditions were used to simulate the complex heat transfer function between the air and ground surface. The climate variability at Salluit over the last decades was assessed by paleoclimatic reconstruction before 1960 (Chouinard et al. 2007), by interpolation of meteorological records at Inukjuak and Iqaluit from 1961 to 1978 (Figs. 1 and 2), by North American Regional Reanalysis (NARR) based on meteorological observations at Salluit airport from 1979 to 2001, and by meteorological observations with an automated station in the valley of Salluit from 2002 to 2007. The mean monthly and mean annual air temperatures for Salluit as reconstructed from the previous methods over the period from 1992 to 2007 appear in Figure 6. Results of numerical modeling are also given in Figure 6.

Discussion

The PS targets located on rock outcrops such as A1MIJ and A1LZW moved toward the satellite with an average velocity of about 1 mm/year (Figs. 4 and 5), which is one-fourth to one-half the rate of land emergence estimated from radiocarbon dates (Gray et al. 1993). Time series of these PS targets do not show any clear periodic variations. Most PS targets with displacement away from the satellite are located in the valley of Salluit on thaw-unstable frozen ground (Fig. 4). However, the A1MAV PS target located on a thin quaternary deposit near a rock outcrop (Fig. 3) has a positive velocity of 0.8 mm/year. The three other selected PS targets have negative velocities ranging from -3.1 to -7.4 mm/year (Figs. 4 and 5, Table 1). At these velocities, a value of 1 mm/year should be subtracted to take the postglacial uplift into account. Annual variations with amplitude close to 8 mm are superposed on the displacement

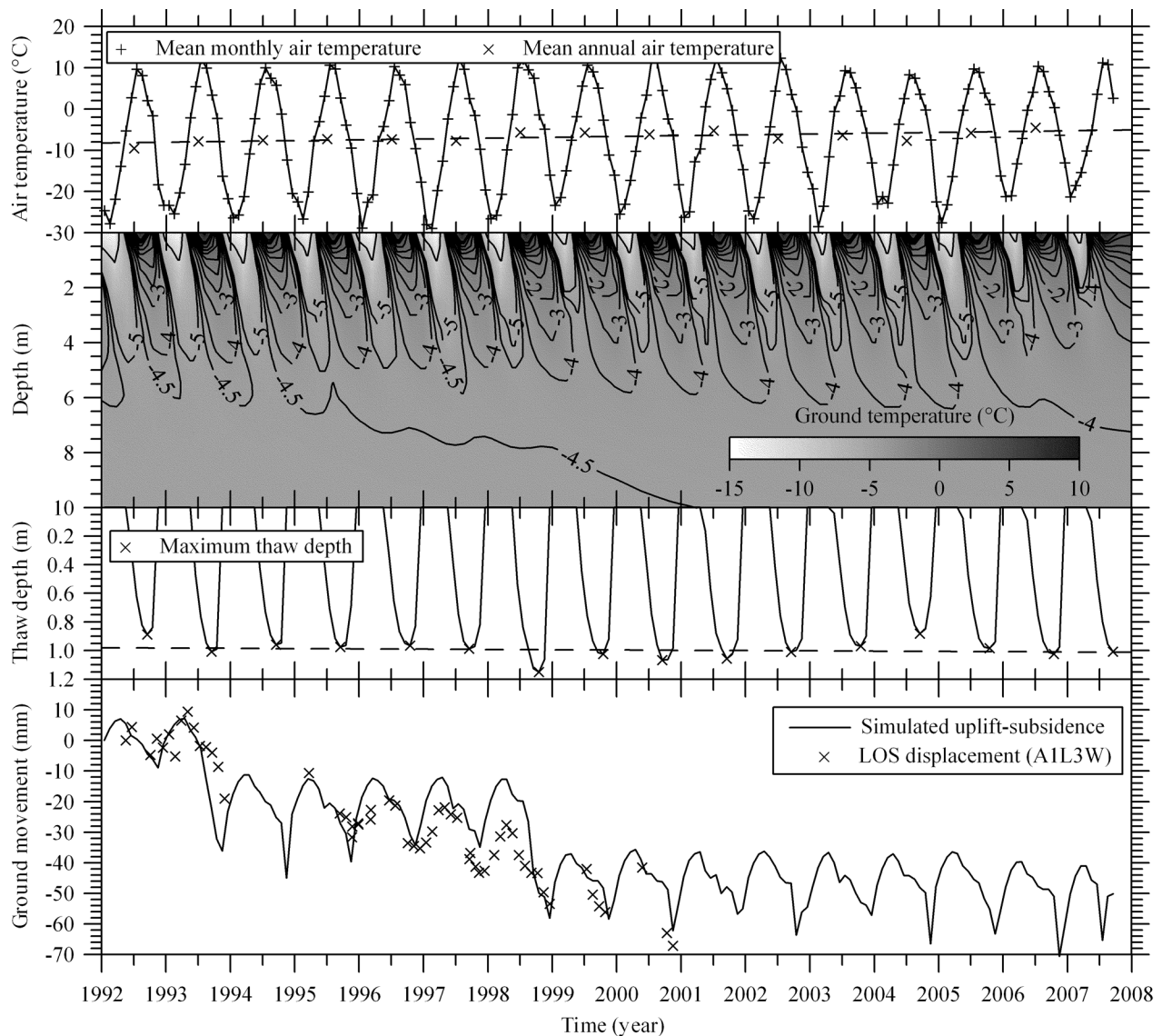


Figure 6. Variations in mean monthly and mean annual air temperature, predicted ground temperature as a function of depth, thaw depth, simulated uplift-subsidence, and LOS displacement of A1L3W PS target (see Figure 3 for the location) over the period from 1992 to 2007.

trend of the last four PS targets (Fig. 5 and Table 1). Clear fitting of a sinusoidal function with a period of one year was not obvious for the A1MAV PS target but it was much easier to fit the last three selected PS targets. Except for the A1MAV PS target, the phase shift of the fitted sinusoidal functions is 0.8 radian or 46 days for a maximum uplift occurring on May 18 ($0.8 + \pi/2$ radian or 138 days) and a maximum subsidence occurring six months later on November 16 ($0.8 + 3\pi/2$ radian or 320 days) of each year.

The mean annual air temperature at Salluit increased by $0.2^{\circ}\text{C}/\text{year}$ from 1992 to 2007 (Fig. 6). The numerical simulations show that, during the same period, permafrost at a depth of 6 m warmed by about 0.5°C (Fig. 6). An increase in the thickness of the active layer of only 2 mm/year was also simulated. However, due to the unusually warm summers in 1993 and 1998 that followed rather warm winters, the thawing front reached its greatest depth ever in the permafrost table. The maximum thaw depth was 1.01 m in 1993 relative to 0.89 m

in 1992 and 1.15 m in 1998 relative to 1.01 m in 1997 (Fig. 6). The permafrost thawing at the permafrost table induced thaw consolidation and subsidence of the ground surface. Assuming a decrease in void ratio of 15% during the thaw consolidation, the thaw subsidence was 18 and 21 mm in 1993 and 1998, respectively, due to the active layer thickening detrimental to the permafrost table. It is also assumed that the phase change occurring in the active layer during the freeze-thaw cycles and in the permafrost during the cooling-warming cycles is associated with an increase or a decrease in void ratio of 9% of volumetric water content or ice content change. Based on the previous assumptions, the annual variations in ground surface elevation were estimated (Fig. 6). Although the phase shift, amplitude, and trend of the simulated uplift-subsidence cycles are similar to those observed by remote sensing at the A1L3W PS target, there are still some discrepancies. The processes taking place in the active layer and permafrost table are too complex to be correctly simulated. The maximum uplift occurs

in May of each year according to the PSInSAR time series, while the simulated one occurs one month earlier in April. Not only does the freeze back of the active layer produce uplift, but the cooling of the frozen active layer and permafrost close to the permafrost table induces further uplift later in the freezing period—the time needed to extract the heat by conduction. The maximum subsidence occurs at the same time in November for both PSInSAR and numerical modeling when the thawing front reaches its maximum depth.

Conclusions

The PSInSAR remote sensing technique is very powerful for monitoring millimetric ground movement when multi-temporal SAR images with proper coverage are available and PS targets are present. Postglacial uplift and ground movement due to active layer thickening, permafrost warming, and freeze-thaw cycles in the active layer of only a few millimeters per year can be detected. Improvement of numerical models is needed to simulate fully coupled processes such as heat transfer by conduction and void ratio change caused by phase change and thaw consolidation.

Acknowledgments

We would like to express our sincere gratitude to the Inuit community of Salluit for its hospitality and friendly support. Funding for this project was provided by the Ministère de la Sécurité Publique du Québec. We acknowledge the major contribution to this project of Michel Allard.

References

- Allard, M., Fortier, R., Gagnon, O., & Michaud, Y. 2004. Problématique du développement du village de Salluit, Nunavik. Final report presented to the Ministère de la Sécurité Publique du Québec, 93 pp.
- Bell, J.W., Amelung, F., Ferretti, A., Bianchi, M., & Novali, F. 2008. Permanent scatterer InSAR reveals seasonal and long-term aquifer-system response to groundwater pumping and artificial recharge. *Water Resources Research* 44: 1-18.
- Chouinard, C., Fortier, R., & Mareschal, J.-C. 2007. Recent climate variations in the subarctic inferred from three borehole temperature profiles in Northern Quebec, Canada. *Earth and Planetary Science Letters* 263: 355-369.
- Couture, R., Smith, S.L., Robinson, S.D., Burgess, M.M., & Solomon, S. 2003. On the hazards to infrastructure in the Canadian North associated with thawing of permafrost. *Proceedings of the Third Canadian Conference on Geotechnique and Natural Hazards, Edmonton, Alberta, June 8-10, 2003*: 97-104.
- Ferretti, A., Prati, C., & Rocca, C. 2001. Permanent scatterers in SAR interferometry. *IEEE Transactions on Geoscience and Remote Sensing* 39: 8-20.
- Ferretti, A., Prati, F., Rocca, N., Casagli, N., Farina, P., & Young, B. 2005. Permanent scatterers technology: a powerful state of the art tool for historic and future monitoring of landslides and other terrain instability phenomena. *Proceedings of the International Conference on Landslide Risk Management, Vancouver, British Columbia, May 31-3 June, 2005*: 1-9.
- Ferretti, A., Savio, G., Barzaghi, Borghi, A., Musazzi, S., Novali, F., Prati, C., & Rocca, F. 2007. Submillimeter accuracy of InSAR time series: experimental validation. *IEEE Transactions on Geoscience and Remote Sensing* 45: 1142-1153.
- Fortier, R., LeBlanc, A.-M., & Yu, W. 2011. Impacts of permafrost degradation on a road embankment at Umiujaq in Nunavik (Quebec), Canada. *Canadian Geotechnical Journal* 48:720-740.
- Gray, J.T., Lauriol, B., Bruneau, D., & Ricard, J. 1993. Postglacial emergence of Ungava Peninsula, and its relationship to glacial history. *Canadian Journal of Earth Sciences* 30: 1676-1696.
- LeBlanc, A.-M. in prep. Modélisation tridimensionnelle du régime thermique du pergélisol de la vallée de Salluit en fonction de différents scénarios de réchauffement climatique. Ph.D. thesis, Université Laval, Québec.
- Liu, L., Zhang, T., & Warh, J. 2010. InSAR measurements of surface deformation over permafrost on the North Slope of Alaska. *Journal of Geophysical Research* 115: 1-14
- Nelson, F.E., Anisimov, O.A., & Shiklomanov, N.I. 2001. Subsidence risk from thawing permafrost. *Nature* 410: 889.
- Romanovsky, V.E., Shender, N.I., Sazonova, T.S., Balobaev, V.T., Tipenko, G.S., & Rusakov, V.G. 2001. Permafrost temperatures in Alaska and East Siberia: Past, present and future. *Proceedings of the Second Russian Conference on Geocryology, Moscow, Russia*: 301-314.
- Therrien, R., McLaren, R.G., Sudicky, E.A., & Panday, S.M. 2008. *HydroGeoSphere – A three-dimensional numerical model describing fully-integrated subsurface and surface flow and solute transport*. Québec: Université Laval, 379 pp.

Linkages between Patterned Ground, Alder Shrubland Development, and Active Layer Temperature in the Northwest Siberian Low Arctic

Gerald V. Frost, Howard E. Epstein

University of Virginia, Department of Environmental Sciences, Charlottesville, VA, USA

Donald A. Walker

Institute of Arctic Biology, University of Alaska Fairbanks, USA

Georgiy Matyshak

Lomonosov Moscow State University, Department of Soil Science, Moscow, Russia

Ksenia Ermokhina

Earth Cryosphere Institute, Siberian Branch of Russian Academy of Sciences, Moscow, Russia

Abstract

Satellite photo-comparisons indicate extensive expansion of alder (*Alnus*) shrubs since 1968 within tundra ecotones near Kharp in northwest Siberia. Field observations reveal that nearly all expansion occurred on exposed circles in patterned ground. We mapped the location of alders and circles and measured surface organic thickness, mineral soil thickness, near-surface soil temperature, shrub height, and Leaf Area Index along transects according to categories of alder stand-age. Young alders occur almost exclusively on circles that lack organic matter and competing vegetation, and are relatively warm in summer. Contrasts in the summer thermal regime of circles and inter-circles diminish during alder colonization and become reversed in older shrublands. We conclude that exposed circles comprise abundant microsites that are susceptible to shrubification in warmer areas of the Low Arctic; summer active layer temperatures decline and circles are inactivated after shrubification, as organic matter buildup and canopy shading reduce the potential for differential frost heave.

Keywords: alder; Arctic; patterned ground; permafrost; shrub expansion; Siberia.

Introduction

Multiple lines of evidence indicate that the abundance of erect shrubs is increasing in the Low Arctic. Experimental studies and simulation modeling have repeatedly shown that expansion of deciduous shrubs is one of the most likely land-cover changes to accompany climate warming in Low Arctic tundra (e.g., Chapin et al. 1995). Recent shrub proliferation has been well documented by observational studies in the North American Arctic, particularly in northern Alaska (e.g., Tape et al. 2006). Shrub expansion in the Eurasian Arctic, however, has received less attention. Here we explore linkages between cryogenic patterned ground and rapid expansion of alder (*Alnus fruticosa* ssp. *sibirica*) within a tundra ecotone near Kharp, Yamalo-Nenets Autonomous Okrug, northwest Siberia (Fig. 1).

Shrub expansion in tundra-dominated regions alters ecosystem structure and can initiate a suite of changes to biophysical attributes of arctic landscapes, including plant community composition (Walker et al. 2006), surface energy balance (Chapin et al. 2005), hydrology (Sturm et al. 2001), and ground thermal regime (Blok et al. 2010). Blok et al. (2010) found that active layer temperatures declined with increasing cover of low shrubs in northeast Siberian tundra. Such findings suggest that even as warming-induced shrub expansion exerts a positive feedback on atmospheric temperature by reducing surface albedo, shading by expanding shrub canopies could buffer permafrost from the effects of warming.

Expansion of alder in tundra-dominated areas represents a fundamental change to the ecosystem state because alder

commonly reaches heights ≥ 2 m and can greatly overtop tundra vegetation and winter snowpack. Thus the development of tall shrublands in tundra is likely to have particularly strong effects on albedo, surface energy balance, hydrology, and, therefore, the thermal regime of permafrost.

Previous studies in the Low Arctic show that alder expansion tends to occur in parts of the landscape that are regularly disturbed, such as floodplains and colluvial slopes (Tape et al. 2006). It also occurs locally after episodic disturbances such as wildfire and retrogressive thaw-slumping (Lantz et al. 2009). Disturbed sites usually lack competing vegetation and the thick accumulations of organic material that are otherwise common in arctic environments. A mechanism for shrubification that has not been previously documented is colonization of mineral-dominated microsites in areas of patterned ground.

Patterned ground features (PGFs) are more or less ubiquitous in arctic landscapes (Washburn 1980). The attributes and mode of formation of PGFs vary according to many factors including climate, soil texture, vegetation cover, and landscape age. Non-sorted circles are common PGFs that are maintained by annual disturbance, which occurs due to sharp gradients in soil thermal properties between circles and inter-circles (Peterson & Krantz 2003). Vegetation and organic matter insulate the subsurface and tend to develop in inter-circle areas; during winter freeze-up, unvegetated circles freeze much more rapidly than inter-circles, resulting in differential frost-heave. Thus the disturbance regime of circles differs from that of permafrost thaw features because disturbance is not episodic but instead is renewed annually.

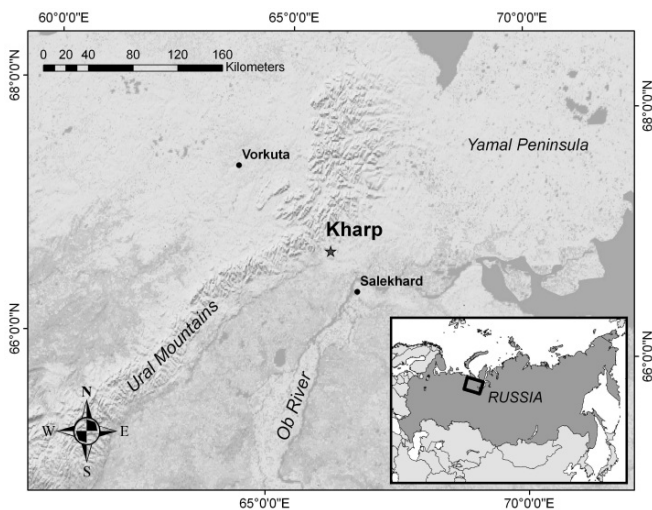


Figure 1. Map of the southern Yamal region showing location of the Kharp study area.

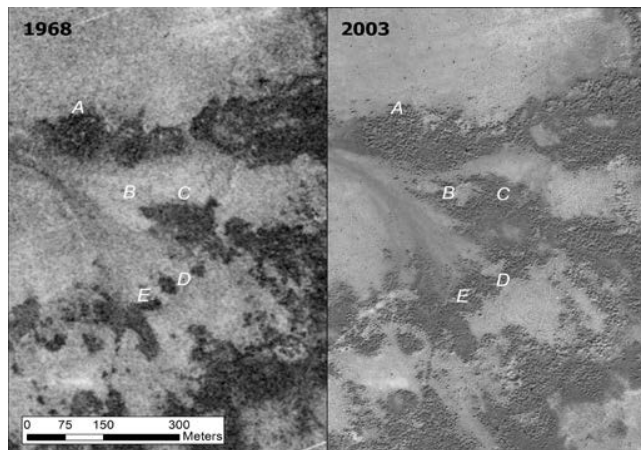


Figure 2. Comparison of 1968 (Corona) and 2003 (QuickBird) imagery showing part of the Kharp study area. Letters indicate areas with recently established alder cover.

During a brief reconnaissance in 2009, we observed that circles are widespread and extensive at Kharp, and it appeared that young alders were concentrated on the exposed centers of circles. These observations prompted us to organize a field expedition to determine important geomorphic site characteristics associated with alder expansion and to evaluate consequences to the ground temperature regime that result from shrubland development.

The objectives of field studies were to (1) test the hypothesis that alder expansion is facilitated by circles; (2) determine if an initial pattern of recruitment on circles explains the distribution of alders in older shrublands; and (3) evaluate changes in the summer active layer thermal regime that occur during shrubland development.

Methods

Study area

We conducted field studies in a 64-km² forest-tundra ecotone in the foothills of the polar Ural Mountains near the

town of Kharp (66.83°N, 65.98°E). Terrain in the study area varies from ~200 to 300 m elevation and consists of gently sloping low hills separated by small alluvial valleys. Common vegetation communities include dwarf shrub tundra dominated by dwarf birch (*Betula nana*) and ericaceous shrubs <30 cm in height; low scrub dominated by dwarf birch and willows (*Salix* spp.); tall alder scrub strongly dominated by alder; and sparse woodlands of Siberian larch (*Larix sibirica*). The Kharp region experiences a continental subarctic climate. Long-term meteorological records at Salekhard, ~35 km southeast of Kharp, indicate a mean annual temperature of -6.5°C and mean annual precipitation of 464 mm.

Sorted and non-sorted circles are common and widespread at the Kharp site. The surficial geology of the area is dominated by ultramafic rocks, which weather directly to silt- and clay-sized particles; the prevalence of fine-grained mineral soils is conducive to differential frost-heave. The size and spacing of circles vary across the study area but typically occur at one of two scales: small non-sorted circles ~70 cm in diameter and spaced ~2 m apart, and larger sorted-circles circles ~2 m in diameter and spaced ~4 m apart. Non-sorted circles are separated by narrow, stony inter-circles that are covered by vegetation. Among sorted-circles, inter-circles typically contain large blocks that often remain barren in exposed locations.

Visual comparison of high-resolution satellite images from 1968 (KH-4B “Corona”) and 2003 (QuickBird) indicates that alder shrubland extent increased ~10% over the 35-year interval (Fig. 2). Using this imagery, we identified expanding and unchanged shrublands for field sampling.

Field data collection

We established a series of transects according to four categories of alder stand-age: tundra, alder colonization zone, mature shrubland, and paludified shrubland (Fig. 3). Tundra transects were placed in alder-free areas of patterned ground adjacent to colonization zones. Colonization zones were along the margins of alder thickets that had not developed until after 1968. Vegetation and geomorphic features in colonization zones were comparable to the tundra transects, except that circle centers were dominated by young alders (<30 cm tall). Mature shrublands were dominated by large alders (typically >2 m in height) that were already evident in 1968 imagery. Paludified shrublands were characterized by open stands of very old alders, often with low vigor (e.g., many moribund or dead ramets), occurring on sites with heavy moss cover, a thick surface organic layer, and wet soils. Observations of soil profiles, alder characteristics, and the spatial distribution of shrublands indicated that the three alder stand-ages described above correspond to a chronosequence of successional stages, and therefore are representative of changes in the summer active layer thermal regime that occur during alder shrubland development over multi-decadal to centennial timescales.

Transect size varied depending on the density of alders and PGFs (20–100 m length, 4–10 m width); we established larger transects where PGFs and alders were widely spaced in order to obtain adequate sample size. We established three transects in each stand-age. At each transect, we made systematic

measurements of surface organic depth, thaw depth/depth to rock, and Leaf Area Index (LAI) at 50-cm intervals (20 m transects) or 1-m intervals (longer transects) along the transect centerline. Transects were placed in areas with homogeneous vegetation and geomorphology, so we assumed that the centerline measurements represented mean conditions. We also recorded surface organic depth and thaw depth/depth to rock at the base of each alder, regardless of size, within each transect. From the soil profile measurements, we calculated the total mineral soil thickness (thaw depth/depth to rock minus surface organic depth). Most thaw probe measurements were of depth to rock (usually frost-shattered blocks), rather than thaw depth. Soil profile measurements were made with a steel thaw probe, and LAI was measured using a LAI-2000 Plant Canopy Analyzer (LI-COR Biosciences, Lincoln NE, USA).

We mapped the locations of alders and the centers of exposed sorted-circles within the transects using X/Y coordinates. When possible, we visually recorded the microsite in which alders were rooted (e.g., center of active circle, margin of active circle, inter-circle). We also measured the height of the dominant ramet of each individual alder. Finally, we embedded 5–10 Thermochron iButton dataloggers (Embedded Data Systems LLC, Lawrenceburg, KY, USA) to measure microsite variation in soil temperature along 1–2 transects in each stand-age. iButtons were distributed at the base of alders and in alder-free inter-circles. All iButtons were placed at a depth of 5 cm; an additional iButton was placed in a shaded location at a height of 2 m to record air temperature at each transect. All iButtons recorded temperatures simultaneously at 4-hour intervals during the 5-day period July 27–August 1.

Data analysis

In order to test if alder establishment is facilitated by circle microsites, we compared surface organic depth and mineral soil thickness between transect centerlines and alders within each stand-age. We also computed the mean soil temperature for each iButton datalogger and compared these means between circles and inter-circles for each stand-age. In order to characterize changes in active layer summer thermal regime that occur during shrubland development, we compared surface organic depth and mean soil temperature for transect centerlines and alders across stand-ages. We also compared LAI and shrub height across stand-age.

We applied two-tailed T-tests for comparison of normally distributed variables, and non-parametric Kruskal-Wallis tests for non-normally distributed variables. We used SAS 9.2 (SAS Institute, Inc., Cary NC, USA) for all statistical procedures. Finally, we generated time series for circle and inter-circle soil temperature for each stand-age; this was done by computing the mean temperature for each time-step and interpolating the time-steps across the 5-day observation period.

Results

Soil properties

Surface organic depth and mineral soil thickness for transect centerlines and alders show strong and consistent patterns of

variation across all stand-ages. Surface organic depth was significantly less, and mineral soil thickness was significantly greater, for alders relative to the centerline measurements (Kruskal-Wallis; $p < 0.001$ for all stand-ages) (Table 1). Mean surface organic depth increases monotonically with increasing alder stand-age.

Transect mapping

In colonization zones, where circle centers were seldom covered by vegetation, observed locations of alders and circles indicated that alder recruitment occurred almost exclusively on exposed circles. Of 272 alders recorded in colonization zones, only 2 were found emerging from inter-circles. Most alders occurred along circle margins rather than in the central part of the circle. This distribution pattern was often visible as a ring of small alders growing around circle margins. In mature and paludified shrublands, circles were usually not visible, but alders typically displayed a distribution pattern of more or less uniformly spaced clumps, similar to what we observed in colonization zones. Where exposed circles did occur in mature and paludified shrublands, we frequently observed seedlings and/or saplings growing on them except on very wet sites.

Active layer temperature and shrub canopy attributes

Mean soil temperatures are warmer at circles than at inter-circles in tundra and colonization zones (T-test; $p < 0.05$) (Table 2). This pattern is reversed in paludified shrublands (T-test; $p < 0.05$). Mean temperatures are not significantly different between microsites in mature shrublands.

Across stand-ages, mean soil temperature at circles declines monotonically from one shrubland stage to the next (T-test; $p < 0.05$). The same pattern is evident at inter-circles, except that there is no significant difference in mean soil temperature between the tundra and colonization stages. LAI and shrub height increase monotonically from tundra to mature stages but decline from the mature to paludified stages (T-test; $p < 0.05$).

Temperature time series for tundra transects show strong microsite variation in mean temperature, maximum temperature, and diurnal variability for circles and inter-circles (Fig. 4). Circle soil temperatures closely track air temperature and are usually $\sim 2^\circ\text{C}$ warmer than adjacent inter-circles. Diurnal fluctuations in temperature are $\sim 6^\circ\text{C}$ for circles and only $\sim 3^\circ\text{C}$ for inter-circles. Microsite variation in temperature is qualitatively similar in alder colonization zones, but the differences are less pronounced. In mature shrublands, the pattern of microsite variation seen in earlier stand-ages is reversed as circle soil temperatures are less variable than at inter-circles. A qualitatively similar pattern exists for paludified shrublands, but there is a sharp decline in temperature for all microsites.

Discussion

Microsite facilitation of alder recruitment

Our field observations, in conjunction with remote-sensing data spanning five decades, demonstrate that rapid and widespread alder expansion has occurred in areas of PGFs at

Table 1. Means and sample sizes of surface organic depth and mineral soil thickness measurements by stage. Ranges are given in parentheses.

| Stage | Surface organic depth (cm) | | Mineral soil thickness (cm) | | n | |
|--------------|----------------------------|-------------|-----------------------------|-------------|----------|--------|
| | Transect | Alders | Transect | Alders | Transect | Alders |
| tundra | 5.7 (0-16) | - | 7.3 (0-33) | - | 22 | |
| colonization | 7.2 (0-27) | 1.1 (0-11) | 9.8 (0-45) | 28.5 (0-69) | 82 | 272 |
| mature | 9.4 (0-38) | 4.3 (0-16) | 12.2 (0-87) | 34.4 (4-96) | 158 | 71 |
| paludified | 25.2 (10-44) | 14.3 (7-25) | 21.0 (0-61) | 44.3 (0-79) | 101 | 59 |

Table 2. Mean and sample size of soil temperature, LAI, and alder height measurements by stage. Standard deviation is given in parentheses.

| Stage | Soil temperature (°C) | | | | LAI | | Shrub height (cm) | |
|--------------|-----------------------|-----------|--------------|--------|-----------|-----|-------------------|-----|
| | Mean | | n | | Mean | n | Mean | n |
| | Inter-circle | Circle | Inter-circle | Circle | | | | |
| tundra | 8.9 (0.4) | 9.9 (0.3) | 7 | 7 | 0.3 (0.3) | 22 | - | - |
| colonization | 8.6 (0.4) | 9.2 (0.5) | 8 | 7 | 0.6 (0.5) | 144 | 23.5 (40.0) | 272 |
| mature | 7.2 (0.5) | 6.6 (1.5) | 6 | 6 | 2.0 (1.0) | 111 | 173.1 (119.9) | 72 |
| paludified | 5.6 (1.2) | 3.7 (0.4) | 6 | 5 | 1.3 (0.7) | 101 | 90.5 (50.3) | 59 |

Kharp. Mean surface organic depth was much less, and mineral horizon thickness much greater, at alders relative to transect centerlines in colonization zones. These measurements, along with the observed distribution pattern of young alders on exposed circles, show that exposed circles facilitate alder recruitment at Kharp.

Unvegetated circles are common across the arctic tundra biome because they are annually disturbed, and most arctic plants grow too slowly to become established during the short growing season. We suggest that alder is able to exploit these circle microsites in warmer parts of the Low Arctic for several reasons. First, alder is a boreal species with much higher potential growth rates than tundra plants. Second, alder seeds are minerotrophic, and seedling survivorship is higher on mineral versus organic soils (Chapin et al. 1994). Third, alder is an N_2 -fixing species, which may enable it to maintain rapid growth on mineral-dominated soils that lack organic N. Finally, although active circles are annually disturbed by differential frost heave, and there is probably high mortality of alder seedlings, circles are favorable seedbeds for alder because soils are warm and there is little competing vegetation.

Legacy of recruitment pattern in alder shrublands

Surface organic depth was much less, and mineral horizon thickness much greater, at alders relative to transect centerlines in mature and paludified shrublands. Although most PGFs were obscured from view in mature and paludified shrublands, subsurface profiles at alders indicate that adult shrubs occupy circle microsites that had become covered by vegetation and organic matter. In mature shrublands, we seldom observed alder seedlings except on a few remaining exposed circles; we almost never recorded seedlings in paludified stands. Therefore, we conclude that (1) the spatial distribution of adult alders is consistent with initial recruitment on circles; and (2) alder recruitment slows dramatically as soil temperatures

decline and circles become covered by vegetation and organic material. Chapin et al. (1989) identified intense nutrient competition as the primary factor driving uniform spacing of alders at an Alaskan site. However, we conclude that patterns of initial recruitment alone are adequate to explain the distribution of shrubs in open alder shrublands (“savannas”) at Kharp.

Alder is a long-lived species; in Interior Alaska, the same species persists from early to late succession in boreal forest despite dramatic changes in soil conditions and competition (Mitchell & Ruess 2009). Observations of alders in paludified shrublands indicate that most shrubs are very old and have slow current rates of growth (e.g., abundant bud scars on small twigs, short internodes and ramet height). Mean circle soil temperature beneath shrubs was 5.5°C lower in paludified shrublands relative to colonization zones. Additionally, the organic-rich soils in paludified shrublands retained water and were frequently saturated at shallow depth. Although adult alders are capable of tolerating cold, wet soils, these conditions are unfavorable for alder recruitment. This would explain in part how “hotspots” of expansion at Kharp are inter-mixed with areas in which shrub cover is identical to that in 1968.

Implications for permafrost

Soil temperature profiles recorded at the Kharp transects indicate that a sequence of changes in microsite and overall active layer thermal regime occur during alder shrubland development in pattered ground. In tundra, prior to alder establishment, temperature profiles of circle centers and inter-circles contrast sharply in mean and maximum temperature and diurnal variability. Circle soil temperatures closely track atmospheric temperature because surface organic material (which reduces thermal conductivity) and overtopping vegetation (which intercepts incident solar radiation) are lacking. These sharp gradients in soil thermal properties



Figure 3. Sample photographs of transects in (top to bottom) tundra (foreground only), alder colonization zone, mature shrubland, and paludified shrubland. Note the low stature of alders in the paludified shrubland.

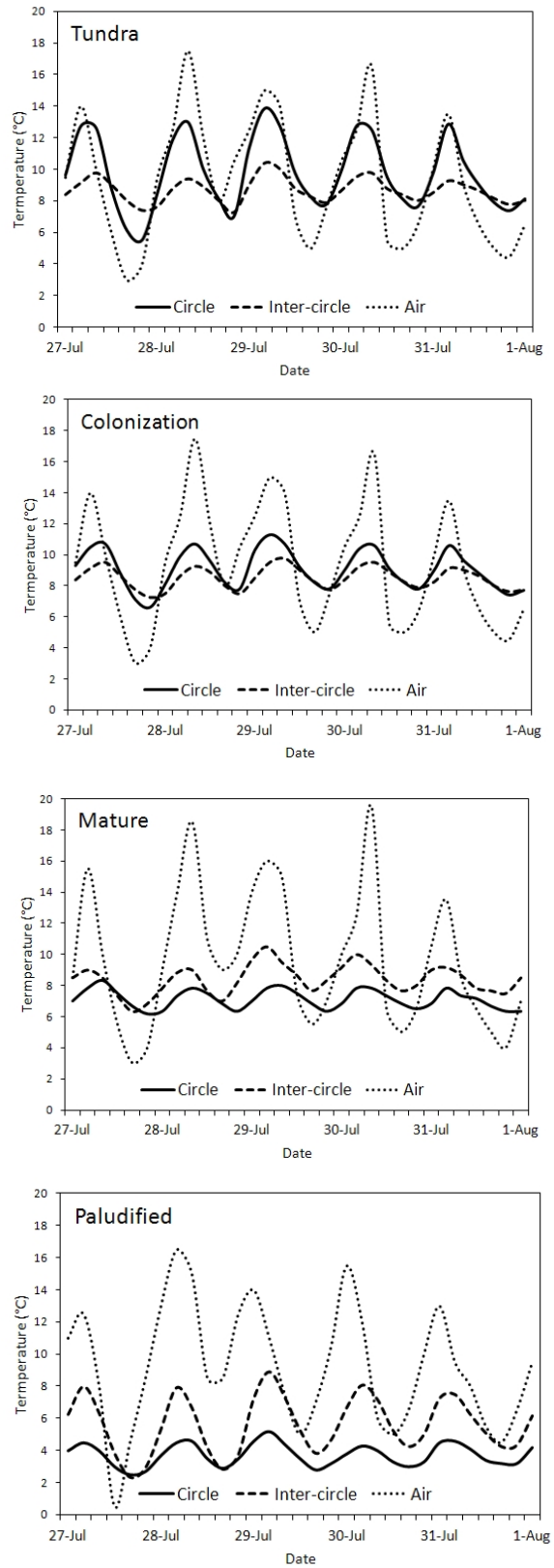


Figure 4. Soil- and air temperature time series recorded along four transects in (top to bottom) tundra, alder colonization zone, mature shrubland, and paludified shrubland. For soil time series, curves are interpolated to mean temperatures for 3 iButtons.

promote differential frost heave as soils freeze in early winter (Peterson & Krantz 2003), maintaining annual disturbance on circles.

Following alder colonization, microsite differences in soil temperature diminish. Our data suggest that this may occur quickly—within only a few years—as diurnal variability in circle soil temperature is significantly lower in colonization zone transects relative to alder-free tundra, with only modest increases in LAI and shrub height. As alders mature and understory vegetation develops, the initial microsite thermal gradient observed in tundra becomes reversed, with circle soils cooler than at inter-circles. This reversal intensifies in moisture-gathering parts of the landscape that are prone to paludification (e.g., toe slopes and lowlands), likely due to positive feedbacks between soil moisture, moss growth, and organic matter accumulation.

A recent dendrochronology study of shrubs at a site ~130 km northeast of Kharp indicates contemporaneous increases in summer temperatures and shrub productivity in recent decades (Forbes et al. 2010), suggesting that climate warming may have played a role in alder expansion at our site. If so, what are the likely implications of land-cover change and climate warming on permafrost at Kharp? Our soil temperature data indicate that alder shrubland development strongly buffers permafrost from changes in atmospheric temperature in the summer. Early in shrubland development, this buffering effect is primarily due to shading by alder canopies, as there is little surface organic matter beneath the colonizing shrubs. As alders grow larger and organic matter begins to accumulate, reduction in differential frost-heave and increased snow-trapping likely allows other vegetation to spread onto circle microsites. The proliferation of vegetation—especially mosses—plays a key role in reducing soil temperature by lowering thermal conductivity. As shrublands age and organic matter accumulates, ground- and atmospheric temperatures become increasingly uncoupled and there is a cessation of cryogenic disturbance.

We conclude that (1) exposed circles in the southernmost Low Arctic are susceptible to rapid changes in land-cover and ecosystem state because they comprise favorable seedbeds for fast-growing, minerotrophic shrubs such as alder; (2) spatial patterns of alder colonization are persistent and may explain the uniform spacing of shrubs in Low Arctic alder “savannas;” (3) shrubland development initiates a cascade of effects on summer soil thermal properties and energy balance due to canopy shading and deposition of organic matter; (4) canopy shading buffers the active layer against atmospheric warming driven by local reductions in albedo and larger-scale forcings; and (5) the breakdown and reversal of microsite thermal gradients following shrub expansion result in inactivation of circles and greatly diminish cryogenic disturbance.

Acknowledgments

This work was funded by the NASA/NEESPI Land-Cover and Land-Use Change Initiative, grants NNG6GE00A and NNX09AK56G, and the Department of Environmental

Sciences at the University of Virginia. We also thank Marina Leibman and Roman Ivanov, Earth Cryosphere Institute, for their indispensable help with field logistics.

References

- Blok, D., Heijmans, M., Schaepman-Strub, G., Kononov, A., Maximov, T., & Berendse, F. 2010. Shrub expansion may reduce summer permafrost thaw in Siberian tundra. *Global Change Biology* 16:1296-1305.
- Chapin, F.S., III, McGraw, J.B., & Shaver, G.R. 1989. Competition causes regular spacing of alder in Alaskan shrub tundra. *Oecologia* 79:412-416.
- Chapin, F.S., III, Walker, L.R., Fastie, C.L., & Sharman, L.C. 1994. Mechanisms of primary succession following deglaciation at Glacier Bay, Alaska. *Ecological Monographs* 64:149-175.
- Chapin, F.S., III, Shaver, G.S., Giblin, A.E., Nadelhoffer, K.J., & Laundre, J.A. 1995. Responses of Arctic tundra to experimental and observed changes in climate. *Ecology* 76:694-711.
- Chapin, F. S., III, Sturm, M., Serreze, M.C., McFadden, J.P., Key, J.R., Lloyd, A.H., McGuire, A.D., Rupp, T.S., Lynch, A.H., Schimel, J.P., Beringer, J., Chapman, W.L., Epstein, H.E., Euskirchen, E.S., Hinzman, L.D., Jia, G., Ping, C.L., Tape, K.D., Thompson, C.D.C., Walker, D.A., & Welker, J.M. 2005. Role of land-surface changes in arctic summer warming. *Science* 310:657-660.
- Forbes, B.C., Fauria, M.M., & Zetterberg, P. 2010. Russian Arctic warming and ‘greening’ are closely tracked by tundra shrub willows. *Global Change Biology* 16:1542-1554.
- Lantz, T.C., Kokelj, S.V., Gergel, S.E., & Henryz, G.H.R. 2009. Relative impacts of disturbance and temperature: persistent changes in microenvironment and vegetation in retrogressive thaw slumps. *Global Change Biology* 15:1664-1675.
- Mitchell, J.S. & Ruess, R.W. 2009. N₂-fixing alder (*Alnus viridis* spp. *fruticosa*) effects on soil properties across a secondary successional chronosequence in interior Alaska. *Biogeochemistry* 95:215-229. doi: 10.1007/s10533-009-9332-x.
- Peterson, R.A. & Krantz, W.B. 2003. A mechanism for differential frost heave and its implications for patterned ground formation. *Journal of Glaciology* 49:69-80.
- Sturm, M., Douglas, T., Racine, C., & Liston, G.E. 2005. Changing snow and shrub conditions affect albedo with global implications. *Journal of Geophysical Research—Biogeosciences* 110:1–13, doi 10.1029/2005JG000013.
- Tape, K., Sturm, M., & Racine, C. 2006. The evidence for shrub expansion in northern Alaska and the Pan-Arctic. *Global Change Biology* 12:686-702.
- Walker, M.A., et al. 2006. Plant community response to experimental warming across the tundra biome. *Proceedings of the National Academy of Sciences* 103:1342-1346.
- Washburn, A.L. 1980. *Geocryology: a survey of periglacial processes and environments*. New York, John Wiley, 406 pp.

Fine-Scale Spatio-Temporal Monitoring of Multiple Thermo-Erosion Gully Development on Bylot Island, Eastern Canadian Archipelago

Etienne Godin, Daniel Fortier

*University of Montreal, Geography Department, Montreal, QC, Canada
Center for Northern Studies, Laval University, Quebec, QC, Canada*

Abstract

Water infiltrating ice-wedge contraction cracks can enable the formation of tunnels in the permafrost, leading to collapse and thermo-erosion gully initiation. The valley of Glacier C-79 on Bylot Island in Canada features dozens of thermo-erosion gullies, ranging from a few meters up to 2 km in main axis length. Five of the largest gullies were chosen for fine-scale spatio-temporal monitoring between 1958 and 2011 using field observations, differential GPS mapping, and aerial and satellite imagery from 1958, 1961, 1972, 1982, 2007, and 2009 to 2011. Gullies developed in aeolian, colluvial, and organic depositional environments. Two gullies were nearly stabilized while three were evolving during the 2007–2011 period at rates ranging from $14 \pm 3 \text{ m y}^{-1}$ to $25 \pm 4 \text{ m y}^{-1}$. One gully mouth has eroded over $82 \pm 6 \text{ m}$ in length during the last three decades by riverbank erosion. Two gullies were formed before 1958, while the other three were initiated at least after 1972 but before the current decade.

Keywords: permafrost; thermo-erosion; ice wedges; gullies; mapping; long-term monitoring; high Arctic; change detection.

Introduction

Ice-wedge polygons are widespread in continuous permafrost terrain characterizing the valley of Glacier C-79 on Bylot Island. Ice wedges grow during spring when water from streams or snowmelt runoff infiltrates thermal contraction cracks and refreezes in contact with the frozen ground to form an ice vein. Several cycles of cracking, water infiltration, and refreezing enable ice-wedge enlargement. Infiltration of concentrated flow into thermal contraction cracks can, in turn, enable the formation and expansion of underground tunnels directly in the ice wedges and the permafrost. Convective heat transfer between flowing water and ice contributes to ground ice melting, permafrost thawing, and tunnel development by thermo-erosion. Repeated water infiltration can enable tunnel enlargement, which regularly leads to tunnel roof brittle failure and collapse, resulting in gully inception. Once the gully is initiated, positive feedback effects can contribute to its rapid development, essentially according to ice wedge location in the ground, and eroding up to several tens of meters per year (Fortier et al. 2007). Gullies in this study were exclusively located on low topographic gradient glacio-fluvial river terraces at the bottom of a U-shaped, glacially eroded valley. In most cases, gullies were expanding and developing in humid low-center ice-wedge polygons representative of the area.

Thermo-erosion gullies in permafrost environments have been observed and studied in several areas of the Northern and Southern hemispheres (e.g., Leffingwell 1919, Hyatt 1992, Mackay 1997, Sidorchuk 1999, Levy et al. 2008, Rowland et al. 2010). While thermo-erosion gullies are mentioned in a few papers, much work needs to be done on the long-term spatio-temporal dynamics of thermo-erosion gullying at a fine-scale level.

The objective of this paper is to present the spatio-temporal development of five thermo-erosion gullies (between ~300 and >1000 m in length) over the period 1958 to 2011, using historical air photography, satellite imagery, and field observations.

Site Characterization

The study site is located in the valley of Glacier C-79 on the southwestern plain of Bylot Island ($73^{\circ}9'N$, $79^{\circ}57'W$) in the Canadian Arctic Archipelago (Fig. 1). The valley is ~65 km² in area, ~17 km long, and $4 \pm 1 \text{ km}$ wide. It is oriented ENE-WSW and bordered by plateaus ~500 m a.s.l. (Fig. 2). The plateau remnants are deeply incised, and alluvial fans are being formed near the base of the valley walls. A braided river flows from the glaciers at the valley head in a sandur, forming a delta in the Navy Board Inlet. On each side of the proglacial river, syngenetic ice-wedge polygon terraces have developed and aggraded since the Late Holocene (Fortier et al. 2004). The terraces are primarily composed of fine to coarse aeolian

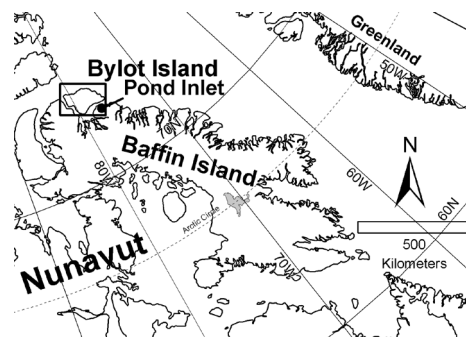


Figure 1. The study site is located on Bylot Island, in the Canadian Arctic Archipelago, ~85 km northwest of the village of Pond Inlet.

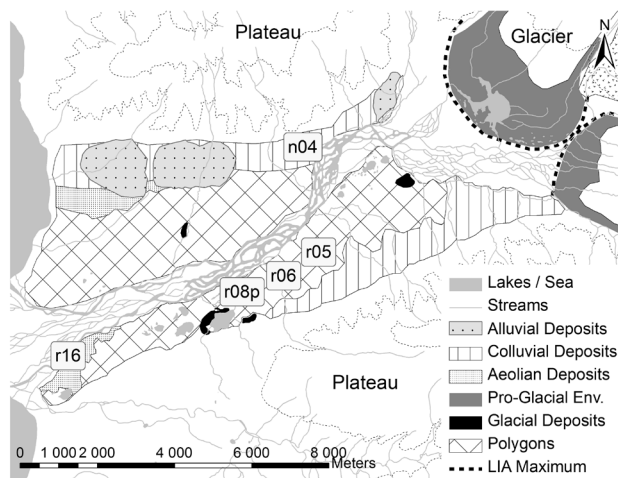


Figure 2. Valley of glacier C-79 geomorphic map, based on Allard (1996) and Klassen (1993). Gully (r05, r06, r08p, r16, and n04) locations are indicated on the map. The dashed line named LIA refers to the Little Ice Age terminal moraine.

silts mixed with poorly decomposed peat. Ice-wedge polygons observed in the valley are either low-centered, high-centered, or flat. Three types of sedimentary environments are active in the valley: 1) aeolian deposition (sand) near the deltaic area adjacent to the Navy Board Inlet; 2) fen peat accumulation with an aeolian component (loess); and 3) colluvial and mass movement deposition (silt to boulders diamicton) at the base of the plateaus. The mean annual temperature (1971–2000) measured at Pond Inlet airport (72°41'N, 77°57'W), some 85 km southeast of the study site, is -15.1°C. Average annual total precipitation (mostly in the form of snow) is around 190 mm (Environment Canada 2002). Permafrost thickness has been estimated to be at least 400 m in the study region (Heginbottom 1995). Active layer depth usually varies between 50 and 60 cm in peaty-silt deposits and up to 1 m in sand and gravel deposits (Fortier et al. 2006).

Methods

The geomorphological features and topographic contours of 36 gullies have been mapped in the valley of Glacier C-79 using a Differential GPS (DGPS) since 2009: six on the northern bank and thirty on the southern bank of the proglacial river. For the current study, only larger active thermo-erosion gullies have been mapped, but several smaller gullies were also observed. The gullies selected for analysis were chosen according to the following criteria: 1) the gully must have been studied in the field; 2) the gully must be large enough to be identified on aerial photography (up to scale = 1:70,000); 3) satellite imagery and aerial photography must be cloud-free over the gullied area; 4) the study area must cover active and nearly stabilized gullies; and 5) gullying in aeolian, organic, and colluvial depositional environments must be included.

Gullies were mapped using a DGPS in 2009, 2010, and 2011. The DGPS used to characterize the gully was a Trimble Pathfinder Pro XRS with a TSC1 data collector. Differential

correction was applied to the DGPS readings by using recordings from Thule reference station, Greenland (496 km from Glacier C-79 valley). (For additional details, see Godin and Fortier 2010). DGPS precision (x,y,z) after differential post-processing was 0.5–1 m for 99% of the records. Post-processed data were transferred to a geographic information system (GIS) built with ESRI's ArcGIS v10.

High-resolution satellite imagery (IKONOS mid-July 2007, 1 pixel = 1 m, GeoEye early September 2010, 1 pixel = 0.5 m) and aerial photography of the study site obtained from the Canadian National Air Photo Library for late June 1958, late July 1961 (scale = 1:60,000), June to August 1972 (1:15,000), and early July to early August 1982 (1: 70,000) were imported in the GIS.

Airborne images were co-registered with the satellite image with a RMSE value ranging from 1.6 m to 30 m (mean RMSE ≈ 17 m). Ten to 12 ground control points were used to register each image. A 2nd to 3rd order polynomial transformation and a nearest neighbor re-sampling was applied to the registration process.

The DGPS mapped gully layer was used as a reference to measure gully development over time. Changes in areas on older or more recent gullies were compared to the reference gully and were manually delineated, thus defining gully sizes for 1958, 1961, 1972, 1982, and 2007. Gully metrics were computed using the 'Measure' tool on each redrawn gully to estimate the length and area for each time segment.

Manual gully delineation implied a level of subjectivity on the subsequent geospatial results generated. The uncertainty was computed based on image resolution. This uncertainty was based on a conservative maximum interpretation error of 0.5 mm on any measurement taken on the images: 1958 and 1961 (scale = 1:60,000, uncertainty = 30 m), 1972 (1:15,000, uncertainty = 7 m), and 1982 (1: 70,000, uncertainty = 35 m). These uncertainty values were used in a relative RMSE calculation for computed length and areas.

Gully Developing in an Aeolian Depositional Environment

The gully r16 developed in an ice-wedge polygon network on the south bank of the braided river ~1.5 km from the delta connecting the river to Navy Board Inlet. The main channel of the gully connected to the proglacial braided river. The gully was incised into an aeolian depositional environment grading into an aeolian-organic transition zone, which is darker on Figure 3. This transitional zone featured some low-centered ice-wedge polygons with ponds and very sparse vegetation. The main body of the gully developed in a dominantly flat surface composed of coarse to fine sand in which ice wedges formed. The gully was already well developed in 1958, and its boundaries did not change significantly during the 1958–1982 period. The gully channel width varied from 10 m downstream to less than 1 m in the gully head area.

Figure 3 shows riverbank erosion where the gully mouth was located in 1958. On the 1982 image, a river channel was migrating toward the bank, but no significant erosion of the

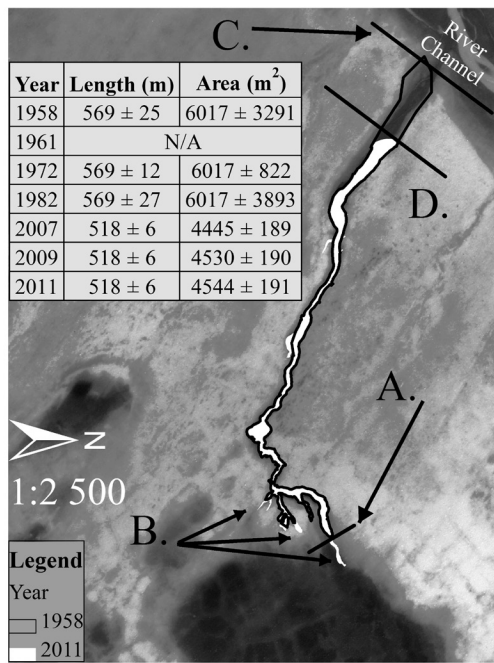


Figure 3. The background image shows the 1972 aerial photography of gully r16 (Fig. 2). Black gully contours show the 1958–1982 gully layout; A) head position for that period; B) 1982–2011 development. Bank erosion between 1982 and 2007 helped to reduce the gully size from C to D. The river channel is shown in the upper right corner.

gully had begun. The gully contours in white, as mapped with the DGPS in 2009 (Fig. 3D), clearly show the recession of the bank compared to the 1958 location of the gully (Fig. 3C). The estimated eroded bank width between 1982 and 2007 was 82 ± 6 m. Consequently, the overall length decreased from 569 ± 25 m to 518 ± 6 m during the 1982–2007 period, while the main channel in the gully head area increased by 30 ± 6 m (Fig. 3A.). Small (few meters) branches and slumps contributed to enlarging the gully slightly during this 35-year period (Fig. 3B). Between 2007 and 2011, the gully length did not increase, but erosion resulted in an overall area increase of $\sim 99 \pm 28$ m².

Gully Developing in a Colluvial Depositional Environment

Gully n04, located in a colluvial depositional environment on the north bank of the braided river, was first observed on the 2007 IKONOS image. On the 1972 and earlier images there was no gully, but rills and water tracks were running over the area where the gully eventually developed. No information could be extracted from the 1982 photo-interpretation due to cloud cover over the gully location. This gully, shown in Figure 4, therefore initiated during the 1972–2007 period, and the gully main axis length was estimated to be 365 ± 5 m in 2007 with an overall calculated area of $4,566 \pm 191$ m² (average 10 ± 1 m y⁻¹ and $\sim 130 \pm 32$ m² y⁻¹ over 35 years). During the DGPS field survey in 2010, this linear gully was affected by thermo-erosion mainly at its head via tunnels and

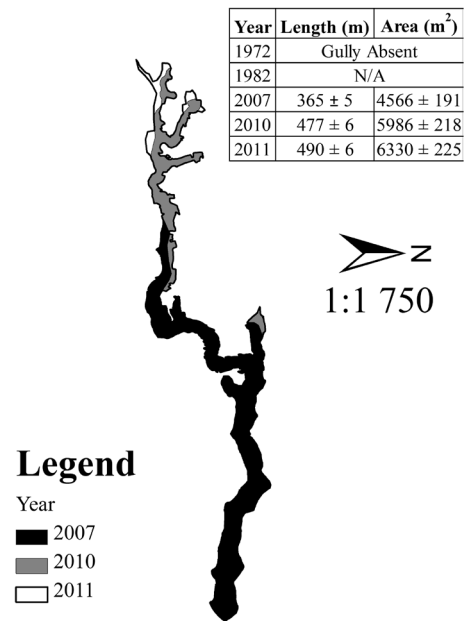


Figure 4. Gully n04 was observed for the first time on a 2007 IKONOS satellite image. Observations of tunnels, sinkholes, and exposed ice wedges near the gully head during summer 2010 and 2011 indicated that the gully was actively developing.

underground water flow, sinkholes, ice-wedge exposures, and recent ground slumping. During a visit in late June 2010, a small stream was continuously flowing into the gully head. Vegetation was present but sparse on the hummocky terrain and polygons near the gully. The colluvial deposits of gully n04 were characterized by a matrix of angular blocks, poorly decomposed peat, and sand. The gully main channel was ~ 13 m wide near its outlet and was ~ 6 m wide in the recently formed channels near the gully head. The gully main axis length and overall area development rate were 25 ± 3 m y⁻¹ and 353 ± 53 m² y⁻¹, respectively, for 2007–2011.

Gully Developing in an Organic Depositional Environment

Gullies r05, r06, and r08p, located on the south shore of the river, all initiated in an organic depositional environment. This area was characterized by well-developed syngenetic ice-wedge polygon networks with polygon width ranging from ~ 8 m to ~ 35 m. Low-centered polygons, often with small ponds in their center, high-centered, and flat polygons were observed near the gullied zones. An almost continuous vegetation cover composed of, among others, *Salicaceae*, *Cyperaceae*, and *Poaceae* was present in this part of the valley. Polygon centers often featured cryoturbation and hummocks. Gullies r05 and r06 were directly connected with the proglacial river. The outlet of r08p was connected to a stream that flowed ~ 1 km downstream in the river. These three gullies were 1–3 km apart from each other and were all oriented in a normal way to the valley walls and to the braided river (NNW-SSE to N-S).

Gully r05

This long gully was already present on 1958 aerial photography. Aerial photographs from 1961 and 1972 did not show any evidence of development by thermo-erosion processes. A 50-m-long channel formed a fork-like pattern in the gully head area between 1972 and 2007, but no significant thermo-erosion was observed for the 2007–2010 interval. No recent thermo-erosion signs, such as exposed ice wedges or evidence of other permafrost thawing, were observed during site visits. Water was observed to be flowing in the gully during early summer. This nearly stabilized gully, formed before 1958, is therefore one of the oldest and largest of the valley, with an estimated main axis length and overall area (not mapped with a DGPS) of 1899 ± 7 m and $29,485 \pm 485$ m², respectively.

Gully r06

The gully r06 (Fig. 5) was not present on the 1972 photograph and the location was hidden by clouds on the 1982 image. The gully therefore initiated during the 1972–2007 interval. Water rills and low-centered polygons with small ponds were present on the 1972 image at the current gully location. The gully main axis length in 2007 was 626 ± 8 m, with an area of $10,004 \pm 283$ m². During a field visit in 2005, narrow but sharp waterfalls were observed entering the gully near its head, favoring thermo-erosion processes. This complex gully was developing linearly toward its water source and laterally through partly melted ice wedges.

The gully continued to enlarge during the following years at a rate of 14 ± 3 m y⁻¹ for the main axis and 343 ± 52 m² y⁻¹

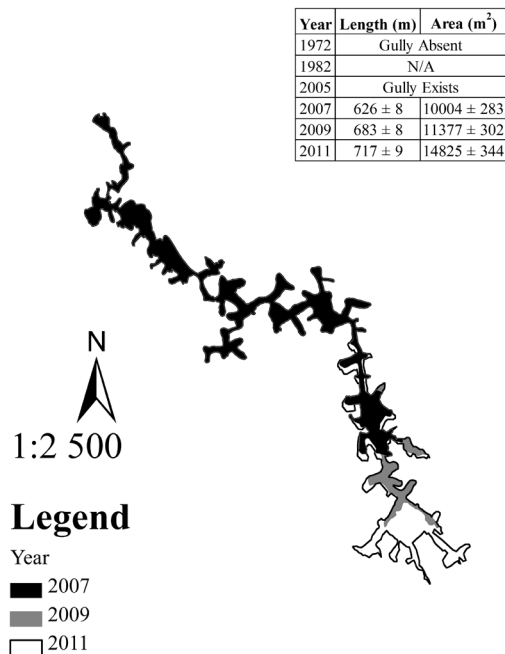


Figure 5. Gully r06 was absent on the 1972 air photography. The first observations of gully development were recorded in 2005. Gully r06 main axis development between 2007 and 2009 was 14 ± 3 m y⁻¹ and 17 ± 3 m y⁻¹ in 2010–2011.

area during the 2007–2009 period. A field visit in 2009, when the gully contours were recorded by DGPS, made it possible to record the presence of recently formed sinkholes, tunnels, thaw slumps and sharp, freshly exposed gully branches.

The channel near the gully head upstream was 6–8 m wide and 2–3 m deep. The channel was narrower downstream near the outlet, with a width of ~3 m and a depth of ~1 m. A second DGPS campaign (2011) provided evidence of gully enlargement over the 2009–2011 period to 717 ± 9 m for the main gully axis and $14,825 \pm 344$ m². Gully r06 had the greatest thermo-erosion and development rate of all gullies, with an overall development of 18 ± 3 m y⁻¹ (main axis length) and 964 ± 88 m² y⁻¹ for the 2007–2011 period.

Gully r08p

This gully (Fig. 6) was monitored since its inception in 1999 (Fortier et al. 2007) and during most years until summer 2011. The 1972 air photograph showed numerous water tracks and rills in the area where gully r08p formed in 1999. Over the 1999–2007 period, the gully expanded by 720 ± 7 m over its main axis (rate of 80 ± 2 m y⁻¹) and $23,130 \pm 430$ m² in overall area (rate of $2,570 \pm 143$ m² y⁻¹).

During 2009 and 2010, gully contours were digitized and field observations were recorded. This non-linear gully was developing simultaneously at six distinct emplacements where significant water flow entering the gully was observed. Sinkholes, waterfalls, ice-wedge exposures, sharp gully walls, and permafrost tunneling were characteristic of the expanding gully. Several baydjarakhs (an advanced stage of erosion of ice-wedge polygons forming a mound) were found in the

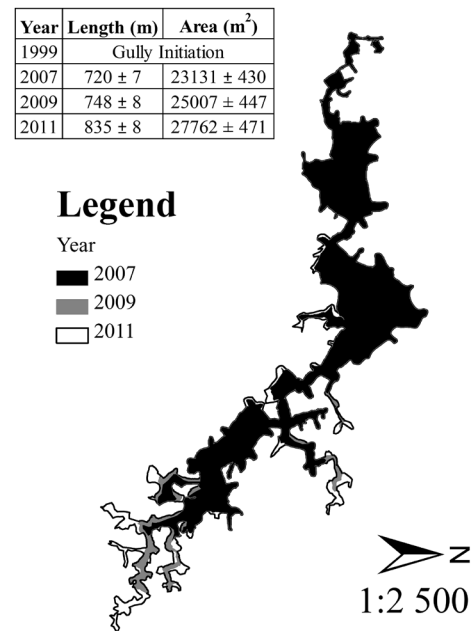


Figure 6. Gully r08p was expanding simultaneously in six distinct axes (light gray and white on the figure). While the overall length of r08p was smaller than other gullies, its area was large due to complete degradation of eroded polygons (baydjarakhs).

older, stabilized parts of the gully. The channel upstream near the gully head was ~8 m wide and ~3 m deep. The channel near the stabilized older sections of the gully in the outlet area was ~3 m wide and ~1 m deep. The gully was actively enlarging during the 2007–2011 period, although slower than the first nine years following its initiation. The gully r08p enlarged during the 2007–2011 period at a rate of $23 \pm 4 \text{ m y}^{-1}$ (main axis) and $872 \pm 83 \text{ m}^2 \text{ y}^{-1}$ of overall eroded area, making this gully one of the most dynamic in the valley.

Development Rates of Thermo-Erosion Gullies

Two of the thermo-erosion gullies covered in this study (r05, r16) initiated and developed before 1958 and have been nearly stable since then. The other three, which initiated at least after 1972 (n04, r06) or more recently (r8p, 1999), were all developing very actively. Consequently, no major gully enlargement was observed between 1958 and 1972 in the valley.

The five gullies studied in the present paper were among the largest found in the valley of Glacier C-79. These thermo-erosion features had distinctive characteristics relative to their depositional environment.

Gullies formed in aeolian and colluvial depositional environments

Gullies formed in colluvial and aeolian depositional environments shared interesting similarities. Channel cross-sections for these gullies were larger and deeper near the outlet than at the head, in opposition to those observed in an organic depositional environment. Their geometry and size were similar. These two types of gullies were characterized by a nearly linear main channel with very few (and small) secondary branches. The overall length and area of these two types of gullies were very similar, with a length of approximately 500 m and an area varying between ~4,500 and 6,500 m². The linear character of these gullies was reflected by a much smaller eroded surface compared to multi-channel gullies formed in an organic depositional environment. The relationship between linearity and overall eroded surface is clear when the 2007–2011 erosion rates of n04 and r08p are compared. For similar main channel erosion rates (n04 = $25 \pm 3 \text{ m y}^{-1}$ and r08p = $23 \pm 4 \text{ m y}^{-1}$), there was 10 times more eroded surface in the multi-channels gully r08p than in n04 (n04 = $353 \pm 53 \text{ m}^2 \text{ y}^{-1}$ and r08p = $872 \pm 83 \text{ m}^2 \text{ y}^{-1}$). The linear character of the gullies can potentially be explained by the high removal rates of sandy material of aeolian and colluvial deposits. Gullies formed in colluvial deposits, however, had a few sinkholes and tunnels which are more like gullies formed in organic depositional environments.

Gullies formed in organic depositional environment

Gullies formed in organic depositional environments were usually longer (~700–900 m in length) than gullies in other depositional environments. They had several channels, which is reflected in a larger eroded surface area (from ~15,000 to 29,000 m² eroded per gully). Active gullies were also

characterized by a large and deep channel near their gully head area, varying from ~2 to 4 m deep and 3 to 8 m wide. Recent (2007–2011) rates of erosion for the main channels varied between 17 ± 3 and $23 \text{ m} \pm 4 \text{ y}^{-1}$, with 306 ± 49 and $872 \pm 83 \text{ m}^2 \text{ y}^{-1}$ of area eroded. These rates of gully development for 2007–2011 were within the same order of magnitude as the erosion rates estimated for the 1972–2007 period, which, in all cases, were much higher than 1958–1972 rates.

Organic depositional environments were characterized by well-developed ice wedges and cohesive silty peat material, enabling the formation and the relative sustainability of forms resulting from thermo-erosion such as sinkholes, tunnels, and sharp, angular gully walls and channels.

Many of the baydjarakhs observed, especially in r06 and r08p, were remnants of a sustained phase of relatively recent thermo-erosion and a rapid development rate. Gullies that developed one or more baydjarakhs were often larger than nearly linear gullies. Many water streams and/or branches were required for enabling the erosion of all sides of ice-wedge polygons.

A fluvial thermo-erosion system has been studied on the Lena River in Siberia (Are 1983), where the river eroded ice complexes (yedoma). Ablation rates of almost pure ice for the Lena River during the flood season varied from 19 m y^{-1} up to 40 m y^{-1} , which is of the same order of magnitude as the most active gullies in the valley of Glacier C-79. This suggests that ground ice is a dominant factor in thermo-erosion rates.

Processes of Gully Development and Stabilization

The gully r16, located near the coast, was eroded and enlarged by tidal currents and river flow over the last 30 years. This changed the base level in the gully, modified the outlet location, and reduced net gully dimensions. For gullies connected to the river, the combination of tidal currents entering the gullies and high pro-glacial river level at the end of the summer contributed to accelerated gully and terrace erosion.

Gullies found in organic depositional environments were the largest observed in the valley and had higher observed development rates. With measured expansion of 50 m in main axis length since 1958, gully r05 was one of the longest, largest, and possibly oldest gullies studied. It was the only gully nearly stabilized. This indicates that several decades are required to achieve gully slope (wall) stabilization and adjacent polygonal landscape equilibrium.

Positive feedback such as thermal denudation following a tunnel collapse, active retrogressive thaw slumps, unstable permafrost thermal regime following denudation, streams flowing through gully heads, and sinkhole enlargement contributed to the accelerate development rate.

Negative feedback such as plant growth, active layer drainage, slope equilibrium, and subsequent ground cooling favored gully stabilization. Feedback effects were therefore central to gully activity. They contributed to acceleration of thermo-erosion (positive feedback) near the gully head and to stabilization (negative feedbacks) in older areas of the gullies.

Conclusions

Following gully initiation, development rates were very high. For instance, during the 1999–2007 period, gully r08p had an average main axis length development rate of ~80 m y⁻¹. It was observed that several years to decades are necessary for gully stabilization.

Gullies formed in aeolian and colluvial depositional environments shared common characteristics such as material erodability, gully size, and gully geometry.

Gullies developed faster during the 1972–2011 period than during the 1958–1972 period. Three new gullies initiated during the 1972–2011 period. Two of these (r06 and r08p) were among the largest in the valley and experienced the highest erosion rates.

Thermo-erosion gullies are long-lasting features in the periglacial landscape. They impact the local hydrology, water availability for vegetation, and therefore plant distribution and assemblages. Ground loss due to permafrost erosion resulting from gullying implies a change in the sedimentary balance of the river system downstream.

Acknowledgments

We would like to thank Dr. Gilles Gauthier (Center for Northern Studies, U. Laval) for providing access to base camp and logistics yearly since 1999. Fieldwork assistance from R. Thériault, A. Guertin-Pasquier, N. Perreault, S. Coulombe, and M. Paquette has been invaluable in the realization of this project. We are grateful to the following organizations and institutions for financial and logistical support: Parks Canada, Polar Continental Shelf Program, Northern Scientific Training Program, NSERC, FQRNT, Center for Northern Studies, ESRI, National Bank of Canada, and the W. Weston Garfield Foundation. We appreciated the technical help from J. Daoust, and profs. F. Cavayas and J. Cardille. Finally, we acknowledge C.R. Duguay and Aiman Soliman for their constructive comments.

References

- Allard, M. 1996. Geomorphological changes and permafrost dynamics: Key factors in changing arctic ecosystems. An example from Bylot Island, Nunavut, Canada. *Geoscience Canada* 23(4): 205-212.
- Are, F.E. 1983. Thermal abrasion of coasts. In *Proceedings of the Fourth International Conference on Permafrost*, Alaska. National Academy Press: Washington DC; 24-28.
- Environment Canada. 2002. Canadian Climate Normals, 1971–2000. Pond Inlet. Environment Canada, Atmospheric Environment Service, Downsview, Ontario, Canada. (Web, Online, 31 January 2012.)
- Fortier, D., Allard, M., & Shur, Y. 2007. Observation of rapid drainage system development by thermal erosion of ice wedges on Bylot Island, Canadian Arctic Archipelago. *Permafrost and Periglacial Processes* 18(3): 229-243.
- Fortier, D., Allard, M., & Pivot, F. 2006. A late-Holocene record of loess deposition in ice-wedge polygons reflecting wind activity and ground moisture conditions, Bylot Island, eastern Canadian Arctic. *Holocene* 16(5): 635-646.
- Fortier, D. & Allard, M. 2004. Late Holocene syngenetic ice-wedge polygons development, Bylot Island, Canadian Arctic Archipelago. *Canadian Journal of Earth Sciences* 41(8): 997-1012.
- Godin, E. & Fortier, D. 2010. Geomorphology of thermo-erosion gullies – case study from Bylot Island, Nunavut, Canada. In: *Proceedings of the 63rd Canadian Geotechnical Conference & 6th Canadian Permafrost Conference*, Calgary, Alberta, Canada. 1540-1547. (Web, Online, 31 January 2012, <http://pubs.aina.ucalgary.ca/cpc/CPC6-1540.pdf>.)
- Heginbottom, J.A. 1995. Canada-permafrost. The National Atlas of Canada, Fifth Edition, Map MCR 4177F 1:1 750000 scale. Natural Resources Canada, Geological Survey of Canada: Ottawa.
- Hyatt, J.A. 1992. Cavity development in ice-rich permafrost, Pangnirtung, Baffin Island, Northwest Territories. *Permafrost and Periglacial Processes* 3(4): 293-313.
- Klassen, R.A. 1993. Quaternary geology and glacial history of Bylot Island, Northwest Territories, Canada. Ottawa, Geological Survey of Canada, Memoir 429, 93 pp.
- Leffingwell, E. 1919. The Canning River region, northern Alaska. Professional Paper. U.S.G. Survey. 109: 247 pp.
- Levy, J.S., Head, J.W., & Marchant, D.R. 2008. The role of thermal contraction crack polygons in cold-desert fluvial systems. *Antarctic Science* 20(6): 565-579.
- Mackay, J.R. 1997. A full-scale field experiment (1978-1995) on the growth of permafrost by means of lake drainage, western Arctic coast: A discussion of the method and some results. *Canadian Journal of Earth Sciences* 34(1): 17-33.
- Rowland, J.C., Jones C.E., et al. 2010. Arctic Landscapes in Transition: Responses to Thawing Permafrost. *Eos Trans. AGU* 91(26): 229.
- Sidorchuk, A. 1999. Dynamic and static models of gully erosion. *CATENA* 37(3-4): 401-414.

A Global View on Permafrost in Steep Bedrock

Stephan Gruber

Department of Geography, University of Zurich, Switzerland

Abstract

Mountainous topography covers a considerable proportion of the global permafrost region. There, temperature changes and the degradation of permafrost in steep bedrock can evoke rapid geomorphic change, some of which may result in natural hazards. Due to the strong relief of most rock walls, corresponding events can have a long runout and transform into cascading events, such as impact to lakes or the damming of rivers that propagate far below the periglacial zone. The identification of areas that potentially have permafrost conditions in steep rock is the important first step in the evaluation of corresponding hazards. During the past decade, researchers have given considerable attention to permafrost in steep bedrock, although most investigations have been conducted in the European Alps. This contribution provides a summary of findings related to the delineation of permafrost in rock walls. Based on this, simple considerations and data sources are outlined that may help the application of current knowledge in remote mountain regions.

Keywords: bedrock slopes; mountains; steep terrain; global; hazard zonation; mapping.

Introduction

A significant proportion of the global permafrost region has mountainous topography (Gruber 2011a). Additionally, coastal cliffs may be subject to permafrost conditions, and changes to permafrost there can alter the stability of rock faces perched high above valleys and thus pose a hazard to human life and infrastructure (cf. Carey 2005). This may occur indirectly through, for example, impacts to lakes that may cause long-distance secondary events (cf. Geertsema & Cruden 2008, Geertsema & Clague 2011). However, non-stationarity, incomplete understanding of processes, and lack of information on local surface and subsurface conditions challenge corresponding hazard zonation. Here, the delineation of permafrost rock slopes can serve as a proxy for areas that may require special attention or surveillance, as they are prone to rapid changes in response to climate forcing (Gruber 2011b). Absent or minimal vegetation, a reduced snow cover, and less important active-layer processes make permafrost in steep rock a system that is simple enough for attempting an extrapolation of findings to environments not measured. In this contribution, I summarize findings on the spatial and temporal variability of mean annual ground temperature (MAGT) and permafrost in steep bedrock. These findings, often based on a narrow range of environmental conditions, are extended with hypotheses for generalization to other environments. This is intended to support the estimation of permafrost conditions in steep rock globally, and to provide a framework to test and improve them by means of measurement, experiment, and observation. Unless stated otherwise, the investigations cited have been performed in the European Alps.

Rock Temperature: Factors and Processes

Basic considerations

The energy fluxes at and near the ground surface are shown for the two conceptual end members of steep and homogenous bedrock and a horizontal debris slope in Figure 1. Longwave

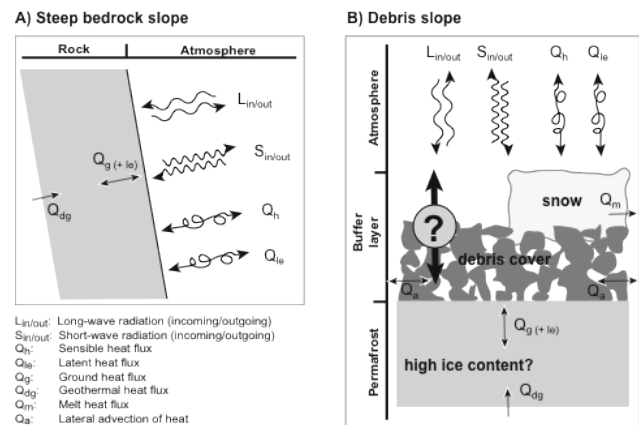


Figure 1. Schematic of energy balance at and near the ground surface in steep bedrock (A) and gentle debris slopes (B).

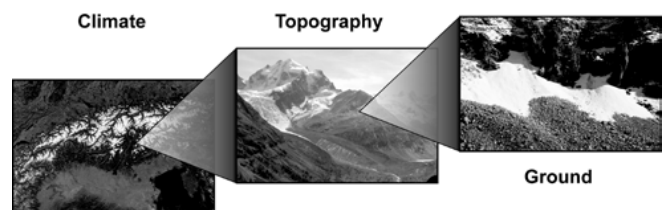


Figure 2. Conceptual scales of influence on ground temperatures.

radiation is mostly affected by air temperature, moisture content, and clouds. Turbulent fluxes mostly depend on air temperature and wind.

Solar irradiation, however, is strongly dependent on cloudiness, sun-terrain geometry, and topography, and results in a high degree of spatial differentiation. Figure 2 shows three conceptual scales that determine ground temperatures. When considering global patterns, differing climate conditions affect the strength of the topographic influence.

For example, in areas with more abundant clouds and diffuse radiation, topographic differentiation is less pronounced than in areas with few clouds and strong direct solar radiation. The

spatial differentiation of MAGT can be conveniently described relative to mean annual air temperature (MAAT) using

$$dT = MAGT - MAAT \quad (1)$$

Because MAAT is a commonly available climate variable, dT helps to estimate local patterns relative to it. MAAT is often subject to strong intra-annual variation, but dT for near-vertical rock remains rather constant (cf. Noetzli & Vonder Muehll 2010).

Near-vertical and compact rock

Near-vertical and compact rock faces exhibit a strong topographic control on subsurface temperatures and a weak thermal influence of snow and active-layer processes typical for debris-covered slopes (Fig. 1). Spatial patterns of dT are dominated by direct solar radiation (cf. Hoelzle 1994) and modified by rock albedo (cf. Hall 1997). For this reason, they are a simple system to investigate and to then gradually expand by considering additional processes. Gruber et al. (2003) present a review of previous investigations and a strategy for measuring in steep rock faces. Corresponding data are available through PERMOS (cf. Noetzli & Vonder Muehll 2010) and a pan-Alpine inventory of permafrost evidence (Cremonese et al. 2011). In near-vertical and compact rock, MAGT is often measured 5–30 cm below the surface and presumed to be equivalent to that just below the active layer.

Based on the work of Allen et al. (2009) summarizing 14 one-year time series from the Southern Alps of New Zealand (44°S), dT in sun-exposed slopes can be estimated to 4.5–6.5°C. In the European Alps (46°N), Boeckli et al. (2012) estimated this to be 5.5–6°C based on 57 locations and a statistical model. A process-based modeling study (Gruber et al. 2004) in the European Alps resulted in dT ranging from 6.5 to 9°C. The model is driven by daily data that do not resolve temperature differences between east and west exposure. This may result from convective clouding in the afternoon lowering the temperature on west-exposed faces by reducing direct solar radiation. Generally, dT increases with elevation due to more shortwave and less longwave radiation, and with decreasing precipitation due to a higher amount of direct radiation. Reflection from surrounding snow-covered slopes can locally increase shortwave irradiation and thus dT . This effect is assumed to have affected dT at two measured locations by 2–3°C (cf. Allen et al. 2009). Without any solar radiation, dT would become slightly negative due to longwave loss.

Summarizing this paragraph, dT likely ranges from 0 to 9°C in steep and compact rock at latitudes near 45°, and varies mostly as a function of solar radiation.

Surface heterogeneity and clefts

Most rock slopes differ from the near-vertical case because micro-topography and fracturing promote patchy covers of debris, snow, and ice (Gruber & Haeberli 2007). The thermal influence of snow, fractures, and active-layer processes can thus contribute to the heterogeneity of dT . Safety issues

and the dominance of lateral heterogeneity in near-surface measurements of MAGT, however, complicate corresponding research. Gubler et al. (2011) found that MAGT on more gentle slopes can already vary by up to 2.5°C within an area of 10 m x 10 m. For heterogeneous bedrock slopes, this value is likely often exceeded.

Using measurements at four depths down to 85 cm in borings and deeper on thermistor strings lowered into clefts, Hasler et al. (2011) estimated a local cooling effect of fractures on the order of 1.5°C. This cooling resulting from ventilation likely depends on cleft aperture and abundance, and its functioning may resemble ventilation effects in coarse blocks (cf. Harris & Pedersen 1998) or, in extreme cases, those in ice caves (Obleitner & Spötl 2011, Schöner et al. 2011). A local lowering of dT by several °C, even in shaded slopes, thus appears possible in rare cases. For practical use, however, an assumption of 1–2°C cooling, increasing from shaded to sun-exposed slopes, appears plausible for heterogeneous conditions. Snow deposited in clefts may have an additional cooling effect by consuming latent heat during melting. At the same time, however, snow cover or infill can inhibit air circulation and thus reduce the associated cooling (Hasler et al. 2011). A thermal diode effect caused by seasonally varying proportions of ice/water/air in pores and fractures can cause a lowering of temperatures at depth (Gruber & Haeberli 2007) similar to the thermal offset described for lowland permafrost (cf. Smith & Riseborough 2002), but this has not been detected in measurements (Hasler et al. 2011).

Snow and perennial ice

Snow on rock faces alters the coupling between the atmosphere and subsurface and thus affects dT . It is usually thinner and spatially and temporally more variable than in gentle terrain. Due to difficult access, corresponding studies are rare (cf. Wirz et al. 2011). Rock faces often extend far above the equilibrium line of glaciers and receive much of their precipitation in solid form. In those conditions, temperature moderates the retention of snow because cohesive snow near melting conditions is more likely to accumulate than cold snow that is prone to be removed by wind and sliding. For cold and shaded faces, this can cause a pronounced snow cover during summer, whereas precipitation in winter barely affects the bare and dark surfaces of ice and rock (cf. Gruber & Haeberli 2007). Depending on the seasonality of precipitation, snow during summer can be common in high-elevation rock faces. For thin snow, the net warming through thermal insulation during winter is reduced and the relative importance of cooling through albedo and latent heat uptake during melt becomes greater. Higher albedo decreases dT more strongly on sun-exposed slopes, whereas the effect of latent heat can cause a lowering of dT in all slope aspects.

Based on numerical experiments under the assumption of laterally homogeneous snow cover, Pogliotti (2011) estimated this cooling to have magnitudes of up to 2°C with respect to snow-free rock. In reality, this is further modified in laterally heterogeneous and discontinuous snow cover because a lateral interaction between snow-covered and snow-free rock facets

exists by heat conduction in rock as well as by radiative and sensible exchange at the surface (cf. Neumann & Marsh 1998). Based on distributed measurements of rock temperature, Hasler et al. (2011) estimated the cooling effect of snow in radiation-exposed faces to be up to 2–3°C.

Ice faces, hanging glaciers, or surface lowering of glaciers can influence the temperature regime in steep rock and can exhibit strong spatio-temporal variations (Fischer et al. 2011). While ice faces and hanging glaciers are diagnostic of permafrost conditions at their rock-ice interface, their absence does not indicate the absence of permafrost. The occurrence of cold firn (Suter et al. 2001, Suter & Hoelzle 2002, Hoelzle et al. 2011), and thus hanging glaciers, follows differing patterns than rock temperature because they are subject to higher albedo and are affected by wind through snow transport. In gently inclined parts of hanging glaciers, the percolation of water into the firn and heat release at depth during refreezing can cause zones of temperate firn and ice (Haeberli & Alean 1985). As a consequence, an inference of temperature below ice cover is difficult. For ice faces that are subject to minimal flow and balance change, a cooling with respect to rock is likely for sun-exposed slopes due to the influence of albedo. For a north-exposed ice face, Hasler et al. (2011) report approximately the same mean annual temperature as in nearby rock.

Three-dimensional and transient effects

Spatial variation of surface conditions and their temporal changes influence permafrost bodies at depth (cf. Gold & Lachenbruch 1973), and in mountain areas this is further complicated by geometric effects (Kohl 1999, Gruber et al. 2004). The combination of a distributed MAGT model and three-dimensional heat-transfer modeling of steep topography (Noetzli et al. 2007) showed complicated permafrost bodies with steeply inclined isotherms near peaks and ridges. Even in steady-state, permafrost can be induced below non-permafrost terrain facets due to nearby cold slopes. Transient simulations were performed with a similar setup (Noetzli & Gruber 2009) and accounted for temperature changes during the past. This revealed the importance of past climate and latent heat that can lead to permafrost bodies persisting at depth below slopes that today would be interpreted as permafrost-free. Because of multi-lateral warming, the reaction of convex topography, such as ridges or rock spurs, can be much faster than that of flat terrain (Noetzli & Gruber 2009). Several new boreholes in steep rock and in ridges (Noetzli et al. 2010, Noetzli et al. 2008, Noetzli & Vonder Muehll 2010) support many of the general findings from the modeling studies.

The Global View: Estimating Spatial Patterns of Rock Temperatures for Diverse Mountain Ranges

In this section, simple approaches for estimating permafrost occurrence in rock faces worldwide are proposed. It is important to keep in mind that this is based on limited point data from a restricted range of environmental conditions.

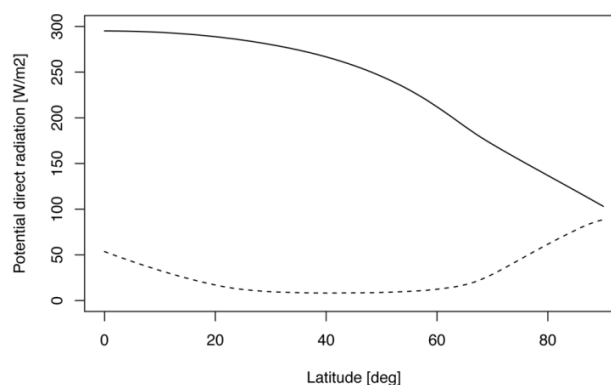


Figure 3. Latitude-dependency of maximum (solid) and minimum (dashed) potential direct solar radiation received in rugged terrain. The experiment shown spans slope angles 0–90°, slope expositions 0–180° (because east and west are identical in this respect), and has no horizon shading.

Furthermore, the derivation of such heuristics has an element of subjectivity, especially where it involves the delineation of permafrost zones.

Global distribution

For strongly shaded rock faces, the 0°C long-term isotherm of the MAAT is a good pointer to determine the elevation above which permafrost must be expected, even though permafrost may sometimes be found at lower elevation. Due to the absence of better data, the zonation shown in Gruber (2011a) can provide an approximation globally at about 1 km resolution. While few rock faces are dominated by inversion effects, inversions are important to consider in the choice of local meteorological stations as possible alternatives. As the extrapolation of MAAT in rugged terrain involves considerable vertical distances, the choice of appropriate lapse rates is important. If suitable ground measurements do not exist, the lapse rate can be approximated based on model data (Gruber 2011a) or regional radiosonde measurements. MAAT data covering a period of several decades helps to minimize the influence of short-term fluctuations. It is sometimes necessary to account for longer-term transient effects that have occurred during the past decades or centuries with respect to the measurement period chosen (cf. Noetzli & Gruber 2009).

Topography and solar radiation

Topography influences dT for individual slopes, mainly through its geometric effect on incoming solar radiation. Generally, steeper and more rugged terrain causes a wider range of dT than more gentle terrain. This effect, however, is modified by latitude and the proportion of direct radiation. As a first approximation, a ruggedness index (e.g., Gruber 2011a) can be used to identify terrain tending to have a higher proportion of steep and strongly shaded rock slopes. Locally, the differentiation of slopes with respect to solar radiation can be estimated based on the calculation of mean annual potential solar irradiation and a decameter-resolution DEM (e.g., Farr et al. 2007). This operation is routinely available in GIS software.

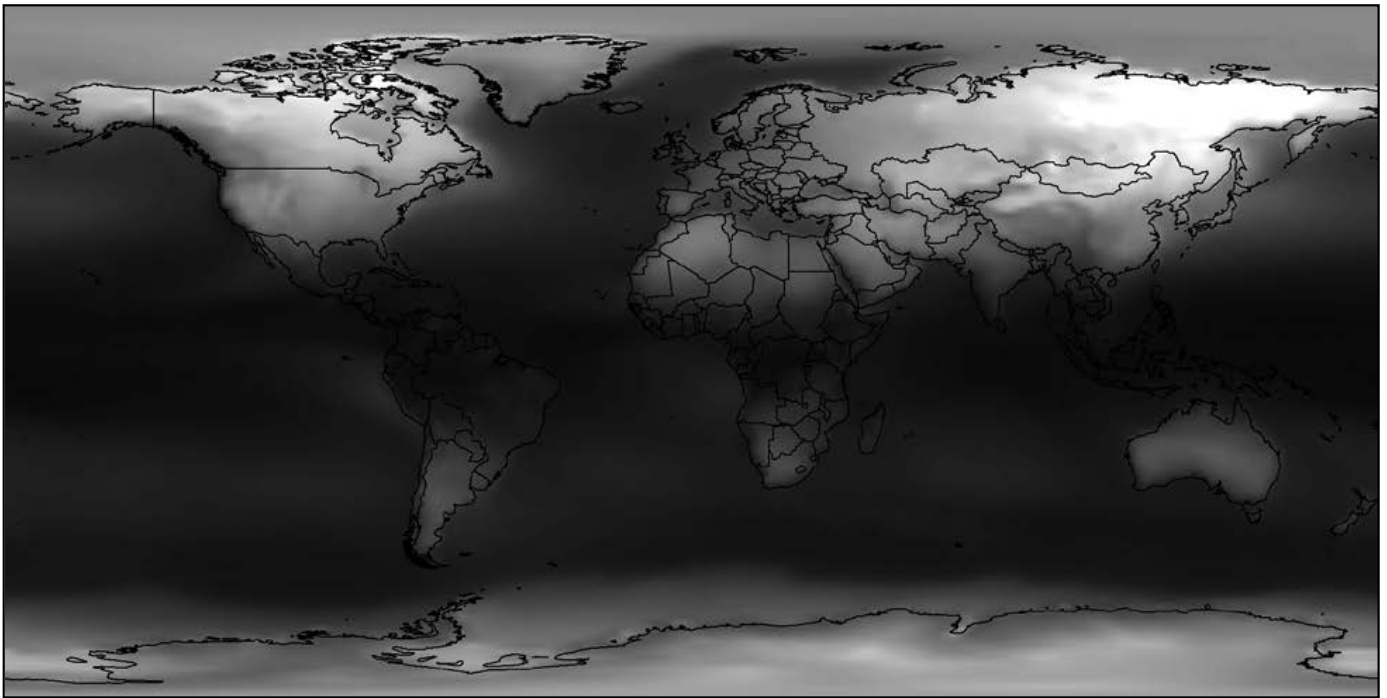


Figure 4. Continentality index derived from 2000–2010 mean monthly surface air temperatures based on ERA-Interim re-analysis data. Dark areas are maritime; light areas are continental climate.

Latitude

Besides its effect on MAAT, latitude influences the maximum amount of total annual solar irradiation received by the most suitably exposed slope. For this reason, the range of dT is also likely to be affected by latitude (Fig. 3). Further, the partitioning of radiation with topography changes with latitude. Toward the poles, increasingly steep slopes receive the highest amounts of radiation; near the tropics, rather gentle slopes receive the highest radiation input. Furthermore, the sensitivity to cast shadowing by obstructed horizons increases toward the poles with the prevalence of low solar elevation angles.

Continental

Continental (as opposed to maritime) climate is characterized by comparably large seasonal thermal variations and dryness, both generally caused by large distances from major water bodies and altered by atmospheric circulation patterns and rain-shadow effects. The dryness in continental areas is usually accompanied by very high amounts of direct solar radiation afforded by often cloud-free skies. Besides MAAT, continentality is often used to describe spatial patterns of cryosphere phenomena (e.g. Holmlund & Schneider 1997, King 1986, Haeberli & Burn 2002, Shumskii 1964) and is frequently characterized by a continentality index defined as the average difference between the coldest and warmest month at a location.

The continentality index shown in Figure 4 provides an appreciation of its global patterns that may help to inform the extrapolation of findings from one mountain range to another. The patterns of temperature range, the proportion of direct

sunlight, and precipitation are jointly described by the concept of continentality. However, these affect rock temperature in differing ways and often correlate much less than expected when plotted based on gridded climate data. Until further analyses help to disentangle these effects, the assumption of subdued spatial differentiation of dT toward maritime areas likely provides a good assumption. This effect of continentality on the degree of spatial differentiation due to solar radiation is, however, not clearly detectable in current measurements (cf. Allen et al. 2009, Boeckli et al. 2012) that span only small gradients.

Surface characteristics

As a general rule, rough surfaces can be assumed to be colder than smooth ones. Cooling is caused by a thin, intermittent, and frequent snow cover and by air circulation in fractures or debris.

At least qualitatively, the roughness of rock walls can be assessed based on field visits, photographs, aerial photographs, or high-resolution satellite imagery. Increasingly, the imagery freely available on GoogleEarth, for example, has sufficient resolution to provide valuable first impressions.

Conclusion

Based on research from a narrow range of environmental conditions and the consideration of what appear to be the processes that govern permafrost distribution in steep bedrock, I have proposed simple considerations to estimate permafrost in rock walls worldwide. Besides the potential for practical application, this contribution points to the wide range of

environmental conditions that drive permafrost in steep terrain. More systematic research in integrating local and regional research to achieve a coherent understanding would be a good avenue to progress beyond the heuristics presented here. Such research would consolidate understanding by basing it on a wider range of environmental conditions.

Acknowledgments

Over the past ten years, many colleagues and friends have contributed toward the synthesis presented here. These contributions have come not only through the works referenced, but also through inspiring discussions and field campaigns. Among these are: Jeannette Nötzli, Andreas Hasler, Marco Peter, Adrian Zraggen, Lorenz Böckli, Jan Beutel, Simon Allen, Martin Hoelzle, Ludovic Ravanel, Paolo Pogliotti, Umberto Morra di Cella, Edoardo Cremonese, and Reynald Delaloye. ECMWF ERA-Interim data used in this study have been obtained from the ECMWF data server. Michael Krautblatter is acknowledged for valuable and insightful reviewer comments.

References

- Allen, S., Gruber, S., & Owens, I. 2009. Exploring steep bedrock permafrost and its relationship with recent slope failures in the Southern Alps of New Zealand. *Permafrost and Periglacial Processes* 20(4): 345–356.
- Boeckli, L., Brenning, A., Gruber, S., & Noetzi, J. 2012. A statistical permafrost distribution model for the European Alps. *The Cryosphere* 6(1): 125–140.
- Carey, M. 2005. Living and dying with glaciers: people's historical vulnerability to avalanches and outburst floods in Peru. *Global and Planetary Change* 47(2-4): 122–134.
- Cremonese, E., Gruber, S., Phillips, M., Pogliotti, P., Boeckli, L., Noetzi, J., Suter, C., Bodin, X., Crepez, A., Kellerer-Pirklbauer, A., Lang, K., Letey, S., Mair, V., Morra di Cella, U., Ravanel, L., Scapozza, C., Seppi, R., & Zischg, A. 2011. Brief Communication: "An inventory of permafrost evidence for the European Alps." *The Cryosphere* 5(3): 651–657.
- Farr, T.G., Rosen, P.A., Caro, E., Crippen, R., Duren, R., Hensley, S., Kobrick, M., Paller, M., Rodriguez, E., Roth, L., Seal, D., Shaffer, S., Shimada, J., Umland, J., Werner, M., Oskin, M., Burbank, D., & Alsdorf, D. 2007. The Shuttle Radar Topography Mission. *Review of Geophysics* 45: RG2004.
- Fischer, L., Eisenbeiss, H., Käab, A., Huggel, C., & Haerberli, W. 2011. Monitoring topographic changes in a periglacial high-mountain face using high-resolution DTMs, Monte Rosa East Face, Italian Alps. *Permafrost and Periglacial Processes* 22(2): 140–152.
- Geertsema, M. & Clague, J.J. 2011. Pipeline routing in landslide-prone terrain. *Innovation* 15(4): 17–21.
- Geertsema, M. & Cruden, D.M. 2008. Travels in the Canadian Cordillera. In *Proceedings of 4th Canadian conference on geohazards*, Quebec City: 383–390.
- Gold, L.W. & Lachenbruch, A.H. 1973. Thermal conditions in permafrost - a review of North American literature. In F. J. Sanger and P. J. Hyde, eds. *Yakutsk, USSR: National Academy of Sciences*, Washington D.C.: 3–25.
- Gruber, S. 2011a. Derivation and analysis of a high-resolution estimate of global permafrost zonation. *The Cryosphere Discussions* 5(3): 1547–1582.
- Gruber, S. 2011b. Landslides in cold regions: making a science that can be put into practice. In *Proceedings of the Second World Landslide Forum*, 3–9 October 2011, Rome, Italy.
- Gruber, S. & Haerberli, W. 2007. Permafrost in steep bedrock slopes and its temperature-related destabilization following climate change. *Journal of Geophysical Research* 112(F2): F02S18.
- Gruber, S., Hoelzle, M. & Haerberli, W. 2004. Rock wall temperatures in the Alps: modelling their topographic distribution and regional differences. *Permafrost and Periglacial Processes* 15(3): 299–307.
- Gruber, S., King, L., Kohl, T., Herz, T., Haerberli, W., & Hoelzle, M. 2004. Interpretation of geothermal profiles perturbed by topography: the Alpine permafrost boreholes at Stockhorn Plateau, Switzerland. *Permafrost and Periglacial Processes* 15(4): 349–357.
- Gruber, S., Peter, M., Hoelzle, M., Woodhatch, I., & Haerberli, W. 2003. Surface temperatures in steep alpine rock faces - A strategy for regional-scale measurement and modelling. In *Proceedings of the 8th International Conference on Permafrost 2003*, Zurich, Switzerland: 325–330.
- Gubler, S., Fiddes, J., Gruber, S., & Keller, M. 2011. Scale-dependent measurement and analysis of ground surface temperature variability in alpine terrain. *The Cryosphere* 5: 431–443.
- Haerberli, W. & Alean, J. 1985. Temperature and accumulation of high altitude firn in the Alps. *Annals of Glaciology* 6: 161–163.
- Haerberli, W. & Burn, C.R. 2002. Natural hazards in forests: glacier and permafrost effects as related to climate change. In R.C. Sidle, ed. *Environmental Change and Geomorphic Hazards in Forests*. Wallingford/New York, CABI Publishing: 167–202.
- Hall, K. 1997. Rock temperatures and implications for cold region weathering. I: New data from Viking Valley, Alexander Island, Antarctica. *Permafrost and Periglacial Processes* 8(1): 69–90.
- Harris, S.A. & Pedersen, D.E. 1998. Thermal regimes beneath coarse blocky material. *Permafrost and Periglacial Processes* 9: 107–120.
- Hasler, A., Gruber, S., & Haerberli, W. 2011. Temperature variability and thermal offset in steep alpine rock and ice faces. *The Cryosphere* 5: 977–988.
- Hoelzle, M. 1994. *Permafrost und Gletscher im Oberengadin. Grundlagen und Anwendungsbeispiele für automatisierte Schätzverfahren*. Ph.D. thesis. Switzerland: ETH Zürich.
- Hoelzle, M., Darms, G., Lüthi, M., & Suter, S. 2011. Evidence of accelerated englacial warming in the Monte Rosa area, Switzerland/Italy. *The Cryosphere* 5: 231–243.

- Holmlund, P. & Schneider, T. 1997. The effect of continentality on glacier response and mass balance. *Annals of Glaciology* 24: 272–276.
- King, L. 1986. Zonation and ecology of high mountain permafrost in Scandinavia. *Geografiska Annaler, Series A* 68(3): 131–139.
- Kohl, T. 1999. Transient thermal effects at complex topographies. *Tectonophysics* 306: 311–324.
- Neumann, N. & Marsh, P. 1998. Local advection of sensible heat in the snowmelt landscape of Arctic tundra. *Hydrological Processes* 12(10-11): 1547–1560.
- Noetzli, J. & Gruber, S. 2009. Transient thermal effects in Alpine permafrost. *The Cryosphere* 3(1): 85–99.
- Noetzli, J., Gruber, S., Kohl, T., Salzmann, N., & Haerberli, W. 2007. Three-dimensional distribution and evolution of permafrost temperatures in idealized high-mountain topography. *Journal of Geophysical Research* 112: F02S13.
- Noetzli, J., Gruber, S. & von Poschinger, A. 2010. Modellierung und Messung von Permafrosttemperaturen im Gipfelgrat der Zugspitze, Deutschland. *Geographica Helvetica* 65(2): 113–123.
- Noetzli, J., Hilbich, C., Hauck, C., Hoelzle, M., & Gruber, S. 2008. Comparison of simulated 2D temperature profiles with time-lapse electrical resistivity data at the Schilthorn crest, Switzerland. In *Ninth International Conference on Permafrost*, University of Alaska Fairbanks: 1293–1298.
- Noetzli, J. & Vonder Muehll, D. 2010. *Permafrost in Switzerland 2006/2007 and 2007/2008*, Cryospheric Commission of the Swiss Academy of Sciences.
- Obleitner, F. & Spötl, C. 2011. The mass and energy balance of ice within the Eisriesenwelt cave, Austria. *The Cryosphere* 5(1): 245–257.
- Pogliotti, P. 2011. *Influence of snow cover on MAGST over complex morphologies in mountain permafrost regions*. Ph.D. thesis. Italy: Scuola di Dottorato in Scienza e Alta Tecnologia, University of Torino.
- Schöner, W., Weyss, G., & Mursch-Radlgruber, E. 2011. Linkage of cave-ice changes to weather patterns inside and outside the cave Eisriesenwelt (Tennengebirge, Austria). *The Cryosphere* 5(3): 603–616.
- Shumskii, PA. 1964. *Principles of structural glaciology*, New York: Dover Publications, Inc.
- Smith, M.W. & Riseborough, D.W. 2002. Climate and the limits of permafrost: A zonal analysis. *Permafrost and Periglacial Processes* 13(1): 1–15.
- Suter, S. & Hoelzle, M. 2002. Cold firn in the Mont Blanc and Monte Rosa areas, European Alps: spatial distribution and statistical models. *Annals of Glaciology* 35: 9–18.
- Suter, S., Laternser, M., Haerberli, W., Frauenfelder, R., & Hoelzle, M. 2001. Cold firn and ice of high-altitude glaciers in the Alps: measurements and distribution modelling. *Journal of Glaciology* 47(156): 85–96.
- Wirz, V., Schirmer, M., Gruber, S., & Lehning, M. 2011. Spatio-temporal measurements and analysis of snow depth in a rock face. *The Cryosphere* 5: 893–905.

Thermo-Erosion along the Yedoma Coast of the Buor Khaya Peninsula, Laptev Sea, East Siberia

Frank Günther, Pier Paul Overduin

Alfred Wegener Institute for Polar and Marine Research, Potsdam, Germany

Aleksandr V. Sandakov

Permafrost Institute, Russian Academy of Science, Siberian Branch, Yakutsk, Russia

Guido Grosse

Geophysical Institute, University of Alaska Fairbanks, USA

Mikhail N. Grigoriev

Permafrost Institute, Russian Academy of Science, Siberian Branch, Yakutsk, Russia

Abstract

Coastal erosion in continuous permafrost regions with high ground ice content is affected by subsidence and mass transport due to thawing of ground ice. Using sites along the western coast of the Buor Khaya Peninsula, we introduce an index for thermo-erosion based on the change in position of the upper and lower edges of the coastal bluff through time. Field surveys of thermo-terraces and an alas were compared with historical elevations and coast-lines. Using survey TINs and photogrammetry-derived DEMs, coastal position change, volumetric land loss, and the Normalized Difference Thermo-erosion Index (NDTI) were calculated. Coastline erosion varied from 0.4 to 3.3 m a⁻¹ over the 36-year period from 1974 to 2010, resulting in volumetric erosion of 7,000 to 67,000 m³ a⁻¹ per km of coastline. NDTI values show coastline erosion dominated by thermo-abrasive to thermo-denudative processes.

Keywords: Arctic coastal erosion; GIS; land-ocean interactions; Laptev Sea; remote sensing; thermo-erosion.

Introduction

Coastal erosion in fine-grained, ice-rich continuous permafrost can be complicated due to the presence of ground ice (Are 1988), resulting in sometimes rapid (Jones et al. 2009) and spatially highly variable (Lantuit et al. 2011a) coastal retreat. In addition to the mechanical action of waves, ground ice renders the shore-face profile vulnerable to thawing below the seabed and above the waterline due to energy inputs at the ground surface. Subsidence and transport of sediment can result.

We adopt the approach of Are (1988) to define the terms thermo-erosion, thermo-abrasion, and thermo-denudation. Thermo-erosion describes the suite of processes eroding the coastline, both above and below the waterline. Thermo-abrasion is due to the combined mechanical and thermal action of sea water and sea ice on the shore face, and thermo-denudation is defined as the combined influence of the energy balance at the ground surface above the waterline. The relative intensities of the latter two processes result in the morphologies typical for arctic coasts (Sovershaev 1992).

Environmental factors driving coastal dynamics, such as bathymetry, geomorphology, ground ice content, sea ice duration, and other larger-scale regional factors, vary spatially and temporally. The relative importance of thermo-abrasion and thermo-denudation therefore also varies spatially and temporally. In this paper we attempt to understand and quantify the geomorphological processes controlling coastal erosion rates in permafrost regions. We use data from the Buor Khaya Peninsula, Siberia, in order to provide a basis for generalizations applicable to other arctic coastal sites.

We introduce the concept of Normalized Difference Thermo-erosion Index (NDTI) as an index of the relative proportions of thermo-denudational and thermo-abrasional erosion above the waterline (Fig. 1). We assume that movement of the top of the coastal bluff is attributable to thermo-denudation as defined above, and the movement of the bluff foot is attributable to thermo-abrasion, in this case the movement of material from the beach to the subaquatic shore face, primarily by wave action. The former assumption is weakened by the fact that movement of the upper edge also depends on the removal of

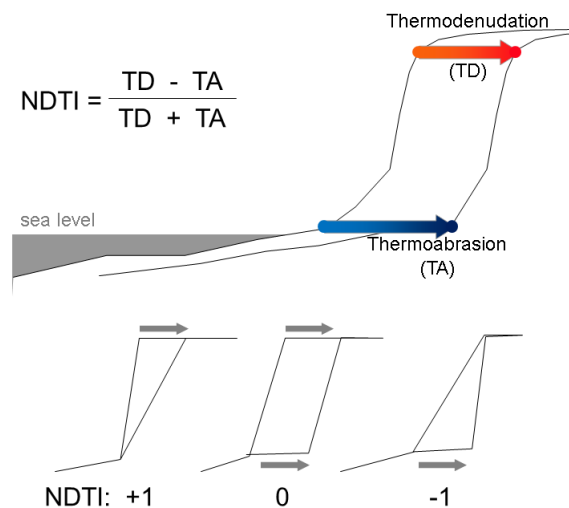


Figure 1. Landward movement of the top and bottom of the coastal bluff are attributed to thermo-denudation and thermo-abrasion, respectively. These values are used to calculate normalized difference thermo-erosion index. The NDTI can vary from +1 (thermo-denudational regime) to -1 (thermo-abrasional regime).

material from the foot, and can proceed via slope failure on slopes for which thermal processes have a negligible influence (e.g. non-permafrost coasts).

However, permafrost coastlines are unique in that landward migration of the upper edge of the coastal bluff can proceed independently (e.g., for retrogressive thaw slumps or thermocirques). Ground ice can also cement permafrost ground, leading to the development of thermo-niches when thermo-abrasion dominates, leading to a decoupling of abrasion and denudation.

Study Area

This study focuses on the western coast of the Buor Khaya Peninsula in the southern part of the central Laptev Sea (Russian Federation). The Buor Khaya Gulf receives most of the Lena River's freshwater and sediment discharge as well as material from coastal erosion (Charkin et al. 2011). The peninsula is part of the ice complex coastal plain (Schirmer et al. 2010, Grosse et al. 2007) and is underlain by continuous permafrost with ground temperatures below -11°C (Drozov et al. 2005). The coastline alternately cuts through yedoma hills (up to 37 m a.s.l.) and flat alas depressions formed by thermokarst (10–15 m a.s.l.). Larger contiguous remnants of yedoma highlands are found only in the hinterland. Coastal erosion and thermokarst features, including inland lakes, contribute to the erosion of the land surface by mobilizing material and changing surface drainage gradients.

Thermo-terrace landslides, which occur on high coasts of ice complex (Are 1988), are very common along the studied coastline and morphologically very similar to retrogressive thaw slumps in the Canadian Arctic (Mackay 1966, Lantuit & Pollard 2008). Unlike most of the latter, they develop in syngenetic permafrost deposits. Syngenetic ice wedges constitute a large part of the subsurface, and the consequent variability in ground composition results in a diversity of coastal profile forms.

Based on our field observations, we selected three coastal study sites: two yedoma exposures from the northern (71.88°N , 132.58°E) and southern (71.42°N , 132.1°E) extremes of the surveyed coastline, as well as an Alas Site (71.59°N , 132.22°E) between the two (Fig. 2).

The North Cliff is a steep, slightly rounded, inland, 25-m-high coastal section with a continuous vertical ice complex outcrop in the upper part and a narrow 35-m-wide terrace with a mean slope of 25° in the lower portion of the slope. The South Cliff is a yedoma hill up to 32 m a.s.l. high, and features an upslope propagating headwall that forms a half-rounded thermo-terrace of uniform self-contained shape, extending 130 m inland with a mean slope of 12° . The Alas Site is part of a coastline section that extends through a 2 km thermokarst depression with a mean height of 10.5 m a.s.l. The steep ($30\text{--}40^{\circ}$) slope is planar with small dissections along polygonal ice-wedge systems. Segregated gravimetric ground ice content is on average 93 and 48 wt% for ice complex and alas deposits, respectively (Strauss & Schirmer 2011). Along the 55 km between the North Cliff and South Cliff sites,

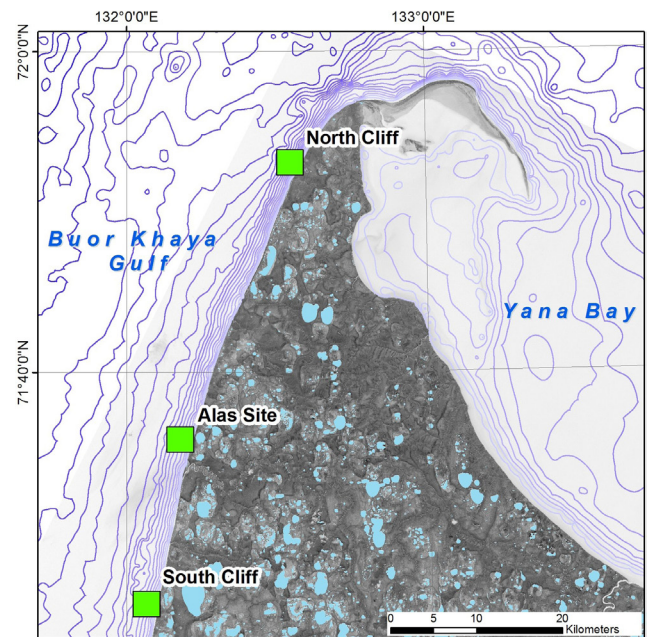


Figure 2. Study site locations are indicated with green squares. Bathymetry is shown with 1 m isobaths. The base image is the 1st channel of the principal component analysis (PCA) of bands 1-5 of a RapidEye image from August 2010.

large sandy beaches up to 2.5 m a.s.l. high protect the shore face from the development of thermo-erosional niches.

Materials and Methods

On-site surveying

During a joint Russian-German expedition in 2010, precise topographic reference measurements were made using a ZEISS ELTA C30 tacheometer and corresponding reflector mirrors. To ensure regular positioning in a local coordinate system and accurate geocoding of all measurements, a network of well distributed anchor points with known absolute coordinates was set up, on which basis the horizontal geocoding *RMS* for all three sites was 1.2 m. Z-values were converted into absolute heights according to the factual sea level, which may oscillate non-periodically up to 80 cm (Dmitrenko et al. 2001). Dense point measurements allowed for interpolation to triangular irregular networks (TIN).

Remote sensing products

Our approach is to create a measure of changing topography over time rather than a traditional 2D shoreline position monitoring and change rate determination. Aerial photographs taken in July 1974 and our field survey conducted in August 2010 span a period of 36 years of coastal change. The former is central perspective stereo imagery and offers the possibility of 3D mapping. Because neighboring image strips were taken at different flight heights, scanning with a high-performance photogrammetric scanner with 14 microns scan interval results in a ground sample distance of 0.7 m for the North Cliff and 1 m over the South Cliff and Alas Site. Providing large

areal coverage at 5 m ground resolution, RapidEye imagery acquired during our expedition and ortho-rectified with a mean *RMS* value of 4.3 m serves as a master dataset for further georeferencing purposes.

Image processing and DEM extraction

Photogrammetric processing of aerial imagery was performed with PCI Geomatica's 10.3 OrthoEngine module. Automatic image correlation based on the PCA-transformed RapidEye scene provided mean horizontal accuracies of 5.6 m for North Cliff, 10.2 m at the Alas Site, and 6.6 m over South Cliff, with mean vertical accuracies of 4.3, 5.1, and 7 m, respectively. Elevation values for stereo ground control points were derived from topographic maps with a contour equidistance of 10 m and using *z*-values of field measurement points. Absolute cumulative error of the geocoded RapidEye (*RMS*₁) and aerial imagery (*RMS*₂) as well as of the independent survey data (*RMS*₃) can reach 11.1 m at North Cliff, 15.7 m along the Alas coast, and 12.1 m on the South Cliff. Regarding planimetric change rate determination over 36 years (ΔT), we estimate uncertainties (E_r) in the erosion rate as follows:

$$E_r = \frac{((RMS_1 + RMS_2) * 2) + (RMS_3 * 2)}{\Delta T} \quad (1)$$

Thus estimated uncertainties were ± 0.62 , ± 0.87 , and ± 0.67 m for erosion rates at North Cliff, Alas Site, and South Cliff, respectively.

Digital elevation models (DEM) were produced with spatial resolutions of 3 m in the north and 4 m for the other two sites. Visual analysis of the historic DEMs shows a systematic underestimation of the rolling hills rather than a random noise signal. Using points of known elevation on undisturbed yedoma tops, the systematic negative height difference was determined and additional correction factors of 1.11, 1.25, and 1.15 m were applied to the DEM extraction process at North Cliff, for the Alas Site, and in the south, respectively. The imagery was ortho-rectified and mosaicked based on the DEMs and ground control points.

Normalized difference thermo-erosion index derivation

Calculation of the NDTI requires digitalization of the lower and upper coastline in each dataset. Due to intense contrast along the beach, the cliff bottom line could be traced in the ortho-photos, and represented the lower coastline in 1974. Despite high spatial resolution, manual digitalization of the coastal bluff top using the black-and-white imagery was highly subjective. We adapted the approach of Liu et al. (2009) of bluff-line estimation by analyzing elevation profiles perpendicular to the mean lower coastline. Cliff profiles were plotted at 50-m intervals using the DEM, and the cliff top position was selected from the cross-section.

Coastline positions in 2010 were surveyed in the field. Based on weighted line segment length and orientation of the 2010 cliff bottom coastline, we derived mean coastline tangents for each site. Along transects perpendicular to these baselines at 50-m intervals, intersections with surveyed, remotely sensed,

and tangentially identified coastlines were constructed with ESRI ArcGIS 10, to calculate planimetric retreat of the cliff bottom and top line, regarded as thermo-abrasion and thermo-denudation, respectively.

Geomorphometric change detection

We defined our study site as the area between the positions of the historic lower coastline (1974) and the contemporary bluff top (2010), bordered laterally using vectors perpendicular to the mean coastline. The resulting total 2D change areas are again divided into comparable pieces of 50-m shoreline but may vary in extent landwards. Eroded sediment volumes were obtained by subtracting the 1974 DEM from the rasterized (1 m) field survey TINs. The resulting 3D surface of changed topography equals effective volumetric erosion.

Results

Coastline digitalization

Based on remote sensing techniques and field survey data, we determined historical and contemporary coastline positions and linear change vectors within a Geographic Information System. Based on vector lengths between bluff top and cliff bottom lines, we calculated mean thermo-denudation and thermo-abrasion rates over a 36-year period (Table 1). In order to maintain consistency with other datasets (e.g., Lantuit et al. 2011a), we adopt thermo-denudation as general coastal erosion. Thus annual coastal erosion rates vary in a range from 0.4 to 3.3 m a⁻¹ and generally show a median from 1.0 m a⁻¹ along the 550-m-long Alas coastline to 1.3 and 2.0 m a⁻¹ along the 350- and 550-m-long yedoma coastline sections at North Cliff and South Cliff, from mean absolute coastal erosion of 29.6, 45.6, and 71.2 m, respectively.

Coastal erosion and mass flux

Analysis of volumetric erosion rates revealed continuously high values around 42,000 m³ km⁻¹ a⁻¹ at North Cliff and slightly lower material displacement of 34,200 m³ per coastline km at South Cliff, but with a three-times higher standard deviation (Table 1). The quantitative continuous erosion at North Cliff is shown in Figure 3a. In comparison to North Cliff, the spatial erosion pattern at South Cliff (Fig. 3b) is more diverse, resulting in quantitatively highly variable planimetric as well as volumetric erosion rates. A common pattern at both sites is that eroded volume diminishes to the north and south as a consequence of changing topography. This is a little less pronounced at North Cliff (25.3 m asl \pm 0.9), but clearly visible at the southern site (31.6 m asl \pm 6.3), where the yedoma hill drops in elevation more steeply. The bluff line at the Alas Site (Fig. 3b) is at 10.5 m a.s.l. throughout the site, resulting in a homogeneous coastal erosion with mean retreat rates around 1 m a⁻¹ and median volume loss of 12,000 m³ km⁻¹ a⁻¹.

Variation of NDTI

The spatial distribution of processes contributing to coastal erosion is also very diverse between all three sites. North Cliff exhibits a clearly uniform thermo-abrasional character

Table 1. Key data of the study sites: geomorphometric characteristics, change detection results, and site specific NDTI values.

| | North Cliff | Alas Site | South Cliff |
|--|------------------------|------------------------|-------------------------|
| Segment length [m] | 350 | 550 | 550 |
| Bluff height [m] ($\pm \sigma$) | 25.3 (± 0.9) | 10.5 | 31.6 (± 6.3) |
| Aspect [$^{\circ}$] | 298 | 287 | 282 |
| Shoreface slope | 0.0042 | 0.0032 | 0.0029 |
| Thermo-denudation rate [m a^{-1}] ($\pm \sigma$) | 1.31 (± 0.22) | 0.97 (± 0.25) | 2.04 (± 0.78) |
| Thermo-abrasion rate [m a^{-1}] ($\pm \sigma$) | 1.77 (± 0.29) | 1.07 (± 0.25) | 1.41 (± 0.24) |
| Vol. erosion rate [$\text{m}^3 \text{a}^{-1}$] per km coastline ($\pm \sigma$) | 42 000 ($\pm 5 700$) | 12 000 ($\pm 3 200$) | 34 200 ($\pm 18 000$) |
| 2D/3D area ratio of DEM difference ($\pm \sigma$) | 0.92 (± 0.005) | 0.94 (± 0.01) | 0.95 (± 0.02) |
| NDTI ($\pm \sigma$) | -0.16 (± 0.11) | -0.04 (± 0.16) | 0.17 (± 0.19) |

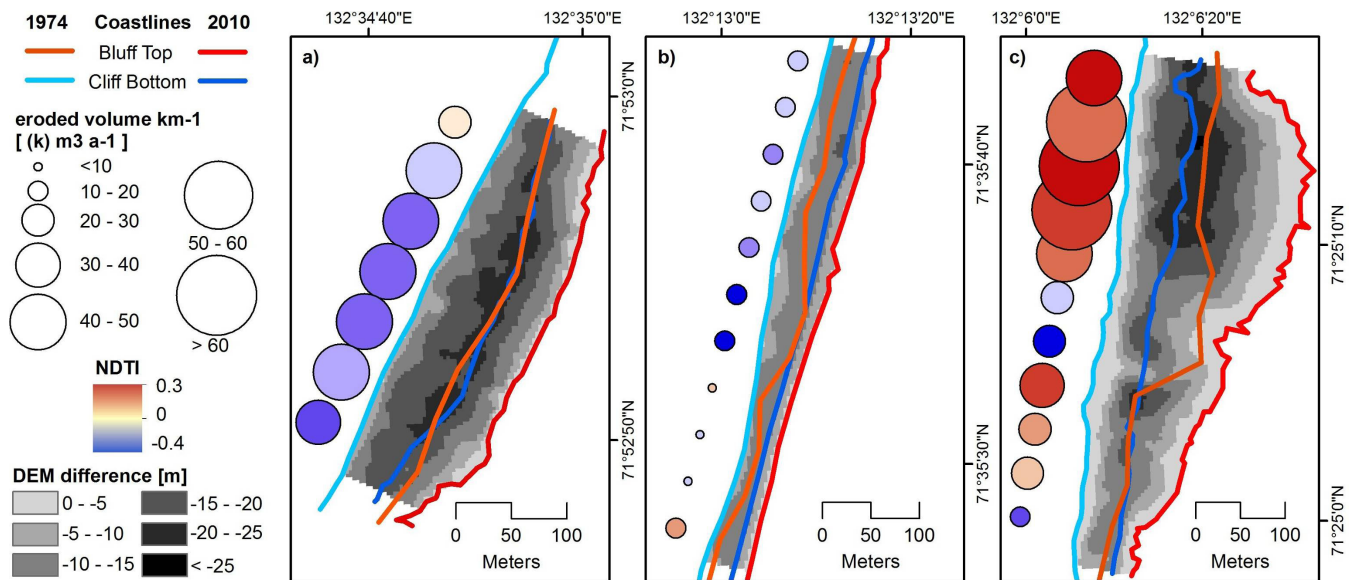


Figure 3. Thematic maps of thermo-erosion for study sites: (a) North Cliff, (b) Alas Site, (c) South Cliff. Positions of coastlines; Circles represent equal pieces of 50 m shoreline, Symbol size shows mean annual quantity of eroded material, scaled to thousands ($\text{k m}^3 \text{ km}^{-1}$ coastline). Circles are color coded with corresponding NDTI value. De facto volumetric erosion is shown through classified DEM difference raster.

with a median NDTI value of -0.16. In marked contrast, the South Cliff site is of more heterogeneous character, showing strong recession of the upper coastline, associated with large erosion volumes and lower rates close to the transition to alas in the southern margins. NDTI at South Cliff is 0.17, but with deviations of the same order (0.19).

The highest NDTI values are observed in the center of the thermo-terrace. Neighboring segments with lower thermo-denudation rates also feature high volume losses. Less difference in 2D/3D area ratio at South Cliff underlines the slope process character of thermo-denudation, if positive NDTI values are involved. In contrast to the yedoma sites, NDTI values along the Alas coast are around 0, with an overall tendency to the negative range (-0.04).

Discussion

Since the coastline examined here is subject to common regional influences (fluvial and sea ice dynamics, for example), and the aspect of the coast varies little between sites

(282 to 298 degrees), we do not expect thermo-abrasion to vary greatly between sites. It varies between 0.5 and 2.1 m a^{-1} , while thermo-denudation varies from 0.4 to 3.3 m a^{-1} . Higher values of thermo-denudation correlate with yedoma sites, where high ground ice contents probably speed erosion of the bluff edge. Presence of ground ice favors coastal erosion. The clastic material component from coasts with high ice contents are quickly removed (Pavlidis et al. 2007). Moreover, the influence of thermo-abrasion depends on whether high ground ice content materials lie below, at, or above the water level (Are 1978). Because of the erosional deposits at the cliff bottom at North Cliff and very little ice exposure in the south, it is difficult to estimate total ground ice contents.

Alas areas next to the 34-m-high yedoma hill in the south are 4 m higher than in the north, while neighboring yedoma hills of the up to 10 m a.s.l. high Alas Site reach even 37 m. Assuming that ice complex within thermokarst basins melted completely, the base at both sites is at the same level, and given that the thickness of alas deposits depends on initial ground ice content (Ulrich et al. 2010), ice content at the thermo-denudational site

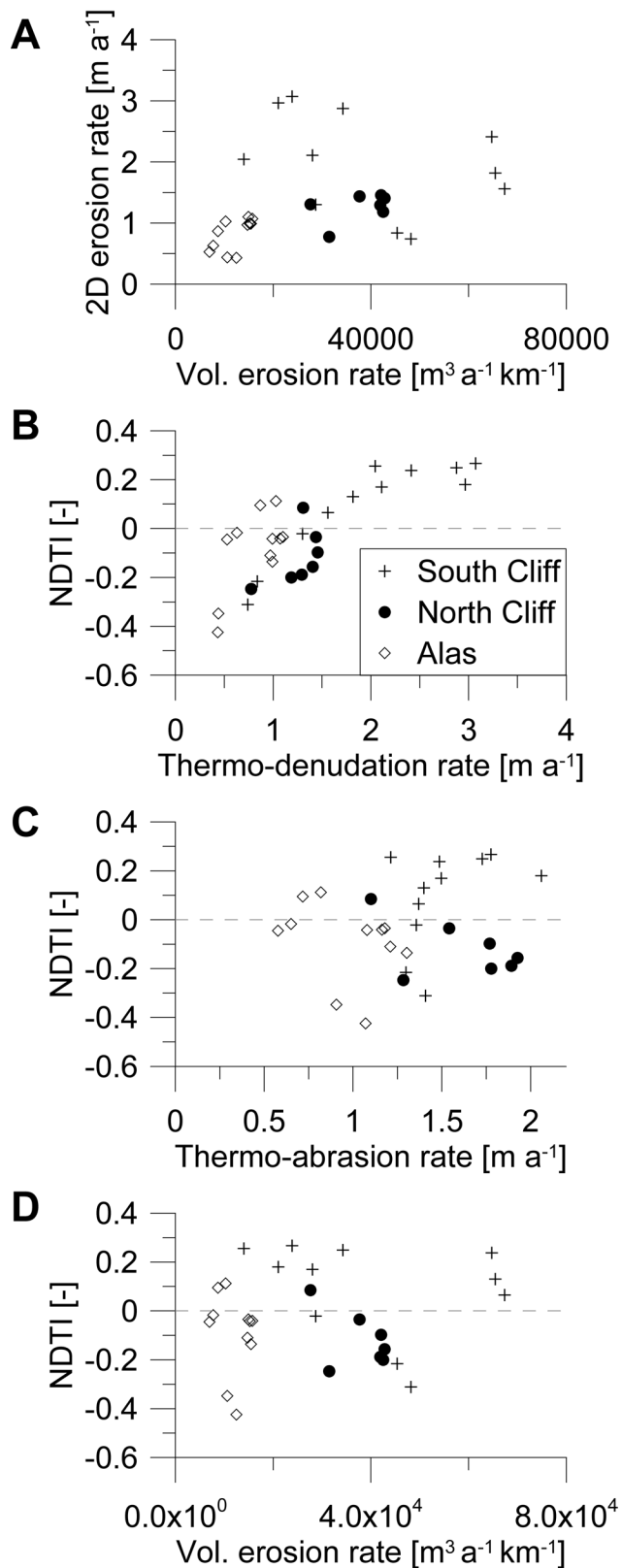


Figure 4. Erosion rates and NDTI values for shoreface profiles at North Cliff, Alas Site, and South Cliff (7, 11, and 11 profiles, respectively). A: 2D coastal erosion rates are plotted against volumetric rates of material loss, normalized to coastline length.

must be lower than at the North Cliff thermo-abrasional site.

The Bykovsky Peninsula on the opposite site of the Buor Khaya Gulf also features thermokarst-dominated relief, including thermokarst lagoons (Grosse et al. 2007). Compared to 1.3 m a⁻¹ mean coastal retreat rate on Buor Khaya, Lantuit et al. (2011b) found a slightly lower erosion rate of 0.59 m a⁻¹ on Bykovsky, but erosional patterns revealed strongest retreat rates of up to 10 m a⁻¹ along a short alas section.

Although aspect, and presumably sea ice, meteorology and sea level affect all three sites similarly, there are differences in 2D and volumetric erosion rates. Sites with higher 2D erosion rates tend to have higher volumes of eroded material (Fig. 4A). However, the values are widely spread, so that observed values yield no predictive relationship. The highest volumes were moved at sites with less than mean erosion rates, suggesting that with increasing positive NDTI values, the cumulative influence on volumetric land loss weakens. Likely explanations include variations between sites in ground ice content, bluff height, and bathymetry. Bathymetry effects are probably small, since thermo-abrasion rates are similar for all sites in terms of magnitude and variance, but slightly higher in magnitude for the yedoma sites than for the Alas Site. The North Cliff site has the highest thermo-abrasion rate and the highest volume of material eroded (42,000 m³ a⁻¹ km⁻¹). Cliff top erosion, the value that would be reported in the international Arctic Coastal Dynamics database (Lantuit et al. 2011a), varies between 1 m (Alas) and 2 m (South Cliff) per year. However, the South Cliff value has triple the standard deviation in rate, reflecting the greater landward progress of portions of the bluff. As a group, the three sites suggest that coastal erosion along the western shore of Buor Khaya, when examined over a 36-year period, is locally more heterogeneous for yedoma than alas sites.

Although the lowest NDTI values were observed at the Alas Site, the North Cliff mean and median NDTI values were lower than those for the Alas Site. At this group of sites, NDTI increases with thermo-denudation but shows no trend with thermo-abrasion (Figs. 4B, 4C). We suggest that this may be an indication that thermo-denudation is generally dominant over thermo-abrasion for these sites.

NDTI can only be calculated for sites where the position of the lower and upper coastlines can be measured in a geo-referenced fashion. In cases where there is more than one upper edge, the method is limited to time intervals short enough to identify the progress of the same edge. In principle, the method can be applied to coasts eroding via block failure, but the landward extent of the thermo-niche at the base of the coastal bluff would need to be measured.

Conclusions

In the coastal zone, thermo-denudation, as a simple slope process in a narrower sense, cannot be dissociated from the abrasional activity of the sea. Since coastal bluffs in ice complex sediments may differ in their spatio-temporal behavior, we considered this relation by looking at effectively eroded volumes in comparison to planimetric erosion rates.

Thermo-erosion along the western coast of Buor Khaya Peninsula impacts a shoreline that has already been affected by thermokarst. In response to this and in connection with littoral drift of accumulated material at the cliff bottoms, a zigzag spatial erosional pattern is pronounced. Applying the NDTI concept, we were able to qualitatively assess the character of thermo-erosion along a permafrost coastline section. It will be necessary to expand analysis to a wider range of sites with different environmental settings.

Acknowledgments

We thank the Arctic and Antarctic Research Institute in St. Petersburg and the staff of the Hydrographical Service in Tiksi (Russia) for logistical support. RapidEye imagery was kindly provided by the DLR. This work was funded in part by the BMBF through PROGRESS: Potsdam Research Cluster for Georisk Analysis.

References

- Are, F.E. 1978. The reworking of shorelines in the permafrost zone, In *Proceedings of the Second International Conference on Permafrost*, Yakutsk, U.S.S.R., July 1973, U.S.S.R. Contribution: 59-62.
- Are, F.E. 1988. Thermal Abrasion of Sea Coasts. *Polar Geography and Geology* 12 (1): 1-81, (2): 87-157.
- Charkin, A.N., Dudarev, O.V., Semiletov, I.P., Kruhmaliev, A.V., Vonk, J.E., Sanchez-Garcia, L., Karlsson, E., & Gustafsson, O. 2011. Seasonal and interannual variability of sedimentation and organic matter distribution in the Buor-Khaya Gulf: the primary recipient of input from Lena River and coastal erosion in the southeast Laptev Sea. *Biogeosciences* 8: 2581-2594.
- Dmitrenko, I.A., Hoelemann, J.A., Kirillov, S.A., Berezovskaya, S.L., & Kassens, H. 2001. Role of barotropic sea level changes in current formation on the eastern shelf of the Laptev Sea. *Doklady Earth Sciences* 377 (2): 243-249.
- Drozhdov, D.S., Rivkin, F.M., Rachold, V., Ananjeva-Malkova, G.V., Ivanova, N.V., Chehina, I.V., Koreisha, M.M., Korostelev, Y.V., & Melnikov, E.S. 2005. Electronic atlas of the Russian Arctic coastal zone. *Geo-Marine Research Letters* 25: 81-88.
- Grosse, G., Schirrmeister, L., Siegert, C., Kunitsky, V.V., Slagoda, E.A., Andreev, A.A., & Derevyagin, A.Y. 2007. Geological and geomorphological evolution of a sedimentary periglacial landscape in Northeast Siberia during the Late Quaternary. *Geomorphology* 86: 25-51.
- Jones, B.M., Arp, C.D., Jorgenson, M.T., Hinkel, K.M., Schmutz, J.A., & Flint, P.L. 2009. Increase in the rate and uniformity of coastline erosion in Arctic Alaska. *Geophysical Research Letters* 36, L03503.
- Lantuit, H., Overduin, P.P., Couture, N., Wetterich, S., Are, F., Atkinson, D., Brown, J., Cherkashov, G., Drozdov, D., Forbes, D., Graves-Gaylord, A., Grigoriev, M., Hubberten, H.-W., Jordan, J., Jorgenson, T., Ødegård, R.S., Ogorodov, S., Pollard, W., Rachold, V., Sedenko, S., Solomon, S., Steenhuisen, F., Streletskaia, I., & Vasiliev, A. 2011a. The Arctic Coastal Dynamics database. A new classification scheme and statistics on arctic permafrost coastlines. *Estuaries and Coasts*, doi:10.1007/s12237-010-9362-6.
- Lantuit, H., Atkinson, D., Overduin, P.P., Grigoriev, M.N., Rachold, V., Grosse, G., & Hubberten, H.-W. 2011b. Coastal Erosion dynamics on the permafrost-dominated Bykovsky Peninsula, north Siberia, 1951-2006. *Polar Research* 30, 7341.
- Lantuit, H. & Pollard, W.H. 2008. Fifty years of coastal erosion and retrogressive thaw slump activity on Herschel Island, southern Beaufort Sea, Yukon Territory, Canada. *Geomorphology* 95: 84-102.
- Liu, J.-K., Li, R., Deshpande, S., Niu, X., & Shih, T.-Y. 2009. Estimation of blufflines using topographic Lidar Data and orthoimages. *Photogrammetric Engineering & Remote Sensing* 75: 69-79.
- Mackay, J.R. 1966. Segregated epigenetic ice and slumps in permafrost, Mackenzie Delta, N.W.T. *Geographical Bulletin* 8: 59-80.
- Pavlidis, Y.A., Leontiev, I.O., Nikiforov, S.L., Rachold, V., Grigoriev, M.N., Razumov, S.R., & Vasiliev, A.A. 2007. General forecast of the evolution of the coastal zone of the Eurasian Arctic Seas in the 21st Century. *Oceanology* 47: 116-126.
- Schirrmeister, L., Kunitsky, V., Grosse, G., Wetterich, S., Meyer, H., Schwamborn, G., Babiy, O., Derevyagin, A., & Siegert, C. 2010. Sedimentary characteristics and origin of the Late Pleistocene Ice Complex on north-east Siberian Arctic coastal lowlands and islands - A review. *Quaternary International* 241:3-25.
- Sovershaev, V.A. 1992. Coastal zone of Arctic seas. In *Geoecology of the North*. Solomatin, V.I. (ed.). Moscow, MGU publishing house, 270 pp. (in Russian).
- Strauss, J. & Schirrmeister, L. 2011. Permafrost sequences of Buor Khaya Peninsula. In *Russian-German Cooperation, System Laptev Sea, The expedition Eastern Laptev Sea - Buor Khaya Peninsula 2010*. Reports on Polar and Marine Research 629: 35-50.
- Ulrich, M., Morgenstern, A., Günther, F., Reiss, D., Bauch, K.E., Hauber, E., Rössler, S., & Schirrmeister, L. 2010. Thermokarst in Siberian ice-rich permafrost: Comparison to asymmetric scalloped depressions on Mars. *Journal of Geophysical Research* 115, E10009.

Shear Strength of Rock Joints Filled with Frozen Sand

Friederike K. Günzel
University of Brighton, Brighton, UK

Abstract

This paper is a first attempt to understand the shear strength of rock joints with frozen infill at temperatures close to melting. Direct shear tests were performed on synthetic samples (concrete-frozen sand) representing rock joints filled with frozen sand; the results are compared with the shear strength of concrete-ice samples representing clear ice-filled rock joints reported by Günzel (2008, 2010). All concrete-frozen sand samples failed by the frozen sand becoming detached from the concrete surface; post-peak behavior was dominated by frictional sliding. Unlike the concrete-ice samples, shear deformation of the frozen sand itself was not observed. Compared to the concrete-ice samples, the peak shear strength of the concrete-frozen sand samples reduced more with increasing temperature. As sand-filled joints cannot close after melting of the ice, the shear strength of the thawed joint is much smaller than that of a clear ice-filled joint after thawing.

Keywords: direct shear; frozen sand; rock joints; rock slopes; shear strength.

Introduction

Rock joints filled with clear ice have been described in permafrost rock slopes and related to temperature induced rock fall and slope failures by many authors (e.g., Gruber & Haerberli 2007). Only recently, joints filled with frozen soil have been mapped in a permafrost area of the Zugspitze (Germany) and brought into connection with rock slope instabilities (Bledow & Krautblatter 2010).

Currently, a large amount of data are available in the literature concerning the mechanical properties of ice and frozen soil for a large number of variables and boundary conditions, such as temperature, ice content, confining pressure, and strain rate (Arenson et al. 2007). Also, over the last decades a large amount of research has been carried out to investigate the shear strength of rock joints filled with soil (de Toledo & de Freitas 1993, Indraratna et al. 2005).

So far, however, only little information is available on the strength properties of rock joints filled with frozen soil. Knowledge of this is important to assess the stability of rock slopes in a warming permafrost environment. The research of rock joints filled with frozen soil is very complex as the number of variables increases by the following: roughness of the rock joint surface, infill thickness, and the relation of the soil grain size to the surface roughness and infill thickness. No doubt more variables can be added to this list.

The current study is a first attempt to understand the behavior of frozen sand filled rock joints by comparing the shear strength of frozen sand-rock interfaces with the shear strength of ice-rock interfaces. Temperature and normal stress are the only variables changed in this study, while the ice content and the grain size of the frozen sand, the surface roughness of the synthetic rock samples, and the strain rate are being held constant.

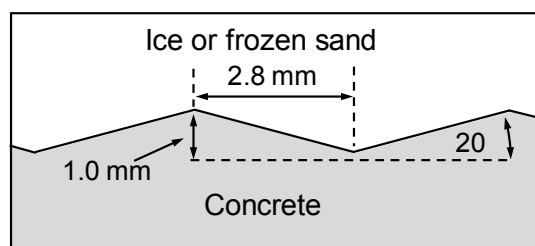


Figure 1. Dimensions of the saw-tooth surface.

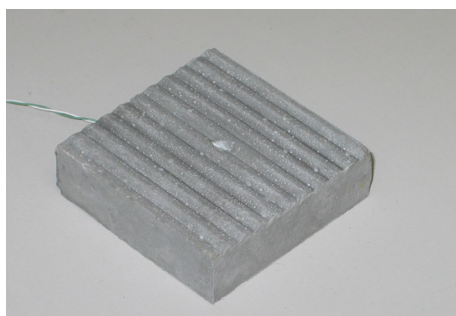


Figure 2. Concrete-block with cast saw-tooth surface; the small cavity in the center holds the tip of the thermocouple.

Laboratory Methods

Preparation of samples

In the experiments, artificial rock samples made of high-strength concrete (Densit Ducorit D4) were used. To simulate the roughness of the natural rock joint surfaces, a regular saw-tooth surface was used with dimensions, as shown in Figure 1. Regular saw-tooth surfaces are a commonly used idealization of rough rock surfaces in the literature (e.g., de Toledo & de Freitas 1993). The dimensions of the samples were 59 mm × 59 mm to fit inside a 60-mm square shear box. The geometry of the sample surfaces was chosen to enable a direct comparison of the frozen sand infill with the clear ice-filled joints previously presented by Günzel (2008, 2010).

A K-Type thermocouple was cast into the concrete samples with the sensitive tip in a small cavity at the center of the sample surface (Fig. 2). This allowed the temperature of the frozen sample to be measured during the shear tests.

For the current study, concrete-frozen sand samples were prepared. These consist of a concrete block with saw-tooth surface overlaid by an equally thick block of frozen sand (Fig.

3). The sand used for the tests was quartz sand, fraction D (150-300 μm), according to BS 1881-131. This grain size was chosen to ensure that the grains would be smaller than the height of the asperities of the concrete surface. The concrete-frozen sand samples simulate a frozen sand-filled joint with the infill thickness being larger than the amplitude of the surface roughness. The samples were prepared by placing the concrete block into a mould (60 mm \times 60 mm \times 40 mm) filled with distilled water. Then 100 g of dry sand was poured on top of the concrete block, the sand surface was levelled, and surplus water removed. The sample was then allowed to freeze overnight at approximately -4°C . With this method, a consistent moisture content of 25.4% (std. dev. = 1.2%) of the sand samples was achieved. This is equivalent to a void ratio of 0.74 for the frozen sand. The frozen sand therefore is grain-supported; the ice content is considered intermediate according to Arenson et al. (2007). The air content of the samples is considered negligible.

Unfrozen concrete-sand samples were prepared in the same way as the concrete-frozen sand samples but directly inside the frame of the shearbox. The samples have the same moisture content as the concrete-frozen sand samples.

Direct shear tests

The direct shear tests were carried out as shown in the schematic overview in Figure 4. Normal stress is provided by hanging weights. Horizontal and vertical displacements are measured with LVDTs.

In the direct shear tests, a constant strain (0.49 mm/h) is

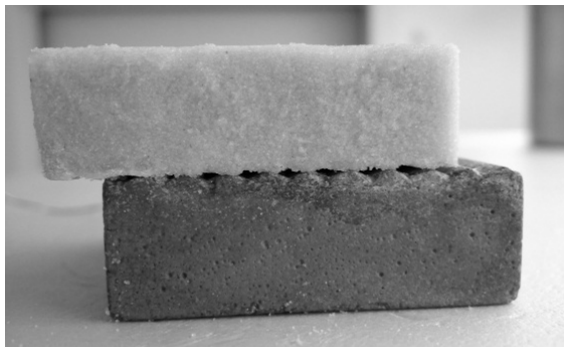


Figure 3. Concrete-frozen sand sample after a direct shear test at -4°C with normal stress = 643 kPa.

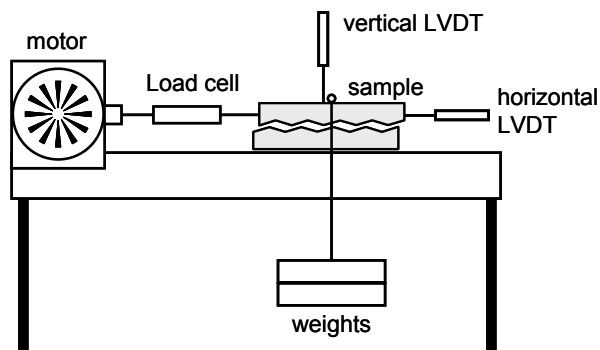


Figure 4. Schematic overview over experimental set-up of the direct shear tests.

applied by an electric motor pulling the upper part of the sample while the lower part remains stationary. The shear stress is measured with a load cell. A total of 50 direct shear tests were carried out with concrete-frozen sand samples at temperatures between -1°C and -4°C ; normal stresses ranged between 135 kPa and 634 kPa. This is equivalent to depths of 5–25 m below ground. This is the depth at which seasonal temperature change can be observed; also warming of permafrost was observed up to 25 m below ground during the past decades (e.g., von der Mühl et al. 1998). The results of these experiments are compared with earlier experiments reported by Günzel (2008), where samples consisting of a concrete block overlaid by clear ice (concrete-ice samples) were tested.

A total of 10 direct shear tests were carried out with unfrozen concrete-sand samples. These were tested at a constant strain of 19 mm/h.

Data of the frictional strength of two concrete blocks without infill (Günzel 2008) are also used for comparison.

Cold room

The experiments were carried out in a cold room. To ensure a constant temperature of the sample during the defrosting cycles of the cooling element, the shear box was encased inside a Styrofoam box with 100 mm wall thickness. However, the electric motor of the shear box apparatus caused the temperature inside the Styrofoam box to increase during the direct shear tests. Therefore, it was very difficult to control the temperature of the sample and subsequently the temperatures at failure varied by about 0.5°C .

Stress-Displacement Curves

Direct shear tests without ice

A typical stress-displacement curve of a concrete sample without infill is shown in Figure 5. The vertical dilation clearly follows the saw-tooth surface of the concrete sample.

Direct shear tests with concrete-ice samples

The concrete-ice samples behaved in two different modes (Günzel 2008). At low normal stresses (below ~ 300 kPa), the ice detached from the concrete surface during the test. A

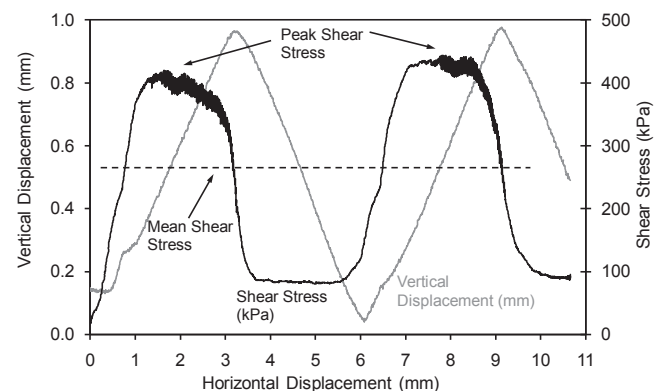


Figure 5. Stress-Displacement curve of saw-tooth concrete samples without infill (normal stress = 207 kPa).

typical stress-displacement curve of a sample tested at low normal stress (207 kPa) is shown in Figure 6. The sharp peak of the shear stress is associated with the detachment of the ice from the concrete surface. The response after 3 mm horizontal displacement is associated with the frictional sliding of the ice-concrete interface.

At high normal stresses, the deformation of the sample was mostly due to a shear deformation of the ice itself or a combination of ice deformation and sliding of ice over concrete. At the end of these tests, the shear deformation of the ice was clearly visible (Fig. 7).

Direct shear tests with concrete-frozen sand samples

The response of the concrete-frozen sand samples differs from the concrete-ice samples inasmuch as, independent of the normal stress and temperature, all concrete-frozen sand samples failed by the frozen sand becoming detached from the concrete surface, as shown in Figure 3. Even at high normal stress (up to 634 kPa), no shear deformation of the frozen sand was observed. It appears that a shear zone inside the frozen sand, as described by Yasufuku et al. (2003), develops only if the attachment of the frozen sand to the concrete surface is stronger than the shear strength of the frozen sand itself.

There is a slight difference in the failure mode of the concrete-frozen sand samples, as demonstrated in Figures

8 and 9. Both curves show a sharp peak at just over 1 mm horizontal displacement associated with the detachment of the frozen sand from the concrete surface. Figure 8 (normal stress = 141 kPa) shows brittle failure just after peak, which is associated with a jump in the vertical displacement curve and some 'overshooting' of the shear stress curve. On the other hand, Figure 9 (normal stress = 634 kPa) shows strain softening, albeit with a steep drop after peak. The majority of samples showed post-peak brittle behavior, but at high sample temperature and high normal stress, strain softening behavior becomes more frequent. This observation follows the description by Arenson et al. (2007) of the effect of different variables on the strength of frozen soil.

The post-peak stress-displacement curve is characterized by frictional sliding of the frozen sand over the concrete surface. The main peaks and troughs can be associated with the sliding movement up and down the asperities. This is very similar to the post-peak behavior of the concrete-ice sample (Fig. 7). However, the double peak (Figs. 8 and 9) was not observed in any of the concrete-ice samples. As yet, no explanation for this phenomenon has been found.

The vertical displacement shown in Figures 8 and 9 clearly shows the movement of the frozen sand over the saw-tooth surface of the concrete. The flattening of the vertical displacement curve at high normal stress (Fig. 9) is due to erosion of the frozen sand during the test. This can clearly be seen when inspecting the detached frozen sand surface of the same sample after the test (Fig. 10).

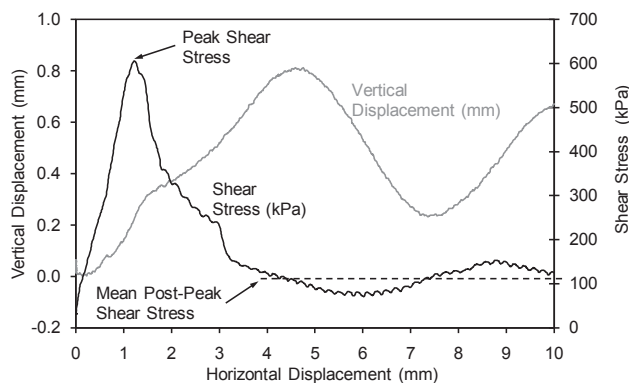


Figure 6. Results of direct shear experiment with a concrete-ice sample at -2°C (normal stress = 207 kPa).

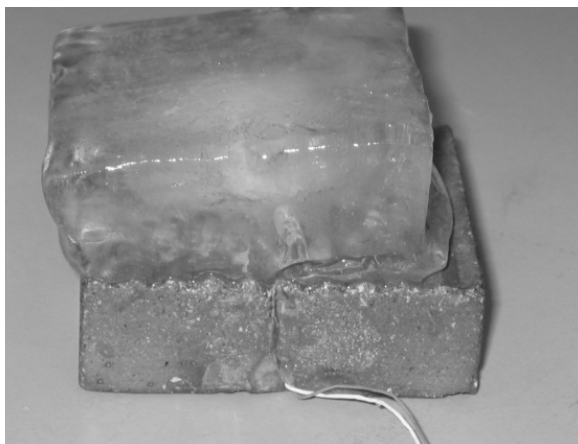


Figure 7. Shear deformation of a concrete-ice sample after a direct shear test with normal stress = 490 kPa.

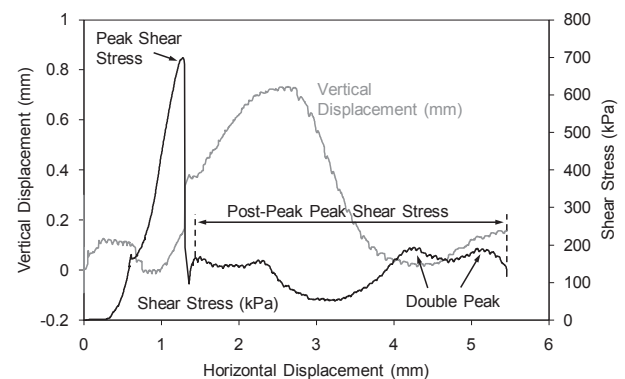


Figure 8. Results of a direct shear experiment with a concrete-frozen sand sample at -3°C (normal stress = 141 kPa).

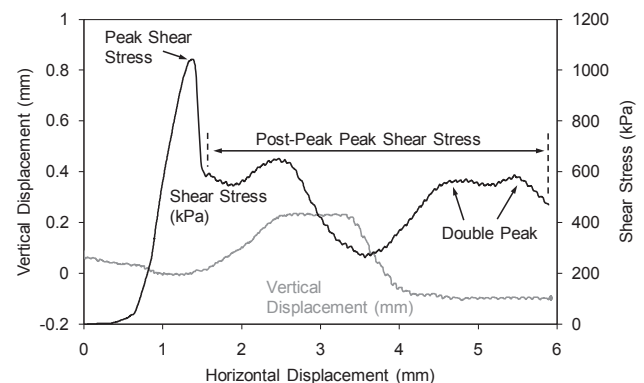


Figure 9. Results of a direct shear experiment with a concrete-frozen sand sample at -4°C (normal stress = 634 kPa).

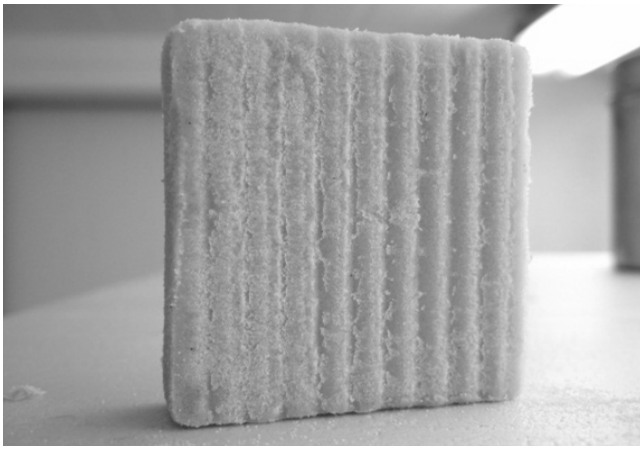


Figure 10. Detached surface of the frozen sand sample after a direct shear test at normal stress = 634 kPa. The erosion of the asperities can be clearly seen.

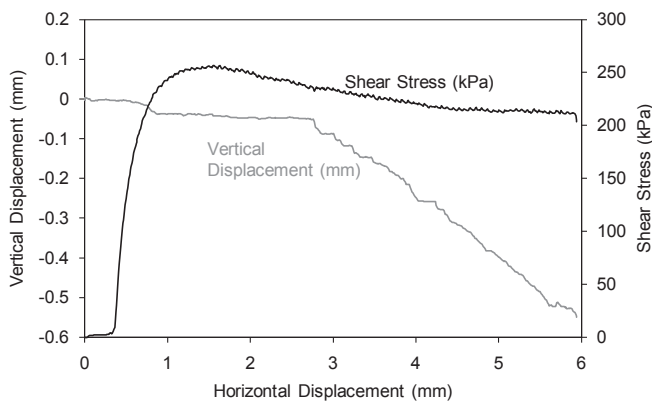


Figure 11. Results of a direct shear experiment with an unfrozen concrete-sand sample (normal stress = 423 kPa).

Direct shear tests with unfrozen concrete-sand samples

The stress-displacement curves of the unfrozen concrete-sand samples (Fig. 11) show strain-softening of the samples during the test. The samples deformed by shearing the sand above the crests of the concrete saw-tooth surface.

Peak Strength and Residual Strength

Peak shear strength of the frozen samples

The peak shear strength of the concrete-ice samples is summarized in Figure 12. A clearly defined maximum peak strength at ~ 300 kPa normal stress is associated with the change between the two failure modes described above (Günzel 2008).

However, the peak shear strength of the concrete-frozen sand samples behaves differently (Fig. 13). The data are much more scattered than for the concrete-ice samples, and no clearly defined maximum is observed within the used range of normal stresses. The linear trendlines show an increase of slope with decreasing temperature from 5.4° (-2°C) to 15° (-4°C). Given the scatter of the data, it is not possible to draw detailed conclusions from these slight differences.

The peak shear strength of the concrete-frozen sand

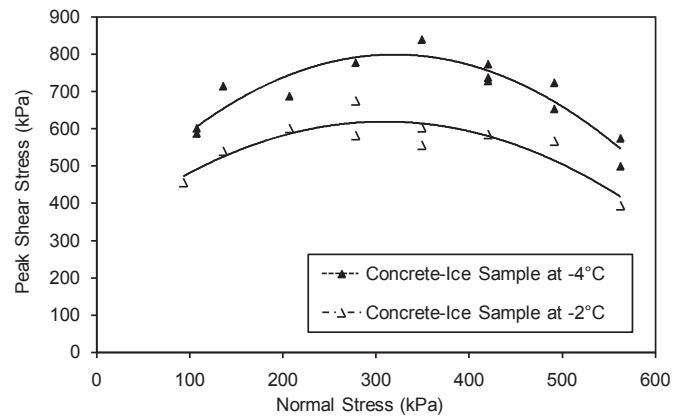


Figure 12. Peak shear strength results of concrete-ice samples.

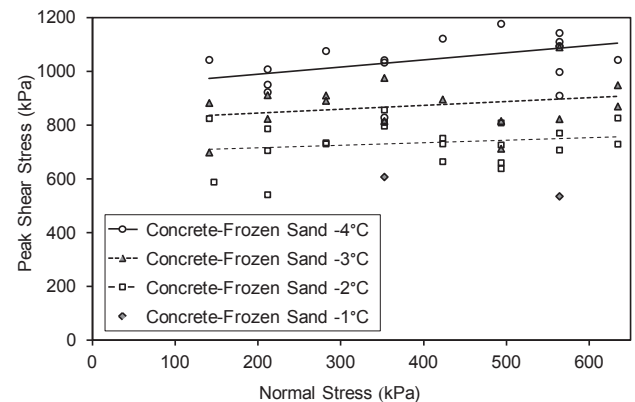


Figure 13. Peak shear strength results of concrete-frozen sand samples.

samples shows more change with temperature than that of the concrete-ice samples. For the concrete-ice samples, a temperature increase from -4°C to -2°C leads to a reduction of the peak shear strength of up to 180 kPa (maximum distance of trendlines in Figure 12); for the concrete-frozen sand samples, the same temperature increase leads to a strength reduction of up to 370 kPa (Fig. 13).

Maximum post-peak shear stress

Figure 14 gives a summary of the maximum post-peak stress of the concrete-frozen sand samples and the concrete-ice samples. The peak shear stresses of the unfrozen samples (concrete-concrete and concrete-sand) are also included. For clarity, only the trendlines of the concrete-ice and concrete-concrete data are shown in Figure 14. All of these data show a linear relationship between shear stress and normal stress indicating frictional behavior. The angles of friction for all sample types are also given in Figure 14.

The main difference between the concrete-frozen sand samples and the concrete-ice samples is that the maximum post-peak stress of the concrete-frozen sand samples is much less dependent on the sample temperature. This indicates that the post-peak strength mainly depends on the properties of the sand grains and less on the strength of the ice.

The angle of friction of the unfrozen concrete-sand samples

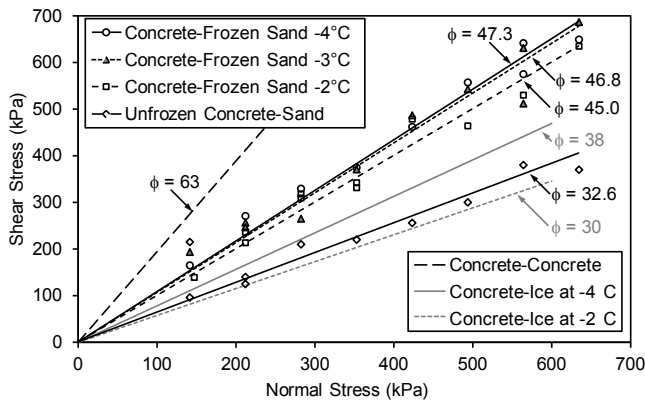


Figure 14. Maximum post-peak shear stress of frozen samples; peak shear stress of unfrozen samples.

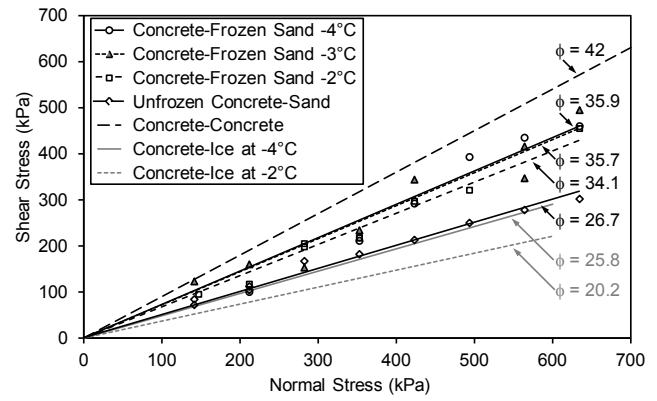


Figure 15. Mean post-peak shear stress of frozen samples; mean shear stress of concrete-concrete samples; residual shear stress of unfrozen concrete-sand samples.

Table 1. Summary of observations on shear behaviour of concrete-frozen sand samples and concrete-ice samples.

| | Concrete-frozen sand | Concrete-ice |
|---|--|--|
| Peak failure mode of sample | Detachment of the frozen sand from the concrete surface (Figs. 8, 9, and 10); | Detachment of ice from concrete surface of shear deformation of ice or combination of both (Figs. 6 and 7); |
| Dependency of peak failure on temperature | Stronger dependency – up to 370 kPa strength reduction with temperature increase from -4°C to -2°C (Fig. 13); Generally higher peak strength than concrete-ice samples | Less dependency – up to 180 kPa strength reduction with temperature increase from -4°C to -2°C (Fig. 12); |
| Dependency of peak failure on normal stress | Less dependency – no maximum; slight increase of peak shear strength with increasing normal stress (Fig. 13); | Stronger dependency – clearly defined maximum peak strength at approx. 300 kPa normal stress (Fig. 12); |
| Dependency of post-peak strength on temperature | No temperature dependency between -4°C and -3°C; slight reduction of angle of friction by 2° at -2°C (Figs. 14 and 15); | Temperature dependency – reduction of angle of friction by 8° with a temperature increase from -4°C to -2°C (Figs. 14 and 15); |
| Dependency of post-peak strength on normal stress | Linear dependency, i.e. frictional sliding predominates (Figs. 14 and 15); | Linear dependency, i.e. frictional sliding predominates in samples where the ice detached from the concrete (Figs. 14 and 15); |
| Other observations on post-peak behavior | The post-peak stress-displacement curves show a double peak as the sample dilates over the saw-tooth surface (Figs. 8 and 9), the reason for this is not yet known; | none |

is approximately 12°–14° less than that of the concrete-frozen sand samples. This is less than the angle of the saw-tooth surface (20°), which can be explained by the different friction within the sand and at the sand-concrete interface.

Mean post-peak shear stress

The normal stresses used in the experiments and the travel distance of the direct shear box are not large enough to completely erode the asperities of the samples. Therefore, the residual shear strength was estimated using the mean shear stress as suggested by Roberds & Einstein (1978). The method is demonstrated in Figure 5. For the concrete-ice and concrete-frozen sand samples, the same method was used, but

here the mean post-peak shear stress was used as demonstrated in Figure 6.

The mean post-peak stresses are summarized in Figure 15. The angle of friction of a regular saw-tooth surface is expected to follow equation 1, given by Hoek & Bray (1981):

$$\tau = \sigma \tan(\phi + i) \tag{1}$$

where τ = shear stress; σ = normal stress; ϕ = angle of friction; and i = angle of the saw-tooth surface.

The angle of friction of the concrete-concrete samples drops nearly 20°, which is expected as the angle of the saw-tooth surface is also 20°. The angles of friction of the frozen samples

reduce by $\sim 11^\circ$, which is only about half the expected value if deformation was purely by frictional sliding. This difference may be explained by the erosion of the frozen samples during the test. The angle of friction of the unfrozen samples reduces by $\sim 6^\circ$ from 32.6° (peak) to 26.7° (residual). These values are very similar to those measured for the saturated sand alone (33.7° and 26.4° , respectively), which shows that the unfrozen samples deform along a shear plane in the sand.

Conclusions and Outlook

Significance of the test results

The data presented in this paper represent the first systematic measurements of rock joints filled with frozen sand and a first attempt to understand the change in the mechanical properties of frozen infill at temperatures close to melting. The most important conclusions from the experiments are the following:

- In comparison with data presented by Günzel (2008 and 2010), there is an even stronger temperature dependency of the peak strength of joints with frozen sand infill than joints with clear ice infill.
- Even more important is the difference of shear strength after melting. In clear ice-filled joints, complete melting of the ice leads to an increase of the shear strength as the rock walls come into contact (Davies et al. 2001). However, sand-filled joints cannot close and therefore the shear strength of thawed sand-filled joints remains lower than that of the frozen joints.

For a more detailed analysis, the observations from both sample types are summarized in Table 1. The following conclusions are made from these observations:

- No shear deformation was observed within the frozen sand part of the samples. This may be explained by the fact that the frozen sand is grain-supported, not ice-supported.
- The peak strength of the concrete-frozen sand samples is higher than the peak strength of the concrete-ice samples. If the attachment of the frozen sample to the concrete is mainly due to adfreezing, this result may be surprising. However, it is assumed that the frictional strength of the angular sand grains has a strong effect on the peak strength.
- The post-peak strength of the concrete-frozen sand samples shows very little dependence of temperature between -2°C and -4°C . This also was an unexpected result. Again, it is assumed that the post-peak strength depends more on the frictional sliding of the sand grains over the concrete surface and less on the strength of the ice matrix.
- The angles of friction of the post-peak data suggest an additional way of deformation other than frictional sliding. One likely suggestion is erosion of the frozen samples.

Outlook

The author is aware that the regular saw-tooth surfaces used in the present study are not a true representation of the natural

roughness of rock joints. However, it is nearly impossible to achieve reproducible results with natural rock samples as the joint surfaces erode quickly during the tests. It is therefore planned to carry out tests with artificial samples cast from natural rock joints and with infill material similar to the naturally occurring joint infill.

References

- Arenson, U., Springman, S.M., & Segó, D.C. 2007. The rheology of frozen soils. *Applied Rheology* 17 (1): 12147-1 – 12147-14.
- Bledow, S. & Krautblatter, M. 2007. The influence of fine-grained fracture infillings on destabilisation processes in permafrost-affected rock walls in the Alps. *Geophysical Research Abstracts* 12: 4163.
- Davies, M.C.R., Hamza, O., & Harris, C. 2001. The effect of rise in mean annual temperatures on the stability of rock slopes containing ice-filled discontinuities. *Permafrost and Periglacial Processes* 12 (2): 137-144.
- de Toledo, P.E.C. & de Freitas, M.H. 1993. Laboratory testing and parameters controlling the shear strength of filled rock joints. *Geotechnique* 42 (1): 1-19.
- Gruber, S. & Haeblerli, W. 2007. Permafrost in steep bedrock slopes and its temperature-related destabilization following climate change. *Journal of Geophysical Research* 112: F02S18.
- Günzel, F.K. 2008. Shear strength of ice-filled rock joints. In *NICOP 2008: Proceedings of the Ninth International Conference on Permafrost*. D.L. Kane, K.M. Hinkel (eds.). Institute of Northern Engineering, University of Alaska Fairbanks, 1: 581-586.
- Günzel, F.K. 2010. Residual strength of ice filled rock joints. *3rd European Conference on Permafrost*, Svalbard, Norway, 2010: 250.
- Hoek, E. & Bray, J.W. 1981. *Rock slope engineering* 3rd ed. Institution of Mining and Metallurgy, Spon, London, 358 pp.
- Indraratna, B., Welideniya, S., & Brown, T. 2005. A shear strength model for idealised infilled rock joints under constant normal stiffness. *Geotechnique* 55 (3): 215-226.
- Roberds, W.J. & Einstein, H.H. 1978. Comprehensive model for rock discontinuities. *Journal of the Geotechnical Engineering Division ASCE* 104 (5): 553-569.
- vonder Mühl, D., Stucki, T., & Haeblerli, W. 1998. Borehole temperatures in Alpine permafrost: A ten year series. *7th International Conference on Permafrost*, Yellowknife, Canada, 1998: 1089-1095.
- Yasufuku, N., Springman, S.M., Arenson, L.U., & Ramholt, T. 2003. Stress-dilatancy behaviour of frozen sand in direct shear. *8th International Conference on Permafrost*, Zürich, Switzerland, 2003: 1253-1258.

Tessellons and “Sand Wedges” on the Qinghai-Tibet Plateau and Their Palaeoenvironmental Implications

Stuart A. Harris

Department of Geography, University of Calgary, Calgary, Alberta, Canada

Huijun Jin

State Key Laboratory of Frozen Soils Engineering, Cold and Arid Regions Environmental and Engineering Research Institute, Chinese Academy of Sciences, Lanzhou, Gansu, China

Abstract

This paper describes tessellons with small, frost-shattered, plate-like rock fragments infilling a wedge structure encountered on the east margin of the Qinghai-Tibet Plateau at 4301 m in China. They are intersected by a sand-filled wedge generally regarded as being 13.49 ka BP by TL dating. The rock tessellon may have been formed during an early phase of the Last Glacial Maximum (LGM) or during an earlier cold event. This geocryological evidence supports the conclusions of the late Yafeng Shi and others that there was not a united ice sheet over the plateau during the LGM. A map of the implied palaeogeography for the LGM of Southeast Asia is provided. Since tessellons have intersecting bedding of the infilling more or less parallel to the sides of the wedge, they are readily distinguished from sand-filled ice-wedge casts. The term “tessellon” should be used for them instead of “sand wedge” with the prefix “rock” or “sand” to avoid confusion.

Keywords: tessellons; sand wedges; ice-wedge casts; sand-wedge infillings; palaeoclimate; Southeast Asia.

Introduction

The term “tessellon” was introduced into permafrost science by Troy Péwé (1959) as a name for sand wedge polygons with a characteristic vertical stratification of the thin layers making up the infilling parallel to the sides of the wedges in the McMurdo Sound region of Antarctica. In the spring, dry sand infills the semi-vertical cavities caused by contraction of the host sediment, and this will leave a narrow depression at the surface of the ground (Berg and Black 1966). The rate of growth appeared to be spasmodic. They were interpreted as being formed under extremely low temperatures resulting in the development of polygonal contraction cracks. The host sediment in Antarctica was sandstone with a variable cover of loose sand derived from it.

Washburn (1979, Figs. 4.34 and 4.35) provided an excellent pair of diagrams showing the difference between ice-wedge casts and these sandy tessellons, while Romanovskij (1973, 1976) discussed apparent transitional forms. They have subsequently been reported from other cold, arid parts of Antarctica (Berg and Black 1966, 70–73, Ugolini et al. 1973), the Alaskan arctic coastal plain (Carter 1981, 1983), and from Prince Patrick Island, Northwest Territories (Pissart 1968). Tessellons have also been reported from the Pleistocene deposits of Wyoming (Mears 1981, 1987) and the Mackenzie Delta (Murton and French 1993).

Unfortunately, subsequent workers have chosen to use the term “sand wedge” instead of tessellon for these features. As noted by Black (1952), sand-filled wedges can also be produced under conditions of extreme wetting and drying in areas without permafrost. They can also form when ice wedges degrade. This inevitably creates difficulties in determining the past conditions under which these formed. A further change is to spell the word with an extra “l” in the more recent literature (AGI 2005).

During field work on the eastern slopes of the Tibetan Plateau in July 2010, the authors discovered wedge-like structures similar to tessellons filled with small, plate-like, angular rock fragments that matched the frost-shattered surface material at the surface of the fissile bedrock. This paper will describe these features, briefly discuss their impact on the nomenclature of tessellons, and explain the significance of these features in interpreting the climate and palaeogeography of China during the last major glaciations (LGM).

Study Area

The study area is located on the upper eastern slopes of the Qinghai-Tibet Plateau at about 35°N and 98°E at an elevation of 4300–4400 m. It is an alpine meadow area which lies on the boundary of the Northern Qinghai Province and the upper Yellow River (Lin Li et al. 2010, zones 3 and 5, Fig. 1, respectively). It is currently on the south boundary of the zone of continuous permafrost (Z. Lin et al. 2010). The mean annual air temperature (MAAT) is -3.9°C, but the area shows an increase of about 0.037°C/a based on the period 1961–2007 (Cheng et al. 2006, Jin et al. 2009). The precipitation (322 mm/a) comes mainly from the East Asian Monsoon in summer, which barely reaches this elevation along the eastern flank of the plateau. A brief summary of the current knowledge of the Quaternary geology of the study area is given by Cheng et al. (2005a). The bedrock consists of metamorphosed sandstone of Triassic age (Cheng et al. 2005b). To the west-southwest is the alpine grassland of the source area of the Yangtze River and northern Tibet (Zone 1 of Lin et al. 2010).

The Qinghai-Tibet Plateau is tectonically unstable, and faults can be found cutting the bedrock and even producing fault scarps cutting across terraces and alluvial fans. In the study area, they were only observed affecting the bedrock. One such fault trace is found in the section shown in Figure 1.

The Section

The critical exposure was found in a road cut at 35°0' 17.7" N, 97°35'58.3" E on the road from Nyöring Lake to Niutoushan at an elevation of 4301 m. The frost shattered bedrock is more than 2.8 m thick, and the products are angular rock fragments up to 200 cm in length, ranging down to plate-like fragments around 2 cm long. A normal fault crosses the section shown in Figure 1 from the left bottom to the top right, and appears to have a downthrow of about 30 cm at the surface of the frost shattered bedrock. Slickensides are absent.

The frost-shattered bedrock is intersected by wedge-like structures filled with the plate-like fragments of the frost shattered bedrock. The long axes of the plate-like fragments of the infilling are oriented parallel to the sides of the wedge. The wedges appear at a spacing of 5–10 m across the section. The upper part of the wedge in Figure 1 is vertical until it meets the fault trace, whereupon it follows the fault trace downwards to the left in the photograph. It extends downwards about 1.8 m from the surface of the shattered bedrock. Similar wedges were seen in another section some 12 km to the south.

Figure 1 also shows the relatively thin deposit of Holocene aeolian or colluvial sandy loam. The latter not only blankets the underlying deposits and bedrock, but also forms a structureless infilling of the younger wedge-like structures which are ubiquitous across the eastern area of the Qinghai-Tibet Plateau. They have a spacing of 4–8 m and are referred to as "sand wedges" in most of the Chinese literature. Cheng et al. (2006) described two types of structureless sand-filled ice-wedges, viz., an earlier form which is up to 2 m in depth and 1 m in width, and a later group of shallower and wider infillings (up to 1.4 m wide and 0.9 m in depth). The first group have been dated by TL dating at 13.49 ka BP, whereas the second shallow group gave a date of 5.69–5.43 ka BP.

In Figure 1, a "sand wedge" cuts through the middle of the upper part of the wedge filled with oriented rock fragments, but instead of following the fault trace it continues downward to about 1.8 m below the upper surface of the surrounding fractured rock. It has the sharp boundary and narrow form of the older of the two kinds of ice-wedge infilling of Cheng et al. (2006).

Interpretation

The extremely deep fracturing of the upper layers of the bedrock indicates that there has been a significant period of very cold conditions. Since the Qinghai-Tibet Plateau is rising fast, this would be expected to be due to the last major cold event (LGM). If so, it would be older than 13.5 ka, presumably being formed near the beginning of the LGM. Cheng et al. (2005) have also reported TL dates of 39.83 ka BP for the cryoturbated, frost-shattered bedrock. This would appear to indicate a younger age for the rock tessellons since they cut through the shattered bedrock. If these TL dates are correct (which can only be confirmed by duplication), the rock tessellons were probably formed at the beginning of the last glaciation, which may have lasted longer at this location than in some other parts of the world. It could also be older,

corresponding to one of the earlier three cold events recorded by ice-wedge casts during the last 150 ka (Pan and Chen 1997). Further work will be needed to confirm the true age of the rock tessellons in this section.

Apparently, minor faulting affected the fractured bedrock shortly after 39.8 ka BP, and subsequently, thermal contraction cracks developed during cold winters when the fractured bedrock was frozen into a solid mass. In Figure 1, the cracking causing the formation of this particular wedge was guided at depth by the fault plane. Since the same wedge features are seen in this section and elsewhere where fault traces are not present, faulting cannot be the only cause of the wedge. In any case, the upper part of the wedge is vertical, unlike the fault trace. The orientation of the rock fragments indicates that it is a tessellon, which is only found today in areas with extremely dry and cold conditions. Wind-blown silts and sands were apparently unavailable during this part of a cold event in this area, but the frost-shattered rock fragments were obviously sliding down any available slope, probably due to icy coatings which occur today on the rock fragments making up the block slopes on the mountains in the higher parts of Tibet (Harris et al. 1998).

The infilling of the younger "sand wedge" exhibits no structure, and examples of the wider, shallower wedges elsewhere in the section show signs of partial collapse of the wall of the wedge during its infilling. This is consistent with the infilling of former ice wedges; i.e., they appear to be the remnants of a former ice wedge network.

They could also be interpreted as soil wedges, though their frequency and the lack of trees in the Holocene in this area (Zhang et al. 1995) suggest otherwise. Both types of sand-filled wedges imply periods of 6–7°C colder but wetter conditions than today (Cheng et al. 2006). Present-day ice wedges have been seen by the authors in the higher parts of the Beiluhe Basin at about 34°N and 92°E at elevations of 4600–4700 m. Professor Zhijiu Cui (personal communication, July 2010) has also found ice wedges on the south slope of the Tanggula Pass (5300m). The MAAT at lower elevations in the Beilehe Basin (Interior Qinghai Plateau) is about -3.8°C (Lin et al. 2010) with a mean annual ground temperature between -0.5 and -1.8°C. This provides an estimate of the degree of cooling required to produce ice wedges at the study site.

Classification of Tessellons

The rock-filled structure is clearly a variety of tessellon, though a rare one. It is the product of intense cold causing fracturing of the fissile bedrock, development of contraction cracks in winter, absence of windblown sand or silt, negligible snowfall, and sliding of ice-coated blocks into the fissures. Its rarity is undoubtedly due to these special requirements for its occurrence, but it means that there are two types of tessellon found in areas of permafrost. The type described above is a rock tessellon as opposed to the sand tessellons previously described by Péwé and others. It is recommended that in the future these names be used for similar structures everywhere so as to avoid problems with confusion with sand-filled ice wedge type structures that formed under warmer and more humid climates.

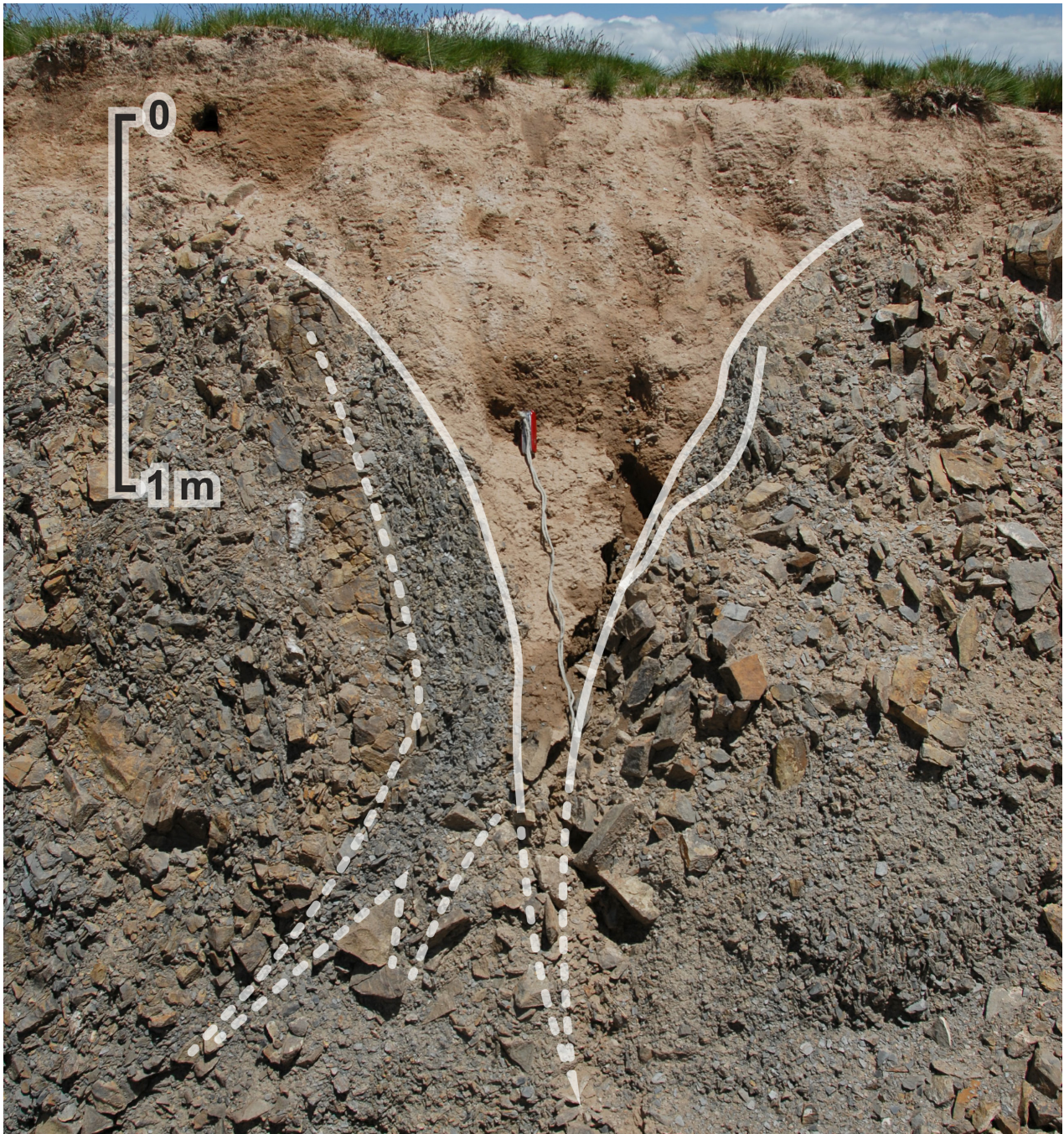


Figure 1. Rock tessellon cut by a younger sandy ice wedge cast.

Implications for the Climate of China during the Last Major Glaciations

Currently, the climate of China is the result of three interacting air masses (Fig. 2). The cA/cP air coming south from Siberia is dominant in Northern and Central China in winter and results in the latitudinal permafrost found in Northeastern China. In summer, it retreats northward into Russia and the westerly winds (cT) replace it across much of West and Central China. The East Asian Monsoon (mT air)

coming in from the Pacific Ocean brings copious quantities of moisture to the coastal lowlands in summer and penetrates almost onto the main eastern margin of the Tibetan Plateau. This air mass is actually part of the Trade Wind system of Easterlies (Gentilli 1967). In winter, it remains offshore. In summer, the westerly continental temperate winds (cT air) bring limited precipitation to the high mountains on the plateau, together with considerable quantities of loess from the desert areas to the west. There is only minor penetration of the Indian Monsoon across the Himalayas.

There are two competing theories regarding the climate

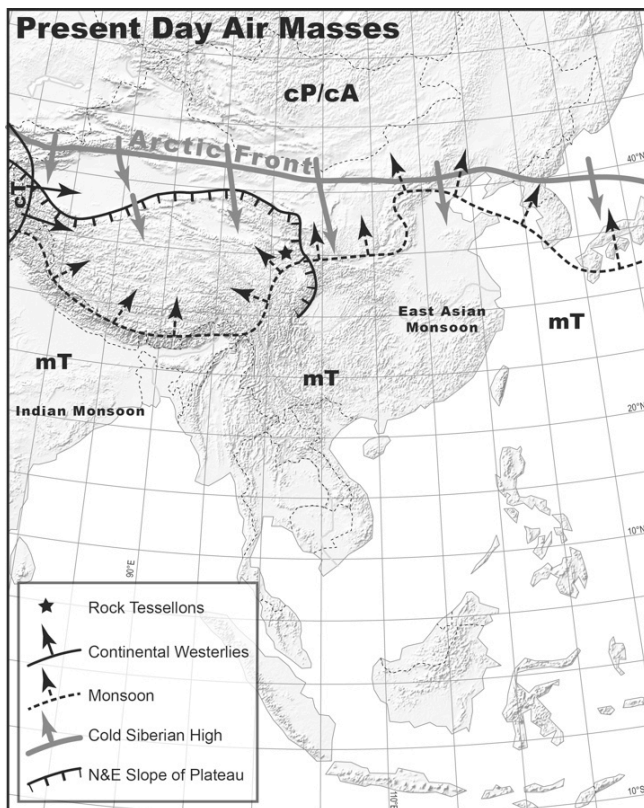


Figure 2. Dominant air masses producing the present-day climate in China.

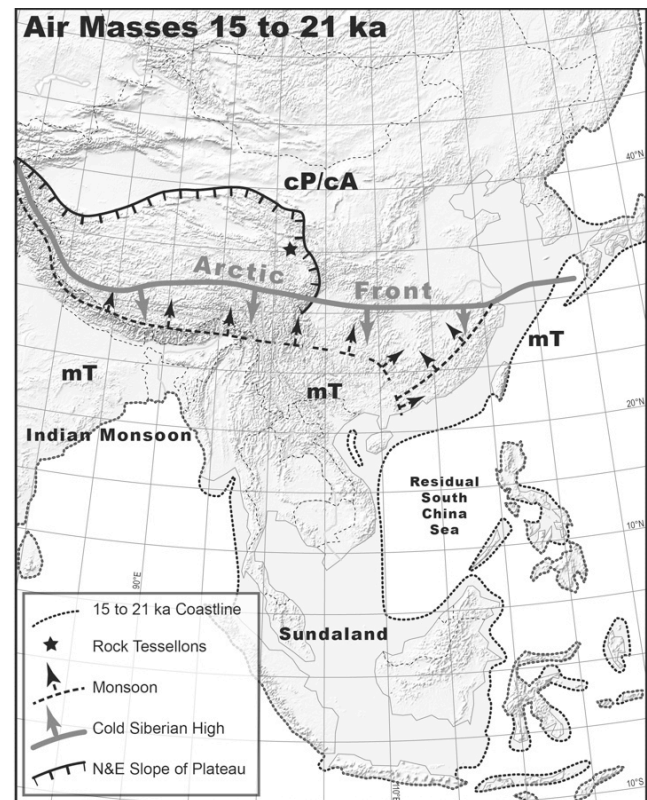


Figure 3. Probable dominant air masses during the last major glaciation in China (note the enormous change in distribution of land and sea due to lower sea level).

during the last glaciation. Matthias Kuhle (1988) has argued that there was a major ice cap over the Tibetan Plateau, but this was challenged by the late Yafeng Shi et al. (1990, 1997) and many other workers (Derbyshire et al. 1991, Rutter 1995). They claim that the only appreciable expansion of glaciers was near the Himalayas. The presence of rock tessellons formed high on the eastern slopes of the plateau during the last glaciations clearly confirms the conclusions of the Chinese glaciologists. This is also supported by the conclusion of anthropologists and zoologists from the Field Natural History Museum in Chicago (Voris 2000) that the area of the South China Sea, between Indonesia and the Philippines, became a wide peninsula that has been called Sundaland (Mollengraaff 1921) during the last glaciations due to the lowering of sea level. Likewise, much of the China Sea east of mainland China would have become land. This would have largely prevented the Indian Monsoon from swinging north because of the lack of hot ocean water needed to maintain it, and greatly reduced the effect of the East Asian Monsoon (Fig. 3). It explains the plant geography of Southeast Asia with its marked floral boundaries (e.g., the Wallace Line), and it explains the widespread evidence of former permafrost phenomena across Tibet (Cui 1982) including areas where it is absent today. It is also consistent with the results of pollen studies from across China (Ni et al. 2010), as well as the results of a study of the centers of plant endemism in China (López-Pujol et al. 2011).

Acknowledgments

This investigation was supported by the Strategic Program of the Chinese Academy of Sciences “Permafrost in China during the Last Glacial Maximum (21 ± 0.10 ka BP) and Megathermal (6 ± 0.05 ka BP)” (Grant No. XDA05120302) and the Global Change Research Program of China “Cryosphere changes in the Northern Hemisphere and Adaptive Policies” (Grant No. 2010CB951404). Robin Poitras drafted Figures 2 and 3.

References

- AGI. 2005. *Glossary of Geology*. Neuendorf, K.K.E., Mehl, J.P. Jr., & Jackson, J.A., Eds. American Geologic Institute, Alexandria, Virginia. 5th Ed.
- Berg, T.E. & Black, R.F. 1966. Preliminary measurements of growth of non-sorted polygons, Victoria Land, Antarctica. In *Antarctic soils and soil-forming processes*. Edited by J.F.C. Tedrow. American Geophysical Union Antarctic Research, Series B 1418: 61-108.
- Black, R.F. 1952. Polygonal patterns and ground conditions from aerial photographs. *Photogrammetrical Engineering* 18: 123-134.
- Carter, L.D. 1981. A Pleistocene sand sea on the Alaskan Arctic Coastal Plain. *Science* 211:381-383.
- Carter, L.D. 1983. Fossil sand wedges on the Alaskan Arctic coastal plain and their environmental significance. In

- Permafrost: 4th International Conference, Proceedings*, National Academy Press, Washington: 109-114.
- Cheng J., Jiang M., Zan L., Lü, X., Xu, X., Lu, P., Zhang, X., & Tian, M., 2005a. Progress in Research on the Quaternary Geology in the source area of the Yellow River. *Geoscience* 19(2): 239-246 (in Chinese).
- Cheng, J., Zhang, X., Tian, M., Yu, W., & Yu, J. 2005b. Ice-wedge casts showing climatic change since the Late Pleistocene in the source area of the Yellow River, north-east Tibet. *Journal of Mountain Science* 2(3): 193-201.
- Cheng, J., Zhang X., Tian, M., Yu, W., Tang, D., & Yue, J. 2006. Ice-wedge casts discovered in the source area of the Yellow River, Northeast Tibetan Plateau and their palaeoclimatic implications. *Quaternary Sciences* 26 (1): 92-98 (in Chinese).
- Cui, Z., 1982. Basic characteristics of periglacial landforms in the Qinghai-Xizang Plateau. *Scientia Sinica* 25 (1): 79-95.
- Derbyshire, E., Shi, Y.F., Li, J.J., Zheng, B.X., Li, S.J., & Wang, J.T. 1991. Quaternary glaciation of Tibet: the geological evidence. *Quaternary Science Reviews* 10: 485-510.
- Gentilli, J. 1967. Monsoons. In: Fairbridge, R.W. (ed.). *The Encyclopedia of Atmospheric Sciences and Astrogeology*. New York: Reinhold Publishing Co., 613-617.
- Harris, S.A., Cheng, C., Zhao, X., & Yongqin, D. 1998. Nature and dynamics of an active block stream, Kunlun Pass, Qinghai Province, People's Republic of China. *Geografiska Annaler* 80A (2): 123-133.
- Jin, H.J., He, R.X., Cheng, G.D., Wu, Q.B., Wang, S., Lü, L., & Chang, X. 2009. Changes in frozen ground in the source area of the Yellow River on the Qinghai-Tibet Plateau, China, and their eco-environmental impacts. *Environmental Research Letters* 4, 1-11.
- Jin, H.J., Luo, D.L., Wang, S.L., Lü, L.Z., & Wu, J.C., 2011. Spatiotemporal variability of permafrost degradation on the Qinghai-Tibet Plateau. *Sciences in Cold and Arid Regions* 3(4): 281-305.
- Kuhle, M. 1988. The Pleistocene Glaciation of Tibet and the onset of Ice Ages - An Autocycle Hypothesis. *Geojournal* 17 (4): 581-596.
- López-Pujol, J., Zhang, F.-M., Sun, H.Q., Ying, T.-S., & Ge, S. 2011. Centres of plant endemism in China: places for survival or for speciation? *Journal of Biogeography* 38: 1267-1280.
- Ni, J., Yu, G., Harrison, S., & Prentice, I.C., 2010. Palaeovegetation in China during the Late Quaternary: Biome reconstructions based on a global scheme of plant functional types. *Palaeogeography, Palaeoclimatology, Palaeoecology* 289: 44-61.
- Li, L., Yang, S., Wang, Z., Zhu, X., & Tang, H.Y., 2010. Evidence of warming and wetting climate over the Qinghai-Tibet Plateau. *Arctic, Antarctic and Alpine Research* 42 (4): 449-457.
- Lin, Z.J., Nui, F.J., Xu, Z., Xu, J., & Wang, P. 2010. Thermal regime of a thermokarst lake and its influence on permafrost, Beiluhe Basin, Qinghai-Tibet Plateau, China. *Permafrost and Periglacial Processes* 21 (4): 315-324.
- Mears, B., Jr. 1981. Periglacial wedges and the Late Pleistocene environment of Wyoming's intermontane basins. *Quaternary Research* 15: 171-198.
- Mears, B. Jr. 1987. Late Pleistocene periglacial wedge sites in Wyoming: An illustrated Compendium. *Geological Survey of Wyoming Memoir* 3.
- Mollengraaff, G.A.F. 1921. Modern deep-sea research in the East Indian archipelago. *Geographical Journal* 57: 95-121.
- Murton, J.B. & French, H.M. 1993. Sand wedges and permafrost history, Crumbling Point, Pleistocene Mackenzie Delta. *6th International Conference on Permafrost, Proceedings*, Beijing, Science Press, 1: 482-487.
- Pan, B.T. & Chen, F.H. 1997. Permafrost evolution in the Northeastern Qinghai – Tibetan Plateau during the last 150,000 years. *Journal of Glaciology and Geocryology* 19 (2): 124-132 (in Chinese with an English abstract).
- Péwé, T. 1959. Sand wedge polygons (tessellations) in the McMurdo Sound region, Antarctica. *American Journal of Science* 257: 545-552.
- Pissart, A. 1968. Les polygones de fente de glace de gel de l'Ile Prince Patrick (Arctique Canadien, 76° lat. N.). *Biuletyn Peryglacjalny* 17: 171-180.
- Romanovskij, N.N. 1973. Regularities in formation of frost-fissures and development of frost-fissure polygons. *Biuletyn Peryglacjalny* 23: 237-277.
- Romanovskij, N.N. 1976. The scheme of correlation of polygonal wedge structures. *Biuletyn Peryglacjalny* 26: 287-294.
- Rutter, N. 1995. Problematic ice sheets. *Quaternary International* 28: 19-37.
- Shi, Y.F., Zheng, B.X., & Li, S J. 1990. Last glaciations and maximum glaciations in Qinghai-Xizang Plateau—A controversy to M. Kuhle Ice Sheet Hypothesis. *Journal of Glaciology and Geocryology* 12(1): 1-16 (in Chinese with an English abstract).
- Shi, Y.F., Zheng, B.X., & Yao, T.D. 1997. Glaciers and environments during the Last Glacial Maximum (LGM) on the Tibetan Plateau. *Journal of Glaciology and Geocryology* 19(2): 97-113 (in Chinese with an English abstract).
- Ugilini, F.C., Bockheim, J.G., & Anderson, D.M. 1973. Soil development and patterned ground evolution in Beacon Valley, Antarctica. *North American Contribution, 2nd International Permafrost Conference*, National Academy of Sciences, Washington. Publication 2115: 246-254.
- Voris, H.K. 2000. Maps of Pleistocene sea levels in Southeast Asia: shorelines, river systems and time durations. *Journal of Biogeography* 27 (5): 1153-1167.
- Washburn, A.L. 1979. *Geocryology*. Edward Arnold, London, 406 pp.
- Zhang, Y.F., Zhang, J., Xu, J.M., & Lin, F. 1995. Paleoclimatic evolution of the Yellow River source areas since Holocene Epoch. *Earth Science – Journal of China University of Geosciences* 20(4): 467-469 (in Chinese with an English abstract).

Estimating Snowdrift Depth Using Differential GPS and a High-Resolution Digital Surface Model

Kenneth M. Hinkel

Department of Geography, University of Cincinnati, Cincinnati, OH, USA

John K. Hurd, Jr.

URS Corporation, Cincinnati, OH, USA

Abstract

A Differential Global Positioning System (DGPS) survey was conducted along a snowdrift formed adjacent to a 2.2-km-long, 4-m-high snow fence constructed near Barrow, Alaska. The objective was to estimate the areal footprint and volume of snow captured by the fence. A snow machine pulled a sled equipped with the DGPS, recording location and elevation every few seconds along five transects parallel to the snow fence. These data were interpolated within a Geographic Information System (GIS) to obtain a digital elevation model representing the snow surface in the area affected by drifting. The base map was a high-resolution digital model of the snow-free tundra surface derived from Interferometric Synthetic Aperture Radar data. Snow depth was calculated for each grid node as the difference between the two surfaces. The snow drift covers an area of 22.72 ha to an average snow depth of 1.87 m as compared to 0.4 m on the nearby unaffected tundra.

Keywords: Alaska; DGPS; Geographic Information Systems; Global Positioning Systems; snow depth; snow fence.

Introduction

The thickness and duration of the snow cover in the Arctic is a key component of the physical, chemical, and biological systems (Zhang & Ling 2003). Due to the varied topography, wind speed and direction, source of precipitation, and vegetative cover, there is a high degree of spatial variability in snow cover depth (Sturm & Benson 2005). Arctic monitoring sites are sparse, the spatial coverage is variable, and the records are of short duration. Advances in remote sensing sensors and software, Geographical Information Systems (GIS), and Differential Global Positioning Systems (DGPS) provide an opportunity to develop and customize a method for quickly measuring snow depth across relatively small areas.

This study incorporates a Digital Surface Model (DSM) collected using remote sensing technology during the summer of 2002, in conjunction with a Digital Elevation Model representing the surface of the seasonal snow cover created by a DGPS survey in April 2005. They are used together to create a raster dataset of snow depth near a snow fence at Barrow, Alaska. The goal is to examine the feasibility of quickly and accurately measuring snow depth at high spatial resolution, defined here as a raster area of 5 m or less (Skidmore 2002). Since modeling snow cover thickness has traditionally proven difficult (Taras et al. 2002), an accurate way of measuring it would be useful.

Study Area and Background

The village of Barrow is located on the Arctic Ocean in northern Alaska at 71.3°N, 156.8°W (Fig. 1). The area is underlain by continuous permafrost to a depth of 400–600 m. The local landscape is relatively flat coastal plain of low relief, dominated by thaw lakes and drained thaw lake basins, and characterized by low-centered ice-wedge polygons.

Barrow has a cold maritime climate and tundra vegetation. The mean annual temperature is -12°C with July the warmest month at 4.7°C and February the coldest month at -26.6°C (NCDC 2008). Mean annual precipitation is 106 mm, with 46% falling as rain in July and August. During the long, dry winters, snow covers the ground to a mean maximum depth of about 40 cm. In summer, the active layer thaws to an average depth of 40 cm (Hinkel & Nelson 2003).

Snow fences in the Arctic are used for both practical and scientific purposes. They are often found near villages and are used to enhance snow capture and supplement local water supplies. Others are constructed to reduce snow drifting around buildings and structures located downwind of the fence.

Researchers have installed snow fences with the intent of modifying the ground thermal regime. Mackay (1978) used them to artificially deepen the snow cover and thus inhibit

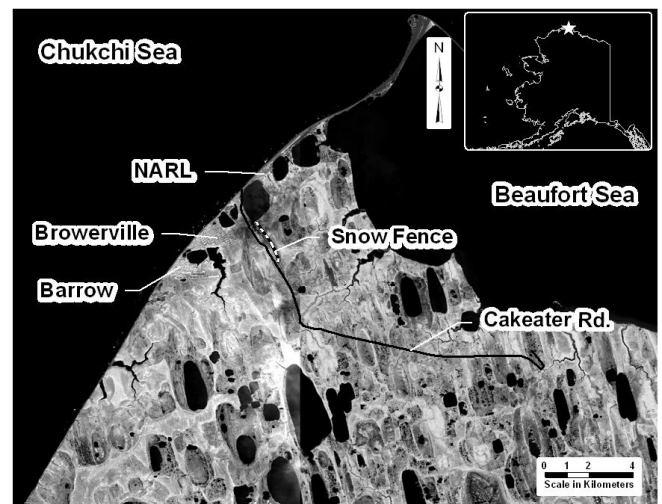


Figure 1. Image of the Barrow area showing Cakeater Road and snow fence.

thermal contraction cracking of ice wedges. Snow fences were installed in Labrador to increase snow depth and reduce ground heat loss in winter (Nicholson 1978). Over five years, the active layer depth increased by a factor of 2.5. Snow fences have been constructed at both the Niwot Ridge, Colorado, and Toolik Lake, Alaska Long Term Ecological Research sites to assess the impact of snow drifting on biophysical factors including snow depth and composition, soil temperature, soil decomposition, CO₂ flux, vegetation type, vegetation quantity and greenness, and active layer depth (Walker et al. 1999).

This project was conducted in conjunction with a long-term study of the Cakeater Road snow fence near Barrow (Hinkel et al. 2003, Hinkel & Hurd 2006, Hurd 2007). The primary scientific objective was to assess the direct and indirect impact of deep snow drifting on near-surface permafrost temperatures, thermokarst and permafrost degradation, and ground subsidence. Construction on the Cakeater Road snow fence began in autumn 1997. It was built to enhance snow capture and mitigate against prevalent drifting that was occurring around buildings in the suburb of Browerville. The fence runs north-south for 2.2 km and has a height of 4 m. Winter winds prevail from the east, and each year a >4-m high, 50–75 m wide drift forms on the downwind (western) side of the fence (Fig. 2). The drift crest is parallel to the fence and is typically positioned about 20 m downwind. Upwind, another smaller drift forms that is usually only 2 m high and no more than 40 m wide. In some years, there is a scour zone near the fence base. Over the 6-year study period, it was found that (1) the average near-surface soil temperature beneath a deep (>4-m) snow drift had warmed 2 to 5°C, (2) ground subsidence of 10 to 20 cm had occurred over most of the impacted area, and (3) widespread but sporadic thermokarst is evidenced where snow meltwater ponds (Hinkel & Hurd 2006).

Base Map and Equipment

The base map used in this study is a high spatial- and radiometric-resolution digital elevation dataset derived from an Interferometric Synthetic Aperture Radar (IfSAR) image collected from a LearJet 36A aircraft during the period 27–29 July 2002. This image of the National Petroleum Reserve of Alaska was acquired by InterMap® for the Bureau of Land Management. The image set has a horizontal resolution of 5 m and was orthorectified to provide the highest possible level of spatial accuracy, resulting in an orthorectified radar image (ORRI). Post-processing was done at the National Snow and Ice Data Center in Boulder, Colorado (Manley et al. 2004).

One of the products derived from the ORRI was a Digital Surface Model (DSM). A DSM represents the elevation at the top of features on the earth's surface; this could be the top of vegetation, buildings, or bare soil (Li et al. 2009). Since the vegetation in the study area is very short (<10 cm) and there are no buildings or roads, the DSM serves as the local base level for estimating snow depth. Nominally, the full-resolution DSM has a 5-m horizontal and 0.5-m vertical resolution.

The DGPS equipment was provided by UNAVCO and managed by the Barrow Arctic Science Consortium (BASC). A



Figure 2. Southern end of snow fence looking north (April 2005).

permanent base station has been established at a Naval Arctic Research Laboratory (NARL) building at 71.324952221°N, 156.6778748°W and positioned 14.595 m above sea level (GEOID99). The base station is approximately 5 km from the study area. There is little relief, and there are no tall structures to hinder radio communication. Base station equipment includes a Trimble 5700 receiver, a Zephyr antenna mounted atop a 10-m pole, and a radio with a long-range antenna. The roving unit consists of a second Trimble 5700 receiver accompanied by a Survey Controller, Zephyr antenna, radio, radio relay and, during the transect survey, a 2-m range pole. The base of the 2-m range pole was placed 30 cm above the snow surface on the sled deck.

UNAVCO provided BASC Trimble Geomatics Office software for processing DGPS field data. The software is installed on a dedicated computer that is connected to the base station.

Methodology

Two DGPS surveys were undertaken. The first was conducted in August 2004 when the snow drift had completely disappeared from the tundra, the second in April 2005 when snow depth was maximized. On the same day in April, snow depth measurements were collected with a probe. These are used as ground truth data to assess the accuracy of the DGPS measurements.

Summer DGPS survey of ground surface elevation

A project-specific assessment was conducted to quantify the local vertical accuracy of the IfSAR-derived DSM. The DGPS survey consists of three parallel transects, separated by 50 m and oriented perpendicular to the snow fence near the southern end (Fig. 4). Established in 1999, these transects have been used to collect annual measurements of snow thickness, active layer depth, and ground subsidence.

For the DGPS survey, readings were collected every 2.5 m and included longitude, latitude, and elevation of the ground surface in Real-Time Kinematic (RTK) mode. During this survey, the DGPS unit recorded a horizontal accuracy



Figure 3. DGPS equipment mounted on a sled behind a snow machine (April 2005).

of 1.0 cm and a vertical accuracy of 1.5 cm. A total of 192 measurements were made.

The DGPS survey point elevations were compared to the DSM elevation at the same locations, and the Root Mean Square Error (RMSE) was 18 cm. The analysis revealed that the DGPS survey recorded consistently higher elevations than the DSM. It is unlikely that the ground surface has been displaced upward by ~20 cm as a result of surface heave over the two-year period between the time that the IfSAR data was collected (2002) and the DGPS survey was conducted (2004). Indeed, Hinkel & Hurd (2006) demonstrated widespread but discontinuous ground subsidence near the snow fence. The discrepancy most likely occurs from systematic error in IfSAR data acquisition or from post-processing.

Winter DGPS survey of snow surface elevation

In April 2005, a DGPS survey was conducted along the entire 2.2-km length of the Cakeater Road snow fence. To travel the length of the snow fence multiple times on foot is not feasible, so a snow machine was used. Any engine that creates a magnetic field while operating can have a deleterious impact on the proper functioning of DGPS equipment and can degrade the integrity of collected measurements. To remedy this, the DGPS equipment was mounted at the rear of a sled that was pulled behind the snow machine with a nylon rope to maintain a safe distance of more than 3 meters from the engine (Fig. 3). On the sled, a radio relay was set up using a 2.5-m antenna. In this way, line of site contact could be maintained between the base station and roving unit even when the snow machine and sled were behind the drift.

The configuration of the DGPS equipment was specific to the task. To continually monitor the vertical and horizontal resolution, RTK mode was used. This method, through the use of radios, allows the two receivers to instantaneously differentially correct the GPS data and display the vertical and horizontal precision to the operator monitoring the receiver. Knowing the quality of the data as it is being collected allows the operator to adjust equipment settings and traveling routes



Figure 4. Location of 1264 DGPS measurement points collected along five transects in April 2005. Middle transect as bold line.

when imprecision becomes excessive.

While the equipment was being pulled behind the snow machine, measurements were sampled every 1 s but recorded only every 5 s. By maintaining a slow, steady speed over the snow cover, data points were measured about every 10 m, depending on the terrain. This method nominally yielded a minimum horizontal precision of 2 cm and vertical precision of 3 cm. However, the operator carries the receiver in a backpack and the antenna is mounted on a short pole. While riding on the sled, the operator is sometimes jostled and forced to adjust position when the terrain becomes rough. This could potentially degrade slightly the accuracy of the DGPS measurements.

To ensure complete coverage of the area impacted by snow drifting, snow machine travel paths were systematically established. Three transects were laid out on the downwind (western) side of the snow fence; the snow machine traveled along the drift crest to measure the tallest point on the snow drift, along the drift margin to identify the spatial extent, and along the back slope of the drift to parameterize the effects of scouring that often occurs on the leeward side. Upwind, the snow machine traveled along both the drift crest to measure its highest point and along the edge to measure the approximate drift extent. A total of 1,264 points were collected during the survey (Fig. 4). The snow in all years was hard packed, so there was no danger of getting stuck; indeed, the heavy snow machine did not depress the snow surface.

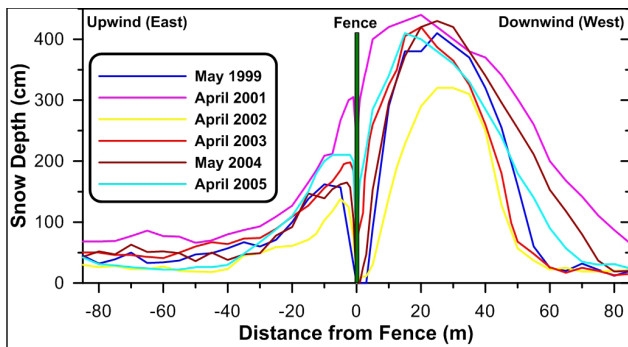


Figure 5. Snow depth measurements collected by probing each spring (except 2000) along middle transect.

Winter manual snow depth measurements

Graduated probes were used to make snow depth measurements used for the accuracy assessment. Snow depth of less than 1.3 m was measured to the nearest cm using a standard active layer probe. In deeper snow, the stainless steel probe is 1 cm in diameter, graduated in decimeter increments, and has 1-m sections that can be added as necessary to a maximum length of 4 m. Snow depth was measured in April 2005 along the middle transect perpendicular to the snow fence. Probing was conducted nominally every 5 m to a maximum distance of 85 m in both the upwind and downwind directions, with higher sampling frequency near the fence to accurately capture the rapid change in snow depth over short distances; a total of 37 measurements were made. The maximum snow depth in April 2005 was 4.1 m with the crest 15 m downwind from the fence (Fig. 5).

Post-Processing

The DGPS measurements were downloaded from the Survey Controller and imported into Trimble Geomatics Office software for processing. The processed data were adjusted to account for the displacement of the range pole above the ground surface and exported to the GIS. The 1,264 data points were interpolated onto a 5-m grid using a natural neighbor algorithm. Given the spatial configuration of the raw dataset, this procedure produced the most accurate results of the available interpolation and geostatistical methods based on the RMSE.

The IfSAR-derived DSM elevation value for each grid node was subtracted from the rasterized snow elevation surface to create a raster data layer representing snow depth across the study area (Fig. 6). Finally, the estimated snow depth was compared to the measured snow depth at each of the 37 locations along the middle transect to assess accuracy.

Results and Discussion

The accuracy assessment of the snow depth interpolation methods yielded an RMSE of 25 cm. However, given that the RMSE of the IfSAR-derived DSM was 18 cm, the net error is likely substantially lower. In addition to this source, error could be introduced by poor satellite coverage or atmospheric turbulence during the acquisition of DGPS survey points.

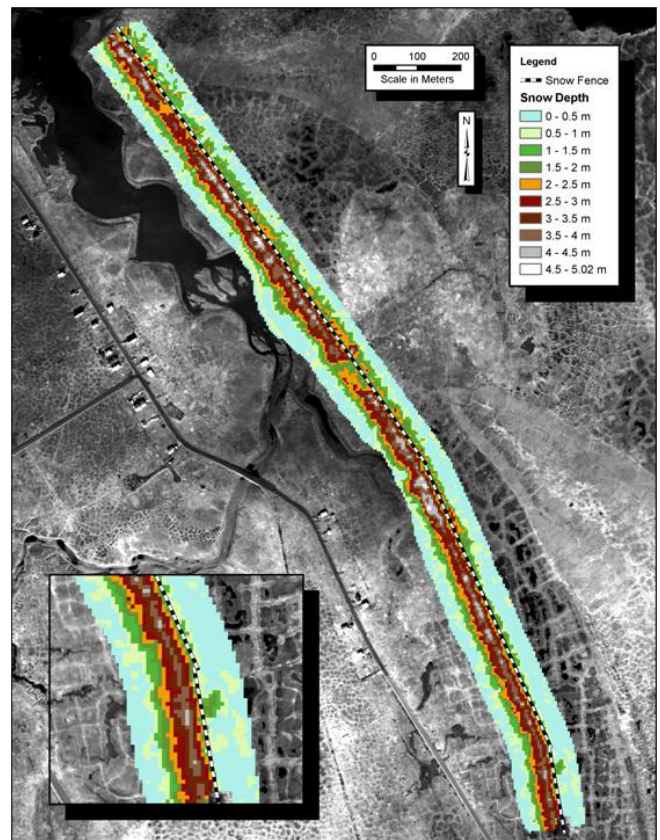


Figure 6. Snow depth raster layer (5-m) interpolated using nearest neighbor algorithm.

Further, interpolation algorithms have inherent limitations and often behave as smoothing operators (Lam 1983). Finally, the method of manually measuring snow depth is limited. Thermokarst and ground subsidence have yielded depressions that form ponds, and these freeze prior to drift development. Mechanical probing for snow depth can penetrate only to the top of the pond ice—not the ground surface. In any event, the difference between the RMS errors is less than the decimeter resolution of the snow probe.

The GIS was used to identify all areas within the study domain that had an estimated snow depth greater 40 cm, which is the mean snow depth of the surrounding unaffected tundra. Snow depth exceeding 40 cm therefore defines the extent of the area affected by snow drifting—the snow fence “footprint” in 2005. Along the entire snow fence, 22.72 ha are impacted and the average snow depth is 1.87 m. The area affected by drifting contained 425,974 m³ of snow in April 2005. On average, the snow depth on both sides of the fence was 4.7 times deeper than snow depth on the unaffected tundra.

Conclusions

The method described here provides a quick and reasonably accurate means of assessing snow drift thickness over areas too large to sample mechanically. Collecting snow cover thickness measurements by manual probing when snow exceeds a depth of 1 m takes considerable time. For example, in April 2005 it

took several hours to collect the 37 snow depth measurements with the probe. By contrast, with the method described here, the April 2005 DGPS survey on snow machine collected 1,264 data points across a large area over the same duration with comparable accuracy. The method is most effective when the high-resolution DSM and DGPS measurements are accurate and there is significant snow thickness. Ground heave will degrade the accuracy, as will sub-pixel variability in the surface elevation and the density of the snow survey sampling points and transects. The recent availability of LiDAR imagery addresses many of these concerns (Tinkham et al. 2010), but the cost of image acquisition remains an issue.

There are a number of potential applications for an accurate high resolution snow depth dataset. Many remote arctic villages have built snow fences to provided fresh water for residents. As the captured snow melts, it can be channeled to a filtration system and used as a viable source of domestic water. Given a known snow water equivalent, the available water within the snow drift can be monitored annually. The available water is estimated by multiplying the volume of the snow drift by the water equivalent.

In addition, there are a number of applications for an accurate high-resolution snow depth dataset in cryospheric research. Since arctic vegetation is sensitive to snow depth, a high resolution snow depth dataset can aid in modeling patterns of and changes in tundra vegetation. The thermal flux between the ground and atmosphere is dependent on snow depth. The methods described here could be applied over micro-scale to meso-scale regions to gain a better understanding of ground / atmosphere coupling. Further, hydrologic modeling on a micro- and meso-scale level is enhanced with the availability of a high spatial resolution snow depth dataset.

Acknowledgments

This research was supported by grants from the National Science Foundation to KMH (OPP-9529783, 9732051, 0094769, and 0713813). Any opinions, findings, conclusions, or recommendations expressed in the material are those of the author and do not necessarily reflect the view of the NSF. We are grateful to the Ukeagvik Inupiat Corporation for access to the Barrow Environmental Observatory, the Barrow Arctic Science Consortium for administrative and logistical assistance, UNAVCO for DGPS training and equipment, and two anonymous reviewers who improved the paper.

References

- Hinkel, K.M. & Nelson, F.E. 2003. Spatial and temporal patterns of active layer depth at CALM sites in Northern Alaska, 1995-2000. *Journal of Geophysical Research-Atmospheres* 108(D2): 10.129.
- Hinkel, K.M., Bockheim, J.G., Peterson, K.M., & Norton, D.W. 2003. Impact of snow fence construction on tundra soil temperatures at Barrow, Alaska. In *Proceedings of the 8th International Conference on Permafrost, Zurich, Switzerland, July 21-25, 2003*: 401-406.
- Hinkel, K.M. & Hurd, J.K., Jr. 2006. Permafrost destabilization and thermokarst following snow fence installation, Barrow, Alaska, U.S.A.. *Arctic, Antarctic and Alpine Research* 38(4): 530-539.
- Hurd, J.K., Jr. 2007. *A GIS model to estimate snow depth using differential GPS and high-resolution digital elevation data*. Masters Thesis, Department of Geography, University of Cincinnati, 59 pp.
- Lam, N.S. 1983. Spatial interpolation methods: A review. *The American Cartographer* 10(2): 129-149.
- Li, Z., Zhu, Q., & Gold, C. 2009. *Digital Terrain Modeling: Principles and Methodology*. Oxford, England: CRC Press, 354 pp.
- Mackay, J.R. 1978. The use of snow fences to reduce ice-wedge-cracking, Garry Island, Northwest Territories. *Current Research, Part A, Geological Survey of Canada Paper 78-1A*: 523-524.
- Manley, W.F., Lestak, L.R., Tweedie, C.E., & Maslanik, J.A. 2004. *High-resolution radar imagery, digital elevation models, and value-added geospatial layers for collaborative research of environmental change at Barrow, Alaska*. National Snow and Ice Data Center, CIRES. Boulder, Colorado.
- National Climate Data Center 2008. <http://www.wrcc.dri.edu/summary/brw.ak.html>.
- Nicholson, F.H. 1978. Permafrost modification by changing the natural energy budget. *Proceedings, Third International Conference on Permafrost, Edmonton, Alberta, July 10-13, 1978*: 61-67.
- Skidmore, A. 2002. *Environmental Modeling with GIS and Remote Sensing*. London: Taylor & Francis, 267 pp.
- Sturm, M. & Benson, C.S. 2005. Scales of spatial heterogeneity for perennial and seasonal snow layers. *Annals of Glaciology* 38: 253-260.
- Taras, B., Sturm M., & Liston, G.E. 2002. Snow-ground interface temperatures in the Kuparuk River Basin, Arctic Alaska: Measurements and model. *Journal of Hydrometeorology* 3: 377-394.
- Tinkham, W.T., Smith, A.M., Link, T.E., Hudak, A.T., Falkowski, M.J., & Marks, D.G. 2010. Spatial assessment of snow volume using Lidar and field measurements. American Geophysical Union, Fall Meeting 2010, 13-17 December, C33C-0555.
- Walker, M.D., Walker, D.A., Welker, J.M., Arft, A.M., Bardsley, T., Brooks, P.D., Fahnestock, J.T., Jones, M.H., Loslebe, M., Parson, A.N., Seastedt, T.R., & Turner, P.L. 1999. Long-term experimental manipulation of winter snow regime and summer temperature in arctic and alpine tundra. *Hydrologic Processes* 13: 2315-2330.
- Zhang, T. & Ling, F. 2003. Impact of the timing and duration of seasonal snow cover on the active layer and permafrost in the Alaskan Arctic. *Permafrost and Periglacial Processes* 14: 141-150.

Recent Hydrological and Ecological Changes in Relation to Permafrost Degradation under Increased Precipitation in an Eastern Siberian Boreal Forest

Yoshihiro Iijima

Research Institute for Global Change, Japan Agency for Marine-Earth Science and Technology, Yokosuka, Japan

Alexander N. Fedorov

Melnikov Permafrost Institute, Siberian Division of Russian Academy of Science, Yakutsk, Russia

Takeshi Ohta, Ayumi Kotani

Nagoya University, Nagoya, Japan

Trofim C. Maximov

Institute for Biological Problem in Cryolithozone, Siberian Division of Russian Academy of Science, Yakutsk, Russia

Abstract

The study presents linkages between permafrost degradation and ecohydrological change in the central Lena River basin in eastern Siberia. Consecutive positive anomalies in winter snow accumulation and summer precipitation after winter 2004 caused abrupt soil warming in the active layer and upper part of the permafrost through increased summer soil thermal conductivity and latent heat storage. Degradation of permafrost resulted in thermokarst in and around alas lakes. Expansion of the alas lake area caused fatal damage to the boreal (larch) forest. The circumference of the water-filled lake floods and erodes the side slopes. Trees surrounding the lake were then perennially waterlogged and they finally withered. Sap flow measurements showed significant reduction in transpiration from the damaged trees, which were located in waterlogged depressions with a deepening active layer.

Keywords: alas; boreal forest; eastern Siberia; soil moisture; thermokarst; transpiration.

Introduction

High-latitude regions of the northern hemisphere have experienced unanticipated environmental change over the last decade. The most prominent feature is the dramatic reduction in summer sea ice extent in the Arctic Ocean. Arctic surface air temperature and associated sea level pressure fields in relation to sea ice reduction have a remarkably different spatial pattern at the beginning of the 21st century, called an “Arctic warm period” (Overland et al. 2008). A terrestrial response, in conjunction with oceanic and atmospheric amplified changes, has also been observed in the boreal and tundra permafrost zones (Shur & Jorgenson 2007). Changes in the hydrological cycle include the precipitation regime, snow distribution and duration, water storage into soil, and river discharge (Muskett & Romanovsky 2009). The water cycle integrates the ocean, atmosphere, and land systems. Changes in the circum-arctic terrestrial water cycle may include water storage and evapotranspiration processes, both of which may affect permafrost conditions.

Continuous observations show evidence of abrupt land surface moistening and soil warming within the active layer and upper part of permafrost in the central Lena River basin, eastern Siberia (Iijima et al. 2010). It should be noted that permafrost degradation near the ground surface is induced by hydrological changes during summer and winter rather than by the global warming trend itself. This result demonstrates that the large amplitude of hydroclimatic changes, in conjunction with arctic climate changes including rainfall, snow amounts, and duration, strongly regulates permafrost-related

environments. These connections have substantial importance in forecasting future changes in energy, water, and carbon circulation over the boreal and tundra region. However, there is still a lack of understanding of the role of the arctic climate on the land surface in continuous permafrost regions.

The present study therefore focuses on the linkages between the hydrothermal changes within the surface layer of the permafrost and the topographical and ecohydrological alterations in the central Lena River basin in eastern Siberia.

Site and Methods

Observation sites

The intensive observational sites were designated as shown in Figure 1.

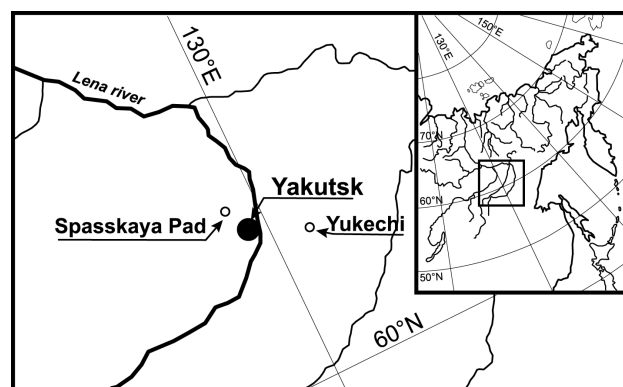


Figure 1. Location of research sites, Spasskayapad and Yukechi near Yakutsk.

Field studies were conducted on a vast boreal forest located approximately 20 km north of Yakutsk in the Republic of Sakha, Russia. The site is in the Spasskaya-pad Experimental Forest (62°15'N, 129°37'E, 220 m a.s.l.) of the Institute for Biological Problems in Cryolithozone (IBPC), Siberian Branch of the Russian Academy of Science (SB RAS), where meteorological data and water, energy, and carbon fluxes have been measured at a 32-m-tall meteorological tower since 1998 (Ohta et al. 2001, Ohta et al. 2008). The site is located on the highest terrace of the left bank of the Lena River and is covered with a thin layer of Quaternary deposits consisting of alluvial deposits with low content of ice complex. The site is on a gentle north-facing slope, covered with pure and mixed stands of larch, birch, and pine forest.

The second site is located 50 km southeast of Yakutsk on the right bank of the Lena River (61°35'N, 130°40'E, 200–220 m a.s.l.). The Yukechi Experimental site (Fig. 2) has been managed by the Melnikov Permafrost Institute (PI), SB RAS since the 1990s. The site represents a typical Central Yakutian landscape containing thick ice wedges, especially in inter-*alas* terrain, sloping gently to the northwest. Silty sandy loams dominate the upper horizons of the Quaternary deposits. The site shows relatively larger undulations due to high activity of thermokarst depletion (*alas* with many lakes) (Fedorov & Konstantinov 2003) and is covered with inter-*alas* larch forest and meadow.

Instruments and methods

We utilized intensive observational data for detecting temporal and spatial variations in hydrothermal conditions in the central Lena River basin.

Soil temperature, soil moisture, and active layer thickness at Spasskayapad and Yukechi have been measured by the observational network on the left and right banks of the Lena River in Yakutsk by the Research Institute for Global Change (RIGC) and the PI. Observations were made twice a month during the warm season (May to October) and once a month during winter (November to April) for soil temperature. Details are described in Iijima et al. (2010).

Soil thermal properties within active layer, such as heat conductivity and capacity, were measured using a portable thermal property analyzer (KD2 Pro, Decagon Devices Inc.) in September of both 2009 and 2010 at Spasskayapad and Yukechi. In Spasskayapad, we measured a pine forest plot, a larch forest tower plot, and a sloping waterlogged larch plot. In Yukechi, we measured a non-degraded larch forest as the control plot and a nearby waterlogged larch forest flooded *alas* as a degraded plot (Fig. 2 line A).

Long-term meteorological observations have been collected at Spasskayapad since 1998 with a 32-m boundary layer tower. Soil temperature and moisture within the active layer have also been monitored near the tower. Soil temperature and moisture were measured using PT-100Ohm temperature and Time Domain Reflectometry (TDR) probes (P2, IMKO), respectively. Net radiation (Q*7, REBS) was measured at 1.2 m above the forest floor. Measurements at the tower site were made every 10 seconds and data recorded as 10-minute

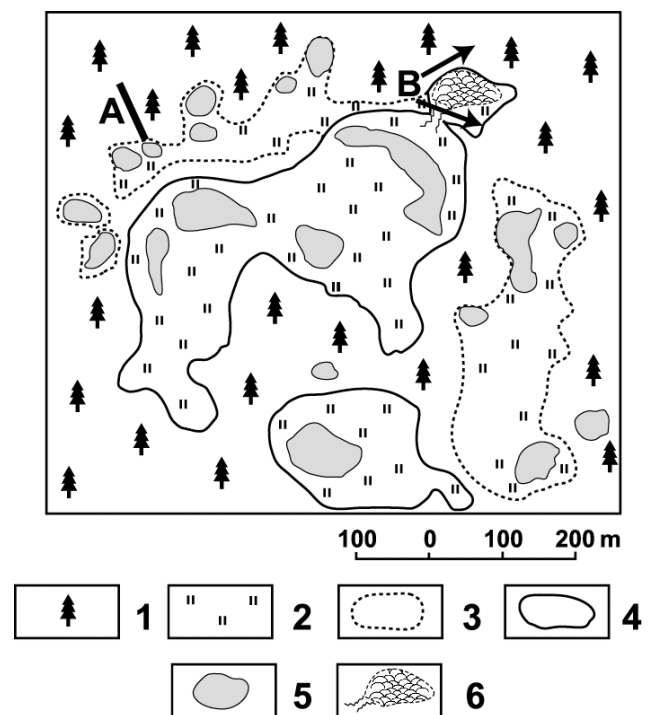


Figure 2. Location map of Yukechi Experimental site (updating Fig. 2 in Fedorov & Konstantinov 2003): 1–larch forest; 2–meadow; 3–meadow contour in inter-*alas*; 4–*alas* contour; 5–lake; 6–collapsed lake; A–Observation site; B–Figure 8.

averages on a datalogger (CR-10X, Campbell Scientific, Inc.). Fifteen larch trees, representing the range in size of mature trees in the stand, were selected for sap flow measurements near the larch tower site at Spasskayapad. Grainer method sensors (cf. Granier et al. 1996) were used to measure sap flow density ($\text{g H}_2\text{O m}^{-2} \text{ sap wood s}^{-1}$). Each sensor consisted of a pair of 20-mm-long, 2-mm-diameter probes; these were inserted above one another in the sap wood 15 cm apart, at a height of approximately 130 cm above ground level on the north-facing side of each tree. The upper probe was constantly heated by a 200 mV heater coil, and the temperature difference between the upper and lower probe was measured in order to calculate sap flow density.

Sap flow measurements were carried out during the growing season (May to September) in 2006 and 2009. Probes in each tree were replaced in April 2009 and moved to positions 5 to 10 cm removed from previous (2006) positions in order to avoid artificial reduction of sap flow surrounding the probes during long-term usage. Temperature differences of all sensors were logged every 10 s and stored as 10-min averages in a datalogger (CR-10X, Campbell Scientific, Inc.).

Results and Discussion

Soil temperature and moisture variations

Figure 3 shows interannual variations in soil temperature and moisture within the active layer from 1998 to 2010 at the larch tower site at Spasskayapad. As described in Iijima et al. (2010), simultaneous increasing trends of soil temperature and moisture within the active layer were prominent after winter

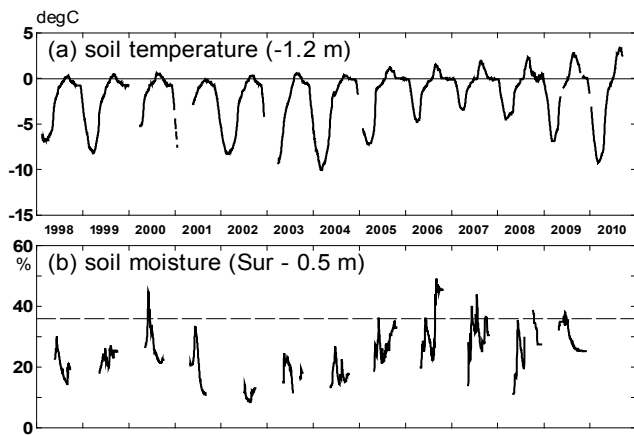


Figure 3. Interannual variations in (a) soil temperature at depth of 1.2 m and (b) soil moisture during the growing season, from 1998 to 2010. Soil temperature shows mean daily value. Soil moisture shows volumetric content from surface to 0.5 m depth. Broken line in (b) denotes soil porosity (36%) observed by GAME-Siberia project.

2004 and persisting through 2010. It should be noted that the soil temperature increase at the 1.2 m depth was first observed during winter 2004 to 2007. The increase during summer was subsequently apparent after 2005. Snow accumulation was above average from 2004 through 2007, with more than 50 cm of maximum snow depth (Iijima et al. 2010). This acted as an effective insulator. Accordingly, cooling of the soil was reduced in winter.

In Yakutsk, the total amount of precipitation from April to September was usually less than 130 mm from 1998 through 2004, whereas the amount exceeded more than 200 mm from 2005 through 2007. Thus the active layer was saturated during both snowmelt and the late growing seasons in 2005–2007. The measured soil moisture during snow melt and the late growing season exceeded soil porosity by 36% (broken line in Fig. 3b; from GAME-AAN data) in 2005–2007, indicating waterlogged conditions.

Figure 4 shows the vertical structure of averaged late-summer soil moisture before (2002–2004) and during (2005–2007) the wet climate at the Spasskayapad and Yukechi sites. Differences in active layer thickness and soil moisture contents are summarized in Table 1. All of the profiles exhibit a steady increase in soil moisture within the active layer from 2002–2004 to 2005–2007. S1 is a mature larch stand near the larch tower site at Spasskayapad. Active layer thickness (ALT) increased from 1.52 m (2002) to 1.74 m (2008). S3 is a pine stand at the top of the hill at Spasskaya pad with sandy soil. ALT at this site was 1.92 m (2002) and 2.28 m (2008). Y1 is a larch stand in the inter-alas at Yukechi. The ALT was 1.41 m in 2008. Y3 is a meadow in alas; ALT was 2.14 m in 2008. The increase in water stored within the active layer was most prominent at Spasskayapad because the active layer was drier than that at Yukechi in 2002–2004. The total increase in amount was 215 mm at S1, 103 mm at S3, while 60 mm at Y1 and 52 mm at Y3. The increased soil moisture likely favored both warmer soil temperature and a deepening of the active layer.

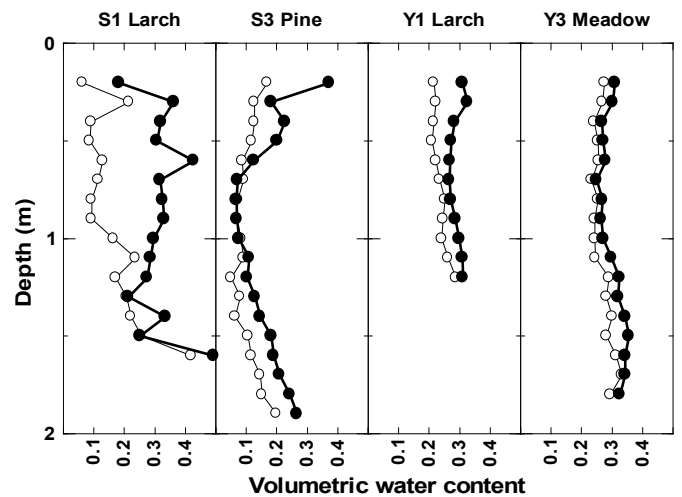


Figure 4. Volumetric soil moisture profile at Spasskayapad (S1 and S2) and Yukechi (Y1 and Y3) sites. Thin and bold lines with open and solid circles denote averaged values in September from 2002 to 2004 and from 2005 to 2007, respectively.

Table 1. Changes in active layer thickness (ALT) and volumetric soil moisture contents (SM) from surface to active layer thickness at Spasskayapad and Yukechi experimental sites. Both data were measured in late September of each year.

| | year | Spasskayapad | | Yukechi | |
|-------------------------|---------|--------------|------|---------|------|
| | | S1 | S3 | Y1 | Y3 |
| ALT (m) in late Sep. | 2002 | 1.52 | 1.92 | 1.30 | 2.10 |
| | 2008 | 1.74 | 2.28 | 1.41 | 2.14 |
| | dif | 0.22 | 0.36 | 0.11 | 0.04 |
| SM (mm) Sur. to ALT | 2002-04 | 257 | 195 | 261 | 461 |
| | 2005-07 | 472 | 297 | 320 | 513 |
| | dif | 216 | 103 | 60 | 52 |

Pure ice content (ice wedges) and thermokarst is limited in the Spasskayapad area (Bosikov 1991) on the left bank of the Lena River, where we observed the active layer and soil moisture increase. We propose that the waterlogged conditions were initially a result of increased summer and winter precipitation, which resulted in impeding larch tree growth. Any reduced transpiration losses may therefore enhance additional soil wetting, which is a mechanism that differs from those commonly associated with permafrost degradation and thermokarst.

On the other hand, activation of thermokarst and enlargement of alas formation are common at the Yukechi site (Fedorov & Konstantinov 2003). During the high-precipitation years after winter 2004, remarkable topographical disturbances, such as a collapsing alas lake in 2008 (Fig. 8), were found in this area. The wet and deep active layer in the inter-alas side slope favored soil instability, which, during the increased precipitation after winter 2004, resulted in erosion during high lake levels.

Soil thermal properties

The increased soil moisture within the active layer affected soil heat capacity and conductivity. The vertical distribution of the soil thermal properties shows well-regulated variations at depth (Fig. 5). At all sites, the upper 10-cm layer showed low heat conductivity having less than $0.5 \text{ W m}^{-1}\text{K}^{-1}$ due to the porous organic layer. The pine forest at the top of a hill at Spasskayapad, which has dry sandy soil, showed low heat conductivity and capacity within the mineral soil (>20 cm). Higher conductivity was observed near the larch tower site with sandy loam soil. The highest heat conductivity and

capacity at Spasskayapad were observed in the larch forest, where the active layer was waterlogged after 2006. Iwasaki et al. (2010) also showed saturated soil moisture distributed in lower and flat surfaces in this larch forest.

The same profile was observed at the Yukechi site (Fig. 5b). Brouchkov et al. (2005) observed heat conductivity at the same area in 2000 and the value was $0.57 \text{ W m}^{-1} \text{ k}^{-1}$ (larch forest) at a depth of 30 cm in mineral soil, which was comparable to the control site in this study ($0.55 \text{ W m}^{-1} \text{ k}^{-1}$). Heat conductivity and capacity at the waterlogged larch plot near the flooding alas exceeded $1.0 \text{ W m}^{-1} \text{ k}^{-1}$ and $2.3 \text{ MJ m}^{-3} \text{ K}^{-1}$, which was similar to the waterlogged larch at Spasskayapad.

Figure 6 shows interannual variations in soil temperature and net radiation at the forest floor at Spasskayapad. In spite of the larger snow accumulation in 2005–2007, the snow disappearance date was earlier: May 7 and 9 (2003 and 2004), compared to April 24, 29, and 18 (2005, 2006, and 2007). Thawing at the 1.2 m depth was earlier in 2005–2007 than 2003–2004. In addition, it should be noted that the zero-curtain effect (Outcalt et al. 1990) at the 1.2 m depth was extended each year. Soil water changed to the ice state at the beginning of December in 2003, whereas it reached mid-February in the 2006–2007 winter. These results indicate that freezing-back of the active layer during winter was weak due to a thick snow cover and increasing latent heat storage. Total amounts of net radiation in subsequent thawing periods were rapidly decreased: 398 MJ m^{-2} in 2003 and 183 MJ m^{-2} in 2007. Excess net radiative energy could then contribute to further heat storage during late summer (July, August, and September) within an active layer moistened by greater infiltration of rainfall. Both effects during winter and late summer accelerated to form a warmer and deeper active layer.

The earlier snow melt resulted in an earlier soil thaw, infiltration of snowmelt water into soils, and snowmelt runoff. In fact, the increase in soil temperature was most rapid at the 1.2 m depth in 2005 (Fig. 6), which suggests that snowmelt water could have penetrated into dry frozen soil with relatively high hydraulic conductivity (Kane et al. 2001). Conversely, high soil moisture content after the snow disappearance in 2006 and 2007 (Fig. 3b) indicates that wet frozen soil suppressed penetration of snowmelt water. The wet active

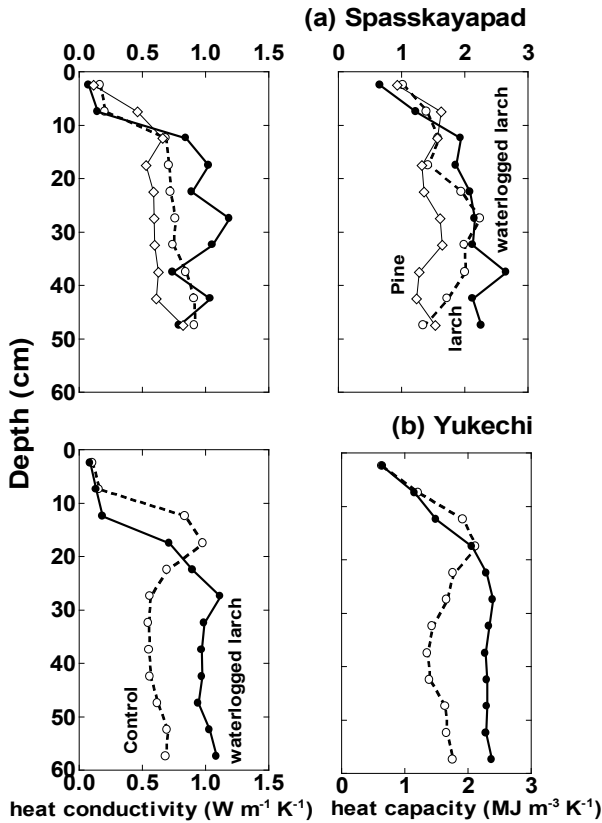


Figure 5. Vertical profiles of soil heat conductivity (left) and capacity (right) at Spasskayapad and Yukechi sites observed in late September 2009.

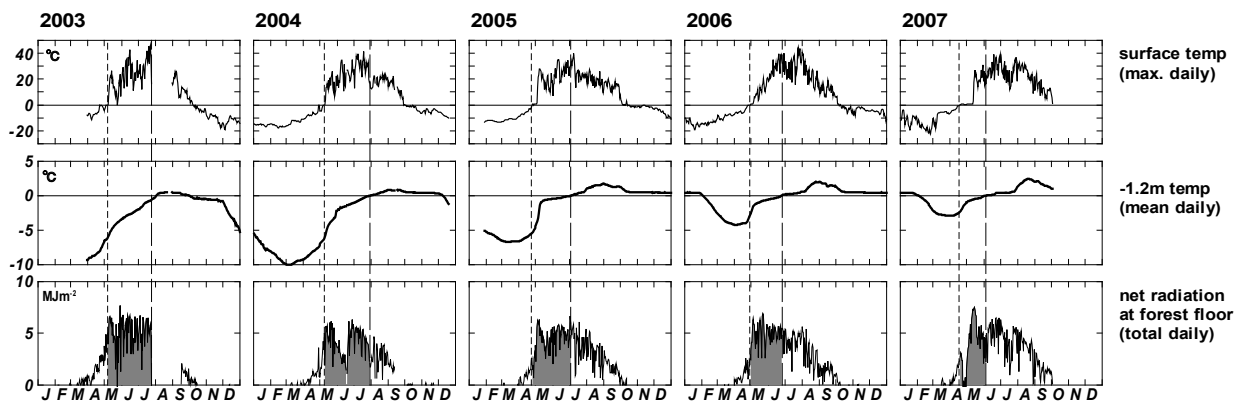


Figure 6. Time series of active layer temperature (surface and 1.2 m depth) and net radiation at a larch forest floor. Dashed and broken lines denote the thawing date at the surface and 1.2 m depth, respectively. Grey area in net radiation indicates total incoming net radiative energy during the thawing period of the active layer within 1.2 m depth.

layer was formed due to infiltration of rainfall in the preceding pre-winter period. The remaining snowmelt water may have flowed into valleys and alases, which resulted in a waterlogged forest combined with thermokarst erosion (Fig. 8).

Sap flow variations

Figure 7a represents seasonal variations in daily totals of sap flow flux from 15 larch trees sampled in 2006 and 2009. Soil moisture was high but larch trees appeared normal in 2006, whereas the active layer had been deepened with remaining saturated soil, and leaf coverage had decreased markedly in 2009. The total amount of sap flow flux, presented as an average of 15 trees between July 15 and September 15, was 12% lower in 2009 (1780 kg H₂O) than in 2006 (2025 kg H₂O). Figure 7b shows mean sap flow flux of control (8) and damaged (7) trees in 2009 as classified by foliation in summer 2009. The control trees maintained active water uptake, having greater daily amounts than the average sap flow flux in 2006 (Fig. 7a), which was likely due to favorable soil moisture conditions throughout the growing season. In contrast, damaged trees exhibited significant reduction with less than 20 kg day⁻¹ in water uptake during the same period.

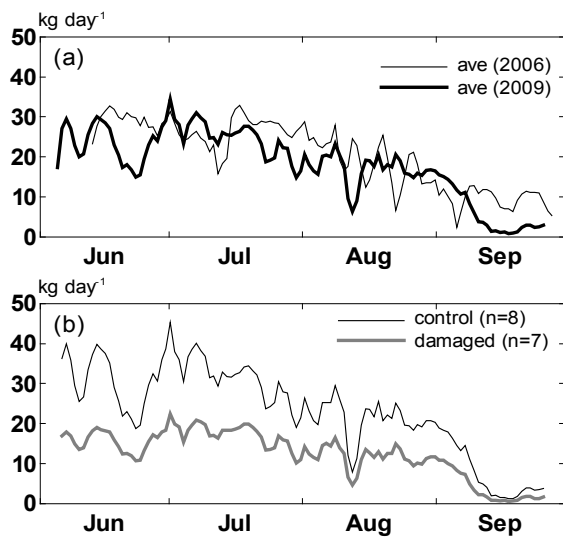


Figure 7. Seasonal variations in daily total sap flow flux (transpiration) of 3-day running mean from 15 larch trees. (a) Averages in 2006 (as denoted by thin line) and 2009 (bold line) and (b) results from control (n=8) and damaged (n=7) trees in 2009.

Larch trees in the Eurasian boreal forest have adapted to continuous permafrost conditions and a typically dry and severely cold climate (Sakai & Saito 1974). Interannual variation in evapotranspiration within larch forests is also more stable than other hydrological components, such as precipitation and soil moisture storage within the active layer (Ohta et al. 2008). Excess water from summer rainfall present in the soil prior to freezing is carried over as ice in the active layer during winter. Water storage thereby stabilizes the rate of evapotranspiration in larch forests (Sugimoto et al. 2003) under dry conditions with large interannual fluctuations in precipitation levels. The consecutive increase in both snow accumulation and summer rainfall after winter 2004 led to a dramatic shift in the hydrothermal environment within the active layer. Elevated levels of snow accumulation and precipitation over a multi-year period had never before been observed in this region, at least during the 20th century (Iijima et al. 2010). The observed environmental change resulted in physiological damage to portions of the larch forest. Consequently, suppression of transpiration within the larch forest emerged under the wet climatic conditions.

According to long-term eddy covariance observations above the canopy of the larch forest at this site during the growing season, evapotranspiration declined in 2007 and 2008 compared to levels observed in 2005 and 2006 (Ohta et al. unpubl.). This fact implies that our findings of changes in sap flow flux from individual trees can also be observed at a larger spatial scale. The central Lena River basin had large amounts of precipitation, and all forests were subject to similar negative effects imposed by a saturated active layer. Thus further attempts should be made to clarify the extent of transpiration reduction from the entire boreal forest in this region.

Conclusions

Atmospheric anomalies in the Arctic may cause intensifying storm activity from summer to early winter (Iijima et al. 2010). An increase in summer and winter precipitation after winter 2004 was observed in the central Lena River basin. The increased precipitation resulted in warming and wetting of the active layer and near surface permafrost.

During this period, subsidence by permafrost thawing is manifested in an open grassland (alase) on the right bank of the Lena River. The surrounding larch forest was exposed to fatal damage due to erosion of the side slope and saturated active



Figure 8. Landscape of a collapsed alase lake on September 28, 2008. Location is shown in Figure 2.

layer. The increased soil water resulted in a delayed freeze-up of the active layer.

The larch forest on the left bank was also damaged by the wet climate. The damaged (ultimately dead) trees were distributed in the concave micro topography with a deeper and oversaturated active layer. Sap flow measurements clearly showed a reduction of transpiration in damaged trees due to the lack of regular foliage.

In conclusion, the increased precipitation after winter 2004 resulted in high soil moisture content, which led to increased thermal conductivity in summer and a deeper active layer. Consequently, the perennial waterlogged active layer could be recognized as a gradual trigger for permafrost degradation under a wet climate. Enhanced thermokarst phenomena and larch forest mortality were unexpected eco-hydrological responses corresponding with permafrost degradation in eastern Siberia.

Acknowledgments

The present study was supported by the Research Institute for Global Change (RIGC), JAMSTEC and by the Ministry of Education, Science, Sports and Culture, Grant-in-Aid for Young Scientists (A) No. 21680057 and for Scientific Research (A) No. 20248016. Our thanks are extended to all the Yakutian personnel at the Institute for Biological Problems of the Cryolithozone and the Melnikov Permafrost Institute for their help during our fieldwork.

References

- Bosikov, N.P. 1991. *Evolution of Alases in Central Yakutia*. Permafrost Institute, Siberian Division of Russian Academy of Science, Yakutsk, Russia, 127 pp. (in Russian).
- Brouchkov, A., Fukuda, M., Iwahana, G., Kobayashi, Y., & Konstantinov, P. 2005. Thermal conductivity of soils in the active layer of eastern Siberia. *Permafrost and Periglacial Processes* 16: 217–222.
- Fedorov, A.N. & Konstantinov, P. 2003. Observations of surface dynamics with thermokarst initiation, Yukechi site, Central Yakutia. *Proceedings of the 8th International Conference on Permafrost, Zurich, Switzerland* 239–243.
- Granier, A., Biron, P., Bréda, N., Pontaller, J.-Y., & Saugier, B. 1996. Transpiration of trees and forest stands: short and long-term monitoring using sap flow methods. *Global Change Biology* 2: 265–274.
- Iijima, Y., Fedorov, A.N., Park, H., Suzuki, K., Yabuki, H., Maximov, T.C., & Ohata, T. 2010. Abrupt increases in soil temperatures following increased precipitation in a permafrost region, central Lena River basin, Russia. *Permafrost and Periglacial Processes* 21: 30–41.
- Iwasaki, H., Saito, H., Kuwao, K., Maximov, T.C., & Hasegawa, S. 2010. Forest decline caused by high soil water conditions in a permafrost region. *Hydrology and Earth System Sciences* 14: 301–307.
- Kane, D.L., Hinkel, K.M., Goering, D.J., Hinzman, L.D., & Outcalt, S.I. 2001. Non-conductive heat transfer associated with frozen soils. *Global and Planetary Change* 29: 275–292.
- Muskett, R.R. & Romanovsky, V.E. 2009. Groundwater storage changes in arctic permafrost watersheds from GRACE and in situ measurements. *Environmental Research Letter* 4: 045009.
- Ohta, T., Hiyama, T., Tanaka, H., Kuwada, T., Maximov, T.C., Ohata, T., & Fukushima, Y. 2001. Seasonal variation in the energy and water exchanges above and below a larch forest in eastern Siberia. *Hydrological Processes* 15: 1459–1476.
- Ohta, T., Maximov, T.C., Dolman, A.J., Nakai, T., van der Molen, M.K., Kononov, A.V., Maximov, A.P., Hiyama, T., Iijima, Y., Moors, E.J., Tanaka, H., Toba, T., & Yabuki, H. 2008. Interannual variation of water balance and summer evapotranspiration in an eastern Siberian larch forest over a 7-year period (1998–2006). *Agricultural and Forest Meteorology* 148: 1941–1953.
- Overland, J.E., Wang, M., & Salo, S. 2008. The recent Arctic warm period. *Tellus* 60A: 589–597.
- Outcalt, S.I., Nelson, F.E., & Hinkel, K.M. 1990. The Zero-Curtain Effect: Heat and Mass Transfer Across an Isothermal Region in Freezing Soil. *Water Resources Research* 26: 1509–1516.
- Sakai, A. & Saito, M. 1974. Dahurian larch trees in Yakutia. *Journal of Forest Research* 56: 247–252 (in Japanese with English abstract).
- Shur, Y.L. & Jorgenson, M.T. 2007. Patterns of permafrost formation and degradation in relation to climate and ecosystems. *Permafrost and Periglacial Processes* 18: 7–19.
- Sugimoto, A., Naito, D., Yanagisawa, N., Ichiyangi, K., Kurita, N., Kubota, J., Kotake, T., Ohata, T., Maximov, T.C., & Fedorov, A.N. 2003. Characteristics of soil moisture in permafrost observed in East Siberian taiga with stable isotopes of water. *Hydrological Processes* 17: 1073–1092.

Engineering Design Utilizing Climate Change Information – Permafrost Application

Arne Instanes
Instanes Polar AS, Bergen, Norway

Abstract

This paper presents a review of present-day codes and regulations related to engineering design and its application to permafrost areas. A methodology is recommended that includes output from downscaled climate models in the geothermal analysis of foundations on frozen ground. The geothermal analysis can then be coupled to time-dependent stress-strain analysis of structures and foundations.

Keywords: engineering; permafrost; design; climate change.

Introduction

Climate modelers claim that due to climate change, historical meteorological and oceanographic data are not suitable for estimating future extreme events and environmental loads on infrastructure and transportation systems (Esau 2011). The magnitude of an extreme event or environmental load is a function of the annual probability of occurrence of the event, the service lifetime of the structure, and the total risk or allowable exceedance probability during the service lifetime of the structure.

Environmental loads for cold region engineering structures are typically ocean waves and currents, wind loads, precipitation, ice loads, and earthquakes. In addition, ground temperature variations have to be incorporated in the design in permafrost regions. Permafrost foundation design always involves an evaluation of the ground thermal regime at the site before construction and during the service lifetime of the structure. Maximum active layer thickness and the maximum permafrost temperature as a function of depth of the foundation soils have to be estimated (Andersland & Ladanyi 2004). Design engineers have to ensure that the structure is not subjected to deformation and settlement that may threaten the structural integrity during the service lifetime of the structure.

Instanes (2003) points out that predicted climate warming may increase the environmental loads the structures are designed for and may increase the ground temperature in areas of permafrost. This may cause increased risk of damage to infrastructure due to increased deformation and settlement, and it may be a threat to human life because of landslides.

Statistical downscaling of climate scenarios has been used to develop climate scenarios for the Scandinavian and Svalbard region (Hanssen-Bauer et al. 2005, Benestad & Engen Skaugen 2009). Statistical downscaling can be used in local climate impact assessments due to its ability to deal with point/station scale (Hanssen-Bauer et al. 2005). For engineering purposes, output from downscaled climate scenarios may be treated in a manner similar to the statistical analysis of observed meteorological data. This means that for impact studies, time series from downscaled models can be used to estimate statistical parameters and probability of occurrence and exceedance probability of environmental loads.

This paper discusses current engineering design methods

and presents a methodology for evaluating climate change scenarios in the design of structures on permafrost.

Codes and Regulations for Engineering Design

In Europe, the Eurocode (www.cen.eu) is intended to be mandatory for European public works and is likely to become the standard for the private sector as well. The objective of the Eurocode is to become the preferred engineering design code in Europe and worldwide. The codes should replace all existing conflicting national codes. The most relevant general codes for foundation and permafrost engineering design in the Eurocode system are Eurocode 0 *Basis for structural design*, Eurocode 1 *Actions on Structures*, and Eurocode 7 *Geotechnical design* (CEN 1998, 2006, Norsk Standard 2004). Eurocode 1 divides structures into three reliability classes depending on the failure consequence to human life, and economic, social and environmental consequences (see Table 1).

Duckett (2004) refers to CIRIA (1977), where the total risk of failure, P , can be expressed as a function of design lifetime of the structure, n , the number of people at risk in the event of failure, n_r , and a structure factor, K_s :

$$P = \frac{10^{-4}}{n_r} K_s n \quad (1)$$

where the structural factor $K_s = 0.005$ for dams and places of public assembly, $K_s = 0.05$ for domestic, office or trade and industry, $K_s = 0.5$ for bridges and $K_s = 5$ for towers, masts, and offshore structures.

Annual or nominal probability is defined as the probability of an extreme event occurring during a one-year period. This is also referred to as the often misunderstood term “return period” of an extreme event. A 100-year return period, or event, corresponds to an annual probability of exceedance of 1%.

Table 1. Reliability class, Eurocode 1. From Duckett (2004).

| Reliability class | Failure consequence | Annual probability of failure |
|-------------------|---------------------|-------------------------------|
| RC1 | Small or negligible | 10^{-5} |
| RC2 | Medium | 10^{-6} |
| RC3 | Considerable | 10^{-7} |

Table 2. Requirements for structures or areas subjected to river flooding or storm surge.

| Safety Class | Consequence | Annual probability of extreme event | “Return period” of extreme event |
|--------------|-------------|-------------------------------------|----------------------------------|
| F1 | Small | $5 \cdot 10^{-2}$ or 5% | 20 years |
| F2 | Medium | $5 \cdot 10^{-3}$ or 0.5% | 200 years |
| F3 | Large | 10^{-3} or 0.1% | 1 000 years |

Table 3. Requirements for structures or areas subjected to avalanches, rock falls, and landslides.

| Safety Class | Consequence | Annual probability of extreme event | “Return period” of extreme event |
|--------------|-------------|-------------------------------------|----------------------------------|
| S1 | Small | 10^{-2} or 1% | 100 years |
| S2 | Medium | 10^{-3} or 0.1% | 1 000 years |
| S3 | Large | $2 \cdot 10^{-4}$ or 0.02% | 5 000 years |

Eurocode 7 gives general recommendations on geotechnical design, but the code does not give specific recommendations for permafrost or cold region engineering design. There are, for example, no guidelines for acceptable limits of probability of failure or level of ground thermal analysis to be performed for a given structure on permafrost, or how possible effects of climate change should be treated.

In Norway, a special regulation in the law deals with requirements and products for construction works (Norwegian Ministry 2010). Chapter 7 in this regulation addresses risks related to environmental loads.

Table 2 shows the design requirements for structures or areas subjected to river flooding and storm surge; Table 3 shows the design requirements for structures or areas subjected to avalanches, rock falls, and landslides. It can be observed from the tables that the annual probability of an extreme event is higher than the annual probability of failure interpreted from Eurocode 1 in Table 1.

Engineering design for offshore structures is regulated through the NORSOK standards (NORSOK 2007, 2010). NORSOK recommends that the probability of environmental actions damaging main safety functions while personnel are on the facility should be less than 10^{-4} per year. This corresponds to an annual probability of 0.01% and gives a total risk of 1% for a structure with a 100-year lifetime. Using equation 1, an oil rig with 100 people on board would have a total risk of $5 \cdot 10^{-4}$, which may be acceptable.

When evaluating the geothermal conditions during the service lifetime of a structure in permafrost regions, the “extreme” event is different from the environmental loads described above. The main difference is that during an arbitrary year, the maximum active layer thickness and maximum permafrost temperature at depth in that particular year occur in most cases only once. The occurrence of the “extreme event” is then limited to once a year, while other environmental loads

Table 4. Design air thawing index for structures on permafrost.

| Safety Class | Consequence | Annual (nominal) probability of extreme event | “Return period” of extreme event |
|--------------|-------------|---|----------------------------------|
| P1 | Small | 1/10 or 10% | 10 years |
| P2 | Medium | 1/100 or 1% | 100 years |
| P3 | Large | 1/1000 or 0.1% | 1 000 years |

(e.g., 3-second wind gusts) have a much higher frequency. Instanes (2003) refers to design methods of frost protection in Norway, where design air freezing indices with various annual probabilities are used in the design. Similarly, air thawing indices with various annual probabilities can be used in permafrost engineering design (see Table 4). It is usually recommended to apply a thawing index with 1% annual probability, but this may be extended to a 0.1% probability for structures sensitive to permafrost warming.

P1 is typically used for road construction, while P2 and P3 are used for buildings and essential infrastructure.

Hayley and Horne (2008) advocate a “project screening process” to address the uncertainty related to future climate warming in the Arctic. The screening process involves an evaluation of the structure’s climate sensitivity and the consequence of failure, similar to the Norwegian approach. The climate sensitivity is dependent on foundation soil type, ice content, and estimates of ground temperatures at the end of the service lifetime of the structure. A risk level is then defined, giving the required level of engineering analysis. Hayley and Horne (2008) recommend including some climate warming trend input in the geothermal analysis and coupling this to failure modes and effects analysis.

However, these approaches do not include an evaluation of reliability as defined by the Eurocode, or risk and/or exceedance probability of the environmental load during the service lifetime of the structure. Neither do they address the time-dependent variations in statistical parameters of the environmental loads.

Exceedance Probability

Clearly, an increased service lifetime of a structure would mean that the accumulated exceedance probability will increase. The relationship between design service lifetime of the structure, return period of extreme events, and probability of this extreme event to occur during the service lifetime can be expressed as (reformulated based on British Standard 2000):

$$P = 1 - \left(1 - \frac{1}{T}\right)^n \quad (2)$$

where P = annual probability of extreme event occurring during service lifetime of structure, T = return period of extreme event, and n = design service lifetime of structure. Equation 2 gives the exceedance probability of an extreme event during the service lifetime of the structure. Equation 2 is plotted in

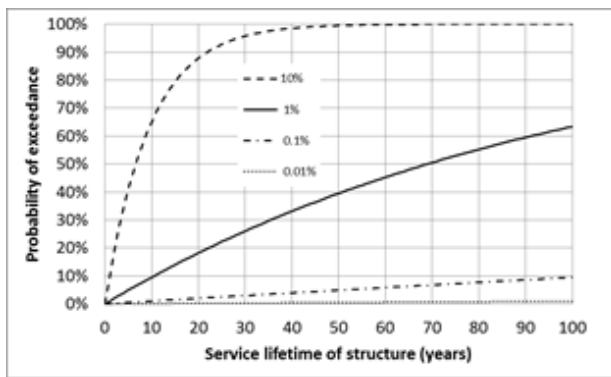


Figure 1. Exceedance probability versus structure service lifetime for return periods of extreme events varying from 0 to 100 years.

Figure 1 for service lifetimes varying from 0 to 100 years and extreme events with nominal probability of 10%, 1%, 0.1%, and 0.01%. From Figure 1 it can be observed that a structure with a service lifetime of 50 years has an approximately 40% chance of experiencing a “100-year-event” during its service lifetime. If the lifetime is increased to 100 years, the exceedance probability will increase to 63.4%.

For structures with considerable failure consequence and service lifetimes over 100 years, the annual probability of an extreme event from Table 2 and 3 will give a total risk during the service lifetime of 9.5% and 2%, respectively. This may be considered an unacceptable risk if human lives are lost. Table 1 may be more appropriate in this case, and reduce the total risk to 0.001%.

In permafrost engineering design, the main interest is, as mentioned above, the predicted maximum active layer thickness during the service lifetime of the structure and the maximum permafrost temperatures of foundation soils. The “extreme event” in this case will be an extreme warm year or number of years. The design “extreme event” has to be used in geothermal analysis in order to calculate maximum thaw depth and permafrost temperature during the service lifetime of the structure. Finally, the maximum temperature profile has to be used in strength and creep evaluations of the permafrost soils, resulting in estimations of deformations and settlements of foundations and structures. The following discussion is restricted to the “extreme event” or warm summer, the effect of structure service lifetime, and climate change impact.

Permafrost Engineering Design

Table 5 gives a review of possible engineering problems related to climate change based on Esch and Osterkamp (1990). It should be noted that these problems are well known after more than 100 years of experience with construction of infrastructure and transportation systems in permafrost areas. Human interaction and engineering construction works often create the impacts shown in Table 4 much faster than a gradual change in climate (Instanes 2003).

Since the strength and creep behavior of frozen soils are temperature and time dependent, the design of foundations

Table 5. Climate change impact and related engineering problems (after Esch and Osterkamp 1990).

| Climate change impact | Engineering problem | Adaptation suggestion |
|----------------------------------|--|---|
| Increased active layer thickness | Thaw settlement during seasonal thawing Increased frost heave forces on piles Increased total and differential frost heave during winter | Insulation Increased pile length Protection/treatment of pile in active layer |
| Warming of permafrost at depth | Increased creep rate of existing piles and footings Reduced ad-freeze bond strength for piles Increased creep of foundations | Increase pile length and depth and area of footings Reduce foundation loads Artificial cooling of foundations |
| Permafrost thaw | Decreased effective pile length Landslides Progressive surface settlements | Increased pile length Relocation Artificial cooling of foundation soils |

on permafrost involves, as mentioned above, geothermal analysis. When the warmest design temperature profile is established, the corresponding strength and creep properties of the foundation soils can be estimated as a function of the service lifetime of the structure. This can ultimately be used to determine if the deformations and settlements of the foundations are within acceptable limits. If not, foundation loads have to be reduced, foundation geometry has to be altered (pile length and diameter, footing depth and area), or alternative foundation techniques found.

Andersland & Ladanyi (2004) propose to use a strength sensitivity index S_T to evaluate the strength loss of frozen soils when climate warming scenarios are not expected to result in complete thaw of the permafrost. The strength sensitivity index is defined as:

$$S_T = w \cdot \left(\frac{\Delta\theta_i}{\theta_i + \theta_0} \right) \quad (3)$$

where w is the laboratory-determined soil sensitivity to temperature change (temperature exponent ≤ 1), θ_i is the absolute value $-T$ of the initial permafrost temperature, θ_0 is a reference permafrost temperature of 1°C, and $\Delta\theta_i$ is the temperature change. In this manner, the change in pile settlement or settlement rates and/or footing deformations can be determined when the sensitivity index is combined with the design warmest permafrost temperature profile.

The design lifetime of a structure in permafrost areas varies typically between 15 and 100 years. Since climate change is a relatively slow process in this timeframe, structures and

infrastructure constructed on permafrost and designed for permafrost conditions are unlikely to be adversely impacted during typical engineering design lifetimes. However, the concept and requirement of “perpetual design” is becoming more common. For high-risk projects such as water retaining structures, tailings, and storage facilities for hazardous waste, the environmental protection agencies can apply such principles to the design. This makes it even more important to evaluate the exceedance probability in permafrost engineering design.

Exceedance Probability and Permafrost Engineering Design

As shown in the above sections, engineering design in permafrost areas includes geothermal analysis that will predict the maximum active layer thickness and maximum permafrost foundation soil temperature. The geothermal analysis is based on assumption of the meteorological conditions on the site during the service lifetime of the structure. Figure 2 presents mean annual air temperatures (MAAT) for Longyearbyen, Svalbard (78°25'N, 15°47'E) for 1912–2100. The squares are based on meteorological observations, the solid line is predicted MAAT based on mean monthly air temperatures 2000–2050 from empirical downscaling (Hanssen-Bauer et al. 2000), and the dotted lines are upper and lower boundaries of the results from empirical downscaling from Benestad and Engen Skaugen (2009). Figure 2 shows that the results from Hanssen-Bauer et al. (2000) are in relatively good agreement with actual observations and that continued warming until 2050 is limited. The more recent results from Benestad and Engen Skaugen (2009) show that the lower boundary indicates a mean annual air temperature in year the 2100 similar to today's value of -5°C . However, the upper boundary predicts extreme warming, giving a mean annual air temperature of $+6^{\circ}\text{C}$ in the year 2100. The corresponding freezing and thawing indices ($^{\circ}\text{C}\cdot\text{days}$) are shown in Figures 3 and 4, respectively. Figure 3 shows that the upper boundary extreme warming will give a freezing index of approximately 0 in the year 2100 (no frost action), while the lower boundary gives a situation similar to the present condition. Similar trends are found in Figure 4 for the thawing index. In geothermal analysis of foundations on permafrost, Andersland and Ladanyi (2004) recommend using the average air thawing index for the three warmest summers in the latest 30 years of record, or the warmest summer in the latest 10 years of record if 30 years of record are not available. Figure 5 shows thawing indices for Longyearbyen based on historical observations.

The consequence will be increased thaw depths, a gradual slow increase of permafrost temperatures with depth, and eventually thawing. Figure 5 also includes observed 30-year mean thawing indices. It is apparent from the figure that the 30-year mean has increased from approximately $400^{\circ}\text{C}\cdot\text{days}$ in 1980 to $500^{\circ}\text{C}\cdot\text{days}$ today. Instanes (2003) recommends using a probabilistic approach where the design thawing index is connected to an annual probability. An annual probability of 1% can be regarded as the design thawing index for structures

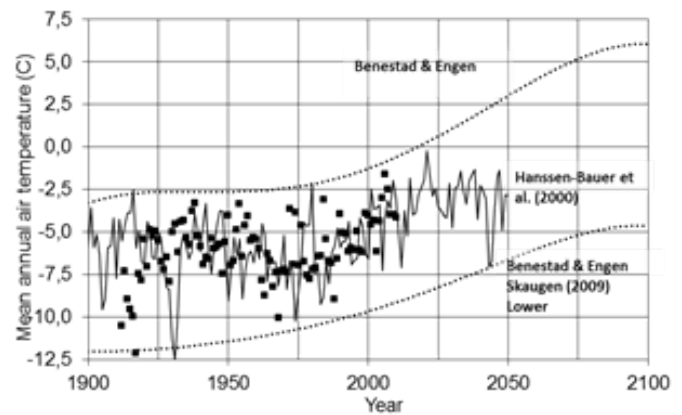


Figure 2. Mean annual air temperature, Longyearbyen, Svalbard.

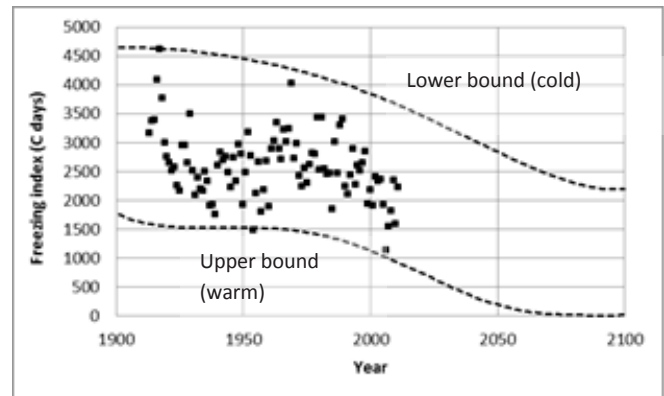


Figure 3. Air freezing index, Longyearbyen, Svalbard. Squares are based on meteorological observations, dotted lines are upper (cold) and lower (warm) boundaries from Benestad and Engen Skaugen (2009).

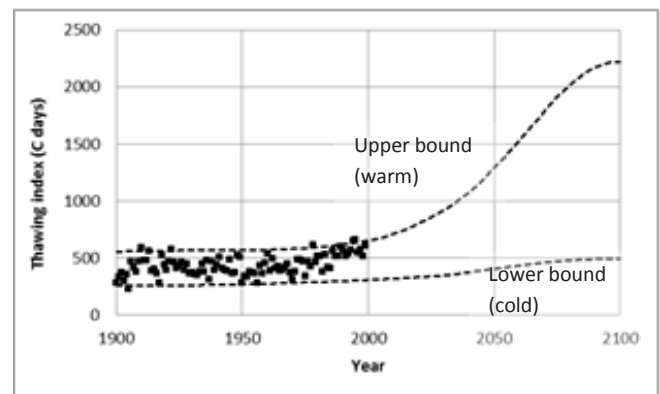


Figure 4. Air thawing index, Longyearbyen, Svalbard. Squares are based on meteorological observations, dotted lines are upper (warm) and lower (cold) boundaries from Benestad and Engen Skaugen (2009).

on permafrost. However, this design exceedance probability versus service lifetime of the structure will follow the solid line in Figure 1 using this criterion. Figure 6 presents the time-dependent variation of thawing indices for Longyearbyen.

The analysis is based on the variation in statistical parameters of the running 30-year mean, and it is assumed for simplicity that each 30-year period has a Gaussian distribution of thawing indices. It can be observed from the figure that the

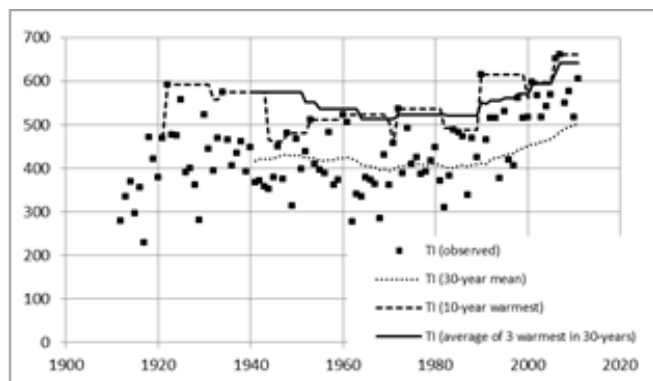


Figure 5. Design air thawing index, Longyearbyen, Svalbard, based on Andersland and Ladanyi (2004).

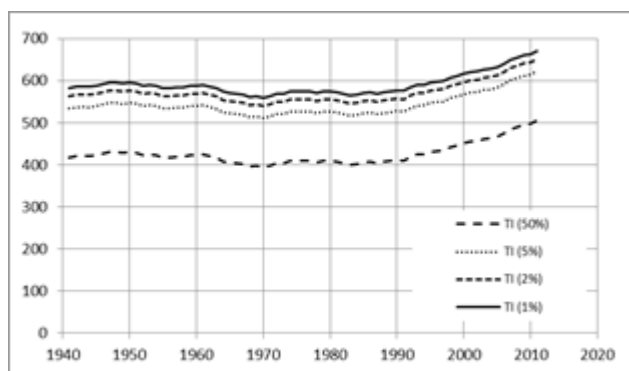


Figure 6. Design air thawing index, Longyearbyen, Svalbard, based on annual probability of occurrence.

thawing index with 1% annual probability has increased from approximately 580 °C-days in 1990 to approximately 670 °C-days today.

A similar analysis has been applied to the mean monthly air temperature data from empirical-statistical downscaled climate scenarios from Benestad & Engen Skaugen (2009) and Hanssen-Bauer et al. (2000). The result of the analysis is shown in Figure 7. The same data are plotted for the time period 1975–2050 in Figure 8. Figure 7 shows that the upper boundary from Benestad and Engen Skaugen (2009) is similar to observed thawing indices from the historical meteorological record from 1975 to 2011. The modelled warming accelerates through the twenty-first century and becomes extremely high at the end of the century. The data from Hanssen-Bauer (2000) give too high warming compared to the observed historical meteorological record, but lower warming compared to Benestad and Engen's upper limit for the period 2012–2050. The lower boundary from Benestad and Engen Skaugen (2009) gives a much cooler summer than the observed records and can be interpreted as a climate cooling trend.

Discussion

Figures 7 and 8 can be used to investigate the performance of a foundation on permafrost during the period of recent warming based on meteorological observations and also under the influence of climate warming scenarios. For example,

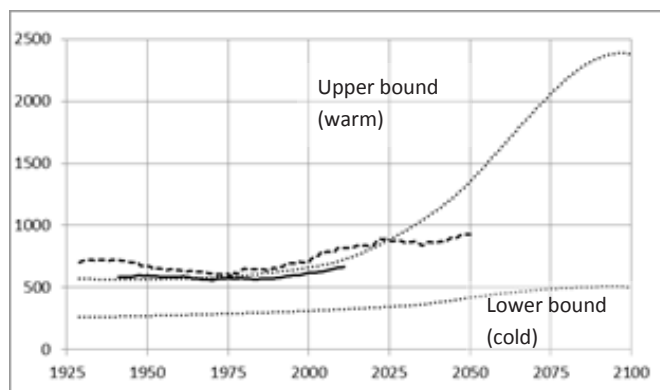


Figure 7. Design air thawing index, Longyearbyen, Svalbard, with annual probability of occurrence of 1%, 1925–2100. Dotted lines are upper (warm) and lower (cold) boundaries from Benestad and Engen Skaugen (2009), dashed line is from Hanssen-Bauer et al. (2000), and solid line is based on meteorological observations.

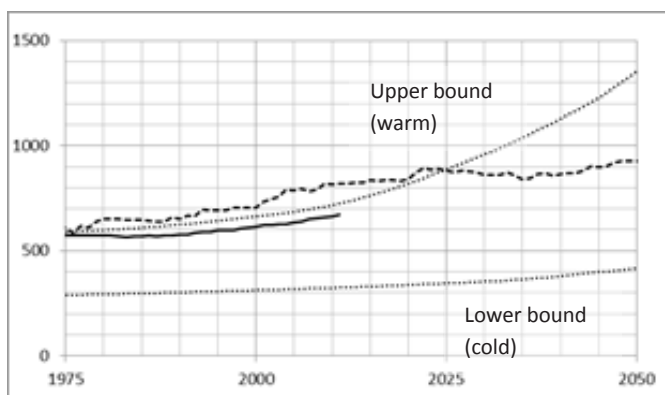


Figure 8. Design air thawing index, Longyearbyen, Svalbard, with annual probability of occurrence of 1%, 1975–2050. Dotted lines are upper (warm) and lower (cold) boundaries from Benestad and Engen Skaugen (2009), dashed line is from Hanssen-Bauer et al. (2000), and solid line is based on meteorological observations.

if a foundation was designed for a 1% annual probability thawing index in 1975 based on 575 °C-days and a 50-year service lifetime, the total probability of exceedance of the design criterion during the service lifetime can be calculated as approximately 40% (equation 3). In 2011, the 1% annual probability thawing index has increased to 670 °C-days. The original design criterion of 575 °C-days has an annual probability of 14% in 2011. However, the remaining service lifetime is reduced from 50 years to 14 years. The total probability of exceedance of the design criterion during the remaining service lifetime can then be calculated using equation 2 and yields 88%. Figure 8 shows that, based on the downscaled models, the 1% annual probability may increase to 900 °C-days in the year 2025. For structures with a 50-year service lifetime, designed and constructed with today's 1% annual probability thawing index of 670 °C-days, the total probability of exceedance of the design criterion during the remaining service lifetime will increase from the initial 40% to nearly 100%.

The next step in the analysis is to calculate the maximum active layer thickness and foundation soil temperatures from

the air temperature records from the downscaled models. Based on this temperature profile, predictions of the time-dependent deformations of the structure can be carried out by using, for example, equation 3 with site specific soil data.

Recommendations and Conclusions

Based on output from downscaled climate models, existing structures on permafrost will experience warm years exceeding design conditions, based on historical observations during the next decades. The upper boundary from climate models from Benestad and Engen Skaugen (2009) is similar to observed thawing indices from historical meteorological records from 1975 to 2011. It is recommended that the geothermal analysis include time series from downscaled climate models to predict maximum thaw depths and permafrost temperatures for the foundation soils. The geothermal analysis can be coupled to time-dependent stress-strain analysis of structures and foundations. Functions giving the sensitivity of the foundation soils to temperature change (such as equation 4) can then be used to investigate the effect on deformations and settlements during the remaining service lifetime of the structure.

Acknowledgments

This study has been carried out as part of the pilot project "A user-defined approach to utilize climate change information in local implementation of national construction standards (RECON)" funded by the Norwegian Research Council as part of the NORKLIMA programme.

References

- Andersland, O.B. & Ladanyi, B. 2004. *Frozen ground engineering*. Second edition American Society of Civil Engineers, John Wiley & Sons. Inc., 363 pp.
- Benestad, R.E. & Engen Skaugen, T. 2009. Simple empirical-statistical downscaling figures. Met.no-note no. 3/2009. The Norwegian Meteorological Institute (met.no) Publication Series, 25 pp.
- British Standard. 2000. Maritime Structures – Part 1: Code of practice for general criteria. BS6349-1: 2000, 254 pp.
- CEN (European Committee for Standardization). 1998. Eurocode 1: Basis of design and actions on structures. ENV 1991-2-7. www.cen.eu.
- CEN (European Committee for Standardization). 2006. Basis for structural design. EN 1991-1-7. www.cen.eu.
- CIRIA (Construction Industry Research and Information Association). 1977. Rationalization of Safety Factors and Serviceability Factors in Structural Codes. CIRIA Report 63.
- Ducket, W. 2004. Risk analysis and the acceptable probability of failure. International Association for Bridge and Structural Engineering. *Designing for the consequence of failure*. Paper 06. 5 pp.
- Esau, I. 2011. Climate change challenge engineers. *Klima* 4-2011: 30-31. www.cicero.uio.no/klima (in Norwegian).
- Esch, D.C & Osterkamp, T.E. 1990. Cold regions engineering: Climate warming concerns for Alaska. *Journal of Cold Regions Engineering* 4(1):8.
- Hanssen-Bauer, I., Tveito, O.E., & Førland, E.J. 2000. Temperature scenarios for Norway: Empirical downscaling from the ECHAM4/OPYC3 GSDIO integration. DNMI Report no. 24/00, Oslo, Norway.
- Hanssen-Bauer, I., Achberger, C., Benestad, R.E., Chen, D., & Førland, E.J. 2005. Statistical downscaling of climate scenarios over Scandinavia. *Climate Research* Vol.29: 255-268, 2005.
- Hayley, D. & Horne, B. 2008. Rationalizing Climate Change for Design of Structures on Permafrost: A Canadian Perspective. In *NICOP 2008: Proceedings of the Ninth International Conference on Permafrost*. D.L. Kane & K.M. Hinkel (eds.). Institute of Northern Engineering, University of Alaska Fairbanks, 1: 681-687.
- Instanes, A. 2003. Climate change and possible impact on Arctic infrastructure. *Proceedings of the 8th International Conference on Permafrost*, Zürich, Switzerland, July 21-26, 2003, pp. 461-466. Balkema publishers, The Netherlands.
- Norsk Standard. 2004. Geotechnical design. NS-EN-1997-1:2004+NA:2008. Eurocode 7: Geotechnical design. National Annex.
- Norwegian Ministry of Local Government and Regional Development. 2010. Technical Regulations under the Planning and Building Act. Regulations concerning requirements for construction works and products for construction works (Byggteknisk forskrift). <http://www.be.no/beweb/english/techreg97.html>.
- NORSOK Standard. 2010. Integrity of offshore structures. N-001 Edition 7, June 2010. 30 pp.
- NORSOK Standard. 2007. Actions and effects. N-002 Edition 2, September 2007.

Thermal State of Mongolian Permafrost

Mamoru Ishikawa

Faculty of Environmental Earth Science, Hokkaido University, Japan

Natsagdorj Sharkhuu, Yamkhn Jambaljav

Institute of Geography, Mongolian Academy of Sciences, Mongolia

Gamboo Davaa

Institute of Meteorology and Hydrology, Mongolia

Kenji Yoshikawa

University of Alaska Fairbanks, USA

Tetsuo Ohata

Japan Agency for Marine-Earth Science and Technology, Japan

Abstract

Mongolian permafrost has temperatures close to 0°C and is expected to thaw drastically due to climate-induced warming. More than 80 boreholes covering almost the entire permafrost region were established recently. This paper discusses the thermal state of permafrost on regional and national scales. Permafrost at higher latitudes tends to be colder than that at lower latitudes, although local topography largely modifies this trend. Ground temperature profiles indicate a strong influence of subsurface materials and vegetation cover on permafrost temperatures. Regions with continuous permafrost in the northern provinces experienced increased warming relative to regions with discontinuous and sporadic permafrost. The greatest warming occurred in the areas where permafrost had already disappeared, suggesting that all energy transferred to the soil was used for ground warming and not for the melting of ice. The warming rates in the permafrost disagree with those measured in the air. We conclude that the warming of Mongolian permafrost is largely controlled by temperature-dependent soil properties.

Keywords: Mongolia; permafrost warming; borehole monitoring network.

Introduction

Permafrost has been degrading over large areas of the world (Brown & Romanovsky 2008, Romanovsky et al. 2010a), as proven by strong local evidence in Alaska (Jorgenson et al. 2001, Osterkamp 2008), Europe (Harris et al. 2003), Siberia (Romanovsky et al. 2010b), Canada (Smith et al. 2005), and Central Asia (Zhao et al. 2010). Studies have reported large spatial variations in warming rates. Hence it is important to organize and sustain continuous observations to monitor the long-term thermal state of permafrost at various locations and in various natural settings around the globe.

Mongolia makes up the southern fringe of the Siberian permafrost region. It is characterized by arid, mountainous land underlain mainly by sporadic-to-continuous permafrost. Mongolian permafrost has temperatures close to 0°C and hence is highly vulnerable to climate-induced warming.

Research of Mongolia's permafrost was initiated at the beginning of the twentieth century when permafrost islands were found in Hovsgol and along the Selenge River (Fig. 1). Official permafrost investigations were performed under the joint Mongolian–Soviet geocryological expedition between 1967 and 1971, and a country-wide map of the Mongolian permafrost (Gravis et al. 1974) was created. The map shows that permafrost occurs mainly in the mountainous regions and reveals an obvious latitudinal shift from the northern to the southern territories (Fig. 1).

In the beginning of the 1990s, most of the research on Mongolian permafrost was interrupted by economic problems. Although numerous permafrost observations were lost, some old data were rescued and are used here for comparison with the recent measurements performed in the late 1990s and the early 2000s.

Permafrost warming is caused by various environmental factors, the most predominant of which is the climate. Most areas of permafrost are not directly connected to the atmosphere. Therefore, warming is also strongly influenced by factors such as micrometeorological conditions, surface and ground water, soil/ground properties, and vegetation. The abovementioned effects are often significant, particularly in Mongolian permafrost, because permafrost occurrences are strongly dependent on various geographical settings such as slope, aspect, and the presence of forest cover (Ishikawa et al. 2005, 2008).

For a better understanding of the thermal state of Mongolian permafrost, there must be an improved borehole monitoring network covering large areas. Toward that end, we drilled new boreholes for research purposes and recovered boreholes that had been abandoned since the late 1990s. The recently established monitoring network comprises more than 80 boreholes (Fig. 1). We evaluated the thermal state of permafrost on regional and national scales and discussed their decadal changes based on the currently available thermal data from 48 research boreholes.

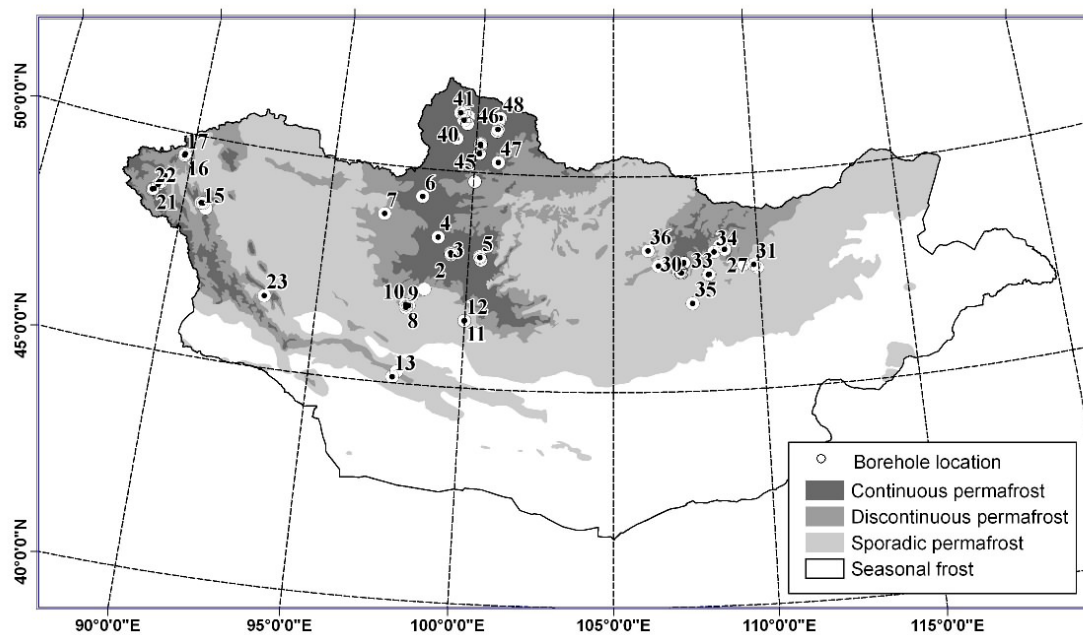


Figure 1. Locations of all research boreholes over the Mongolian permafrost. Numbered and dotted circles indicate the locations of the boreholes used for analysis in this study. See Table 1 for coordination and other geographic information. Some of the boreholes that are located close to those used in study are not shown.

Geographical and Climatic Settings of the Boreholes

A gradual temperature and moisture change is reflected in the prevailing climatic pattern along a latitudinal gradient (IMH 2009). Winter air temperatures often dip to -50°C in the northern territory, and to 4°C in the south. In the warmest month, air temperatures range between 10 and 15°C in the northern provinces (Hovsgol, Northern Hangai, Altai, and Hentii) and reach up to 20°C in the southern province (Gobi-Altay). The air temperatures are the lowest in mid-January and range between -25 and -30°C in the northern regions and between -15 and -20°C in the southern regions. Annual total precipitation is 300 – 400mm in Northern Hangai, Hentii, and Hovsgol, and it decreases to 100 – 200mm in Southern Hangai and Gobi-Altay. These climatic transitions produce a latitudinal shift in vegetation cover from north to south. Deciduous needle leaf forests extend over the northern provinces, while grasslands are seen in most parts of the country and in the desert in the southern regions. The Hangai Mountain ridges prevent moist air from flowing southward, resulting in wet climatic conditions in Northern Hangai, in contrast to the dry climate in the Southern Hangai provinces.

Eighty-six boreholes, spanning almost all the permafrost regions in Mongolia, are available for research. The boreholes cover Hovsgol, Northern Hangai, and Altai provinces, which have continuous permafrost, and Southern Hangai, Hentii, and Gobi-Altay provinces, which have discontinuous permafrost (Fig. 1 and Table 1). Most of the boreholes are in the sedimentary layers, while a few are in the ice-rich or bedrock layers (Table 1).

These boreholes enable us to evaluate the thermal state of permafrost on a national scale. Further, local topographic

dependencies on permafrost temperatures can be evaluated by studying some of the boreholes set in the north, its adjacent south-facing slopes, and the intermediate valley bottom (Terkh of northern Hangai [#1, 2, 3] and Bayanbulag [#8, 9, 10] and Galuut of Southern Hangai) (Table 1). The boreholes at Galuut are on the northern talus slope (#11) and its adjacent valley bottom (#12), where degrading pingos are observed (Babinski 1982). Two boreholes (#24, 25) are in the south-facing pasture and the forested north-facing slopes in Terelj, Hentii.

Decadal changes in permafrost temperatures are evaluated for the borehole sites, where ground temperatures were observed more than one time over three decades from the 1960s to the 1980s. For the Bayanbulag3, Tsagaannuur1, Tsagaannuur2, Khentii36, and Gurvanturuu sites, the boreholes were reconstructed between 2008 and 2010 at a place close to the abandoned boreholes (less than several tens of meters apart).

Measurements and Analysis

Ground temperatures were measured manually and automatically in the open-cased (PVC or metallic tubes) borehole. Manual measurements were performed using a movable thermistor string, and readings were taken in the same month at the same depth using a digital multi-meter (see Anarmaa et al. 2008 for more details). Automatic measurements were made by HOBO U-12 (with an accuracy of 0.1°C or better), CR10x, or CR1000 data-loggers using calibrated TMC-HD and other types of thermo-sensors (see Ishikawa et al. 2006, 2008 for more details).

As of September 2011, we successfully acquired temperature data from 48 boreholes (Table 1) and defined the 10-m depth ground temperatures (GT10m) measured once during summer

Table 1. Inventory of research boreholes analyzed in this paper.

| Province | Research Borehole | | Coordination | | | Year of data available | Analysis | Contributor (References) | |
|----------|-------------------|----------------------|------------------|--------|--------|------------------------|----------------|--------------------------|-------|
| | # | Name(Geology) | N | E | Elev | | | | |
| NH | 1 | Terkh ar(1) | 48.05 | 99.38 | 2180 | 2009- | G,M,P | J, I | |
| | 2 | Terkh ubur(1) | 48.10 | 99.37 | 2100 | 2009- | P | J, I | |
| | 3 | Terkh valley(1) | 48.08 | 99.38 | 2050 | 1988 2009- | G,M,C,P | S,J, I (3,4) | |
| | 4 | Sharga_M8(1) | 48.45 | 98.90 | 1896 | 1981 2008- | G.M.C | S,J, I (3,4) | |
| | 5 | Chuluut Pingo M7A(2) | 48.04 | 100.39 | 1870 | 1969 2007 | G.M.C | S (4) | |
| | 6 | Mungut pingo(2) | 49.35 | 98.24 | 1781 | 2009- | G.M | Y, S (5) | |
| | 7 | Numrug(1) | 48.87 | 96.96 | 1853 | 2009- | G.M.P | J, I | |
| SH | 8 | Bayanbulag1(1) | 46.83 | 97.98 | 2418 | 2009- | G,M,P | J, I | |
| | 9 | Bayanbulag2(1) | 46.76 | 98.00 | 2517 | 2009- | P | J, I | |
| | 10 | Bayanbulag3(1) | 46.81 | 98.09 | 2253 | 1981 2009- | G.M,C,P | J, I | |
| | 11 | Galuu1(1) | 46.55 | 99.98 | 2100 | 2009- | G,M,P | J, I | |
| | 12 | Galuu2(2) | 46.56 | 99.99 | 2046 | 2009- | G.M.P | J, I | |
| GA | 13 | Erdene2(1) | 45.14 | 97.75 | 2415 | 1982 2009- | G.M,C,P | J, I | |
| AT | 14 | Hashaat2(1) | 48.50 | 90.69 | 2498 | 2009- | G.M | J, I | |
| | 15 | Hongor ulun(1) | 48.50 | 90.62 | 2390 | 2009- | G.M | J, I | |
| | 16 | Tsagaannuur1(1) | 49.52 | 89.74 | 2135 | 1985 2009- | G.M,C | J, I | |
| | 17 | Tsagaannuur2(1) | 49.49 | 89.73 | 2113 | 1983 2009- | G.M,C | J, I | |
| | 18 | Tsengel1(1) | 48.94 | 89.21 | 1995 | 2010- | G | D, J | |
| | 19 | Tsengel2(1) | 48.77 | 89.11 | 2240 | 2010- | G | D, J | |
| | 20 | Tsengel3(1) | 48.71 | 89.04 | 2338 | 2010- | G | D, J | |
| | 21 | Tsengel4(1) | 48.60 | 88.93 | 2500 | 2010- | G | D, J | |
| | 22 | Tsengel5(1) | 48.58 | 88.89 | 2567 | 2010- | G | D, J | |
| | 23 | Tsetseg(1) | 46.64 | 93.25 | 1714 | 2010- | G | D, J | |
| | HT | 24 | Terej-ND(1) | 47.98 | 107.43 | 1629 | 2002- | P | I (2) |
| | | 25 | Terej-SD(1) | 47.99 | 107.42 | 1656 | 2002- | G,M,P | I (2) |
| | | 26 | Nalikh-D(1) | 47.75 | 107.34 | 1422 | 2002- | G.M | I (2) |
| | | 27 | Udieg(1) | 48.28 | 108.85 | 1388 | 2009- | G | I |
| | | 28 | Nalikh SE M2E(3) | 47.77 | 107.29 | 1441 | 1999 2004 2007 | G | S |
| | | 29 | Nalikh SE M2C(3) | 47.77 | 107.29 | 1439 | 2000 2003 | G | S |
| | | 30 | Argalant M3(1) | 47.92 | 106.55 | 1385 | 1988 2007 | G,C | S (4) |
| 31 | | Khentii36(1) | 47.87 | 109.83 | 1289 | 1984 2009- | G.M,C | J, I | |
| 32 | | Baganuur LS M1A(1) | 47.69 | 108.26 | 1345 | 1976 2002 2007 | G | S (1) | |
| 33 | | Baganuur DPR M1A(1) | 47.69 | 108.29 | 1350 | 1976 2006 | G,C | S (4) | |
| 34 | | Mungunmorit1(1) | 48.21 | 108.49 | 1450 | 2010- | G | D, J | |
| 35 | | Guvanturuu(1) | 47.04 | 107.69 | 1399 | 1978 2010- | G,C | J, I | |
| 36 | | Borhujii M15(1) | 48.28 | 106.19 | 1160 | 1970 2007 | G,C | S | |
| HV | 37 | Hatgal1(1) | 50.44 | 100.14 | 1679 | 2009- | G | J, I | |
| | 38 | Hatgal2(1) | 50.45 | 100.13 | 1690 | 2009- | G | J, I | |
| | 39 | Munguushiin sair(1) | 50.76 | 99.29 | 1629 | 2010- | G | J, I | |
| | 40 | Darhad Huurch(1) | 51.19 | 99.50 | 1558 | 2008- | G.M | S | |
| | 41 | Tsagaannuur(1) | 51.36 | 99.36 | 1550 | 2008- | G.M,C | S (3,4) | |
| | 42 | Hatgal WS M11(1) | 50.44 | 100.15 | 1662 | 1983 2005 | G.M,C | S (5) | |
| | 43 | Ardag SE M5(3) | 50.63 | 100.17 | 1870 | 1987 2002 | G | S (5) | |
| | 44 | Ardag M5A(3) | 50.66 | 100.16 | 2057 | 1987 2007 | G | S (5) | |
| | 45 | Ardag M5B(3) | 50.66 | 100.16 | 2055 | 1987 2007 | G | S (5) | |
| | 46 | Dalbay M12(1) | 51.02 | 100.76 | 1648 | 2005 2007 | G | S (3) | |
| | 47 | Shagnul M12C(1) | 50.25 | 100.84 | 1700 | 2003 2005 | G | S (3) | |
| | 48 | Turag M12D(1) | 51.29 | 100.83 | 1677 | 2003 2007 | G | S (3) | |

Note: **Province:** northern Hangai (NH), southern Hangai (SH), Gobi-Altay (GA), Altay (AT), Hentii (HT), Hovsgol (HV). **Geology:** (1) Sediments (silt, sand, gravel and their composition), (2) ice-rich sediments beneath ice-cored mound (Pingo), (3) bedrock. **Year of data available:** The year followed by a hyphen shows the starting year of continuous temperature monitoring. **Analysis:** Temperature values are used to analyze a snapshot of permafrost temperature (GT10m; G), recent mean annual ground temperature at a 10-m depth (MAGT; M), comparison between past and recent ground temperatures at a 10-m depth (C), and ground temperature envelopes (P). See text for more information. **Contributors:** (J) Y. Jambaljav, (I) M. Ishikawa, (S) N. Sharkhuu, (D) G. Davaa, (Y) K. Yoshikawa. **References:** (1) Sharkhuu (2003), (2) Ishikawa et al. (2005), (3) Anarmaa et al. (2007), (4) Sharkhuu et al. (2008), (5) Sharkhuu & Anarmaa (2011).

(August to October) between 2005 and 2010 (Table 1) as the representative parameter for the current thermal state of permafrost. Since GT10m was measured more than one year after drilling, thermal disturbances are negligible. Further mean annual ground temperatures (MAGTs) were available for the sites, where ground temperatures were monitored continuously for more than one year. Year-round temperature measurements at several depths provide ground temperature profiles, often represented graphically as an envelope of the maximum, minimum, and mean annual ground temperature

profiles. The profile shapes reflect the influences of specific local environmental settings and the physical properties of the ground material on the ground temperatures.

Since shallow ground temperatures are strongly influenced by short-term atmospheric variations, they are not very useful to assess long-term trends in permafrost temperature changes. We compared the temperatures observed in the 1960s, 1970s, and 1980s with those recently measured for the same month. The differences in the ground temperature between two observations for all sites were more than 0.2°C, which exceeded the observational accuracy. Data from the sites that had surface disturbance (e.g., forest clearance) were excluded from the analysis.

Air temperatures are from the University of Delaware Air Temperature & Precipitation, version 2.01, which has horizontal resolutions of 0.5°×0.5° and is available from 1960 to 2008. We interpolated these gridded temperature values using Cressman and Kriging methods to estimate the air temperatures at the borehole sites. We evaluated the accuracy of this dataset using meteorological data from 31 permanent stations ($r = 0.773$, $p < 0.001$).

Results and Discussion

State of modern permafrost temperatures and their relation to climate

Permafrost temperatures generally corresponded well with permafrost continuity (Fig. 2). The coldest temperatures (GT10m < -1.4°C) occur in continuous permafrost, as in Hovsgol (#39, 40, 41, 46), at high elevations of Northern Hangai (#3, 4), and at Altay (#14, 20, 21, 22). In the other sites (Hentii, Gobi-Altay, Southern Hangai, and low elevations of Altay and Northern Hangai), permafrost temperatures are slightly higher. The colder permafrost (GT10m < 1.0°C) is restricted to the sites with ice-rich sediments (#6, 12). In Hentii, ground temperatures are generally high and permafrost is absent at three sites (#25, 35, 31).

The correlation between MAGT and MAAT ($r = 0.59$, $p < 0.01$, Fig. 3b) indicates climatic dependencies of ground temperatures on a national scale. Almost all ground temperatures ranged from -1.5 to 0°C, with an insignificant relation between MAGT and latitude (Fig. 3a). Since the research boreholes are mainly located in mountainous areas, topography will be more important than latitude.

Long-term changes in permafrost temperature and their relation to climate

Long-term (more than one decade) changes in permafrost temperatures can be evaluated at 14 sites distributed over all the provinces (Table 1, Fig. 4). A significant correlation existed between the annual rate of ground temperature increase and latitude ($r = 0.60$, $p < 0.05$), excepting one outlier (#31), where the permafrost disappeared during 1984 and 2009, and a very strong annual increase in ground temperatures (0.055°C/a) was observed. On the other hand, the relationship between the rates of increase in the ground and air temperatures is insignificant, although these temperatures keep increasing at almost all sites (Fig. 4b).

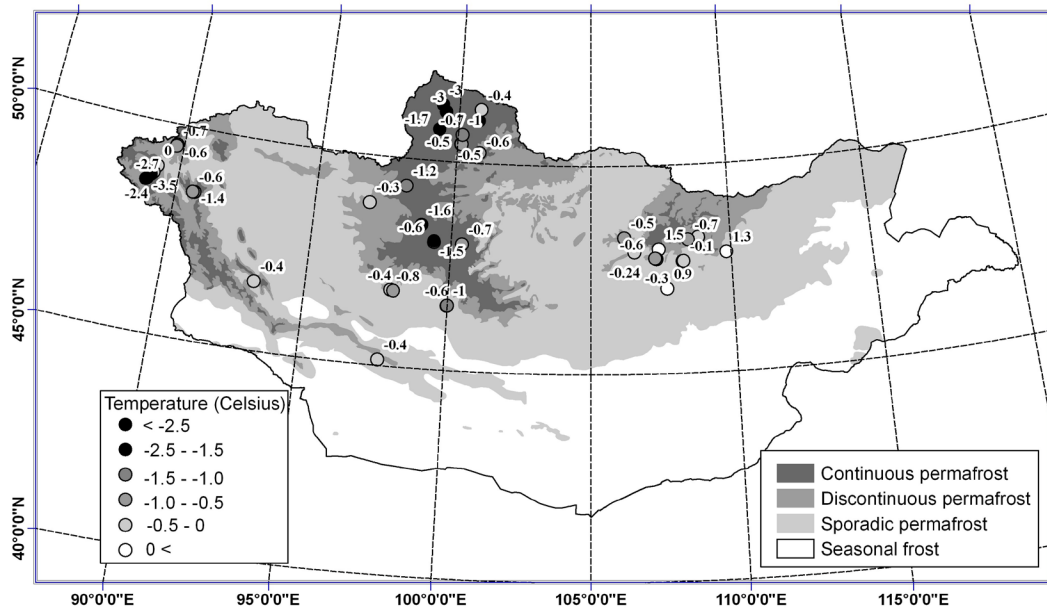


Figure 2. Snapshot of ground temperature at 10 m depth between August and September for the years 2000–2010. The temperature values are shown on the permafrost distribution map.

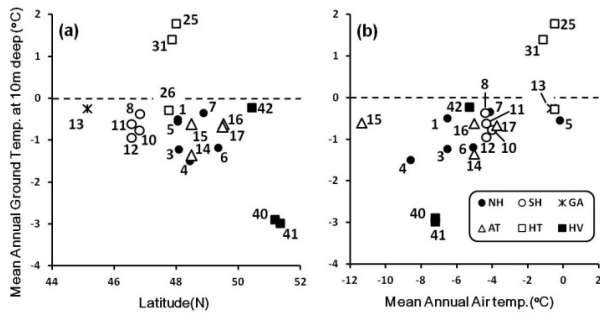


Figure 3. Scatter plots of (a) mean annual ground temperature at 10-m depth vs. latitude and (b) vs. 10-year-averaged mean annual air temperature. Refer to the caption of Table 1 for abbreviations of the province names.

We deduce that temperature-dependent soil thermal properties in the soil largely control the rate of permafrost warming. The cold permafrost of the northern provinces is easily warmed (#38, 40) (Fig. 4) even if the rate of air temperature increase is similar. We postulate that the colder permafrost tends to contain a lesser amount of unfrozen water. Therefore, the apparent heat capacity is lower than that in the southern provinces, where apparent heat capacity of warmer permafrost is higher. This is because the warmer permafrost contains a higher amount of unfrozen water that increases exponentially as ground temperatures approach the melting point, preventing the ground from warming further. Rapid ground warming at Hentii (#31) probably indicates that once the permafrost disappears, warming is accelerated because all the energy transferred to the soil is used for soil warming and not for the melting of ice.

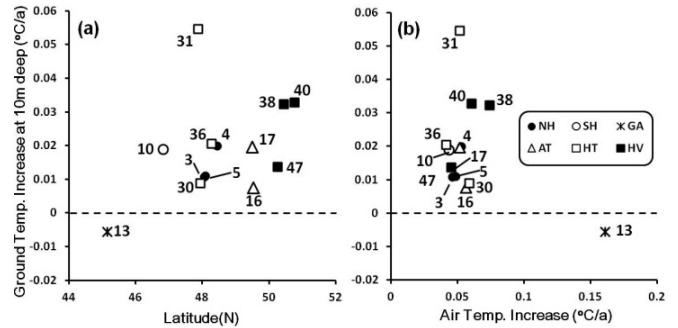


Figure 4. Scatter plots of (a) latitude vs. ground temperature increases at 10-m depth, and (b) linear trend of air temperature increase between two measurement years vs. ground temperature increases at 10-m depth.

Influences of local topographic settings on permafrost temperatures

The thermal state of modern permafrost and the rate of ground temperature increase varied largely even at similar latitudes (Figs. 3a and 4a). For example, MAGT at a 10-m depth ranged between -0.5 and -1.5°C in North Hangai, while the annual rate of ground temperature increase ranged between 0.1 and 0.3°C, indicating a strong influence of local topographical settings even on the deep ground temperatures. We evaluated this by comparing the ground temperature profiles of nearby sites. Among three adjacent boreholes (#8, 9, 10 in Southern Hangai), the lowest MAGT at a 10-m depth (-0.76°C) was found at the valley-bottom site, where the freezing and thawing fronts penetrated to a great depth and intensive winter cooling was observed near the ground surface (Fig. 5).

Colder permafrost will be maintained by intensive near-surface air temperature inversions that concentrate cold air mass on topographic depressions. These meteorological situations are typical for cold and dry regions.

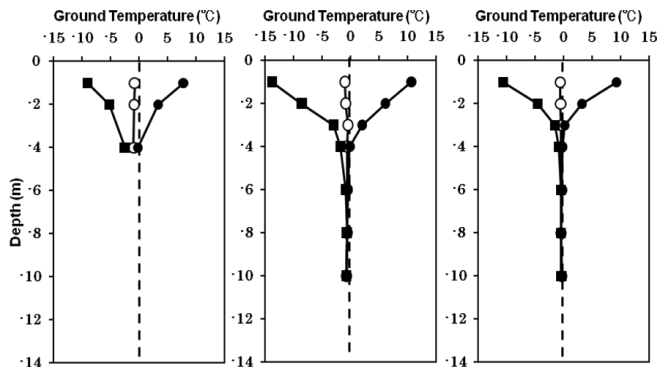


Figure 5. Ground temperature profiles at Bayanbulag sites, Southern Hangai. Left: northern slope (#9), center: valley bottom (#10), right: southern slope (#8).

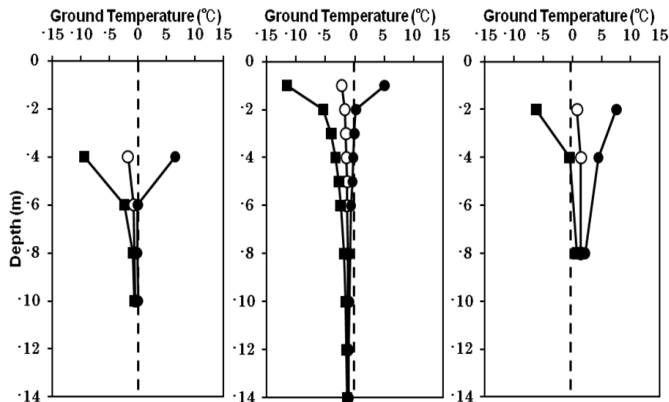


Figure 6. Ground temperature profiles of Terkh sites, Northern Hangai. Left: northern slope (#1), center: valley bottom (#3), right: southern slope (#2).

The lowest ground temperature was also observed at the valley-bottom site (MAGT at a 10-m depth; -1.2°C) among the three immediate adjacent boreholes of Terkh, Northern Hangai province. The three ground temperature profiles (Fig. 6) show that ground thawing is restricted to the near surface at the valley-bottom site but extends to a depth of approximately 6 m at the northern slope, probably because of different conditions of the soil water. At the valley-bottom site, higher production and consumption of latent heat due to the high soil water content would dampen deeper migration of the freezing and thawing fronts. Accordingly, permafrost at the northern slope (MAGT_{10m} = -0.49°C) may be more vulnerable to atmospheric warming than is that at the valley bottom.

The effects of latent heat on ground temperature are more clearly seen at the Galuut sites (Fig. 7). Ground temperatures remained almost stable for a year at the valley-bottom site, where the borehole was installed in ice-rich sediments. Although the ground temperatures at the two sites are similar (MAGTs at a 10-m depth are -0.61 and -0.94°C for Galuut1 and Galuut2, respectively), the former site with permafrost would be more vulnerable than the latter, where atmospheric fluctuations are restricted to a shallower depth.

Ground temperatures differed significantly between two immediately adjacent sites at Terej (Fig. 8). The MAGTs at

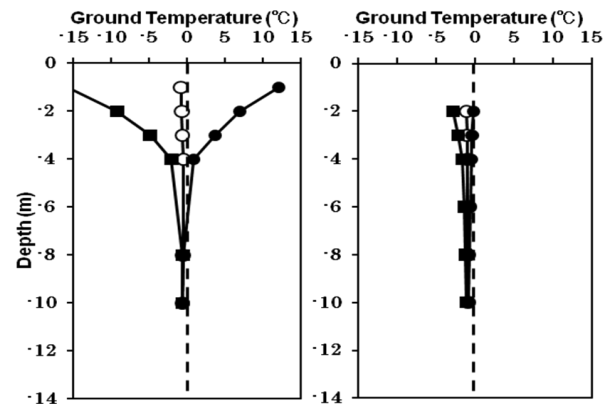


Figure 7. Ground temperature profiles of Galuut sites, Southern Hangai. Left: northern slope (#11), right: valley bottom (#12).

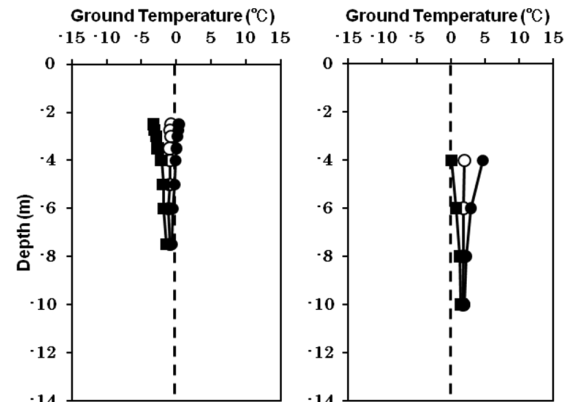


Figure 8. Ground temperature profiles of Terej sites, Hentii. Left: northern forested slope (#24), right: southern pasture slope (#25).

a depth of 8 m at the northern and southern slopes were -0.63 and 1.83°C , respectively, yielding the largest spatial variation among our measurements. Comparing the land-surface heat budget components between two sites, Ishikawa et al. (2008) indicated the importance of the combined effects of forest shading and the presence of organic- and pore-rich soils on the maintenance of permafrost underneath forested northern slopes. Disturbance of such symbiotic systems between forest and permafrost by, for example, deforestation, would accelerate permafrost degradation greatly. This was shown by the 10-year averaged MAAT, which was close to 0°C (-0.49°C).

Conclusions

This paper introduces a national monitoring network of permafrost boreholes for research purposes and discusses the thermal state of Mongolian permafrost. The main results are summarized as follows.

- 1) Ground temperatures of continuous permafrost are lower than -2.0°C , while those of discontinuous permafrost range between -1 and 0°C .
- 2) The rate of permafrost warming ranges between 0.01

and 0.03°C/a and is more pronounced in the northern provinces with continuous permafrost. Permafrost disappeared between the 1980s and 2009 at the southern boundary of the permafrost region.

- 3) Permafrost in colder regions warmed faster than that in warmer regions. Permafrost warming is mainly disassociated from atmospheric warming, but it does have temperature-dependent soil properties (unfrozen water content).
- 4) Strong influences of local topography on permafrost temperatures could be observed. Cold permafrost occurs beneath topographic depressions, within ice-rich soils, and under forested slopes. Knowledge of these effects will be fundamental to predicting the future thermal state of Mongolian permafrost.

References

- Anarmaa, S., Sharkhuu, N., Etzelmüller, B., Heggem, F.B., Nelson, F.E., Shiklomanov, N.I., Goulden, C.E., & Brown, J. 2007. Permafrost monitoring in the Hovsgol mountain region, Mongolia. *Journal of Geophysical Research* 112: doi:10.1029/2006JF000543.
- Babinski, Z. 1982. Pingo degradation in the Bayan-Nuurin-Khotnor Basin, Khangai Mountains, Mongolia. *Boreas* 11: 291-298.
- Brown, J. & Romanovsky, V.E. 2008. Report from the International Permafrost Association: State of permafrost in the first decade of the 21st century. *Permafrost and Periglacial Processes* 19: 255-260.
- Gravis, G.F., Zabolotnik, S.I., Sukhodrovsky, V.L., Gavrilo, M.K., & Lisun, A.M. 1974. *Geocryological Conditions in the People's Republic of Mongolia*. Moscow: Nauka Publishing, 200 pp. (in Russian).
- Harris, C., Vonder Mühl, D., Isaksen, K., Haeberli, W., Sollid, J.L., King, L., Holmlund, P., Dramis, F., Guglielmin, M., & Palacios, D. 2003. Warming permafrost in European mountains. *Global and Planetary Change* 39: 215-225.
- Institute of Meteorology and Hydrology (IMH), Mongolian Academy of Science. 2009. Mongolia: Assessment report on climate change. 228 pp.
- Ishikawa, M., Sharkhuu, N., Zhang, Y., Kadota, T. & Ohata, T. 2005. Ground thermal and moisture conditions at the southern boundary of discontinuous permafrost, Mongolia. *Permafrost and Periglacial Processes* 16: 209-216.
- Ishikawa, M., Zhang, Y., Kadota, T., & Ohata, T. 2006. Hydrothermal regimes of the dry active layer. *Water Resources Research* 42: W04401, doi:10.1029/2005WR004200.
- Ishikawa, M., Iijima, Y., Zhang, Y., Kadota, T., Yabuki, H., Ohata, T., Dorjgotov, B., & Sharkhuu, N. 2008. Comparable energy balance measurements on the permafrost and immediately adjacent permafrost-free slopes at the southern boundary of Eurasian permafrost, Mongolia. In *NICOP 2008: Proceedings of the Ninth International Conference on Permafrost*. D.L. Kane, K.M. Hinkel (eds.). Institute of Northern Engineering, University of Alaska Fairbanks, 1: 795-800.
- Jorgenson, M.T., Racine, C.H., Walters, J.C., & Osterkamp, T.E. 2001. Permafrost degradation and ecological changes associated with a warming climate in central Alaska. *Climatic Change* 48(4): 551-571.
- Osterkamp, T.E. 2008. Thermal state of permafrost in Alaska during the fourth quarter of the twentieth century. In *NICOP 2008: Proceedings of the Ninth International Conference on Permafrost*. D.L. Kane, K.M. Hinkel (eds.). Institute of Northern Engineering, University of Alaska Fairbanks, 2: 1333-1338.
- Romanovsky, V.E., Smith, S.L., & Christiansen, H.H. 2010a. Permafrost Thermal State in the Polar Northern Hemisphere during the International Polar Year 2007–2009: a Synthesis. *Permafrost and Periglacial Processes* 21: 106-116. doi: 10.1002/ppp.689.
- Romanovsky, V.E., Drozdov, D.S., Oberman, N.G., Malkova, G.V., Kholodov, A.L., Marchenko, S.S., Moskalenko, N.G., Sergeev, D.O., Ukraintseva, N.G., Abramov, A.A., Gilichinsky, D.A., & Vasiliev, A.A. 2010b. Thermal State of Permafrost in Russia, *Permafrost and Periglacial Processes* 21: 136-155, doi: 10.1002/ppp.683.
- Sharkhuu, N. 2003. Recent changes in the permafrost of Mongolia, In *Proceedings of the Eighth International Conference on Permafrost*, Zürich, 1029-1034.
- Sharkhuu, N., Anarmaa, S., Romanovsky, V.E., Yoshikawa, K., Nelson, F.E., & Shiklomanov, N.I. 2008. Thermal State of Permafrost in Mongolia. In *NICOP 2008: Proceedings of the Ninth International Conference on Permafrost*. D.L. Kane, K.M. Hinkel (eds.). Institute of Northern Engineering, University of Alaska Fairbanks, 2: 1633-1638.
- Sharkhuu, N. & Anarmaa, S. 2011. *Guidebook to field trip on mountain permafrost in the Hovsgol and Hangai mountainous regions, Mongolia*, Ulaanbaatar Mongolia, 47 pp.
- Smith, S.L., Burgess, M.M., Riseborough, D., & Nixon, F.M. 2005. Recent trends from Canadian permafrost thermal monitoring network sites. *Permafrost and Periglacial Processes* 16: 19-30.
- Zhao, L., Wu, Q., Marchenko, S.S., & Sharkhuu, N. 2010. Thermal State of Permafrost and Active Layer in Central Asia during the International Polar Year. *Permafrost and Periglacial Processes* 21:198-207.

Thermokarst Lake and Shore Fen Development in Boreal Alaska

M. Torre Jorgenson

Alaska Ecoscience, Fairbanks, AK, USA

Mikhail Kanevskiy, Yuri Shur, Thomas Osterkamp

University of Alaska Fairbanks, USA

Daniel Fortier

University of Montreal, Canada

Tim Cater, Patricia Miller

ABR, Inc., Fairbanks, AK, USA

Abstract

Patterns and rates of thermokarst lake and shore fen development were studied across three lowland ecoregions in the discontinuous permafrost zone of boreal Alaska. The organic-rich and fine-grained surficial deposits varied from glacio-lacustrine in the Copper River Basin, to abandoned floodplain cover deposits in the Tanana-Kuskokwim lowlands, to collapsed eolian silt and lacustrine deposits on the Koyukuk flats. Soils were ice rich and dominated by micro-lenticular, reticulate, ataxitic, and braided cryostructures within the top 2–3 m. Soil volumetric water contents generally ranged from 70 to 90%. Airphoto analysis showed that thermokarst lakes decreased from 18.7 to 17.8% in area over ~57 years and shore fens increased from 4.2 to 5.8% overall. A total of 76 lakes decreased, while 48 increased in size. Rates of shoreline change averaged -0.06 m/yr (lake contracted) where shore fens were continuous along the margins and averaged 0.12 m/yr (lake expanded) where fens were absent. Thermokarst dynamics varied due to multiple processes, including rapid expansion in ice-rich glacio-lacustrine deposits, rapid lateral drainage in one lake, widespread infilling by shore fens, and continuing thermokarst along the forest edge with replacement by shore fens instead of open water.

Keywords: Alaska; thermokarst; lake; permafrost; ground ice; change.

Introduction

Thermokarst lakes are prevalent in ice-rich lowlands across the boreal forest region of central Alaska. Although thermokarst lakes have been extensively studied in the continuous permafrost zone of northern Alaska (Carson and Hussey 1962, Hinkel et al. 2005), there have been few studies that have evaluated the patterns and processes involved in thermokarst lake development in the discontinuous zone of Alaska. Thermokarst lakes in central Alaska were first described by Wallace (1948), and regions with abundant thermokarst lakes have been mapped by Jorgenson et al. (2008a). Several studies have quantified the rates of overall lake change (Riordan et al. 2006, Roach et al. 2011), but there is little information assessing the development of thermokarst lakes in relation to surficial geology or ground ice.

Lakes in central Alaska have been found to be mostly shrinking, but there is substantial variability in patterns for differing regions of Alaska (Riordan et al. 2006). While lake shrinking was attributed by Riordan et al. (2006) to increased evaporation under a warming climate, Roach et al. (2011) attributed lake shrinking to paludification and lake expansion to thermokarst. Some lake shrinking has been attributed to subsurface drainage caused by thawing of surrounding permafrost (Yoshikawa and Hinzman 2003). In ice-rich regions, such as in central Alaska and Yukon, lake expansion due to thermokarst can be fairly rapid (Burn and Smith 1990, Osterkamp et al. 2000, Shur and Osterkamp 2007, Burn 1992, Jorgenson et al. 2008b). Complicating the assessment

of lake development, however, is the differing genesis of lake bodies that include fluvial oxbow lakes, glacial kettle lakes, interdunal lakes, bedrock controlled lakes, and thermokarst lakes (Jorgenson and Shur 2007). Thermokarst lakes have been differentiated into shallow (<1.5 deep) thermokarst lakes, which freeze to the bottom during the winter, and deep thermokarst lakes typically formed in extremely ice-rich Pleistocene silt (yedoma).

In this study, we evaluated the patterns and rates of thermokarst lake and shore fen development across three lowland regions in the discontinuous permafrost zone of central Alaska including the Copper River Basin, the Tanana-Kuskokwim lowlands, and the Yukon River lowlands. Lake development was assessed by measuring topographic cross-sections, describing geomorphic settings and soil stratigraphy, quantifying ground ice morphology and volume, permafrost table variation, and mapping thermokarst lake and shore fen distribution using a time series of airphotos and satellite imagery.

Methods

Three small study areas were established across three ecoregions in areas with abundant thermokarst lakes. The sites included Billy Lake (62.483°N, 144.727°W, 1005 ha) in the Copper River Basin sampled in 2005, Gosling Lake (63.909°N, 151.895°W, 536 ha) in the Mud River region the Tanana-Kuskokwim lowlands sampled in 2005, and Finger Lake (65.256°N, 157.042°W, 117 ha) on the Koyukuk flats

in the Yukon River lowlands sampled in 2006 (Fig. 1). Data collected at each site included topographic surveys, soil stratigraphy, ground ice morphology and content, soil samples, soil temperatures, and vegetation composition. Ground and water surface elevations were measured along 200–300-m transects oriented across a lake, fen, bog, and forest toposequence using an autolevel. Soil stratigraphy was described from bank exposures and from 2–3-m soil cores obtained with a SIPRE corer using standard methods. Cryostratigraphy was described according to French and Shur (2010). Soil samples were taken every ~20 cm for analysis of water content, bulk density, pH, and electrical conductivity. A few organic-rich samples were sent to the NOSAMS lab at Woods Hole for radiocarbon dating. Thaw depths along transects were measured using an extendable tile probe.

For analysis of lake change, historical black-and-white (ca. 1950) and color-infrared (ca. 1980) airphotos were compared to recent (2008–2010) airphotos or satellite imagery. New high-resolution airphotos were collected in 2010 at Gosling and Finger lakes, and Ikonos satellite imagery (1-m fused panchromatic and multispectral) was obtained in 2008 at Billy Lake. For Gosling and Finger lakes, the ~1980 CIR airphotos were georectified to the NASA Geocover Landsat product, and other time periods were georectified to these base images using ArcMap software (ESRI, Redland, CA). At Billy Lake, the 1949 and 1981 airphotos were georectified to the 2008 Ikonos image. Georectification errors were 0.3 to 2.2 m RMS. Margins of lakes and shore fens were manually interpreted, digitized using ArcMap, and coded for year, thermokarst type (lake, shore fen, drained basin), lake ID, basin ID, and continuity of shore fen surrounding the lake. Thermokarst bogs and pits away from the lakes were not mapped. Rate of average shoreline change for each lake was calculated by subtracting areas between periods, dividing by the shoreline length averaged for the two periods, and then dividing by the number of years.

Results

Thermokarst lakes across the three lowland regions developed in very different geomorphic settings. At Billy Lake in the Copper River Basin, the lakes developed in poorly stratified, peat-rich silts associated with glacio-lacustrine deposits of Late Pleistocene to early Holocene age (Ferrians et al. 1989). At Gosling Lake on the Mud River flats, parent materials are thick peat deposits over stratified silts and sands, interpreted as abandoned floodplain deposits. At Finger Lake on the Koyukuk flats, lakes developed in very thick peats over massive silts, interpreted as remnants of collapsed extremely ice-rich silt (yedoma).

At each of the sites, the transects crossed a range of ecosystem types including black spruce woodlands, sphagnum collapse-scar bogs, sphagnum and sedge-rich shore fens, and open lakes (Fig. 2). Differences in ground surface and lake bottom elevations at Billy, Gosling, and Finger lakes indicate there was a maximum of 5.2, 3.6, and 1.9 m of thaw settlement, respectively. Due to development of outlets in the

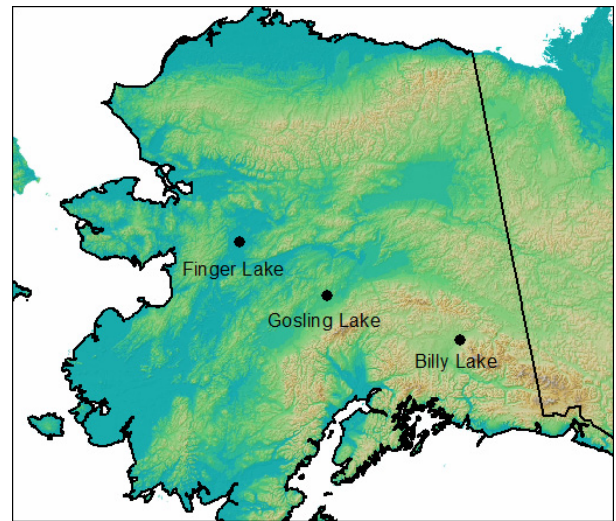


Figure 1. Location of thermokarst lake study areas in Alaska.

lake basins, water depths were approximately 3.5, 1.0, and 0.6 m, respectively.

Soil stratigraphy and cryostructure descriptions revealed that all sites were ice rich, but there were some important differences (Fig. 3). At Billy Lake, the surface peat was 35 to 40 cm thick over slightly pebbly silt and clayey silt derived from glacio-lacustrine material. Micro-lenticular, reticulate, and ataxitic cryostructures dominated the top 0.5 to 1.5 m of the upper permafrost, while braided cryostructures were dominant below. Radiocarbon dates from two profiles indicate that the glacio-lacustrine deposition ended around $7,370 \pm 47$ to $7,438 \pm 62$ ^{14}C ybp. At Gosling Lake, surface peat and silty peat ranged from 1.3 to 2.8 m in depth and was underlain by silt and silty sand, interpreted to be of fluvial origin. In the thick surface peat, cryostructures were dominated by lenticular and braided forms. In mineral soils, layered and braided cryostructures with ice lenses up to 20 cm thick were common. Radiocarbon dates near the base of the surface peat layers ranged from 5,253 to $6,722 \pm 47$ ^{14}C ybp.

Soil analyses showed the soils at the sites to be extremely ice rich. At Billy Lake, volumetric water contents typically ranged from 80 to 90% in the top 0.5 to 1.5 m, where the soils were dominated by peat (Fig. 4). The underlying silty glacio-lacustrine material mostly had water contents of 70 to 90% extending to the bottom of the profiles, although a couple of boreholes had contents dropping below 40% at depth. At Gosling Lake, water contents generally ranged from 70 to 90% at 0.5 to 1.5 m depth, but one profile maintained contents of 90 to 96% down to almost 3 m. At Finger Lake, water contents generally ranged from 70 to 90% to the 2 m depth in peats, and 60 to 80% in underlying silt. Densities of 0.1 to 0.4 g/cm^3 were indicative of organic matter near the surface.

Shore fens were prominent thermokarst features along the lake margins in this boreal region. They had very low density organic mats that floated or extended to the lake bottom. They often transitioned from herbaceous fen vegetation at the water's edge to sphagnum-dominated bog or ericaceous low shrub vegetation on older portions of the mat away from the lakeshore.

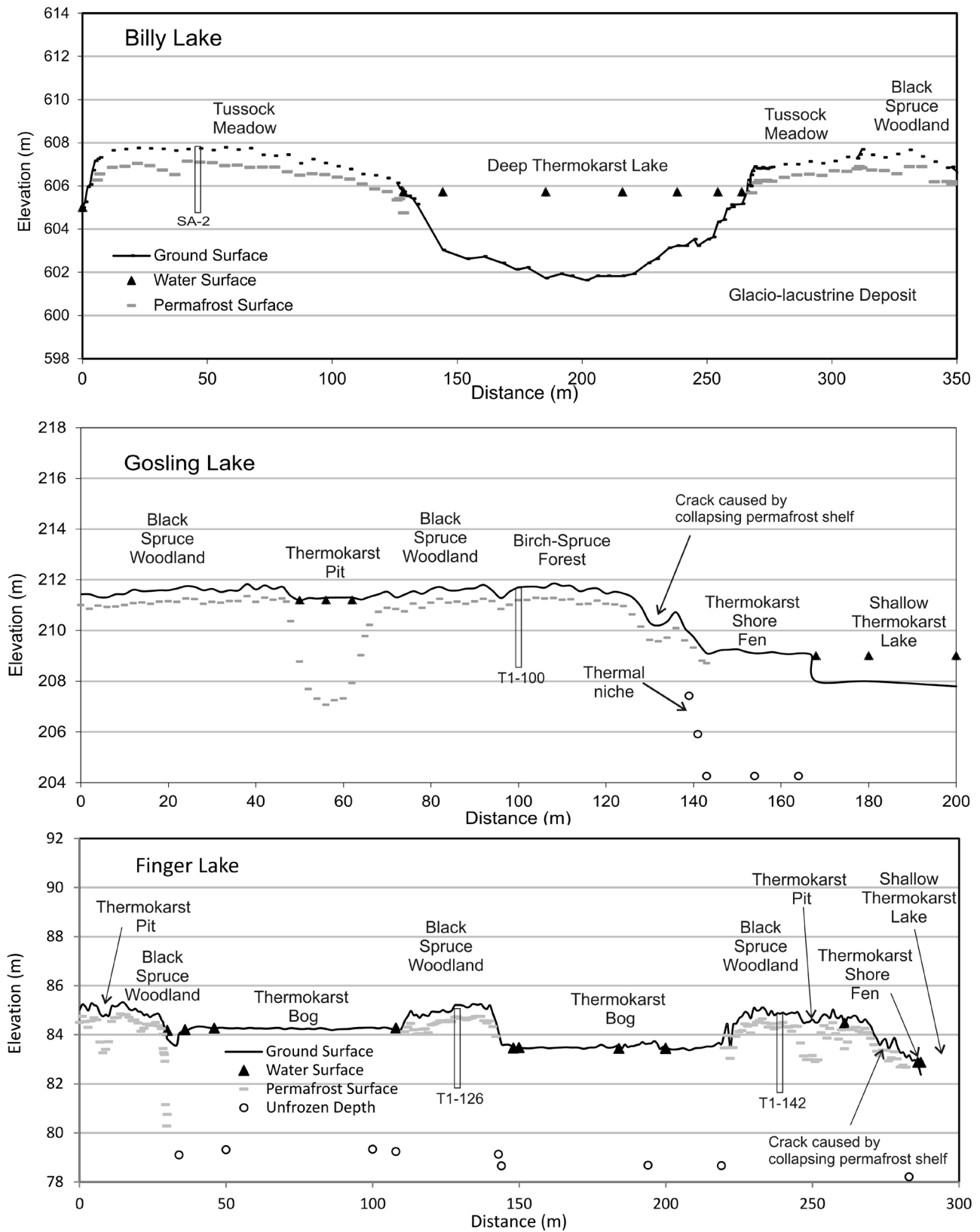


Figure 2. Toposequences for Billy, Gosling, and Finger lakes showing relative elevations of ground surface, water surface, permafrost surface, and unfrozen soil at maximum probing depth.

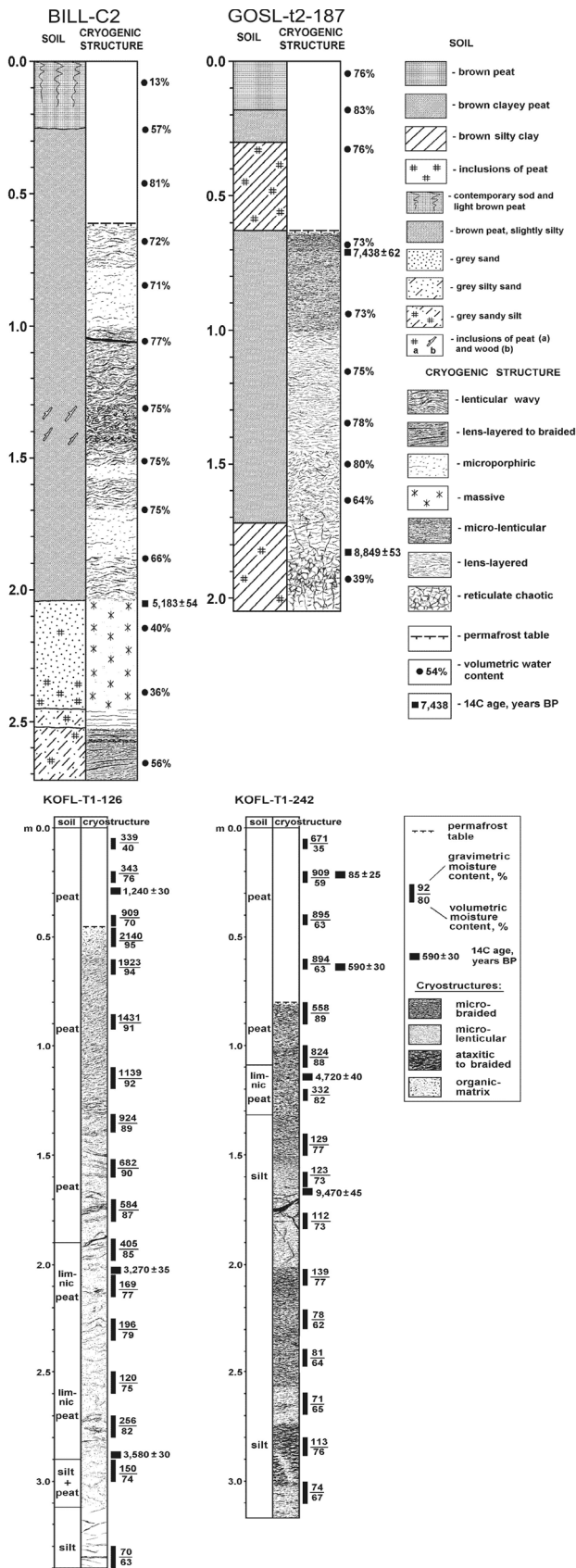


Figure 3. Representative borehole for Billy (top left), Gosling (top right), and Finger lakes (bottom).

Mapping of thermokarst lakes and shore fens on a time series of airphotos and satellite images in areas of prominent thermokarst-lake development showed overall that thermokarst extent in 2008–2010 varied from 11% at Billy Lake to 42% at Gosling Lake to 51% at Finger Lake (Fig. 5). At Billy Lake, several of the lakes showed large rates of shoreline collapse, while one lake showed extensive drainage. Overall, the 124 lakes across all sites decreased from 18.7 to 17.8% in total lake area over ~57 years. At Billy Lake, total lake area decreased from 9.6 to 8.5% from 1949 to 2008. At Gosling Lake, area remained constant at 32.7%. At Finger Lake, area decreased from 32.2 to 29.3% from 1952 to 2010 (Figs. 5 and 6). Overall, 76 lakes increased and 48 lakes decreased in size (Fig. 7).

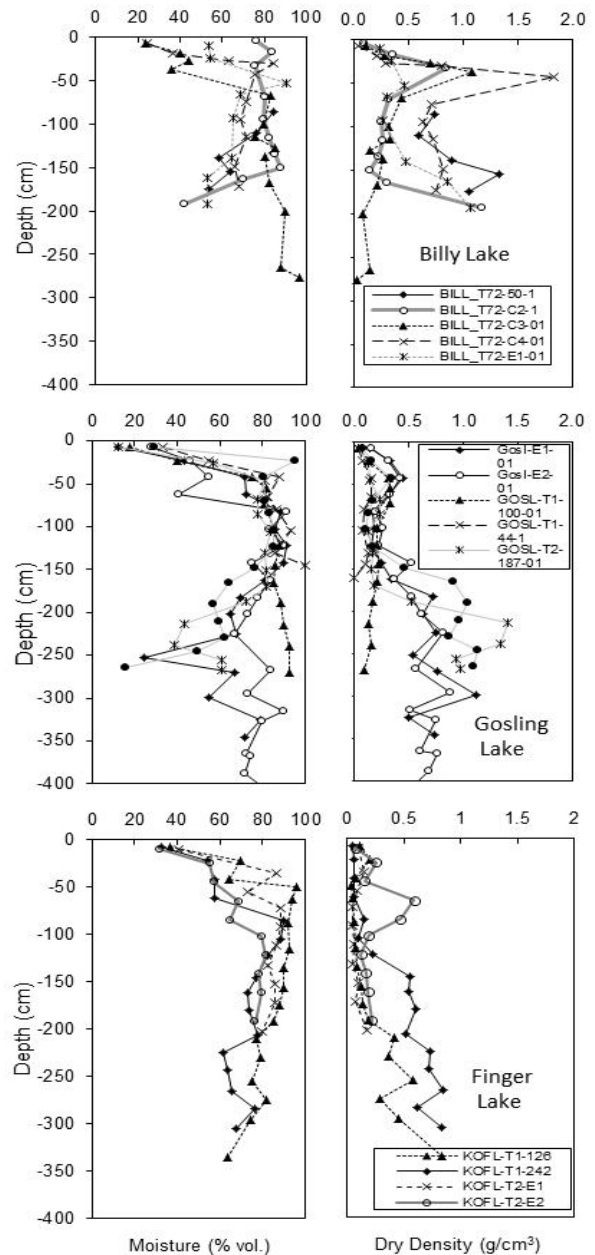


Figure 4. Volumetric water content and bulk density profiles.



Figure 5. Lake and shore fen boundaries (white) from circa 1950 overlaid on recent imagery showing changes in thermokarst.

Shore fens increased in width along most lake margins due to both expansion into the lakes and continued collapse of permafrost along the forest edge. Shore fen area increased from 0.8 to 1.7% at Billy Lake, from 7.6 to 10.0% at Gosling Lake, and from 17.5 to 21.5% at Finger Lake. Shore fens had a large effect on lake change. At lakes where shore fens were continuous along the margins, more lakes shrank and there was a substantial net decrease in area. Where fens occurred only as isolated patches along the margins, lakes increased in size. Rates of shoreline change averaged -0.06 m/yr (lake contracted) where shore fens were continuous and averaged 0.12 m/yr (lake expanded) where fens were absent (Fig. 7). Overall, lake area decreased along the shores by -0.06 m/yr.

Discussion

Thermokarst lakes are prevalent in areas with ice-rich permafrost formed in fine-grained deposits in lowland regions throughout central Alaska. They are particularly abundant in the Copper River Basin, Nabesna flats, Innoko flats, Koyukuk

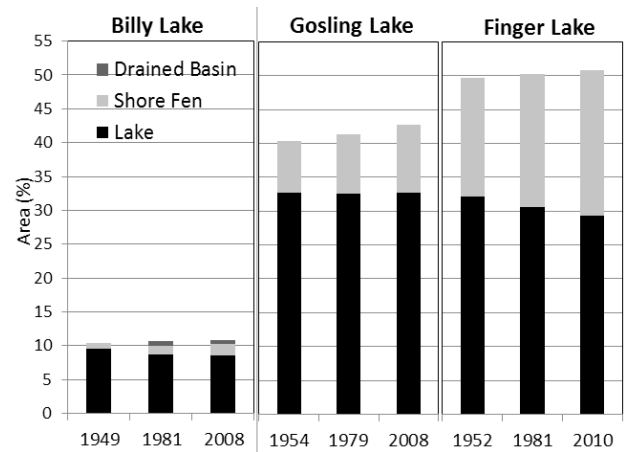


Figure 6. Changes in areal extent of thermokarst lakes, shore fens, and drained-lake basins at the Billy Lake, Gosling Lake, and Finger Lake areas from 1949–1954 to 2008–2010.

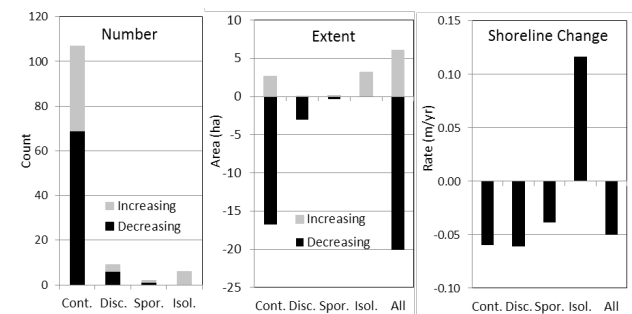


Figure 7. Thermokarst lake development across all sites. Number and cumulative extent of lakes differentiated by whether they were increasing or decreasing, and by continuity (continuous >90%, discontinuous 50–90%, sporadic 10–50%, sporadic <10%) of shoreline fen surrounding the lake. Rates of shoreline change (positive when lake expanding) were differentiated by shore fen continuity.

flats, and Kanuti flats. They typically occur on flat areas with glacio-lacustrine, abandoned overbank floodplain, lowland loess, and lacustrine deposits. Deep thermokarst lakes in extremely ice-rich loess (yedoma) in upland areas also are common but not covered in this study. Thermokarst lakes on retransported deposits on the toe slopes of hillsides are less abundant because of the runoff of water from slopes.

Cryostructures are effective at differentiating soils with high volumetric water contents. Micro-lenticular, reticulate, ataxitic, and braided cryostructures generally had ice contents of 70 to 90%. These cryostructures and high ice contents of the upper permafrost are a prerequisite to the formation of shallow thermokarst lakes.

Differentiation of thermokarst lakes from lakes of other genesis can be problematic (Jorgenson and Shur 2007), but there are some key attributes that help identify thermokarst lakes. Thermokarst lakes usually are round to elliptical in shape due to thermal and mechanical erosion; riverine lakes have oxbow shapes; and morainal and bedrock controlled lakes have irregular shorelines. Shorelines of thermokarst lakes in our area had steep banks that extend well below the water line, while other lake types tend to have gradual, shallow margins with wave cut benches caused by wave erosion. Finally, thermokarst lakes must have extremely ice-rich banks, often with thermo-erosional niches above or below water line. We found thaw bulbs or niches that extended at least 3 m under the permafrost shelf at the bank edge (Fig. 2). Usually the banks are blanketed by peat slumping over the collapsing shoreline and obscuring the ice-rich sediments. In boreal Alaska, the shorelines typically have a shore fen growing along the slowly collapsing margin protecting the banks from wave erosion and convective heat transfer.

Airphoto analysis showed a wide range of thermokarst lake development. Rapidly expanding lakes in extremely ice-rich glacio-lacustrine deposits, where water was in direct contact with the collapsing bank, was relatively uncommon. Rapid drainage, which left small remnant water bodies within much larger lake basins, was observed in only one lake basin due to lateral drainage through a breached surface outlet. Shrinking of thermokarst lakes by infilling from shore fens was widespread across the three areas. In these situations, however, there was continuing thermokarst along the forest edge with replacement by shore fens instead of open water. Thus thermokarst is continuing in all areas, but the open water portions of the basin usually are shrinking.

Acknowledgments

The research was supported by grants ARC-0454985 and ARC-0454939 from the National Science Foundation. The report represents the findings of the authors and not the opinions of NSF.

References

- Burn, C.R. 1992. Thermokarst Lakes. *Canadian Geographer* 36(1): 81–85.
- Burn, C.R. & Smith, M.W. 1990. Development of thermokarst lakes during the Holocene at sites near Mayo, Yukon Territory. *Permafrost and Periglacial Processes* 1(2): 161-176.
- Carson, C.E. & Hussey, K.M. 1962. The oriented lakes of arctic Alaska. *Journal of Geology* 70, 417-439.
- Ferrians, O.J., Nichols, D.R., & Williams, J.R. 1989. Copper River Basin. In *Glacial Geology and Geomorphology of North America*, Vol. 1. American Geophysical Union, Washington, DC., pp. 39-43.
- French, H. & Shur, Y. 2010. The principles of cryostratigraphy. *Earth-Science Reviews* 101: 190-206.
- Hinkel, K.M., Frohn, R.C., Nelson, F.E., Eisner, W.R., & Beck, R.A. 2005. Morphometric and spatial analysis of thaw lakes and drained thaw lake basins in the western Arctic Coastal Plain, Alaska. *Permafrost and Periglacial Processes* 16, 327-341.
- Jorgenson, M.T. & Shur, Y. 2007. Evolution of lakes and basins in northern Alaska and discussion of the thaw lake cycle. *J. Geophysical Research* 112:F02S17.
- Jorgenson, M.T., Yoshikawa, K., Kanevskiy, M., Shur, Y.L., Romanovsky, V., Marchenko, S., Grosse, G., Brown, J., & Jones, B. 2008a. In *Extended Abstracts, NICOP 2008: Proceedings of the Ninth International Conference on Permafrost*. D.L. Kane, K.M. Hinkel (eds.). Institute of Northern Engineering, University of Alaska Fairbanks, pp. 121-122.
- Jorgenson, M.T., Shur, Y.L. & Osterkamp, T.E. 2008b. Thermokarst in Alaska. In *NICOP 2008: Proceedings of the Ninth International Conference on Permafrost*. D.L. Kane, K.M. Hinkel (eds.). Institute of Northern Engineering, University of Alaska Fairbanks, pp. 869-876.
- Osterkamp, T.E., Viereck, L., Shur, Y., Jorgenson, M.T., Racine, C., Doyle, A., & Boone, R.D. 2000. Observations of thermokarst and its impact on boreal forests in Alaska, U.S.A. *Arctic, Antarctic, and Alpine Research* 32(3): 303-315.
- Riordan, B., Verbyla, D., & McGuire, A.D. 2006. Shrinking ponds in subarctic Alaska based on 1950-2002 remotely sensed images. *Journal of Geophysical Research*, 111, G04002.
- Roach, J., Griffith, B., Verbyla, D., & Jones, J. 2011. Mechanisms influencing changes in lake area in the Alaskan boreal forest. *Global Change Biology* 17(8): 2567–2583.
- Shur, Y. & Osterkamp, T.E. 2007. *Thermokarst*. Institute of Northern Engineering, University of Alaska Fairbanks, Fairbanks, AK. Rep. INE06.11, 50 pp.
- Wallace, R.E. 1948. Cave-in lakes in the Nabesna, Chisana, and Tanana River Valleys, Eastern Alaska. *J. Geology* May:171-181.
- Yoshikawa, K. & Hinzman, L.D. 2003. Shrinking thermokarst ponds and groundwater dynamics in discontinuous permafrost near Council, Alaska. *Permafrost and Periglacial Processes* 14(2): 151-160.

Investigating Hydrologic Storage in Catchments Underlain by Continuous Permafrost

Douglas L. Kane, Emily K. Youcha, Robert E. Gieck

Water and Environmental Research Center, Institute of Northern Engineering, University of Alaska Fairbanks, USA

Abstract

It is very difficult to quantify storage in a watershed; however, we know that the hydrologic runoff response of a catchment is intimately tied to the storage in that catchment. In the Arctic, several types of storage are possible, each having its own residence time. We investigate storage in two arctic watersheds underlain by continuous permafrost: one where the main storage mechanism is the active layer and another where surface storage (lakes, ponds, and wetlands) is dominant. In both cases, the snow water equivalent of the late winter snowpack is sufficient to fill these storage reservoirs and produce runoff. However, by summer's end, a wide range of storage conditions can prevail in these catchments depending on the warm season precipitation, evapotranspiration, and runoff. These late summer conditions carry over the winter and impact the next spring's snowmelt response.

Keywords: hydrology; catchments; continuous permafrost; water balance; storage.

Introduction

Fluxes and stores are the two main components of the hydrologic cycle. Historically, government networks have monitored the fluxes of precipitation and discharge at selected sites. Occasionally, evapotranspiration flux has been estimated using a variety of methods, some as simple as the evaporation pan (and a pan coefficient), some as complex as the energy balance method, and numerous others ranging in difficulty between these two examples (Shutov et al. 2006). Direct measurement of evapotranspiration for small footprints (10s of m) have been made recently using eddy covariance methods (Vourlitis & Oechel 1997). Traditionally, no program or methodology has been available to continually monitor changes in storage that occur in a watershed, although storage is capable of significantly altering watershed runoff response. Often the storage change in a watershed is assumed not to have undergone any change (which is more likely for periods of a year or more), so the water balance can be completed; this often makes it possible to solve for an unknown flux such as evapotranspiration (ET) in the hydrologic cycle. Recently, the role of storage in its numerous forms has undergone greater scrutiny (Spence 2010, McNamara et al. 2011).

The water balance equation for a selected watershed contains both fluxes and storage terms. In simple form, it is:

$$P - (Q + ET) \pm \Delta S = \eta \quad (1)$$

where (all terms are in depth [mm] over the watershed area) P = precipitation, both solid and liquid; Q = runoff leaving the watershed; ET = evapotranspiration; ΔS = change in various forms of storage; and η = closure error.

Ideally, all storage terms and fluxes should be measured so that the closure error (η) can be determined. There are only a handful of catchments (generally small) where the closure error has actually been determined (Kane & Yang 2004). Even in these cases, some assumptions about storage change were made to complete the water balance.

Reported here is the change in modeled storage over the warm season (from break-up to freeze-up) on the North Slope

of Alaska for a range of wet to dry conditions in examples of both moderate- and low-gradient catchments.

Storage

Although a challenge to quantify, various forms of storage play an important role in tempering hydrologic fluxes such as runoff and ET from a catchment.

High-latitude watersheds have a variety of possible storage reservoirs that vary both spatially and temporally:

$$P - ET - Q \pm \Delta S_{wpl} \pm \Delta S_{glac} \pm \Delta S_{snow} \pm \Delta S_{auf} \pm \Delta S_{vad} \pm \Delta S_{gw} \pm \Delta S_{ice} = \eta \quad (2)$$

where ΔS_{wpl} = volume change in storage of water in wetlands, ponds, and lakes (could include constructed reservoirs); ΔS_{glac} = volume change in glacial storage; ΔS_{snow} = volume change of seasonal snow, persistent snow fields, etc.; ΔS_{auf} = volume change in aufeis formations, both growth and decay; ΔS_{vad} = volume change in subsurface water in unsaturated (vadose) soils; ΔS_{gw} = volume change in subsurface saturated (groundwater) soils/bedrock; and ΔS_{ice} = volume change in many forms of ice including rivers, streams, permafrost, etc.

These storage reservoirs vary both spatially and temporally. Surface storage can take many forms: aufeis mentioned above, glaciers, snowfields, seasonal snow cover, and surface storage (lakes, ponds, and wetlands). The first four storage terms in the previous sentence require energy for phase change to produce hydrologic fluxes such as runoff or evapotranspiration. All of these reservoirs are likely to enhance runoff, although the timing may vary. Water trapped in permafrost as ice could become an important source of liquid water in a warmer climate due to thawing at the bottom and top of the permafrost (deeper active layer).

Catchments underlain by continuous permafrost have altered runoff responses due to the presence of frozen ground. In general, watersheds underlain by permafrost have higher runoff ratios and higher peak flows for a given watershed area; this is usually attributed to the lack of subsurface hydraulic connectivity between water at the surface and deep subsurface

Results

groundwater aquifers. In areas of continuous permafrost, the only subsurface storage reservoir is the active layer. The amount of supra-permafrost groundwater storage in the active layer is roughly equivalent to the annual precipitation; this can be compared to areas of no permafrost or discontinuous permafrost where the volume of subsurface storage can be orders of magnitude greater than the total annual precipitation.

The potential volume of water stored in lakes, ponds, and wetlands varies from little to a considerable amount, depending upon the number and depth of surface water bodies. In the Arctic, lakes, ponds, and wetlands are much more common in regions having a low hydraulic gradient, such as the coastal plain on the North Slope of Alaska.

Setting

The two catchments reported here, Upper Kugaruk (142 km²) and Putuligayuk (471 km²) Rivers, are located on the treeless North Slope of Alaska (Fig. 1). The Upper Kugaruk has mid- to high-hydraulic gradients that result in well-drained slopes; a few very small lakes exist within the drainage network. The Upper Kugaruk catchment (basin length 16 km, stream length 25 km, and elevation range 698 to 1464 m) has been studied since 1993, and Putuligayuk catchment (basin length 60 km, stream length 54 km, and elevation range 1 to 109 m) since 1999 (Kane et al. 2000). The Putuligayuk was gauged earlier by the U.S. Geological Survey, but no other complementary hydrological or meteorological data were collected at that time. The Upper Kugaruk basin is characterized by rolling foothills, with a few small mountains in the headwaters, glaciated terrain, a few small lakes, shrubs, and continuous permafrost (~300 m thick). Vegetation is diverse in this catchment, from shrubs and tussocks at the lower elevations to alpine vegetation at higher elevations, with widespread vegetation-free areas in the headwaters. Slightly more than 25% of the headwater area of the basin is classified as bedrock; this is primarily in the steepest terrain. Storage is confined to the few lakes and the active layer, which averages a depth of thaw of about 50 cm at summer's end.

The Putuligayuk basin (Fig. 1) is a low-gradient, unglaciated drainage dominated by lakes, ponds, and wetlands. Permafrost is continuous in this basin (~600 m thick) and permafrost features such as ice-wedge polygons, pingos, drained-thaw lake basins, strangmoor ridges, and hummocky ground are common. These permafrost features in low-gradient watersheds have their greatest hydrologic impact during the summer when they retard drainage and enhance storage (Kane et al. 2003). This further enhances the loss of water by vertical evaporation fluxes during the warm season while reducing the runoff volume. Considerable storage is afforded by the lakes, ponds, and wetlands, plus the active layer. Hall et al. (1994) have classified 83% of the coastal plain on the North Slope of Alaska as wetlands. In response to early summer runoff and ET during the remainder of summer, the watershed dries out as summer precipitation is usually not sufficient to offset the losses due to these two processes. Sedges, grasses, and some small shrubs are the prominent vegetation types. More information on these north-draining basins is found in Kane et al. (2000).

This paper is a first attempt at trying to evaluate and quantify the change in amount of storage throughout the warm season in two dissimilar catchments (Upper Kugaruk and Putuligayuk) in the Alaska Arctic. Earlier studies (Bowling et al. 2003, Bowling & Lettenmaier 2010) examined changes over the summer of surface storage both through remote sensing and hydrologic modeling. To accomplish our task of estimating continuous storage change, the terms in equation 1 are either measured (Q or P), estimated (ET), or set equal to zero (η), or solved for ($\Delta S = P - Q - ET$). The winter accumulation of snow could be a storage process; however, we do not measure snowfall at the time that it occurs but at winter's end, after wind redistributes the snow and sublimation takes place. Redistribution of snow in this windy and treeless setting is a major process that has significant hydrologic implications.

One of the problems we encounter in this process is that we do not know the initial amount of storage when we initiate a water balance determination. We can calculate the relative change in storage but not the absolute amount as we do not know at any given time the true amount of storage.

Figures 2 and 3 show plots of cumulative P , Q , ET , and ΔS for three distinctly different warm seasons; in terms of precipitation, 2006 was a typical year, 2007 was a very dry year, and 2008 was a wet year until late in the summer. The 2007 drought produced little summer runoff that year and also very low runoff during snowmelt the following year (Tables 1 and 2). A large storage deficit developed, especially in the

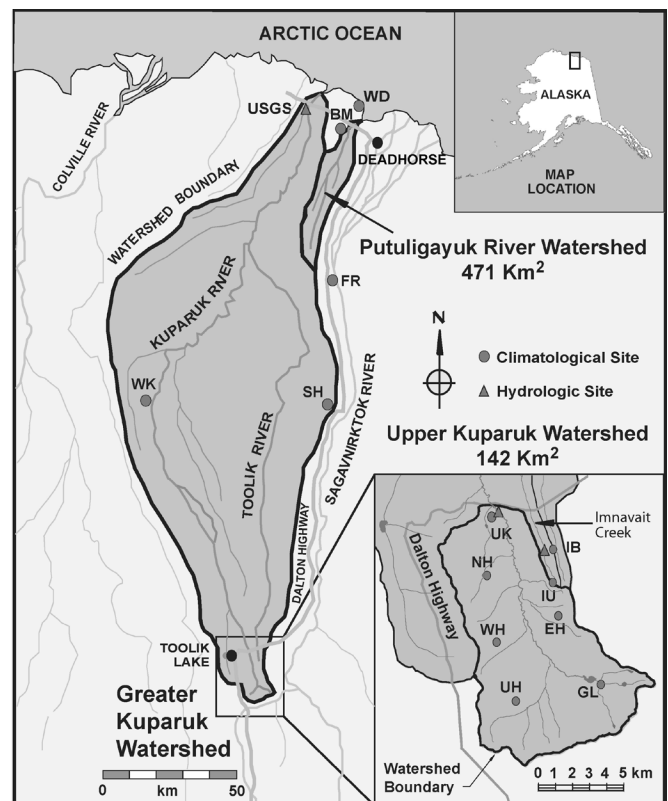


Figure 1. Location map of Upper Kugaruk and Putuligayuk catchments with meteorological and hydrological stations shown.

Upper Kuparuk, where the 2008 runoff ratio ($Q_{\text{snow}}/P_{\text{snow}}$) was 0.13 (the 2007–2008 snowpack was also quite light) and the 13-year average was 0.46. The plot of precipitation (Figs. 2 and 3) shows the initial snow water equivalent (SWE) at winter's end as a single-step input plus summer rainfall. The SWE is determined through several spatially distributed sites over the watersheds, where 50 depth measurements and 5 density measurements are made at each site. Because of the redistribution of snow on the ground by wind, there is considerable spatial variability and it is a challenge to quantify the average SWE in the watershed. One unstudied aspect of arctic snow hydrology is the importance of snow redistribution on the runoff ratio. One net result of snow redistribution is that snow gets moved closer to the drainage network, as it tends to collect in low-lying areas.

Rainfall is measured with the standard 8-in. (~20 cm) diameter orifice gauge with an Alter shield. These unmanned gauges are put into operation during snowmelt and decommissioned in late summer. Flow is measured intensely during snowmelt and occasionally during the summer, using standard U.S. Geological Survey methods. Stage-discharge relationship is developed for the channel ice-free season. During snowmelt, attempts are made to measure discharge once or twice daily. Evapotranspiration is estimated by a modified Priestley-Taylor method without soil conduction. A weighted α value was determined for each watershed based on percent dry, wet, and standing water surface conditions; a higher value of α was used early in the warm season and a lower value later in the warm season as the system dried out. The value of α ranged from 0.9 for dry upland to 1.5 for lakes. Heat conduction into the soil was not measured; however, from other studies the magnitude is about 15% of total net radiation. Past studies, water balance calculations, and evaporation pan data are used to guide our estimates of parameters in the Priestley-Taylor algorithm for ET. Past intense ET studies (Mendez et al. 1998, Rovensek et al. 1996) near the Putuligayuk have helped guide our ET estimates there; however, our ET estimates for the Upper Kuparuk at the basin-wide scale are lacking in confidence because of the wide range of soil moisture conditions that exist across the watershed given the numerous ground cover types such as shrubs, tussocks, alpine vegetation, glacial deposits, and rock outcrops.

The typical hydrology of these Alaska Arctic watersheds is the spring snowmelt freshet, followed by a drying of the system as combined Q and ET exceed summer P , and eventually a late summer rewetting of the system as ET tapers off and P increases (Bowling et al. 2003). August is generally the wettest month of the year, although in any one year, June, July, and September have been the wettest months. This pattern can be seen in Figures 2a, b, and c and 3a, b, and c, with some differences because of the large variation in summer P (Tables 1 and 2) between the three years (198, 109, and 185 mm for Upper Kuparuk in 2006, 2007, and 2008, respectively, and 107, 15, and 90 mm for the Putuligayuk for 2006, 2007, and 2008, respectively). For 13 years, the Upper Kuparuk average is 222 mm of summer rainfall, while for 10 years the Putuligayuk average is 85 mm (Tables 1 and 2). Typically,

the amount of water stored increases during ablation and then decreases continuously as ET ramps up. Some recovery of this storage deficit may occur if there is ample late-summer rainfall; however, this can vary considerably due to natural variability in both amount and timing of precipitation events.

The change in storage for three years for the Upper Kuparuk catchment is shown in Figures 2a, b, and c. As mentioned earlier, 2007 was a relatively dry year, although all three years were below the average rainfall (222 mm, Table 1). The main storage mechanism for the Upper Kuparuk is the active layer. While positive storage followed immediately after snowmelt, relative storage went from positive to negative during the summer and remained negative for the remainder of the summer as $ET + Q$ exceeded P . The timing of this transition was later for those years with greater rainfall. Note that a large tundra wildfire in 2007 northwest of the Upper Kuparuk burned from early summer into early winter and was the largest documented tundra fire on the North Slope of Alaska.

A similar plot (Fig. 2c) for 2008 shows the storage remaining positive much longer into the summer and then going negative in late July. The lack of precipitation in August ensured that the storage would stay negative. Considerable precipitation in early summer and the lack of it in late summer, which is generally not the case, explains the pattern seen this year. In normal years, when there is late summer precipitation, much of the storage deficit can be made up.

The pattern for the Kuparuk in all three years is quite similar, with a positive storage amount following snowmelt and a gradual decline over the summer that can be buffered by rainfall, ending with a negative deficit that needs to be satisfied the next spring before there is a runoff response.

Water balance plots (Figs. 3a, b, and c) for three years for the Putuligayuk show a wide range in response. While there was a decrease in storage in mid-summer of 2006, which was a wetter than normal year (Table 2), the amount of storage never went negative. In contrast, 2007 was the drought year when $ET + Q$ was greater than P , with this transition occurring in late June. In terms of precipitation, 2008 was a normal year (Fig. 3c, Table 2), but the estimate of ET was low this year. Thus there was a positive storage throughout the summer. Note that the Putuligayuk has very low flows during the summer (Figs. 3a, b, and c), with minimal response to rainfall.

Discussion

Recent publications have highlighted the importance of revisiting the role of storage on hydrological processes of watersheds (McNamara et al. 2011, Spence 2010). The runoff response, both from snowmelt and rainfall, is a function of available storage in a watershed. The active layer storage in areas of permafrost is a poor buffer to both drought and floods because of limited storage. Bowling et al. (2003) showed that for a three-year period (1999–2001) at the Putuligayuk drainage, a significant percentage of the SWE went into satisfying storage deficit, mainly of surface water bodies. They found that a reduction in surface saturation over the course of the summer was 58% in 1999 and 73% in 2000, which resulted

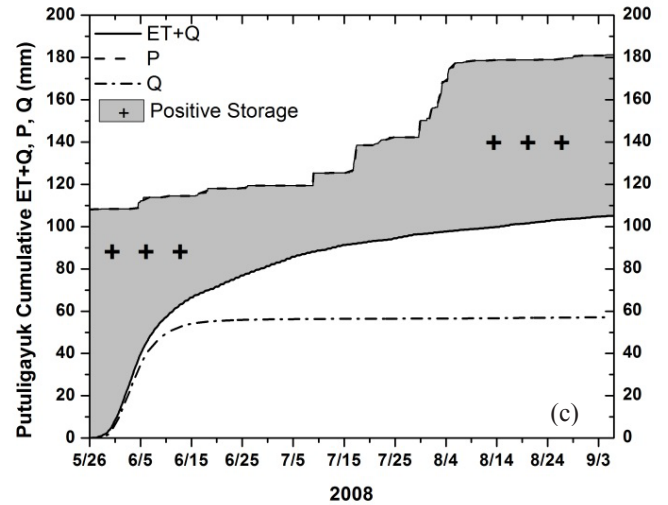
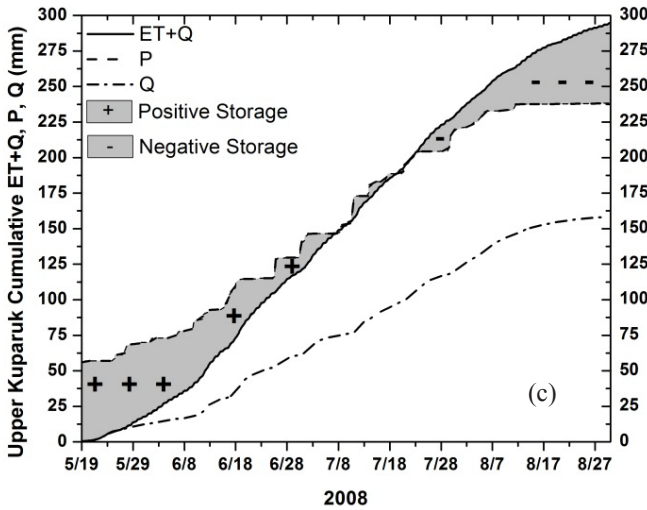
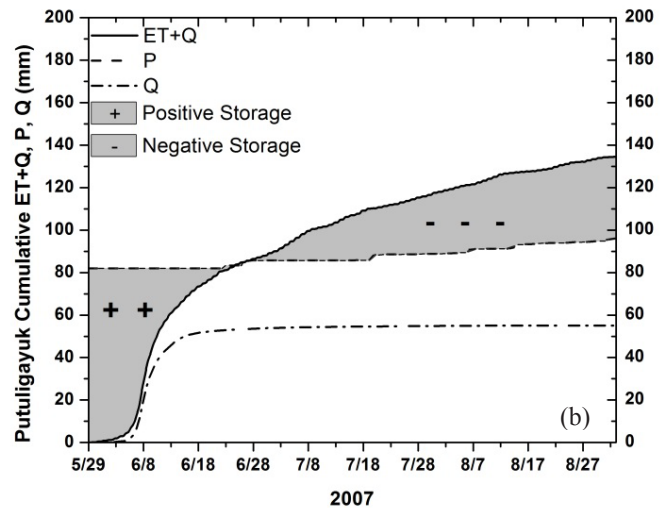
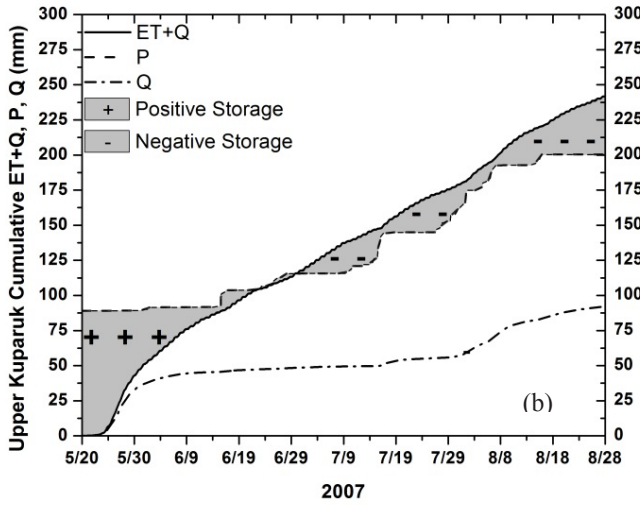
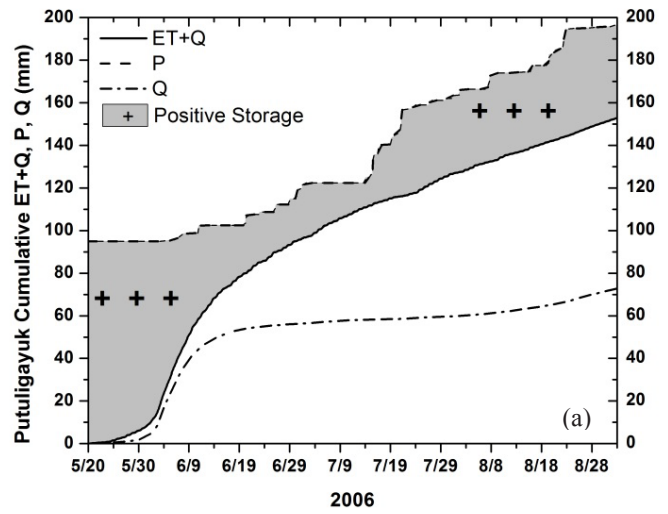
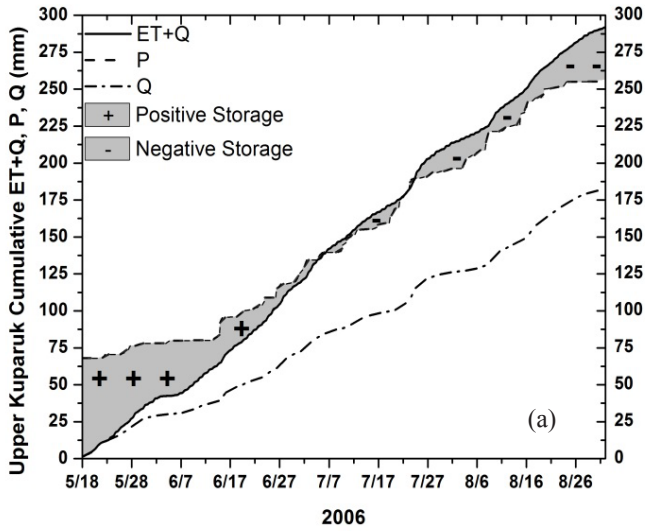


Figure 2. Change in storage (shaded area mainly active layer) for the moderate- to steep-gradient Upper Kuparuk River catchment in (a) 2006, (b) 2007, and (c) 2008.

Figure 3. Change in storage (shaded area mostly lakes, ponds, and wetlands) for the low-gradient Putuligayuk River catchment in (a) 2006, (b) 2007, and (c) 2008.

Table 1. Upper Kuparuk River hydrological summary for 2006–2008 and overall average, maximum, and minimum based on the 13-year period of record.

| Year | P _{snow} | P _{rain} | P _{total} | ET _{Priestley Taylor} | Q _{snow} | Q _{rain} | Q _{total} |
|----------------|--------------------|-------------------|--------------------|--------------------------------|-------------------|-------------------|--------------------|
| | Precipitation (mm) | | | Evapotranspiration (mm) | Runoff (mm) | | |
| 2006 | 79 | 198 | 276 | 109 | 27 | 150 | 177 |
| 2007 | 90 | 109 | 198 | 154 | 36 | 58 | 94 |
| 2008 | 58 | 185 | 243 | 140 | 7 | 148 | 155 |
| Average (n=13) | 108 | 222 | 330 | n/a | 50 | 157 | 207 |
| Maximum (n=13) | 152 | 324 | 460 | n/a | 104 | 274 | 324 |
| Minimum (n=13) | 54 | 98 | 198 | n/a | 7 | 54 | 94 |

Table 2. Putuligayuk River hydrological summary for 2006–2008 and overall average, maximum, and minimum based on the 10-year period of record.

| Year | P _{snow} | P _{rain} | P _{total} | ET _{Priestley Taylor} | Q _{snow} | Q _{rain} | Q _{total} |
|----------------|--------------------|-------------------|--------------------|--------------------------------|-------------------|-------------------|--------------------|
| | Precipitation (mm) | | | Evapotranspiration (mm) | Runoff (mm) | | |
| 2006 | 95 | 107 | 202 | 80 | 55 | 28 | 83 |
| 2007 | 82 | 15 | 97 | 66 | 52 | 3 | 55 |
| 2008 | 96 | 90 | 186 | 48 | 54 | 3 | 57 |
| Average (n=10) | 95 | 85 | 180 | 59 | 72 | 31 | 102 |
| Maximum (n=10) | 112 | 137 | 231 | 80 | 105 | 71 | 173 |
| Minimum (n=10) | 82 | 15 | 97 | 48 | 51 | 3 | 55 |

in the development of a storage deficit. One other significant observation of this group was that, as the system dries out, the hydraulic connectivity of the drainage network becomes fragmented. This explains the lack of a runoff response to precipitation in the summer months mentioned above and shown in Figure 3. In a macroscale hydrologic modeling effort, Bowling & Lettenmaier (2010) demonstrated the importance of storage at a larger scale; they concluded that 46% of the variance in the volume of snowmelt water entering into storage can be explained by the year-to-year variation in maximum SWE and the lake storage deficit from the previous year.

The challenge for hydrologists is that it is very difficult to measure the absolute amount of storage at the watershed scale at a given time. However, we can document the amount of change or relative storage in a catchment each year, which is what we have done here. The maximum amount of water that can be stored in the active layer in this case is equivalent approximately to the annual precipitation. Of course, some of this storage is only for a brief period, as the ability of watershed soils (especially surficial organic soils) to retain storage is also limited. Figures 2 and 3 show that storage, both for the active-layer case (Upper Kuparuk basin) and the surface-storage case (ponds, lakes, and wetlands of Putuligayuk catchment), is continually in flux, and the amount of water in storage is dependently linked not only to the physical characteristics of

the storage reservoir, but also to the patterns of P, ET, and Q. The figures also illustrate that, although these catchments start out with positive relative storage after snowmelt, at summer's end the storage in these basins varies substantially and can vary in sign from one year to the next. One limitation of the water balance approach is that all of the error in measuring P and Q and estimating ET is reflected in the ΔS estimate. On the other hand, however, the spatial heterogeneity of each watershed makes it almost impossible to quantify storage accurately at a selected time.

Conclusions

Storage can, and often does, play a dominant role in the hydrologic cycle of watersheds; at the same time, permafrost plays a role in dictating the type and extent of storage. Although the absolute value of storage is not known, through the exercise carried out here we can begin to develop an understanding of the range of variation in storage and how it may affect the runoff response. Hydrologic data from three years with significantly different precipitation amounts were analyzed to determine the change in storage for a moderate-gradient and a low-gradient watershed underlain by continuous permafrost. Results of this study show that although considerable storage is guaranteed after snowmelt, by summer's end a wide range of storage conditions can exist in Alaska Arctic watersheds

underlain by continuous permafrost. It is only a coincidence that the magnitude of the storage changes in the two catchments illustrated here are similar; the range of change possible is highly constrained by the continuous permafrost and low amounts of annual precipitation.

Acknowledgments

This paper is based on work supported by the National Science Foundation, Office of Polar Programs, Grants OPP-9814984 and OPP-0335941. We are also grateful to faculty, staff, and students who over the years of the Kuparuk River research helped collect data that made these computations possible.

References

- Bowling, L.C. & Lettenmaier, D.P. 2010. Modeling the effects of lakes and wetlands on the water balance of Arctic environments. *Journal of Hydrometeorology* 11:10.1175/2009JHM1084.1.
- Bowling, L.C., Kane, D.L., Gieck, R.E., Hinzman, L.D., & Lettenmaier, D.P. 2003. The role of surface storage in a low-gradient arctic watershed. *Water Resources Research* 39(4): 1087, doi:10.1029/2002WR001466.
- Hall, J.V., Frayer, W.E., & Wilen, B.O. 1994. Status of Alaska Wetlands. U.S. Fish and Wildlife Service, Alaska Region, Anchorage, AK, 32 pp.
- Kane, D.L. & Yang, D. 2004. Overview for water balance determinations for high latitude watersheds. *Int. Assoc. of Hydrological Sciences Publication 290*: 1–12.
- Kane, D.L., Hinzman, L.D., McNamara, J.P., Zhang, Z., & Benson, C.S. 2000. An overview of a nested watershed study in Arctic Alaska. *Nordic Hydrology* 4/5:245–266.
- Kane, D.L., Gieck, R.E., & Bowling, L.C. 2003. Impacts of surficial permafrost landforms on surface hydrology. *Proceedings of the Eighth International Conference on Permafrost, Zurich, Switzerland, July 21–25, 2003*, Phillips, M. et al. (eds.), A.A. Balkema Publishers: 507–512.
- McNamara, J.P., Tetzlaff, D., Bishop, K., Soulsby, C., Seyfried, M., Peters, N.E., Aulenbach, B.T., & Hooper, R. 2011. Storage as a metric of catchment comparison. *Hydrological Processes* DOI:10.1002/hyp.8113.
- Mendez, J., Hinzman, L.D., & Kane, D.L. 1998. Evapotranspiration from a wetland complex on the Arctic Coastal Plain of Alaska. *Nordic Hydrology* 29(4/5): 303–330.
- Rovensek, R.J., Hinzman, L.D., & Kane, D.L. 1996. Hydrology of a tundra wetland complex on the Alaskan Arctic Coastal Plain. *Arctic and Alpine Research* 28(3): 311–317.
- Shutov, V., Gieck, R.E., Hinzman, L.D., & Kane, D.L. 2006. Evaporation from land surface in high latitude areas: A review of methods and study results. *Nordic Hydrology* 37(4/5): 393–411.
- Spence, C. 2010. A paradigm shift in hydrology: Storage thresholds across scales influence catchment runoff generation. *Geography Compass* 4(7): 819–833, 10.1111/j.1749-8198.2010.00341.x.
- Vourlitis, G.L. & Oechel, W.C. 1997. Landscape-scale CO₂, H₂O vapour and energy flux of moist-wet coastal tundra ecosystems over two growing seasons. *Journal of Ecology* 85:575–590.

Study of Ice-Rich Syngenetic Permafrost for Road Design (Interior Alaska)

Mikhail Kanevskiy, Yuri Shur, Billy Connor
University of Alaska Fairbanks, USA

Matthew Dillon
Golder Associates Inc., Anchorage, AK, USA

Eva Stephani
Golder Associates Inc., Quebec, Qc, Canada

Jonathan O'Donnell
USGS, Boulder, CO, USA

Abstract

Geotechnical investigations along the proposed alignment of the Dalton Highway between MP 8 and MP 12 included core logging and laboratory testing of soil samples. The cryofacies method by Katasonov was used to identify the origin of permafrost. Ice-rich syngenetic permafrost with large ice wedges (yedoma) in the area was formed in the late Pleistocene by simultaneous accumulation of silt and upward permafrost aggradation. Four sections with different properties of frozen soils were distinguished. Thickness of ice-rich silt varied from several meters to more than 26 m, and the wedge-ice volume can be nearly 50%. Extremely high ice content of syngenetic permafrost determined its high thaw susceptibility. Thaw strain varied from 20% to 60%. Yedoma soils in the study area are separated from the base of the active layer by two protective layers: a 0.5- to 1-m-thick ice-rich intermediate layer, and a 1- to 4-m-thick ice-poor layer of thawed and refrozen soils. Road construction can cause thaw settlement and slope failures in cut areas.

Keywords: Alaska; geotechnical investigations; ice wedges; syngenetic permafrost; thaw settlement; yedoma.

Introduction

The Alaska Department of Transportation (AKDOT) recently proposed a new alignment of the Dalton Highway between Mile Post (MP) 8 and MP 12 (Fig. 1). The study area is located approximately 20 km north-west of Livengood and about 100 km north of Fairbanks. The Trans-Alaska Pipeline in this area is located about 2 km east of the Dalton Highway. The area is drained by the Yukon River and belongs to the Yukon-Tanana Upland formed by generally rolling low mountains (Wahrhaftig 1965). The 4.5-km-long alignment is sloping gently to the northwest from approximately 470 m to 320 m above sea level.

The proposed alignment crosses the area with extremely complex permafrost conditions. The Alaska University Transportation Center (AUTC) of the University of Alaska Fairbanks (UAF) was involved in geotechnical investigations for this project. An analysis of existing data from previous geotechnical investigations in the area identified the existence of ice-rich permafrost including massive ice. Boreholes drilled for the Trans-Alaska Pipeline in 1970 (Kreig & Reger 1982) showed the presence of more than 18 m of ice-rich silt. Large ice wedges were exposed nearby during construction of the Dalton Highway (Lotspeich 1971, Smith & Berg 1973).

In the 1990s, AKDOT investigated geotechnical conditions in the area to find a safer alignment between MP 8 and MP 12. In 1990, 45 test holes were drilled, and an additional 29 test holes were drilled in 1991. It was found that permafrost in the study area was continuous, and the thickness of massive ice varied from less than one meter to dozens of meters; high

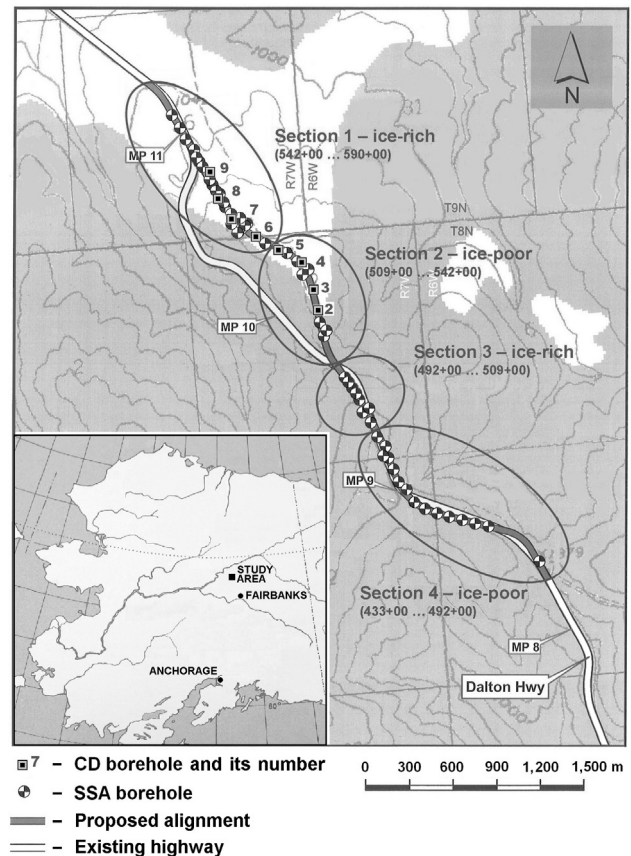


Figure 1. Location of the proposed alignment of the Dalton Highway and position of boreholes drilled in 2008.

contents of ice and organic matter were reported (Schlichting & Darrow 2006). In this paper, we present the main results of geotechnical investigations performed in the project area in 2008 as a cooperative effort between AUTC and AKDOT.

Methods

Hollow stem core drilling (CD) was conducted in May 2008 with a drill rig equipped with a modified CME (Central Mine Equipment Company) sampler (5 cm inside diameter). Eight CD boreholes (Fig. 1) from 7.5 m to 21.5 m deep were cored by an AKDOT crew (drillers Tom Johnson and Jason Cline) and logged by the authors (Shur et al. 2010). The total length of all cores was 109.4 m. An additional 54 boreholes, with a maximum depth of 26 m, were drilled without coring by solid-stem augering (herein referred to as SSA boreholes) and logged by AKDOT personnel (Rowland 2010).

For geotechnical investigations in areas with ice-rich permafrost, specific methods of permafrost field studies have been successfully applied. In this work, we used the cryofacies method (Katasonov 1969, 1978). This method is based on a close relationship between the shape, size, and spatial pattern of ice inclusions in soils (i.e., cryostructures) and specific terrain units, and reveals the nature of permafrost formation. The study of cryostructures allows researchers to identify the nature of permafrost and to estimate the ice distribution within it. The cryofacies method has been especially useful for study of syngenetic permafrost (Katasonov 1969, 1978, Shur & Jorgenson 1998, Kanevskiy et al. 2008, 2011). For description of soil cryogenic structure, we used a classification of cryostructures (patterns formed by ice inclusions in the frozen soil) that was adapted from several Russian and North American classifications (Gasnov 1963, Katasonov 1969, Kudryavtsev 1978, Zhestkova 1982, Shur & Jorgenson 1998, French & Shur 2010). Particle size distribution analyses were performed on 25 samples obtained from six CD boreholes (CD-2–CD-7) according to ASTM D 422 to quantify particle size distribution.

Wedge-ice occurrence and its distribution with depth were evaluated on the basis of data from 8 CD and 54 SSA boreholes. Ice content of frozen soil between ice wedges was evaluated by soil oven-drying (90°C, 72 h). Gravimetric moisture contents (on a dry-weight basis) were calculated for 189 soil samples. For volumetric moisture contents, 99 samples with accurate sample volume measurements were prepared. Thaw strain of ice-rich soil without external load was studied on 44 samples, and a consolidation test of thawed soils upon different loads was performed on five samples.

Results and Discussion

Area description

The study area is located within the discontinuous permafrost zone (Péwé 1975, Jorgenson et al. 2008). Permafrost temperatures at the site vary from -1.5°C to -0.5°C (Rowland 2010). Active layer thickness varies mostly from 0.5 to 1 m. There is no contemporary growth of ice wedges in the area. Wedge-ice development in Interior Alaska can be expected only

in organic soils, usually on flat surfaces with limited drainage and mostly in peat bogs (Hamilton et al. 1983). Despite the recent forest fire (2003 Erickson Creek fire) and subsequent increase in the active layer thickness, thermokarst features in the project area are limited to shallow irregular thermokarst scars; thaw settlement does not exceed 0.5 to 1 m. We did not observe any distinct thermokarst troughs above melting ice wedges using both high-resolution aerial photographs and our surface observations. Numerous old gullies in the study area have not shown any evidence of the recent rejuvenation.

Soil characteristics

The surficial deposit is frozen silt (loess). The particle-size distribution analysis of the sediments from six boreholes (CD-2–CD-7) performed on 25 samples showed that the content of silt particles comprised 70% to 80% of bulk soils. The percentage of sand did not exceed 15%, and clay content varied between 10% and 20%. According to loss-on-ignition measurements by AKDOT (Rowland 2010), organic matter content varied from 2% to 20% with an average value of 6.7%. In most CD boreholes, horizons of organic-rich silt and peat were encountered at different depths. Thickness of silt varied from 0.5 m to more than 26 m. Radiocarbon age of sediments ranged from 22,600 to 43,100 yr BP (eight samples were obtained from the CD boreholes). Radiocarbon ages of similar sediments from 18,000 to 27,000 yr BP were reported for the adjacent area (O'Donnell et al. 2011). Silt deposits are underlain by colluvial and fluvial gravelly soils up to 3 m thick or weathered bedrock. Bedrock in the study area is represented mostly by highly deformed weathered sedimentary rocks. Neither CD nor SSA boreholes (the deepest hole was about 26 m deep) located at the base of the slope at elevations from 320 to 380 m reached the base of silt deposits.

Cryogenic structure and ice content

Study of the cryogenic structure of cores obtained from eight CD boreholes showed the prevalence of micro-cryostructures typical of syngenetic permafrost (Kanevskiy et al. 2011). An example of cryostructures and properties of soil between the ice wedges studied in one of the boreholes is shown in Figure 2. Soil presented here can be divided into the following cryostratigraphic units: (1) active layer (0–0.71 m); ice-rich intermediate layer (0.71–1.50 m); (2) ice-poor thawed and refrozen sediments (1.50–3.05 m); (3) ice-rich syngenetic permafrost (3.05–10.00 m); and (4) ice-poor epigenetic permafrost (10.00–12.20 m).

Most of the other CD boreholes revealed a similar structure of the upper permafrost. Five of eight boreholes showed a well-developed ice-rich intermediate layer (Shur 1988) from 0.7 m to 1.0 m thick. A rudimentary intermediate layer up to 0.3 m thick was encountered in two more boreholes. We related the formation of these poorly developed layers to the recovery of the upper permafrost after the forest fire, which had triggered an increase in the active layer thickness and degradation of the original intermediate layer.

In five boreholes, the ice-poor layer of thawed and refrozen sediments (ranging from 0.3 to 8.0 m thick) was encountered

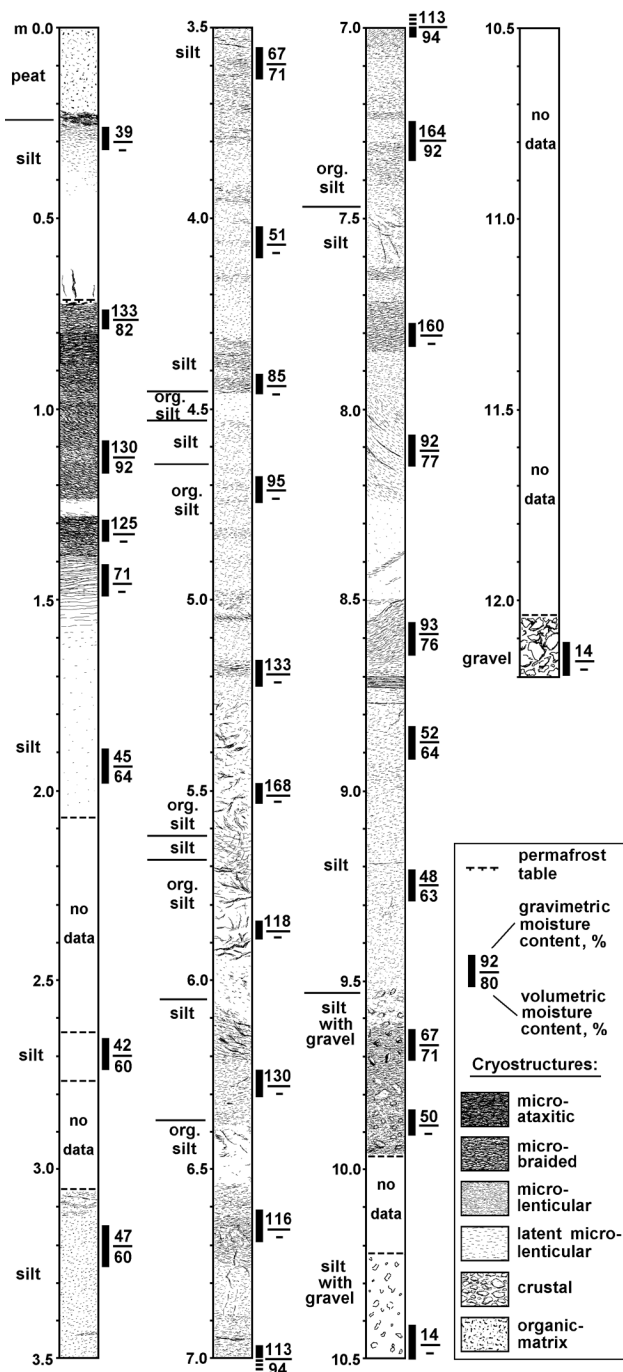


Figure 2. Cryogenic structure and ice content of frozen soils, borehole CD-4 (ice is black).

below the intermediate layer. The wide occurrence of thawed and refrozen sediments in Interior Alaska was previously documented by Péwé (1975). Wedge ice was encountered at various depths in all boreholes except CD-2, CD-4, and CD-5. In boreholes CD-8 and CD-9, ice wedges appear just below the ice-rich intermediate layer, from depths 1.2 m and 1.5 m respectively. Soils between ice wedges are mostly ice-rich. The wide range (from ~40% up to 200% and more) and high values (85.5% average) of gravimetric moisture content, which do not change significantly with depth, are typical of syngenetic permafrost.

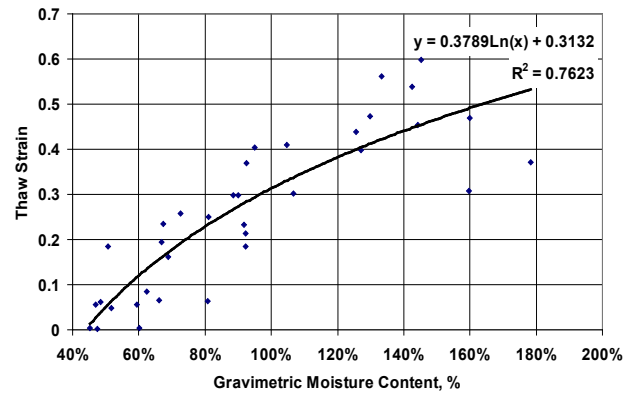


Figure 3. Logarithmic relationship between thaw strain of mineral soil (without external load) and gravimetric moisture content (based on the data for 35 samples from CD boreholes).

Thaw strain

Evaluation of thaw strain of frozen soils was based on 44 tests of thawing without external load (free thawing) and five consolidation tests. Average thaw strain was 0.23. Average thaw strain values for mineral and organic soils were 0.26 (35 samples) and 0.13 (9 samples) respectively. Figure 3 shows the correlation between thaw strain and gravimetric moisture content for 35 samples of mineral soils. We found that organic soils behaved differently from mineral soils, and their thaw strain in free thawing was much lower. In consolidation tests, the part of the thaw strain of organic soils related to the impact of a load was greater than that of mineral soils, and the total thaw strain of organic-rich silt was comparable to the thaw strain of mineral soils.

Wedge-ice volume and identification of alignment sections with different permafrost characteristics

Wedge ice is the main type of ground ice in syngenetic permafrost and the only one identified in boreholes in the studied area. Gray- and brown-colored wedge ice with a distinct vertical foliation due to mineral and organic inclusions was encountered at various depths in both CD and SSA boreholes. Our experience shows that during the drilling in the areas with the ice-rich syngenetic permafrost (yedoma), wedge ice can be found at different depths. It can be related to the occurrence of ice wedges buried at different depths, irregular boundaries of ice wedges, variability of the wedges' thickness with depth, and inclination of wedges. The penetration of wedges through the entire silt stratum is typical of yedoma. Wedge ice was found in most of the CD and SSA boreholes, but its occurrence varied along the alignment. On the basis of the wedge-ice occurrence, we identified four sections, two of which (sections 1 and 3) are defined as rich in massive ice and two (sections 2 and 4) defined as poor in massive ice. Boundaries between these sections are shown in Figure 1. A cryostratigraphic profile for sections 1 and 2 of the study site is shown in Figure 4.

Section #1 was characterized by the sequence of ice-rich syngenetically frozen silt from 12 m to more than 26 m thick. Wedge ice was observed at various depths in 24 of

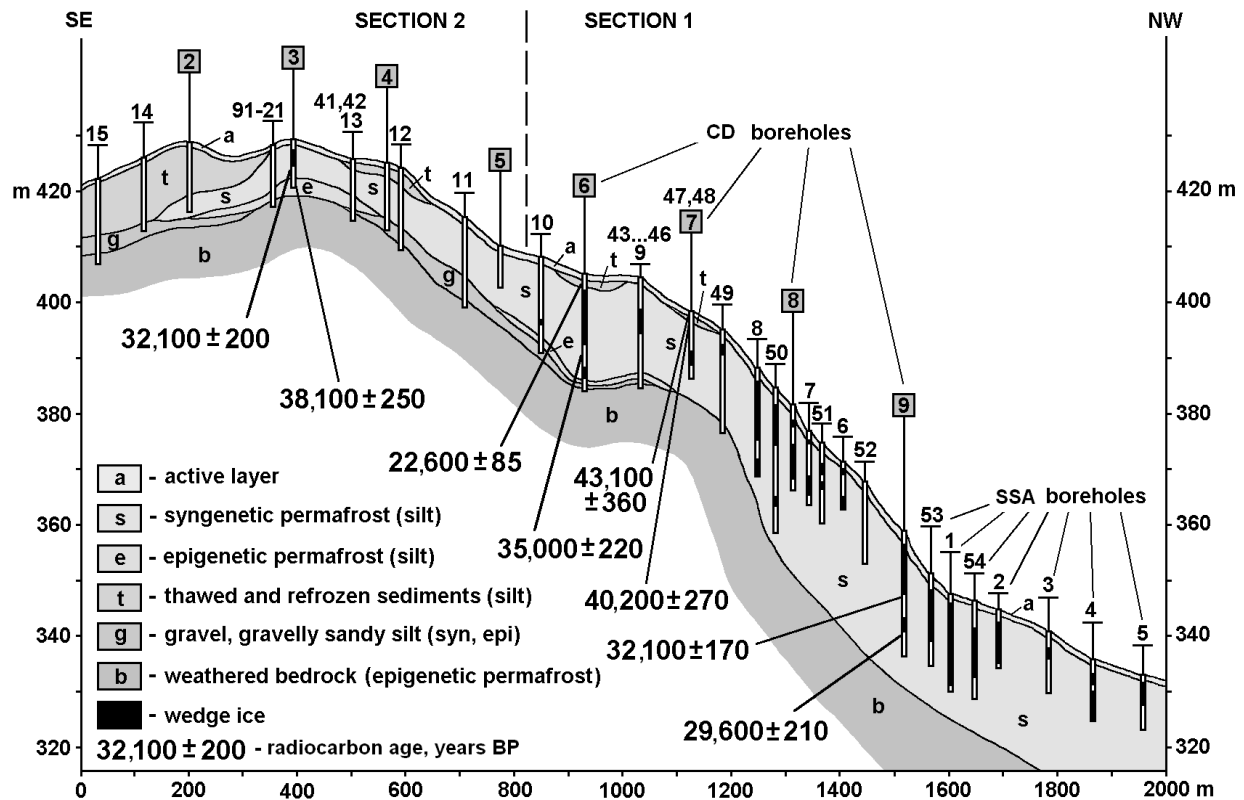


Figure 4. Cryostratigraphic profile. CD boreholes are marked by squares, and the rest are SSA boreholes.

26 boreholes. Average wedge-ice occurrence in this section reached 35%, but the wedge-ice volume was not distributed evenly with depth. Absence of ice wedges in the upper meter of the sequence can be explained by the occurrence of an intermediate layer beneath the active layer. Relatively small wedge-ice volume (less than 15%) at a depth interval of 1 to 2 m occurs in the ice-poor layer of thawed and refrozen soils. The highest values (more than 40%) were at depth intervals from 6 to 10 m and 17 to 20 m. Average gravimetric moisture content of silt between ice wedges was 102% (based on measurements of 85 samples from four CD boreholes). The lowest values of moisture content were obtained mostly at the depth interval from 0 to 3 m (they correspond to the active layer and the layer of thawed and refrozen sediments). The estimation of average thaw strain due to segregated ice was 0.32, so the total thaw strain (due to wedge ice and segregated ice) was 0.56. This thaw strain estimation was not conservative because it reflected only the settlement upon thawing without load.

In the ice-poor section #2, wedge-ice was found in only one of 12 boreholes at depths ranging from 1.8 to 4.8 m, and wedge-ice occurrence in this section was about 2%. Syngenetic permafrost was identified in every CD borehole in section #2, although it can be overlain by the layer of thawed and refrozen sediments up to 9 m thick. The thickness of silt in this section varied from 10 m to 12 m. Ice content of the soil in section #2 is 79% (based on measurements of 88 samples from four CD boreholes), which is lower than in section #1. The

lowest values corresponded to the active layer and the layer of thawed and refrozen sediments. The average thaw strain due to segregated ice was 0.23, and the total thaw strain estimation was 0.25.

In the ice-rich section #3, wedge-ice was found in 8 of 9 boreholes and occupied 47% of the combined length of all boreholes. Wedge-ice was not observed from 0 to 2 m, and from 2 to 4 m its volume did not exceed 17%. We relate this to occurrence of the ice-poor layer of thawed and refrozen soils. Wedge-ice volume more than 50% was observed from 6 to 14 m, and at 8 to 14 m it reached more than 80%. The thickness of silt in this section varied from 9 to 14 m. Average gravimetric moisture content of the silt was 81% (based on measurements of 38 samples from nine SSA boreholes). The lowest values of soil moisture content were obtained mostly at the depth interval from 0 to 4 m (they correspond to the active layer and the layer of thawed and refrozen sediments) and from 12 to 17 m (gravelly soil and bedrock). The average thaw strain due to segregated ice was 0.23, and the total thaw strain was 0.59.

In the ice-poor section #4, wedge ice was found in one of 15 boreholes. Wedge-ice occurrence is very small (about 3%), but the gravimetric moisture content of perennially frozen silt is relatively high (63% average, based on measurements of 21 samples obtained from 15 SSA boreholes). This section was characterized by a 0.5- to 4-m-thick sequence of silt overlaying gravel and weathered bedrock. The average thaw strain due to segregated ice was 0.13, and total thaw strain was 0.16.

Genesis of permafrost

Our study of soils and ground ice show that the frozen silt in the study area is mostly ice-rich syngenetic permafrost formed in the late Pleistocene (yedoma). The evidence includes thick deposits of homogeneous silt with poorly decomposed organic matter, age of sediments (22,600 to 43,100 yr BP, Fig. 4), very high ice content, prevalence of micro-cryostructures, and occurrence of large foliated ice wedges penetrating through the entire silt sequence. Yedoma deposits were formed by simultaneous accumulation of windblown silt partly reworked by slope and fluvial processes (Péwé 1975) and upward permafrost aggradation. Ice-rich syngenetic Pleistocene permafrost widely occurs in Interior Alaska, on the Seward Peninsula, and on the Arctic Foothills of the Brooks Range, and it can be encountered in other areas that had remained unglaciated during the late Pleistocene (Kanevskiy et al. 2011). Until recently, this type of permafrost has been understudied in Alaska, and investigations for engineering projects usually do not provide sufficient information for its characterization. In Interior Alaska, the cryogenic structure of these sediments has been studied extensively in the well-known CRREL permafrost tunnel at Fox, near Fairbanks (Sellmann 1967, Hamilton et al. 1988, Shur et al. 2004, Bray et al. 2006, Fortier et al. 2008, Kanevskiy et al. 2008). A comparison of ice-rich soils in the study area with those of the CRREL permafrost tunnel showed that they had similar age, cryogenic structure, and ice content. Wide occurrence of yedoma in Alaska presents a great challenge to development and should be closely considered during geotechnical investigations in Interior Alaska.

Conclusions

The thick layer of syngenetic permafrost in the studied area was formed during the late Pleistocene by simultaneous accumulation of silt and upward permafrost aggradation. Most of the soils in the project area are extremely ice-rich and display excessive thaw settlement upon thawing. The thickness of ice-rich silt usually varies from 10 m to more than 26 m, and wedge-ice volume can reach more than 45%. Extremely high ice content of syngenetic permafrost with ice wedges determines its high thaw susceptibility. Thaw strain values generally vary from 20% to 60%. Four sections with different permafrost properties are identified along the proposed alignment. Sections #1 and #3 are extremely ice-rich, and permafrost thawing in these parts of the alignment will bring significant thaw settlement. Ice wedges in sections #2 and #4 are rare, but thaw settlement of silt cannot be neglected. The main potential hazards related to road construction in this area are (1) significant differential thaw settlement of soils beneath the road; (2) rapid retreat of permafrost slopes in cut areas resulting in slope failures; and (3) contamination of surface water due to thawing of organic and ice-rich silt at the slopes. Mitigation of these hazards will result in extremely high maintenance costs.

Ice-rich soils with large ice wedges are usually separated from the base of the active layer by two protective layers: a 0.5- to 1-m-thick ice-rich intermediate layer, and a 1- to 4-m-thick ice-poor layer of thawed and refrozen soils. Formation of the

latter could be related to climate changes during the Holocene or to frequent wildfires. Occurrence of the ice-poor layer on top of the ice-rich syngenetic permafrost is extremely important for resilience of ecosystems to environmental changes and to the integrity of the road in fill areas. In cut areas, this protective layer can be completely destroyed, and permafrost becomes thaw sensitive and vulnerable to climatic impacts and local disturbances. The ice-poor layer is favorable to stabilization of exposed permafrost slopes in cut areas.

Acknowledgments

This work was funded by the Alaska University Transportation Center (project #207122) and the Alaska Department of Transportation. Data analysis was also supported by the National Science Foundation (NSF grant EAR 0630257). We appreciate the good job done by AKDOT drillers Tom Johnson and Jason Cline, cooperation in the field with AKDOT geologists Julie Rowland and Ronald Brooks, and discussion at the different stages of the project with AKDOT engineers and geologists Jessie Reinikainen, Steve Masterman, James Sweeney, and Leo Woster. We also thank Vladislav Roujanski and James Rooney for valuable comments and suggestions.

References

- Bray, M.T., French, H.M., & Shur, Y. 2006. Further cryostratigraphic observations in the CRREL permafrost tunnel, Fox, Alaska. *Permafrost and Periglacial Processes* 17 (3): 233-243.
- Fortier, D., Kanevskiy, M., & Shur, Y. 2008. Genesis of reticulate-chaotic cryostructure in permafrost. In *NICOP 2008: Proceedings of the Ninth International Conference on Permafrost*. D.L. Kane & K.M. Hinkel (eds.). Institute of Northern Engineering, University of Alaska Fairbanks, 1: 451-456.
- French, H. & Shur, Y. 2010. The principles of cryostratigraphy. *Earth-Science Reviews* 110, 190-206.
- Gasnov, S.S. 1963. *Morphogenetic classification of cryostructures of frozen sediments*. Trudy SVKNII, Vol. 3, Magadan (in Russian).
- Hamilton, T.D., Ager, T.A., & Robinson, S.W. 1983. Late Holocene ice wedges near Fairbanks, Alaska, USA: environmental setting and history of growth. *Arctic and Alpine Research* 15 (2): 157-168.
- Hamilton, T.D., Craig, J.L., & Sellmann, P.V. 1988. The Fox permafrost tunnel: a late Quaternary geologic record in central Alaska. *Geological Society of America Bulletin* 100: 948-969.
- Jorgenson, T., Yoshikawa, K., Kanevskiy, M., Shur, Y., Romanovsky, V., Marchenko, S., Grosse, G., Brown, J., & Jones, B. 2008. Permafrost Characteristics of Alaska. In *Proceedings of the Ninth International Conference on Permafrost, extended abstracts*. D.L. Kane & K.M. Hinkel (eds.). Institute of Northern Engineering, University of Alaska Fairbanks: 121-122.

- Kanevskiy, M., Fortier, D., Shur, Y., Bray, M., & Jorgenson, T. 2008. Detailed cryostratigraphic studies of syngenetic permafrost in the winze of the CRREL permafrost tunnel, Fox, Alaska. In *NICOP 2008: Proceedings of the Ninth International Conference on Permafrost*. D.L. Kane & K.M. Hinkel (eds.). Institute of Northern Engineering, University of Alaska Fairbanks, 1: 889-894.
- Kanevskiy, M., Shur, Y., Fortier, D., Jorgenson, M.T., & Stephani, E. 2011. Cryostratigraphy of late Pleistocene syngenetic permafrost (yedoma) in northern Alaska, Itkillik River exposure, *Quaternary Research* 75(3), 584-596.
- Katasonov, E.M. 1969. *Composition and cryogenic structure of permafrost*. National Research Council of Canada, Ottawa, Technical Translation 1358, 25-36.
- Katasonov, E.M. 1978. Permafrost-facies analysis as the main method of cryolithology. *Proceedings of the Second International Conference on Permafrost*, July 13-28, 1973. USSR Contribution. Washington: National Academy of Sciences, 171-176.
- Kreig, R.A. & Reger, R.D. 1982. *Air-photo analysis and summary of landform soil properties along the route of the Trans-Alaska Pipeline System*. DGGs, College, Alaska, Geologic report 66: 149 pp.
- Kudryavtsev, V.A. (ed.). 1978. *General Permafrost Science (Geocryology)* 2nd edn. Moscow: Moscow University Press, 463 pp. (in Russian).
- Lotspeich, F.B. 1971. *Environmental guidelines for road construction in Alaska*. Environmental Protection Agency, Alaska, Water Laboratory, College, Alaska, Report No. 1610 GOI 08/71, 127 pp.
- O'Donnell, J.A., Harden, J.W., McGuire, A.D., Kanevskiy, M.Z., Jorgenson, M.T., & Xu, X. 2011. The effect of fire and permafrost interactions on soil carbon accumulation in an upland black spruce ecosystem of interior Alaska: implications for post-thaw carbon loss. *Global Change Biology* 17, 1461-1474.
- Péwé, T.L. 1975. *Quaternary geology of Alaska*. United States Geological Survey, Professional Paper 835, 145 pp.
- Rowland, J. 2010. *Geotechnical report – supplemental, Dalton Highway 9 mile North*. Federal Project No. NH-F-06502(3) / State Project No. 64899. Alaska Department of Transportation and Public Facilities, Northern Region Material Section.
- Schlichting, S.J. & Darrow, M.M. 2006. *Geotechnical report, Dalton Highway 9 mile Hill North*. Federal Project No. NH-F-065-2(3) / State Project No. 64899, Northern Region. Alaska Department of Transportation and Public Facilities, Northern Region.
- Sellmann, P.V. 1967. *Geology of the USA CRREL permafrost tunnel, Fairbanks, Alaska*. Hanover, New Hampshire, US Army CRREL Technical Report 199, 22 pp.
- Shur Y.L. 1988b. The upper horizon of permafrost soils. In *Proceedings of the Fifth International Conference on Permafrost*, Vol. 1. Tapir Publishers, Trondheim: Norway, 867-871.
- Shur, Y. & Jorgenson, M.T. 1998. Cryostructure development on the floodplain of the Collville River Delta, northern Alaska. In *Proceedings of the Seventh International Conference on Permafrost*. Yellowknife, Canada: 993-999.
- Shur, Y., French, H.M., Bray, M.T., & Anderson, D.A. 2004. Syngenetic permafrost growth: cryostratigraphic observations from the CRREL Tunnel near Fairbanks, Alaska. *Permafrost and Periglacial Processes* 15 (4): 339-347.
- Shur, Y., Kanevskiy, M., Dillon, M., Stephani, E., & O'Donnell, J. 2010. *Geotechnical investigations for the Dalton Highway innovation project as a case study of the ice-rich syngenetic permafrost*. Report # FHWA-AK-RD-10-06, prepared for AK DOT & PF, AUTC assigned project # 207122. Institute of Northern Engineering, University of Alaska Fairbanks.
- Smith, N. & Berg, R. 1973. Encountering massive ground ice during road construction in central Alaska. *Proceedings of the Second International Conference on Permafrost*, July 13-28, 1973. Washington: National Academy of Sciences, 730-736.
- Wahrhaftig, C. 1965. *Physiographic divisions of Alaska*. USGS professional paper 482. Washington: United States Government Printing Office, 52 pp.
- Zhestkova, T.N. 1982. *Formation of the cryogenic structure of ground*. Moscow: Nauka, 209 pp. (in Russian).

Two-Dimensional Frost Heave Simulation Based on Takashi's Equation

Shunji Kanie, Hao Zheng

Faculty of Engineering, Hokkaido University

Satoshi Akagawa

Cryosphere Engineering Laboratory, Hachioji, Tokyo, Japan

Abstract

This research aims to simulate interactive two-dimensional behavior between a chilled gas pipeline and frost heave. Among several frost heave models, the authors adopted Takashi's equation, which has been applied for one-dimensional frost heave estimation according to the Japanese Geotechnical Standard. We expanded this model for two-dimensional evaluation of frost heave and verified the possibility of applying Takashi's equation to two-dimensional interaction. Takashi's equation was originally derived from numerous one-dimensional experiments and it becomes necessary to include the anisotropic expansion due to frost heave. The authors introduced an anisotropic parameter named β , which distributes the frost heave ratio in two different directions. The simulation program was originally developed by coupling a heat transfer calculation and a mechanical equilibrium analysis in a Finite Element Model (FEM). In order to confirm its applicability, the simulation results are compared with data obtained in a real-scale experiment in Fairbanks, Alaska. The influence of the anisotropic property of frost heave and the thermal conductivity of soil are reported in this paper. The results by the numerical model based on Takashi's equation show good agreement with the observed data in the real-scale experiment in Alaska when we choose an appropriate value for the anisotropic parameter β . The thermal conductivity of the soil has a complex influence on frost heave because it affects both the freezing rate and the size of the frost bulb formed around the pipe.

Keywords: chilled gas pipeline; frost heave; interaction; simulation; Takashi's equation.

Introduction

A chilled gas pipeline buried in the ground suffers damage from unexpected settlement and rise by complicated interactions such as frost heave with the neighboring ground. It is important to evaluate the interaction between the pipeline and neighboring frozen ground and to establish predictive methods of frost heave. The purpose of this study is to validate this prediction method and evaluate its influence on the pipeline.

Buried chilled gas pipelines are threatened with frost heave since frost bulbs can form around the pipe in frost-susceptible soil. Numerous researchers have studied this phenomenon. Razaqpur and Wang (1996) proposed practical models for frost heave estimation by considering water migration based on the Clausius-Clapeyron equation. Additionally, Mikkola (2001) developed a mathematical model in which the physical-chemical structure of the soil is described using remeshing techniques with the Galerkin method. From an engineering standpoint, several evaluation methods using segregation potential theory have been developed by Nixon (1982, 1987a, b), Konrad (1987), Shen & Ladanyi (1991), and Selvadurai & Shinde (1993). Kanie (2006) also developed a practical evaluation method based on Takashi's equation with a beam on the elastic foundation model. Although the frost heave behavior of a pipe following the growth of a frost bulb has been researched, the interactive bending behavior with frost bulb development has rarely been discussed.

In this paper, the authors introduce an anisotropic parameter to expand Takashi's equation and combine a heat transfer calculation with a mechanical equilibrium analysis within an FEM. This makes it possible to evaluate the interactive behavior of soil and structure due to frost heave.

Takashi's Equation as a Frost Heave Model

There are several models proposed for frost heave estimation. The Clausius-Clapeyron equation, named after Rudolf Clausius and Benoît Paul Émile Clapeyron, is a way of characterizing a discontinuous phase transition between two phases of matter. By applying this idea to frost heave, water migration can be expressed based on the gradient of coexistence curve between two phases. The segregation potential method is an experimental way to estimate frost heave with confining stress and the gradient of temperature, as well as the segregation potential reflecting the characteristics of soil. Takashi's equation is also an experimental method for frost heave estimation, and it has been widely used based on the Japanese Geotechnical Standard.

Takashi's equation relates the frost heave ratio with the constraining stress and freezing rate as equation 1.

$$\xi = \xi_0 + \frac{\sigma_0}{\sigma} \left(1 + \sqrt{\frac{U_0}{U}} \right) \quad (1)$$

ξ : frost heave ratio, σ : constraining stress in the freezing direction, U : freezing rate. ξ_0 , σ_0 and U_0 are constants for the material obtained by experiment regulated by the JGS. It is obvious that U and σ are two critical variables for obtaining the frost heave ratio. For example, if the confining stress σ is small, there will be a larger frost heave ratio. If the soil was frozen quickly, which means that the freezing rate U is large, there will be a small frost heave ratio.

In the two-dimensional analysis, U is obtained by heat transfer calculation and σ is obtained by mechanical equilibrium analysis at each time step. Then the frost heave ratio is converted into equivalent strains in two directions with

the anisotropic parameter corresponding to the volumetric change due to frost heave.

If we assume that it is an isotropic problem in three dimensions or, in other words, that all strains in different directions are equal to each other, the strains are related with the frost heave ratio, as equation 2.

$$\xi = \varepsilon_x + \varepsilon_y + \varepsilon_z = 3\varepsilon_x \quad (2)$$

Here we assume the problem as a two-dimensional anisotropic problem with a plain strain condition. If ε_{1t} is the strain in the freezing direction, ε_{2t} is a strain in the other direction, as given in equation 3.

$$\beta = \frac{\varepsilon_{2t}}{\varepsilon_{1t}} \quad (3)$$

$$\xi = (1 + \beta)\varepsilon_{1t} \quad (4)$$

Simulation Method

In this simulation, a heat transfer calculation and a mechanical equilibrium analysis are carried out at each time step. The flow of the simulation is shown in Figure 1.

The aim of this research is to evaluate the interactive behavior between the chilled gas pipe and the frozen soil around it. This process can be divided into two parts: heat transfer analysis and mechanical equilibrium analysis. Before each time step, we need to analyze the initial condition and boundary condition. Following that, the distribution of temperature in the soil will be known in every step. One important thing in this process is that we need to consider the latent heat during freezing. Based on the temperature distribution, the freezing direction and freezing rate can be calculated. These are two critical parameters for evaluation of the frost heave ratio. With the help of freezing direction and the initial stress analysis, we can obtain the constraining stress in the freezing direction. At this point, all the parameters used in Takashi's model are ready. Consequently, applying Takashi's equation, we can get the frost heave ratio. Because this is a multi-dimensional problem, the anisotropic parameter β is introduced to distribute the frost heave ratio in each direction.

Calculation assumptions and modeling

In the simulation, the following assumptions are adopted:

- Soil is assumed to be fully saturated.
- Water absorbed for frost heaving is provided from the boundary.
- Water flow after thawing is not considered.
- Water migration is implicitly included in Takashi's equation. Then water pressure within the soil is not evaluated for the calculation of frost heave.

The finite element modeling is done as follows:

- All the FEM elements are modeled as two-dimensional solid elements.
- The stress-strain relationship of soil is assumed to be linear regardless of its temperature. Cracks in the element are also neglected.
- Plain strain condition is assumed.

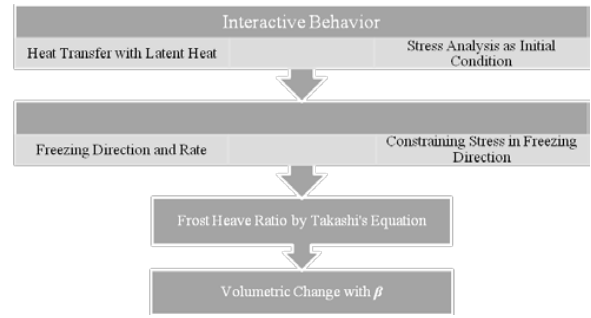


Figure 1. Flow chart of soil-pipeline interaction simulation.

Heat transfer calculation

The governing equation is given by equation 5:

$$\rho c \frac{\partial \theta}{\partial t} = \nabla(k \nabla \theta) \quad (5)$$

where ρ is the density, c is the characteristic heat of the material, k is the thermal conductivity, and θ is the temperature. By applying the Galerkin method to this governing equation, we can obtain the weak form formulation.

$$\rho c \int_A \frac{\partial \theta}{\partial t} \boldsymbol{\theta} \, d\mathbf{a} = \int_S q \boldsymbol{\theta} \, ndS - k \int_A \nabla \boldsymbol{\theta} \nabla \boldsymbol{\theta} \, d\mathbf{a} \quad (6)$$

For time step repetition, we adopted the Crank-Nicolson method, and the temperature at the next time step is computed implicitly.

In order to evaluate latent heat contained in the soil element, the equivalent heat capacity method is adopted. That idea is to give an additional heat capacity during the phase change equivalent to the latent heat. We introduce the solid phase limit temperature as T_s , and the liquid phase limit temperature as T_L . In addition, the latent heat of water is given as L (kcal/kg), and the weight of water in a unit volume of soil is expressed by m_w (kg). First the weight of water is calculated by the following equation using the void ratio and density of water:

$$m_w = \frac{e}{1+e} \rho_w$$

where e is the void ratio and ρ_w is the density of water. Then the soil heat capacity $c_p \rho$ is increased as the equivalent heat capacity $c_2 \rho$ with its latent heat when the temperature is between T_s and T_L .

$$\int_{T_s}^{T_L} c_2 \rho dT = L m_w + \int_{T_s}^{T_L} c_1 \rho dT \quad (7)$$

$$c_2 \rho = \frac{L m_w}{T_L - T_s} + c_1 \rho$$

We assume that T_L is equal to 0 and T_s is equal to -0.5 degrees in centigrade. As a result, the equivalent heat capacity method defines the relation between the heat capacity of soil and its temperature as Figure 2.

$$\rho C_{PE}(T_L - T_{t+\Delta t}) = \rho C_P(T_L - T')$$

$$T_{t+\Delta t} = T_L - \frac{C_P}{C_{PE}}(T_L - T')$$

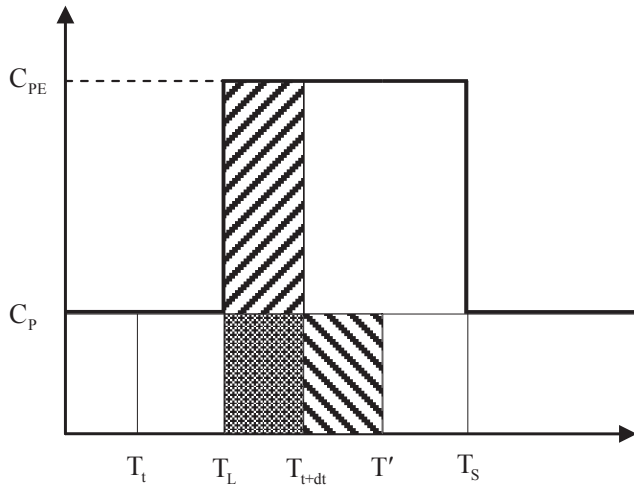


Figure 2. Equivalent heat capacity method.

The freezing direction and the freezing rate obtained by the heat transfer calculation are used to evaluate the frost heave ratio by Takashi's equation. The freezing direction α , the angle from x axis, can be calculated by equation 8 by using the temperature gradient at the center of an element after the heat transfer calculation.

$$\alpha = \tan^{-1} \frac{\partial \theta / \partial y}{\partial \theta / \partial x} \quad (8)$$

The gradient in temperature is also calculated as shown in equation 9.

$$\frac{\partial \theta}{\partial s} = \sqrt{\left(\frac{\partial \theta}{\partial x}\right)^2 + \left(\frac{\partial \theta}{\partial y}\right)^2} \quad (9)$$

If the temperature at this point changes from θ_t to $\theta_{t+\Delta t}$ during time duration of Δt , the freezing distance Δs is calculated as equation 10.

$$\Delta s = \frac{(\theta_t - \theta_{t+\Delta t})}{\partial \theta / \partial s} \quad (10)$$

Then the freezing rate U can be obtained as shown in equation 11.

$$U = \Delta s / \Delta t \quad (11)$$

According to the freezing direction, the confining stress can be computed by the mechanical analysis. The frost heave ratio and two-dimensional strains for a frozen element are given with the freezing rate.

Mechanical equilibrium analysis with frost heave

The FEM formulation for mechanical equilibrium is derived from the governing equations as shown below.

$$\frac{\partial \sigma_x}{\partial x} + \frac{\partial \tau_{xy}}{\partial y} + X = 0$$

$$\frac{\partial \sigma_y}{\partial y} + \frac{\partial \tau_{xy}}{\partial x} + Y = 0$$

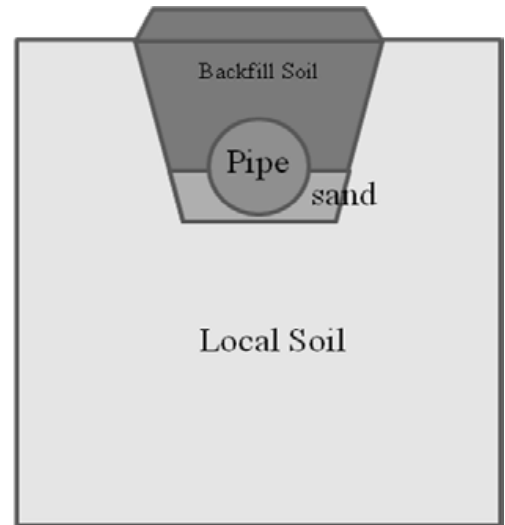


Figure 3. Cross sectional view.

The stress-strain relationship is given by equation 12 when we give the strain due to frost heave calculated by equation 1 and equation 4.

$$\{\sigma\} = [D]\{\{\varepsilon\} - \{\varepsilon_f\}\} \quad (12)$$

Here the D matrix is shown below under the plain strain condition.

$$[D] = \frac{E}{(1-\nu)(1-2\nu)} \begin{bmatrix} 1-\nu & \nu & 0 \\ \nu & 1-\nu & 0 \\ 0 & 0 & (1-2\nu)/2 \end{bmatrix}$$

Real Scale Experiment in Alaska

The primary purposes of this experiment were to evaluate the effects of differential frost heave and induced stresses in the pipe around the boundary between permafrost and non-permafrost. In this paper, however, only the two-dimensional problem is considered for comparison with analytical results, and consequently frost heave interaction at a cross section of the pipeline is analyzed. In December 1999, a 0.914-m-diameter, 105-m-long chilled pipeline with X65 grade and 9-mm wall thickness was constructed in Fairbanks, Alaska. The cross section is illustrated in Figure 3. Cold anti-freeze at almost -8°C was then run through the pipe, and a frost bulb was formed around the pipe with gradual frost heave. In this study, the frost heave at the bottom of the pipe is evaluated for comparison.

Simulation of Interactive Behavior

Calculation conditions and modeling

Due to the symmetry of the model, displacement in the x direction along the symmetric boundary is restricted and no heat flux through this boundary is assumed. The displacements of the outside boundary in x direction, where $x=5\text{m}$, are fixed and the temperatures are also assumed to be 0°C . At the bottom boundary of the model, displacements in the y direction are constrained and their temperatures are always set at 0°C .

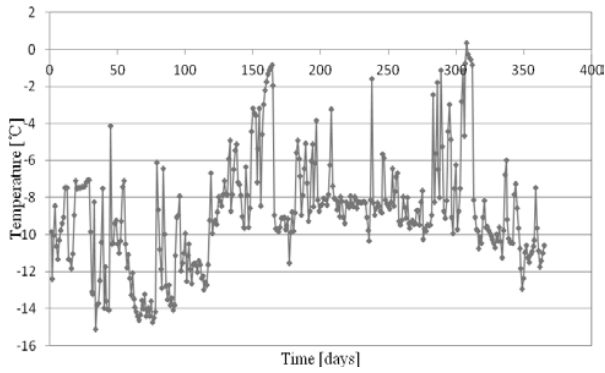


Figure 4. Real pipe gas temperature in the first year.

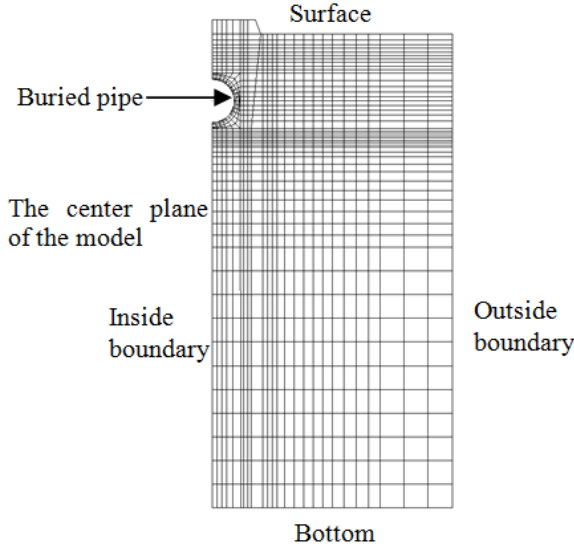


Figure 5. Meshing of numerical model.

On the top surface of the model, we give air temperature as 0°C with no restrictions in any direction for displacements. The frost bulb around the pipe is induced by the low temperature of the chilled gas. We adopted the real fluctuant temperature observed in the experiment as shown in Figure 4.

Figure 5 shows the meshing of the numerical model, and Figure 4 is the real fluctuant gas temperature in the pipe for the first year. The size of the model is 5m×10m.

Effect of anisotropic parameter β

Figure 6 and Figure 7 show the displacements at the bottom of the pipe. A comparison of results from Takashi’s model proposed in this study with the experimental results obtained in Alaska is presented in these figures. With an increase in β , the value of the calculated result decreases. When $\beta=0.75$, the simulation result is very close to the observed data in Alaska. $\beta=0.75$ means that most of the frost heave ratio is distributed to the vertical direction (4/7 of the frost heave ratio is distributed in the vertical direction and 3/7 is in the horizontal direction), which also proves that the soil is a kind of anisotropic material.

Figure 8 indicates the relationship between β and frost heave under the pipe. It is known that the vertical frost heave decreases when the value of β increases, which can be

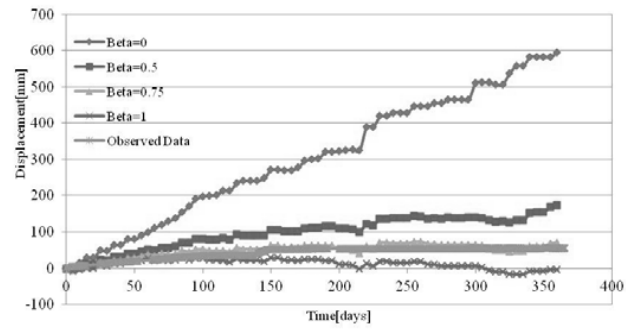


Figure 6. Comparison of different β values and the observed data (the frost heave under the pipe).

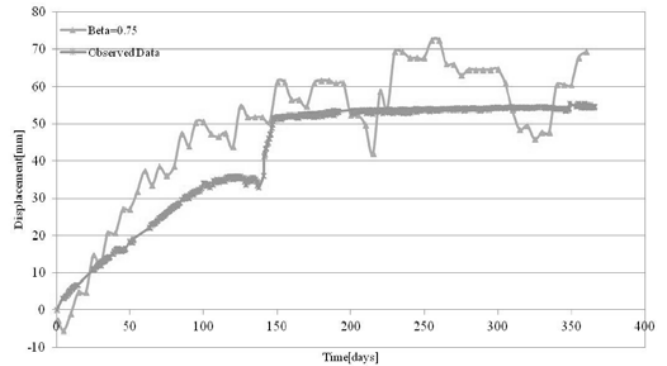


Figure 7. Comparison of calculation result with the observed data (when $\beta=0.75$).

Table 1. Material Properties.

| Properties | Local Soil | Sand | Steel (Pipe) |
|-------------------------------------|------------|----------|--------------|
| Elasticity E(N/m ²) | 2.80E+08 | 2.10E+11 | 2.80E+08 |
| Poisson’s ratio ν | 0.200 | 0.3 | 0.200 |
| Density ρ [kg/m ³] | 1900 | 7890 | 1550 |
| c[Whr/kg · K] | 0.28 | 0.48 | 0.28 |
| k[W/mK] | 1.00 | 45* | 1.00 |
| Water content | 0.25 | 0.000 | 0.25 |
| ξ_0 | 2.50E-02 | 0.000 | 2.79E-02 |
| σ_0 [N/m ²] | 800 | 0.000 | 0.000 |
| U_0 [m/hr] | 2.5E-04 | 0.000 | 0.000 |

* The heat conductivity of steel is 45 W/mK, but considering the Courant number, it is assumed to be 1. Because the thickness of the pipe is so thin, there is no obvious influence on the final result of the simulation.

explained by equation 4. Further, the relationship between β and frost heave is not linear.

Effect of thermal conductivity

The thermal conductivity k can obviously affect the freezing rate. Meanwhile, the freezing rate influences the frost heave ratio. Figure 9 illustrates the calculation results of frost heave at the bottom of the pipe with various soil conductivities k . When k is equal to 0.9 and 1.2, the computed frost heave is larger than those for the cases of $k=1.0$ and $k=1.1$. After

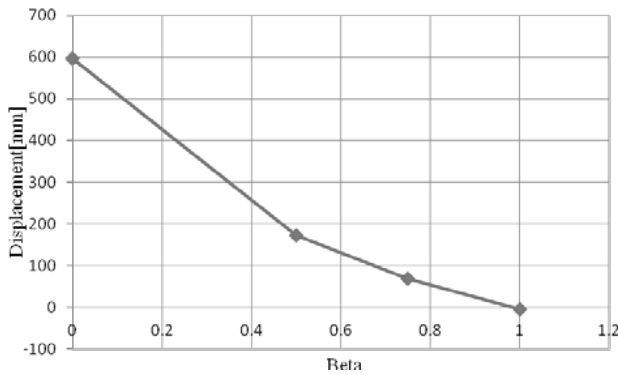


Figure 8. Relationship between β and frost heave under the pipe.

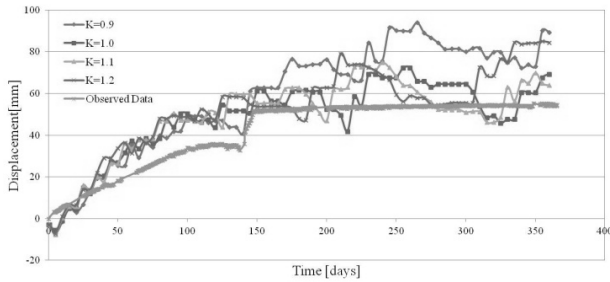


Figure 9. Chronicle relationship between thermal conductivity k and frost heave.

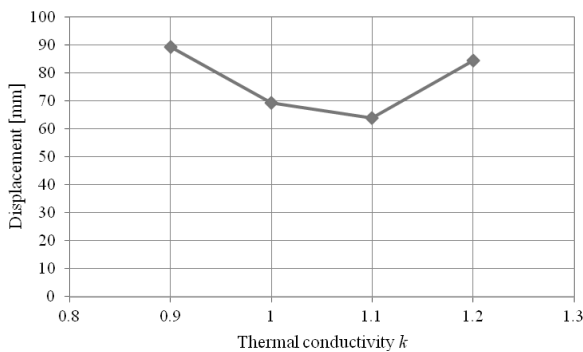


Figure 10. Relationship between thermal conductivity k and the maximum of frost heave.

comparison with the experimental results, it can be understood that $k=1.0$ or $k=1.1$ gives better estimation for the observed data. This trend is illustrated more clearly in Figure 10, which also demonstrates that the relationship between k and maximum frost heave is not linear.

These results can be explained by the freezing rate and the size of the frost bulb. If we assume a large thermal conductivity for soil, the freezing rate at the frozen front becomes faster. At the same time, it is natural that the size of the frost bulb goes up with an increase of thermal conductivity. The frost heave is calculated in this model as the product of the size of the frost bulb and the frost heave ratio. According to Takashi's equation, however, a large freezing rate leads to a small frost heave ratio. In Figure 11, the influence of thermal conductivity on the size of the frost bulb is presented. With an increase in k , the maximum size of the frost bulb becomes larger.

On the other hand, we introduced a new parameter to estimate the mean frost heave ratio, using the ratio of frost

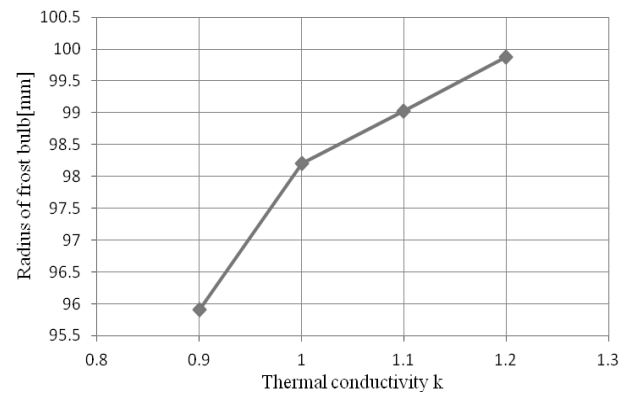


Figure 11. Relationship between thermal conductivity k and the maximum of frost bulb radius.

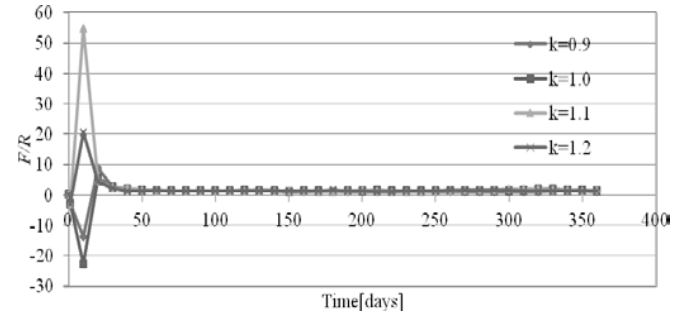


Figure 12. Chronicle relationship between thermal conductivity k and F/R .

heave to frost bulb radius, F/R . This value can be thought of as an average frost heave ratio at each time step. In Figure 12, the relationships between F/R and time with different k are presented. It is confirmed that thermal conductivity actually can significantly affect the frost heave. At the beginning stage, both frost heave and the frost bulb are very small, but the ratio between them is large. As time passed, this ratio converges to a specific value and it becomes stable.

Practical Significance of Test Results

According to the above discussions concerning the anisotropic parameter β and thermal conductivity k , two suggestions could be given for practical engineering:

- 1) The anisotropic property of local soil is important. An accurate estimation of β is critical for the prediction of frost heave. Thus some experiments are recommended in order to evaluate β during the design process. Based on our understanding of the anisotropic parameter β , it may have a significant relationship with the permeability of soil in different directions. This point should be verified in future studies.
- 2) According to our research concerning thermal conductivity, there is a critical point of k which can result in a minimal amount of frost heave. This is contrary to some previous research, which concluded that using some insulating material to wrap the buried pipe (which means decreasing the k value of the pipe and slowing the freezing rate) can decrease or even prevent the occurrence of frost

heave. According to our study, this may be not true. It requires further study to provide a definitive conclusion about what k value can lead to a minimal amount of frost heave.

Conclusion

In this research, a simulation model is proposed based on Takashi's equation, which is expanded into two-dimensional problems. The calculation results are compared with observed data from Alaska. After the influences of some parameters in this research are discussed, we obtained some important findings:

- Takashi's equation is successfully expanded to a multi-dimensional problem. The results of a numerical model based on Takashi's model are very similar to the observed data from Alaska.
- In this situation, $\beta=0.75$ is recommended for calculations. β is a very critical parameter and can significantly affect the results. If possible, some simple experiments and numerical calculations are recommended to determine a suitable value of β .
- Thermal conductivity k has a complex influence on frost heave. Through this research, we can make some conclusions concerning k . A large k can increase the size of the frost bulb, cause a faster freezing rate, but yield a small frost heave ratio.
- Occasionally, a critical thermal conductivity k may exist. If so, the frost heave becomes minimal.

For better estimation of the frost heave, several points need more consideration in future research.

- More analysis should be done concerning the freezing rate. Factors that can affect the freezing rate are the most important in estimating the frost heave.
- The actual fluctuating air temperature should be introduced. In this numerical model, it is assumed that the surface air temperature is 0°C , but it is indeed fluctuating with the change of seasons. If the fluctuating air temperature is introduced, we need to consider the thawing process in our program.
- Expanding this model into a three-dimensional problem should be considered.
- The differential heave along the pipe based on this model should be discussed in the future.

References

- ACPA, American Concrete Pavement Association.
- Bray, M.T. 2003. Field Observations of a Large Diameter Chilled Pipeline Experiment, Fairbanks, Alaska.
- Henry, K.S. 2000. A Review of the Thermodynamics of Frost Heave. Cold Regions Research and Engineering Laboratory. US Army Corps of Engineers. ADA381842.
- Huang, S.L., Bray, M.T., Akagawa, S., & Fukuda, M. 2004. Field Investigation of Soil Heave by a Large Diameter Chilled Gas Pipeline Experiment, Fairbanks, Alaska. ASCE, ISSN 0887-381X/20041-2-34.
- JGS. JGS 0171-2003. Japanese Geotechnical Standards.
- Kanie, S., Akagawa, S., Kim, K., & Mikami, T. 2006. Estimation Method of Frost Heaving for Chilled Gas Pipeline Buried in Frost Susceptible Soil. Current Practices in Cold Regions Engineering *Proceedings of 13th International Conference on Cold Regions Engineering. ASCE Conference Proceedings* 210, 33.
- Konrad, J.M. & Morgenstern, N.R. 1984. Frost Heave Prediction of Chilled Pipelines Buried in Unfrozen Soils. *Canadian Geotechnical Journal* 21, 1, pp. 100-115
- Konrad, J.-M. & Shen, M. 1996. 2-D frost action modeling using the segregation potential of soils. *Cold Regions Science and Technology* Vol. 24, pp. 263-278.
- Mikkola, M. & Hartikainen, J. 2001. Mathematical Model of Soil Freezing and Its Numerical Implementation. *International Journal for Numerical Methods in Engineering* Vol. 52, pp. 543-557.
- Nixon, J.F. (Derick). 1992. Discrete Ice Lens Theory for Frost Heave beneath Pipelines. *Can. Geotech. J.*29, pp. 487-497.
- Razaqpur, A.G. & Wang, D.Y. 1996. Frost-Induced Deformations and Stresses in Pipelines. *Int. J. Pres. Ves. & Piping* 69, pp. 105-118.
- Selvadurai, A.P.S., Hu, J., & Konuk, I. 1999. Computational Modelling of Frost Heave Induced Soil-Pipeline Interaction. *Cold Regions Science and Technology* Vol. 29, pp. 215-228.
- Taber, S. 1991. Frost heaving. *Journal of Geology*, vol. 37, pp. 428-461. In CRREL Special Report 91-23, *Historical Perspectives in Frost Heave Research*, USA Cold Regions Research and Engineering Laboratory, Special Report 91-23, pp. 9-26.
- Williams, P.J. 1988. *Pipelines and Permafrost: Science in a Cold Climate*. Oxford University Press, USA; 2nd edition.

Regional and Local Variability of Modern Natural Changes in Permafrost Temperature in the Yakutia Coastal Lowlands, Northeastern Siberia

A. Kholodov

*Geophysical Institute, University of Alaska Fairbanks, USA
Institute of Physical-Chemical and Biological Problems of Soil Science RAS*

D. Gilichinsky, V. Ostroumov, V. Sorokovikov, A. Abramov
Institute of Physical-Chemical and Biological Problems of Soil Science RAS

S. Davydov
North-East Scientific Station Pacific Institute of Geography FEB RAS

V. Romanovsky
Geophysical Institute, University of Alaska Fairbanks, USA

Abstract

Northern Yakutia is characterized by a cold continental climate (mean annual air temperature is from -10.6 to -13.5°C) and thick continuous permafrost. It is the most ancient permafrost in the Northern Hemisphere that was never completely thawed during the Quaternary period. A network of geothermal observations includes 10 boreholes located in different natural zones within the region. Mean annual ground temperature (MAGT) ranges from -12.3°C to -2.6°C , depending on latitude and landscape. Comparison of modern observations and published data shows that the most significant changes in permafrost temperatures took place on the Kolyma Lowland. Here permafrost temperature increased by 1.5 – 2°C since 1980. At the same time, the thermal state of permafrost in the western part of the region did not change until recent years. However, as observations show, temperature here is rising now by hundredths to tenths of a degree Celsius per year. At some sites, modern changes in the vegetation and micro-topography have led to a stabilization of permafrost temperatures.

Keywords: permafrost; mean annual ground temperature; climate change; Northern Yakutia.

Introduction

Permafrost continues to receive much attention as observed climate change brings it to the edge of widespread degradation and thawing in many regions (Romanovsky et al. 2008, 2010a, 2010b). Some regions, such as the area investigated here, are not expected to be subjected to permafrost degradation anytime soon, but it is still very important to record and understand the dynamics of the thermal state of permafrost. The arctic ecosystem in this region is extremely vulnerable, and therefore even a slight increase in active layer thickness induced by permafrost warming would lead to dramatic changes in the hydrological regime and in the entire ecosystem. Such an increase could be a trigger for hazardous natural processes such as thermokarst or landslides.

Northern Yakutia has the oldest permafrost in the Northern Hemisphere. The presence of middle Pleistocene ice bodies in Quaternary deposits in the region (Sher 1971, Andreev et al. 2011), as well as permafrost dating using the ^{36}Cl isotope (Gilichinsky et al. 2007, Blinov et al. 2009), confirm that permafrost here never completely thawed in the last 1 million years. Evidence suggests that local permafrost thaw has occurred only under lakes. The thermal state of permafrost in this region could be a good indicator of the scale of modern climate warming.

The recent increase of permafrost temperature is a climate-driven process. It is necessary to consider that regional

variations of atmospheric circulation, local landscapes, vegetation, topography, and hydrology can affect the response of permafrost to rising air temperature in different places.

Investigation Area

The study area covers the Arctic Ocean coastal zone from the Lena River delta to the Kolyma River. In the south, it is adjacent to the Verhoyansk-Kolyma mountain zone (Fig. 1).

Climate

Northern Yakutia is characterized by cold continental climate. The average mean annual air temperature over the last 30 years varied from -10.6 to -13.5°C (Fig. 2). Due to the influence of the ocean, there is no clear latitudinal air temperature zonality, although the amplitude of seasonal variation increases from 40.6°C at the sea shore (Tiksi) to 47.4°C inland (Chokurdah, Chersky).

The thickness of the snow cover at the end of winter usually does not exceed 0.2 – 0.3 m at the sea coast and 0.5 m in the continental part of the region. It is important to note that within the tundra zone, the thickness of snow cover is controlled mainly by wind redistribution, especially on hilltops.

In terms of air temperature dynamics, the period of the last 30 years can be divided into 2 stages: from 1980 to 1996–97, when the air temperature was relatively stable, and from 1997 to the present—the period of sustained warming. It is necessary

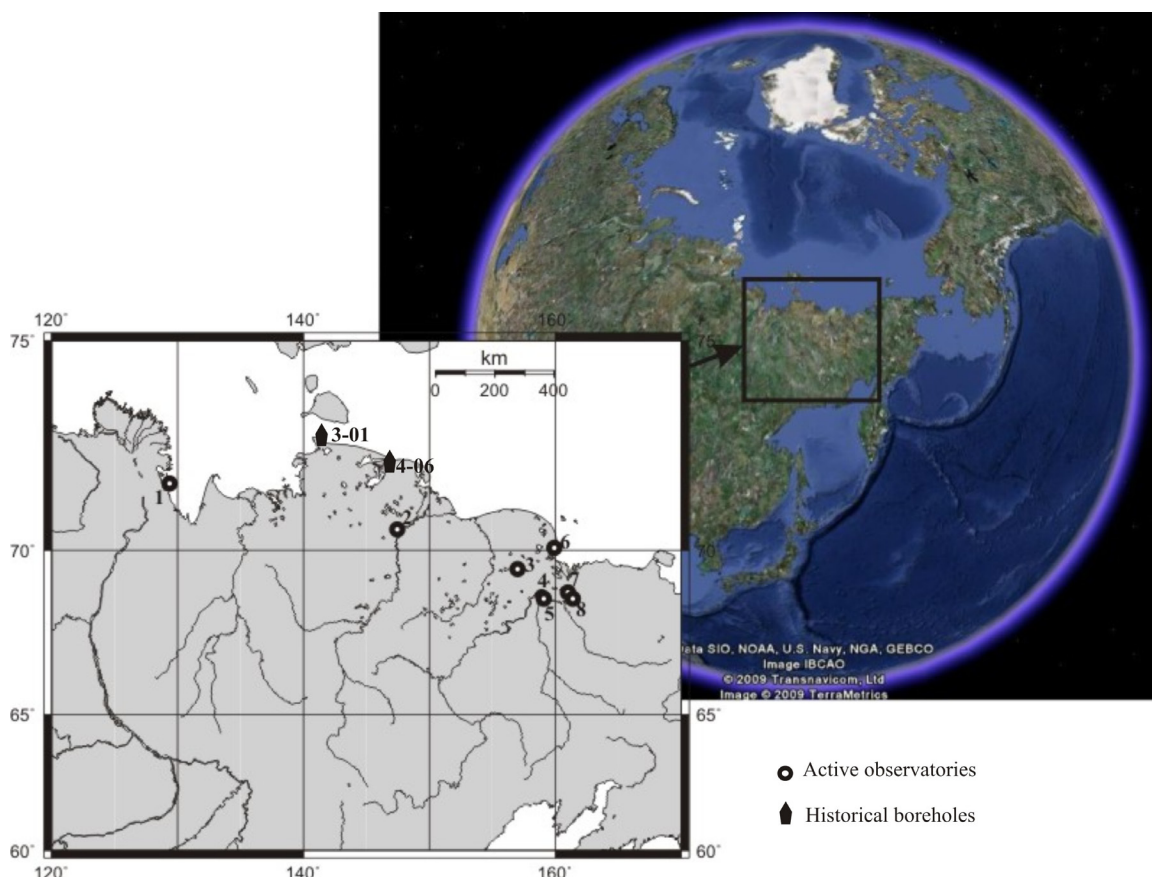


Figure 1. Map of investigated area with observation locations. Observatories: 1 – Bykovsky peninsula; 2 – Allaiha river; 3- Chukochya river; 4 – Omolon river mouth; 5 – Duvanny Yar; 6 – Chukochy cape; 7 – Ahmelo lake; 8 – Amboliha channel.

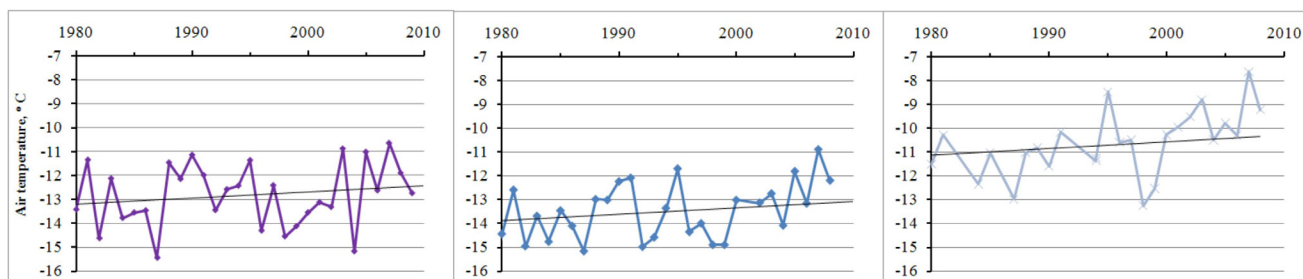


Figure 2. Mean annual air temperature records at the meteorological stations of the region: Tiksi (left), Chokurdah (center), and Chersky (right).

to note that the increase in the mean annual air temperature in the western part of the region was caused mainly by winter warming, while the increase in the eastern part was due to both winter and summer warming.

Typical landscapes

The modern topography of the region represents the remnants of the Late Pleistocene accumulation plain, called “Yedomá” after the name of the sediments that compose this plain. Elevations are from 20 to 60 m a.s.l. It is dissected by thermokarst depressions or “alases” (with elevations from 2 to 20 m a.s.l.), gullies, and valleys of rivers and streams (up to 5 m a.s.l.).

Various vegetation types are found in the region, including tundra in the northwestern and northern parts of the region

(sites 1, 2, 3, 6, and both historical boreholes) and boreal forest in the southeastern part (sites 4, 5, and 7). Willow shrub vegetation is typical for rivers and stream valleys (site 8).

Most of the observation sites are characterized by polygonal ground patterns. Tussocks are common only on the floodplains of rivers and streams.

Permafrost conditions

Northern Yakutia is a continuous permafrost region with permafrost thickness of 300 to 700–800 m (Geocryology of USSR 1989). Closed taliks up to 50–60 m deep can be found only under lakes and large rivers.

Active layer thickness is 0.3–0.6 m and up to 1 m at some locations. The MAGT in terrain dominated by late Pleistocene watersheds varies from -12.3°C at 72°50'N, to -9.9°C at

69°30'N. Within alas depressions, MAGT is somewhat warmer (-10°C at 71°40'N and -7°C at 68°50'N). Despite the absence of air temperature latitudinal zonality, mean annual ground temperature decreases by approximately 1°C per 1° of latitude. This can be explained by the previously mentioned difference in snow thickness and by the northward decreasing seasonal air temperature variation, which reduces the warming effect of snow on permafrost temperature (Ershov 1989). From a rough estimate using the Kudryavtsev approach (Kudryavtsev 1974), the warming influence of the snow is 0.5 to 1.5°C in the northwestern part with a relatively maritime climate, while in the southern and eastern parts with a more continental climate it is 3.5 to 4.5°C.

The upper part of the geological cross-section is composed of ice-rich sediments with large ice bodies. This makes permafrost very sensitive to any changes in surface conditions such as warming or surface disturbances.

Methods and Equipment

The main method used to conduct this study involved temperature measurements from boreholes located at sites that are representative of a range of different natural conditions. Currently, the observational network includes 2 historical (mea-

sured once and not instrumented for long-term observations) and 10 active boreholes located at 8 sites (Fig. 1).

We used two types of measurement strategies:

- 1) Long-term, high-frequency (hourly to daily) continuous observations in boreholes.
- 2) Occasional or periodic measurements in deep boreholes (if possible annually or more frequently).

The second type of observation was used until 2006. Since then, within the framework of IPY Project #50 “Thermal State of Permafrost” (Brown et al. 2010), boreholes have been instrumented for continuous observations.

HOBO U12 (4-channel) and HOBO U23 (2-channel) dataloggers with TMC-HD thermistors designed and produced by Onset Computer Corp. have been used as standard equipment. The high resolution and accuracy ($\pm 0.02^\circ\text{C}$) of this equipment allow us to obtain precise temperature records and to register even slight changes in permafrost temperature that are very important for a short period of observation.

Before installation, the equipment was calibrated at 0°C using the ice-bath method (i.e., in a eutectic mixture of crushed ice or snow and distilled water).

Each borehole was instrumented with one HOBO U12 datalogger. Additionally, near 7 of the 10 boreholes, HOBO

Table 1. Observation borehole inventory.

| Borehole ID | Site # (fig. 1) | Equipment | Sensor spacing | History of observations | Current monitoring status |
|-------------|-----------------|----------------------------|---|--|---------------------------|
| RU_06_0002 | 1 | HOBO U12 | 5; 10; 15; 26 m | Observed occasionally since 2003, instrumented for continuous measurements since 2007. Destroyed in 2009, recovered in 2010. | Active |
| RU_06_0003 | 1 | 2 of HOBO U23; HOBO U12 | 0.05, 0.2, 0.3, 0.5 m 3; 5; 10; 15 m | Observed occasionally since 2004, instrumented for continuous measurements since 2006. Destroyed in 2009, recovered in 2010. | Active |
| RU_06_0005 | 2 | 2 of HOBO U23; HOBO U12 | 0, 0.1, 0.2, 0.6 m 3, 5, 10, 15 m | Continuous measurements 2006-2007. Destroyed in 2008, recovered in 2010. | Active |
| RU_06_0008 | 6 | 2 of HOBO U23; HOBO U12 | 5, 10, 15, 25 m | Annual measurements in 2002 and 2006. Continuous since 2007 | Active |
| RU_06_0013 | 4 | 2 of HOBO U23; HOBO U12 | 5, 10, 15, 25 m | Continuous measurements since 2007. | Active |
| RU_06_0014 | 8 | HOBO U12 | 4, 10, 14, 21 m | Monthly measurements in 1980. Recovered for continuous measurements in 2007. | Active |
| RU_06_0015 | 7 | 2 of HOBO U23; HOBO U12 | 3, 5, 10, 16 m | Continuous measurements since 2007. | Active |
| RU_06_0017 | 5 | HOBO U12 | 5, 10, 15, 25 m | Continuous measurements since 2008. | Active |
| RU_06_0018 | 3 | HOBO U12 | 3, 5, 10, 15 m | Annual measurements during 1979-82 and 1990-92. Recovered for continuous observations in 2009. | Active |
| RU_06_0019 | 1 | HOBO U12 | 0, 1.5, 3, 5 m | Annual measurements during 2001-2005. Recovered for continuous observations in 2010. | Active |
| 3_01 | 3_01 | Thermistor string | | Measured once in 2001. | Not active |
| 4_06 | 4_06 | Thermistor string | | Measured once in 2006. | Not active |

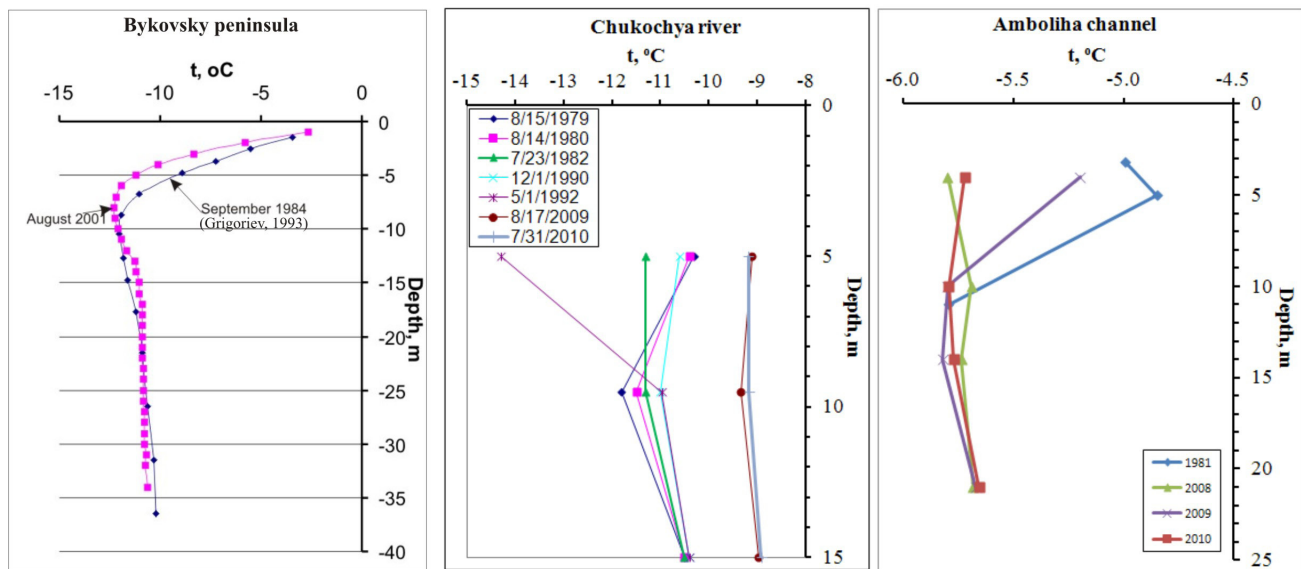


Figure 3. Comparison of the modern observation results with historical data at the observation sites 1 (left), 3 (middle) and 8 (right) (see Fig. 1 for site locations).

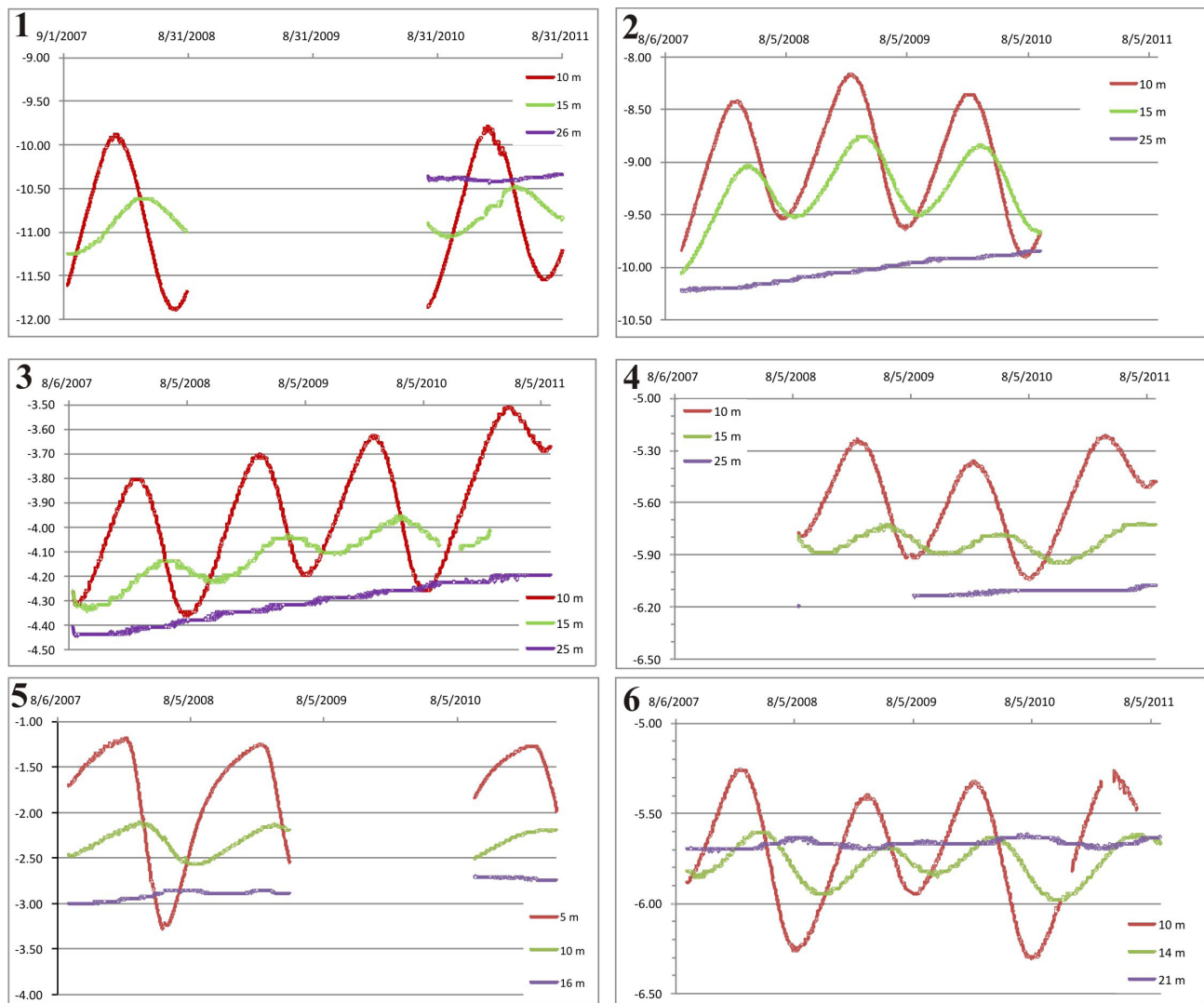


Figure 4. Permafrost temperature dynamics at the observation sites located at the tundra (upper panel); boreal forest (middle), and the Kolyma river valley (lower). Boreholes: 1 – RU_06_0002; 2 –RU_06_0008 ; 3 – RU_06_0013; 4 – RU_06_0017; 5 – RU_06_0015; 6 – RU_06_0014 (see Table 1 for borehole descriptions).

U23 2-channel loggers were installed in the active layer. For sensor spacing, see Table 1.

Most boreholes (7 of 10) are associated with CALM grids for active layer thickness monitoring (Fedorov-Davydov et al. 2004).

Results and Discussion

Comparison of modern results with historical and published data (Fig. 3) shows that the permafrost temperature in the region was stable until the beginning of the twenty-first century, as is typical for central and eastern Siberia (Romanovsky et al. 2008, 2010a).

Climate warming effects became apparent at the end of the 1990s (Fig. 2) and induced an increase in permafrost temperature. The most significant changes are observed on the Kolyma Lowland, where permafrost temperature increased by 1.5–2°C since 1980.

Results of the modern observations are shown in Figure 4. Recent dynamics of MAGT in the region are similar to those of the entire Northern Hemisphere (Romanovsky et al. 2010b). Most monitoring sites show a sustained positive trend in permafrost temperature at the bottom of the layer of seasonal temperature variations during the last several years.

The most significant changes are apparent within the tundra zone near the Arctic Ocean. Here the rate of MAGT increase at depths of 15 and 25 m is up to 0.2°C per year (Fig. 4, upper panel). In the boreal forest zone, permafrost warming does not exceed 0.1°C per year (Fig. 4, middle panel).

An observational site, located in the Amboliha channel of the Kolyma River floodplain and characterized by tussock micro-topography, is the only spot where the MAGT is relatively stable. It is also one of the places in the Chersky vicinity with the coldest permafrost. Comparison of the 1980 data and modern observations does not show any significant changes (Fig. 3-right, see also Fig. 4-6). This can be explained by snow redistribution at the beginning of the winter season in this type of landscape. At the beginning of snow cover formation, and until the snow thickness is less than tussock height, the tussock sides are open to the impact of cold air; this results in very fast active layer freezing and permafrost cooling. During the last 30 years, tussock grooving was observed at the Amboliha research site. This makes the duration of this process longer because it takes more time for snow to completely cover all the tussocks. This leads to a decrease in the average winter ground temperature and reduction of the impact of warming air.

Conclusions

Based on observations and analysis of published data, the following conclusions can be made.

- Modern mean annual ground temperature in this region varies across a wide range from -12.3°C to -2.6°C.
- Despite the absence of a latitudinal zonality in the air temperature, the reduced warming influence of snow at coastal sites in this region leads to a northward decrease in mean annual permafrost temperature (1°C per 1° of latitude).

- Permafrost temperatures in this region did not change significantly from 1980 to the end of the twentieth century. However, a permafrost warming trend is very noticeable over the entire region over the last several years, with a rate of increase in the mean annual ground temperature of up to 0.2°C per year.
- Climate-affected local changes in ecosystems, especially vegetation and micro-topography, can reduce the warming effect on permafrost temperature within some specific landscapes.

Acknowledgments

This project is supported by NSF (ARC-0520578, ARC-0632400, and ARC-0856864) and joint RFBR-CRDF project RUG1-2986-PU-10.

The observational data presented in this paper are available to download at the CADIS data portal (www.aoncadis.ucar.edu).

References

- Andreev, A., Schirrmeister, L., Tarasov, P., Ganopolsky, A., Brovkin, V., Siegert, C., Wetterich, S., & Hubberten, H.-W. 2011. Vegetation and climate history in the Laptev Sea region (Arctic Siberia) during Late Quaternary inferred from pollen records. *Quaternary Science Reviews* (in press).
- Blinov, A., Alfimov, V., Beer, J., Gilichinsky, D., Schirrmeister, L., Kholodov, A., Nikolsky, P., Opel, T., Tihomirov, D., & Wetterich, S. 2009. Ratio of $^{36}\text{Cl}/\text{Cl}$ in ground ice of East Siberia and its application for chronometry. *Geochemistry, Geophysics, Geosystems* 10. Q0AA03.
- Brown, J., Kholodov, A., Romanovsky, V., Yoshikawa, K., Smith, Sh., Christiansen, H., Viera, G., & Noetzi, J. 2010. The Thermal State of Permafrost: the IPY-IPA snapshot (2007-2009). *Proceedings of the 63rd Canadian geotechnical conference & 6th Canadian permafrost conference*, Calgary, Canada, September 12-16.
- Ershov, E.D. (ed.). 1989. *Geocryology of USSR. East Siberia and far East*. Moscow, Nedra publ., 515 pp.
- Fyodorov-Davydov, D., Sorokovikov, V., Ostroumov, V., Kholodov, A., Mitroshin, I., Mergelov, N., Davydov, S., Zimov, S., & Davydova, A. 2004. Spatial and Temporal Observations of Seasonal Thaw in the Northern Kolyma Lowland. *Polar Geography* Vol. 28, No. 4: 308-325
- Gilichinsky, D., Nolte, E., Basilyan, A., Beer, J., Blinov, A., Lazarev, V., Kholodov, A., Meyer, H., Nikolsky, P., Schirrmeister, L., & Tumskpy, V. 2007. Dating of syngenetic ice wedges in permafrost with ^{36}Cl and ^{10}Be . *Quaternary Science Reviews* 26. pp. 1547-1556.
- Grigoriev, M.N. 1993. *Kriomorphogenesis of the Lena river mouth region*. Yakutsk, Permafrost Institute SB RAS, 173 pp. (in Russian).
- Kudryavtsev, V.A. 1974. *Basics of the permafrost forecast for engineering researches*. Moscow, MSU publ., 432 pp.

- Romanovsky, V.E., Kholodov, A.L., Marchenko, S.S., Drozdov, D.S., Malkova, G.V., Moskalenko, N.G., Vasiliev, A.A., Sergeev, D.O., & Zheleznyak, M.N. 2008. Thermal state and fate of permafrost in Russia: first results of IPY. In *Proceedings of the Ninth International Conference on Permafrost*. Edited by D.L. Kane and K.M. Hinkel. Fairbanks, Alaska. Institute of Northern Engineering, University of Alaska Fairbanks, Vol.2, pp. 1511-1518.
- Romanovsky, V.E., Drozdov, D.S., Oberman, N.G., Malkova, G.V., Kholodov, A.L., Marchenko, S.S., Moskalenko, N.G., Sergeev, D.O., Ukrainsteva, D.G., Abramov, A.A., & Vasiliev, A.A. 2010a. Thermal state of permafrost in Russia. *Permafrost and Periglacial Processes* 21: 106-116.
- Romanovsky, V.E., Smith, S.L., & Christiansen, H.H. 2010b. Permafrost thermal state in the polar Northern Hemisphere during the International Polar Year 2007-2009: a synthesis. *Permafrost and Periglacial Processes* 21: 106-116.
- Sher, A.V. 1971. *Mammals and Pleistocene stratigraphy of the extreme Northeast of the USSR and North America*. Moscow. Nauka publ.

Modeling Permafrost Response of the Last Glacial Termination: First Results of the VAMPER Model

D.C. Kitover, H. Renssen, R.T. Van Balen, J. Vandenberghe
Vrije Universiteit Amsterdam, The Netherlands

Abstract

This paper introduces the VAMPER model, a 1-D numerical finite-difference permafrost model designed for eventual coupling with an earth system model of intermediate complexity (EMIC). The purpose of such coupling is to examine the relationship between permafrost and climate at millennial timescales with specific focus on possible feedback effects of a changing permafrost regime. First results here include 1) an equilibrium experiment where the VAMPER model simulated the current depth of permafrost at Barrow, Alaska; 2) validation of the VAMPER model by comparing results to two other previously published models; and 3) a deglaciation transient experiment done for Wyoming, USA, forced by surface temperatures from the EMIC LOVECLIM.

Keywords: Barrow; climate model; deglaciation; permafrost; permafrost evolution; Wyoming.

Introduction

According to the 2007 report from the Intergovernmental Panel on Climate Change, permafrost has experienced both degradation and warming in recent decades (Lemke et al. 2007). Because the governing factor influencing permafrost growth and decay is surface temperature, it is expected that these recent changes are primarily due to Earth's current warming (Nelson 2003, Osterkamp 2007). Apart from increased atmospheric emissions (Zimov et al. 2006) and increasing ground water flow due to a thickening active layer (Hinzman & Kane 1992), an additional positive feedback effect comes from the energy balance at the surface. Because frozen ground provides an additional heat buffer via latent heat exchange, degrading permafrost reduces the long-term heat sink of the subsurface, which leads to warmer surface and air temperatures.

An important consideration for examining the interaction between climate and permafrost is the time period; ideally model simulations should run at millennial timescales. This is because permafrost has a relatively slow response time, taking up to tens of thousands of years to acquire a new thermal equilibrium when there is a significant climate change (Lunardini 1995). However, there have been only a handful of studies that have numerically modeled permafrost dynamics over geologic time periods. Kukkonen & Šafanda (2001) looked at permafrost formation during the Holocene in Northern Fennoscandia. Osterkamp & Gosink (1991) used a paleotemperature model of Prudhoe Bay, Alaska, to simulate permafrost depths during the last 120 k years. Delisle et al. (2003) modeled permafrost conditions during the Weichselian in Western and Central Europe. And more recently, Mottaghy & Rath (2006) ran their permafrost model for 150 k years to test the inferred ground temperature history for a borehole in Poland.

It is clear that more research is needed to investigate the long-term effect of permafrost on climate. To address this gap, the Vrij Universiteit Amsterdam Permafrost (VAMPER) model has been designed to simulate deep permafrost and

later be coupled with an existing Earth System Model of Intermediate Complexity (EMIC) called LOVECLIM (Goosse et al. 2010). It is then anticipated that some or all of the abovementioned feedback implications, and thus the role of permafrost in the climate system, can be more closely examined. The objective of this paper is to demonstrate the capability of the VAMPER model as a stand-alone permafrost model, simulating permafrost growth/decay at millennial timescales. Since it is capable of taking a variety of input data from the LOVECLIM suite of modules, it is thus ready to be coupled with LOVECLIM. After description of the model, it is calibrated by simulating the current depth of permafrost at Barrow, Alaska, USA. The model is then validated by comparing results to two similar studies of Delisle (1998) and Osterkamp & Gosink (1991). Finally, a deglaciation experiment is performed using surface temperature forcings from LOVECLIM for a location in Wyoming, USA. Similar to many sites that exhibit cryogenic features such as ice and sand pseudomorphs, Wyoming is a region where permafrost likely formed during the last glacial period and then degraded in postglacial times (French 2007, Nissen & Mears 1990).

Methods

The VAMPER model is built with the underlying motivation to couple it with LOVECLIM 1.2, a three-dimensional Earth system model of intermediate complexity (Goosse et al. 2010). Specifically, the VAMPER model will be coupled via the surface heat budget calculation of the land-surface construct of the atmosphere component ECBilt. Therefore, the thermal energy calculations will be made at the same resolution as in ECBilt, which is approximately 560 km x 560 km. Due to this large areal size of grid cells, it is not necessary to go beyond a 1-D vertical solution for resolving permafrost.

The permafrost model is based on the heat conduction equation:

$$\rho C_p \frac{\partial T}{\partial t} = \frac{\partial}{\partial z} \left(K_e \frac{\partial T}{\partial z} \right) \quad (1)$$

where T is temperature (Kelvin), K_e is thermal conductivity (W/mK), ρ is density (kg/m³), and C_p is specific heat capacity (J/kg K). Radiative and convective heat transport are neglected.

Latent heat effect

Permafrost dynamics involve phase change during freezing and thawing. Therefore, the latent heat released (absorbed) during freeze (thaw) must be considered. This problem is treated using the apparent heat capacity method (Williams & Smith 1989, Zhang et al. 2008). With this method, the heat capacity is replaced by an effective heat capacity, which accounts for the additional heat released or absorbed during phase change. The amount of added heat capacity is a function of the temperature-water content relationship where freezing/thawing occurs over a given temperature range. To incorporate effective heat capacity, we follow the approach used by Mottaghy & Rath (2006). The percent liquid water content (θ) is assumed to be a continuous function of temperature in a specified freezing/thawing range (w) in the following equation (Mottaghy & Rath 2006 taken from Lunardini 1987):

$$\dot{E} = \begin{cases} \left(\exp \left[- \left(\frac{T - T_f}{w} \right)^2 \right] \right) & T < T_f \\ 1 & T \geq T_f \end{cases} \quad (2)$$

where T_f is the freezing temperature.

If T is above T_f , the effective heat capacity is determined using a weighted average of the mass heat capacities of soil (C_m) and liquid water (C_w):

$$C_p = (1-n)\rho_m C_m + n\rho_w C_w \quad (3)$$

In equation 3, subscript 'm' stands for matrix (i.e., solid particles) and 'w' for water. Porosity (n) is expressed as a fraction of 1.

If T is in the freezing/thawing range, two additional terms are added in the heat capacity calculation as shown in equation 4 below:

$$C_p = (1-n)\rho_m C_m + n\theta\rho_w C_w + (n-n\theta)\rho_f C_f + n\rho_w L \frac{d\theta}{dT} \quad (4)$$

where L is the latent heat of fusion (kJ/kg) and the subscript f stands for ice (frozen). The last two terms represent the heat capacity of ice and the latent heat released (absorbed) as the soil freezes (thaws).

Typically, $d\theta/dT$ is empirically determined from soil freezing curves, which vary based on soil type (Williams & Smith 1989). However, Mottaghy & Rath (2006) found that by using the derivative of equation 2, a smoother function can be applied:

$$\frac{d\theta}{dT} = \begin{cases} - \frac{2(T-T_f)}{w^2} \exp \left[- \left(\frac{T-T_f}{w} \right)^2 \right] & T < T_f \\ 0 & T \geq T_f \end{cases} \quad (5)$$

In the VAMPER model, the thermal conductivity, K_e , is also dependent on temperature. Using a geometric mean from Farouki (1986) the effective thermal conductivity (K_e) is calculated as follows:

$$K_e = K_m^{1-n} K_f^n - \theta K_w \quad (6)$$

Farouki (1986) reports that equation 6 gave similar results to the De Vries' method, the other most commonly used parameterization in estimating thermal conductivity in frozen soil models (Zhang et al. 2008). The assumption with this method is that soil is saturated. In the stand-alone version of the VAMPER model, saturated soil is the only option. However, when coupled to LOVECLIM, where more variable soil conditions may occur, a modified version of the Johansen method (Farouki 1986) will be followed.

For simplicity, porosity is assumed to be a function of depth using a common exponential depth-porosity equation (e.g., Sclater & Christie 1980):

$$n = \varphi e^{-0.00395 d} \quad (7)$$

where d is depth (m) and φ is porosity at the surface. Groundwater flow is neglected, and soil water content therefore remains constant. Similar to soil saturation discussed above, this assumption will change when coupled to LOVECLIM, where a bucket model already exists. It is anticipated that in the least a multi-layered soil hydrology module will be integrated to replace the top layers of soil within the VAMPER model and, likewise, the bucket model within LOVECLIM. This improvement would allow limited vertical subsurface flow.

Numerical solution

The heat conduction equation is solved numerically using a volume-centered implicit finite difference scheme with variable grid spacing. The bottom boundary condition is the geothermal heat flux. The upper boundary is the ground surface temperature provided by LOVECLIM.

Spatial/temporal resolution

Linking the VAMPER model to LOVECLIM implies some unique prerequisites for the spatial parameterization. The soil profile should be deep enough to allow the potential aggradation and degradation of permafrost through glacial/interglacial transitions. The depth is thus set to 1000 meters, following the guidelines from Alexeev et al. (2007). On the other hand, the model should also be able to capture seasonal changes at the surface and active layer. Considering that the active layer usually stays within 0.5 to 2 meters below the surface (Williams & Smith 1989), the spatial parameterization in the first two meters is at 10-cm spacing. Beyond this point, the spatial resolution becomes progressively coarser with depth on a logarithmic scale.

As the different model components of LOVECLIM run at varying time steps, the VAMPER model calculates at a monthly time step, which is the maximum temporal resolution to capture the seasonal response but is still computationally efficient.

Because the VAMPER model will eventually be coupled to an already existing land-surface system and a vegetation model, VECODE (Brovkin et al. 2002) within LOVECLIM, the effects of snow cover and vegetation will be applied upon coupling. They are therefore not included in the stand-alone version. Similarly, LOVECLIM already has a mechanism to calculate surface runoff.

Results and Discussion

Calibration using present-day simulation

An equilibrium experiment was performed at Barrow, Alaska, USA ($71^{\circ}18'N$, $156^{\circ}47'W$) to model the current estimated permafrost thickness. This site was chosen because there is sufficient available knowledge including 1) a monthly surface temperature series from Hinkel (1998) covering the years 1993 to 2004, 2) an estimated geothermal heat flux of 56 mW/m^2 from Lachenbruch et al. (1982), and 3) a known permafrost thickness of 350–400 m (Lachenbruch et al. 1982). There have been previous studies attempting to model permafrost at Barrow (Nakano & Brown 1971, Zhang & Stamnes 1998, Ling & Zhang 2004), but they kept their scope to the active layer and near-surface permafrost. The VAMPER model will capture the entire thickness. The soil temperature data for this study were collected by sensors at 1 cm below the surface (Hinkel 1998). This depth was assumed to be characteristic of surface temperature and therefore used as the upper boundary condition in the VAMPER model. The average annual temperature of this dataset is approximately -8°C , which is a few degrees warmer than the equilibrium surface temperature interpreted by Lachenbruch et al. (1982).

The VAMPER model found an equilibrium depth of permafrost at 420 m (Fig. 1a). This result is reasonably close to the estimated thickness, given the uncertainties in the observed Barrow data (see Hinkel 1998) and warming during the last century (Lachenbruch et al 1982).

Figure 1b shows the top 30 m where the active layer is approximately 1 m thick and the depth of zero annual amplitude is 15–20 m. Although the latter of these two attributes is close to expected values according to Williams & Smith (1989), the active layer thickness is modeled deeper than the actual 35 cm near the surface (Hinkel et al. 2001). It is likely that this deeper active layer is due to the absence of an organic layer within the VAMPER model. The organic layer serves as a buffer to subsurface warming due to its low thermal conductivity. However, testing the impact of an organic layer within the model is beyond the scope of this paper.

Validation

The VAMPER model was validated by comparing results with other models specifically parameterized for paleoclimate experiments. The two studies used are those of Osterkamp & Gosink (1991) and Delisle (1998). Both applied numerical approximation schemes of the heat equation (1) to simulate permafrost growth and decay over millennia, expressed in values of permafrost thickness. The values of the model parameters used in the studies and subsequently applied in the VAMPER model are listed in Table 1.

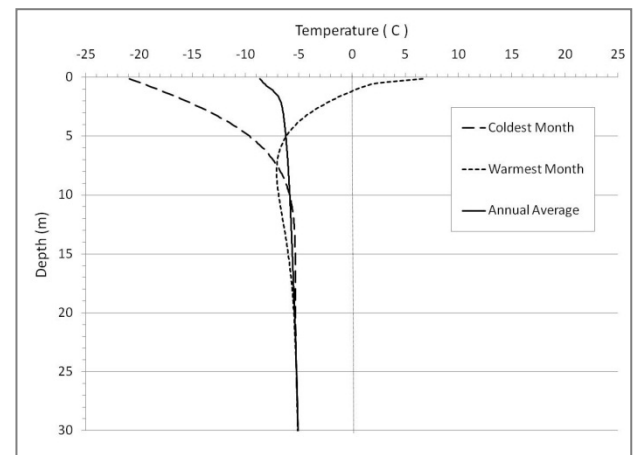
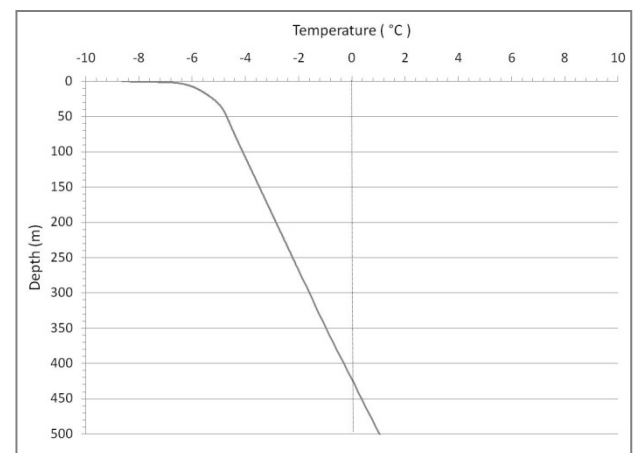


Figure 1. a) VAMPER model results for Barrow, AK showing the equilibrium temperature-depth profile 500 m deep and b) the top 30 m.

Table 1. Model parameters for each study as applied in simulations of the VAMPER model.

| Model Parameters | Osterkamp & Gosink (1991) | Delisle (1998) |
|----------------------|----------------------------|--------------------------------|
| Time period | 120 ka – Present | 50 ka – 8 ka |
| Time step | 100 years | 100 years* |
| Thermal conductivity | $K_e = 3.39 \text{ W/mK}$ | $K_e = 2.2 \text{ W/mK}$ |
| Porosity | $n = 0.40$ | $n = 0.30$ |
| Geothermal heat flux | 57 mW/m^2 | 60 mW/m^2 |
| Freezing temp. | $T_f = -1^{\circ}\text{C}$ | $T_f = 0.0001^{\circ}\text{C}$ |

Osterkamp & Gosink (1991) applied a near-surface paleotemperature model based on geological reconstructions from Brigham & Miller (1983) adjusted for Prudhoe Bay, Alaska, over the last 120,000 years to achieve the current state of permafrost. This temperature series (applied in two repeating cycles) was the forcing for the VAMPER model simulation. First, the model was spun-up to achieve an initial permafrost depth similar to that of Osterkamp & Gosink (1991): approximately 710 m, as compared to theirs of 630 m. Figure 2a shows this initial state at 240 ka with results of

the transient simulation. As Osterkamp & Gosink (1991) point out, the effect of initial conditions is more prominent in the first cycle of forcing (240–120 ka) than the following 120,000 years (120–0 ka) when the temperature series is repeated.

For the second study, the VAMPER model was run according to the same model configuration and temperature curve of Delisle (1998), who simulated permafrost behavior in western Europe during the Weichselian/Wisconsinian glacial (MIS 2–4) (Fig. 2b). The model was first spun-up to achieve equilibrium conditions with a constant annual average surface temperature of 0°C and lower boundary heat flux, which was specified by Delisle (1998).

As is evident from Figure 2, the VAMPER model is able to reproduce reasonably well the long-term growth and decay of permafrost of the two previous model studies. There are reasons why the results of the VAMPER model differ from Osterkamp & Gosink (1991) and Delisle (1998). Particularly, we had no insights for the code produced by either of these models, and therefore it is likely that the equations used are somewhat different than in the VAMPER model. Additionally, Delisle (1998) does not disclose how latent heat is treated and therefore it is assumed that the VAMPER model is likely different in this respect. This is also the case for Osterkamp & Gosink (1991) who use an apparent heat capacity approach but presumably not a continuous function to characterize the freezing temperature range, as described in the Methods section. In summary, validation of the VAMPER model is considered successful.

Deglaciation experiment

To demonstrate how the VAMPER model responds during a climate change scenario, a transient experiment was performed during the last deglaciation. The site is in Wyoming, USA (41°31'N, 106°52'W), where permafrost is believed to have formed during the late Pleistocene, as evidenced from sand wedges and other periglacial indicators (Nissen & Mears 1990). The first 12,000 years (21 ka–9 ka) of monthly surface temperatures used to force the VAMPER model come from a published LOVECLIM model setup parameterized specifically for the warming period following the Last Glacial Maximum (LGM) beginning approximately 21,000 years (ka) BP (Roche et al. 2011). The aim of Roche et al. in this transient LOVECLIM experiment was to capture the long-term deglaciation trend.

A present-day (1998–2008) evaluation of LOVECLIM's accuracy in capturing Wyoming surface temperatures revealed an annual average warm bias of approximately 6°C. LOVECLIM temperatures were checked against observational data from the National Resources Conservation Services (NRCS) soil temperature monitoring station Torrington #1 (site no. 2018) in southeast Wyoming (42°4'N, 104°7'W). This observation site was used because historic records are available and because the location and elevation are similar to the region mentioned in Nissen & Mears (1990). Although the observed soil temperatures, with a 10-yr annual average of 9.9°C, were taken 5 cm below the surface, the expected difference between these and actual surface temperatures is considered negligible.

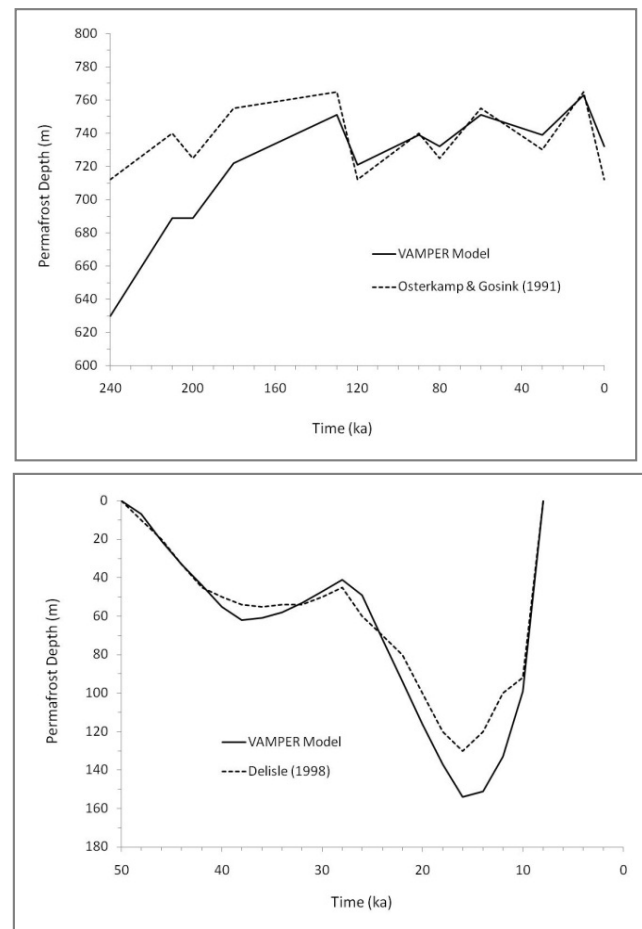


Figure 2. Comparison of simulation results from the VAMPER model to the redrawn curves of a) Osterkamp & Gosink (1991) for Prudhoe Bay, AK and b) Delisle (1998) for Western Europe.

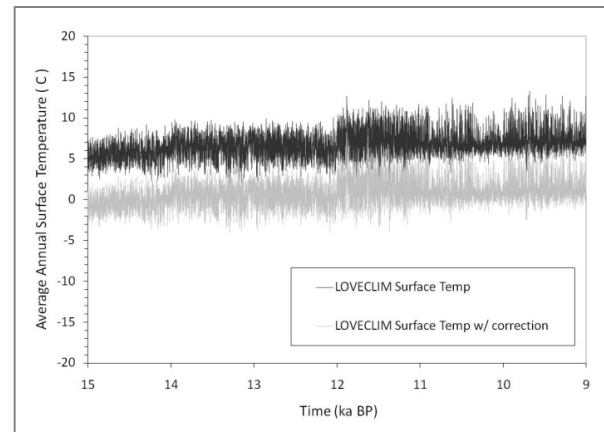


Figure 3. LOVECLIM average annual surface temperatures, with and without correction, for deglaciation experiment.

Assuming that this 6°C represents a structural LOVECLIM model bias for Wyoming, we subsequently subtracted a correction factor of 6°C from the paleotemperature series from Roche et al. (2011). Figure 3 shows the original temperature series with the corrected one.

The model was first spun-up using a repeating cycle of the first 100 years of the corrected surface temperature data. After

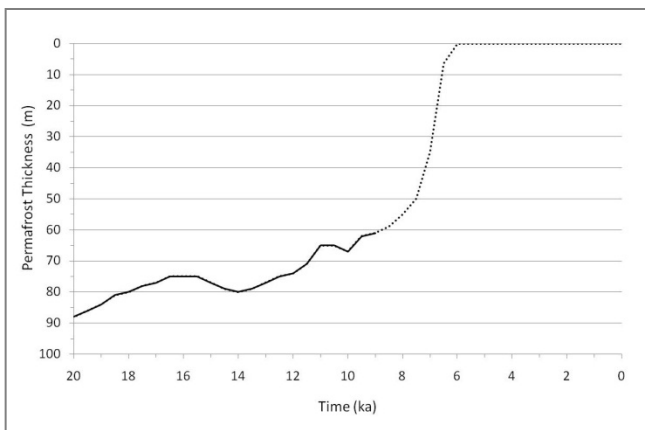


Figure 4. VAMPER model results for Wyoming showing permafrost degradation and aggradation following the LGM. The dashed line represents permafrost response to a linear regression of LOVECLIM surface temperatures.

100,000 model years, a steady-state permafrost thickness of 89 m was reached.

Permafrost at the Wyoming site degraded from 89 m to about 60 m (Fig. 4). There are two periods of permafrost aggradation (~15 ka and ~11ka) where the VAMPER model responded to cooler surface temperatures. Speculating on the causes of these two periods lies within the makeup and testing of LOVECLIM and is beyond the scope of this paper.

Because the LOVECLIM temperature dataset ended at 9 ka, the remaining 9,000 years of surface temperatures were interpolated using a linear regression of $1^{\circ}\text{C}/1000$ years (dashed line in Fig. 4). This rate of change is based on the approximate warming that occurs between 9 ka (1°C) and 0 ka (10°C).

Although the surface temperatures found by LOVECLIM and the subsequent correction factor are reasonable, there are influences still to be considered. For example, Renssen et al. (2009) recently suggested the Laurentide ice sheet may have had a cooling effect on the regional climate between 9 and 7 ka. Also, around this time, North America experienced a thermal maximum, which is not represented in the interpolation. It is expected that a few degrees warmer or cooler around the juncture of 9 ka would have a measurable effect on the timing and rate of disappearing permafrost in Wyoming. Therefore, our results for the early Holocene part (9 to 7 ka) should be interpreted with caution.

Forced by the interpolation, permafrost completely disappeared around 6 ka. However, in reality, it is expected that permafrost would have disappeared earlier if the Holocene thermal maximum had been reflected in the temperature data. But given the forcing from both the actual LOVECLIM data and the interpolated temperatures, we are satisfied with model performance. Results are reasonable based on an average thawing of the permafrost base (0.002–0.012 m/yr), which is similar to rates from Osterkamp & Gosink (1991). Further, the rapid permafrost decay beginning about 8 ka is due to the already warm permafrost, making it particularly susceptible to thaw at both the base and top of the permafrost (Kane et al. 1991).

Conclusions

This study has demonstrated that the VAMPER model is sufficiently calibrated to simulate the depth of permafrost at Barrow, Alaska, assumed to be in equilibrium with today's surface temperatures. The VAMPER model was also validated by reproducing the results of two previous transient millennia-scale studies comparably well. Finally, the VAMPER model produced results for a transient experiment of the last deglaciation in Wyoming, USA. Based on these three demonstrations, it can be concluded that the VAMPER model is capable of simulating permafrost dynamics and is therefore ready to be coupled with LOVECLIM.

References

- Alexeev, V.A., Nicolsky, D.J., Romanovsky, V.E., & Lawrence, D.M. 2007. An evaluation of deep soil configurations in the CLM3 for improved representation of permafrost. *Geophysical Research Letters* 34 L09502, doi:10.1029/2007GL029536.
- Brigham, J.K. & Miller, G.H. 1983. Paleotemperature estimates of the Alaskan Arctic Coastal Plain during the last 125,000 years. *Proceedings of the Fourth International Conference on Permafrost*, Fairbanks, Alaska, July 17-22, 1983: 80-85.
- Brovkin, V., Bendtsen, J., Claussen, M., Ganopolski, A., Kubatzki, C., Petoukhov, V., & Andreev, A. 2002. Carbon cycle, vegetation, and climate dynamics in the Holocene: Experiments with the CLIMBER-2 model. *Global Biogeochemical Cycles* 16(4), 1139, doi:10.1029/2001GB001662.
- Delisle, G. 1998. Numerical simulation of permafrost growth and decay. *Journal of Quaternary Science* 13(4): 325-333.
- Delisle, G., Caspers, G. & Freund, H. 2003. Permafrost in north-central Europe during the Weichselian: how deep? *Proceedings of the Eighth International Conference on Permafrost*, Zurich, Switzerland, July 21-25, 2003: 187-191.
- Farouki, O.T. 1986. Thermal Properties of Soils. *Series on Rock and Soil Mechanics* 11. 136 pp.
- French, H.M. 2007. *The Periglacial Environment*. West Sussex: John Wiley & Sons Ltd, 450 pp.
- Goosse, H., Brovkin, V., Fichefet, T., Haarsma, R., Huybrechts, P., Jongma, J., Mouchet, A., Selten, F., Barriat, P.Y., Campin, J.M., Deleersnijder, E., Driesschaert, E., Goelzer, H., Janssens, I., Loutre, M.F., Morales Maqueda, M.A., Opsteegh, T., Mathieu, P.P., Munhoven, G., Pettersson, E.J., Renssen, H., Roche, D.M., Schaeffer, M., Tartinville, B., Timmermann, A., & Weber, S.L. 2010. Description of the Earth system model of intermediate complexity LOVECLIM version 1.2. *Geoscientific Model Development* 3: 603-633.
- Hinkel, K.M. 1998, updated 2004. *Soil temperatures for Happy Valley and Barrow, Alaska, USA*. Boulder, CO: National Snow and Ice Data Center. Digital media.

- Hinkel, K.M., Paetzold, F., Nelson, F.E., & Bockheim, J.G., 2001. Patterns of soil temperature and moisture in the active layer and upper permafrost at Barrow, Alaska: 1993–1999. *Global and Planetary Change* 29: 293-309.
- Hinzman, L.D. & Kane, D.K. 1992. Potential Response of an Arctic Watershed During a Period of Global Warming. *Journal of Geophysical Research* 97 (D3): 2811-2820.
- Kane, D.K., Hinzman, L.D., & Zarling, J.P. 1991. Thermal response of the active layer to climatic warming in a permafrost environment. *Cold Regions Science and Technology* 19: 111-122.
- Kukkonen, I.T. & Šafanda, J. 2001. Numerical modelling of permafrost in bedrock in northern Fennoscandia during the Holocene. *Global and Planetary Change* 29: 259–273.
- Lachenbruch, A.H., Sass, J.H., Marshall, B.V., & Moses, T.H., Jr. 1982. Permafrost, Heat Flow, and the Geothermal Regime at Prudhoe Bay, Alaska. *Journal of Geophysical Research* 87(B11): 9301-9316.
- Lemke, P., Ren, J., Alley, R.B., Allison, I., Carrasco, J., Flato, G., Fujii, Y., Kaser, G., Mote, P., Thomas, R.H., & Zhang, T. 2007. Observations: Changes in Snow, Ice, and Frozen Ground. In: Solomon, S., Qin, D., Manning, M., Chen, Z., Marquis, M., Averyt, K.B., Tignor, M. & Miller, H.L. *Climate Change 2007: The Physical Science Basis. Contribution of Working Group I to the Fourth Assessment Report on the Intergovernmental Panel on Climate Change*. Cambridge, United Kingdom and New York, NY, USA: Cambridge University Press, 337–383.
- Ling, F. & Zhang, T. 2004. A numerical model for surface energy balance and thermal regime of the active layer and permafrost containing unfrozen water. *Cold Regions Science and Technology* 38: 1-15.
- Lunardini, V.J. 1987. Freezing of soil with an unfrozen water content and variable thermal properties. CRREL report 88-2, 23 pp.
- Lunardini, V.J. 1995. Permafrost Formation Time. CRREL Report 95-8: 44 pp.
- Mottaghy, D. & Rath, V. 2006. Latent heat effects in subsurface heat transport modelling and their impact on palaeotemperature reconstructions. *Geophysical Journal International* 164: 236-245.
- Nakano, Y. & Brown, J. 1972. Mathematical Modeling and Validation of the Thermal Regimes in Tundra Soils, Barrow, Alaska. *Arctic and Alpine Research* 4(1): 19-38.
- Nelson, F.E. 2003. (Un)frozen in time. *Science* 299: 1673-1675.
- Nissen, T.C. & Mears, B. Jr. 1990. Late Pleistocene Ice-wedge Casts and Sand-wedge Relics in the Wyoming Basins, USA. *Permafrost and Periglacial Processes* 1: 201-219.
- Osterkamp, T.E. & Gosink, J.P. 1991. Variations in Permafrost Thickness in Response to Changes in Paleoclimate. *Journal of Geophysical Research* 96 (B3): 4423-4434.
- Osterkamp, T.E. 2007. Characteristics of the recent warming of permafrost in Alaska. *Journal of Geophysical Research* 112: 1-10.
- Renssen, H., Seppä, H., Heiri, O., Roche, D.M., Goosse, H., & Fichet, T. 2009. The spatial and temporal complexity of the Holocene thermal maximum. *Nature Geoscience* 2: 411 – 414.
- Roche, D.M., Renssen, H., Paillard, D., & Levavasseur, G. 2011. Deciphering the spatio-temporal complexity of climate change of the last deglaciation: a model analysis. *Climate of the Past* 7: 591–602.
- Sclater, J.G. & Christie, P.A.F. 1980. Continental Stretching: An Explanation of the Post-Mid-Cretaceous Subsidence of the Central North Sea Basin. *Journal of Geophysical Research* 85(B7): 3711-3739.
- Williams, P.J. & Smith, M.W. 1989. *The Frozen Earth: Fundamental of Geocryology*. Cambridge: Cambridge University Press, 306 pp.
- Zhang, Y., Carey, S.K., & Quinton, W.L. 2008. Evaluation of the algorithms and parameterizations for ground thawing and freezing simulation in permafrost regions. *Journal of Geophysical Research* 113: 1 -17.
- Zhang, T. & Stamnes, K. 1998. Impact of Climatic Factors on the Active Layer and Permafrost at Barrow, Alaska. *Permafrost and Periglacial Processes* 9: 229-246.
- Zimov, S.A., Shuur, E.A.G., & Chapin, F.S. III. 2006. Permafrost and the Global Carbon Budget. *Science* 312: 1612-1613.

Monitoring of Permafrost Creep on Two Rock Glaciers in the Austrian Eastern Alps: Combination of Aerophotogrammetry and Airborne Laser Scanning

Christoph Klug, Erik Bollmann, Rudolf Sailer, Johann Stötter
Institute of Geography, Innsbruck University, Austria

Karl Krainer
Institute of Geology, Innsbruck University, Austria

Andreas Kääb
Department of Geosciences, University of Oslo, Norway

Abstract

The aim of this study is to quantify vertical and horizontal surface changes of two rock glaciers (Reichenkar and Äusseres Hochebenkar) for a period of 56 years. The quantification of the surface changes is based on the comparison of multitemporal digital elevation models (DEM) and orthoimages over the period 1953/54–2003. By combining digital photogrammetry and airborne laser scanning (ALS) data from 2006 and 2009, the time series was extended to 2009. For the calculation of the vertical and horizontal changes, DEMs were generated from aerial photographs. The vertical changes were derived through subtraction of the multitemporal DEMs over the different periods. Additionally, the horizontal flow velocity was computed with the implementation of two image correlation programs. Furthermore the results were compared with dGPS-measured flow velocities. For different periods within 1953/54–2009, the surface displacements of the well-investigated rock glaciers Reichenkar and Äusseres Hochebenkar are reconstructed and analysed in this paper.

Keywords: active rock glaciers, aerophotogrammetry, airborne laser scanning; flow velocity; image correlation.

Introduction

Active rock glaciers, indicators of mountain permafrost, are lobate or tongue-shaped landforms composed of a mixture of perennially frozen rock debris and ice. They slowly creep downslope by inner deformation of ice and forces of gravity (Barsch 1996). As a result, the surface shows a typical topography of transverse or longitudinal ridges and furrows.

Most rock glaciers show average surface velocities of a few decimetres per year (Krainer & Mostler 2000), although higher velocities of more than 2 m a⁻¹ have been observed throughout the Alps (e.g., Roer 2005, Haerberli et al. 2006, Avian et al. 2009). The highest flow velocities (5–7 m a⁻¹) in the Alps have been measured on the Äusseres Hochebenkar and Reichenkar rock glaciers discussed here (Schneider & Schneider 2001, Krainer & Mostler 2006). In the last 20 years, several alpine rock glaciers show increasing creep velocities (Roer et al. 2005). A relation may be supposed between the increasing flow velocity of rock glaciers and global warming.

According to Kääb & Vollmer (2000), a long-time survey of the distribution of rock glacier surface velocities, combined with terrestrial point measurements, can improve the understanding of the underlying processes.

Nevertheless, long-term measurements of flow velocities on active rock glaciers are rare. During the last few decades, a variety of methods for the quantification of rock glacier creep have been developed. Early approaches used field surveying and triangulation techniques (Pillewizer 1957). Recently, differential GPS (dGPS) has proved to be an effective direct method for studying rock glacier flow (Lambiel & Delaloye 2004). The main disadvantage of these methods is the lack of area-wide data coverage.

Airborne remote sensing techniques enable area-wide data acquisition. Aerial photogrammetry allows area-wide monitoring of rock glacier geometry, thickness changes, and surface creep (Kääb et al. 1997). Recently, techniques like space-borne differential synthetic aperture radar interferometry (DInSAR) (Strozzi et al. 2004) or terrestrial and airborne laser scanning have been used for surveying rock glaciers and measuring displacement rates (Bauer et al. 2003, Bollmann et al. submitted).

The objective of this paper is to reconstruct and analyse the surface displacements derived from aerial images and ALS data over the period 1953/54–2009 on two active rock glaciers in the Austrian Alps. Furthermore, the novel approach of using ALS data, especially for validating the photogrammetrical-derived DEMs, is pointed out.

Study Area and Data

Äusseres Hochebenkar rock glacier (AHK)

The Äusseres Hochebenkar (AHK) rock glacier (46°50'N, 11°01'E) is a tongue-shaped, talus-derived rock glacier about 2 km south of Obergurgl (Ötztal Alps, Austria). It expands from about 2830 m down to about 2360 m a.s.l. and reaches a length of up to 1.6 km. A detailed characterization of the physiognomy of AHK is given by Vietoris (1972) and Haerberli & Patzelt (1982). Since 1938, systematic terrestrial investigations on surface flow velocities, front advance rates, and surface elevation changes of AHK have been carried out on an annual scale (Schneider & Schneider 2001). Remote sensing methods, such as terrestrial and aerial photogrammetry, have also been applied (Kaufmann & Ladstätter 2002).

The AHK is characterized by very high surface velocities of up to several meters per year. According to Schneider & Schneider (2001), maximum displacement rates (6.6 m a^{-1}) were measured below a terrain edge at about 2570 m a.s.l. in the 1960s. Following Haerberli & Patzelt (1982), these high values are most likely a result of a significant increase of slope steepness below the terrain edge. The related velocity gradients result in deep cross cracks in the rock glacier body.

Reichenkar rock glacier (RK)

The Reichenkar (RK) rock glacier ($47^{\circ}02'N$, $11^{\circ}01'E$) is located in the western Stubai Alps (Tyrol, Austria). It is situated in a small, northeast-facing valley called Inneres Reichenkar. RK is a tongue-shaped, ice-cored rock glacier 1400 m long with widths that reach 260 m near the head and 170–190 m near the front. The rock glacier covers an area of 0.27 km^2 and extends in altitude from 2750 m to 2310 m a.s.l.

Detailed information about this rock glacier can be found in Krainer & Mostler (2000) and Hausmann et al. (2007). Investigations on surface flow velocities have been carried out in the period 1997–2003 with dGPS measurements (Chesi et al. 2003). These data are used to validate the derived horizontal displacement rates.

Data acquisition

The basic data applied in the presented analysis are greyscale aerial photographs, provided by the Austrian Federal Office of Metrology and Survey (BEV), with a scale from 1:16.000 to 1:30.000. For the study sites, analogue aerial stereoscopic pairs are available for the years (Table 1), taken with Wild/Leica-Cameras of different types. Additionally, the federal province of Tyrol provided high-resolution orthoimages from the years 2003 and 2009.

To best pursue the objective target, the recording date and time are important, because snow cover or topographic shadowing make DEM generation impossible. For that reason, only aerial photographs with a certain standard were used.

ALS data acquisition campaigns at AHK and RK were carried out in 2006 (by the federal province of Tyrol) and 2009 (within the project C4AUSTRIA). A summary on the exact data acquisition dates is given in Bollmann et al. (submitted). DEMs out of these ALS flight campaigns were generated and integrated in the analysis.

Methods

Generation of DEM & orthoimages

For the photogrammetric analyses, the analogue data were provided as scanned aerial photographs ($\sim 1600 \text{ dpi}$) with the required calibration reports. Image orientation, automatic DEM extraction, and digital orthophoto generation were the first steps in this study. For a detailed description of the methods, see Baltsavias et al. (2001). The DEMs were generated from the mono-temporal stereo models with 1 m spacing. Additionally, the orthoimages were calculated with the cubic convolution resampling method with 0.2 m ground resolution.

Table 1. Calculated RMSE for the generated DEM vs. 2009. (-) Aerial images not available for acquisition in winter.

| DEM | RK - RMSE | AHK -RMSE |
|-------------|-----------|-----------|
| 2009 (ALS) | ref | ref |
| 2006 (ALS) | 0.13 m | 0.10 m |
| 1997 | - | 0.41 m |
| 1994 | 0.22 m | - |
| 1989 /1990 | 0.26 m | 0.42 m |
| 1977 | - | 0.25 m |
| 1973 | 1.29 m | - |
| 1971 | - | 0.55 m |
| 1969 | - | 0.29 m |
| 1953 / 1954 | 0.78 m | 0.58 m |

Accuracy assessment

In a first step, the quality of the used ground control points, as well as the calculated exterior orientation, were checked and evaluated by an automatic residual error tool to minimize processing errors and to improve accuracy.

Afterwards, an accuracy assessment was performed by comparing the generated DEM with the high-quality DEM of the ALS flight campaign of 2009. Therefore, 3 areas that represent the surface structure (slope, aspect, height) of the rock glaciers are detected in stable regions. On the basis of this analysis, the root mean square error (RMSE) could be calculated. The computed RMSE figures (Table 1) show values of 0.2–1.3 m.

For the analyses of the RMSE, it has to be kept in mind that the accuracy is strongly influenced by systematic errors such as shadowing, steep terrain, and low image contrast. According to Käab (2010), a vertical RMSE for automatic generated DEM corresponding to 1–3 times the image pixel size is possible in relatively flat areas (e.g., alpine meadows). For slopes and ridges, a RMSE of 5–7 times the image pixel size can be expected. Steep slopes with shadowed areas reveal RMSE on the order of 60–100 times the image pixel size. This assessment is reflected in the results of this study. For detailed information on automatic photogrammetric-derived DEM vertical error analysis, see Baltsavias et al. (2001).

Calculation of horizontal displacements

The horizontal displacement rates from the orthoimages were calculated with the Correlation Image Analysis (CIAS) Software (Käab & Vollmer 2000). CIAS has already been applied to a variety of glaciers and rock glaciers to calculate flow velocities from orthoimages or satellite images (Käab 2004). CIAS identifies displacement rates as a double cross-correlation function based on the grey values of the used input images (Käab 2010). The correlation algorithm searches via block matching a predefined corresponding reference section in the image of acquisition time 1 (t_1) in a sub-area of image of acquisition time 2 (t_2). If the reference block is successfully matched, the differences in central pixel coordinates show the horizontal displacement between t_1 and t_2 . The output file consists of the x- and y-coordinates of the reference block, the displacement rates in the x- and y-direction, as well as the Euclidean distance, the direction, and the correlation

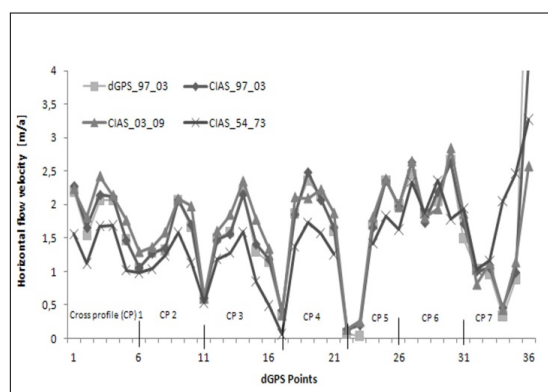


Figure 1. Comparison of the measured (dGPS) and computed (CIAS) flow velocities for the periods 1997–2003, 2003–2009, and 1954–1973.

coefficient. Matching errors can be detected and eliminated by analyzing the correlation parameters, the expected range for surface velocity, and direction. Because of the varying lengths of the periods, CIAS was run with different parameter combinations regarding the size of the reference and search area, as well as the window spacing.

For measuring changes in geometry, relative accuracy is more important than the absolute position of the images (Kääb 2010). Therefore, the multitemporal orthoimages have been co-registered using tie points in addition to the initial georeferencing.

Additionally, the horizontal displacement rates are calculated from shaded reliefs of ALS DEM with the open source image correlation software Imcorr (Scambos et al. 1992), which has been applied to calculate flow velocities of glaciers using different input data acquired from aircraft or satellites. Detailed information about this software is given in Bollmann et al. (submitted).

Accuracy assessment

The accuracy of the calculated horizontal displacement rates was evaluated using dGPS data from the 1997–2003 RK record. The original CIAS output point files were compared to the dGPS displacement rates using a buffer of 3 m around the dGPS points.

For the time period 1997–2003, an absolute mean deviation of 0.4 m (Std 0.46 m) between the dGPS values and the corresponding nearest CIAS point measurements was calculated. Figure 1 shows the computed and the 36 dGPS measured flow velocities within the investigated period. Additionally, the dGPS points were used as reference for the periods 1954–1973 and 2003–2009. In contrast to the latter epoch, the velocities between 1954 and 1973 were slower in evidence, but there is still a good relative correlation within the profiles.

Table 2 presents the calculated differences by CIAS, considering the mean absolute error (Amean) in combination with the standard deviation (Std) to be the most appropriate accuracy indicators.

Table 2. Comparison between horizontal displacement rates calculated from CIAS and measured by dGPS (CIAS – dGPS).

| CIAS - dGPS | Mean [m] | Amean [m] | Std [m] | Max [m] | Min [m] | RMSE [m] | R ² |
|-------------|----------|-----------|---------|---------|---------|----------|----------------|
| 1997/2003 | 0.24 | 0.4 | 0.46 | 1.28 | 0.02 | 2.05 | 0.91 |

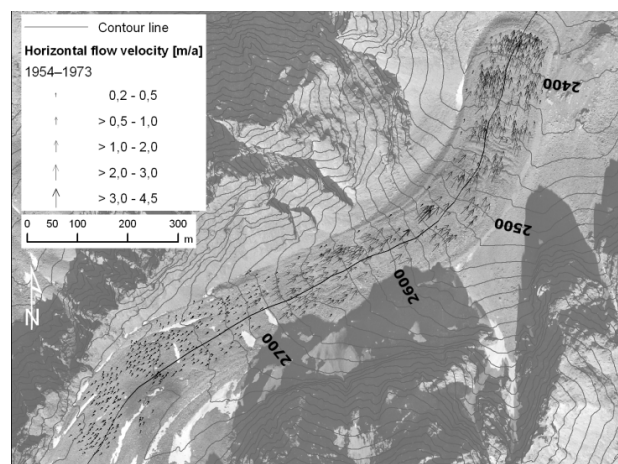


Figure 2. Mean annual horizontal flow velocity on RK 1954–1973. Contour lines indicate the steep midsection.

Results and Discussion

Reichenkar

The horizontal surface velocity fields (cf. Figs. 2 and 3) and the thickness changes on RK (Fig. 4) varied between the individual investigated epochs. From 1954–2009, an average vertical loss of the rock glacier of nearly 3.2 m ($\sim -6 \text{ cm a}^{-1}$) can be observed. In the rooting zone surface, lowering of up to -0.5 m a^{-1} in various periods indicates massive loss of ice. The average elevation change in this zone lies within the range of -0.10 m a^{-1} .

The increase in thickness at the front of individual flow lobes suggests that elevation changes are influenced by mass advection. Over the investigated periods, the surface of RK was creeping with average rates of 0.9 m a^{-1} (Table 3). Maximum creep rates occur in a transition zone (2540–2660 m a.s.l.), a steeper mid-section before the flat tongue, where compressive flow with development of transverse ridges and furrows can be observed. The measured surface displacements depict acceleration since the late 1990s from the middle to the front part of the rock glacier. The displacement rates in the root zone seem to be constant over the whole period ($0.2\text{--}0.5 \text{ m a}^{-1}$), whereas flow rates at the tongue, which were consistent over the periods from 1954 to 1997 with average rates of $1\text{--}2 \text{ m a}^{-1}$ along the central axis, increased to $2.0\text{--}3.0 \text{ m a}^{-1}$ since 1997. The increasing velocities cannot be explained by the gradient of the slope, which measures only $11\text{--}12^\circ$ on the lower part of RK.

The front of RK advanced 53 m from 1954 to 2009 (0.76 m a^{-1}). Figure 5 depicts the mentioned acceleration, which increased from an average of 0.6 m a^{-1} to 1.55 m a^{-1} during the last 20 years. The measurements show displacement rates at the front of up to 3 m a^{-1} . At the orographic left part of the flat

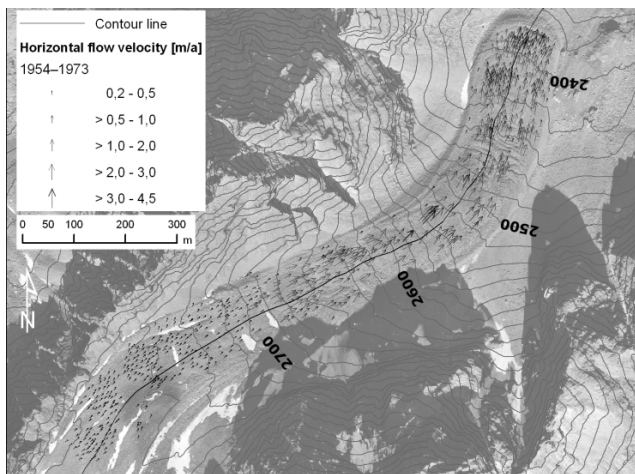


Figure 3. Mean annual horizontal flow velocity on RK 1997–2003. Points indicate 36 dGPS points measured along seven cross profiles.

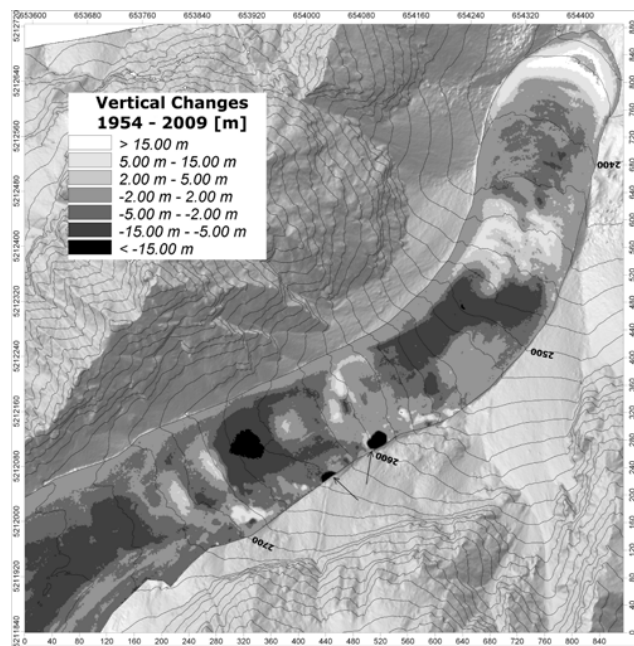


Figure 4. Cumulated vertical changes of RK between 1954 and 2009. Arrows indicate errors because of bad contrast.

tongue (2520–2460 m a.s.l.), one portion features relatively high movement rates (~ 3.3 m a⁻¹) since 1994. In combination with the general topography, the distinct speed gradients indicate that the lower part of the frozen body is overridden from above by a new lobe.

Hochebenkar

The rock glacier is characterized by a comparatively high flow velocity of several meters per year and periodically changing flow rates between 1953 and 2009 (Table 3). A transverse terrain edge at an altitude of about 2580 m a.s.l. divides the rock glacier into a lower steep part and an upper flat part. Within all periods, the rooting zone shows constant velocities (0.2–0.5 m a⁻¹), whereas in the adjacent zone toward the terrain edge displacement rates differ during the investigation periods.

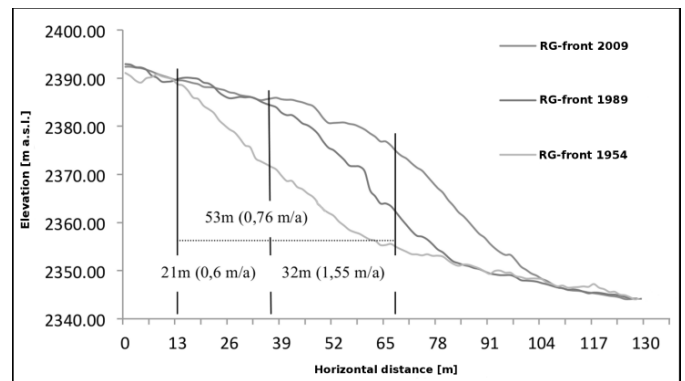


Figure 5. Front advance depicted by longitudinal profiles.

Table 3. Calculated horizontal velocities (mean, maximum, and acceleration dv) on RK and AHK. The rock glaciers were separated into three sections (root zone, transition zone, and tongue), and in every zone the same amount of measured blocks was used for calculation of the annual mean.

| Reichenkar | | | | |
|-------------|-----------------|---------------------|---------------------|--------|
| Period | Measured blocks | Mean velocity [m/a] | Max. velocity [m/a] | dv [%] |
| 1954 - 1973 | 841 | 0.75 | 3.4 | - |
| 1973 - 1989 | 871 | 0.73 | 3.5 | - 2.7 |
| 1989 - 1994 | 909 | 0.73 | 4.2 | 0.0 |
| 1994 - 1997 | 987 | 0.76 | 5 | + 3.2 |
| 1997 - 2003 | 830 | 1.12 | 4.9 | + 47.4 |
| 2003 - 2009 | 811 | 1.3 | 4.1 | + 16.1 |
| Hochebenkar | | | | |
| 1953 - 1969 | 2438 | 0.84 | 5.2 | - |
| 1969 - 1971 | 2479 | 0.64 | 6.9 (?) | - 14.3 |
| 1971 - 1977 | 2711 | 0.42 | 4.1 | - 34.4 |
| 1977 - 1990 | 2283 | 0.54 | 1.85 | + 28.6 |
| 1990 - 1997 | 2865 | 0.63 | 1.7 | + 16.7 |
| 1997 - 2003 | 2308 | 0.77 | 2.3 | + 22.2 |
| 2003 - 2009 | 2439 | 0.86 | 2.5 | + 11.7 |

In the period from 1953 to 1969, high movement rates (1.0–2.5 m a⁻¹) were measured in this zone. At the same time, the upper part of the tongue showed the development of massive transverse cracks, where the loss of mass was extremely high. From the early 1970s to the beginning of the 1990s, a phase with relatively slow average annual velocity rates (0.5–1.0 m a⁻¹, Table 3) could be observed. From the 1990s onward, the movement rates increased, showing velocities (1.0–2.5 m a⁻¹) similar to those of the late 1960s (Fig. 6). On the terrain edge, creep velocities increased to about 2.5 m a⁻¹. Maximum creep rates (6.9 m a⁻¹) have been measured in this transition zone from 1953 to 1969, although rockfall may be a significant process here and cannot be attributed to permafrost creep exactly.

The measurements show elevation changes within the range of -0.10 m a⁻¹ in the upper part, whereas the changes increase to nearly -0.6 m a⁻¹ at the zone below the terrain edge (Fig. 7). Thinning of the frozen debris at the terrain edge of around 2580 m a.s.l. is compensated to a large extent by corresponding thickening in the lowest part. Below 2580 m, which marks the

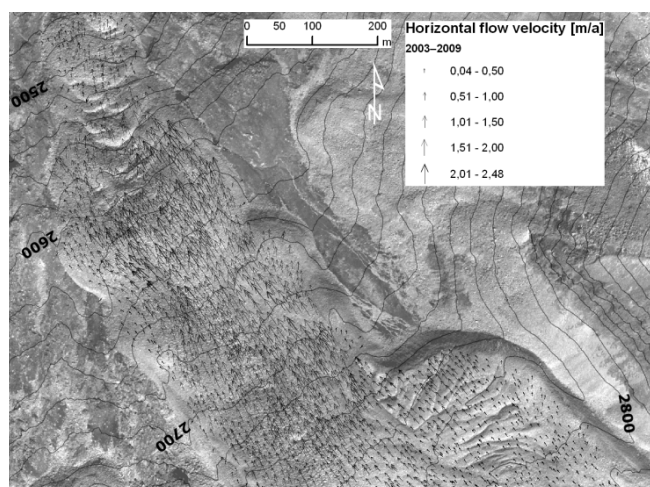


Figure 6. Mean annual horizontal flow velocity on AHK 2003–2009. Contour lines indicate the terrain edge at 2580 m a.s.l.

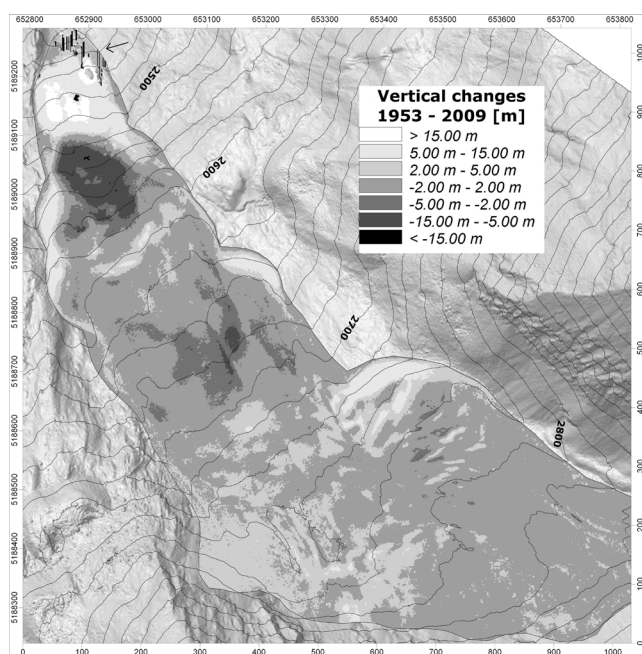


Figure 7. Cumulated vertical changes of AHK between 1953 and 2009. Arrow at the front indicates errors because of bad contrast.

end of the steady-state creeping zone, the tongue has moved into very steep terrain. In this area, landslides have occurred due to the specific topographic situation and make image correlation nearly impossible. The front of AHK advanced 135 m (2.4 m a^{-1}) from 1953 to 2009. Since 1969, the rates of front advance decreased from 4.1 m a^{-1} to 1 m a^{-1} in the 1990s, and since that time an increase could be observed to the current 1.6 m a^{-1} .

Conclusion

In the case of RK and AHK, permafrost creep is the most important factor governing surface elevation changes. Computer-based aerial photogrammetry in combination with ALS allows detailed determination and analysis of surface

elevation changes in, and horizontal displacements on, the investigated rock glaciers over a period of 56 years. These calculations build an important analytical component for identifying the state of activity of rock glaciers.

Using ALS data in rock glacier research, especially for validating the photogrammetrical-derived DEMs and for calculating flow velocities, has proved to be a useful data source for area-wide investigations on rock glaciers. The results show the potential of the method combination to quantify spatio-temporal variations of rock glacier surface changes.

The obtained spatial patterns agree with the dGPS measurements and the existing knowledge about the flow behavior of the two rock glaciers. Furthermore, the length of the time series allows the investigation of temporal variations of flow velocities, on which little has been previously done for fast creeping types like RK and AHK. The study reveals an acceleration of the rock glaciers since the late 1990s. In contrast to AHK, where the displacement rates in the 1950s and 1960s have been similar to current rates, the RK shows acceleration over all periods from 0.75 to 1.3 m a^{-1} currently. In addition to the temporal variation, spatial variation in the velocity field of RK could be detected. The orographic left portion in the middle and lower section shows higher velocities.

Although some regional-scale studies have been conducted (e.g., Roer 2005), most investigations are still concentrated on single rock glaciers, and meso-scale information on this topic is limited. Area-wide data about the flow behavior of rock glaciers provide useful input for understanding rock glacier dynamics. In order to obtain detailed information of rock glacier dynamics, more data about the internal structure are needed. Furthermore, the temporal resolution of temperature and velocity measurements has to be increased to get more detailed information about the interrelation of rock glacier creep and global warming.

Acknowledgments

This study was embedded in the project C4AUSTRIA, which is funded by the Austrian Climate Research Program (ACRP Nr. A963633). We acknowledge two anonymous referees whose constructive comments helped to improve the paper.

References

- Avian, M., Kellerer-Pirklbauer, A., & Bauer, A. 2009. LiDAR for Monitoring Mass Movements in Permafrost Environments at the Cirque Hinteres Langtal, Austria, between 2000 and 2008. *Natural Hazards and Earth System Sciences*, Special Issue: LIDAR and DEM techniques for landslides monitoring and characterization.
- Barsch, D. 1996. Rockglaciers. Indicators for the Present and Former Geocology in High Mountain Environments. *Berlin, Springer Verlag*, 331 pp.
- Baltsavias, E.P., Favey, E., Bauder, A., Boesch, H., & Pateraki, M. 2001. Digital surface modelling by airborne laser scanning and digital photogrammetry for glacier monitoring. *Photogrammetric Record* 17(98), 243-273.

- Bauer, A., Paar, G., & Kaufmann, V. 2003. Terrestrial laser scanning for rock glacier monitoring. In: Phillips, M., Springman, S.M., Arenson, L.U. (Eds.), *Proceedings of the 8th international conference on permafrost*. Swets and Zeitlinger, Lisse, 1: 55-60.
- Bollmann, E., Abermann, J., Klug, C., Sailer, R., & Stötter, J. (submitted). Quantifying Rock Glacier Creep using Airborne Laser Scanning. A case study from two Rockglaciers in the Austrian Alps. Proceedings of the tenth International Conference on Permafrost, Tyumen, Russia.
- Chesi, G., Geissler, S., Krainer, K., Mostler, W., & Weinold T. 2003. 5 Jahre Bewegungsmessungen am aktiven Blockgletscher Inneres Reichenkar (westlichen Stubai Alpen) mit der GPS-Methode, XII. Int. Geodätische Woche Obergurgl, 201-205.
- Haerberli, W. & Patzelt, G. 1982. Permafrostkartierung im Gebiet der Hochebenkar-Blockgletscher. Obergurgl, Öztaler Alpen. *Zeitschrift für Gletscherkunde und Glazialgeologie* 18(2), 127-150.
- Haerberli, W., Hallet, B., Arenson, L., Elconin, R., Humlum, O., Kääb, A., Kaufmann, V., Ladanyi, B., Matsuoka, N., & Vonder Mühl, D. 2006. Permafrost creep and rock glacier dynamics. *Permafrost and periglacial processes* 17 (3): 189-214.
- Hausmann, H., Krainer, K., Brückl, E., & Mostler, W. 2007. Internal Structure and Ice Content of Reichenkar Rock Glacier (Stubai Alps, Austria) Assessed by Geophysical Investigations. *Permafrost and Periglacial Processes* 18, 351-367.
- Kääb, A., Haerberli, W., & Gudmundsson, H. 1997. Analysing the creep of mountain permafrost using high precision aerial photogrammetry: 25 years of monitoring Gruben rock glacier, Swiss Alps. *Permafrost and periglacial processes* 8: 409-426.
- Kääb, A. & Vollmer, M. 2000. Surface geometry, thickness changes and flowfields on creeping mountain permafrost: automatic extraction by digital image analysis. *Permafrost and Periglacial Processes* 11(4), 315-326.
- Kääb, A. 2004. Mountain glaciers and permafrost creep. Research perspectives from earth observation technologies and geoinformatics. Habilitation, Department of Geography, ETH Zürich.
- Kääb, A. 2010. Aerial photogrammetry in glacier studies. London, P. Pellikka & W. G. Rees (Hrsg.), *Remote Sensing of Glaciers. Techniques for Topographic, Spatial and Thematic Mapping of Glaciers*. 331 pp.
- Kaufmann, V. & Ladstädter, R. 2002. Monitoring of active rock glaciers by means of digital photogrammetry. ISPRS Commission III, Symposium "Photogrammetric Computer Vision." Austria, Graz.
- Krainer, K. & Mostler, W. 2000. Reichenkar Rock Glacier: a Glacier-Derived Debris-Ice System in the Western Stubai Alps, Austria. *Permafrost and Periglacial Processes* 11, 267-275.
- Krainer, K. & Mostler, W. 2006. Flow velocities of active rock glaciers in the Austrian Alps. *Geografiska Annaler* 88(a), 267-280.
- Krainer, K., Mostler, W. & Span, N. 2002. A glacier-derived, ice-cored rock glacier in the western Stubai Alps (Austria): Evidence from ice exposures and ground penetrating radar investigation. *Zeitschrift für Gletscherkunde und Glazialgeologie* 38, 21-34.
- Lambiel, C. & Delaloye, R. 2004. Contribution of real-time kinematic GPS in the study of creeping mountain permafrost: examples from the Western Swiss Alps. *Permafrost and Periglacial Processes* 15: 229-241.
- Pillewizer, W. 1957. *Untersuchungen an Blockströmen der Öztaler Alpen*. Abhandlungen des Geographischen Institutes der Freie Universität Berlin 5: 37-50.
- Roer, I. 2005. Rockglacier kinematics in a high mountain geosystem. – Dissertation, Geographisches Institut, Universität Bonn. http://hss.ulb.uni-bonn.de/diss_online/math_nat_fak/2005/roer_isabelle
- Roer, I., Kääb, A., & Dikau, R. 2005. Rockglacier kinematics derived from small-scale aerial photography and digital airborne pushbroom imagery. *Zeitschrift für Geomorphologie* 49(1): 73-87.
- Scambos, T.A., Dutkiewitz, M.J., Wilson, J.C., & Bindschadler, R.A. 1992. Application of image cross-correlation software to the measurement of glacier velocity using satellite data. *Remote sensing of environment* 42: 177-186.
- Schneider, B. & Schneider, H. 2001. Zur 60jährigen Messreihe der kurzfristigen Geschwindigkeits-schwankungen am Blockgletscher im Äusseren Hochebenkar, Öztaler Alpen, Tirol. *Zeitschrift für Gletscherkunde und Glazialgeologie* 37(1), 1-33.
- Strozzi, T., Kääb, A., & Frauenfelder, R. 2004. Detecting and quantifying mountain permafrost creep from in-situ, airborne and spaceborn remote sensing methods. *International journal of remote sensing* 25(15): 2919-2931.
- Vietoris, L. 1972. Über die Blockgletscher des Äußeren Hochebenkars. *Zeitschrift für Gletscherkunde und Glazialgeologie* 8, 169-188.

Active Layer Processes in the McMurdo Dry Valleys, Antarctica: Decadal Trends and Experimental Responses to Changes in Soil Moisture

Joseph Levy, Andrew Fountain
Portland State University, Portland, OR, USA

Michael Gooseff
Penn State University, University Park, PA, USA

John Barrett
Virginia Tech, Blacksburg, VA, USA

Diana Wall, Uffe Nielson
Colorado State University, Fort Collins, CO, USA

Byron Adams
Brigham Young University, Provo, UT, USA

W. Berry Lyons
Byrd Polar Research Center, Columbus, OH, USA

Abstract

This paper analyzes active layer data collected at a permafrost experimental site near the Lake Hoare camp (77.63°S, 162.89°E) and at sampling sites across the McMurdo Dry Valleys (MDV) of Antarctica. The experimental site was selected to directly test the effects of soil water content on soil thermal properties (conductivity, heat capacity, thermal diffusivity) and active layer thickness in a cold, polar desert. Results show a strong dependence of thermal properties and heating hysteresis on soil water content. Wet soils (volumetric water content >10%) are ice-rich in the winter but thaw deeply in the summer (~50 cm). Dry soils (volumetric water content <10%) are largely ice-free and experience shallower depths of thaw (~20 cm). These results suggest that additions of soil moisture to MDV soils (through increased snowfall/snowmelt, glacier runoff, ground ice melt, and/or lake level rise) will result in a deepening of active layer thaw in the Dry Valleys, potentially resulting in rapid, melt-related landscape and ecosystem change.

Keywords: active layer; Antarctica; ecology; connectivity; water tracks.

Introduction

The polar desert of the McMurdo Dry Valleys (MDV) of Southern Victoria Land, Antarctica, is a mosaic of permafrost, glaciers, streams, and ice-covered lakes that together constitute the geological setting for the southernmost functioning terrestrial ecosystem (Kennedy 1993, Lyons et al. 2000). Water is scarce across the McMurdo Dry Valleys (MDV) landscape and is thought to limit soil ecosystem function (Kennedy 1993). Water is also critically important to permafrost active layer dynamics in the MDV, where soil moisture shapes the thermal behavior of permafrost in response to both seasonal and secular change (Ikard et al. 2009, Levy et al. 2011).

Taylor Valley (77.6°S, 162.9°E), one of the MDV, provides an ideal natural laboratory for determining the effects of soil moisture on permafrost thermal behavior, the role of permafrost in hydrological connectivity, and active layer ecosystem response to changes in soil water and energy budgets (Fig. 1). Taylor Valley contains examples of both ice-cemented permafrost (with pore ice present in the upper 100 cm of the soil column) as well as “dry-frozen” permafrost (which lacks ice in the upper 100 cm of the soil column) (Bockheim et al. 2007). Desiccation of Taylor Valley permafrost is thought to result largely from a net water vapor flux out of MDV soils due to high potential evaporation rates of ~30 cm/year (Chinn

1981, Clow et al. 1988, Gooseff et al. 2003b) coupled with low precipitation, 3–50 mm/year water equivalent, all of which falls as snow (Fountain et al. 2010). Hydrologic connectivity is facilitated by seasonal meltwater input into permafrost soils from snowbanks, glaciers, seasonal glacial runoff streams, and water tracks (Barrett et al. 2009, Campbell et al. 1998, Fountain et al. 2011, Gooseff et al. 2003a, Gooseff et al. 2011, Levy et al. 2011, McKnight et al. 1999). Meltwater input into the active layer is highly seasonal, occurring only during summer months. Taylor Valley has a mean annual air temperature of c. -18°C (Doran et al. 2002a) and soil surface temperatures that span from -43°C to +20°C, with a mean of -18°C.

MDV permafrost is unusual because of its low organic carbon content as well as its low water content. Taylor Valley soils typically contain <0.5 wt.% organic carbon (Virginia & Wall 1999). In addition, MDV soils are overwhelmingly dry; average active layer gravimetric water content (mass mixing ratio) in the MDV is 5%, while surface water contents (in the upper 3 cm of the soil column) are typically <1% (Campbell et al. 1998). These low water contents translate into extremely low ionic migration rates, averaging 0.3 m/year (Claridge et al. 1997) as well as low apparent thermal diffusivities, typically <1x10⁻⁸ m²/s (Ikard et al. 2009). Taken together, these observations suggest that typical MDV soils, as measured in Taylor Valley, are neither chemically nor thermally dynamic.

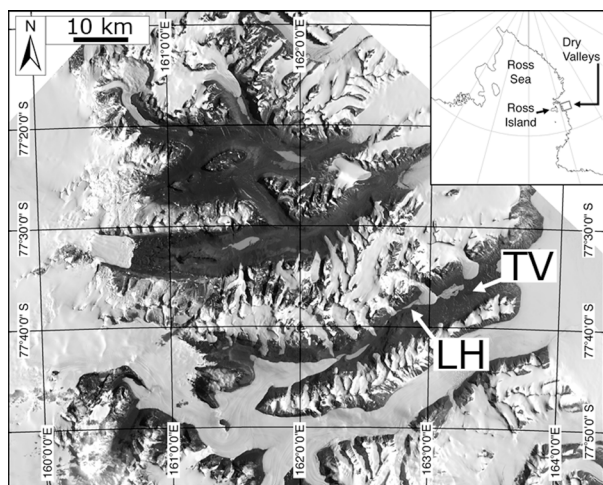


Figure 1. Taylor Valley (TV), Antarctica, one of the McMurdo Dry Valleys (MDV). LH marks the location of Lake Hoare.

The MDV is also unusual in that it is a polar environment that has experienced a decadal cooling trend (Doran et al. 2002b). MDV air temperatures decreased 0.7°C/decade between 1986 and 2000, part of a broader Antarctic cooling trend spanning 1966–2000, with cooling most pronounced during summer and autumn (Doran et al. 2002b). These trends have largely continued to the present in the MDV, making Taylor Valley a “thermal refuge” for pre-Anthropocene permafrost physical conditions (in contrast to warming in the Arctic and along the Antarctic Peninsula). Changes in southern hemisphere circulation are expected to result in reversal of this trend, resulting in MDV warming of 1.6–3.5°C by 2100 (Arblaster & Meehl 2006, Chapman & Walsh 2007, Shindell & Schmidt, 2004).

As a consequence of these climatological conditions,

several questions remain outstanding regarding the future of cold desert permafrost in the MDV: 1) Will active layers in the MDV become wetter or dryer in a warming world? 2) What are the thermal/stability consequences of wetter or dryer active layers? Active layer monitoring undertaken by the McMurdo Dry Valleys Long Term Ecological Research program provides preliminary answers to these fundamental Antarctic permafrost questions.

Active Layer Thermal Properties

The Lake Hoare experimental site (Fig. 2) consists of two vertical arrays of thermistors and TDR soil moisture probes designed to operate in concert with the MDV-wide MCM-LTER meteorological station network (Doran et al. 2002a). One array (W0-W40) is present in the path of a water track (Levy et al. 2011), which is a sub-linear depression in the ice cement table that routes fluids downslope through the active layer. This array samples “wet” soil conditions. The second array (D0-D30) is located across a sand-wedge polygon trough (a natural drain that acts as a barrier to active layer fluid flow) within the polygon interior and thus represents more typical “dry” soil conditions. Soil probes were installed in December 2010, with W40 and D30 placed at the top of the ice-cement table. Probe W0 was installed in November 2011 to provide complementary surface data. Soil temperature and soil moisture content measurements are made every 15 minutes and are logged on CR10X dataloggers.

Near-surface temperature and soil moisture records from the Lake Hoare experimental site are summarized in Figure 3 and Table 1. Volumetric water contents (VWC) are calculated from measured TDR travel times based on a soil-specific calibration formulated using gravimetric water content and bulk density analyses of 24 Lake Hoare basin soils (VWC =

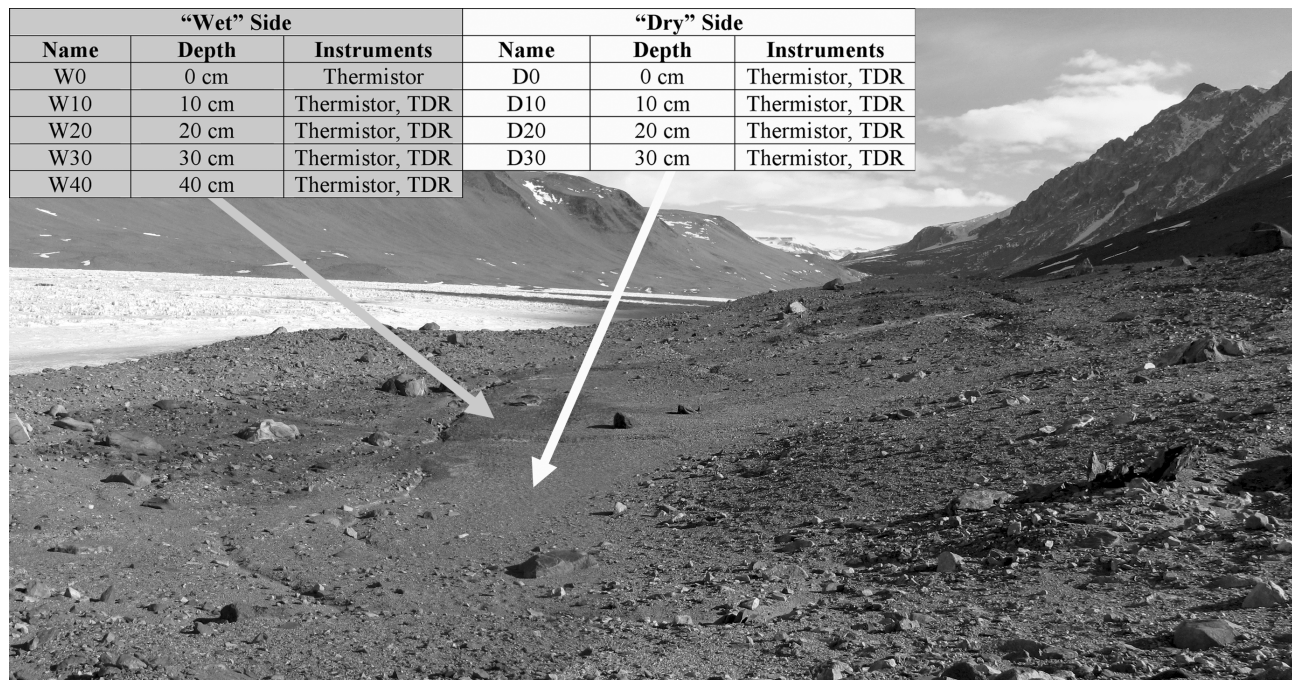


Figure 2. The Lake Hoare experimental site. Sensor arrays were installed at the locations indicated by arrows.

$(0.0009t^2)-(0.0178t)+0.0817$, where t is the TDR travel time in ms). Differences between wet soil temperatures and dry soil temperatures are shown in Figure 4, which summarizes these data by depth in the soil column. Maximum temperatures are higher on the “wet” side at every depth, while minimum temperatures are comparable across depths, consistent with

conduction/air-temperature-dominated winter temperatures, and insolation/albedo-dominated summer temperatures. “Dry” soils are typical of MDV soils in terms of water content, seldom exceeding 10% by volume. In contrast, “wet” soils are saturated at depth, and wicking from the saturated layer results in transport of moisture to the surface throughout the

Table 1. Summary of Lake Hoare Experimental station temperatures and VWC by depth. (s) indicates summer-only records. T indicates temperature, VWC indicates volumetric water content.

| T (°C) | W0 | W10 | W20 | W30 | W40 | D0 | D10 | D20 | D30 |
|---------|-----------|-------|-------|-------|-------|-------|-------|-------|-------|
| Max | 21.5 (s) | 12.4 | 7.0 | 4.6 | 1.7 | 19.7 | 9.9 | 5.6 | 1.1 |
| Min | -10.7 (s) | -39.5 | -37.7 | -35.9 | -34.7 | -42.9 | -39.3 | -37.6 | -32.9 |
| Mean | 4.1 (s) | -17.2 | -17.4 | -17.3 | -17.5 | -17.7 | -17.7 | -17.9 | -17.3 |
| VWC (%) | W0 | W10 | W20 | W30 | W40 | D0 | D10 | D20 | D30 |
| Max | NA | 15% | 21% | 32% | 32% | 10% | 8% | 8% | 8% |
| Min | NA | 7% | 7% | 8% | 8% | 4% | 5% | 5% | 5% |
| Mean | NA | 8% | 10% | 12% | 11% | 5% | 5% | 6% | 5% |

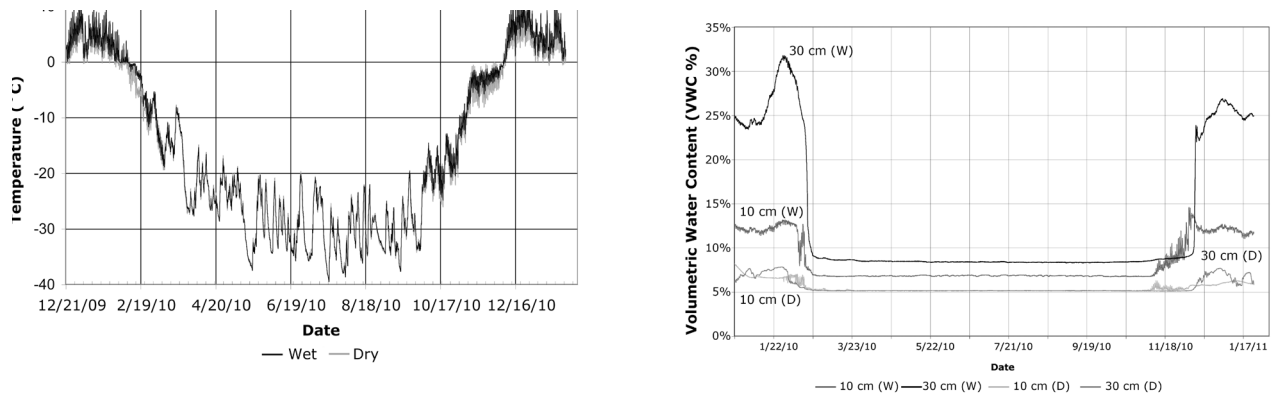


Figure 3. (Left) Soil temperature measurements at 10 cm depth from the Lake Hoare experimental station at 1-hour intervals. (Right) Measured volumetric water contents at 10 cm and 30 cm depth from wet (W) and dry (D) soil columns.

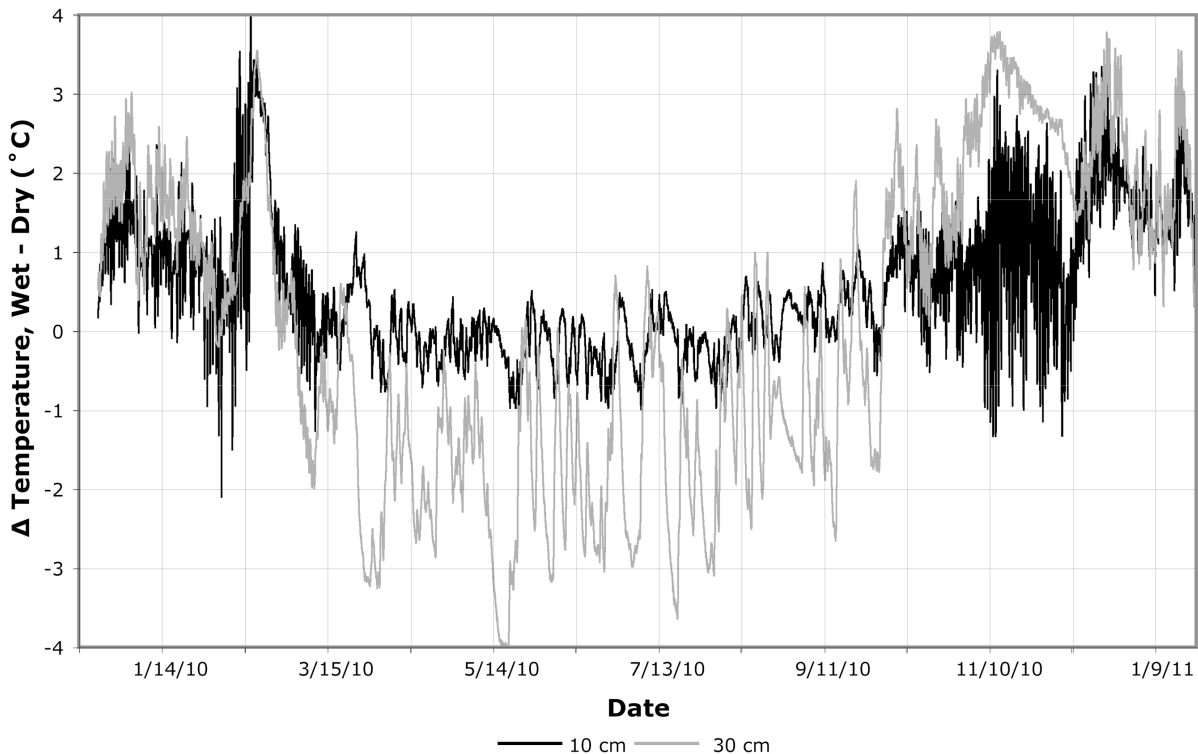


Figure 4. Difference between wet soil and dry soil temperatures at the Lake Hoare experimental site. Wet soils are colder (negative differences) in the winter, and warmer (positive differences) in the summer. Note that wet soils are isothermal at 0°C during autumn freezing (February 2010), producing a positive excursion on the plot.

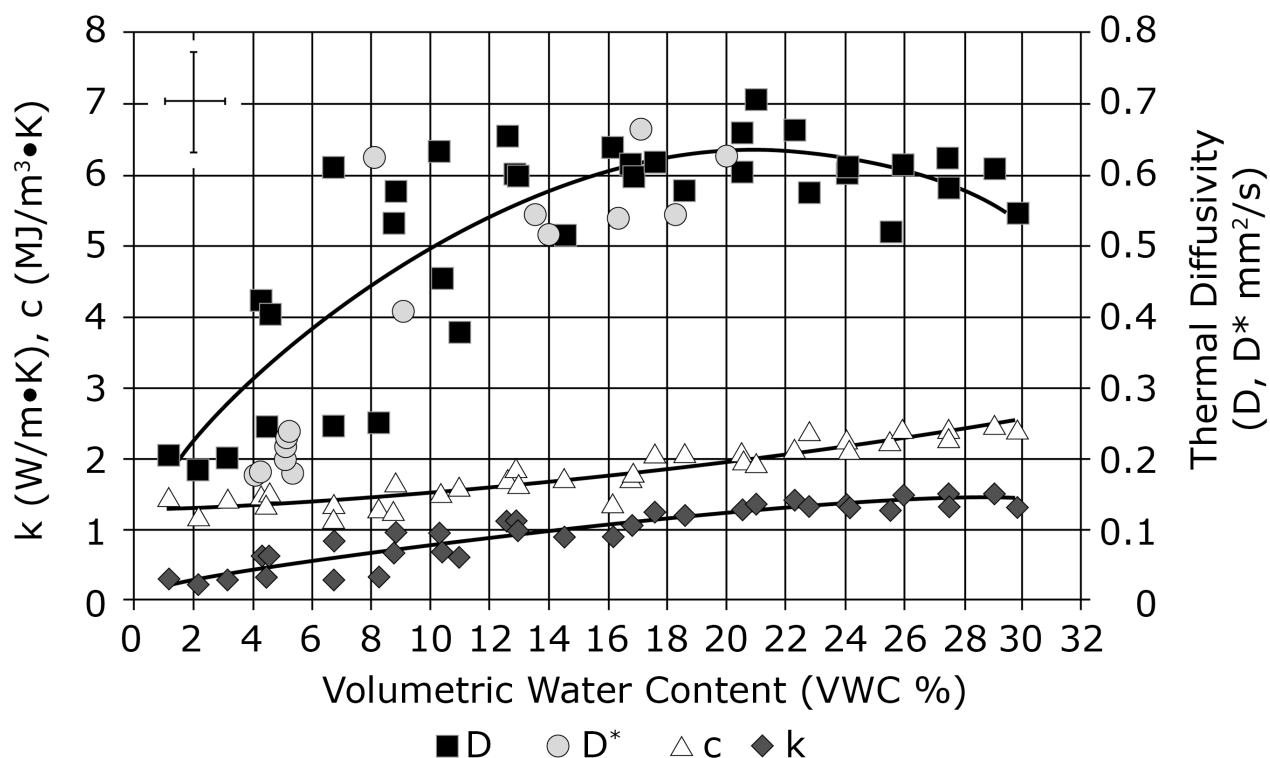


Figure 5. Lake Hoare basin soil thermal properties as a function of volumetric water content. D is thermal diffusivity measured in laboratory analysis of soil samples. D^* is field measurements of thermal diffusivity, c is soil heat capacity, and k is soil thermal conductivity. Lines represent polynomial best fits. Maximum error bars for D and D^* are shown in the upper left corner. Error bars for c and k are smaller than the symbols.

austral summer, resulting in high near-surface water contents (manifest as visible darkening at the ground surface). Visibly dark, damp soils typically have summer volumetric water contents of $\sim 12\%$, while dry soils have VWC values of $< 5\%$. Active layer thicknesses in dry soils at the experimental site average 19 cm, while wet soils have an average thaw depth of 45 cm. Winter depth to ice cement typically averages 0–1 cm for wet soils and ~ 10 cm for dry soils.

Laboratory analysis of thermal properties

Thermal diffusivity (D) is the ratio between soil thermal conductivity (k) and soil volumetric heat capacity (c). Because k and c are sensitive functions of soil water content, D is sensitive to the volumetric water content. A detailed view of the effects of soil moisture on thermal diffusivity was achieved by directly measuring the changes of D , k , and c resulting from known additions of water to Lake Hoare Basin soil samples (sandy haploorthels, 75%–80% sand by mass) using a KD2 Pro thermal properties analyzer. Figure 5 shows the composite results from five soil samples typical of the Lake Hoare basin (36 measurements) at $\sim 15^\circ\text{C}$. The best-fit regression lines are: $D = -0.001(\text{VWC})^2 + 0.048(\text{VWC}) + 0.132$ ($R^2 = 0.705$); $c = 0.001(\text{VWC})^2 + 0.020(\text{VWC}) + 1.262$ ($R^2 = 0.868$); and $k = -0.001(\text{VWC})^2 + 0.078(\text{VWC}) + 0.114$ ($R^2 = 0.866$).

For comparison, the D values measured in the field for a range of wet soils are also shown (D^*). As anticipated, D

increases with increasing soil moisture. However, as with the experimental plot, the decrease in D with increasing soil moisture above ~ 20 – 22% , typical of classic soil thermal properties measurements (e.g., Baver et al. 1972), is not a major feature of the dataset. This may be because the KD2 is partially sensitive to apparent thermal diffusivity (here used to indicate heat transport via a combination of both conduction and small-scale fluid convection).

Comparisons with meteorological network data

Decadal temperature trends for MCM-LTER meteorological stations located throughout Taylor Valley and the MDV are shown in Table 2. Temperature trends were calculated by performing a linear regression on available temperature records. The Lake Hoare, Lake Fryxell, Lake Bonney, and Explorer's Cove stations are all located in Taylor Valley. cursory analysis indicates that MDV soils have undergone decade-scale cooling of a similar magnitude to MDV air temperatures.

Lake levels have risen during the observation period recorded in Table 2 (Barrett et al. 2008). This suggests the possibility that the expansion of lake margin hyporheic zones (wetted zones) into monitored soil patches (typically located adjacent to lakes) has influenced the long-term temperature record through modification of lake shore permafrost thermal properties and energy balance (Ikard et al. 2009).

Table 2. Average temperature change (°C/year) at MCM-LTER meteorological station sites as a function of depth.

| Site | 0 cm | 5 cm | 10 cm | Years Sampled |
|-----------------|--------------|--------------|--------------|---------------|
| Lk Brownworth | -0.02 | -0.08 | -0.12 | 1995-2008 |
| Lake Vida | -0.03 | -0.07 | -0.09 | 1996-2008 |
| Lake Fryxell | +0.02 | -0.08 | -0.01 | 1995-2008 |
| Beacon Valley | -0.09 | -0.13 | -0.14 | 2001-2008 |
| Lake Hoare | +0.32 | +0.48 | +0.22 | 1994-2008 |
| Lake Bonney | -0.10 | -0.12 | -0.10 | 1995-2008 |
| Lake Vanda | +0.02 | -0.04 | +0.04 | 1995-2008 |
| Explorer's Cove | -0.08 | +0.43 | +0.35 | 2003-2008 |

Discussion and Conclusions

The important result to stem from the ATD measurements is that there appear to be two major styles of heat transport in ADV soils. For dry soils, insulation is the norm. Dry soils neither warm excessively in the summer nor cool deeply in the winter due to low thermal conductivity and low thermal diffusivity. In contrast, wet soils have high ratios of conductivity to heat capacity. These soils freeze deeply but also thaw deeply, producing active layers that can be twice as deep as adjacent dry soils (Levy et al. 2011). Interestingly, the dominance of latent heat effects in active layer soils near 0°C typically reduces the apparent thermal diffusivity of warm/wet soils by up to an order of magnitude as compared to cold/dry soils (Romanovsky et al. 2010). The dominance of latent heat effects in Taylor Valley permafrost can be clearly seen in the relative long zero curtain (Fig. 4), the prevalence of isothermal conditions in wet soils, and the strong thermal offsets between wet and dry soils (Romanovsky et al. 2010).

What may be important over time is the transition between dry (VWC < 10%) and wet soils (VWC > 10%) in the MDV. Soils that have had low VWC for tens of thousands of years (or, in cases, millions of years, for example, in Beacon Valley) may become seasonally wetter with increasing snowfall, enhanced glacier runoff, or slightly deeper thawing into ice-cemented (or massive ice) permafrost. These soils are at risk for entering a new thermal regime characterized by high VWC, high thermal diffusivity (Fig. 5), and deep thaw. If soil moisture remains available, potentially runaway thawing could form increases in D driven by increased VWC, which in turn increases ground ice thaw and soil VWC. As a result, there is the potential for MDV permafrost to reach a soil-moisture driven “tipping point.” Transitions from “dry” to “wet” soils will fundamentally change the thermal character of MDV permafrost and may promote rapid landscape change as stable permafrost begins to thaw, slump, and cryoturbate. If saturated active layer conditions develop across broad sections of the MDV, where dry permafrost now persists (Bockheim et al. 2007), it is possible that water track drainage systems will spread beyond their current extent (Levy et al. 2011), resulting in considerably greater geochemical, hydrological, and ecological connectivity at the hillslope scale. Understanding the ecological effects of newly wetted soils on organisms

habituated to dry, stable soils (Virginia & Wall 1999, Wall, 2007) may represent a new frontier in MDV ecosystem research.

Acknowledgments

This work is supported by the Antarctic Organisms and Ecosystems Program in the Antarctic Sciences Division of the National Science Foundation (grant #ANT-0851965 to JSL). This project has benefited greatly from discussion with MCM-LTER team members (www.mcmlter.org).

References

- Arblaster, J.M. & Meehl, G.A. 2006. Contributions of external forcings to southern annual mode trends. *Journal of Climate* 19: 2896-2905.
- Barrett, J.E., Gooseff, M.N., & Takasc-Vesbach, C. 2009. Spatial variation in soil active-layer geochemistry across hydrologic margins in polar desert ecosystems. *Hydrology and Earth Systems Science* 13: 2349-2358.
- Barrett, J.E., Virginia, R.A., Wall, D.H., Doran, P.T., Fountain, A.G., Welch, K.A., & Lyons, W.B. 2008. Persistent effects of a discrete climate event on a polar desert ecosystem. *Global Change Biology* 14: 2249-2261.
- Baver, L.D., Gardiner, W.H., & Gardiner, W.R. 1972. *Soil Physics*, 4th ed. New York, NY: Wiley.
- Bockheim, J.G., Campbell, I.B., & McLeod, M. 2007. Permafrost distribution and active-layer depths in the McMurdo Dry Valleys, Antarctica. *Permafrost and Periglacial Processes* 18: 217-227.
- Campbell, I.B., Claridge, G.G.C., Campbell, D.I., & Balks, M.R. 1998. The soil environment of the McMurdo Dry Valleys, Antarctica. In: J.C. Prisco (eds) *Ecosystem Dynamics in a Polar Desert*. American Geophysical Union, Washington, D.C.: 297-322.
- Chapman, W.L. & Walsh, J.E. 2007. A synthesis of Antarctic temperatures. *Journal of Climate* 20: 4096-4117.
- Chinn, T.J. 1981. Hydrology and climate in the Ross Sea area. *Journal of the Royal Society of New Zealand* 11: 373-386.
- Claridge, G.G.C., Campbell, I.B., & Balks, M.R. 1997. Ionic migration in soils of the Dry Valley region. In: W.B. Lyons, C. Howard-Williams and I. Hawes (eds) *Ecosystem Processes in Antarctic Ice-Free Landscapes*. Balkema, Rotterdam: 137-143.
- Clow, G.D., Mckay, C.P., Simmons, G.M., Jr., & Wharton, R.A., Jr. 1988. Climatological observations and predicted sublimation rates at Lake Hoare, Antarctica. *Journal of Climatology* 1: 715-728.
- Doran, P.T., Mckay, C.P., Clow, G.D., Dana, G.L., Fountain, A.G., Nylen, T., & Lyons, W.B. 2002a. Valley floor climate observations from the McMurdo dry valleys, Antarctica, 1986-2000. *Journal of Geophysical Research* 107: doi:10.1029/2001JD002045.
- Doran, P.T., Prisco, J.C., Lyons, W.B., Walsh, J.E., Fountain, A.G., Mcknight, D.M., Moorhead, D.L., Virginia, R.A., Wall, D.H., Clow, G.D., Fritsen, C.H., Mckay, C.P.,

- & Parsons, A.N. 2002b. Antarctic climate cooling and terrestrial ecosystem response. *Nature* 415: 517-520.
- Fountain, A.G., Hoffman, M., Levy, J.S., Nysten, T.N., & Lyons, W.B. 2011. The hydrology of the McMurdo Dry Valleys, Antarctica, an energy-dominated system. In *International Symposium on Antarctic Earth Sciences*. Edinburgh, Scotland.
- Fountain, A.G., Nysten, T.N., Monaghan, A., Basagic, H.J., & Bromwich, D. 2010. Snow in the McMurdo Dry Valleys, Antarctica. *International Journal of Climatology* 30: 633-642.
- Gooseff, M.N., Barrett, J.E., Doran, P.T., Fountain, A.G., Lyons, W.B., Parsons, A.N., Porazinska, D.L., Virginia, R.A., & Wall, D.H. 2003a. Snow-patch influence on soil biogeochemical processes and invertebrate distribution in the McMurdo Dry Valleys, Antarctica. *Arctic and Alpine Research* 35: 91-99.
- Gooseff, M.N., Mcknight, D.M., Doran, P., Fountain, A.G., & Lyons, W.B. 2011. Hydrological connectivity of the landscape of the McMurdo Dry Valleys, Antarctica. *Geography Compass* 5: 1-16.
- Gooseff, M.N., Mcknight, D.M., Runkel, R.L., & Vaughn, B.H. 2003b. Determining long time scale hyporheic zone flow paths in Antarctic streams. *Hydrological Processes* 17: 1691-1710.
- Ikard, S.J., Gooseff, M.N., Barrett, J.E., & Takacs-Vesbach, C. 2009. Thermal characterisation of active layer across a soil moisture gradient in the McMurdo Dry Valleys, Antarctica. *Permafrost and Periglacial Processes* 20: 27-39.
- Kennedy, A.D. 1993. Water as a limiting factor in the Antarctic terrestrial environment: a biological synthesis. *Arctic and Alpine Research* 25: 308-315.
- Levy, J.S., Fountain, A.G., Gooseff, M.N., Welch, K.A., & Lyons, W.B. 2011. Water Tracks and Permafrost in Taylor Valley, Antarctica: Extensive and Shallow Groundwater Connectivity in a Cold Desert Ecosystem. *Geological Society of America Bulletin* 123: doi:10.1130/B30436.1.
- Lyons, W.B., Fountain, A.G., Doran, P.T., Priscu, J.C., Neumann, K., & Welch, K.A. 2000. Importance of landscape position and legacy: the evolution of the lakes in Taylor Valley, Antarctica. *Freshwater Biology* 43: 355-367.
- Mcknight, D.M., Niyogi, D.K., Alger, A.S., Bomblied, A., Conovitz, P.A., & Tate, C.M. 1999. Dry valley streams in Antarctica: Ecosystems waiting for water. *BioScience* 49: 985-995.
- Romanovsky, V.E., Smith, S.L., & Christiansen, H.H. 2010. Permafrost thermal state in the polar northern hemisphere during the International Polar Year 2007-2009: a synthesis. *Permafrost and Periglacial Processes* 21: 106-116.
- Shindell, D.T. & Schmidt, G.A. 2004. Southern hemisphere climate response to ozone changes and greenhouse gas increases. *Geophysical Research Letters* 31: doi:10.1029/2004GL020724.
- Virginia, R.A. & Wall, D.H. 1999. How soils structure communities in the Antarctic Dry Valleys. *BioScience* 49: 973-983.
- Wall, D.H. 2007. Global change tipping points: above- and below-ground biotic interactions in a low diversity ecosystem. *Philosophical Transactions of the Royal Society of London, Biology* 362: doi:10.1098/rstb.2006.1950.

Thermal Conductivity and Freezing Temperature of Oil-Contaminated Foundation Soils Surrounding the China-Russia Crude Oil Pipeline

Guoyu Li, Wei Ma, Wenjie Feng, Yanhu Mu

State Key Laboratory of Frozen Soils Engineering, Cold and Arid Regions Environmental and Engineering Research Institute, Chinese Academy of Sciences, Lanzhou, Gansu, China

Xingbai Li

School of Energy and Power Engineering, Lanzhou University of Technology, Lanzhou, China

Abstract

Thermal properties of soils surrounding an oil pipeline might vary greatly after being contaminated by oil. This study investigates this variation and its mechanisms by laboratory measurement of the thermal conductivity and freezing temperature of typical oil-contaminated foundation soils surrounding the China-Russia Crude Oil Pipeline (CRCOP). The results show that the thermal conductivity of the contaminated soils increases with increasing water content when the dry density remains constant. The conductivity initially decreases and then sharply increases, finally decreasing again with increasing oil content. The influence of temperature on thermal conductivity depends mainly on whether the pore water is frozen or unfrozen. The thermal conductivity is jointly controlled by location (absorbed around soil particles or freely existing in pore space), phase state (liquid or solid state), amount of liquid phase in soil (water and oil), and soil type. The freezing temperature of the contaminated soil decreases with increasing oil content. The varying mechanisms of the thermal conductivity and freezing temperature are described in detail. Results are important and valuable for the evaluation and forecast of oil migration, for environmental protection, for permafrost degradation, and for engineering stability.

Keywords: China-Russia Crude Oil Pipeline; environmental engineering; freezing temperature; oil contamination and migration; permafrost; thermal conductivity.

Introduction

In recent years, more oil pipelines have been constructed in cold regions to support rapid economic growth, especially in developing countries. The crude oil might be spilled on and under the ground surface as it is transported by the buried pipes. The spilled oil contaminates the soils and underground water, causing serious environmental and engineering problems. Generally, it is very difficult to rehabilitate the polluted environment and repair the damaged engineering structures in cold regions. Investigations of this environmental pollution and the associated engineering stability require appropriate thermal, hydrological, and mechanical parameters of the contaminated soils in both frozen and unfrozen state. To date, little information about these parameters is available.

Laboratory experiments have been conducted to study the effects of dry density, water content, temperature, salt content, soil type, and external loadings on the thermal conductivity of uncontaminated soils (Li & Cheng 1995, Wen et al. 2005, Xu et al. 2009, Li 2009). It is found that the thermal conductivity increased with increasing density, water content, salt content, and the loadings. The conductivity could be calculated by regarding the soil as the porous material; it has a greater value in the frozen soil than that in the unfrozen state (Liu et al. 2002, Xu & Zhan 2010). Investigations of freezing temperature are similar to research that has been carried out in past decades. The conductivity of oil-contaminated soils has been experimentally performed (Motenko & Nefedieva 2004, Motenko et al. 2003, Zhuravlev & Motenko 2004). Published research has shown that the thermal conductivity and freezing temperature of contaminated soil decrease with increasing

oil content. However, the effects of crude oil on the thermal conductivity, freezing temperature, and changing mechanisms have not been sufficiently quantified.

In this paper, soil adjacent to the China-Russia Crude Oil Pipeline (CRCOP) was collected in permafrost areas in Northeastern China. The soil samples were prepared in the laboratory and the thermal conductivity of the sample was measured under different temperatures, water contents, and oil contents in order to study the influence of these factors on the conductivity. In addition, the freezing temperature of samples with varying oil content was measured to investigate the effect of oil. The testing reports numerous thermal parameters for the quantitative evaluation and prediction of pipeline engineering stability in cold regions.

Testing Procedure

Sampling and instruments

The subsurface soil was collected from the specific location (50°42.086'N, 124°18.584'E) where the CRCOP passed across an underlying permafrost layer. The physical parameters of the collected soil were tested in the laboratory. The liquid and plastic limits were 48.3% and 30.8%, respectively. The plastic index was 17.5. The specific weight was 2.44. The grain-size distribution of soil is shown in Table 1. The crude oil for testing was collected from the Kelamayi Oil Field, Xijiang Province, in Northwestern China.

The QL-30 thermo-physical instrument was used to measure the thermal conductivity with unsteady heat flow (Wen et al. 2005, Xu et al. 2009). Samples can be tested in a short time. A cooling bath was employed to lower the temperature of

Table 1. Grain-size distribution of soil.

| Diameter (mm) | >0.05 | 0.05-0.01 | 0.01-0.005 | <0.005 |
|----------------|-------|-----------|------------|--------|
| Percentage (%) | 6.64 | 51.34 | 5.59 | 36.43 |

samples to determine the freezing temperature (Li et al. 2009). The steady temperature at the cooling curve versus time was defined as the freezing temperature after supercooling and temperature rise due to the latent heat induced by phase change from water to ice (Grechishcheva et al. 2001).

Testing procedure for thermal conductivity

The oil-contaminated soil is a multiple-phase (soil particle, water, oil, air) porous material. Air, water, and oil jointly occupy the pore volume in soil as the dry density is kept constant. The amount and state (liquid or solid) of various phases in soil commonly determine the magnitude of the thermal conductivity.

The dry soil, water, and oil were combined into a uniform mixture in a laboratory according to the experimental requirements (SBQTSMC 1999). The mixture was compressed into cylindrical soil samples with a height of 50 mm and a diameter of 61.8 mm. The completed samples were allowed to equilibrate for 24 hours to ensure a uniform distribution of water and oil. Then the thermal conductivity of the soil samples was measured according to the different testing requirements.

Testing procedure for freezing temperature

Soil collection and preparation were the same as that presented above for the thermal conductivity. Keeping the water content and dry density constant, soil samples with different oil contents were prepared to test the freezing temperature. The samples were placed in a small steel cell. The thermal sensor was inserted in the middle of the soil to measure the temperature, and the cell was fully sealed. The cooling bath was used to cool the sealed cell and to lower the temperature of samples. Testing continued until the temperature of the soil started to decrease again after a sharp rise due to the latent heat of phase change.

Results and Discussion

Variation in thermal conductivity with water content

The dry density and oil content of the tested samples were 1.38 g/cm^3 and 5.8%, respectively. The water contents were 11.7%, 16%, and 24%, respectively. Testing reveals that the thermal conductivity increases with increasing water content (Fig. 1), which is similar to previous experimental results (Li & Cheng 1995, Xu et al 2009). This is because water that replaces the pore air in soil as water content increases leads to a rise in thermal conductivity. The thermal conductivity of water is generally greater than that of air. Additionally, the thermal conductivity of frozen soil is greater than that of unfrozen soil because ice appears at negative temperatures.

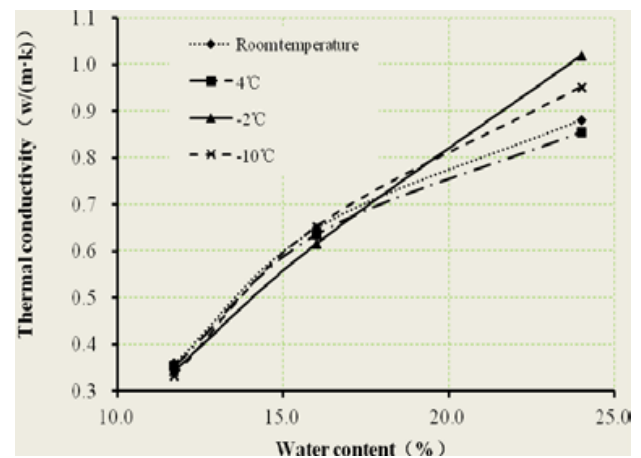


Figure 1. Response of thermal conductivity to increasing water contents.

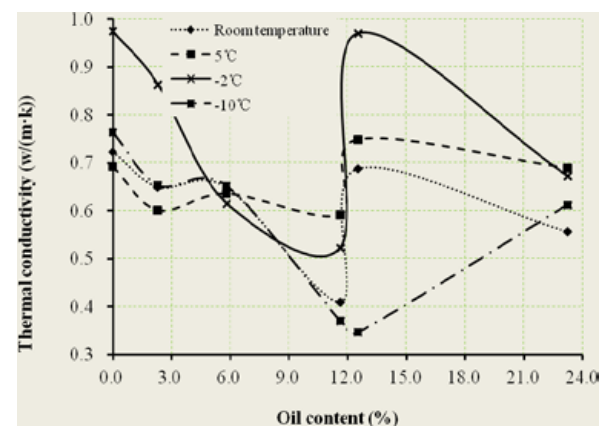


Figure 2. Response of thermal conductivity to increasing oil content.

Influence of oil content

Soil samples with oil contents of 0% (uncontaminated), 2.3%, 5.8%, 11.6%, 12.5%, and 23.2% were prepared. The dry density and water content were 1.38 g/cm^3 and 16%, respectively.

The results of the thermal conductivity versus oil content are shown in Figure 2. At lower oil contents, the thermal conductivity decreased gradually with increasing oil content. We attribute this to the weakened contact among soil particles due to the absorption of oil around soil particles as the oil content rises. At higher oil contents, some oil is absorbed around the soil particles and some oil replaces air in the soil pore space. This replacement results in an increase in thermal conductivity because the thermal conductivity of oil is much greater than that of air (no convection occurs). It reaches the maximum value when the oil content is 12.0% because the pore air is almost fully replaced by oil when soil is approximately saturated by oil (the saturation oil content is 12.5%); while oil content in soil continues to increase, the soil sample is saturated by oil. The saturation enables soil particles to separate, which weakens the contact among soil matrix.

Influence of temperature

Soil samples with varying oil contents were prepared to

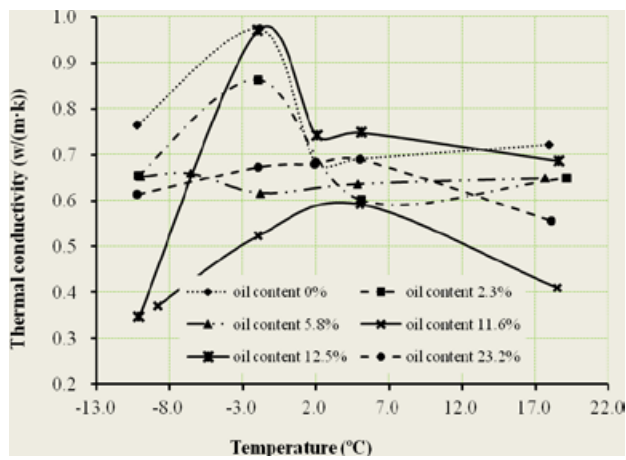


Figure 3. Response of thermal conductivity to different temperatures.

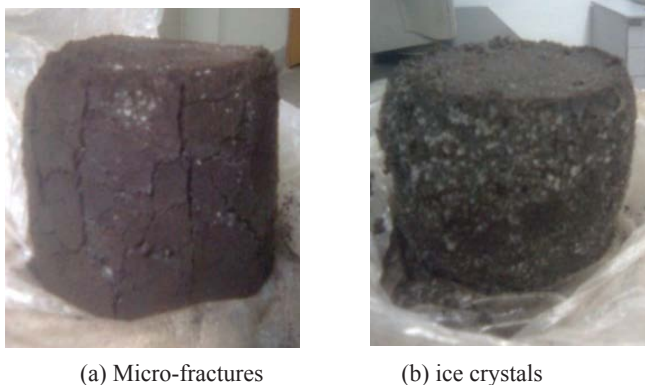


Figure 4. Visible micro-fractures and ice crystals in soil at negative temperature.

measure the thermal conductivity at different temperatures and oil content. The dry density and water content were kept constant at 1.38 g/cm^3 and 16%, respectively. The results are shown in Figure 3.

Results indicate that the changing curve can be divided into three phases. In the first phase, when temperatures were positive, the thermal conductivity of soil samples, having different oil contents of 0%, 2.3%, and 5.8%, decreased with decreasing temperature. However, the thermal conductivity of samples with oil contents of 11.6%, 12.5%, and 23.2% rose slightly with decreasing temperature. The possible reason is that some petroleum hydrocarbons were condensed to the solid state. The thermal conductivity of solid-state oil is always greater than that of the liquid state. In the second phase, close to 0°C , the thermal conductivity varied abruptly except for samples with oil contents of 5.8%, 11.6%, and 23.2%. The sudden variation is mainly caused by phase change from water to ice, partially by condensation of oil. In the third phase, when temperatures were negative, the thermal conductivity gradually decreased with decreasing temperature. This is attributed to volume dilation and micro-fractures induced by ice growth occurring in soil samples (Fig. 4).

Influence of oil on freezing temperature

Three soil samples were prepared with oil contents of 2%, 5%, and 20% to study the effect of oil on freezing temperature.

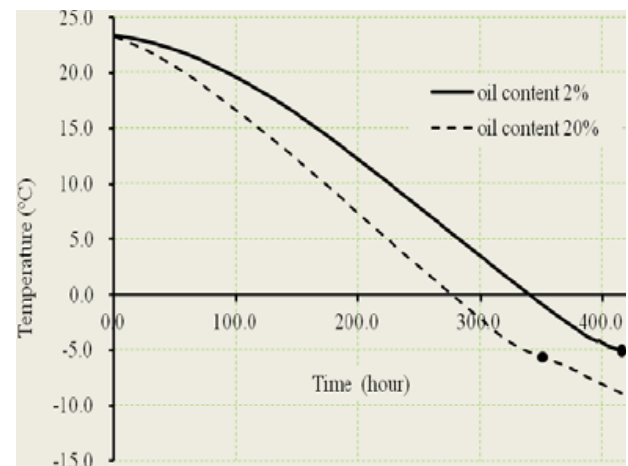


Figure 5. Cooling process of soil samples for determination of freezing temperature.

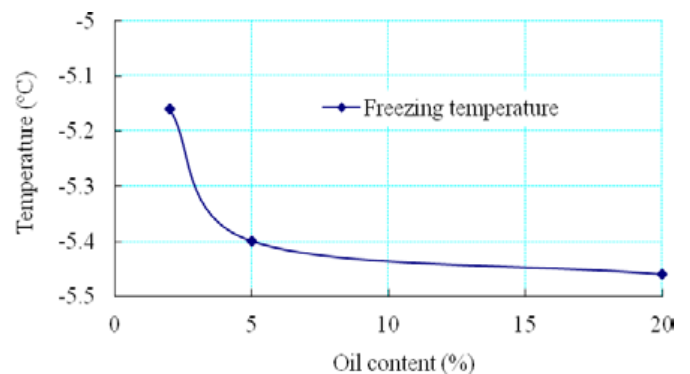


Figure 6. Variation in freezing temperature with oil content.

The dry density and water content were kept constant at 1.25 g/cm^3 and 16%, respectively.

The freezing temperature is determined by the cooling curve of the soil sample. Generally, the temperature change can also be described by three phases when the soil sample was cooled (Grechishcheva et al. 2001). In the first phase, the temperature was reduced below the freezing point. The soil sample was cooled and super-cooled. Ice crystals did not appear in the soil. In the second phase, the soil sample was further cooled. Ice nucleation was generated and crystallized in the soil. During this period, the temperature abruptly increased due to the latent heat induced by strong phase change from water to ice. In the third phase, the soil sample continued to be cooled. The temperature remained constant until ice and water distribution became homogeneous. After this, the temperature began to decrease again. The cooling curves are shown in Figure 5 and the testing results are shown in Figure 6.

The effects of temperature rise due to phase change in oil-contaminated soil are not clear (Fig. 5). Freezing temperatures are -5.16°C , -5.40°C , and -5.46°C , corresponding to oil contents of 2%, 5%, and 20%, respectively (Fig. 6). The freezing temperature falls with increasing oil content. This suggests that oil causes soil to have a lower freezing point. It is more difficult for pore water to change into ice in oil-contaminated soil, probably due to dissolved hydrocarbons.

Conclusions

The thermal conductivity of oil-contaminated soil increases with increasing water content. At equal water content, the thermal conductivity of frozen soil is greater than that of unfrozen soil.

The thermal conductivity of soil first decreases, then abruptly increases, finally decreasing again with increasing oil content.

The influence of temperature on the thermal conductivity is mainly dependent on the phase state of pore water. Phase change, volume dilation, and micro-fracturing play key roles in determining the thermal conductivity.

The thermal conductivity of oil-contaminated soil is jointly controlled by location, amount, phase state, thermal property of water and oil, and soil type.

The freezing temperature of oil-contaminated soil falls with increasing oil content. More oil causes the soil sample to have a lower freezing point.

Acknowledgments

This work was supported by the Chinese Academy of Sciences (CAS) Western Project (No. KZCX2-XB2-10), National Natural Science Foundation of China (Nos. 40821001, 40801022, 41023003, and 40971046), Funds of the State Key Laboratory of Frozen Soils Engineering, CAS (Nos. SKLFSE-ZY-03 and SKLFSE-ZQ-02), and the Western Communications Construction Scientific and Technological Project (No. 200831800025).

References

- Grechishcheva, S.E., Instanes, A., & Sheshin, J.B. 2001. Laboratory investigation of the freezing point of oil-polluted soils. *Cold Regions Science and Technology* 32: 183-189.
- Li, G., Yu, W., & Ma, Wei et al. 2009. Experimental study of characteristics of frost and salt heaves of saline highway foundation soils in seasonally frozen regions in Gansu Province. *Rock and Soil Mechanics* 30(8): 2276-2280 (in Chinese).
- Li, J. 2009. Testing and analysis of thermal properties of reservoir rocks. *Journal of Daqing Petroleum Institute* 33(5): 23-26 (in Chinese).
- Li, S. & Cheng, G. 1995. Problem of Heat and Moisture Transfer in Freezing and Thawing Soils. Lanzhou, *Lanzhou University Press*. pp.16-24 (in Chinese).
- Liu, W., He, P. & Zhang, Z. 2002. A calculation method of thermal conductivity of soils. *Journal of Glaciology and Geocryology* 24(6): 770-773 (in Chinese).
- Motenko, R.G., Ershov, E.D., & Chuvilin, E.M. 2003. Heat and mass transfer in freezing soils contaminated by oil. *Proceedings of the Eighth International Conference on Permafrost*. A.A. Publishers, Switzerland. Pp. 795-799.
- Motenko, R.G. & Nefedieva, Y.A. 2004. The influence of addition on thermal properties of oil contaminated frozen soils of different ground-size composition. *Journal of Glaciology and Geocryology* 26 (Suppl.1): 56-59.
- State Bureau of Quality and Technical Supervision and Ministry of Construction (SBQTSMC), People's Republic of China 1999. Standard for Soil Test Method. Beijing, China Planning Press.
- Wen, Z., Sheng, Yu. & Ma, Wei., et al. 2005. Experimental studies on thermal conductivity of undisturbed permafrost at Beiluhe testing site on the Qinghai-Tibet plateau. *Journal of Glaciology and Geocryology* 27(2): 182-187 (in Chinese).
- Xu, T. & Zhan, S. 2010. Theoretical calculation of thermal conductivity for moisture-content for porous building materials. *Low Temperature Architecture Technology* (6): 119-120 (in Chinese).
- Xu, X., Wang, J. & Zhang, L. 2009. *Frozen Soil Physics*. Beijing, Science Press. pp. 121-131 (in Chinese).
- Zhuravlev, I.I. & Motenko, R.G. 2004. The oil contamination influence on heat transfer in frozen soils. *Journal of Glaciology and Geocryology* 26 (Suppl.1): 128-132.

Ice-Wedge Polygon Type Controls Low-Gradient Watershed-Scale Hydrology

A.K. Liljedahl

Water and Environmental Research Center and International Arctic Research Center, University of Alaska Fairbanks, USA

L.D. Hinzman

International Arctic Research Center, University of Alaska Fairbanks, USA

J. Schulla

Hydrologic Software Consultant, Zurich, Switzerland

Abstract

Ice-wedge polygons and related microtopographic variations are ubiquitous in landscapes underlain by permafrost. High- and low-centered polygons are typical, but surprisingly their role on hydrologic fluxes and stocks is not well quantified. We performed hydrologic modeling analyses using the physically-based model WaSiM-ETH which was forced by data from the Biocomplexity Experiment, Barrow, Alaska (1999 to 2009), to assess the effect of ice-wedge polygon type on watershed-scale hydrology. Low-centered polygons, through elevated rims, reduced runoff while increasing evapotranspiration and surface water storage. The high-centered polygon landscape produced more than twice the runoff than the low-centered polygons, while storage and runoff drastically decreased. It is evident that microtopography plays an important role on the watershed-scale hydrologic fluxes and stocks of low-gradient arctic wetlands. Permafrost degradation could transform low- into high-centered polygons, which could potentially dominate the direct effects of climate change on arctic wetland hydrology.

Keywords: ice-wedge polygons; watershed; hydrology; water balance.

Introduction

Wetlands are common across the pan-arctic landscape (Tarnocai and Zoltai 1988) and their unique geomorphological and hydrologic features are important components of the tundra ecosystem (Walker et al. 2004) and the global climate system (Chapin et al. 2005). Landforms associated with arctic wetlands, such as vegetated drained thaw lakes and patterned ground may play an important role in basin hydrology (Kane et al. 2003). It has been proposed that not accounting for the role of tundra micro-scale heterogeneity could lead to large uncertainty in regional estimates of carbon and energy exchange (Sellers et al. 1997, Ostendorf et al. 2001).

Changes to the surface topography of arctic wetlands can be abrupt and easily initiated. Despite the cold and continuous permafrost in Northern Alaska, Jorgenson et al. (2006) documented a widespread degradation of ice wedges occurring over a decadal time scale of moderate climate warming (2–5°C). Further, Fortier et al. (2007) demonstrated that in just four summers, infiltration of snowmelt runoff into ice-wedge cracks can result in a continuous system of gullies through thermo-erosion. Thus, in a relatively short time period, a low-centered polygon landscape can turn into a high-centered polygon landscape due to melting of ice wedges.

Projected effects on the tundra ecosystem may not have properly accounted for the dynamic control of geomorphology under a changed climate (Ellis and Rocherfort 2004). Considering that a) a substantial portion of the pan-arctic landscape is represented by polygon mires (250,000 km²) (Minke et al. 2007) with b) dynamic low- and high-centered polygons, and c) that the air temperature and precipitation is projected to increase (Walsh 2008), more research is needed to examine the effect of patterned ground on hydrology. This

paper assesses the watershed-scale hydrologic impact as a low-centered polygon landscape is transformed into high-centered polygon tundra. We evaluate the change in the basin water balance through simple modeling experiments forced by data collected at a vegetated drained thaw lake basin in Barrow, northern Alaska. The model experiments represent a first approximation in assessing the effects of ice-wedge polygon type on watershed hydrology as we did not include the effects of frozen ground on hydraulic conductivity and subsurface storage capacity.

Background

In the field of geocryology, the term polygon refers to closed, multisided, roughly equidimensional patterned ground features, bounded by more or less straight sides (van Everdingen 1998). The two major types of ice-wedge polygons are low-centered and high-centered polygons. Both of these features strongly influence the hydrologic, pedological, and biological variations in low-land tundra (Brown et al. 1980) including meter-scale variations in near-surface soil moisture (Engstrom et al. 2005), plant distribution (Webber 1978), snow accumulation (Webber et al. 1980), active layer depth (Minke et al. 2009), soil biological activity (Mueller et al. 1999), and the export of natural chlorine and bromine to the stratosphere (Teh et al. 2009). Even though the tundra wetlands may at first appear as a featureless plain, its typical polygonal landforms result in a highly variable and dynamic environment.

The mosaic in surface hydrology results in extensive spatial variations in soil respiration (Sommerkorn 2008) and net ecosystem carbon fluxes (Olivas et al. 2011). Basins of low-centered polygons are either temporary or continuously flooded during the summer (Liljedahl 2011). High-centered polygons

are well drained with the troughs often serving as effective pathways for the movement of water and nutrients, especially during snowmelt (Woo and Guan 2006). Rims of the low-centered polygons and centers of the high-centered polygons are both exposed to summer and winter climate extremes (Brown et al. 1980). A topographic reversal of a low-centered polygon into the formation of troughs and, thus, eventually a well-drained high-centered polygon can therefore have major implications for ecosystem structure and functioning.

Field studies have shown complex micro- and watershed-scale lateral hydrologic connectivity of arctic wetlands. Widespread flooding (Rovaneck et al. 1996) allows effective surface flow connectivity during freshets (Woo and Guan 2006). In summer, the shallower thaw in combination with a higher ground surface of low-centered polygon rims form ridges of frozen ground (Minke et al. 2007), which can serve as hydrologic barriers (Donner 2007). Accordingly, the threshold water level that allows for a subsurface lateral connection varies in time due to the seasonal development of the active layer. Adding to the complexity is the advective heat transfer, where lateral flow can produce pathways within these barriers (Donner 2007). Such thermal erosion is an effective positive feedback mechanism that results in further lowering of the threshold water levels. Thus hydrologic fluxes and stocks are intrinsically and dynamically linked to the unique tundra microtopographic units. Still the role of low- and high-centered polygonal ground on watershed-scale water balance is poorly constrained and rarely, if ever, represented in hydrologic models.

Site Description

The site, here referred to as the Biocomplexity Experiment (71°16'51"N, 156°35'47"W, elevation 4.5 m), is located a few kilometers from the Beaufort Sea near Barrow on the Arctic Coastal Plain in northern Alaska. Mean annual air temperature at the Barrow Airport is -12.0°C (1977–2009) where summer (June through August) averages 3.3°C. About 55% of the annual precipitation (173 mm, 1977–2009) falls during June through September (99 mm) and represents adjusted precipitation following the WMO method described by Yang et al. (1998).

The Biocomplexity Experiment site is largely represented by a vegetated drained thaw lake basin (DTLB). DTLBs occupy approximately 26% of the western Arctic Coastal Plain (Hinkel et al. 2005) and 50% of the Barrow Peninsula north of ~71° latitude (Hinkel et al. 2003). The site has poorly drained wet tundra meadow with Typic Aquiturbels soils (Bockheim et al. 1999) underlain by 600 m of ice-rich permafrost (Brown and Johnson 1965). Low-centered polygons are common within the lake bed, while high-centered polygons dominate the upland tundra. Interannual variation of the mean active layer depth at nearby locations varied from 29 to 35 cm (1995–2009) (Shiklomanov et al. 2010).

Mosses represent most of the live above ground biomass at the site (Zona et al. 2009). Vascular plant composition is represented by sedges (*Carex aquatilis*) and grasses (*Eriophorum* and *Dupontia*) with an average LAI in mid-

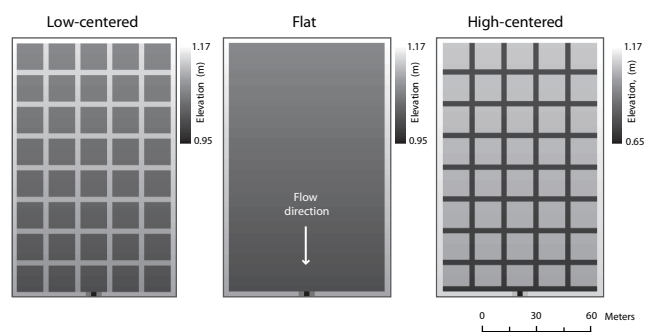


Figure 1. The schematic digital elevation models used in the modeling analysis representing low-centered polygons with 8-cm-high rims, a flat surface, and high-centered polygons with 30-cm-deep troughs. The surface has a general slope of 0.03% as determined by airborne Lidar surveys of a vegetated drained lake basin near Barrow, Alaska.

August 2006 of 0.43, 0.13, and 0.02, respectively (Zona et al. 2011). Senescence in the region begins in August (Myers and Pitelka 1979).

Methods

Schematic DEMs

The effect of polygon rims on the water balance was quantified using three artificially produced DEMs (Fig. 1). The artificial DEM represent a simplistic DTLB by having the same slope (0.03%) as the DTLB at the Biocomplexity Experiment, Barrow, Alaska (Liljedahl 2011). Airborne Lidar and field surveys of the Barrow DTLB show low-centered polygon rims up to about 10 cm height. Accordingly, low-centered polygon rims were represented by a network of elevated pixels (+8 cm) within the schematic DTLB. A second schematic DEM represents the DTLB as a featureless surface, while the third presents a DTLB having high-centered polygons and a connected network of 30 cm deep troughs.

Hydrologic model

We chose the physically-based hydrologic model Water Balance Simulation Model (WaSiM-ETH) (Schulla 1997, Schulla and Jasper 2007). WaSiM-ETH is a well-established tool for modeling the spatial and temporal variability of hydrologic processes in complex basins ranging from less than 1 km² to more than 500,000 km². Its application has ranged from water management in arid and semi-arid regions (Bharati et al. 2008), flood forecasting (Jasper et al. 2002), water balance analyses of wetlands within lowland floodplains (Krause et al. 2007) and, in the Arctic (Liljedahl 2011), to the distribution of water and phosphorus yield-producing areas (Lindenschmidt et al. 2004), and many other hydrologic studies.

The WaSiM-ETH includes the Richards equation to represent the fluxes within the unsaturated soil zone. It is a 1-D finite difference scheme with multiple user-defined discrete soil layers. Here the infiltration into the soils was presented as if the soils were thawed. The lower boundary condition to the unsaturated zone is the groundwater layer (i.e., saturated zone), which is constant for a specific time step but variable

in time. The extraction of water from the different soil layers is done separately for soil evaporation and for transpiration before calculating the soil water fluxes. The first step is the extraction through transpiration (Penman-Monteith), which includes stress induced by soil moisture. The second step is the extraction of soil evaporation from bare soil (or moss), which is also linked to soil moisture status. The modeling of the groundwater and lateral flow is 2-D where the flux is estimated from the continuity and Darcy equations through an implicit finite difference approach (Gauss-Seidel-Algorithm with automatic estimation of successive over-relaxation factors).

Lateral flow is represented through channel routing (Manning-Strickler), base flow, interflow, and a surface routing module designed for small-scale applications. Infiltration excess and direct runoff from snow melt is used as input for the surface routing model. The surface runoff flows from cell to cell until a river cell is reached. In diverging areas, up to three flow paths are possible, while only one flow direction is allowed in converging areas (the steepest slope). The flow velocity depends on slope, roughness, and water film depth (Manning-Strickler) where the slope depends upon the elevation model plus the water storage. The dynamic generation of ponds occurs when elevation and local storage lead to a zero or inverted gradient. The time step of surface routing is dynamically decreased but, if necessary, it can also be parameterized.

Two different approaches were applied to represent surface flow. We utilized the surface routing module in the low-centered polygon and flat ground scenarios, while the troughs were parameterized as a channel network in the high-centered polygon landscape.

WaSiM-ETH was forced with 11 summers of hourly meteorological data collected near Barrow, Alaska, by the Center for Climate Change at San Diego State University, Circumpolar Active Layer Monitoring program, NOAA, ARM, and the National Weather Service. The model simulations were started just prior to each year's snow ablation and stopped during the onset of winter. The latter was defined as being the first day of ten consecutive days experiencing mean daily air temperatures below 0°C. In this particular application we did not represent the seasonal changes in the active layer nor the presence of permafrost. Instead, the model sensitivity analysis is solely based upon the change DEM and surface routing parameterization. Model parameters were given the same values as those presented by Liljedahl (2011).

Results

The polygon rims affect several components of the water balance. The multi-week-long ponding (hydroperiod) of the DTLB was only replicated when low-centered polygons were represented (Fig. 2). When no elevated rims were present, the hydroperiod was limited to 5.2 (flat) and 0 days (high-centered) compared to 36 days in the low-centered polygon scenario. The mean inundated depth at low-centered polygons was 40 mm compared to 11 mm at the flat wetland scenario. Water levels were higher throughout the summer in the low-

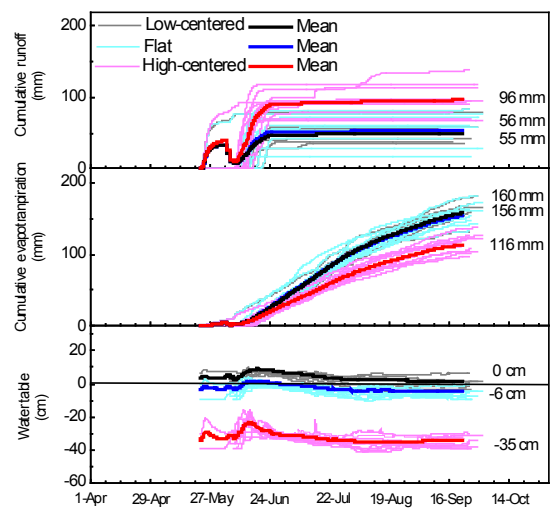


Figure 2. Simulated water table and cumulative runoff and evapotranspiration from the three schematic DEMs. Thin lines represent individual years, while thick lines are the long-term average. The mean runoff was about twice as high from the high-centered polygons compared to the low-centered polygons and the flat wetland. Evapotranspiration and soil water storage were reduced at the high-centered polygon. The typically observed multi-week-long ponding was only produced by the low-centered DEM.

centered polygon DTLB, where the absence of rims resulted in larger soil water storage deficits prior to freeze-up. In five of the 11 years, the ground surface was inundated prior to freeze-up in the low-centered polygon scenario, while the fall water table was always below the ground surface in late summer on the flat and high-centered polygon ground. The change in soil water storage, ΔS , was negligible on a decadal time scale, but year-to-year variations were found in all three scenarios.

Despite the larger soil water storage deficit, total runoff was higher in the high-centered polygon (96 mm) than the flat (53 mm) and low-centered polygon (49 mm) scenarios. The runoff ratio (runoff/SWE) was nearly doubled from the high-centered polygons (0.83) compared to the low-centered and flat basins (0.44 and 0.47, respectively).

Total evapotranspiration was reduced when troughs were present and also less variable among years. The flat and the low-centered polygon scenario had nearly identical evapotranspiration losses (156 and 160 mm, respectively), while the high-centered polygon area lost on average 116 mm. Total transpiration was the same amongst the scenarios (mean 55 mm). Accordingly, the role of transpiration on total evapotranspiration was increased during the high-centered polygon scenario (47% of total evapotranspiration) compared to the low-centered (34%).

Discussion

Micro-scale variations in surface topography, induced by ice-wedge polygons, control the water balance in these extremely low-gradient arctic watersheds. A transition from low- to high-centered polygon landscape resulted in a

dramatic alteration in the partitioning of the water balance. Overall, losses from the low-centered polygon scenario were dominated by evapotranspiration but total runoff was similar to evapotranspiration at the high-centered polygon landscape. We show that structural changes in the arctic soils at the order of centimeters can have dramatic effects on the watershed-scale hydrology.

Soil and surface water storage

The near-surface was typically saturated when rims were present. The autumn water table fluctuated above and below the ground surface amongst the years in the low-centered polygon scenario, while the fall water table of high-centered polygons always remains at depths where one would normally expect the permafrost table (see Shiklomanov et al. 2010). In that sense, the water table of high-centered polygons was less variable by supporting a consistently deep water table.

The 11 years of simulations suggest that it is typical for these systems, whether they are dominated by low- or high-centered polygons, to experience interannual variations in the soil water storage, ΔS . Annual water balance calculations based on assumptions of no change in ΔS would, according to the simulations, result in errors of up to 90 mm, which is half of the long-term mean annual precipitation in the Barrow area. Our simulations suggest that such methods should only be applied to datasets representing approximately a decade.

Lateral flow

The type of polygon feature affects the total discharge as well as the timing of the runoff. About half of the SWE did not contribute to streamflow from the low-centered polygon (56%) and flat wetland (53%). The limited difference was due to the larger soil water storage deficit (fall water table depth) at the flat scenario, which was of similar magnitude as the surface storage capacity of the low-centered polygons. The high-centered polygon scenario resulted in 27% of the SWE recharging the soils. In comparison, field studies performed by Kane et al. (2008) showed that on average 22% (1999–2007) of the SWE did not contribute to runoff in the Putuligayuk River watershed (471 km²), Arctic Coastal Plain, Alaska. In addition, the simulated runoff exits the basin earlier from the high-centered polygon scenario due to an effective network of channels and steeper micro-topographical gradients when compared to the other scenarios. Runoff is therefore drastically reduced and evaporation increased due not only to the presence of larger-scale features such as lakes and wetlands (Bowling and Lettenmaier 2010), but also to micro-scale features such as the presence of rims and the absence of a connected network of troughs and short, relatively steep slopes typical of high-centered polygons.

The high-centered polygon scenario represented an extreme scenario of the basin-scale lateral surface connectivity through the unified drainage network. Field observations have shown that the ground subsidence may not necessarily form a continuous network but rather disconnected channels and therefore small water bodies (Jorgenson et al. 2006).

Vertical fluxes

Total evapotranspiration from the high-centered polygon scenario was similar to the total amount of runoff. This is due partly to a larger runoff compared to flat and low-centered scenarios and to reduced evaporation. Open water/moss evaporation was lower from the high-centered polygons as the surface was water-limited due to the deeper water tables (~30 cm). The simulated water table in the flat scenario rarely dropped below 10 cm depth, which was within the parameterized zone of water accessible for evaporation (*Sphagnum* moss has shown to effectively transport water from a 10–15 cm deep water table through capillary flow (Price et al. 2009)). Hence, the position of the water table resulted in similar total evapotranspiration amongst the flat and low-centered polygon scenario, while reduced at the high-centered polygons.

Future directions

The modeling analysis presented a first-order approach in simulating the role of low- and high-centered polygons on arctic wetland hydrology. Neither the freeze-thaw dynamics within the active layer nor the permafrost was represented, both of which have shown to be important in tundra wetland hydrology. Consequently, the modeling did not include the differential distribution of lateral and vertical hydrologic barriers caused by the presence of ice-rich frozen ground. In addition, the trough network was continuous. Therefore, both the lateral hydrologic connectivity and the (liquid) soil water storage were likely overestimated, which suggests an overall underestimation in surface water storage. A representation of frozen ground would likely result in an increased hydrologic sensitivity to polygon type, although any disconnected channels (troughs) could partly offset the differences between ice-wedge polygon type on watershed-scale fluxes and stocks.

Conclusions

The model experiments presented a first-order approach in evaluating the role of microtopography on watershed-scale hydrology. A shift from low-centered to high-centered polygon dominated landscape results in drastic changes to watershed-scale water storage, runoff, and evapo-transpiration. Low-centered polygons promote extensive ponding, while high-centered polygons enhance runoff. Evapotranspiration is suppressed at high-centered polygon landscapes as the near-surface soil moisture is reduced. Therefore, not accounting for the role of microtopographical variability on hydrology can have dramatic consequences when estimating regional scale water and energy exchange. It is necessary to account for the microtopography and the dynamic role of geomorphology in regulating tundra microclimate in order to reduce the uncertainty in present and future pan-arctic hydrologic fluxes and stocks.

Acknowledgments

The Atmospheric Radiation Measurement Program provided radiation measurements. B. Cable and J. Long provided technical assistance. Financial support for this research was provided through the National Science Foundation (grants 0652838, 0632263, and 0421588) and student grants from the Swedish-America Foundation, Gemzeus Foundation, American Water Resources Association-Alaska Section, and the Center for Global Change and Arctic System Research.

References

- Bharati, L., Rodgers, C., Erdenberger, T., Plotnikova, M., Shumilov, S., Vlek, P., & Martin, N. 2008. Integration of economic and hydrologic models: Exploring conjunctive irrigation water use strategies in the Volta Basin. *Agr. Water Manag.* 95: 925-936.
- Bockheim, J.G., Everett, L.R., Hinkel, K.M., Nelson, F.E., & Brown, J. 1999. Soil organic carbon storage and distribution in arctic tundra, Barrow, Alaska. *Soil Sci. Soc. Am. J.* 63: 934-940.
- Bowling, L.C. & Lettenmaier, D.P. 2010. Modeling the effects of lakes and wetlands on the water balance of arctic environments. *J. Hydrometeorol.* 11(2): 276-295. doi: 10.1175/2009JHM1084.1
- Brown, J., & Johnson, P.L. 1965. Pedo-ecological investigations at Barrow, Alaska. *Tech. Rep.*, 159:32, 32 pp., US Army CRREL, Hanover, USA.
- Brown, J., Everett, K.R., Webber, P.J., MacLean, S.F., & Murray, D.F. 1980. The coastal tundra at Barrow. In *An arctic ecosystem: the coastal tundra at Barrow, Alaska*, editors Brown, J., Tieszen, P.C., and Bunnell, F.L., pp. 1-29, Dowden, Hutchinson and Ross Inc., Stroudsburg, PA.
- Chapin III, F.S., Sturm, M., Serreze, M.C., McFadden, J.P., Key, J.R., Lloyd, A.H., McGuire, A.D., Rupp, T.S., Lynch, A.H., Schimel, J.P., Beringer, J., Chapman, W.L., Epstein, H.E., Euskirchen, E.S., Hinzman, L.D., Jia, G., Ping, C.-L., Tape, K.D., Thompson, C.D.C., Walker, D.A., & Welker, J.M. 2005. Role of land-surface changes in arctic summer warming. *Science* 310: 657-660.
- Donner, N. 2007. Hydrological windows in low-centered arctic polygons: A landscape ecological perspective on polygon mires. M.S. thesis, Greifswald University, Germany.
- Ellis, C.J. & Rochefort, L. 2004. Century-scale development of polygon-patterned tundra wetland, Bylot Island (73°N, 80°W). *Ecol.* 85(4): 963-978.
- Engstrom, R., Hope, A., Kwon, H., Stow, D., & Zamolodchikov, D. 2005. Spatial distribution of near surface soil moisture and its relationship to microtopography in the Alaskan Arctic coastal plain. *Nordic Hydrol.* 36(3): 219-234.
- Fortier, D., Allard, M., & Shur, Y. 2007. Observation of rapid drainage system development by thermal erosion of ice wedges on Bylot Island, Canadian Arctic Archipelago. *Permafrost and Periglac. Process.* 18: 229-243.
- Hinkel, K.M., Eisner, W.R., Bockheim, J.G., Nelson, F.E., Peterson, K.M., & Dai, X. 2003. Spatial extent, age, and carbon stocks in drained thaw lake basins on the Barrow Peninsula, Alaska. *Arctic, Antarctic, and Alpine Res.* 35: 291-300.
- Hinkel, K.M., Frohn, R.C., Nelson, F.E., Eisner, W.R., & Beck, R.A. 2005. Morphometric and spatial analysis of thaw lakes and drained lake basins in the western Arctic Coastal Plain, Alaska. *Permafrost Periglacial.* 16(4): 327-341.
- Jasper, K., Gurtz, J., & Lang, H. 2002. Advanced flood forecasting in Alpine watershed by coupling meteorological observations and forecasts with a distributed hydrological model. *J. Hydrol.* 327: 40-52.
- Jorgenson, M.T., Shur, Y.L., & Pullman, E.R. 2006. Abrupt increase in permafrost degradation in Arctic Alaska. *Geophys. Res. Lett.* 33, L02503, doi:10.1029/2005GL024960.
- Kane, D.L., Gieck, R.E., & Bowling, L.C. 2003. Impacts of surficial permafrost landforms on surface hydrology. In *Proceedings of the Eighth International Conference on Permafrost*, edited by Phillips, Springman and Anderson, pp. 507-511, Balkema Publishers, Zurich, Switzerland.
- Kane, D.L., Gieck, R.E., & Hinzman, L.D. 2008. Water balance for a low-gradient watershed in Northern Alaska. In *Proceedings Ninth International Conference on Permafrost*, edited by D. L. Kane and K. M. Hinkel, University of Alaska Press, Fairbanks, AK.
- Krause, S., Jacobs, J., & Bronstert, A. 2007. Modelling the impacts of land-use and drainage density on the water balance of a lowland-floodplain landscape in northeast Germany. *Ecol. Modell.* 200: 475-492.
- Liljedahl, A.K. 2011. *The hydrologic regime at sub-arctic and arctic watersheds: present and projected*. Ph.D. Dissertation, University of Alaska, Fairbanks, AK.
- Lindenschmidt, K.-E., Ollesch, G., & Rode, M. 2004. Physically-based hydrological modeling for non-point dissolved phosphorous transport in small and medium sized river basins. *Hydrol. Sci. J.* 49(3): 495-510.
- Minke, M., Donner, N., Karpov, N., De Klerk, P., & Joosten, H. 2007. Distribution, diversity, development and dynamics of polygons mires: Examples from Northeast Yakutia (Siberia). *Peatlands Int.* 1: 36-40.
- Minke, M., Donner, N., Karpov, N., De Klerk, P., & Joosten, H. 2009. Patterns in vegetation composition, surface height and thaw depth in polygon mires in the Yakutian Arctic (NE Siberia): A microtopographical characterization of the active layer. *Perm. Perigl. Process.* 20: 357-368.
- Mueller, G., Broll, G., & Tarnocai, C. 1999. Biological activity as influenced by microtopography in a cryosolic soils, Baffin Island, Canada. *Perm. Periglac. Process.* 10: 279-288.
- Myers, J.P. & Pitelka, F.A. 1979. Variations in summer temperature patterns near Barrow, Alaska: Analysis and ecological interpretation. *Arct. Alp. Res.* 11: 131-144.
- Olivas, P.C., Oberbauer, S., & Kuchy, A. 2011. Effects of fine-scale topography on CO₂ flux components of Alaskan Coastal Plain Tundra: Response to contrasting growing seasons. *Arctic, Antarctic, and Alpine Res.* 43(2): 256-266.

- Ostendorf, B., Hilbert, D.W., Kostner, B., Tappeiner, U., & Tasser, E. 2001. The importance of understanding spatial pattern for scaling up plot-level matter and energy fluxes to regional scales. *Syst. Analys. Model. Sim.* 41(3): 391-408.
- Price, J., Edwards, T.W.D., Yi, Y., & Whittington, P.N. 2009. Physical and isotopic characterization of evaporation from Sphagnum moss. *J. Hydrol.* 369: 175-182.
- Rovaneck, R.J., Hinzman, L.D., & Kane D.L. 1996. Hydrology of a tundra wetland complex on the Alaskan Arctic Coastal Plain, U.S.A. *Arctic, Alp Res.* 28(3): 311-317.
- Schulla, J. 1997. Hydrologische Modellierung von Flussgebieten zur Abschätzung der Folgen von Klimaänderungen (Hydrological modelling of river basins for estimating the effects of climate change). *Zurcher Geographische Schriften* 69, ETH Zurich, Switzerland.
- Schulla, J. & Jasper, K. 2007. Model description WaSiM-ETH, *Internal Report*. Institute for Atmospheric and Climate Science, ETH Zurich, Switzerland.
- Sellers, P.J., Heiser, M.D., Hall, F.G., Verma, S.B., Desjardins, R.L., Schuepp, P.M., & MacPherson, J.I. 1997. The impact of using area-averaged land surface properties - topography, vegetation condition, soil wetness - in calculations of intermediate scale (approximately 10 km²) surface-atmosphere heat and moisture fluxes. *J. Hydrol.* 190:269-301.
- Shiklomanov, N.I., Streletskiy, D.A., Nelson, F.E., Hollister, R.D., Romanovsky, V.E., Tweedie, C.E., & Brown, J. 2010. Decadal variations of active-layer thickness in moisture-controlled landscapes, Barrow, Alaska. *J. of Geophys. Res.* doi:10.1029/2009 JG001248.
- Sommerkorn, M. 2008. Micro-topographic patterns unravel controls of soil water and temperature on soil respiration in three Siberian tundra systems. *Soil Biol. Biochem.* 40: 1792-1802, doi:10.1016/j.soilbio. 2008.03.002.
- Tarnocai, C. 2006. The effects of climate change on carbon in Canadian peatlands. *Global Plan. Ch.* 53, 222-232.
- Tarnocai, C. & Zoltai, S.C. 1988. Wetlands of Arctic Canada. In *Wetlands of Canada. Ecological Land Classification Series No. 24.*, pp. 29-53, Environment Canada and Polysciences Publications Inc., Montreal, Canada.
- Teh, Y.A., Mazeas, O., Artwood, A.R. Abel, T., & Rhew, R.C. 2009. Hydrologic regulation of gross methyl chloride and methyl bromide uptake from Alaskan Arctic tundra. *Glob. Ch. Biol.* 15: 330-345, doi: 10.1111/j.1365-2486.2008.01749.x.
- van Everdingen, R.O. 1998. *Multilanguage glossary of permafrost and related ground-ice terms*. International Permafrost Association, The Arctic Institute of North America, Calgary, Canada.
- Walker, D.A., Epstein, H.E., Gould, W.A., Kelley, A.M., Kade, A.N., Knudson, J.A., Krantz, W.B., Michaelson, G., Peterson, R.A., Ping, C.-L., Raynolds, M.K., Romanovsky, V.E., & Shur, Y. 2004. Frost-boil ecosystems: Complex interactions between landforms, soils, vegetation and climate. *Perm. Periglac. Process.* 15: 171-188.
- Walsh, J.E. 2008. Climate of the Arctic Marine Environment. *Ecol. App.* 18(2): 3-22.
- Webber, P.J. 1978. Spatial and temporal variation of the vegetation and its productivity. In *Vegetation and Production Ecology of an Alaskan Arctic Tundra*, edited by L.L. Tieszen, pp. 37-112. Springer-Verlag, New York, NY.
- Webber, P.J., Miller, P.C., Chapin, F.S. III, & McCown, B.H. 1980. The vegetation: Pattern and succession. In *An arctic ecosystem: the coastal tundra at Barrow, Alaska*, edited by J. Brown et al., pp. 30-56, Dowden, Hutchinson and Ross Inc., Stroudsburg, PA.
- Woo, M.-K. & Guan, X.J. 2006. Hydrological Connectivity and Seasonal Storage Change of Tundra Ponds in a Polar Oasis Environment, Canadian High Arctic. *Perm. Perigl. Process.* 17: 309-323.
- Zona, D., Oechel, W.C., Peterson, K.M., Clements, R.J., Paw, K.T., & Ustin, S.L. 2009. Characterization of the carbon fluxes of a vegetated drained lake basin chronosequence on the Alaskan Arctic Coastal Plain. *Global. Ch. Biol.* doi: 10.1111/j.1365-2486.2009.02107.x
- Zona, D., Oechel, W.C., Richards, J.H., Hastings, S., Kopetz, I., Ikawa, H., & Oberbauer, S. 2011. Light stress avoidance mechanisms. In Sphagnum dominated wet coastal Arctic tundra ecosystem in Alaska. *Ecology* 92(3): 633-644.

Compression Test and Pore-Water Pressure Measurement for Warm and Ice-Rich Frozen Soil

Shiwei Liu, Jianming Zhang, Hu Zhang

State Key Laboratory of Frozen Soils Engineering, Cold and Arid Regions Environmental and Engineering Research Institute, Chinese Academy of Sciences, Lanzhou, Gansu, China

Bo Zheng

China Railway Southwest Research Co., Ltd., Chengdu, Sichuan, China

Abstract

In order to investigate the deformation mechanism of warm and ice-rich frozen soils, compression tests were conducted using two methods: (1) a traditional compression test under a constant temperature with a stepped load (CTSL), and (2) a compression test under a constant load and a stepped temperature (CLST), which is the more reasonable way to simulate the settlement process of engineering structures on permafrost under the conditions of global warming. Two types of compressibility coefficients were employed to describe the degree of deformation sensitivity to warming temperature and increasing load, respectively. The pore-water pressure variations were measured using an antifreeze agent during the compression tests in order to explore the consolidation effect of the warm and ice-rich frozen soil.

Keywords: warm and ice-rich frozen soil; compression test; pore water pressure; consolidation effect.

Introduction

Warm frozen soil refers to frozen soil in the temperature range that experiences severe phase changes, and it is usually warmer than -1.5°C . The proportion of ice to unfrozen water in the soil is extremely sensitive to temperature variations, so the warm frozen soil is prone to considerable variation in physical-mechanical properties. At the same time, if the soil contains a large amount of ice, namely ice-rich frozen soil, its rheological properties are more obvious. Upon thawing, such as that expected during global warming, ice-rich frozen soils will become a slurry, completely losing their load-bearing capacity. Even minor thawing can substantially deteriorate the soil's engineering properties. Therefore, it is important to study the physical-mechanical properties of warm and ice-rich frozen soils (WIRFS). Current research on the deformation mechanisms of WIRFS is rare and immature. Compression tests on warm frozen soils at various temperatures were first carried out in Russia (Tsyтович 1975); then Zhu and Zhang (1982) proposed an equation for estimating the relative compressibility coefficient of warm frozen soils. Arenson and Springman (2005a, b) developed a mathematical model to describe the thermo-mechanical behavior of ice-rich frozen soils at temperatures near 0°C .

Pore-water pressure measurements have been used to study frost heave mechanisms as well as freezing and thawing cycles (Eigenbrod et al. 1996, Akagawa et al. 2008). It is particularly interesting to explore the methods of pore-water pressure measurement and the law of pore-water pressure dissipation for warm frozen soil during the compression process. Currently, in the coupled heat-moisture-mechanic model of frozen soil, the governing equations are established on the assumption that the seepage flow of the unfrozen water follows Darcy's law; however, this assumption needs further justification.

To address the problem of the deformation mechanism of WIRFS, we conducted compression tests using two methods: (1) a traditional compression test under a constant temperature and a stepped load (CTSL), and (2) a compression test under a constant load and a stepped temperature (CLST). Pore-water pressure variation was measured simultaneously.

Equipment and Methods

Temperature control

We developed a set of high-precision temperature control equipment to ensure the accuracy of temperature in the compression tests. The equipment mainly consists of a cooling system, a temperature-control system, a loading system, a data acquisition system, and the K_0 consolidation test apparatus. The cooling system is based on a modified refrigerator. In our tests, the temperature was controlled both in the laboratory and in the refrigerator. The laboratory temperature was controlled with an air-conditioner unit, which limited the fluctuation of the temperature within 5°C . The temperature in the refrigerator was modulated with a high-precision numerical control apparatus, which automatically calibrated the refrigerator's temperature with an accuracy of 0.01°C . The data acquisition system employed a Datataker500 data logger (<http://www.datataker.com>). The details of our equipment and temperature control system can also be found in the literature (Qin et al. 2009, Zheng et al. 2009).

Sample preparation

There is a close relationship between water content and dry density in the naturally frozen soils. According to Wang (1983), we initially identified the dry density (ρ_d) of our soil sample, and then determined the total water content (ice + water; w) in the soil. Our samples are 40 mm high with a diameter of 61.8

mm and a volume of 120 cm³. The mass (*m*) of soil grain, ice, and water needed for a sample were determined by:

$$m_s = \rho_d v \tag{1}$$

$$m_w = w m_s \tag{2}$$

$$m_{\text{unfrozen}} = \chi m_w \tag{3}$$

$$m_i = (1 - \chi) m_w \tag{4}$$

where χ is a dimensionless empirical parameter related to soil type. For clay, the value of χ can be set at 0.13~0.25. For sand, χ can be set at 0.07~0.10. For our clay samples, $\chi = 0.15$ provided the best sample quality, and $\chi = 0.08$ provided the best sand sample quality. Table 1 shows the water content and dry density for our samples.

We created ice crystals from distilled water. In the cold room at about -6°C, we ground the prepared ice into ice powder and mixed it with the pre-cooled soil in a plastic bag. Then a calculated amount of pre-cooled water close to 0°C was sprinkled on the soil-ice mixture. Finally, the ice-soil-water composite was mixed and put into a pre-cooled uniform mold. The thickness of samples was controlled with a hydraulic hoisting jack. Molds were placed in the refrigerator to freeze for 24 h, forming isotropically uniform frozen soil samples. Samples were then wrapped with a plastic film to inhibit evaporation.

Compression tests

The experiments were conducted at the State Key Laboratory of Frozen Soil Engineering in Lanzhou, China. The CTSL model used a frozen soil sample that was loaded under temperatures of -1.5, -1.0, -0.5, and -0.3°C. At each temperature, the sample was subjected to a stepped load of 0.1, 0.2, 0.3, 0.4, 0.5, 0.6, and 0.7MPa. According to the National Standard for Soil Test Method (GB/T50123-1999), we measured the deformation of each loaded sample after 24 h. For the CLST model, we put a constant load on the samples and varied the temperature in a stepwise manner. We used three constant loads of 0.1, 0.2, and 0.3MPa. At each load, we varied the temperature from -1.5 to -1.0, -0.5, and -0.3°C.

Pore-water pressure measurement

Liquid water can exist in frozen soil only on the surfaces of mineral grains and ice crystals; once released from these surfaces, the liquid water immediately turns into ice. Thus we needed to find an appropriate antifreeze agent to use during our pore-water pressure measurements. The antifreeze agent must have the following characteristics: unfrozen at temperatures below 0°C, insoluble in water, and with a viscosity similar to water. Both decane and low-viscosity dimethyl silicone oil meet these requirements. Decane is an alkane hydrocarbon [CH₃(CH₂)₈CH₃] with a freezing point at -29.7°C and a density of 0.73g/cm³ (at 20°C). The viscosity of decane at -2°C is similar to that of water at 15°C (Andersland et al. 1996). Low-viscosity dimethyl silicone oil (LDSO) has a viscosity of 0.65mPa.s (at 25°C). We chose LDSO due to its superiority to decane in safety, chemical stability, and accessibility.

Table1. Water content and dry density of the samples.

| Water content (%) | Dry density (g/cm ³) | |
|-------------------|----------------------------------|------|
| | clay | sand |
| 40 | 1.21 | 1.15 |
| 80 | 0.82 | 0.77 |
| 120 | 0.61 | 0.53 |

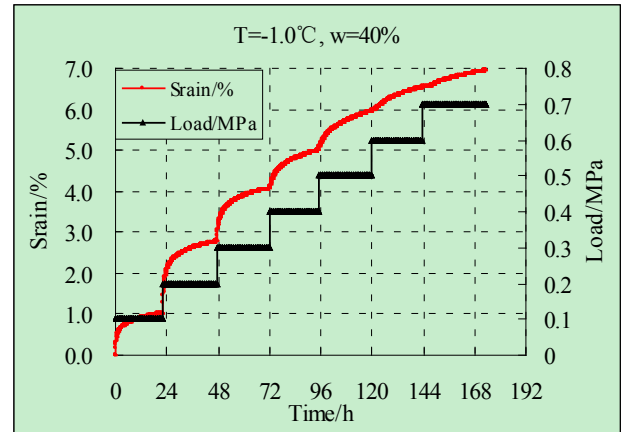


Figure 1. Typical compression curves under stepped loads.

Results and Discussion

Compression tests

Figure 1 shows the deformation process of the frozen soil sample under each load in the CTSL model. Vertical strain increases with the load steps, with larger strain variation in the initial load steps, but less sensitive to the applied load at the end of the test.

For the CTSL model, the strain of the sample under each load was converted to the void ratio of the soil. Figure 2 shows that the *e-p* curve under relatively low temperature (-1.5°C) is a straight line, but takes the form of a power function under relatively higher temperatures. When the pressure increases from *P*₁ to *P*₂, the void rate correspondingly decreases from *e*₁ to *e*₂. The compressibility coefficient can be expressed as:

$$\alpha_{1-2} = \frac{e_1 - e_2}{p_2 - p_1} \tag{5}$$

We used the compressibility coefficient α_{1-2} , corresponding to the pressure interval from *P*₁ = 0.1MPa to *P*₂ = 0.2MPa, to evaluate the compressibility of frozen soil. The tests results are shown in Table 2.

In the CLST model, we used frozen soil samples with three water contents (*w* = 40, 80, and 120%) under three different constant loads (0.1, 0.2, and 0.3 MPa), respectively. Typical compression curves under a constant load and a stepped temperature are shown in Figure 3. Temperature is the main factor influencing the compression strain. With the increase of each temperature step, the strain rate increases markedly at the beginning of the test, and then produces a smooth step toward the end.

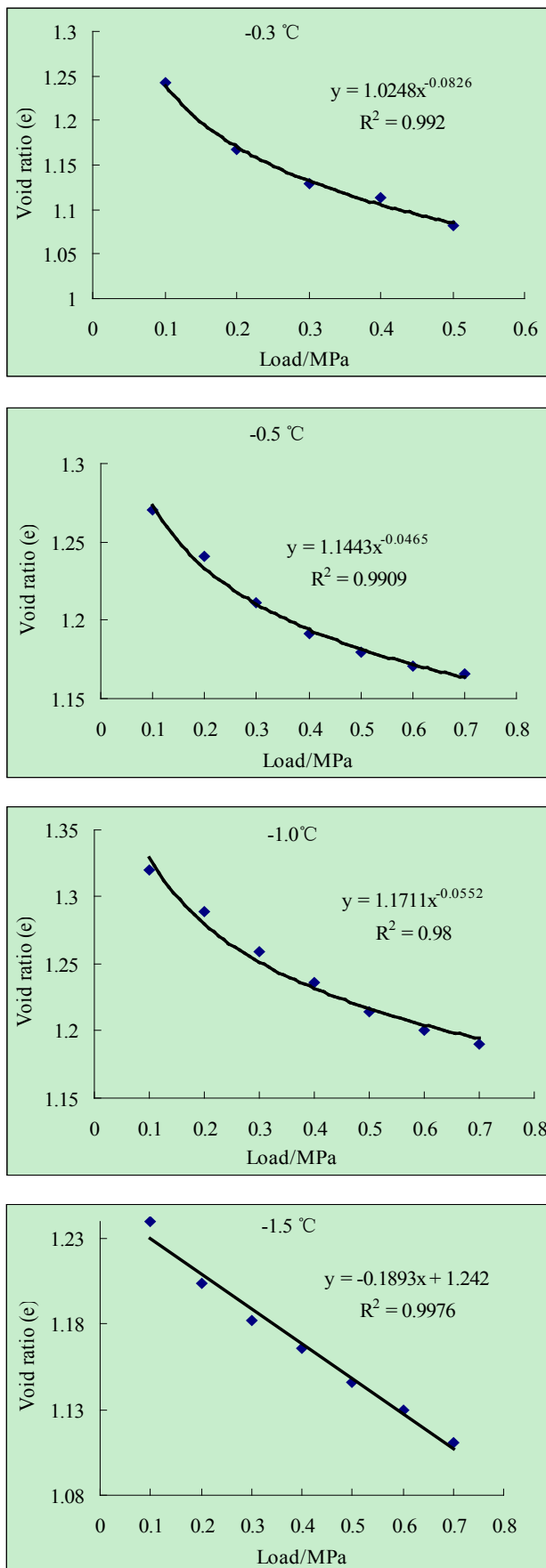


Figure 2. The $e-p$ curves under various temperatures.

Table 2. Compressibility coefficient under varying temperatures ($w = 40\%$).

| Temperature (°C) | α_{1-2} (MPa ⁻¹) |
|------------------|-------------------------------------|
| -1.5 | 0.218 |
| -1.0 | 0.413 |
| -0.5 | 0.479 |
| -0.5 | 0.751 |

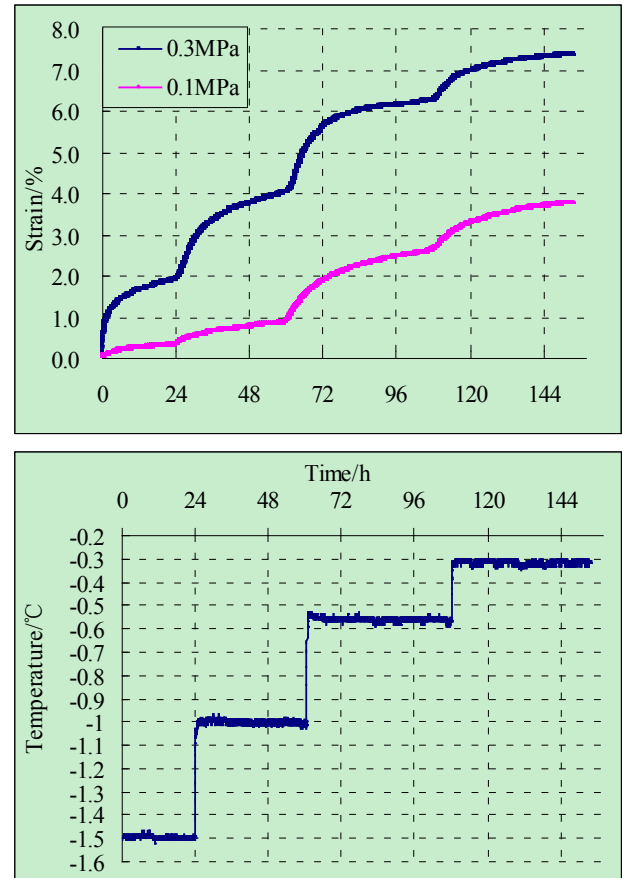


Figure 3. Typical compression curves under a constant load and a stepped temperature ($w=40\%$).

For this model, the compressibility coefficient was defined to evaluate the compressibility of frozen soil subjected to the incremental temperatures under a constant load. It can be expressed as:

$$\dot{a}^\Sigma = \frac{\Sigma S_\infty}{Ph} \tag{6}$$

where h is the original specimen height, P is the constant load, and ΣS_∞ represents the cumulative compression after deformation stabilizes.

Figure 4 shows the relationship between the compressibility coefficient and the temperature. The compressibility coefficient increases nonlinearly with increasing temperature, and their correlation can be approximated by the exponential law:

$$\alpha^\Sigma = A \exp(BT) \tag{7}$$

where T is the temperature of frozen soil, and A and B are experimental parameters depending on soil type, water

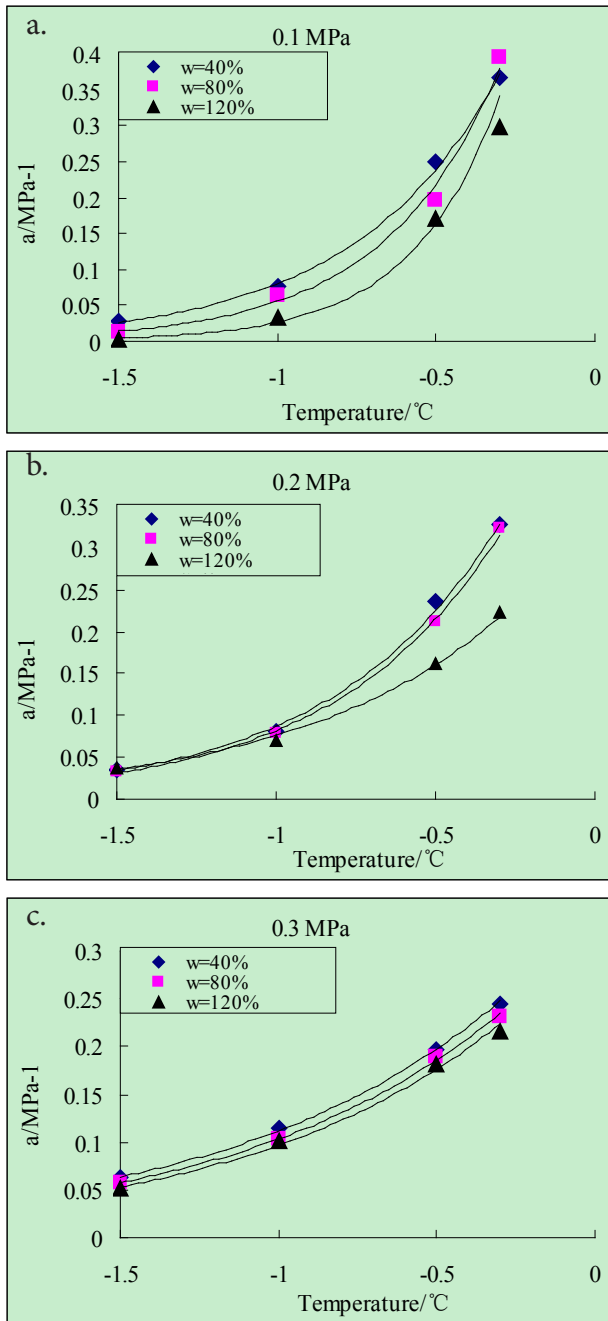


Figure 4. Compressibility coefficient vs. temperature under various constant loads (a,b,c).

content, and load. The values of these two parameters can be obtained by regression analysis, as shown in Table 3.

For comparison, we calculated the compression coefficient using equation 6 for CTSL again, and the results are illustrated in Figure 5.

Under relatively higher temperatures, the compressibility coefficient is more sensitive to temperature variations. However, at relatively lower temperatures, the applied load is the key factor influencing the compressibility coefficient. Therefore, compression deformation is more sensitive to temperature variation than to increased load. The compressibility coefficient α_{1-2} is usually used to express

Table 3. Results of regression analysis of the experiment parameters.

| Parameters Load/MPa | W/% | A | B | R ² |
|------------------------|-----|--------|--------|----------------|
| | 0.1 | 40 | 0.718 | 2.1947 |
| | 80 | 0.8667 | 2.7474 | 0.9945 |
| | 120 | 1.0154 | 3.6445 | 0.9927 |
| 0.2 | 40 | 0.5808 | 1.8972 | 0.9965 |
| | 80 | 0.5627 | 1.9278 | 0.9988 |
| | 120 | 0.3405 | 1.501 | 0.9952 |
| 0.3 | 40 | 0.3481 | 1.1363 | 0.9993 |
| | 80 | 0.5217 | 0.8373 | 0.9928 |
| | 120 | 0.3213 | 1.1997 | 0.9964 |

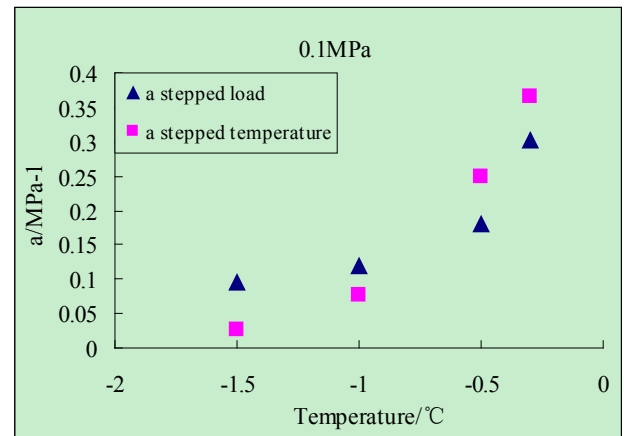


Figure 5. Compressibility coefficient vs. temperature (a,b); (a) comparison between CTSL and CLST (0.1MPa).

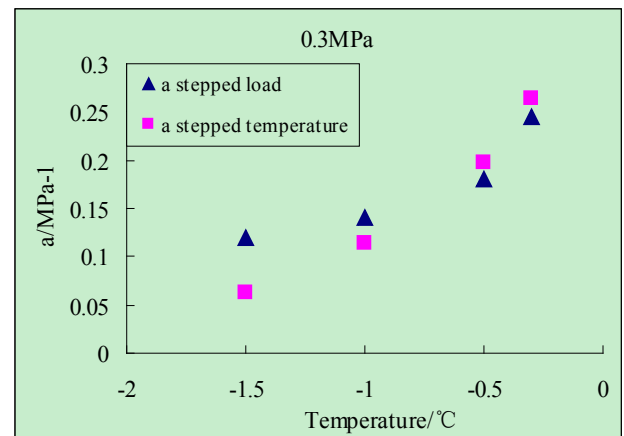


Figure 5 (b) comparison between CTSL and CLST (0.3MPa).

the compressibility of WIRFS from the perspective of load, and the relative compressibility coefficient α^z is used to describe the compressibility of WIRFS from the perspective of temperature increase.

Pore-water pressure measurements

Pore-water pressure measurement results show that temperature is the primary factor influencing the pore-water pressure variation in frozen soil. The higher the temperature,

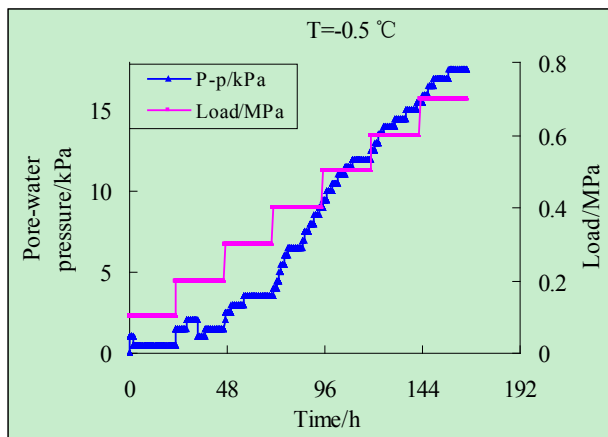


Figure 6. Pore-water pressure variation with time.

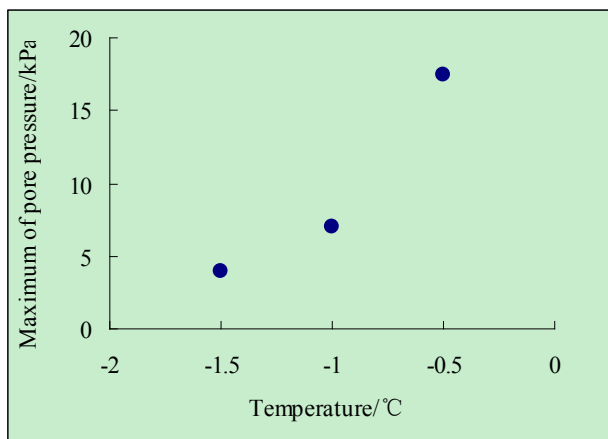


Figure 7. Maximum of pore-water pressure vs. temperature.

the greater the pore-water pressure. However, when the temperature is maintained at a higher level, the pore-water pressure variation is more sensitive to the load, as shown in Figure 6. Data at -0.3°C are incomplete due to an unexpected power failure during the experiment. However, we found that the phenomenon of pore-water pressure dissipation did not appear in most of the tests. The reason for this may be that the hydraulic conductivity of frozen soil is very weak, and the test period was not long enough. Therefore, the test period in future studies should be substantially increased so as to trace the phenomenon of pore-water pressure dissipation.

Practical Significance of the Test Results

The compressibility coefficient is an important parameter for the numerical simulation of warm and ice-rich frozen soil. This coefficient can be used to evaluate the compressibility of frozen soil in geotechnical engineering. However, further numerical simulations should be conducted in order to predict soil settlement in cold regions, such as that found in the embankment of the Qinghai-Tibet Railroad, where warming soil poses a potential adverse effect on the operation of the railroad.

The relative compressibility coefficient α^2 in the CTCLST model clearly shows that the considerable deformation of

frozen soil caused by warming temperature is similar in magnitude to that caused by additional loading.

Our study found that, in order to use consolidation theory to explain the deformation mechanism of WIFS, the pore-water pressure must first be determined. Our use of an antifreeze agent in the compression test when measuring pore-water pressure in frozen soil is a novel development. Preliminary test results show that the pore-water pressure variation is closely related to temperature. Our test results may provide a preliminary theoretical basis for the analysis of deformation and stability of building foundations in permafrost regions.

Conclusions

We used two models to study the compressibility of WIRFS when subjected to increasing load and warming temperatures, respectively. We measured the pore-water pressure variation during the compression tests by using an antifreeze agent. Our conclusions are as follows:

- 1) The compression of WIRFS is sensitive to both increasing load and warming temperature. When WIRFS is subjected to an incremental rise in temperature, the strain-time curve is similar to the strain-time curve when the soil is subjected to stepwise loads. However, under relatively higher temperatures, the compressibility of WIRFS is more sensitive to temperature variation than to increasing load.
- 2) We found an appropriate antifreeze agent to measure the pore-water pressure in WIRFS. Our test results show that temperature is the main factor influencing the pore-water pressure variation. However, the phenomenon of pore-water pressure dissipation did not appear during our tests due to the small hydraulic conductivity of frozen soil.
- 3) For the CTSL model, the $e-p$ curve takes on the form of a power function under relatively higher temperatures (-1.0 , -0.5 , and -0.3°C), but forms a straight line under relatively lower temperatures (-1.5°C). For the CLST model, however, the relationship between compressibility coefficient and temperature can be approximated by the exponential law.

Acknowledgments

This research was supported by the National Natural Science Foundation of China (grant No. 40971045) and the State Key Laboratory of Frozen Soil Engineering (China), Cold and Arid Regions Environmental and Engineering Research Institute, Chinese Academy of Sciences (grant No. 09SF102007).

References

- Akagawa, S., Hiasa, S., Kanie, S., & Huang, S. 2008. Pore water and effective pressure in the frozen fringe during soil freezing. In *NICOP 2008: Proceedings of the Ninth International Conference on Permafrost*. D.L. Kane, K.M. Hinkel (eds.). Institute of Northern Engineering, University of Alaska Fairbanks, 1: 13-18.

- Arenson, L.U. & Springman, S.M. 2005a. Mathematical descriptions for the behavior of ice-rich frozen soils at temperatures close to 0°C. *Canadian Geotechnical Journal* 42: 431-442.
- Arenson, L.U. & Springman, S.M. 2005b. Triaxial constant stress and constant strain rate tests on ice-rich permafrost samples. *Canadian Geotechnical Journal* 42: 412-430.
- Eigenbrod, K., Knutsson, S., & Sheng, D. 1996. Pore-water pressures in freezing and thawing fine-grained soils. *Journal of Cold Regions Engineering* 10(2): 77-91.
- Qin, Y.H., Zhang, J.M., Zheng, B., & Ma, X.J. 2009. Experimental study for the compressible behavior of warm and ice-rich frozen soil under the embankment of Qinghai-Tibet railroad. *Cold Regions Science and Technology* 57:148-153.
- Tsytoovich, N.A. 1975. *The mechanics of frozen ground*. McGraw Hill, New York, NY, 426 pp.
- Wang, Y.Q. 1983. Professional papers on permafrost studies of Qinghai-Xizang plateau: moisture content and density of frozen soils. Science press, 60-66 (in Chinese).
- Zheng, B., Zhang, J.M., & Qin, Y.H. 2010. Investigation for the deformation of embankment underlain by warm and ice-rich permafrost. *Cold Regions Science and Technology* 60:161-168.
- Zhu, Y.L. & Zhang, J.Y. 1982. Elastic and compressive deformation of frozen soils. *Journal of Glaciology and Geocryology* 4(3): 29-40.

Distribution of Permafrost in the Source Area of the Yellow River on the Northeastern Qinghai-Tibet Plateau, China

Dongliang Luo, Huijun Jin, Lin Lin

State Key Laboratory of Frozen Soils Engineering, Cold and Arid Regions Environmental and Engineering Research Institute, Chinese Academy of Sciences, Lanzhou, Gansu, China

Abstract

Based on data from permafrost boreholes set up from July to November 2010, the spatial characteristics of permafrost temperatures and thickness, and the lower limit of permafrost in the Source Area of the Yellow River (SAYR), have been studied and presented in this paper. According to in situ measurements, the lowest mean annual ground temperature (MAGT) is -1.9°C , and the deepest permafrost is 74 m at Chalaping at elevations of more than 4700 m in the Bayan Har Mountains. Permafrost is generally warm ($>-1^{\circ}\text{C}$) and thin (<40 m). There are abrupt changes of the MAGT from a negative value (-0.2°C) to a positive value ($+1.3^{\circ}\text{C}$) in Yeniugou at an elevation of 4400 m. The lower limits of discontinuous permafrost are at 4330 m on the north slope of the Bayan Har Mountains and at 4450 m on the south slope of the Buqing Mountains. The lower limits of permafrost have risen by 130 m on the south slope and 50 m on the north slope of the Bayan Har Mountains during the past 30 years. The changes in the distribution of permafrost in the SAYR are attributed to climate warming and increasing anthropogenic activities.

Keywords: mountain permafrost; ground temperature; permafrost thickness; lower limit of permafrost; Source Area of the Yellow River; Northeastern Qinghai-Tibet Plateau.

Introduction

The permafrost features along the Qinghai-Tibet Engineering Corridor have been studied intensively to provide information for large engineering projects along the Qinghai-Tibet Railway/Highway and for national climate change adaptation strategies (Tong & Li 1983, Jin et al. 2000, Zhou et al. 2000, Cheng & Wu 2007, Jin et al. 2008, Wu et al. 2010). It has been widely accepted that permafrost degradation is caused by climate warming (Lachenbruch et al. 1986, Osterkamp et al. 1999, Marchenko et al. 2007, Harris et al. 2009). The source areas of the Yellow, Yangtze, and Lancang/Mekong rivers, the so-called "Source Areas of the Three Rivers," are located on the northeastern Qinghai-Tibet Plateau (QTP), where permafrost degradation has caused significant water resource imbalance and runoff cutoff (Cheng and Wu 2007). Unfortunately, the spatial characteristics of permafrost in this region are largely unknown, which makes the evaluation of the causes and adaptive strategies for water resources and ecological management difficult. Particularly in the Source Area of the Yellow River (SAYR), only qualitative and empirical descriptions for permafrost distribution exist. There are very few systematic and long-term investigations, surveys, and reports on permafrost temperatures and thickness from direct borehole measurements (Jin et al. 2009). Hence it is important and urgent to study the permafrost features and their changes in the SAYR.

Study Region and Data

The SAYR is located in the northeastern Qinghai-Tibet Plateau. It encompasses the catchment area above Duoshixia ($34^{\circ}46'25.10''\text{N}$, $98^{\circ}20'59.03''\text{E}$, 4197 m a.s.l.) along the

Yellow River, with a total catchment area of 2.8×10^4 km² (Jin et al. 2009). The elevations range from 4197 to 5267 m a.s.l., with an average of 4491 m a.s.l. (Luo et al. 2011). It is separated from the watershed of the Yangtze River by the Bayan Har Mountains to the south and by the Geshigeiya Mountains to the west, and bordered by the Buqing Mountains on the north. The Bayan Har Mountains provide a natural barrier to the warm-wet air flow from the Indian Ocean, resulting in great differentiations in thermal and moisture regimes between the northern and southern sides (Wang et al. 1999). Hence permafrost distribution is very complicated, and alternating zones of continuous, discontinuous, sporadic, and sometimes deeply buried permafrost, as well as seasonally frozen ground, occur (Li et al. 1996, Jin et al. 2010).

From July to September 2010, 12 boreholes were drilled at 100-m intervals in elevation along National Highway No. 214, which runs through the eastern part of the SAYR (Fig. 1). One borehole reached a depth of 100 m, one had a depth of 30 m, and ten had depths of 20 m. Thermistor cables were installed and read manually almost every month (in the middle of month). These temperature thermistors, with an accuracy of $\pm 0.033^{\circ}\text{C}$, were made by the State Key Laboratory of Frozen Soils Engineering (SKLFSE) at Lanzhou, Chinese Academy of Sciences. Measurement results show that thermal disturbances after drilling are negligible after 3 to 6 months. From October to November in 2010, several automatic weather stations were installed for monitoring climate variables and active layer processes. By analyzing some initial data and information from borehole drillings and temperature measurements, the spatial characteristics of permafrost distribution, temperatures, thickness, and the lower limits of permafrost were revealed and are presented in this paper.

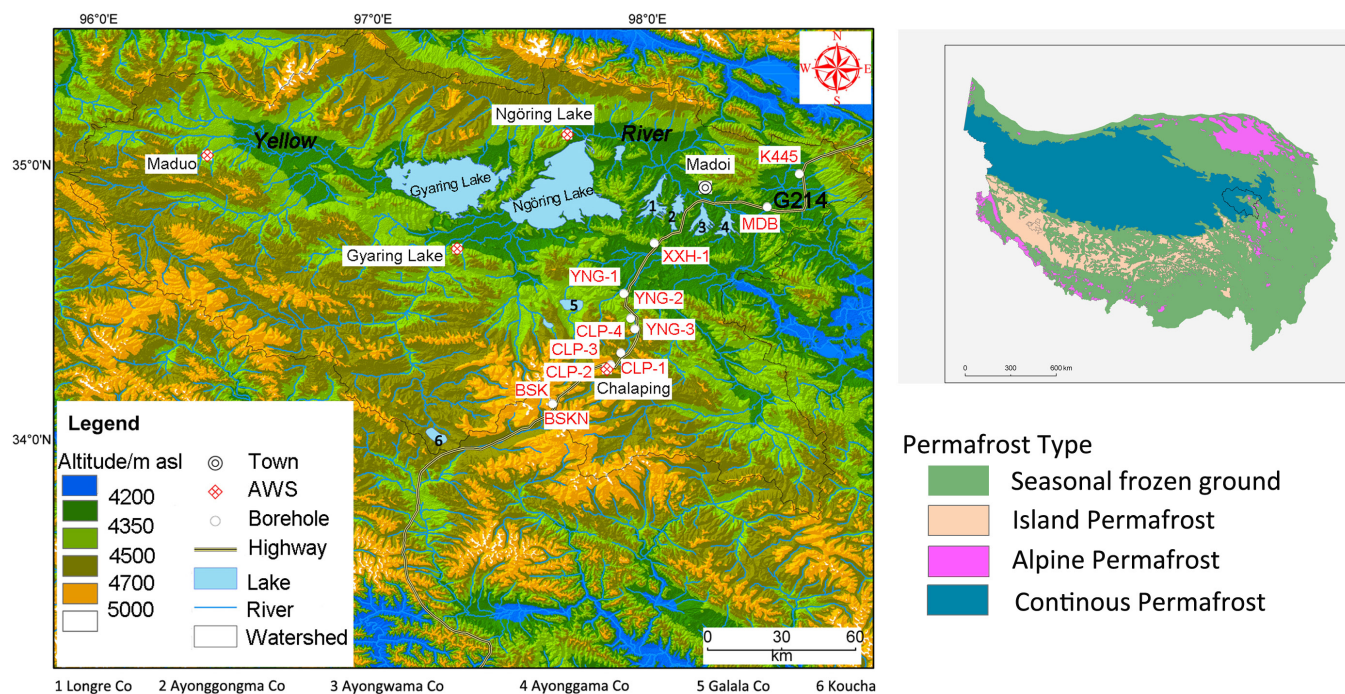


Figure 1: Permafrost boreholes and monitoring network in the SAYR set up in 2010.

Results

Permafrost temperature and thickness

Permafrost distribution in the SAYR is complicated due to the rugged terrain, which includes numerous mountains and hills, valleys and intermontane basins, high plains, lakes and rivers, specific soil textures and moisture content, and vegetative cover on the ground surface. Permafrost in the Bayan Har and Buqing Mountains is mainly elevational. The mean annual ground temperatures (MAGT) were colder than -1°C above 4700 m a.s.l. on the south slope of the Bayan Har Mountains, and above 4630 m a.s.l. on the north slope of the Bayan Har Mountains. The MAGTs are generally colder than -0.5°C at elevations higher than 4560 m a.s.l. on the south slope of the Bayan Har Mountains, and above 4450 m a.s.l. on the north slope of the Bayan Har Mountains. At elevations below 4400 m a.s.l., there is only island permafrost in specific topographic settings such as piedmont gentle slopes and intermontane basins with favorable ground surface cover. Due to the influence of the latitudinal zonation, the MAGTs ranged from -0.7°C to -1.3°C , even when the elevations were lower than 4400 m in the eastern Buqing Mountains along National Highway No. 214 (Fig. 2).

Comprehensive field surveys show that the lowest MAGT is -1.9°C and the thickest permafrost is 74 m, at Chalaping at an elevation of 4720 m a.s.l. Permafrost is generally warm ($>-1^{\circ}\text{C}$) in the eastern part of the SAYR. Abrupt changes, from a slightly negative temperature (-0.2°C) in borehole YNG-1 to a positive temperature ($>+1^{\circ}\text{C}$) in borehole YNG-2, were observed at Yeniugou at an elevation of 4395 m a.s.l. The horizontal distance between the two boreholes was less than 2 km and the elevation difference was no more than 70

m. From the Bayan Har Mountain Pass to Yeniugou Town, the elevation decreases by 500 m and the northern latitude increases by $30'$, whereas the MAGTs increase almost 3°C . From borehole XXH-1 in Yematan south of Xingxinghai Lake to borehole YNG-3, the latitude increases by $10'$, elevation decreases by 100 m, and the MAGTs decrease to $+0.5^{\circ}\text{C}$. The MAGTs abruptly change from positive to negative temperature in the Buqing Mountains. There is little change in elevation on the north slope of the Eastern Buqing Mountains. The latitude increase is only $20'$ from Madoi County Town and Huangheyuan (Yellow Riverside) to borehole K445, whereas the MAGTs ranged from -0.7 to -0.9°C . These temperatures are much lower than those at similar elevations in river valleys and basins with high soil moisture contents along the Yellow River.

Permafrost thickness was obtained through direct measurements and indirect estimates using permafrost temperature profiles and thermal gradients. The thermal gradient in Borehole CLP-2 was approximately $0.3^{\circ}\text{C}/100\text{ m}$; this value was then used for calculating permafrost thickness with the MAGTs. A permafrost base deeper than 40 m appears at the Bayan Har Mountains, Chalaping, and the north slope of the Buqing Mountains (Fig. 3). The permafrost thickness increases at higher elevations from east to west in the SAYR as well. For example, the elevations in Borehole ZK6, ZK8803, and ZK7 were 4272, 4400, 4472 m, respectively, while the horizontal distances between them was less than 25 km. Permafrost thicknesses were 6.5, 18.2, and 44.3 m, respectively (Jin et al. 2010). According to the empirical statistical relationship of permafrost thickness with elevation and latitude, permafrost thickness could exceed 100 m on the northwest bank of the Sister Lakes (the Ngöring Lake and the

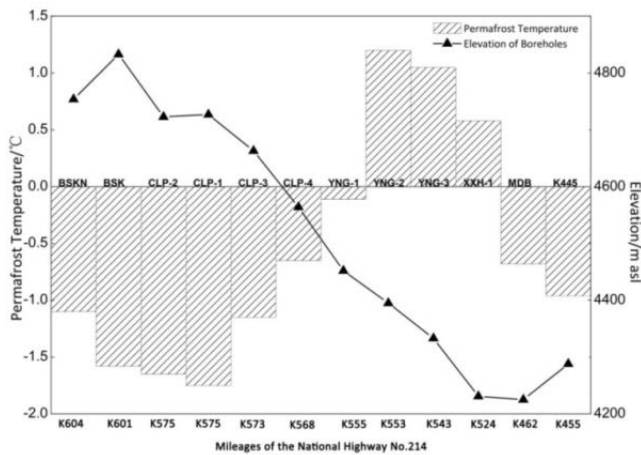


Figure 2. Permafrost temperatures along the National Highway No. 214 in the SAYR.

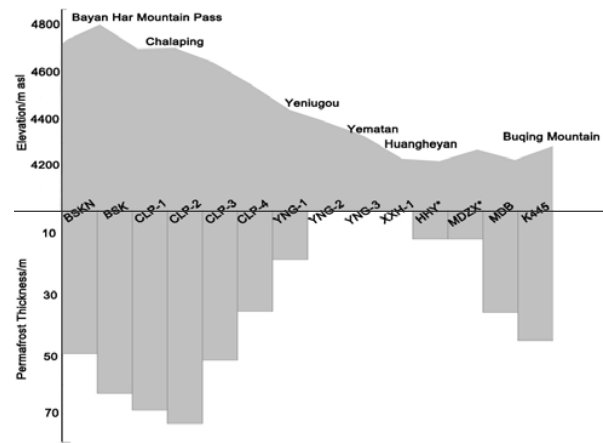


Figure 3. Thickness of permafrost along National Highway No. 214 in the SAYR. Note: the data for the borehole number with an asterisk were cited from Wang et al. (1999).

Table 1. The lower limits of permafrost on the north slope of the Bayan Har (BHM) and Buqing Mountains (BQM).

| Geomorphic Location | Northern Latitude | Lower limit of continuous permafrost (m a.s.l.) | Lower limit of discontinuous permafrost (m a.s.l.) | | | | Lower limit of isolated patches of permafrost (m a.s.l.) |
|------------------------|-------------------|---|--|---------|---------|-----------------------|--|
| | | | In 1991 | In 1998 | In 2010 | Rise in 1991~2010 (m) | |
| North slope of the BHM | 34° 20' | 4650 m | 4320 m | 4370 m | 4450 m | 130m | 4395 m |
| South slope of the BQM | 34° 48' | 4300 m | 4200 m | / | 4300 m | 100m | 4350 m |

Gyaring Lake). Permafrost thickness increases at rates of 13 to 20 m for every 100-m rise in elevation in the Bayan Har Mountains. It may reach a thickness of 120 m on Lenadongze Mountain (5267 m a.s.l.), the highest peak in the SAYR. The changing rates of permafrost thickness with latitude are unclear because of very different moisture and thermal regimes on the sunny and shadowy slopes, rugged mountains and hills, and river valleys. The rates are also influenced by complicated local factors such as hydrology, ground surface cover, and lithology.

Lower limit of permafrost

The elevations of the lower limits of permafrost in the SAYR are higher than the western and northern edges of the Qinghai-Tibet Plateau. However, they differ with local factors such as microrelief and ground surface cover. Wang et al. (1991) proposed that the lower limit of permafrost on the northeastern Qinghai-Tibet Plateau rises by a rate of 130 m per 1° decline in northern latitude, and that the lower limits of permafrost on the north and south slopes could differ by 200 to 400 m; the mean annual air temperatures (MAAT) at the belts of the lower limits of permafrost are between -2.5 and -3.5°C. Ding et al. (1983) estimated the lower limit of alpine permafrost from the regression function (1) of the MAATs with the elevations, latitudes:

$$H = \frac{56.02 - T - 1.02L}{0.562} \times 100 \tag{1}$$

Here *H* is the lower limit of permafrost (m), *T* is mean annual air temperatures, and *L* is the northern latitude.

Because of high maintenance expenses and difficult logistics of permafrost stations, these estimates of lower limits of permafrost prior to the 1990s were based on drillings of hydrogeological boreholes, instead of measuring ground temperatures. Harris and Brown (1978) suggested that the lower limits of continuous permafrost largely coincide with the isotherms of -1°C in MAGTs, and height differences between continuous permafrost and discontinuous permafrost are 70 m. Based on this rule of thumb and extensive field investigations, the lower limits of discontinuous permafrost in the SAYR appear at elevations where the MAGTs are -0.5°C, and the lower limits of island permafrost appear at elevations where the MAGTs are 0°C. Hence the spatial distribution of permafrost in the SAYR could be characterized through direct borehole measurements and indirect estimates of the MAGTs using elevation and latitude. According to drillings and extensive investigations, the lower limit of continuous permafrost on the north slope of the Bayan Har Mountains, also the southern boundary of the SAYR, is 4630 m; the lower limit of discontinuous permafrost is 4450 m. For the Buqing Mountains, the elevations of the lower limit on south slope are 4300 m for continuous permafrost, 4250 m for discontinuous permafrost, and 4200 m for the isolated patches of permafrost (Table 1). When compared with lower limits of permafrost in the 1990s, it rose by 130 m on the north slope of the Bayan Har Mountains, and by 100 m on the south slope of the Buqing

Mountains in the SAYR (Table 1). In the central part of the SAYR, there are large taliks around the margins of the Sister Lakes, and only patchy permafrost appears at elevations lower than 4350 m. In Yeniugou and Yematan, and in the Hei'he River area, sometimes deep buried sporadic permafrost was encountered in drilling, but otherwise it is seasonally frozen ground below an elevation of 4250 m (Jin et al. 2009). Therefore, it is impossible and unnecessary to study the lower limits in the river valleys of the SAYR, such as Da Yemaling and Xiao Yemaling, and Yematan in between.

Summary and Conclusions

Based on extensive field investigations, direct borehole measurements, and indirect estimates from permafrost temperature profiles and geothermal gradients, the spatial characteristics of permafrost temperature and thickness and the lower limits of permafrost in the southern and northern boundaries of the SAYR are presented in this paper. Some preliminary conclusions were drawn as follows:

- 1) The directly measured lowest MAGT is -1.9°C , and the deepest permafrost by direct borehole measurement is 74 m in Chalaping at elevations greater than 4700 m a.s.l. Indirect estimates from permafrost temperatures and latitude, elevation, and thermal gradients show that permafrost thickness may reach 120 m, and the MAGT may be lower than -3°C on Lenadongze Mountain, the highest peak in the SAYR with an elevation of 5267 m a.s.l. Permafrost may reach a thickness of more than 100 m in the Buqing Mountains.
- 2) It is evident that permafrost temperatures in the SAYR are much higher than those along the Qinghai-Tibet Railway/Highway (QTR/H, or National Highway No. 109), which has the lowest MAGT of -3.8°C . Most permafrost is warm ($>-1^{\circ}\text{C}$) in the SAYR. Permafrost thickness from direct borehole measurement is also much thinner than along the QTR/H, where the thickest permafrost is 312 m. There are abrupt changes in ground temperatures from -0.2 to $+1.3^{\circ}\text{C}$ at Yeniugou on the north slope of the Bayan Har Mountains.
- 3) The lower limits of permafrost in the SAYR are higher than those on the northern and western edges of the Qinghai-Tibet Plateau. The lower limits change with aspect, slope, and latitude. The latitudinal influence on the lower limits of permafrost is hard to quantify at a small watershed scale because of the complicated permafrost distribution. The lower limits of discontinuous permafrost on the north slope of the Bayan Har Mountains and on the south slope of the Buqing Mountains are at 4450 and 4250 m a.s.l., respectively. These have risen 130 and 100 m from 1991 to 2010.
- 4) Due to high temperatures and low thickness of permafrost, the thermal state of permafrost in the SAYR is unstable and sensitive to disturbances to the cold environments and climate warming. Therefore, it is recommended that permafrost be protected during the construction of highways, hydropower stations, and buildings in

consideration of the spatial characteristics of the thermal state of permafrost in the SAYR. Long-term monitoring with a permafrost-climate network needs to be improved and operated for long-term studies.

In addition, more investigations need to be conducted for permafrost conditions in the future, especially in the east-west direction such as along the north bank of the Sister Lakes, the upper streams of the Yellow River in the Geshigeya Mountains, and the middle part of the Bayan Har Mountains in the southern SAYR.

Acknowledgements

This project was supported by the State Key Laboratory of Frozen Soils Engineering (SKLFSE) at Lanzhou, Chinese Academy of Sciences (Grant No SKLFSE-ZY-01) and China National Science Foundation (Grant No 40821001).

References

- Cheng, G.D. & Wu, T.H. 2007. Responses of permafrost to climate change and their environmental significance, Qinghai-Tibet Plateau. *Journal of Geophysical Research* 112, F02S03. Doi: 10.1029/2006JF000631.
- Ding, D.W. & Wu, Z.W. 1983. A new method to determine the permafrost thickness—Method to calculate geothermal (ground temperature gradient). *The Symposium of Permafrost Research in Qinghai-Xizang Plateau*. Science Press: Beijing; 157-162 (in Chinese).
- Harris, C., Arenson, L.U., Christiansen, H., Etzemüller, B., Frauenfelder, R., Gruber, S., Haeblerli, W., Hauck, C., Hölzle, M., Isaksen, K., Käab, A., Kern-Lutschg, M. A., Lehning, M., Matsuoka, N., Murton, J.B., Nötzli, J., Phillips, M., Ross, N., Seppälä, M., Springman, S.M., Ross, N., & Mühlh, D.V. 2009. Permafrost and climate in Europe: Monitoring and modelling thermal, geomorphological and geotechnical responses. *Earth-Science Reviews* 92: 117-171.
- Harris, S.A., & Brown, R.J.E. 1978. Plateau Mountain: A case study of alpine permafrost in the Canadian Rocky Mountains. *Proceedings of the 3rd International Conference on Permafrost*, Edmonton, Alberta, Canada : 385-391.
- Jin, H.J., He, R.X., Cheng, G.D., Wu, Q.B., Wang, S.L., Lü, L.Z., & Chang, X.L. 2009. Changes in frozen ground in the Source Area of the Yellow River on the Qinghai-Tibet Plateau, China, and their eco-environmental impacts. *Environmental Research Letters* 4(4): 1-11.
- Jin, H.J., Li, S.D., Cheng, G.D., Wang, S.L. & Li, X. 2000. Permafrost and climatic change in China. *Global and Planetary Change* 26: 387-404.
- Jin, H.J., Wang, S.L., Lü, L.Z., He, R.X., Chang, X.L., & Luo, D.L. 2010. Features and degradation of frozen ground in the Source Area of the Yellow River, China. *Journal of Glaciology and Geocryology* 32(1): 10-17 (in Chinese with English Abstract).

- Jin, H.J., Yu, Q.H., Wang, S.L. & Lü, L.Z. 2008. Changes in permafrost environments along the Qinghai-Tibet engineering corridor induced by anthropogenic activities and climate warming. *Cold Regions Science Technology* Vol. (issue): 317-333.
- Lachenbruch, A.H. & Marshall, B.V. 1986. Changing climate: geothermal evidence from permafrost in the Alaskan Arctic. *Science* 234: 689-696.
- Marchenko, S.S., Gorbunov A.P., & Romanovsky, V.E. 2007. Permafrost warming in the Tien Shan Mountains, Central Asia. *Global and Planetary Change* 56(3-4): 311-327.
- Osterkamp, T.E. & Romanovsky, V.E. 1999. Evidence for warming and thawing of discontinuous permafrost in Alaska. *Permafrost and Periglacial Processes* 10(1): 17-37.
- Tong, B.L. & Li, S.D. 1983. Some characteristics of permafrost on the Qinghai-Xizang Plateau and a few factors affecting them. Professional Papers on Permafrost Studies of the Qinghai-Xizang Plateau. Beijing, China, Science Press: pp. 1- 11 (in Chinese).
- Wang, S.L., Lin, Q., & Zhao, L. 1999. Permafrost along the Qing-Kang Highway (National Highway No.214). *Arid Land Geography* 22(2): 42-49 (in Chinese with English Abstract).
- Wang, S.L. & Luo, X.R. 1991. The distribution characteristics of frozen ground in the east of the Qinghai-Xizang Plateau. *Journal of Glaciology and Geocryology* 13(2): 131-140 (in Chinese with English Abstract).
- Wu, Q.B., Zhang, T.J., & Liu, Y.Z. 2010. Permafrost temperatures and thickness on the Qinghai-Tibet Plateau. *Global and Planetary Change* 72: 32-38.
- Zhou, Y.W., Guo, D.X., Qiu, Cheng, G.Q., & Li, S.D. 2000. *Frozen ground in China*. Beijing, China, Science Press (in Chinese).

Progress in Frozen Soil Mechanics Research in China: A Review

Wei Ma, Dayan Wang, Zhi Wen

State Key Laboratory of Frozen Soils Engineering, Cold and Arid Regions Environmental and Engineering Research Institute, Chinese Academy of Sciences, Lanzhou, Gansu, China

Abstract

In China, 2.15 million square kilometers of land is covered by permafrost, thus making it third in the world on the list of countries with the most permafrost. However, China is a relative latecomer to the synthetic and systematic study of permafrost, and especially to the study of frozen soil mechanics. Since the 1950s, studies have been conducted to characterize the frozen soil for economic and social development in permafrost regions. This paper summarizes the achievements in stress-strain relationship, constitutive modeling, thermal-moisture process, frozen soil-structure interaction, and the testing methodologies of frozen soil mechanics research in China. Finally, we forecast the developing trend for frozen soil mechanics research from the perspective of integrating principles of frozen soil mechanics, the requirements for engineering construction on frozen soil mechanics, and the state of the art of related subjects.

Keywords: frozen soil mechanics; strength and deformation; thermal-moisture process; constitutive relationship; prospect.

Introduction

In China, perennially frozen ground is widely distributed on the Tibet Plateau, the northwestern mountains, and the Daxinanling, Xiaoxinanling, and Songnen plains in the north and northeast. Seasonally frozen ground lies in the vast areas of western China along the Helan Mountains and Ailao Mountains, and north of the Qinglin Mountains and Huai River. There is a freezing-thawing stratum that freezes in winter and thaws in summer in both perennially and seasonally frozen ground areas. In cold regions, this freezing-thawing stratum is often used as the structural foundation. When subjected to freeze-thaw cycles, soil properties within the freezing-thawing stratum will change accordingly and thus affect the stability of constructed facilities. Therefore, to ensure stability, durability, and economic rationality of structures in frozen ground, it is necessary to address a series of theoretical and practical questions about cryopedology, the study of frozen soils and the interaction between frozen soil and structure foundations.

Frozen Soil Mechanics Research in China

It is a great challenge to develop a synthetic theory in evaluating frozen soil due to its extremely complex multiphase medium. Thanks to the long-term efforts of a number of scholars in this field, great achievements have been made in understanding frozen soil mechanics. Generally, the experiences could be divided into three stages since 1950s: experimental study stage, phenomenological constitutive model study stage, and meso-microcosmic constitutive model stage. At the experimental study stage, the physical-mechanical parameters and their functional relationship of frozen soil were determined with lab and field experimental results. The phenomenological constitutive model study stage was the second stage and is characterized by continuous medium mechanics theory combined with the elastic, plastic, and viscous theory. The third stage was a meso-microcosmic constitutive model stage, in which the material microcosmic

structure and moisture-thermal process were carefully considered. Therefore, we will summarize the achievements of frozen soil mechanics research in China by addressing five aspects that include 1) strength and deformation of frozen soil; 2) a frozen soil constitutive model; 3) the thermal-moisture-processes of frozen soil; 4) the interaction between frozen soil and structures; and 5) testing techniques in frozen soil mechanics.

The strength and deformation of frozen soil

With regard to traditional studies of the mechanical properties of frozen soil, Wu et al. (1983a, b, 1993) put forward a method to determine the long-term strength of frozen soils based on a field loading sheet test, plastic flow equation, and stress-strain curve. On the basis of the study of the plastic and strain hardening of Lanzhou sands, under the influences of confining pressure and temperature, Wu et al. (1996, 1997) elaborated on the proliferation and expansion of structural defects during the process of frozen soil creep, which controls the strengthening and weakening of soil structure. By analyzing the uniaxial experimental data of frozen silt and sand, Zhu (1983, 1984) proposed a mathematical model to identify the silt and sand uniaxial ultimate stress variations with strain rate and temperature. Ma et al. (1995) proved that the volume changes of the frozen soil were not zero when frozen soil creeps. Ling et al. (1999) explained that the stress-strain curve of frozen soil was a step-like curve in a uniaxial test with irreversible deformation. Mandelbrot's fractal geometry theory was introduced into frozen soil mechanical studies by applying a linear hyperbolic iterated function system, and a new method was developed to simulate the stress-strain curve of frozen soil as well as to calculate its fractal dimension by using a computer. He et al. (2002) presented a reasonable and more convenient calculation expression for unsaturated frozen soil strength by studying the frozen soil strength relationship between unsaturated and saturated soil, and analyzing the formation mechanism of unsaturated frozen soil strength. In order to study the whole deformation process in frozen soils,

extending from small cracks to macro-cracks and ending with failure under loading, Miao et al. (1995) presented the failure mechanics relating to frozen soil. Based on a series of creep tests and microstructure observation, and using the so-called "duplication-electronmicroscope" technique, Miao found that cohesive force created by ice, orientation of soil grains, and late extension of micro-cracks control the entire creep process in frozen soil. This technique was used to develop a three-dimensional failure theory for creep deformation on the assumption of continuum mechanics and the frame of failure mechanics. This procedure was successfully used to describe the strengthening and weakening phenomena during frozen soil creep. Based on timely CT experimental investigation of uniaxial compression, Liu et al. (2002) separated the failure process of frozen reconstructed-soil into plastic failure and micro-crack failure, and then presented a formula to calculate the failure values for saturated and unsaturated frozen soil under each different stage.

In order to extract minerals at depths of hundreds or even a thousand meters, where there are complex geotechnical conditions, the environmentally friendly technique of artificial ground freezing is routinely used as a means of providing groundwater control and soil support in the construction of shafts and underground openings. In the artificial freezing process, the in situ pore-water is frozen into ice, which becomes a bonding agent, fusing together adjacent particles of soil or blocks of rock and thus increasing their combined strength and making them impervious. Excavation can then proceed safely either within or adjacent to the created barrier of strong, watertight, frozen earth. However, since investigations of frozen soils were limited to relatively low confining pressures, problems with pressure thawing of pore-ice under higher confining pressures and consolidation of frozen soil have not been dealt with. The traditional theories were not suitable for predicting the strength of deep artificial frozen soil while experiencing consolidation before freezing. In view of this, much research has been conducted to investigate testing techniques, the physical parameters, and the mechanical characteristics of deep artificial frozen soils (Cui 1998, Ma Wei & Wu Ziwang 2002). Wang et al. (2004, 2005, 2008) utilized the Duncan-Chang hyperbolic model to analyze the stress-strain behavior of frozen soils to evaluate strength and deformation characteristics.

The constitutive relationship research of frozen soil

Early studies on the frozen soil constitutive model are all based on the continuous medium hypothesis. Generally, it begins with analyzing the frozen soil stress-strain relationships after loading, and then applies the curve fitting method using the elastic theory, plastic theory, and other theories to build a constitutive model. The model, ignoring some contact characteristic details among particles, describes the mechanical properties of granular materials by state parameters such as the porosity ratio, temperature, relative density, and the anisotropy tensor, so the mathematical analysis tools can be easily applied. However, due to the existence of ice within frozen soil, the force analysis for frozen soil should not only consider

macroscopic performance after loading, but also should address inner temperature changes and subsequent phase transition. As a consequence, the research progress for frozen soil constitutive relationship has been relatively slow. Miao (1995) introduced a failure mechanics theory, which found a new way to study the frozen soil constitutive model by the failure mechanics theory. In the following years, based on the failure mechanics theory and microcosmic view, explanation of frozen soil strength and failure became an effective tool for studying the frozen soil constitutive model.

Study of thermal-moisture processes in the frozen soil

1) Unfrozen water content in frozen soil

The unfrozen water content in frozen soil is an important index for evaluating the moisture migration characteristics and is generally used in the calculation of the soil thermal regime. However, experiments for unfrozen water content determination are expensive and time-consuming. To solve this problem, Xu et al. (1985) proposed an expression to calculate the unfrozen water content using two different initial moisture contents and the corresponding freezing temperature. An improved model was then presented to predict how unfrozen water content varied with the initial moisture content, the initial concentration, as well as the change of external loads on the assumption of the additivity of freezing point depression (Xu et al. 1995). The two-phase transition theory showed the influence of salt type and concentration on unfrozen water content, which was also used to explain the reason why the initial moisture and initial concentration exhibited trivial effects on unfrozen water content of sulfate soil. This result involves the electrolyte and changes of the coefficient in the empirical relationship function of unfrozen water and temperature (Zhang et al. 1993). The study of the influence of pressure and temperature on unfrozen soil revealed that the freezing temperature decreases linearly with an increase in the confining pressure, while the unfrozen water content increases with an increase in the confining pressure. The research showed that the unfrozen water content during the freezing process is always greater than that during the thawing process due to hysteresis. Moreover, the difference in the unfrozen water content between the freezing and thawing process decreases with the decrease of negative temperature (Zhang et al. 1994). The known one-way accumulation effect of unfrozen water in the seasonal freezing-thawing layer was presented and provided a theoretical basis to explain the formation of the thick upper layer of ground ice in permafrost (Cheng 1981).

2) Moisture migration in freezing soil

Moisture migration in freezing soil leads to ice segregation and frost heave, which is the reason why freezing soil exhibits special physical and mechanical characteristic. Xu et al. (1985, 1988, 1991) conducted a series of experiments related to the moisture migration in freezing soil, frozen soil, and thawing soil. The experiments showed that moisture in freezing non-saturated semi-intensive sand in a closed system will migrate to the freezing front under a constant temperature, and the

migration flux decreases with the increase of initial moisture content (Xu et al. 1991). The migration flux of the saturated freezing soil in an open system under the condition of constant temperature was proved to be proportional to the square root of time (Xu et al. 1988). The relationship between moisture migration flux and frozen duration time, temperature, and temperature gradient in frozen soil in a closed system was studied by Xu et al. (1985). To describe the moisture migration in freezing soil, the migration potential was presented, and a mathematical model was proposed to calculate moisture distribution in freezing soil (Sheng et al. 1993). The freezing front is a key parameter to understanding the moisture migration in freezing soil. Xu et al. (1997) proved that the thickness of the freezing front depends on freezing velocity and frost heave rate. The variation of the freezing front has three patterns including increases, stays constant, and then decreases during the soil freezing processes. The experiments validated that the ice segregation temperature decreases with the temperature depression of the cooling side. A method for estimating the ice segregation temperature was proposed by using freezing temperature, cooling side temperature, and the relation curve of unfrozen water content with temperature (Xu et al. 1997).

Up to now, four hypothetical mechanisms were put forward to explain the formation of thick-layered ground ice including ice segregation, cementation and ice segregation, repeated-segregation, and intrusive ice. In 1982, the known theory of repeated-segregation was put forward by the Chinese scholar Cheng Guodong to explain the mechanism for formation of extensive thick ground ice layers on the Qinghai-Tibetan Plateau (Cheng 1982). To apply the artificial freezing method in the construction of mine and underground engineering construction, an intermission freezing method was introduced in order to avoid the disadvantages when applying the artificial freezing method (Zhou et al. 1999). The experiments showed that the intermission freezing method can mitigate frost heave. The measurement technology has been improved greatly and many new instruments, such as the optical microscope, scanning electron microscopy, CT scanners, and pressure mercury, have been applied in frozen soil research. This is helpful for the systematic study of the influence of five main elements—soil, moisture, temperature, salinity, and pressure. Many interesting and insightful results have been achieved by applying these new techniques, especially when based on computer photo-digitizing processing. Li et al. (1999) evaluated the dynamics of freezing front, ice segregation front, and ice edge thickness in freezing soil, which reflects a new way of understanding moisture migration and ice segregation.

3) Moisture-thermal-stress coupling model

The interaction between temperature, moisture and stress field is an extraordinarily complex question related to thermodynamics, physical chemistry, and mechanics. The moisture-thermal-stress coupling mathematical model of frozen soil presents the best way to understand the thermal-moisture dynamics and solve frozen ground problems. Studies on soil thermal-moisture relations have been conducted for

more than 60 years and have achieved significant progress in last 20 years. Shen et al. (1987) presented a quasi-three-fields coupled model based on Harlan's hydrodynamics model and the simplification of deformation resulting from moisture migration. Since then, a series of coupling models related to soil freezing processes were put forward (He et al. 2000, Wang et al. 2003, Li et al. 1998). The coupled moisture-thermal-stress model has been used to calculate the ground temperature and the deformation of frozen embankment along National Road No. 214, and it showed the feasibility of application in frozen ground engineering (Li et al. 2003). However, the study on the coupled moisture-thermal-stress model is still in development and further research is necessary.

The interaction between frozen soil and structure

The interaction between frozen soil and foundation structure is an important concern when addressing engineering safety in seasonal frozen and permafrost regions. In the 1980s, soil frost heave and thaw settlement classification systems were presented and applied in China (Wu et al. 1982). Research has been focused on frost heave forces acting on structures placed in frozen ground. Research covered many aspects including mechanisms of frost-heave force, calculation methods, and countermeasures. Finally, several National standards related to foundations, hydraulic structures, and geotechnique applications were established to guide the engineering construction, and it subsequently achieved significant success (Huang 1988, Liu 1981, Zhu et al. 1988). In recent years, tunnel construction in cold regions has become more and more popular. Frost action generally results in serious damages to the tunnels in cold regions, such as cracks, leaking water, and icing. To support tunnel construction, the frost heave force between surrounding rock and the tunnel lining has become a hot research topic. Tunnel heat transfer models have been developed, and coupled models were used to calculate the thermal regime and seepage field during the operation of tunnels in cold regions. The application of the above research achievements provides powerful support for the design and construction of tunnels in cold regions (Lai 1999, Zhang et al. 2004).

The development of a test technique for frozen soil mechanics

Permafrost and frozen soil mechanical experiments provide an important way to study the physical and mechanical properties of frozen soil. After decades of development, the test techniques for frozen soil mechanics and its level have been greatly improved in China. In terms of the frozen soil physical parameters test, the pulsed NMR technique is used to measure unfrozen water content in the laboratory, and TDR is applied in field investigations. These provide a simple method to measure and understand moisture variation in the laboratory as well as in permafrost and seasonally frozen ground. After breaking through the traditional temperature controlling way using a signal fixed boundary, the improved freeze-thaw process test system can simulate the stochastic change of external temperature, which achieves the indoor experiments of the actual freezing-thawing process. As for measurement of

frozen soil mechanical parameters, the improved material test machine (MTS-810, USA) has the capability of controlling the negative temperature with high accuracy during the test and operational process. This machine allows study of the elastic modules, creep characteristics, failure strength, and constitutive model of frozen soils and unfrozen soils under either dynamic or static load. Along with the development of electronic microscope scanning technology and computer image processing systems, the electronic microscope scanning technology and CT technology have been introduced into frozen soil mechanics research. Using new techniques, changes in frozen soil engineering properties can be evaluated by understanding the change in frozen soil structure. By developed K_0 consolidation equipment with higher pressure and lower temperature, the formation and loading process of deep artificially frozen soils can be simulated in the laboratory. The abovementioned methods are important symbols that demonstrate how frozen soil mechanics and permafrost studies in China have greatly progressed.

Future Research on Frozen Soil Mechanics in China

In China, we should pay more attention to the following aspects of the study of permafrost and frozen soil mechanics in the next few years.

- 1) Further study of the physical characteristics and the mechanical behavior of frozen soils, and how to model the mechanical behavior and thermodynamic properties. Currently, simplified hypotheses are inevitably adopted when studying frozen soil. For example, frozen soil is seen as an elastic body or a rigid plastic body, according to the specific problems. This allows us to learn frozen soils from only a one-sided perspective. Therefore, future research should comply with frozen soils as they actively exist.
- 2) In order to apply theoretical results to engineering applications to solve practical problems, strength relations of samples recovered from field sites should be investigated. Although the study of frozen soil mechanics is a basic science, the purpose of the research is to serve engineering construction directly. Only when the frozen soil mechanics theory is applied in engineering practice and tested will it have validity.
- 3) Non-deterministic methodology should be advocated in the study of frozen soils. Frozen soil is a special soil category and it also has large spatial and temporal variability similar to other geological materials. In addition, permafrost engineering belongs to the category of geotechnical engineering and it has many uncertainties ranging from the stage of investigation, designation, and test studies, as well as construction design and operations. Addressing these aspects as a deterministic problem is limited only for its randomness. Therefore, use of the non-deterministic method in the study of frozen soil mechanics is recommended.
- 4) Meso-cosmic methods should be combined with the

microcosmic method. The microcosmic method is used to recognize the origin, composition, texture, and structure of frozen soil (as well as grain orientation in the process of loading) during mutual transformation between ice and water. Meso-cosmic methods should be employed to reveal the essence of frozen soil characteristics, to explain mechanical phenomena, and to recognize many other issues such as frozen soil yield and failure conditions, shear zone, and localized deformation. To combine the meso-cosmic with microscopic method provides a way to recognize nonlinearity, elasto-plasticity, anisotropy, and rheological behavior of frozen soils. In addition, we can obtain a better understanding about pore ice thawing under higher pressure, water, and migration during freezing and ice formation processes.

- 5) The testing technology of frozen soil mechanics should be improved. This includes the technology of laboratory testing, field testing, monitoring, and other aspects. With regard to field testing technology, more attention should be paid to field displacement testing, field stress and temperature test, field soil pressure testing on the surface of underground structures, strength and deformation testing of foundation soil, and so on. These conventional difficulties can be solved with the entire test technology progress.
- 6) Numerical methods have achieved great advances in dealing with engineering and scientific problems in recent decades. With the development of large high-speed electronic computers and large-scale software, the universality and flexibility of these different methods have been enhanced significantly. Therefore, development and application of numerical simulations in the study of frozen soil mechanics will greatly improve experimental efficiency.

Acknowledgments

This research was supported by the National Natural Science Foundation of China (No. 41071048), the Innovation Research Group of National Natural Science Foundation of China (No. 41121061), CAS Knowledge Innovation Project for the Youth Fund projects (KZCX2-YW-QN307), and the 100 Talent Young Scientists Project granted to Dr. Zhi Wen.

References

- Chen, Feixiong, Li, Ning, & Cheng, Guodong. 2002. The theoretical frame of multi-phase porous medium for the freezing soil. *Chinese journal of geotechnical engineering* 24: 213-217 (in Chinese).
- Cui, Guangxin. 1998. Mechanics of frozen soil for deep alluvium—A new field of frozen soil mechanics. *Journal of glaciology and geocryology* 20(2): 97-100 (in Chinese).
- Dayan, Wang, Wei, Ma, & Xiaoxiao, Chang. 2004. Analyses of behaviour of stress-strain of frozen Lanzhou loess subjected to K_0 consolidation. *Cold regions science and technology* 40: 19-29.

- Da-yan, Wang, Wei, Ma, & Xiao-xiao, Chang, Ai-guo Wang. Study on the resistance to deformation of artificially frozen soil in deep alluvium. *Cold regions science and technology* 42: 194-200.
- Da-yan, Wang, Wei, Ma, & Zhi, Wen. 2008. Study on strength of artificially frozen soils in deep alluvium. *Tunneling and underground space technology* 23: 381-388.
- He, Ping, Cheng, Guodong, & Yu, Qihao. 2000. A couple model of heat, water and stress fields of saturated soil during freezing. *Journal of glaciology and geocryology* 22:135-138 (in Chinese).
- He, Ping, Cheng, Guo-dong, & Yang, Cheng-song. 2002. Analysis of strength of unsaturated frozen soil. *Journal of glaciology and geocryology* 24(3):260-263 (in Chinese).
- Huang, Xiaoming. 1988. Review about the research on permafrost problems of road engineering in cold region, in China. *Journal of glaciology and geocryology* 10: 344-351 (in Chinese).
- Lai, Yuanming. 1999. Nonlinear analysis for the coupled problem of temperature, seepage and stress fields in cold regions tunnels. Graduate university of the chinese academy of sciences dissertation for Ph.D. (in Chinese).
- Li, Hongsheng, Liu, Zengli, & Li, Nansheng. 1998. A frost heave model based on moisture temperature and applied load interaction in frozen soil. *Journal of Dalian university of technology* 38: 29-33 (in Chinese).
- Li, Ning, Chen, Bo, & Chen, Feixiong. 2003. Heat-moisture-deformation coupled model for composite foundation in cold zone. *China civil engineering journal* 36: 66-71 (in Chinese).
- Li, Ping, Xu, Xiaozu, & PU, Yibin. 1999. Analyses of characteristics of frozen fringe using the digital technique of picture. *Journal of glaciology and geocryology* 21: 175-180 (in Chinese).
- Ling, Feng, Wu, Ziwang, & Zhu, Yuanlin. 1999. Fractal approximation of the stress-strain curve of frozen soil. *Science in China* 42 supp.:17-22.
- Liu, Hongxu. 1981. On calculation of normal frost heaving force. *Journal of glaciology and geocryology* 2: 13-17 (in Chinese).
- Liu, Zengli, Li, Hongsheng, & Zhu, Yuanlin. 2002. Damage characteristics and micro-crack damage measurement of frozen soil under uni-axial compression. *Journal of Dalian university of technology* (2):223-227 (in Chinese).
- Ma, Wei, et al. 2002. Analyses of strength and deformation of an artificially frozen soil wall in underground engineering. *Cold regions science and technology* 1: 11-17.
- Ma, Wei, Wu, Ziwang, & Sheng, Yu. 1995. Effect of confining pressure on strength behavior of frozen soil. *Chinese journal of geotechnical engineering* 17(5):7-11 (in Chinese).
- Miao, Tiande, Wei, Xuexia, & Zhang, Changqing. 1995. Microstructural damage theories of creep of frozen soil. *Science in China* (Series B) 25(3): 309-317 (in Chinese).
- Shen, Mu & Ladanyi, B.. 1987. Modeling of coupled heat, moisture and stress field in freezing soil. *Cold regions science and technology* 14: 237—246.
- Sheng, Yu, Ma, Wei, & Hou, Zhongjie. 1993. A model of migration potential for moisture migration during soil freezing. *Journal of glaciology and geocryology* 15: 140-143 (in Chinese).
- Wang, Tiexing & Hu, Changshun. 2003. Study on the problem of coupled temperature field and moisture migration field of subgrade in permafrost region. *China civil engineering journal* 36: 93-97 (in Chinese).
- Wu, Ziwang. 1982. Classification of frozen soils in engineering constructions. *Journal of glaciology and geocryology* 4: 43-48 (in Chinese).
- Wu, Ziwang, Liu, Yongzhi, & XIE, Xiande. 1983. Field experiments of bearing capacity of frozen soils. Professional papers on permafrost studies of Qinghai-Xizang plateau. Beijing: Science Press, 112-119 (in Chinese).
- Wu, Ziwang, Zhang, Jiayi, & Zhu, Yuanlin. 1983. Experimental research on determination of the long-term strength of frozen Soils. Professional papers on permafrost study of Qinghai-Xizang plateau. Beijing: Science Press, 120-123 (in Chinese).
- Wu, Ziwang, Ma, Wei & Cang, Xiaoxiao, Shen Zhongyan. 1993. Uniaxial stress relaxation of frozen loess. *Journal of glaciology and geocryology* 15(1): 125-128 (in Chinese).
- Wu, Ziwang, Ma, Wei, Pu, Yibin, & Chang, Xiaoxiao. 1996. Monitoring the change of structures in frozen soil in uniaxial creep process by CT. *Journal of glaciology and geocryology* 18(4): 306-311 (in Chinese).
- Wu, Ziwang, Ma, Wei, Pu, Yibin, & Chang, Xiaoxiao. 1997. Submicroscopic analysis on deformation characteristics in creep process of frozen soil. *Chinese journal of geotechnical engineering* 19(3): 1-6 (in Chinese).
- Xu, Xiaozu, Zhang Lixin, & Wang, Jia-cheng. 1995. Establishment of a model for predicting unfrozen water content. *Proceedings of 7th International Symposium on Ground Freezing*: 65-68.
- Xu, Xiaozu, Alfried, I.L., & Tax, A.R. 1985. The soil water potential, unfrozen soil water content, and temperature. *Journal of glaciology and geocryology* 7: 1-14 (in Chinese).
- Xu, Xiaozu. 1991. Water and solute migration of freezing soils in the closed system under temperature gradients. *Proceedings of the 6th International Symposium on Ground Freezing*: 93-98.
- Xu, Xiaozu, Deng, Yousheng, & Wang, Jiacheng. 1988. Water migration saturated freezing soil. *Proceedings of 5th Intern. Conf. on Permafrost*: 516-521.
- Xu, Xiaozu, Oliphant, J.L., & Tice, A.R. 1985. Experimental study on factors affecting water migration in frozen morin clay. *Proceedings of 4th intern. symp. on ground freezing* 1: 123-128.
- Zhang, Lixin, Xu, Xiaozu, & Tao, Zhaoxiang. 1993. Two phase transition analysis for saline solute. *Progress in natural science* 3: 48-52.
- Zhang, Lixin & Xu, Xiaozu. 1994. The influence of freezing-thawing process on the unfrozen water content of frozen saline soil. *Proceedings of 7th international symposium on ground freezing*: 93-97.

- Zhang, Xuefu, Su, Xinmin, & Lai, Yuanming. 2004. Non-linear analysis for three-dimensional temperature fields in cold-region tunnels. *China civil engineering journal* 37: 47-53 (in Chinese).
- Zhou, Guoqing. 1999. Analysis of mechanism of restraining soil freezing swelling by using intermission method. *Journal of china university of mining & technology* 28: 413-416 (in Chinese).
- Zhu, Qiang, Fu, Sining, & Wu, Fuxue. 1988. On the frost heave distribution along depth. *Journal of glaciology and geocryology* 10: 1-7 (in Chinese).
- Zhu, Yuanlin & Carbee, D.L. 1983. Creep behavior of frozen silt under constant uniaxial stress. In *proc. of 4th Inter. Conf. Permafrost*, Fairbanks, Alaska: 1507-1512.
- Zhu, Yuanlin & Carbee, D.L. 1984. Uniaxial compressive strength of frozen silt under constant deformation rates. *Cold Regions science and Technology* 9: 3-15.

Reassessment of Lakes and Ponds in an Arctic River Delta Using Modern Spatial Technology

Molly McGraw

Southeastern Louisiana University, Hammond, LA, USA

H. Jesse Walker

Louisiana State University, Baton Rouge, LA, USA

Abstract

The study of Arctic delta lakes has been limited to a few lake deltas such as those of the Colville, Lena, and Mackenzie rivers. Early studies classified and quantified delta lakes using manual methods and aerial photography. Later studies used satellite imagery and computers to count delta lakes. In this study, the authors used both high resolution aerial photography and satellite imagery to quantify and classify all of the lakes and ponds within the entire 600 km² Colville River delta. The imagery was classified, and the resulting classified file was converted into a shape file, which was used to calculate the frequency, area, and distribution of the ponds and lakes. The study determined that the Colville delta contains 238,803 ponds and lakes, which range in size from a few square meters to ~6 km² and occupy ~19 % of the surface area of the delta.

Keywords: Alaska; Arctic; Colville River; delta; lakes; remote sensing.

Introduction

One of the most striking features over much of the Arctic is the great number of lakes that dot its surface. Lakes occupy more than one-third of the area in some locations. Like natural lakes elsewhere, Arctic lakes vary greatly in size, shape, depth, and manner of origin. However, they differ from lakes in some other climatic regions in that, during many months of the year, shallow lakes are frozen to the bottom and deeper lakes are frozen to depths of two to three meters. In addition, permafrost and its associated features play a major role in the formation, maintenance, and destruction of most Arctic lakes.

Research on Arctic lakes has been limited. Until recently it has mostly been devoted to studies related to the orientation of lakes in many parts of the Arctic, including the Alaskan Arctic Coastal Plain (AACP) (Carson and Hussey 1962, Black 1969, Sellman et al. 1975, Frohn et al. 2005, Jorgenson et al. 2007). In contrast to the relative uniformity in shape of oriented lakes, those in Arctic deltas such as the Kolyma, Indigirka, and Lena in Russia, the Mackenzie in Canada, and the Colville in Alaska have a very distinctive orientation.

Very few researchers have attempted to classify Arctic deltaic lakes; exceptions include Mackay (1963), Lewis (1988), Mouchot et al. (1991), and most recently Boyes (1999) and Brown & Young (2006) for the Mackenzie and the Canadian Arctic; Morgenstern et al. (2008), Schneider et al. (2009), and Ulrich et al. (2009) for the Lena; and Dawson (1975 and 1977) for the Colville. Morgenstern et al. (2008), Mouchot et al. (1991) and Boyes (1999) used satellite imagery and computerized technology in their studies.

Prior to the production of Landsat images, the development of Geographic Information Systems (GIS), and high-speed computers, most surface analyses were done manually and often with the aid of aerial photographs. Such was the case with the first lake study of the Colville River delta (Dawson 1975). This paper updates some of those results through the use of

current technology, and fills a void in the current scientific knowledge on the frequency and size of the lakes and ponds within the delta.

Colville River Delta

The Colville River delta, located about 75 km west of Prudhoe Bay, was formed by the Colville River where it debouches into the Beaufort Sea of the Arctic Ocean (Fig. 1). The 53,000 km² drainage basin of the Colville River lies entirely within the zone of continuous permafrost. Ice wedges are common features within the delta, which is subjected to more than 5000 degree days of freezing (Fig. 2). After bifurcation, about 40 km from the ocean, river water flows mainly through two channels, the Niglik (Netchlik) Channel to the west and the main channel on the east. Interlaced between these two channels are numerous smaller active and abandoned distributaries and thousands of lakes and ponds of various shapes and sizes. In addition, the delta supports mudflats, sand bars, sand dunes, ice-wedge polygons, frost mounds, and some pingos.

During most of the year, the delta is in a frozen state. Snow melt and river flow begin in May and river breakup flooding soon follows. The major flooding period lasts for three to four weeks during which much of the delta, including many of its lakes and ponds, is flooded (Walker 1983). Most of the geomorphic activity in the delta, including that related to lakes, occurs between spring breakup and winter freeze up.

Research on the Delta Lakes in the Arctic

Many descriptions of Arctic deltas commonly refer to the large number of lakes and their variation in size (Fig. 3). For example, within the Colville River delta, early measurements determined that lake and pond areas ranged from less than 0.01 km² to more than 2 km² (Dawson 1975, 1977, Walker 1978). Dawson's classification, however, stemmed from an analysis

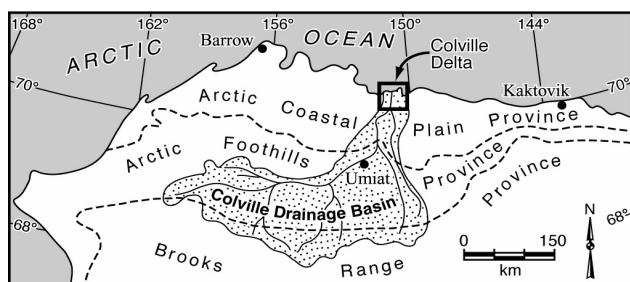


Figure 1. Location of the Colville River delta.

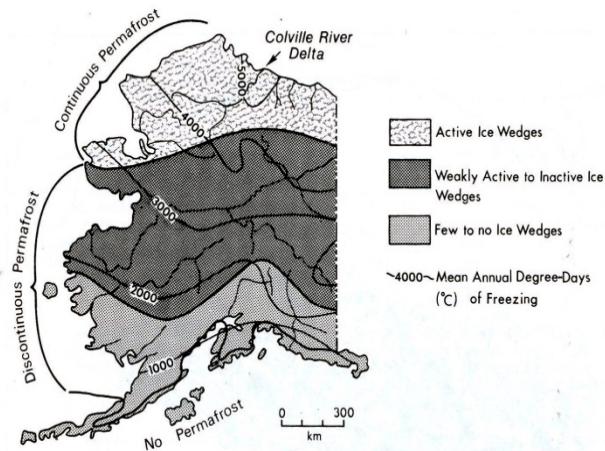


Figure 2. Degree-days of freezing, permafrost zones, and ice-wedge activity in Alaska (after Walker 1983, modified from Péwé 1966).

of three sets of aerial photographs and ground information and photographs acquired during several years of fieldwork during the 1960s and 1970s. This field information included channel and lake profiles and field maps of lake distribution (Dawson 1975).

Dawson (1975) identified four types of lakes within the delta: 1) thermokarst (thaw) lakes, 2) oriented lakes, 3) perched lakes, and 4) channel lakes. Thermokarst lakes range in size from small thaw ponds occupying the center of low-centered polygons to large lakes. Many of the large lakes are the result of the coalescence of smaller thaw lakes and may have drowned polygonal shelves. A small group of lakes near the northwestern mouth of the river appears to be a remnant of larger oriented lakes that are typical of the upper tundra surface. Perched lakes are mainly found in sand dunes, especially just west of the main channel. These dunal lakes were divided by Walker (1967) into inter-dune and intra-dune types. Inter-dune lakes are found in deflation hollows within a dune, whereas intra-dune lakes are those perched between dune bands. The perched category of lakes also includes those lakes found in meander swales. Within the channel-lake category is a variety of lake types including linear point bar ponds, mid-channel bar ponds, oxbow lakes, and other abandoned channel lakes.

In addition to Dawson's classification work on the Colville River delta, individual lake studies include detailed research on the erosion and deposition of lakes that have been tapped by migrating distributaries (Walker 1978, Roselle and Walker 1996), ice wedge and pond degradation (McGraw 2008), and perched ponds (Walker and Harris 1976).

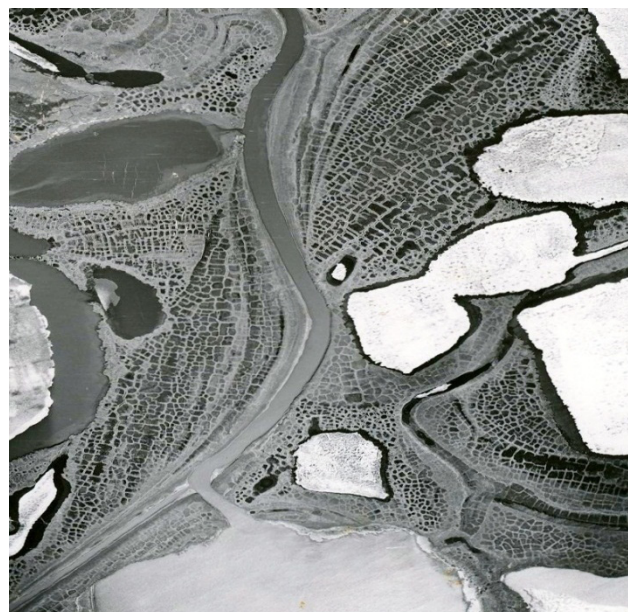


Figure 3. Example of lake variety in shape and size in the Colville River delta. The aerial photograph was taken after river breakup but before total lake-ice melt. Note that the tapped lakes are ice free.

Permafrost, Ice Wedges, and Deltaic Lake Modification

Permafrost-free locations (taliks) in the Colville delta lie beneath the deeper lakes (~2 m) and beneath the thalweg portions of the distributaries. The rest of the surface (sand dunes, sand bars, mudflats, and tundra surfaces) is underlain by permafrost. Each environment has an active layer that varies in depth at the height of the thaw season from a few centimeters in areas with peat and tundra vegetation, to more than two meters in sand dunes. Much of the surface is covered with ice-wedge polygons. Low-centered polygons support small water bodies and/or marsh-type vegetation. Thus most of the ponds of the delta are the result of the nature of ice-wedge growth (Lachenbruch 1962). Even high-centered polygons often have small ponds between the polygons where ice-wedges have melted.

Those large bodies of water that are not bordered by dunes usually have a serrated edge caused by ice-wedge melt. Enlargement, especially of the larger lakes, is aided by the mechanical erosion of wind-driven lake ice during the lake-ice melt season and some wave action during the ice-free season. Most large untapped lakes maintain an ice cover long after river breakup, even until July during some years. The unique enlargement of such lakes results in an inverted topography. Low-centered polygons become high-centered polygons that form a submerged shelf around the lake (Fig. 4).

The most distinctive of the many processes involved in lake and pond modification in Arctic deltas is tapping by migrating river channels (Walker 1978). Since 1948, when the first aerial photographs of the delta were made, innumerable near-channel ice-wedge polygons and no fewer than a dozen large lakes have been tapped. The most recent of the large lakes to be

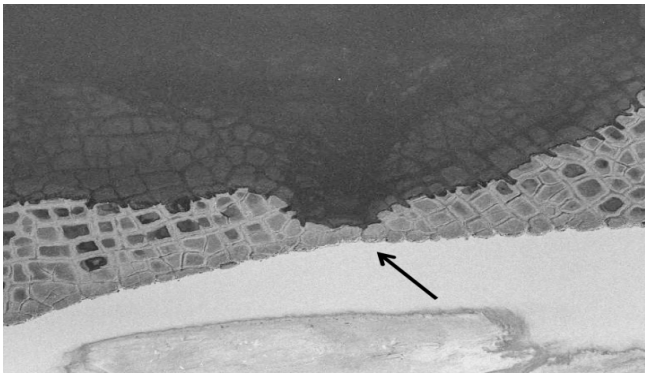


Figure 4. Submerged polygons forming a lake shelf. An arrow shows the location of tapping 2008.

tapped was in 2008 just northwest of the ConocoPhillips Al-pine Oil Drilling facility (Parrett 2009). Usually breaching of the lake/river barrier occurs along ice wedges that have melted and have been eroded by fluvial activity (Fig. 4). Once tapped, the lake is in essence a stilling pond subject to river stage variation and sediment load of the river. Lake deltas form rapidly and, depending on the variation in relief of the lake bottom, the lake becomes divided into distinctive lakes and ponds (Fig. 5).

Another unique factor affecting lakes in permafrost zones is that permafrost becomes an aquiclude at the base of the active layer (Walker and Harris 1976). By preventing percolation downward, any basin deeper than the thickness of the active layer can become a pond. Blowouts in sand dunes, depressions between dune bands, and ice-shove troughs along river banks are all potential ponds, even if ephemeral. Even large lakes maintain higher levels than they might otherwise because of restricted flow through their permafrost-bound banks.

Methodology

Data

This study was conducted using ESRI's ArcGIS 10.0, along with the extensions Image Analysis and Spatial Analyst, and ERDAS' Imagine 10.0. Orthorectified aerial photographs were used for the bulk of the study. The aerial photography, which was acquired in 2004 and has a resolution of 2.5 m, was supplied by ConocoPhillips and the Michael Baker Corporation. Additionally, Band 4 (Near Infrared) Landsat 5 TM imagery, dated July 14, 2011, and US Geological Survey (USGS) National Hydrography Dataset (NHD) - Alaska (resolution 1:100,000) were used. The Landsat 5 imagery was downloaded from Earth Resources Observation and Science (EROS) Center. Landsat 5, Band 4 was used in the study because it is very good at differentiating between land and water. The USGS NHD consisted of various types of GIS data for the entire United States, including Alaska. The dataset includes polyline channel data (NHD Flowline) and polygon lake/pond (NHD Waterbody) data of the Colville delta. Both datasets were in a geodatabase format and contained information collected between 2002 and 2010.

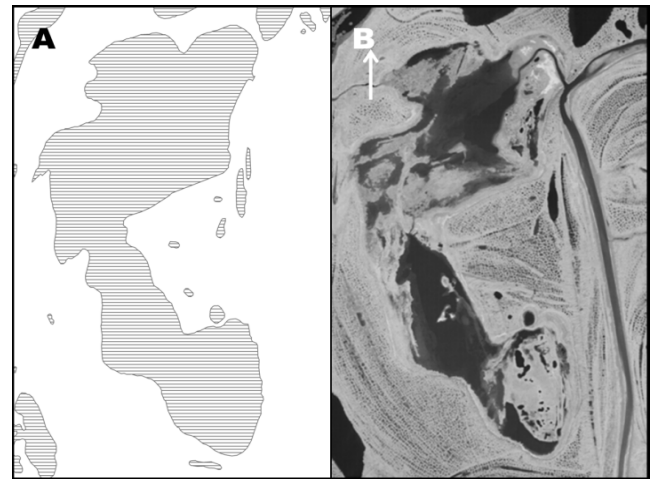


Figure 5. Tutut (Caribou) Lake, A. Prior to tapping in 1971 and as depicted in the USGS NHD data. B. After tapping in 1971 showing present-day morphology.

Data preparation

Since the Colville delta is a myriad of lakes, channels and sand bars, image classification is difficult and complex. To aid lake/pond classification, all extraneous material had to first be removed from the imagery. This was accomplished using a series of masks to block or eliminate the unwanted spatial data. The basic mask covered the entire 600 km² delta and was used to clip the 2004 aerials and the Landsat imagery to the perimeter of the delta. Two additional masks were developed to 1) remove the channels and large lakes (≥ 0.05 km²) from the 2005 aerial photograph, and 2) remove the channels from the 2011 Landsat image (Figs. 6 and 7).

Classification

Due to the enormous size and variety of lakes found in the delta, it was decided to classify both the 2011 Landsat image and the 2004 aerial mosaic. The Landsat image was used to capture large (≥ 0.05 km²) lakes, and the 2004 aerial was used to analyze small (< 0.05 km²) ponds. Both images were classified into 30 classes using ISO cluster unsupervised classification in ArcGIS's Image Analysis. Signatures containing no data and background were deleted and another ISO cluster unsupervised classification, using 4 classes, was run on the first classified images. The overall classification accuracy (Kappa coefficient) was 0.70 for the 2011 imagery and 0.84 for the 2004 imagery. Next, sieving was performed on both reclassified images (2004 and 2011) using a 3-by-3 majority filter. Finally, the 4 classes were merged into water and "other," and the "other" class was deleted. The resulting raster images (2004 and 2011) were converted into shape files to enable spatial calculations (Fig. 8).

Discussion

Frequency

The focus of this study is to calculate the frequency, size, and distribution of lakes and ponds in the Colville delta using modern technology. During the 1960s, the number and size of

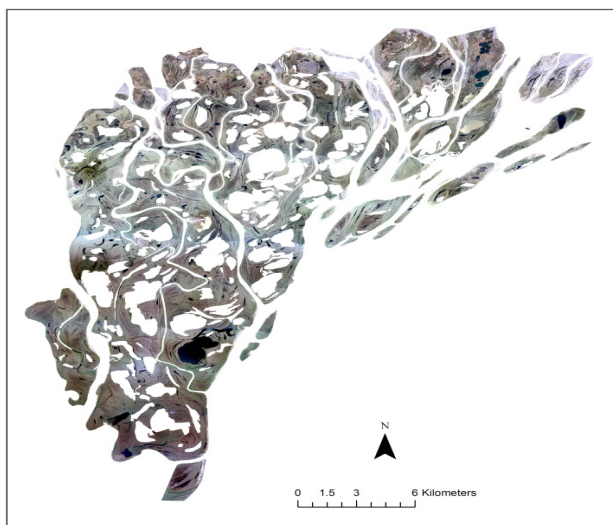


Figure 6. 2004 Mosaic with channels and lakes $\geq 0.05 \text{ km}^2$ removed.

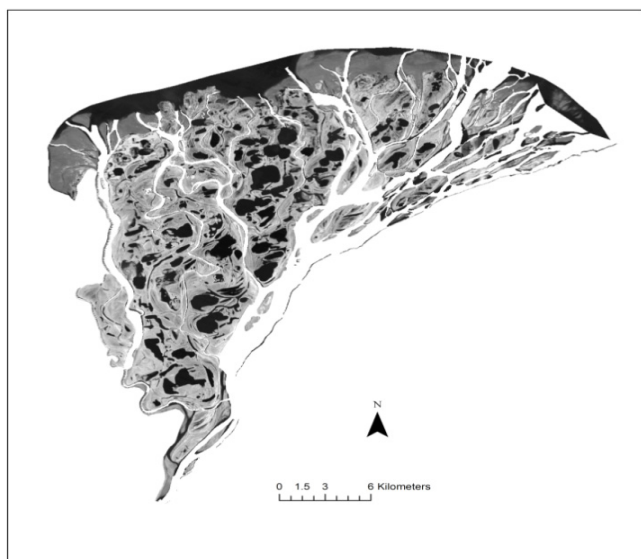


Figure 7. 2011 Landsat 5 TM, Band 4 with channels removed.

the Colville lakes were manually calculated (Table 1) using aerial photography and USGS topographic maps. Same-sized representative areas of the delta were selected and the number of lakes and ponds was manually counted in each area. This number was then extrapolated to determine the total number of lakes for the delta and the results placed into one of eight classes based on size. These calculations yielded a total count of 645 lakes; however, due to limitations of manual counts, only lakes larger than 0.0125 km^2 were included.

Forty years later, the USGS, using satellite imagery and high speed/capacity computers, released GIS files that contained data on the Colville lakes. The USGS data identified 1,469 lakes within the delta. At this resolution, only lakes larger than 10 m^2 could be discerned. It should be noted that the USGS data contains lakes ranging in size from $\sim 20 \text{ m}^2$ to 6 km^2 (Table 1). The number of larger lakes was similar to that of 1960 (Table 1), but the USGS was able to estimate the number

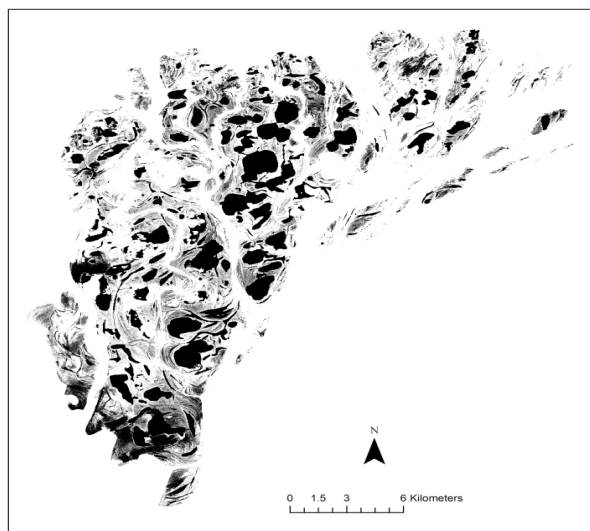


Figure 8. Classified lakes of the delta. Note that everything colored black is a lake/pond.

of small lakes at 1,001, something that was impossible before.

There is one notable error in the USGS data involving several large tapped lakes. For example two lakes (Caribou Lake and Lake Nanook), located in the center of the delta, were tapped in the 1940s and 1970, respectively. Today, both of these lakes are being in-filled with sediment and consist of several connected ponds (Fig. 5). However, the USGS data show each as a single polygon, instead of a series of polygons. The second error involved the small thaw/polygonal ponds that the USGS did not include.

Using better data and technology, this current study was able to estimate the number of all lakes within the delta as 238,803, ranging in size from $\sim 5 \text{ m}^2$ to greater than 6 km^2 (Table 1). Note that this count includes the small polygon lakes, which had eluded the previous researchers (Figs. 8 and 9).

Upon comparing the present data with previous studies, one finds a large disparity in the number of the small ($< 0.0125 \text{ km}^2$), large ($> 1.0 \text{ km}^2$), and a narrow range of medium ($0.10\text{--}0.25 \text{ km}^2$) sized lakes. As alluded to previously, the disparity involving the small lakes is due to the better data and technology. Because the 1960s study was conducted manually, it did not include lakes smaller than 0.0125 km^2 . The USGS estimated that 1,001 small ($< 0.0125 \text{ km}^2$) lakes were in the delta. However, it should be noted that the USGS only includes lakes larger than 20 m^2 in its dataset.

The number of large lakes varies from 25 in the 1960s study, to 22 in the USGS data, to 17 in the current study. This decrease in the number of lakes over time is likely due to changes in individual lake morphology, differences in data resolution, and in manual versus computerized counts. As discussed above, several large lakes within the delta have been tapped and drained and are currently experiencing differential sedimentation, resulting in the creation of several small ponds where there was once a single large lake. During the 1960s, some of the large tapped lakes still contained a large volume of water and were not completely drained; each was thus manually counted as a single lake. The USGS was able to

Table 1: Comparison of the frequency and percent coverage of lakes in the Colville River delta.

| Size (km ²) | Number of Lakes | | | | | |
|-------------------------|-----------------|---------|-------------|---------|----------------|---------|
| | 1960s Values | | USGS Values | | Current Values | |
| | No. | % delta | No. | % delta | No. | % delta |
| 0.00-0.0125 | * | ? | 1,001** | 0.62 | 238,288 | 4.62 |
| 0.0125-0.05 | 393 | 1.3 | 263 | 1.12 | 289 | 1.19 |
| 0.05-0.10 | 84 | 1.0 | 69 | 0.79 | 92 | 0.99 |
| 0.10-0.25 | 79 | 2.0 | 59 | 1.60 | 59 | 1.49 |
| 0.25-0.50 | 42 | 2.5 | 35 | 2.12 | 39 | 2.43 |
| 0.50-1.00 | 18 | 2.2 | 20 | 2.30 | 19 | 2.24 |
| 1.00-2.00 | 20 | 4.4 | 14 | 3.12 | 10 | 2.28 |
| > 2.00 | 5 | 2.5 | 8 | 3.88 | 7 | 3.60 |
| Total No. | 645 | 16.2 | 1,469 | 15.6 | 238,803 | 18.84 |

* not determined; ** does not include lakes less than 20 m²

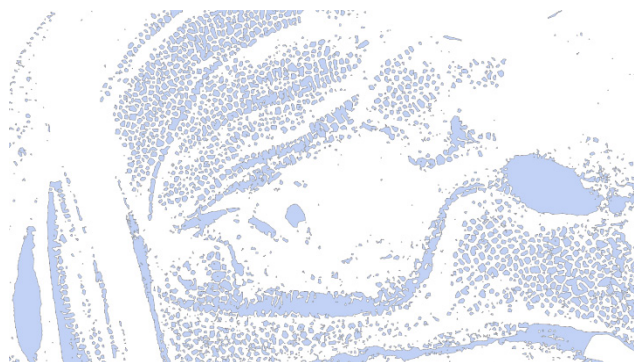


Figure 9. Example of the classified lakes/ponds file (from aerial photograph).

distinguish some of the changes in the tapped lakes, but not all. It took the high resolution aerial photos of this study to distinguish the numerous ponds where there was once only a single large lake. Conversely, several medium-size lakes have undergone thermal erosion and are now hydraulically connected, creating a single large lake. Thus lakes that were once counted individually in the 1960s were counted as a single large (>2 km²) lake in both the USGS data and this study.

Similarly, the disparity in the number of the medium (0.10–0.25 km²) lakes, from a high of 79 in the 1960s to 59 in both the USGS data and the current study, is likely due to changes in lake morphology. Also, higher resolution data allows easier delineation between water and land.

In summary, the discrepancies between the numbers (Table 1) for the three systems used mainly represent actual changes

in lake numbers among the different size categories. These changes have occurred because of three factors: 1) the tapping of a number of lakes during the past 40 years, thus reducing the number of large lakes but increasing the number of lakes and ponds; 2) thermal and mechanical erosion that has resulted in the coalescence of adjacent lakes and thus increased the number of large lakes while reducing the number of smaller ones; and 3) the higher quality of calculations made possible by the use of modern technology. An example of the coalescence of adjacent lakes is illustrated by one of the lake systems in the north-central part of the delta. The lake that displays an area of about 6 km² in today's calculations was, in the 1960s, actually four lakes that were minimally connected.

Distribution

As expected, the area of the delta covered by lakes differed with each study (Table 1). In the 1960s study, lakes larger than 0.0125 km² occupied 16.2% of the delta. The USGS data indicated that lakes occupied 15.6% of the delta, compared to the current study, which shows that 18.8% of the delta is covered by lakes and ponds. The approximately 3% difference in lake areas between the current study and older data is undoubtedly due to the quantification of the small polygonal lakes in the current study (Table 1). As expected, the small (<0.0125 km²) polygonal lakes and large (>2 km²) lakes occupied the most area (4.6% and 3.6%, respectively) of the delta.

Summary

The ponds and lakes of the Colville delta were quantified using aerial photography and satellite imagery. The imagery was classified and the resulting classified file was converted to a shape file. The shape file was used to calculate the frequency, area, and distribution of the ponds and lakes. The study determined that the Colville delta contains 238,803 pond and lakes, which range in size from a few square meters to ~6 km² and occupy about 19% of the surface area of the delta.

Acknowledgments

The authors would like to thank ConocoPhillips and the Michael Baker Corporation for the 2004 aerial photography of the Colville River delta, and two anonymous reviews for their constructive comments.

References

- Black, R.F. 1969. Thaw depressions and thaw lakes—a review. *Biuletyn Peryglacjalny*. 19: 131-150.
- Boyes, D. 1999. *Morphometry, Spatial Analysis and Development of Lakes on the Mackenzie Delta Plain*. Unpublished Doctoral Diss., University of Western Ontario: 310 pp.
- Brown, L. & Young, K.L. 2006. Assessment of three mapping techniques to delineate lakes and ponds in a Canadian High Arctic wetland complex. *Arctic* 59(3): 283-293.
- Carson, C. & Hussey, K. 1962. The oriented lakes of Arctic Alaska. *Arctic* 21: 12-26.

- Dawson, A.G. 1975. *Landforms of the Colville River delta, Alaska, as interpreted from aerial photographs*. Unpublished M.S. Thesis. Baton Rouge, LA: Louisiana State University: 93 pp.
- Dawson, A. G. 1977. *The Nature and Distribution of Lake types in the Colville River Delta, Alaska*. *Edinburgh Research Discussion Paper* 11: 22 pp.
- Frohn, R.C., Hinkel, K.M., & Eisner, W.R. 2005. Satellite remote sensing classification of thaw lakes and drained thaw lake basins on the North Slope of Alaska. *Remote Sensing of Environment* 97 (1): 116-126.
- Jorgenson, T.M. & Shur, Y. 2007. Evolution of lakes and basins in northern Alaska and discussion of the thaw lake cycle. *Journal of Geophysical Research* 112: 1-12.
- Lachenbruch, A. 1962. *Mechanics of Thermal Contraction Cracks and Ice-Wedge Polygons in Permafrost*. U. S. Geological Survey Special Paper No. 70.
- Lewis, C. 1988. *Mackenzie Delta Sedimentary Environments and Processes*, Draft Copy, Inland Waters Directorate, Environment Canada. As quoted by Boyes, 1999.
- McGraw, M. 2008. The degradation of an ice wedge and its role in pond development. In *NICOP 2008: Proceedings of the Ninth International Conference on Permafrost*. D.L. Kane, K.M. Hinkel (eds.). Institute of Northern Engineering, University of Alaska Fairbanks, 2: 1161-1166.
- Mackay, J. 1963. *The Mackenzie Delta Area, N.W.T. Department of Mines and Technical Surveys*, Geographical Branch, Canada, Memoir 8.
- Morgenstern, A., Grosse, G., & Schirrmeyer, L. 2008. Genetic, morphological, and statistical characterization of lakes in the permafrost dominated Lena delta. In *NICOP 2008: Proceedings of the Ninth International Conference on Permafrost*. D.L. Kane, K.M. Hinkel (eds.). Institute of Northern Engineering, University of Alaska Fairbanks, 2: 1238-1244.
- Mouchot, M.-E., Alföldi, T. DeLisle, D., & McCullough, G. 1991. Monitoring water bodies of the Mackenzie River Delta using remote sensing methods. *Arctic* 44 (Suppl. 1): 21-28.
- Parrett, J. Personal communication, June 2, 2009.
- Péwé, T. 1966. Ice-wedges in Alaska; classification, distribution, and climatic significance. *Proceedings of the Permafrost International Conference*, Lafayette, Indiana. 76-81.
- Roselle, D. & Walker, H. 1996. Erosional and depositional history of two delta lakes in Arctic Alaska. In: *Festschrift für Dietrich Barsch*. Geographischen Instituts der Universität Heidelberg: 413-426.
- Schneider, J., Grosse, G., & Wagner, D. 2009. Land cover classification of tundra environments in the Arctic Lena Delta based on Landsat 7 ETM+ data and its application for upscaling of methane emissions. *Remote Sensing of Environment* 113(2): 380-391.
- Sellman, P.V., Brown, J. Lewellen, R.I., McKim, H., & Merry, C. 1975. *The classification and geomorphic implications of thaw lakes on the Arctic coastal plain, Alaska*, CRREL Report 344.
- Ulrich, M., Grosse, G., Chabrilat, S., & Schirrmeyer, L. 2009. Spectral characterization of periglacial surfaces and geomorphological units in the Arctic Lena Delta using field spectrometry and remote sensing. *Remote Sensing of Environment* 113(6): 1220-1235.
- United States Geological Survey National Hydrography Dataset*. Denver, Colorado: US Geological Survey National Geospatial Technical Operations Center. <ftp://nhdftp.usgs.gov/DataSets/Staged/States/FileGDB/HighResolution> (June 4, 2011).
- Walker, H.J. 1967. Riverbank dunes in the Colville River Delta, Alaska. Coastal Studies Institute, Louisiana State University. *Bulletin* 1: 7-14.
- Walker, H.J. 1978. Lake tapping in the Colville River Delta, Alaska. In: *Third International Conference on Permafrost, Proceedings*: 233-238.
- Walker, H.J. 1983. *Guidebook to Permafrost and Related Features of the Colville River Delta Alaska*. Fourth International Conference on Permafrost, Guidebook 2: 34 pp.
- Walker, H. & Harris, M. 1976. Perched ponds: an Arctic variety. *Arctic* 29: 233-238.

Thermal Performance of the Permafrost Protection Techniques at Beaver Creek Experimental Road Site, Yukon, Canada

Julie M-Lepage, Guy Doré

Department of Civil Engineering, Laval University, Québec, Canada

Daniel Fortier

Geography Department, University of Montréal, Québec, Canada

Paul Murchison

Yukon Highways and Public Works, Transportation Engineering, Whitehorse, Yukon, Canada

Abstract

To better understand permafrost degradation under roadways, 12 experimental sections were constructed on the Alaska Highway near Beaver Creek in April 2008. These sections study one or several combined methods of thermal stabilization, such as air convection embankment, heat drains, grass-covered embankment, reflecting surfaces, and snow clearing on embankment slopes. This paper presents the results of the analysis of the ground thermal regime and the heat balance for the 12 sections during their first three years in service to determine the thermal impact of the construction and the short-term effectiveness of the techniques experimented.

Keywords: thermal regime; permafrost mitigation technique; Alaska Highway; embankment; heat extraction index.

Introduction

In the Canadian North, permafrost is thawing at an accelerated rate due to climate warming and other factors. As a result, subgrade soils underlying roadways are settling and experiencing a loss of bearing capacity. This is reducing the level of service and increasing the risks of accidents for road users. Maintenance costs are also considerably higher for affected sections of the road (Remchein et al. 2009). Furthermore, road construction techniques developed in southern Canada need to be adapted to the northern environment to prevent dramatic permafrost thawing after new road construction. Preventing permafrost warming or thawing by simply increasing the thermal resistance (e.g., by increasing the embankment height or by using more thermal-resistant materials) is a passive method and lacks long-term effectiveness (Zhang et al. 2010). To find better solutions, 12 experimental sections have been constructed on the Alaska Highway near Beaver Creek, Yukon (Fig.1).

The main objectives of this paper are to 1) analyze the ground thermal regime for the 12 sections during their first

three years in service, and 2) determine the thermal impact of the construction and the short-term effectiveness of the protection technique.

Problem Statement

In permafrost regions, there has been very limited success building linear infrastructure that does not undergo deformations resulting from thawing of ice-rich soils or frost heave induced by freezing of wet foundation soil (Kondratiev 2010). During construction of an embankment on ice-rich soils, the thermal regime can be significantly impacted, causing rapid thawing of permafrost. The main types of resulting distresses are differential settlement and cracking along the road shoulder.

This phenomenon causes an important loss of the functional and structural capacities of the Alaska Highway over a 200-km

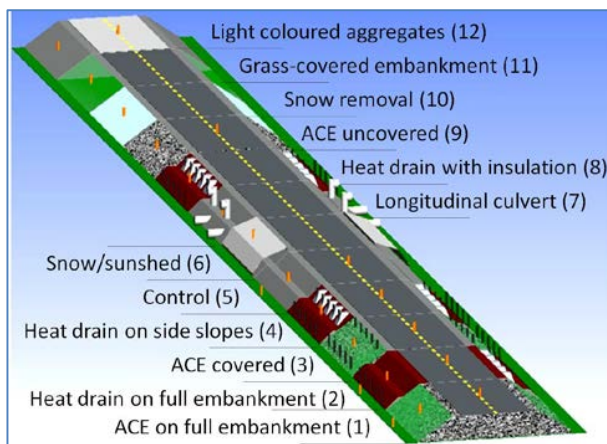


Figure 1. Schematic of Beaver Creek experimental test site.



Figure 2. Left: thaw-settlements causing water to pond in the depression near the centerline of the road (km 1858). Right: longitudinal cracking observed along the Alaska Highway (km 1760).

section, mainly from Destruction Bay to the Alaska border. Every year, an estimated \$22,000 per kilometer is spent on maintenance directly related to damage caused by degrading permafrost. In fact, in these areas, highway resurfacing is required every 3–4 years compared to every 15–20 years for sections constructed on stable ground.

The techniques used at the Beaver Creek experimental site were designed to prevent permafrost thawing either by extracting ground heat under the embankment or by reducing absorbed solar radiation at the embankment surface. It is expected that these methods will allow the control of the active layer thickness and limit the occurrence of differential settlements and cracks if thawing occurs. In the discontinuous permafrost zone near the study site, the active layer thickness averages 40–60 cm in peat-covered soils. However, road construction is one of the main factors causing permafrost degradation, and the active layer thickness can easily reach to 3 or 4 meters locally under these embankments.

Methodology

The results presented in this paper are based on the analysis of thermal data collected at each test section. Temperature monitoring at each of the test sections was done using thermistor strings. As a minimum, a vertical thermistor string was installed in the middle of the section at mid-slope (south side) to a depth of 15 m from the surface. Sections including protection systems extending across the embankment also included a thermistor string positioned at the center of the cross section of the embankment. Finally, a few sections included an additional thermistor string located at the toe of the embankment slope (south side). These sections are the reference section, the full air-convection embankment, and the full embankment heat drain.

The thermal data record starts in October 2008 and includes six daily readings. Data were made available to researchers by Yukon Highways and Public Works (YHPW). The raw data have been analyzed to extract useful information including evolution of temperature with depth and time, thermal regimes at specific times, and thermal gradients using EXCEL and SURFER software.

To characterize the effectiveness of the sections, a new method based on heat flux measurements at the interface

between the embankment and natural soil has been used in this study. Heat fluxes have been calculated to obtain the heat extraction H_x and induction H_i indices for each protection technique at the road/embankment interface (Fig. 3).

The proposed method is based on three assumptions:

- 1) The first 2 m of the natural ground under the embankment is homogenous.
- 2) Only conduction governs heat transfer into the natural ground.
- 3) There is no water flow under the road embankment.

Fourier’s law of heat conduction (equation 1) has been used to compute heat fluxes.

$$q = k_{soil} \times \frac{\partial T}{\partial z} \tag{1}$$

where q : heat flux [W/m^2]; k_{soil} : thermal conductivity [$W/m^{\circ}C$] (Type of soil at the test site: gravelly muddy sand); T : temperature measured at 0 m and -2 m [$^{\circ}C$]; Z : depth [m].

Based on field measurements (De Grandpré 2011), k_{frozen} has been set at 1.337 $W/m^{\circ}C$ and $k_{unfrozen}$ at 0.907 $W/m^{\circ}C$. The definition of the heat extraction/induction indices is based on the quantity of heat extracted H_x or inducted H_i during a year. The heat induction index is computed by adding all positive heat fluxes obtained based on thermal gradients measured every 14 days (equation 2). The heat extraction index is obtained by adding all negative heat fluxes (equation 3).

$$H_x \left[\frac{KJ}{m^2} \right] = k_{frozen} \times -\frac{\partial T}{\partial z} \times \Delta t \tag{2}$$

$$H_i \left[\frac{KJ}{m^2} \right] = k_{unfrozen} \times \frac{\partial T}{\partial z} \times \Delta t \tag{3}$$

where $\Delta t = 14$ days = 1 209 600 seconds.

The heat balance at the interface is obtained by adding H_i and H_x . A negative heat balance means that more heat is extracted than heat is induced. The upper portion of the natural ground should then be cooling.

Control Section

The control section has been constructed using standard Alaska Highway construction practices. This section is used as a reference to compare the thermal performance of the other sections and to assess the relative effectiveness of the protection techniques.

The kriging interpolation graph shown (Fig. 4) has been created using the daily mean temperature data from the control section between October 2008 and October 2009. The dashed line located at the 0 m depth illustrates the interface between the embankment and the natural ground. The dark solid line corresponds to the 0°C isotherm. The shaded region represents a critical temperature zone where the soil has temperature values between -1°C and 0°C. In 2008 and 2009, the 0°C isotherm confirms that the active layer is at a depth of 1.4 meters. This graph shows the importance of heat intake in a standard bituminous surface treatment road during the summer season.

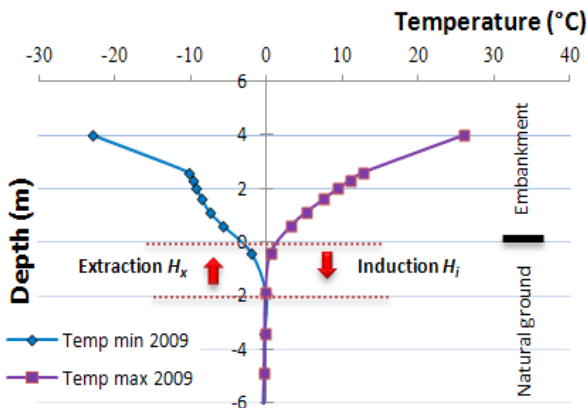


Figure 3. Schematic of the heat extraction and induction indices in the longitudinal culvert in 2009.

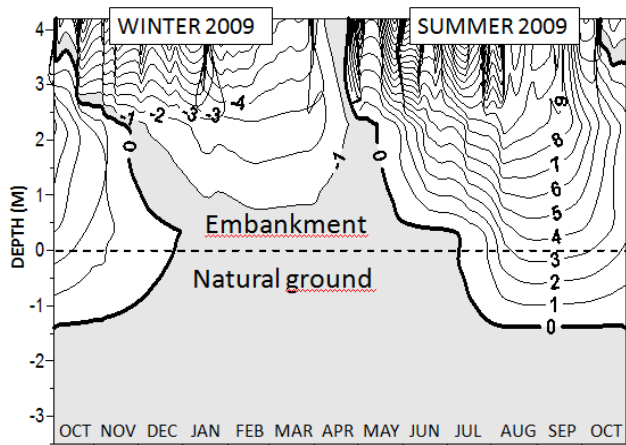


Figure 4. Kriging interpolation of the control section thermal regime ($^{\circ}\text{C}$).

Mitigation Technique Tested

Sections protected with air convection embankment

This thermal stabilization method uses natural air convection to activate heat loss during winter, increasing winter cooling rates. The section was constructed using 150 mm to 300 mm diameter crushed rock for the embankment slopes or across the full width of the embankment to form interconnected convective cells (Fig. 5). During winter, air cooled in the upper part of the convective material sinks down into the embankment, displacing warm air upward. Heat is then extracted at the top of the embankment by conduction. During summer, the 5-m-thick porous material insulates the ground and reduces warming by keeping warm air near the surface and cool air at the base of the air convection embankment. Three Air Convection Embankment (ACE) test sections were constructed. Section 1 is characterized by the presence of a convective layer across the full width of the embankment. The embankment's slopes are also covered by an organic soil layer to impede heat intake and reduce warming of the ACE material during summer. Section 3 differs from section 1 as the application of ACE material was limited to the embankment slopes. In an attempt to maximize the effectiveness of the convective system, two ventilation pipes have been placed at the base and at the top of the convective layer. Section 9 is similar to section 3, but the ACE material is exposed at the surface.

Longitudinal culvert

This method uses a 750-mm-diameter waterproof plastic culvert, buried under the embankment slope and parallel to the road, to generate air circulation and convection cooling (Fig. 6). During winter, warm air tends to move upward through the vertical outlets drawing cold air in at the base of the embankment through the inlets. During summer, the inlet and outlet are shut by lids to impede warm air circulation in the embankment.

Snow/sun sheds

This method provides embankment slope protection during winter (snow accumulation) and summer (solar radiation). In the winter, the technique enhances cooling by preventing snow

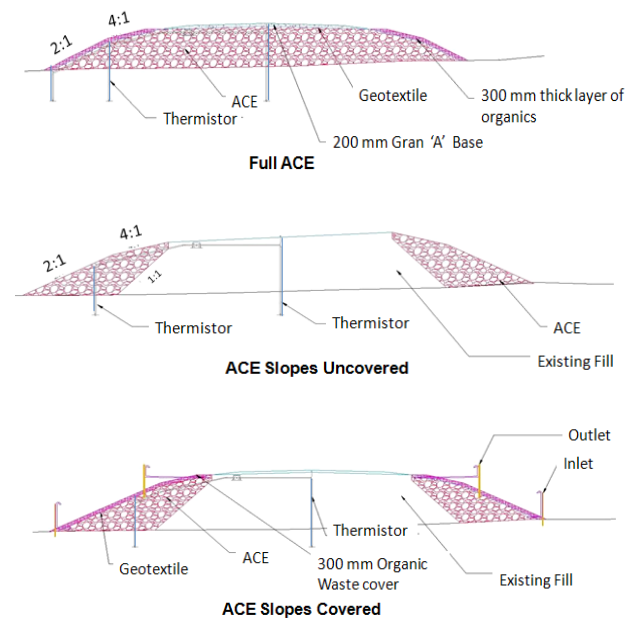


Figure 5. Schematic of the air convection embankment sections.

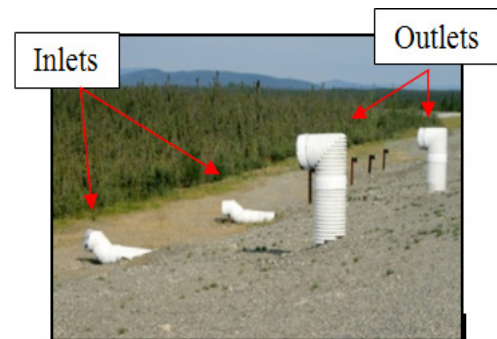


Figure 6. Inlets and outlets of the longitudinal culvert system.



Figure 7. Snow/Sun shed on the west side of the Alaska Highway.

accumulation on the ground, thereby eliminating the insulating effect of snow and allowing cold air circulation over the ground surface (Fig. 7). The technique reduces solar radiation on the embankment slopes during the summer.

Snow clearing

The objective of this technique is to reduce the insulating effect of snow accumulation on the embankment and allow heat to be removed more effectively in the winter. This is accomplished by mechanically removing the snow from the embankment slope.

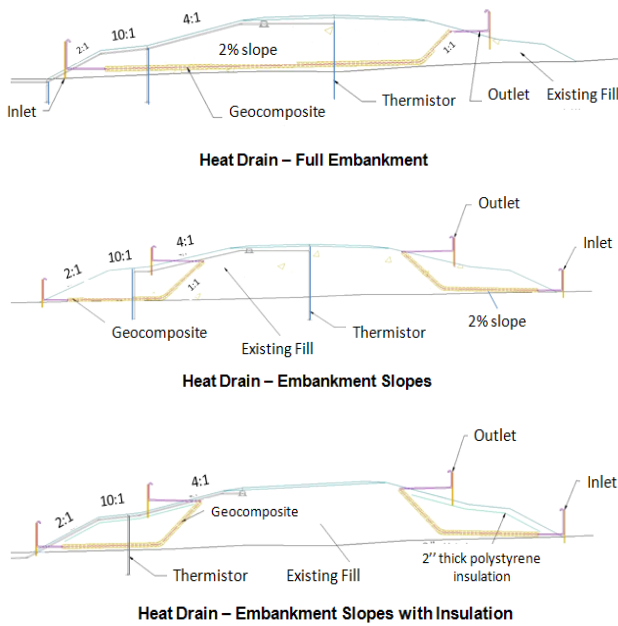


Figure 8. Schematic of the heat drain sections.

Heat drains

This protection technique uses a 25-mm-thick geocomposite drainage layer (dimple board/drain board) to induce cold air circulation by natural convection through the embankment (Fig. 8). Inlet and outlet pipes are attached to the geocomposite at regular intervals along the road. During winter, warm air moves upward in the drain and is expelled by the outlets. This movement draws cold air into the inlets and through the heat drain at the base of the embankment. The heat drain technique was used in three sections. Section 2 was constructed using a heat drain extending across the full width of the embankment. In section 4 the heat drain was limited to the embankment shoulders. Finally, the system used in section 8 includes the use of a 50-mm-thick insulation layer above the heat drain.

Light-colored bituminous surface treatment

This section uses light-colored aggregates in the bituminous surface treatment to reduce heat absorption from solar radiation.

Heat Balance from the Embankment Slopes

Figure 9 represents the heat balance computed for selected sections during the 2010 monitoring year. The heat balance represents the sum of the heat induction and extraction indices for a given section.

Based on temperature measurements under the embankment, five sections appeared to have cooler ground temperatures than the control section in 2010. These were the longitudinal culvert, the snow/sun shed, and the 3 sections using air convection embankments. However, based on heat balance measurements, only 3 of those sections—the snowshed, the longitudinal culvert, and the ACE uncovered—have successfully cooled the natural ground and show a negative heat balance (Fig. 9). For the ACE uncovered, the upper half of the

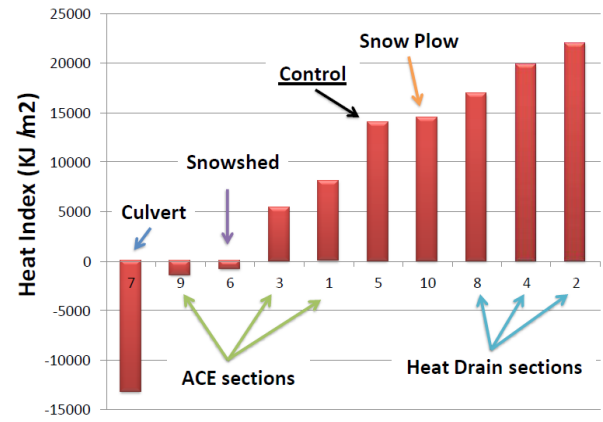


Figure 9. Heat balance in the embankment slope in 2010. Positive index means net heat intake, and negative index net heat outtake.



Figure 10. West slope of the ACE uncovered contaminated with gravels by snow removal in March 2011.

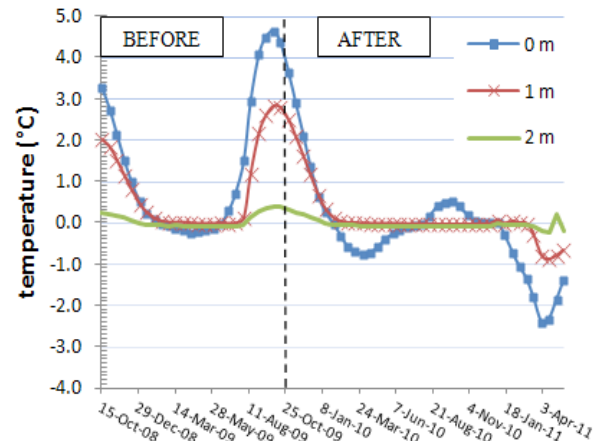


Figure 11. Thermal regime at 0, 1, and 2 meters depth in the natural ground before and after the snow/sun shed construction.

slope is being contaminated by sand and gravel from winter maintenance operations (Fig. 10). This might cause the section to be less effective in the future if the voids become obstructed.

The snow/sun shed was constructed in fall 2010, one year after the construction of the other sections. Figure 11 shows how quickly the ground temperatures are reduced right after construction of the shed.

The poor performance of the heat drain sections at the Beaver Creek site was not expected based on the good performance reported for the heat drain section tested on the Tasiuaq airstrip in northern Quebec (Ficheur & Doré 2010). All of the systems tested at the Beaver Creek site have a higher heat balance than the control section. It is suspected that the heat drain sections are not functioning based on their lack of performance. YHPW completed smoke tests in August 2011 to determine if air could be circulated through the heat drains. Smoke was injected in section 4 using two of the air inlets. Smoke was detected in the other inlets but not at any of the outlets. The results of the test suggest that there may be a blockage or a break in this section of heat drain that is preventing it from working as expected. It is possible that some part of the geocomposite was crushed or intake/outlet connections were damaged during construction. The problem may also be associated with air leakage at the joints of the ventilation pipe system.

Variation in air temperature between 2009 and 2010

The air temperature is recorded at the test site by a weather station located adjacent to the Alaska Highway. The annual mean air temperatures registered in 2009 and 2010 were -3.9°C and -2.9°C, respectively. The Beaver Creek climatic normal from 1971 to 2000 is -5.5°C (Environment Canada 2011). However, it can be noted that the warming mainly occurred in 2010 during the winter period, when most of the techniques were active (Table 1).

The thermal regime in the embankment slopes of only one section was not affected by the winter climate variation recorded during the monitoring period. The longitudinal culverts extracted more heat from the ground while the mean air temperature was 1°C higher. In fact, this technique extracted 1626 KJ/m² more in 2010 than in the previous year (Fig. 12).

Table 1. Freezing and thawing index registered at the Beaver Creek test site in 2009–2010 compared to the 30-year average.

| | Freezing Index (°C) | Thawing Index (°C) |
|-----------------|---------------------|--------------------|
| 2009 | 3170 | 1745 |
| 2010 | 2782 | 1717 |
| 30-year average | 3534 | 1532 |

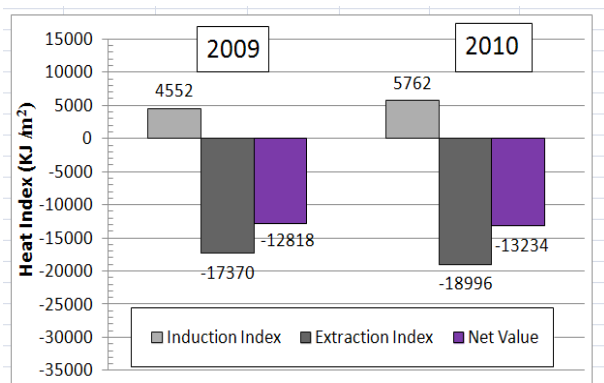


Figure 12. Induction index, extraction index, and heat balance in the longitudinal culvert section in 2009 and 2010.

Heat Balance under the Centerline of the Road

Only seven techniques are represented in Figure 13 because thermistor strings are not located at the centerline of the road for every section. Therefore, knowing the cooling effect induced by the longitudinal culverts and the snowshed under the center of the road is not possible. However, an interesting effect can be observed with the ACE sections.

Using the convective material across the full embankment helps to significantly cool the embankment in the middle of the road (1). For the uncovered ACE (9), the cooling of the slopes appears to extend under the centerline of the road. Finally, for the ACE with the vegetation cover on the slopes combined with the ventilation system (3), there is a significant warming effect under the road. This warming could be associated with malfunctioning of the ventilation system. The light-colored aggregate bituminous surface treatment has a

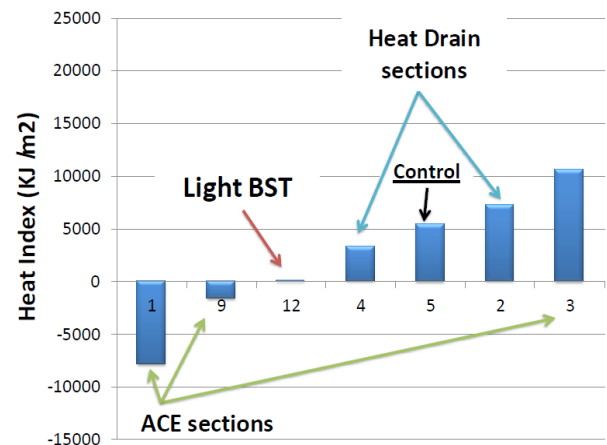


Figure 13. Heat balance under the centerline of the road (2010).

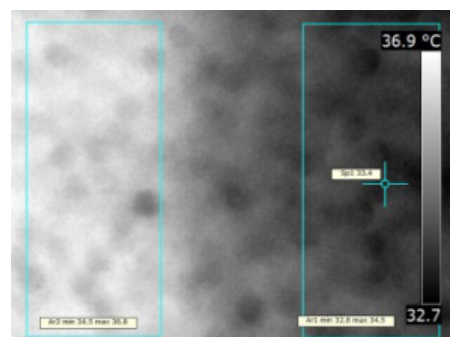


Figure 14. Infrared image comparing dark- and light-colored bituminous surface treatment.

heat balance of 104 KJ/m², which is 5338 KJ/m² lower than the control section. This high albedo surface appears to significantly reduce the embankment heat intake caused by absorption of solar radiation by darker surface material. Equilibrium is reached throughout the year between heat induction and extraction. The beneficial effect of the light-colored aggregated surface has also been measured with an FLIR infrared camera (Fig. 14). This infrared image was taken at the beginning of August on a sunny day around 4:30 p.m. The dark bituminous surface treatment zone on the left had a mean temperature of 36.2°C. The right zone that is the light-colored aggregate had a mean temperature of 33.7°C. During March in the morning, a difference of 1°C was measured between the two surfaces. It appears to be a promising technique to prevent permafrost differential thawing on the road and could be combined with other mitigation techniques in areas highly affected by permafrost degradation.

Conclusion

This analysis of the temperature data and heat balance from the Beaver Creek experimental site has led to preliminary conclusions on the thermal performance of permafrost mitigation techniques. Some permafrost protection systems have shown good potential during their first two years in service. This is the case for sections 1, 3, and 9 (air convection embankments), section 7 (longitudinal culverts), section 6 (snow/sun shed), and section 12 (light-colored aggregates). More tests will be required to understand the non-effectiveness of the heat drain sections. It is necessary to continue the thermal monitoring and analysis for a few more years to assess section performance under various climatic conditions. The durability of these sections, as well as their long-term economic potential, must also be assessed.

Acknowledgments

The authors would like to acknowledge the technical and the financial support of Yukon Highways and Public Works for this project.

References

- Environment Canada. 2011. *National Climate Data and Information Archive*, Beaver Creek A (Yukon Territory), www.climate.weatheroffice.gc.ca.
- Ficheur, A. & Dore, G. 2010. *Expérimentation de techniques de mitigation des effets de la fonte du pergélisol sur les infrastructures de transport du Nunavik : Aéroport de Tasiujaq*, Rapport final, 177 pp.
- Kondratiev, V.G. 2010. Some geocryological problems of railways and highways on permafrost of Transbaikai and Tibet, *63rd Canadian Geotechnical Conference and the 6th Canadian Permafrost Conference*: 541-548.
- M-Lepage, J., Doré, G., & Fortier, F. 2010. Experimentation of mitigation techniques to reduce the effects of permafrost degradation on transportation infrastructures at Beaver Creek experimental road site (Alaska Highway, Yukon), *63rd Canadian Geotechnical Conference and the 6th Canadian Permafrost Conference*: 526-533.
- Remchein, D., Fortier, D., Dore, G., Stanley, B., & Walsh, R. 2009. Cost and Constructability of Permafrost Test Sections Along the Alaska Highway, Yukon. *Proceedings of Transport Association of Canada Annual Conference, Vancouver, October 2009*, 1-20.
- De Grandpré, I. 2011. *Impacts de l'écoulement souterrain sur la dégradation du pergélisol*, mémoire de maîtrise, département de géographie, faculté des Arts et Sciences, Université de Montréal, 132 pp.
- Zhang, M., Lai, Y., & Dong, Y. 2010. Three-Dimensional Nonlinear Analysis for the Cooling Characteristics of Crushed-Rock Interlayer Embankment with Ventilated Duct along the Qinghai-Tibet Expressway in permafrost Regions. *Journal of Cold Regions Engineering* Volume 24, Number 4: 126-141.

Monitoring Instruments for Freeze-Thaw Depth

Junko Mori, Toshio Sone

Institute of Low Temperature Science, Hokkaido University, Sapporo, Japan

Abstract

Frost tubes are useful instruments for measuring ground freezing and thawing at point locations. However, few frost tubes have been designed to make automatic readings. We report an automatic recordable frost tube to measure freeze-thaw at multiple depths in the soil column. Using this device, which we call the “freeze-thaw sensor (FTS),” it is possible to detect the frozen or unfrozen state of the ground from the surface to more than 3 m depth at 5 mm intervals. FTS uses little power and will operate for more than one year at hourly intervals under field conditions. Installation requires a small-diameter drill hole. Laboratory experiments showed that FTS is able to detect the depth of freeze-thaw with accuracy comparable to temperature measurements at 5 cm intervals. The device can be more suitable for multi-depth freeze-thaw measurements than soil temperature measurements.

Keywords: active layer depth; automatic monitoring; freeze-thaw depth; freeze-thaw sensor; frost tube.

Introduction

Frost tubes are useful instruments for measuring the depths of freezing and thawing in the ground (Rickard & Brown 1972, Mackay 1973). Most, however, do not provide time series data automatically. In Canada, a thaw tube was developed by Nixon (2000) for the measurement of active-layer thickness. This instrument has been used extensively in Canada and elsewhere in the Circumpolar Active Layer Monitoring (CALM) network (CALM, <http://www.udel.edu/Geography/calm/index.html>). However, for the purpose of monitoring the number of freeze-thaw cycles during a year, more precise automatic measurements of ground freezing and thawing are needed.

Automatic measurements of the depth of freezing in soils have been attempted since 1963 in Japan (e.g., Ishikawa & Suzuki 1963). Yahagi (1993, 1995) successfully invented frost meters to automatically detect the seasonal state of freezing and thawing from the surface to a depth of 72 cm, at intervals of 1 cm, and at hourly intervals, over a single winter. For multi-depth ground temperature measurements, multiple sensors are obviously necessary, and this leads to the requirement for a thick buried pipe containing many sensor cables. This, in turn, causes thermal disturbance at the site. With Yahagi's device, only five wires are necessary for the measurement. However, his devices were not widely adopted. He described the concept of the electronic components of the sensors in detail but inadequately explained the other components of the sensors and the logging systems in his publications (Yahagi 1993, 1995).

We have applied Yahagi's method to produce freeze-thaw monitoring instruments. Our instruments were designed to detect the freeze-thaw status of the ground at depths greater than 3 m, at 5 mm intervals, and to operate in the field for

more than one year using only AA dry batteries. The apparatus was designed to create minimal thermal disturbance. The instruments were tested in a cold laboratory to confirm their effectiveness. In this paper we present an example of the results of the one-directional freeze-thaw process.

Concept of Monitoring Instruments for Freeze-Thaw Depth

Because the resistivity of ice is much greater than that of water, the frozen or unfrozen state of water can be detected by the electric property of water. Using this method, we monitored the freeze-thaw depth of ground automatically. Our new device consists of two parts: a sensor and a datalogger. The sensor is composed of an electric board (Fig. 1) and a frost tube, with points of electric contact (Fig. 2). Sixty points of contact are placed at 5-mm intervals on each side of the sensor electric board. The electric contacts are inserted into the frost tube and touch the water in the frost tube. They detect freezing and thawing of the water in the frost tube by the change of resistivity between the pair of electric contacts. The sensor's electric board is 300 mm long and 15 mm wide. Multiple sensor boards can be linked to extend the measurement depth. The frozen-thawed condition of ground to more than 3 m depth can be detected by adding sensor boards. The sensor part can be installed into a thin PVC tube of 16–20 mm inner diameter. The principles employed in the sensor board were published by Yahagi (1993, 1995).

The logger's electric board is 75 mm long and 50 mm wide (Fig. 3). The data logger operates at 4.5 V with three AA dry batteries. A new lithium battery will last one year using logging intervals greater than one hour. Logging interval time is adjustable and ranges from 1 minute to 24 hours. The readings are stored in a memory card. The connection between

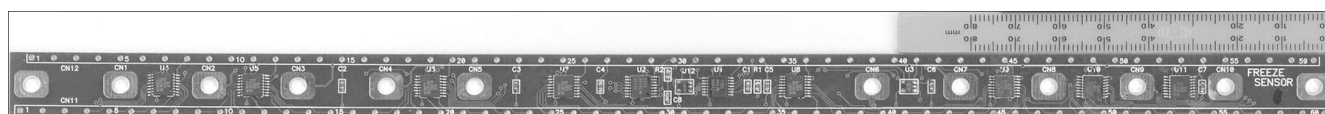


Figure 1. Electric board of freeze-thaw sensor.

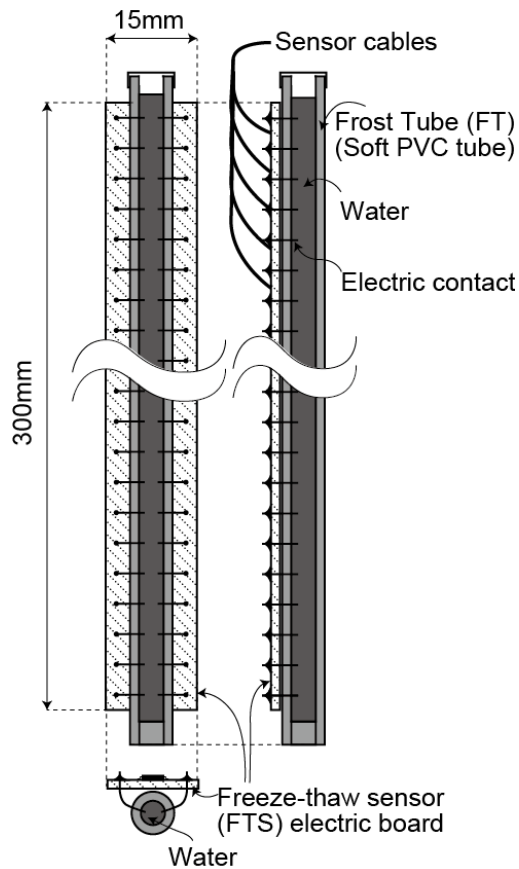


Figure 2. Schematic figure of FTS.

the logger and the sensor requires only 5 wires and does not depend on the number of sensor boards. An RS232 cable is used to connect the logger to a computer.

The sensor and logger are designed for at least one year's use. To date, testing in the field for four months during a winter season has not revealed any problems with the system. Durability tests for longer period in the field should be done in the future.

Experiment Methods

Figure 4 shows the experimental setup. A square container, 60 cm x 60 cm and 45 cm deep, was filled with medium sand up to 40 cm deep. The container was thermally insulated with extruded polystyrene foam (XPS) at the sides and at the bottom so that the freezing was one-dimensional. To avoid frost heaving, sand was used. Volumetric water content of the sand was 20%.

An FTS sensor was inserted into a 16-mm inner diameter PVC pipe, which was vertically buried in the sand. Dataloggers with thermistor sensors (TR-52S, T and D Corporation) are used for temperature measurements. The thermistors are 2 mm in diameter and fixed on the FTS board at depths of 0, 5, 10, 15, 20 cm. The sensors were calibrated at 0.0°C. Freezing and thawing of the sand was monitored over a range of depths extending from 0 cm to 29.5 cm, using intervals of 0.5 cm. Freeze-thaw conditions and temperature were automatically logged every 10 minutes.

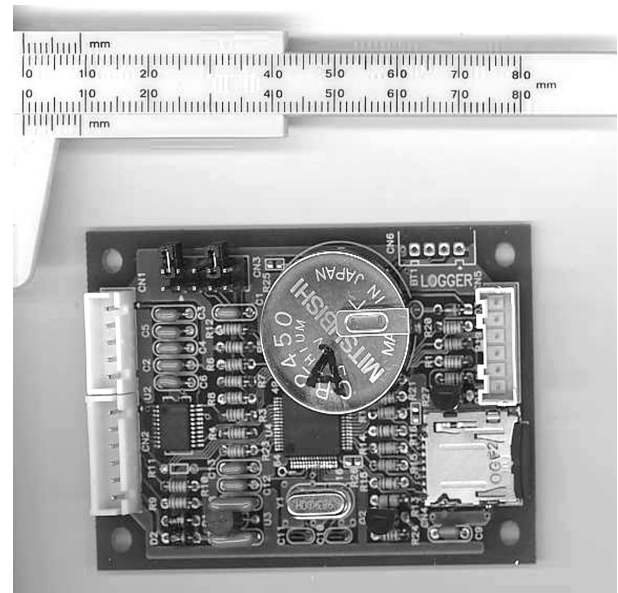


Figure 3. Electric board of data logger.

Three frost tubes (FT) were installed vertically into the sand around the FTS. Each frost tube consisted of a rigid acrylic outer pipe, 6 mm in diameter, with a removable inner tube. The inner tube was filled with water dyed with methylene blue to detect the frozen part. Freezing and thawing depth were manually measured at an appropriate interval. In a previous experiment, we confirmed that the depth of the frost table measured with the frost tube was coincident with a probed depth to within ± 1 cm. Probing and frost tube methods are widely used by the CALM program for the measurement of active-layer thickness.

Results and Discussion

The experiment was started with the soil at a temperature of +20°C (Fig. 5). After 85 hours of cooling at an air temperature of -20°C, thawing at +20°C air temperature was initiated. The freeze-thaw sensor operated for logging at air temperatures as low as -20°C. Maximum freezing depths were indicated as 25 cm and 23 cm by the FTS and FT methods, respectively.

During downward freezing, the differences in the readings between FTS, FT1, and FT2 were approximately 2 cm, except for the reading of FT1 at 94 hours. As the freezing front penetrated deeper than 15 cm, the zero degree isotherm interpolated from the temperature data (Fig. 5) showed deeper freezing than those obtained by the other two methods. The 0.0°C isotherm error tends to increase.

During the thawing stage, the readings of FTS preceded those of FT1 and FT2. During the thawing period, despite the constant air temperature after 89 hours, the 0.0°C isotherm did not decline constantly and stayed flat at the depths of each thermistor. During the time when a zero-curtain effect was apparent at certain sensor depths, the sensor logs 0.0°C. Therefore, the incorporated zero degree isotherm is drawn as remaining at that sensor's depth during the period of the zero-curtain effect. As the zero-curtain has restricted extent in time

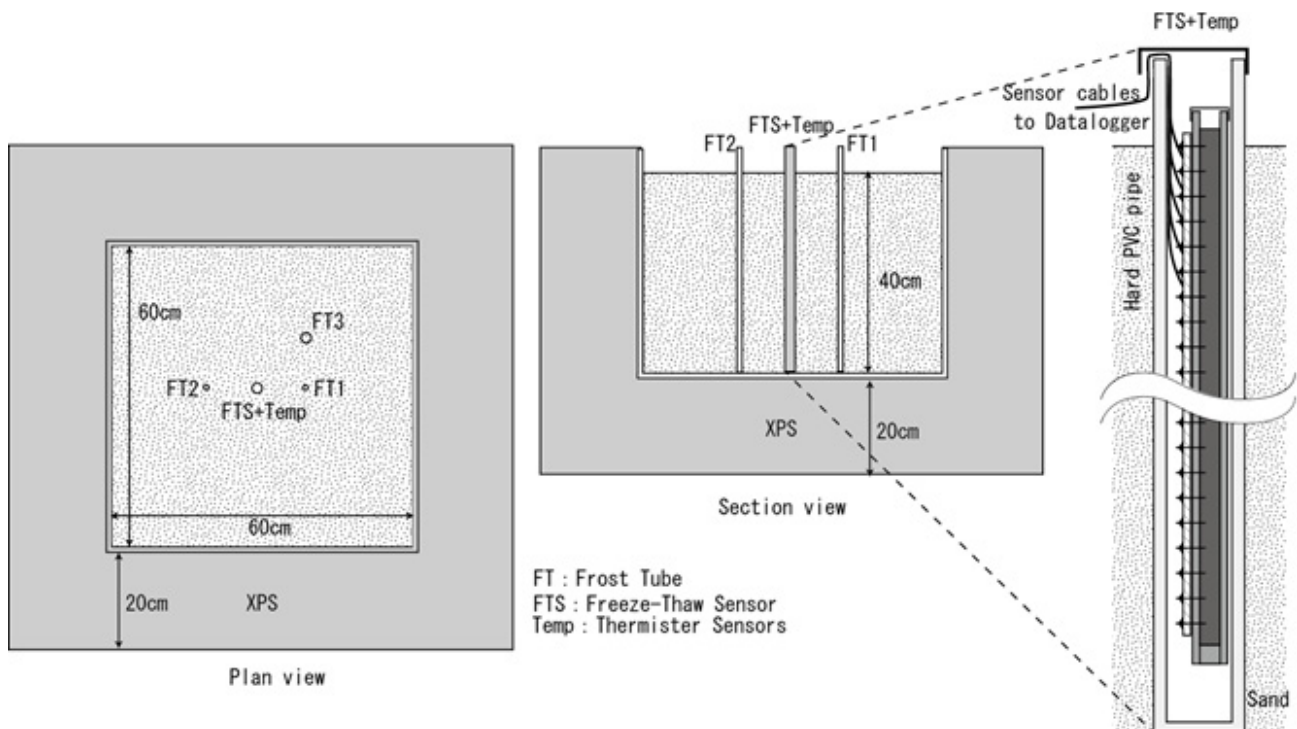


Figure 4. Settings of the experiments.

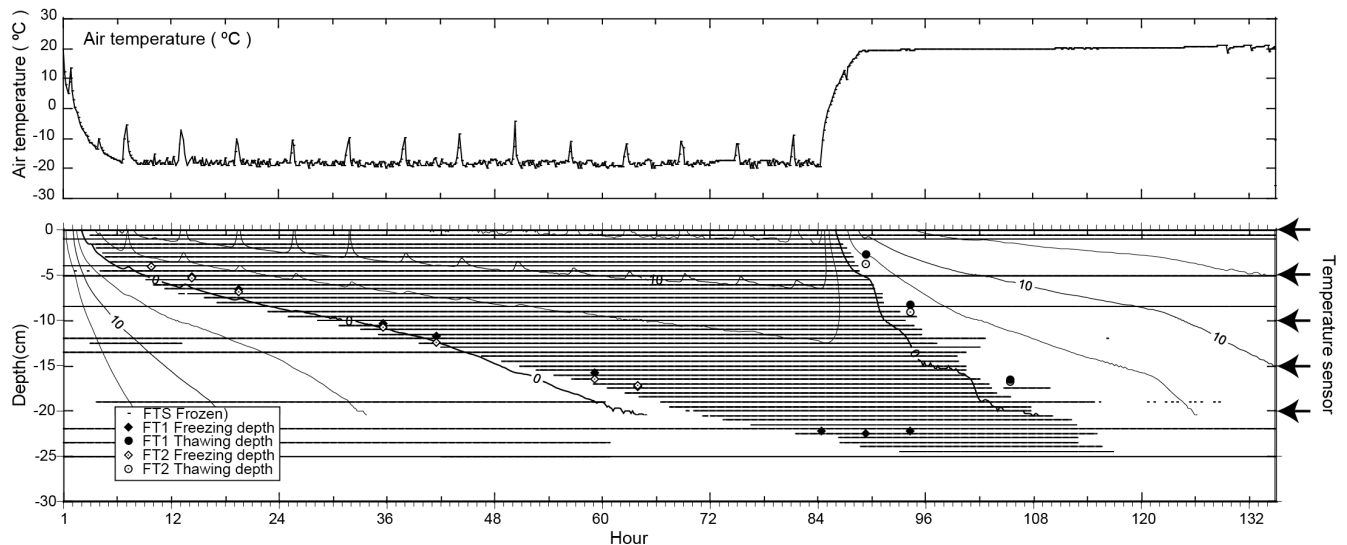


Figure 5. Upper graph shows the air temperature of the cold chamber. Lower graph shows freezing and thawing depth, measured with the freeze-thaw sensor (small black dot represents a frozen condition), with the frost tube (FT)(open and closed circles show thawing depth, open and closed diamonds show freezing depth). The isotherms (°C) were interpolated using kriging on the temperature data measured by the thermistors. The depths of thermistors are shown on the right axis with arrows.

and space, thawing could take place somewhere between the initiation and termination of the zero-curtain effect.

The small difference in readings between FTS and FT might be caused by the difference in the diameter of the FTS and FT tubes.

As noted above, the zero degree isotherms were interpolated with ground temperature data, and are affected by the sensor depth. To obtain the freeze-thaw condition with ground temperature data, it is best to use as many sensors as possible. However, the number of sensors that can be practically used is

limited. Furthermore, sensor cables would disturb the ground thermal and structural conditions. FTS was able to detect the freeze-thaw depth with sufficient accuracy (as compared to results from temperature measurements) using 5-cm intervals. The device needs a drill hole of 16 mm inner diameter from the ground surface to more than 3 m deep at every 5-mm interval. In terms of achieving minimal ground disturbance, FTS is more suitable for multi-depth freeze-thaw measurements and detection of the active layer depth than is soil temperature measurement.

The behavior of FTS at several depths (e.g., 5, 8.5 cm) is cause for concern. It appears that there may have been a problem with the connection between the wire of the electric contact and water inside the frost tube. This should be improved by changing the wire length touching the water. Dew condensation on the electric sensor board could result in erroneous readings. Preventive measures against condensation will be necessary before the device goes into production.

Conclusions

The effectiveness of the freeze-thaw sensors described in this paper has been confirmed by laboratory experiments. To detect ground freeze-thaw conditions, compared with results from thermometers and frost tubes, this device has acceptable accuracy; one advantage is that it can be installed with less ground disturbance. The sensor and logger are designed for at least one year of field use. Durability tests for longer periods in the field should be done in the future.

Acknowledgments

We are grateful to Mr. Y. Naito, Umezawa Musen Denki Corporation, for producing the electric boards for sensors and dataloggers, and to Dr. H. Yahagi, Emeritus Professor of Hokkaido University of Education, for his useful advice. We also thank the referees for providing constructive comments and help in improving the contents of this paper.

References

- Ishikawa, M. & Suzuki T. 1963. A gypsum block recorder for measuring freezing depth of soils. Annual report of the Hokkaido Branch Forestry Experiment Station 1963: 306-313 (in Japanese with English summary).
- Mackay, J.R. 1972. A frost tube for the determination of freezing in the active layer above permafrost. *Canadian Geotechnical Journal* 10: 392-396.
- Nixon F.M. 2000. Permafrost monitoring. In *The physical environment of the Mackenzie Valley, Northwest Territories: a base line for the assessment of environmental change*. Dyke, L.D., Brooks, G.R.. Geological Survey of Canada, Bulletin 547, 119-126.
- Rickard, W. & Brown, J. 1972. The performance of a frost-tube for the determination of soil freezing and thawing depths. *Soil Science* 113: 149-154.
- Yahagi, H. 1993. On the new "ECHO" type frost-meter for detecting active layers. 92 Cold Region Technology Conference Proceedings, No.9: 710-715 (in Japanese).
- Yahagi, H. 1995. *Kushiro and frozen ground*. Kushiro, Kushiro City, 366 pp. (in Japanese).

Evaluation of the ERA-Interim Reanalysis for Modeling Permafrost on the North Slope of Alaska

R.I. Mugford, P. Christoffersen, J.A. Dowdeswell
Scott Polar Research Institute, University of Cambridge, Cambridge, UK

A. Consonni
Eni S.p.A E&P Division, San Donato Milanese, Italy

Abstract

The suitability of using ERA-Interim reanalysis data to force a fully coupled thermal and hydrological soil model, GEOTop, is assessed. ERA-Interim data are compared to in situ observations of atmospheric parameters, and the ability to capture inter-annual and seasonal variability is evaluated. GEOTop 1.145 is used to model the thermal state of the subsurface in the Imnavait basin, Alaska, forced by ERA-Interim reanalysis data. Model results of soil temperature profiles are validated using borehole observations. The use of atmospheric reanalysis products to force models such as GEOTop enables simulations to be performed in regions where in situ meteorological measurements are sparse.

Keywords: Alaska; ERA-Interim reanalysis; GEOTop Model; numerical modeling.

Introduction

This study uses ERA-Interim data (Dee et al. 2011) to force GEOTop, which is a fully coupled thermal and hydrological model of subsurface permafrost soil. We analyze how accurately ERA-Interim represents atmospheric forcing by comparing with observations from meteorological stations. The main difference between ERA-Interim and the previous reanalysis, ERA-40, is the implementation of a 12-hourly 4D-Var data assimilation system. The models used to produce ERA-40 and ERA-Interim reanalyses, including details of the observations assimilated, are

described by Uppala et al. (2005) and Dee et al. (2011). Previous studies by Betts et al. (2003, 2009) assessed the bias of ERA-40 and ERA-Interim reanalyses compared to meteorological observations in the Mackenzie River basin. They found that ERA-Interim performs better than ERA-40 for shortwave radiation, temperature, and precipitation. In ERA-40, a spin-up in the precipitation, which is forecast on a daily basis, was detected and this affected the diurnal cycle; however, this has been improved in ERA-Interim. This study focuses on the Kuparuk basin, as part of a wider project funded by Eni S.p.A., which aims to understand permafrost changes in Alaska.

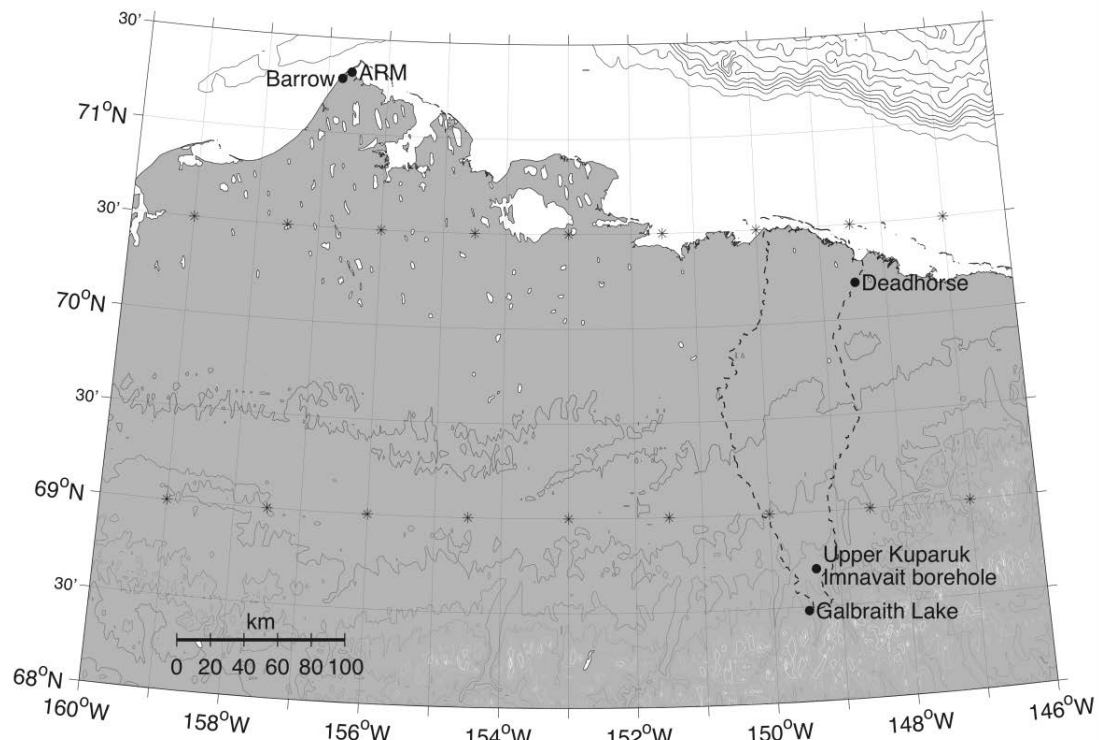


Figure 1. Map of the North Slope of Alaska showing meteorological and radiation stations used in this study, as well as the Imnavait borehole site (black dots), and the location of ERA-Interim data points shown by *.

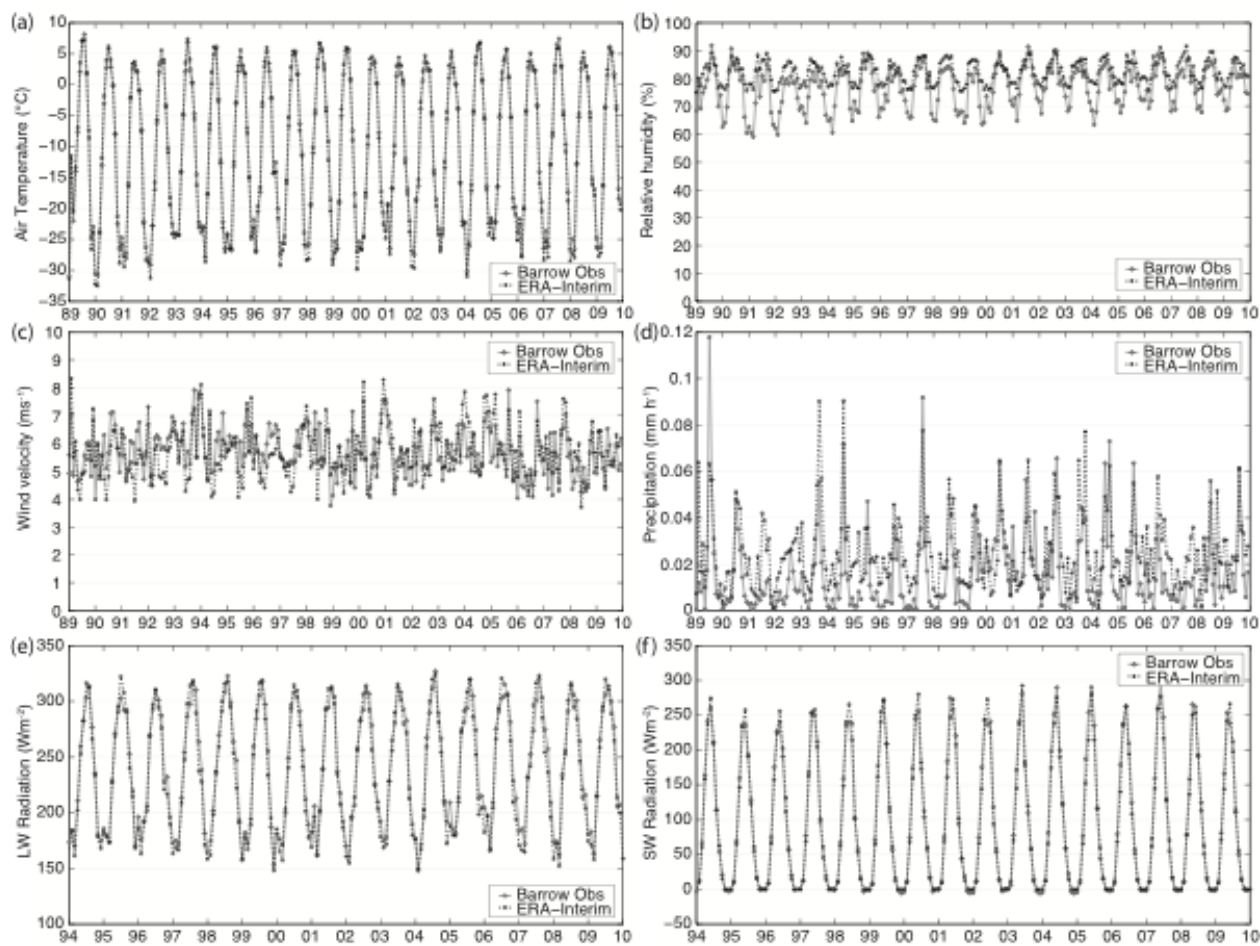


Figure 2. Time series of monthly means (a) temperature, (b) humidity, (c) wind velocity, (d) precipitation, (e) longwave radiation, and (f) shortwave radiation. (a)-(d) are from NCDC station at Barrow, and (e)-(f) are from ARM station at Barrow.

ERA-Interim Validation

ECMWF ERA-Interim data used in this study have been obtained from the ECMWF data server. The ERA-Interim reanalysis data used is on a 1.5° grid, as shown in Figure 1.

Observations

The temperature, humidity, wind speed, and precipitation measurements used were from the global surface summary of day product produced by the National Climatic Data Center (NCDC) (<ftp://ftp.ncdc.noaa.gov/pub/data/g sod>). The input data used to create this product are the Integrated Surface Data (ISD). Further meteorological data were used from the Water and Environmental Research Center (WERC) at the University of Alaska Fairbanks, and the North Slope Hydrology Research Projects (Kane and Hinzman 2011).

Measurements of shortwave and longwave radiation were collected by the NOAA/ESRL/GMD radiometers (NOAARAD) at the Atmospheric Radiation Measurement (ARM) Climate Research Facility site at Barrow (<http://www.arm.gov/>). These observations are not directly assimilated by ERA-Interim, although rawinsonde data are collected here, which will improve the calculation of surface radiation in the reanalysis.

Time series Comparison

Time series from 1989 to 2009 for ERA-Interim and concurrent observations are shown in Figure 2. The ERA-Interim monthly mean air temperature shows very good agreement with observations at Barrow, capturing interannual variability and absolute monthly temperatures well.

Humidity is not as well represented, with smaller seasonal variability and in general overestimating the winter values in ERA-Interim compared to observations.

Wind speed is a more chaotic picture, and ERA-Interim captures some of the variability well but is less accurate with the absolute values.

Precipitation gauges are plagued by biases due to wind-induced undercatch, wetting losses, evaporation losses, and trace levels of precipitation, which introduce significant uncertainty to measurements (Yang et al. 2005). For example, Bowling and Lettenmaier (2010) corrected WERC precipitation measurements for gauge undercatch in the Kuparuk River basin, which resulted in a 70% increase in cumulative precipitation over the simulation period. Therefore, it is not surprising that ERA-Interim does not fit the data precisely; however, it does capture the seasonal cycle reasonably well, with a peak in summer. Although the absolute values are higher in ERA-Interim than the measurements, this difference can be attrib-

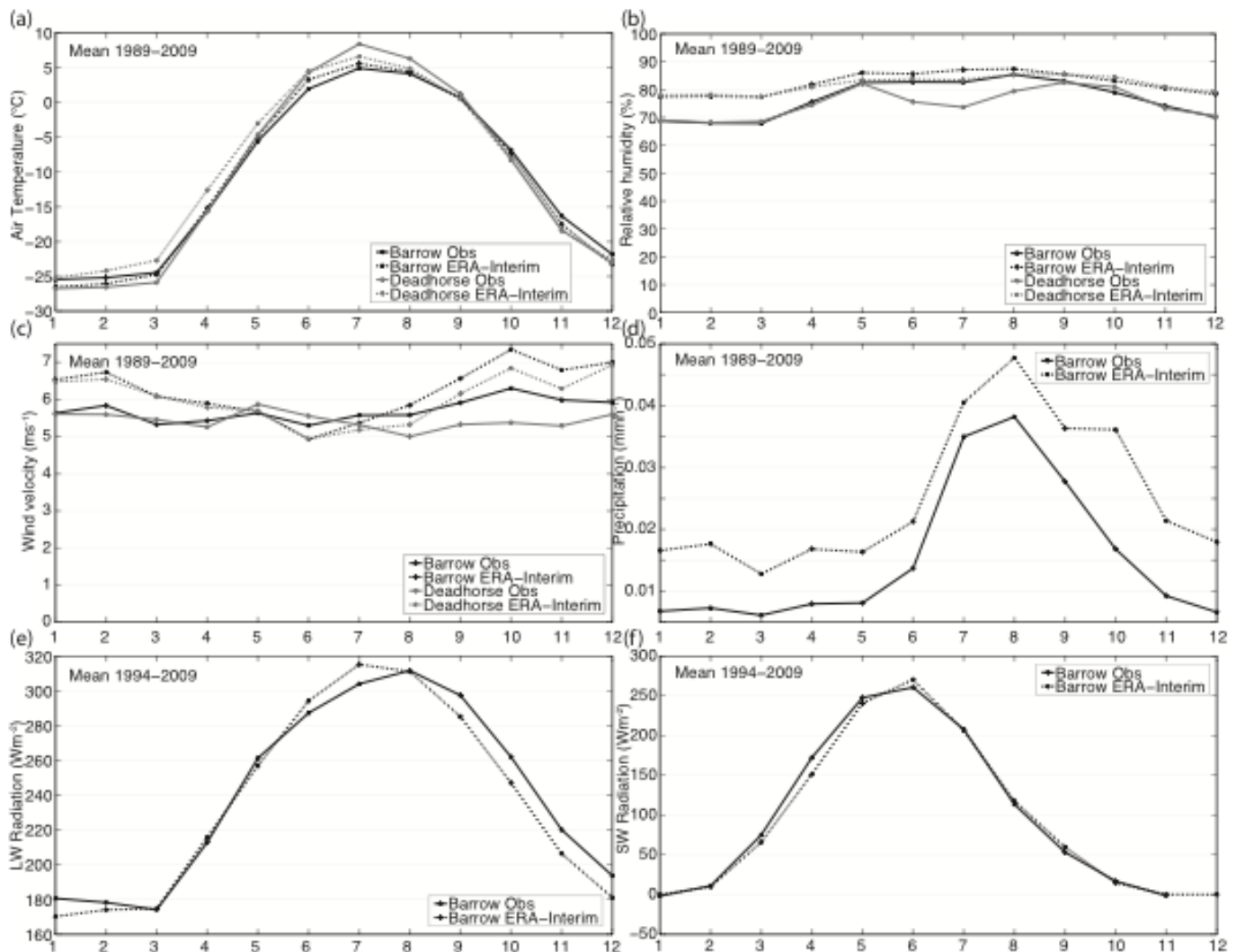


Figure 3. Monthly means for the period of observations (a) temperature, (b) humidity, (c) wind velocity, (d) precipitation, (e) longwave radiation, (f) shortwave radiation. (a)–(d) mean 1989–2009, NCDC stations at Barrow and Deadhorse; (e)–(f) mean 1994–2009, ARM station at Barrow.

uted to an underestimation bias of the measurements for the reasons discussed above.

Longwave and shortwave radiation at Barrow show very good correlation, although this could be due to assimilation of rawinsonde data at this location.

Seasonal cycle

Monthly means calculated over the period of observations for both observations and ERA-Interim at Barrow and Deadhorse are shown in Figure 3. There is a warm bias from January to May at Deadhorse, followed by a cold bias from July to August, and good agreement toward the end of the year. Barrow has a good agreement for air temperature, with a small warm bias in summer and cold bias in January and February.

Relative humidity shows an almost constant bias through the year at Barrow, while at Deadhorse the bias is smallest in spring and autumn and largest in winter and summer. ERA-Interim represents wind velocity and relative humidity best in summer, with a larger winter bias.

The observations of precipitation at Deadhorse had too many

missing data points to make a comparison. At Barrow, there is an almost constant difference between ERA-Interim and measurements. The longwave and shortwave radiation fluxes, as discussed previously, are consistent with observations at Barrow, and this is the case throughout the seasonal cycle.

Cumulative distribution functions

The cumulative distribution functions of the seven atmospheric parameters that force the model are shown for both ERA-Interim reanalysis data and observations from the Upper Kuparuk and Barrow in Figure 4. The Upper Kuparuk meteorological station is at an elevation of 774 m and is in close proximity to the Innavait Creek borehole (location shown in Fig. 1). Measurements were collected at the Upper Kuparuk meteorological station by the WERC North Slope Hydrology Research project (Kane & Hinzman 2011). The ERA-Interim reanalysis compares well to these observations with negligible bias for temperature and longwave and shortwave radiation. There is a bias in wind velocity, in particular at higher wind speeds. There is a more significant bias in humidity.

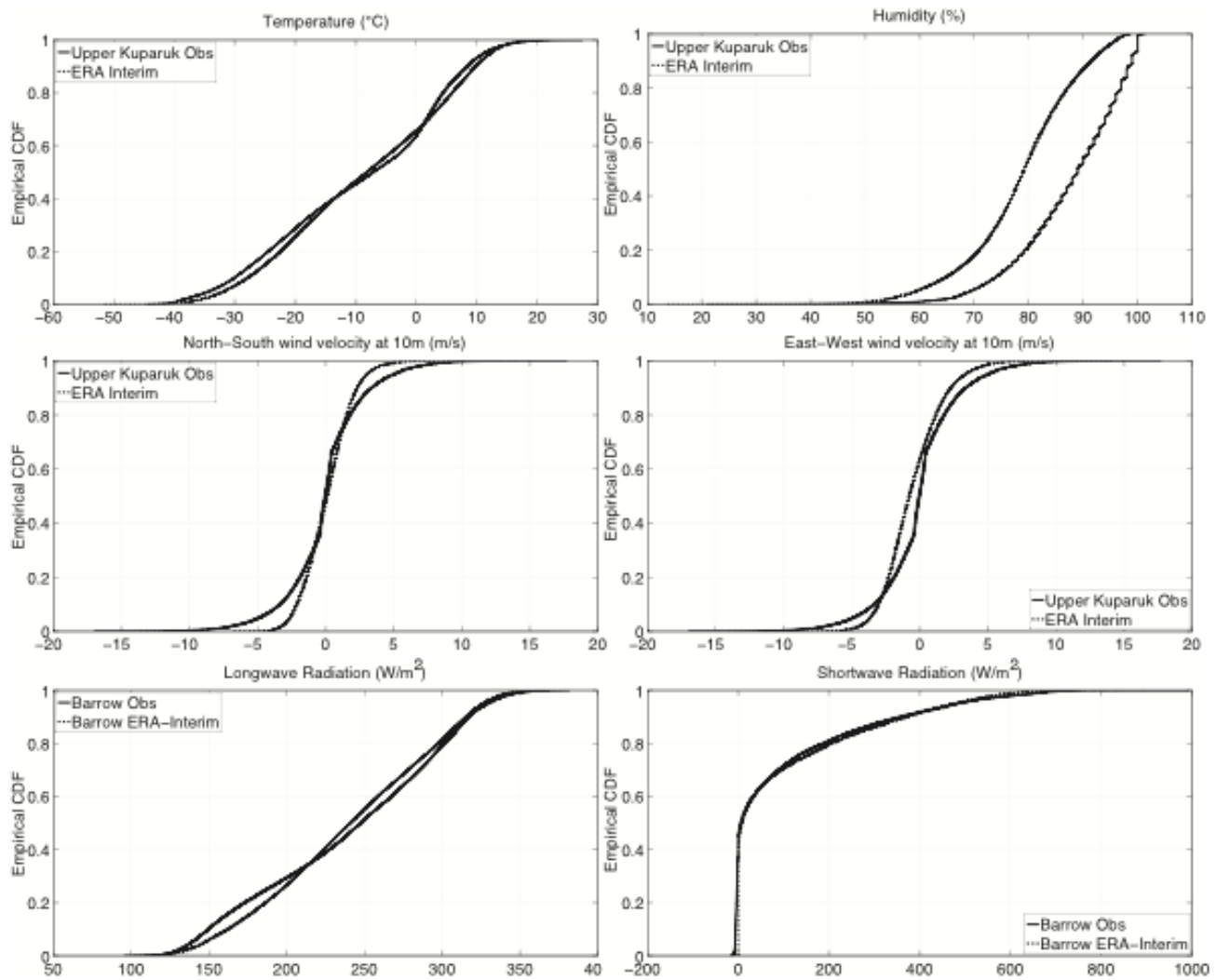


Figure 4. Empirical cumulative distribution function (a) temperature, (b) humidity, (c) north-south wind velocity, (d) east-west wind velocity, (e) longwave radiation, and (f) shortwave radiation. Observations (a)-(d) from a meteorological station located in the Imnavait Basin (Kane & Hinzman 2011), observations (e)-(f) from ARM station in Barrow.

Permafrost Modeling Using ERA-Interim

GEOtop model

GEOtop is a distributed hydrological model that has been developed over the past ten years, originally at the Department of Civil and Environmental Engineering of the University of Trento (Bertoldi, 2004, Bertoldi et al. 2006, Rigon et al. 2006, Zanotti et al. 2004). The version used here is GEOtop 1.145, which includes a three-dimensional representation of water fluxes in the soil and a one-dimensional description of the energy exchanges at the soil-atmosphere interface. The thermal and hydrological characteristics of the soil are simulated by solving equations describing the coupled mass and energy system. In addition, it includes a detailed representation of the topographic controls on solar radiation. GEOtop has been developed in the past few years to improve the energy balance description and the snow cover module, which now solves the snow energy and water balance in a fully coupled way in a multilayer representation of the snowpack (Endrizzi

2007). It solves the heat equation using the Crank-Nicolson method, and the apparent heat capacity parameterization method for simulating latent heat has been implemented. The method for solving the energy equation in freezing soil uses a splitting method to couple the energy equation with the Richards equation and, therefore, approximates water flow in unsaturated soils near the liquid-solid phase transition (Dall'Amico 2011).

Application to Imnavait Creek

Imnavait Creek was chosen as a case study for assessing the validity of using ERA-Interim to force the GEOtop model. A borehole was instrumented from 2006 to 2010 in Imnavait Creek by Romanovsky et al. (NSF projects ARC-0520578 and ARC-0632400), and these observations are compared with the modeled temperature.

Two one-dimensional simulations of the Imnavait borehole are presented here with the hydrology routine switched off and on to investigate the impact that water advection has on the soil

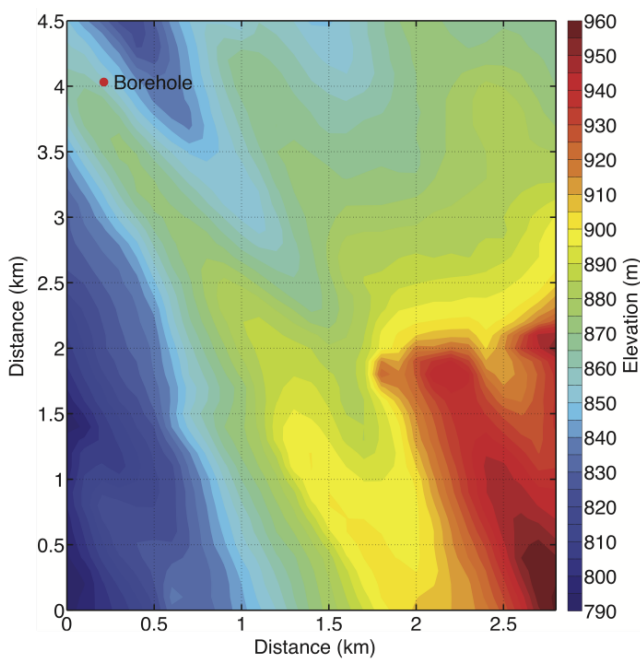


Figure 5. The location of the 1D simulation on the USGS Alaska North Slope 100-m-resolution digital elevation model (ARCSS301) of Imnavait Creek.

Table 1. Thawed soil thermal parameters calibrated using Imnavait Creek borehole data and 100-year spin up.

| Depth of soil layer (cm) | 0-25 | 25-80 | 80-120 | 120-base |
|--|--------|--------|-----------------|----------|
| Thermal Conductivity ($\text{Wm}^{-1}\text{K}^{-1}$) | 0.08 | 0.1 | 0.5 | 1 |
| Heat Capacity ($\text{Jkg}^{-1}\text{K}^{-1}$) | 10^5 | 10^5 | 5×10^5 | 10^6 |

temperature. In the run with hydrology switched off, the water content is assumed to be at saturation, and with hydrology switched on, water can advect through the soil layers.

The forcing data was bilinearly interpolated from the ERA-Interim grid to the location of the Imnavait borehole. Three-hourly forcing was derived from the reanalysis, and accumulation terms were calculated from forecast steps. The simulation time step was one hour. The location of the 1D simulation on the USGS Alaska North Slope 100-m-resolution digital elevation model (ARCSS301) is shown in Figure 5.

The soil properties were determined by an initial calibration run, which was performed with forcing from 2006–2009 repeatedly for a period of 50 to 100 years. This spin up of the model allows the soil temperature to reach equilibrium for the applied forcing. Various configurations of soil layer thickness and soil properties were tested. Once the run had stabilized, the modeled subsurface temperature profile was compared with the borehole observations. The soil properties used in the run that achieved the closest fit to the observations were then applied for the subsequent run over the ERA-Interim period of 1989–2009. The soil properties are shown in Table 1 and represent a surface organic layer 25 cm thick underlain by mineral soil with a mixed layer between. The total model thickness was 20

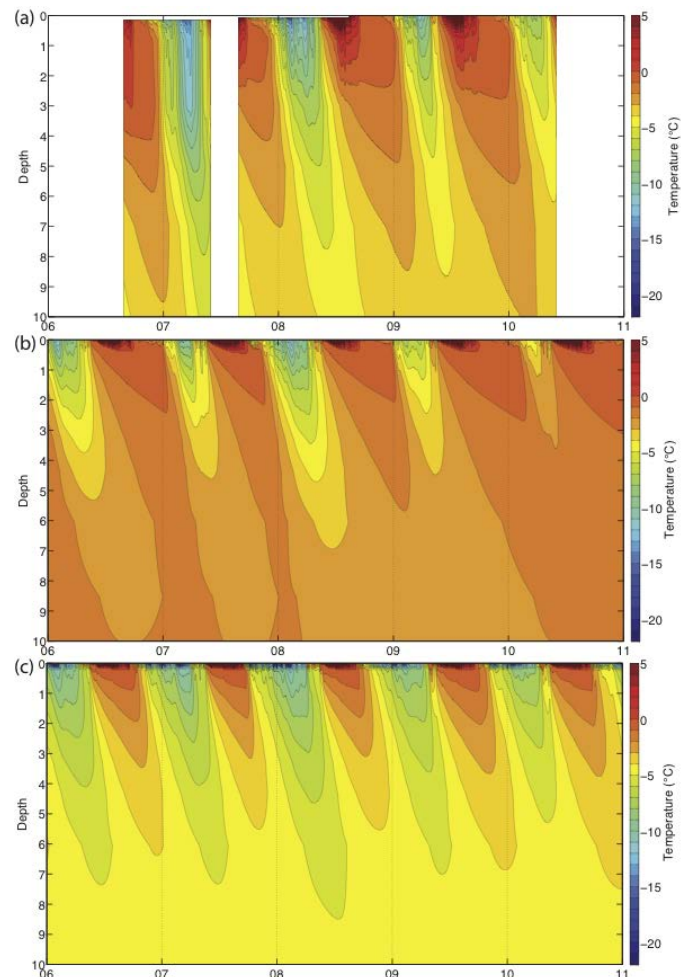


Figure 6. Depth vs. time plots from 2006–2009 (a) Observations collected by Romanovsky et al. (NSF projects ARC-0520578 and ARC-0632400) in the Imnavait drainage basin 68.639656°N 149.352341°W (b) Point simulation- thermal only (c) Point simulation- thermal and hydrological.

m, consisting of 31 layers varying in thickness from 10 mm at the surface to a deepest layer of 5 m.

Using these soil thermal properties, the model was then allowed to spin up using a 4-year cycled forcing from 1989–1992, before the simulation from 1989–2010 was performed. It took about 50 years before the temperature of the 20-meter-thick soil stabilized.

Model results

GEOtop model results from 1D simulations with the hydrology routine turned off and on, and observations of soil temperature plotted as depth versus time, are shown in Figure 6.

The run with hydrology turned on produces results much closer to observations than the run neglecting hydrology; including water advection results in cooling of the deeper soil layers. The interannual pattern of maximum temperature depth in summer and minimum temperature depth in winter is reproduced reasonably well compared to observations. However, the cold temperatures penetrating to deeper depths than the other years in spring 2007 are not fully replicated by the model runs.

The deep soil temperatures in the simulation with hydrology

turned on and observations agree well. The run with hydrology turned on also reproduces the observed relatively warmer maximum summer temperatures in summer 2006, followed by a cooler maximum summer temperature in 2007 and increasingly warmer maximum summer temperatures from 2008 to 2010.

Neither model simulation reproduces the depth of penetration of the summer temperature maximum and the winter temperature minimum seen in the observations. This could be because of errors in the representation of soil parameters. The soil parameterizations in GEOtop have been developed for mineral soils and at present there is no alternative treatment of organic soils. Organic soils have different soil-water characteristic curves, with much less suction than mineral soils. This results in the surface soil layers becoming dryer in the model than they should (not shown). The thermal properties of organic soils are strongly dependent on water content, with thermal conductivity and heat capacity increasing with water content. This would mean that if the surface layers had a higher water content, there would be increased heat transported through the organic layer, which could help to improve the penetration depth of the maximum temperature in summer and the minimum temperature in winter.

Summary

This study has demonstrated that ERA-Interim reanalysis data closely resemble atmospheric observations on the North Slope of Alaska. Systematic biases in temperature, precipitation, and radiation have been assessed by comparing monthly mean time series and climatologies with observations from meteorological stations at Deadhorse, Barrow, and in the Kuparuk basin. Temperature and longwave and shortwave radiation all demonstrate good correlation between ERA-Interim reanalysis and observations. Humidity, wind velocity, and precipitation do not show such close correlations. In the case of wind velocity, this is probably because ERA-Interim does not capture extreme wind gusts. With precipitation it is difficult to determine whether the discrepancy is due to measurement inaccuracy or a shortcoming of the ERA-Interim reanalysis product. Nonetheless, there is an overall good agreement between the reanalysis and independent observations.

Forced by ERA-Interim with a spin up period to allow the soil temperature to stabilize, the GEOtop model performed well in comparison to borehole measurements, especially at depth. However, differences were highlighted in the maximum penetration depth of the summer maximum temperature and the winter minimum temperature. In conclusion, ERA-Interim has proved to be a useful dataset for forcing the current generation of thermal and hydrological numerical models. Future work will involve running 3D simulations of GEOtop over the North Slope, with ERA-Interim providing a spatially varying atmospheric forcing field.

Acknowledgments

We thank Eni S.p.A for funding this study. We extend our gratitude to the members of the GEOtop development team

and in particular Stefano Endrizzi and Stephan Gruber for their help and support. ECMWF ERA-Interim data used in this study were obtained from the ECMWF data server.

References

- Bertoldi, G. 2004. The water and energy balance at basin scale: a distributed modeling approach. Ph.D. thesis, University of Trento, Italy.
- Bertoldi, G., Rigon, R., & Over, T.M. 2006. Impact of watershed geomorphic characteristics on the energy and water budgets. *Journal of Hydrometeorology* 7:389–403.
- Betts, A., Ball, J., & Viterbo, P. 2003. Evaluation of the ERA-40 surface water budget and surface temperature for the Mackenzie River basin. *Journal of Hydrometeorology* 4 (6): 1194–1211.
- Betts, A.K., Koehler, M., & Zhang, Y. 2009. Comparison of river basin hydrometeorology in ERA-Interim and ERA-40 reanalyses with observations. *Journal of Geophysical Research* 114: D02101, doi:10.1029/2008JD010761.
- Bowling, L.C. & Lettenmaier, D.P. 2010. Modeling the effects of lakes and wetlands on the water balance of Arctic environments. *Journal of Hydrometeorology* 11 (2): 276–295, doi: 10.1175/2009JHM1084.1.
- Dall'Amico, M., Endrizzi, S., Gruber, S., & Rigon, R. 2011. A robust and energy-conserving model of freezing variably saturated soil. *The Cryosphere* 5 (2): 469–484, doi:10.5194/tc-5-469-2011.
- Dee, D.P., Uppala, S.M., Simmons, A.J., Berrisford, P., Poli, P., and 31 others 2011. The ERA-Interim reanalysis: configuration and performance of the data assimilation system. *Quarterly Journal of the Royal Meteorological Society* 137 (656): 553–597, doi: 10.1002/qj.828.
- Endrizzi, S. 2007. Snow cover modelling at a local and distributed scale over complex terrain. Ph.D. thesis, University of Trento, Italy.
- Kane, D.L. & Hinzman, L.D. 2011. Climate data from the North Slope Hydrology Research project. University of Alaska Fairbanks, Water and Environmental Research Center, [http://ine.uaf.edu/werc/projects/NorthSlope/\[04/2011\]](http://ine.uaf.edu/werc/projects/NorthSlope/[04/2011]).
- Rigon, R., Bertoldi, G., & Over, T.M. 2006. GEOtop: a distributed hydrological model with coupled water and energy budgets. *Journal of Hydrometeorology* 7: 371–388.
- Uppala, S., Kallberg, P., Simmons, A., Andrae, U., Bechtold, V., and 41 others 2005. The ERA-40 reanalysis. *Quarterly Journal of the Royal Meteorological Society* 131 (612): 2961–3012, doi:10.1256/qj.04.176.
- Yang, D., Kane, D., Zhang, Z., Legates, D., & Goodison, B. 2005. Bias corrections of long-term (1973–2004) daily precipitation data over the northern regions. *Geophysical Research Letters* 32 (19), doi:10.1029/2005GL024057.
- Zanotti, F., Endrizzi, S., Bertoldi, G., & Rigon, R. 2004. The GEOtop snow module. *Hydrological Processes* 18: 3667–3679, doi:10.1002/hyp.5794.

Multi-Satellite-Derived Changes in Energy and Mass of Russian Permafrost Regions

Reginald R. Muskett, Vladimir E. Romanovsky
Geophysical Institute, University of Alaska Fairbanks, USA

Abstract

We report on energy and mass changes by satellite-based geodetic measurements from August 2002 through December 2008 for the region from 75° to 165°E and 50° to 80°N. Our focus is on the geopotential field changes of gravity, land-surface temperature, and CO₂ sources relative to the terrestrial reference frame. Our analysis of the gradient fields and regionalized time series indicates coupled water equivalent mass, land-surface temperature, and carbon fluxes in Mays and Septembers. The inflection point in the seasonal energy and mass cycle indicates ecosystem respiration. We hypothesize that this response is driven in part by permafrost degradation and thawing, talik formation, and microbial activity.

Keywords: permafrost; energy; mass; GRACE; MODIS; AIRS.

Introduction

Land- and ocean-surfaces form a fundamental physical boundary of the Earth (Salzman 1983). Processes acting on decadal and interannual scales include energy and water cycles, soil-atmosphere micrometeorology, evaporation, evapotranspiration, cloudiness, aerosol chemistry, albedo, and ecosystem vitality and phenology (Flanner et al. 2011, Zhang et al. 2004). In the terrestrial northern high latitudes, land-surface temperature changes form the boundary condition for warming and degradation of permafrost, development and expansion of taliks, and the mobility and exchange of groundwater that are driven by climate change (Flanner et al. 2011, Romanovsky et al. 2010).

Our region of interest is the northern high latitudes from 50° to 80°N and 75° to 165°E (Figure 1). Within this region, the Lena River and neighboring watersheds provide a physical reference frame to evaluate energy and mass transfers. The Lena, the Yenisei, and the Ob' are the three great Siberian rivers. The Lena is the easternmost of them. The continuous permafrost zone mostly underlies the Lena and Yenisei River watersheds. The discontinuous zone underlies their upper-southern parts at the latitude of Lake Baikal (Lena). The central and northern parts of the region are well noted for permafrost wetlands and thaw-lakes in central Yakutia. It is one of the regions of the thick subsurface ice- and carbon-rich deposits known as Yedoma. The Taymyr Peninsula and Kolyma River areas are noteworthy thaw-lake regions as well.

Our recent investigations of the northern hemisphere permafrost watersheds have revealed diversity in the character of water mass changes (Muskett & Romanovsky 2009, 2011a, b). The Siberian watersheds show increasing runoff and groundwater storage while regionally averaged winter snow-load shows no trend. In western North America, the Mackenzie River and Yukon River watersheds, mostly underlain by discontinuous permafrost, show no trend in runoff yet show trends of decreasing groundwater storage and increasing regionally averaged winter snow-load. These changes in water loads continued through the period 2002 through 2008.

Using measurements from a multi-satellite sensor suite, we will frame our investigation toward surface energy and

mass transfers. This will aid investigations of energy balance on Earth's land-surfaces and physical processes which draw from the balance and feedbacks, both negative and positive, with drivers of solar energy input and its feedbacks with atmosphere, vegetation, and anthropogenic modification.

The thermal state of the land-surface is the boundary condition for changes of active layer, permafrost, and talik that are coupled with climate change (Romanovsky et al. 2010). Water is a fundamental substance on Earth, which through its heat capacity can re-distribute energy through the atmosphere and ocean, on the land-surface, and within the subsurface (Salzman 1983). Recent studies have revealed that the carbon sequestered in Earth's permafrost regions exceeds by twice the troposphere load (Schuur et al. 2009). Thermokarst and other permafrost degradation processes associated with thaw-lakes in the permafrost zones have been identified as emitters of methane (Walter et al. 2007). Carbon storage is vulnerable to changes in ecosystem, hydrogeology, and land-surface characteristics from climate change (Walter et al. 2007, Grosse et al. 2011). Our investigation seeks to elucidate the coupling of land-surface temperature with near-surface water and atmospheric CO₂ mass changes relative to permafrost and terrain.

Data

Our source data for change of surface energy come from 1) the Moderate Resolution Imaging Spectroradiometer (MODIS) on NASA-Terra satellite daily land-surface temperature, 2) the Gravity Recovery and Climate Experiment (GRACE) mission for water equivalent mass, and 3) the Atmospheric InfraRed Sounder (AIRS) (includes the Atmospheric Microwave Sounding Unit) onboard NASA-Aqua for tropospheric CO₂. Our source of topography data, including river and lake elevation, is the ESA funded Altimetry Corrected Elevation version 2 Digital Elevation Model (DEM) (Berry et al. 2008).

MODIS

MODIS land-surface temperature, product MOD11A1, Level-3 version-5 grids are global at 1-km posting from March 2000 at twice-daily intervals (Wan 2008, Coll et al. 2009).

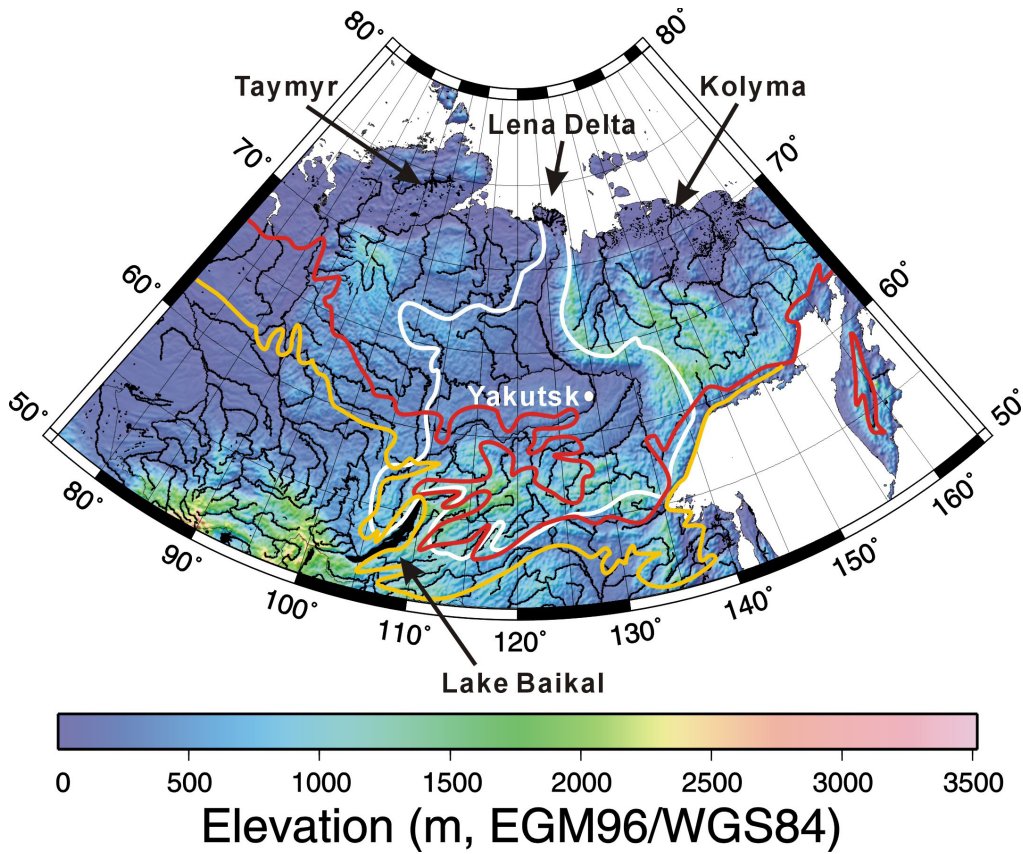


Figure 1. Investigation region centered on the Lena River watershed (white line extent). Digital elevation data from the ESA funded ACE2 DEM (Muskett and Romanovsky 2011). Red line represents the extent of the continuous zone and the yellow line represents the extent of the combined discontinuous and sporadic zone. Permafrost and thaw-lake regions of Kolyma, Taymyr, and Yakutsk are identified.

We re-project the grid to be consistent with the international terrestrial reference frame of the GRACE data. Land-surface temperature in Kelvin is derived by algorithm using clear-sky day/night thermal emission and emissivity in the 10.78 to 11.28 μm and 11.77 to 12.27 μm bands. Input data derive from the L1B Level 2 swath product using cloud-cover detection routines with corrections for atmosphere column water vapor and boundary level temperatures and off-zenith-angle pointing (Wang et al. 2008). We use only those temperatures with the highest quality flag. The accuracy of the MODIS land-surface temperatures is at 1-kelvin (Wang et al. 2008). The trend of MODIS (Aqua and Terra sensors) land-surface temperature shows high correlations with near-ground air temperature and sub-surface (3 to 5 cm) soil temperature measurements (Hachem et al. 2011).

GRACE

The international Gravity Recovery and Climate Experiment provides nominal-monthly near-surface water equivalent mass changes (Wahr et al. 1998, Tapley et al. 2004). The tandem satellites measure variations in gravity/mass indirectly through changes of the inter-satellite range and range rate from an initial orbit altitude of 485 kilometers, in a controlled free-fall (down to about 200 km) non-repeating ground track mode. The mass changes are coupled to high-accuracy onboard GPS and

star-tracking instruments to reference them to the International Terrestrial Reference Frame 2005.

Data for water equivalent mass change comes from Release-04 (R4) Level-3 products provided by the GRACE Science Team centers. Grids are produced at 1-arc-degree global coverage complete to degree and order 40. The GRACE solution to the gravity potential formulated as an equivalent water mass change (length scale) is given by

$$\Delta h(\phi, \lambda, t) = \rho \sum_{l=0}^{40} \sum_{m=0}^l \frac{(2l+1)}{1+k_l} W_l P_{lm} \sin(\phi) \Delta f_{lm} \quad (1)$$

with

$$\rho = \frac{a_e \rho_e}{3\rho_w} \quad (2)$$

$$W_l = \exp\left[\frac{(lr/a_e)^2}{4 \ln(2)}\right] \quad (3)$$

$$\Delta f_{lm} = \Delta C_{lm}(t) \cos(m\lambda) + \Delta S_{lm}(t) \sin(m\lambda) \quad (4)$$

P_{lm} : Normalized Legendre polynomials, $\Delta C_{lm}(t)$, and $\Delta S_{lm}(t)$: Normalized time-varying Stokes spherical harmonic geopotential coefficients, a_e – Earth mean radius, r – spatial

radius, k_l – Love numbers, ρ_e – Earth mean density, ρ_w – water density, t – time, and ϕ , λ are latitude and longitude (Wahr et al. 1998). Beyond degree (order) 40 to 70, the inherent noise level in the mass change signal becomes significant (Tapley et al. 2004). Processing includes downward propagation and adjustments to remove the time-variable mass change effects from tides and atmosphere and mean variation (GRACE geoid model). A normalized Gaussian smoother filter mitigates striping artifacts produced by the orbit non-crossing and control-descent geometry (Wahr et al. 1998, Tapley et al. 2004). Differences in processing (de-aliasing) and error sources and products are attributable to differences in assumed zero-degree and order Stokes harmonics, tide (liquid and solid) models, and the modeled atmosphere mass change removal, respectively in decreasing order of magnitude (Quinn & Ponte 2010, Zenner et al. 2010).

Glacial isostatic adjustment (GIA) is a global phenomenon by way of mantle flow following the decay of the Pleistocene ice sheets in North America and Euro-Scandinavia (Peltier 2004). We remove modeled GIA from the GRACE grids (Paulson et al. 2007).

AIRS

CO₂ free-troposphere measurements (concentration in parts per million) derive from the Atmospheric InfraRed Sounder onboard the NASA-Aqua (Barkley et al. 2006, Xiong et al. 2008). The Level 3 data are in the form of monthly near-global grids, 60°S to 90°N, from October 2002. Grid spacing is 2 degrees latitude by 2.5 degrees longitude. Daytime and nighttime CO₂ concentrations are derived from a suite of spectral channels with 15 μ m bandwidth and peak sensitivities at about 450 hPa with accuracy better than 2 parts per million (Chahine et al. 2008). Validations have been accomplished using ground-based upward viewing spectro-radiometers, aircraft-based spectro-radiometers, model simulations and with other satellite sensor comparisons (Xiong et al., 2008, Chahine et al. 2008). AIRS has proven capability to measure both mid-troposphere transport and surface sources of CO₂ of natural and anthropogenic origin (Chahine et al. 2008, Neelin et al. 2010, Muskett and Romanovsky 2011b).

Methodology

Our mathematical basis derives from Linear & Non-Linear Algebras of Hilbert Space applied to the Generalized Inverse and Potential Theory (Scales et al. 2001). We use this methodology to derive regional gradients of geopotential fields, error analysis, and statistical significance drawing from other works by Brockwell & Davis (1991) and Borradaile (2003).

On the MODIS, GRACE, and AIRS datasets we apply the Sandwell biharmonic method (Sandwell 1987, Wessel & Bercovici 1998, Wessel 2009) with Greens Functions zero-curvature constraint to produce global grids at 0.2-degree (about 22-km) spatial resolution. This method is useful for MODIS products to mitigate cloud-voids. The MODIS grids remain at daily temporal resolution and the GRACE and

Table 1. Comparison of the MOD11A1 derived mean land-surface temperature changes within the region of Figure 1, before and after interpolation with the Sandwell biharmonic method.

| 2008 05 | 2008 09 |
|--|--|
| +7.98 \pm 4.90 °C (Original) | -5.63 \pm 3.80 °C (Original) |
| +7.46 \pm 5.75 °C (Interpolation) | -5.69 \pm 4.59 °C (Interpolation) |

AIRS grids remain at monthly temporal resolution. Statistical evaluation tests are performed to monitor validity of the resultant grids using techniques of Borradaile (2003). Tests of this method on MODIS MOD11A1 daily 1-km land-surface temperature data over the region of Figure 1 show satisfactory results with P-values better than the α -level of 0.05, 95% significant (Table 1). From May 1 through 31, 2008, within the region of Figure 1, land-surface temperatures increased by about 8°C, on average. From September 1 through 30, 2008, within the region of Figure 1, land-surface temperatures decreased by about 6°C, on average.

Results and Discussion

Time series

Our ongoing investigation builds on research applying methods of satellite geodesy to issues of water equivalent storage changes and their sources in the permafrost watersheds of the northern hemisphere (Muskett & Romanovsky 2009, 2011). The Lena and Yenisei River watersheds indicate substantially increasing water equivalent storage (Muskett & Romanovsky 2009). Mays (mass loading) and Septembers (mass unloading) are distinctive in the seasonal cycle of water mass changes. The pattern of runoff (water mass unloading) is distinctive of high-latitude watersheds with the maximum runoff occurring in June (Muskett & Romanovsky 2009, 2011a, 2011b). During the winter months, base flow from groundwater discharge is increasing as well as the spring flows (Yang et al. 2002). While yearly runoff is strongly increasing, winter snow loads show no trend on the largest Siberian watersheds of the continuous permafrost zone of Eurasia. Using techniques of signal reduction, we find ground water storage significantly increasing (Muskett & Romanovsky 2011a, 2011b). Regionalized vegetation and shallow (~ 1 to 2 cm) soil moisture monthly series show only small seasonal-latitudinal variations without trend (Muskett & Romanovsky 2011b). Bias-corrected summer precipitation trends are very weak, with high uncertainty and very low significance. The strongly increasing trends of total water storage and runoff changes have very low correlation to precipitation trends (Muskett and Romanovsky 2011b). Regionalized CO₂ time series on the Arctic Ocean and coastal seas indicate strong emissions during Aprils-Mays correlated with springtime lead formation (Muskett and Romanovsky 2011b).

Spatiotemporal gradient fields

Figure 2 illustrates the geopotential gradient fields (left

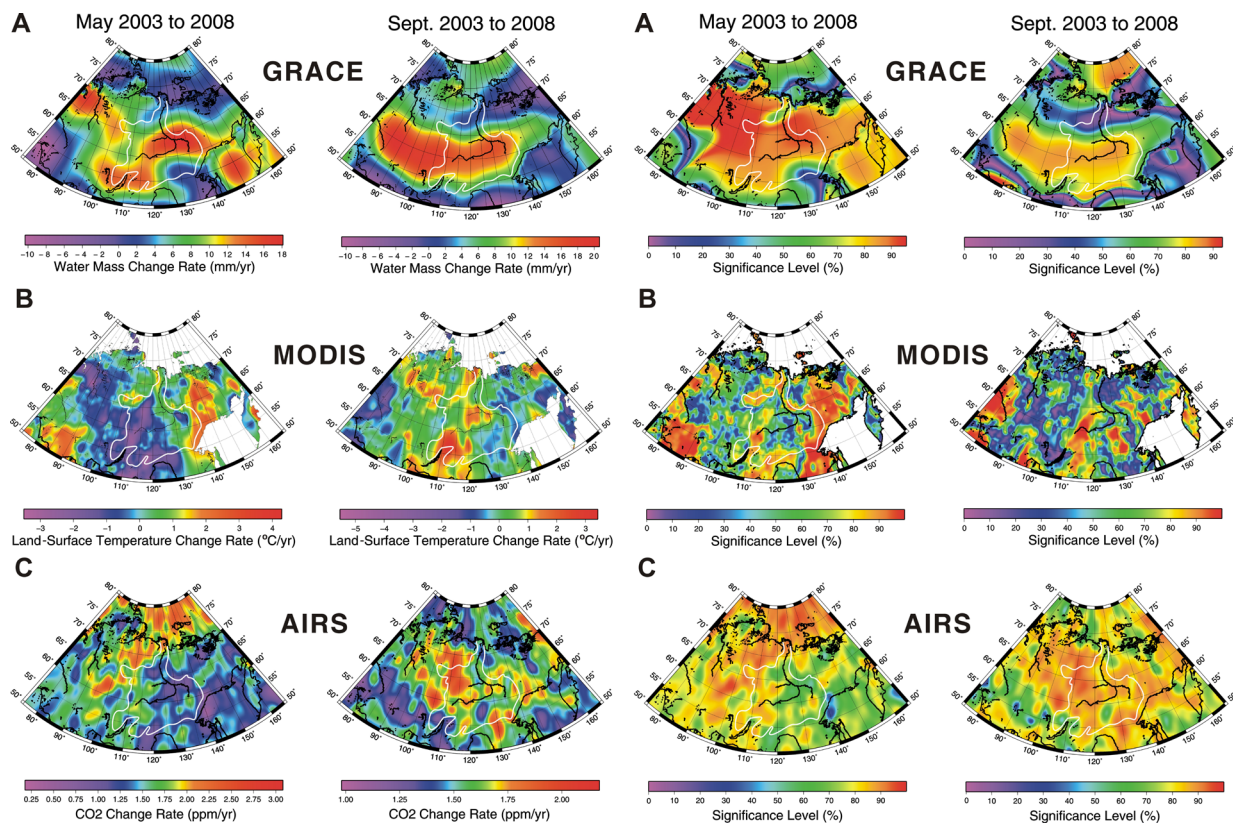


Figure 2. Coupled geopotential gradient fields (left side) and significance level fields (right side) of GRACE (A), MODIS (B) and AIRS (C) (Muskett and Romanovsky 2011).

side) of changes in water equivalent mass (A), land-surface temperature (B), and CO_2 (C) during May and September from 2002 through 2008, and the associated significance levels (right side). Root Mean Square deviation levels (uncertainty) from variance-covariance matrices is typically about 30% and less on the strongest gradients with significance up to and above 95%. Weak gradients near zero magnitude do not rise above their RMS values and have low significance.

The gradient fields indicate coupled ecosystem-energy-mass response to forcing and feedback over the period of measurement. Results from the gradient fields are summarized:

- 1) Arctic uplands such as the Siberian Plateau show strongly positive water equivalent mass and strongly negative land-surface temperature gradients during May months.
- 2) Arctic lowlands such as the thaw-lake regions of Kolyma, Lena Delta, and Taymyr show strongly negative water equivalent mass and strongly positive land-surface temperature gradients during September months.
- 3) Areas with strongly positive water equivalent mass and negative land-surface temperature gradients during May months have weakly positive CO_2 gradients.
- 4) Areas with strongly negative water equivalent mass and strongly positive land-surface temperature gradients during September months have strongly positive CO_2 gradients.

This indicates permafrost ecosystem microbial response is correlated and in phase with energy and mass changes over the period of measurements. GRACE positive gradients

are particularly strong on the central and southern Lena continuous and discontinuous permafrost zone during May and September 2002 through 2008. On the northern Yenisei River, the watershed continuous permafrost zone on the west side of the Lena, GRACE positive gradients are particularly strong during May. The northern Yenisei River watershed continuous permafrost zone shows strong positive water equivalent mass gradients during Mays. During Septembers, the center and southern Yenisei River watershed continuous and discontinuous zones show strongly positive water equivalent mass gradients, while the northern part becomes weakly positive water equivalent mass gradients. Lowland regions in the continuous permafrost zone with abundant thermokarst-lakes in the Taymyr, Lena Delta, and Kolyma regions have strong negative water equivalent mass and positive CO_2 gradients during September 2002 through 2008. These regions are also noteworthy for their CH_4 emissions (Walter et al., 2007, Schuur et al. 2009). CO_2 and CH_4 emissions are in part driven by lake expansion by shoreline erosion and limited by lake drainage through lakebed taliks that are linked to permafrost degradation (van Huissteden et al. 2011).

Our investigations of the arctic permafrost watersheds point to the strong role of groundwater storage changes (Muskett & Romanovsky, 2009, 2011a, b). Permafrost regions can contain liquid water in large quantities (Kalabin 1973). The increasing groundwater storage of the Eurasian arctic watersheds and the decreasing groundwater storage of the western North American arctic watersheds are not simply linked to water

volume changes. Rather, as permafrost thaws and degrades to taliks, internal flow paths can form and those existing can become connected. In the continuous and discontinuous permafrost zones there are regions of increasing capacity and residence time that can be a function of newly closed taliks, as well as regions of decreasing residence time that can be a function of new through taliks. In the western North American Yukon River watershed, the latter is the case, whereas in the Arctic Coastal Plain of Alaska, the former is the case, on average. Our measurements indicate that observations of the increasing number of thaw lakes in the continuous permafrost zones are not simply linked to precipitation increases (see Smith et al. 2005). The decreasing number of thaw lakes in the discontinuous permafrost zone that are linked to subsurface drainage (see Yoshikawa and Hinzman 2003) are manifestations of the changing groundwater mass storage and residence times.

Permafrost is vulnerable to climate-driven forcing and feedbacks (Grosse et al. 2011). During Septembers the Taymyr, Lena Delta, and Kolyma regions (thaw-lakes) of the continuous zones have strong negative gradients in water equivalent mass, strong positive gradients in land-surface temperature, and strong positive gradients in CO₂. These changes point to permafrost thaw and degradation and carbon release.

Current estimates of the global CH₄ emission budget points to arctic wetlands contributing up to 12% (Bloom et al. 2010). Arctic methanogenesis is keyed to thaw lake thermokarst and permafrost degradation processes (Walter et al. 2006, van Huissteden et al. 2011). We hypothesize that increasing numbers of thaw lakes by permafrost thawing and degradation in the continuous permafrost zones will likely be a strong positive feedback, increasing CH₄ emissions that can offset the negative feedback of decreasing numbers of thaw lakes and reducing CH₄ emissions in the discontinuous zone on an area-average basis.

Acknowledgments

This work was funded through supporting grants from NASA (NNOG6M48G), the National Science Foundation (NSF) ARC0632400, ARC-0612533, and ARC0856864 projects, Alaska EPSCoR NSF award #EPS-0701898 and the State of Alaska. The Alaska Region Supercomputing Center is thanked. NASA, GSFC and JPL and Deutsches GeoForschungsZentrum are thanked for the GRACE, MODIS and AIRS datasets. The Generic Mapping Tools were used in this research.

References

- Barkley, M.P., Monks, P.S., & Engelen, R.J. 2006. Comparison of SCIAMACHY and AIRS CO₂ measurements over North America during the summer and autumn of 2003. *Geophys. Res. Lett.* 33 (L20805), doi:10.1029/2006GL026807.
- Berry, P.A.M., Smith, R.G., Freeman, J.A. & Benveniste, J. 2008. Towards a New Global Digital Elevation Model. In Sideris, M.G. (ed.), *Observing Our Change Earth*, 133, Part 2, 431-435. International Association of Geodesy Symposia 2008, Springer-Verlag Berlin, Germany, doi:10.1007/978-3-540-85426-5_52.
- Bloom, A.A., Palmer, P.L., Fraser, A., Reay, D.S., & Frankenberg, C. 2010. Large-scale controls of methanogenesis inferred from methane and gravity data. *Science* 327: 322-325, doi:10.1126/science.1175176.
- Borradaile, G.J. 2003. *Statistics of Earth Science Data: Their Distribution in Space, Time and Orientation*. Springer-Verlag, Berlin, Germany.
- Brockwell, P.J. & Davis, R.A. 1991. *Time Series: Theory and Methods* 2nd Ed. Springer-Verlag, New York, USA.
- Chahine, M., Chen, L., Dimotakis, P., Jiang, X., Li, Q.B., Olsen, E., Pagano, T., Randerson, J., & Yung, Y. 2008. Satellite remote sounding of middle tropospheric CO₂. *Geophys. Res. Lett.* 35 (L17807), doi:10.1029/2008GL035022.
- Coll, C., Wan, Z., & Galve, G.M. 2009. Temperature-based and radiance-based validations of the V5 MODIS land surface temperature product. *J. Geophys. Res.* 114: D20102, doi:10.1029/2009JD12038.
- Flanner, M.G., Shell, K.M., Barlage, M., Perovich, D.K., & Tschudi, M.A. 2011. Radiative forcing and albedo feedback from the Northern Hemisphere cryosphere between 1979 and 2008. *Nature, Geosci.* 4: 151-155, doi: 10.1038/ngeo1062.
- Grosse, G., Marchenko, S., Romanovsky, V., Wickland, K. P., French, N., Waldrop, M., Bourgeau-Chavez, L., Striegl, R., Harden, J., Turetsky, M., McGuire, A. D., Camill, P., Tarnocai, C., Frolking, S., Schuur, E., & Jorgenson, T. 2011b. Vulnerability of high latitude soil organic carbon in North America to disturbance. *J. Geophys. Res.*, 116, doi:10.1029/2010JG001507.
- Hachem, S., Duguay, C.R., & Allard, M. 2011. Comparison of MODIS-derived land surface temperatures with near-surface soil and air temperature measurements in the continuous permafrost terrain. *The Cryo. Discuss.* 5: 1583-1625, doi: 10.5194/tcd-5-1583-2011.
- Kalabin, A.I. 1973. Scientific-procedural principles of investigation and the main features of the hydrogeology of northern countries (exemplified by northeastern USSR). In USSR Contribution - *Permafrost, 2nd International Conference*, July 13-28 1973, Sanger, F.J. & Hyde, P.J. Eds., National Academy of Sciences, Washington, D.C.
- Muskett, R.R. & Romanovsky, V.E. 2009. Groundwater storage changes in arctic permafrost watersheds from GRACE and in situ measurements. *Envir. Res. Lett.* 4, doi:10.1088/1748-9326/4/4/045009.
- Muskett, R.R. & Romanovsky, V.E. 2011a. Alaskan Permafrost Groundwater Storage Changes Derived from GRACE and Ground Measurements. *Remote Sens.* 3: 378-397, doi:10.3390/rs3020378.
- Muskett, R.R. & Romanovsky, V.E. 2011b. Energy and mass changes of the Eurasian permafrost regions by multi-satellite and in-situ measurements. *Natural Science* 3 (10), 827-836, doi:10.4236/ns.2011.310108.

- Neelin, J.D., Lintner, B.R., Tian, B., Li, Q., Zhang, L., Patra, P.K., Chahine, M.T., & Stechmann, S.N. 2010. Long tails in deep columns of natural and anthropogenic tropospheric tracers. *Geophys. Res. Lett.* 37 (L05804), doi:10.1029/2009GL041726.
- Paulson, A., Zhong, S., & Wahr, J. 2007. Inference of mantle viscosity from GRACE and relative sea level data. *Geophys. J. Int.* 171: 497-508, doi:10.1111/j.1365.246X.2007.03556.x.
- Peltier, W.R. 2004. Global glacial isostasy and the surface of the Ice-Age Earth: The ICE-5G (VM2) model and GRACE. *Annu. Rev. Earth Planet. Sci.* 32: 111-149, doi:10.1146/annurev.earth.32.082503.144359.
- Quinn, K.J. & Ponte, R.M. 2010. Uncertainty in ocean mass trends from GRACE. *Geophys. J. Int.* 181: 762-768, doi:10.1111/j.1365-426X.201004508.x.
- Romanovsky, V.E., Drozdov, D.S., Oberman, N.G., Malkova, G.V., Kholodov, A.L., Marchenko, S.S., Moskalenko, N.G., Sergeev, D.O., Ukrainseva, N.G., Abramov, A.A., Gilichinsky, D.A., & Vasiliev, A.A. 2010. Thermal State of Permafrost in Russia. *Perma. & Peri. Process.* 21: 136-155, doi:10.1002/ppp.683.
- Saltzman, B. (ed.). 1983. *The Theory of Climate. Advances in Geophysics 25* Academic Press, New York, USA.
- Sandwell, D.T. 1987. Biharmonic spline interpolation of GOES-3 and SEASAT altimeter data. *Geophys. Res. Lett.* 14 (2): 139-142.
- Scales, J.A., Smith, M.L., & Treitel, S. 2001. *Introductory Inverse Theory*. Samizdat Press, Golden, CO, USA.
- Schuur, E.A.G., Vogel, J.G., Crummer, K.G., Lee, H.L., James, O., Sickman, J.O., & Osterkamp, T.E. 2009. The effect of permafrost thaw on old carbon release and net carbon exchange from tundra. *Nature* 459: 556-560, doi:10.1038/nature08031.
- Smith, L.C., Sheng, Y., MacDonald, G.M., & Hinzman, L. D. 2005. Disappearing Arctic Lakes. *Science* 308 (5727), 1429, doi:10.1126/science.1108142.
- Tapley, B.D., Bettadpur, S., Watkins, M., & Reigber, C. 2004. The gravity recovery and climate experiment: Mission overview and early results. *Geophys. Res. Lett.* 31 (L09607), doi:10.1029/2004GL019920.
- van Huissteden, J., Berrittella, C., Parmentier, F.J.W., Mi, Y., Maximov, T.C., & Dolman, A.J. 2011. Methane emissions from permafrost thaw lakes limited by lake drainage. *Nature Climate Change* 1, 119-123, doi:10.1038/nclimate1101.
- Wahr, J., Molenaar, M., & Bryan, F. 1998. Time variability of the Earth's gravity field: Hydrologic and oceanic effects and their possible detection using GRACE. *J. Geophys. Res.* 103 (B12): 30205-30229, doi:10.1029/98JB02844.
- Walter, K.M., Edwards, M.E., Grosse, G., Zimov, S.A., & Chapin, F.S. III. 2007. Thermokarst lakes as a source of atmospheric CH₄ during the last deglaciation. *Science* 318: 633-636, doi:10.1126/science.1142924.
- Wan, Z. 2008. New refinements and validation of MODIS land-surface temperature/emissivity products. *Remote Sens. Env.* 112: 59-74, doi:10.1016/j.rse.2006.06.026.
- Wang, W., Liang, S., & Meyers, T. 2008. Validating MODIS land surface temperature products using long-term nighttime ground measurements. *Remote Sens. Env.* 112: 623-635.
- Wessel, P. & Bercovici, D. 1998. Interpolation with splines in tension: A Green's function approach. *Math. Geol.* 30(1): 77-93, doi:10.1023/A:1021713421882.
- Wessel, P. 2009. A general-purpose Green's function-based interpolator. *Comp. & Geosci.* 35 (6): 1247-1254, doi:10.1016/j.cageo.2008.08.012.
- Xiong, X., Barnet, C., Maddy, E., Sweeney, C., Liu, X., Zhou, L., & Goldberg, M. 2008. Characterization and validation of methane products from the Atmospheric Infrared Sounder (AIRS). *J. Geophys. Res.* 113 (G00A01), doi:10.1029/2007JG000500.
- Yoshikawa, K. & Hinzman, L.D. 2003. Shrinking thermokarst ponds and groundwater dynamics in discontinuous permafrost near Council, Alaska. *Perma. & Peri. Process.* 14, 151-160, doi:10.1002/ppp.451.
- Yang, D., Kane, D.L., Hinzman, L.D., Zhang, X., Zhang, T. & Ye, H. 2002. Siberian Lena River hydrologic regime and recent changes. *J. Geophys. Res.* 107 (D23), 4694 doi:10.1029/2002JD002542.
- Zenner, L., Gruber, T., Jäggi, A., & Beutler, G. 2010. Propagation of atmospheric model errors to gravity potential harmonics—impact on GRACE de-aliasing. *Geophys. J. Int.* 182 (2): 797-807, doi: 10.1111/j.1365-246X.2010.04669.
- Zhang, X., Friedl, A.M., Schaaf, B.C., & Strahler, A.H. 2004. Climate controls on vegetation phenological patterns in northern mid- and high latitudes inferred from MODIS data. *J. Global Change Biology* 10: 1133-1145, doi: 10.1111/j.1365-2486.2004.00784.x.

“The Worst Thing We Had To Contend With”: Permafrost and Construction of the Alcan Highway

Frederick E. Nelson

American Geographical Society Library, University of Wisconsin-Milwaukee, Milwaukee, WI, USA

Abstract

The 2250-km Alaska-Canada (“Alcan”) Highway was developed through nearly uncharted wilderness over a period of only seven months in 1942. The road was one of the largest engineering projects undertaken in North America to that time. The largest single obstacle to the construction and efficient operation of the initial road was ice-rich permafrost. Despite prior experience with permafrost engineering in North America and repeated warnings by arctic experts about the use of mid-latitude engineering procedures in permafrost regions, the U.S. Army initially adopted conventional construction techniques, with disastrous consequences. To remediate the situation, a permafrost engineering manual was commissioned and prepared by Dr. Siemon W. Muller, a Stanford University geology professor of Russian extraction. The manual, based almost entirely on Russian-language literature, was used to guide the reconstruction and realignment of permafrost-affected sections of the road. Muller’s book was used widely in subsequent engineering projects in Alaska and northern Canada.

Keywords: Alcan Highway; engineering; ground ice; permafrost; roads; World War II.

Introduction

When the administration of U.S. President Andrew Johnson acquired Alaska from Russia in 1867 for \$7,200,000, the transaction was referred to derisively by many as “Seward’s Folly,” after Secretary of State William Seward, who negotiated the purchase. Although a few pleas for rational exploration and development and for fair treatment of Native peoples appeared in the territory’s early years (e.g., Kane 1868), Alaska remained a largely unexplored and unexploited backwater until the Klondike gold strike of 1896 brought thousands of prospectors and support personnel north. The discovery of rich mineral resources in the vast territory awakened the U.S. federal government to its potential, and systematic surveys across its extent began in earnest during the first decade of the 20th century, largely through the work of the U.S. Geological Survey (e.g., Moffit 1905, Prindle 1905).

Early USGS surveys in Alaska were not concerned entirely with economic geology. Most of the scientists responsible for these expeditions were generalists, well versed in survey methods, topographic mapping, physiography, botany, and anthropology. Many of the publications growing out of these surveys documented the existence of ground that remained frozen throughout the summer, often with large inclusions of ground ice. Referring to this phenomenon variously as “permanently frozen ground,” “eternal frost,” and “ever-frozen ground,” these reports conveyed recognition that it could cause severe problems for engineering projects.

Unlike the situation in Russia, knowledge in North America about perennially frozen ground developed in piecemeal fashion. Although information was sufficient by the late 1920s to enable publication of a treatise about its effects on placer mining operations (Wimmler 1927), an extensive knowledge base was not developed in systematic fashion and made available in accessible form to the engineering community. Information about perennially frozen ground was (a) acquired

by personnel on expeditions to the North American Arctic sponsored by such private organizations as the American Geographical Society (e.g., Russell 1890, Stefansson 1910, Leffingwell 1915); (b) written by Russian expatriates (e.g., Nikiforoff 1928), or (c) gained through field experience in Russia (e.g., Cressey 1939). Articles about frozen ground were scattered through the literature of several basic scientific disciplines (e.g., geography, geology, botany), and operating engineers in North America were generally unaware of this knowledge base.

At the dawn of World War II, advances in basic understanding of perennially frozen ground and its disruptive potential had not been introduced to North American engineering literature (French & Nelson 2008b). This lack of understanding set the stage for costly and dangerous engineering blunders in several of the continent’s largest and strategically most important infrastructure projects.

The Alcan (Alaska) Highway

Routing

Shortly after German forces launched a surprise attack on the Soviet Union on June 22, 1941, the Soviet ambassador to the U.S. made a formal request that the Lend-Lease program, already in effect with Great Britain and other countries, be extended to the USSR. After a great deal of back-and-forth wrangling about the types and numbers of aircraft and the most appropriate route, it was agreed that an “ALSib” route (Hays 1996) should be created between Alaska and Siberia, using Ladd Field (now Fort Wainwright) in Fairbanks as the transfer point. Aircraft were brought to Fairbanks using the “Northwest Staging Route,” a string of airfields extending from Great Falls, Montana, through Alberta, British Columbia, and Yukon Territory. The Northwest Route, built in 1941–42 to supply Alaska, was an extension of Canadian prewar aeronautical ambitions (Hays 1996).

Concerns about Alaska's vulnerability were at extremely high levels after the Japanese attack on Pearl Harbor in December 1941. These concerns, coupled with the need to contain costs in servicing the airfields of the Northwest Staging Route, convinced authorities of the need for an overland route to Alaska. Four routes were proposed and bitter arguments arose over their relative advantages and disadvantages (Finnie 1942, Stefansson 1944). Recriminations, including congressional investigations, continued long after the Rocky Mountain route was chosen. This route was selected ostensibly because its distance from the sea rendered attack by naval forces improbable (see Stefansson 1944) and because it offered the best proximity to the airfields of the Northwest Staging Route. At the outset of the project, much of the route was uncharted wilderness. The CANOL ("Canadian Oil") project, concerned with bringing oil from Norman Wells on the lower Mackenzie River to Whitehorse, also began during 1942.

Initially, the general course of the Canadian-Alaskan Military ("Alcan") Highway through the largely uncharted territory making up the route was determined using 1:250,000 National Geographic Society maps, 1:1,000,000 aeronautical charts, and the services of a bush pilot (Greenwood 1992). Beginning in July 1942, the route was determined through stereoscopic interpretation of air photographs obtained on missions flown by the U.S. Army Air Forces specifically for that purpose (Lane 1942, Richardson 1943). Working with air photos marked with local segments of the route, field parties determined routing details on the ground using plane tables, optical instruments, and chains where possible, but often reverting to compass-and-pace, line-of-sight, and offset survey methods. Where heavy vegetation obscured terrain, bulldozers were run along compass lines connecting treetop reconnaissance stations. Grades were established using hand (Abney) levels (Lane 1942).

Construction Methods

Construction of the Alcan Highway began in March 1942 under the command of Brigadier General William M. Hoge, only a month after President Franklin D. Roosevelt signed legislation authorizing the road. An unusual two-phase plan involved immediate construction of a "pioneer road" by military engineers and troops, followed by development of an improved "PRA road" administered by the U.S. Public Roads Administration, using private contractors. The sense of urgency accompanying construction of the pioneer road is apparent in the instructions issued to troop commanders from the Army's Chief of Engineers:

A pioneer road is to be pushed to completion with all speed within the physical capacity of the troops. The objective is to complete the entire route at the earliest practicable date to a standard sufficient only for the supply of troops engaged on the work. Further refinements will be undertaken only if additional time is available (Sturdevant 1943:173).

Seven engineering regiments (nearly 11,000 troops) had

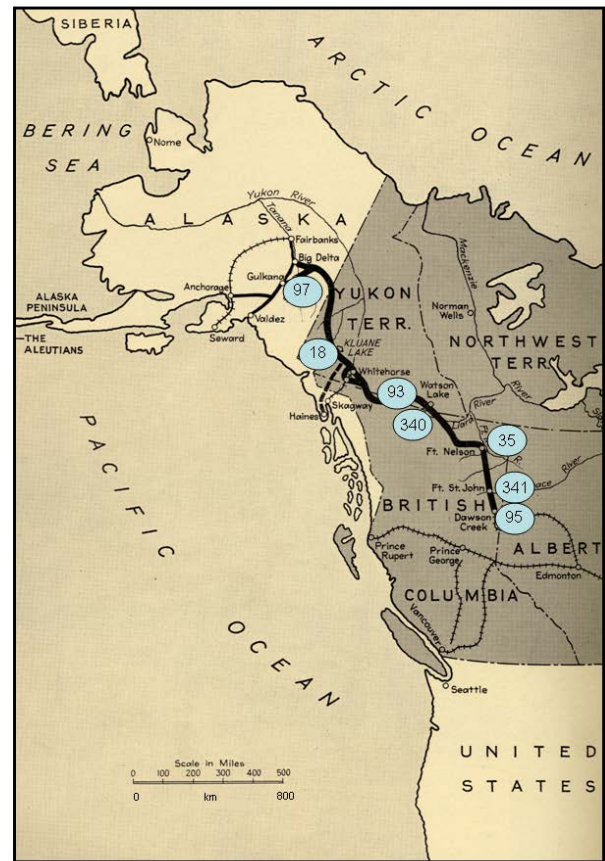


Figure 1. Alcan Highway route in 1942, showing approximate locations of regimental sectors. Base map from Richardson (1942a: 82).

begun working by the second quarter of 1942. The 35th, 341st, and 95th Engineers worked northward from Dawson Creek and Fort St. John (Fig. 1). The 18th Engineering Regiment worked westward from Whitehorse, while the 97th Engineers progressed southward from Alaska. The 93rd and 340th regiments worked in difficult terrain in Yukon Territory east of Whitehorse (Richardson 1942b, Sturdevant 1943). The PRA phase involved a large number of U.S. and Canadian contractors employing thousands of civilian workers. The project used three supply routes: (a) by rail to Dawson Creek; (b) via ship to Skagway and rail to Whitehorse; and (c) by ship to Valdez and road to Big Delta, Alaska (Richardson 1942b). Working conditions for the road crews were often primitive, involving horse-drawn water wagons, tents and wanigans, canned field rations, and extreme isolation. Frigid winter temperatures, hazardous water crossings, and hordes of insects added misery to the three eight-hour shifts each day of the week (Hardin 1942, Richardson 1942b, Greenwood 1992).

Each of the seven regiments charged with constructing the pioneer road was issued 20 D-8 (23-ton) diesel bulldozers, 24 lighter tractors and bulldozers, six tractor-drawn graders, three patrol graders, six router plows, 50-90 dump and cargo trucks, 11-20 jeeps ("quarter-ton trucks"), 12 pickup trucks, two 0.5-yard gas shovels, one truck crane, six 12-yard scraper/carriers, one portable sawmill, two pile drivers, as well as light tools, water purification equipment, and electricity generation

plants (Richardson 1942a, Sturdevant 1943). Nearly all of the equipment was new.

Following in the wake of the survey crews were mechanized units composed of a lead D-8 Caterpillar bulldozer used to fell trees along the centerline, flanked by two or more Cats clearing the path to a 100-foot (30.5 m) right-of-way in most sections. Additional bulldozers followed to clear fallen timber, remove brush, and scrape surface materials. Roadcuts were used extensively. The heavy bulldozers were able to clear up to three miles per day, allowing them to stay well ahead of specialized companies responsible for follow-up tasks (Greenwood 1992). Extending 30 to 50 miles (48 to 80 km) behind the mechanized companies were “soldier units” responsible for grading, culverting, and constructing small bridges (Richardson 1943). An alternative deployment divided regiments into companies that were responsible for all major tasks and “leap-frogged” one another along their assigned portion of the construction route. Major river crossings were bridged by relatively stationary crews operating quasi-independently of the road builders. Richardson (1943) provided a detailed account of construction procedures.

Once the effects of the spring thaw abated, progress was rapid, and the entire route was open to traffic by late October of 1942. Detailed accounts of early passages on the Alcan route (Lanks 1944, Correll 1981) provide fascinating insights into travel on the pioneer road.

Permafrost and the Alcan Highway

Despite the Klondike Gold Rush era experiences, engineering practice in North America had taken little systematic notice of permafrost by 1940, and little applied (engineering) literature had been published in the English language. In contrast, the Russian approach to permafrost science was systematic and holistic; both basic and applied aspects of the subject were treated in unified fashion under the rubric of “geocryology” (e.g., Sumgin 1940, French & Nelson 2008b). This approach imparted great benefits to the design and operation of engineered works, such as the Trans-Siberian Railway (Shiklomanov 2005), and at the beginning of World War II an extensive Russian-language literature about permafrost had appeared. Engineers had developed detailed design criteria for construction projects, and manuals for engineered works in permafrost regions were widely available.

Consequences of Alcan construction methods

The “brute force” construction methods used to develop the Alcan pioneer road guaranteed degradation of ice-rich permafrost beneath the road surface and major problems from thaw subsidence. Although the military commanders in charge of the Alcan and CANOL projects had been warned repeatedly by locals and arctic experts, the use of bulldozers to remove vegetation and scrape the resulting bare surfaces thawed ice-rich permafrost in many locations, creating major problems in the sections where the 18th and 340th Engineers were operating. Removal of insulating layers of vegetation,



Figure 2. Small bulldozer mired in mud after thaw of ice-rich permafrost.

peat, and humus meant that ice-rich permafrost was exposed directly to solar radiation and high surface temperatures. Under such conditions, a right-of-way that had appeared smooth and dry immediately after clearance could become a morass only a day or two later, as ground ice melted. Both heavy and light bulldozers frequently became mired (Fig. 2). Muller (2008:118) cited anecdotal evidence about one bulldozer disappearing completely, never to be recovered. Roadcuts also created localized problems of thaw settlement and slumping.

Another “AlSib Connection”

Although unclassified literature published during 1942–43 glossed over the deleterious effects of thaw settlement on the pioneer road (e.g., Lane 1942, Richardson 1943), great administrative concern was generated by continuing thaw-related problems. Remedial actions, such as corduroy road segments covered with insulating layers of brush, soil, and gravel (Fig. 3) slowed the pace of construction substantially, and there was general concern about continuing thaw in 1943 and beyond. Decades after the pioneer road was completed, General Hoge stated in an interview that permafrost “was the worst thing we had to contend with” (Greenwood 1985, Twichell 1992).

A search was initiated to find an individual who possessed both knowledge about engineering problems relating to frozen ground and the linguistic skills necessary to access Russian-language literature on the subject. It is unclear why authorities did not tap Constantin C. Nikiforoff, a U.S. Soil Conservation Service scientist who had completed doctoral studies at St. Petersburg University during the pre-revolutionary period and had published an English-language paper about frozen ground in Siberia (Nikiforoff 1928). Nonetheless, an extremely capable scientist was found. Siemon W. Muller, a professor of geology at Stanford University, was engaged as a civilian consultant to the Army (French and Nelson 2008a). Muller was the son of a Danish engineer who had worked on the Trans-Siberian Railway’s telegraph line. At the time of the 1917 revolution, Siemon Muller was a cadet in the Naval Academy in Vladivostok. After a well-advised escape to China, Muller made his way to the United States and eventually earned a doctorate in geology. At the opening of World War II, Muller was a respected professor at Stanford, specializing in stratigraphy and paleontology.



Figure 3. Corduroy road construction used to mitigate damage to the pioneer road caused by thaw of ice-rich permafrost. Timbers were obtained from slash created by road construction and covered with brush and gravel to inhibit thaw. Three of the seven U.S. Army regiments (93rd, 95th, 97th) involved in construction of the pioneer road were composed of African-American troops (Twichell 1992, Brinkley 2002).

When the magnitude of the problems associated with frozen ground along the Alcan route became apparent, Muller was recruited by the Army to create a compilation of appropriate engineering methods based on Russian-language literature (French & Nelson 2008a). Working at the Library of Congress and the U.S. Geological Survey Library, Muller compiled a construction manual representing a distillation of the Soviet experience with frozen ground. Issued to military engineers as a classified report early the following year (Muller 1943), the compilation provided a firm basis for constructing and maintaining engineered works in regions of perennially frozen ground. Following completion of the initial version of his report, the U.S. Army Air Forces Air Transport Command assigned Muller, still a civilian, to study frozen-ground phenomena along the Alcan route and at air bases throughout Alaska. This work resulted in an expanded version of his classified report, issued in 1945. A series of shorter reports on specialized topics (e.g., Muller 1944) was also issued to military engineers late in the war. After being declassified, the report received wide distribution (Muller 1947) and functioned for many years as the premier English-language permafrost text. It remains an authoritative work to the present time (French & Nelson 2008a).

Muller's report also performed the critically important function of providing an instantly recognizable name for the phenomenon. Muller's book introduced the term *permafrost* ("permanent frost"), a loan translation from the Russian *Vechnaya merzlota* ("eternal frost"). Although concerns were raised about the term's etymological purity (e.g., Bryan 1948), *permafrost* quickly became firmly rooted in the scientific vocabulary and remains the preferred term for perennially frozen ground.

Applications to Alcan

Permafrost science is an integrative discipline, mastery of which requires an understanding of elements of many other branches of science, including geology, botany, hydrology, soil physics, and civil engineering. Muller's 1943 report was a masterful blend of these topics, and it allowed operating engineers to understand and predict the behavior of frozen ground. Probably more importantly at the time, the manual provided a wealth of information about how to recognize and avoid potential problems involving permafrost and how to implement practical solutions to existing problems.

During the summer of 1943, nearly a third of the Alcan route had to be relocated, in many cases because of recurrent thaw-related problems. On the basis of his extensive 1943–45 investigations along the Alcan route, Muller (2008:114) summarized the types of problems likely to cause damage to roads in permafrost terrain:

- cracking resulting from thermal contraction;
- differential frost heave;
- differential settling as the active layer thaws;
- turbation induced by differences in moisture content;
- differential settling due to thaw of underlying permafrost;
- mass movements induced by cut-and-fill operations;
- erosion along drainage ditches and culvert margins;
- roads impeding drainage, creating localized *icings*.

He emphasized the need for proactive strategies:

The choice of a route in permafrost terrain should not be dictated by either the usual evaluation of topography or the premise that the shortest and most direct route is the most satisfactory.... During the construction of the Alaska [Alcan] Highway, costly experience showed that every effort should be made to preserve permafrost in its frozen state beneath the roadbed and in the immediately adjacent ground. Once the original insulating cover of vegetation and topsoil had been removed and permafrost allowed to thaw, the thawing process spread like cancer and in many cases could not be checked (Muller 2008: 114-118).

Muller's approach to construction has stood the test of time and has been implemented widely in subsequent construction projects in arctic and subarctic regions of North America.

The Alcan Legacy

The Alcan Highway was one of the largest North American engineering projects undertaken to that time. The urgency with which it was implemented led to costly construction blunders that could have been avoided if information about permafrost behavior and effective construction methods had been readily available to North American engineers at the time the highway was built.

Siemon Muller's work during the 1940s led to widespread recognition of permafrost-related problems (e.g., Barnes 1946, Wilson 1948), development of methods for detecting

the presence of permafrost (e.g., Woods et al. 1948), and improved technical understanding of its behavior (e.g., Jaillite 1947, Terzaghi 1952). An important factor in the success of Muller's contribution derived from his having assigned a "catchy," easily retained name for the phenomenon.

Following a permafrost conference held in St. Paul, Minnesota, in January 1945, the U.S. Army's Corps of Engineers created a Permafrost Division. Responsibility for permafrost research in the U.S. military continued through a succession of Corps of Engineers reorganizations, culminating in the Cold Regions Research and Engineering Laboratory in Hanover, New Hampshire (Wright 1986). In 1948, the Military Geology Branch of the U.S. Geological Survey established the Alaska Terrain and Permafrost Section, which was funded jointly with the Army Corps of Engineers. This unit, which replaced the USGS Alaska Branch, produced a large number of maps and studies before its dissolution in 1972 (Terman 1998). Current responsibility for other governmental research and publication on permafrost is diffused through a wide array of government agencies (U.S. Arctic Research Commission 2003).

Despite these organizational and dissemination efforts, the permafrost-related lessons of the Alcan project were not learned completely by the North American engineering community for many years. After major oil reserves were discovered at Prudhoe Bay in 1968, the rush to create overland access to the area involved a new, heavier generation (D-9) of Caterpillar bulldozers employing virtually the same methods used in the early stages of Alcan construction (Nelson & Outcalt 1982). Initial industry plans for bringing the petroleum to refining facilities included an astonishing plan to bury a hot-oil pipeline in ice-rich permafrost terrain over much of its route (Lachenbruch 1970). After the bitter, expensive, and widely publicized debate about implementing the Trans-Alaska Pipeline (Coates 1991), engineering practice in permafrost regions improved considerably. Today, specialized texts and manuals are widely available (e.g., Andersland & Ladanyi 2004).

Unbeknownst to almost everyone (including permafrost scientists), Siemon Muller continued to compile information about permafrost and had nearly completed a lengthy integrative text at the time of his retirement in the early 1960s. This book (Muller 2008) remained in manuscript form until discovered in the effects of one of his students and brought to publication many years after Muller's death (French and Nelson 2008a). Had it been published at the time of completion (c. 1962), the book would have advanced North American permafrost science by well over a decade (French & Nelson 2008b).

The road was renamed "Alaska Highway" in 1943. It was turned over to Canadian authorities in 1946 and, after construction of suitable service facilities, was opened to civilian traffic (Nelson 1947). Today, after decades of continuous improvements and realignments, the road is an all-weather, hard-surfaced route carrying large volumes of tourist and commercial traffic. The Alaska Highway has its own annual publication, *The Milepost*.

A trained eye can discern many permafrost-related features along the route of the Alaska Highway (e.g., Denny 1952). Frost heave and thaw settlement still plague highway maintenance crews. Little remains, however, to focus the attention of casual travelers on the existence of permafrost, aside from potholes, undulating surfaces, "drunken forest," and place names (e.g., Snafu Lake, Tarfu Lake) that serve as reminders of the problems Army engineers encountered during the early 1940s.

References

- Andersland, O.B. & Ladanyi, B. 2004. *Frozen Ground Engineering*. Hoboken, NJ: Wiley, 363 pp.
- Barnes, L.C. 1946. Permafrost: a challenge to engineers. *The Military Engineer* 38: 9-11.
- Brinkley, D. 2002. *The World War II black regiment that built the Alaska Military Highway*. Jackson: University of Mississippi Press, 112 pp.
- Bryan, K. 1948. The study of permanently frozen ground and intensive frost action. *The Military Engineer* 40: 304-308.
- Coates, P.A. 1991. *The Trans-Alaska Pipeline controversy: technology, conservation and the frontier*. Bethlehem, PA: Lehigh University Press, 447 pp.
- Correll, D.S. 1981. *Alaska Highway Adventure*. Printed privately, 170 pp.
- Cressey, G.B. 1939. Frozen ground in Siberia. *Journal of Geology* 47: 472-488.
- Denny, C.S. 1952. Late Quaternary geology and frost phenomena along the Alaska Highway, northern British Columbia and southeastern Yukon. *Geological Society of America Bulletin* 63: 883-921.
- Finnie, R. 1942. A route to Alaska through the Northwest Territories. *Geographical Review* 32: 403-416.
- French, H.M. & Nelson, F.E. 2008a. Introduction to *Frozen in time: Permafrost and engineering problems* by S.W. Muller. Reston, VA: American Society of Civil Engineers, ix-xxiv.
- French, H.M. & Nelson, F.E. 2008b. The permafrost legacy of Siemon W. Muller. In *NICOP 2008: Proceedings of the Ninth International Conference on Permafrost*. D.L. Kane, K.M. Hinkel (eds.). Institute of Northern Engineering, University of Alaska Fairbanks, 1: 475-480.
- Greenwood, J.T. 1985. General Bill Hoge and the Alaska Highway. In: K. Coates (ed.), *The Alaska Highway: Papers of the 40th Anniversary Symposium*. Vancouver: University of British Columbia Press, 39-53.
- Greenwood, J.T. 1992. Building the road to Alaska. In: B.F. Fowle, (ed.) *Builders and fighters: U.S. Army Engineers in World War II*. Fort Belvoir, VA: Office of History, U.S. Army Corps of Engineers, pp. 117-135.
- Hardin, J.R. 1942. Engineers rush Alaskan defenses. *The Military Engineer* 34: 1-3.
- Hays, O., Jr. 1996. *The Alaska-Siberia connection*. College Station, TX: Texas A&M University Press, 184 pp.
- Jaillite, W.M. 1947. Permafrost research area. *The Military Engineer* 39: 375-379.

- Kane, T.L. 1868. Alaska and the polar regions: lecture of Thomas L. Kane before the American Geographical Society in New York City, Thursday Evening, May 7, 1868. New York: Journeymen Printers' Co-operative Association.
- Lachenbruch, A.H. 1970. Some estimates of the thermal effects of a heated pipeline in permafrost. *U.S. Geological Survey Circular* 632.
- Lane, A.L. 1942. The Alcan Highway: road location and construction methods. *The Military Engineer* 34: 492-499.
- Lanks, H.C. 1944. *Highway to Alaska*. New York: D. Appleton-Century Company, 200 pp.
- Leffingwell, E. de K. 1915. Ground-ice wedges: the dominant form of ground-ice in the north coast of Alaska. *Journal of Geology* 23: 635-654.
- Moffit, F.H. 1905. The Fairhaven gold placers, Seward Peninsula, Alaska. *U.S. Geological Survey Bulletin* 247.
- Muller, S.W. 1943. *Permafrost or permanently frozen ground and related engineering problems*. Special Report, Strategic Engineering Study. 62. Intelligence Branch, Office of the Chief of Engineers, 136 pp.
- Muller, S.W. 1944. *Permafrost: studies in connection with engineering projects in Arctic and Subarctic regions. Part I. Instructions for Measuring Ground Temperatures*. Air Installation Division, Headquarters Alaskan Division, U.S. Army Air Forces, Alaska Transport Command, 37 pp.
- Muller, S.W. 1947. *Permafrost or permanently frozen ground and related engineering problems*. Ann Arbor: J.W. Edwards, Inc., 231 pp.
- Muller, S.W. 2008. *Frozen in Time: Permafrost and engineering problems*. H.M. French & F.E. Nelson (eds.). Reston, VA: American Society of Civil Engineers, 280 pp.
- Nelson, F. & Outcalt, S.I. 1982. Anthropogenic geomorphology in northern Alaska. *Physical Geography* 3(1): 17-48.
- Nelson, H.E. 1947. The long trail revisited. *The Military Engineer* 39: 157-162.
- Nikiforoff, C. 1928. The perpetually frozen subsoil of Siberia. *Soil Science* 26: 61-78.
- Prindle, L.M. 1905. The gold placers of the Fortymile, Birch Creek and Fairbanks regions, Alaska. *U.S. Geological Survey Bulletin* 251.
- Richardson, H.W. 1942a. Alcan—America's glory road. Part I—Strategy and Location. *Engineering News-Record* 129 (25): 82-95.
- Richardson, H.W. 1942b. Alcan—America's glory road. Part II—Supply, Equipment and Camps. *Engineering News-Record* 129 (27): 35-42.
- Richardson, H.W. 1943. Alcan—America's glory road. Part III—Construction Tactics. *Engineering News-Record* 130: 131-138.
- Russell, I.C. 1890. Notes on the surface geology of Alaska. *Bulletin of the Geological Society of America* 1: 99-162.
- Shiklomanov, N.I. 2005. From exploration to systematic investigation: Development of geocryology in 19th-and early-20th-century Russia. *Physical Geography* 26: 249-263.
- Stefansson, V. 1910. Underground ice in northern Alaska. *Bulletin of the American Geographical Society* 42: 337-345.
- Stefansson, V. 1944. The North American Arctic. In *Compass of the world: a symposium on political geography*. H.W. Weigert & V. Stefansson (eds.). New York: The Macmillan Company, 215-265.
- Sturdevant, C.L. 1943. The military road to Alaska: Organization and administrative problems. *The Military Engineer* 35: 173-180.
- Sumgin, M.I. 1940. *Obshcheye merzlotovedeniya* (General permafrostology): Akad. Nauk SSSR.
- Terman, M.J. 1998. Military Geology Branch of the U.S. Geological Survey. In *Military geology in war and peace*. J.R. Underwood Jr. & P.L. Guth (eds.). Boulder, CO: Geological Society of America, 75-82.
- Terzaghi, K. 1952. Permafrost. *Journal of the Boston Society of Civil Engineers* 39(1): 319-368.
- Twichell, H. 1992. *Northwest epic: the building of the Alaska Highway*. New York: St. Martin's Press, 368 pp.
- U.S. Arctic Research Commission Permafrost Task Force (F.E. Nelson & L.W. Brigham, Lead Authors), 2003. *Climate change, permafrost, and impacts on civil infrastructure*. Washington, DC: U.S. Arctic Research Commission, 62 pp.
- Wilson, W.K., Jr. 1948. The problem of permafrost. *The Military Engineer* 40: 162-164.
- Wimmler, N.L. 1927. Placer-mining methods and costs in Alaska. *U.S. Bureau of Mines Bulletin* 259.
- Woods, K.B., Hittle, J.E., & Frost, R.E. 1948. Use of aerial photographs in the correlation between permafrost and soils. *The Military Engineer* 40: 497-499.
- Wright, E.A. 1986. *CRREL's first 25 years, 1961-1986*. Hanover, NH: U.S. Army Corps of Engineers, Cold Regions Research and Engineering Laboratory, 61 pp.

Thermal Status of Traditional Roadbed and Roadbed with Slopes Covered by Crushed Rocks along the Qinghai-Tibet Railway

Fujun Niu, Zhanju Lin, Hua Liu, Jiahao Lu

State Key Laboratory of Frozen Soils Engineering, Cold and Arid Regions Environmental and Engineering Research Institute, Chinese Academy of Sciences, Lanzhou, Gansu, China

Zhengping Liu

The First Railway Survey and Design Institute of China, Xi'an, Shanxi, China

Abstract

The Qinghai-Tibet Railway has been in service for five years in a permafrost region. The roadbed is generally stable and train speed reaches 100 km/h, which achieves one of the design requirements. The roadbed was constructed under the principle of a cooling roadbed. One technique used to cool the roadbed is covering the slopes with crushed rocks, and this technique is also strongly proposed for maintaining the railway. A traditional roadbed was used in some sections where permafrost was cold and ice-poor. In situ measurements indicate that thermal stability of the roadbed is much better where slopes were covered by crushed rocks than on the traditional roadbed. Measurements on roadbed covered by crushed rocks showed reduced ground temperature, good symmetry in the temperature field, and upward migration of the artificial permafrost table.

Keywords: permafrost; Qinghai-Tibet Railway; roadbed structure; thermal stability.

Introduction

It is generally believed that settlement, especially settlement caused by thawing permafrost, is the most serious problem for roadbed stability in permafrost regions. The key problem influencing successful construction and service of the Qinghai-Tibet Railway (QTR) was how to keep the roadbed stable in permafrost regions. As permafrost is sensitive to temperature change, roadbed stability has been facing great challenges under global warming and the intensifying trend of engineering activities on the plateau (Liu et al. 2000, Wu et al. 2004, Wu & Zhang 2008).

The QTR is expected to operate for more than 100 years at an average speed of 100 km/h. Considering the influence of global warming and engineering activities on permafrost, the principle of “active cooling” was adopted to lower temperatures of the underlying permafrost in the construction of the QTR (Cheng 2003, Cheng 2005). Given the fact that the current train speed of about 100 km/h achieves one of the design requirements, this principle has proved to be a success. The roadbed is stable at present. Some settlement has occurred in a few sections, but it has not affected the service of the railway (Lin et al. 2008, Niu et al. 2010).

In the design, a traditional roadbed was used where permafrost was thought to be cold and ice-poor because it cannot cause serious thaw settlement. However, roadbeds in warm or ice-rich permafrost were required to be designed under the “active cooling” principle. The main types of cooling-roadbed adopted were the crushed-rock basement roadbed, the roadbed with slopes covered by crushed rocks, and the U-type crushed-rock roadbed. Among these, the roadbed with slopes covered by crushed rocks (RSCCR) is easiest to construct and is the most convenient for railway maintenance during the lifetime of the roadbed.

Some research results show that the temperature of embankments consisting of coarse rocks with high porosity is lower than the temperature of embankments with other soil types (Goering & Kumar 1996). As explained, this is caused by the Balch Effect (Mikhailov 1971). The coarse rocks act as thermal semi-conductors and cool the underlying soils during the natural cyclic variation in air temperature (Narasimhan 1999). Therefore, the porous rock layer covering the embankment slopes is expected to provide natural air convection during winter and a stable layer of insulating air and solar shading during summer.

In this paper, the thermal status of the RSCCR is discussed based on seven years of in situ measured ground temperature, and the RSCCR is compared to the traditional roadbed.

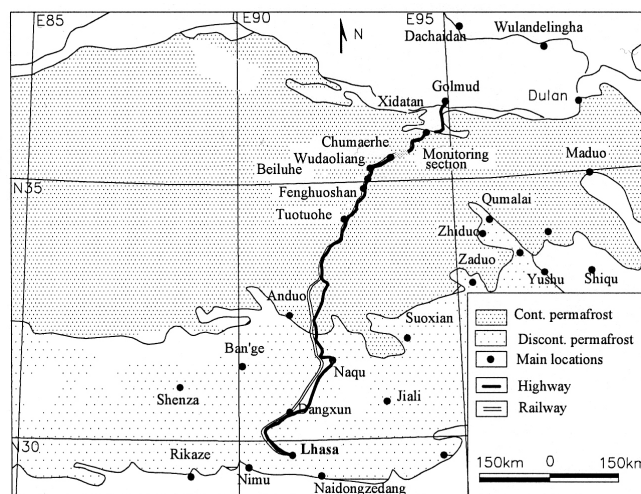


Figure 1. The permafrost distribution and the monitoring section of the different roadbeds of the QTR.

Monitoring Section and Methods

The monitoring section is located in the hinterland of the Qinghai-Tibet Plateau (Fig. 1), where the mean annual air temperature is around -3°C . The ground temperature was manually monitored in boreholes twice a month just after the roadbeds were constructed in 2003. Data were not collected in 2008, when the monitoring work was halted for a year. The monitored traditional roadbed is 4.14 m in embankment height, and the RSCCR is 3.15 m. Ground temperature monitoring boreholes were drilled at the two shoulders and the two slope toes of the railway embankments. Also, a borehole was drilled in the undisturbed ground to monitor ground temperature under natural conditions.

Thermal Regimes of the Traditional Roadbed and the RSCCR

Figure 2 shows the ground temperature in the boreholes beneath two shoulders of the traditional roadbed. Figure 2a shows the temperature changing with time and depth in the borehole on the sunny side shoulder. It indicates that the maximum seasonal thaw depth showed an increasing trend from 2003 to 2006, marked as the changes of the depth of the 0°C isotherm. The depth was 5.8 m from the embankment surface in 2003, and it was 6.6 m in 2006. After that time, the

thaw depth decreased slowly, and the value was 5.3 m from the embankment surface in 2010. The natural permafrost table was 2.1 m in depth during this time. On the other hand, the ground temperature in the deeper soil increased markedly. There was a small part enclosed by the isotherm of -1°C before 2004 which disappeared to a depth of more than 10 m. It is more obvious that the -0.5°C isotherm inclined downward with time. This indicates that the permafrost beneath the sunny side shoulder of the traditional roadbed was degrading.

Figure 2b was drawn with the data obtained from the borehole on the shady side shoulder of the traditional roadbed. The figure shows that the maximum seasonal thaw depth was decreasing during the monitoring period. Just after roadbed construction, the thawing part was within the embankment part, and the maximum thaw depth was 3.8 m from the embankment surface in 2010. Therefore, the depth was much lower than that beneath the sunny side shoulder. Another phenomenon noted is that the ground temperature in the deep soil remained stable, shown by the relatively unchanged position of the -1°C isotherm.

The large differences between the ground temperatures and their development beneath the two shoulders of the traditional roadbed indicate the influence of solar radiation. Such differences should be prevented for the long-term maintenance of the roadbed.

According to the thermal regime characteristics of the traditional roadbed, it was deduced that the upward

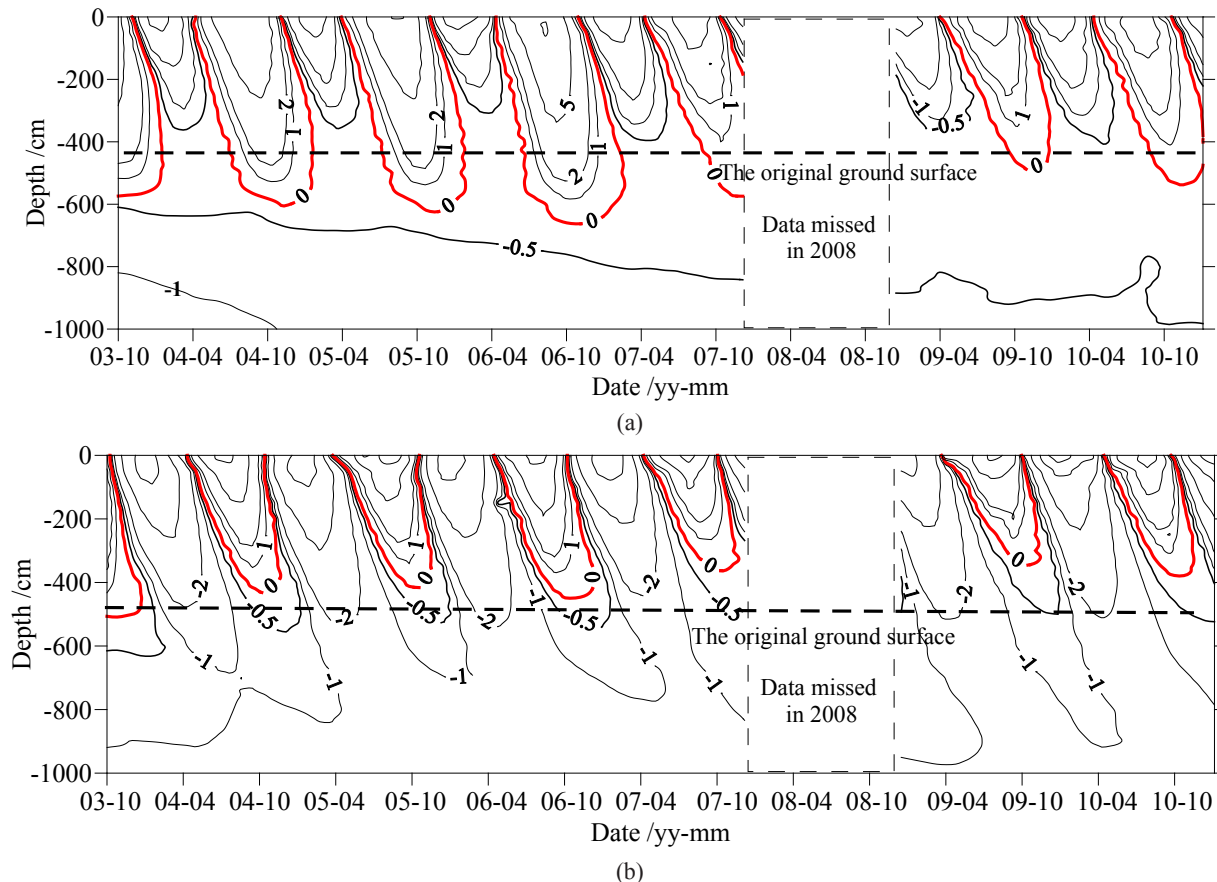


Figure 2. Thermal regime of the boreholes (2003–2010) beneath two shoulders of the traditional roadbed (unit: $^{\circ}\text{C}$). (a) Borehole on the sunny side shoulder; (b) Borehole on the shady side shoulder.

movement of the permafrost table in the traditional roadbed area was at the expense of ground temperature increasing in the deeper soil. This process was an adaptation between the embankment soils and the underlying permafrost through heat exchange; the height of the embankment provided thermal insulation.

Figure 3 shows the ground temperature in the boreholes beneath two shoulders of the RSCCR. On the whole, the maximum thaw depth in the RSCCR was limited to within the embankment portion one year after the slopes were covered by rocks, indicating that the ground temperature under the crushed rocks decreased rapidly. The maximum thaw depth was 2.5 m (Fig. 3a) beneath the sunny side and 2.8 m (Fig. 3b) beneath the shady side embankment surface in 2010. As the embankment height was 3.15 m, the part under the original ground surface was frozen permanently when the roadbed was constructed. Comparing the depth of the natural permafrost table, which was 2.1 m, the artificial permafrost table in the RSCCR did not change too much, considering the depth from the embankment surface.

The two figures in Figure 3 indicate that although the ground temperature beneath the sunny side shoulder was warmer than that beneath the shady side, the maximum thaw depths were nearly same. Such a situation might benefit roadbed stability since the freeze-thaw influences on roadbed soil deformation of both sides were nearly same.

Ground Temperature Fields of the Traditional Roadbed and RSCCR

Figure 4 shows the ground temperature field of the traditional roadbed at the time when the thaw depth reached the maximum value in different years (2003, 2005, 2007, and 2010). As the boreholes at the slope toe on the shady side broke in 2007, the temperature contours in the right part of the figures are missing after that time. However, the temperature fields beneath the main part of the embankment are shown in the figures.

From Figure 4, it is clear that the temperature field was symmetrical in 2003, and the artificial permafrost table was positioned at nearly the same depth as the original permafrost table. However, the temperature beneath the sunny side was higher than that beneath the shady side, as shown by the deepening of the -1°C isotherm on the left side in Figure 4a (September 27, 2003). The difference persisted, apparent as deeper -1°C and -0.5°C isotherms, and as a result the artificial permafrost table beneath the sunny side was progressively deeper before 2007. Meanwhile, the artificial permafrost table and the isolines of negative temperature beneath the shady side moved toward the surface. Therefore, the disadvantages of the traditional roadbed in terms of thermal stability include the increase in the ground temperature, lowering of the artificial permafrost table beneath the sunny side, and also the

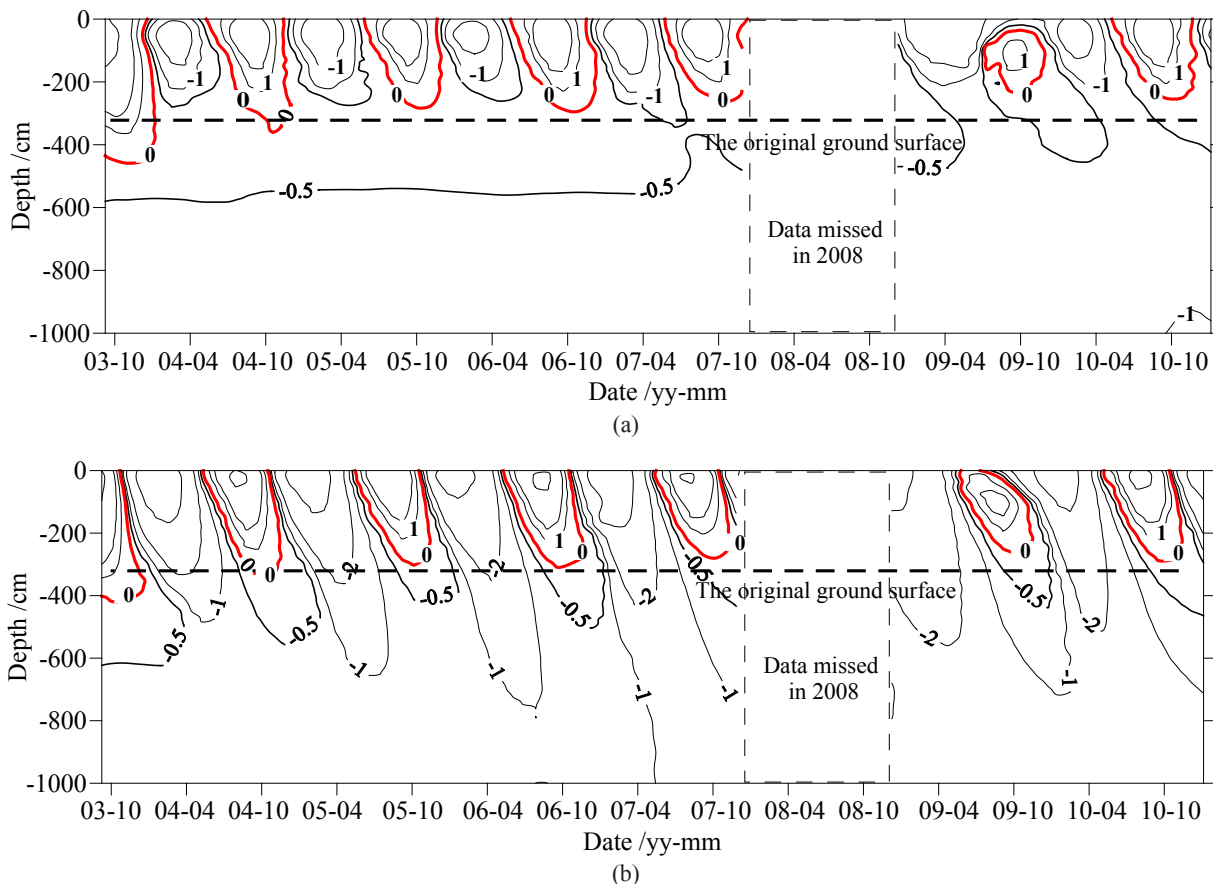


Figure 3. Thermal regime of the boreholes (2003-2010) beneath two shoulders of the RSCCR (unit: $^{\circ}\text{C}$). (a) Borehole on the sunny side shoulder; (b) Borehole on the shady side shoulder.

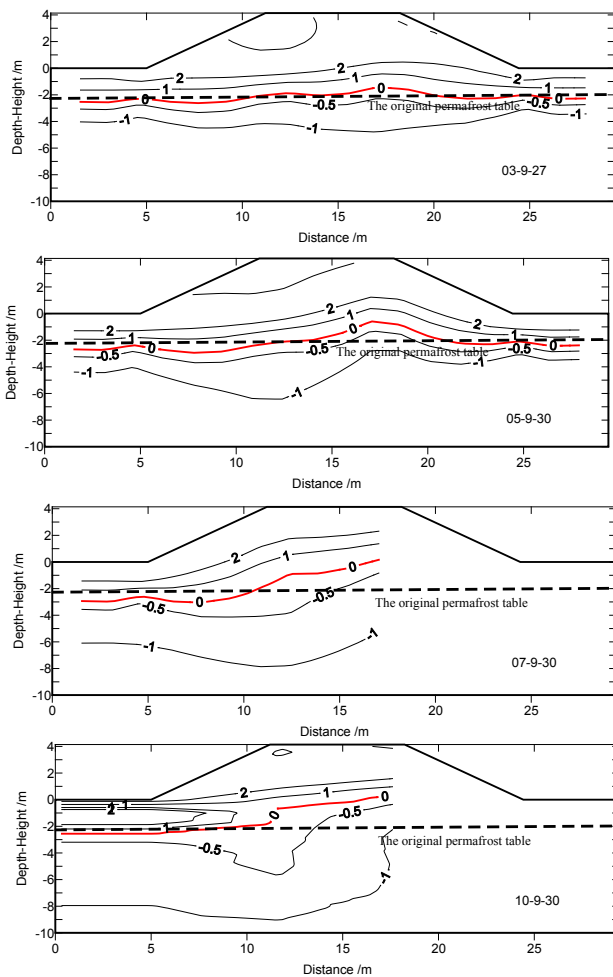


Figure 4. Ground temperature field of the traditional roadbed in different years (unit: °C).

asymmetry of the entire ground temperature field (Zhang et al. 2003).

To compare the ground temperature fields of the traditional roadbed and the RSCCR, Figure 5 was generated based on the measured data. This figure shows the ground temperature field beneath the RSCCR at maximum thaw depth in the years 2003, 2005, 2007, and 2010. The most remarkable characteristic demonstrated in Figure 5 is that the temperature field is highly symmetric. Furthermore, the temperature just beneath the permafrost table was stable, as shown by the shape of the -0.5°C isotherm. Before 2007, the thermal disturbance induced by the embankment fill caused the subsurface temperature to increase slightly, as indicated by the depression of the -1°C isotherm. The increase was limited to 1°C . After 2009, the -1°C isotherm began to rise toward the surface, suggesting that the permafrost at depth was cooling. The depth of this isotherm rose to its original position, except for a small portion in 2010, demonstrating the effectiveness of the crushed rocks on the embankment slope in protecting the underlying permafrost.

The cooling effects of a thickness of crushed rocks have been discussed (Harris & Pedersen 1998, Goering & Kumar 1999, Cheng 2004). In Figure 5, the thickness of the rocks

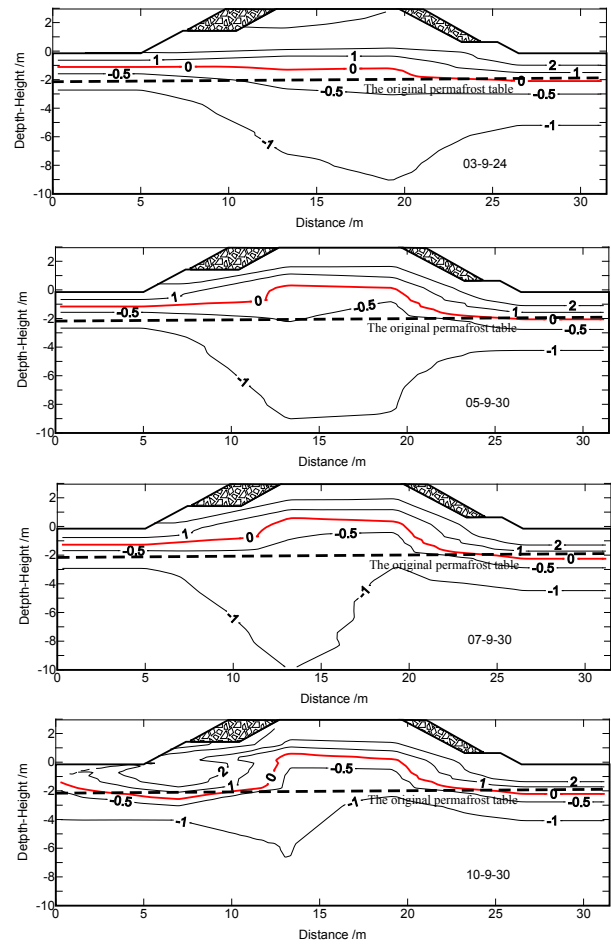


Figure 5. Ground temperature field of the RSCCR in different years (unit: °C).

was 1.6 m on the sunny slope and 0.8 m on the shady slope. The different thickness was applied to adjust the symmetry of the ground temperature field. Comparing the temperature field of the traditional roadbed (Fig. 4), it is clear that RSCCR is a more effective method for cooling the subgrade soils and adjusting the temperature field.

Conclusions

- 1) The traditional roadbed can passively protect the underlying permafrost through the thickness of the embankment. However, the increasing ground temperature beneath the sunny side, the asymmetry of the ground temperature, and the artificial permafrost table might lead to settlement and uneven deformation of the roadbed.
- 2) The most remarkable characteristic of the roadbed with the slopes covered by crushed rocks was that the temperature field was highly symmetric. The ground temperature decreased and the permafrost table was elevated when the slopes were covered by crushed rocks.
- 3) The roadbed with crushed-rock slopes has a much better ability to cool the subgrade soils and adjust the temperature field compared to the traditional roadbed.

Thus it was extensively used in construction of the Qinghai-Tibet Railway and was adopted in the railway maintenance plan.

Acknowledgments

This work was supported in part by the State Key Program of National Natural Science of China (Grant No. 41030741), the Foundation for Innovative Research Groups of the National Natural Science Foundation of China (Grant No. 41121061), the State Key Development Program of Basic Research of China (973 Plan, 2010CB434813), and the Innovation Project of the State Key Laboratory of Frozen Soil Engineering (SKLFSE-ZY-07). Sincere thanks to the editors and reviewers of the Proceedings of the Tenth International Conference on Permafrost.

References

- Cheng, G.D. 2003. Constructing of the Qinghai-Tibet Railroad using the principle of cooling the roadbed. *China Railway Science* 24(3): 1-4 (in Chinese with English abstract).
- Cheng, G.D. 2004. Influences of local factors on permafrost occurrence and their implications for Qinghai-Xizang Railway design. *Science in China (Series D)* 47(8): 704-709.
- Cheng, G.D. 2005. A roadbed cooling approach for the construction of Qinghai-Tibet Railway. *Cold Regions Sciences and Technology* 42: 169-176.
- Goering, D.J. & Kumar, P. 1996. Winter-time convection in open-graded embankments. *Cold Regions Science and Technology* 24(1): 57-74.
- Goering, D.J. & Kumar, P. 1999. Permeability effects on winter-time natural convection in gravel embankments. *Advances in Cold Regions Thermal Engineering and Sciences*. Springer, 455-464.
- Harris, S.A. & Pedersen, D.E. 1998. Thermal regimes beneath coarse blocky materials. *Permafrost and Periglacial Processes* 20(9): 107-120.
- Lin, Z.J., Niu, F.J., & Xu, J. 2008. Secondary freezing-thawing hazards and analysis on their causes along permafrost regions Qinghai-Tibet railway roadbed. *Journal of Engineering Geology* 16(Supp.): 666-673 (in Chinese with English abstract).
- Liu, Y.Z., Wu, Q.B., & Zhang, J.M. 2000. Study on ground temperature field in permafrost regions of Qinghai-Tibet Plateau. Highway 2: 4-8 (in Chinese with English abstract).
- Mikhailov, G.P. 1971. Temperature regime of embankments consisting of coarse rock on permafrost. *Transportation Construction* 12: 32-33 (in Russian).
- Narasimhan, A. 1999. Rayleigh-Be'nard convection: physics of a widespread phenomenon, resonance. *Journal of Science Education* 4 (6): 82-90.
- Niu, F.J., Lin, Z.J., Lu, J.H., Liu, H., & Xu, Z.Y. 2010. Characteristics of roadbed settlement in embankment-bridge transition section along the Qinghai-Tibet Railway in permafrost regions. *Cold Regions Sciences and Technology* 65: 437-445.
- Wu, Q.B., Cheng, G.D., & Ma, W. 2004. The impact of climate warming on Qinghai-Tibetan Railroad. *Science in China (Series D)* 47(Supp.I): 122-130.
- Wu, Q.B. & Zhang, T.J. 2008. Recent permafrost warming on the Qinghai-Tibetan Plateau. *Journal of Geophysical Research* 113 (D13): 148-227.
- Zhang, L.X., Yuan, S.C., & Yang, Y.P. 2003. Mechanism and prevention of deformation cracks of embankments in the permafrost region along Qinghai-Tibetan Railway. *Quaternary Sciences* 23 (6): 604-610.

Effect of Vegetation on Soil-Surface Temperatures in Northern Alaska

Kelsey E. Nyland, Nikolay I. Shiklomanov, Dmitry A. Streletskiy
Department of Geography, George Washington University, Washington, DC, USA

Anna E. Klene
Department of Geography, University of Montana, Missoula, USA

Fredrick E. Nelson
Department of Geography, University of Delaware, Newark, USA

Abstract

This study quantitatively evaluates the degree to which different categories of tundra vegetation, characteristic of the North Slope of Alaska, affect the thermal regime at the soil surface. Data collected from a series of sites representing diverse climatic and landscape settings over a 15-year period (1995–2010) were used to study the spatial and temporal variability of temperatures immediately beneath the vegetation. Evaluation of the thermal effect of vegetation was based on temperature differences between the air and soil surface and thawing n -factors. This assessment of the insulating effects of vegetation helps to better understand the relationship between climatic forces and heterogeneous tundra landscapes. The findings from this research may enhance future permafrost modeling by improving landcover parameterization and understanding of active-layer dynamics.

Keywords: active layer; climate change; N -factor; thawing period; temperature difference; tundra vegetation.

Introduction

Anthropogenic climatic changes are well underway, and the Arctic has been impacted significantly (e.g., Hinzman et al. 2005). However, the relationship between the permafrost system and the warming climate is not direct. Unlike much of the cryosphere lying above or at the ground surface, which can be influenced directly by the climate, permafrost receives a climatic signal that is modified substantially by processes occurring at the surface and within the active layer. In particular, the climatic signal is altered by the insulating effect of natural ground covers such as snow and vegetation. As a result, the magnitude and timing of the signal, even at shallow depths, may not correspond closely to those of the initial climatic forcing. Moreover, the combined effect of climate-induced changes in surface and subsurface processes on the thickness of the active layer and thermal regime of the permafrost can be opposite to the effect of atmospheric warming. For example, an expansion of deciduous shrubs in tundra regions of the Arctic triggered by climate warming may reduce summer thaw propagation and thus offset further permafrost degradation by future temperature increases (Bolk et al. 2010). Several studies have dealt specifically with climate-induced changes to terrestrial vegetation, including an earlier onset of the growing season and more active photosynthesis in the mid-summer months (e.g., Jia et al. 2003, 2009, Goetz et al. 2011). However, these trends do not continue uniformly in time or space but instead vary significantly by vegetation type (e.g., Bunn & Goetz 2006). Previous studies (e.g., Klene et al. 2001, Shiklomanov & Nelson 2002) have demonstrated that vegetation type can serve as a generalized indicator of the spatial variability of soil-surface temperature and active-layer thickness.

In this paper we relate the effects of generalized vegetation type to the soil-surface thermal regime by estimating simple

indices that indirectly account for the complex energy exchange processes within the atmosphere-soil complex. The analysis is based on long-term observations (1995–2010) of air and soil-surface temperatures at an array of sites on the North Slope of Alaska.

Study Area

The study sites are distributed along two parallel north-south transects across the North Slope of Alaska. The North Slope comprises three distinct physiographic provinces, each with distinctive ecological characteristics: the Arctic Coastal plain, Arctic Foothills, and the northern portion of the Brooks Range (Wahrhaftig 1965).

The Arctic Coastal Plain is the northernmost physiographic region in Alaska. Its poorly drained terrain rises very gradually from sea level toward the adjacent foothills. The region has an arctic climate with very low mean annual temperature and annual precipitation. The Arctic Foothills region is a wide area of rolling hills and ridges that grades between the coastal plain on the north and the Brooks Range on the south. The hills and valleys of the region have better-defined drainage patterns than those found in the coastal plain to the north, and have fewer lakes. An arctic climate dominates this region.

A sharp ecological contrast on the North Slope is associated with a difference in pH of the subsurface. Based on soil pH, the foothills province can be classified into nonacidic ($\text{pH} > 6.5$) and acidic ($\text{pH} < 5.5$) components (Walker et al. 1998). While glacial, alluvial, and loess deposits dominate soils of the region, the younger nonacidic tundra has a thin discontinuous organic layer and a mineral horizon relatively unaffected by soil-forming processes. In contrast, soils in older acidic tundra have a thick continuous organic horizon (Bockheim et al. 1998, Walker et al. 1998).

For this study we used the vegetation classification developed by the Circumpolar Arctic Vegetation Map project (CAVM) (Walker et al. 2005). The CAVM broadly classifies North Slope vegetation, from north to south, into bioclimatic tundra subzones C, D, and E. Subzone C has a mean July air temperature of 7 to 9°C and is dominated by wet graminoid and non-acidic tundra with rare inclusions of low semiprostrate and prostrate dwarf shrubs (Jia et al. 2009). Subzone D has a mean July temperature of 9 to 11°C. The vegetation types include predominantly moist acidic and nonacidic tundra with some prostrate dwarf shrubs. The southernmost subzone (E) has a mean July air temperature of 11 to 13°C (Jia et al. 2009) and complex patterns of vegetation. Tussock tundra and extensive water tracks with shrub communities dominate the acidic surfaces while nonacidic surfaces are predominantly covered by sedge, dwarf shrubs, forbs, and mosses (Walker et al. 2005).

Study sites were selected along the dominant regional climatic gradient and are arranged in two (western and eastern) parallel transects. The eastern transect runs along the Dalton Highway, the only road traversing the region from north to south. The western transect includes sites in Barrow, Atqasuk, and Ivotuk (Fig. 1). The landcover categories derived from remote-sensing-based landcover maps of the Kuparuk Region (50 m resolution, Auerbach et al. 1996) and the North Slope of Alaska (1 km resolution, Walker 1999) were used to guide selection of individual site locations. The sampling strategy was based on fieldwork within the Kuparuk River basin showing that areas with similar landcover categories possess similar properties that influence the ground thermal regime.

Five 1-ha sites were selected to represent relatively homogeneous landcover types found in particular physiographic provinces/bioclimatic zones, while two 1-ha sites represent complexity introduced by the water tracks common in the Foothills region. Eight 1-km² sites were selected to represent more generalized conditions found in each physiographic province/bioclimatic zone. All 1-ha and 1-km² sites are part of the Circumpolar Active Layer Monitoring (CALM) network. An array of supplementary point locations were established in areas with climatic and/or edaphic conditions underrepresented by CALM sites. Detailed site descriptions can be found on the CALM website (www.udel.edu/Geography/calm). Three of the point locations were selected to represent barren and/or very sparsely vegetated areas characteristic of mountain tops and the valleys of braided rivers.

Methodology

Each site was instrumented with one to five Onset™ miniature dataloggers connected to probe-type thermistors. Each logger/thermistor unit has an effective temperature range of -50°C to +33°C and resolution of approximately 0.32°C. At each site, one thermistor was placed in a radiation shield approximately 2 m above the ground surface. One to nine thermistors were placed in organic material about 0.02 m below the soil surface, which in turn lies beneath the vegetation layer and in various microtopographic positions within the site.

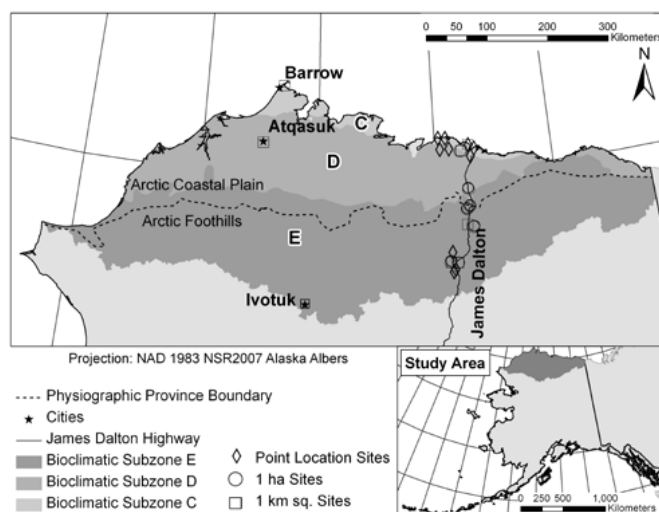


Figure 1. Study site locations and the three bioclimatic subzones of the North Slope of Alaska.

Temperature measurements were collected at intervals of 15 min, 1 hr, and 2 hr, depending on site, season, and year. Details on field procedures can be found in Nelson et al. (1997) and Klene et al. (2001). Data were downloaded annually.

Statistical and Geographic Analysis

Data analysis

Analysis consisted primarily of calculating mean daily temperature from the raw data recorded by loggers. Missing daily temperature values were estimated by correlating data records between at least two neighboring stations (for air temperature) or locations with similar climatic and edaphic conditions. Details about processing of air temperature and soil temperature data can be found in Shiklomanov and Nelson (2003) and Klene et al. (2001), respectively. Auxiliary air temperature data provided by the University of Alaska Fairbanks Water and Environment Research Center (WERC) (<http://ine.uaf.edu/werc/>), the U.S. Department of Agriculture Natural Resources Conservation Service (USDA-NRCS Soil Survey) (<http://www.nrcs.usda.gov/wps/portal/nrcs/home>), and the International Tundra Experiment (ITEX) (<http://www.geog.ubc.ca/itex/>) were used to fill gaps in the data record and to validate trends.

The daily temperature records from 1995 to 2010 were used to estimate mean annual and seasonal temperatures and degree days of thawing (DDT) and freezing (DDF) at 2 m height and at the soil-surface beneath natural covers (vegetation and snow) for each site. Site-specific daily soil-surface temperature records were used to evaluate the length of thawing periods, defined as the number of days in which surface temperatures were consistently above 0°C. Short-term periods of negative surface temperatures occurring during the summer were considered as part of the thawing period.

Site-specific temperature differences associated with the insulating properties of natural covers were estimated by evaluating the difference between seasonal (winter and

summer) and annual temperature values from the air and soil surface (Zhang et al. 1997). In addition, site-specific empirical summer n-factors were calculated as the ratio of annually accumulated DDT at the soil surface to those of the air (Klene et al. 2001).

Spatial integration and mapping

Mean annual/seasonal surface temperatures, length of thawing periods at the soil surface, temperature differences, and summer n-factors from sites possessing similar vegetation and physiographic characteristics were averaged to obtain values characteristic of each vegetation type found within each bioclimatic subzone. Parameters for each bioclimatic subzone were obtained by averaging vegetation-specific values weighted by the area occupied by each vegetation type within that bioclimatic subzone. Estimates of areas occupied by each vegetation type were obtained from the 1-km² resolution landcover map of the North Slope of Alaska (Walker et al. 2005). To produce maps of temperature differences and summer n-factors, vegetation-specific values of these parameters were assigned to corresponding vegetation types on the landcover map of the North Slope of Alaska. The resulting raster maps cover the geographic extent of the North Slope at 1-km² resolution.

Results

Air and soil-surface temperature trends

Subzone specific values of annual, winter (December–February), and summer (June–August) mean values of air and soil-surface temperatures are shown in Figure 2. Regionally, mean annual air temperatures increase inland from the northernmost (Subzone C) to the southernmost (Subzone E) parts of the study area. In summer, the moderating effect of the Arctic Ocean keeps the coastal plain, represented by subzone C, within several degrees of freezing (Kittel et al. 2011). The foothills of the Brooks Range (Subzones D and E) have warmer mean annual air temperatures, owing to the transition from maritime to continental climate (Haugen & Brown 1980). The southernmost subzone (Subzone E) has experienced the most substantial increase in annual temperatures over the past 15 years, with a trend of 0.3°C per year. Subzones C and D show less pronounced annual air temperature trends, with increases of 0.09° and 0.04°C per year, respectively.

Surface temperature exhibits a strong relationship with air temperature in the summer. The soil surface is consistently colder during summer and consistently warmer during winter owing to the insulating properties of vegetation and snow. The temporal variation and magnitude of the differences between the air and soil-surface temperatures in all three bioclimatic subzones is greater in winter than in summer, owing to the insulating effects of snow in addition to that of vegetation (Fig. 2). The greater temporal variability in winter is attributable to the interannual variability in snow depth (Stieglitz et al. 2003, Ling & Zhang 2007). In summer, temperature differences are more consistent on an interannual basis, facilitating climatologic and regional analysis of vegetation effects on soil-surface temperature.

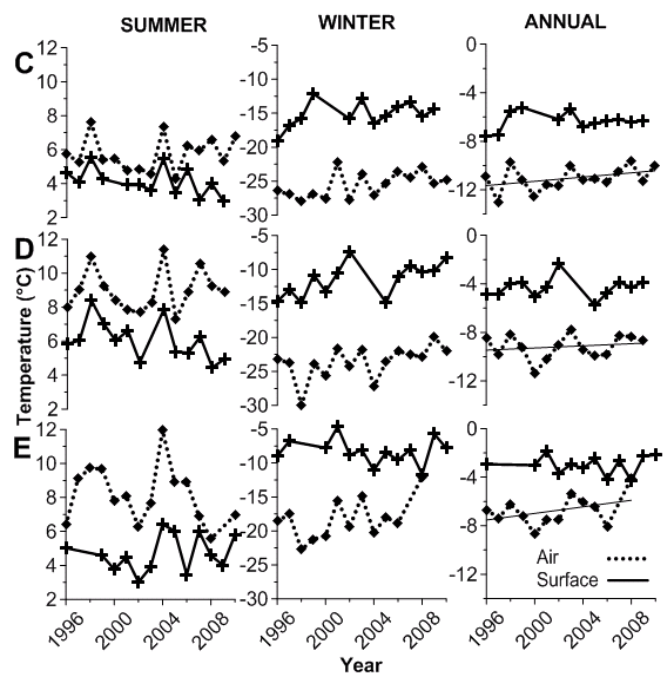


Figure 2. Temporal variability in mean annual, summer, and winter air and soil temperatures. Note differences in y-axes between seasons.

Thermal insulation effects of vegetation

Mean 15-year temperature differences and mean summer n-factors characteristic of each vegetation type and bioclimatic zone are presented in Tables 1 and 2, respectively. Because sites are representative of major landcover categories and because the effect of vegetation on soil-surface temperature, at least during summer, tends to vary in a systematic manner, it is possible to extrapolate local findings to the entire study area based on the landcover map of the North Slope of Alaska by Muller et al. (1999). Calculated vegetation-specific values were assigned to each landcover category in each bioclimatic subzone and extrapolated for the entire region of the North Slope (Figs. 3, 4).

The vegetated surfaces in both physiographic provinces show positive temperature difference values (ΔT) and n-factor values of less than unity, indicating the cooling influence of vegetation on soil surface temperatures during the warm period of the year. The distinct values of ΔT and n-factors indicate the thermal influence of different landcover types characteristic of the three bioclimatic subzones. The moist low-shrub tundra of bioclimatic Subzone E has the largest value of ΔT at 3.85°C and the smallest n-factor value of 0.50. The smallest negative ΔT value of 0.53°C and the highest n-factor value of 0.73 were found in the wet graminoid tundra of bioclimatic Subzone C.

Regionally, ΔT and n-factor values for similar landcover units vary from north to south in response to the increase in density of the vegetation cover. This effect is evident from differences in ΔT and n-factors for moist nonacidic tundra in the three bioclimatic subzones. The thermal influence of vegetation increases along the bioclimatic gradient from Subzone C to Subzone E (north to south). Unvegetated surfaces, which consist primarily of sand, gravel, and bedrock

Table 1. Mean summer differences between air and surface temperature by landcover unit, weighted by area occupied within each bioclimatic subzone. Negative differences indicate a lack of insulation and a warmer soil surface than the air; higher positive differences indicate increased interference through insulation afforded by landcover.

| Landcover Unit | C | D | E |
|------------------------|------|-------|-------|
| Barrens/dry tundra | | -0.18 | -0.88 |
| Moist nonacidic tundra | 1.55 | 1.93 | 2.98 |
| Moist acidic tundra | | | 3.82 |
| Moist low-shrub tundra | | | 3.85 |
| Wet graminoid tundra | 2.43 | 3.29 | 2.43 |
| Weighted Avg. | 1.00 | 2.38 | 3.07 |

Table 2. Summer n-factors by landcover units, weighted by area occupied within each bioclimatic subzone.

| Landcover Unit | C | D | E |
|------------------------|------|------|------|
| Barrens/dry tundra | | 1.05 | 1.14 |
| Moist nonacidic tundra | 0.66 | 0.70 | 0.67 |
| Moist acidic tundra | | | 0.53 |
| Moist low-shrub tundra | | | 0.50 |
| Wet graminoid tundra | 0.73 | 0.57 | 0.72 |
| Weighted Avg. | 0.51 | 0.66 | 0.62 |

along streams and atop hills and mountains, show negative values of ΔT and n-factors greater than unity, indicating the warming influence of barren surfaces on the ground thermal regime. The zonal values presented in Tables 1 and 2 account for areas occupied by each landcover category and, as such, do not directly reflect the arithmetic average of landcover-specific values. Relatively high proportions of barrens are associated with higher elevations in subzone E, substantially decreasing the associated weights assigned when averaging the n-factor values.

Duration of thawing period

Fifteen-year trends for the duration of thawing periods at the soil-surface for each bioclimatic subzone are presented in Figure 5. Subzone E experienced the largest increase in thawing period, with a rate of 0.34 days/year. This increase is attributed to both later dates of freezing and earlier dates of thawing. Subzone C experienced a slight lengthening in the duration of thaw (0.14 days/year) primarily due to later dates of freezing. Although dates of freezing were consistently moving to later dates in Subzone D, much later dates of thawing contributed to overall shortening of the duration of the thawing period. This effect can be partially attributed to a possible increase of snow accumulation and/or an increase in soil moisture and related prolonging of the zero-curtain effect. However, the reason for later initiation of thawing in Subzone D requires further investigation. Considering the 15-year means, Subzone C experienced the shortest duration of thawing season (110 days), while Subzones D and E experienced thawing periods of equal length (118 days).

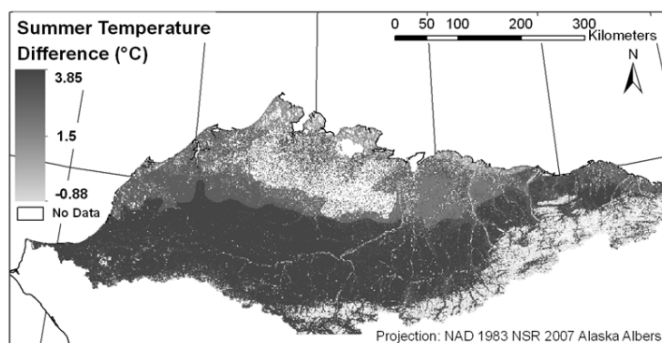


Figure 3. Map of summer temperature difference ($^{\circ}\text{C}$). Each of the landcover units was assigned a calculated value, which was then projected across the entire North Slope to produce this 1-km² resolution map.

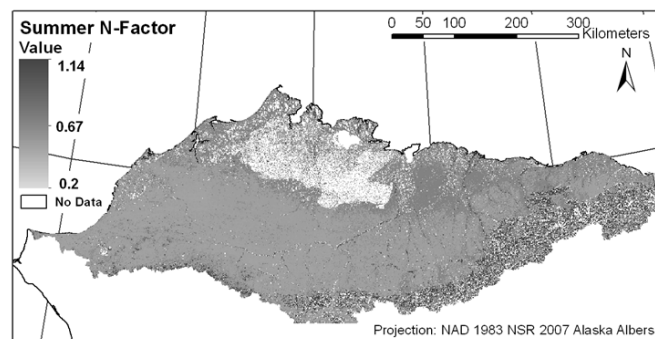


Figure 4. Map of summer n-factors by landcover unit. Each of the landcover units was assigned a calculated n-factor value that was then projected across the North Slope, producing the 1-km² resolution map.

Conclusions

Long-term (1995–2010), regional monitoring of air and soil temperature, conducted as a part of the CALM observational program, has allowed for the quantitative assessment of vegetation effects on soil-surface temperatures. Our results indicate that there are significant differences in the insulation properties between different types of characteristic vegetation on the North Slope of Alaska. The greatest insulation is attributed to shrublands and moist acidic tundra, which at present occur predominantly in bioclimatic Subzone E. These results further confirm the presence of strong negative feedbacks to the permafrost system associated with the thermal insulation effects of vegetation. The northward expansion of taller and denser vegetation associated with climate warming (“arctic greening”) (Blok et al. 2010, Jia et al. 2003, Sturm et al. 2001) may offset permafrost warming because of some of the insulating effects of increased vegetation cover.

This integrative analysis of recent changes in the duration of the thawing period at the soil surface indicates a consistent shift in the onset of freezing to a later date in all three bioclimatic zones. However, thawing begins earlier only in the southernmost subzone (E). Subzone D experienced shortening of the thaw season due to shifting of the onset of thaw to a slightly later date.

The spatial sampling strategy implemented by the CALM program allows for effective extrapolation of field

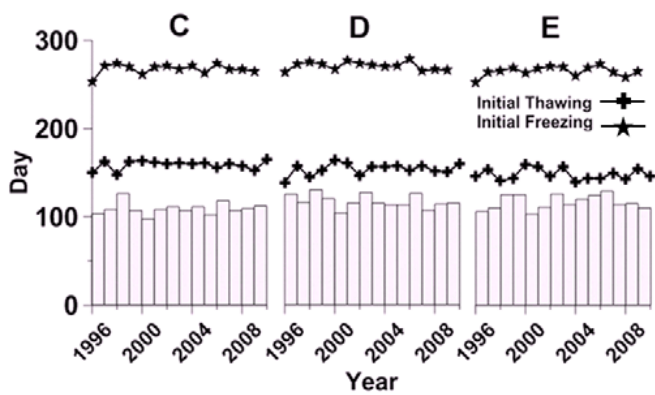


Figure 5. Interannual variability of onset of thawing, freezing, and duration of thaw period. Thawing and freezing days are expressed as Julian days of each year when the temperature begins to remain consistently above or below 0°C (black solid lines) and duration is the total number of days above 0°C per year (vertical grey bars).

observations to the regional scale and development of gridded fields with potential application for a wide range of analytical and modeling studies addressing the effects of climate change on permafrost-affected landscapes.

Acknowledgments

This research was sponsored by U.S. National Science Foundation (NSF) grants OPP-0352957, OPP0352958, and OPP-0856421. Logistical support for fieldwork to collect data was provided by CH2M-Hill, the Barrow Arctic Science Consortium (BASC), and UMIAQ Scientific Services. We thank British Petroleum for granting access to sites located within the Prudhoe Bay oil field. The conclusions expressed in this paper and the use of specific trademark brands do not constitute endorsement by NSF.

References

- Auerback, N.A., Walker, D.A., & Bockheim, J. 1996. *Landcover of the Kuparuk River Basin, Alaska*. (Scale 1:500,000). Joint Facility for Regional Ecosystem Analysis, University of Colorado, Boulder, Colorado.
- Blok, D., Heijmans, M.M.P.D., Schaepman-Strub, G., Kononov, A.V., Maximov, T.C., & Berendse, F. 2010. Shrub expansion may reduce summer permafrost thaw in Siberian tundra. *Global Change Biology* 16: 1296–1305.
- Bunn, A.G. & Goetz, S.J. 2006. Trends in satellite-observed circumpolar photosynthetic activity from 1982 to 2003: The influence of seasonality, cover type, and vegetation density. *Earth Interactions* 10(12): 1–19.
- Goetz, S.J., Epstein, H.E., Alcaraz, J.D., Beck, P.S.A., Bhatt, U.S., Bunn, A., Comiso, J.C., Jia, G.J., Kaplan, J.O., Lilschke, H., Lloyd, A., Walker, D.A., & Yu, Q. 2011. Recent changes in Arctic vegetation: Satellite observations and simulation model predictions. *Eurasian Arctic Land Cover and Land Use in a Changing Climate*. Springer. New York. VI pp. 9–36.

- Jia, G.J., Epstein, H.E., & Walker, D.A. 2003. Greening of Arctic Alaska, 1981–2001. *Geophysical Research Letters* 30(20): doi:10.1029/2003GL018268.
- Jia, G.J., Epstein, H.E., & Walker, D.A. 2009. Vegetation greening in the Canadian Arctic related to decadal warming. *Journal of Environmental Monitoring* 11: 2231–2238.
- Haugen, R.K. & Brown, J. 1980. Coastal-inland distributions of summer air temperature and precipitation in northern Alaska. *Arctic and Alpine Research* 12(4): 403–412.
- Hinzman, L.D., Bettez, N.D., Bolton, W.R., Chapin, F.S., Dyurgerov, M.B., Fastie, C.L., Griffith, B., Hollister, R.D., Hope, A., Huntington, H.P., Jensen, A.M., Jia, G.J., Jorgenson, T., Kane, D.L., Klein, D.R., Kofinas, G., Lynch, A.H., Lloyd, A.H., McGuire, A.D., Nelson, F.E., Oechel, W.C., Osterkamp, T.E., Racine, C.H., Romanovsky, V.E., Stone, R.S., Stow, D.A., Strum, M., Tweedie, C.E., Vourlitis, G.L., Walker, M.D., Walker, D.A., Webber, P.J., Welker, J.M., Winker, K.S., & Yoshikawa, K. 2005. Evidence and implications of recent climate change in northern Alaska and other arctic regions. *Climatic Change* 72: 251–298.
- Kittel, T.G.F., Baker, B.B., Higgins, J.V., & Haney, J.V. 2011. Climate vulnerability of ecosystems and landscapes on Alaska's North Slope. *Regional Environmental Change* 11: S249–S264.
- Klene, A.E., Nelson, F.E., Shiklomanov, N.I., & Hinkel, K.M. 2001. The n-factor in natural landscape: Variability of air and soil-surface temperatures, Kuparuk River basin, Alaska, USA. *Arctic, Antarctic, and Alpine Research* 33(2): 140–148.
- Ling, F. & Zhang, T. 2007. Modeled impacts of changes in tundra snow thickness on ground thermal regime and heat flow to the atmosphere in northernmost Alaska. *Global and Planetary Change* 57: 235–246.
- Muller, S.V., Racoviteanu, A.E., & Walker, D.A. 1999. Landsat MSS-derived land-cover map on northern Alaska: extrapolation methods and a comparison with photo-interpreted and AVHRR-derived maps. *International Journal of Remote Sensing* 20 (15 & 16): 21921–2946.
- Nelson, F.E., Shiklomanov, N.I., Mueller, G.R., Hinkel, K.M., Walker, D.A., & Bockheim, J.G. 1997. Estimating active-layer thickness over a large region: Kuparuk River basin, Alaska, U.S.A. *Arctic and Alpine Research* 29(4): 367–378.
- Shiklomanov, N.I. & Nelson, F.E. 2002. Active-Layer Mapping at regional scales: A 13-year spatial time series for the Kuparuk region, North-Central Alaska. *Permafrost and Periglacial Processes* 13: 219–230.
- Shiklomanov, N.I., Nelson, F.E. 2003. Climatic variability in the Kuparuk Region, North-Central Alaska: optimizing spatial and temporal interpolation in a sparse observation network. *Arctic* 56(2): 136–146.
- Stieglitz, M., Déry, S.J., Romanovsky, V.E., & Osterkamp, T.E. 2003. The role of snow cover in the warming of Arctic permafrost. *Geophysical Research Letters* 30(13): 1721.

- Sturm, M., Racine, C., & Tape, K. 2001. Increasing shrub abundance in the Arctic. *Nature* 411: 546–547.
- Wahrhaftig, C. 1965. Physiographic Divisions of Alaska, U.S. Geological Survey Professional. Paper 482, 52 pp.
- Walker, D.A. 1999. An integrated vegetation mapping approach for northern Alaska (1:4 M scale). *International Journal of Remote Sensing* 20 (15-16): 2895–2920.
- Walker, D.A., Auerback, N.A., Bockheim, J.G., Chapin, F.S., Eugster, W., King, J.Y., McFadden, J.P., Michaelson, G.J., Nelson, F.E., Oechel, W.C., Ping, C.L., Reeburg, W.S., Regli, S., Shiklomanov, N.I., & Vourlitis, G.L. 1998. Energy and trace-gas fluxes across a soil pH boundary in the Arctic. *Nature* 394(6692): 469–472.
- Walker, D.A., Raynolds, M.K., Daniëls, F.J.A., Einarsson, E., Elvebakk, A., Gould, W.A., Katenin, A.E., Kholod, S.S., Markon, C.J., Melnikov, E.S., Moskalenko, N.G., Talbot, S.S., & Yurtsev, B.A., (CAVM Team). 2005. The Circumpolar Arctic Vegetation Map. *Journal of Vegetation Science* 16(3): 267–282.
- Zhang, T., Osterkamp, T.E., & Stamnes, K. 1997. Effects of climate on the active layer and permafrost on the North Slope of Alaska, U.S.A. *Permafrost and Periglacial Processes* 8: 45–67.

Preliminary Development of a Field Tool to Assess the Load Capacity of Frozen Muskeg

James M. Oswell

Naviq Consulting, Inc., Calgary, Alberta, Canada

Ron Coutts

Ardent Innovation, Inc., Calgary, Alberta, Canada

Russell Stancliffe

Imperial Oil Resources Limited

Abstract

This paper documents the development of a preliminary methodology for assessing the short-term load capacity of frozen muskeg. Numerical analyses were used to assess the general behavior of wheel loading on a frozen organic stratum underlain by weak unfrozen soil. The numerical results and the measurement of in situ strength of the frozen stratum can be linked to the factor of safety against a bearing type failure. The Standard Penetration Test (SPT) may be a useful quantitative method to assess the in situ strength, which is a function of organic content, air content, temperature, and other factors. Data are presented for two sites in northern Alberta, Canada, where SPT values were collected, and compared to the unconfined compressive strength from laboratory tests to establish a field strength–laboratory strength relationship. This can then be correlated to the factor of safety for one specific tire load.

Keywords: frozen muskeg; wheel loads; bearing capacity.

Introduction

The strength of frozen subgrades in northern terrain often controls the mobilization of heavy equipment across muskeg and similar organic soils. In these cases, the operators of such equipment presently rely on anecdotal information (traditional knowledge) or rules of thumb as to the necessary frozen thickness needed to facilitate travel on frozen organic soils. If a more rational approach to this problem can be developed, then mobilizing heavy equipment could potentially occur earlier and with greater certainty of safety.

The allowable loading of frozen peat or muskeg terrain by a heavy drill rig was considered in a study by Oswell et al. (2011), in which a numerical analysis of the loading of a 64,000 kg (gross vehicle mass) drill rig over a thin layer of frozen muskeg and underlain by unfrozen muskeg was reported. Figure 1 illustrates a suite of failure surfaces for a heavy vehicle on a thin (0.4 m) layer of frozen muskeg. Rationally, there are a large number of combinations of muskeg thicknesses and frozen strengths that could be used to support any given vehicle load. The numerical modeling and factor of safety calculations provide a theoretical basis to assess the load capacity of frozen muskeg. The modeling shows that the load capacity of frozen muskeg is controlled by both the strength (as quantified by the frozen muskeg cohesion) and the thickness of the frozen muskeg layer.

The numerical study reported by Oswell et al. (2011) was very useful in showing that there were certain combinations of frozen strength and frozen thickness that could achieve a safe travel layer. However, the question remained as to how to assess the strength of the frozen layer and how to then translate that strength into an allowable wheel load for a vehicle.

Figure 2 presents factors of safety for the critical failure mode as determined by Oswell et al. (2011); it represents a potential assessment tool to determine the required thickness of the frozen surface layer. It requires only knowledge of the frozen layer strength and the frozen thickness. This paper explores how this information can be applied to develop a field assessment tool.

Strength of Frozen Organic Soils

The strength of frozen muskeg is a function of many factors including temperature, loading (strain) rate, ice content, unfrozen water content, air content, salinity, muskeg fabric, and likely others. It may be useful to consider combining these factors into a single strength parameter. One such potential field tool that could provide an assessment of the frozen strength of organic soils is the Standard Penetration Test (SPT) (ASTM 2008). The SPT uses a thick-walled split sample tube with an outside diameter of 50 mm, an inside diameter of 35 mm, and an overall length of 650 mm. This sampler is driven into the ground by blows from a slide hammer with a weight of 63.5 kg (140 lb), dropping a fixed distance of 760 mm (30 inches). The sample tube is driven into the ground 450 mm with the number of blows per 150 mm of penetration recorded. The SPT N-value is the number of blows for the final 300 mm of penetration. The blow count provides an indication of the density or consistency of the material. The N-value has been correlated to the unfrozen strength of both fine-grained and coarse-grained soils (Terzaghi & Peck 1948). However, data on the N-values recorded in frozen soils are very limited, and there is even less information on frozen muskeg and peat materials.

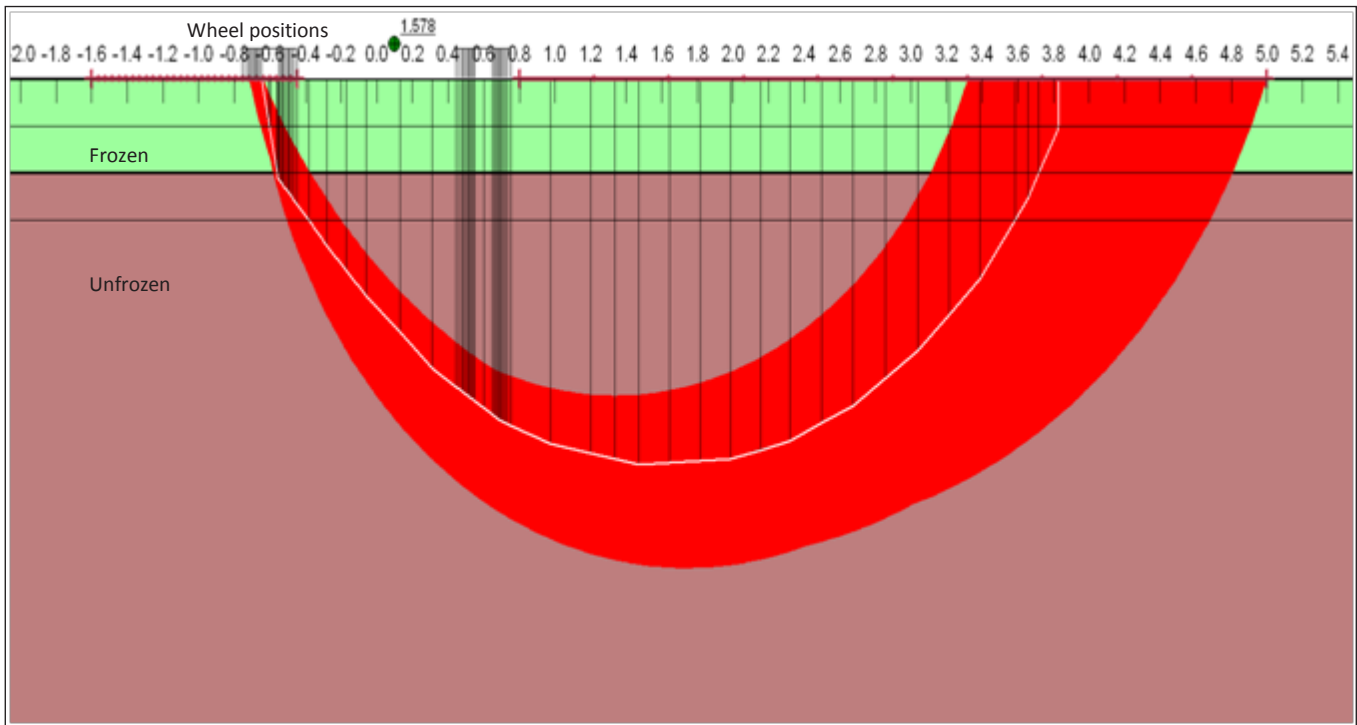


Figure 1. Stability analysis for a frozen thickness of 0.4 m with a cohesion intercept of 50 kPa. The red band represents the zone of similar failure planes, and the white line represents the critical failure plane. This deep failure plane, encompassing both axles, extends into the unfrozen muskeg underlying the frozen layer (from Oswell et al. 2011).

The desire of using the SPT as a field assessment tool is its simplicity. The derived N-values may be a combined function of many independent variables including ground temperature, water content, muskeg fabric, and other factors.

As part of this study, SPT blow counts were gathered from a number of sites in two different geographic areas in northern Alberta. Figure 3a presents the SPT blow count for the in situ testing at two geographic locations. Examination of this figure shows that there are two important aspects to consider. First, there is a clear difference in blow counts between Site M and Site C, with Site M blow counts consistently higher than the Site C values. The differences in blow counts, which reflect strength differences, may be the result of either muskeg fabric differences, or ground temperatures, or both. In situ temperature measurements showed that at the 0.6 m depth ground temperatures at Site C were generally warmer (and in some cases above freezing) than the Site M test locations. The warmer ground temperatures render weaker muskeg and lower blow counts.

Second, for both datasets, there is a consistent shape to the blow count with depth response. The blow counts increase and then decrease with depth. It is likely that the response is a function of the frozen strength of the muskeg. Near the ground surface the muskeg may be weakening in response to the warming air temperatures (the testing was completed in early spring at a period of rising daily air temperatures). With depth, the frozen strength of the muskeg is higher, but then it decreases as the ground temperature warms toward 0°C at the seasonal frost line. For both geographic locations, the peak blow counts occur at about 0.45 m depth.

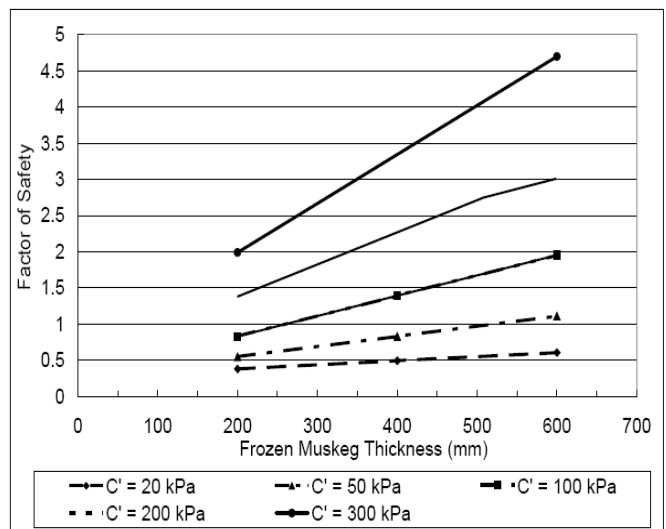


Figure 2. Factor of safety as a function of frozen muskeg thickness for a variety of effective cohesion values (from Oswell et al. (2011)).

Figure 3b presents the blows per 150 mm penetration. The data follow the same trend as the SPT N-values but include the near surface layer.

Nottingham and Christopherson (1983) reported limited data on the penetration of the SPT sampler based on 150 mm penetration rather than the full 300 mm penetration specified for the official blow counts. These data are shown graphically on Figure 4, combined with ground temperatures. The relationship between the 1/2N-value and soil temperature is

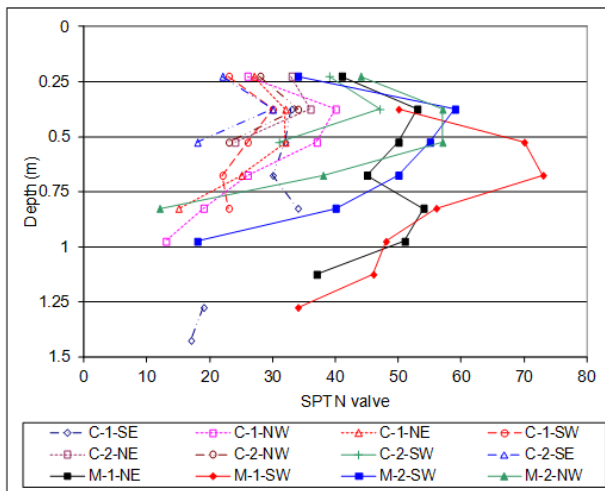


Figure 3a. SPT blow counts per 300 mm penetration by SPT sampler versus depth. Locations denoted “C” are from Site C and locations denoted “M” are from Site M.

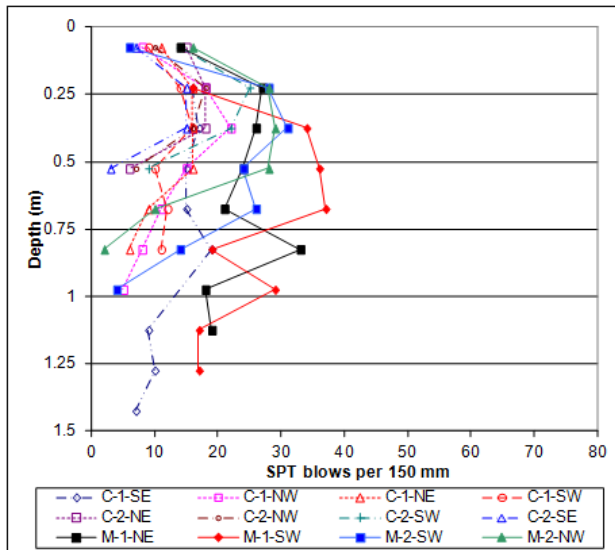


Figure 3b. Blow counts per 150 mm penetration by SPT sampler versus depth. Locations denoted “C” are from Site C and locations denoted “M” are from Site M.

very linear ($R^2 = 0.99$). It is interesting to observe how the muskeg data lie along the same general trend as the mineral silt soil data reported by Nottingham & Christopherson (1983).

While the relationship in Figure 4 is interesting, it is insufficient to estimate the strength of frozen materials. For the present study, a number of unconfined compression tests on frozen muskeg samples were conducted to assist in the development of a relationship between SPT N-value and shear strength. The shear (undrained) strength (C_u) is taken as one-half of the unconfined compressive strength, as measured in the laboratory tests. Figure 5 presents the undrained strength as a function of the SPT N-value (at approximately the same depth) for the available data. These data have been presented separately for the Site C and Site M geographical areas, as there appears to be a clear difference between the two datasets. A tentative relationship between the cohesion and SPT value. In the case of Site C, two high-strength values were ignored in

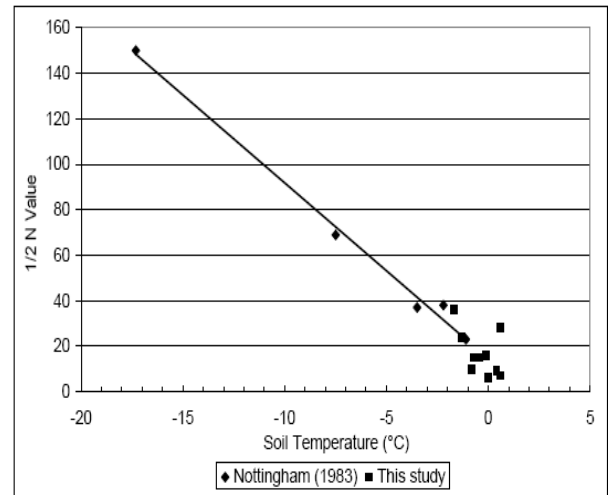


Figure 4. The $\frac{1}{2}N$ -value (SPT blows for 150 mm penetration) as a function of soil temperature. Data presented from Nottingham & Christopherson (1983) for silt and from this study for muskeg. The solid line is the linear correlation for the Nottingham & Christopherson (1983) data ($R^2 = 0.99$).

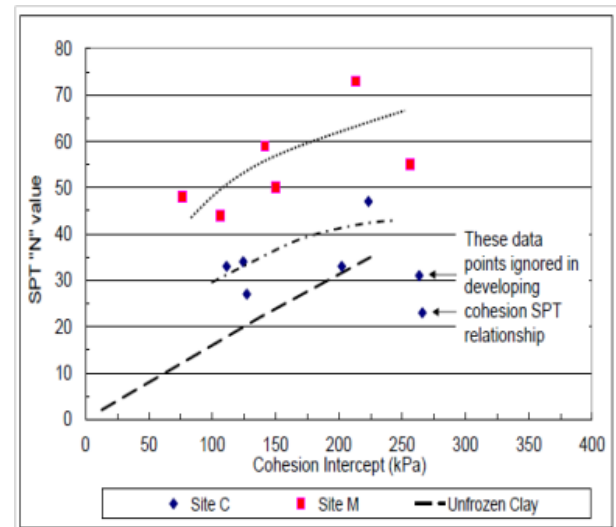


Figure 5. SPT “N” value as a function of cohesion intercept. An approximate correlation curve for each data set is shown. The black dashed line is a commonly used relationship between SPT value and undrained (cohesion) shear strength (data from Terzaghi and Peck, 1948).

developing the Site C relationship. Also shown on the figure is the published relationship between undrained strength (cohesion) and SPT value for unfrozen clay (Terzaghi & Peck 1948).

There are conceptual issues with the relationships shown in Figure 5. Intuitively one would expect or hope that a single relationship could be derived between the cohesion intercept and SPT value rather than the site-specific relationships shown. No information is available as to why the two sites exhibited different responses. As presented, the data suggest that site-specific data, including laboratory testing of undisturbed samples to determine the compressive strength, are required. This may impede the development of a general muskeg

loading relationship or tool. It is considered that additional field and laboratory testing will be needed to further develop this relationship.

Other relationships could also be considered, pending collection of sufficient data. For example, the frozen strength dependency on temperature is known to be an important issue. Relationships of in situ and laboratory strength as a function of temperature could provide additional insights into the behavior of the frozen materials. Measurement of the temperature profile through the frozen layer could also be performed.

Development of a Preliminary Frozen Muskeg-Vehicle Load Capacity Tool

Figure 6 (Oswell et al. 2011) presents a derived relationship between frozen layer strength and frozen layer thickness for two factors of safety. Figure 5, used in conjunction with Figure 6, represents a preliminary form of the field tool to assess the safety axle loading of frozen layers. Figure 5 uses field measurements to estimate the frozen layer strength on a site-specific basis. Figure 6 then estimates the required frozen layer thickness necessary to support the modeled axle load of 37,500 kg. In theory, if a single frozen strength versus SPT value can be developed for a wide range of muskeg materials, then a single plot of SPT value versus frozen thickness can be developed for fixed factors of safety for a specified load criterion. As noted, temperature dependency on frozen strength needs to be considered and verified that strength increases with declining (colder) temperatures are reflected by the SPT values.

This approach considers only the strength of the frozen muskeg material. It does not address environmental impacts or the need to protect the muskeg surface from tire damage, or longer term impacts of muskeg damage. To provide some level of protection to the muskeg, a layer of compacted snow or ice is often used to reduce damage of the vegetative mat.

It may be argued that to confirm the strength of the muskeg necessary to support a vehicle, a vehicle equipped with an SPT device needs to be mobilized. However, it is likely that such testing equipment can be mounted on a 4x4 pick-up truck with a gross vehicle mass much less than the very heavy (e.g., 65,000 kg) mobile drill rig that would need to traverse the muskeg.

Conclusions

As noted, the combined application of Figure 5 and Figure 6 represents a potential tool for assessing the necessary thickness of a frozen muskeg layer for a specified factor of safety. The factors of safety are specific to a wheel axle load of 37,500 kg. They assume that the muskeg fails in a general shear, bearing capacity-type failure, and that the underlying unfrozen materials have non-zero shear strength.

Additional development of this procedure is needed in several areas. First, the lack of a unique correlation between SPT N-value with depth (or undrained strength) for different muskeg materials (Fig. 5) is problematic. It is desirable that

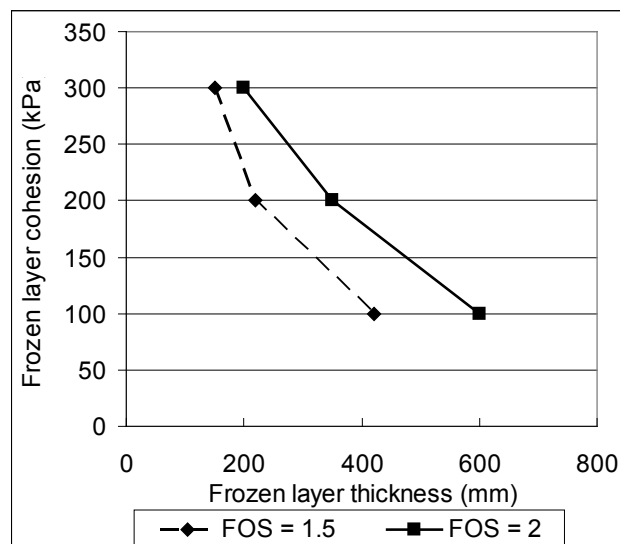


Figure 6. Relationship between frozen layer strength and required frozen layer thickness for fixed factors of safety. The loading scenario consists of two axles of eight wheels with each axle carrying a total load of approximately 37,500 kg. (from Oswell et al. 2011).

a single relationship be developed such as that reported for unfrozen fine-grained soils. Additional field testing and measurements are needed to explore this issue further. Second, the factor of safety for any frozen muskeg thickness (Figure 6) is a function of the applied wheel load. Additional numerical modeling is desirable to develop a normalized relationship for factor of safety and frozen thickness.

This study has shown that a methodology for assessing the bearing capacity of frozen muskeg to heavy traffic loads could likely be developed with additional assessment of the strength and load capacity of frozen muskeg. Application of such a methodology would be used by transport and exploration companies to rationally assess the muskeg strength at the onset of winter and thus maximize the available time window for winter operations.

References

- American Society for Testing and Materials. 2008. *ASTM D1586 - 08a Standard Test Method for Standard Penetration Test (SPT) and Split-Barrel Sampling of Soils*. West Conshohocken, Pennsylvania, USA. America Society for Testing and Materials.
- Nottingham, D. & Christopherson, A.B. 1983. Design criteria for driven piles in permafrost. Prepared for State of Alaska, Department of Transportation and Public Facilities. 40 pp.
- Oswell, J.M., Stancliffe, R., Coutts, R., Karambelkar, V., & Wood, M. 2011. Allowable drill rig wheel loads on frozen muskeg. *Proceedings, Arctic Technology Conference*, Houston TX, February 7-9, 2011. Paper OTC 22035.
- Terzaghi, K. & Peck, R.B. 1948. *Soil Mechanics in Engineering Practice*. New York, NY, Wiley & Sons.

Ground Ice Conditions in University Valley, McMurdo Dry Valleys, Antarctica

W.H. Pollard

Department of Geography, McGill University, Montreal, Canada

D. Lacelle

Department of Geography, University of Ottawa, Ottawa, Canada

A.F. Davila, D. Andersen

SETI Institute/Carl Sagan Center for the Study of Life in the Universe, Mountain View, California, USA

C.P. McKay, M. Marinova, J. Heldmann

NASA Ames Research Center, Space Science Division, Moffat Field, California, USA

Abstract

This paper presents preliminary observations on the distribution and nature of ground ice in University Valley located in the Quartermain Mountains of the McMurdo Dry Valleys. University Valley lies in the ultraxerous soil zone characterized by extreme cold and aridity. Shallow coring and excavations in 2009 and 2010 documented widespread ice-cemented ground beneath polygonal terrain that displayed an increasing depth to the ice table in a down valley direction. Two bodies of massive ground ice were also discovered. The first, adjacent to a small glacier at the head of University Valley, is interpreted as glacier ice buried by a rock slide. The second body of massive ice is at the mouth of the valley in an area of polygonal moraine. GPR surveys revealed that the first ice body is continuous and extends about 5–6 m beneath a thin boulder-rich debris layer. Geochemical analyses support a buried glacier origin for both massive ice bodies and indicate that they are undergoing sublimation at a rate of 3.0 to $5.0 \times 10^{-5} \text{ mm yr}^{-1}$.

Keywords: ground ice; ice-cemented sediment; massive ice; GPR; McMurdo Dry Valleys; stable isotopes.

Introduction

Ground ice is an important geologic component of near surface sediments in areas underlain by permafrost. The study of ground ice characteristics and its environmental significance have been part of permafrost and engineering studies in the North American Arctic since the 1940s and even earlier in Russia. Recently the investigation of ground ice has become a focus of cryostratigraphic and paleoenvironmental studies in the McMurdo Dry Valleys (MDV) of Antarctica (e.g., McKay et al. 1998, Marchant et al. 2002, Pollard et al. 2002, Dickinson & Rosen 2003, Levy et al. 2006, Swanger et al. 2010). Apart from a few earlier studies that mention ground ice, ice wedges and ice-cemented sediments (Black 1973), the main source of ground ice information for the MDV was related to descriptions of ice-cored moraines (Stuiver et al. 1981), rock glaciers (Hassinger & Mayewski 1983), and soils (Campbell & Claridge 1969, Ugolini 1963). The paleo-environmental emphasis in Antarctic ground ice studies, and questions concerning its long-term stability and sublimation processes, are the result of the identification of buried Miocene glacier ice in Beacon Valley by Sugden et al. (1995) and Marchant et al. (2002). Beacon Valley is part of a small group of inland ice-free valleys located in the Quartermain Mountains (Fig. 1). This group of dry valleys is notable not only because of extreme cold and arid conditions, but also because of the very old and complex nature of the landscapes and sediments; for example, some glacial drift sequences date 11.3 Ma (Marchant et al. 1993, 2002).

The aim of this paper is to characterize ground ice conditions in University Valley based on observations from shallow

excavations, coring, geophysical surveys, and geochemical measurements. These observations yield insights on the distribution, nature, and stability of ground ice under extreme conditions. This study also suggests that the higher tributary valleys have been subject to geomorphic regimes that differ from Beacon and Arena Valleys.



Figure 1. Location of University Valley in the Quartermain Mountains. (Source: Antarctic Geospatial Information Center. Satellite imagery copyright Digital Globe, Inc. Provided by NGA Commercial Imagery Program.)

Background

The MDV is an area of hyper-arid, cold polar desert conditions located between 76–79°S and 158–170°E along the western coast of the Ross Sea in southern Victoria Land, Antarctica. The MDV is the largest ice-free region in Antarctica covering roughly 15,000 km² of which ~6700 km² is snow and ice free (Vincent 1996, Bockheim et al. 2007). Mean annual air temperatures in the MDV range between -20°C and -35°C (Marchant et al. 2002), typically less than 100 mm (water equivalent) of precipitation per year, and measured sublimation rates of 150 to >1000 mm a⁻¹ (Clow et al. 1988). The MDV is divided into three microclimatic/soil zones: Zone 1, the coastal or subxerous zone, where summer temperatures exceed 0°C and hence a seasonal melt phase develops; Zone 2, an intermediate, or xerous zone typical of the inland valleys, where temperatures rise above 0°C for short periods and liquid water is periodically present; and Zone 3, the ultraxerous zone located adjacent to the polar plateau, where summer maximum air temperatures do not exceed 0°C and little or no melting of snow and/or ice occurs (Campbell & Claridge 1969, 1987, Marchant & Denton 1996, Bockheim et al. 2007, Marchant & Head 2007). The ultraxerous zone is perhaps the most extreme terrestrial permafrost environment where unique processes can occur.

Study Site

University Valley (77°52'S, 163°45'E; 1700–1750 m a.s.l.) is one of four small, north-facing valleys perched about 450 m above Beacon Valley in the Quartermain Mountains. University Valley is approximately 1.5 km wide and 4 km in length, with a small glacier (University Glacier) and perennial snowfield at the head of the valley (Fig. 2). The uneven valley floor is mantled with a thin veneer of glacial drift in which (non-sorted) polygonal ground has formed that covers more than 80% of the surface.

The bedrock consists of Devonian-Triassic sandstones and siltstones of the Beacon Supergroup intruded by Jurassic sills and dikes of Ferrar Dolerite (Marchant et al. 2002). University Valley lies in the ultraxerous zone which, together with the steep valley sidewalls, contributes extensive shading that limits potential soil warming by insolation. According to Bockheim (2007), surfaces higher than 1500 m a.s.l. in this region are covered by the highly oxidized, salt-rich Altar till that dates to 11.3 Ma. Bockheim's (2007) map also shows a rock glacier covering most of the University Valley floor.

Methods

To investigate distribution and conditions of ground ice under different ice table depths, we collected four cores of ice-cemented permafrost from ice table depths of 0, 1, 10, and 40 cm, and also cores from two bodies of massive ground ice using a SIPRE corer (Figs. 2, 3). Additionally, samples of loose cryotic sediments overlying the massive ice were collected from shallow excavations. The ground ice cores were sub-

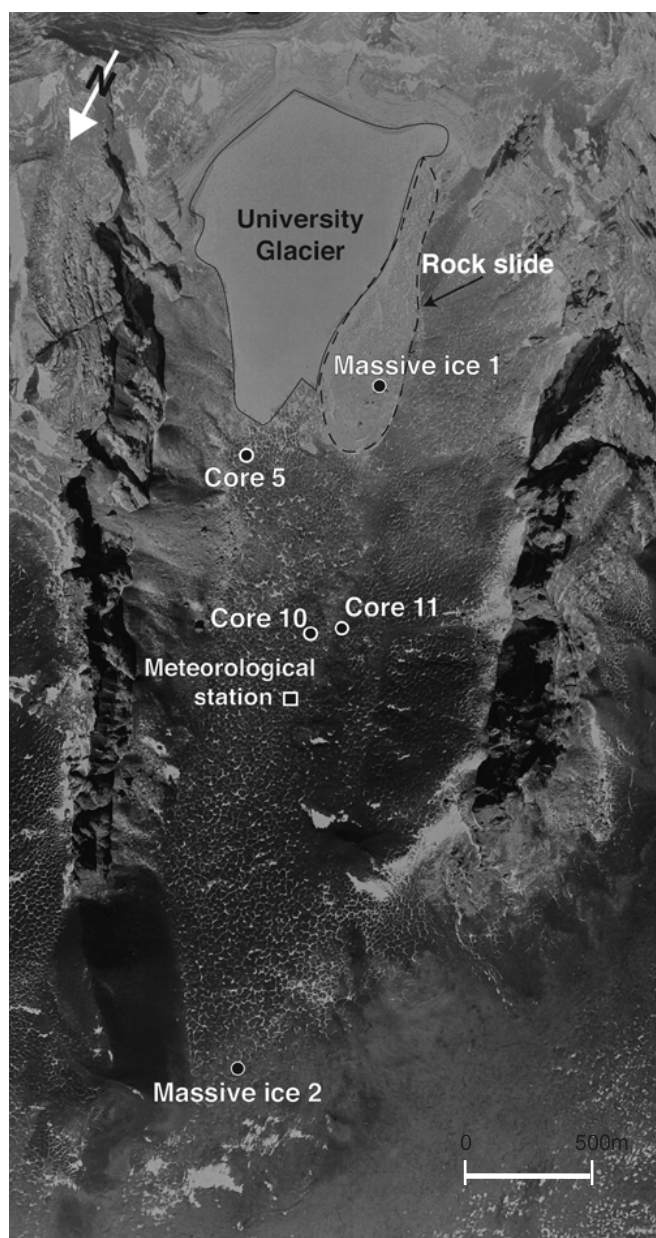


Figure 2. Vertical air photograph of University Valley, MDV, showing location of the two bodies of massive ground ice and coring sites of ice-cemented soils (1993). TMA ID: CA30790299, 11/21/1993 courtesy of the U.S. Geological Survey & the Polar Geospatial Center.

sampled at 2 cm intervals using a circular rock saw, allowed to melt in sealed plastic bags, filtered, and then transferred into 50 ml polypropylene centrifuge tubes. Once in the bottles, the excess ice content was determined based on the volume of water and sediments. For all samples, the pH and conductivity were measured using a VWR multi-parameter meter and then analyzed for major anions and stable O-H isotopes. Only the water isotope measurements are presented here as these parameters yield insights into processes that affect their origin and stability such as condensation, absorption, sublimation, freezing, and melting (Lacelle 2011, Lacelle et al. 2011). The ¹⁸O/¹⁶O and D/H ratios of water samples were determined using a liquid water analyzer (Los Gatos Research Liquid water

analyzer model 908-0008) with an analytical reproducibility for $\delta^{18}\text{O}$ and δD is $\pm 0.3\%$ and $\pm 1\%$, respectively.

The depth, thickness, and extent of the two massive ice bodies were determined by a combination of shallow excavations (along a series of longitudinal transects) and ground penetrating radar (GPR). In the latter, a series of single fold fixed-offset reflection profiles were collected, using a Sensors and Software (S&S) PulseEKKO Pro system with 100 and 200 MHz center frequency unshielded transmitter and receiver. Antenna separations (in a parallel broadside configuration) of 100 cm and 50 cm, and step sizes of 25 and 10 cm, respectively, provided signal penetration to depths of 5–8 m. GPR data were analysed using S&S EKKO View Deluxe software. We collected 64 stacks at each position along the survey line, and fiducial marks were inserted into the data file every few meters and at critical structures to ensure that the recorded transect spacing was in agreement with the on-ground geometry.

Results

The ubiquitous presence of polygonal terrain throughout the floor of University Valley suggests the extensive presence of ground ice (Levy et al. 2009). As such, there is a need to characterize the ground ice conditions in University Valley, where unique climatic conditions are encountered, to facilitate comparisons with visually similar ground ice deposits in adjacent Beacon Valley and elsewhere in the MDV.

Ground ice distribution

Based mainly on observations from Beacon and Arena Valleys, Bockheim (1995) and Bockheim et al. (2007) suggest that permafrost in the Quartermain Mountains is predominantly dry (59%) in nature (lacking ground ice) with only 37% ice-cemented and 4% characterized by excess ground ice. Our field surveys in University Valley provided a very different ground ice picture. First, two separate bodies of massive ice have been identified. The first is located at the head of the valley immediately south of University Glacier, while the second is near the mouth of the valley in an area of low hummocky moraine. These ice bodies occupy 14–15% of the shallow permafrost in the valley. Approximately 75% is underlain by ice-cemented ground dominated by pore ice, thin ice lenses, and ice coatings. The remaining 10–11% was either bedrock, loose talus, or simply dry cryotic, which occurred as small outliers of Beacon sandstone in the mid-valley and as talus aprons that line both sides of the valley but better developed on the north side.

Soil pits and shallow coring at more than 50 locations in University Valley provided a clear pattern of increasing depth to ice table in a down valley direction, measuring 0 cm at the foot of the glacier to more than 70 cm at the mouth of the valley (Marinova et al. in review). However, in any one area, the ice table is relatively uniform and smooth. At all locations, sediments above the ice table consist of dry cryotic sediments. This variation in depth to ice table may be the result of varying snow recurrence intervals, with higher snow recurrence near the head of the valley acting as a recharge mechanism and resulting in

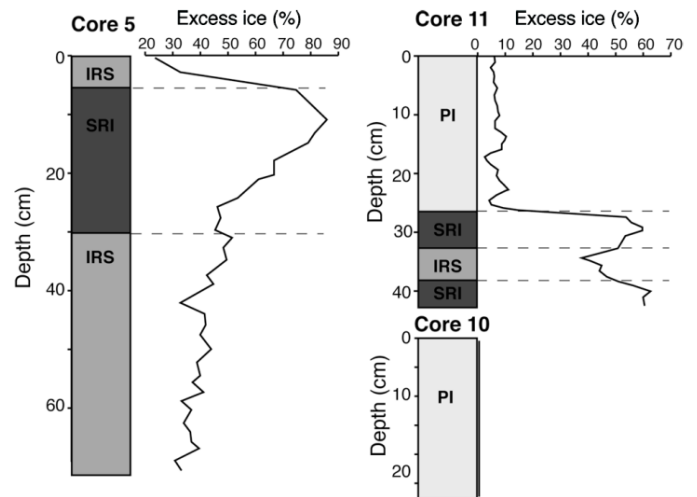


Figure 3. Excess ice content in near-surface permafrost in University Valley. Core 11: ice table depth 0 cm; Core 5: ice table depth 1 cm; Core 10: ice table depth 10 cm. See Figure 2 for location of cores in University Valley. (Legend for cryofacies – IRS=ice-rich sediment, PI=Pore ice and SRI=sediment-rich ice.)

stable shallow ice (McKay 2009, Marinova et al. in review).

The ice-cemented ground cores collected under increasing ice table depth (0, 1, and 10 cm) show varying excess ice content (Fig. 3). Core 11, obtained directly below a perennial snow patch (ice table depth of 0 cm), has an excess ice content of 10% within the upper 25 cm of the core (pore ice cryofacies). Below 25 cm, the ice content rapidly increases to values between 35 and 62%, producing two zones of sediment-rich ice (25–34 cm and 39–43 cm) separated by an ice-rich sediment cryofacies. The excess ice content in Core 5 (ice table depth of 1 cm) rapidly increases from 25% at the surface to 84% at 11 cm depth. Below this level, the ice content in the sediments progressively decreases to 30%. Based on this excess ice content, three units are defined: 1) 65–27 cm, ice-rich sediments; 2) 27–6 cm, sediment-rich ice; and 3) 6–0 cm, ice-rich sediments. Finally, Core 10 (ice table depth of 10 cm), which measures 20 cm and was collected 10 m adjacent to Core 11, has no excess ice and corresponds to a pore ice cryofacies.

Extent of massive ground ice

Two separate bodies of massive ground ice have been identified. The first is located at the head of the valley immediately south of University Glacier, while the second is near the mouth of the valley in an area of low hummocky moraine (see Fig. 2).

The first massive ice body forms the core of an elongated tongue of white, non-sorted, poorly weathered Beacon Sandstone immediately below Slump Mountain (Fig. 4). This unit includes angular sandstone boulders (but no dolerite) ranging in diameter from a few decimeters to more than 4–5 meters in a 15–30 cm thick coarse to medium sand matrix. Large boulders frequently have numerous cobbles and small boulders perched on them. The surface debris layer is dry and loose and rests on the ice. The unconformable contact between the sediments and the underlying massive ice is abrupt and uneven; the ice

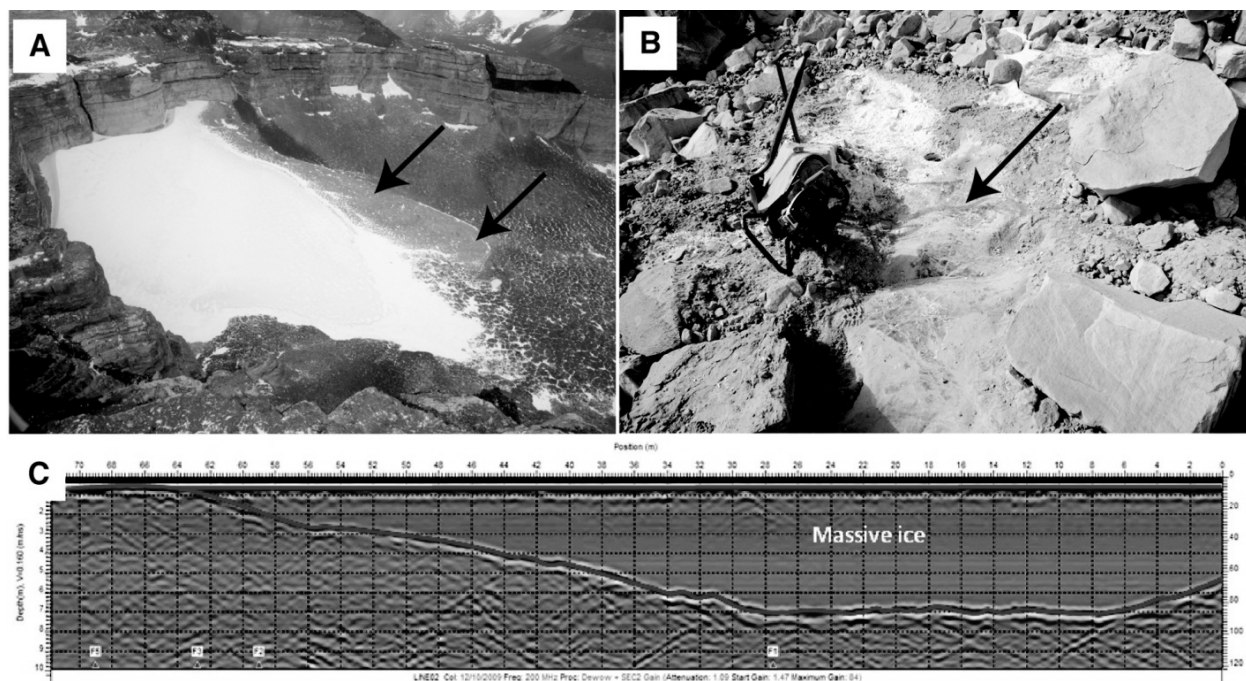


Figure 4. A) University Glacier and rock slide, denoted by arrows. B) Massive ice (arrow) deposit formed by burial of glacier ice by a rock slide (corer and ice axe for scale). C) GPR profile of the lower part of the debris slide along a transect from middle of the slide (position 1) to the down slope edge (position 62) and 10 m of run out. This survey used 200MHz antenna, 50 cm separation and a 10 cm step. A velocity of 0.16 m/ns derived from CMP surveys was used to interpret ice thickness.

surface is characterized by shallow depressions beneath larger clasts and high points between boulders. GPR profiles indicate that the massive ice ranges in thickness from 3 to 7 m and underlies most of the debris layer, but is thickest in the middle of the deposit (Fig. 4C). The massive ice appears relatively clean with an abrupt lower contact. Excavation at the side of the deposit revealed ice cemented drift similar to the materials down valley. The overlying sediments had also buried areas of polygonal ground. Based on the shape of the deposit, the angular nature of the debris, and the fan shape of the lower part of the feature, it would appear that a rock slide buried a section of University Glacier (Fig. 2). Other evidence for a rock slide burial origin includes the absence of any of the overlying sediment within the ice body, the fresh unweathered nature of debris slide material compared with the highly weathered sandstone on the valley floor, and that the down slope and south sides of the slide material buries the weathered sandstone and dolerite that covers the valley floor. Further, δD - $\delta^{18}O$ composition of the ice body plots along a regression slope similar to that of the adjacent University Glacier (Lacelle et al. 2011), supporting the interpretation that the ice body represents a portion of the glacier buried by rock slide.

The second massive ice body occurred near the mouth of the valley in hummocky moraine terrain. Excavation and coring revealed 200+ cm of brownish, bubble-rich ice unconformably overlain by 30–45 cm of light brown (7.5YR 6/4) to pinkish (7.5YR 7/4) drift characterized by a fine sand silt matrix and sub-angular sandstone cobbles and boulders and rounded dolerite cobbles. The ice was accessible along the sides of polygon troughs, while in polygon centres the

massive ice is overlain by 15–25 cm of ice cemented drift and 20–25 cm of dry drift. Ice contents ranged from 85 to 95%vol for the massive ice, 30 to 40%vol in the ice-cemented drift, to <15%vol in the loose surface materials. The massive ice was bubble-rich and contained disseminated fine sediment and fine gravel. GPR surveys suggest that this ice body is highly non-uniform in thickness and distribution. Further, δD - $\delta^{18}O$ composition of the ice body plots along a regression slope similar to that of the adjacent University Glacier (not shown), supporting the interpretation that the ice body is buried glacier.

Discussion

Stability and age of buried glacial ice bodies

Lacelle et al. (2011) assessed the stability of the body of massive ground ice adjacent to the glacier by measuring $\delta^{18}O$ with depth. Here we assess the stability of a second body of massive ground ice discovered in 2010 at the mouth of University Valley and compare the results to those of the up-valley ice body (Fig. 5). The $\delta^{18}O$ values of the massive ground ice body at the valley mouth show an exponential decrease in the uppermost 15 cm, from a maximum value of -25.6‰ at the top of the ice to -29.9‰ at 15 cm depth. Below this, the $\delta^{18}O$ values progressively decrease from -29.6 to -30.2‰. Although with higher $\delta^{18}O$ values, this $\delta^{18}O$ profile is very similar to that measured in the massive ground ice body situated adjacent to the glacier (Fig. 5). By comparison, the $\delta^{18}O$ values of the glacier fluctuate between -30.9 and -28.1‰ with depth; however, the $\delta^{18}O$ values do not trend along an upward convex profile.

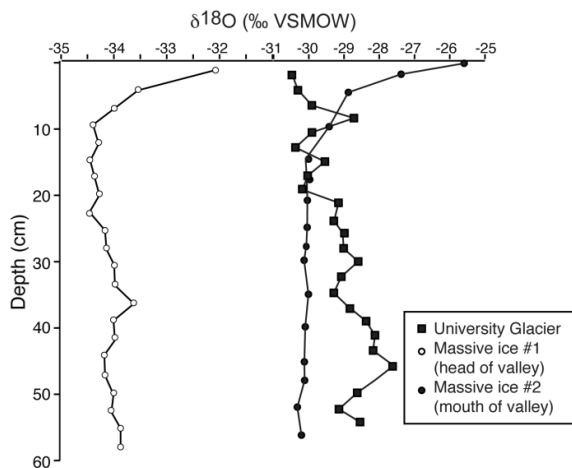


Figure 5. $\delta^{18}\text{O}$ depth profiles of glacier and massive ice bodies in University Valley, MDV.

The upward convex $\delta^{18}\text{O}$ profiles measured in both massive ground ice bodies suggest that the ice is undergoing sublimation, and such profiles have been observed in firm ice (e.g., Sommerfield et al. 1986, Friedman et al. 1991, Stichler et al. 2001, Sokartov & Golubev 2009). The upward convex $\delta^{18}\text{O}$ profiles reflect two competing processes during sublimation: the downward diffusion of heavy water molecules (HD^{16}O and H_2^{18}O) concentrated at the surface during evaporation/sublimation, and the upward migration of light water molecule that sustains the evaporation/sublimation flux. Lacelle et al. (2011) used a modified sublimation-diffusion model to calculate net ice loss rate and time expected to reach the measured $\delta^{18}\text{O}$ profile. Using equations 1, 2, and 3 in Lacelle et al. (2011) with an estimated ice temperature of -20°C (the average annual temperature of near-surface permafrost in Beacon Valley) (Kowalewski et al. 2011), the calculated net ice loss rate of the massive ground ice body at the mouth of the valley is $3.0 \times 10^{-5} \text{ mm yr}^{-1}$. The net ice loss rate is similar to that from the head of the valley ($5.0 \times 10^{-5} \text{ mm yr}^{-1}$ at -20°C), but slower than the predicted sublimation rate in Beacon Valley using a 2D numerical model ($2.2 \times 10^{-3} \text{ mm yr}^{-1}$) (Kowalewski et al. 2012). However, net ice loss rates are very sensitive to changes in air temperatures, with ice loss rates decreasing with colder air temperatures. Therefore, the colder air temperatures in University Valley due to the higher elevation (ca. 450 m above the floor of Beacon Valley) can result in a lower net ice loss rate.

Using Ramseier ^{18}O diffusion coefficient and the calculated net ice loss rates, the time required to achieve the $\delta^{18}\text{O}$ profile can be calculated, which yields insights into the time of burial of the glacial ice bodies. Although both buried glacial ice bodies yielded similar net ice loss rate values, the time required to achieve the $\delta^{18}\text{O}$ profile is much longer at the mouth of the valley (1,150 ka yr) compared to the ice body adjacent to the glacier (414 ka yr). This result suggests that University Valley was most likely glaciated at about 1,150 ka yrs ago, which corresponds to an early Pleistocene glacial period (marine isotope stage 34 or 36) (Williams et al. 1988).

Conclusions

Our observations indicate that ground ice is a more common component of near-surface permafrost (upper 1–5 m) in University Valley than reported for Beacon and Arena Valleys. We show that ice-cemented ground is present beneath 75% of the valley while massive ice underlies up to 15%. The massive ice is buried glacier ice related to at least two different burial and preservation processes. In one case, a rock slide has buried a portion of University Glacier, and subsequent retreat of the glacier has isolated the ice-cored slide as a distinct landform. Although lobate in shape, this feature lacks any discernible flow structure related to ice creep; hence, a rock glacier designation as suggested by Bockheim et al. (2007) is not considered. Our interpretation is further supported by the structure of this feature in that the debris layer associated with the original rock slide rests on the ice and has not been incorporated into the ice body. Accordingly, the area mapped as a rock glacier by Bockheim (2007) is incorrect.

The second body of massive ice occurs in an area of hummocky moraine near the valley mouth. The young age of this ice relative to the age of ice and sediments in Beacon Valley suggests that this ice body is derived from a relatively recent period of alpine glaciation. The paucity of active melt features (fresh channels, frozen runoff, or frozen pools) reflects the extreme cold. Furthermore, isotope geochemical data indicate a sublimation-dominated cryogenic system, which is unique to the upper MDV. Given that University Valley is perched 450 m above Beacon Valley, and its orientation and narrow width limit insolation, it is reasonable to conclude that this cryological system represents one of the most extreme ground ice environments in the McMurdo Dry Valley area.

Acknowledgements

This research was supported by NASA's ASTEP program with field support from NSF-OPP (Project B302). We wish to acknowledge Brad Herried and the Antarctic Geospatial Information Center (AGIC) for help with Antarctic mapping. Satellite imagery copyright Digital Globe, Inc. Provided by NGA Commercial Imagery Program. The authors also wish to acknowledge comments from two anonymous reviewers.

References

- Black, R., 1973. Growth of patterned ground in Victoria Land, Antarctica. In *Permafrost: North American Contribution*. Second International Conf. NAS, Washington DC; 193-203.
- Bockheim, J., 1995. Permafrost distribution in the southern circumpolar region and its relation to the environment: a review and recommendations for future research. *Permafrost and Periglacial Processes* 6, 27-45.
- Bockheim, J. 2007. Soil processes and development rates in the Quartermain Mountains, upper Taylor Glacier region, Antarctica. *Geografiska Annaler* 89A: 153-165.
- Bockheim, J., Campbell, I., & McLeod, M. 2007. Permafrost distribution and active-layer depths, McMurdo Dry Valleys, Antarctica. *Permafrost and Periglacial Processes* 18, 217-227.

- Campbell, I. & Claridge, G. 1969. A classification of frigid soils – the zonal soils of the Antarctic. *Soil Science* 107, 75-85.
- Campbell, I. & Claridge, G. 1987. *Antarctica: Soils, Weathering Processes and Environment*. Elsevier: Amsterdam, 368 pp.
- Clow, G.D., McKay, C.P., Simmons, G. Jr., & Wharton, R. 1988. Climatological observations and predicted sublimation rates at Lake Hoare, Antarctica. *Journal of Climate* 1, 715 – 728.
- Dickinson, W. & Rosen, M. 2003. Antarctic permafrost: an analog for water and diagenetic minerals on Mars. *Geology* 31, 199–202.
- Friedman, I., Benson, C., & Gleason, J. 1991. Isotopic changes during snow metamorphism. In *Stable Isotope Geochemistry: a tribute to Samuel Epstein*. Geochemical Society, Special Publication No.3. Eds. H.P. Taylor Jr., J.R. O'Neil, I.R. Kaplan. pp. 211-221.
- Hassinger, J. & Mayewski, P. 1983. Morphology and dynamics of rock glaciers in southern Victoria Land, Antarctica. *Arctic and Alpine research* 15, 351-368.
- Kowalewski, D.E., Marchant, D.R., Swanger, K.M., & Head, J.W. III. 2011. Modeling vapour diffusion within cold and dry supraglacial tills of Antarctica: Implications for the preservation of ancient ice. *Geomorphology* 126, 159-173.
- Kowalewski, D.E., Marchant, D.R., Head, J.W. III, & Jackson, D.W. 2012. A 2D model for characterizing first-order variability in sublimation of buried glacier ice, Antarctica: assessing the influence of polygon troughs, desert pavements and shallow subsurface salts. *Permafrost and Periglacial Processes* doi:10.1002/ppp.731
- Lacelle, D. 2011. On the $\delta^{18}\text{O}$, δD and D-excess relations in meteoric precipitation and during equilibrium freezing: theoretical approach and field examples. *Permafrost and Periglacial Processes* DOI: 10.1002/ppp.712.
- Lacelle, D., Davila, A., Pollard, W., Andersen, D., Heldmann, J., Marinova, M., & McKay, C. 2011. Stability of massive ground ice bodies in University Valley, McMurdo Dry Valleys of Antarctica: using stable O-H isotopes as tracers of sublimation in hyper-arid regions. *Earth and Planetary Science Letters* 301, 403-411.
- Levy, J., Head, J., & Marchant, D. 2009. Cold and dry processes in the martian Arctic: geomorphic observations at the Phoenix landing site and comparisons with terrestrial cold desert landforms. *Geophys. Res. Lett.* 36, doi:10.1029/2009GL040634.
- Levy, J., Marchant, D., & Head, J. 2006. Distribution and origin of patterned ground on Mullins Valley debris covered glacier, Antarctica: the roles of ice flow and sublimation. *Antarctic Science* 18 385-397.
- Marchant, D.R. & G.H. Denton. 1996. Miocene and Pliocene paleoclimate of the Dry Valleys region, southern Victoria Land: A geomorphological approach. *Marine Micropaleontology* 27, 253-271.
- Marchant, D. & Head, J. 2007. Antarctic Dry Valleys microclimate zonation, variable geomorphic processes and implications for assessing climate change on Mars. *Icarus* 192, 187-222
- Marchant, D., Denton, G., & Swisher, C. 1993. Miocene-Pliocene-Pleistocene glacial history of Arena Valley, Quartermain Mts, Antarctica. *Geographiska Annaler* 75A, 269-302.
- Marchant, D.R., Lewis, A.R., Phillips, W.M., Moore, E.J., Souchez, R.A., Denton, G.H., Sugden, D.E., Potter, N., & Landis, G.P. 2002. Formation of patterned ground and sublimation till over Miocene glacier ice in Beacon Valley, southern Victoria Land, Antarctica. *Geological Society of America*. Bulletin, 114, 718-730.
- Marinova, M.M., McKay, C.P., Pollard, W.H., Heldmann, J.L., Davila, A.F., Andersen, D.T., Jackson, W.A., Lacelle, D., Paulson, G., & Zacny, K. (in review). Distribution of the depth to ice-cemented soils in the high-elevation Quartermain Mountains, Dry Valleys of Antarctica. *Antarctic Science*.
- McKay, C.P., Mellon, M.T., & Friedmann, E.I. 1998. Soil temperatures and stability of ice-cemented ground in the McMurdo Dry Valleys, Antarctica, *Antarctic Sci.*, 10, 31-38.
- McKay, C.P. 2009. Snow recurrence sets the depth of dry permafrost at high elevations in the McMurdo Dry Valleys of Antarctica. *Antarctic Science* 21, 89-94.
- Pollard, W.H., Doran, P., & Warton, R. 2002. The nature and significance of massive ground ice in Ross Sea Drift, Garwood Valley, McMurdo Sound. *Royal Society of New Zealand Bulletin* 35, pp. 397-404.
- Sokratov, S. & Golubev, V. 2009. Snow isotopic content change by sublimation. *Journ. of Glaciology* 55, 823-828.
- Sommerfeld, R.A., Friedman, I., & Nilles, M. 1986. The fractionation of natural isotopes during temperature gradient metamorphism of snow. Chemistry of Seasonal Snowpacks. NATO Advanced Study Institute, Les Arcs, France, July 1986.
- Stichler, W., Schotterer, U., Fröhlich, K., Ginot, P., Kull, C., Gäggeler, H., Pouyaud, B. 2001. Influence of sublimation on stable isotope records recovered from high-altitude glaciers in the tropical Andes. *Journal of Geophysical Research* 106, 22,615-22,620.
- Stuiver, M., Yang, I., Denton, G., & Kellogg, T. 1981. Oxygen isotope ratios of Antarctic permafrost and glacier ice. In: McGinnis, L.D. (ed.) Dry Valley Drilling Project. AGU Ant. Res. Series, 33, 131-139.
- Sugden, D.E., Marchant, D.R., Potter, N., Souchez, R.A., Denton, G.H., Swisher, C.C., & Tison, J.-L. 1995. Preservation of Miocene glacier ice in East Antarctica. *Nature* 376, p. 412-414.
- Swanger, K.M., Marchant, D.R., Kowalewski, D.E., & Head, J.W. III. 2010. Viscous flow lobes in central Taylor Valley, Antarctica: origin as remnant buried glacial ice. *Geomorphology* 120, 174-185.
- Ugolini, F. 1963. Soil investigations in the lower Wright Valley. In *Proceedings of the First International Permafrost Conference*. NAS/NRC, 1287, 55-61.
- Vincent, W. (ed.). 1996. Environmental management of a cold desert ecosystem: the McMurdo Dry Valleys, DRI. University of Nevada, spec. pub, 57 pp.
- Williams, D.F., Thunell, R.C., Tappa, E., Rio, D., & Raffi, I. 1988. Chronology of the Pleistocene oxygen isotope record: 0-1.88 m.y. B.P. *Palaeogeography, Palaeoclimatology, Palaeoecology* 64, 221-240.

Numerical Estimation for Settlement of Roadway Embankment in Permafrost Regions

Jilin Qi, Songhe Wang, Fan Yu

State Key Laboratory of Frozen Soils Engineering, Cold and Arid Regions Environmental and Engineering Research Institute, Chinese Academy of Sciences, Lanzhou, Gansu, China

Abstract

Settlement is one of the main engineering problems for roadway embankments in permafrost regions. It results from a series of physical and mechanical processes (e.g., thaw consolidation, creep, and freeze-thaw cycling). To analyze the multi-source settlement, a three-dimensional thaw consolidation theory and the Lubby2 creep model were numerically implemented. The settlement of an embankment section along the Qinghai-Tibet highway was selected for analysis. Results show that the simulated settlement agrees in general with in situ monitoring data. Within the section considered, thaw consolidation and creep mainly occur in a silty clay layer. Displacement from thaw consolidation and creep were analyzed.

Keywords: cold regions engineering; settlement source; thaw consolidation; creep.

Introduction

Permafrost degradation has been aggravated due to global warming and increasing engineering activities in cold regions over the last century. As a consequence, engineering problems related to freezing and thawing pose a potential threat to the long-term stability of cold regions engineering. Among these problems, settlement is one of the main and prevalent occurrences in permafrost regions (Cheng & Yang 2006).

In situ observation indicates that settlement results from a series of complicated physical and mechanical processes. Andersland & Ladanyi (1994) pointed out that settlement of shallow foundations can be attributed to five types of deformation, including instantaneous elastic, instantaneous plastic, viscoelastic, consolidation, and creep. As far as a permafrost embankment is concerned, further compaction of fill soil, thaw settlement, and compression of warm frozen soil were considered to be the main settlement sources (Wu & Liu 1989, Liu et al. 2002). Zhang et al. (2003) highlighted the effects of freeze-thaw cycling. Zhang et al. (2007) further proposed that thaw consolidation and compression of permafrost are the main causes of embankment settlement. Considering the mechanism, Qi et al. (2007) suggested that thaw consolidation, creep of the warm frozen layer, and compression due to freeze-thaw cycling in the active layer are the three sources of settlement.

Previous work has focused primarily on the computation of a single settlement source. For reasonable estimation of settlement of infrastructures in cold regions, the idea of multi-source settlement proposed by Qi et al. (2007) will be numerically implemented by ADINA finite element analysis software in this paper.

Constitutive Model for Each Settlement Source

Thaw consolidation

In situ monitoring data reveal that thaw consolidation was the primary source of the settlement in cold regions. In previous

studies, it was generally described by two separate processes: thaw settlement (free of load) and consolidation. For the former, it was usually estimated by a thaw-settlement coefficient and has been applied in the design of civil engineering structures in cold regions. However, the thaw-settlement coefficient is only a rough estimation as it does not consider consolidation under surcharge loads. For the later, the consolidation theory of unfrozen soils was used. Taking it as one entire process, a one-dimensional thaw consolidation theory was first proposed by Morgenstern & Nixon (1971). Yao (2010) further proposed a three-dimensional thaw consolidation theory by combining the heat transfer equation with phase change and Biot consolidation theory. The equation for heat conduction in the soil layers can be described as follows:

$$-\nabla \cdot \mathbf{q}^T + q_v^T = \rho c \frac{\partial T}{\partial t} \quad (1)$$

where q and q_v represent the heat flux vector and volumetric heat-source intensity, respectively. ρ and c are the unit weight and heat capacity of soil, respectively.

A linear elastic model is used for simulating the stress-strain relationship of soil while the fluid movement is described by Darcy's law.

Numerical implementation and application in the analysis of test results demonstrated its efficacy, and is therefore used in the subsequent analysis.

Creep

Creep of frozen soil generally occurs under a relatively high state of stress. However, in situ monitoring of settlement of different layers showed that within a warm frozen layer, obvious creep deformation occurred beneath the subgrade under the stress range of highway engineering. Thus it cannot be neglected for settlement analysis, especially in terms of continuous permafrost degradation.

In previous studies, the engineering model (Ladanyi 1972) and viscoplastic model (Vyalov 1987) were usually applied in the analysis. Moreover, thermodynamic models (Andersland

& Akili 1967, Andersland & Noury 1970, Fish 1980, 1983) and damage theories (Miao et al. 1995, He et al. 1999) were introduced, although limited to theoretical studies to date. Among the abovementioned models, the element model (based on the combination of basic mechanical elements) was suggested to describe creep in a permafrost subgrade for convenience in numerical implementation.

In practical application, the Lubby2 model in ADINA was selected for the calculation of creep deformation. It can be expressed as (ADINA R&D Inc. 2008):

$$e^c = \left[-\frac{1}{G_k} \exp\left(-\frac{G_k}{\eta_k} t\right) + \frac{t}{\eta_M} + \frac{1}{G_k} \right] \sigma \quad (2)$$

where

$$\eta_M = \eta_M^* \exp(m\sigma)$$

$$G_k = G_k^* \exp(k_1\sigma)$$

$$\eta_k = \eta_k^* \exp(k_2\sigma)$$

and $m, k_1, k_2, \eta_M^*, G_k^*,$ and η_k^* are material parameters, corresponding to the required input parameters a_0, a_1, a_2, a_3, a_4 and a_5 in the ADINA platform; e^c is the effective creep strain at time t . Due to the closed form relationship with stress state and temperature, the Lubby2 model can reasonably describe the rheological behavior of geo-materials under a complex thermal regime.

Freeze-thaw cycling

The physical and mechanical properties of soil under freeze-thaw cycling clearly alter (e.g., permeability, cohesion, and internal friction angle) (Qi et al. 2006). The permeability of fine-grained soil generally increases after a certain number of freeze-thaw cycles. The porosity of densely compacted soil increases from the disturbance, while in loose soil it decreases due to freeze-thaw induced compaction. Currently, the freeze-thaw induced deformation cannot be reflected by any constitutive model. At the same time, it has been found that freeze-thaw cycling may lead to further deformation in the first 5–6 cycles (Eigenbrod 1996). Therefore, the effect of freeze-thaw will not be taken into consideration in this study.

Numerical Implementation of Multi-Source Settlement in Permafrost Subgrade

An embankment section along the Qinghai-Tibet highway was selected for study. The specific geometric model for numerical calculation was assumed symmetric. The engineering geological conditions are illustrated in Figure 1.

Determination of model parameters

The mechanical properties of frozen soil varied with temperature. Young’s modulus and Poisson’s ratio can be estimated by the following equations:

$$E = a_1 + b_1 * \text{abs}(T)^m \quad (3)$$

$$v = a_2 + b_2 * \text{abs}(T) \quad (4)$$

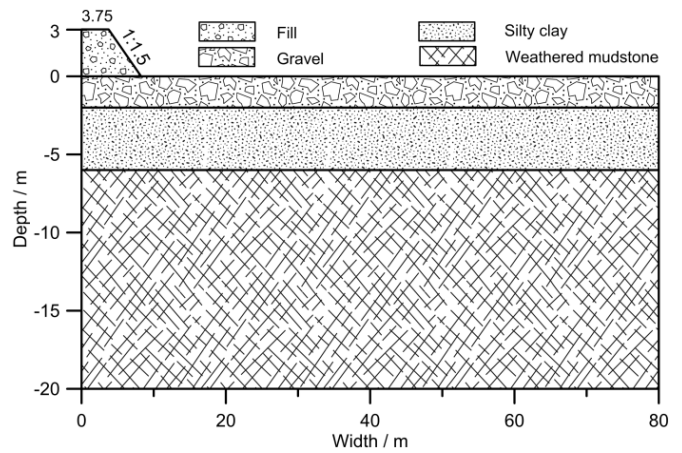


Figure 1. Engineering geological conditions for the section.

Table 1. Mechanical parameters for soil in each layer.

| Media type | T/°C | -15 | -5 | -1 | 0 | 15 |
|--------------------|-------|-------|-------|------|------|------|
| Fill | E/MPa | 9.27 | 5.59 | 3.15 | 1.65 | 1.65 |
| | v | 0.25 | 0.32 | 0.34 | 0.35 | 0.35 |
| Gravel | E/MPa | 7.50 | 4.43 | 2.40 | 1.15 | 1.15 |
| | v | 0.25 | 0.32 | 0.34 | 0.35 | 0.35 |
| Silty clay | E/MPa | 3.36 | 2.02 | 1.12 | 0.57 | 0.57 |
| | v | 0.28 | 0.36 | 0.39 | 0.40 | 0.40 |
| Weathered mudstone | E/MPa | 27.85 | 16.82 | 9.50 | 5.00 | 5.00 |
| | v | 0.19 | 0.23 | 0.24 | 0.25 | 0.25 |

Table 2. Thermal parameters for each soil layer.

| Thermal properties | Fill | Gravel | silty clay | Weathered mudstone |
|---|------|--------|------------|--------------------|
| λ_r (W/m·°C) | 1.71 | 1.28 | 0.86 | 0.96 |
| λ_u (W/m·°C) | 1.31 | 1.45 | 1.45 | 0.91 |
| C_r (J/kg·°C) | 2183 | 2484 | 1794 | 2191 |
| C_u (J/kg·°C) | 1693 | 1844 | 1283 | 1907 |
| L (10 ⁶ J/m ³) | 20.4 | 15.6 | 60.3 | 37.7 |

The parameters in the equations above were obtained from laboratory test results (Li et al. 2009, Wu & Ma 1994, Wang et al. 1993), as shown in Table 1.

An enthalpy is defined in ADINA to numerically calculate the transient thermal field with phase change. It reasonably solves the complicated thermal problem at the phase-change interface (Rolph III & Bathe 1982). Thermal parameters for each layer of subgrade are obtained from a work report generated during design and construction of the Qinghai-Tibet highway and railway and are given in Table 2.

As to the creep, parameters for the Lubby2 model were obtained by fitting the laboratory test results and in situ measured results (Ma et al. 2008, Wu & Ma 1994, Wang et al. 1993). It is worth mentioning that the creep of gravel layers was not taken into account. Considering the length limit of the paper, only the parameters for the fill soil are listed in Table 3.

Table 3. Parameters for the fill soil.

| T/°C | $a_0/10^{-4}$ | $a_1/10^{-4}$ | $a_2/10^{-4}$ | $a_3/10^{10}$ | $a_4/10^4$ | $a_5/10^7$ |
|------|---------------|---------------|---------------|---------------|------------|------------|
| -15 | -7.0 | -8.0 | -13.0 | 12.0 | 6.7 | 10.0 |
| -5 | -7.0 | -8.0 | -13.0 | 12.0 | 6.7 | 10.0 |
| -2 | -7.0 | -8.0 | -13.0 | 12.0 | 6.7 | 10.0 |
| -1 | -7.0 | -8.0 | -9.0 | 8.0 | 6.8 | 8.0 |
| -0.5 | -10.0 | -11.0 | -9.0 | 5.0 | 6.0 | 7.0 |
| 1 | -20.0 | -21.0 | -9.0 | 3.0 | 5.5 | 5.0 |
| 5 | -17.0 | -18.0 | -9.0 | 2.0 | 5.3 | 3.0 |
| 15 | -21.0 | -11.0 | -9.0 | 2.0 | 5.4 | 3.0 |

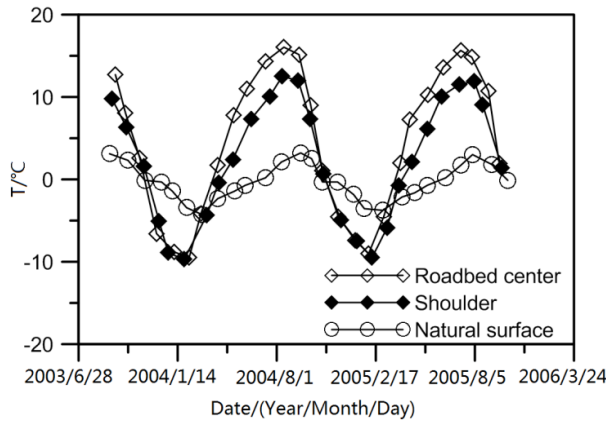


Figure 2. Ground temperature fluctuations at a working site.

Boundary conditions

Thermal boundary conditions for the road surface, shoulder, and natural ground surface can be simplified as a sine function:

$$T=T_0+\alpha t+l\sin(2\pi t/365+n\pi) \tag{5}$$

where T_0 is the mean annual ground temperature (°C), l is the temperature amplitude (°C), and $n\pi$ is the initial phase angle, which can be fitted from Figure 2. At the base of the computational model, a temperature gradient α is assumed to be 0.02 °C/a. Both sides of the model are assumed to be adiabatic boundaries. The heat flux in the bottom boundary is taken as 0.06 W/m².

The frozen soil is assumed permeable in each layer of the subgrade section (Englemark 1984, Watanabe & Flury 2008), which avoids additional development of arrays recording mechanical information for each element in the computational model.

Results and analysis

The development of the thermal field in the subgrade section presented in Figure 3 shows that the permafrost table descends relatively slowly in the first 30 years after construction; with the passage of time, the range of thawed and warm frozen soil increases rapidly.

In Figure 4, the comparison between calculated and in situ measured settlement shows that the simulated results agree in general with those monitored. The comparison in Figure 5 shows that thaw consolidation in the very early stage is inferior

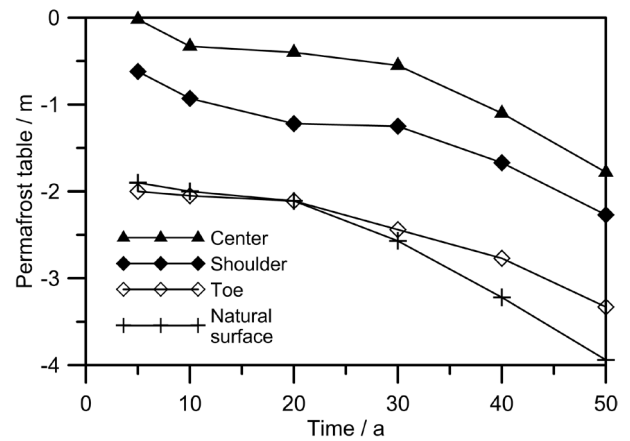


Figure 3. Development of the permafrost table at different positions along the embankment.

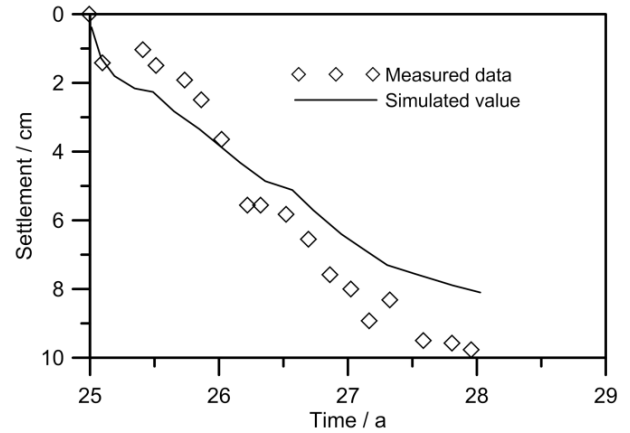


Figure 4. Comparison between measured and simulated settlement.

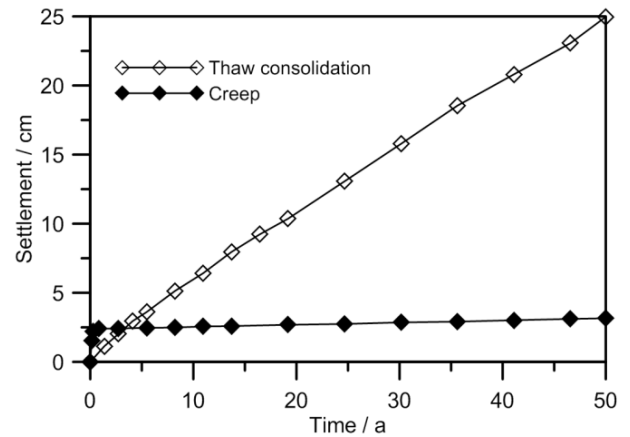


Figure 5. Comparison between thaw consolidation and creep.

to the creep settlement. However, with continuous descent of the permafrost table, thaw consolidation dominates the total settlement. This may provide a basis for future construction and maintenance of cold regions embankments.

Figure 6 presents the amount of settlement for each layer. It can be seen that after about five years, thaw consolidation of fill soil tends to stabilize; in subsequent decades, small settlement occurs within this layer. Slightly more settlement occurs in the gravel layer. Compared with the layers discussed

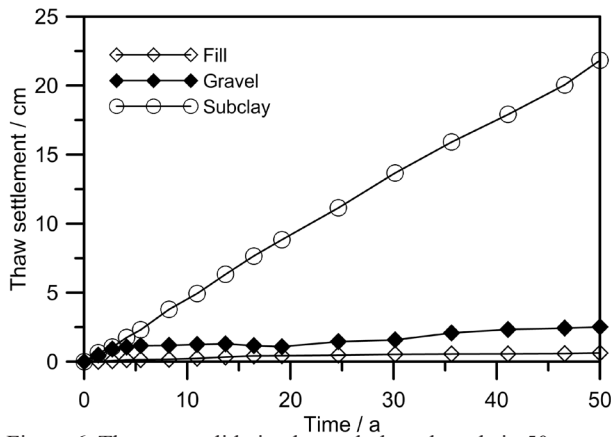


Figure 6. Thaw consolidation beneath the subgrade in 50 years.

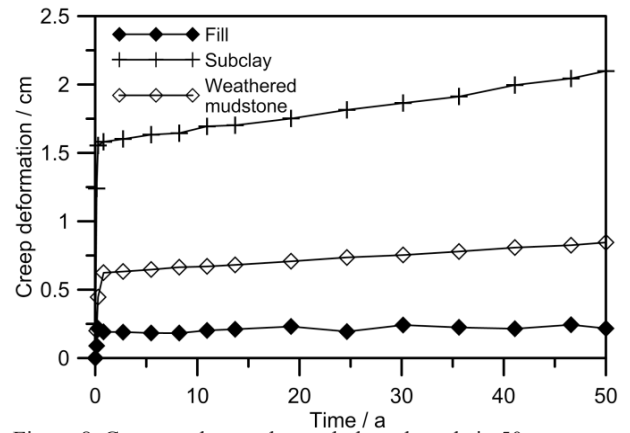


Figure 8. Creep settlement beneath the subgrade in 50 years.

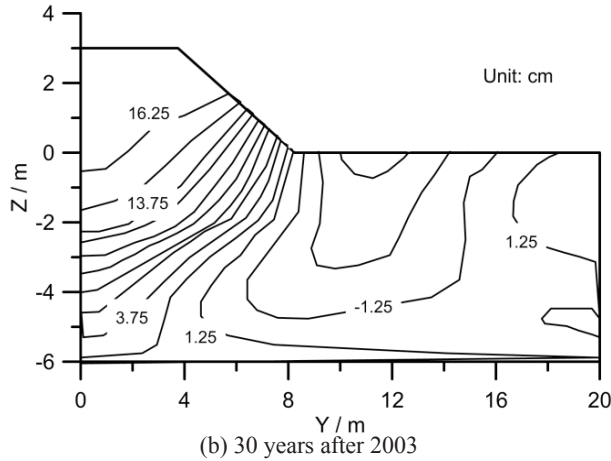
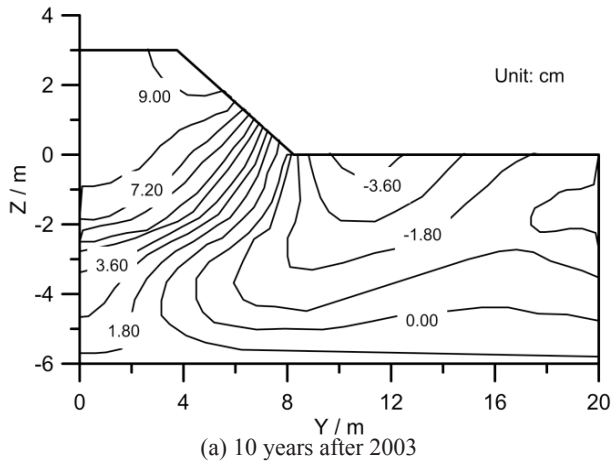


Figure 7. Displacement distribution within the subgrade section.

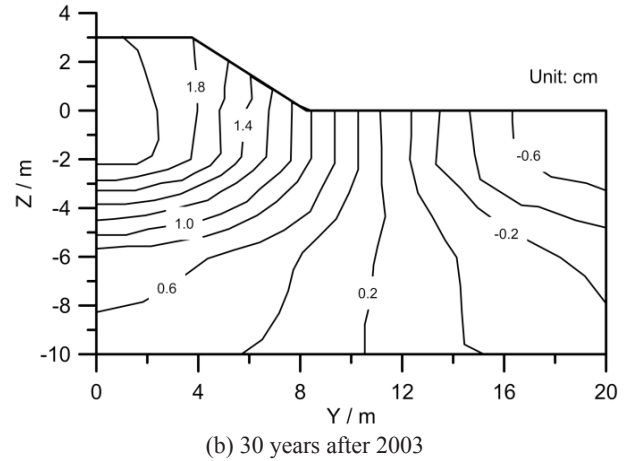
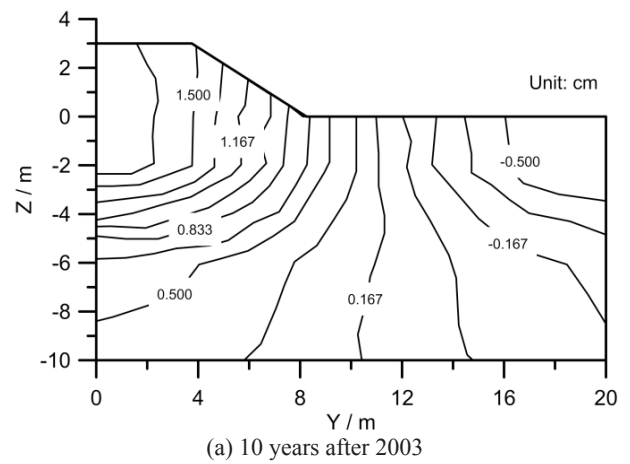


Figure 9. Displacement distribution within the subgrade section.

above, significant thaw consolidation occurs within the silty clay layer, especially with ground temperature warming.

The displacement distributions 10 and 30 years after construction are illustrated in Figure 7. Note that thaw settlement occurs primarily beneath the embankment center with some heave at the slope toe.

The creep settlement of each layer is shown in Figure 8. In the fill soil layer, the creep deformation is about 0.25 cm while larger settlement occurs in the weathered mudstone. The creep of silty clay dominates the total creep with an increase in the

range of warm frozen soil. The displacement isoline tends to be vertical, as shown in Figure 9.

Practical significance of the numerical estimation

The numerical computation provides a rough method for estimating long-term settlement of the embankment in a permafrost region. The numerical results show that thaw consolidation and creep occur mainly in the silty clay layer beneath the subgrade, and minor settlement in fill soil, gravel, and weathered mudstone. Therefore, for maintenance of

constructed structures, the silty clay beneath the subgrade may be replaced by coarse-grained soil or artificially improved soil for the sake of stability.

In addition, different embankment structures may result in different magnitudes of settlement (Lai et al. 2009). Thus reasonable computation of settlement would be important for the selection of appropriate designs.

Discussion

A typical embankment section along Qinghai-Tibet highway was taken as the study object. The possible sources of settlement were theoretically analyzed and numerically implemented. The following conclusions can be drawn:

- 1) Thaw consolidation is described by the combination of the heat conduction equation and Biot consolidation theory. A finite element creep model is used to determine the creep in each layer of the subgrade. Multi-source settlement was numerically implemented based on the three-dimensional thaw consolidation theory and the Lubby2 creep model in ADINA.
- 2) Calculated settlement agrees fairly well with the measured data.
- 3) Within the subgrade section, thaw consolidation and creep occur primarily in the silty clay layer.

The computation work described in this paper presents a new approach to consideration of so-called multiple deformation sources. However, the deformation induced by freeze-thaw cycling may be integrated in the next step so as to account for all possible processes during the entire time period following construction. In subsequent research, the optimization of theoretical models for each settlement source may be fulfilled.

Acknowledgments

This work was supported in part by the National Natural Science Foundation of China (No. 41172253 and 40871039), and the 100 Young Talents project granted to Dr. Jilin Qi.

References

ADINA. Research and Development Inc. 2008. ADINA Theory and Modeling Guide Report ARD 08-7. ADINA R&D Inc., Watertown, MA.

Andersland, O.B. & Akili, W. 1967. Stress effect on creep rates of a frozen clay soil. *Geotechnique* 17(1): 27-39.

Andersland, O.B. & Ladanyi, B. 1994. *An introduction to frozen ground engineering*. New York, Chapman and Hall, 195 pp.

Andersland, O.B. & Noury, J.A. 1970. Time dependent strength behaviors of frozen soils. *Journal of the soil mechanics and foundations division* 96(4): 1249-1265.

Cheng, G.D. & Yang, C.S. 2006. Mechanics related with frozen ground in construction of Qinghai-Tibet railway. *Mechanics in Engineering* 28(3): 1-8 (in Chinese).

Engelmark, H. 1984. Infiltration in unsaturated frozen soil. *Nordic Hydrology* 15: 243-252.

Engenbrod, K.D. 1996. Effects of cyclic freezing and thawing on volume changes and permeabilities of soft fine-grained soils. *Canadian Geotechnical Journal* 33:529-537.

Fish, A.M. 1980. Kinetic nature of the long-term strength of frozen soils. In *proceedings of the Second International Symposium on Ground Freezing*. Trondheim, Norwegian Institute of Technology, 95-108.

Fish, A.M. 1983. Thermal dynamic model of creep at constant stresses and constant strain rates. US Army, Corps of Engineers, Cold Regions Reserch and Engineering Laboratory (CRREL), Technical Report, 83-33.

He, P., Cheng, G.D., & Zhu, Y.L. 1999. Permafrost vicoelastic-damage coupled plastic constitutive theory. *Science in China (Series D)* 29(Supp.):34-39 (in Chinese).

Ladanyi, B. 1972. An engineering theory of creep of frozen soil. *Geotechnical Journal* 22(9): 88-99.

Li, S.Y., Lai, Y.M., Zhang, M.Y., & Dong, Y.H. 2009. Study on long-term stability of Qinghai-Tibet Railway embankment. *Cold Regions Science and Technology* 57(2): 139-147.

Liu, Y.Z., Wu, Q.B., Zhang, J.M., & Sheng, Y. 2002. Deformation of highway roadbed in permafrost regions of the Tibetan Plateau. *Journal of Glaciology and Geocryology* 24(1): 10-15 (in Chinese).

Ma, X.J., Zhang, J.M., Zheng, B., & Li, S.Y. 2008. Study on warm and ice-rich permafrost beneath Qinghai-Tibet railway embankment with pressiometer. *Rock and Soil Mechanics* 29(3): 764-768 (in Chinese).

Miao, T.D., Wei, X.X., & Zhang, C.Q. 1995. Microstructural damage theories of creep of frozen soil. *Science in China (Series B)* 25(3): 309-317 (in Chinese).

Morgenstern, N.R. & Nixon, J.F. 1971. One-dimensional consolidation of thawing soils. *Canadian Geotechnical Journal* 8(4): 558-565.

Qi, J.L., Sheng, Y., Zhang, J.M., & Wen, Z. 2007. Settlement of embankments in permafrost regions in the Qinghai-Tibet Plateau. *Norwegian Journal of Geography* 61(2): 49-55.

Qi, J.L., Vermeer, P.A., & Cheng, G.D. 2006. A Review of the influence of Freeze-thaw cycles on soil geotechnical properties. *Permafrost and Periglacial Processes* 17: 245-252.

Rolph, W.D. III & Bathe, K.J. 1982. An Efficient Algorithm for Analysis of Nonlinear Heat Transfer with Phase Changes. *International Journal for Numerical Methods in Engineering* 18: 119-134.

Sykes, J.F., Lennox, W.C., & Charlwood, R.G. 1974. Finite element permafrost thaw settlement model. Journal of Geotechnical Engineering Division. *Proceedings of the American Society of Civil Engineers* 100(GT11): 1185-1201.

Vyalov, S.S. 1987. *Rheological Fundamentals of soil mechanics*. Beijing, Science Press, 186-187 pp. (in Chinese).

Wang, J.P., Wang, Z.Y., & Wu, Q.J. 1993. Three-dimensional finite element analysis of stress and deformation of frozen wall in deep thick clay layer. *Journal of Glaciology and Geocryology* 15(2): 309-316 (in Chinese).

- Watanabe, K. & Flury, M. 2008. Capillary bundle model of hydraulic conductivity for frozen soil. *Water Resources Research* 44: W12402.
- Wu, Z.W. & Liu, Y.Z. 1989. In *Prediction about the Qinghai-Tibet highway roadbed with adoption of asphalt surface*. Beijing, Science Press, pp. 333-338 (in Chinese).
- Wu, Z.W. & Ma, W. 1994. *Strength and creep of frozen soil*. Lanzhou. Lanzhou University Press, 26 pp. (in Chinese).
- Yao, X.L. 2010. Theoretical and application study on thaw settlement of frozen soils. Ph.D. Dissertation, Beijing, Graduate University of the Chinese Academy of Sciences (in Chinese).
- Zhang, J.M., Liu, D., & Qi, J.L. 2007. Estimation on the settlement and deformation of embankment along Qinghai-Tibet railway in permafrost regions. *China Railway Science* 28(3): 12-17 (in Chinese).
- Zhang, L.X., Yuan, S.C., & Yang, Y.P. 2003. Mechanism and prevention of deformation cracks of embankments in the permafrost region along Qinghai-Xizang railway. *Quaternary Sciences* 23(6): 604-610 (in Chinese).
- Lai, Y.M., Zhang, M.Y., & Li, S.Y. 2009. *Engineering theory and application in cold regions*. Beijing: Science Press (in Chinese).

Estimation of the Mean Annual Surface Temperature and Surface Frost Number Using the MODIS Land Surface Temperature Products for Mapping Permafrost in China

Youhua Ran, Xin Li, Rui Jin

State Key Laboratory of Frozen Soils Engineering, Cold and Arid Regions Environmental and Engineering Research Institute, Chinese Academy of Sciences, Lanzhou, Gansu, China

Abstract

In this paper, we propose a pragmatic scheme for estimation of MAST and surface frost number, based on the assumption that the average of maximum and minimum land surface temperature (LST) represents the daily mean LST, using MODIS Aqua/Terra LST products. The advantage of this approach is that it allows the full use of every value at any time at any pixel of MODIS LST products to estimate the two important indices for mapping permafrost: mean annual surface temperature and surface frost number. This scheme is simple and easy to implement, and it does not depend on other observations. The accuracy of the method depends only on the accuracy of MODIS LST products. Eight years of datasets from 2003 to 2010 were generated. These datasets are validated primarily by comparison with in situ observations and analysis of the spatial pattern over China. Results show that the datasets have a high level of accuracy, although some uncertainty such as the complicated scale effect does exist. These datasets can be used to support permafrost mapping in China.

Keywords: permafrost, MAST, surface frost number, remote sensing, MODIS, China.

Introduction

Permafrost is a major element of the cryosphere and is extremely sensitive to climate warming and human activity (Li et al. 1996a, Jin et al. 2000, Haeberli & Hohmann 2008, Li et al. 2008, Wu et al. 2002). China's permafrost area ranks third in the world in terms of area and is the largest in terms of middle- and high-altitude permafrost areas, which are particularly sensitive to global climatic change. The Qinghai-Tibet Plateau (QTP) in particular plays a very important role in global change (Wu et al. 2002, Li et al. 2008). Significant permafrost degradation has occurred and is occurring in most permafrost regions in China, resulting in increased environmental fragility and related hazards. All of these factors underline the importance of permafrost mapping in China.

In the past 50 years, many maps have been compiled to investigate the distribution and thermal status of permafrost (LIGG/CAS 1988, Li & Cheng 1996, Qiu et al. 2000, CAREERI/CAS 2006). This has been done in an effort to study the response and feedback of permafrost to global change and human engineering activities and to decrease and prevent permafrost hazards. All of these maps are based on a few in situ air temperature observations and a small amount of mean annual ground temperature (MAGT) investigation data. The accuracy of these observations and data largely depends on the mapper's empiricism. However, many investigators suggest that air temperature is not an optimal predictor of permafrost distribution because the very large effects of snow cover and other variables influencing permafrost occurrence are ignored. Instead, land surface skin temperature (LST) should be used (Nelson 1987, Cheng, personal communications). The mean annual surface temperature (MAST) and "surface frost number" (Nelson 1987) are quantitative criteria in mapping permafrost.

Satellite image data have been successfully used to retrieve the LST since the advent of the Advanced Very High Resolution

Radiometer (AVHRR) instrument on board the NOAA series of satellites in the 1970s and the MODIS (Moderate-resolution Imaging Spectro radiometer) instrument, which was launched in 2000 as a payload on the Terra satellite. In 2002, a second MODIS instrument was launched on the Aqua satellite. MODIS improves upon the performance of AVHRR by providing both higher spatial resolution and greater spectral resolution. The polar-orbiting MODIS sensors produce daily land surface temperature (LST) maps with global coverage.

Based on remote sensing LST observations, many studies have been made to estimate the mean LST. A simplified method proposed by Jin (1999, 2000) includes two steps: the neighboring-pixel approach (NP) and surface air temperature adjustment. The scheme has a clear theoretical basis, but there are problems; for example, many parameters are difficult to achieve, and spatial coverage is inadequate. Langer et al. (2010) and Westermann et al. (2011) examine the spatial and temporal variability of summer surface temperatures using a ground-based high-resolution thermal imaging system at a northern Siberia polygonal tundra site and at a high-arctic tundra site on Svalbard, Norway, respectively. Langer et al. (2010) point out that cloudy conditions can lead to biased weekly temperature averages inferred from MODIS LST data. They recommend a solution to improve the accuracy of average LST by combining cloud cover information with a gap filling procedure. Westermann et al. (2011) conclude that a reliable gap filling procedure to moderate the impact of prolonged cloudy periods would be of high value for a future LST-based permafrost monitoring scheme. Hachem et al. (2009) proposed a more practical method to estimate the annual mean LST. This method involves fitting a sinusoidal model over the daily LST of MODIS readings to reproduce seasonal thermal variations near the ground for each 1-km² pixel. This method is simple and practical. However, it does take advantage the MODIS LST products that are available four times daily.

This paper proposes a pragmatic scheme for estimating MAST and surface frost number using MODIS Aqua/Terra LST products, i.e., four times daily LST observations.

Method

Assumption

The assumption that the arithmetic average of maximum and minimum LST can represent the daily mean LST is well-founded (Liu et al. 2006). Thus the MODIS Terra/Aqua daytime and nighttime LST products (MOD11C1 and MYD11C1 version 041) with 0.05° spatial resolution were acquired from NASA Distributed Active Archive Center (DAAC) and used to estimate the daily mean LST. The reason for the use of MODIS Aqua is that Aqua overpass time is later than Terra (13PM vs. 10AM for daytime, 1AM vs. 10PM for nighttime) and therefore has a better chance of capturing the daytime maximum and nighttime minimum temperature (Kogan et al. 2010).

Figure 1 shows that the MODIS Terra/Aqua daytime and nighttime LST products have a high degree of correlation with daily maximum and minimum in situ LST. The higher temporal

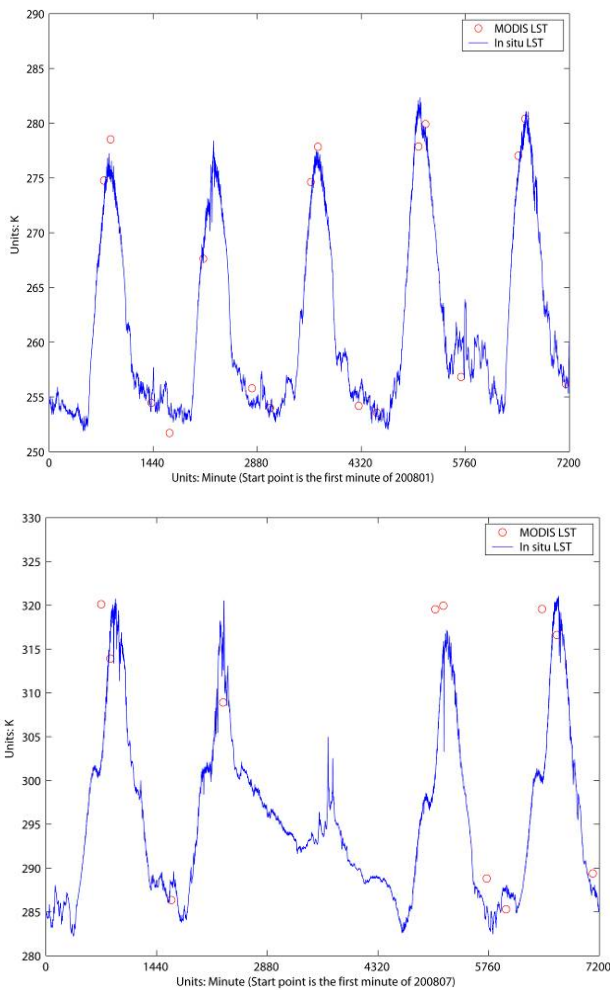


Figure 1. The representation of MODIS Aqua/Terra daytime and nighttime LST products for maximum and minimum LST. (Top: 20080101–20080105 in cold season; Bottom: 20080701–20080705 in warm season.)

resolution in situ LST is obtained from the WATER (Watershed Allied Telemetry Experimental Research) experiment (Li et al. 2009) in 2008. The in situ LST observations from the Linze grassland station are used to assess the representation of MODIS Terra/Aqua daytime and nighttime LST products for daily maximum and minimum LST. The land cover types at the station are diverse in this area, with a distribution of wetland, grassland, salinized meadow, and farmland.

Workflow

Based on the assumption given above, we present a scheme to estimate the annual mean LST. The workflow of this scheme is shown in Figure 2. This scheme includes four steps.

Step 1: Select daytime and nighttime LST.

For one day, the daily mean LST is calculated using equation 1. At least once, daytime and nighttime observation was selected from both sensors.

$$T_{daily} = (T_d + T_n) / 2 \tag{1}$$

Step 2: Identify the LST amplitude and interpolate it over the region.

To estimate the daily mean LST for the pixels that did not have a pair of LST observations (typically owing to cloud cover), the daily LST amplitude is interpolated according to the near LST pair pixels. Experiment shows that the LST amplitude is more spatially homogeneous than the LST itself. This provides the possibility for interpolating LST amplitude for the entire region of China. The amplitude is calculated using equation 2. Based on this step, any one observation is sufficient to estimate the daily average surface temperature. We believe that observation is stronger than no observation in this process.

$$D = T_{max} - T_{min} \tag{2}$$

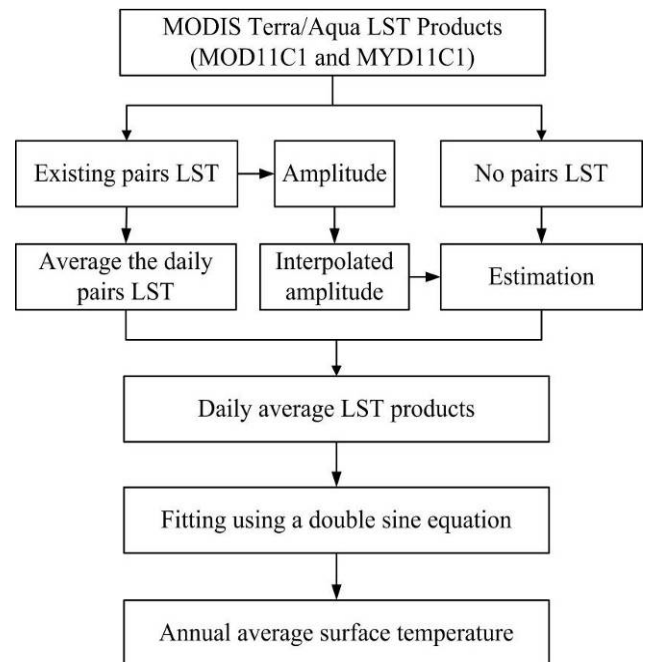


Figure 2. The workflow to estimate the annual mean LST using MODIS Aqua/Terra daytime and nighttime LST products.

Step 3: Calculate the daily mean LST for pixels that did not contain a pair generally due to cloud cover.

When the daily LST amplitude is known, we can calculate the daily mean LST for pixels that did not contain an LST pair using equation 3.

$$T_{daily} = \begin{cases} T_{dt} - D_d / 2 & t = 1 \text{ or } 3 \\ T_{dt} + D_d / 2 & t = 2 \text{ or } 4 \end{cases} \quad (3)$$

where t represents the time for one day. 1 and 3 show the daytime LST, 2 and 4 show the nighttime LST; d denotes one day in a certain year; ‘daily’ is the daily mean LST, and T represents the LST.

Step 4: Fitting the seasonal cycle of LST.

The daily mean LST is expanded spatially as much as possible by steps 2 and 3. For step 4, a continuous double sine function model reproducing the seasonal cycle of LST in each pixel was adopted by fitting a sinusoidal interpolation between the daily average LSTs for each pixel year by year as follows:

$$T_a = a_1 \times \sin(b_1 \times x + c_1) + a_2 \times \sin(b_2 \times x + c_2) \quad (4)$$

where x is the Julian day and T_a represents the MAST. The coefficients are derived from fitting expanded spatially daily mean LST.

Step 5: According to the double sine function, the annual average LST and surface frost number are produced. Here the surface frost number (Nelson 1987) was used.

$$F = \frac{DDF^{1/2}}{DDF^{1/2} + DDT^{1/2}} \quad (5)$$

where DDF and DDT are surface freezing and thawing indices, respectively, expressed in degree days, and F indicates surface frost number. The freezing and thawing indices (TC days) are derived from the double sine function model, i.e., equation 4 and integrating this curve below and above the 0°C axis.

Result and Validation

Annual average LST and surface frost number datasets from 2003–2010 were generated by implementing the workflow described above. An example result is shown in Figures 3 and 4.

Figure 3 shows the estimated MAST over China and the pattern of temperature distribution. Temperatures in the Northeast and the QTP are colder than in other regions. The temperature in the northern region of the QTP is colder than in the south. This gives a clear outline of permafrost distribution in China. Figure 4 also shows that the estimated surface frost number reveals the pattern of permafrost distribution in China.

In situ daily land surface temperature data from 664 sites were obtained from the Chinese Meteorological Administration (CMA) and are used to validate the estimated annual average LST and surface frost number, as shown in Figures 5 and 6. The correlation coefficient (R) of the linear relationship between in situ annual average LST and estimated annual average LST

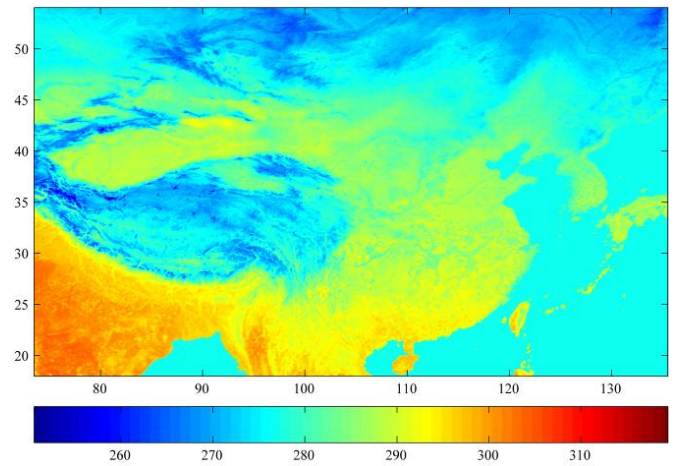


Figure 3. The MAST over China in 2004 (Units: K).

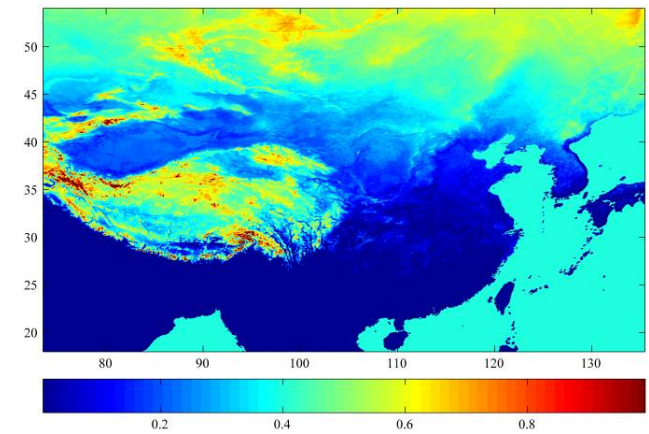


Figure 4. Surface frost number in 2004.

in 2004 is 0.88, and the standard deviation (SD) is 3.14 ($p < 0.0001$). For the surface frost number, R is 0.95, and the SD is 0.047 (both $p < 0.0001$). This strong linear relationship indicates that the estimated MAST and surface frost number have a high level of accuracy.

However, the permafrost boundary is very sensitive to MAST and the surface frost number, and is complicated by the coarse spatial resolution of the data which makes validation difficult.

Summary and Future Prospects

A pragmatic scheme for estimating the MAST and surface frost number using MODIS Aqua/Terra LST products is presented. The advantage of this approach is the use of every value at any time at any pixel of MODIS LST products in estimating the two important indices for mapping permafrost: mean annual surface temperature and surface frost number. The scheme is simple and easy to implement, and it does not depend on other observations. The accuracy of the method depends only on the accuracy of MODIS LST products. Eight years of datasets from 2003–2010 were generated using this scheme to provide mean annual surface temperature and surface frost number to map permafrost in China. These

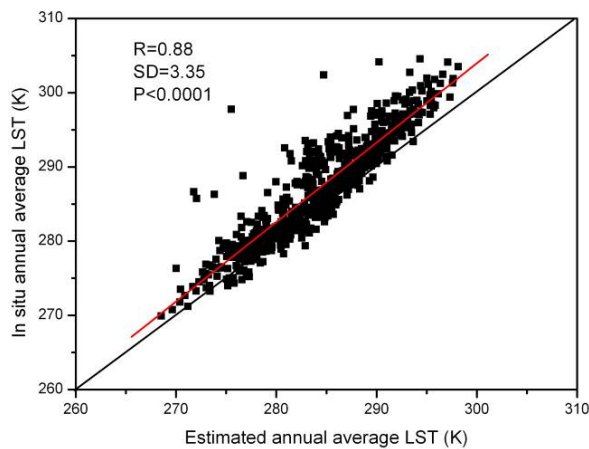


Figure 5. The correlation of estimated MAST and observation MAST in 2004.

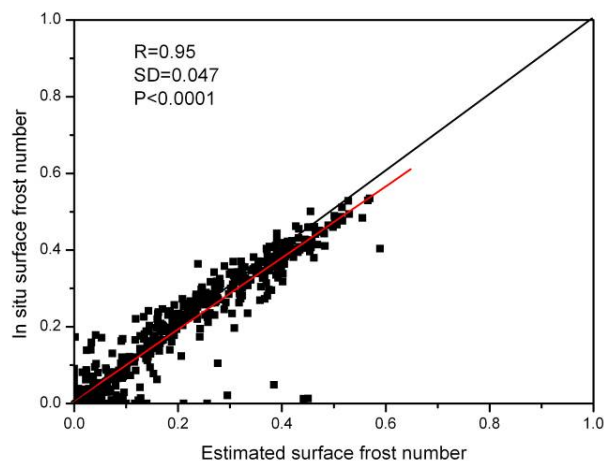


Figure 6. The correlation of estimated surface frost number and observation surface frost number in 2004.

datasets were validated primarily by comparison with in situ observations and analysis of the spatial distribution pattern over China. Results show that the datasets have a high level of accuracy, although some uncertainty, such as the complication of scale effects, does exist.

However, the permafrost boundary is very sensitive to MAST and surface frost number. The accuracy of this proposed method has much room for improvement. Snow cover should be considered in mapping permafrost processes in the near future, especially in regions that maintain a snow cover. Remote sensing observations can be assimilated into a land surface model that would output land surface temperature with more accuracy and a higher spatial/temporal resolution.

Acknowledgments

This work is supported by the Foundation for Excellent Youth Scholars of CAREERI, CAS. We thank the editor and the anonymous reviewers for their extremely helpful suggestions in revising the article.

References

- Cold and Arid Regions Environmental and Engineering Research Institute (CAREERI), Chinese Academy of Sciences (CAS). 2006. *Map of the glaciers, frozen ground and desert in China*. 1:4,000,000. SinoMaps Press, Beijing (in Chinese).
- Haerberli, W. & Hohmann, R. 2008. Climate, glaciers and permafrost in the Swiss Alps 2050: scenarios, consequences and recommendations. In *NICOP 2008: Proceedings Ninth International Conference on Permafrost*. Edited by D.L. Kane and K.M. Hinkel, K.M. Institute of Northern Engineering, University of Alaska Fairbanks, 1: 607–612.
- Hachem, S., Allard, M., & Duguay, C. 2009. Using the MODIS Land Surface Temperature Product for Mapping Permafrost: An Application to Northern Quebec and Labrador, Canada. *Permafrost and Periglacial Processes* 20(4): 407-416.
- Jin, M.L. & Dickinson, R.E. 1999. Interpolation of surface radiative temperature measured from polar orbiting satellites to a diurnal cycle - 1. Without clouds. *Journal of Geophysical Research-Atmospheres* 104(D2): 2105-2116.
- Jin, M.L. 2000. Interpolation of surface radiative temperature measured from polar orbiting satellites to a diurnal cycle 2. Cloudy-pixel treatment. *Journal of Geophysical Research-Atmospheres* 105(D3): 4061-4076.
- Jin, H.J., Li, S.X., Cheng, G.D., Wang, S.L., & Li, X. 2000. Permafrost and climatic change in China. *Global and Planetary Change* 26 (4): 387-404.
- Kogan, Felix; Powell, Alfred; Fedorov, Oleg (ed.) *Use of Satellite and In-Situ Data to Improve Sustainability* Springer Netherlands. 2010, 362 pp.
- Langer, M., Westermann, S., & Boike, J. 2010. Spatial and temporal variations of summer surface temperatures of wet polygonal tundra in Siberia - implications for MODIS LST based permafrost monitoring. *Remote Sensing of Environment* 114(9): 2059–2069.
- Lanzhou Institute of Glaciology and Geocryology, Chinese Academy of Sciences (LIGG/CAS). 1988. *Map of Snow, Ice and Frozen Ground in China (1: 4,000,000)*. Cartographic Publishing House, Beijing, China.
- Li, S., Cheng, G., & Guo, D. 1996a. Numerical simulation on the changes of permafrost on the Qinghai–Tibet Plateau under a persisting warming climate. *Science in China Series D: Earth Sciences* 26(4): 342–347.
- Li, S. & Cheng, G.D. (eds). 1996b. *Map of permafrost on the Qinghai-Tibet Plateau (1:3,000,000)*. Gansu Culture Press, Lanzhou (in Chinese).
- Li, X., Cheng, G.D., Jin, H.J., Kang, E.S., Che, T., Jin, R., Wu, L.Z., Nan, Z.T., Wang, J., & Shen, Y.P. 2008. Cryospheric Change in China. *Global and Planetary Change* 62(3-4): 210-218.

- Li, X., Li, X. W., Li, Z. Y., Ma, M. G., Wang, J., Xiao, Q., Liu, Q., Che, T., Chen, E.X., Yan, G.J., Hu, Z.Y., Zhang, L.X., Chu, R.Z., Su, P.X., Liu, Q.H., Liu, S.M., Wang, J.D., Niu, Z., Chen, Y., Jin, R., Wang, W.Z., Ran, Y.H., Xin, X.Z. & Ren, H.Z. 2009. Watershed Allied Telemetry Experimental Research. *Journal of Geophysical Research* 114(D22103), doi:10.1029/2008JD011590.
- Liu, X., Yin, Z.-Y. Shao, X. & Qin, N. 2006. Temporal trends and variability of daily maximum and minimum, extreme temperature events, and growing season length over the eastern and central Tibetan Plateau during 1961–2003. *Journal of Geophysical Research* 111(D19109), doi:10.1029/2005JD006915.
- Nelson, F.E. & Outcalt, S.I. 1987. A computational method for prediction and regionalization of permafrost. *Arctic and Alpine Research* 193: 279–288.
- Qiu, G.Q., Zhou, Y.W., Guo, D.X., & Wang, Y.X. 2000. *The Map of Geocryological Regionalization and Classification in China*. Science Press, Beijing (in Chinese).
- Westermann, S., Langer, M., & Boike, J. 2011. Spatial and temporal variations of summer surface temperatures of high-arctic tundra on Svalbard - implications for MODIS LST based permafrost monitoring. *Remote Sensing of Environment* 115: 908–922.
- Wu, Q.B., Zhu, Y.L., & Liu, Y.Z. 2002. Evaluation model of permafrost thermal stability and thawing sensibility under engineering activity. *Cold Regions Science and Technology* 34(1): 19-30.

Encounters with Relict Permafrost in the Anchorage, Alaska, Area

Charles H. Riddle

R&M Consultants, Inc., Anchorage, Alaska, USA

James W. Rooney

J&F Rooney, LLC., Anchorage, Alaska, USA

Abstract

Within the Anchorage, Alaska, area, only limited information has been published regarding the existence of relict permafrost and actual occurrences of frozen ground. Many of the reported encounters with frozen ground conditions occurred during a very active period of development from the 1960s through the 1980s. At that time, development of commercial buildings and residential housing extended into marginal areas having less desirable soil and terrain conditions, most with relatively deep overlying wet organic and fine-grained soil deposits. Resultant problems with frozen ground in Anchorage have not received much attention from permafrost researchers because very little information was made available to them by either private developers, their consultants, or governmental agencies. This paper represents an effort to document information retrieved from various sources on relict permafrost encounters in the Anchorage area.

Keywords: Anchorage, Alaska; climate warming; permafrost; urban planning.

Introduction

Over the past 50 or so years of continued development, very little information has been published on the existence of relict permafrost and actual occurrences within the Anchorage area. "Relict permafrost" is defined as permafrost reflecting past climatic conditions differing from those of today (Harris et al. 1988). Many of the encounters with these reported frozen ground conditions occurred during the more active period of development within the Anchorage bowl from the 1960s to the 1980s. During that time, development of commercial properties and residential housing extended into marginal areas that had less desirable soil and terrain conditions, most with relatively deep overlying wet organic and fine-grained soil deposits. The frozen ground problems that occurred within these residential and commercial development projects have not received much attention from permafrost researchers because very little information was made available to them by either private developers, their consultants, or governmental agencies.

In 1979, the Municipality of Anchorage (MOA) issued a report titled "Geotechnical Hazards Assessment Study" (MOA 1979). This report briefly discussed permafrost issues and indicated its "potential existence throughout much of the Municipality." It stated that frozen ground "is occasionally encountered to depths of between 5 and 12 m, often with massive ice layers." The report also stated that "localized microclimate well below the ambient temperature" was conducive to these existing permafrost conditions. A map showing isolated, discontinuous permafrost areas within shaded zones was provided with the report. The shaded areas were divided into three severity ratings. The highest incidence area is shown with a rating of Zone 3. Areas suspected to have deeper lying frozen ground in lower lying areas were given a permafrost potential rating of Zone 2. All other areas, where no assessment has been made (including those outside the Anchorage bowl), were classified as Zone U (unknown). The

report also noted that "movements on the order of 1,200 mm have been observed in extreme permafrost cases."

In 1980, the Municipality of Anchorage republished the 1979 permafrost mapping information in the "Anchorage Coastal Resources Atlas" (MOA 1980). The base map, presented at a scale of 1:25,000, indicates a zone of "high potential for isolated permafrost conditions" as shown by the hatched pattern (see Fig. 1). The 1980 map is commonly used for planning and evaluation efforts in areas of potential permafrost.

The earliest known documentation on the presence of permafrost in the Anchorage area was presented by Harry Lee, P.E., at the Second International Symposium on Cold Regions Engineering in 1976 (Lee 1977). The Generalized Geologic Map of Anchorage and Vicinity (Schmoll & Dobrovolsky 1972), on which Lee marked areas of both "Confirmed" and "Suspected" permafrost, was included in this technical paper. This work appears to be the primary reference source for the 1979 MOA study.

In this paper, we further document information retrieved from various sources on relict permafrost. Specific locations where permafrost was encountered and documented are shown in Figure 1. These identified locations should not be considered to be all inclusive since other areas may not have been reported or may still remain to be encountered. As an example, the recent discovery of deeper underlying permafrost along an Alaska Railroad realignment just north of Anchorage and near the community of Eagle River provides such an example of encountering permafrost conditions in a warm frozen ground area.

Soil and Climate Conditions

Anchorage is located within the Cook Inlet-Susitna Lowland physiographic province. The area is characterized as a glaciated lowland containing areas of ground moraine and stagnant ice topography, drumlin fields, eskers, and outwash

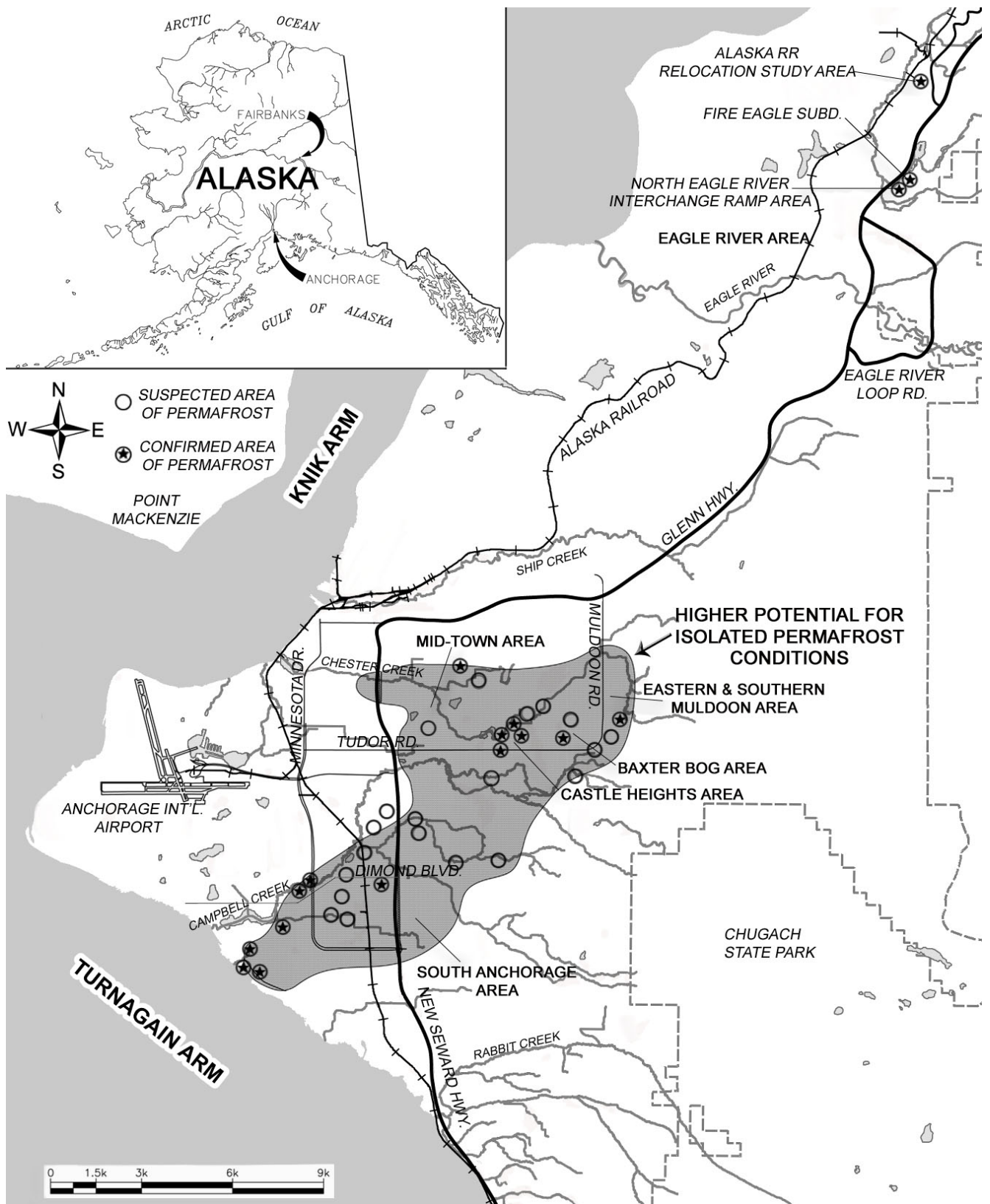


Figure 1. Map of Anchorage, Alaska, showing zone for higher potential of isolated permafrost and actual site locations (modified after Lee 1977 and MOA 1980).

plains, with rugged mountains located immediately to the east (Wahrhaftig 1965). This region of Alaska is considered to be generally free of permafrost. One exception is where isolated masses of permafrost occur in lowland areas with high ground insulation, such as peat bogs and swamps (Ferrains 1965).

Lying between Cook Inlet and the Chugach Mountains, Anchorage has a transitional climate that may be characterized as variable owing to the influence of both maritime and continental conditions. Anchorage receives about 400 mm of precipitation per year. The temperature ranges in extremes from about -37°C to 29°C with an annual mean of 2.3°C . The mean monthly temperature ranges from about -9°C in January to 15°C in July.

The Anchorage area is known to contain numerous microclimate zones. However, the study areas discussed in this paper do not have the necessary long-term data required for detailed climate analysis. The official recording station at Anchorage International Airport (Fig. 1) is generally considered to be warmer in winter and cooler in summer than many other locations within Anchorage. Much of the shaded area (Fig. 1) that is characterized as having a higher potential for isolated permafrost conditions is low-lying and often much cooler in winter than the official recording station located adjacent to Knik Arm and Turnagain Arm of Cook Inlet. Ground temperature data are not available for the study areas discussed below.

Areas with Permafrost Encounters

Mid-Town area

Early encounters with relict permafrost within the Chester Creek Valley were identified on mostly north-facing slopes in the 1960s and 1970s, when the Alaska Department of Transportation and Public Facilities (ADOT&PF) was doing road improvements (Long & Weaver, pers. com.). These encounters appear to have involved permafrost at shallow enough depths that allowed excavation of the frozen material. Harry Lee's marked-up map also identifies locations within this region that extend east toward the Lake Otis Parkway.

Castle Heights Subdivision area

One of the earliest encounters with deeper lying frozen ground in the Anchorage area was in the early 1970s in the Castle Heights residential subdivision. A few years after construction, several homes began to experience various forms of structural deformation and building subsidence. Several homes were eventually removed from their failing foundations and relocated to other property, and others were re-leveled and placed on new foundations. The contractors and home owners eventually filed suit against the developer, the engineers, and the geological consultant. The case, which focused on the issue of whether the consultants had followed current "Standards of Practice" in performing the site subsurface investigation, ultimately was carried to the Alaska State Supreme Court which decided in favor of the developer and geological consultant. The court ruled that the "Standards of Practice" had been followed and that frozen

ground conditions had not been encountered previously and thus represented a unique situation (Pacific Reporter 1979). Harry Lee's technical paper, which identified revised site exploration procedures, subsequently became the "unofficial" minimum standard for Anchorage.

Terrain and soil conditions in the Castle Heights Subdivision involved both slightly upland and lower lying deposits of fine- and coarse-grained glacial and fluvial material (R&M 1973). The frozen layer extended from a depth of 2.4 to 6 m below ground surface and contained a number of ice seams ranging up to 200 mm in thickness.

This relatively shallow permafrost was not detected during construction at these problem house locations. However, during rehabilitation of one house, the uncovered five-course block wall on a footing foundation was observed to have been capped with a concrete leveling sill that ranged from 75 mm at one end to nearly 250 mm at the opposite end, indicating that the foundation had already settled during construction. Typically, the residents of these homes did not experience deformation problems during the first few years, but problems began to show up when heat from the homes extended down to the frozen ground. Figure 2 provides a test hole log for a residence located on Knights Way; Figures 3a and 3b are photographs showing interior wall damage and a recovered frozen core sample containing an ice seam. This residence was moved to another location and ultimately a new home was constructed on the lot.

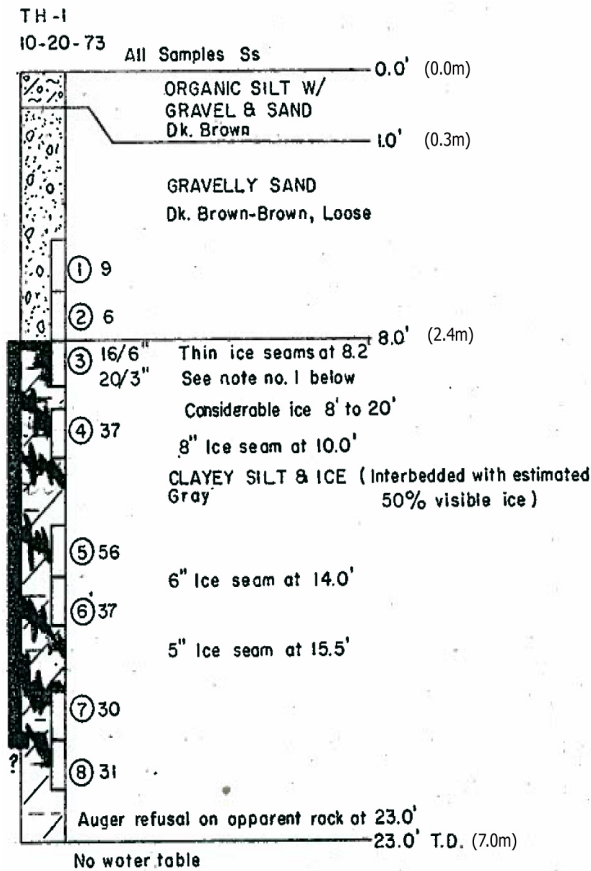
Baxter Bog area

During early 1970s, a four-unit townhouse development was partially constructed along the east side of Baxter Bog. The initial group of occupied townhouse units was located uphill from the adjacent separated garage structures. A second group of townhouse foundation footings was just completed when ground settlement problems began to appear. Subsurface investigations revealed a deep-lying layer of frozen ice-rich soil that was thawing. Deformation of the garage units in the initial group was substantial, but these were renovated. However, the second group of townhouse foundations had to be abandoned and the area remains open to this day.

Another multi-unit subdivision development, Rainbow Terrace located just to the north, was being planned when site subsurface investigations fortunately revealed the presence of frozen ice-rich soil along the lower lying western portion of the property (R&M 1975). A test boring indicated frozen ground from the surface to a depth of 11.5 m with a talik from 8.2 to 9.1 m. A 180-mm-thick ice lens was recovered in a sample taken at 6.3 m. Two adjacent borings also revealed frozen ground extending to a depth of 8.5 m. Modifications were made to the development layout, and the area identified with frozen ground conditions was converted to open space and an owner vehicle parking and storage area.

Eastern and southern Muldoon area

Several other areas of relict permafrost have been identified in a section lying east of Muldoon Road and bordering adjacent military land. Some of the residential areas had



NOTE No. 1) Auger refusal on apparent rock. Moved rig ahead 3.0' and started new boring.

Figure 2. Boring log for Knights Way residence (Castle Heights Subdivision).



Figure 3a. Interior wall damage at a house located on Knights Way (Castle Heights Subdivision).



Figure 3b. Recovered frozen core sample containing an ice seam taken from Test Hole TH-1 (see Fig. 2).

units that experienced ground deformation both during and after construction. These sites were all situated on fairly level terrain having a relatively thick cover of organic and fine-grained material.

In an effort to improve and provide secondary backup water supply to the Anchorage bowl area, the Anchorage Water and Wastewater Utility (AWWU) proceeded with needed development of a 1,220-mm-diameter water transmission line loop connection along the eastern edge of the city. A portion of this alignment was located adjacent to some subdivision areas that had experienced prior encounters with localized permafrost. In 1984, a 213-m length of sanitary sewer (installed in 1976) required reconstruction because of excessive pipeline settlement resulting from permafrost degradation. This sanitary sewer line was just 25 m west of and parallel to the water transmission main alignment. Because of these concerns, a very detailed effort was made to explore subsurface conditions along this proposed pipeline segment. Both ground penetrating geophysical techniques and many closely spaced test borings were placed in those areas identified to be of most concern. Unfortunately, no evidence of frozen ground was detected and the project proceeded with a conventional pipeline burial design during the 1996–1997 winter season.

About one year after project completion, a pipeline water leak was detected and ice-rich frozen ground was revealed by test borings to extend over a 45-m alignment segment. Depth to the top of permafrost was on the order of 5 m and varied from 0.5 to 2.7 m in thickness.

Considerable visible ice in the form of layers and lenses up to 100 mm thick was observed in the frozen zone. An interpreted ground profile is presented in Figure 4. In this particular critical situation, AWWU elected to solve the problem by supporting the pipeline on piles through this short section because of environmental, access, and time constraints, rather than using other slightly longer-term ground treatment solutions. This site was evaluated in detail, and the results were presented in a technical paper (Barber-Wiltse & Rast 2000).

Some permafrost was encountered by ADOT&PF during exploration for the south end of the Muldoon Road curve connection to Tudor Road. The alignment was reported to have avoided much of the frozen ground, although it was reported that some deeper excavation was required to remove frozen material (Weaver, pers. com.).

South Anchorage area

One of the southernmost locations of deeper-lying permafrost was detected in the area to the southeast of the intersection of the Old Seward Highway and Dimond Boulevard. Frozen ground was detected during preliminary site subsurface investigations for property development. The initial development was then terminated, and an effort was initiated to accelerate ground thawing by covering a large portion of the site with black plastic sheeting material in order to increase heat flow into the

ground. Ultimately, thawing of the frozen layer was confirmed and a few years later development of the site proceeded.

ADOT&PF reported encountering some shallower permafrost on the north side of the Minnesota/Diamond interchange during field studies. The frozen ground was successfully excavated during construction (Weaver, pers. com.).

Eagle River area

ADOT&PF encountered permafrost in Eagle River along the Glenn Highway at the North Eagle River interchange. This segment of highway was constructed in multiple phases, and significant ground subsidence experienced at several locations within the interchange area was attributed to permafrost degradation. ADOT&PF elected to take a passive approach and allow subsidence to be addressed by maintenance repairs. Unfortunately, this encounter with frozen ground was not well documented.

During the period 2003 to 2005, a very large multi-unit housing development (Fire Eagle Subdivision) was constructed in the area immediately adjacent to the northbound entrance ramp of the North Eagle River interchange. Within a short time, some of these condominium units began to settle and deform (Tracy 2006). Subsequent subsurface investigations found permafrost with frozen ground to depths of up to 12 m. At least six structures, involving about 18 condo units, required major remedial underpinning using helical piles (Helical Pier Systems undated).

Frozen ground containing massive ice was also detected during recent geotechnical investigations for realignment of a segment of the Alaska Railroad in an area just north of Eagle River. Various materials were encountered, including massive ice, thaw-stable frozen soil, very soft silty clay to clayey silt, silty sand, and gravelly sand (Krzewinski et al. 2007). Massive ice thickness ranged from about 1.5 to 12 m and contained 20 to 95% visible ice content interbedded with the silt and clay soils. A generalized subsurface profile is presented as Figure 5. Artesian groundwater flow of about 75 to 110 liters per minute was encountered within the frozen silty sand in several borings, as shown in Figure 5.

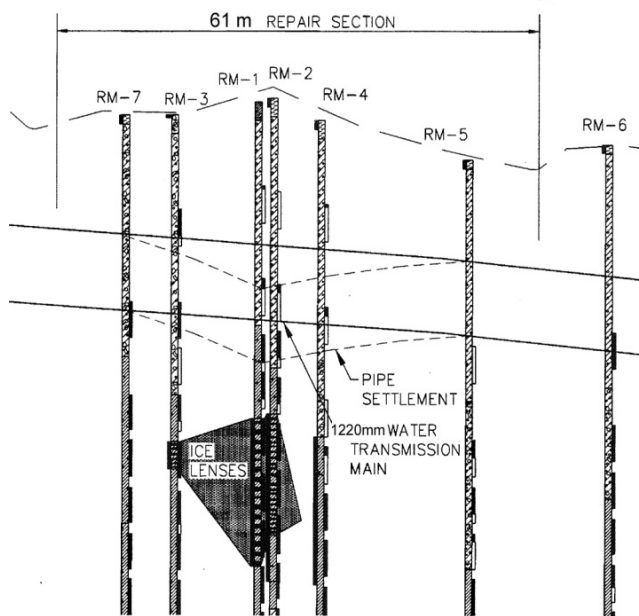


Figure 4. Interpreted AWWU ground profile (from Barber-Wiltse & Rast 2000).

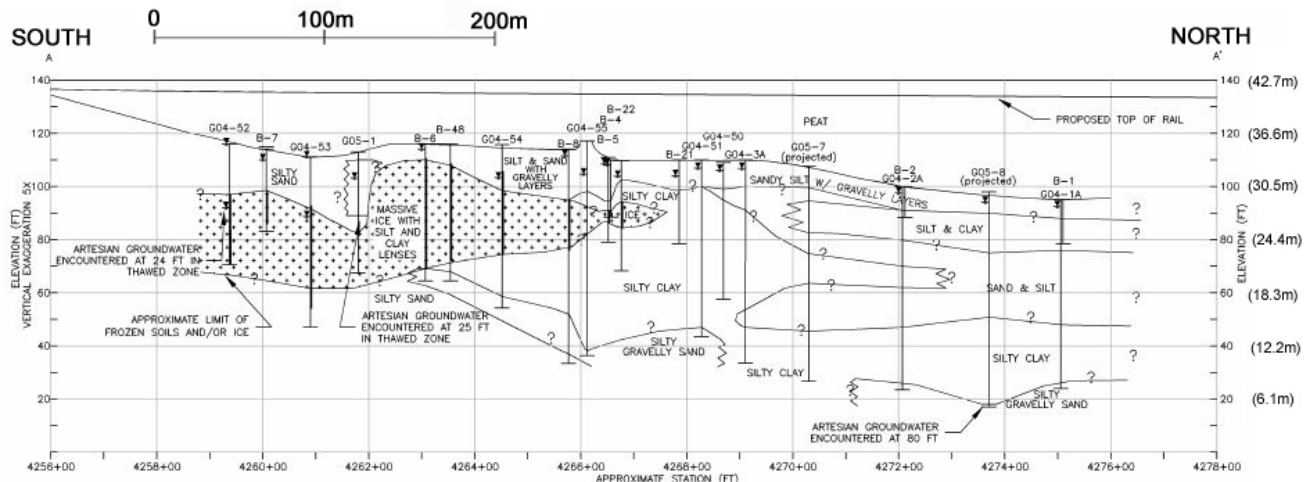


Figure 5. Generalized subsurface profile of proposed railroad realignment (from Krzewinski et al. 2007).

Closure

The importance of proper site investigation in areas of relict permafrost cannot be overemphasized. Adequate knowledge of subsurface conditions (including how they may change in response to infrastructure construction and operation) is critical for appropriate infrastructure design in permafrost environments under both stable and changing climate conditions. A changing climate presents an additional challenge, and adequate knowledge of subsurface conditions is required. In addition, the ways in which subsurface conditions (in particular the thermal regime) may change in response to climate warming needs to be considered.

Due to the occurrence of isolated relict permafrost, “unofficial” minimum standards for site exploration in the Anchorage area were revised; engineering and geological consultants typically are now drilling test borings to greater depths in areas of suspected permafrost. Additionally, “official” Anchorage minimum standards now require that a subsurface investigation be performed at any building site within areas delineated on the 1980 MOA map as having a high potential for isolated permafrost conditions (MOA 2011).

With continued development and expansion into areas having less desirable terrain and soil conditions, additional areas containing relict permafrost will surely be encountered. However, with proper site investigation and subsequent design, the detrimental effects of frozen ground on foundations and infrastructure can be minimized.

References

- Barber-Wiltse, L. & Rast, F. 2000. Anchorage loop water transmission main repair. *Proceedings of the Sixth International Symposium on Cold Region Development*, ISCORD 2000, Hobart, Tasmania, Australia, January 31–February 4, 2000: 41-44.
- Ferrains, O.J., Jr. 1965. Permafrost map of Alaska. USGS Miscellaneous Geologic Inventory Map I-445, Scale 1:2,500,000.
- Harris et al. 1988. Glossary of permafrost and related ground-ice terms. National Research Council of Canada. Technical Memorandum No. 142, 156 pp.
- Helical Pier Systems. Undated. Subdivision underpinning. Manufacturer’s literature, http://helicalpiersystems.com/products-services/featured_projects/subdivision_underpinning/.
- Krzewinski, T.G., Wachholz, M.J., Miller, D., & Lotakis, G. 2007. ARRC rail alignment improvements Birchwood, Alaska railroad design – construction in marginally frozen relict ice and soil. *Proceedings of 13th International Conference on Cold Regions Engineering*, Orono, Maine, July 23-26, 2006, 10 pp.
- Long, E.L. Personal communication, March, 2011.
- Lee, H.R. 1977. Permafrost in Anchorage. *Proceedings of the Second International Symposium on Cold Regions Engineering*, University of Alaska Fairbanks, August 12-14, 1976: 283-288.
- Municipality of Anchorage (MOA). 1979. Geotechnical hazards assessment study. Prepared by Harding-Lawson Associates, June 15, 1979, 102 pp. with plates.
- Municipality of Anchorage (MOA). 1980. Anchorage coastal resource atlas. Municipality of Anchorage Planning Department. Vol. 1: Anchorage bowl.
- Municipality of Anchorage (MOA). 2011. Chapter 23.15. Local amendments to the International Building Code 2009 Edition, Subsection 1803.5.13, Permafrost, 26 pp.
- Pacific Reporter. 1979, 2nd Series. George and Lora Stepanov, Tom and Rita Gittens, Steiner Eidum Hansen, Reid and Eunice Dresser, and Turner Construction Co, Inc., Appellants v. Louis Gavrilovich, Milanka Gavrilovich and Hewitt V. Lounsbury and Associates, Appellees. No. 3236, Supreme Court of Alaska, March 30, 1979.
- R&M Consultants, Inc. (R&M). 1973. Private residence-5039 Knights Way boring log. Castle Heights No. 2 subdivision, Anchorage, Alaska, October, 1973.
- R&M Consultants, Inc. (R&M). 1975. Proposed Rainbow townhouse development geotechnical report. Anchorage, Alaska, December, 1975, 13 pp. with appendices.
- Schmoll, H.R. & Dobrovlny, E. 1972. Generalized geologic map of Anchorage and vicinity. USGS Folio of Anchorage and Vicinity, Anchorage, Alaska Map I-787-A, Scale 1:24,000.
- Tracy, Kate. 2006. 24 Sue condo builder. *Alaska Star*, Thursday, June 29, 2006.
- Wahrhafting, Clyde. 1965. Physiographic divisions of Alaska. USGS Professional Paper 482, 52 pp.
- Weaver, Monte. Personal communication, July, 2011.

Vegetation Cover on Alpine Rock Glaciers in Relation to Surface Velocity and Substrate

Lorenzo Rieg, Rudolf Sailer, Johann Stötter
Institute of Geography, University of Innsbruck

Dieter Burger
Institute of Geography and Geoecology, Karlsruhe Institute of Technology

Abstract

This study analyzes the relationship between vegetation cover and surface velocity on alpine rock glaciers. Fieldwork was conducted in four areas in the Tyrolean Alps (Austria). Total vegetation cover and cover of each distinct species were assessed. In addition, the percentage of fine-grained material was measured. The results were compared to surface movement, calculated from two DSMs derived from multitemporal airborne laser scanning data. The assumption that surface movement is a limiting factor for plant growth could be confirmed. No direct relationship between surface movement and vegetation cover could be established. Especially, the availability of fine-grained substrate has to be taken into account in the explanation of vegetation cover on rock glaciers. The vegetation cover and amount of fine-grained material correlate in areas with surface movement below 1.5m/a. In areas with velocities >1.5m/a, vegetation cover seems to be mainly affected by surface velocity.

Keywords: alpine flora; extreme environments; permafrost; rock glaciers; vegetation cover.

Introduction

Active rock glaciers are widespread features in alpine environments and are commonly regarded as indicators of discontinuous permafrost (Barsch 1996).

Vegetation on rock glaciers has been investigated mainly by Burga (1987, 1999), Cannone (1997), Cannone & Gerdol (2003), and Burga et al. (2004). A key question regarding the special environmental conditions on active rock glaciers is which parameters are crucial in controlling the establishment of plants on such unstable surfaces. The substrate character and surface deformation are responsible for the growth of primarily pioneer plants (Burga et al. 2004), mainly the same plants that are growing in glacier forefields (Burga 1999). The crucial factors for colonization of alpine glacier forefields are the availability of fine detritic material, water supply, and favorable microclimatic conditions (Matthews 1992). These also seem to be important factors for vegetation on active rock glaciers. According to Burga (1999), there is also a correlation between the grain size of the substrate and the occurrence of some vascular plant species in glacier forefields, where some species grow mainly on silt and fine sand while others prefer rather coarse-grained materials. Surface deformation is a locally crucial parameter of plant occurrence, but it can affect the vegetation cover also as a secondary factor by modifying the quality of the substrate. For example, it can occur through the creation of pockets containing fine-grained material on the rock glacier surface, or the accumulation of fine substrate in the furrows caused by the moving surface. The movement of substrate undoubtedly plays a major role for the plant cover on active rock glaciers, but factors such as grain size and other plant growth controlling parameters, such as the availability of fine-grained substrate or water and microclimate, must

also be considered. While less vegetation occurs in areas with high surface instability (Cannone & Gerdol 2003), a clear relation between vegetation cover, surface change, and other parameters has yet to be proved.

All previous studies have focused on smaller parts of rock glaciers, where flow velocity was measured. Hence the spatial distribution of areas in which a comparison between vegetation cover, surface parameters, and surface change is possible has been limited. With surface velocities calculated from airborne laser scanning (ALS) to derive high-resolution and accurate digital surface models (DSMs), the possibilities for calculating surface change and velocity of rock glaciers increase drastically. Velocities can, for example, be calculated for the entire surface of a rock glacier. Therefore, this study aims at improving the understanding of the relationship of surface velocity and substrate on rock glaciers with the occurrence of vegetation.

Study Areas, Methods, and Data

Study areas

The four study areas are high alpine cirques containing one or several active rock glaciers located in the Stubai and Ötztal Alps, Tyrol (Austria) (see Figs. 1 and 2).

The rock glacier Äusseres Hochebenkar (AHK) (Fig. 2.1) is located in the Gurgler Tal south of Obergurgl. It is a big, tongue-shaped rock glacier with a length of about 1600 m, and it fills the entire cirque. The history of investigation goes back to the 1930s (Pillewitzer 1938), with a long record of flow velocity and other data (Victoris 1958, 1972, Haerberli & Patzelt 1982, Schneider & Schneider 2001). The rock glacier AHK covers relatively steep terrain and, with velocities of up to 5 m/a, is one of the fastest moving rock glaciers known

(Barsch 1996:126ff). It reaches from 2830 m to ca. 2360 m altitude.

The Innere Ölgrube (OGR) (Fig. 2.3) is a small side valley of the Kauner Valley containing a composite rock glacier. The OGR has been thoroughly investigated recently (Berger et al. 2004, Krainer & Mostler 2002, 2006, Hausmann et al. 2007a,

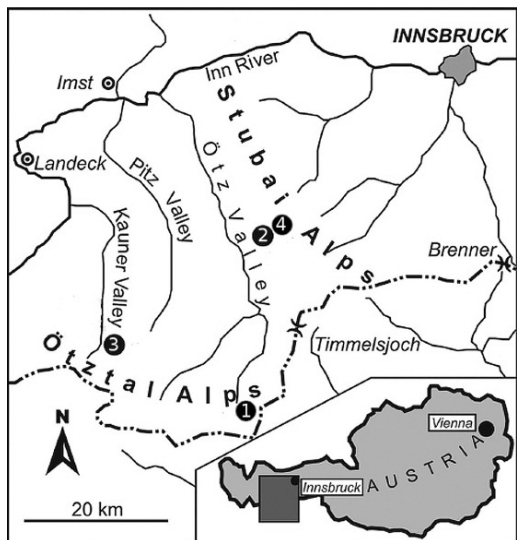


Figure 1. Location of the study sites: (1) Äusseres Hochebenkar, (2) Innere Ölgrube, (3) Inneres Reichenkar, and (4) Schrankar.

Krainer et al. 2007) with special regards to its surface velocity and internal structure. It consists of two separate tongue-shaped rock glaciers that lie side by side and therefore appear as one (see Fig. 2). The study areas Inneres Reichenkar (RKR) and Schrankar (SKR) are located in the westernmost part of the Stubai Alps, in the Sulztal, a side-valley of the Ötztal. The rock glacier Reichenkar, one of the longest and most active rock glaciers in Austria (Hausmann et al. 2007b), has also been intensively investigated, especially during the last decade (Chiesi et al. 1999, 2003, Krainer & Mostler 2000, 2002, 2006, Hausmann et al. 2007b, Krainer et al. 2002, 2007). A large amount of surface velocity, discharge, and geophysical data have been collected.

The SKR is a big cirque enclosed by high peaks with a steep cirque threshold to the south, containing several rock glaciers of different activity and material. In this study, two rock glaciers were investigated, both of which are significantly smaller and less active than the rock glaciers at the other study sites.

Field data

For this study, the total vegetation cover and the cover of each distinct species were assessed in squares of 3 x 3 m, located roughly every 15 m, along several longitudinal and transversal transects on each rock glacier, using the Braun-Blanquet method (Braun-Blanquet 1964) with a percent scale (Dierschke 1994). In addition, the percentage of fine-grained

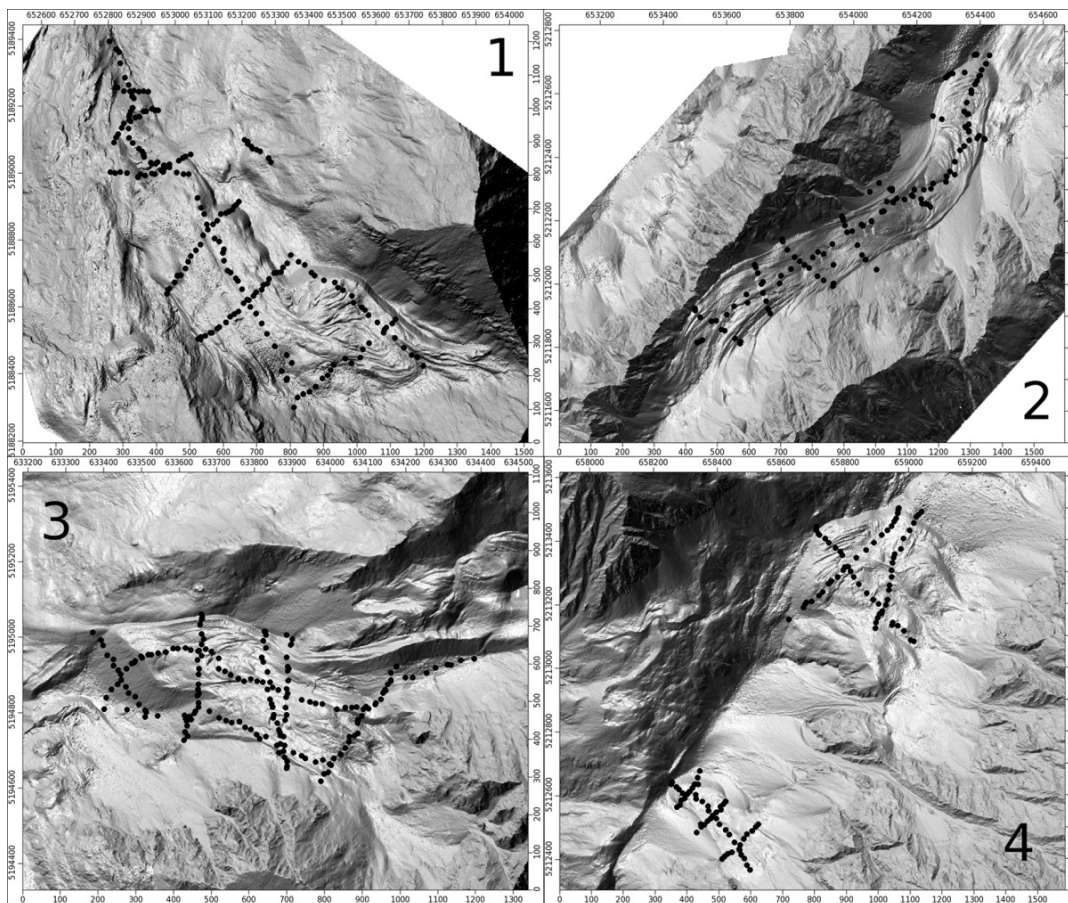


Figure 2. Location of the mapped squares in the study sites. (1) Äusseres Hochebenkar, (2) Inneres Reichenkar, (3) Innere Ölgrube, and (4) Schrankar.

material (silt, clay and sand combined) was estimated visually in each square, while the average size of the blocks was measured. For comparison, adjacent stable areas alongside the rock glaciers were also mapped. In total, 622 squares were mapped during August and September 2010; 541 of them were located on rock glaciers ranging from elevations of 2300 m to 2800 m.

Calculation of surface velocity

Surface velocity data were acquired using the image correlation program Imcorr, developed by Scambos et al. (1992), which uses two images and attempts to match small subsequences from both images. The program can be used to calculate the displacement rates of moving features. Of course, surfaces and their features on active rock glaciers change, but not much in the relatively short period of three years. The program is also widely used to measure glacier velocities (e.g., Scambos et al. 1992, Bucher 2006), where the change of the glacier surface features is a much bigger problem.

Detailed hillshades, derived from Lidar-DSMs with a resolution of 0.5 m, were used as input images for the feature detection and correlation. For all successfully matched features, Imcorr gives the x and y coordinates and a displacement value as output. These files were used to interpolate velocity-rasters. For details on the dataset, the process of surface movement calculation, and the accuracy of the results, see Bollmann et al. (2011) and Bollmann et al. (submitted). The first Lidar-acquisition campaign took place in autumn 2006 and the second in autumn 2009. Therefore, velocities were calculated over a period of three years, but mean annual values are given in this study to facilitate the comparison to other studies.

Results

Vegetation cover and frequency

Although the vegetation cover and patterns are in some ways similar on all studied rock glaciers, there are differences (see Figs. 3 and 4 and Tables 1 and 2). AHK shows the lowest number of different species, which might be explained by the scarcity of fine-grained substrate and therefore low vegetation cover. The higher vegetation cover at OGR is seen as being related to the high percentage of fine-grained material.

The values at SKR and OGR are comparable (see Figs. 3 and 4), while RKR shows less fine-grained material, which could be an explanation for the lower vegetation cover, especially in combination with the higher surface velocities.

Only six species—*Poa laxa*, *Cerastium uniflorum*, *Saxifraga bryoides*, *Oxyria digyna*, *Leucanthemopsis alpine*, and *Geum reptans*—occur at all study sites (see Table 2). These are also the most frequent species, except for *Minuartia sedoides*, which was found only at OGR but at such a high cover and frequency that it is still one of the most frequent species overall. All other species occur rarely, probably due to individual site-specific factors or coincidental germination. More field data would be needed to seriously compare the vegetation patterns of the different study areas.

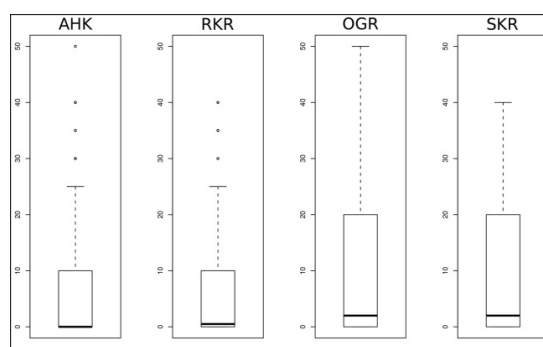


Figure 3. Values of fine-grained material in the squares on rock glaciers in all study sites. 1st quartile, median, 2nd quartile, range (95%) and outliers.

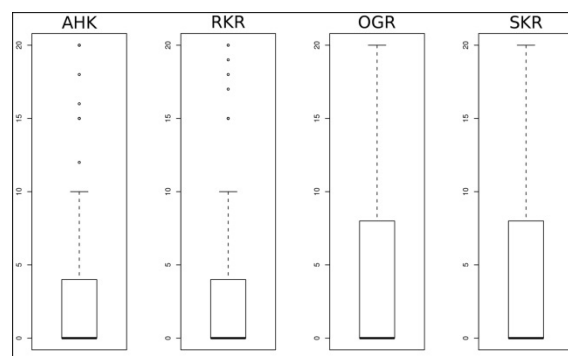


Figure 4. Total vegetation cover (%) in the squares on rock glaciers in all study sites. 1st quartile, median, 2nd quartile, range (95%) and outliers.

Table 1. Number of different species and average values for fine-grained material and total vegetation cover in the squares on rock glaciers for all study sites.

| Area | Species | Fine-grained material | Vegetation cover |
|------|---------|-----------------------|------------------|
| AHK | 9 | 8.45% | 3.19% |
| OGR | 15 | 13.49% | 5.57% |
| RKR | 15 | 9.62% | 4.17% |
| SKR | 14 | 13.51% | 4.77% |

Surface velocity

The highest velocities occur at the steep parts of the tongues of rock glaciers RKR and AHK with values of up to 3 m/a. These values are comparable to those given by several authors (e.g., Schneider & Schneider 2001, Hausmann et al. 2007a). At OGR, the fastest moving part of the rock glacier is the tongue of the smaller, southern rock glacier, which reaches velocities over 1.5 m/a. Big portions of the composite rock glacier seem to move slower, with values below 0.5 m/a. At SKR, surface velocities are very low in general. Only the steepest part of the smaller rock glacier reaches values of over 0.6 m/a, while the bigger, spatula-shaped rock glacier shows no clear movement at all. This could be expected due to the relatively flat topography of the area; unfortunately there are no other measurements available to validate the results.

Table 2. Average cover (Cov.) and frequency (Fr.) of all species in the different study areas and combined for all areas in percent.

| Study area | AHK | | OGR | | RKR | | SKR | | All | |
|---------------------------------|------|-----|------|-----|------|-----|------|-----|------|-----|
| | Cov. | Fr. | Cov. | Fr. | Cov. | Fr. | Cov. | Fr. | Cov. | Fr. |
| <i>Poa laxa</i> | 0.7 | 20 | 1.69 | 44 | 1.08 | 32 | 0.85 | 34 | 0.86 | 32 |
| <i>Cerastium uniflorum</i> | 1.28 | 26 | 0.81 | 17 | 0.72 | 28 | 0.83 | 14 | 0.73 | 21 |
| <i>Saxifraga bryoides</i> | 0.02 | 1.3 | 0.01 | 0.6 | 0.6 | 25 | 1.31 | 26 | 0.39 | 11 |
| <i>Oxyria digyna</i> | 0.42 | 0.6 | 0.16 | 4.4 | 0.45 | 17 | 0.28 | 11 | 0.26 | 7 |
| <i>Leucanthemopsis alpina</i> | 0.38 | 10 | 0.58 | 11 | 0.09 | 4.6 | 0.16 | 6 | 0.24 | 8.5 |
| <i>Minuartia sedoides</i> | 0 | 0 | 1.02 | 29 | 0 | 0 | 0 | 0 | 0.2 | 8.5 |
| <i>Geum reptans</i> | 0.02 | 1.3 | 0.28 | 9 | 0.12 | 7 | 0.11 | 6 | 0.11 | 5 |
| <i>Taraxacum alpinum</i> | 0 | 0 | 0 | 0 | 0 | 0 | 0.25 | 6 | 0.05 | 1.3 |
| <i>Sedum alpestre</i> | 0.2 | 4.5 | 0.04 | 1.9 | 0 | 0 | 0.3 | 2.7 | 0.05 | 2.4 |
| <i>Rhododendron ferrugineum</i> | 0 | 0 | 0 | 0 | 0.24 | 3.6 | 0 | 0 | 0.05 | 0.7 |
| <i>Veronica alpina</i> | 0 | 0 | 0.18 | 5 | 0 | 0 | 0 | 0 | 0.04 | 1.5 |
| <i>Senecio incanus</i> | 0 | 0 | 0.15 | 6 | 0.01 | 1.8 | 0 | 0 | 0.03 | 2 |
| <i>Saxifraga spec.</i> | 0.09 | 2 | 0.01 | 0.6 | 0 | 0 | 0 | 0 | 0.02 | 0.7 |
| <i>Salix retusa</i> | 0 | 0 | 0.04 | 1.2 | 0.04 | 0.9 | 0 | 0 | 0.02 | 0.5 |
| <i>Poa alpina</i> | 0 | 0 | 0 | 0 | 0.06 | 1.8 | 0.04 | 1.8 | 0.02 | 0.7 |
| <i>Erigeron uniflorus</i> | 0 | 0 | 0 | 0 | 0 | 0 | 0.09 | 2.7 | 0.02 | 0.5 |
| <i>Doronicum clusii</i> | 0 | 0 | 0.06 | 1.8 | 0.04 | 1.8 | 0 | 0 | 0.02 | 0.7 |
| <i>Campanula barbata</i> | 0 | 0 | 0.02 | 0.6 | 0.04 | 0.9 | 0 | 0 | 0.02 | 0.4 |
| <i>Loiseleuria procumbens</i> | 0 | 0 | 0.3 | 1.9 | 0 | 0 | 0.3 | 1.9 | 0.01 | 1.1 |
| <i>Linaria alpina</i> | 0 | 0 | 0 | 0 | 0 | 0 | 0.03 | 2.7 | 0.01 | 0.5 |
| <i>Carex curvula</i> | 0 | 0 | 0 | 0 | 0.03 | 0.9 | 0 | 0 | 0.01 | 0.5 |
| <i>Androsace alpina</i> | 0.06 | 0.6 | 0 | 0 | 0.01 | 0.9 | 0 | 0 | 0.01 | 0.4 |
| <i>Artemisia mutellina</i> | 0 | 0 | 0 | 0 | 0 | 0 | 0.01 | 1.8 | 0 | 0.2 |

Discussion

While very high surface movement certainly prevents plant growth, vegetation seems to tolerate much higher intensities of surface movement than was previously assumed. The most species and the highest values for vegetation cover were found in squares with relatively low surface velocity, but vegetation covers of up to 20% were found in several squares with surface velocities of about 2 m/a (see Fig. 5). The only squares in which no vascular plants at all were found were those with velocity of over 2.8 m/a.

These results contradict the findings of Cannone & Gerdol (2003) and Burga et al. (2004). Cannone & Gerdol (2003) state that vascular species tolerate surface movement only up to a velocity of 0.35 m/a, with *Geum reptans* and *Cerastium uniflorum* being the species most resistant to stress induced by surface movement. However, Burga et al. (2004) give 0.3 m/a as the maximum surface movement value that is tolerated by vascular plants. Caccianiga et al. (2011) proved that several species, such as *Linaria alpina*, tolerated much higher velocities on the debris-covered Miage glacier.

The relationship of total vegetation cover to surface movement was analyzed for all mapped squares. The values for total

vegetation cover do not clearly correlate with those for surface movement (see Fig. 5), but total vegetation cover is related to the percentage of fine-grained material (see Figs. 6 and 7). This correlation is noticeable for all squares ($R^2=0.43$), but it gets better if squares with values for surface velocity exceeding a certain level are removed (Fig. 7).

The correlation gets much better if squares with a surface velocity of over 1.5 m/a are excluded ($R^2=0.70$), but it improves only slightly if more squares are removed from the comparison (e.g., $R^2=0.75$ if all squares with surface velocities of over 0.17 m/a are excluded). Nearly all squares with high percentages of fine-grained material (over 40%), which show no or very little vegetation cover, fall within the range of surface velocities above 1.5 m/a (see Fig. 6).

Therefore, we conclude that vegetation cover is at first regulated by the availability of fine-grained material, as long as the surface velocity is below a threshold of 1.5 m/a. If this threshold is exceeded, vegetation cover is heavily influenced by surface instability and therefore shows much lower values in relation to the fine-grained material. Below this threshold, vegetation seems to tolerate movement reasonably well, and its occurrence is mainly related to the percentage of fine-grained material.

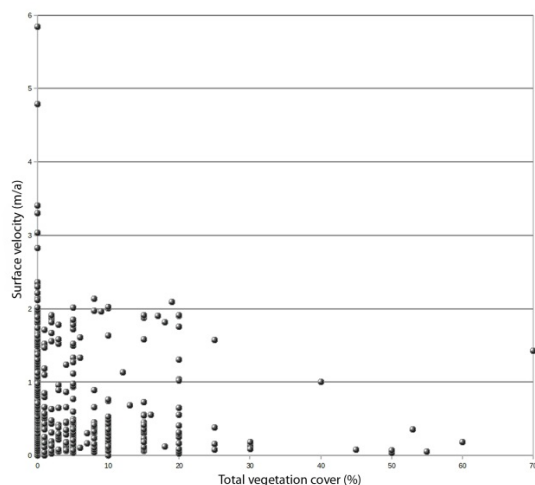


Figure 5. Relation of vegetation cover and surface velocity.

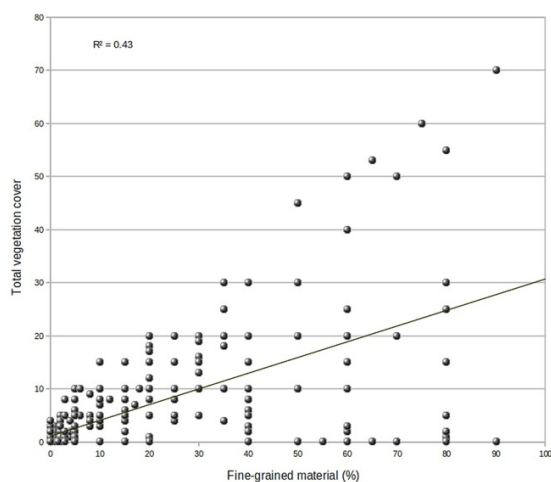


Figure 6. Relation of total vegetation cover and fine-grained material for all squares.

Conclusions

Analysis of vegetation showed that all species that occur on the rock glaciers in all study areas have also been found on other rock glaciers in the Alps (Cannone & Gerdol 2003, Burga et al. 2004). Especially *Cerastium uniflorum* and *Saxifraga bryoides*, and to a lesser extent *Geum reptans* and *Loiseleuria procumbens*, occurred frequently on all botanically investigated rock glaciers. Of course, these are widespread alpine plants, but they can be assumed to be well-suited to the stress caused by environments as extreme as active rock glaciers. As expected due to the transect-approach, fewer different species were found than in other studies. On the other hand, the complete rock glacier surfaces could be covered, even in a less detailed way, while the majority of other studies focus on the easily accessible rock glacier tongues. This might also be the reason for the relatively low total vegetation cover in comparison to other studies.

The comparison of calculated surface velocities with the data acquired during the field campaign showed interesting results. Relatively high vegetation covers (up to 20%) were

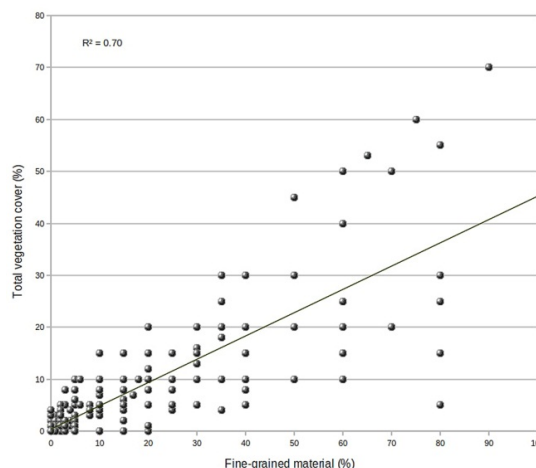


Figure 7. Relation of vegetation cover and fine-grained material for squares with surface movement below 4.5 m/a during three years.

mapped in areas with surface movement rates of over 1.5 m/a and scarce vegetation even in areas with surface velocity exceeding 2.5 m/a.

The relationship between vegetation cover and the percentage of fine-grained substrate is also dependent on surface velocity. A threshold of 1.5 m/a for surface velocity could be defined. Below this threshold, the vegetation cover is mainly dependent on the availability of fine-grained material, while it is heavily affected by surface instability if the surface velocity exceeds the threshold. Of course, it has to be kept in mind that other factors can influence plant growth if not hindered by surface instability or the lack of fine-grained substrate. Topographic parameters such as elevation, aspect, and slope have been tested as well, but no clear correlation between them and the total vegetation cover was found. For other parameters, such as air temperature and water availability, no data were available for the investigated areas. Further research and data would be required to answer the remaining questions.

Acknowledgments

This study was funded by the Austrian Climate Research Program through the project C4AUSTRIA (Climate Change Consequences for the Cryosphere ACRP Nr. A963633). Further acknowledgements go to Erik Bollmann, who provided the surface velocity data, and two reviewers who helped improve this paper.

References

Barsch, D. 1996. Rockglaciers. Indicators for the Present and Former Geocology in High Mountain Environments. Springer Verlag, Berlin, 331 pp.

Berger, J., Krainer, K., & Mostler, W. 2004. Dynamics of an active rock glacier (Ötztal Alps Austria). *Quaternary Research* 62, 233-242

- Bollmann, E., Sailer, R., Briese, Ch., Stötter, J., & Fritzmann P. 2011. Potential of airborne laser scanning for geomorphologic feature and process detection and quantifications in high alpine mountains. *Zeitschrift für Geomorphologie* 54, Supplementary Issue "Laser scanning applications in in geomorphology."
- Bollmann, E., Abermann, J., Klug, C, Sailer, R., & Stötter, J. (submitted). Quantifying Rock Glacier Creep using Airborne Laserscanning. A case study from two rock glaciers in the Austrian Alps. *Proceedings of the tenth International Conference on Permafrost*, Tyumen, Russia.
- Braun-Blanquet, J. 1964. Pflanzensoziologie. 3. Auflage, Wien, 865 pp.
- Bucher, K., Geist, T., & Stötter, J. 2006. Ableitung der horizontalen Gletscherbewegung aus multi-temporalen Laserscanning-Daten Fallbeispiel: Hintereisferner, Ötztaler Alpen. *Angewandte Geoinformatik 2006 – Beiträge zum AGIT-Symposium Salzburg*, 277-286
- Burga, C.A. 1987. Gletscher- und Vegetationsgeschichte der Südrätischen Alpen seit der Späteiszeit. *Denkschrift der SNG 101*.
- Burga, C.A. 1999. Vegetation development on the glacier forefield Morteratsch (Switzerland). *Applied Vegetation Science* 2, 17-24.
- Burga, C.A., Frauenfelder, R., Ruffet, J., Hoelzle, M., & Kääh, A. 2004. Vegetation on Alpine rock glacier surfaces: a contribution to abundance and dynamics on extreme plant habitats. *Flora* 199, 505-515.
- Caccianiga, M, Andreis, C., Dilaiuti, G., D'Agata, C., Mihalcea, C., & Smiraglia, C. 2011. Alpine debris-covered glaciers as a habitat for plant life. *The Holocene* 21(6), 1011-1020
- Cannone, N. 1997. Vegetazione periglaciale e crionivale: caratteristiche, modelli di aggregazione e rapporti con forme processi periglaciali. Ph.D. Thesis, University of Pavia.
- Cannone, N. & Gerdol, R. 2003. Vegetation as an Ecological Indicator of Surface Instability in Rock Glaciers. *Arctic, Antarctic and Alpine Research* 35(3). 384-390.
- Chiesi, G., Krainer, K., Mostler, W., & Weinold, T. 1999. Bewegungsmessungen am aktiven Blockgletscher Inneres Reichenkar mit der GPS-Methode. *X. Internationale Geodätische Woche, Obergurgl*. 223-227.
- Chiesi, G., Krainer, K., Mostler, W., & Weinold, T. 2003. 5 Jahre Bewegungsmessungen am aktiven Blockgletscher Inneres Reichenkar (westliche Stubaier Alpen) mit der GPS-Methode. *XII. Internationale Geodätische Woche, Obergurgl*. 201-205.
- Dierschke, H. 1994. Pflanzensoziologie. Grundlagen und Methoden. *Ulmer Verlag* Stuttgart, 683 pp.
- Haeberli, W. & Patzelt, G. 1982. Permafrostkartierung im Gebiet der Hochebenkar-Blockgletscher. Obergurgl, Ötztaler Alpen. *Zeitschrift für Gletscherkunde und Glazialgeologie* 18(2), 127-150.
- Hausmann, H., Krainer, K., Brückl, E., & Mostler, W. 2007a. Creep of two alpine rockglaciers – Observation and Modelling (Ötztal- and Stubai Alps, Austria). *Grazer Schriften der Geographie und Raumforschung* 43, 145-150.
- Hausmann, H., Krainer, K., Brückl, E., & Mostler, W. 2007b. Internal Structure and Ice Content of Reichenkar Rock Glacier (Stubai Alps, Austria) Assessed by Geophysical Investigations. *Permafrost and Periglacial Processes* 18, 351-367.
- Krainer, K. & Mostler, W. 2000. Reichenkar Rock Glacier: a Glacier-Derived Debris-Ice System in the Western Stubai Alps, Austria. *Permafrost and Periglacial Processes* 11, 267-275.
- Krainer, K. & Mostler, W. 2002. Hydrology of active rock glaciers in the Austrian Alps. *Arctic, Antarctic and Alpine Research* 34, 142-149.
- Krainer, K. & Mostler, W. 2006. Flow velocities of active rock glaciers in the Austrian Alps *Geografiska Annaler*. 88(a), 267-280.
- Krainer, K., Mostler, W., & Span, N. 2002. A glacier-derived, ice-cored rock glacier in the western Stubai Alps (Austria). Evidence from ice exposures and ground penetrating radar investigation. *Zeitschrift für Gletscherkunde und Glazialgeologie* 38, 21-34.
- Krainer, K., Mostler, W., & Spötl, C. 2007. Discharge from active rock glaciers, Austrian Alps: a stable isotope approach. *Austrian Journal of Earth Sciences* 100, 102-112.
- Matthews, J.A. 1992. *The ecology of recently-deglaciated terrain: A geoecological approach to glacier forelands and primary succession*. Cambridge University Press, Cambridge, 386 pp.
- Pillewitzer, W. 1938. Photogrammetrische Gletscheruntersuchungen im Sommer 1938. *Zeitschrift für Erdkunde*, 9(19), 367-372.
- Schneider, B. & Schneider, H. 2001. Zur 60 jährigen Messreihe der kurzfristigen Geschwindigkeits-schwankungen am Blockgletscher im Äusseren Hochebenkar, Ötztaler Alpen, Tirol. *Zeitschrift für Gletscherkunde und Glazialgeologie* 37(1), 1-33.
- Scambos, T.A., Dutkiewicz, M.J., Wilson, J.C., & Bindshadler, R.A. 1992. Application of image cross-correlation to the measurement of glacier velocity using satellite image data. *Remote Sensing of Environments* 42(3), 177-186.
- Vietoris, L. 1958. Der Blockgletscher des Äußeren Hochebenkars. *Gurgler Berichte*, 1, 41-45.
- Vietoris, L. 1972. Über die Blockgletscher des Äußeren Hochebenkars. *Zeitschrift für Gletscherkunde und Glazialgeologie* 8, 169-188.

Simplified Climate Statistics for Permafrost Modeling: Yellowknife Case Study

Daniel Riseborough, Stephen Wolfe, Caroline Duchesne
Geological Survey of Canada

Abstract

Climate variables were examined to evaluate their simplification for use in permafrost models, using data for Yellowknife Northwest Territories, Canada, as an example. Results suggest that conversion of the annual temperature cycle to a sine wave is an acceptable approximation, as long as the wave retains the correct values for the annual freezing and thawing degree-day totals. Evolution of the annual snow cover can be approximated by a parabolic accumulation function; the delay of snow cover initiation with respect to the start of the freezing season, the snow accumulation function, and snow density are all critical, while end-of-season snowpack evolution is of secondary importance.

Keywords: permafrost; numerical models; climate data.

Introduction

Numerical permafrost simulation models are used to estimate the thermal state of the ground, including predicted future changes. A critical process in model building is to balance scientifically realistic complexity with practically realistic simplicity (Ferguson 1999). Model outputs are influenced by model inputs, so it is important to consider the effect of simplifying assumptions on the accuracy of simulation results. This paper examines some of the simplifying approaches that can be applied to climate data input, using data for Yellowknife, Northwest Territories, Canada (62°30'N, 114°29'W), as a case study.

It is assumed in this analysis that the goal of simplified modeling is to characterize ground thermal behavior at an annual time scale, rather than to predict the seasonal progression of the ground thermal regime. For example, results for maximum active layer thickness are more important than the timing of the freezing front position over the thaw season. As such, trends and inter-annual variation in freezing and thawing degree-days should be represented in model input, but daily or synoptic-scale variations are not required. Conceptual descriptions of permafrost-climate interactions (Smith and Riseborough 2002), model-based sensitivity analyses (Goodrich 1982, Ling and Zhang 2006, 2007), and field studies (Smith et al. 2009) suggest that the key climate variables for model input are

- Mean annual air temperature (MAAT)
- Annual total freezing degree-days (FDD_{Ann})
- Annual total thawing degree-days (TDD_{Ann})
- MAAT, FDD_{Ann} and TDD_{Ann} trends ($^{\circ}$, $^{\circ}$ -days/decade)
- Inter-annual variability
- Snow cover initiation
- Snow density
- Seasonal pattern of snow accumulation
- Snow ablation

These parameters are discussed in the following sections.

Temperature and Degree-Days

For multi-year studies of permafrost conditions, the annual temperature cycle can be converted to a sine wave that

retains the correct values for FDD_{Ann} and TDD_{Ann} . For an air temperature wave with amplitude A (i.e., an annual temperature range of $2A$) and mean T_{Ann} (= MAAT), temperature T at time t (ignoring the phase of the wave) is

$$T(t) = T_{Ann} + A \sin(2\pi t / P) \quad (1)$$

where t = time, A = air temperature amplitude, T_{Ann} = mean annual temperature (MAAT), P = Period (365 days). The surface temperature first reaches 0°C at time t_0 , defined as

$$t_0 = \left(\frac{P}{2\pi} \right) \sin^{-1} \left(\frac{-T_{Ann}}{A} \right) \quad (2)$$

Thawing ends (and freezing begins) at $t = (P/2) - t_0$ and freezing ends at $t = P + t_0$, so that the seasonal freezing and thawing degree-day totals for this sine wave are

$$FDD_{Ann} = - \int_{\frac{P}{\pi} - t_0}^{P+t_0} T_{Ann} + A \sin(2\pi t / P) \partial t \quad (3)$$

$$TDD_{Ann} = \int_{t_0}^{\frac{P}{\pi} - t_0} T_{Ann} + A \sin(2\pi t / P) \partial t \quad (4)$$

Letting $t_U = P/2 - t_0$, equation 4 resolves to

$$TDD_{Ann} = \left(T_{Ann} \cdot t_U - \left(\frac{A \cdot P}{2\pi} \right) \right) 2\pi \cos \left(\frac{t_U}{2\pi P} \right) - \left(T_{Ann} \cdot t_0 - \left(\frac{A \cdot P}{2\pi} \right) \right) 2\pi \cos \left(\frac{t_0}{2\pi P} \right) \quad (5)$$

FDD_{Ann} can be calculated from MAAT and TDD_{Ann} , given that $MAAT = (TDD_{Ann} - FDD_{Ann})/365$. For example, Figure 1a shows the Yellowknife annual daily-mean temperature cycle for 2009, with the equivalent sine wave included ($MAAT = -4.42^{\circ}$; $FDD_{Ann} = 3365$; $TDD_{Ann} = 1753$; $A = 21.4^{\circ}$). Using this approach, the 66-year degree-day time series in Figure 1c can be recreated within the model using means (Fig. 1b) and amplitudes (Fig. 1d).

Figure 2a shows the 2009 thaw-season daily temperatures

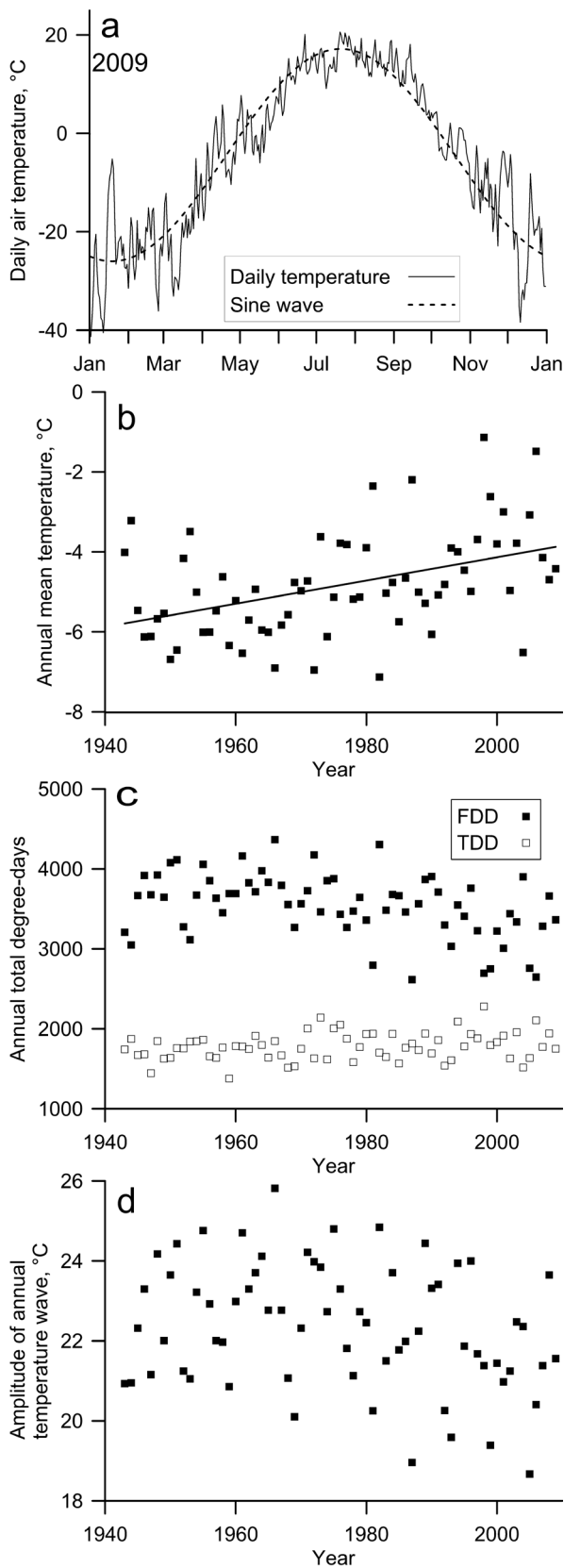


Figure 1. Air temperature data for Yellowknife, Northwest Territories, Canada: a) annual cycle of daily mean for 2009, with equivalent sine wave included; b) trend of mean annual temperature 1943–2009; c) trend of annual freezing and thawing degree-day totals 1943–2009; d) trend of annual sine wave amplitudes calculated from FDD and TDD in (c).

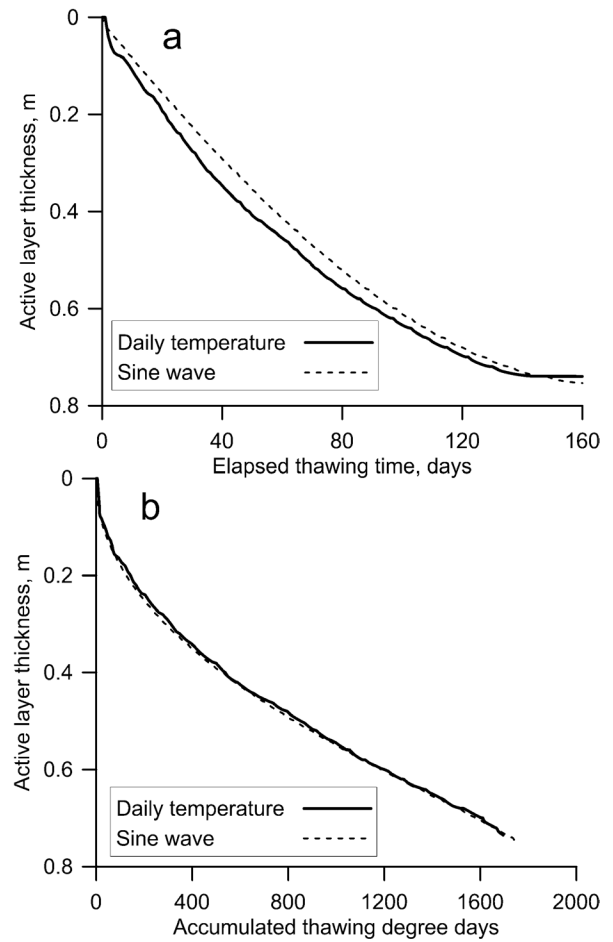


Figure 2. a) Simulated seasonal active layer development, using thawing season air temperature data of Figure 1a, and with equivalent sine wave; b) simulated active layer development of (a), plotted versus accumulated thawing degree-days.

from Figure 1a, together with the thaw-season part of the sine wave (note that season dates have been shifted by about 11 days compared to Figure 1a so that the beginning of the thaw season coincides). Figure 2a shows simulated seasonal active layer development using these temperatures with a typical Yellowknife-area peatland substrate, obtained with the finite element model TONE (details in Riseborough 2007). Results show that the sine wave simulates active layer development reasonably well over the course of the thaw season, never departing from the results using daily temperatures by more than 0.05 m. Figure 2b shows the same results as 2a, but plotted as a function of accumulated TDD; in this case, thaw depth results are consistently within 0.01 m, suggesting that the temporal discrepancy is primarily due to the timing of TDD accumulation. The maximum annual active layer thickness differs between the curves due to the early termination of the thaw season by a brief cold period in the simulation with daily variability. Additional simulations (not presented here) with simple step and saw-tooth temperature functions gave essentially the same active layer development curves shown in Figure 2b.

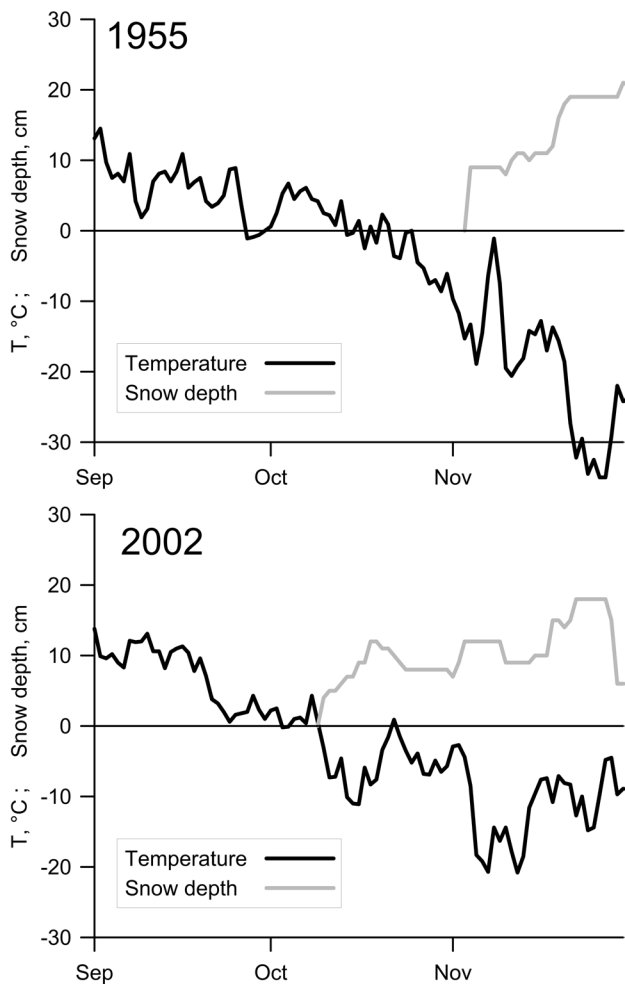


Figure 3. Daily mean air temperature and snow depth at the beginning of the freezing season, 1955 and 2002.

Snow Cover

The properties of snow cover change continuously, from the start of snow accumulation in late autumn or early winter until its disappearance in spring, with variations that influence its effect on the ground thermal regime (Zhang 2005). The challenge that snow cover presents for permafrost-climate models is to describe this variability in a way that allows it to be used in predicting its effect on permafrost temperature. In permafrost models, the thermal resistance of the snow pack determines its thermal effect rather than its thickness alone.

Initiation

The relationship between the beginning of the snow accumulation season and the beginning of the freezing season is critical to the thermal effect of the snow cover (Goodrich 1982, Ling and Zhang 2007). Figure 3 shows extreme examples from the Yellowknife record where snow cover and freezing conditions arrive simultaneously (2002), or after a delay of two weeks (1955). Riseborough (2004) found that delayed snow cover reduces ground temperatures far more than can be attributed to the increase in surface FDD alone; earlier active layer freeze-up affected the ground thermal regime for the rest of the season.

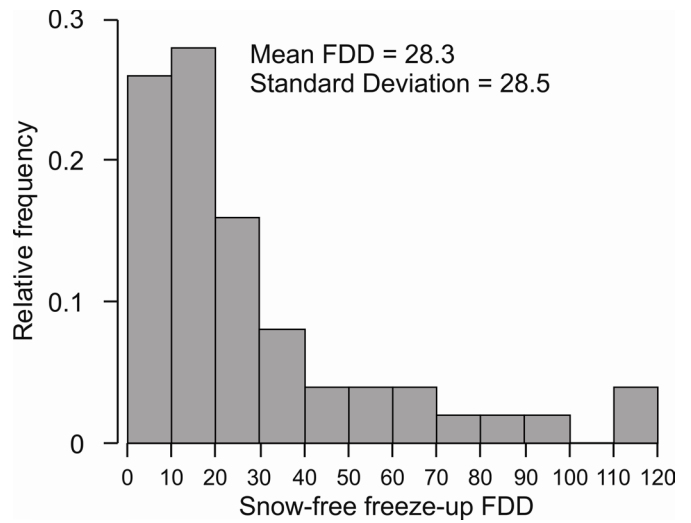


Figure 4. Distribution of FDD totals for the snow-free period at the beginning of the freezing season.

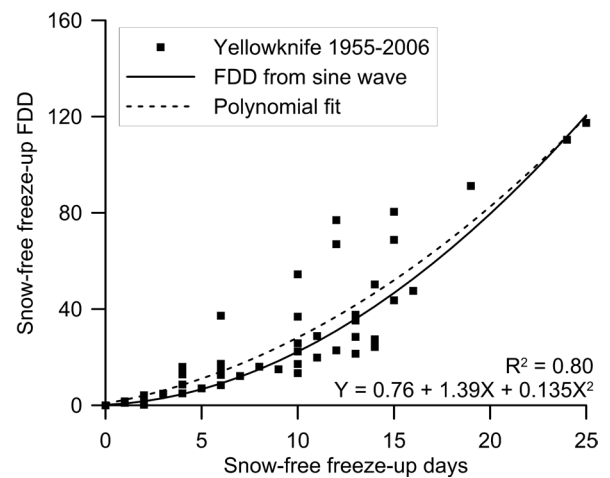


Figure 5. Snow-free accumulation for the beginning of the freezing season as a function FDD of the duration of the snow-free period.

Figure 4 shows the distribution of snow-free FDD at the beginning of the annual freezing season for the Yellowknife climate record. The mean length of the snow-free freeze-up period is 8.9 days with a standard deviation of 5 days; the mean FDD for this period is 28.3 degree-days, with a standard deviation of 28.5 degree-days.

Figure 5 shows the relationship between length of the snow-free period at the beginning of the annual freezing season for the Yellowknife climate record, and the FDD total for that period. Data for individual years of the record are shown as points, with a polynomial fit through the data shown as a dashed line. Also included is the FDD accumulation expected for a sine wave (solid line), using the mean and amplitude calculated for the mean FDD and TDD for the Yellowknife data. The approximate agreement between the polynomial fit and the theoretical result suggests that the use of a specified time delay in conjunction with the sine wave produces the appropriate FDD value.

Snow accumulation

Based on an analysis of the climate record for Barrow, Alaska, Zhang et al. (1996) characterized the snow accumulation rate as a parabolic function:

$$Z_t = Z_{max} \left(\frac{t - t_{init}}{t_{max} - t_{init}} \right)^{0.5} \tag{6}$$

where t = time, Z_t = snow depth at time t , Z_{max} = maximum snow depth, t_{init} = time of snow cover initiation, t_{max} = time of maximum snow depth. Osokin et al. (2000) found that the exponent in equation 6 varied between 0.4 and 0.6 for a number of climate stations in Russia. Zhang et al. (1996) modeled deflation of the snow pack at the end of the snow cover season using a similar function:

$$Z_t = Z_{max} \left(\frac{t - t_{max}}{t_{end} - t_{max}} \right)^{1.5} \tag{7}$$

Figure 6a shows the annual snow depth record for all years of the Yellowknife record, superimposed. Figure 6b shows the mean and median snow depth from these data, together with

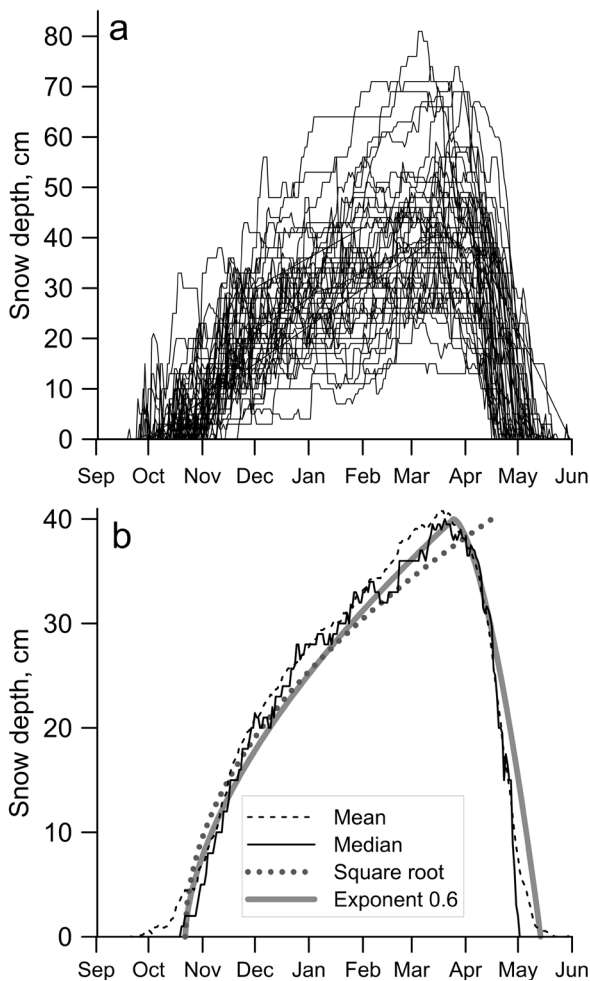


Figure 6. a) Yellowknife snow accumulation curves for individual years 1955–2005. b) Mean and median daily snow depth from data in (a), with different accumulation curves derived for seasonal maximum and freezing-season end, and with/without deflation at season end.

two possible accumulation functions. Both use the average snow season delay of Figure 4 and the maximum of the median snow depth curve of Figure 6a. The exponent 0.6 function reaches maximum at the mean date of maximum snow depth from the climate record, with end-of-season deflation using equation 7, while the exponent 0.5 function reaches the maximum at the end of the accumulation season (so that the snow disappears by ablation without deflation). The square root curve over-predicts snow depth early in the season and under predicts it late in the season, whereas the 0.6 exponent function is closer to the data curve, albeit with extended periods of over and under prediction. Handling of the end-of-season snow cover is discussed in the section below on ablation.

Density variation

Although many other factors have an influence, density is the most common parameter used to model the thermal properties of snow cover (Sturm et al. 1997). Snow naturally develops a layered structure as it undergoes compaction and metamorphism between discrete deposition events. Whereas many processes are critically dependent on the distribution of properties of the strata, the use of average density is usually sufficient for thermal studies (Colbeck 1991).

Unfortunately, snow density (or snow water equivalent—SWE—the parameter that allows its calculation from snow depth) is not usually collected at meteorological sites. Although it is possible to estimate snowpack densities from precipitation data using a viscous compaction model such as Kojima (1967), this approach does not account for the development of depth hoar.

For the Canadian context, Brown et al. (2003) developed a Canada-wide grid of mean snow density at 15-day intervals over the winter season based on historical snow course records. Figure 7 shows the seasonal trend in snow density for the grid points within the Slave province of the Northwest Territories. This can be used to determine appropriate parameters for use in empirical densification schemes such as in Verseghy (1991) to approximate the evolution of snow thermal properties over time.

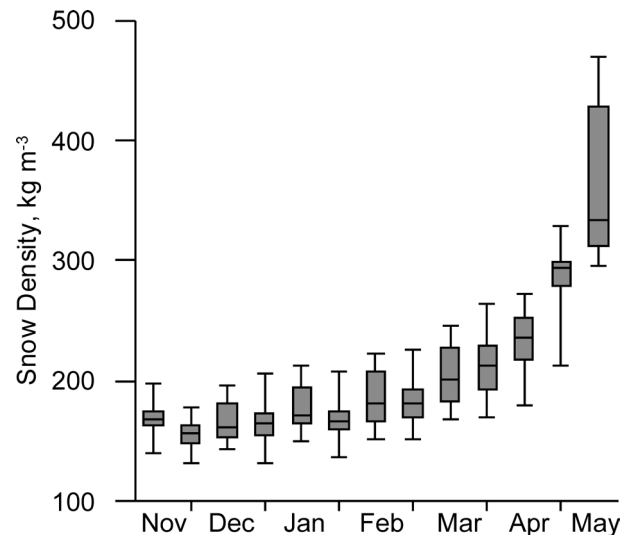


Figure 7. Seasonal trend in snow density for grid points near Yellowknife from the snow density database provided in MSC (2000).

Ablation

For ground thermal modeling purposes, the thickness and density profile of the ablating snow cover has a negligible effect once it has reached the “ripe” stage (isothermal at 0°C), since the ablation process keeps the ground surface temperature at 0°C until the snow is gone. The simplest model for the ablation process (Pomeroy and Goodison 1997) relates snowmelt to the thawing degree-day total:

$$\text{SWE}_A = M_f \text{TDD} \quad (7)$$

where SWE_A = Ablated snow water equivalent, and M_f = melt factor, $\text{kg m}^{-2}\text{TDD}^{-1}$.

Numerical thermal models with relatively simple routines to handle snow evolution (such as TONE, described in Riseborough 2004, 2007) use M_f to ablate the snow. For a given time step, snow cover loss is modeled using the calculated SWE_A mass to determine a decrease in snow layer thickness, converted to layer thickness using the snow density. Figure 8a shows the relationship between snow depth at the end of the freezing season, and the accumulated TDD for the period of ablation. The relationship is weak, in part because the density of the snow cover is unknown and because mean daily temperatures do not capture the melt that can occur on days with mean air temperature below 0°C but a high above 0°. The relationship is weak also because of the effect of rising temperatures on the accelerated mechanical densification of the snow pack. Figure 8b shows the distribution of values for M_f based on these data, with the assumption that the snow in all years has a density equal to the regional mean for April 15 (from Fig. 7).

Discussion

The particular parameter choices for this study were determined in part by the functional capabilities of the numerical model being used and the continental climatic regime under study; in mountainous regions or high-altitude plateaus, the snow regime may be very different. For permafrost (and active layer) modeling, retaining accurate values for TDD_{Ann} and FDD_{Ann} is the most important aspect of parameterizing the surface climate. While it is relatively straightforward to evaluate the effect of assumptions in the air temperature regime, it is much more difficult to perform this type of analysis on the effect of simplifying the snow accumulation regime. With the temperature regime, the effects being removed occur within the annual cycle; simplification of the snow cover replaces the unique annual accumulation with a parabolic function for all years, so that the effect of the snow cover is almost certainly misrepresented in any single year. Riseborough (2007) demonstrated that long-term (multi-year) simulations with variability in a suite of parameters produced a long-term average thermal regime that was very close (mean annual temperature at the base of the active layer within 0.15°C) to the thermal regime of similar simulations without variability.

The snow cover disappears at the start of the thaw season as a result of the ablation process, in which radiant and convective

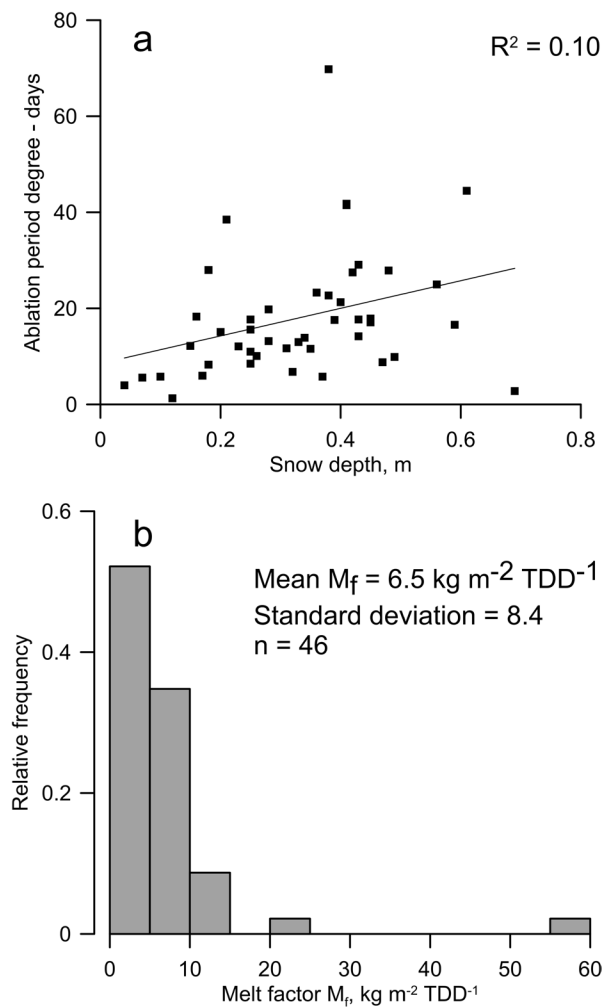


Figure 8. a) Relationship between maximum snow depth and ablation-period TDD for Yellowknife 1955–2005; b) distribution of calculated M_f from data in (a), assuming a snow density of 212. kg m^{-2} (mean for April 15 in Figure 7) derived for seasonal maximum and freezing-season end.

energy from the atmosphere is sufficient to melt the snow. On average, however, the Yellowknife snow cover reaches its maximum height on March 10, or about 73% of the way through the freezing season, about a month before the average date that the daily mean air temperature rises above 0°C (April 11). This makes it impractical to rely on the ablation process alone to parameterize the evolution of the snowpack at the end of the snow season.

Riseborough (2004) found that snow accumulation at a number of Canadian arctic climate stations conformed reasonably well to the parabolic accumulation function of equation 6. The analysis did not include an evaluation of the seasonal timing of the maximum snow depth, although the data suggest that this varied from about 65% to 90% of the freezing season length. The climatology of this effect needs to be evaluated to allow the best empirical fit and application of equation 7.

Table 1 summarizes a preliminary sensitivity analysis evaluating the effects of the simplifying assumptions on the mean ground temperature at the base of the active layer. All

Table 1. Results of sensitivity analysis.

| | Air T | Snow depth exponent | Max. snow timing ¹ | Deflate snow ? | Snow density | MAGT °C |
|----|-------|---------------------|-------------------------------|----------------|--------------|---------|
| 1 | Data | Data | Data | Data | Constant | 0.92 |
| 2 | Sine | 0.5 | 0.75 | Yes | Constant | 1.29 |
| 3 | Sine | 0.5 | 0.75 | No | Constant | 1.43 |
| 4 | Sine | 0.5 | 0.99 | No | Constant | 0.85 |
| 5 | Sine | 0.4 | 0.75 | Yes | Constant | 1.81 |
| 6 | Sine | 0.6 | 0.75 | Yes | Constant | 0.94 |
| 7 | Data | Data | Data | Data | f (time) | 2.03 |
| 8 | Sine | 0.5 | 0.75 | Yes | f (time) | 2.34 |
| 9 | Sine | 0.5 | 0.75 | No | f (time) | 2.37 |
| 10 | Sine | 0.5 | 0.99 | No | f (time) | 1.93 |
| 11 | Sine | 0.4 | 0.75 | Yes | f (time) | 2.58 |
| 12 | Sine | 0.6 | 0.75 | Yes | f (time) | 1.97 |

¹ Timing of snow cover maximum relative to the length of the freezing season.

simulations had the same substrate (1 m saturated peat over 8 m clay over bedrock) and were run for a minimum of 100 annual cycles to approach equilibration. Surface climates were based on 1955–2006 multi-year averages, and were either daily average temperature and snow depth (“Data” in Table 1) or a degree-day appropriate sine wave (“Sine”) with a range of snow cover treatments. Differences in mean annual ground temperature (MAGT) allow a ranking of the relative importance of the various simplifications to the accuracy of model results.

The daily-data-based simulations (1 & 7 in Table 1) were closest in temperature to the simplified climate simulations with a snow cover most closely resembling the daily data (6 & 9), although simulations with the simplest snow cover (4 & 10) differed from 1 and 7 by 0.1°C or less. The largest temperature differences (>1°C) are between simulations with constant (1–6) and time varying (7–12) snow cover.

Conclusions

This paper presents an analysis of the Yellowknife climate record in order to extract a set of simple parameters for use in numerical modeling.

For permafrost (and active layer) modeling, retaining accurate values for TDD_{Ann} and FDD_{Ann} is the most important aspect of the surface temperature climate.

The parabolic accumulation function was shown to represent the mean snow accumulation function for the Yellowknife record with the proper parameters, although the seasonal trend in snow density and the timing of the maximum snow depth within the season was identified as an additional parameter to be collected. Details of end-of-season snowpack evolution are of secondary importance.

Acknowledgments

This research was undertaken as part of the TRACS project, Geological Survey of Canada (GSC Contribution number). The authors also thank Mark Ednie and two anonymous reviewers for their useful comments.

References

- Brown, R.D., Brasnett B., & Robinson, D. 2003. Gridded North American Monthly Snow Depth and Snow Water Equivalent for GCM Evaluation. *Atmosphere-Ocean* 41 (1): 1–14.
- Colbeck, S.C. 1991. The layered character of snow covers. *Reviews of Geophysics* 29(1): 81–96.
- Ferguson, R.I. 1999. Snowmelt runoff models. *Progress in Physical Geography* 23: 205–227.
- Goodrich, L.E. 1982. The influence of snow cover on the ground thermal regime. *Canadian Geotechnical Journal* 19: 421–432.
- Kojima, K. 1967. Densification of seasonal snow cover. *Physics of Snow and Ice* 2: 929–952, Institute of Low Temperature Science, Sapporo.
- Ling, F. & Zhang, T. 2006. Sensitivity of ground thermal regime and surface energy fluxes to tundra snow density in northern Alaska. *Cold Regions Science and Technology* 44: 121–130.
- Ling, F. & Zhang, T. 2007. Modeled impacts of changes in tundra snow thickness on ground thermal regime and heat flow to the atmosphere in northernmost Alaska. *Global and Planetary Change* 57: 235–246.
- Osokin, N.I., Samoylov, R.S., Sosnovskiy, A.V., Sokratov, S.A., & Zhidkov, V.A. 2000. Model of the influence of snow cover on soil freezing. *Annals of Glaciology* 31: 417–421.
- Pomeroy, J.W. 1998. An evaluation of snow accumulation and ablation processes for land surface modelling. *Hydrological Processes* 12: 2339–2367.
- Riseborough, D.W. 2007. The effect of transient conditions on an equilibrium permafrost-climate model. *Permafrost and Periglacial Processes* 18: 21–32.
- Riseborough, D.W. 2004. Exploring the parameters of a simple model of the permafrost-climate relationship. Ph.D. Dissertation, Carleton University, Ottawa. 330 pp.
- Smith, M.W. & Riseborough, D.W. 2002. Climate and the limits of permafrost: a zonal approach. *Permafrost and Periglacial Processes* 13: 1–15.
- Smith, S.L., Wolfe, S., Riseborough, D.W., & Nixon F.M. 2009. Active-layer characteristics and summer climatic indices, Mackenzie Valley, Canada. *Permafrost and Periglacial Processes* 20: 201–220.
- Sturm, M., Holmgren, J., König, M., & Morris, K. 1997. The thermal conductivity of seasonal snow. *Journal of Glaciology* 97 (B2): 2129–2139.
- Verseghy, D.L. 1991. CLASS: A Canadian land surface scheme for GCMs I: Soil model. *International Journal of Climatology* 11, 111–133.
- Zhang, T., Osterkamp, T.E., & Stamnes, K. 1996. Influence of the depth hoar layer of the seasonal snow cover on the ground thermal regime. *Water Resources Research* 32: 2075–2086.
- Zhang, T.J. 2005. Influence of the seasonal snow cover on the ground thermal regime: an overview. *Reviews of Geophysics* 43: RG4002.

Foundation Engineering in Svalbard, 1950–2012

Johanna Lohne Rongved
Sweco Norge AS, Bergen, Norway

Arne Instanes
Instanes Polar AS, Bergen, Norway

Abstract

This paper presents an analysis of foundation engineering design on Svalbard during the last 60 years. Most buildings on Svalbard were built after 1950, and some of the older buildings have severe damage due to warm foundations on saline, ice-rich permafrost. In the last 30 years, development of new technology has led to a partial change in foundation design from shallow footings to piles and more active methods of heat pump cooling and air duct ventilation. Case-studies involving rehabilitation of old structures and design of recent infrastructure are presented.

Keywords: air duct foundation; foundation reconstruction; heat pump cooling; piles; shallow foundation.

Introduction

Svalbard is an archipelago in the Arctic Circle, north of mainland Norway; the islands range from 74° to 81° north latitude. The main settlement in Svalbard is Longyearbyen. Other settlements include the research community of Ny Ålesund, the mining outpost of Sveagruva, and the Russian mining community of Barentsburg. A map of Svalbard is shown in Figure 1.

Most buildings and infrastructure in Svalbard were built after 1950. Building on warm, saline permafrost generally leads to a short life expectancy of the building. Some of the buildings that were constructed in Svalbard around 1950 are still in use today, but most of them have experienced severe settlement damage. This paper will focus on buildings in Longyearbyen and Sveagruva and the different engineering designs most commonly used over the last 60 years.

Temperature and Climate

Svalbard is characterized by continuous permafrost and an annual mean temperature around -5°C. The annual mean temperatures in Longyearbyen and Sveagruva are presented in Figure 2 with blue and red color, respectively. The dots represent the mean monthly temperatures, dotted lines represent 10-year averages, and the solid lines represent 30-year averages.

Temperatures in Sveagruva have been recorded only since 1978. For Longyearbyen, temperature data exist from as far back as 1911, although the location of measurements was changed in 1975 from Longyearbyen to the Svalbard airport 7 km west.

The permafrost in populated areas in Svalbard is generally relatively warm and ice-rich. It often has a high concentration of salts due to low-lying areas in close vicinity to the ocean. For the case studies presented in this paper, salinity has been registered from 1 to 27 ppt. Both in Longyearbyen and in Sveagruva it is not uncommon to encounter layers of pure ice in the ground, which increases the risk of severe settlement in the case of thawing.

Common Foundation Methods

Until 1980, the traditional method of foundation construction in Svalbard was restricted to shallow footings, embankments, and concrete slabs directly on grade. In the early 1980s, a pile rig was developed that enabled piled foundations (Instanes, B 2000). Pile foundations are still commonly used, but the ice-

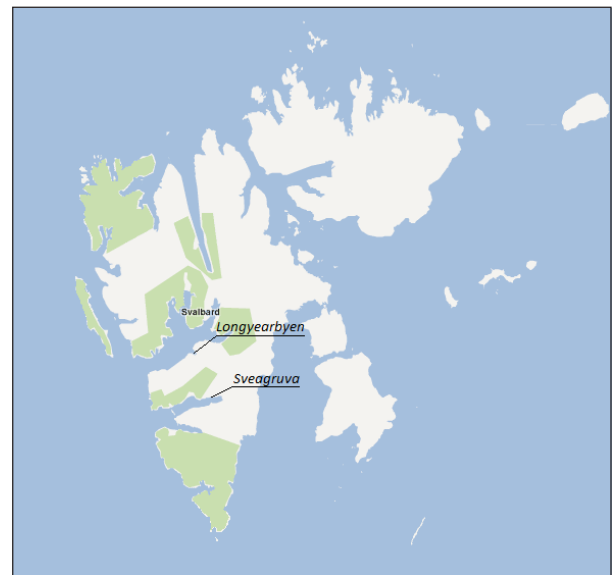


Figure 1. Svalbard (from Google maps).

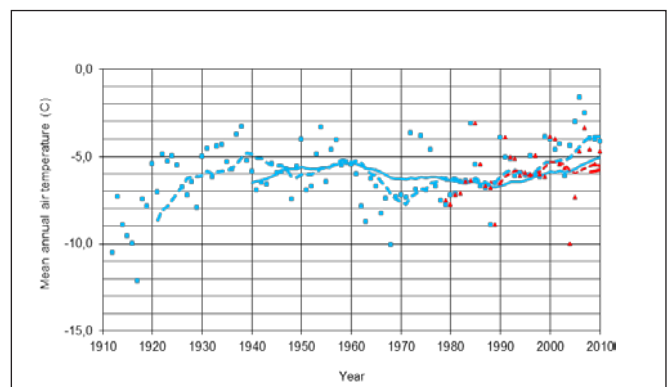


Figure 2. Air temperatures, Longyearbyen (blue) and Sveagruva (red).

rich, warm permafrost often found in Svalbard decreases the bearing capacity of traditional pile foundations, and increases the settlement rate (Instanes, D & Instanes, A 1998). With the prospect of global warming, buildings on pile foundations are increasingly vulnerable to settlement damages and frost jacking. Active methods used to increase heat loss from foundation soils have therefore become more accepted as practical and often necessary solutions.

Piles and shallow foundations

Residential buildings and other lightweight and flexible constructions are still commonly built on pile foundations. Wooden piles are most common, but concrete piles and steel beam piles are also used to some extent. Embedded pile length typically varies from 6 to 10 m. Although wood piles have been preferred as the fastest and most cost-effective foundation design, the warm permafrost in Longyearbyen leads to relatively high settlement rates. Over the last few years severe rot damage has also been observed in several wood pile foundations.

Shallow foundations have also been a commonly accepted foundation design in Svalbard. Examples of buildings on shallow foundation are the old university building from 1995 (UNIS), and also parts of the *Telegrafbygningen* (the Telegraph building) in Longyearbyen. The locations of some relevant buildings in Longyearbyen are shown in Figure 3.

To avoid frost jacking and thawing of foundation soils, shallow foundations are placed beneath the permafrost table. A precondition when using either piles or shallow foundation is that heat from the building must be prevented from penetrating the ground. This is solved by raising the building above ground level, which allows air circulation beneath the building. Water should also be led away from the construction to avoid pooling water around the foundations.

In order to prevent unauthorized access under the buildings, the ventilated space beneath structures is often blocked by fencing. This causes snow to build up around the building and restricts air ventilation. Drainage of surface water is a challenge, and water can often be observed under buildings and around foundations during spring and summer. These problems will lead to increased thaw depth and permafrost temperatures in the foundation soils.

Heat pump cooling

Foundation design using a heat pump cooling system has been used in Svalbard since 1986 (Instanes & Rongved 2009). The method uses a cooling system underneath the foundations to prevent thawing of the underlying permafrost. For heavy structures, or buildings with low tolerance for differential settlement, this will often be the preferred foundation design. This foundation method also offers the possibility of using excess heat from the ground to heat the building, and it can also be combined with floor heating without risk of thawing foundation soils. Another advantage is that the ground floor of the building will be at ground level, thus improving access. The heat pump cooling design was most recently used for the new cultural building in Longyearbyen.



Figure 3. Map of Longyearbyen (from Google maps).

In addition to its use for several new buildings over the last 25 years, this cooling system can also be used for foundation reconstruction for older buildings placed directly on permafrost.

The disadvantages with the method are mainly the constant need of electric power to run the system, and the need for maintenance to ensure the system is switched on and functioning properly. Both Longyearbyen and Sveagruva have a large turnover of personnel, and to minimize the risk of human error it is recommended to combine the cooling system with temperature sensors for automatic control of the system.

Air duct foundation

An air duct foundation works on the principle of ventilation ducts cooling the ground under the building. As with the heat pump foundation design, the air duct foundation also allows for a ground floor at terrain level.

The ventilation ducts are installed in a gravel embankment, on top of which the building is constructed. To minimize heat transfer to the ground, an insulating layer is placed under the concrete floor slab. The ventilation ducts are kept open during winter, allowing cold air to circulate and cool the ground. In summer, the ducts are closed to minimize heat transfer to the underlying frozen ground. It is recommended to combine the system with temperature sensors for automatic opening and closing of the ducts at appropriate temperatures.

Unlike the heat pump system, air duct ventilation does not extract heat from the ground during summer. Some thawing must therefore be expected during the summer months, and any frost susceptible soil under the building must be replaced by thaw-stable materials to the maximum thaw depth. For this reason, this foundation design is mainly recommended for industrial buildings, storage buildings, or other constructions with a relatively low indoor temperature. It is not advisable to combine this foundation design with floor heating.

Over the last couple of years, three buildings in Sveagruva have been constructed using the principle of a ventilated gravel embankment. For one of these buildings, ventilation ducts with temperature sensors and automatic controlling were



Figure 4. *Sysselemannsgården* during reconstruction of foundation.

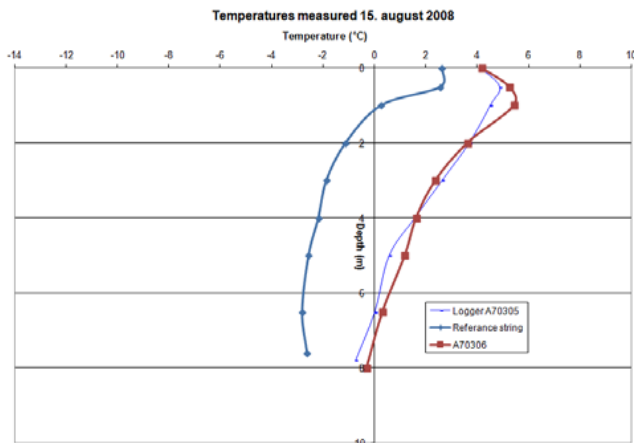


Figure 5. Ground temperatures next to *Sysselemannsgården*.

used. The other two sites used a simplified design, where the insulating material underneath the concrete slab was stacked to create ventilation space along the ground surface.

Case Studies

Warm foundations

The *Sysselemannsgården* houses the Governor of Svalbard. It was built in 1950 and consists of four connected buildings. The two lighter, one-story buildings have a pile foundation with a ventilation space underneath and have no noticeable settlement damage. The main building and the tower, which are heavier concrete structures, both have problems with settlement. Both buildings have a heated lower story beneath terrain level, and the foundations consist of a 20-cm slab of plain concrete with an underlying layer of timber placed directly on permafrost. Figure 4 is a photograph taken during reconstruction of the foundations in 2010. The white and the red parts of the building had severe settlement damage. The structures on the left are constructed on a pile foundation and have suffered no apparent damage.

Temperature data from thermistor strings installed near the building showed that the ground was thawed to around 7 m, nearly down to bedrock. A reference string installed nearby indicates that the normal depth of the active layer is about 1 m for this area. The ground temperature is shown in Figure 5.

Collected soil samples show that the ground around the structure consists mainly of sand and gravel over silt and clay. The investigations also revealed an upper layer of fill material, with bits of wood, bricks, and coal. From the investigation report, it is estimated that bedrock is at approximately 8 m below terrain level. Salinity was found to vary from 1 to 4 ppt.

It was concluded that the cause of the settlement damage was melting of the permafrost under the building due to the heated basement (Rongved 2010). Several methods for foundation reconstruction were considered. Mainly due to the risk of frost heave during refreezing of the soil, artificial freezing methods were disregarded. It was decided to reconstruct the foundation using bored steel core piles to bedrock. This is a method often used in non-permafrost areas, and the piles are not designed for frost heave or frost jacking. Precautions are therefore taken to keep the ground underneath the building permanently thawed.

Another old building that experienced settlement damage due to inadequate foundation design is the *Bergmesterboligen*. This building, located about 100 m from *Sysselemannsgården*, was constructed in 1948 and has a foundation placed directly on the ground. The building has a basement that was traditionally used for melting snow and as a heating center, and large quantity of heat has therefore been transferred to the ground. The ground consists mainly of moraine with a large content of fine-grained materials. Salinity at this site is assumed to correlate largely to the values found at *Sysselemannsgården*. Thawing of the permafrost led to settlement and deformation of the building.

The engineering company Instanes Svalbard compiled a report in 1991, proposing reconstruction of the foundations using the heat pump cooling method. During the reconstruction, the existing concrete floor was demolished and the upper ca 0.5 m of underlying soil was excavated and replaced with thaw-stable material. The cooling pipes were placed in a 100-mm concrete slab over which was added 200 mm of insulating material and then a 70-mm concrete floor slab.

The cooling system has generally proved to be efficient, since after reconstruction the ground stabilized and the settlement stopped. However, additional settlement was observed a few years after reconstruction when the cooling system was not restarted after a power failure, thus proving the need for proper maintenance.

Piles and shallow foundations

The Telegraph building, originally built in 1952, was added to in 1967 and again in 1980. The original part of the building is constructed on what appears to be wooden piles. The foundation depth for the original building is not known, but with the available equipment in the 1950s foundation depth is assumed to be less than 2 m.

The two newer additions to the building are both constructed on shallow concrete foundations, and settlement was observed in 2009 for these parts of the building.

The building is raised above the ground to create a ventilated space underneath, but a concrete "wall" has been added around the perimeter of the ventilation space, blocking the airflow under the construction. All access hatches have been blocked

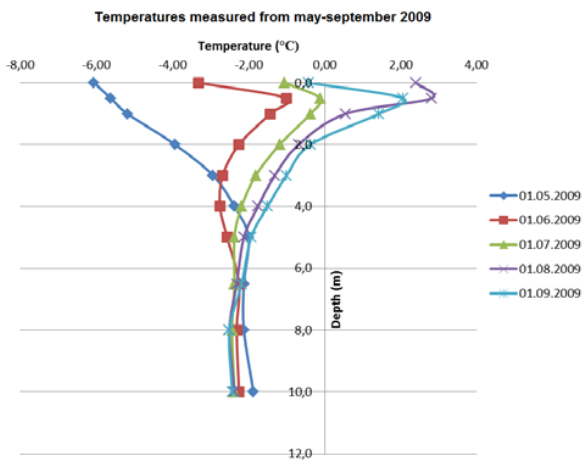


Figure 6. Ground temperatures next to the Telegraph building.

off, effectively cutting off air circulation. During an inspection under the building in April 2009, a pool of water was observed under the newest addition to the building. The water suggested relatively high temperatures beneath the building.

A thermistor string installed approximately 1 m from the building showed relatively constant temperatures of around -2°C at 8 to 10 m depth. The active layer is shown to have a depth of about 2 m (Fig. 6)

In connection with drilling for the thermistor string, a simplified site investigation was performed and soil samples were collected from the boring debris. Based on a visual classification, the material appeared to consist of mainly sand and gravel, but with a varying content of organic material and fine grained soil. No pure ice was observed.

In 2011 a second thermistor string was installed under the building. The string was installed to a depth of 0.8 m and showed a temperature of about 0°C .

Based on the temperature data, inspection beneath the building, and the original construction drawings, it was concluded that the most likely cause of the observed damages was heating of the permafrost, with a resulting reduction in bearing capacity. Old drawings indicate a placement of the shallow foundations of approximately 2.5 m below ground level. Temperature data show that the ground outside the building thaws to a depth of approximately 2 m during summer. Due to the observed water and the elevated temperatures under the building, thaw depth is likely to be greater than the foundation depth for most parts of the building.

Heat pump cooling

Since 1986, the heat pump cooling system has been used for one building in Sveagruba and four in Longyearbyen. In addition, it has been used for reconstruction of the foundation for *Bergmesterboligen*. The site conditions for all these buildings are characterized by high ice content, high salinity, and silty clay (Instanes & Rongved 2009).

The most recent building utilizing this design is the new cultural building in Longyearbyen. Site investigations showed mainly silty, clayey soils, with a relatively high ice content. Salinity was found varying from 5 to 27 ppt. The temperature

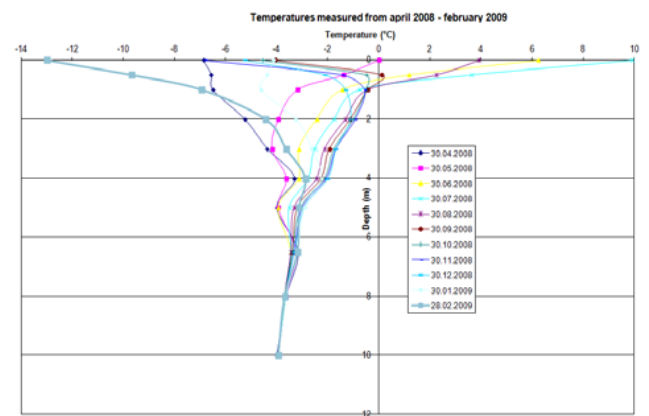


Figure 7. Ground temperature next to the Cultural building.

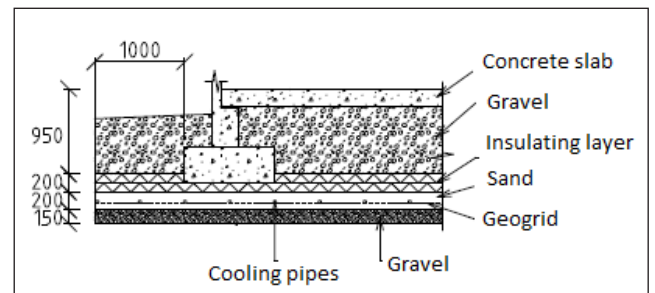


Figure 8. Foundation using heat pump cooling.

profile from the site is presented in Figure 7 and shows permafrost temperature measured at approximately -4°C .

The building was planned with a large glass façade, and it has a low tolerance for differential settlement. In addition, the building was planned as an extension to an existing building constructed on a heat pump cooling foundation, thus making it difficult to establish a ventilated space underneath the new building without conflicting with the cooling slab of the existing one.

Based on these considerations, it was decided to construct the new cultural building on a cooling slab using a heat pump system. Figure 8 shows the principal design for a foundation with heat pump cooling.

The site was prepared by first excavating the top layer of frost-susceptible and organic soils. The site was then leveled using a 150-mm-thick layer of gravel. The cooling pipes were placed in a 200-mm layer of sand and were fastened to a geogrid to prevent the pipes from shifting. Insulating material (200 mm) was placed on the sand layer, and the foundations of the building were placed on this insulating layer. Gravel was filled around the foundations up to the concrete floor slab. To prevent freezing of the gravel layer, no insulation was used underneath the floor slab.

The cooling slab extends about 1 m outside the outer walls of the building and, to prevent ice from building up over the cooling slab surface, water is drained away from the construction. Along the eastern edge of the cooling slab existing infrastructure made proper drainage difficult, and a geomembrane was therefore used to keep the water above the insulating layer.

Air duct ventilation

Industrial buildings commonly need vehicular access, which is most easily obtained by placing the building on ground level. This makes either a cooling slab or air duct ventilation a suitable foundation design. Over the last couple of years, air duct ventilation has been used in two variations for industrial buildings in Sveagruva. A simplified design was used for two storage buildings during 2010 and 2011. For the simplified design, insulating material was stacked to create ventilation ducts along the ground surface. Foundations and the floor slab were constructed on top of the insulating layer.

In 2011 a new coal preparation plant was built in Sveagruva. The plant was constructed using an air duct ventilation foundation with fans used to help circulate air through the ventilation ducts installed in the gravel embankment under the building. During summer, the ventilation ducts are closed to minimize heat transfer to the ground. Temperature sensors monitor the temperature inside the ducts and the outside temperature. The system is designed to open and close the ventilation ducts automatically at specific temperatures.

The plant is approximately 100 m from the fjord, and temperature measurements show that ground temperatures at the site are largely influenced by the sea. The permafrost temperature was measured at approximately -2°C , with salinity varying from 15 to 25 ppt. Also, site investigations showed a layer of pure ice in the ground, varying up to 2 meters in thickness. It can be discussed whether air duct ventilation actually is the best foundation design for cases with temperatures as high as measured here and with salinity up to 25 ppt, or if heat pump cooling should have been chosen as the safer option.

For preparation of the site, pure ice and ice-rich soils were excavated and replaced by freeze-stable rock and gravel. The site was then leveled off before the 300-mm ventilation ducts were installed through a gravel embankment. To minimize heat transfer, a 200-mm insulating layer was placed beneath the concrete floor slab.

The finite element program Temp/W (GeoSlope 2007) was used to design the diameter and spacing of the ventilation ducts. Figure 9 shows the input model for the ventilation ducts installed in the rock/gravel layer. Figure 10 shows the modeled thaw depth at end of the summer season. The model shows that maximum thaw depth does not exceed the depth of the thaw-stable material underneath the building.

Summary and Conclusion

This paper has given a brief introduction to the main foundation designs used in Svalbard. Prior to 1980, the most common foundation design usually involved shallow footings. Piles were sometimes used but, due to lack of equipment, the installed depth of the piles was limited. The paper has also described examples of older buildings constructed on warm foundations. The few buildings of this kind still standing today all suffered severe damage from settlement, and a couple of these buildings have undergone substantial foundation reconstruction in order to maintain their structural integrity.

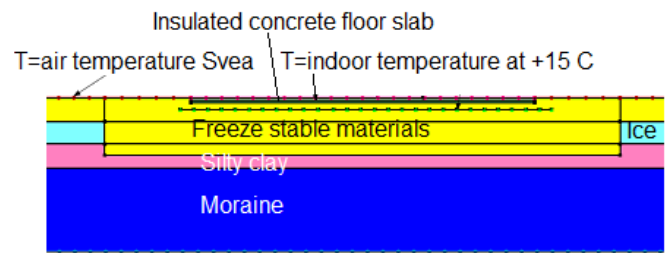


Figure 9. Temp/W model for air duct ventilation.

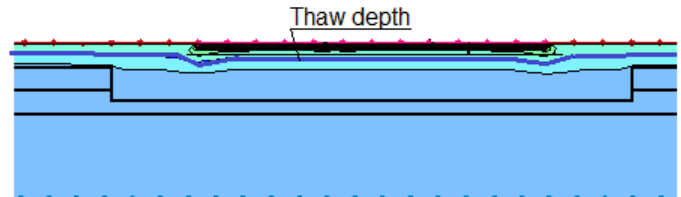


Figure 10. Modeled thaw depth at end of summer.

After the early 1980s, piled foundations were increasingly used; by then the proper equipment had been developed to allow installation of piles to greater depths. Piles are still the most accepted method of building foundations in Svalbard, and a piled foundation is normally a good solution for lightweight and flexible buildings that will tolerate some settlement.

In 1986, a new foundation design that utilizes a heat pump system to extract heat from the permafrost under the building was developed. This system lowers the permafrost temperature, thereby reducing settlement rates and making the cooling system a suitable foundation design for constructions vulnerable to differential settlement. Another advantage using this kind of foundation is that the ground floor of the building can be placed at ground level, thereby improving access. This will be especially beneficial for industrial buildings or any other building dependent on the transportation of large or heavy items.

Air duct ventilation has been less common in Svalbard but has been used for several industrial buildings over the last couple of years. The foundation design depends on air circulation through ventilation ducts installed in a gravel embankment underlying the construction. The ventilation ducts are open during winter but must be closed during summer to prevent thawing. Proper maintenance is important in order to prevent blocking of the ventilation ducts during winter and to ensure that the ducts are closed in summer. Thawing during summer must be expected to some extent, and any frost-susceptible soils beneath the building must be replaced by freeze-stable materials. This method is best suited for industrial buildings or storage halls where the inside temperature will be kept relatively low. Floor heating should not be used for buildings constructed on a foundation using air duct ventilation.

References

- Geo-slope International. 2007. GeoStudio 2007. Thermal modeling with TEMP/W. www.geo-slope.com.
- Instanes, A. & Rongved, J.L. 2009. Foundation design in Svalbard by artificial cooling – 20 years' experience. Proceedings of "Geoteknikkdagen 2009", Oslo, Norway, pp.41-1 to 41-12 (in Norwegian).
- Instanes, B. 2000. Permafrost engineering on Svalbard. *Proceedings from the International Workshop on Permafrost Engineering*, Longyearbyen, Svalbard, 18.-21.juni 2000, pp.1-24.
- Instanes, D. & Instanes, A. 1999. Pile design in saline permafrost at Longyearbyen. *Proceedings of the 10th International Conference on Cold Regions Engineering*, Lincoln, NH, USA, August 16-19, 1999: 222-231.
- Rongved, J.L. 2010. Foundation reconstruction for the Governor's residence in Longyearbyen. Statens Vegvesen publication nr 111, *Frost in Ground* 2010, pp. 17-20.

City of Kotzebue's Vortac Earthen Dam: A Review of the Naturally Frozenback Embankment and Reservoir Slopes

James W. Rooney

J&F Rooney, LLC., Anchorage, Alaska, USA

Charles H. Riddle

R&M Consultants, Inc., Anchorage, Alaska, USA

Abstract

The City of Kotzebue's water supply system evolved from an early expansion of Vortac Lake by construction of a small earthen dam that was allowed to completely freeze back during a three year construction period ending in 1970. By the early 1980s, the city's water supply needs were exceeding the Vortac Dam's reservoir capacity. Development of the adjacent Devil's Lake into a larger reservoir then placed the Vortac reservoir in standby status. Since construction of Vortac Dam was completed, a number of technical reviews of have been written by various agencies and consultants. These reviews have provided some insight into the dam's frozen core thermal, slope, and overall reservoir performance.

Keywords: Kotzebue, Alaska; climate warming; permafrost; water supply dam.

Introduction

The design of Vortac Dam was prepared by the U.S. Public Health Service (USPHS), and earthwork began in 1967 under the direction of that agency. The naturally frozenback earthen dam design was based on the concept of maintaining a stable frozen core and underlying foundation over the life of the structure (Crum, pers. com.). The USPHS final project report stated, "The dam at Vortac Lake was to be constructed of silt to provide an impermeable fill with a permanently frozen core. The only way to work with the silty soil was to excavate it in a frozen or semi-frozen state" (USPHS n.d.). Progress of construction was slowed when workers found the frozen ground to be harder than expected, and "crews

discovered that fill material for the dam could only be worked for approximately two weeks in the spring and fall, when the soil was in a semi-frozen state..." (USPHS n.d.). A location map for Kotzebue and Vortac Dam is presented in Figure 1.

A limited thermal analysis was performed by the University of Alaska Arctic Engineering Laboratory on construction related concerns (Peyton 1966). This brief evaluation only addressed seasonal active layer depth and the effect of summer and winter fill placement. Upslope slope thermal conditions and the influence of reservoir warming impacts were not addressed.

Because the frozen fine-grain foundation soil underlying the dam and abutments is ice-rich and contains massive ice segments (Rooney 1986, Riddle 1989, Scher 1994), it is critical that a frozen state be maintained. Over time, some significant upslope thawing and slope slumping has occurred, particularly in the area of the southern segment of the dam and the adjacent abutment. The City of Kotzebue made repairs to these areas in the mid-1990s by reconstructing the failing upslope areas and widening and slightly raising the dam crest. However, upslope embankment sloughing and displacement have continued, and recommended procedures for completing repairs have not been implemented. A site map showing the dam and reservoir is shown in Figure 2. Figure 3 presents a cross section of Vortac Dam and reservoir.

Site Conditions and Geology

Early documentation of Kotzebue's frozen terrain was provided by Otto von Kotzebue from his 1815–1818 Russian expedition (von Kotzebue 1817). "We saw masses of the purest ice, of the height of a hundred feet, which are under cover of moss and grass," von Kotzebue wrote. His journal included a graphic sketch of exposed massive ice inclusions along the Kotzebue bluffs. The extent of remaining massive ice is still significant but unknown; however, von Kotzebue's sketch does help provide insight into the amount of massive ice contained within the bluffs.

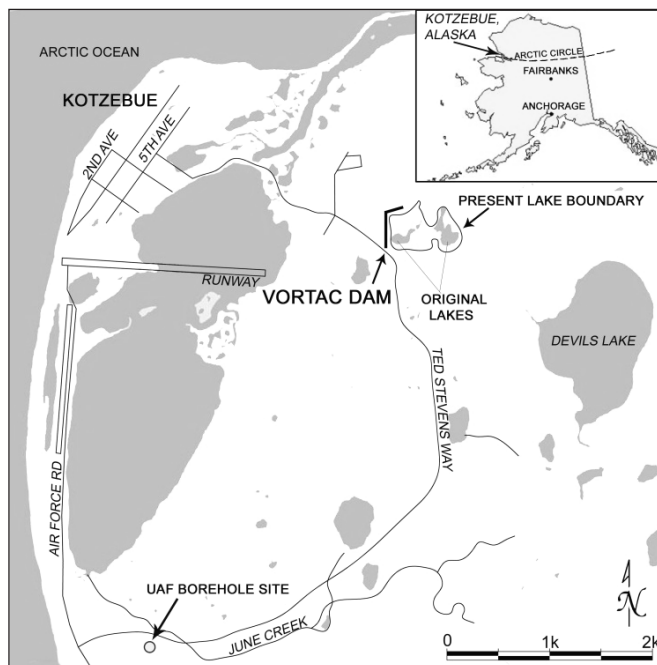


Figure 1. Vortac Dam location map. City of Kotzebue, Alaska (67°53'N, 162°31'W).

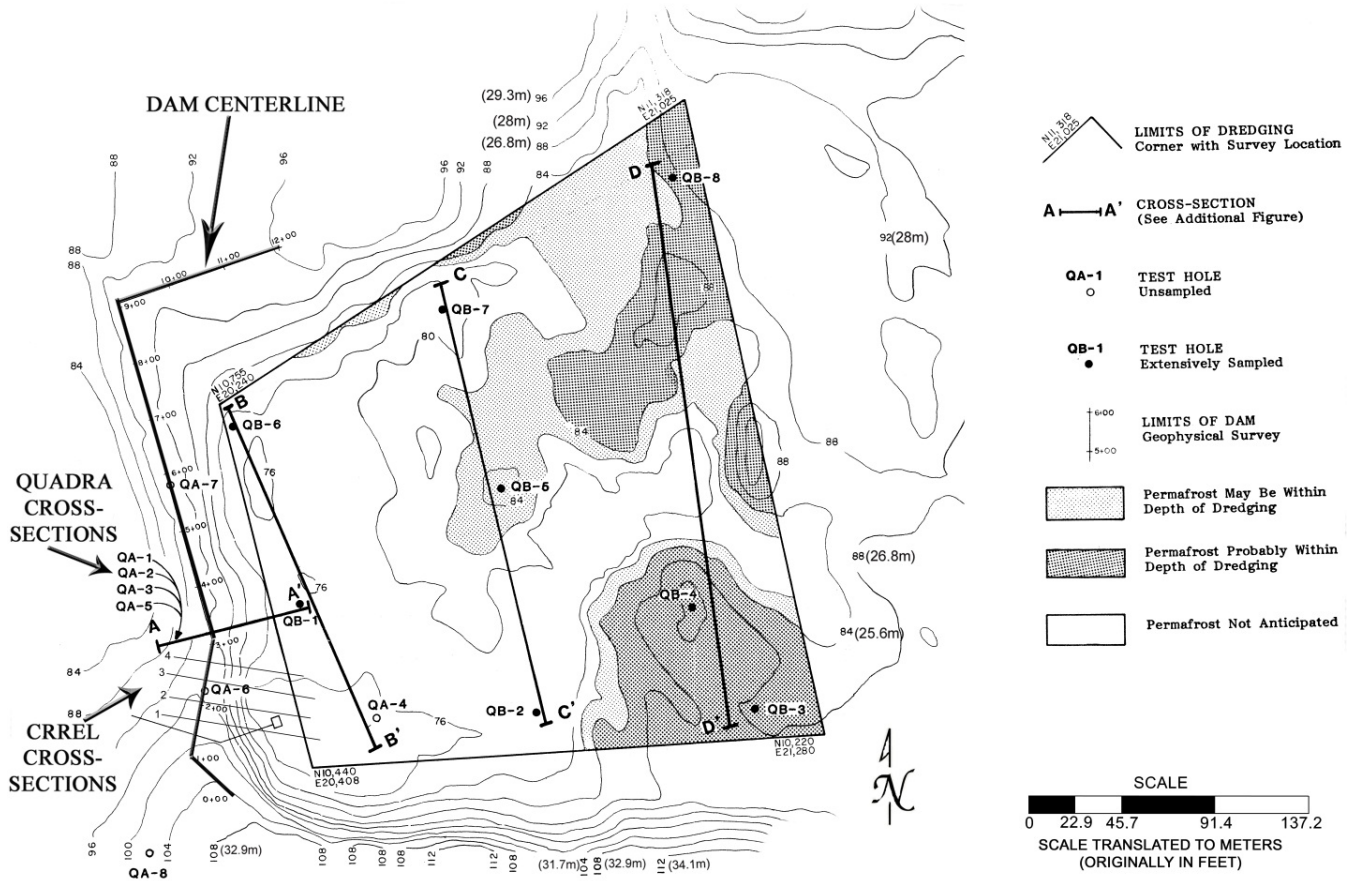


Figure 2. Site map showing dam and reservoir investigations including test holes, temperature instrumentation, and resistivity measurements (from Bendz 1983).

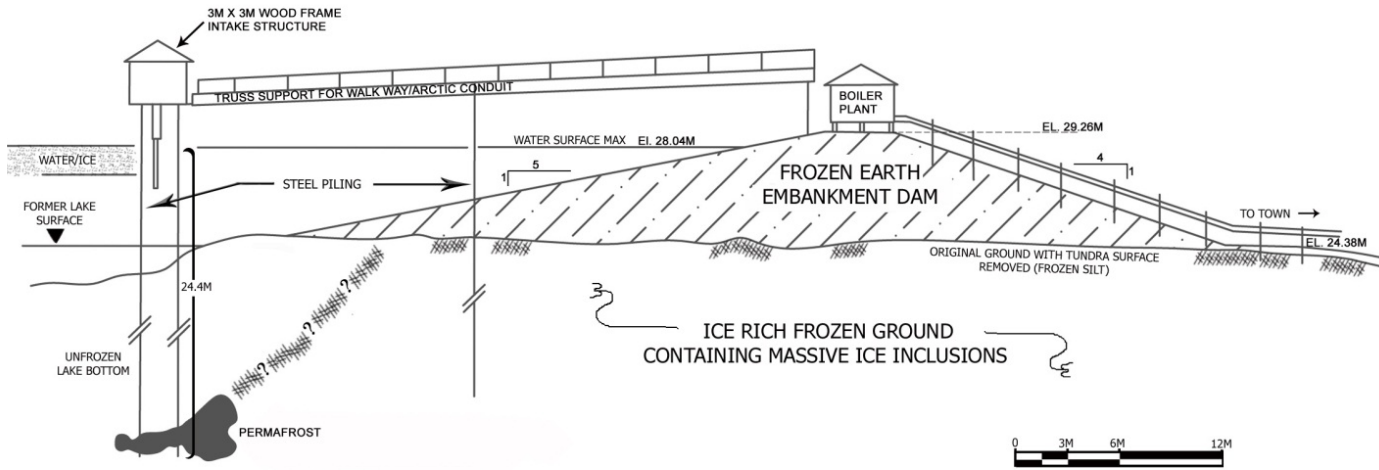


Figure 3. Cross-section of Vortac Dam and reservoir illustrating initial constructed conditions (after USPHS n.d.).

Kotzebue lies just north of the Arctic Circle. It is on the northwestern end of the Baldwin Peninsula, which is reported to be a terminal “push moraine” created by advancing glaciers pushing up marine sediments (Plafker 1994). The marine sediments are overlain by glacialfluvial outwash deposits, wind-blown loess, and organic-rich lake deposits. The Kotzebue area is renowned for its large masses of segregated ice in the form of horizontal lenses up to 3 m or more in thickness and vertical wedges up to 9 m or more in depth. Kotzebue lies in an area of moderately thick to thin permafrost (Ferrains 1965). Locally, in close proximity to large water bodies, permafrost is absent. Pro-glacial dunes containing eolian silts and sands are the predominant soil deposit at the dam site. Profiles of subsurface soil conditions are shown in Figures 4, 5, and 6.

The Kotzebue region has an arctic climate and an average annual temperature of -3.6°C. The average annual surface thawing and freezing indexes are 1,333°C-days and 4,278°C-days, respectively. Average annual precipitation is 23 cm.

Engineering Issues

A number of site investigations and studies for Vortac Dam have been done since completion of construction in 1970. The first was in 1976, when USPHS requested the Corps of Engineers, US Army, Cold Regions Research and Engineering Laboratory (CRREL) to evaluate dam upslope failure concerns. Eleven deep test holes were drilled and instrumented for ground temperature measurements (Collins & McFadden 1977). These test holes provided information

on subsurface soil and ground temperatures at several cross sections of the dam site. In 1983, Quadra Engineering, Inc. completed an engineering study for potential expansion of the lake reservoir. This study included placement of six test holes with ground temperature instrumentation (Bendz 1983). In 1997, Crowther Associates drilled six shallower test holes and installed temperature instrumentation (Crowther 1998). No additional subsurface investigations have been completed since that time.

Under the Alaska Department of Natural Resources Dam Safety Program, a number of periodic inspections of the Vortac Dam have been conducted. The first and second efforts were completed in 1984 and 1990 by Dames & Moore (Krzewinski et al. 1984). The third inspection was performed in 1997 by Crowther Associates, and the most recent inspection was completed by Golder Associates in 2005. All of these inspections came to nearly the same conclusions and recommendations.

The primary concern has always been with the dam’s upslope instability, slumping induced by thawing, and bank erosion remediation needs. Thawing of the massive ice below the upstream slope has continued to create large voids that induce upslope embankment slumping and instability within the unfrozen upslope portion of the dam.

The 2005 Golder Associates report stated that “the upstream dam embankment and south abutment face have continued to experience erosion and slope instability since the last inspection. Similar to historical observations, most of the damage appears to be occurring near the southern abutment, possibly due to the prevailing wind direction, taller slopes,

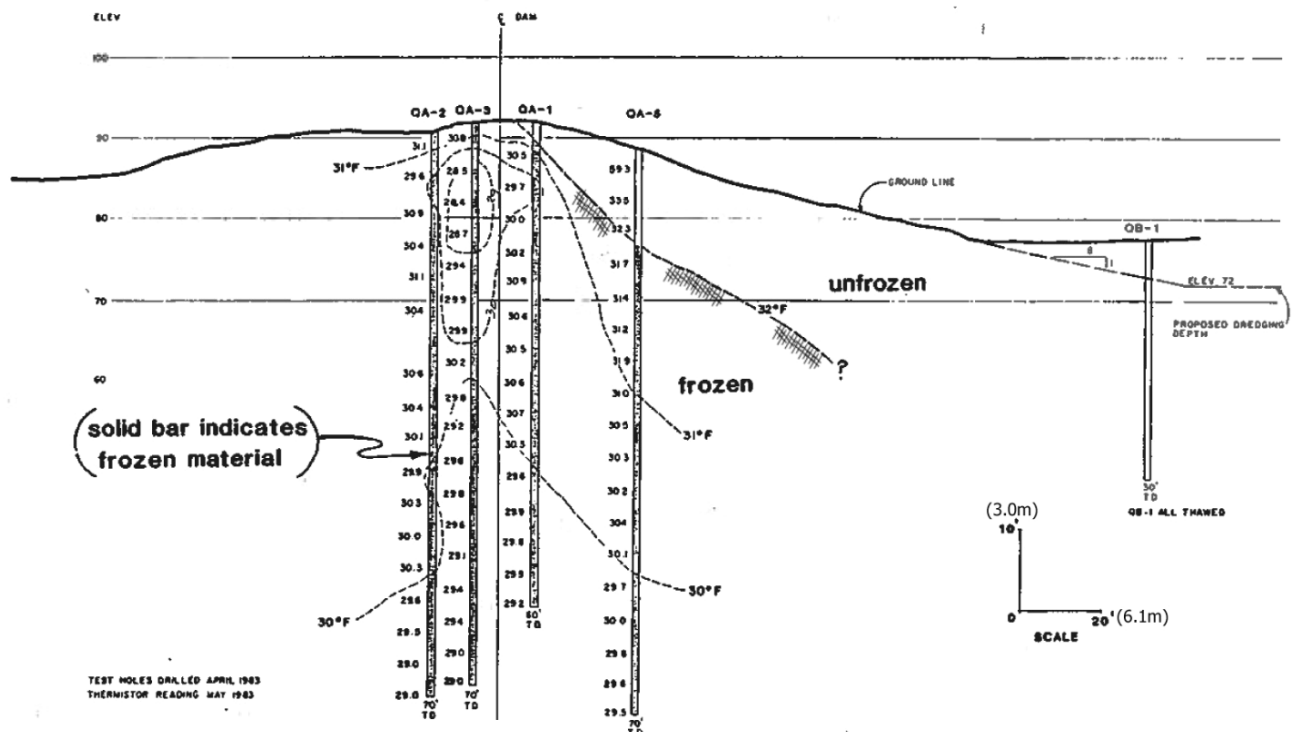


Figure 4. Profile of subsurface soil conditions in 1983 (from Bendz 1983).

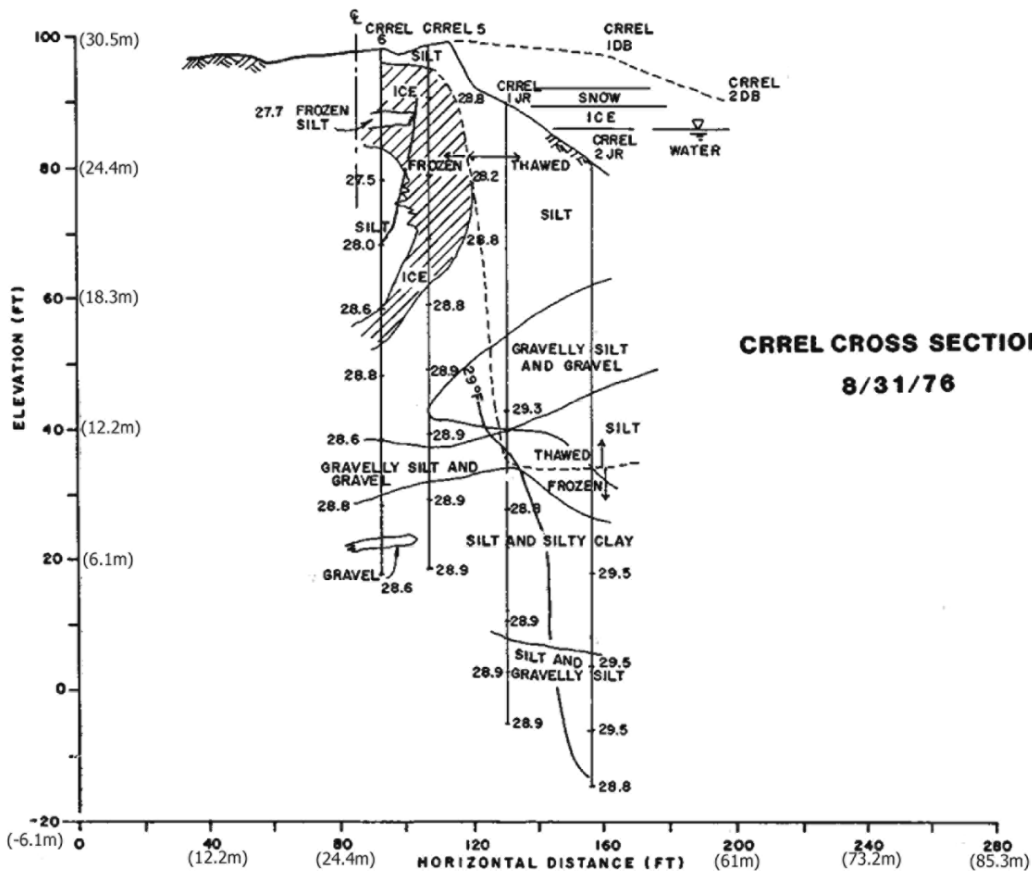


Figure 5. Profile of subsurface soil conditions in 1976 (from Collins and McFadden 1977).

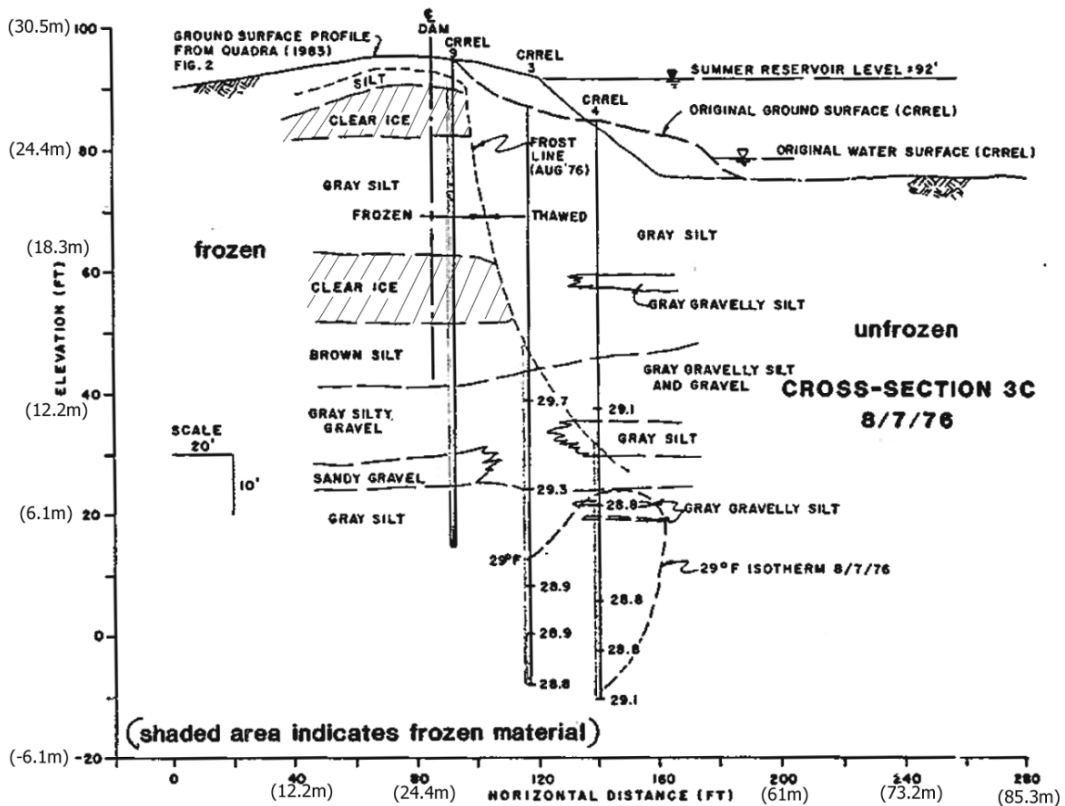


Figure 6. Profile of subsurface soil conditions in 1976 (from Collins and McFadden 1977).

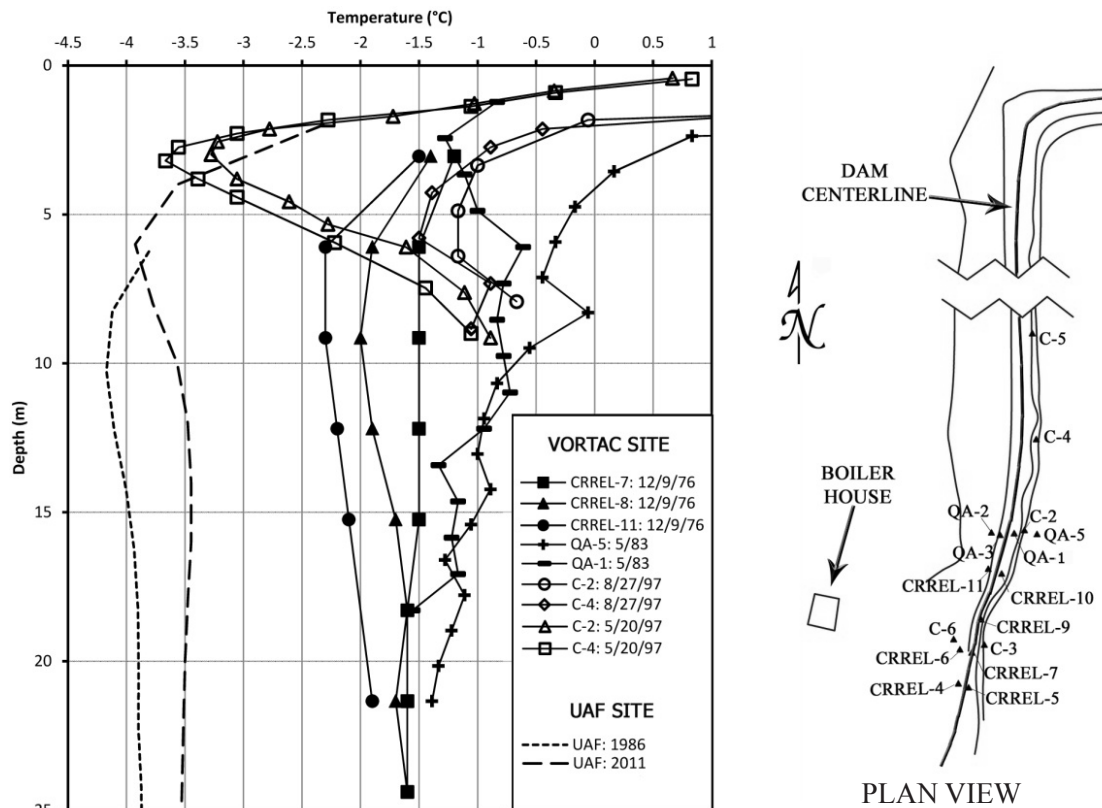


Figure 7. Comparison of historical ground temperatures at designated test hole locations (after Anderson & Krzewinski 2005).



Figure 8. Vortac Dam site photograph with visible upslope active slumping (September 9, 2010). FAA Vortac structure visible in background.

and higher ice content. If left unchecked without repairs, the dam would likely fail through a breach after several years and could be accelerated by seasonal storm events” (Anderson & Krzewinski 2005).

Almost all the involved technical groups addressed the geotechnical and frozen ground concerns and repair needs in a similar manner; however, with the exception of the 1994

repair effort, funding limitations seem to have prevented implementation of these recommendations. A program for continuous thermal monitoring (necessary for potential upslope thermal degradation evaluation) has never been implemented.

The Crowther study concluded that, from comparison with the earlier temperature measurements, the foundation soil and dam core have cooled slightly over the measured time period. It also stated that thawing of the frozen soil below the lake bed had increased significantly, and that the upstream slope of the dam would continue to be subjected to further thermal degradation, wave erosion, solifluction, and local instability.

The 2005 review by Golder Associates stated that “historical ground temperature data indicates that the depth of temperature changes due to seasonal variability is about 9 m below the ground surface, the active layer can reach depths up to about 2.4 m deep, and that ground temperature below this depth have increased by one or two degrees Fahrenheit since 1976, probably due to heat from the lake.”

Figure 7 provides a plot summarizing ground temperature data from the 1976, 1983, and 1997 measurements, as well as recent UAF data. Unfortunately, the 1997 measurements extend only to a depth of 10 m, but they do seem to confirm the slight warming trend that was observed in 1983. Information from a nearby UAF ground temperature monitoring site, located away from possible lake warming influence, is also plotted on Figure 7 and shows a corresponding temperature rise of approximately 1°C (UAF Permafrost Laboratory n.d.).

Conclusion

Vortac Dam has been in service for more than 40 years and is expected to remain functional for an undetermined period. With the continuing climate warming trend, the observed slight ground warming within the dam core, and the limited temperature datasets, it would be interesting to now apply thermal modeling techniques to address future thermal performance and design concerns.

At the time the dam was built, thermal modeling capabilities were limited. Alaska was then experiencing a “slight” cooling trend, which allowed refreezing of the embankment core lifts being placed through the three-year construction period. More recently, the newly developed thermal modeling capability (Cavanagh & Tchekhovski 2010) provides insight into possible ground thermal impacts. This project, even with the limited database, has the potential to provide an opportunity for refining thermal modeling capabilities and to assess continuing climate warming impacts. The apparent slight warming of portions of the dam and underlying foundation materials are of particular interest. Both the dam’s upslope and downslope stability are always of concern (Figure 8). While the frozen portion of the earth embankment is relatively ice-free, stability of the underlying ice-rich permafrost is an ongoing issue, particularly when considering the potential for underlying piping and erosion that may result from any thawing within the more ice-rich segments. These concerns do not appear to be highly significant over the reservoir’s remaining useful life, but they should be taken into consideration in all repairs and future evaluations.

References

- Anderson, S.L. & Krzewinski, T.G. 2005. Geotechnical assessment of Vortac Dam in Kotzebue, Alaska, report prepared by Golder Associates, Inc. Report AK000640, Kotzebue, Alaska, Dec., 2005, 31 pp. with appendices.
- Bendz, J. 1983. Geotechnical investigation, Vortac Lake – reservoir at Kotzebue, Alaska, report prepared by Quadra Engineering, Inc. June, 1983, 13 pp. with appendices.
- Cavanagh, P.C. & Tchekhovski, A. 2010. Design and performance of a frozen core dam in Cape Dorset, Nunavut, Canada. GEO2010: 63rd Canadian Geotechnical Conference & 6th Canadian Permafrost Conference, Calgary, Alberta, Canada, September 12-16, 2010: 625 – 633.
- Collins, C.M. & McFadden, T.T. 1977. Investigation of slumping failure in an earth dam abutment at Kotzebue, Alaska, U.S. Army Corps of Engineers Cold Regions Research and Engineering Laboratory (CRREL) Special Report 77-21, July, 1977, 21 pp.
- Crowther, G.S. 1998. Geotechnical assessment-Vortac Reservoir Dam safety evaluation, Kotzebue, Alaska, report prepared by Crowther Associates, January, 1998, 4 pp. with attachments.
- Crum, J. Personal Communication, August, 2011.
- Ferrains, O.J., Jr. 1965. Permafrost map of Alaska. USGS Miscellaneous Geologic Inventory Map I-445, Scale 1:2,500,000.
- Krzewinski, T.G., Webb, W.D., & Prakash, A. 1984. Kotzebue water supply dam (Vortac Dam), report prepared by Dames and Moore. Report AK00064, Kotzebue, Alaska, Dec., 1984, 19 pp. with appendices.
- Peyton, H.R. 1966. USPHS Kotzebue dam thermal analysis. Arctic Engineering Laboratory, University of Alaska, Fairbanks, Alaska.
- Plafker, G. (ed.). 1994. The Geology of Alaska, In *The Geology of North America*, Vol. G-1, Geological Society of America, 1055 p.
- Riddle, C.H. 1989. Kotzebue water improvement project, report prepared by R&M Consultants, Inc., May, 1989.
- Rooney, J.W. 1986. City of Kotzebue – Vortac Dam and abutment repairs study, report prepared by R&M Consultants, Inc., November, 1986, 17 pp. with attachments.
- Scher, R.L. 1994. Vortac Lake dam, Devil’s Lake road erosion, and Shore Avenue beach erosion, report prepared by R&M Consultants, Inc., September, 1994, 6 pp. with attachments.
- U.S. Dept. of Health, Education Welfare, Public Health Service (USPHS). N.d. Final report on the sanitation facilities construction for the City of Kotzebue, Alaska, Project No’s: AN-66-451, AN 68-600, An-69-609, AN-70-687EM, AN-71-619, AN-71-911, An-72-620, AN-72-687EM, AN-72-931, Public Law 86-121, p. 16 & 20.
- UAF Permafrost Laboratory. N.d. Process studies: permafrost observations, analysis, and interpretation, Geophysical Institute, University of Alaska Fairbanks.
- von Kotzebue, O. 1817. Journal entry for August 8, 1817, Science Under Sail – Russia’s Great Voyages to America - 1728 to 1867, Anchorage Museum of History and Art, 2000.

Warming Permafrost Temperatures at Two Mine Sites in the North Slave Region, Northwest Territories, Canada

Vladislav E. Roujanski, Bill Horne, Gordon Zhang, Shirley McCuaig, Michelle Blade
EBA, a Tetra Tech Company, Edmonton, Alberta, Canada

Michael Regular
Tyhee Development Corp., Vancouver, BC, Canada

Abstract

Geotechnical investigations conducted by EBA, a Tetra Tech Company, at two proposed mine sites (Tyhee and NICO) in the Canadian Northwest Territories have revealed warming trends in permafrost temperatures. Very warm, locally ice-rich, discontinuous permafrost with ground temperatures ranging from 0.0° to -0.6°C at the depth of zero annual amplitude was identified at the Tyhee site. The recent Tyhee ground temperature data indicate a warming trend with an increase of up to 0.2°C in the permafrost temperature since 2007. At the NICO site, warm discontinuous permafrost was found to be locally ice-rich, with ground temperatures ranging from -1.0°C to -1.8°C at the depth of zero annual amplitude. An increase of up to 0.6°C in the permafrost temperature has been observed at the NICO site since 2004. Permafrost distribution mapping at these two sites was carried out using *Ikonos* satellite imagery, borehole and testpit logs, and ground temperature monitoring data. The delineated areas of sensitive permafrost terrain were avoided during mine infrastructure siting.

Keywords: geotechnical investigations; discontinuous permafrost; ground ice; ground temperature cables; permafrost temperatures; warming trend.

Introduction

Recent characterizations (Romanovsky et al. 2010, Smith et al. 2010) of trends in permafrost temperatures show that ground temperature change rates for warming permafrost across the Northern Hemisphere are much smaller for warm permafrost at temperatures close to 0°C than for colder permafrost.

This paper adds new information on warming permafrost trends in the central Northwest Territories. Geotechnical investigations have been conducted recently by EBA, A Tetra Tech Company (EBA), at two proposed mine sites (Tyhee and NICO) located in the North Slave Region of the Northwest Territories (Fig. 1).

The Yellowknife Gold Project, operated by Tyhee Development Corp. (Tyhee), is an advanced gold exploration

project located approximately 85 km north of Yellowknife. Geotechnical investigations of various components of the project were completed by EBA in 2005, 2006, 2009, and 2010 (EBA 2006, EBA 2010). An understanding of near surface permafrost conditions is critical for all northern developments so that geotechnical problems associated with permafrost degradation can be avoided. The investigations at Tyhee consisted of the drilling, logging, and sampling of thirty vertical and angle boreholes and the installation of thirteen ground temperature (thermistor) cables (GTCs) to depths ranging from 10 m to 217 m. The boreholes provide pertinent data on overburden and bedrock conditions.

The NICO gold-bismuth deposit, operated by Fortune Minerals Ltd. (Fortune), is located approximately 170 km northwest of Yellowknife. EBA was retained by Fortune to conduct geotechnical investigations (in 2004, 2010, and 2011) that would provide feasibility stage geotechnical information for the design of proposed site facilities (EBA 2005, EBA 2011). To this end, EBA oversaw drilling of forty-five vertical boreholes and installed six GTCs to a depth of 15 m. Ground temperature monitoring has been carried out at the NICO site since October 10, 2004, and at the Tyhee site since August 22, 2007.

The objectives of this paper were to examine recent trends in permafrost temperatures and to determine permafrost distribution patterns at the two mine sites.

Methods

Geotechnical boreholes for the GTC installations were drilled using a diamond drill. Overburden and bedrock core samples were recovered using either HQ (63 mm core diameter) or NQ (47 mm core diameter) wireline core barrels and conventional

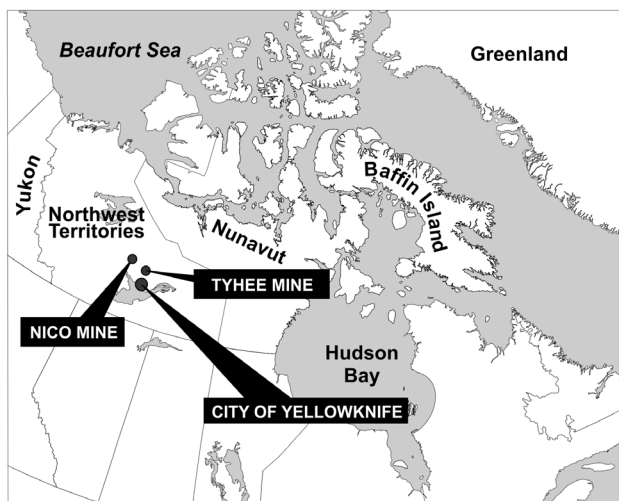


Figure 1. Location map of NICO and Tyhee mine sites.

diamond drilling techniques. To obtain frozen core samples, chilled brine was used as the drilling fluid when coring the overburden and the uppermost portion of the bedrock.

The overburden and bedrock core were examined and logged in the field. Soil and rock index parameters were determined immediately after sample recovery. Soil logging was based on the Modified Unified Soil Classification System guidelines and also included classification of ground ice within the cores.

Ground temperatures at both sites were monitored with EBA-made multi-bead GTCs installed in watertight PVC pipes (25 mm inside diameter) filled with dry fine sand. The annulus between the PVC pipe and the borehole wall was filled with coarse sand. The GTCs were calibrated in an ice-water bath with an accuracy of 0.01°C. Most of the ground temperature data were collected manually with a multi-meter. One GTC, which was installed in a borehole with only seasonal access (BH10-01), was connected to a “Lakewood Systems” datalogger. Temperatures were recorded at all GTCs at least once or twice per month throughout each year; however, only selected ground temperature measurements are presented in the ground temperature profile figures in this paper for clarity.

The collected ground temperature monitoring data and the results of the geotechnical drilling were used to compile permafrost distribution maps for both sites. Ground temperature, borehole, and testpit log data, along with field observations of permafrost-related terrain features, were used to identify and delineate areas (terrain units) characterized by perennially frozen vs. unfrozen ground conditions. *Ikonos* satellite imagery was used as the base map. Textures and tones were identified for frozen and for unfrozen ground types (e.g., bedrock exposed at the surface is unfrozen and appears as light-toned rough-textured areas on the satellite imagery). This information was extrapolated to the rest of the study areas in order to create maps of permafrost distribution and calculate the percentages of areas underlain by permafrost.

Tyhee Study Area

Geological setting

The Yellowknife Gold Project (Tyhee) area is situated within the southern Slave Province of the Canadian Shield. The study area is underlain primarily by variably metamorphosed greywacke, tuffaceous wacke, siltstone, mudstone, mafic metavolcanic amphibolite, and minor granodiorite.

Terrain

Satellite imagery analysis shows that the landscape of the Tyhee study area is dominated by a series of southwest-northeast trending glacially sculpted ridges and elongated hills separated by inter-ridge valleys and depressions created by folds and other structural elements in the bedrock. The depressions are occupied by lakes and ponds of variable size.

Glacial till deposits, the most widespread sediment type in the area, are characterized by a sandy texture with minor silt and clay (EBA 2010). Poorly drained surfaces in the inter-ridge valleys, depressions, and low-lying areas are covered by clayey and silty lacustrine sediments and organic peat

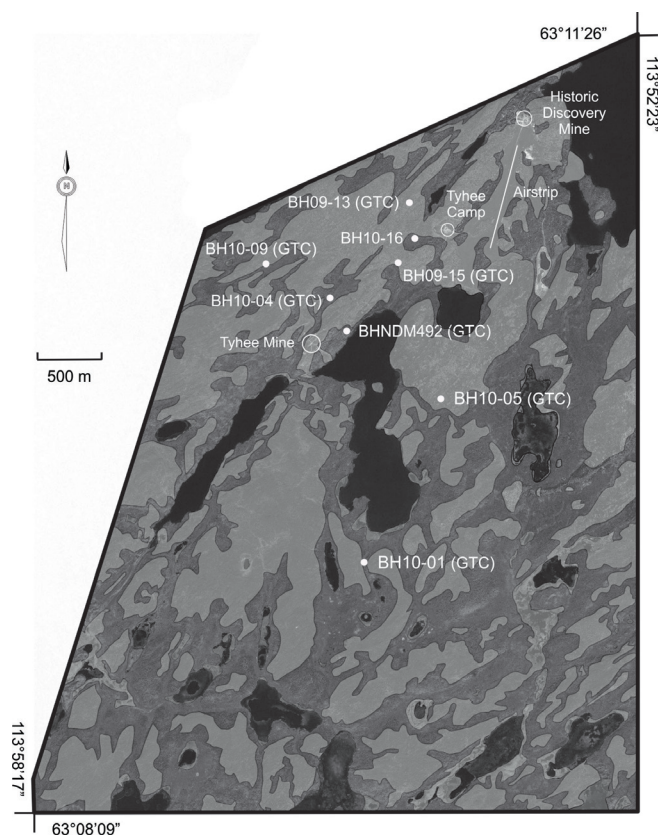


Figure 2. Permafrost distribution map, Tyhee Mine Site. Light grey areas (exposed bedrock, fens, etc.) and black areas (lakes) are unfrozen. Dark grey areas (peat-covered low-lying areas, bogs and north-facing slopes) are perennially frozen. Boreholes fitted with a multi-bead GTC are marked with (GTC) (compiled by Roujanski, McCuaig, and Blade).

deposits up to 3 m thick (penetrated by BH10-16; Fig. 2 and Fig. 3). Glaciofluvial deposits are of limited extent within the study area. There are numerous bedrock outcrops cleared of sediment by meltwater flow during the waning stages of the Late Wisconsinan glaciation.

Permafrost distribution, ground ice, and ground temperatures

Satellite imagery analysis (substantiated by borehole logs and ground temperature monitoring data) of the permafrost distribution shows that approximately 40% of the study area is underlain by very warm, locally ice-rich permafrost (Fig. 2). Visually estimated ground ice content (by volume) comprises up to 60% of the perennially frozen soil at the Tyhee site.

A massive icy bed 0.9 m thick encountered at a depth of 2.8 m in BH10-16 (Fig. 2) consisted of interbedded sub-horizontal layers of ice and light grey silt with some fine- to coarse-grained sand and a trace of fine gravel. Visually estimated volumetric ice content of the bed was 50–60%. Gravimetric ice content determined in the laboratory (on an ice-to-dry-soil weight basis) was 112%. The massive icy bed was covered by 2.8 m of peat with a gravimetric ice content ranging from 653% at a depth of 1.0 m to 392% at a depth of 2.2 m. The

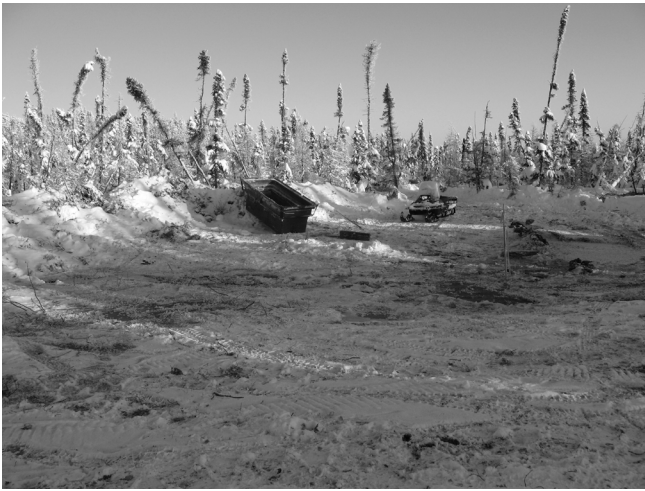


Figure 3. Borehole BH10-16 site with drunken forest indicative of ice-rich permafrost (in background). Foreground is area cleared for drilling.

massive icy bed was underlain by bedrock at a depth of 3.7 m. The shallow ice-rich permafrost at the BH10-16 site resulted in the tree stand condition known as the drunken forest. Some of the stunted trees of the predominantly black spruce forest were observed leaning in random directions (Fig. 3).

The maximum measured thickness of the permafrost layer in the study area is approximately 70 m. This thickness was recorded at BH10-04 (Fig. 4), the location of which is shown in Figure 2. Permafrost temperatures at the depth of zero annual amplitude within the study area range from 0.0° to -0.6°C (Fig. 4). The measured ground temperatures in the two deep boreholes (BHNDM492 and BH10-04) indicate that the geothermal gradient at depth at the Tyhee Mine site is 0.01 to 0.03°C/m.

The recent ground temperature data collected at the Tyhee site indicates a warming trend in permafrost temperatures, with an increase of up to 0.2°C in the permafrost temperature at a depth of 15 m below the ground surface since 2007 (BHNDM492, Fig. 4). This finding was taken into consideration during the pre-feasibility study completed by EBA (EBA 2010). Potentially unstable areas underlain by warming, locally ice-rich permafrost were avoided during the proposed mine infrastructure siting.

NICO Study Area

Geological setting

The NICO study area is underlain by volcanic and plutonic rocks. These include metasedimentary rocks and intermediate to felsic intrusive and extrusive, predominantly volcanic rocks (rhyolite) with sill-type intrusions.

Terrain

The terrain of the NICO study area is characterized by glacially sculpted, rounded bedrock ridges and hills separated by valleys and depressions. Valley bottoms and depressions are underlain by metasedimentary rocks covered by perennially

frozen unconsolidated deposits of glacial (till) and post-glacial (glaciofluvial, lacustrine, and organic) origin. Hills and bedrock ridges in the study area correspond to the exposed unfrozen intrusive and extrusive, predominantly volcanic (rhyolite) rocks.

Hills and ridges in the study area exhibit well-developed cryoplanation terraces (i.e., step-like benches) formed on the exposed bedrock slopes by intense frost wedging associated with snowdrifts. The terraces and the lower portions of the bedrock slopes are mantled by colluvium.

Two distinctive organic terrain types (fens and bogs) separated by bedrock outcrops were observed in low-lying areas.

Permafrost distribution, ground ice, and ground temperatures

Warm, locally ice-rich discontinuous permafrost was mapped at the NICO site, and several boreholes with GTC cables are present in the area (Fig. 5 and Fig. 6).

In the study area, permafrost is confined to low-lying areas covered by organic deposits, where it is found predominantly in bogs. Fens are seasonally frozen within the uppermost layer. Permafrost is also found at the bottoms of valleys and depressions and on north-facing slopes.

Satellite imagery analysis (substantiated by borehole logs and ground temperature monitoring data) of the permafrost distribution shows that approximately 36% of the NICO study area is underlain by warm, locally ice-rich permafrost (Fig. 6). Visually estimated ground ice content (by volume) varies from up to 30% (in organic deposits, BH04-01) to greater than 40% (interbedded layers of ice and clay encountered at a depth of 1.7 m in BH04-05).

Permafrost temperatures were found to range from -1.0°C to -1.8°C at a depth of 15 m below the ground surface (BH 04-05 and BH11-37, Fig. 5). An increase of up to 0.6°C in the permafrost temperature at a depth of 15 m below the ground surface has been observed at the NICO site since 2004 (BH04-05 in Fig. 5). This equates to a warming rate of approximately 0.09°C/year. The ground temperature increase makes areas underlain by ice-rich warm permafrost susceptible to further change in response to a warming climate.

Air Temperatures

Historical mean annual air temperatures for Yellowknife are shown in Figure 7. The air temperature data were downloaded from the Environment Canada climate/weather website (http://www.climate.weatheroffice.gc.ca/climateData/canada_e.html).

A long-term warming trend of 0.03°C/year has been observed. The warming trend from 2004 to 2010 is 0.08°C/year; however, there is considerable scatter in the data. It is interesting to note that the warming trend at the NICO mine site is of a similar rate.

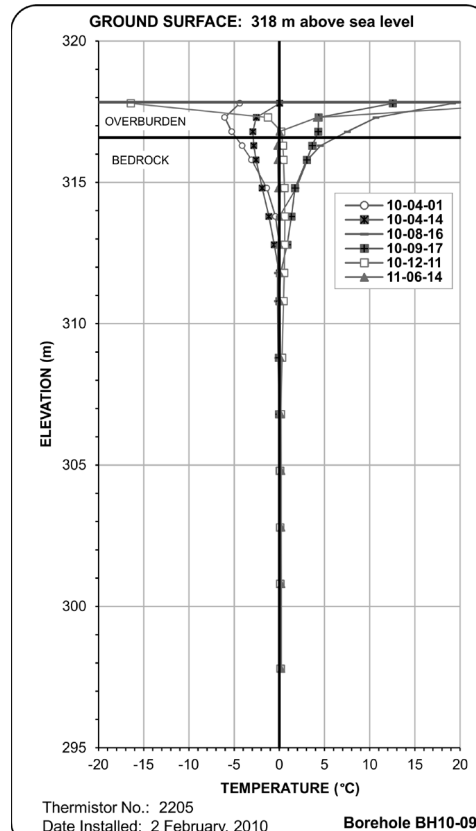
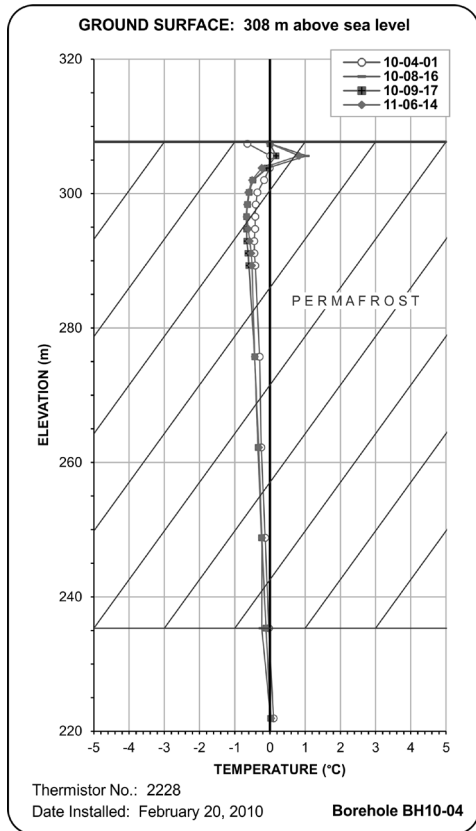
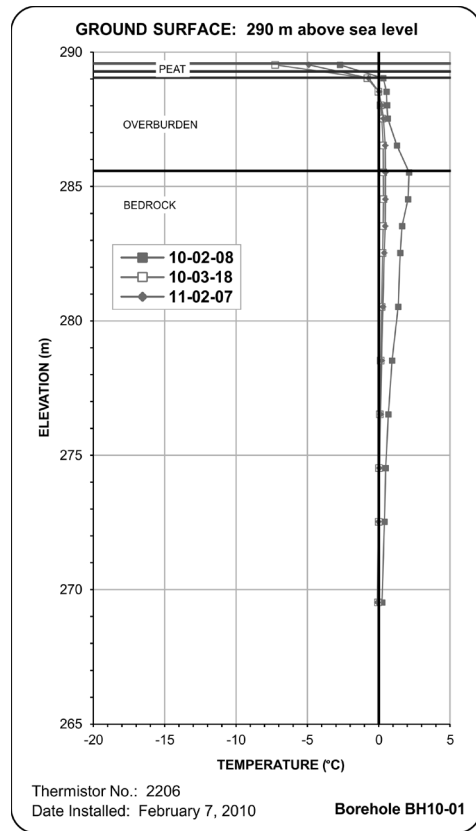
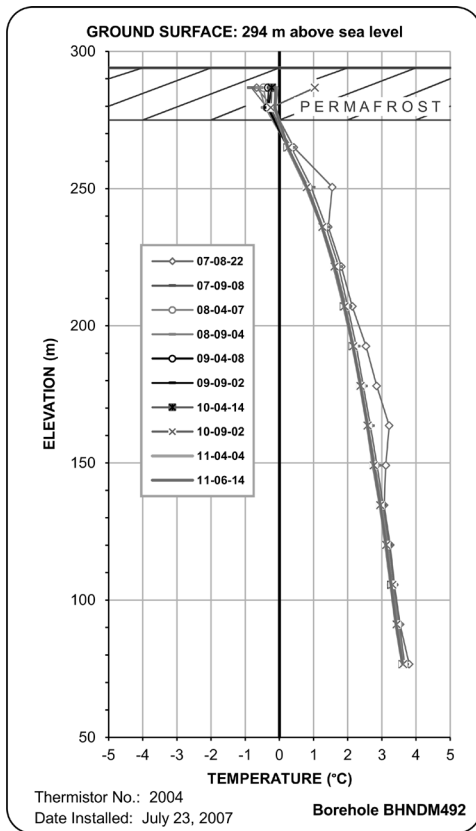


Figure 4. Measured ground temperature profiles in selected boreholes drilled at the Tyhee mine site.

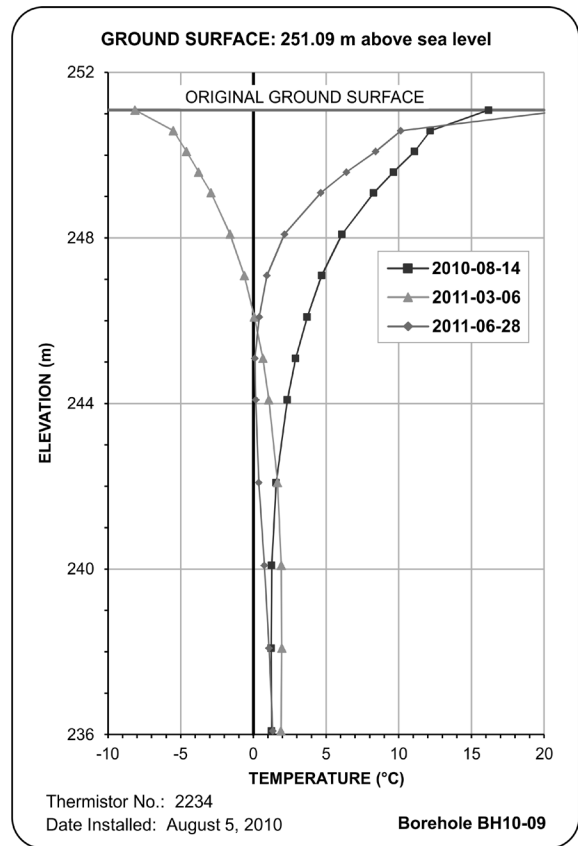
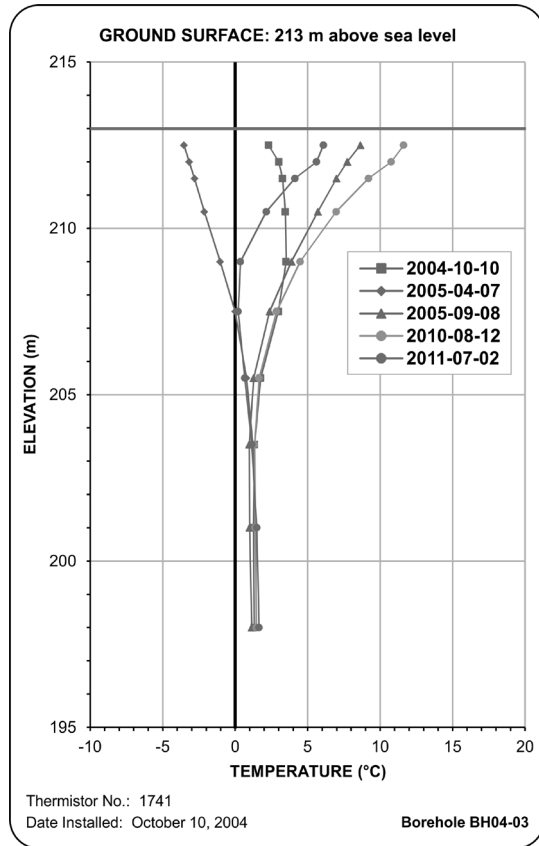
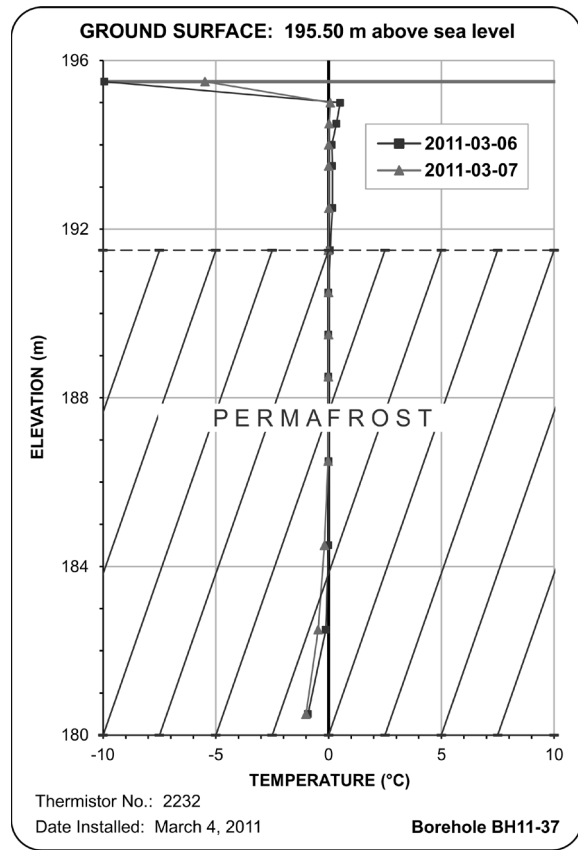
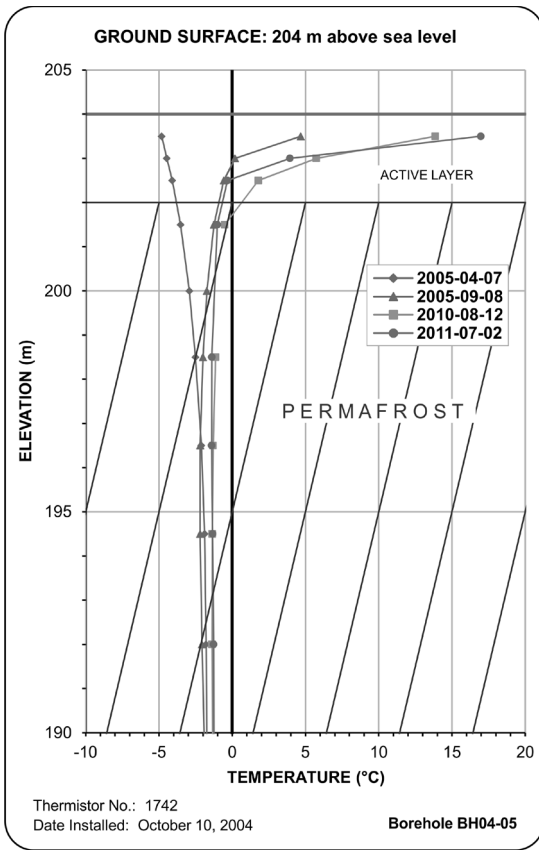


Figure 5. Measured ground temperature profiles in selected boreholes drilled at the NICO site.

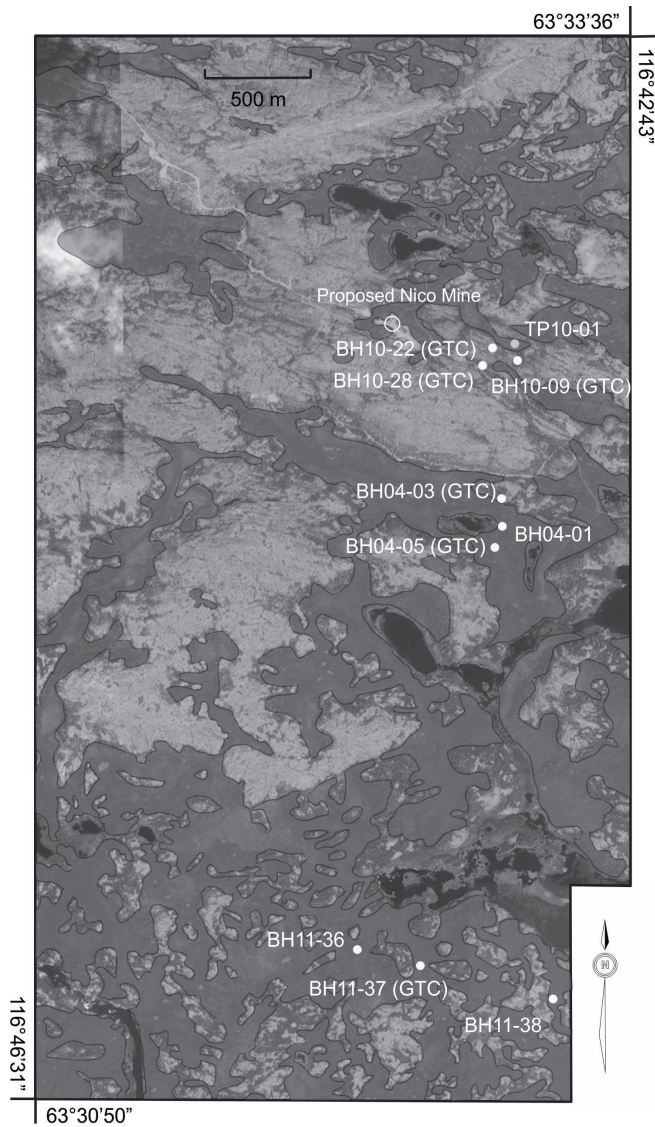


Figure 6. Permafrost distribution map, NICO Mine Site. Light grey areas (exposed bedrock, fens, etc.) and black areas (lakes and stream channels) are unfrozen. Dark grey areas (peat-covered low-lying areas, bogs and north-facing slopes) are perennially frozen. Boreholes fitted with a multi-bead GTC are marked with (GTC) (compiled by Roujanski, McCuaig, and Blade).

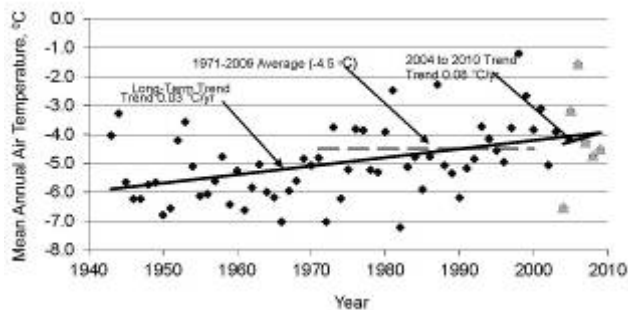


Figure 7. Yellowknife mean annual air temperatures.

Conclusions

Approximately 40% of the Tyhee study area is underlain by very warm, locally ice-rich permafrost up to 70 m thick, with ground temperatures ranging from 0.0° to -0.6°C at the depth of zero annual amplitude.

Approximately 36% of the NICO study area is underlain by warm, locally ice-rich permafrost with ground temperatures ranging from -1.0°C to -1.8°C at the depth of zero annual amplitude.

Warming ground temperature trends were observed at two boreholes at the NICO and Tyhee sites. Areas underlain by ice-rich permafrost close to 0°C are susceptible to further temperature changes and possibly thaw in response to warming climate. Where possible, mine infrastructure should be placed to avoid these potentially unstable areas.

Acknowledgments

This paper is published with the approval of the Tyhee Development Corporation and Fortune Minerals Ltd.

The authors wish to acknowledge assistance offered by Debashis Das, Corrie Schofield, Kimberly Turner-De Vries, and Laili Abolghasemi of EBA with the preparation of this paper.

The authors are thankful for the constructive comments provided by the reviewers and the editor.

References

- EBA Engineering Consultants Ltd. 2011. NICO 2010 Process Plant Facilities and 2011 Airstrip Geotechnical Investigations. Report prepared for Fortune Minerals Ltd., File No. Y14101101.004, April 2011.
- EBA Engineering Consultants Ltd. 2010. Technical Report on the Pre-Feasibility Study of the Yellowknife Gold Project, Northwest Territories, Canada. Report prepared for Tyhee Development Corp., July 22, 2010.
- EBA Engineering Consultants Ltd. 2006. Yellowknife Gold Project – Winter Lake Tailings Dams Geotechnical Investigations. Report prepared for Tyhee NWT Corp., File No. 1740082.027, May 2006.
- EBA Engineering Consultants Ltd. 2005. NICO Tailings Dam and Process Plant Facilities, 2004 Geotechnical Site Investigation. Report prepared for Fortune Minerals Ltd., File No. 1700127.002, April 2005.
- Romanovsky, V.E., Smith, S.L., & Christiansen, H.H. 2010. Permafrost thermal state in the Polar Northern Hemisphere during the International polar Year 2007-2009: a Synthesis. *Permafrost and Periglacial Processes* 21: 106-116.
- Smith, S.L., Romanovsky, V.E., Lewkowicz, A.G., Burn, C.R., Allard, M., Clow, G.D., Yoshikawa, K., & Throop, J. 2010. Thermal state of permafrost in North America: a contribution to the International Polar Year. *Permafrost and Periglacial Processes* 21: 117-135.

Thermo-Mechanical Modeling of a Glacier-Permafrost System in Spitsbergen: Implications for Subglacial Hydrology

Nicolas Roux, Christophe Grenier

Laboratoire des Sciences du Climat et de l'Environnement, UMR 8212 CNRS-CEA-UVSQ, Orme des merisiers, 91191 Gif-sur-Yvette Cedex, France

Christelle Marlin, Emerick Delangle, Albane Saintenoy

IDES, UMR 8148 CNRS – Université Paris Sud, 91405 Orsay Cedex, France

Jean-Michel Friedt

FEMTO-ST, UMR 6174 CNRS, Université de Franche-Comte, France

Madeleine Griselin

THEMA, UMR 6049 CNRS, Université de Franche-Comte, France

Abstract

To study the hydro-glaciological response of glaciers impacted by recent climate change, a polar glacierized watershed (10 km²) was monitored in West Spitsbergen (79°N). Field surveys show winter discharges causing large icings. A 2D modeling approach along the main axis of the system is developed to study the evolution of the glacier-bed system. Two codes are chained (for the glacier and for the underground). Results confirm that the glacier is polythermal with a cold-based terminus. Its rapid retreat (ca. 18 m a⁻¹) should lead to a cold glacier within decades to a century. Simulations show that permafrost development precedes glacier retreat (thin glacier tongue with -5°C MAAT at Ny Alesund), while in the mountainous part a somewhat stable glacier position allows permafrost to develop over longer times and at greater depths. The unfrozen soil extent below the glacier will progressively shrink, causing the disappearance of winter discharges probably within the next century.

Keywords: permafrost; numerical modeling; glacier-permafrost interaction; glacial hydrology; Spitsbergen.

Introduction

As concluded by the ACIA-group (2004), one of the greatest impacts of climate change in the mass of arctic land ice over decade-to-century timescales is likely to be a change in the freshwater input to the high-latitude oceans. Spitsbergen, the main island of the Svalbard archipelago, is a key region in the High Arctic to study the impact of climate change on ice masses, as glaciers and ice caps cover about 60% of its surface. The smaller glaciers, which display a rapid hydrological response and a quick change of front position and ice volume over years to decades, are particularly interesting.

Several small glaciers are located along the Broggerhalvoya peninsula (Northwestern Spitsbergen). For instance, Midtre Lovénbreen was extensively studied (Björnsson et al. 1996). The neighbor glacier, Austre Lovénbreen, has been recently investigated to compare glacier and water mass-balance. The Austre Lovénbreen catchment is optimal for hydrological studies because the catchment's surface outlet is separated from the sea by a thick, calcareous stable outcrop through which flow has carved a canyon, making flux measurement complete and conservative. The glacier system has been extensively studied as well (Griselin 1982, Saintenoy et al. 2011, Friedt et al. 2010, Friedt et al. 2011). According to the results obtained on the Midtre Lovénbreen glacier, Austre Lovénbreen is expected to be polythermal with a cold-based terminus. Glacial hydrology is classically complex, involving various reservoirs as well as flow paths within and beneath the glacier, including subglacial groundwater flow (Fountain

& Walder 1998, Flowers & Clarke 2002). One especially interesting feature concerns evidence of winter flow. It appears as icings during winter (Griselin 1982, 1985), partly covering the proglacial moraine. Griselin (1985) estimated the total volume of these icings. Considering the water geochemistry, this winter flow may be related to the discharge of a subglacial reservoir, possibly linked to an underground storage volume, recharged in the upper parts of the glacier catchment in spring and summer.

Our objective here is to study the thermal state of a polar glacier and its substrate. The extent of permafrost is indeed a key feature controlling the extent of this likely subglacial/underground reservoir. Due to the highly transitory evolution of the glacier/underground coupled system, a transient simulation is considered, involving some future perspectives.

The 2D modeling approach used in this work involves a glacier model and a heat transfer simulation code for porous media. Both models are simply chained; glacier evolution is simulated and basal temperature evolution is used as the forcing signal to the porous medium heat transfer model. The uncovered parts of the profile are imposed mean air temperatures as a function of altitude. This approach is similar to that of Boulton and Hartikainen (2004). (In the framework of nuclear waste storage studies and considering ice sheets, see Chan et al. 2005.) Similarly again, the model is a 2D cross-section through the catchment from the mountain range in the upper part to the external ridge of the proglacial moraine.

The key idea is that a sufficiently thick and active glacier should maintain ice temperatures at the pressure melting point

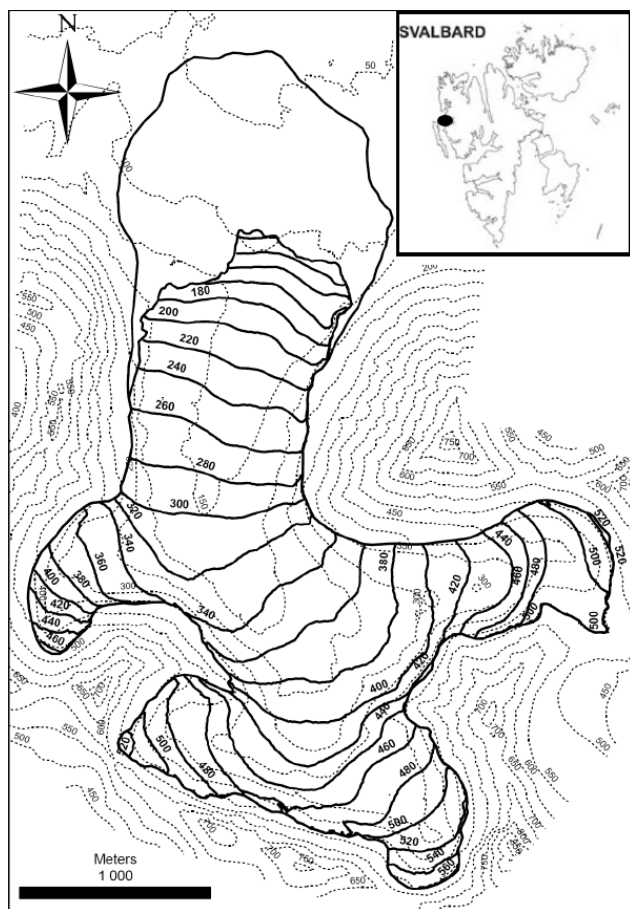


Figure 1. On the upper right corner, the study area (black oval) in Northwestern Spitsbergen: the Broggerhalvoya Peninsula. Main panel: study glacier with 2009 surface and bed topography (respectively solid and dotted lines). Bed and surface contour intervals are 50 m and 20 m, respectively. The past extent from the 1962 DEM is shown as well (outermost solid line).

at its base. Indeed the glacier insulates the ground from the atmosphere, and geothermal flux accumulates at the glacier base, resulting in an elevation of basal ice temperature. As observed by the surveys, the glacier has been retreating over the last decades and its thinning is leading to the freezing of its base due to the reduction of glacier activity and curtain effect (annual mean air temperatures are well below zero).

In the following section, we present the Thermo-Mechanical glacier model, the permafrost model, and the simulations.

Glacier Modeling

Glacier and bedrock geometry

Since 2006, both the glacier surface and bedrock topography have been mapped with Differential GPS for the surface and Ground Penetrating Radar for the ice thickness. Digital Elevation Models (DEM) corresponding to 2009 that include the glacier surface and bedrock are used. The horizontal resolution is 10 m (see Figure 1 for the contour plot). DEMs for the 1995 and 1962 surfaces also exist (Friedt et al. in prep.). We extract from each DEM a south-to-north central flowline profile as an input for the 2D glacier model (Fig. 2). The glacier

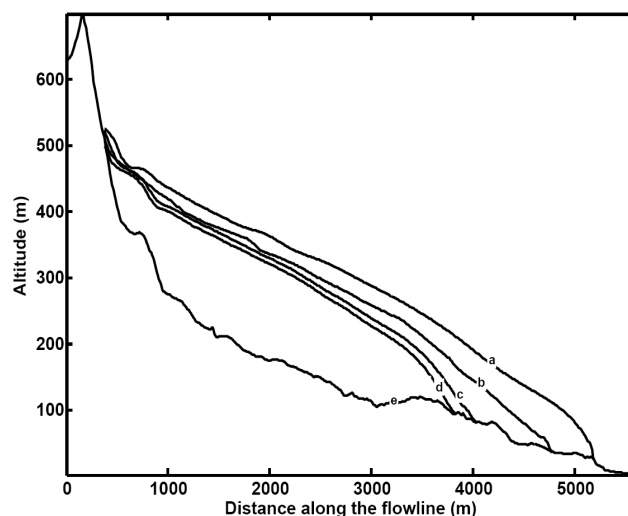


Figure 2. Altitudinal profiles along the central flowline (Austre Lovenbreen). “a” is the glacier surface profile for 1925. “b”, “c” and “d” are from the 1962, 1995, and 2009 DEM respectively. “e” is the surface of the bedrock.

has been retreating rapidly (at roughly 18 m a^{-1}) over the last 50 years. The first profile (a) in Figure 2 corresponds to an initial reconstruction of glacier geometry at its last maximum extent, just before the beginning of the last century retreat (estimated around 1925). The other curves refer to the glacier geometry in 1962, 1995, and 2009, respectively, for (b), (c), and (d).

Glacier mass balance and air temperature profiles

Glacier mass balance measurements are available for three years between 2007 and 2010. The mean equilibrium line altitude is close to 350 m. We use a linear relationship between mass balance and altitude, with an altitudinal gradient of 0.8 m a^{-1} per 100 m that we will apply to any surface geometry. The constant relationship over the years is justified by the fact that the glacier net mass balance in this area has been fairly constant, though negative, over the past few decades (Hagen et al. 1990, Hagen et al. 2003).

Temperature measurements at the glacier surface give a rather well constrained and constant altitudinal temperature gradient (-0.57°C per 100 m). We thus may apply this gradient to the mean annual air temperature over the last 70 years measured at Ny Alesund (approximately -5°C at 8 m a.s.l., data from the Norsk Meteorological Institute) to estimate the surface temperature over the entire profile (ice or ground).

The thermo-mechanical model

We used the thermo-mechanically coupled model developed by Sam Pimentel at Simon Fraser University, Vancouver, Canada. Only the glacier dynamics portion has been published in Pimentel et al. (2010), where a full description of the model can be found. In the mechanical portion, the momentum and mass conservation equations with the constitutive flow law, which depends on stress and temperature, are resolved in a Picard iteration loop. Surface boundary is stress-free, whereas sliding can be applied at the glacier base. Modifications have been made in the original thermal portion, resulting in an

Table 1. Constants and model parameters used for both glacier and porous media numerical models.

| Parameters | Value | Units |
|--------------------------|----------------------|----------------------------------|
| Flow rate factor | $2.4 \cdot 10^{-24}$ | $\text{Pa}^{-3} \text{s}^{-1}$ |
| Ice density | 910 | kg m^{-3} |
| Water density | 1000 | kg m^{-3} |
| Rock density | 2600 | kg m^{-3} |
| Ice heat capacity | 2009 | $\text{J kg}^{-1} \text{K}^{-1}$ |
| Water heat capacity | 4187 | $\text{J kg}^{-1} \text{K}^{-1}$ |
| Rock heat capacity | 840 | $\text{J kg}^{-1} \text{K}^{-1}$ |
| Ice thermal conductivity | 2.1 | $\text{W m}^{-1} \text{K}^{-1}$ |
| Water heat conductivity | 0.58 | $\text{W m}^{-1} \text{K}^{-1}$ |
| Rock heat conductivity | 2.9 | $\text{W m}^{-1} \text{K}^{-1}$ |
| Geothermal heat flux | 0.084 | W m^{-2} |
| Latent heat of fusion | $3.34 \cdot 10^5$ | J kg^{-1} |
| Porosity | 0.1 | (-) |

energy conservation equation reduced to the simplest, which is vertical heat conduction and volumetric heat source due to the internal deformation of ice.

Simulations

The current thermal state of Austre Lovenbreen is certainly not in balance with today's climate. It is indeed likely to be the result of a past thermal equilibrium because of the high heat storage capacity of ice. We infer a former glacier geometry that would correspond to the "Little Ice Age" (LIA), probably marked by the external boundary of the proglacial moraine (Fig. 2). Similar to Zwinger & Moore (2009), we let the glacier with the "LIA" geometry equilibrate between the surface air temperature and the geothermal heat flux applied at the glacier base. A constant parameter for the flow law of ice is used. This thermal state provides an initial condition for the prognostic simulations. We then simulate the glacier evolution (geometry and temperature) over 200 years from 1925 to 2125 (see Table 1 for the numerical parameters) in order to provide the current thermal state and the future evolution. This will be the base for permafrost modeling.

Permafrost Modeling

The model

Régner et al. (2010) developed a thermo-hydraulically coupled code within the Cast3M finite element and finite volume code (www-cast3m.cea.fr). The purely thermal model used here simulates transient heat transfers with conduction and phase change. The equation (e.g., similar to McKenzie et al. 2007) is nonlinear. The conductive properties depend on the thermal state of the porous medium. The liquid water saturation curve is a linear function of temperature, providing a temperature range of 1.5°C for phase change (from full liquid water saturation to full ice saturation). The non-linearity is dealt with by a Picard convergence loop.

Simulations

The simulated domain is 2D, and spreads 500 m deep below

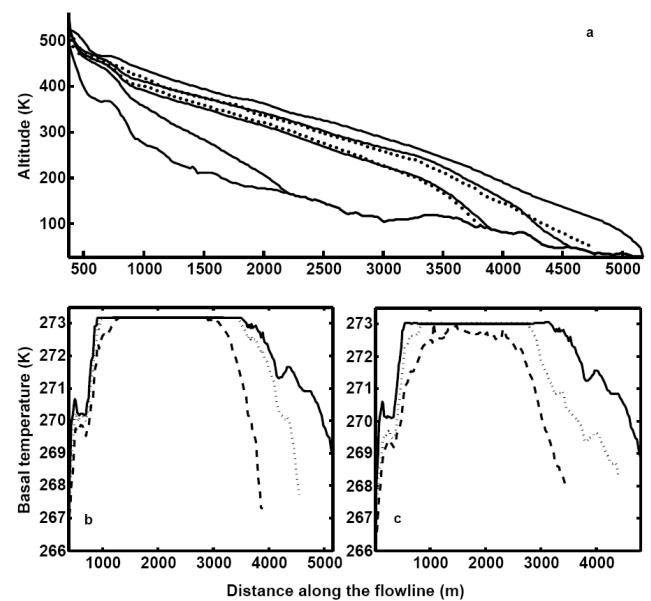


Figure 3. (a) 1962 and 2009 modeled surface (solid) compared with the data (dotted line). Smallest glacier extent corresponds to the 2125 predicted surface. (b) & (c) Modeled basal temperature: 1925 initial state (solid), 1962 (dotted), and 2009 (dashed).

the ground surface (curve "e" in Figure 2). The domain lateral extension is different than for the glacier simulations since we take into account the mountain peak and the proglacial area down to the sea. The lower boundary is imposed by the geothermal flux, and lateral sides are constrained to no heat flux. Table 1 provides the ground thermal properties used for the simulations.

Initial conditions correspond to a steady state calculation of ground temperatures. They result from a spin up to equilibrium simulating the initiation of permafrost with imposed surface temperature (meaning ground surface, which is in contact either with the atmosphere or the glacier base). Under the mountain peak, air temperature is imposed on the ice-free surface. For the proglacial area (from 3.5 km down to the sea), two extreme scenarios are considered. For the first, air temperature is imposed, whereas zero degree is maintained for the second, preventing permafrost development.

We then study the underground thermal evolution forced by glacier basal and air temperature over 200 years as the glacier retreats.

Results

Glacier evolution and basal temperature

Glacier surface evolution over 200 years is plotted in Figure 3. Modeled surfaces for 1962 and for 2009 are in good agreement with the DEMs. Figure 3b shows the basal temperature along the profile modeled at the initial state and that calculated for 1962 and 2009 with the transient coupled method. Figure 3c is the same as Figure 3b, but for each geometry the simulation is carried on until steady state is

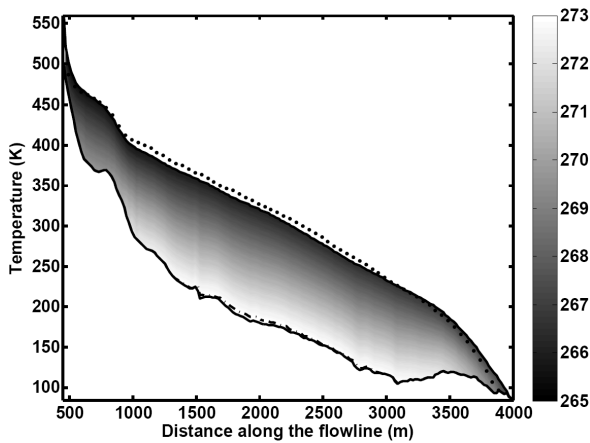


Figure 4. Austre Lovénbreen temperature modeled for 2009. Dotted line is the 2009 profile from DEM. The dashed-dotted line is the zero-isotherm through the glacier.

reached. It shows the importance of thermal inertia and thus how important it is to go back in time as far as possible to model the best current thermal state. In Figure 3c, a glacier in equilibrium with today's climate would have an entirely cold base (dashed line).

The present-day modeled thermal state of Austre Lovénbreen is shown in Figure 4. The temperate part of the glacier is very small and will certainly vanish within the next decades. Nevertheless, today's thermal state should still largely allow the presence of liquid water at its base.

Permafrost extent

Permafrost evolution is represented in Figure 5 for both scenarios. The simulations have been performed for a period of 200 years, from 1925 to 2125. Figure 5 encompasses the present-day state and also includes a prospective view of permafrost development over longer timescales.

The upper panel in Figure 5 provides modeled glacier thicknesses through time, which controls the underground thermal evolution. It shows the rapid glacier evolution: overall mass loss, and retrogradation (ca. 18 m a^{-1}). The maximum glacier extent is represented as a dotted line, corresponding to the 1925 initial reconstruction given in Figure 2. The dashed line represent the current (2009) state, while the other curves (from 1 to 4) correspond to situations spaced with a 50-year interval.

The lower panel of Figure 5 provides the position of the -0.5°C isotherm in the porous medium, interpreted here as the permafrost depth.

The lower part (glacier snout) displays rapid lateral permafrost evolution as the glacier retreats. Permafrost precedes the glacier tongue due to the reduced ice thickness, allowing the penetration of the cold wave. In both scenarios, permafrost doesn't evolve through time in the first kilometer below the mountain peak. Indeed, ice thickness is fairly constant on the upper glacier and air temperatures are held constant over time. In the first scenario (black lines), permafrost is already developed under the glacier snout, extending over 1.5 km

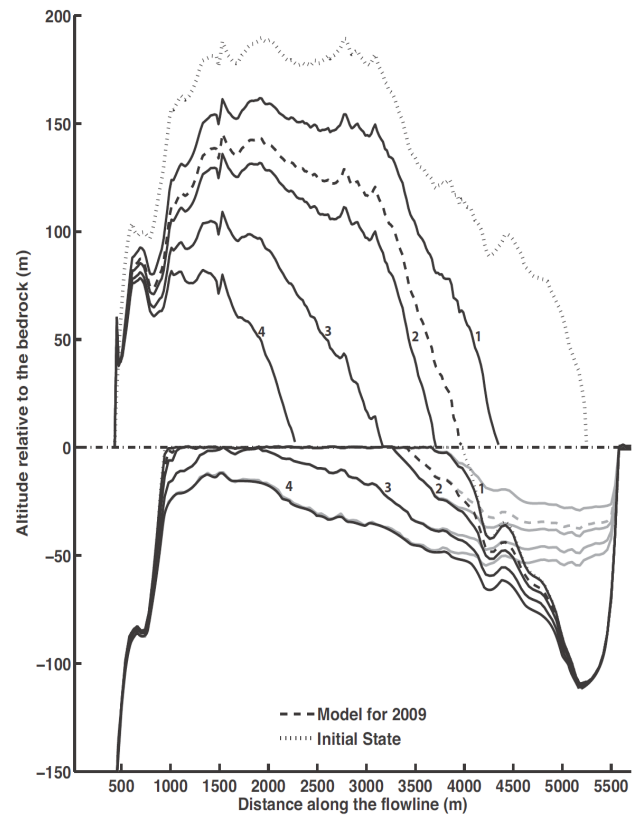


Figure 5. Permafrost development as a function of glacier retreat. Upper panel: ice thickness profiles plotted with a 50-year interval. Lower panel: depth of the -0.5°C isotherm (as an approximation for the permafrost table position) in the porous medium. Black and grey lines are for two different scenarios with two initial conditions. The dashed line corresponds to the situation in 2009, and the dotted line is the initial state in 1925.

laterally with a maximum depth around 100 m. The porous medium is permafrost-free in that same area for the second scenario (gray lines). The results from the two scenarios show differences in the permafrost evolution only from 3.5 km to the sea. Yet lateral extensions of both the grey and black lines are the same at each time. In particular, the permafrost-free area between kilometer 1 and 3.5 coincides for both cases. Only the depth in the proglacial zone is different, with the first scenario having permafrost twice as thick as the second.

In these simulations, permafrost should underlie the whole glacier by 2075, and by 2125 the minimal depth of the -0.5°C isotherm should be around 20 m.

Discussion

The results of the models indicate that the Austre Lovénbreen glacier is in a transient condition, out of equilibrium with the present-day climatic conditions. It is hard to provide a good initial state, sufficiently far back from today, both for the glacier and the underground system. The reconstructed glacier geometry for 1925 is the best estimate of its last maximum extent that we can provide, the proglacial moraine being a geomorphological witness of its last maximum extent. The

year 1925 should be taken as the beginning of its retreat (Hansen et al. 2003). Ideally, the same guess of a probable initial state should be done for the underground medium, but there is no such feature as the moraine to enable us to guess at the former extent of permafrost. To get around this problem, we let the permafrost develop for thousands of years with some realistic upper temperature profile for the mountain peak. This only gave us an idea of “a maximum” depth of high mountain permafrost. By doing so, we obtained permafrost depths of the order of 350 m, developing over 5000 years, which is in fairly good agreement with former estimates of Humlum (2005). It is more difficult to simulate in the same fashion a maximum depth for coastal permafrost due to the uncertainties in the glacier maximal extent over the last millennia. Our first scenario assumed the glacier stayed at its 1925 thermal state for thousands of years, which is not true but probably gives a rather realistic permafrost initial extent. The other endmember situation was to start with a permafrost-free proglacial area as in the second scenario. These two scenarios provide bounds for the dynamics of permafrost development at depth. Indeed, in a few hundred years (scenario 2), permafrost develops half as deep as it would in a few thousand years (scenario 1). This means that the vertical progression of permafrost is slower as it extends deeper (conductive wave propagation). Only a really small area should have been exposed to air temperatures for a long period of time, since the glacier, before terminating on land, was most certainly calving to the sea. Thus reality is expected to land somewhere between the two endmember situations.

More importantly from a hydrological point of view is the lateral extension of the unfrozen substrate. The modeled horizontal extent of permafrost, even below mountain peaks, should be close to reality. Having a wrong initial state for the underground system has a greater impact on the depth of permafrost than its lateral extent (forced by glacier retreat for both cases) since permafrost can develop over a few meters only after a few years of exposure to negative air temperatures.

The model thus provides a simplified but coherent view of the glacier-substrate system, at least for our hydrological purposes. Some quantitative features are probably reasonably estimated. Its retreat reduces the unfrozen bed zone roughly at the same speed (18 m a^{-1}). The upper part of the profile under the mountain peaks does not present any evolution of glacier cover but the temperature signal penetrates into the mountain range and permafrost propagates at depth and partly below the glacier. The reduction of the unfrozen bed extent is slower.

According to the model and the scenarios considered here, the time required to obtain complete freezing of the porous medium below the glacier ranges between 20 years and a century. Thus winter flows will probably decrease in coming decades. A hydrogeological model should take these extensions into account, considering that the permafrost is a no-flow zone. The water recharge of an under glacier storage is probably achieved in summer along the bergschrund while winter discharge, limited by permafrost at the base of the snout, requires channels for subglacial discharge. This is consistent with field observations and interpretations of Griselin (1985).

Conclusion

We studied here the quantitative evolution of a glacier-porous medium system with a view to understanding the implications on the unfrozen subglacial porous medium layer. It is probably responsible for permanent subglacial-underground flows, particularly visible in winter when surface meltwater stops flowing.

Our results provide a basis to explain winter flows. The glacier system is still polythermal with a warm base core, experiencing rather rapid evolution forced by climate. Permafrost development is forced by glacier retreat downstream of Austre Lovénbreen. It is in transition to becoming cold, and time scales are probably on the order of some decades to a century. As a consequence, winter flow will change quite significantly as we expect that most of it comes from underground storage. Indeed, underground flow should stop as permafrost grows. Yet winter icing might continue, maybe with less intensity, as winter flows can be the result of water stored in cut and closure channels as suggested by Baelum and Benn (2011).

Improvements of the approach are currently expected. Several scenarios should be considered to address the uncertainties and sensitivity of the system. Among them, the initial permafrost extent is subject to debate. The underground heat transfer model could be made more complex to treat snow cover and the presence of winter icing. The actual nature of the interface between the glacier and its bed is highly uncertain, including the type of heat transfer between glacier and bed. Especially, would groundwater flow delay permafrost development under the glacier? The retroaction of ground temperatures on glacier evolution is an open topic.

In the future we will focus on the unfrozen porous medium extent at the base of the glacier as deduced from permafrost development. The simulation of winter discharge with a hydrogeological model will allow us to assess the credibility of these hypotheses and study the range of variations of associated properties.

Acknowledgments

Data acquisition and fieldwork were granted by the French National Agency for Research (ANR). We especially thank Sam Pimentel and Gwenn Flowers for kindly letting us use their glacier code. This work would have taken so much longer without this model.

References

- ACIA. 2004. Hydrology and Cryosphere, Arctic Climate Impact Assessment report, chapter 6: 183-242.
- Baelum, K. & Benn, D.I. 2011. Thermal structure and drainage system of a small valley glacier (Tollbreen, Svalbard), investigated by ground penetrating radar. *The Cryosphere* 5: 139-149.
- Boulton, G., & Hartikainen, J. 2004. Thermo-Hydro-Mechanical Impacts of Coupling Between Glaciers and Permafrost, In:

- Ove Stephanson, Editor(s), Elsevier Geo-Engineering Book Series, Elsevier, 2004, Volume 2, 293-298.
- Bjornsson, H., Gjessing, Y., Hamran, S.E., Hagen, J.O., Liestol, O., Palsson, F., & Erlingsson, B. 1996. The thermal regime of sub-polar glaciers mapped by multi-frequency radio-echo sounding. *Journal of Glaciology* 42: 23-32.
- Chan, T., Christiansson, R., Boulton, G.S., Ericsson, L.O., Hartikainen, J., Jensen, M.R., Mas Ivars, D., Stanchell, F.W., Vistrand, P., & Wallroth, T. 2005. DECOVALEX III BMT3/BENCHPAR WP4: The thermo-hydro-mechanical responses to a glacial cycle and their potential implications for deep geological disposal of nuclear fuel waste in a fractured crystalline rock mass. *International Journal of Rock Mechanics and Mining Sciences* 42, 5-6, 805-827.
- Flowers, G.E. & Clarke, G.K.C. 2002. A multicomponent coupled model of glacier hydrology, I, Theory and synthetic examples, *J. Geophys. Res.* 107(B11), 2287.
- Fountain, A.G. & Walder, J.S. 1998. Water flow through temperate glaciers. *Reviews of Geophysics* 36: 299-328.
- Friedt, J.-M., Tolle, F., Bernard, E., Griselin, M., Laffly, D., & Marlin, C. 2011. Assessing Digital Elevation Models relevance to evaluate glacier mass balance: application to the Austre Lovénbreen (Spitsbergen, 79°N), in prep.
- Friedt, J.-M., Laffly, D., Saintenoy, A., Bernard, E., Griselin, M., & Marlin, C. 2010. Evaluating the Austre Lovénbreen (Svalbard) glacier ice volume, area and its bedrock topography using Ground Penetrating Radar and differential GPS measurements. 11th International Circumpolar Remote Sensing Symposium, September 2–24, 2010, Cambridge, UK.
- Griselin, M. 1985. Les marges glacées du Loven Est, Spitsberg : un milieu original lié aux écoulements sous-glaciaires. *Revue de Géologie Alpine* tome LXXIII, Num. 4, 389-419.
- Griselin, M. 1982. Les modalités de l'écoulement liquide et solide sur les marges polaires : exemple de bassin Loven Est, côte nord-ouest du Spitsberg. Thèse de troisième cycle, Volume III des travaux du Laboratoire de Géographie Physique de Nancy II.
- Hagen, J.O. & Liestol, O. 1990. Long-term glacier mass-balance investigations in Svalbard, 1950-88. *Annals of Glaciology* 14: 102-106.
- Hagen, J.O., Kohler, J., Melvold, K., & Winther, J.G. 2003. Glaciers in Svalbard: mass balance, runoff and freshwater flux. *Polar Research* 22: 145-159.
- Hansen, S. 2003. From surge-type to non-surge-type glacier behaviour: midre Lovénbreen, Svalbard. *Annals of Glaciology* 36: 97-102.
- Humlum, O. 2005. Holocene permafrost aggradation in Svalbard. In: *Cryospheric Systems: Glacier and Permafrost*. Geological Society, London, Special publication, 242, 119-130.
- McKenzie, J.M., Voss, C.I., & Siegel, D.I. 2007. Groundwater flow with energy transport and water-ice phase change: Numerical simulations, benchmarks, and application to freezing in peat bogs. *Advances in Water Resources* 30, 4, 966-983.
- Pimentel, S., Flowers, G.E., and Schoof, C.G. 2011. A hydrologically coupled higher-order flow-band model of ice dynamics with a Coulomb friction sliding law. *J. Geophys. Res.* 115.
- Régnier, D., Grenier, C., Davy, P., & Benabderrahmane, H. 2010. A coupled Thermo-Hydro model to study permafrost. Proc. EUCOP III in Longyearbyen, Svalbard.
- Saintenoy, A., Friedt, J.-M., Tolle, F., Bernard, E., Laffly, D., Marlin, C., & Griselin, M. 2011. High density coverage investigation of the Austre Lovénbreen (Svalbard) using Ground Penetrating Radar. 6th International Workshop on Advanced Ground Penetrating Radar 2011, Aachen, Germany, 22. – 24.06.2011.
- Zwinger, T. & Moore, J.C. 2009. Diagnostic and prognostic simulations with a full Stokes model accounting for superimposed ice of Midre Lovénbreen, Svalbard. *The Cryosphere* 3: 217-229.

Mountain Permafrost Distribution in the Andes of Chubut (Argentina) Based on a Statistical Model

Lucas Ruiz, Dario Trombotto Liaudat

Instituto Argentino de Nivología Glaciología y Ciencias Ambientales (IANIGLA) CCT- Mendoza, CONICET. Mendoza Argentina

Abstract

An important debate generated by a new federal regulation in Argentina places mountain permafrost distribution and the potential of ground ice for water storage at the center of the scene. The main problem is related to the lack of field data on a regional scale. With the aim of solving this problem, in the Precordillera of Chubut, Argentina, a statistical model of mountain permafrost distribution based on measured BTS (Bottom Temperature of Snow cover) was presented. A multiple linear regression analysis was used to reproduce BTS distribution with elevation and potential short-wave radiation as independent variables. A threshold classification was then applied to BTS distribution in order to discriminate between probable, possible, and no possible permafrost zones. The model results suggest that mountain permafrost may exist, and is related to high- elevation south-facing slopes or highly cast shadow zones. Although the model was statistically significant, it is necessary to confirm the presence of permafrost by ground validation.

Keywords: BTS; Andes of Patagonia; statistical modeled permafrost distribution; ground ice.

Introduction

Mountain permafrost distribution and its response to climate change has become an area of major importance during recent years in Argentina and other countries with mountain environments. The main issues are (1) the occurrence of ice in mountain permafrost as water storage, especially in arid mountain regions, and (2) the risk of natural hazards related to mountain permafrost degradation in populated regions.

In Argentina, mountain permafrost and glacier distribution has been the focus of an intense social, political, and scientific debate in relation to the recently approved Federal Glacier and Periglacial Protection Law (Ley 26.639, 2010), most commonly called “Glacial Law.” This law protects glaciers and rock glaciers as strategic fresh water resources for the future, prohibiting any human activity on or close to them that could modify their natural behavior. Another important aspect of the “Glacial Law” is the creation of a National Inventory of Glaciers and Rock Glaciers using remote sensing.

One concern of the scientific community is the problem of mapping the distribution of mountain permafrost using satellite imagery. In this context, mountain permafrost distribution models based on indirect information such as the BTS (Bottom Temperature of Snow cover) method (Haeberli 1973) could help identify the zones where permafrost is developed and also indicate zones where rock glaciers or ice-rich permafrost landforms may exist.

In this paper, we present modeled permafrost distribution for the Andes of Northern Patagonia, based on BTS data and topoclimatic factors.

Background

Permafrost in Patagonia

Permafrost in Patagonia is mainly associated with fossil cryogenic sedimentary structures related to cold episodes associated with the Pleistocene Glaciations (Trombotto 2008).

Garleff & Stingl (1998) describe different periglacial features for the Patagonian Andes and point to temperature as the most important cryogenic factor. Trombotto (2000) indicates that it is possible to find continuous permafrost above 2,000 m a.s.l. at a regional scale in North Patagonia. Ruiz & Trombotto (2011) present a detailed periglacial geomorphology map of Cordón Leleque and they recognize, among other landforms, relict rock glaciers, active protalus lobes, and protalus ramparts; the latter are related to present permafrost.

BTS

First introduced by Haeberli (1973), BTS consists of measuring the temperature at the base of the mid-winter snow cover. It is based on two assumptions: (1) BTS remains constant in mid-winter below a snow cover of at least 0.8 m thickness, and (2) the BTS value is determined by the heat flux from the subsurface and serves as proxy of subsurface thermal conditions. Haeberli (1978) empirically established BTS thresholds of -3°C and -2°C for discrimination between likely permafrost, possible permafrost, and no permafrost.

Although the method was developed for the Swiss Alps (Hoelzle 1992, Gruber & Hoelzle 2001), it has been tested and used in other mountain ranges of the world with positive results (Brenning et al. 2005). However, data do not yet exist to date that would prove its validity for application in the Andes.

Mountain permafrost distribution models

Different types of models have been used to simulate and predict mountain permafrost distribution, based on topoclimatic parameters, BTS, and morphological terrain expressions (Gruber & Hoelzle 2001, Brenning & Trombotto 2006, Arenson & Jakob 2010, and others). In this study, we used the multiple linear regression approach presented by Gruber & Hoelzle (2001). These authors demonstrated that mountain permafrost distribution in the Swiss Alps could be replicated using a model distribution of BTS and Haeberli's (1978) thresholds.

Brenning et al. (2005) present the typical problems with BTS and statistical models of permafrost. These authors suggest that common errors are associated with (1) the distribution and distances between each measurement; (2) early or late snow cover; (3) early snow melting, both local and regional; and (4) operational errors associated with observer and instrumental bias.

Study Area

The study was carried out in the Precordillera of Chubut (42°–43°S, 71°–71.5°W) (Figs. 1A, 1B). At this latitude, the Andes can be separated in two main mountain ranges: the Lake Region Andes where, due to high precipitation, it is possible to find valley glaciers terminating close to 1,000 m a.s.l., and an east mountain range, informally called Precordillera, which is similar in elevation to the Lake Region Andes but receives much less precipitation. The Andes constitute a massive barrier to the atmospheric westerly flow, generating steep west-east precipitation gradients (Prohaska 1976). According to Condom et al. (2005), the climatic Equilibrium Line Altitude for glaciers (~2,200 m a.s.l.) is higher than the 0°C isotherm (~1,980 m a.s.l.) at the Precordillera, favoring the development of mountain permafrost (Haerberli 1985) (Fig. 1B).

The Rivadavia Range (RIV) (Z1, Fig. 1C) at the western margin of Precordillera, Esquel Range (ESQ) (Z2, Fig. 1C) and the Leleque Range (LEL) (Z3, Fig. 1C) at the eastern margin, were the areas selected for the BTS measurements. Although all three ranges reach 2,100 m a.s.l., ESQ is the one with the largest area above the treeline (~1,500 m a.s.l.).

With the exception of ESQ, where the ski resort of La Hoya is located, these mountain ranges are extremely remote, without road access. The only human activities are forestry and/or livestock.

These ranges are located within the watersheds of very important rivers in the region. RIV (eastern margin), LEL (western margin), and ESQ (western margin) are the watersheds of the Percey and Esquel. These rivers deliver water to the communities of Esquel and Trevelin, the most important towns in the west of the Chubut province. LEL (eastern margin) and ESQ (eastern margin) are part of the watershed of the Chubut River, the most important river in the province. This allochthonous river is the water source for the main agricultural activity of Chubut province, located more than 400 km from its source area.

Method

The model

The theory behind this model is presented in Gruber & Hoelzle (2001) and will be discussed only briefly here. Permafrost is a thermal phenomenon that can be described in terms of energy balance and heat transfer capacity. The most important incoming sources of energy are turbulent heat (i.e., air temperature) and radiation (both short and long wave). It has been shown that air temperature and solar radiation are closely related to the presence or absence of permafrost

(Hoelzle 1994). Gruber & Hoelzle (2001) propose elevation as proxy of temperature, and potential short-wave radiation (PSWR) during summer as model parameters. They also use a vegetation index (Soil Adjusted Vegetation Index, SAVI) as proxy of vegetation cover to tune the model. Brenning et al. (2005) have shown that the importance of SAVI, as a normal explanatory variable, does not improve the predictability of the model. In this study, we were dealing with an area above the tree line where vegetation is largely absent, so we also discard this parameter.

For the model, the SRTM Digital Elevation Model (DEM) was used. Although it is a medium spatial resolution source, it reproduces the terrain with great fidelity and has a global accuracy of 20 m (Jarvis et al. 2008). The DEM with a 95-m grid cell in Universal Transversal Mercator (Zone 19S) projection and WGS 84 Datum formed the common basis on which all other data have been entered and processed in a GIS environment (SAGA GIS 2.07). The PSWR for each grid cell was calculated using the Potential Incoming Solar Radiation module of SAGA GIS (Wilson et al. 2000). It takes into account the effects of topography and shading for every grid cell. It is possible to use different parameters to tune the model, primarily related to atmospheric conditions. Here the total PSWR for “summer” (December 1 to April 30) was calculated using an incremental period of 1 hr with an arbitrary Lumped Atmosphere Transmittance of 70%. Total PSWR was divided by the number of days in order to obtain a mean daily PSWR, expressed in mega joule by square meter per day (MJ/m²d).

BTS measurements

For this study, a total of 80 BTS readings during the winters of 2009, 2010, and 2011 were used. Measurements were conducted with a snow probe of 2-m length with a Grant temperature sensor at its tip and a digital tester (precision 0.8%). Resistivity was measured in the field and then converted to temperature. Locations in the field were determined using a handheld GPS, and the altitude for each point was extracted from the DEM in the GIS environment for consistency in the model tuning. A description of the 80 BTS measurements is presented in Figures 2 and Figure 3. Two different biases were detected. The first was related to the slope of the BTS point, where no slope greater than 35° was detected. This is related to two causes: (1) because of the coarse cell size of the DEM and the algorithm used to calculate the slope angle, only a huge steep face could achieve high values, and (2) on steep slopes there is no possibility for a thick snow cover to accumulate (Fig. 2). The second bias is related to the aspect of the BTS point, where a deficit in south-facing slopes was observed. This was mainly related to the difficulties of accessing the study zone; in general, the approach to the mountain areas was from the east (Fig. 3).

Of the 80 BTS, 15 were excluded from the model validation. The remaining 65 were used to run the model. In order to eliminate the possibility for pseudo replication and autocorrelation (Brenning et al. 2005), BTS were resampled to the spatial size of the DEM. If more than one BTS was located in the same grid cell, the mean value was used. With this

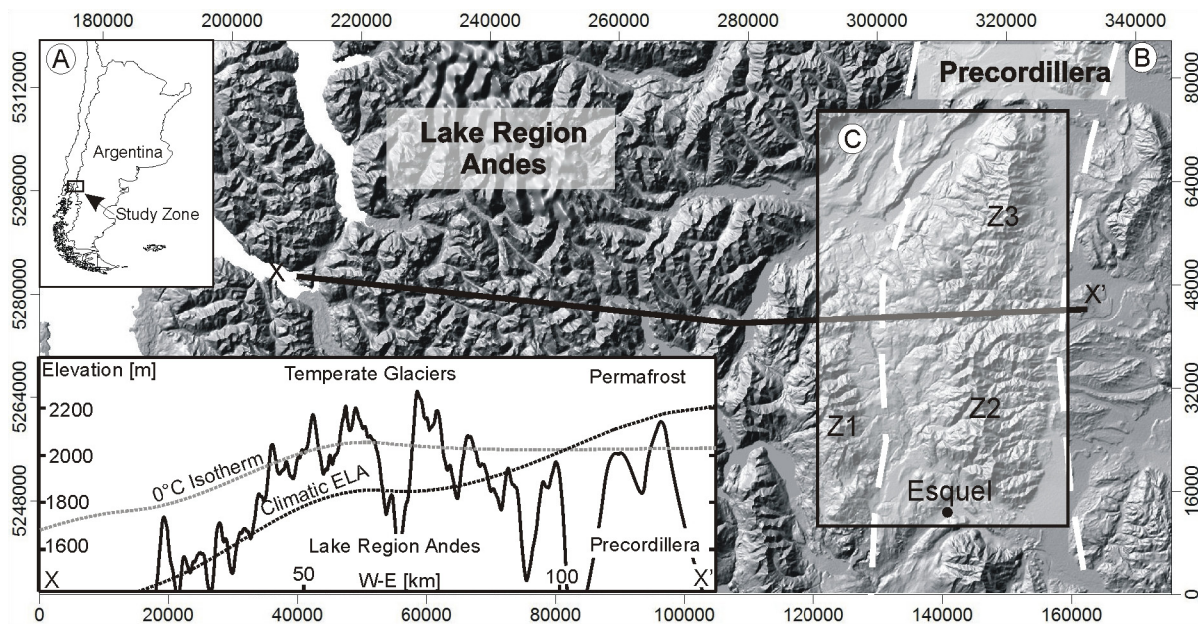


Figure 1. A) Location of the study area in the context of southern South America. B) Andes of North Patagonia, major cities of Argentina (Esquel) are shown as reference, white long dash line indicates the limits between Lake Region Andes, Precordillera and Patagonian Steppe, black line indicates the position of X to X' profile. The profile indicates the elevation distribution, 0°C isotherm and Climatic ELA of Lake Region Andes and Precordillera. C) The study zones where BTS were measured, Z1= RIV, Z2= ESQ, Z3= LEL (WGS 84, UTM Zone 19S).

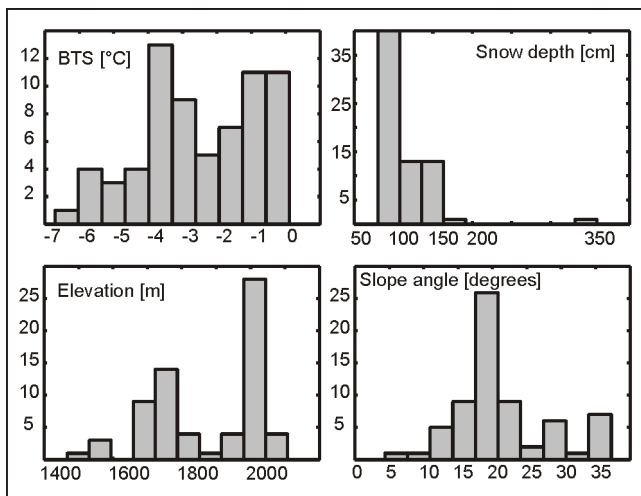


Figure 2. Histograms illustrating the characteristics of BTS used in this study. Ordinates indicate the number of BTS contained in each histogram class.

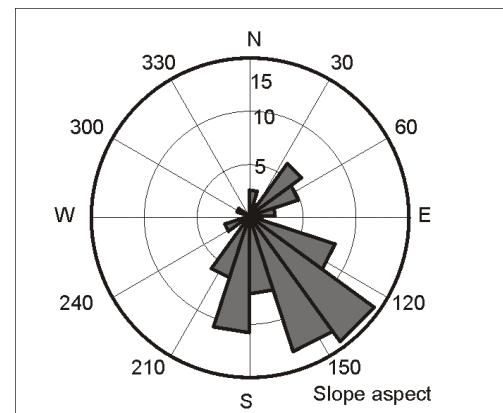


Figure 3. Rose diagram illustrating the aspect of BTS used in this study.

approach, the number of BTS to make the model decreases to 36.

Based on the 36 driving points, a multiple linear regression analysis was performed in order to predict the BTS, using elevation (Z) and PSWR as independent variables.

The regression yields a relation of the form:

$$BTS = a + b * Z + c * PSWR \tag{1}$$

where a, b, and c are coefficients obtained from the analysis.

In order to assess whether the BTS remains constant throughout winter, a simple experiment was conducted in LEL (Fig. 1B). A miniature temperature logger (UTL-2), measuring

temperature every 4 hours throughout the year, was introduced at the interface between the air and blocky surfaces to monitor BTS. The sensor was located in a protalus lobe that could be active (frontal slope angle >45°).

In order to test the model, BTS and the permafrost distribution model output were compared with a recent periglacial map of Cordón Leleque (Ruiz & Trombotto 2011). The correlation between the landform distribution and the permafrost distribution model was analyzed using zonal statistics and visual inspection on a screen.

Finally, the importance of permafrost areas as water storage was analyzed. This property is related to the ice content, which is largely correlated to ground porosity. Rock glaciers, as ice-rich creeping permafrost landforms (Barsch 1996), are where ground ice is concentrated in a mountain permafrost environment. A simple slope analysis was conducted to assess

how much of the area that was detected as possible permafrost (PP) and as likely permafrost (LP) could indeed have ground ice. In general, debris-covered surfaces and rock glacier surfaces had slopes from 0 to 25°, and it is possible to assume that slopes of more than 25° could be related to rocky outcrops (totally impermeable) or high slope screes (low ground ice content). In this respect, PP and LP areas for each mountain zone were subdivided between two categories: potential to contain ground ice (PGI) (slope < 25°, and no potential to contain ground ice (NPGI) (slope > 25°). It is important to note that this simple analysis does not take into account two important factors related to the generation and behavior of rock glaciers: (1) *debris supply*, without which it is not possible to form rock glaciers, and (2) *creep phenomena* that allow rock glaciers to transport ground ice downslope from its source zone.

Results

Significance of BTS measurements

In Figure 4, the mean daily temperatures at the ground surface in LEL are shown. Throughout the year, four different periods of time could be distinguished: (1) *Dry snow cover less than 1 m*. Although there was some variation, temperature was attenuated by an increasing snow cover; (2) *Dry snow cover more than 1 m*. During winter (mid July to mid October) the temperature reached a stable value around $-2.7 \pm 0.1^\circ\text{C}$ and indicates likely permafrost conditions; (3) *Snow melting*, a temperature-stable period, close to 0°C , was detected in spring and is related to melting of the snow cover. At the end of this period the temperature decreased below zero because of a very cold day which refroze and cooled the snow; (4) *Bare surface*. During summer all the snow melted, and the temperature was free to oscillate with air temperature. The difference between the measured BTS during winter (16/08/2010) and the temperature of the miniature data logger (-0.3°C) could be related to the accuracy of the thermistors.

Permafrost distribution model

After running the multiple regression analysis, two outliers were identified in the residual plot (Fig. 5A). They were discarded and a new regression analysis was conducted. The coefficients obtained were $a=2.6$, $b=-0.0049$, and $c=0.24$. The overall $R^2=0.48$, with a P-value of 0.000062 ($\alpha=0.001$), indicates the result is statistically significant (i.e., the relation is unlikely to have occurred by chance). Nevertheless, these coefficients should not be used in other areas without new analysis (Gruber & Hoelzle 2001). The RMSE (root mean square error) between the BTS measurement and the BTS modeled was 1.0°C .

The regression was then applied to the entire project area, generating a continuous field of simulated BTS, and subsequently grouped into classes to obtain a permafrost distribution model for the study area:

- < -3°C likely permafrost (LP)
- 3 to -2°C possible permafrost (PP)
- > -2°C no permafrost (NP)

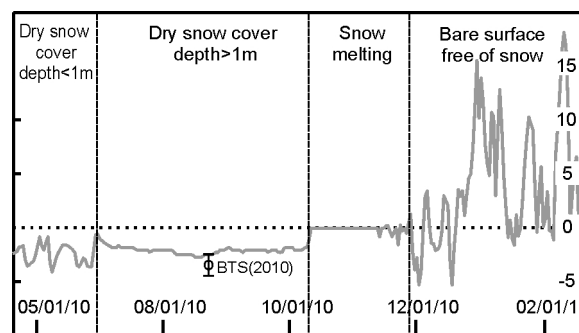


Figure 4. Mean daily temperature at the air/surface interface in a protalus lobe, Cordon Leleque. The curve could be divided into 4 different periods of time. BTS measurement for that year is indicated.

Table 1. Permafrost class area and percentage of area with potential to contain ground ice for each mountain range.

| Range | CLASS | AREA km ² | PGI % |
|-------|-------|----------------------|-------|
| RIV | LP | 2.1 | 38 |
| | PP | 13.0 | 53 |
| ESQ | LP | 4.5 | 62 |
| | PP | 31.0 | 76 |
| LEL | LP | 1.3 | 69 |
| | PP | 14.0 | 90 |

Testing the significance of the model

Fifteen BTS data points were not used in the regression analysis and used for cross-validation. The RMSE of modeled and BTS used for cross validation is 1.01°C . The agreement between the model and the measured BTS is shown in Figure 5B. Although the residual could exceed $\pm 2^\circ$, the model fails in only one case to reproduce the permafrost class (Fig. 5B). In this case, the model overestimates the presence of permafrost.

Permafrost distribution in Precordillera of Chubut and its comparison with periglacial landforms

The statistical permafrost distribution obtained in this study is presented in Figures 5C and 5D and Table 1. Although the area covered by PP and LP was small (~16% and ~2% of the area above tree line, respectively), the model indicates permafrost conditions for all the highest zones in the study area.

An example of the periglacial landform map of Ruiz and Trombotto (2011) is shown in Figure 5E. In general, the distribution of active permafrost landforms (protalus ramparts and lobes) coincided with the LP area (Figs. 5D and 5E). The zonal statistics by landforms indicate that active protalus ramparts and lobes have a mean BTS of $-3.1 \pm 0.1^\circ\text{C}$ and $-2.9 \pm 0.4^\circ\text{C}$, respectively. In contrast, relict rock glaciers have a mean BTS of $-1.3 \pm 0.5^\circ\text{C}$. This also indicates a good agreement.

Potential of permafrost areas as water storage

Results of the threshold classification (PGI) are shown in Figure 5D and Table 1. More than 60% of LP area in ESQ and

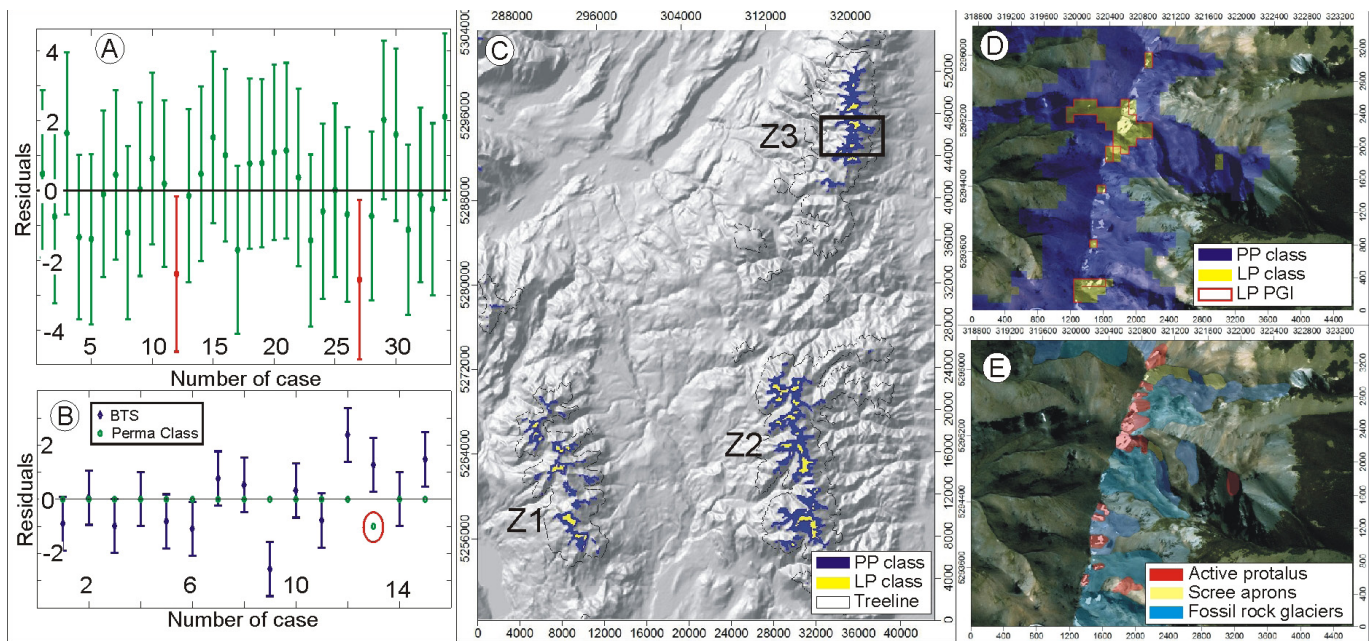


Figure 5. A) Residual plot between the BTS used to perform the model and the model results. Error bar indicates the residual intervals. Outliers are identified in red. B) Residual plot between the model result, the BTS used for corroboration and their corresponding permafrost class. Error bar of BTS represents the RMSE. Red circle show where the model over-estimated the permafrost class. C) Modeled permafrost distribution for Precordillera of Chubut, black box indicates the area of figures D and E. D) A closer view of LEL with Spot RGB images as background. E) The same zone as in Figure D but with a simplified version of the periglacial map of Ruiz & Trombotto (2011). PP class= Possible Permafrost; LP class= Likely Permafrost; LP PGI= Likely Permafrost with potential for ground ice (WGS 84, UTM Zone 19S).

LEL, and only 38% of LP area in RIV, could be PGI. Although the classification selected with good agreement the active protalus distribution (Fig. 5E), it also includes some of the little cliffs on arêtes (Fig. 5D) and over-estimated the actual distribution. The misclassification is highly dependent on the MDE resolution.

Discussion

Combined BTS surveys using both mapping and monitoring have shown significant differences in the evolution of BTS values throughout the winter, depending on the thermal characteristics of surface material and annual snow cover history at a site (Brenning et al. 2005).

Since no attempt has been undertaken to map the permafrost distribution in North Patagonia by means of BTS or other methods, the spatial and temporal characteristics of BTS values, and thus their applicability to map permafrost distribution, is unclear.

The only independent result came from the periglacial landforms map of Ruiz & Trombotto (2011). We found good agreement between the LP and active landform distribution in LEL, which indicates that at least in this range the model is a good approximation.

The difference between the total area of PP and LP between mountain ranges (Fig. 5C, Table 1) is related to the parameters (elevation, solar radiation) used in the model and the hypsometry of each range. ESQ, which has more area distribution above 1,600 m a.s.l., is also the one with more PP and LP. The threshold classification used to identify PGI zones

overestimated the actual distribution mainly because the MDE used to derive the slope is too coarse to resolve small cliffs or outcrops.

The R^2 of ~ 0.5 indicates that only half of the variability is explained by the model. In order to improve the model, it is necessary to (1) increase the number of independent BTS measurements, (2) improve the PSWR calculation, (3) take into consideration the transient effects of ground temperature, and (4) improve the resolution of the DEM.

Conclusions

In this work, the first BTS measurements conducted in North Patagonia were presented. With a multiple linear regression, the measurements were used to model the distribution of mountain permafrost in the Precordillera of Chubut. The model indicates that although not aerially extensive, permafrost conditions are related to high-altitude zones (mainly between 1,750 m a.s.l. and 2,100 m a.s.l.) that received low radiation (i.e., southwest facing slopes or highly shaded areas). In order to estimate how much of this area could have ground ice and be considered as a long-term water storage reservoir, a simple slope classification approach was conducted. This approach overestimates the presence of ground ice and does not provide any information on permafrost thicknesses.

The presence of permafrost and ground ice content in the Precordillera of Chubut must be confirmed by ground verification before the permafrost distribution obtained here can be used for legislative and binding actions.

Acknowledgments

Thanks to Jose Hernández (Técnico Principal IANIGLA-CONICET) for constructing the probes. The research was funded by CONICET (PIP 114-200801-00156) and Agencia de Promoción Científica (PICT 2007-0379). Thanks to Andres Errasti, Lucas Bianchi, Gabriel Rocamora, and Gabriel Moretta for their help during the fieldwork. The manuscript was improved by the comments of Lukas Arenson and another anonymous referee.

References

- Arenson, L. & Jakob, M. 2010. A new GIS based Mountain Permafrost Distribution Model. *63rd Canadian Geotechnical Conference & 6th Canadian permafrost Conference*. Calgary, Alberta, September 12-15, 452-458.
- Barsch, D. 1996. *Rockglaciers. Indicators for the Present and Former Geocology in High Mountain Environments*. Springer, 331 pp.
- Brenning, A., Gruber, S., & Hoelzle, M. 2005. Sampling and Statistical Analyses of BTS Measurements. *Permafrost and Periglacial Processes* 16 (4), 383-393.
- Brenning, A. & Trombotto, D. 2006. Logistic regression modeling of rock glacier and glacier distribution: Topographic and climatic controls in the semi arid Andes. *Geomorphology* 81, 141-154.
- Garleff, K. & Stingl, H. 1988. Geomorphologische Untersuchungen in der nivalen und subnivalen Stufe der argentinischen Anden –Ergebnisse und paläoklimatische Interpretation. Deutscher Geographentag München, Tagungsbericht und wissenschaftliche Abhandlungen, Stuttgart, 46, 419-425.
- Gruber, S. & Hoelzle, M. 2001. Statistical Modelling of Mountain Permafrost Distribution: Local Calibration and Incorporation of Remote Sensed Data. *Permafrost and Periglacial Processes* 12 (1), 69-77.
- Haerberli, W. 1973. Die Basis-Temperatur der winterlichen Schneedecke als möglicher Indikator für die Verbreitung von Permafrost in den Alpen. *Zeitschrift für Gletscherkunde und Glazialgeologie* 9, 221-227.
- Haerberli, W. 1978. Special effects of high mountain permafrost methodology and zonation in the Alps. *Third International Conference on Permafrost*, NRC Ottawa, Vol I, 374-384.
- Haerberli, W. 1985. Creep of mountain permafrost: internal structure and flow of alpine rock glaciers. *Mitteilungen der Versuchsanstalt für Wasserbau, Hydrologie und Glaziologie*, ETH Zürich, 77pp.
- Hoelzle, M. 1992. Permafrost occurrence from BTS measurement and climate parameters in the Eastern Swiss Alps. *Permafrost and Periglacial Processes* 3 (2), 143– 147.
- Hoelzle, M. 1994. Permafrost und Gletscher im Oberengadin. Grundlagen und Anwendungsbeispiele für automatisierte Schätzverfahren. *Mitteilungen der Versuchsanstalt für Wasserbau, Hydrologie und Glaziologie*, ETH Zürich, 132.
- Jarvis, A., Reuter, H.I., Nelson, A., & Guevara, E. 2008. Hole-filled SRTM for the globe Version 4, available from the CGIAR-CSI SRTM 90 m Database (<http://srtm.csi.cgiar.org>).
- Ruiz, L. & Trombotto, D. 2011. Glaciares de Escombros Fósiles en el Cordón Leleque, Noroeste de Chubut. Significado Paleoclimático y Paleogeográfico en el Contexto Regional de los Andes Patagónicos Norte. *Revista de la Asociación Geológica Argentina*, in press.
- Trombotto, D. 2000. Survey of Cryogenic Processes, Periglacial Forms and Permafrost Conditions in South America. *Revista do Instituto Geológico* 21 (1/2), São Paulo, 33-55.
- Trombotto Liaudat, D. 2008. Geocryology of Southern South America. En: “Late Cenozoic of Patagonia and Tierra del Fuego,” Jorge Rabassa (Editor). *Developments in Quaternary Sciences*, Elsevier, The Netherlands, 11, 255-268.
- Wilson, J.P. & Gallant, J. 2000. Secondary Topographic Attributes. In *Terrain Analysis, Principles and Applications*, edited by John P. Wilson and John C. Gallant, 447 pp.

Perennial Frost Mounds in Mongolia

N. Sharkhuu

Institute of Geography, Mongolian Academy of Sciences, Mongolia

K. Yoshikawa

Water and Environmental Research Center, Institute of Northern Engineering, University of Alaska Fairbanks, USA

Sh. Anarmaa

Department of Earth and Environmental Science, University of Pennsylvania, USA

Abstract

Perennial frost mounds are widespread in both large and small intermountain lake basins in Mongolia. They are found in areas where permafrost is geographically discontinuous as well as those underlain continuously by permafrost. Initial data are presented from boreholes drilled at the top of selected Mongot, Chuluut, and Nalayh mounds, and the thermal and hydrological conditions of these sites. In addition, some results of pingo formation and development are reported. Most of the pingos in Mongolia are of the open system type, developed by perennial freezing of artesian waters. At present, most of the investigated frost mounds are stable or show only a slight degrading tendency.

Keywords: artesian water; ice core; lithalsa; Mongolia; perennial frost mound; permafrost; pingo.

Introduction

“Perennial frost mound” is an internationally well-accepted general term referring to permafrost mounds of any size and shape. In addition, there are some national and scale-specific terms for perennial frost heave mounds in the literature, including pingos (Alaska and Canada), hydro-laccoliths and bulgunniakh (Russia and Yakutia), palsa, and lithalsa. At present, the term *pingo* is used widely in the scientific literature as an international term. Pingos are perennial frost mounds consisting of a core of massive ice, produced primarily by injection of water (although other ancillary processes such as ice segregation may be involved), and covered with soil and vegetation. Most pingos are conical, somewhat asymmetric, and have a circular or oval base and a fissured top that may be cratered (Everdingen 2002). Pingos are of two general origins based on hydrological environments: an open-system (hydraulic) and a closed-system (hydrostatic). Scientists from Canada, Alaska, and Russia have studied the mechanism of the formation of the open-and closed-system pingos based on analysis of stable isotopes ($\delta^{18}\text{O}$ and δD) of the pingo ice (Mackay & Black 1978, Yoshikawa 2008). The distribution and morphology of pingos in Mongolia have been studied by Russian and Mongolian researchers (Gravis et al. 1974, Sharkhuu 1970, 1999). However, the formation and development of pingos have not been well studied in Mongolia.

In contrast, *palsas* are smaller frost mounds that often are formed by processes, such as ice segregation, that do not involve the injection of water. They are often associated with peatlands and the unusual thermal properties of peat can play an important role in their formation and maintenance, particularly near the equatorward limit of permafrost (Nelson et al. 1992). *Lithalsa* is a term first introduced by S. Harris (1993) to describe mineral ice mounds of segregation ice origin in Yukon Territory, Canada. Lithalsas, often called mineral

palsas, are similar to *palsas* but are lacking a thick cover of peat. After degradation, lithalsas leave closed depressions surrounded by a rampart. Remnants of lithalsas formed during the Younger Dryas are found in northern Europe (Ireland, Wales, and Belgium). These remnants, which for years have been considered pingo remnants, are likely lithalsa remnants (Pissart 2000). Many mounds that do not contain intrusive ice, but consist of a large volume of ice lenses, are today classified as *palsas* or *lithalsas*. The purpose of this paper is to describe the main features of selected perennial frost mounds in Mongolia.

Study Methods and Selected Sites

The study of perennial frost mounds in Mongolia is based on data from borehole drillings. During drilling operations, we investigated ice formation and size, permafrost, and hydrological conditions. We made detailed descriptions of ground and ice core profiles in boreholes, determined ice content and density, monitored active layer thickness and mean annual ground temperature, and used leveling and temperature measurements to estimate recent dynamics of frost mounds. In addition, stable isotope analysis of pingo ice was employed in 2009–2010.

For this investigation, we selected three well-studied sites at Mongot, Chuluut, and Nalayh possessing perennial frost mounds. Based on the borehole drillings and visual observations at these sites, the initial data of the selected mounds are presented in Table 1.

Permafrost and Hydrological Conditions of the Study Sites

Mongot pingo site

Several groups of pingos, named Mongot, Asgat, and Eleet, are in the study area of Tes Valley, which is located in

Table 1: Characteristics of the selected perennial frost mounds.

| <i>Mountain region</i> | <i>Hovsgol</i> | <i>Hangai</i> | <i>Hentei</i> |
|--|----------------------|------------------|-----------------|
| Name | Mongot | Chuluut | Nalayh |
| Latitude N | 49°20'50" | 48°02'28" | 47°46'35" |
| Longitude E | 99°14'32" | 100°23'30" | 107°20'18" |
| Elevation, m a.s.l | 1800 | 1870 | 1400 |
| Mound height, m | 20 | 10 | 5 |
| Diameter of the base, m | 80–120 | 60–90 | 45–60 |
| Thickness of ice layer | 28 | 20 | 9 |
| Density of ice layer, g/cm ³ | 0.7–0.9 | 0.6–0.8 | 0.5–0.7 |
| Active layer thickness, m | 1.2 | 1.6 | 1.4 |
| MAGT at 15 m depth, °C | -0.5 | -0.4 | -1.3 |
| Permafrost thickness, m | 32.5 | 34.5 | about 40 |
| Thermal gradient below 15 m depth, °C/m | 0.029 | 0.022 | 0.051 |
| Present artesian waters | with little pressure | | absent |
| Recent development of permafrost and mound | almost stable | little degrading | very changeable |

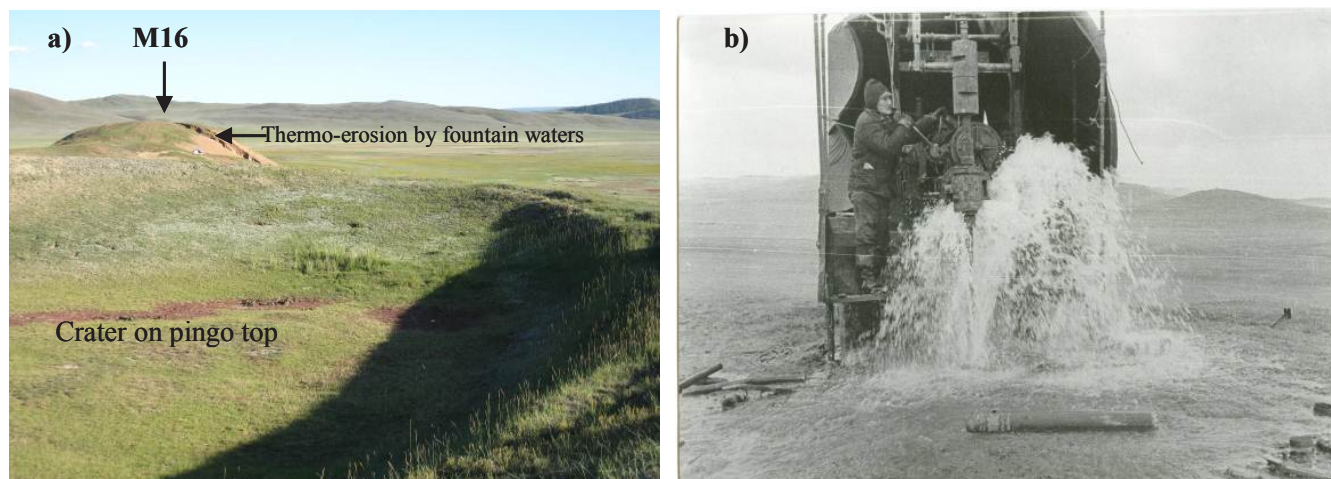


Figure 1: a) Several of the Mongot pingos in Tes Valley, Hovsgol region: A crater atop the pingo (foreground) and location of the 32-m-deep borehole on the top of the pingo in rear (Sharkhuu 2009); b) 1.2-m-high water fountain of sub-pingo artesian waters during borehole drill (Sharkhuu 1968).

the southwestern part of the Hovsgol mountainous region. The Mongot pingo group consists of two separate pingos, located about 200 m apart. There is a closed crater about 1 m in depth and 10–15 m in diameter atop the pingo, located in the west (Fig. 1a). In early October 1968, Borehole No. 10 was drilled by Gravis and Sharkhuu down to 32-m depth atop the eastern Mongot pingo. During this drilling operation, sub-pingo artesian water with high pressure was encountered at 32-m depth and formed a water fountain through a 13.5 cm diameter casing with an initial height of 100–120 cm above the soil surface (Fig. 1b). The water flow ceased after 120 hours. During this period, the height, discharge, and volume of the fountain water were monitored. The temperature of the artesian water, the discharge of which was accompanied by the strong odor of hydrogen sulphate gas, was -0.15°C . On October 3, 1968, active layer thickness in the borehole was 110 cm (Sharkhuu 1970).

In late September 1969, the 82-m-deep Borehole No. 11 was drilled by Sharkhuu in the broad plain of the Tes River

valley, located about 4 km southwest of the Mongot pingo. Interpolation of borehole temperature indicates that the thickness of permafrost is about 90 m. In addition, Mongolian geologists drilled a deep borehole, located about 10 km west of the Mongot pingo. Intra-permafrost artesian water in the thick lacustrine sediments was found at a depth of 120 m and gushed forth to the surface. These sediments were formed during the Pliocene to upper Pleistocene and Holocene.

Chuluut frost mound site

During the lower and middle Pleistocene, the valley of the Chuluut River was blocked by volcanic lava flows in its middle and lower parts. As a result, a large lake was formed during the upper Pleistocene, and a 10- to 20-m-thick section of interlayered silt and clay lacustrine sediments was deposited (Selvanov 1972). Epigenetic permafrost formed in the valley bottom gradually as the lake disappeared. At present, permafrost thickness in the valley ranges from 15 m to 30 m. The cryogenic structure of the lacustrine sediments

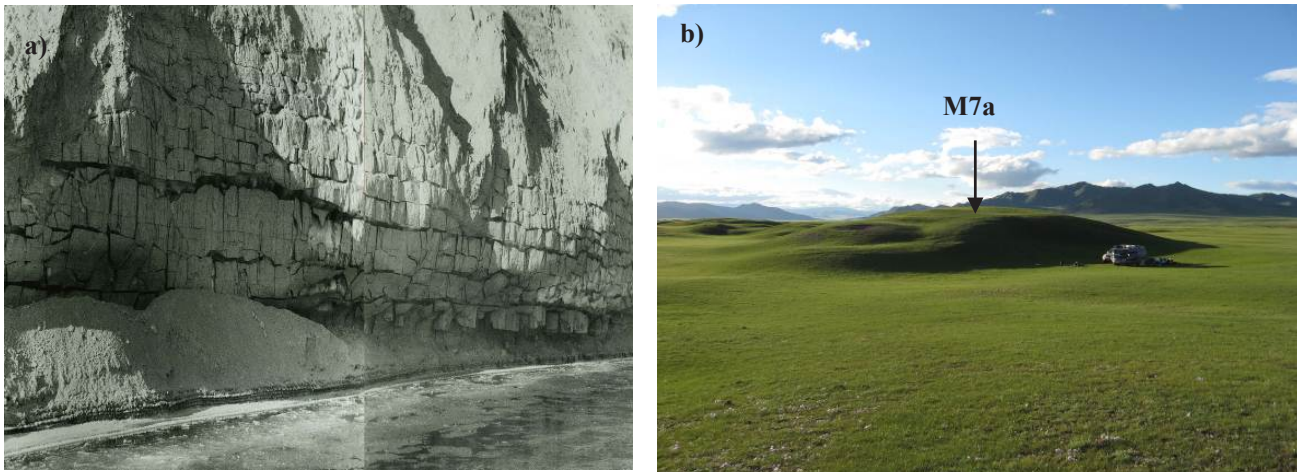


Figure 2: a) Cryostructure of lacustrine sediments on exposure of 8-m-high Chuluut riverbank (Sharkhuu 1969); b) 10-m-high frost mound in Chuluut Valley, Hangai region (Sharkhuu 2010).

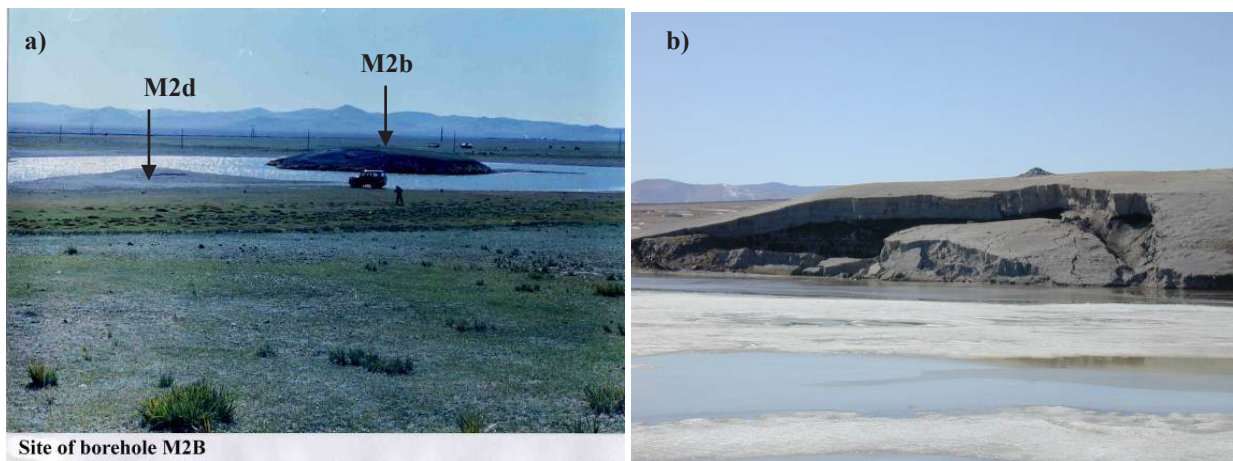


Figure 3: a) Bus nuur Lake, perennial frost mound, and borehole locations in Nalayh depression, Hentei region (Sharkhuu, July 1999); b) thaw slumping of 1.3-m-thick active layer on permafrost table (ice layer) occurred suddenly in late August 2004 on the southeastern slope of this degrading frost mound (Sharkhuu, April 2005).

was observed in a 6- to 8-m-high bank exposure along the Chuluut River (Figure 2a). The section contains epigenetic, ice-rich permafrost with predominantly segregated ice layers and structures, mostly 5–20 cm thick and up to 80 cm thick. Borehole No. 17 reached a depth of 36 m on the Chuluut mound in October 1969, and Borehole M7a at the same site was re-drilled to a depth of 15 m in June 2002 for monitoring permafrost temperatures.

Nalayh frost mound site

The Nalayh mound is located in the center of a small lake basin, which is composed of inter-bedded, semi-consolidated fine sandy silt, clay, coal, gravel, and pebbles of lower Cretaceous age. This mound is surrounded by lake water. The level or depth of the lake water has been highly variable during recent decades. According to topographic maps, in the early 1940s the lake was larger than its current size. However, by Sharkhuu's observation in July 1967, the lake depth and mound height did not exceed 0.5–0.7 m and 2.5 m, respectively. In the 1980s and 1990s, the size and depth of the lake was larger than at present. In the late 1990s, water surrounding the

4.5-m-high mound reached a depth of 3 m (Fig. 3a). In early March, the depth of seasonal freezing of lake water was 1.5 m. It is therefore likely that a closed, unfrozen ground mass (talik) exists, at least under the lake bottom. During the last 10 years, the lake level has decreased by 1.2–1.5 m, and water in the western part of the lake has disappeared. In 1999 and 2003, 6- to 8-m-deep boreholes (M2b and M2d) were drilled atop the mound and in the lake basin by Fukuda and Sharkhuu to monitor the thermal state of the permafrost in, and possibly below, the mound and in the adjacent lake sediments. In addition, during 2010 a 30-m-deep borehole (M2b) on the top was re-drilled by Yoshikawa and Sharkhuu for sampling the ice core and for monitoring the thermal state of the mound.

Some Results of the Study of the Formation and Development of Perennial Frost Mounds

Mongot pingo

The Mongot pingo is characterized by relatively massive ice-core, sub-pingo artesian waters, thick lacustrine sediments, and surrounding thick permafrost (Fig. 4).

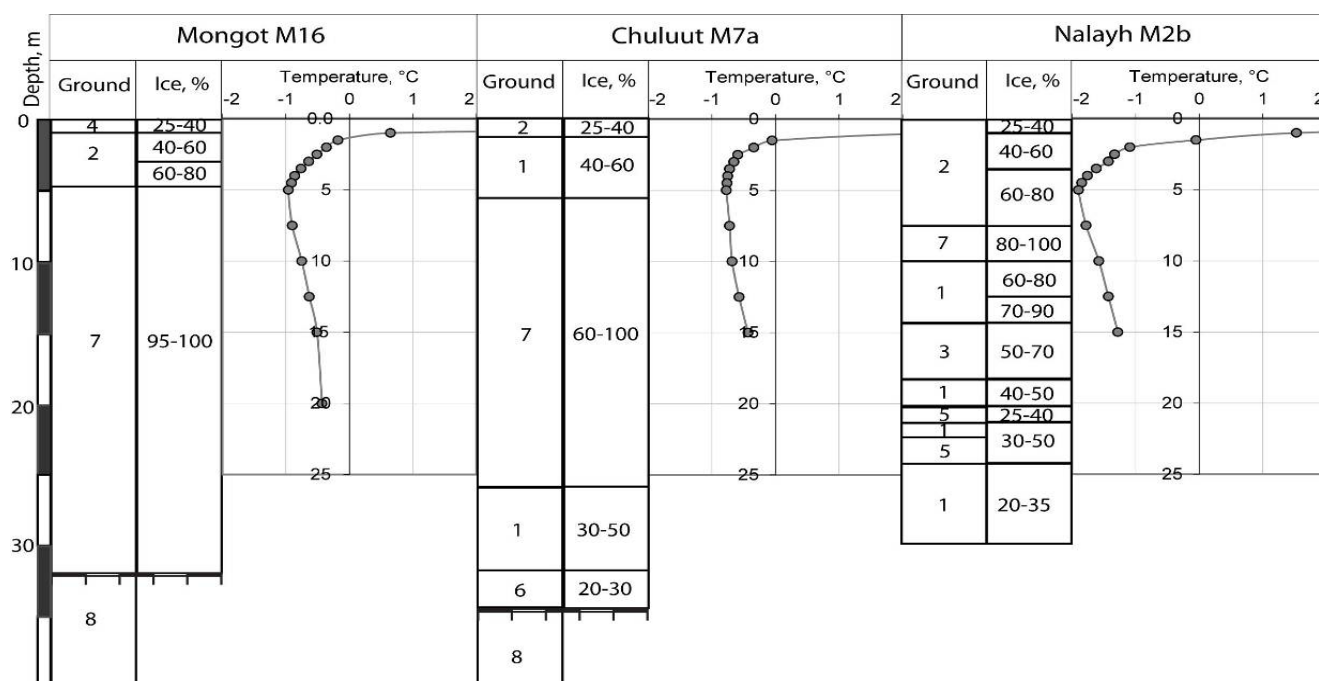


Figure 4. Ground-ice content and temperature profiles in the selected mound boreholes. Ground profile: 1, clay; 2, silt; 3, coal; 4, sandy loam; 5, gravely sand; 6, sandy gravel; 7, ice; 8, water.

To study the formation and evolution of the Mongot pingo, in early August 2009 Yoshikawa and Sharkhuu drilled a 33-m-deep borehole (M16) atop the pingo at a distance of 3 m from the old borehole. This time, the depth at which sub-pingo artesian water was encountered was 32.6 m, and the height of the water fountain above the ground surface was 60–70 cm. Based on analysis of stable isotopes and the chemical composition of ice samples and samples of adjacent surface water, spring water, and sub-pingo water, we concluded that Mongot Pingo formed under conditions of repeated open and semi-closed systems of artesian water environments. An open-system pingo undergoes relatively rapid freezing at the top of the ice layer in an open environment, and this represents the main growth period. At the end of this growth period, or when interrupted, the groundwater reservoir is isolated and freezes slowly, forming a closed environment. This is a typical process for the formation of an open system pingo. The stable isotope signals indicate that the early formation stage of the Mongot pingo occurred under more arid conditions. In addition, the ^{14}C dating of the plant remnant at a depth of 13.8 m was 8790 ± 50 yr BP (BETA 271760), indicating that ice formed after the plant remnant entered the groundwater flow (Yoshikawa and Sharkhuu 2012). On August 6, 2009, the depth of ground thaw in the borehole was 110 cm, which corresponds to about 88% of thaw for the final seasonal active layer thickness (ALT), estimated as 125 cm. On October 3, 1968, active layer thickness in the borehole was 110 cm, as described above. Therefore, the rate of increase in the ALT of this pingo during the last 40 years is determined as 0.4 cm per year. In spite of the small increase in the ALT, the development of the Mongot pingo during the last 40 years was relatively stable.

Chuluut frost mound

The Chuluut mound is characterized by mostly segregated ice-core and relatively warm permafrost temperatures (Fig. 4). The Chuluut mound is composed of inter-layering clay and silt, with a core of ice at depths between 5 and 26 m. The volumetric ice content of different sections (layers) in this core is quite variable, however, ranging from 40% to 100%. The ice in some parts of the section is very loose and has a white color resembling dense glacier snow. It was very difficult to determine with confidence the mechanism by which this ice formed. The ice layers of the Chuluut mound might have formed both as segregation and injection freezing, which rhythmically alternated with each other in certain sections. The predominantly cryogenic structure of the mound is characterized by segregated ice. This mound might be the remnant of the thermal erosion in the surrounding thermokarst depression. Permafrost at the Chuluut mound site is slowly degrading under the influence of recent climate warming. Long-term monitoring of permafrost temperatures at the top of this mound (borehole M7a) has revealed trends of increase in active layer thickness and mean annual ground temperature under the influence of climate warming during the last 40 years of 4.3 cm and 0.06°C per decade, respectively (Sharkhuu et al 2008, Zhao et al 2010).

Nalayh mound

The Nalayh mound is characterized by semi-consolidated fine sediments, predominantly segregated loose ice, relatively low temperature permafrost, and a lack of artesian water (Fig. 4).

Although the Nalayh mound is larger than most, we

consider it to be analogous to lithalsas. The formation and development of this mound was variable depending on hydrological conditions at the bottom of the permafrost. Especially during the last 10 years, lake levels decreased and grass cover on the mound disappeared. These hydrological changes led to the degradation of this mound. In late August 2004, thaw slumping of the 1.3-m-thick active layer over the ice-rich layer suddenly occurred on the southeastern slope of this degrading mound (Fig. 3b). According to leveling measurements, the southeastern part of the mound subsided by 50 cm in 2005, 40 cm in 2006, and 45 cm between 2007 and 2009. This subsidence was caused by melting of the ice layer in the upper permafrost. A small (1-m-high) mound is located at the northern edge of the Bus Lake, along with the 4.5-m-high Nalayh mound. This small mound was formed 20–30 years ago, when the highest level of lake water decreased. Apparently, the Nalayh mound was formed 50–100 years ago.

Concluding Remarks

The frost mounds investigated for this study show a relationship between mound height and the integrated thickness of injected and segregated ice. Higher mounds are associated with thicker unconsolidated sediments, artesian waters, and thicker permafrost.

Most pingos in Mongolia located in intermountain depressions and valleys are related to open systems of perennial freezing of lacustrine and alluvial sediments with artesian waters. Ice types within the frost mounds include both injected massive and segregated layered lenses.

At present, most of the perennial frost mounds in the study area are stable or degrading slightly. The degradation of the mound usually occurs on the southeastern or southern sides of the slopes.

We recognize that there are difficulties with widely accepted frost mound classifications and terminological schemes. Some of the mounds investigated in this study do not fit neatly into classificatory niches because their combinations of size, morphology, and genesis are inconsistent with criteria established by previous investigators. As suggested by Nelson et al. (1992) it may be useful to use a terminological scheme in which these variables are expressed separately.

Acknowledgments

The authors thank the editor and anonymous reviewers of this paper for their helpful comments, suggestions, and revision of English. We are also grateful to the University of Alaska Fairbanks, which provided financial support for drilling two 30- to 35-m-deep boreholes at the Mongot and Nalayh sites.

References

- Everdingen, R.V. 2002. *English language glossary of permafrost and related ground-ice terms*. Arctic Institute of North America, Calgary.
- Gravis, G.F., Zabolotnik, S.I., Sukhodrovsky, V.L., & Gavrilo, M.K. 1974. *Geocryological conditions of the Mongolian People's Republic*. Moscow, Nauka Press, 197 pp. (in Russian).
- Harris, S.H. 1993. Palsa-like mounds developed in a mineral substrate, Fox Lake, Yukon Territory. *Proceedings of the Sixth International Conference on Permafrost, 5-9 July, Beijing, China, South China University of Technology*: Vol.1: 238-243.
- Mackay, J.R. & Black, R.F. 1978. Origin, composition, and ground ice. *Proceedings of the Permafrost, Second International Conference, Yakutsk. Washington, National Academy of Science*: 185-193.
- Nelson, F.E., Hinkel, K.M., & Outcalt, S.I. 1992. Palsa-scale frost mounds. In *Periglacial Geomorphology*, Dixon, J.C. and Abrahams, A.D. (eds.), *Proceedings of the 22nd Annual Geomorphology Symposium*. Wiley. New York: 305-325.
- Pissart, A. 2000. Remnants of lithalsas of the Hautes Fagnes, Belgium: a summary of present-day knowledge. *Permafrost and Periglacial Processes* 11:327-355.
- Sharkhuu, N. 1970. Perennial frozen ground on northern plateau of Bulnai Mountain range. *Geographic problems of Mongolia* 9:86-113 (in Mongolian).
- Sharkhuu, N. 1999. Occurrence of frost heaving in the Selenge River Basin, Mongolia. *Permafrost and Periglacial Processes* 10: 187-192.
- Sharkhuu, N., Sharkhuu, A., Romanovsky, V.E., Yoshikawa, K., Nelson, F.E., & Shiklomanov, N.I. 2008. Thermal State of Permafrost in Mongolia. In *NICOP 2008: Proceedings of the Ninth International Conference on Permafrost*. D.L. Kane, K.M. Hinkel (eds.). Institute of Northern Engineering, University of Alaska Fairbanks, 2: 1633-1638.
- Selvanov, E.I. 1972. *Neotectonics and geomorphology of the Mongolian People's Republic*. Moscow, "Nedra" Press, 292 pp. (in Russian).
- Yoshikawa, K. 2008. Stable isotope composition of ice in seasonally and perennially frozen mounds. In *NICOP 2008: Proceedings of the Ninth International Conference on Permafrost*. D.L. Kane, K.M. Hinkel (eds.). Institute of Northern Engineering, University of Alaska Fairbanks, 2: 1997-2003.
- Yoshikawa, K. & Sharkhuu, N. 2012. Open-system pingo hydrology at Mongot pingo, Mongolia. (in review). *Permafrost and Periglacial Processes*.
- Zhao, L., Wu, Q., Marchenko, S.S., and N. Sharkhuu . 2010. Thermal State of Permafrost and Active Layer in Central Asia during the International Polar Year. *Permafrost and Periglacial Processes* 21: 198–207

Northern Hemisphere Component of the Global Circumpolar Active Layer Monitoring (CALM) Program

Nikolay I. Shiklomanov, Dmitry A. Streletskiy

Department of Geography, George Washington University, Washington, DC, USA

Frederick E. Nelson

Department of Geography, University of Delaware, Newark, DE, USA

Abstract

The Circumpolar Active Layer Monitoring (CALM) program is the world's primary source of empirical information about the active layer, its spatial patterns, and its temporal trends. Established in the early 1990s, the CALM network currently comprises 260 sites distributed throughout the Arctic and parts of Antarctica. Active-layer observations and auxiliary information from the network provide a circumpolar database, which has been used extensively by the broader scientific community in biochemical, ecologic, geomorphologic, hydrologic, and climatic research. An overview is provided of the observational strategy and data availability for CALM's Northern Hemisphere component. Generalized active-layer trends in the Arctic are also summarized.

Keywords: active layer; data analysis; data archive; permafrost; polar regions; sampling design.

Introduction

The Circumpolar Active Layer Monitoring (CALM) program is a network of sites at which active-layer thickness (ALT) data are collected. CALM is the world's primary source of empirical information about the active layer, its spatial patterns, and temporal trends. The concept of a CALM program was developed in the early 1990s to observe the long-term response of the active layer and near-surface permafrost to changes in climatic parameters. Together with the International Permafrost Association's (IPA's) Thermal State of Permafrost (TSP) program, CALM comprises the Global Terrestrial Network for Permafrost (GTN-P). The CALM network's history and organizational structure are reported in Brown et al. (2000), Nelson et al. (2004, 2008), and Shiklomanov et al. (2008).

The CALM program initially focused on developing monitoring and sampling methodologies to provide spatial and temporal assessment of the active layer and near-surface permafrost conditions within representative landscapes. In addition to standardized active-layer observations, most sites were instrumented for continuous temperature monitoring within the active layer and upper permafrost. Periodic snow, soil moisture, and ground subsidence measurements are conducted at a large number of these sites. Several sites serve as bases for intensive ecological, biochemical, and geomorphological observations. The CALM III project was launched in 2009 with the objective of maintaining established programs of long-term active-layer, near-surface permafrost, landscape, and geomorphologic observations in existing Alaskan and Russian networks. It emphasized closer cooperation with the TSP program, continuing development and refinement of data management for the CALM program, and expansion of outreach activities.

The CALM III project is currently administered through

George Washington University's Department of Geography. Analysis, archiving, and distribution of CALM's long-term observations are integral components of the project. Measurements are provided by participants to the CALM office at GWU, where they are subsequently incorporated into several databases and disseminated through the program's website and Cooperative Arctic Data and Information Service of the Arctic Observing Network (AON-CADIS).

Although substantial efforts have been made to develop CALM in the permafrost areas of the Southern Hemisphere (CALM-S), this paper focuses on the Northern Hemisphere component of the CALM program. Details on CALM-S can be found elsewhere in these proceedings.

CALM Network

Significant efforts have been made over the past decade to expand geographical coverage in the CALM program, and these are reflected in the substantial growth that has occurred in the number of observational sites.

The present distribution of CALM observational sites in the Northern Hemisphere is shown in Figure 1. The CALM network incorporates sites in arctic, subarctic, and mountain regions. The distribution of sites is not uniform, a circumstance attributable to historical factors and logistical constraints. The sites were established in regions of extensive economic activity and/or in areas of long-term climatic, permafrost, and ecosystem research. This logistically driven approach to site selection was adopted to ensure regularity and periodicity of measurements.

The inception and funding of the Thermal State of Permafrost (TSP), under the stimulus of the International Polar Year (IPY) and the International Permafrost Association (IPA) in a large number of countries, provided a basis for more comprehensive assessment of permafrost conditions at the global scale. It also

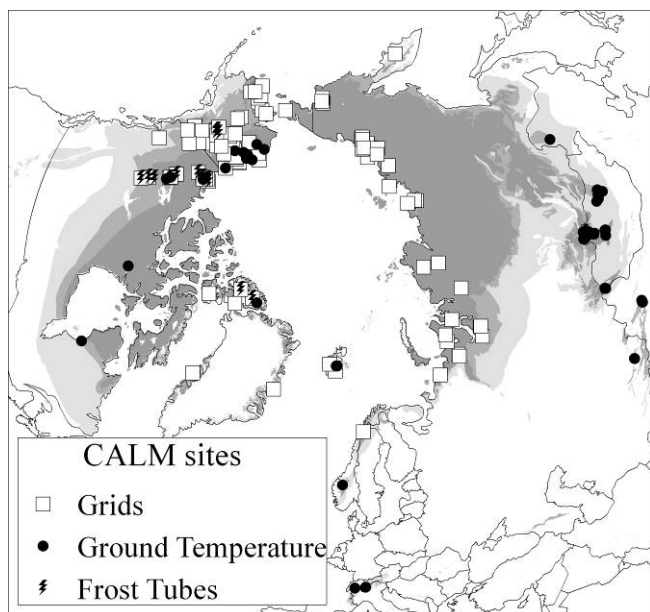


Figure 1. Distribution of CALM observational sites in the Northern Hemisphere

allowed a more detailed, topical focus on different components of the climate-active-layer-permafrost system. The active layer and near-surface permafrost are characterized by high spatial variability and high sensitivity to disturbance as a result of the complex interplay between climatic, surface, and subsurface conditions. As such, they cannot be adequately represented by traditional ground temperature observations at point locations, especially in areas with shallow annual thaw propagation and high ice content. The spatial heterogeneity of the active layer and near-surface permafrost requires a monitoring strategy designed to capture their natural spatial variability. The CALM III observational program therefore focuses on direct spatial active-layer and near-surface permafrost observations over representative arctic landscapes. As such, the CALM III project no longer supports sites where active layer is inferred from the ground temperature measurements at deep boreholes. This primarily includes sites in mountain regions. However, CALM continues to archive and distribute data from these locations as they became available.

The CALM program continues to maintain its open, community-based structure involving participation in its monitoring and analytical activities by all elements of the global permafrost research community. The strategy for incorporating new sites into the network requires conformity with the CALM observational protocol. Specifically, the following guidelines are used for incorporating new sites: a) sites should be located in areas underrepresented in the current CALM observational network; b) investigators should be able to provide observations that include annual thaw depth measurements and active-layer and near-surface temperature monitoring; c) observations should be distributed over diverse landscape units that are characteristic of the area; and d) observations should be sustainable over multi-year periods, preferably a decade or more.

Methodology

CALM III continues to employ existing observation strategies and types of instrumentation (Brown et al. 2000). Three complementary methods are currently used to determine the thickness of the active layer: 1) mechanical probing using a graduated metal rod; 2) temperature measurements; 3) frost/thaw tubes. Observations on snow, vegetation, landscapes, and soils are conducted at the majority of sites. Because many permafrost and landscape processes operate over long time periods (decades or even centuries, depending on site characteristics and process intensity), process-based investigations are supplemented with cryostratigraphic investigations aimed at determining the long-term behavior of the permafrost system at some locations. Many sites are instrumented for air, ground surface, and upper permafrost temperature monitoring. Vertical ground movement observations associated with frost heave/thaw subsidence are measured using traditional optical survey instruments (e.g., Mazhitova et al. 2008) or variants of the “heavometers” used in geomorphological studies. Several sites in Alaska are monitored using Differential Global Positioning Systems technology (Streletskiy et al. 2008). Several Canadian sites employ frost/thaw tubes to detect the magnitude of annual frost heave and thaw subsidence (e.g., Smith et al. 2009). Frost/thaw tubes can be particularly useful for tracking interannual trends.

These strategies were reviewed and evaluated by Brown et al. (2000), Nelson et al. (2004, 2008), Shiklomanov et al. (2008), and during a series of CALM workshops.

Data Availability

At present, active-layer and temperature data are distributed through the CALM web site, (www.udel.edu/Geography/calm) and through the Cooperative Arctic Data and Information Service of the Arctic Observing Network (AON-CADIS). The web-based summary table contains average ALT at all stations for all years and is linked to metadata and individual datasets. About 260 sites were registered in the CALM database at the time of this manuscript’s submission. The following subsections provide a brief inventory of available direct active-layer observations and auxiliary data-specific geographic regions.

Alaska

Alaska is represented by 67 sites. Active-layer measurements are conducted on regular grids of various sizes at 48 sites and three transects with thaw tubes. The North Slope of Alaska has 41 sites, the Alaska Interior region has 24, and two sites are located in the Seward Peninsula. The length of the observational records varies greatly, but more than 40% of the sites have records exceeding 15 years. Several sites originally established by the U.S. Army’s Cold Regions Research and Engineering Laboratory have active-layer records dating back to the 1960s and 1970s (Barrow, Pearl Creek, and Wickersham Dome). A total of 19 new sites have been established in Interior Alaska since 2008.

Canada

Of the 31 Canadian sites registered in the CALM database, 19 are currently active. The majority of the sites are located along the Mackenzie River Valley. Three sites were recently established near the Alaska border. The most comprehensive datasets are available for eight 1-ha grids in the Mackenzie River Valley (Smith et al. 2009). The data include 10 or more years of active-layer observations on grids and thaw tubes, spatial characterization of subsurface conditions (organic layer thickness, organic composition, mineral strata), and several snow surveys from the 2000–2003 period.

Nordic Region

The seven Nordic CALM sites are located in several areas surrounding the North Atlantic: two 1-ha grids in northeast Greenland at Zackenberg; one 1-ha grid in west Greenland on Disko Island (Christiansen 2004); a 1-ha grid on the west coast of Svalbard at Kapp Linne; four transects constituting two sites at Calypostranda, Svalbard (Repelewska-Pekalowa & Pekalowa 2004); and an alpine subarctic 1-ha grid in the vicinity of Abisko, northern Sweden. With the exception of Disko and one of the Calypostranda sites, the active-layer record for the Nordic region grids is available for 10 or more years. The record for the Abisko site extends back to 1972 and includes thickness of active layer in different landscapes. The Zackenberg database includes weekly active-layer observations for the 1996–2010 thawing periods and snow thickness surveys for selected years.

Russia

There are 50 sites in the Russian Arctic registered in the CALM database, including 16 sites that have not reported data for more than two years. Measurements at all sites are conducted by probing grids ranging from 100 to 10,000 m². Several sites have additional thaw tubes and temperature boreholes installed.

European North: Three 1-ha grids are located in the discontinuous permafrost region of the European tundra—Ayach-Yakha and Talnik near Vorkuta and Bolvansky in the Pechora lowlands (Mazhitova et al. 2008). All sites have more than 12 years of active-layer record. The auxiliary data include detailed soil and vegetation characterization, soil temperature, and soil moisture records. Since 1999, periodic, spatially oriented frost heave and ground subsidence measurements using optical leveling have been conducted at Talnik and the Ayach-Yakha site (Mazhitova & Kaverin 2007).

West Siberia: Eight active CALM sites are located in West Siberia. Long-term observations are available from two 1-ha grids at Maere Sale and Vaskiny Dachi in the continuous permafrost zone (established in 1978 and 1991, respectively), and the 1-km² Nadym grid in the discontinuous zone established in 1972 (Vasiliev et al. 2008). An additional four grids were established during the 2003–2007 period in underrepresented areas (Kurchatova and Boytsov 2008).

Central Siberia: In association with the GEWEX Asian Monsoon Experiment (GAME) program in the Siberian Arctic, a 1-km² CALM grid was established in 1997 near Tiksi

on the Lena River (Watanabe et al. 2003). Since 2004, periodic thaw depth measurements are also conducted at two 1-ha grids representing different landscapes of the Lena Delta. Two grids were established around Norilsk and Igarka in 2005 and 2008, respectively (Zepalov et al. 2008).

Lower Kolyma River: In 1996, a series of 15 1-ha grids, spanning a distance of approximately 1300 km, was established to represent characteristic climatic and environmental conditions in the Kolyma-Indigirka lowlands on the northeast Eurasian tundra (Fyodorov-Davydov et al. 2008). Logistical problems have led to some interruptions in observations at six of these sites.

Chukotka and Kamchatka Peninsulas: In 1996, a Mt. Dionisy site was established on the Chukotka Peninsula. A new site was initiated at Lavrentia along the Chukchi Sea coast in 2000 (Zamalodchikov et al. 2008). Both sites consist of 1-ha grids. Three 1-ha grids were established on Kamchatka in 2003.

Although temperature observations in boreholes formally compose the Thermal State of Permafrost program, the CALM database contains site information and available summary active-layer data from 79 borehole sites. Out of these, 40 are located in Mongolia, 16 in Alaska, 11 in China, 7 in Canada, 3 in Kazakhstan, and 2 in Switzerland.

Regional Active-Layer Trends in the Arctic

Below we provide an abbreviated summary of regional active-layer trends and comparative regional analysis based on available continuous long-term data from selected CALM sites. Details about active-layer dynamics are presented regularly at national and international meetings, and have been published widely in international scientific journals and symposia proceedings. Several papers focused on CALM appear elsewhere in these proceedings.

Figure 2 shows temporal active-layer dynamics for several characteristic arctic regions. The regional mean, minimum, and maximum of CALM site-specific thaw depth observations from the end of the thawing season were used to evaluate long-term active-layer trends. Availability of at least ten years of continuous spatial thaw depth observations extended to the 2010/2011 thawing seasons was the only criterion used for site selection. The number of CALM sites within each region varies. For comparative purposes, the data are presented as annual deviations, expressed in percentages, from the mean value over the period of observations.

Thaw depth observations in permafrost regions indicate substantial interannual fluctuations in active-layer thickness, primarily in response to variations in summer air temperature (e.g., Smith et al. 2009). Decadal trends in ALT vary by region. A progressive increase in ALT has been observed in all regions, with the exception of Northern Alaska and West Siberia. For example, observations conducted in Greenland show an increase in active-layer thicknesses since the late 1990s, although the increase is not spatially and temporarily uniform (Christiansen et al. 2010). Scandinavian sites,

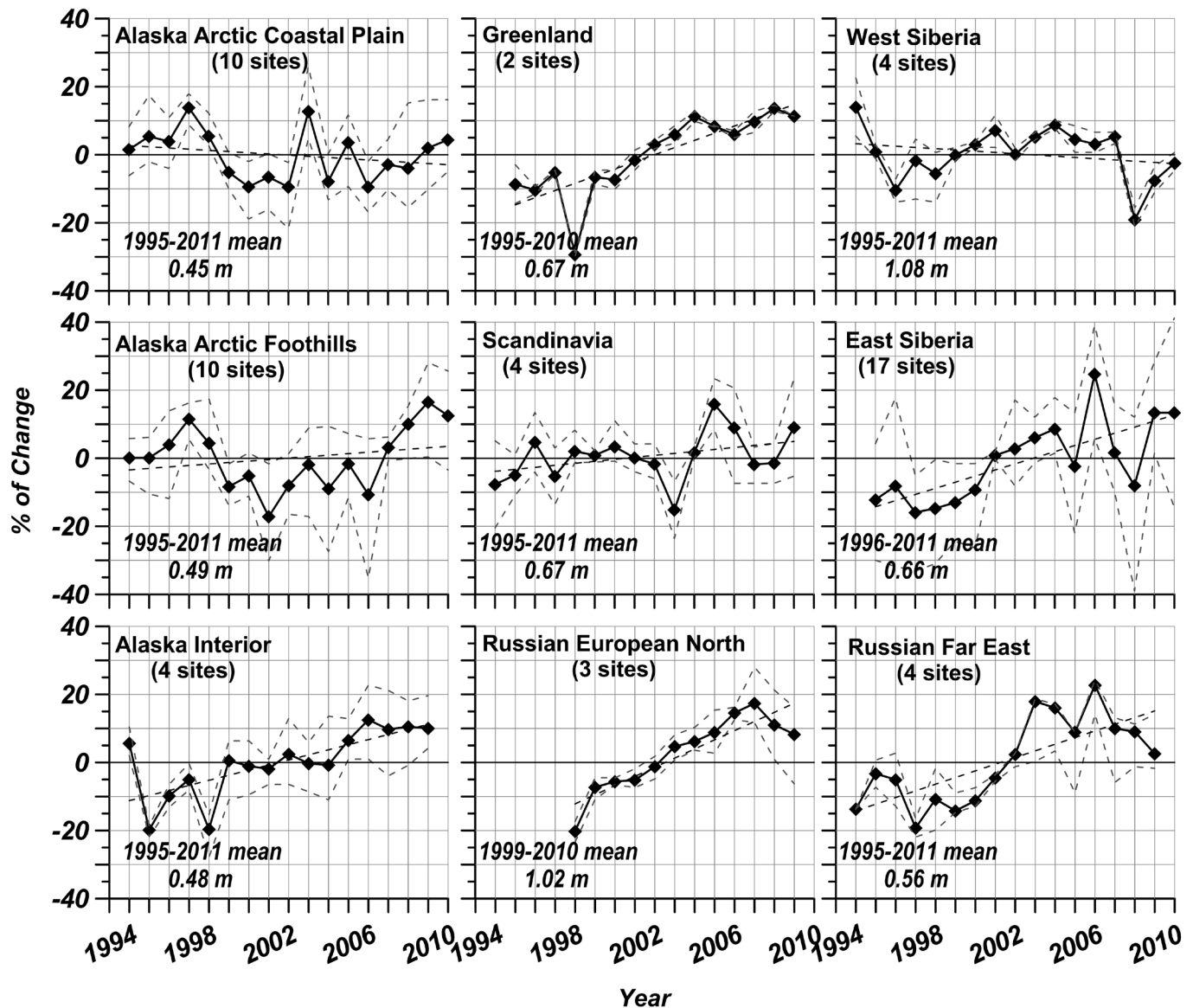


Figure 2. Temporal active-layer dynamics for several characteristic arctic regions. The change is expressed in % from the long-term mean. Solid black line and symbols represent average relative change from multiple CALM sites within the region. Dashed grey lines indicate minimum and maximum relative change. The number of sites used in analysis, the length of the period of observations, and the long-term means for each region are indicated.

which include locations in Arctic Sweden and Svalbard, are collectively characterized by a small positive trend in active-layer thickness. However, the aggregated data presented in Figure 2 can be misleading. For example, the progressive active-layer thickening in the Abisko area of Arctic Sweden has been observed since the 1970s and has accelerated since 1995, resulting in disappearance of permafrost in several mire landscapes (e.g., Åkerman & Johansson 2008, Callaghan et al. 2010). The degraded sites were not included in the analysis.

Significant permafrost degradation has been reported in the Russian European North. As a result of recent climatic warming, the thickness of the active layer has increased significantly (Mazhitova et al. 2008) and permafrost patches that were 10–15 m thick thawed completely in the Vorkuta area (Oberman 2007), causing a significant reduction of the

near-surface permafrost area over the 1970–2005 period. Although permafrost degradation has been reported in the discontinuous zone of West Siberia (e.g., Romanovsky et al. 2010), West Siberia CALM sites are located within the continuous permafrost zone, which has not shown pronounced active-layer trends (Vasil'ev et al. 2008). An increase in active layer thickness has been observed in East Siberia (e.g., Fyodorov-Davydov et al. 2008) and the Russian Far East (e.g., Zamolodchikov et al. 2008).

Active-layer trends are different for North American sites. There, a progressive increase of ALT is evident only at sites in the Alaskan Interior. Active-layer thickness on the Alaskan North Slope is relatively stable, without pronounced trends over the 1995–2011 period.

Similar results are reported from the western Canadian

Arctic. Smith et al. (2009) found that there was no definite trend in active-layer thickness over the 1998–2005 period in the Mackenzie Valley. There are, however, no data available to extend the observational record.

Thaw penetration into an ice-rich layer at the base of the active layer is accompanied by loss of volume (thaw consolidation), manifested as ground subsidence at the surface. Results from monitoring of the position of the ground surface at representative locations on the North Slope of Alaska indicate that up to 11 cm of ground subsidence had occurred over the 2001–2008 period (Streletskiy et al. 2008). Similar results have been obtained from the Russian European North, where increases in active-layer thickness caused ground subsidence of 20 cm over the 1998–2007 period (Mazhitova et al. 2008).

Conclusion

At present, CALM is the world's primary source of empirical information about the active layer, its spatial patterns, and temporal trends. The CALM database consists of submissions from 260 sites, and includes ALT, soil temperature, soil moisture (where available), and heave/subsidence data (where available). Active-layer observations and auxiliary information from the CALM network provide a circumpolar database that has been used extensively by the broader scientific community in biochemical, ecologic, geomorphologic, hydrologic, and climatic research. Because CALM investigators adhere to a standardized observational protocol, data from the program have been widely used for validation of modeling efforts at a variety of geographic scales. CALM is, in the first instance, a global-change observational program. The CALM data serve as a source of fundamental information for climate change assessments such as the Arctic Climate Impact Assessment (ACIA) and the Intergovernmental Panel on Climate Change (IPCC) reports. CALM is the oldest and most comprehensive permafrost-oriented international global-change monitoring program, and has achieved considerable success in this role.

Acknowledgments

The components of the CALM program operating in Alaska and Russia have been partially supported through the U.S. National Science Foundation's Office of Polar Programs under grants OPP-9732051 to the University of Cincinnati, OPP-0352958 to the University of Delaware, and ARC-1002119 to George Washington University. We are grateful to numerous researchers from different countries for conducting CALM observations and for providing data.

References

- Åkerman, H. J. & Johansson, M. 2008. Thawing permafrost and thicker active layers in sub-arctic Sweden. *Permafrost and Periglacial Processes* 19: 279–292. doi:10.1002/ppp.626
- Brown, J., Hinkel, K.M., & Nelson, F.E. 2000. The Circumpolar Active Layer Monitoring (CALM) program: research designs and initial results. *Polar Geography* 24: pp. 258.
- Burn, C.R. & Kokelj, S.V. 2009. The environment and permafrost of the Mackenzie Delta area. *Permafrost and Periglacial Processes* 20: 83–105.
- Callaghan, T.V., Bergholm, F., Christensen, T.R., Jonasson, C., Kokfelt, U., & Johansson, M. 2010. A new climate era in the sub-Arctic: Accelerating climate changes and multiple impacts. *Geophysical Research Letters* 37: L14705, doi:10.1029/2009GL042064.
- Christiansen, H.H., Etzelmüller, B., Isaksen, K., & 15 others. 2010. The thermal state of permafrost in the Nordic area during the international polar year 2007–2009. *Permafrost and Periglacial Processes* 21: 156–181. doi: 10.1002/ppp.687.
- Christiansen, H.H. 2004. Meteorological control on interannual spatial and temporal variations in snow cover and ground thawing in two northeast Greenlandic Circumpolar-Active-Layer-Monitoring (CALM) sites. *Permafrost and Periglacial Processes* 15: 155–169.
- Federov, A.N. 1996. Effects of recent climate change on permafrost landscapes in central Sakha. *Polar Geography* 20: 99–108.
- Fedorov, A.N. & Konstantinov P.Y. 2008. Recent changes in ground temperature and the effect on permafrost landscapes in Central Yakutia. In *NICOP 2008: Proceedings of the Ninth International Conference on Permafrost*. D.L. Kane, K.M. Hinkel (eds.). Institute of Northern Engineering, University of Alaska Fairbanks, 1: 433–438.
- Fyodorov-Davydov, D.G., Kholodov, A.L., Ostroumov, V.E., Kraev, G.N., Sorokovikov, V.A., Davudov, S.P., & Merkalova, A.A. 2008. Seasonal thaw of soils in the North Yakutian ecosystems. In *NICOP 2008: Proceedings of the Ninth International Conference on Permafrost*. D.L. Kane, K.M. Hinkel (eds.). Institute of Northern Engineering, University of Alaska Fairbanks, 1: 481–486.
- Harris, C., Haerberli, W., Vonder Muehll, D., & King, L. 2001. Permafrost monitoring in the high mountains of Europe: the PACE Project in its global context. *Permafrost and Periglacial Processes* 12: 3–11.
- Isaksen, K., Sollid, J.L., Holmlund, P., & Harris C. 2007. Recent warming of mountain permafrost in Svalbard and Scandinavia. *Journal of Geophysical Research* 112: F02S04, doi:10.1029/2006JF000522.
- King, L., Herz, T., Hartmann, H., Hof, R., Jiang, T., Ke, C., Wei, Z., Liu, J., & Yi, C. 2006. The PACE monitoring strategy: A concept for permafrost research in Qinghai-Tibet. *Quaternary International* 154: 149–157.
- Kurchatova, A.N. & Boytsov A.V. 2008. Temperatures of upper permafrost in northern West Siberia. In *NICOP 2008: Proceedings of the Ninth International Conference on Permafrost*. D.L. Kane, K.M. Hinkel (eds.). Institute of Northern Engineering, University of Alaska Fairbanks, 2: 1659–1664.
- Marchenko, S., Gorbunov, A. & Romanovsky, V. 2007. Permafrost warming in the Tien Shan Mountains, Central Asia. *Global and Planetary Change* 56: 311–327.

- Mazhitova, G., Malkova, G., Chestnykh, O., & Zamolodchikov, D. 2008. Recent decade thaw depth dynamics in the European Russian Arctic based on the Circumpolar Active Layer Monitoring (CALM) data. In *NICOP 2008: Proceedings of the Ninth International Conference on Permafrost*. D.L. Kane, K.M. Hinkel (eds.). Institute of Northern Engineering, University of Alaska Fairbanks, 2: 1155-1160.
- Mazhitova, G.G. 2008. Soil temperature regimes in the discontinuous permafrost zone in the East European Russian Arctic. *Eurasian Soil Science* 41: 48-62.
- Nelson, F.E., Shiklomanov, N.I., Christiansen, H.H., & Hinkel, K.M. 2004. The circumpolar-active-layer-monitoring (CALM) Workshop: Introduction. *Permafrost and Periglacial Processes* 15: 99-101.
- Nelson, F.E., Shiklomanov, N.I., Hinkel, K.M., & Brown, J. 2008. Decadal results from the Circumpolar Active Layer Monitoring (CALM) program. In *NICOP 2008: Proceedings of the Ninth International Conference on Permafrost*. D.L. Kane, K.M. Hinkel (eds.). Institute of Northern Engineering, University of Alaska Fairbanks, 1: 1273-1280.
- Nixon, F.M. 2000. Thaw-depth monitoring. In: *The Physical Environment of the Mackenzie Valley, Northwest Territories: a base line for the assessment of environmental change*. Geological Survey of Canada Bulletin 547: 119-126.
- Nixon, F.M. & Taylor, A.E. 1998. Regional active layer monitoring across the sporadic, discontinuous and continuous permafrost zones, Mackenzie Valley, northwestern Canada. In: *Proceedings of the Seventh International Conference on Permafrost*. Quebec: Centre d'Etudes nordiques, Université Laval, 815-820.
- Oberman, N.G. 2007. Global warming and permafrost changes in Pechora-Urals region. *Exploration and Protection of Natural Resources* 4: 63-68.
- Repelewska-Pekalowa, J. & Pekala, K. 2004. Active-layer dynamics at the Calypsostranda CALM site, Recherche Fiord Region, Spitsbergen. *Polar Geography* 28: 326-340.
- Romanovsky, V.E., Drozdov, D.S., Oberman, N.G. & 9 others. 2010. Thermal state of permafrost in Russia. *Permafrost and Periglacial Processes* 21: 136-155. doi: 10.1002/ppp.683
- Romanovsky, V.E., Sergueev, D.O., & Osterkamp, T.E. 2003. Temporal variations in the active layer and near surface permafrost temperatures at the long-term observatories in northern Alaska. In: *Proceedings of the Eighth International Conference on Permafrost*, Lisse, A.A. Balkema, Vol. 2, 989-994.
- Sharkhuu, N., Sharkhuu, A., Romanovsky V.E., Yoshikawa K., Nelson F.E., & Shiklomanov, N.I. 2008. Thermal state of permafrost in Mongolia. In *NICOP 2008: Proceedings of the Ninth International Conference on Permafrost*. D.L. Kane, K.M. Hinkel (eds.). Institute of Northern Engineering, University of Alaska Fairbanks, 2: 1633-1639.
- Shiklomanov, N.I., Nelson, F.E., Streletskiy, D.A., Hinkel, K.M., & Brown, J. 2008. The Circumpolar Active Layer Monitoring (CALM) Program: Data collection, management, and dissemination strategies. In *NICOP 2008: Proceedings of the Ninth International Conference on Permafrost*. D.L. Kane, K.M. Hinkel (eds.). Institute of Northern Engineering, University of Alaska Fairbanks, 2: 1647-1652.
- Smith, S.L., Wolfe, S.A., Riseborough, D.W. & Nixon, F.M. 2009. Active-layer characteristics and summer climatic indices, Mackenzie Valley, Northwest Territories, Canada. *Permafrost and Periglacial Processes* 20: 201-220. doi:10.1002/ppp.651.
- Streletskiy, D.A., Shiklomanov, N.I., Nelson, F.E., & Klene, A.E. 2008. 13 Years of observations at Alaskan CALM sites: Long-term active layer and ground surface temperature trends. In *NICOP 2008: Proceedings of the Ninth International Conference on Permafrost*. D.L. Kane, K.M. Hinkel (eds.). Institute of Northern Engineering, University of Alaska Fairbanks, 2: 1727-1732.
- Vasiliev, A.A., Leibman, M.O. & Moskalenko, N.G. 2008. Active layer monitoring in West Siberia under the CALM II Program. In *NICOP 2008: Proceedings of the Ninth International Conference on Permafrost*. D.L. Kane, K.M. Hinkel (eds.). Institute of Northern Engineering, University of Alaska Fairbanks, 2: 1815-1821.
- Viereck, L.A., Werdin-Pfistere, N.R., Phyllis, C.A., & Yoshikawa, K. 2008. Effect of wildfire and fireline construction on the annual depth of thaw in a Black Spruce permafrost forest in Interior Alaska: A 360 Year Record of Recovery. In *NICOP 2008: Proceedings of the Ninth International Conference on Permafrost*. D.L. Kane, K.M. Hinkel (eds.). Institute of Northern Engineering, University of Alaska Fairbanks, 2: 1845-1850.
- Watanabe, K., Kiyosawa, H., Fukumura, K., Ezaki, T., & Mizoguchi, M. 2003. Spatial and temporal variation in thaw depth in Siberian tundra near Tiksi. In: *Proceedings of the Eighth International Conference on Permafrost*, Lisse: A.A. Balkema, Vol. 2, 1211-1216.
- Zamolodchikov, D., Kotov, A., Karelin, D., & Razzhiving, V. 2008. Recent climate and active layer changes in Northeast Russia: regional output of Circumpolar Active Layer Monitoring (CALM) In *NICOP 2008: Proceedings of the Ninth International Conference on Permafrost*. D.L. Kane, K.M. Hinkel (eds.). Institute of Northern Engineering, University of Alaska Fairbanks, 2: 2021-2027.
- Zepalov, F.N., Grebenets, V.I., Streletskiy, D.A., & Shiklomanov, N.I. 2008. Active-layer monitoring at a new CALM Site, Taimyr Peninsula, Russia. In *NICOP 2008: Proceedings of the Ninth International Conference on Permafrost*. D.L. Kane, K.M. Hinkel (eds.). Institute of Northern Engineering, University of Alaska Fairbanks, 2: 2037-2042.

Permafrost Degradation and Thaw Settlement under Lakes in Yedoma Environment

Yuri Shur, Mikhail Kanevskiy, Torre Jorgenson, Matthew Dillon, Eva Stephani, Matthew Bray
University of Alaska Fairbanks, USA

Daniel Fortier
University of Montreal, Montreal, QC, Canada

Abstract

Yedoma, ice-rich syngenetic permafrost with large ice wedges formed during the Late Pleistocene, occurs widely in parts of Alaska that were unglaciated during the last glaciation, including Interior Alaska, the Brooks Range foothills, and the Seward Peninsula. Since the Late Pleistocene, most yedoma has been destroyed by thermokarst and thermal erosion, and the resulting features occur in different forms. Thermokarst lakes are the most obvious and one of the most damaging forms of yedoma degradation. The contemporary yedoma environment is not favorable for new development of mature thermokarst lakes. The initial stages of thermokarst are numerous in yedoma, but their further development is often restricted by drainage associated with yedoma relief and by accumulation of organic matter in initial thermokarst ponds and troughs. Development of thermokarst lakes under favorable conditions occurs at rates comparable to those of kettle lakes in terrain with buried glacier ice, and only sudden drainage can prevent yedoma from complete thawing.

Keywords: Alaska; ice wedges; thaw settlement; thermokarst lakes; yedoma.

Yedoma in Alaska

The Late Pleistocene was extremely favorable for syngenetic permafrost development, which led to formation of thick deposits of yedoma. Yedoma is one of the most prominent features of the periglacial environment in the Arctic. In the contemporary permafrost region, yedoma is characterized by extremely ice-rich, loess-like silt with wide ice wedges penetrating through its entire thickness. The thickness of yedoma typically ranges from 10 to 30 m, but in some areas of Siberia it can be 50 m or more (Ivanov 1984).

Ice wedges form in a polygonal network. In exposures, the ice is visible in varying orientations, but only one (when an exposure is vertical and perpendicular to the ice wedges) reveals the real width of wedges, typically 2–6 m. Other orientations can be confusing and lead to an exaggerated estimate of the amount of massive ice in yedoma (Shumskii 1959). Ice wedges in yedoma usually occupy 30–50% of their total volume and even more in the high Arctic. Wedge ice is gray or brown in color because it contains numerous inclusions of silt and organics. Ice wedges in yedoma can be easily distinguished from Holocene ice wedges, which are white due to fewer soil inclusions and have more air bubbles.

Yedoma has numerous characteristic features. It has a specific cryogenic structure (patterns of ice distribution within the soil) that has been documented by many studies in Russia (Katasonov 1954, Popov 1967, Romanovskii 1977, Shur 1988). Gravimetric moisture content of soil between the ice wedges reaches 200% and more. The total volumetric ice content of yedoma usually reaches 70–80% or greater. Plant remains occur throughout the yedoma thickness. Roots of grasses are the main part of these remains, but peat layers also occur occasionally. Yedoma contains well-preserved remains of Pleistocene fauna.

The ecosystem during yedoma formation had been changing from typical tundra to tundra-steppe (Yurtsev 1981). The

time of yedoma formation ranges from more than 40,000 to 12,000 years ago (Hamilton et al. 1988, Kanevskiy et al. 2011, Vasil'chuk 1992). O¹⁸ data show that the climate during the entire period of yedoma formation was relatively stable and much more severe than at present. The permafrost temperature during this period was 7–10°C colder than today (Vasil'chuk 1992). Yedoma was the dominant type of permafrost in the areas unglaciated during the Late Pleistocene.

Yedoma has been widely studied in Russia since the 1950s, and the literature related to Siberian yedoma contains hundreds of papers and dozens of books. In Alaska, works related to yedoma are very limited. Péwé (1975) described an exposure of the Late Pleistocene permafrost at Eva Creek (Interior Alaska). Hamilton et al. (1988) studied and dated Late Pleistocene deposits in the CRREL permafrost tunnel near Fairbanks, Interior Alaska. Carter (1988) described three exposures of ice-rich silt in the Brooks Range foothills and found them similar to yedoma in Central Yakutia. He also extrapolated the area of yedoma to the silt belt of northern Alaska. Yedoma sites in the Brooks Range foothills were also studied by Lawson (1982). In Canada, yedoma was described in the Klondike area by Fraser & Burn (1997) and Kotler & Burn (2000).

Yedoma in the CRREL permafrost tunnel has been intensively studied by Shur et al. (2004), Bray et al. (2006), Kanevskiy et al. (2008), and Fortier et al. (2008). Using methods of cryofacies analysis (Katasonov 1954), they distinguished between original yedoma and later modifications. They reconsidered the genesis of tabular ice in the tunnel, which for decades had been described as buried pond ice, and proposed a new type of cryostructure associated with thermokarst-cave ice. An outstanding yedoma exposure was recently described at the Itkillik River (Kanevskiy et al. 2011).

While the distribution of yedoma in Alaska is inadequately known, a preliminary map of yedoma in Alaska (Fig. 1) has been developed based on field observations, interpretation of

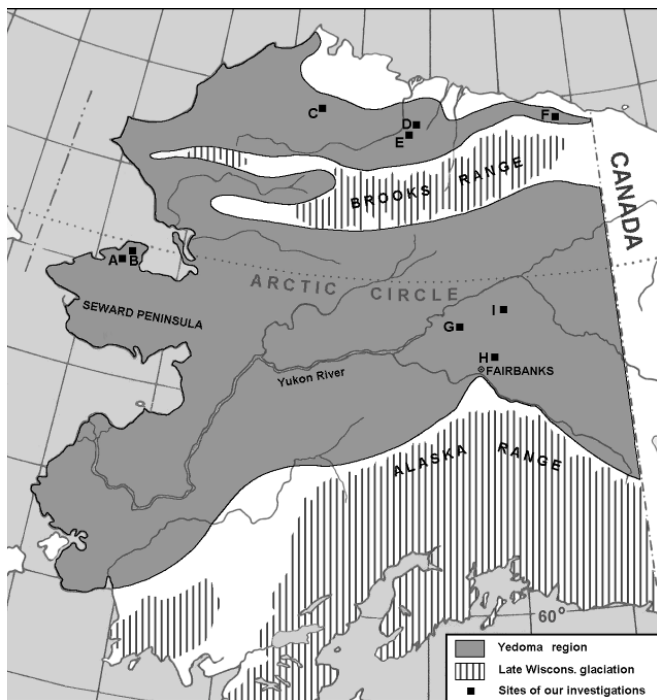


Figure 1. Preliminary map of yedoma distribution in Alaska (based on Kanevskiy et al. 2011). Field sites: A – Devil Mountains, B – Cape Espenberg, C – Oumalik, D – Itkillik, E – Umiat, F – Jago, G – Hess Creek, H – CRREL tunnel, I – Boot Lake.

aerial images, and existing data (Kanevskiy et al. 2011). We consider Alaska to be the world's second largest region with yedoma, after Russia.

Stages of Thermokarst Lake Development

Deep lakes and drained-lake basins (alases) are parts of the yedoma environment from the high Arctic to its southern boundaries, and they are related to its degradation in the Holocene. Soloviev (1962) described the stages of thermokarst lake development in yedoma using native Yakutian names. His conceptual model considered progressive development of thermokarst from small depressions caused by an increase in the active layer depth, to complete yedoma degradation beneath thermokarst lakes, and eventual formation of vast drained-lake basins. The model was originally developed with the assumption that ice in yedoma was buried glacier ice, a common misperception at that time. Soloviev's model was adapted by Russian scientists and later presented in English by Czudek and Demeck (1970), Washburn (1973), and French (1975). Based on the experience of our permafrost studies in Russia and Alaska (Kanevskiy 1985, Shur 1988, Kanevskiy et al. 2011), we revised Soloviev's model with the following.

Stage Ia develops from an increase in the active-layer thickness and thawing of the upper permafrost over ice wedges and inside polygons, which results in thaw settlement of soils.

In Stage Ib, thawing of the upper ice wedges and

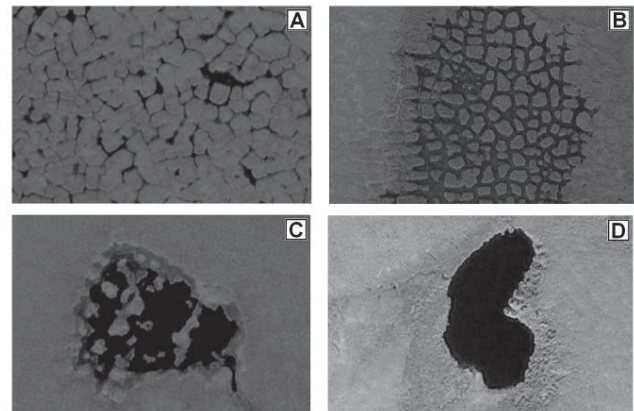


Figure 2. Stages I – IV of thaw-lake basin development (images from Google Earth). A – Stage Ib (formation of thermokarst troughs above ice wedges); B – Stage II (deepening of troughs); C – Stage III (formation of thermokarst pond above polygons); D – Stage IV (deepening of thermokarst lake).

formation of ice-wedge troughs (especially above ice-wedge intersections), begins when the deepening active layer reaches the ice wedges (Fig. 2A).

Stage II reflects the deepening of ice-wedge troughs with accumulation of water in the troughs, especially above ice wedge intersections where initial thermokarst ponds can form. Settlement of the soil surface above the ice wedges occurs faster than at polygon centers, so high-centered polygons rise over troughs as low and flat thermokarst mounds (Fig. 2B).

Stage III involves formation of thermokarst ponds above polygons. Continuous melting of ice wedges and thawing of soil in polygon centers adjacent to water-filled troughs trigger the partial degradation of thermokarst mounds. Redistribution of soil from the central region of the polygons to initial ponds and troughs increases the rate of permafrost thaw inside polygons and decreases the rate of ice-wedge melting. Further melting of ice wedges and thaw settling within polygons finally leads to accumulation of water over the entire site (Fig. 2C).

Stage IV involves lake deepening, which results in accelerated development of thermokarst when the depth of the thermokarst lake becomes greater than critical (Fig. 2D).

Stage V denotes the complete thawing of yedoma under the lake, accompanied by thermal erosion of the shores. At this stage, the lake is similar to lakes of non-thermokarst origin in terms of the thermal impact on the underlying permafrost.

Stage VI results from the drainage of the lake and formation of alases, alas valleys, and alas plains (Soloviev 1962).

Shur (1988) quantified development of Stages I and II in relation to cryostratigraphy and soil properties of the upper permafrost and defined conditions for the transition from Stage III to Stage IV. Degradation of permafrost is enhanced when water depth is greater than critical (when

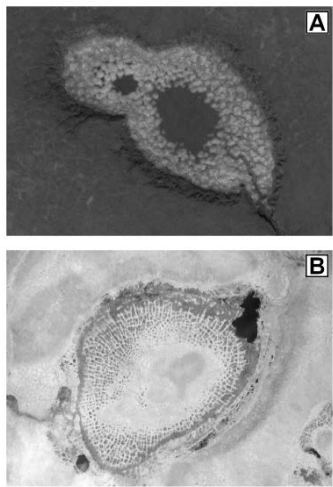


Figure 3. Alases of the Seward Peninsula (images from Google Earth). A – formation of a shallow alase as a result of lake drainage at Stage IV; B – mature alase with modern ice-wedge development; yedoma soils under the lake had thawed completely before the drainage occurred (stage VI).

combined water depth and snow thickness leads to mean annual temperature $>0^{\circ}\text{C}$). The process of thaw-lake formation can be terminated at any stage by surface water drainage (Fig. 3A).

Rate of Yedoma Degradation Under Lakes

From studying yedoma on the Seward Peninsula, we were able to evaluate thermokarst development at Stage IV and its impact on yedoma. In 1994, we visited a freshly drained lake in the Devil Mountains area (Fig. 1) and found that the lake was drained by underground piping (not by surface thermal erosion and breaching). The underground piping occurred through a layer of tephra with particle sizes of fine and medium gravel. A mechanism of underground lake drainage on the Seward Peninsula was previously described by Hopkins (1949). The drained-lake basin was 120×140 m. The depth in the central part of the basin was 11–13 m below the main yedoma surface, which is equal to the thaw settlement of yedoma under the lake. We observed exposures with thick ice wedges and syngenetic permafrost. The studied drained lake belongs to an area of wide yedoma occurrence that had typical yedoma thermokarst stages varying from young forms to well developed alases and alas valleys. Slopes of alases and thermokarst lakes had baidjarakhs (thermokarst mounds), typical of yedoma.

In 2009, we revisited this site and surveyed three transects across the drained-lake basin (Fig. 4). We drilled 21 boreholes in the middle of the basin, on its slopes, and on the original yedoma surface along two transects (Figs. 4–6). Fifteen years after lake drainage, the unfrozen soil in the talik had been completely refrozen. The boundary between original yedoma soil and the refrozen upper part was evaluated by comparing cryostructures typical of yedoma with cryostructures of the refrozen soil. Thawed and refrozen soil over ice wedges had an average gravimetric water content of 64% ($n=23$), while the

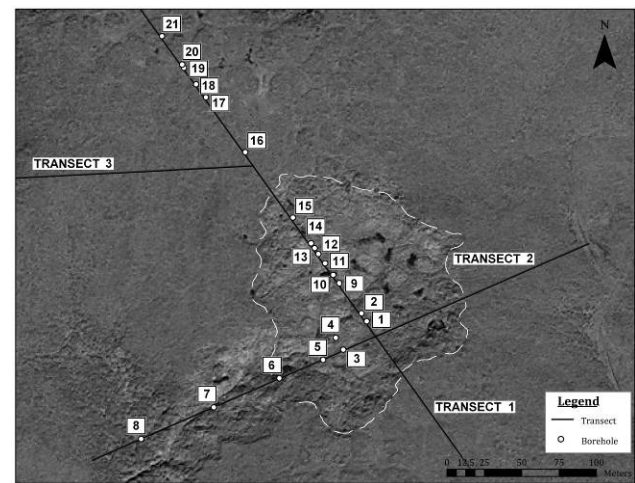


Figure 4. Location of boreholes at the 2009 study site near Devil Mountains, Seward Peninsula. Dashed line shows boundaries of the lake basin.

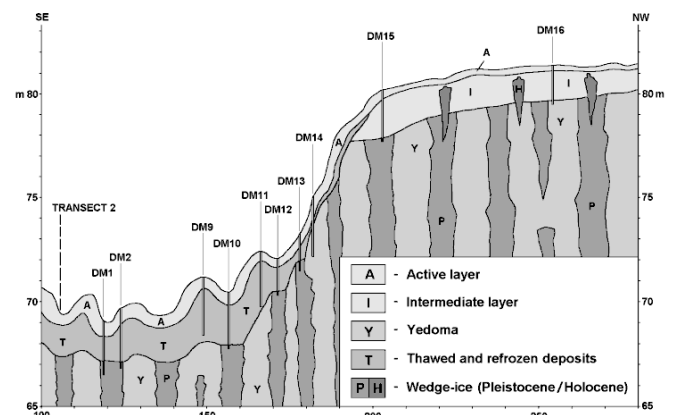


Figure 5. Schematic section across the thaw-lake basin and undisturbed yedoma, Transect 1 (ice-wedges not to scale).

water content of refrozen soil over polygons was 48% ($n=27$). The water content of the intermediate layer (Shur 1988) was 142% ($n=15$) for the main yedoma surface and 116% ($n=26$) for underlying yedoma. Cryostructures indicate the talik under the lake was about 2 m thick over ice wedges, and about 3–4 m in the centers of polygons. The heights of thermokarst mounds over ice-wedge troughs in the central part of the drained-lake basin did not exceed 2 m.

Airphoto analysis of polygonal relief in the thaw-lake basin found a volumetric content of wedge ice of 61%. Volumetric ice content of yedoma inside polygons was equal to 76%, and total volumetric ice content, including both components, was 90%. Average thaw strain (ratio of a thickness of thawed soil to an initial thickness before thawing) of yedoma at the studied site was estimated as 0.8.

The depth of the shallow talik evident from the cryostructures in the cores was small in comparison to the width of the lake basin. It was previously shown (Shur 1988) that a one-dimensional model describes thawing under lakes as effectively as two-dimensional and three-dimensional models, if the ratio of the thickness of the talik to the width of

the lake is smaller than 0.2. In our case, this ratio was about 0.03. This indicates that thawing of permafrost under the lake can be considered as one-dimensional, and the rate of talik development can be estimated using equations describing one-dimensional thawing and taking into account soil settlement from thawing. Such equations were developed by Are et al. (1974) and Shur (1977). The depth of yedoma thawing under a lake with mean annual water temperature above 0°C can be found from the following simple equation (Shur 1977):

$$\xi = \sqrt{h^2 + \frac{2kt\tau}{(1-\delta)\rho W}} \quad (1)$$

where: ξ = depth from the initial surface to the permafrost table; h = thickness of seasonally frozen soil layer over yedoma before the Stage IV of the lake formation; k = thermal conductivity of thawed soil; t = mean annual water temperature; τ = time; δ = thaw strain of soil; ρ = latent heat of phase change; W = weight of ice in one volumetric unit of yedoma.

Equation 1 does not include a parameter describing convection at the bottom of a lake. It was shown that the impact of convection should be taken into account when the thickness of soil above ice is on the order of only centimeters, which is much smaller than a thickness of unfrozen soil above ice wedges and ice-rich soil of yedoma. The magnitude of the first parameter (h) under the square root (equation 1) is around 1 m and can be neglected when ξ is greater than 3 m. In our case, it was more than 10 m.

The equation neglects the sensible heat of soil. This assumption is appropriate for ice-rich permafrost for which the latent heat of phase change in one volumetric unit of soil during thawing is more than 100 times greater than the change in sensible heat with a warming of 1°C.

Using equation 1 and assuming the mean annual water temperature in the lake was between 1 and 4°C, we calculate that it would take only 50 to 100 years for the lake to reach a depth of 10 m from the initial surface to the permafrost table during Stage IV, when talik development and settlement were occurring. It is of interest to compare the rate of yedoma thawing and settling with melting of buried glacier ice, which can be described by equation 2 (Shur 1977):

$$\xi = \frac{k t \tau}{h \rho W} \quad (2)$$

where: h – thickness of the soil above buried ice. For other parameters see equation 1.

With h equal to 1 m, and using the above assumptions, we calculate it would take 25 to 100 years to develop a kettle lake of similar depth. This comparison indicates that the development of thermokarst lakes in ice-rich yedoma at Stage IV is similar to that of kettle lakes derived from buried glacier ice.

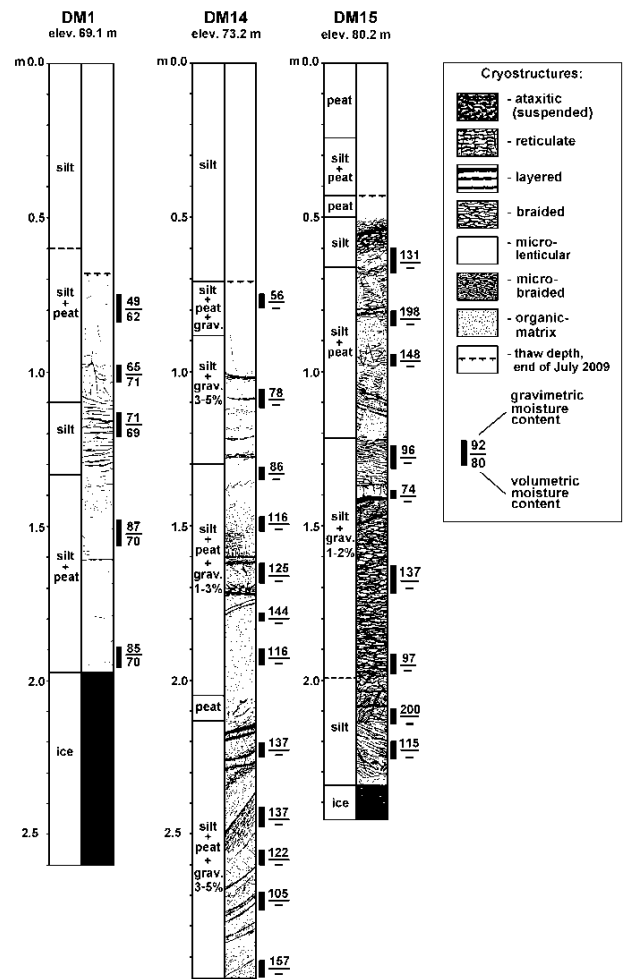


Figure 6. Cryogenic structure of frozen soils. DM1 – refrozen soil above ice wedge, DM14 – yedoma soil at the slope of thaw-lake basin, DM15 – ice-rich intermediate layer above undisturbed yedoma (for location of boreholes, see Figs. 4 and 5).

Yedoma Changes During the Holocene

Yedoma was in balance with the cold environment of the Late Pleistocene, even with an almost thermally unprotected soil surface of cold steppe terrain (Yurtsev 1981). Vast yedoma plains were formed during the Late Pleistocene. The transition from a cold and dry climate of the Late Pleistocene to a warmer and wetter Holocene climate led to widespread degradation of yedoma. It completely disappeared in Eastern Europe (Velichko 1973), and in the Arctic on the previously exposed continental shelf as a result of marine transgression. In the contemporary permafrost region, a significant part of yedoma has been destroyed by thermal erosion and thermokarst since the Late Pleistocene, and both processes are still affecting yedoma. In some areas of East Siberia and Alaska, human activities, such as mining and farming, have had severe impacts on yedoma (Soloviev 1962, Péwé 1954).

Yedoma is a relic of the Late Pleistocene. Other unique deposits that formed during this period in the discontinuous permafrost zone of Alaska are frozen glacio-lacustrine sediments and buried glacier ice. The main property of relic permafrost

deposits is their irreversible nature; once destroyed, they do not recover. The Holocene history of yedoma can be considered from two points of view: as yedoma degradation or as yedoma adaptation to a new environment. The first approach is focused on the sensitivity of yedoma to climatic changes, and on the processes and factors leading to yedoma destruction. The focus of the second approach is yedoma stability, and those factors and properties that affect the persistence of yedoma in an environment significantly different than the environment during which it formed. We note that the first approach has overwhelmingly prevailed in the literature.

Development of thermokarst lakes from the initial surface to the latest stages is rather unusual in the contemporary environment. There are numerous examples of Stages I and II, but in most cases thermokarst does not proceed further. Starting with Stage II, the possibility of development to the next stage diminishes. Our observations in western and northern Alaska and in northern Yakutia, and our analysis of aerial photographs, revealed thousands of sites at Stages I and II and only a few sites where newly developing thermokarst might progress to Stages III and IV. Initial thermokarst stages are often interrupted by drainage associated with sloping relief and by accumulation of organic matter in wet and warm initial thermokarst pits. This creates a powerful negative feedback to thermokarst (Jorgenson et al. 2006).

Grave (1944, p. 20) found that "First what catches your eye in the lake – alas terrain is overwhelming prevalence of old forms over young ones." This observation is applicable to all areas of yedoma occurrence. In the contemporary permafrost region, evolution of yedoma terrain has continued for more than 10,000 years. What used to be yedoma plains are now occupied by yedoma remnants shaped as hills with gentle to moderate slopes. Thermokarst and erosional processes modify slopes and integrate drainage networks that enhance water removal and help stabilize ice-rich permafrost. This leaves less opportunity for development of new thermokarst lakes. Drainage systems and thermokarst lakes divided and shaped a previously flat surface. A significant part of yedoma was destroyed by these processes before yedoma remnants became more stable. The other very important factor contributing to yedoma stability was environmental change from steppe to tundra, with accumulation of organic matter on the soil surface in the early Holocene (Shur 1988). Formation of lakes in areas of poor drainage was accompanied by the development of a wetland type vegetation in better drained areas, with accumulation of thermally insulating mosses and peat (Shur 1988). In northern Yakutia, extremely ice-rich yedoma is currently degrading mainly by erosion along shores of rivers and seas, and to a smaller degree along shores of old thermokarst lakes (Shur 1988). We found that this observation is also applicable to yedoma in Alaska.

Conclusions

Yedoma, ice-rich syngenetic permafrost with large ice wedges that formed during the Late Pleistocene, occurs widely in unglaciated regions of Alaska including Interior Alaska, the

Brooks Range foothills, and the Seward Peninsula. Since the Late Pleistocene, yedoma has been partly destroyed by thermokarst and thermal erosion. Degradation of yedoma occurs in different forms. Thermokarst lakes are the most obvious and one of the most damaging forms of yedoma degradation. The other is coastal thermal erosion. Unlike most thermokarst lakes in permafrost regions, which are not deeper than 1 to 3 m, thermokarst lakes in yedoma often are 10 to 20 m deep.

Thermokarst lakes in yedoma have several stages of development. The first stage is triggered by thickening of the active layer and partial thaw of ice wedges. During the second stage, small ponds form over ice wedges and especially at their intersections. Only under favorable conditions do these ponds grow deeper and coalesce to form a shallow initial thermokarst lake in the third stage. The fourth stage of lake formation includes fast melting of ice wedges and ice-rich sediment between them, which results in rapid deepening of the lake. At this stage, only shallow taliks develop beneath thaw lakes, and only sudden, complete lake drainage can prevent yedoma from complete thawing. Yedoma sections we studied are characterized by total volumetric ice content ranging from 70 to 90%, and thaw strain from 0.5 to 0.8. With such high ice content, the formation of thaw lakes in yedoma is comparable to the formation of kettle lakes in glacial terrain. During the fifth stage, thawing reaches the base of the ice-rich stratum, and further yedoma destruction is restricted to thermal erosion of the lake shore. The final sixth stage of thermokarst in yedoma is related to its complete thawing, lake drainage, and subsequent freezing of soils in a drained-lake basin. This stage produces alases (thaw-lake basins), alas valleys, and alas plains. All these forms are common in the northern part of the Seward Peninsula.

For continued thermokarst development over time, accumulation of water in thermokarst depressions is the most important factor. Without impounded water, thermokarst can proceed only in the discontinuous permafrost zone as part of overall permafrost degradation. In the continuous permafrost zone, remnants of yedoma are stable when well drained and are not affected by erosion.

Acknowledgments

This study was funded by the National Science Foundation (NSF) grant ARC-0454939. Helpful suggestions by Kenneth Hinkel and two reviewers are appreciated.

References

- Are, F.E., Balobaev, V.T., & Bosikov, N.P. 1974. Peculiarities of the reworking of shores of thermokarst lakes in Central Yakutia. In *Lakes of the cryolithozone of Siberia*. F.E. Are (ed.). Novosibirsk, "Nauka", pp. 39-53 (in Russian).
- Bray, M.T., French, H.M., & Shur, Y. 2006. Further cryostratigraphic observations in the CRREL permafrost tunnel, Fox, Alaska. *Permafrost and Periglacial Processes* 17 (3), 233-243.

- Carter, L.D. 1988. Loess and deep thermokarst basins in Arctic Alaska. *Proceedings Fifth International Conference on Permafrost* 706-711.
- Czudek, T. & Demek, J. 1973. Thermokarst in Siberia and its influence on the development of lowland relief. *Quaternary Research* 1, pp. 103-120.
- Fortier, D., Kanevskiy, M., & Shur, Y. 2008. Genesis of reticulate-chaotic cryostructure in permafrost. In *NICOP 2008: Proceedings of the Ninth International Conference on Permafrost*. D.L. Kane, K.M. Hinkel (eds.). Institute of Northern Engineering, University of Alaska Fairbanks, 1, 451-456.
- Fraser, T.A. & Burn, C.R. 1997. On the nature and origin of 'muck' deposits in the Klondike area, Yukon Territory. *Canadian Journal of Earth Sciences* 34, 1333-1344.
- Grave, N.A. 1944. Ground ice of the Lena-Aldan watershed. In *Trudy of Obruchev's Permafrost Institute* Vol 4. USSR Academy of Sciences: 10-32 (in Russian).
- Hamilton, T.D., Craig, J.L., & Sellmann, P.V. 1988. The Fox permafrost tunnel: a late Quaternary geologic record in central Alaska. *Geological Society of America Bulletin* 100, 948-969.
- Hopkins, D.M. 1949. Thaw lakes and thaw sinks in the Imuruk Lake area, Seward Peninsula, Alaska. *Journal of Geology* 57, 119-131.
- Ivanov, M.S. 1984. *Cryogenic structure of Quaternary deposits of Lena-Aldan Depression*. Novosibirsk: Nauka, 124 pp. (in Russian).
- Jorgenson, M.T., Shur, Y., & Pullman, E.R. 2006. Abrupt increase in permafrost degradation in Arctic Alaska. *Geophysical Research Letters* 33: L022503.
- Kanevskiy, M. 1985. *Alases of Northern Yakutia*. MS thesis. Moscow State University (in Russian).
- Kanevskiy, M., Fortier, D., Shur, Y., Bray, M., & Jorgenson, T., 2008. Detailed cryostratigraphic studies of syngenetic permafrost in the winze of the CRREL permafrost tunnel, Fox, Alaska. In *NICOP 2008: Proceedings of the Ninth International Conference on Permafrost*. D.L. Kane, K.M. Hinkel (eds.). Institute of Northern Engineering, University of Alaska Fairbanks, 1, 889-894.
- Kanevskiy, M., Shur, Y., Fortier, D., Jorgenson, M.T., & Stephani, E. 2011. Cryostratigraphy of Late Pleistocene syngenetic permafrost (yedoma) in northern Alaska, Itkillik River exposure. *Quaternary Research* 75(3), 584-596.
- Katasonov, E.M. 1954. *Lithology of frozen Quaternary deposits (cryolithology) of the Yana Coastal Plain*. Ph.D. Thesis, Obruchev Permafrost Institute (published in 2009, Moscow, PNIIS), 176 pp. (in Russian).
- Kotler, E. & Burn, C.R. 2000. Cryostratigraphy of the Klondike 'muck' deposits, westcentral Yukon Territory. *Canadian J. Earth Sciences* 37, 849-861.
- Lawson, D.E. 1982. *Long-term modifications of perennially frozen sediment and terrain at East Oumalik, northern Alaska*. CRREL Rep. 82-36, 33 pp.
- Péwé, T.L. 1954. *Effect of permafrost upon cultivated fields*. U.S. Geological Survey Bulletin, 989F, pp. 315-351.
- Péwé, T.L. 1975. *Quaternary geology of Alaska*. U.S. Geological Survey professional paper 835. Washington: Government Printing Office, 145 pp.
- Popov, A.I. 1967. *Permafrost features in Earth crust (Cryolithology)*. Moscow State University Press: Moscow (in Russian).
- Romanovskii, N.N. 1977. *Formation of polygonal-wedge structures*. Nauka, Novosibirsk, 212 pp. (in Russian).
- Shumskii, P.A. 1959. Ground ice. In *Principles of Geocryology Part 1. General Geocryology*. P.F. Shvetsov, and B.A. Dostovalov (eds.). Moscow, USSR Academy of Sciences, pp. 274-327 (in Russian). Technical translation 1130 Ottawa, National Research Council of Canada, 1964.
- Shur, Y. 1977. *Thermokarst (on thermo-physics fundamentals of the development of the process)* Moscow: Nedra (in Russian).
- Shur, Y. 1988. *Upper horizon of permafrost and thermokarst*. Novosibirsk: Nauka (in Russian).
- Soloviev, P.A. 1962. Alas relief of Central Yakutia and its origin. In *Permafrost and Related Features in Central Yakutia*. N.A. Grave (ed.). Moscow: The Academy of Sciences of USSR Press, pp. 38-54 (in Russian).
- Yurtsev, B.A. 1981. *Relic steppe complexes of North-East Asia*. Novosibirsk, Nauka, 168 pp. (in Russian).
- Vasil'chuk, Y.K. 1992. *Oxygen isotope composition of ground ice*. Moscow, Moscow State University (in Russian).
- Velichko, A.A. 1973. *The natural process in Pleistocene*. Moscow, Nauka (in Russian).
- Washburn, A. 1973. *Periglacial Processes and Environment*. New York: St. Martin Press.

Vegetation Patterns of Retrogressive Thaw Slumps, Herschel Island, Southern Beaufort Sea, Yukon Territory, Canada

Heather A. Sloan, Wayne H. Pollard
McGill University, Montreal, Canada

Abstract

Arctic landscapes underlain by massive ground ice and ice-rich permafrost are inherently unstable and often display surficial evidence of past thaw subsidence. Retrogressive thaw slumps are permafrost thaw features that are progressively backwasting and result in dramatic changes to the landscape. The cyclic pattern of disturbance and stabilization related to these thaw slumps results in a patchy tundra landscape where geomorphic units reflect the stage of stabilization and the time since disturbance. This work describes the vegetation and soil characteristics of these geomorphic units for three active, polycyclic retrogressive thaw slumps on Herschel Island, YT. Three geomorphic units were defined for each slump. Species presence, diversity, and cover are used to describe the plant community. Soil characteristics measured include pH, active-layer depth, and soil temperature. Distinct vegetation communities are associated with the geomorphic units of each retrogressive thaw slump studied, representing their relative age and the degree of stabilization.

Keywords: biogeomorphology; ecology; Herschel Island; permafrost; thaw slump; vegetation.

Introduction

Vegetation exerts strong controls on local ecosystem processes. Therefore, understanding the effects of disturbance on short-term and long-term revegetation patterns is a critical component of understanding the effects of climate change on the Arctic. Arctic landscapes underlain by massive ground ice and ice-rich permafrost are inherently unstable, and even moderate warming is likely to cause a massive increase in surface subsidence due to thawing (Forbes et al. 2001). Despite this, successional relationships related to permafrost degradation are very poorly understood (Burn & Friele 1989).

While the examination of individual ecosystem components (e.g., geomorphology and vegetation) have their particular uses, the linking and aggregating of components into ecosystems with covarying climate, geomorphology, surface forms, hydrology, and smaller scale features such as vegetation can provide a much broader range of information necessary for ecosystem management (Jorgenson et al. 1999). The tundra landscape is perhaps best understood as a mosaic of interactions between past and present disturbances nested in energy, moisture, nutrient, and disturbance gradients. These, in turn, are affected by climate, physiography, soils, hydrology, flora, and fauna (Jorgenson et al. 1999).

Retrogressive thaw slumps are a particularly dynamic type of thaw subsidence in permafrost environments. Retrogressive thaw slumps are permafrost thaw features that are progressively backwasting (characterized by a retreating headwall) and tend to go through cycles of activity, resulting in dramatic changes to the landscape. Due to their dynamic nature, thaw slumps have their own unique set of variables that influence patterns of revegetation.

In an attempt to determine if distinct vegetation communities are related to current and previous episodes of disturbance in the ice-rich Western Arctic, this study investigates vegetation communities and corresponding soil properties associated with different geomorphic units related to retrogressive thaw slumps.

Study Area

Field activities were undertaken at three retrogressive thaw slumps on Herschel Island, Yukon Territory, Northern Canada. Field activities were performed from July 29 to August 8, 2009, on Herschel Island, (69°36'N, 139°04'W), located in the Yukon Coastal Plain (Fig. 1). Herschel Island is composed primarily of deformed, fine-grained marine sediment dredged from the Herschel Basin and pushed into place by the Laurentide ice sheet during the Buckland Stage of the Wisconsin Glaciation (Mackay 1959, Lantuit & Pollard 2008). Ground ice is widespread on Herschel Island and underlies most of the island in the form of ice wedges, pore ice, segregated ice lenses, intrasedimental ice, and buried snowbank/glacier ice (Pollard 1990). These ice-rich sediments are easily eroded following any geomorphic disturbance, and the island is therefore subject to high rates of surface and coastal erosion, as evidenced by the more than 100 active retrogressive thaw slumps on the island (Lantuit & Pollard 2008).

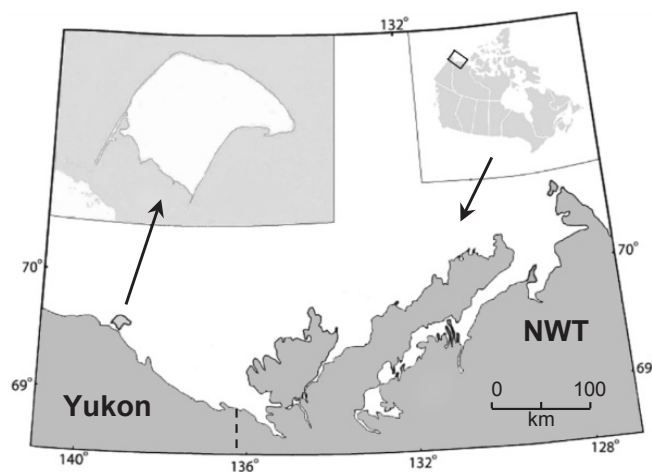


Figure 1. Herschel Island, located on the Yukon North Slope.

Retrogressive thaw slumps are initiated when ice-rich soil is exposed by disturbance and generally become stabilized within 30 to 50 summers (Burn & Friele 1989, French 1996). Due to their extent and varying moisture regimes, stabilized and semi-stabilized slump floors provide an environment where the recovery and re-establishment of natural conditions after disturbance may be studied (Burn & Friele 1989).

Methods

For each thaw slump selected for study, three geomorphic landscape units reflecting distinct stages of recovery were visually delineated with the use of aerial photography and on-site assessment (Fig. 2). A transect parallel to the thaw slump headwall and completely contained within the geomorphic unit was established at each site, and six 1 x 1 m sample plots were randomly placed along each transect for a total of 18 plots per thaw slump. At each sample plot, vegetation data collected included the estimated percent cover of each species present. Species diversity was calculated using the Shannon Index and the Simpson Index of alpha diversity (α -diversity). The Simpson Index takes into consideration both the number of species present and the relative abundance of each species, and therefore it expresses the probability of two randomly selected individuals belonging to different species (Brower et al. 1997). It is calculated according to the following equation:

$$SIDI = 1 - \sum_{i=1}^N p_i \times p_i \quad (1)$$

where N is the number of species and p_i is the relative abundance of each species (i) (Nagendra 2002). The Shannon Index expresses the average uncertainty in predicting which species a randomly selected organism will belong to. It is calculated as follows:

$$SHDI = 1 - \sum_{i=1}^N p_i \times \ln p_i \quad (2)$$

where N is the number of species and p_i is the proportional abundance of the i th type (Nagendra 2002).

Soil temperature was recorded at depths of 1 cm and 10 cm using a calibrated digital thermometer. Active-layer depth was also measured at each plot using a steel permafrost probe, and soil grab samples of the upper 10 cm of soil were collected adjacent to each plot. Laboratory analysis of pH was performed and followed McKeague (1978). The voucher specimens of the vascular plants collected in this study are housed in the McGill Herbarium and at the Aurora Research Institute, Inuvik, NWT.

Results and Discussion

Soil

All three retrogressive thaw slumps studied displayed distinct and consistent differences between the soil and plant characteristics of each geomorphic zone. Even though the study slumps have different aspects and locations (coastal versus inland), there is a consistent trend in the pH values recorded at

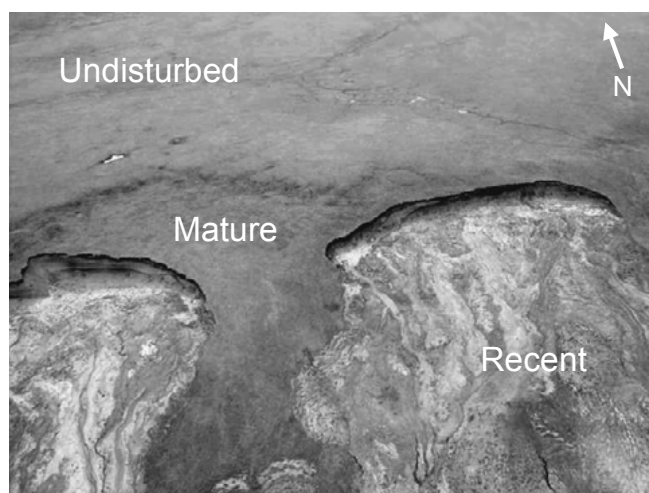


Figure 2. Geomorphic zones of study site A.

Table 1. Active-layer depth, soil temperature, and pH of tundra units of different ages.

| Geomorphic unit | Avg. active-layer depth (cm) | Avg. pH | Avg. surface temp. (°C) | Avg. 10cm temp. (°C) |
|-----------------|------------------------------|---------|-------------------------|----------------------|
| Undisturbed | 33.5 | 5.8 | 11.1 | 5.3 |
| Mature | 53.0 | 7.2 | 10.3 | 5.8 |
| Recent | >77.2 | 7.7 | 14.7 | 11.0 |

each geomorphic unit of each slump. In all cases, the lowest soil pH was recorded in the Undisturbed unit, followed by the Mature unit and the Recent unit (Table 1). Consistent with the existing literature concerning active-layer depths at thaw slump sites, the active layer is at its greatest thickness within the Recent unit, followed by the Mature unit, and is shallowest beneath the Undisturbed unit (Lambert 1972, Lantz et al. 2009) (Table 1). Temperatures recorded at a depth of 10 cm also follow this pattern, while surface soil temperature is highest at the Recent unit, followed by the Undisturbed unit, reaching its lowest in the Mature unit (Table 1).

The absence of vegetation cover and the prevalence of dark colored mud surfaces in the Recent zone result in the highest surface and 10-cm temperatures recorded in this study. As would be expected, the depth of the permafrost table follows this general trend; as plant cover and canopy complexity increase following disturbance, the active-layer depth decreases. Since the Mature zone lacks the diversity of vegetation canopy layers that are present in the Undisturbed zone, there is less microclimate variation, and the lack of the insulating air pockets created by plant cover might explain the difference of temperature between the Mature and Undisturbed zones.

The pH values recorded in this study directly reflect the stages of slump maturity, where the most acidic soils are found in the Undisturbed zone, followed by the Mature and Recent zones. These findings are consistent with Lambert's (1972)

study of thaw slumps, which concluded that the exposed soil of a mudflow is only moderately to slightly acidic compared to the strongly acidic condition of the surrounding climax community (pH 4.6). The recorded pH values are also consistent with the study by Kokelj et al. (2002), which showed that at disturbed sites the soluble cation concentrations in the active layer were greater than in the undisturbed active layer by 1–2 orders of magnitude, but that the concentration declined with the age of disturbance. Kokelj et al. (2002) also found higher concentrations of soluble cations in the underlying permafrost than in the active layer at all study sites on Herschel Island, suggesting that the higher observed pH of the Recent zone is likely a result of it being composed of newly reconstituted material from the cation-rich slump headwall. The increasing acidity recorded in the Mature and Undisturbed zones is likely the result of both an acidic organic surface layer developing at pace with vegetation regrowth and cation leaching from the active layer. This leaching is highest when the slump headwall is actively melting and large amounts of supernatant water and fluidized sediment are flowing downslope in leveed channels (Lantuit & Pollard 2008). Even in stabilized areas of the slump floor, cation leaching likely continues as the supersaturated sediments slowly dewater through deeply incised drainage channels that persist for decades (Lantuit & Pollard 2008).

Vegetation

As part of the Northern Mountains and Coastal Plain Ecoregion, the predominant Undisturbed vegetation type is sedge and cottongrass tussocks, described by Smith et al. (1989) as

the characteristic terrain of the oldest and most stable land surface on Herschel Island (Oswald & Senyk 1977). Undisturbed sites surrounding retrogressive thaw slumps are hummocky and support ericaceous shrubs, prostrate willows, forbs, and moss (Table 2). This zone has the highest plant community diversity, and several species occur exclusively in this geomorphic unit (Tables 2, 3). This is consistent with the conclusions of previous arctic vegetation studies, which found that species richness is typically lower at disturbed sites than at undisturbed sites because low germination rates combine with reduced habitat heterogeneity at disturbed sites to decrease species richness (Ebersole & Webber 1983, Forbes et al. 2001).

The plant community diversity of the Mature zone is lower than the Undisturbed zone, having been disturbed at all sites by a previous cycle of slumping (Table 3). As air photos show that the Mature geomorphic zone at each study site has been stable for over 60 years, the altered abiotic conditions such as pH, nutrient availability, and ground thermal regime observed suggest that the effects of disturbance endure for decades to centuries, and that the vegetation community in the Mature zone is still developing (Lantz et al. 2009). Since this zone is a reconstituted slump scar, the hummock/hollow and tussock surfaces characteristic of the Undisturbed zone are absent. Thus there are fewer microhabitats for species to inhabit, and species diversity is therefore reduced (Smith et al. 1989). In the case of thaw slump scars specifically, the residual concave morphology can likely be sustained for centuries, meaning that elevated snow accumulation and distinct abiotic conditions also persist, inhibiting ground heat loss and delaying freeze-

Table 2. Vegetation summary for the four geomorphic zones: Undisturbed (U), Mature (M), and Recent (R).

| Species | U (n= 18) | | M (n= 18) | | R (n= 18) | |
|---|-----------|----|-----------|----|-----------|----|
| | F | %C | F | %C | F | %C |
| <i>Eriophorum vaginatum</i> | 6 | 37 | | | | |
| <i>Lupinus arcticus</i> | 5 | 10 | | | | |
| <i>Salix planifolia</i> ssp. <i>pulchra</i> | 7 | 8 | | | | |
| <i>Salix reticulata</i> | 10 | 16 | 2 | 5 | | |
| <i>Dryas integrifolia</i> | 17 | 22 | 11 | 11 | | |
| <i>Pedicularis lanata</i> | 12 | 2 | 10 | 2 | | |
| <i>Astragalus umbellatus</i> | 9 | 1 | 10 | 4 | | |
| <i>Oxytropis deflexa</i> | 2 | 1 | 6 | 11 | | |
| <i>Alopecurus alpinus</i> | 1 | 1 | 10 | 4 | | |
| <i>Festuca</i> sp. | | | 8 | 2 | | |
| <i>Arctagrostis latifolia</i> | 6 | 4 | 10 | 2 | 3 | 12 |
| <i>Salix arctica</i> | 13 | 8 | 18 | 34 | 6 | 7 |
| <i>Poa</i> sp. | 7 | 3 | 3 | 1 | 6 | 2 |
| <i>Senecio congestus</i> | | | | | 9 | 2 |
| <i>Matricaria ambigua</i> | | | | | 3 | + |

n, number of quadrats placed in each geomorphic zone

F, frequency of occurrence in n quadrats, each 1 x 1m

%C, average percent cover in n quadrats; +, a value less than 1%

Table 3. Average Simpson Index and Shannon Index value for each geomorphic zone.

| Geomorphic unit | Average Simpson Index value | Average Shannon Index value |
|-----------------|-----------------------------|-----------------------------|
| Undisturbed | 0.71 | 1.68 |
| Mature | 0.60 | 1.3 |
| Recent | 0.30 | 0.51 |

back compared to the undisturbed tundra (Lantz et al. 2009). The specific vegetation community repeats at each stabilized slump scar in this study and many others observed on Herschel Island. This consistency is likely due in part to the fact that in arctic environments, a shortage of efficient colonizers means that many of the same species occur repeatedly in disturbances of different ages and origins (Forbes et al. 2001).

The most dynamic geomorphic unit is the Recent unit, and this is reflected in its characteristic vegetation community. As the permafrost in the headwall of a thaw slump melts, the headwall retreats upslope, and soil falls onto the footslope to produce a zone of viscous mud (Lantuit & Pollard 2008). As the exposed ground ice melts, the overlying vegetation mat and active layer collapse into the slump and appear as islands of vegetation surrounded by liquid mud or water; these islands are often drowned and overtaken by successive mud flows (Lambert 1976) (Fig. 3). As the distance from the headwall increases, pools of supersaturated sediment and standing water transition to plastic mud and finally to dry, desiccated mud (Lantuit & Pollard 2008). In large slumps, the distance from the headwall to the dry area may be 30 to 40 m (Lantuit & Pollard 2008). The process of stabilization is not uniform, however, as headwall sections with low ice contents tend to stabilize while retreat continues in adjoining areas that are ice rich, creating a dynamic pattern of slump floor stability. The degree of disturbance associated with a retrogressive thaw slump means that the seed bank is all but destroyed and a few pioneer species compose most of the vegetation community of the Recent zone (Table 2). The exception to this rule is at the edges of the slump, or where “islands” of vegetation from the headwall have managed to survive the journey to a more stable area of the slump floor. Initially these turf blocks may be species-rich, but with successive mud flows and desiccation of the soil, the majority of the species are eliminated (Figs. 4, 5).

Very few species occur in every geomorphic zone, and the overall tendency is for overlapping species to occur in adjacent zones (e.g., Undisturbed and Mature, Mature and Recent). In terms of a successional timeframe for Herschel Island, it is clear that the revegetation process proceeds over a long period of time, and though the Mature zone vegetation community may otherwise achieve the physical and floristic characteristics of the Undisturbed zone, this is interrupted by the polycyclic nature of these slumps. Indeed, Kokelj et al. (2002) attribute the high floristic diversity of Herschel Island in part to the cycle of permafrost degradation, resulting soil salinization, and cation leaching from the active layer created by polycyclicly.

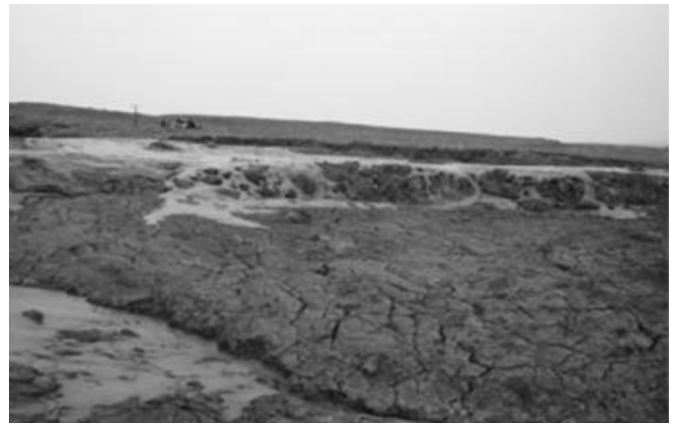


Figure 3. Previously established vegetation islands being consumed by new headwall melt.



Figure 4. A recent vegetation island containing living *Salix arctica*, *Myosotis alpestris*, and *Arctagrostis latifolia*.



Figure 5. As the turf block dries out and much of it is buried, often only *Salix arctica* survives.

Landscapes underlain by massive ground ice and ice-rich permafrost, such as those on Herschel Island, are inherently unstable and often display evidence of past and present thaw subsidence. Thermokarst and other forms of thaw induced erosion and mass wasting are naturally occurring processes on Herschel Island and play an important role in the evolution of permafrost landscapes. Local variation within

these landscapes is driven by factors such as topography, surface processes, and vegetation. Given the cyclic pattern of disturbance, stabilization, and subsequent revegetation of stabilized surfaces, there exists a patchy landscape surrounding disturbed surfaces where the vegetation pattern is a reflection of geomorphic stage and time since disturbance. In the case of retrogressive thaw slumps, distinct vegetation communities are associated with the geomorphic units of each retrogressive thaw slump, representing their relative age and the degree of stabilization. Where vegetation community overlap occurs, the tendency is for adjacent units to share species, and anomalies in this overall pattern of vegetation fidelity can be explained by the presence of vegetation remnants.

Changes in arctic vegetation may have already begun as a result of recent warming in the Arctic (Chapin et al. 1995, Tape et al. 2006), and the problem could be further complicated by successional species changes resulting from climate warming (Lantz et al. 2009). Given the expected increase of permafrost thawing and the importance of the resulting thaw-related landscape features, it is increasingly important to characterize the 'typical' revegetation patterns following disturbance in order to understand the geomorphic history of an area and predict future changes in the landscape. To this end, it is the recommendation of this paper that these patterns of revegetation should be studied in depth.

Acknowledgments

This research was supported by the Natural Science and Engineering Research Council of Canada (USRA and grant to W. Pollard) and ArcticNet (project 4.4). Exceptional field logistical support was provided by the Polar Continental Shelf Project (PCSP). Additional funds were provided through grants from the Northern Scientific Training Program (NSTP). Special thanks to M. Angelopoulos and N. Couture for their excellent field assistance. This manuscript has been enhanced by the insightful recommendations of two anonymous reviewers.

References

- Brower, J.E., Zar, J.H., & von Ende, C.N. 1997. *Field and laboratory methods for general ecology*, 4th Edn. New York: McGraw-Hill, 288 pp.
- Burn, C.R., & Friele, P.A. 1989. Geomorphology, vegetation succession, soil characteristics and permafrost in retrogressive thaw slumps near Mayo, Yukon Territory. *Arctic* 42: 31-40.
- Chapin, F.S., Shaver, G.R., Giblin, A.E., Nadelhoffer, K.J., & Laundre, J.A. 1995. Responses of arctic tundra to experimental and observed changes in climate. *Ecology* 76: 694-711.
- Ebersole, J.J. & Webber, P.J. 1983. Biological decomposition and plant succession following disturbance on the arctic coastal plain, Alaska. *Proceedings of the Fourth International Conference on Permafrost*, Fairbanks, Alaska, July 17-23, 1983: 266-271.
- Forbes, B.C., Ebersole, J.J., & Strandberg, B. 2001. Anthropogenic disturbance and patch dynamics in circumpolar arctic ecosystems. *Conservation Biology* 15: 954-969.
- French, H.M. 1996. *The Periglacial Environment*, 2nd Edn. Harlow, United Kingdom: Addison Wesley Longman Ltd., 341 pp.
- Jorgenson, M.T., Roth, J.E., Reynolds, M.K., Smith, M.D., Lentz, W., Zusi-Cobb, A.L., & Racine C.A. 1999. An ecological land survey for Fort Wainwright, Alaska. CRREL Report 99-9, US Army Corp of Engineers, Cold Regions Research & Engineering Laboratory, Hanover, NH.
- Kokelj, S.V., Smith, C.A.S., & Burn, C.R. 2002. Physical and chemical characteristics of the active layer and permafrost, Herschel Island, western arctic coast, Canada. *Permafrost and Periglacial Processes* 13: 171-185.
- Lambert, J.D.H. 1972. Plant succession on tundra mudflows: preliminary observations. *Arctic* 25: 99-106.
- Lambert, J.D.H. 1976. Plant succession on an active tundra mud slump, Garry Island, Mackenzie River Delta, Northwest Territories. *Canadian Journal of Botany* 54: 1750-1758.
- Lantz, T.C., Kokelj, S.V., Gergel, S.E., & Henry, H.R. 2009. Relative impacts of disturbance and temperature: persistent changes in microenvironment and vegetation in retrogressive thaw slumps. *Global Change Biology* 15: 1664-1675.
- Lantuit, H. & Pollard, W.H. 2008. Fifty years of coastal erosion and retrogressive thaw slump activity on Herschel Island, southern Beaufort Sea, Yukon Territory, Canada. *Geomorphology* 95: 84-102.
- Mackay, J.R. 1959. Glacier ice-thrust features of the Yukon coast. *Geographical Bulletin* 13: 5-21.
- McKeague, J.A. 1978. *Manual on soil sampling and methods of analysis*, 2nd Edn. Ottawa: Soil Research Institute, Agriculture Canada, 212 pp.
- Nagendra, H. 2002. Opposite trends in response for the Shannon and Simpson indices of landscape diversity. *Applied Geography* 22: 175-186.
- Oswald, E.T. & Senyk, J.P. 1977. *Ecoregions of Yukon Territory*. Canadian Forestry Service, Environment Canada, 115 pp.
- Pollard, W.H. 1990. The Nature and origin of ground ice in the Herschel Island area, Yukon Territory. *Proceedings of the Fifth Canadian Conference on Permafrost*, Quebec City, June 6-8, 1990: 23-30.
- Smith, C.A.S., Kennedy, C.E., Hargrave, A.E., & McKenna, K.M. 1989. *Soil and vegetation of Herschel Island, Yukon Territory*. Ottawa: Agriculture Canada, 101 pp.
- Tape, K., Sturm, M., & Racine, C. 2006. The evidence for shrub expansion in northern Alaska and the pan-arctic. *Global Change Biology* 12: 686-702.

A Community-Based Permafrost/Active Layer Monitoring Program

Elena Sparrow, Kenji Yoshikawa
University of Alaska Fairbanks, USA

Abstract

The Permafrost/Active Layer Monitoring Program is a science research and education project to establish long-term permafrost and active layer monitoring in Alaskan communities and in other regions with permafrost. Teachers and their students in almost 200 schools in Alaska collect temperature data on permafrost and the seasonal length and depth of the active layer. The project collects baseline data with wide spatial coverage. It contributes to Alaskan students' scientific knowledge, and it improves their science process skills and their ability to conduct research even in remote communities.

Keywords: active layer; communities; frost tube; GLOBE; permafrost; season.

Introduction

The Arctic Impact Assessment Report (ACIA 2004) examined arctic climate change and found that between the 1950s and 2003 average annual temperatures have risen 2 to 3°C and up to 4°C in winter. Permafrost regions occupy about one-quarter of the earth's land surface. Permafrost is one of the most important components of the arctic terrestrial system, and it is one of the most sensitive physical elements of the landscape to climate change.

Therefore, observing the interactions between permafrost and other components of the arctic system (climate, hydrology, biogeochemistry, vegetation), especially during a period of possible climatic warming, is among the most important aspects of arctic research. The changing properties of permafrost play an important role in driving the ecosystem balance, and they affect carbon and water cycles as well (Oechel et al. 2000). Additionally, man-made structures on or near ice-rich permafrost can suffer severe damage from thaw-induced ground settling, which will accelerate if mean annual temperatures continue to rise (Osterkamp et al. 2000, Romanovsky & Osterkamp 2001).

Within the sensitive permafrost region, the zone of discontinuous permafrost is the most likely to respond to climatic warming. Most rural communities in Alaska are located in this zone. Throughout the circumpolar North, the boreal forest widely overlaps the area of discontinuous permafrost (Péwé 1975). Thermal conditions of discontinuous permafrost are quite unstable, with the ground being close to thawing, and temperatures often hovering at -1°C or warmer.

The Permafrost/Active Layer Monitoring Program (PALM) is a long-term research and education project at the University of Alaska Fairbanks (UAF). It monitors ground permafrost temperature and depth of the active layer in arctic communities. This builds on work begun in 2005 to establish long-term monitoring of permafrost and in 2007 to monitor the active layer in sites adjacent to schools in Alaskan communities. In addition to extending our knowledge of the arctic environment, the program involves school-age students in urban and rural communities. This is a unique collaboration opportunity in that it 1) uses scientifically accurate instruments, 2) is led and supervised by scientists, including instrumentation set-

up and data quality check, and 3) has an observation network organized by teachers and students.

Most of the monitoring sites are located in remote communities, where the majority of residents depend on a subsistence lifestyle. Changes in climate, length of seasons, and permafrost conditions directly impact natural resources and subsistence activities. Changes in permafrost conditions also affect local ecosystems and hydrological regimes and can influence the severity of natural disasters.

Project Goals

The overall goals of the project are 1) to increase understanding of the thermal state of permafrost and its effect on the natural environment and local ecosystem in the Arctic, and to contribute to the general knowledge of the earth's climatic pattern, and 2) to provide a strong educational outreach program involving remote communities.

The objectives are 1) to monitor the permafrost temperature of the ground and the depth of the active layer in Alaskan communities, 2) to increase the spatial coverage of monitoring sites to include all Alaskan communities, 3) to provide students in local schools with hands-on scientific experience and an opportunity to see the connection between science education and science research, and 4) to increase student understanding of permafrost, the active layer, hydrology, and the arctic climate system.

Methods

We established monitoring sites to track permafrost and active layer change over time, at or near communities throughout the permafrost region in Alaska and in other areas where there is permafrost, such as Canada, Greenland, Mongolia, China, Japan, Scandinavia, and Russia. This paper focuses on research and data collection in Alaska. Students and teachers in local schools, including remote Alaskan sites, participate in the program by reading measurements at the monitoring sites, recording data, comparing data on-line with other schools, and discussing what they learn.

To ensure scientific integrity, the scientist installed all of the monitoring instruments and selected the sites representa-

tive of the surrounding biome and thermal conditions. We used a borehole, casing pipes, and drill equipment to establish monitoring stations. For each monitoring station we drilled a borehole 3 to 6 m deep for measuring ground temperatures, and another borehole 1 to 5 m deep for monitoring the seasonal/active layer. In one borehole, we placed a datalogger attached to thermistors inserted at different depths. In the other, we inserted a frost tube. We also installed a small one-channel datalogger connected to an air temperature sensor next to the frost tube. Freezing degree days (freezing index) and thawing degree days (thawing index), as well as mean annual temperature, can be calculated from the surface temperature data. The remote location of most villages necessitated the development of a portable, lightweight, small-diameter drill system and a method of drilling through frozen ground.

As part of this project and in collaboration with the GLOBE–Seasons and Biomes program, we developed a frost tube or active layer measurement protocol for teachers and students in Alaska and other parts of the world. This includes field guides for students on how to make the frost tube as described below, how to set up a study site, and how to do the measurements and record data. These materials are currently posted at our website (<http://www.uaf.edu/permafrost>). GLOBE (Global Learning and Observations to Benefit the Environment) is an international earth/environmental science and education program in more than 110 countries, which engages primary and secondary students and their teachers in conducting research investigations at or close to their schools and in collaboration with scientists (www.globe.gov). Seasons and Biomes is one of four GLOBE earth system science projects and an IPY project.

A frost tube is an instrument that measures when and how deeply soil freezes. It is made of 3 tubes that fit inside each other and are inserted in the hole drilled in the ground. The innermost tube is marked every 5 cm and filled with colored water; it fits inside a radiant heat tube (sealed on the bottom), which fits inside a PVC pipe, open on both ends (Figs. 1, 2). The innermost tube in the frost tube is about 12 mm in diameter. The frost tube's underground end reaches to the deepest level of frost or to the permafrost layer. The aboveground end (about 1 m long) is capped to prevent air temperature from influencing the underground temperatures and to keep snow and water out. The innermost tube with colored water shows where ice has formed underground when it is lifted out from the two outer tubes, and the depth where ice has formed is noted. It is easy to see the boundary between ice and unfrozen water because the ice looks clear and the water is colored. During frost heave, only the outermost tube is affected. Figure 3 shows seasonal ground freezing during the year.

Classroom lessons on permafrost have been developed for students at all grade levels. Learning activities help students to understand the science concepts in the frost tube protocol. In addition to the scientific measurement protocols and learning activities, we developed videos of the adventures of a superhero, Tunnel Man. The videos were made available on the project website as well as on YouTube.

Results

More than 200 monitoring sites have been established in Alaska. Several students have been using the data for their projects and have been inspired to continue their studies. The data gathered from these stations are shared with other schools and made available to the public through the project website.

Pre- and post-assessments administered to students provided data on growth in student knowledge and learning of permafrost science and inquiry/process skills. Students demonstrated an average increase in achievement of 74.9%. Analysis of the pre- and post-tests showed significant student improvement from pre-test to post-test in all three years of the program. Overall, students' average improvement was 74.9% ($n = 867$), a significant improvement ($Z = 25.201$, $P < 0.001$) (Larson et al. 2009).

Active layer monitoring using the frost tube protocol includes the rationale for student involvement given below:

Purpose

The purpose of the project is to monitor the timing and depth of freezing in soil at a frost tube site or a designated GLOBE study site.

Overview

Students will construct a frost tube that is inserted into a hole in undisturbed and uncompacted soil. During the cold months, students measure the depth at which water in the frost tube has frozen to get an indication of when the surrounding soil has also frozen.

Student Outcomes

Students will be able to:

- Observe when water in the frost tube freezes.
- Collect and analyze data related to freezing of soil to understand how soil temperature and moisture coincide with changes in seasons across different biomes.
- Examine relationships among air, soil, and permafrost.
- Communicate project results to other GLOBE schools.
- Collaborate with other GLOBE schools (within your country or in other countries).
- Share observations by submitting data to the GLOBE archive.
- Compare the timing and depth of freezing in soils in different regions around the world.
- Predict the timing and depth of freezing for upcoming seasons (for advanced students).

Science Concepts

Earth and Space Sciences

- Some regions of the world have freeze/thaw cycles, and these occur seasonally. Other regions do not have these cycles, as the soil never freezes or thaws.
- Water infiltrates into the soil and freezes at certain depths during the seasonal cycles.
- Depending on the geographical location of the soil being tested, some water in soil may never thaw or freeze.

- Water circulates through soil, changing the properties of both the soil and the water.
- The depth of snow and/or organic material (moss, leaf litter, etc.) can impact how deep soil freezes.

Life Sciences

- The temperature of the soil will impact the type of life growing on and in it and how it grows. (Organisms' functions relate to their environment.)
- The type of vegetation growing on soil can influence how deep soil freezes and thaws as well as the rate at which it freezes and thaws. (Organisms change the environment in which they live.)

Scientific Inquiry Abilities

- Use appropriate tools and techniques including mathematics to gather, analyze, and interpret data.

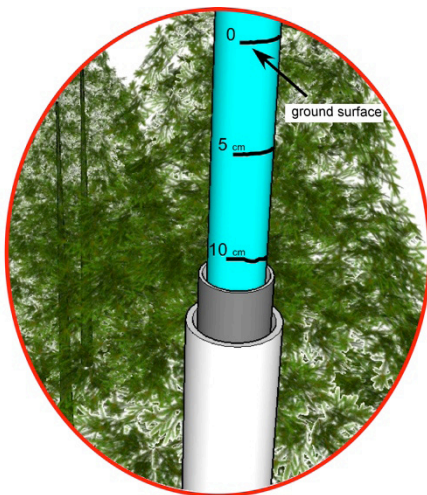


Figure 1. A view of the frost tube showing inner, middle, and outer tubes.

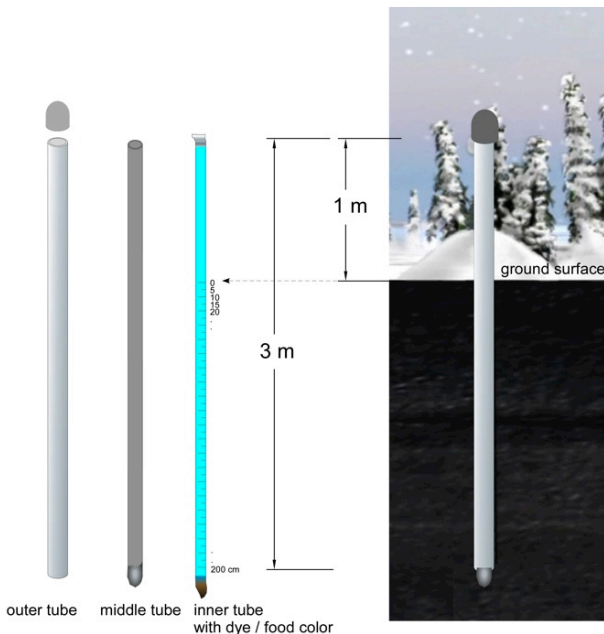


Figure 2. Components of a frost tube showing inner, middle, and outer tubes.

- Develop descriptions and predictions using evidence.
- Recognize and analyze alternative explanations.
- Communicate procedures and explanations.

The Frost Tube program has been a great success in Alaskan communities because it was relatively easy to install and cost efficient and because it is a highly dynamic activity for students. Examples of data collected are given in Figures 4 and 5. In Figure 4, using the surface temperature data (obtained from the air temperature sensor near the frost tube), freezing degree days (freezing index) and thawing degree days (thawing index) as well as mean annual temperature were calculated. Igiugig had more freezing degree days and showed soil freezing at lower depths than Homer, with lower freezing degree days.

Frost depth measurements from different schools are shown in Figure 5. The graph from Fairbanks Moosewood Farm Home School show what data look like when students/teachers are able to monitor daily or, in the case of Igiugig, weekly. The graph suggests that more frequent data collection gives a more complete picture, but the once-a-week regimen still gives enough useful information. Also, the deepest frost depths occurred in the spring months.

Permafrost Temperature Monitoring

For maintenance purposes and educational outreach, the majority of our permafrost monitoring sites are located at or near schools or national park headquarters. This allows easier access to equipment, provides educational opportunities by involving students and teachers in research, and facilitates data collection. Figure 6 shows the locations of the monitoring

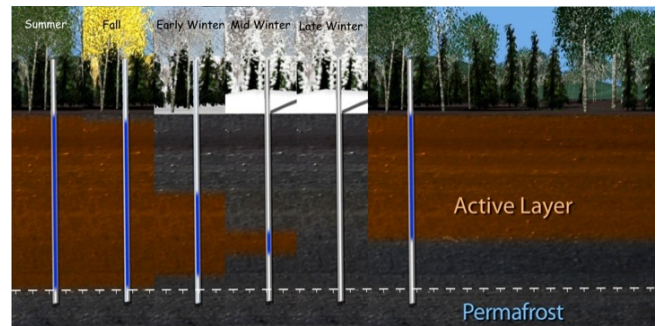


Figure 3. Progression of freezing through the seasons.

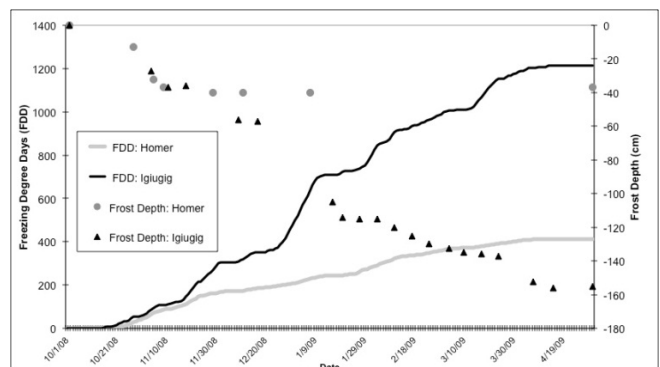


Figure 4. Freezing degree days and frost depths at Homer and Igiugig, Alaska.

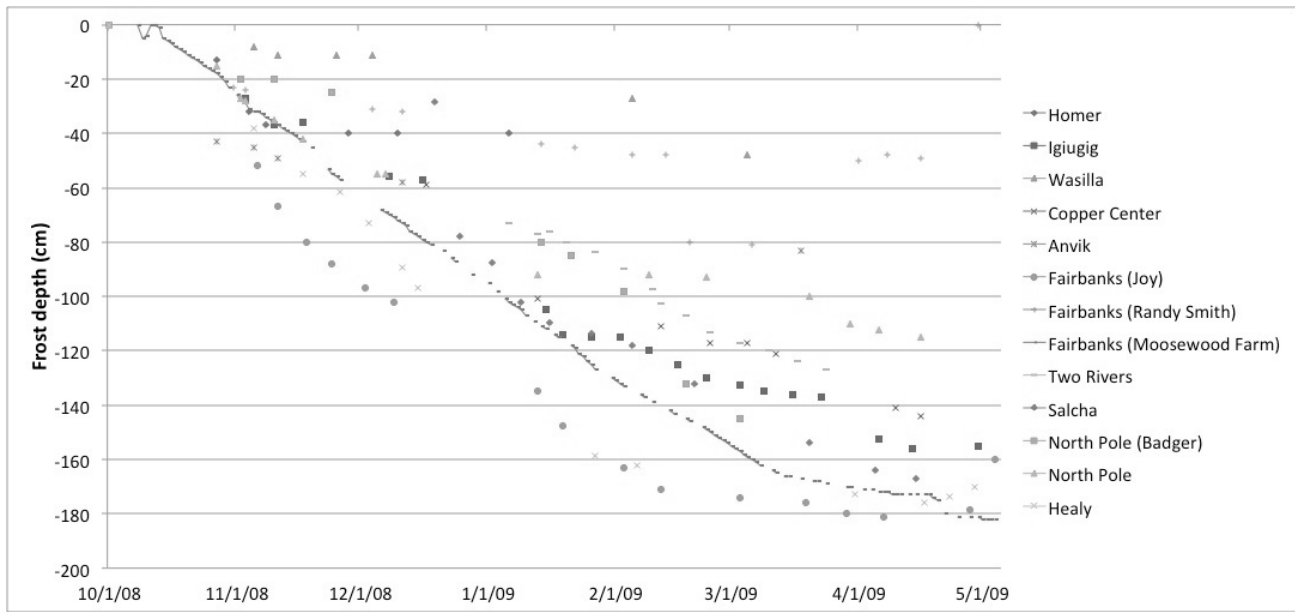


Figure 5. Frost depth measurements in some urban and rural communities in Alaska.

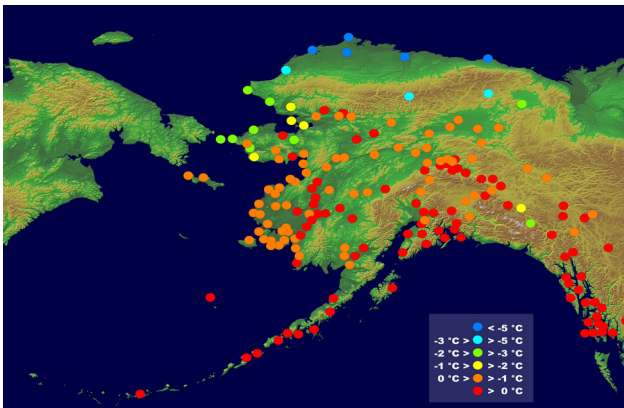


Figure 6. Map of monitoring network and ground temperature distributions in Alaska

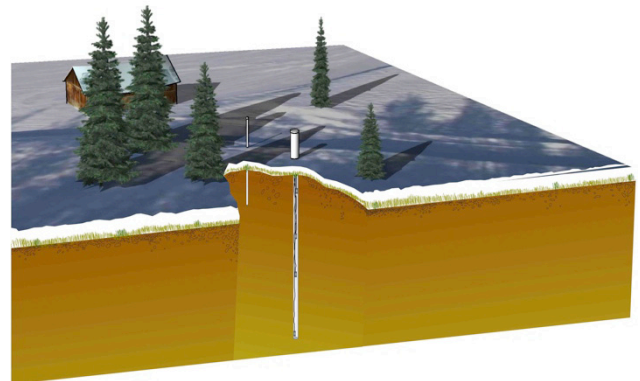


Figure 7. Temperature borehole and frost tube.

sites and ground temperature distributions in Alaska. Figure 7 shows a diagram of installed instruments, and Figures 8a and 8b are examples of permafrost temperatures for the villages of Emmonak and Wainwright, respectively.

This project establishes baseline data for long-term data collection on ground temperature and conditions in situ over a wide area, including almost all Alaska communities. These data will be useful to scientists for their research in the same way that GLOBE data are useful to scientists in their research (Gazal et al. 2008, Robin et al. 2007). The data in this project will contribute to the Global Temperature Network on Permafrost and perhaps even to the Thermal State of Permafrost project, and will be useful to scientists who will be looking for long-term data for the next IPY.

The biggest contributions of the project are the spatial distribution of baseline data and the involvement of teachers in helping students to collect data. Data quality is kept high and reliable through scientist involvement. The project needs at least one dedicated scientist and funding to set up the monitoring program. For example, instruments such as the datalogger, thermistors, and pipes cost \$300. Datalogger batteries need to

be changed periodically and the data downloaded. There are other costs such as travel, drilling equipment, and time. The main cost of installing permafrost and active layer monitoring stations has already been covered. The hope is to maintain the instruments and measurements until the next IPY. The challenge is how to maintain the funding stream, as well as community interest and involvement (teachers, students, and community members), especially with the high teacher turnover rate in remote villages.

Permafrost Failure Impacts Rural Communities

The discontinuous permafrost region in northwestern America is particularly sensitive to climatic change. Intense summer rain or extreme summer drying can accelerate rates of thermal erosion by changing the surface conditions in areas of ice-rich permafrost. Parts of Yukon Territory in Canada and parts of northwestern Alaska that were covered by glaciers during the Last Glacial Maximum are widely recognized as being among the most ice-rich and thaw-sensitive areas. In particular, glaciated areas are prone to develop retrogressive

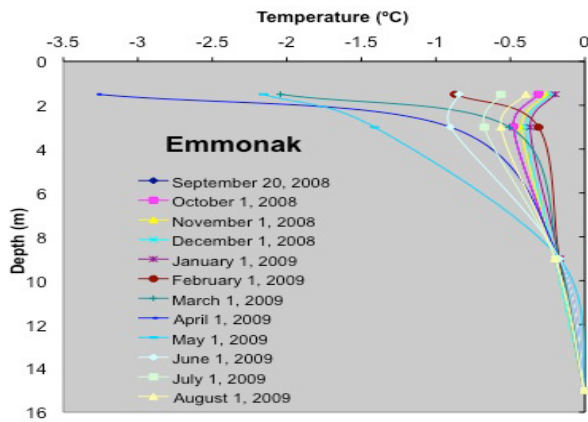


Figure 8a. Permafrost temperature profile from the village of Emmonak.

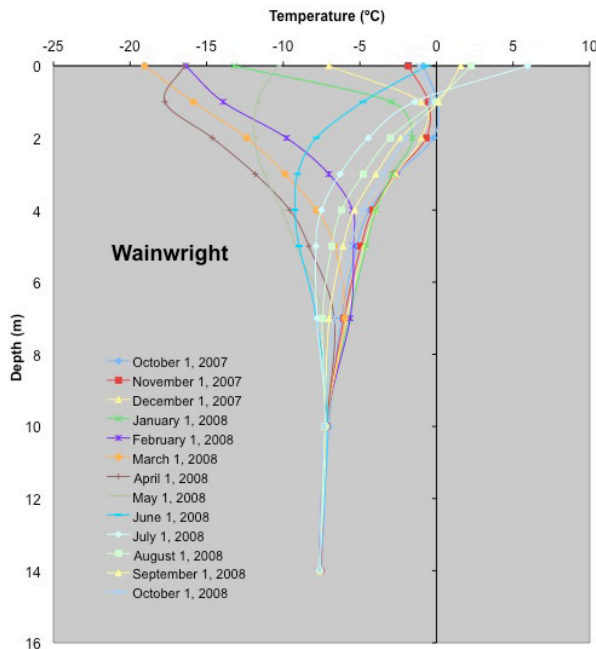


Figure 8b. Permafrost temperature profile from the village of Wainwright

thaw slumps by the thawing of buried glacial ice bodies. The volume of sediment and ground ice eroded by retrogressive thaw slump activity has discharged large amounts of suspended sediments into river systems (Fig. 9). Large quantities of suspended sediments have impacted drinking water sources for rural communities and may jeopardize critical fish spawning habitat.

Conclusions

This community-based permafrost/active layer monitoring program is successful from both scientific and education viewpoints. Nearly 200 sites of temperature measurements reveal the thermal state of permafrost in Alaska, especially in communities located in the discontinuous or southern limit of the permafrost zone. We have a better understanding of and more accurate information on the distribution of the



Figure 9. Retrogressive thaw slump near Selawik.

permafrost and ground thermal conditions of each community in the program. At the same time, these datasets help inform engineering practices used by the community. From the educational viewpoint, students have gained knowledge in permafrost science and inquiry/process skills and the opportunity to conduct research in their communities close to their schools.

Communities have also become increasingly interested in this project, not only as an educational program, but also for its implications for disasters such as mud slides, loss of the capability to store food in the ground, and water pipes bursting from ground freezing at shallower depths. Challenges in education outreach include the high cost (dollars and time) of reaching the remote study sites scattered across the vast Alaskan landscape, and how to increase student understanding of the scientific concepts in the long-term study of permafrost and the active layer. Through this project, students in remote Alaskan communities learn science in a way that is meaningful to their daily lives. In addition, they experience research investigations within a larger scientific community and thus expand their worldview.

Acknowledgments

We thank Kathy Bertram and staff of the UAF Geophysical Institute Education Department for working on the PALM program as part of ACMP. We thank Drs. Ming-Ying Wei (NASA), David Campbell (NSF), Renee Crain (NSF), Sharon Locke (NSF), Panya Lipovsky, and Sarah Laxton (Yukon Geological Survey), and the staff of CH2MHill for logistical support. We also thank Martha Kopplin, Fran Pedersen, Tohru Saito, and all science teachers, students, and principals of our network schools for field support and data collection. Main project funding was provided by NSF/NASA Grant DRL-0731739, NSF GLOBE Seasons and Biomes GEO-0627941 and Alaska EPSCoR.

References

- ACIA. 2004. Impacts of a Warming Climate: Arctic Climate Impact Assessment. Cambridge University Press. Available at <http://www.uaf.edu/acia/numbers>.

- Gazal, R., White, M., Gillies, R., Rodemaker, E., Sparrow, E., & Gordon, L. 2008. GLOBE students, teachers, and scientists demonstrate variable differences between urban and rural leaf phenology along a multi-continent bioclimatic gradient. *Global Change Biology*, 14, 1-13, doi:10.1111/j.1365-2486.2008.01602.x.
- Larson, A.M., Crevensten, D., & Corven, B. 2009. Arctic Climate Modeling Program Final Evaluation Report, Fairbanks, Alaska USA, Goldstream Group Inc. 35 pp.
- Oechel, E.C., Vourlitis, G.L., Hastings, S.J., Zulueta, R.C., Hinzman, L.D., & Kane, D.L. 2000. Acclimation of ecosystem CO₂ exchange in the Alaskan Arctic in response to decadal climate warming. *Nature* 406:978-981.
- Osterkamp, T.E., Viereck, L. Shur, Y., Jorgenson, M.T., Racine, C., Doyle, A., & Boone, R.D. 2000. Observations of thermokarst and its impact on boreal forests in Alaska, USA. *Arctic, Antarctic, and Alpine Research* 32: 303-315.
- Péwé, T.L. 1975, Quaternary geology of Alaska. US Geological Survey Prof. Paper 835, 145 pp.
- Robin, J.H., Dubaya, R., Sparrow, E., & Levine, E. 2007. Monitoring start of season in Alaska with GLOBE, AVHRR and MODIS data. *Journal of Geophysical Research–Biogeosciences*. 113, G01017, doi:10.1029/2007JG000407.
- Romanovsky, V.E. & Osterkamp, T.E. 2001. Permafrost: Changes and impacts. In *Permafrost Response on Economic Development, Environmental Security and Natural Resources*. R. Paepe and V. Melnikov (eds.). Kluwer Academic Publishers, 297-315.

High-Resolution Permafrost Simulations in Western Greenland and an Assessment of Permafrost Degradation Risk

Martin Stendel, Jens Hesselbjerg Christensen

Danish Meteorological Institute, Copenhagen, Denmark; Greenland Climate Research Centre, Nuuk, Greenland

Sergei Marchenko, Ronald Daanen, Vladimir Romanovsky

Geophysical Institute, University of Alaska Fairbanks, USA

Abstract

Observations and model studies indicate warming of frozen ground in northern regions. We address these processes by using high-resolution versions (25 km and 5 km) of a regional climate model to create boundary conditions for an advanced permafrost model, which allows for simulation at very high resolutions. Since ensembles of different model combinations do not exist at such high resolutions, we estimate the bias of our approach with a quantile-quantile ranking of an ensemble of existing coarser simulations. We compare time-slice integrations for present-day climate and two future periods for most of Greenland. Permafrost is projected to degrade in most ice-free regions south of 76°N toward the end of the century, faster in the 5 km simulation than at the 25 km scale. We discuss a permafrost thaw potential based on modeled active layer thickness increase to assess the risk of permafrost degradation depending on surface properties and ice content.

Keywords: climate change; Greenland; permafrost degradation; permafrost model; regional climate model; risk assessment.

Introduction

There is ample observational evidence of recent warming in high latitudes, affecting permafrost (perennially frozen ground) and the seasonally thawed layer between it and the surface—the active layer. Climate change scenarios (e.g., Christensen et al. 2007) indicate that warming due to anthropogenic activities will be largest in polar regions. Changes involving permafrost may affect infrastructure and regional ecosystems due to thawing of the ground and development of thermokarst depressions (Romanovskii et al. 2000), or they may contribute to the release of greenhouse gases from partly decomposed organic material presently frozen in the ground.

Many model studies with comprehensive coupled general circulation models (GCMs) show that the area of the Northern Hemisphere underlain by permafrost could be reduced substantially in a warmer climate (e.g., Nelson et al. 2001, Stendel & Christensen, 2002 and references therein). However, thawing of permafrost, particularly ice-rich permafrost, is subject to a time lag due to the large latent heat of fusion of ice. State-of-the-art GCMs cannot adequately model these processes because (a) even the most advanced subsurface schemes rarely treat depths below 5 m explicitly, (b) soil thawing and freezing processes are not dealt with directly due to the coarse resolution, and (c) the required simulations covering millennia cannot be conducted due to computer power limitations.

Any attempt to model subsurface processes needs information about soil properties, vegetation, and snow cover, but these are hardly realistic on a typical GCM grid. Furthermore, simulated GCM precipitation is often underestimated due to the coarse underlying topography. Consequently, the spatial distribution of precipitation and the proportion of rain and snow are incorrect (e.g., Christensen & Kuhry 2000).

One possible way to address resolution-related problems is to

use regional climate models (RCMs). As no specific treatment of soil freezing and thawing is done in these RCMs, the same limitations as for the GCM apply, and these simulations, like those for coarser-scale models, also lack sufficient information about soil properties. Therefore, we use the RCM to create boundary conditions for an advanced permafrost model that solves the nonlinear heat transfer equation. The approach is described in Stendel et al. (2007). The RCM (and therefore the permafrost model) is run on horizontal resolutions of 25 km and 5 km for a region covering the southwestern two-thirds of Greenland.

Model Hierarchy and Downscaling Procedure

The three models used in this study are briefly described below. The driving GCM is the state-of-the-art model ECHAM5/MPI-OM1 (Roeckner et al. 2003, Marsland et al. 2003, Jungclaus et al. 2006), which consists of submodels for atmosphere, ocean, cryosphere, etc. All the forcing data for the Greenland simulation have been taken from a transient simulation with this model (May 2007) at T63 resolution (~1.8° by 1.8°).

As RCM we use HIRHAM5 (Lucas-Picher 2011, Mottram et al. 2011), which is based on the adiabatic part of the HIRLAM (High-Resolution Limited Area Model) short-range weather forecast model (Källén et al. 1996). For climate modeling purposes, HIRLAM's standard physical parameterization was replaced by that of ECHAM5, so that HIRHAM5 can be thought of as a high-resolution limited area version of ECHAM5.

For numerical stability reasons, it is not possible to directly downscale from the GCM to the 5 km grid. Therefore, the GCM data were first downscaled to 25 km (Stendel et al. 2008), and HIRHAM was run in a transient mode on a circumpolar domain, and it was then further downscaled to the target 5 km grid. Both simulations are considered here.

The boundary forcing from the GCM is updated every six hours in a region 10 grid points wide with a simple relaxation of all prognostic variables. We note that HIRHAM5 has been upgraded in several aspects with regard to the predecessor versions. The surface scheme has an improved interactive snow model over ice sheets and glaciers, and an ice sheet model has been added.

Varying concentrations of well-mixed greenhouse gases (CO_2 , CH_4 , N_2O , CFC-11, and CFC-12) as well as ozone (O_3), and sulphate aerosols (SO_4) were prescribed from observations over the period 1861–2000 and according to the SRES A1B scenario (Nakicenovic et al. 2000) thereafter. In this scenario, the CO_2 concentration in 2100 is near 700 ppm, and the globally averaged warming with respect to present-day climate is 3.5°C .

The third component is the GIPL 2.1 permafrost model (Geophysical Institute Permafrost Lab) of the University of Alaska Fairbanks (Sergeev et al. 2003), which is a one-dimensional, spatially distributed, physically based, multi-processor numerical model for the solution of the non-linear heat transfer equation. The model solves for ground temperatures and active layer thickness. The input data are air temperature, snow depth, soil composition, water content and thermal properties as well as characteristics of vegetation cover, geomorphologic features, and the geothermal flux as a bottom boundary. All these are taken from the regional climate model. Snow depth is calculated from snow water equivalent (which is an output field in HIRHAM) using a constant snow density of 0.15 kg dm^{-3} , which generates snow depths that are comparable to measured snow depths from Ilulissat (Olesen 2003). Further details of the model setup are given in Daanen et al. (2011). The permafrost model is run on the grid of the RCM, which excludes for the detailed discussion of edaphic factors (soil properties, vegetation), since these fields are given on the RCM grid. On the other hand, there is a consistency between climate data and boundary conditions on the horizontal scale we are able to resolve here. Further downscaling to the site level would seem desirable, but it would add another (statistical) model which is not the scope of this study. Verification at this scale is by no means a straightforward task because observational data are generally lacking.

A Metric of Uncertainty for Regional Climate Simulations

High-resolution climate simulations on rather large domains such as the one discussed here are challenging in terms of computer performance. Therefore, assuming that the SST forcing of the GCM is consistent with that of the RCM climatology (e.g., Giorgi 2008), we restrict ourselves to three “time-slices”: for present day (1980–1999) and two future periods in the middle (2046–2065) and end (2080–2099) of the twenty-first century.

This study relies on only one RCM forced by one GCM. This is because running such high-resolution models is very time consuming and because, at least at the 5 km scale, no

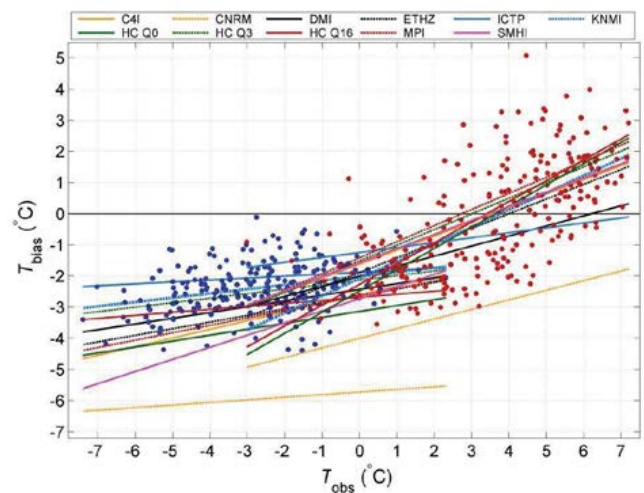


Figure 1. Model temperature biases, 1961–2000. Linear fits to ERA40-driven monthly mean model temperature biases as a function of observed monthly mean temperatures for an arbitrarily chosen grid point on Iceland. Points are for KNMI RACMO (blue for November–April and red for May–October).

other simulations exist yet. It is therefore important to assess the plausibility of the GCM/RCM combination and to put it into context with other setups. Fortunately, such information is available from the ENSEMBLES project (van der Linden & Mitchell 2009). In this huge multinational project, a number of RCMs were forced by several different GCMs. Based on monthly mean temperatures from 11 reanalysis-forced RCMs on a 25-km grid, Christensen et al. (2008) found a temperature-dependent temperature bias, here shown as an example for Iceland (Fig. 1). Other polar regions (not shown) are similar. It is obvious that the common assumption of bias cancellation in climate change projections is challenged.

This approach can be extended to facilitate a comparison with GCM scenario data (Boberg & Christensen 2012). Since such a setup is running freely, unconstrained by observations (other than defining the initial state), the simulated weather represents the real world only in a statistical sense.

We can construct quantile-quantile (Q-Q) plots where, for the RCMs, the ranked monthly mean temperatures are plotted, modeled against observed (not shown). For the GCMs, only such Q-Q plots can be constructed since the actual month cannot be compared to a particular month from the observations (Fig. 2).

It is evident that many GCMs exhibit an upward curvature in the Q-Q diagram, which supports the findings of Christensen et al. (2008) for RCMs. The EC-Earth model, marked in green in Figure 2, and ECHAM5, which behaves similarly, represent models that have comparatively small biases, at least according to the metric discussed here. This corroborates findings by Walsh et al. (2008) who found in a comparison study between 14 of the CMIP3 models (Meehl et al. 2007) that ECHAM5 is top ranking with respect to simulated present-day conditions in the Arctic.

We note that the findings presented in Figure 2 do not

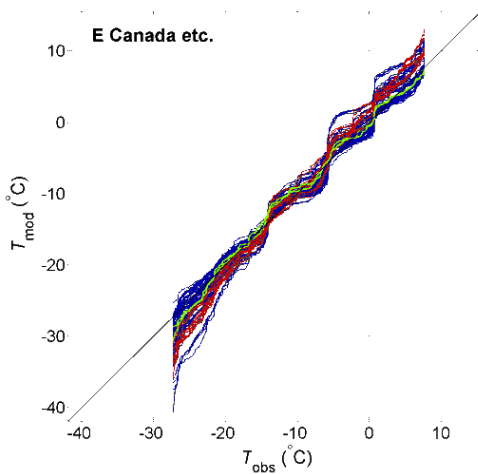


Figure 2. Ranked monthly mean temperatures, modeled against observed, for Greenland and Northeastern Canada, 1961–2000. Data for 64 GCMs from the CMIP3 (Meehl et al. 2007, blue lines) and for the new CMIP5 experiments (red lines), centered to obtain a zero mean in model temperature with respect to the diagonal $T_{\text{GCM}} = T_{\text{obs}}$. One particular model, EC-Earth, is highlighted in green; ECHAM5, the GCM used in this study, is very similar. Observations are from the CRU dataset.

imply that all models are too warm in the warmest months. It is rather the curvature in the temperature dependency we are emphasizing.

Future Evolution of Permafrost

As discussed above, the driving model for the HIRHAM simulation is a coupled atmosphere-ocean GCM (i.e., the atmosphere is forced by modeled SSTs and sea ice concentrations rather than by observed ones). This implies that in order to assess variability and change, the considered periods need to be long enough (i.e., cover several decades). The three 20-year time slices (1980–1999, 2046–2065, and 2080–2099) can be compared to results from the transient 25 km simulation mentioned above (Stendel et al. 2008).

The evolution of ground temperatures depends on the thermal properties of the subsurface material. Ice-free areas in Greenland are generally dominated by exposed bedrock with sediment-filled depressions, often covered by a layer of organic material. Since the resolution applied here is too coarse to resolve the distribution of surface material, we consider both cases separately. For details of soil classes used in the sediment run and associated thermal properties, we refer to Daanen et al. (2011).

As an example, Figure 3 shows the temperature distribution and active layer depth on the 25 km scale for the sediment run. Due to the offset as a result of thermal conductivity differences between thawed and frozen porous media, it is generally colder than the bedrock run. For the period 2065–2075, compared to 1995–2005, the temperature at 2 m depth in sediment is projected to increase by 2 K.

Figure 4 shows results from the new 5 km simulation.

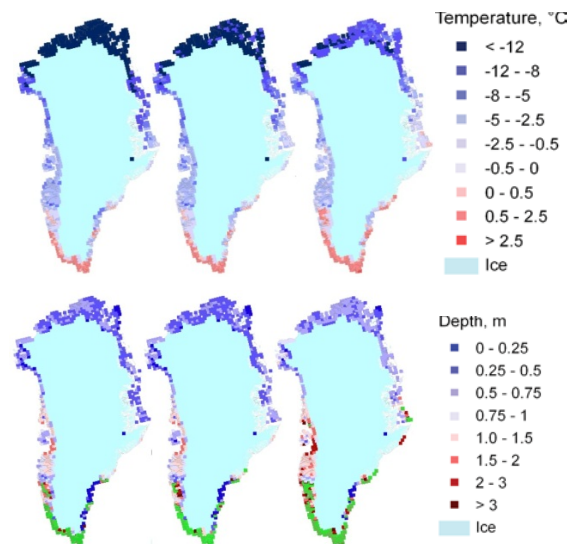


Figure 3. Top: Annual average ground temperature at 2 m depth. Bottom: Active layer thickness. Average for 1955–1965 (left), 1995–2005 (middle), and 2065–2075 (right). Sediment with organic layer, 25 km run. Green color in bottom panel stands for permafrost-free zone.

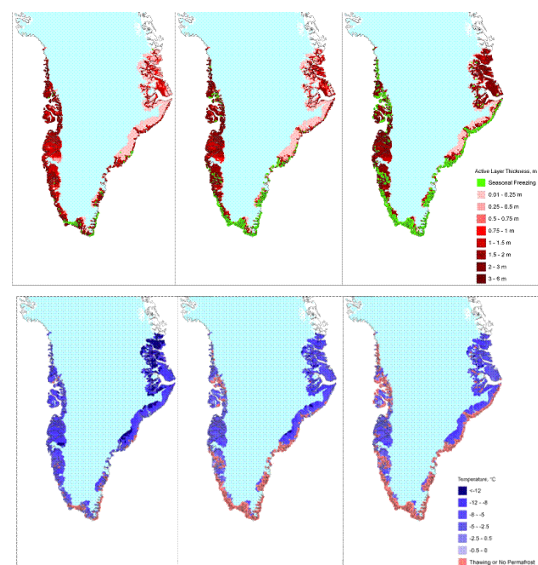


Figure 4. Top: Mean annual temperature distribution at 1 m depth. Bottom: Active layer thickness at 1 m depth for 1980–1999 (left panels), 2046–2065 (middle panels), and 2080–2099 (right panels), sediment with organic layer, 5 km run.

Despite the slightly different time periods in Figures 3 and 4, we can conclude that higher temperatures and an increased active layer thickness are found in the 5 km run compared to the coarser resolution. This is particularly true along the east coast of Greenland, a feature that is completely absent in the lower resolution (25 km) simulation.

Another striking difference between the low- and the high-resolution simulation is the considerably more substantial degradation of permafrost along the west coast of Greenland, even in higher latitudes. Assuming that higher resolution yields a more realistic topography and therefore more realistic

temperature and snow cover, these results indicate that permafrost degradation may already be ongoing by the end of the twenty-first century as far north as Upernavik. Active layer depths show a strong gradient decreasing from the coastal regions toward the ice sheet, in particular along the east coast. Also these features do not show up in the 25 km resolution. In particular along the west coast, the degradation of permafrost is probably still underestimated, since part of the sediment is marine silty clay, in particular around Ilulissat and Sisimiut. This material is much more sensitive to warming even at relatively low temperatures just below the freezing point.

Risk Assessment by Means of the Permafrost Thaw Potential

Population growth, developing tourism, and the increasing need for infrastructure outside the traditional settlements result in an extension of constructions from bedrock to unconsolidated sediments and ice-rich permafrost. An assessment of risk during the planning phase of such construction is required. Existing risk assessment strategies (e.g., Nelson et al. 2001) are rather complex. For reason of simplification and to allow for downscaling from the regional to a local scale, Daanen et al. (2011) introduced the permafrost thaw potential (PTP), which is based on the change in active layer thickness as obtained from the spatially distributed permafrost model.

The risk of permafrost degradation is evaluated from three environmental properties: (a) surface properties (bedrock or sediment), (b) grain size (gravel, sand, silt or clay), and (c) the ice content. The risk is also evaluated with one model-generated quantity, namely, the PTP (i.e., the potential increase in active layer depth from present to future conditions) (Daanen et al. 2011). Figure 5, which can serve as a kind of “worst-case” scenario for sediment, indicates that most of the ice-free area of Greenland is at risk (decreasing from south to north) of permafrost degradation.

We note that most of the ice-free part of Greenland has a PTP of more than 2.5 m, which means that in these regions almost all sedimentary basins can be classified as high-risk areas. This finding can be applied on a local scale, given that the ice content of the sediment (condition (c) above) is high.

The results presented in Figure 5 can be validated for the towns of Sisimiut (66.2°N, 53.7°W) and Ilulissat (69.2°N, 51.1°W), both of which are located in the discontinuous permafrost zone (Christiansen & Humlum 2000) and for which observations from the 1960s and 1970s exist. Figure 6 (compare Daanen et al. 2011) shows as an example modeled and observed time series of temperature near Ilulissat for two depths, two observation periods (described in Olesen 2003 and Daanen et al. 2011, respectively), and for saline and non-saline conditions.

For both locations, the comparison to observed data gives reasonably realistic results given that the snow cover, which is an input to the permafrost model, is entirely model-generated, so that one cannot expect perfect agreement with observations on a particular day. Based on this assessment, the permafrost within the marine silty clay in Sisimiut is projected to be

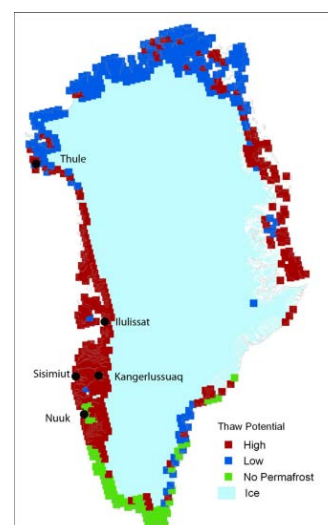


Figure 5. Permafrost thaw potential (PTP) for Greenland for sediment with organic layer, 25 km run, expressed as the difference between future (2065–2075) and present (1995–2005) active layer depth. High PTP corresponds to an active layer depth increase of more than 2.5 m, a value chosen according to observations at Thule Air Force Base (Birkholm et al. 2007).

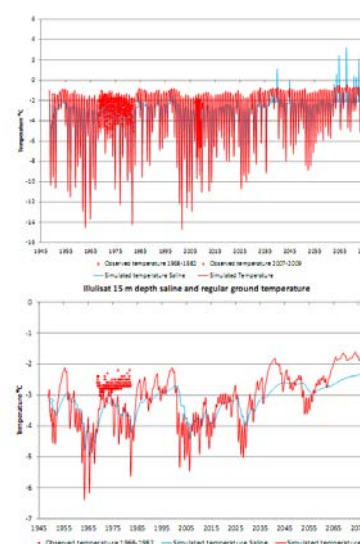


Figure 6. Temperature time series for Ilulissat for depths of 2.5 m (top) and 15 m (bottom), comparing saline and non-saline temperature simulations for the sediment case. Also shown are observations from the 1960s and 1970s (Olesen 2003) and more recent data from 2007 on (Daanen et al. 2011).

actively degrading, with an increase of the active layer depth of more than 4 m. For Ilulissat with its saline permafrost (Ingeman-Nielsen et al. 2008), an increase in active layer depth of nearly 4 m is projected. This suggests that all permafrost areas with marine silty clay need to be classified as high-risk zones.

Conclusions

Comparing Figures 3 and 4, it becomes obvious that there is a considerable potential in high-resolution permafrost modeling. A PTP evaluation on the 5 km scale is underway.

High-resolution permafrost simulations driven by a chain of models, as presented here, cannot be run in large ensembles due to computer constraints. By means of the quantile-quantile distribution, one can indirectly make use of large ensembles of simulations that have been conducted at a coarser resolution and thus put an individual simulation (one RCM driven by one GCM) into a larger context.

Even though the thaw potential presented in Figure 5 cannot be used for an assessment of the stability of individual buildings, it can demonstrate the general risk potential if such constructions would be conducted on sediment.

A quantification of the risk of permafrost degradation by means of the permafrost thaw potential (PTP) suggests that most of the ice-free regions in Greenland south of 76°N can be classified as high-risk areas. A careful risk evaluation in the initial phase of construction projects is therefore deemed useful. In particular, for Ilulissat, the presence of ice-rich saline permafrost with temperatures close to the freezing point and a high PTP suggest that construction on fine-grained sediments with permafrost should be avoided.

The present risk assessment is based on high-resolution climate simulations but, in terms of individual engineering applications, more sophisticated formulations of snow, the surface energy balance, and the hydrological parameters will be required. The present paper thus can serve as a proof-of-concept study.

Acknowledgments

The ECHAM/MPI-OM GCM and HIRHAM RCM simulations were conducted on DMI's supercomputers (NEC-SX6 and Cray XT5, respectively). The RCM run was sponsored by the Danish Environment Agency under grant no. M127/001-0237. Funding was partly by the National Science Foundation under grant no. ARC-0612533. Computational support was given by ARSC. We thank our collaborators from ASIAQ and DTU.

References

- Birkholm, J., Brandt, I., & Foged, N. 2007. Deterioration of permafrost in Thule – implication for road constructions in Greenland. International Conference: Arctic Roads, operating, maintaining and building roads in a climatically challenging environment, Sisimiut, 1, 70-78.
- Boberg, F. & Christensen, J.H. 2012. Overestimation of Mediterranean summer temperature projections due to model deficiencies. Submitted to *Nature*.
- Christensen, J.H. & Kuhry, P. 2000. High-resolution regional climate model validation and permafrost simulation for the East European Russian Arctic. *J. Geophys. Res.* 105, 29647–29658.
- Christensen, J.H. et al. 2007. Regional climate projections. In *Climate Change 2007: The Physical Science Basis*. Edited by Solomon et al. Cambridge University Press.
- Christensen, J.H. et al. 2008. On the need for bias correction of regional climate change projections of temperature and precipitation. *Geophys. Res. Lett.* 35, 10.1029/2008GL035694.
- Christiansen, H.H. & Humlum, O. 2000. In *Topografisk Atlas Grønland*. Edited by Jakobsen et al., pp. 32-35. Det Kongelige Geografiske Selskab og Kort- og Matrikelstyrelsen.
- Daanen, R.P. et al. 2011. Permafrost degradation risk zone assessment using simulation models. *The Cryosphere* 5, 1-14, doi:10.5194/tc-5-1-2011.
- Giorgi, F. 2008. Regionalization of climate change information for impact assessment and adaptation. *WMO Bulletin* 57(2), 7 pp.
- Ingeman-Nielsen, T. et al. 2008. Geophysical investigations of saline permafrost at Ilulissat, Greenland. *Proc. Of the Ninth International Conference on Permafrost*, Fairbanks, Alaska, 1, 773-778.
- Jungclaus, J.H. et al. 2006. Ocean circulation and tropical variability in the AOGCM ECHAM5/MPI-OM. *J. Climate* 19, 3952–3972.
- Källén, E. (ed.). 1996. *HIRLAM Documentation Manual, System 2.5*. Swed. Meteorol. and Hydrol. Inst., Norrköping, 126 pp.
- Lucas-Picher, P. 2011. Very high-resolution regional climate modelling over Greenland with HIRHAM5. In preparation.
- Marsland, S.J. et al. 2003. The Max-Planck-Institute global ocean/sea ice model with orthogonal curvilinear coordinates. *Ocean Mod.* 5, 91–127.
- May, W. 2007. Climatic changes associated with a global “2°C-stabilization” scenario simulated by the ECHAM5/MPI-OM coupled climate model. *Clim. Dyn.* 31, 283-313.
- Meehl, G.A. et al. 2007. The WCRP CMIP3 multimodel ensemble – a new era in climate change research. *Bull. Amer. Met. Soc.* 88, 1383-1394.
- Mottram, R.H. et al. 2011. Surface mass balance of the Greenland Ice Sheet 1989-2005 using the regional climate model HIRHAM5. In preparation.
- Nakicenovic, N. et al. 2000. IPCC special report on emissions scenarios. Cambridge University Press, Cambridge, UK, 599 pp.
- Nelson, F.E., Anisimov, O.A., & Shiklomanov, N.I. 2001. Subsidence risk from thawing permafrost. *Nature* 410, 889-890.
- Olesen, O.B. 2003. Shallow borehole temperatures, Ilulissat, Greenland. Greenlandic Geological Survey (GEUS), distributed by National Snow and Ice Data Center/World Data Center for Glaciology.
- Roeckner, E. et al. 2003. The atmospheric general circulation model ECHAM 5. Part I: Model description. Max Planck Institute for Meteorology Report 349, 127 pp.
- Romanovskii, N.N. et al. 2000. Thermokarst and land-ocean interactions, Laptev Sea region, Russia. *Permafrost: Periglac. Proc.* 11, 137–152.
- Sergeev, D.O., Tzipenko, G.S., & Romanovsky, V.E. 2003. Mountain permafrost thickness evolution under influence of long-term climate fluctuations (results of numerical

- simulations). In Phillips et al., (eds.) *8th International Conference on Permafrost*. Balkema, Zurich, 1017-1021.
- Stendel, M. & Christensen, J.H. 2002. Impact of global warming on permafrost conditions in a coupled GCM. *Geophys. Res. Lett.* 29, 10.1029/2001GL014345.
- Stendel, M., Romanovsky, V.E., Christensen, J.H., & Sazonova, T. 2007. Global warming and permafrost: Closing the gap between climate model simulations and local permafrost dynamics. *Glob. Plan. Change* 56, 203-214.
- Stendel, M., Christensen, J.H., & Petersen, D. 2008. Arctic climate and climate change with a focus on Greenland. In: The dynamics of a High Arctic ecosystem in relation to climatic variability and change - Ten years of monitoring and research at Zackenberg Research Station, Northeast Greenland. Edited by H. Meltofte et al. *Adv. in Ecol. Res* 40, 13-43, doi: 10.1016/S0065-2504(07)00002-5., Elsevier.
- van der Linden, P. & Mitchell, J.F.B. 2009. ENSEMBLES; climate change and its impacts. Summary of research and results from the ENSEMBLES project. Met. Office Hadley Centre, Exeter, UK.
- Walsh, J.E., Chapman, W.L., Romanovsky, V., Christensen, J.H., & Stendel, M. 2008. Global Climate Model Performance over Alaska and Greenland. *J. Climate* 21, 2156-2174, doi: 10.1175/2008JCLI2163.1

Infrastructure and a Changing Climate in the Russian Arctic: A Geographic Impact Assessment

Dmitry Streletskiy, Nikolay Shiklomanov, Ellen Hatleberg
Geography Department, George Washington University, Washington, DC, USA

Abstract

Air temperature increases observed over the last few decades in the Arctic affect economic activities and human infrastructure. This paper focuses on geographic evaluation of such impacts associated with climate change including duration of heating season, duration of winter road operations, and stability of infrastructure foundations in the Russian Arctic. Climate datasets and modeling techniques were used to quantitatively evaluate the changes between the 1970s and the 2000s. Our analysis shows negative effects from observed climate change, particularly on the stability of building foundations and the duration of winter road operations. Results are presented as a series of maps portraying spatial variability of changes found in several administrative regions of the Russian Arctic.

Keywords: Arctic; climate change; permafrost; winter roads; foundation stability; bearing capacity.

Introduction

The Arctic has experienced a warming trend over the last few decades. Warming temperatures are raising concerns among the engineering community, land use planners, and policy makers because the trend may have negative impacts on socio-economic development and human activities in the northern regions (ACIA 2005). However, a warming climate could also have positive economic effects, which might include development of maritime transportation as sea ice retreats; development of hydropower energy as river runoff increases; a decrease of energy consumption; and enhanced agricultural production due to warmer temperatures and a longer growing season. Yet these benefits may be negligible compared to the many negative impacts on transportation accessibility and stability of existing infrastructure, especially in permafrost regions. Permafrost regions occupy about a quarter of the land surface in the Northern Hemisphere (Zhang et al. 2008). Russia and Canada contain permafrost areas of approximately 66% and 50% of their respective territories. In the United States, permafrost regions occupy about 80% of the state of Alaska. The majority of Russian territory is considered to be northern to at least some extent, with some regions largely occupied by permafrost (Fig. 1). According to recent delineations, 16 federal subjects are fully included in the Russian North and 11 are partly included (Klütter 2000).

Population in the Arctic is generally sparse, but the Russian Arctic is heavily urbanized. Data from the 2002 Russian census (Goskomstat Rosii 2002) showed that urbanization in five Russian Arctic administrative regions ranged from 59 to 94% (Fig. 2), indicating that a majority of the population lives in cities such as Vorkuta, Salekhard, Nadym, Noviy Urengoy, Noril'sk, Magadan, Yakutsk, or other settlements with more than 12,500 people. Although only about 5% of the Russian population resides in arctic regions, their contribution to the country's economy is disproportionately large: 20% of the Russian GDP and 22% of Russian exports are produced in arctic regions (Khrustalev et al. 2011). Therefore, a changing

climate in the northern regions could profoundly affect the Russian economy. Permafrost plays an important role in the functioning of arctic ecosystems and largely influences human activities in the North. Observed climate warming has resulted in a permafrost temperature increase of 0.5–2°C over the last 20–30 years in the Russian Arctic (Romanovsky et al. 2010).

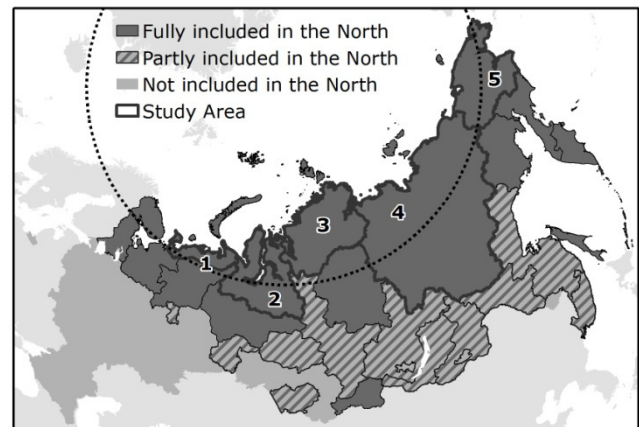


Figure 1. Federal subjects fully or partly included in the Russian North. Federal subjects that are part of the study include: (1) Nenets AO; (2) Yamalo-Nentes AO; (3) Taymyr AO; (4) Yakutia; and (5) Chukchi AO. 'AO' denotes Autonomous Okrug.

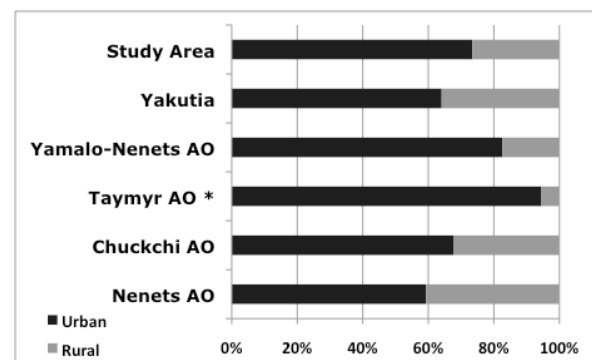


Figure 2. Percent of the total population that was urban or rural in 2002 for specific administrative regions.

Changes in permafrost environments have been observed in most regions of the Russian Arctic. For example, in the Russian European North from 1970 to 2005 the southern permafrost boundary has retreated northward by 30–40 km in the Pechora lowland (Malkova 2008) and by 70–100 km in the foothills of the northern Urals (Oberman & Shesler 2009). Thawing of ice-rich permafrost is also occurring in the southern fringes of the permafrost zone in West Siberia (Vasilev et al. 2008). A permafrost temperature increase of 1°C was observed in the Urengoy gas field from 1975 to 1993 due to climate warming. However, more recent years showed no significant changes until 2005, when a warming trend continued (Drozdov et al. 2008). Northeastern Yakutia experienced permafrost warming of up to 1.5°C beginning in 1980. Previously stable areas of Northwestern Yakutia are beginning to show permafrost warming in recent years (Romanovsky et al. 2010). Although warming trends in the Arctic are mostly attributable to the winter season, with only a slight increase during summer months (Pavlov & Malkova 2005, Skachkov 2008), an increase in permafrost temperature was accompanied by an increase of active-layer thickness (ALT) in a majority of regions. Thickening of the active layer was reported from the Russian European North and eastern and western Siberia (Fyodorov-Davydov et al. 2008, Malkova 2010, Melnikov 2004, Vasiliev et al. 2008, Zamolodchikov et al. 2008).

Changes in the natural environment are already affecting human infrastructure. Observed increases in near-surface permafrost temperatures are decreasing the ability of foundations to support structures. The rates of temperature increase may not have been anticipated at the time of construction (Khrustalev & Davidova 2007, Streletskiy et al. 2012). Similarly, a thicker active layer decreases the effective area of foundation adfreezing with permafrost and intensifies the processes of frost heave and thaw subsidence. It also increases corrosion of foundation materials. This situation is already affecting infrastructure in arctic regions, as a large number of structural deformations have been reported in a majority of settlements built on permafrost in Russia (Kronic 2001, Khrustalev et al. 2011). Similarly, more than three hundred residential buildings have been reported to have experienced deformation in Fairbanks, Alaska (Permafrost Technology Foundation 2009). The permanent transportation network is also affected as warming permafrost and a thickening active layer may induce differential heave and settlement leading to the deterioration of railroad embankments, pavement, and pipelines. Warmer air temperatures are limiting accessibility of remote regions as the length of winter road operation on land is shrinking (Stephenson et al. 2011).

Projected climate warming in the Arctic has the potential to cause further deterioration and deformation of structures on permafrost. This can have severe socio-economic consequences because most of the existing infrastructure will require expensive mitigation measures to maintain support. In this paper, we attempt to geographically evaluate how climate change affects human activities that may already be occurring in the Russian Arctic. Knowledge of the temporal and

geographic patterns of these changes may provide an essential key for both environmental and socio-economic development in arctic regions.

Methodology

In order to quantitatively address the impacts of climate change on human infrastructure in the Arctic, the historical changes of three vital, climate-dependent types of economic activity were considered for analysis: stability of foundations, energy consumption, and land transportation. This research anticipated infrastructure change in the locations where climate conditions have changed significantly. The methodology, briefly described below, was developed to depict spatial trends at a small (regional to continental) geographic scale. As such, it relies on the broad spatial characterization of major climatic, vegetation, soil, and infrastructure-specific parameters. More detailed investigations are necessary to provide assessment at finer geographic scales.

Foundation stability: Urban architecture in the Russian Arctic is predominantly represented by a mixture of prefabricated panel or standard-design brick buildings of five to nine floors. The majority of such structures on permafrost are built using piling foundations according to passive principles (Shur & Georing 2008). To assess changes in potential stability of arctic infrastructure, we have used the bearing capacity (ability to support load) of the standard 0.35 x 0.35 x 10 m concrete foundation pile. Such an approach is frequently used in Russia for preliminary assessments of large territories (CNR 1990). It effectively shows diversity in possible construction designs and practices and focuses on changes in engineering properties of permafrost landscapes in response to climatic forcing. Foundation bearing capacity was calculated using evaluations provided by the Russian Construction Norms and Regulations (CNR 1990). These evaluations relate active-layer thickness and permafrost temperature to stresses experienced by the foundation pile embedded in the permafrost. Changes in permafrost parameters (e.g., active-layer thickness, permafrost temperature) were estimated using a spatially distributed equilibrium model of permafrost-climate interactions (Anisimov et al. 1997, Sazonova & Romanovsky 2003, Shiklomanov & Nelson 2002). Details on calculation procedures are provided in Streletskiy (2010) and Streletskiy et al. (2012).

Energy consumption: The majority of the Russian Arctic population lives in buildings with a centralized heating system. The local and municipal governments establish standardized location-specific requirements for building insulation and heating load. As a result, the heating degree-days (HDDs) and the length of the heating season can be used as proxies for energy consumption. According to Russian government standards, the beginning of the heating season starts on the day following five consecutive days with temperatures below 8°C and ends when the temperature exceeds 8°C for five consecutive days (Russian Government Resolution N307 from 23.05.2006).

Land transportation: Since arctic countries rely heavily on

seasonal road networks, the changes in land transportation were evaluated through the estimated potential annual operational period of winter/ice roads. Russian construction norms (e.g., VSN 137-89) do not implicitly use climate (e.g., air temperature) as a parameter determining suitability of winter road operation. We have relied on North American regulations, which indicate that an accumulation of more than 300 degree-days of freezing (DDF) can be used to estimate the onset of winter road construction. The mean daily temperature of more than 0°C determines the closing date of safe winter road operation (Vinson 1996, Kuryk 2003). The operational period was estimated by counting days between the beginning of construction (> 300 DDF in the autumn) and the closing date (daily air temperature >0°C in spring).

Data availability: Climatic input consisted of National Center for Environmental Prediction (NCEP, Kalnay et al. 1996) gridded datasets of daily temperatures and precipitation scaled to 15x15 km horizontal resolution. The assessments were focused on two reference periods: 1965–1975 and 1995–2005. Daily climate data were averaged over these periods to provide climatologic means. Decadal periods were chosen to illuminate interannual variability in climate data. The decade centered around 1970 was chosen as a baseline period due to extensive construction in the Russian Arctic at this time. It was assumed that structures were designed to withstand climatic conditions of the period. The decade around 2000 was selected to represent contemporary conditions because, at the time of analysis, the most recent standardized gridded data were available through 2005. In the following discussion, the 1965–1975 and 1995–2005 period are referred to as the 1970 and 2000 periods, respectively. Land surface data were represented by a uniform sand profile with low ice content. All results presented in this paper are in the form of relative change between two selected periods.

Geographically, the analysis was focused on five Russian Administrative regions: Nenets Autonomous Okrug (AO), Yamalo-Nenets AO, Taymyr AO, Republic of Sakha (Yakutia), and Chukchi AO. Collectively these regions comprise a significant portion of the Russian Arctic (Fig. 1).

Results and Discussion

Climate data show that the majority of the studied areas experienced warming, with the exception of the western part of Nenets AO and Northern Yakutia (Fig. 3).

Energy consumption

The most pronounced change in energy consumption is found in northern and southeastern Yamal-Nenets AO and northern Chukchi AO (Fig. 4). However, warmer mean annual air temperatures do not necessarily translate to a corresponding decrease in the length of the heating period.

While the absolute values of HDDs have decreased by up to 700 in West Siberia and 1300 in the Chukchi AO, the length of the heating period did not change significantly. Nadym, Noviy Urengoy, Noyabrsk, Labytnangi, and Salekhard potentially benefited the most due to a reduced number of HDD. Small

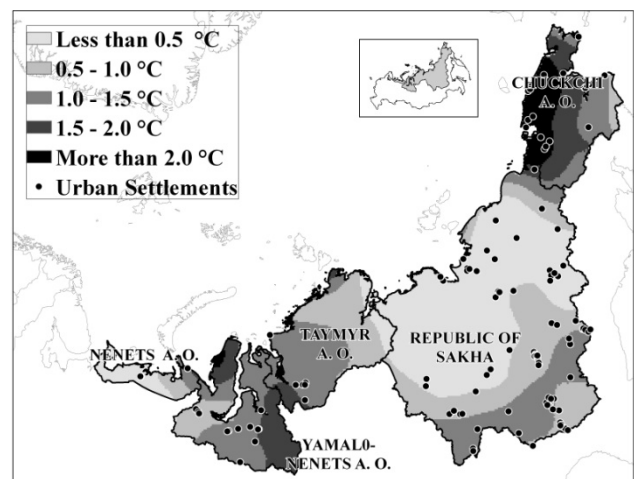


Figure 3. Change in mean annual air temperature between the 1970 and the 2000 periods showing magnitude (°C) of warming.

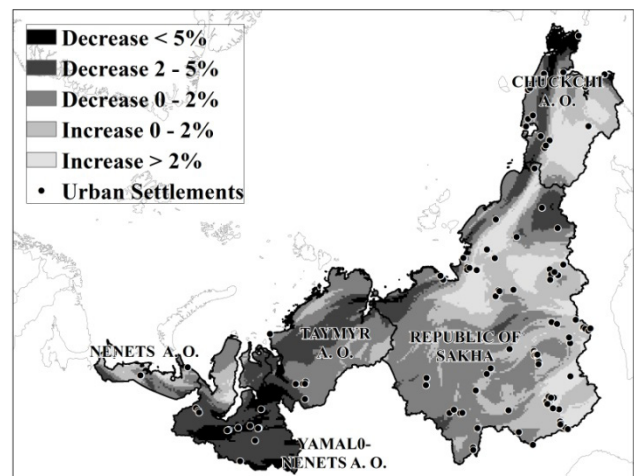


Figure 4. Temporal changes in percent of number of heating degree-days between the 1970 and the 2000 periods.

(~1%) decreases were also found in Yakutsk, Noril'sk, Dudinka, and Chersky.

Increases in the heating season by more than 1% were found predominantly in northern Yakutia in settlements such as Tommot, but also in southern areas of Neryungri and Aldan. However, the majority of the study area did not show any significant changes.

The number of HDDs for the 2000 period was within $\pm 2\%$ of values from the 1970 period. This suggests that the significant warming observed in the Russian Arctic did not result in a significant positive economic effect with respect to reduced energy consumption.

Land transportation

Paved roads built on permafrost are likely to suffer from subsidence associated with the melting of ground ice. The projected increase in snow accumulation and, as a consequence, larger volumes of redistributed snow to the roadsides, will further enhance permafrost warming and result in development of thermokarst and waterlogging. Railroads

can also suffer significant deformation due to differential frost heave and thaw settlement. However, arctic countries, including Russia, rely heavily on winter roads and drivable ice pavements to supply communities in remote areas. As a result, many areas of the Russian Arctic are land-accessible only during winter.

Our results indicate that changes have already occurred in the length of time winter roads can be used. However, these changes are not uniform. Some regions, such as Yakutia, show an increase in operational road duration while West Siberia is characterized by a significant decrease. It is important to note that the decrease in the period of potential winter road operation was found in areas of intensive oil and gas exploration and development, including areas around Noyabrsk, Noviy Urengoy, and Nadym. Other economically vital regions with a decrease in potential accessibility include areas along the Yenesei River north of Igarka up to Dickson; around Chersky in Northeastern Yakutia; and Pevek and Anadyr in Chukchi AO (Fig. 5).

The comprehensive study of the effects of climate change on transportation in Northern Canada concluded that a shorter winter road operational season will be compensated by the longer navigation season on lakes and rivers during summer months (Lonergan et al. 1993). However, a large number of small settlements in the Russian Arctic are located far from major river routes.

A decrease in winter road operation could also be offset by improving maritime transportation conditions in the Arctic (Stephensen et al. 2011). While shrinking sea ice and the opening of arctic passages look promising, the coastal infrastructure will have to be built in accordance with conditions of increased wave activity and coastal erosion. Increased rates of coastal erosion have already resulted in a series of negative consequences for Native settlements in Alaska, especially Kivalina in northwestern Alaska. This coastal settlement is planning to relocate due to sea wave erosion, and such relocation will cost around \$176 million (Wilson 2007). While no comparative studies have been done in the Russian Arctic, the possible loss of existing coastal infrastructure, especially along the Northern Sea Route, should not be ignored.

Foundation stability

A majority of foundations built on permafrost utilize piling foundations. Piles embedded in permafrost allow for much heavier loads compared to those in non-permafrost regions because the majority of the bearing capacity can be gained by the adfreeze of pile surfaces with permafrost. The shear stress per surface unit of a pile is much lower compared to the normal stress at the bottom of a pile, but the much larger adfreeze area of the pile surface relative to the bottom allows redistribution of up to 80% of the pile bearing capacity to its wall surface. Dependence of adfreeze strength on permafrost temperature along the piles makes a foundation's bearing capacity highly dependent on climatic conditions influencing the thermal regime of permafrost. An increase in permafrost temperature is accompanied by an increase in unfrozen water content and decreasing cohesion of soil particles, resulting

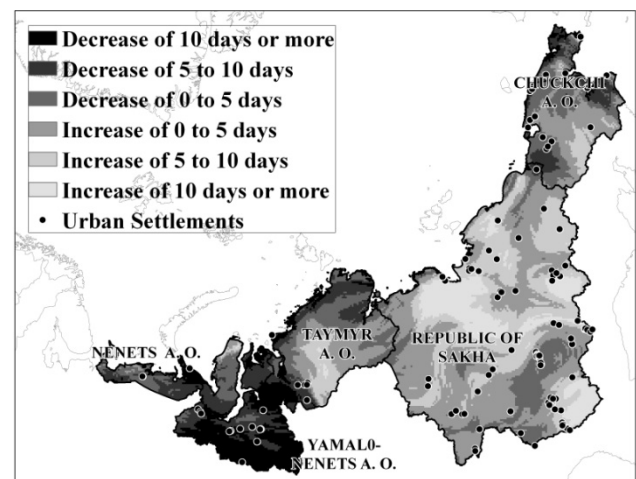


Figure 5. Temporal changes in winter road operable days between the 1970 and the 2000 periods.

in a substantial loss of adfreeze strength. A thickening of the active layer increases the depth to which freeze/thaw cycles extend, which leads to an increase in settlement. It also decreases the effective contact area of the pile with permafrost.

Effective permafrost engineering designs are aimed at protecting permafrost from warming by ensuring permafrost isolation during the summer and by providing heat exchange between the permafrost and atmosphere during the winter. With adequate maintenance, this allows for relatively stable and sometimes decreasing permafrost temperature. In the ideal case, the permafrost temperature beneath a structure built using the passive method of an elevated first floor is near the mean annual air temperature of the area.

Actual conditions, however, are far from ideal. A substantial number of reports on the deformation of structures built on permafrost, both in the scientific literature (e.g., ACIA 2005) and the public media, have prompted speculation that climate warming is at least partially responsible. Our results indicate that observed climate warming has the potential for decreasing bearing capacity of permafrost foundations built in the 1970s in the majority of settlement cases in all five study regions. Substantial decreases in potential foundation bearing capacity occur in regions of eastern Chukotka, southern parts of Yamalo-Nenets AO, and Sakha Republic (Fig. 6). According to our estimates, a climate-induced decrease in bearing capacity by 15–20% occurred in Salekhard, Noviy Urengoy, Nadym, Pevek, Anadyr; by 10–15% in Bilibino and Dudinka; and by 5–10% in Noril'sk, Neryungri, Mirny, Yakiusk. At the same time, Chersky, Noyabrsk, and Provideniya experienced a decrease of more than 20%.

While climate warming is a plausible cause for the decrease in foundation bearing capacity, other technogenic factors, such as inadequate structural design or lack of proper maintenance, should also be considered. Undetected leaks in sewage and water pipes are well known for causing rapid warming and chemical contamination of permafrost below building foundations. The resulting decrease in the soil's ability to support foundations has resulted in serious deformation

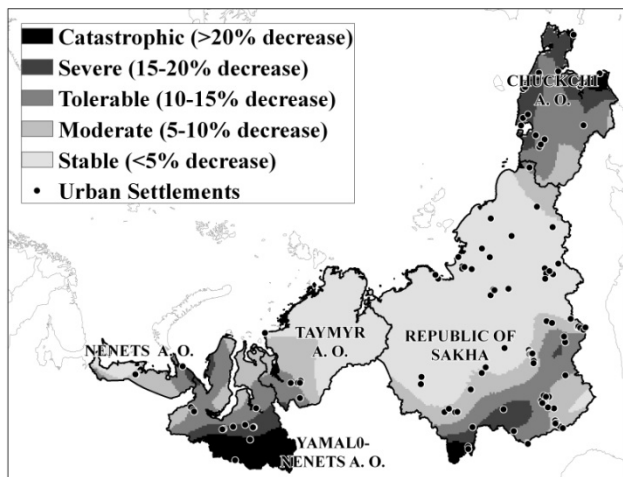


Figure 6. Temporal changes in foundation bearing capacity between the 1970 and the 2000 periods.

of many structures (Grebenets et al. 2001). The detailed investigations required to assess foundation deformation caused by technogenic factors are well beyond the scope of the present study. However, our results clearly indicate that climate warming has a significant potential for undermining the structural stability of structures built on permafrost.

Summary

Geographic assessment of the potential impacts of observed climate change on several economic parameters representing infrastructure, transportation, and energy consumption indicate that deleterious impacts due to observed climate warming may exceed those that have a positive economic impact. A decrease in the length of the heating season is almost negligible despite warmer temperatures. Decreasing operational time of winter roads reduces accessibility of remote regions, resulting in negative consequences, especially for small isolated arctic communities. The most profound climate change impact is associated with increases in permafrost temperature and active-layer thickness, which will decrease the bearing capacity of foundations. Projected warming is likely to enhance observed trends and to further deteriorate living conditions in the Arctic. The effect will be most significant for highly urbanized communities in the Russian Arctic.

Acknowledgments

This research was sponsored by the U.S. National Science Foundation grant ARC-1002119 to George Washington University, and NASA grants NNX09AI94G and 09-040 to George Washington University, the University of Delaware, and the University of New Hampshire. Opinions, findings, conclusions, and recommendations expressed in this paper are those of the authors and do not necessarily reflect the views of NSF or NASA.

References

- ACIA. 2005. *Arctic Climate Impact Assessment*. Cambridge: Cambridge University Press.
- Anisimov, O.A., Shiklomanov, N.I., & Nelson, F.E. 1997. Global warming and active-layer thickness: results from transient general circulation models. *Global and Planetary Change*. 15: 61-77.
- CNR. 1990. *Stoitelnie Normi i Pravila (Construction Norms and Regulations)*. Foundations on Permafrost 2.02.04-88. State Engineering Committee of the USSR. 56. (In Russian)
- Drozdov, D.S., Malkova, G.V., & Melnikov, V.P. 2008. Recent Advances in Russian Geocryological Research: A Contribution to the International Polar Year. *Proceedings of the Ninth International Conference on Permafrost*, Fairbanks, Alaska, June 29–July 3, 2008: 2: 379-384.
- Fyodorov-Davydov, D.G., Kholodov, A.L., Ostroumov, V.E., Kraev, G.N., Sorokovikov, V.A., Davudov, S.P., & Merekalova, A.A. 2008. Seasonal Thaw of Soils in the North Yakutian Ecosystems. In *NICOP 2008: Proceedings of the Ninth International Conference on Permafrost*. D.L. Kane, K.M. Hinkel (eds.). Institute of Northern Engineering, University of Alaska Fairbanks, 1: 481-486.
- Goskomstat Rosii. 2002. 12. Present and resident population of the Russian Federation by cities, towns and urban areas as of 1 January 2001. *Demograficheskiy yezhegodnik* (in Russian).
- Grebenets, V.I. & Kerimov, A.G. 2001. Geocryolithic and Geocologic Construction Problems in Regions of the Extreme North. Evolution of natural and man-made complexes in the Noril'sk Region, Scientific-Practical Seminar, 130–135 (in Russian).
- Kalnay, E., Kanamitsu, M., Kistler, R., Collins, W., Deaven, D., Gandin, L., Iredell, M., Saha, S., White, G., Woollen, J., Zhu, Y., Leetmaa, A., Reynolds, R., Chelliah, M., Ebisuzaki, W., Higgins, W., Janowiak, J., Mo, K.C. Ropelewski, C., Wang, J., Jenne, R., & Joseph, D. 1996. The NCEP/NCAR 40-year reanalysis project. *Bulletin of American Meteorological Society* 77: 437–471.
- Khrustalev, L.N. & Davidova, I.V. 2007. Forecast of climate warming and account of it at estimation of foundation reliability for buildings in permafrost zone. *Earth Cryosphere* 11(2): 68-75.
- Khrustalev, L.N., Parmuzin, S.Y., & Emelyanova L.V. 2011. *Reliability of northern infrastructure in conditions of changing climate*. Moscow: University Book Press, 260 pp. (in Russian).
- Klüter, H. 2000. Der Norden Russlands - vom Niedergang einer Entwicklungsregion. *Geographische Rundschau*, 52(12), 12-20.
- Kronic, Y.A. 2001. Accident rate and safety of natural-technogenic systems in cryolithozone. *Proceedings of the Second Conference of Geocryologists of Russia*, Moscow, June 6-8, 2001: 4: 138-146.

- Kuryk, D. 2003. Winter Roads in Manitoba. *12th Workshop on the Hydraulics of Ice Covered Rivers*, Edmonton, Alberta, June 19-20, 2003: Internet resource: http://cripe.civil.ualberta.ca/Downloads/12th_Workshop/Kuryk-2003.pdf. Accessed [14.09.11].
- Lonergan, S., Difrancesco, R., & Woo, M.K. 1993. Climate change and transportation in Northern Canada: an integrated impact assessment. *Climatic Change* 24: 331-351.
- Malkova, G.V. 2008. The last twenty-five years of changes in permafrost temperature of the European Russian Arctic. In *NICOP 2008: Proceedings of the Ninth International Conference on Permafrost*. D.L. Kane, K.M. Hinkel (eds.). Institute of Northern Engineering, University of Alaska Fairbanks, 2: 1119-1124.
- Malkova, G.V. 2010. Mean-annual ground temperature monitoring on the steady-state-station "Bolvansky". *Earth Cryosphere* 14(3): 3-14.
- Melnikov, E.S., Leibman, M.O., Moskalenko, N.G., & Vasiliev, A.A. 2004. Active-layer monitoring in the cryolithozone of West Siberia. *Polar Geography* 28 (4): 267-287.
- Mintransstroy. 1991. Departmental construction norms: Design, Construction and Maintains of Winter Roads in Siberia and the Northeast of the USSR. Ministry of Transport Construction of the USSR, 1991, 180 p. (VSN 137-89). Internet resource: http://gost-rf.ru/view_post.php?id=1175 (in Russian).
- Oberman, N.G. & Shesler, I.G. 2009. Observed and projected changes in permafrost conditions within the European North-East of the Russian Federation. *Problemy Severa i Arctiki Rossiiskoy Federacii (Problems and Challenges of the North and the Arctic of the Russian Federation)* 9: 96-106 (in Russian).
- Pavlov, A.V. & Malkova, G.V. 2005. Recent climate change in the north of Russia. Series of small-scale maps. Novosibirsk: Geo Press, 54.
- Permafrost Technology Foundation. 2009. Internet resource: <http://permafrost.org>.
- Romanovsky, V.E., Drozdov, D.S., Oberman, N.G., Malkova, G.V., Kholodov, A.L., Marchenko, S.S., Moskalenko, N.G., Sergeev, D.O., Ukraintseva, N.G., Abramov, A.A., Gilichinsky, D.A., & Vasiliev, A.A. 2010. Thermal state of permafrost in Russia. *Permafrost and Periglacial Processes* 21: 136-155.
- Russian Federation Government Resolution № 307 of May 23, 2006 "On Approval of the Provision which Allows Citizens to be Granted a License to Sell Electric Power." Internet resource: <http://base.consultant.ru/cons/cgi/online.cgi?req=doc;base=LAW;n=78806>. Accessed [14.09.11].
- Shiklomanov, N.I. & Nelson, F.E. 2002. Active-layer mapping at regional scales: a 13-year spatial time series for the Kuparuk Region, north-central Alaska. *Permafrost and Periglacial Processes* 13: 219-230.
- Shur, Y. & Goering, D. 2008. Climate change and foundations of buildings in permafrost regions. *Soil Biology* 16: 251-260.
- Sazonova, T.S. & Romanovsky, V.E. 2003. A model for regional-scale estimation of temporal and spatial variability of active layer thickness and mean annual ground temperatures. *Permafrost and Periglacial Processes* 14: 125-139.
- Skachkov, Y.B. 2008. Recent Climatic Changes in Yakutia. In *Extended Abstracts: Proceedings of the Ninth International Conference on Permafrost*. D.L. Kane, K.M. Hinkel (eds.). Institute of Northern Engineering, University of Alaska Fairbanks, 291-292.
- Stephenson, S.R., Smith, L.C., & Agnew, J.A. 2011. Divergent long-term trajectories of human access to the Arctic. *Nature Climate Change* 1: 156-160.
- Streletskiy, D.A. 2010. Spatial and temporal variability of the active-layer thickness at regional and global scales. Ph.D. Dissertation. University of Delaware, 243 pp.
- Streletskiy, D.A., Shiklomanov N.I., & Nelson F.E. 2012. Permafrost, infrastructure and climate change: A GIS-based landscape approach. *Arctic, Antarctic and Alpine Research* (in press).
- Vasiliev, A.A., Leibman, M.O., & Moskalenko, N.G. 2008. Active Layer Monitoring in West Siberia under the CALM II Program. In *NICOP 2008: Proceedings of the Ninth International Conference on Permafrost*. D.L. Kane, K.M. Hinkel (eds.). Institute of Northern Engineering, University of Alaska Fairbanks, 2:1815-1820.
- Vinson, T.S., Rooney, J.W., & Haas, W.H. (eds.). 1996. Roads and Airfields in Cold Regions: A State of the Practice Report (ASCE Technical Council on Cold Regions Engineering Monograph). Reston: ASCE, 324 pp.
- Wilson, K. 2007. Environmental Assessment and Finding of No Significant Impact. Section 117 Expedited Erosion Control Project Kivalina, Alaska. US Army Corps of Engineers, Alaska District, September 2007.
- Zamolodchikov, D., Kotov, A., Karelin, D., & Razzhivin, V. 2008. Recent climate and active layer changes in Northeast Russia: regional output of Circumpolar Active Layer Monitoring (CALM). In *NICOP 2008: Proceedings of the Ninth International Conference on Permafrost*. D.L. Kane, K.M. Hinkel (eds.). Institute of Northern Engineering, University of Alaska Fairbanks, 2: 2021-2027.
- Zhang, T., Barry, R.G., Knowles, K., Heginbottom, J.A., & Brown, J. 2008. Statistics and characteristics of permafrost and ground-ice distribution in the northern hemisphere. *Polar Geography* 31(2): 47-68.

Feasibility Study of Using Active Microwave Data for Examination of Thaw Lake Drainage Patterns over the Yamal Peninsula

Anna Maria Trofaier, William Gareth Rees
Scott Polar Research Institute, University of Cambridge, Cambridge, UK

Annett Bartsch, Daniel Sabel, Stefan Schlaffer
Vienna University of Technology, Institute of Remote Sensing and Photogrammetry, Vienna, Austria

Abstract

The applicability of radar data for monitoring the seasonal changes in permafrost thaw lake surface extent on the Yamal Peninsula is investigated. Data from the European Space Agency's ENVISAT Advanced Synthetic Aperture Radar (ASAR) operating in wide swath mode are used to map water bodies by applying simple threshold classification algorithms. A change detection analysis of lake surface extent shows that there are inundation variations between seasons. These preliminary results allow for the identification of summer drainage of certain lakes. However, due to the sensor-related limitations, the reason for this seasonal lake drainage pattern cannot be established. We assume that the interplay between the lakes and rivers should be taken into account for a complete understanding of lake dynamics. This paper hopes to communicate that ENVISAT ASAR WS data can be successfully used in the first instance to identify hotspots of lake change.

Keywords: active microwave; remote sensing; Russia; thermokarst lakes; Yamal Peninsula.

Introduction

Landscape evolution is a natural process. Periglacial environments have undergone modifications throughout the Quaternary. Nonetheless, the current trend of increasing air temperatures is raising concerns about the implications these temperatures may have on permafrost landscapes in arctic and subarctic regions.

Thermokarst is a process related to the thawing of frozen ground in ground-ice-rich regions. Ground ice ablation results in topographic slumping, known as thermokarst subsidence. Thaw waters accumulate in the resulting depressions. These thaw waters are known as thermokarst lakes or ponds, depending on their respective sizes. Tundra thaw ponds are of limited size; their diameter often being below 2 km (French 2007).

Thermokarst lakes and ponds are abundant in arctic and subarctic regions; in particular they cover the vast tundra lowlands. They are subject to seasonal variations due to snowmelt and fluctuations in precipitation, both of which can lead to changes in lake extent. The interaction of water bodies with permafrost is crucial to permafrost hydrology. Water has a high heat capacity, which results in further ground thawing. Hence surface water itself and changes in its extent affect permafrost processes.

During recent decades, a warming trend in the upper permafrost layers has been observed in high-latitude regions (Romanovsky et al. 2010). This warming affects permafrost processes. We hypothesize that changes in permafrost terrain are not necessarily attributed to climate-induced landscape evolution. Seasonal effects, associated with distinct change patterns, also need to be considered. This study provides preliminary data of an ongoing investigation on changes in thermokarst lakes. The paper focuses on the technical aspect of using ENVISAT ASAR WS as a means of identifying lake change. The assumption is that frequent monitoring

over consecutive years provides insight into any interannual variations in changes in lake extent.

Satellite data have been used in many studies to monitor lakes over the vast tundra regions. However, due to their limited size, tundra ponds are not captured in satellite-based global land cover datasets (Frey & Smith 2007, Bartsch et al. 2008). High spatial resolution data are required. Such data are available from optical sensors. The availability of acquisitions depends on daylight and cloud conditions. Aerial photographs are most suitable, but their availability is constrained due to acquisition difficulties. Satellite data provide an alternative means for more extensive archived material. Landsat data have been available since the 1970s, and multispectral instruments—the Thematic Mapper (TM) and, in later missions, the Enhanced Thematic Mapper (ETM)—have frequently been used to capture land cover changes in thermokarst regions (e.g., Frohn et al. 2005, Grosse et al. 2006, Ulrich et al. 2009, Arp et al. 2011). Other optical data are available for even longer periods back in time. Corona data, which date back to the 1960s, and the more recent Ikonos data have been of interest for permafrost studies (Yoshikawa & Hinzman 2003, Grosse et al. 2005). Less extensive archives for active microwave data are available. However, these sensors, such as synthetic aperture radar (SAR), are independent of cloud cover and illumination and have proved to be a useful method for providing observations and monitoring features of the hydrosphere (Bartsch et al. 2009). The feasibility of using radar for monitoring thermokarst lakes is explored in this study. In particular, our interest lies in exploiting active microwave data for the analysis of lake drainage patterns.

Representative data for the phenomenon of lake change are restricted to late summer acquisitions, since most lakes are often still frozen at the beginning of summer. Lake drainage and shrinkage have been reported based on optical satellite data from Alaska (Yoshikawa & Hinzman 2003), Siberia (Smith et

al. 2005), and Canada (Plug et al. 2008, Labreque et al. 2009). However, both decreasing and increasing lake surface extent are reported, depending on geographical location (Grosse et al. 2011).

The aim of this study is to analyze ENVISAT ASAR WS data of the Yamal Peninsula for the years 2007 to 2009, and to quantify the magnitude of changes in lake surface extent that are identified by the sensor. This paper evaluates the use of ENVISAT ASAR WS and discusses the implications of strategies of thermokarst monitoring with satellite data.

Study Area

The topography of the Yamal Peninsula is a ground-ice-rich lowland with gently rolling hummocky terrain; it is a typical thermokarst landscape. The greatest elevation on the Yamal Peninsula is about 40 m a.s.l. (Mahaney et al. 1995). Numerous streams meander through this landscape, many of which lie below the spatial resolution of ENVISAT ASAR operating in wide swath mode. These streams are to be kept in mind because the interactions between lakes and the river systems may play a key role in lake dynamics.

The focus has been on two study areas where changes in lake extent are identified by the sensor. One is located near the Bovanenkovo gas field in the west of the Yamal Peninsula (ROI 1). The other area lies south of this (ROI 2). Both regions are indicated in Figure 1. Stratified silts and organic materials containing fibrous peat are found in these areas (Mahaney et al. 1995).

Materials and Methods

Satellite data

This study uses data from the European Space Agency's ENVISAT Advanced Synthetic Aperture Radar (ASAR) instrument operating in wide swath (WS) mode. ASAR data have been collected since 2003 at several modes. In wide swath, which is a ScanSAR mode, a high number of images are available for certain areas in the Arctic, although not at regular intervals, and the data are acquired only on request. ASAR is a C-band sensor which has a center frequency of 5.331 GHz. The spatial resolution for ASAR WS is 150 m. This is rather coarse, but it allows improved mapping over larger regions and the majority of tundra ponds are captured (Bartsch et al. 2008). The data for this study were taken in HH polarization.

The first few stages in the processing chain are usually referred to as pre-processing steps. These can be divided into calibration and georeferencing, where the former encompasses the conversion of the raw digital numbers, which are measured by the sensors, into their representative physical quantities (Rees 2006). The pre-processing steps are as follows:

1. Radiometric calibration
2. Geometric correction
3. Normalization - Local incidence angle correction

Advanced data handling is required for change detection applications, which rely on a high number of samples. The

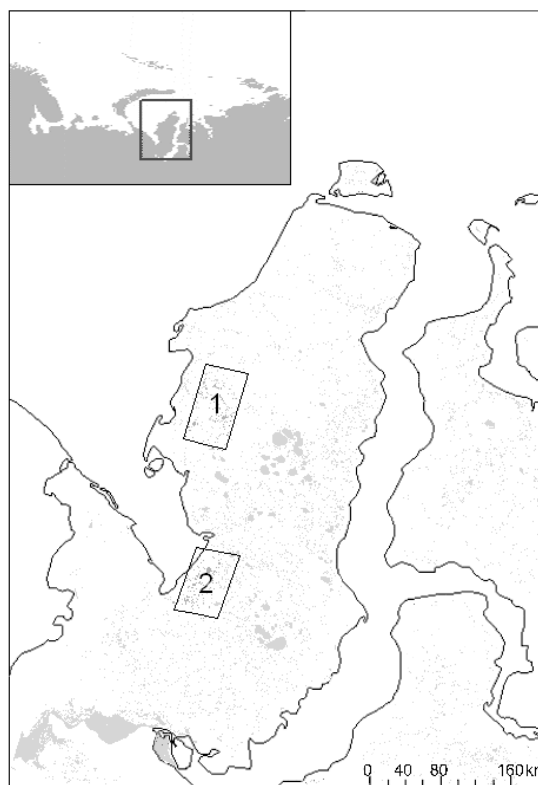


Figure 1. Map of the Yamal Peninsula. Grey areas represent ASAR WS classified water bodies, many of which fall below the map resolution.

datasets are resampled to pre-defined tiles (Pathe et al. 2009, Sabel et al. in press), and single acquisitions are stored as layer stacks. Only datasets from the snow- and freeze-free period have been selected. Snowmelt is usually complete by mid-June over the Yamal Peninsula (Bartsch 2010).

Inundation mapping

The method of thresholding is applied to the ASAR WS data for classification purposes. Specular reflection of the radar beam at the air-water interface of lakes on wind-free days allows for a clear distinction of water from the surrounding neighborhood. The backscatter value of a lake with low surface roughness (i.e., for low wind conditions) in an ASAR normalized image is about -14 dB, when normalized to an incidence angle of 30° (Bartsch et al. 2011). This backscatter value is set to be the threshold.

An automated classification of the summer months July and August in each year is done on a fortnightly basis. The classification routine is set to identify any pixels that lie below the aforementioned threshold, which are then classified as water pixels. In a post-processing step, a further condition is introduced: at least two ASAR measurements within the given time period for each pixel. Hence four classifications for each year, two in each month, are established. The classification details are given in Table 1. This classification method provides a means for identifying lake surfaces at their greatest extent within a two-week period.

Table 1. Classifications.

| Classification | Time period for each year | |
|----------------|---------------------------|-----------|
| | Start date | End date |
| A | 01 July | 14 July |
| B | 15 July | 31 July |
| C | 01 August | 14 August |
| D | 15 August | 31 August |

Table 2. Number of ENVISAT measurements for each classification.

| Classification | Maximum number of images used for ROI 1 | | | Maximum number of images used for ROI 2 | | |
|----------------|---|------|------|---|------|------|
| | 2007 | 2008 | 2009 | 2007 | 2008 | 2009 |
| A | 12 | 14 | 4 | 8 | 13 | 3 |
| B | 15 | 14 | 9 | 13 | 12 | 7 |
| C | 12 | 9 | 8 | 11 | 7 | 8 |
| D | 13 | 11 | 7 | 10 | 8 | 4 |

Change detection

The classification procedure is then followed by a Geographic Information System (GIS) lake surface analysis as a means of change detection. This is done by subtracting each classification from its temporally preceding classification, thereby arriving at three classifications for changes that have occurred over July and August (classification A-B, B-C, and C-D).

Optimum threshold sensitivity analysis

The classification procedure is dependent on the chosen threshold of -14 dB. This threshold is selected in accordance with previous studies that have explored the threshold approach and found it to produce satisfactory results (Bartsch et al. 2007, Bartsch et al. 2008). Nonetheless, an optimum threshold evaluation for a set of randomly chosen lakes is performed for further sensitivity analysis of the water pixel classification to the chosen threshold.

This procedure was done in the ImageJ software environment (Abramoff et al. 2004). The optimum threshold for a set of 12 randomly selected lakes for five ASAR WS images was determined manually. The software was then used to calculate the area and perimeter of each lake. The error in the threshold value was investigated by analyzing the change in mean lake diameter and area as a function of threshold value.

Results

There are two regions on the Yamal Peninsula where larger variations are identified by the sensor. The first region of interest (ROI 1) is situated in the northwest of the Yamal Peninsula. The Bovanenkovo gas field lies in the north within ROI 1. The second region of interest (ROI 2) is located south of ROI 1. Both regions are shown in Figure 1, and their geographical coordinates are given in Tables 3 and 4.

Table 3. Geographic coordinates for ROI 1.

| Corner points | Latitude (N) | Longitude (E) |
|---------------|---------------|---------------|
| Upper left | 70°30' 1.744" | 67°53' 59.15" |
| Lower right | 69°48' 5.265" | 68°59' 57.25" |

Table 4. Geographic coordinates for ROI 2.

| Corner points | Latitude (N) | Longitude (E) |
|---------------|---------------|---------------|
| Upper left | 68°35' 60.00" | 68°44' 52.82" |
| Lower right | 67°56' 11.99" | 69°32' 43.23" |

The manually determined optimum threshold for each lake in each image showed that this optimum threshold varied significantly from lake to lake and was also image dependent. The values range from -15 to -9.8 dB. The standard deviation of the entire set of optimum threshold values was found to be 1.22 dB. It was therefore decided to proceed with a threshold sensitivity analysis in steps of 1 dB.

The sensitivity analysis of the threshold conditions showed that an increase in threshold by 1 dB results in an average change in mean lake diameter of ~21.84 m. The choice of using a threshold value that is at the lower end of the optimum threshold range is related to the loss in separability of the lakes from the surrounding neighborhood. At a threshold of -10 dB, most of the selected lakes merge with neighboring lakes. In addition, the increase in noise from pixels that are classified as water but cannot be identified as lakes, due to spatial resolution constraints, provides the reasoning for setting the threshold value at -14 dB.

The total pixel count change for each classification is shown in Figure 4. The total change can be divided into changes due to pixel loss versus pixel gain. A map of lake change due to loss in pixel count is given in Figure 2.

Pixel count of lake area is highly dependent on the number of measurements available from ENVISAT ASAR for each classification. Figure 3 shows the pixel count for each classification of ROI 1 in 2007 as a function of ASAR measurements.

The cumulative changes in water pixel count for ROI 1, for both loss and gain, are given in Figure 5, where loss and gain in pixel count are represented by negative and positive values, respectively. The greatest change in loss in both regions occurs between the first two classifications. In each case, loss in water pixel count decreases steadily thereafter. This holds for ROI 1. Similarly, this behavior is also found for ROI 2 in 2007. Unfortunately, the number of measurements available that meet the threshold conditions was greatly limited in 2008 and 2009 for ROI 2.

The bottom right panel of Figure 2 shows the water pixel counts for each classification in 2008 for ROI 2 as a function of ASAR measurements.

In addition to loss, the gain in water pixel count was also identified. This gain is primarily around the margins of the water bodies and could be attributed to mixed pixels.

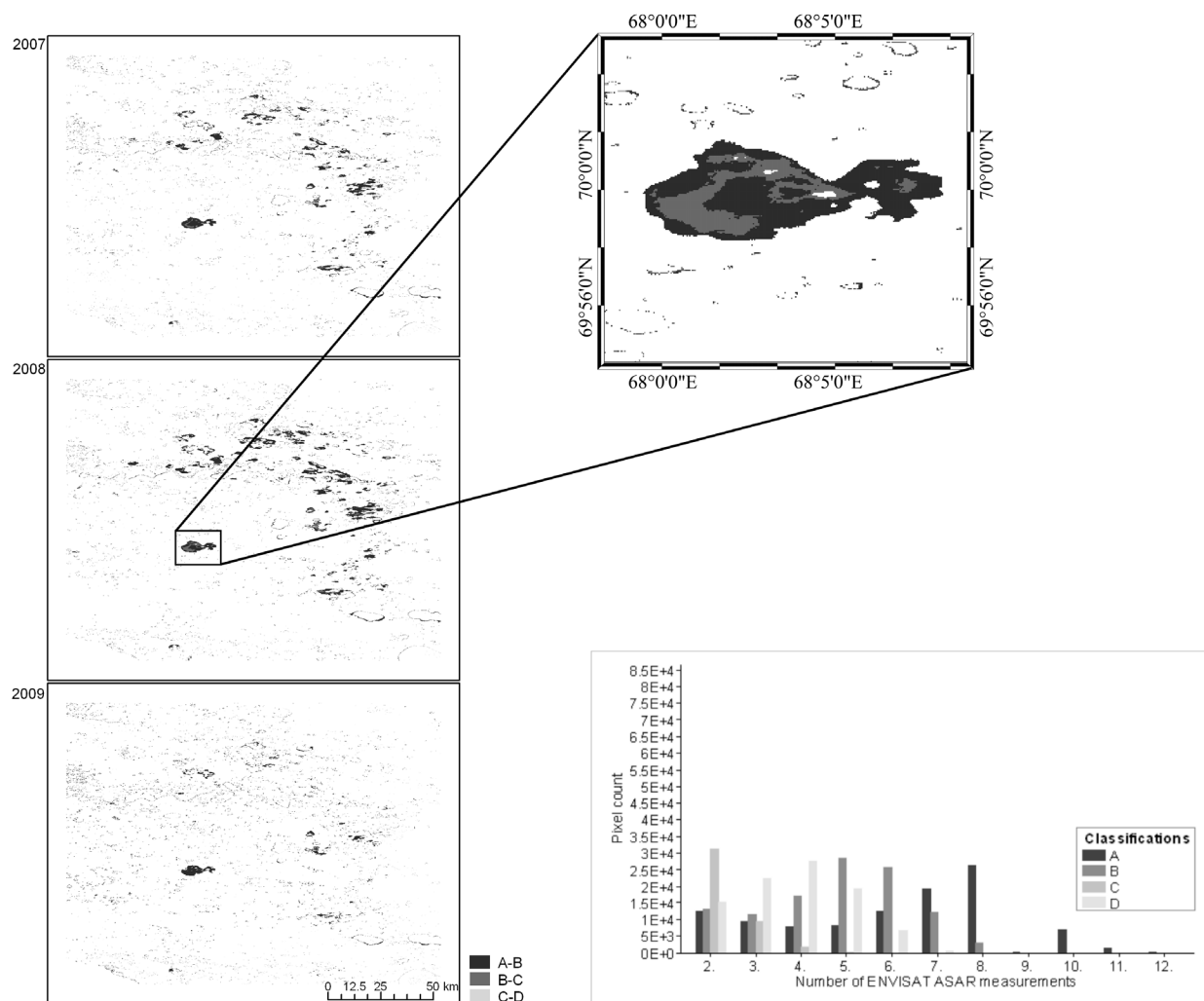


Figure 2. Map of water pixel loss for ROI 1 (left). Number of measurements and associated pixel count for each classification for ROI 2 in 2008 (bottom right).

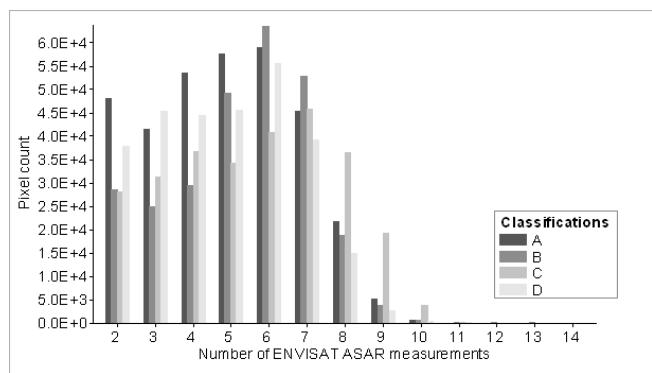


Figure 3. Number of measurements and associated pixel count for each classification for ROI 1 in 2007.

Furthermore, wind conditions seem to play a crucial role, in particular concerning large lakes. At high wind speed, an increase in the surface roughness of these lakes will result in loss of separability from their surroundings, and these data will not be classified as water bodies. The classifications, and hence the results for the change analysis, will be affected by this problem. Therefore, gain in lake extent is also associated

with an increase in data (i.e., better wind conditions). This issue is particularly prominent in ROI 2 in both 2008 and 2009, as can be seen from the pixel counts for each classification depicted in the bottom panel of Figure 4.

Discussion

The ASAR WS analysis of lake surface extent on the Yamal Peninsula shows that there are two regions in which a sudden decrease in the number of water pixels in the first few weeks of July is visible. It is hypothesized that this is related to a distinct seasonal pattern in lake drainage, which may in turn result from river-lake interactions. However, due to spatial resolution constraints of the sensor, these interactions cannot be investigated by the current method. Further research into this phenomenon is necessary.

The automated thresholding approach is used as a time efficient means to produce a fairly accurate classification. The choice of threshold is at the lower end of the optimum threshold range of the random lake sample. However, our error investigation showed that given the great range of

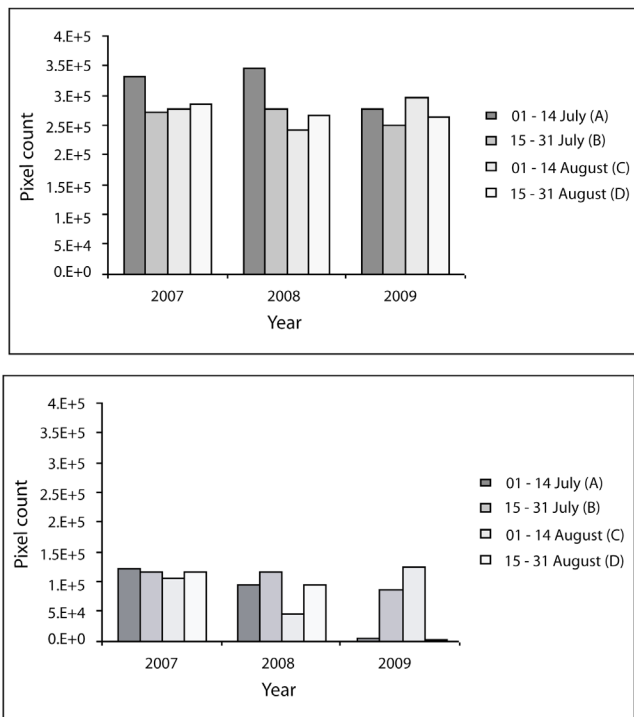


Figure 4. Pixel count of each classification for ROI 1 (top) and ROI 2 (bottom).

optimum thresholds and the lower signal to noise ratios at higher thresholds, the average change in mean lake diameter was sufficiently low to use a threshold value of -14 dB. Indeed, given the sensor's spatial resolution of 150 m and an average change in mean lake diameter of less than 22 m, the applicability of the thresholding approach is clearly justifiable.

The results show that the regular monitoring of these water bodies with the aid of ASAR WS is restricted by the impact of local wind conditions. The high variability of wind speed produces skewed classification results, which hinder a comprehensive analysis based solely on SAR data. Bartsch et al. (2011) have discussed the effects of wind on this classification technique. The classification problem is distinctly noticeable for ROI 2 in both 2008 and 2009, when the number of ASAR WS measurements is greatly limited.

These restrictions have implications for continuous monitoring of lake dynamics. Advanced knowledge of weather conditions from meteorological records provides complementary information and allows a pre-selection of wind-free datasets. However, such records are not always available. Further, this knowledge will have no impact on the number of ASAR WS measurements. The ASAR WS sensor is a highly capable device for frequent monitoring, but severe wind conditions common to high-latitude regions impinge on its temporal resolution.

Conclusions

This study addresses the use of active microwave data as a preliminary method for investigating seasonal patterns in inundation dynamics. Permafrost thaw lakes on the Yamal

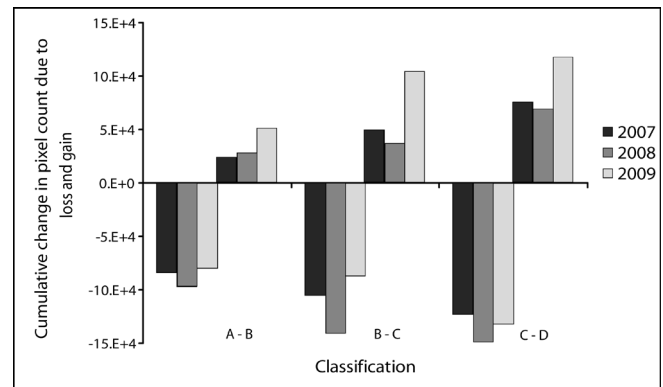


Figure 5. Cumulative change in pixel count due to water pixel loss and gain for ROI 1.

Peninsula are monitored with the aid of synthetic aperture radar. The information retrieved from such sensors can be translated into classifications of inundation extent. Changes in lake surface extent are examined; both loss and gain in water pixel counts are established. As with many remotely sensed studies, data availability (both sensor and weather-related) poses a more complex issue that needs to be tackled for effective monitoring.

Acknowledgments

Satellite data processing has been supported by ESA initiatives DUE Permafrost (ESRIN Contr. No. 22185/09/I-OL) and STSE ALANIS-Methane (ESRIN Contr. No. 4000100647/10/I-LG). A.M. Trofaier is a recipient of a DOC-fFORTE-fellowship of the Austrian Academy of Sciences at the Scott Polar Research Institute. A. Bartsch has been a recipient of a research fellowship by the Austrian Science fund (FWF Elise Richter Program, V150- N21) during the course of the study.

References

- Abramoff, M.D., Magalhaes, P.J., & Ram, S.J. 2004. Image Processing with ImageJ. *Biophotonics International* 11(7): 36-42.
- Arp, C.D., Jones, B.M., Urban, F.E., & Grosse, G. 2011. Hydrogeomorphic processes of thermokarst lakes with grounded-ice and floating-ice regimes on the Arctic coastal plain, Alaska. *Hydrological Processes*.
- Bartsch, A. 2010. Ten Years of SeaWinds on QuikSCAT for Snow Applications. *Remote Sensing* 2: 1142-1156.
- Bartsch A., Kidd, R., Pathe, C., Wagner, W., & Scipal, K. 2007. Satellite radar imagery for monitoring inland wetlands in boreal and sub-arctic environments. *Journal of Aquatic Conservation: Marine and Freshwater Ecosystems* 17: 305-317.
- Bartsch, A., Pathe, C., Wagner, W., & Scipal, K. 2008. Detection of Permanent Open Water Surfaces in Central Siberia with ENVISAT ASAR Wide Swath Data with Special Emphasis on the Estimation of Methane Fluxes from Tundra Wetlands. *Hydrology Research* 39: 89-100.

- Bartsch, A., Trofaier, A.M., Hayman, G., Sabel, D., Schläffer, S., Clark, D., & Blythe, E. 2011. Detection of wetland dynamics with ENVISAT ASAR in support of methane modeling at high latitudes. *Biogeosciences Discuss* 8: 8241-8268.
- Bartsch, A., Wagner, W., Scipal, K., Pathe, C., Sabel, D., & Wolski, P. 2009. Global monitoring of wetlands - the value of ENVISAT ASAR global mode. *Journal of Environmental Management* 90:2226-2233.
- French, H.M. 2007. *The Periglacial Environment*, 3rd edition. Chichester, John Wiley & Sons, 191 pp.
- Frey, K. & Smith, L.C. 2007. How Well Do We Know Northern Land Cover? Comparison of Four Global Vegetation and Wetland Products with a New Ground-Truth Database for West Siberia. *Global Biogeochemical Cycles* 21: GB1016.
- Frohn, R.C., Hinkel, K.M., & Eisner, W.R. 2005. Satellite remote sensing classification of thaw lakes and drained thaw lake basins on the North Slope of Alaska. *Remote Sensing of Environment* 97:116-126.
- Grosse, G., Jorgenson, T., Walter, K., Brown, J., & Overduin, P.P. 2011. Vulnerability and Feedbacks of Permafrost to Climate Change. *EOS Transactions, American Geophysical Union* 92: 73-80.
- Grosse, G., Schirrmeyer, L., Kunitzky, V.V., & Hubberten, H.-W. 2005. The use of CORONA images in remote sensing of periglacial geomorphology: An illustration from the NE Siberian coast. *Permafrost and Periglacial Processes* 16: 163-172.
- Grosse, G., Schirrmeyer, L., & Malthus, T. 2006. Application of Landsat-7 satellite data and a DEM for the quantification of thermokarst-affected terrain types in the periglacial Lena-Anabar coastal lowland. *Polar Research* 25(1): 51-67.
- Labreque, S., Lacelle, D., Duguay, C.R., Lauriol, B., & Hawkings, J. 2009. Contemporary (1951–2001) Evolution of Lakes in the Old Crow Basin, Northern Yukon, Canada: Remote Sensing, Numerical Modeling, and Stable Isotope Analysis. *Arctic* 62(2): 225-238.
- Mahaney, W.C., Michel, F.A., Solomatin, V.I., & Hütt, G. 1995. Late Quaternary stratigraphy and soils of Gydan, Yamal and Taz Peninsulas, northwestern Siberia. *Palaeogeography, Palaeoclimatology, Palaeoecology* 113: 249-266.
- Pathe, C., Wagner, W., Sabel, D., Doubkova, M., & Basara, J. 2009. Using ENVISAT ASAR Global Mode Data for Surface Soil Moisture Retrieval Over Oklahoma, USA. *IEEE Transactions on Geoscience and Remote Sensing* 47(2): 468-480.
- Plug, L.J., Walls, C., & Scott, B.M. 2008. Tundra lake changes from 1978 to 2001 on the Tuktoyaktuk Peninsula, western Canadian Arctic. *Geophysical Research Letters* 35: L03502.
- Rees, W.G. 2006. *Remote Sensing of Snow and Ice*. Cambridge, Taylor and Francis, 76 pp.
- Romanovsky, V.E., Smith, S.L., & Christiansen, H.H. 2010. Permafrost thermal state in the polar Northern Hemisphere during the International Polar Year 2007–2009: A synthesis. *Permafrost and Periglacial Processes* 21: 106-116.
- Sabel, D., Bartalis, Z., Wagner, W., Doubkova, M., & Klein, J.-P. 2011. Development of a Global Backscatter Model in support to the Sentinel-1 mission design. *Remote Sensing of Environment*, in press.
- Smith, L.C., Sheng, Y., MacDonald, G.M., & Hinzman, L.D. 2005. Disappearing Arctic Lakes. *Science* 308: 1429.
- Ulrich, M., Grosse, G., Chabrillat, S., & Schirrmeyer, L. 2009. Spectral characterization of periglacial surfaces and geomorphological units in the Arctic Lena Delta using field spectrometry and remote sensing. *Remote Sensing of Environment* 113:1220-1235.
- Yoshikawa, K. & Hinzman, L.D. 2003. Shrinking thermokarst ponds and groundwater dynamics in discontinuous permafrost near Council, Alaska. *Permafrost and Periglacial Processes* 14: 151-160.

Inventory and Monitoring of Rock Glaciers and Cryogenic Processes in the Central Andes of Mendoza, Argentina: Birth and Extinction of a Periglacial Lake

Dario Trombotto Liaudat, M. Gabriela Lenzano
IANIGLA, CCT CONICET Mendoza, Casilla de Correo 330, 5500 Mendoza

Mariano Castro
IANIGLA, CCT CONICET Mendoza, Casilla de Correo 330, 5500 Mendoza

Abstract

New inventories of rock glaciers in the Cordillera del Tigre (32°11'S, 32°45'S) and the Cordón del Plata (32°40'S, 33°24'S) were made with manual digitizing of ASTER images and interpretation of photographs. The Cordillera del Tigre (NW Mendoza) has a surface with possible permafrost of approximately 1171 km², and the Cordón del Plata has 956 km². The lower permafrost limit was estimated to be 3600 m a.s.l. In the Cordillera del Tigre, 182 new active rock glaciers were counted, with an average surface of 0.35 km² and an area of about 64 km². The largest rock glacier comprises a surface of 2.37 km². Rock glaciers appear preferably when their detritic and nival feeding zone has a southerly orientation. The lower limit of uncovered ice lies at approximately 4300 m a.s.l. A build-up of the creeping permafrost generated a lake of approximately 7.9 ha on one of the tributaries of the Mendoza River.

Keywords: Argentina; Central Andes; periglacial lake; permafrost; inventory of rock glaciers.

Introduction

In 1981 an inventory of rock glaciers of the Cordillera Frontal of Argentina was presented as part of the Glacier Inventory of the Mendoza River (Corte & Espizúa 1981). This pioneer work helped to reconstruct the environment of the cryospheric system, but today these data need to be updated and revised due to changes observed in the glaciers caused by global warming during recent years. Moreover, this early publication does not take into account rock glaciers and the cryodynamics of creeping permafrost as an independent topic, apart from the distinction between covered and uncovered glaciers. That work only linked the origin of a rock glacier as a landform depending on glaciers. Hence a logistical regression model based on aerial photographs and digital elevation models was employed (Brenning & Trombotto 2006). This model considered the topography and climate of the Central Andes of Chile and Argentina in order to study the distribution of glaciers and rock glaciers of glacial and cryogenic origin.

The law that promotes the National Inventory of Glaciers has included rock glaciers as part of the periglacial environment for their hydrological importance and their significance as a strategic ice reservoir. At the same time, the melting of the active layer of the rock glaciers is considered to be an important annual hydrological contribution to Andean rivers. It has to be noted, though, that Andean rock glacier hydrology is far from being really well known. According to the results of different geophysical, geoelectrical, seismic, and GPR studies of the structure of the Andean rock glaciers (Barsch & King 1989, Trombotto et al. 1999, Götz et al. 2008, Arenson et al. 2010, Otto et al. 2010, among others), the latter display a wide range of vertical and areal varieties in terms of their ice content. This makes it difficult to quantify the water volume equivalent to the ice of a rock glacier. Moreover, rock glaciers differ greatly

from one another, and these differences complicate a model-based generalization.

An inventory of rock glaciers and other ice bodies was compiled for two particular sections of the Cordillera Frontal of Argentina: the Cordón del Plata (Novero 2003, Trombotto 2003) and the Cordillera del Tigre (Castro 2010). The latter was part of a final work of Technician in Geography at the Universidad Nacional de Cuyo, and it corresponded to a first step of recognition and monitoring. The aims of this presentation are to further study the periglacial environment of the two mentioned sectors, to characterize rock glaciers, map permafrost, monitor the area, and try to distinguish rock glaciers from covered glaciers. It must be pointed out, however, that while rock glacier activity depends on the existence or not of permafrost, covered glaciers are in fact glaciers and have glacier dynamics. At the same time, the intention is to detect more rock glaciers and to substantially improve the existing inventory thanks to technological advances in remote sensing.

Study Area

The study area belongs to the Cordillera Frontal (32°–34°30'S) of Mendoza (Trombotto et al. 1999). It is an intermediate mountain area of the Cordillera Principal, which borders with Chile. It belongs to the Andean orogenic cycle of the Tertiary and the Precordillera, which is part of an old mountain system with initial orogenic activity and rocks of Palaeozoic age. Volcanic rocks (andesites, rhyolites) are predominant in the study area but greywacke, lutites, sandstone, and intrusive granitic rocks of Palaeozoic age are also present. From a cryogenic point of view, two important sectors of the Cordillera Frontal were chosen: Cordón del Plata (32°40'S and 33°34'S) and Cordillera del Tigre (32°11'S and 32°45'S). Climatically, the area belongs to a mountain climate, polar Tundean climate, or Altoandean region (Trombotto 1991) with

mean annual air temperatures below 0°C at an approximate height of 3600 to 3700 m a.s.l. and upward. Precipitation ranges from 300 to 450 mm/y (at the meteorological stations Aguaditas at 2250 m a.s.l. and Vallecitos at 2550 m a.s.l., respectively, between 1972 and 1985, on the SE slope of the Cordón del Plata) to a precipitation optimum of approximately 600–650 mm at a height of 4000 m a.s.l. and higher. During the winter season, snowfalls are more frequent but the zonda (a foehn-like wind) plays a major role in the redistribution and disappearance of snow. The area receives precipitation from the Atlantic as well as from the Pacific with important yearly peaks in summer (February) and in winter (July). Permafrost is observed in situ and also as creeping permafrost (Trombotto & Borzotta 2009).

Methodology

For the inventory of rock glaciers, ASTER (Advanced Spaceborne Thermal Emission and Reflection Radiometer) images of the TERRA sensor were used to obtain information on two sectors of the Cordillera Frontal of Mendoza, Argentina. Different scenarios were selected according to their availability in the archive. For Cordillera del Tigre, the image from February 24, 2007, was selected, and for Cordón del Plata, the image from April 8, 2011, was chosen. It was easier to detect rock glaciers on this last image because it contains a smaller area with snow cover and fewer clouds than others. Level 1B of ASTER was chosen to carry out the inventory because it has the capability of generating a product with projected coordinates (Iwasaki & Fujisada 2005), and it comes in pre-processed format. All data were referenced using WGS84 and reprojected in the Argentine GK2 system. The rock glacier areas were expressed as projected surfaces (2D).

Rock glaciers larger than 0.01–0.02 km² m were selected for the inventory and classified according to their origin. Rock glaciers were classified as glacial (i.e., debris rock glaciers) (Barsch 1996) or cryogenic (i.e., talus rock glacier) (Barsch 1996). In this inventory, both active and inactive rock glaciers are included for several reasons. Because of the use of different images in inaccessible areas or areas unknown through field campaigns, it is very difficult to distinguish between them. In pilot zones such as the Morenas Coloradas rock glacier, frozen bodies are often entangled or superposed. Field trips are always necessary, for instance, to corroborate the inclination of the slopes of the active fronts > 30°, marked ridges and furrows, unstable surfaces with blocks, lack of vegetation, and vertical selection at the fronts for indication of activity. The height of the active rock glacier fronts helped determine the lower limit of Andean creeping permafrost and to disregard lower areas with fossil rock glaciers. The presence of cirques in relation to the rock glaciers was also mentioned and considered when they were classified.

In order to make an inventory of rock glaciers, the technique of manual delineation in the image was applied (Stokes et al. 2007). The cryospheric map obtained for the two sectors of the Cordillera Frontal of Mendoza was vectorized to produce the boundaries of the rock glaciers through photo-interpretation.

Because of the limitation of digitizing rock glaciers from the available imagery, aerial photographs (but not of the entire region) and Google Earth images were used.

Possible and probable permafrost occurrence from a regional point of view was marked on the maps by extrapolating from in situ detection or deduced from active rock glaciers at certain key sites according to similar conditions of topography, orientation, and location. For the general distribution of mountain permafrost and in the first approximation, active and inactive rock glacier fronts were used as the lower limit. This limit was considered as “possible permafrost occurrence” for the region. A more precise limit for probable permafrost was based on data (permafrost presence) from different sites and monitoring outside the range of rock glaciers, from the presence of perennial snow patches, the presence of gelifluction, and the sole presence of cryogenic rock glaciers in certain field trip areas.

Analysis of different historic LANDSAT and ASTER images also allowed us to determine the formation of a periglacial lake, its evolution until its extinction, and the creation of a new lake. The area and evolution of the lake were studied through manual digitization of the perimeter.

Table 1 identifies the satellite images used for this work.

Results and Discussion

Cordón del Plata

A new inventory of rock glaciers (Fig. 1) conducted at the Cordón del Plata area shows that the estimated area of possible permafrost extends upward from 3600 m a.s.l. and covers 956 km²; the area of probable permafrost extends upward from 4500 m a.s.l. and covers 498 km².

The lower limit of uncovered ice lies at approximately 4300

Table 1. Satellite images.

| Type of sensor | Date |
|---|--|
| LANDSAT 7, 4-5 TM (Path:232, Row: 83), resolution: 30 m | 1984-04-21; 1986-02-22; 1987-02-09 |
| ASTER, resolution: 15 m | 2005-02-18; 2007-02-24; 2008-12-27; 2010-03-27; 2010-09-28; 2011-04-08 |

Table 2. Inventory of rock glaciers in the Cordón del Plata.

| | glaciers and perennial snow patches | glacial rock glaciers | cryogenic rock glaciers | composed rock glaciers |
|-----------|-------------------------------------|-----------------------|-------------------------|------------------------|
| number | 354 | 101 | 264 | 38 |
| ∑ | 85 km ² | 38 km ² | 39 km ² | 17 km ² |
| \bar{X} | 0.2 km ² | 0.8 km ² | 0.1 km ² | 0.4 km ² |
| min. | 0.01 km ² | 0.55 km ² | 0.01 km ² | 0.08 km ² |
| max. | 9 km ² | 1.6 km ² | 1.1 km ² | 2.5 km ² |

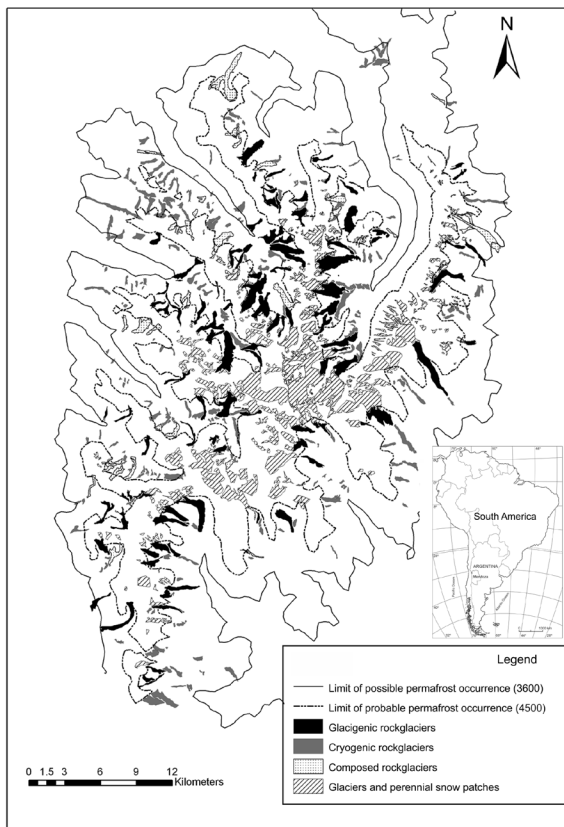


Figure 1. Rock glaciers in the Cordón del Plata.

m a.s.l. Thermokarst zones are usually combined with covered ice and identified in 30% of the inventoried debris covered glaciers between about 4300 and 4100 m a.s.l. However, ice bodies not attached to the main body of the covered glacier display thermokarst down to 3700 m.

A total of 354 uncovered glaciers, glacieretes, and perennial snow patches linked with the glaciers were identified. Their size varied from 0.01 km² to 9 km², and their surface covered an area of 85 km². Moreover, 365 rock glaciers (Table 2) were counted, 101 of which were of glacigenic origin (377 km²), 264 (39 km²) were of cryogenic origin, and 38 were composed rock glaciers (of glacigenic and cryogenic origin), covering an area of 17 km². Thermokarst was not inventoried in this step because these features will have to be separated into two types according to whether they are found in covered glaciers or in rock glaciers, where they are irregularly dispersed along their fronts and in different units of rock glaciers.

Data of the rock glacier Morenas Coloradas (Trombotto & Borzotta 2009) were used as a reference zone and a model of composed rock glaciers (cryogenic/glacigenic), multi-root, multi-unit, and with superposed lobes in order to know the parameters that condition the presence of permafrost. It has three active layer monitoring sites with data that, in some cases (Balcón I), date back to 1989.

The rock glacier Morenas Coloradas at its lower altitudinal limit tends to have aggradating permafrost at about 3600 m (Balcón I); presumably this is a recovery of the equilibrium

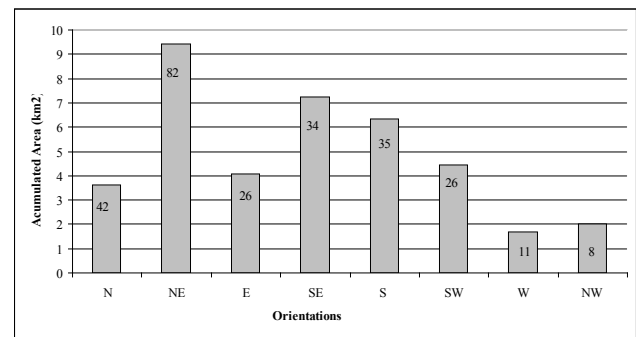


Figure 2. Orientation versus accumulated area of rock glaciers in the Cordón del Plata. The numbers inside the histogram indicate the quantity of rock glaciers.

state of the former cryogenic system. The present analysis reveals a tendency toward a gradual reduction in the thickness of the unfrozen sediments in the upper part of the rock glacier. The active layer thickness of ~5 m found in 1992 at 3560 m a.s.l. was measured at an approximate elevation of 3600 m a.s.l. in 2008, some 40 m higher (Trombotto Liaudat et al. 2008). Another monitoring site, Balcón II, shows a smaller variation in the active layer with a trend toward reduced thickness.

Figure 2 shows the predominant orientation of the cryogenic rock glaciers. These rock glaciers were chosen in order to obtain a direct link with the factors of temperature, exposure, and height in the mountain system, which are reliable indicators of the lower permafrost limit. The high number (82) of NE orientated rock glaciers in the Cordón del Plata is remarkable, but these bodies are small and appear at high altitude (> 4300 m a.s.l.). They seem to be associated with the same general alignment as the predominant structures of the Cordón del Plata that are NE-SW. Glacigenic rock glaciers are of great size (various km). Many of them however are composed rock glaciers, such that their genesis results by contribution from talus rock glaciers. The latter incorporate cryosediments through their numerous roots or areas of cryosediment production at the talus foot or as superimposed lobes. Among the orientations, a preference of the bodies toward the S was found. However, there was also a significant number with an NE orientation that might be associated with the fact that they are composed rock glaciers, which therefore achieve great magnitude and also move along valleys which respond to preferential tectonic structures. The directions of glacigenic rock glaciers are controlled by the pre-existing geological structures. Predominant NW-SE faults force the prevailing orientation of glaciers and covered glaciers which produce glacigenic rock glaciers. These move along the valley because of the covered glaciers. Glacigenic rock glaciers interact with covered glaciers.

Additional results of the inventory in the Cordón del Plata: detection of a periglacial lake

Monitoring a shallow lake at the central part of the Cordón del Plata at an approximate height of 3800 m a.s.l., in an area of possible permafrost in a N-S valley of U-shape with many rock glaciers and glaciers, allowed us to corroborate its cryogenic

Table 3: Evolution of a periglacial lake.

| Image | Length (m) | Area (m ²) |
|------------|------------|------------------------|
| 1984-04-21 | 0.0 | 0.0 |
| 1986-02-22 | 1581 | 59085 |
| 1987-02-09 | 1792 | 64441 |
| 2005-02-18 | 1825 | 60071 |
| 2008-12-27 | 1913 | 76063 |
| 2010-03-27 | 1495 | 48949 |
| 2010-09-28 | 0.0 | 0.0 |
| 2011-04-08 | 690 | 16275 |

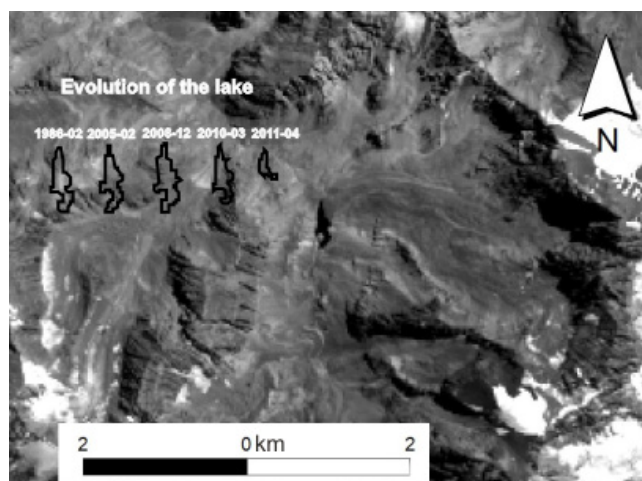


Figure 3. Evolution of a periglacial lake in the Central Andes of Mendoza.

origin. The lake is located near 32°57'S, 69°33'W and is generated by the accumulation of water from the cryospheric system of the surrounding areas, melted snow, glacial ice, and the annual thawing of the active layer. A build-up formed in an area of outcrop shaped by glacial ice which cuts the valley transversally and combines with a blockade of periglacial sediments from the active rock glaciers of the surroundings, particularly from a SW-oriented rock glacier. The foot of the front slope of this glacier has experienced variations, as it was formally an active body of a larger complex. The rock glacier, however, is active, with clear signs of half moon furrows on its surface. The body of the lowest rock glacier is part of a group of superposed units and gradual steps building a composed group of rock glaciers, which interact with each other during the transport of cryosediments downslope. They possess cryogenic as well as glacial roots according to the follow-up of satellite images and Google Earth.

The lake apparently formed between 1984 and 1986. On the LANDSAT scene from February 22, 1986, the lake can already be identified with its maximum extension in length of ~550 m, width of ~200 m, and an estimated maximum depth of 10 m. The analysis of different images shows the evolution of the lake between 1984 and 2011 (Table 3). Since the scene from March 27, 2010, the surface of the lake has decreased by 35%, and in the image of September 28, it has completely disappeared. Figure 3 shows the evolution of the periglacial lake and its new appearance in 2011.

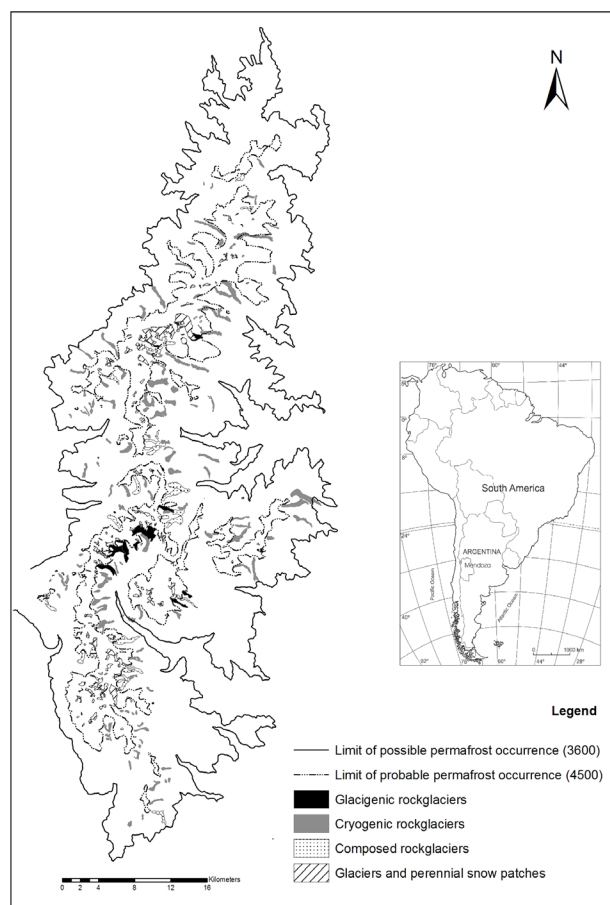


Figure 4. Cordillera del Tigre.

The increase in the water volume coincides with a period of intense snowfalls between 2007 and 2009, whereas the drainage of the lake in 2010 coincides with an extraordinarily dry year, according to a precipitation transect traced from Colonia Suiza (1200 m a.s.l.) to Balcón I (3560 m a.s.l.), which might have influenced its evolution. Conversely, permafrost could be important for impeding water percolation. On February 27, 2010, an earthquake in Maule in Chile strongly impacted Mendoza and might also have caused a weakening of the precarious periglacial blockade of the lake. In April of 2011, a newly formed lake was observed.

Cordillera del Tigre

The Cordillera del Tigre in the northwest of the province of Mendoza has possible permafrost covering ~1171 km² (Figure 4). The lower permafrost limit was found at 3600 m a.s.l. through interpolation of direct data (temperature registers) from the province of San Juan (northern limit of the Cordillera del Tigre) and data obtained from the Cordón del Plata, Mendoza (Trombotto & Borzotta 2009). One hundred eighty-two active and inactive rock glaciers were counted, covering 64 km². The average area is 0.35 km², the minimum area of a cryogenic rock glacier was 0.02 km², and the largest rock glacier comprises a surface of 2.37 km². It is of composed and glacial roots.

Table 4. Inventory of rock glaciers in the Cordillera

| | glaciers and perennial snow patches | glacigenic rock glaciers | cryogenic rock glaciers | composed rock glaciers |
|-----------|-------------------------------------|--------------------------|-------------------------|------------------------|
| number | 152 | 10 | 144 | 28 |
| Σ | 21 km ² | 8 km ² | 41 km ² | 15 km ² |
| \bar{X} | 0.1 km ² | 0.8 km ² | 0.3 km ² | 0.5 km ² |
| minimum | 0.02 km ² | 0.26 km ² | 0.02 km ² | 0.08 km ² |
| maximum | 2,9 km ² | 2.3 km ² | 1.7 km ² | 1.6 km ² |

The limit of the probable permafrost occurrence within the curve of 4500 m height covered an area of ~315 km². There are 144 rock glaciers of cryogenic origin and 38 rock glaciers close to covered glaciers or perennial snow patches (including composed rock glaciers), with total surface areas of 41 km² and 23 km², respectively.

Rock glaciers, particularly of cryogenic origin, tend to preferentially appear when their detritic and nival feeding zone has a southerly orientation.

Conclusions

Based on direct observations at key monitoring sites, the estimated surface of probable permafrost at the Cordón del Plata is around 500 km²; in the Cordillera del Tigre it is ~315 km². Possible permafrost occurrence is found in an area of ~2127 km² (including Cordillera del Tigre). According to the new inventory of rock glaciers of the Cordón del Plata and the Cordillera del Tigre, the area with creeping permafrost or rock glaciers would comprise 94 km² and 64 km², respectively. This is a significant water reservoir for the semiarid region east of the oasis of northern Mendoza. Above all, it justifies the fact that the Cordón del Plata has recently been declared a Provincial Park in order to protect the cryospheric system as strategic for the region.

Most of the rock glaciers have a S, SE, and E orientation in the Cordillera del Tigre, and a S, SE, NE, and E orientation in the Cordón del Plata. The prevailing S and SE orientation seems to be strongly associated with the presence of mainly glacigenic and composed rock glaciers; thus it is associated with those rock glaciers that interact with covered glaciers, as explained by Trombotto et al. (2008) following a pattern that is characteristic for the Central Andes. On the other hand, the importance of these cryofoms in terms of an E orientation in accordance with tectonic structures may be a strong meteorological component. In the Dry Andes, precipitation plays a more important role than temperature for the generation of cryogenic processes. The Cordillera Frontal, where both areas are located, receives precipitation not only from the W (SW) but also from the Atlantic Ocean to the E. There is a remarkably higher density of rock glaciers in the NE, where more freeze-thaw cycles might occur, than in the SE, and therefore there is major production of cryosediments

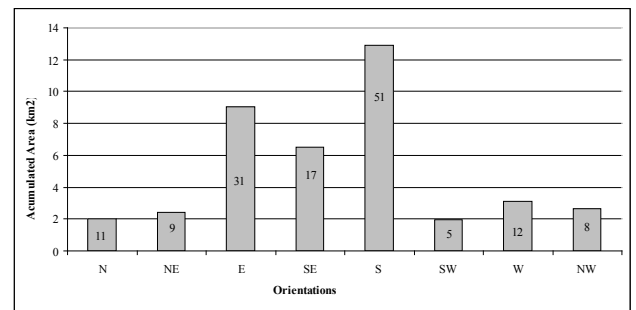


Figure 5. Orientations versus accumulated area of rock glaciers in the Cordillera del Tigre. The numbers inside the histograms indicate the quantity of rock glaciers.

which feed the rock glaciers. The latter are small and are found at great height, where temperatures are lower; nevertheless, their occurrence is associated with a precipitation optimum due to altitude.

Small and shallow inter-Andean lakes at great heights frequently appear correlated with rock glaciers. Monitoring a periglacial lake of this type with a size < 8 ha, which appears and disappears on a time series of different satellite images analysed for the inventory of rock glaciers of the Cordón del Plata, is another key indicator to be taken into account for the regional monitoring of rock glaciers. This also applies when deducing periglacial processes and cryodynamics of the Central Andes of Mendoza, given its hydrological importance and also because of its location in a seismic zone, as this might produce GLOF phenomena in the proximity of human settlements, villages, and cultivated land.

Acknowledgments

We thank GLIMS for its support in obtaining the satellite images and Daniel Dueñas for his collaboration with the maps. The fieldwork in the mountains of the Cordón del Plata was possible through the financial support of CONICET (project PIP 2008-2011).

References

- Arenson, L.U., Pastore, S., Trombotto, D., Bölling, S., Quiroz, M.A., & Ochoa, X.L. 2010. Characteristics of two Rock Glaciers in the arid Argentinean Andes based on initial surface investigations. In *Proceedings of the 63rd Canadian Geotechnical Conference / 6th Canadian Permafrost Conference*, September 12-16, 2010, Calgary, AB, Canada, 1501-1508.
- Barsch, D. & King, L. 1989. Origin and geoelectrical resistivity of rock glaciers in semi-arid subtropical mountains (Andes of Mendoza, Argentina). *Z. f. Geomorph.* V.33, pp. 151-163.
- Brenning, A. & Trombotto, D. 2006. Logistic regression modelling of rock glacier and glacier distribution: Topographic and climatic controls in the semi-arid Andes?. *Geomorphology* 81: 141-154.

- Castro, M. 2010. Mapeo de crioformas y ambiente periglacial en la Cordillera del Tigre, Mendoza, Argentina. Seminario de la Tecnicatura Universitaria en Sistemas de Información Geográfica, Cartografía y Teledetección (Geografía, Universidad Nacional de Cuyo), Mendoza, 55 pp.
- Corte, A.E. & Espizúa, L. 1981. *Inventario de Glaciares de la Cuenca del Río Mendoza*. IANIGLA – CONICET, Imprenta Farras. Mendoza, 64 pp.
- Götz, J., Keuschnig, M., Hartmeyer, I., Trombotto, D., & Schrott, L. 2008. Geophysical prospection on a complex rock glacier system - Morenas Coloradas, revisited (Cordón del Plata, Mendoza, Argentina). 3. *Mittleuropäischen Geomorphologietagung, Tagungsband (Hrsg. Schrott & Otto)*, p. 80, Salzburg.
- Iwasaki, A. & Fujisada, H. 2005. ASTER Geometric Performance. *IEEE Transactions on Geoscience and Remote Sensing*. Vol. 43, 129.
- Novero, N. 2003. Aspectos hidrológicos de los cuerpos de hielo del Cordón del Plata. Seminario de Integración, Teledetección y S.I.G. Universidad Nacional de Cuyo, Mendoza, 54 pp.
- Otto, J-Ch., Götz, J., Keuschnig, M., Hartmeyer, I., Trombotto, D., & Schrott, L. 2010. Geomorphological and geophysical investigation of a complex rock glacier system - Morenas Coloradas valley (Cordon del Plata, Mendoza, Argentina). European Geosciences Union, Viena, *Geophysical Research Abstracts, EGU2010-3625*, Vol. 12.
- Stokes, C. R., Popovnin, V., Aleynikov, A., Gurney, S. D., & Shahgedanova, M. 2007. Recent glacier retreat in Caucasus Mountains, Russia, and associated increase in supraglacial debris cover and supra-proglacial lake development. *Annals of Glaciology*, 46, 95-213.
- Trombotto, D. 1991. *Untersuchungen zum periglazialen Formenschatz und zu periglazialen Sedimenten in der 'Lagunita del Plata', Mendoza, Argentinien*. Heidelberger Geographische Arbeiten, Heft 90, Germany, 171 pp.
- Trombotto, D. 2003. Mapping of permafrost and the periglacial environment, Cordón del Plata, Argentina. *Extended Abstracts of the 8th International Conference on Permafrost*. In W. Haeblerli & D. Brandová (ed.), Zürich, 161-162.
- Trombotto, D., Buk, E., & Hernández, J. 1999. Rock glaciers in the Southern Central Andes (appr. 33° S.L.), Mendoza, Argentina: a review. In *Bamberger Geographische Schriften* 19, Selbstverlag des Faches Geographie an der Universität Bamberg, Germany, 145-173.
- Trombotto Liaudat, D., Arena, L., & Caranti, G. 2008. Glacial Ice as Cryogenic Factor in the Periglaciation Zone of the Composed Rockglacier Morenas Coloradas, Central Andes of Mendoza, Argentina. *Proceedings of the Ninth International Conference on Permafrost, University of Alaska, Fairbanks* Vol 2: 1781-1786.
- Trombotto, D. & Borzotta, E. 2009. Indicators of present global warming through changes in active layer-thickness, estimation of thermal diffusivity and geomorphological observations in the Morenas Coloradas rock glacier, Central Andes of Mendoza, Dry Andes, Argentina. *Cold Regions Science. and Technology* 55: 321-330.
- Trombotto Liaudat, D., Blöthe, J.H., Keuschnig, M., Hernández, P., Götz, J., Hartmeyer, I., & Schrott, L. 2008. Detection of permafrost aggradation at Balcón I, Morenas Coloradas Rockglacier, Mendoza, Argentina. 3. *Mittleeuropäischen Geomorphologietagung. Tagungsband (Hrsg. Schrott & Otto)*, p. 81, Salzburg.

Spatial and Temporal Dynamics of Erosion along the Elson Lagoon Coastline near Barrow, Alaska (2002–2011)

C.E. Tweedie, A. Aguirre, R. Cody, S. Vargas
The University of Texas at El Paso, USA

J. Brown
Woods Hole, MA, USA

Abstract

As a contribution to the Arctic Coastal Dynamics program and the International Polar Year, this study updates the decade-long time series of erosion surveys made along 10.7 km of the Elson Lagoon on the Beaufort Sea coast of northern Alaska near Barrow. Seasonal erosion rates are calculated from repeat ground surveys of the 2–4-m-high coastal bluffs using a differential global positioning System (DGPS). Rates of erosion, which averaged 1–4 meters per year from 2003 to 2011, are lower than other areas of the Beaufort Sea coast that lack protective barrier islands but higher than historic decadal-scale rates for this site. Since 2003, 16.72 ha of land eroded from the study site. Regression analyses indicated no significant change to the rate of erosion during the past decade. Analyses of our seasonal data indicate that rates of erosion are higher in summer survey periods when losses are normalized to the number of ice-free days.

Keywords: arctic coastal dynamics; Arctic Coastal Plain; coastal erosion; DGPS; permafrost.

Introduction

Ice-rich permafrost coastlines in the Arctic are subject to erosion during periods of ice-free seas. The duration and extent of seasonal ice-free seas in the Arctic are increasing (Richter-Menge & Overland 2010) and the five lowest extents of arctic sea ice cover in the satellite record have been observed over the last five years (2007–2011, NSIDC 2011). With continued climate warming and loss of sea ice, and the consequent increase in wave action (Overeem et al. 2011), arctic coastlines are likely to become one of the most climate-change impacted environments on Earth (Lantuit et al. 2011).

Increased rates of coastal erosion can impact communities, affect industry (USACE 2009), and alter habitats and biogeochemical processes in coastal terrestrial and marine ecosystems (Michaelson et al. 2008, Schuur et al. 2008, Lantuit et al. 2009). Two recent assessments of arctic coastlines (Forbes et al. 2011, Lantuit et al. 2011) report that mean decadal timescale rates of coastal retreat are typically in the order of 0.5–2 m/year, but vary up to 10–30 m/year at some locations. The highest mean rates of coastal erosion have been documented for the Beaufort, East Siberian, and Laptev seas. Large declines in the extent of sea ice have also been recorded in these regions (Bhatt et al. 2010).

To date, most studies documenting rates of erosion in the Arctic have focused on the use of high-spatial-resolution aerial or satellite imagery to document trends over decadal timescales (e.g., Jorgenson & Brown 2005, Jones et al. 2009a). In concert with these studies has been an increased recognition of the range of marine, terrestrial, and atmospheric properties and processes that interact to control erosion at multiple spatial and temporal scales (Hoque & Pollard 2009, Aguirre 2011, Wobus et al. 2011). A remaining challenge is to understand, at the process level, how factors interact to control erosion at small scales and how these

manifest at larger spatial scales and longer temporal scales. Coupled to this challenge is an understanding of if and/or how change in other components of the Arctic System (e.g., ocean, atmosphere, cryosphere) constrain or exacerbate coastal erosion. Based on sampling methodologies and analytical approaches that have underpinned advances in understanding the relative importance of interacting processes controlling coastal erosion elsewhere in the world (e.g., Esteves et al. 2002, Quinn et al. 2010), seasonal high spatial and temporal resolution ground-based observations of erosion appear to be essential. To date, such studies have been scant in the Arctic.

Observations of coastal erosion near Barrow date back to the late 1940s (MacCarthy 1953). More recently, a relatively comprehensive knowledge base of coastal erosion has been established for the area including a set of historical aerial and satellite images (Aguirre 2011, Lestak 2007). This study presents an update to records derived from high-spatial and high-temporal resolution ground-based surveys of the northernmost Elson Lagoon coastline, an area situated on the Beaufort Sea coast of northern Alaska near Barrow. The current project was initiated as part of the Arctic Coastal Dynamics (ACD) program (Rachold et al. 2004). Results from observations recorded at the site have been previously described by Brown et al. (2003), Serbin et al. (2003), Aguirre et al. (2008), and Aguirre (2011). Records documented in this study now form one of the longest continuous studies of its type in the Arctic (2002–2011). Like other ACD-affiliated projects, this project also serves as a training ground for a new generation of young researchers, and it contributed to the International Polar Year and its legacy. Data from this project have been incorporated into the interactive and freely available Barrow Area Information Database-Internet Map Server (www.baidims.org).

Study Area

The Elson Lagoon study site is situated on the Alaskan Beaufort Sea coastline and forms the eastern boundary of the 7,466-acre Barrow Environmental Observatory (BEO). The studied coastline is approximately 10.7 kilometers in length (71°19'53"N, 156°34'4"W) (Fig.1). The terrain is composed of ice wedge polygons, shallow elliptically shaped lakes, drained lake basins, and small ponds (Brown et. al 1980). Vegetation cover consists of mostly moist and wet tundra with acidic soils.

The ACD-BEO coastline is divided into four segments. Sections A, B, and D face eastward, and section C faces predominantly north. The highest coastal bluffs reach 4.4 m in section B. Water depth in Elson Lagoon ranges from approximately 0.5 m to 3.5 m. Maximum bottom water temperatures in August range between 9 and 12°C (pers. comm. M.T. Jorgenson). Mean annual permafrost temperatures at nearby inland sites are approximately -9.5°C at a depth of 40 meters (Smith et al. 2010).

The lagoon is bounded on the northeast by a series of low-elevation barrier islands. Shallow but submerged bars lie at the mouth of most tidal inlets, and a submerged shoal extends northwest from Tekegakrok Point, which marks the junction between Sections C and D. Fourteen permanent ACD transect sites are oriented perpendicular to the coastline along Elson Lagoon (Fig. 1).

Methods

Repeat foot surveys of the breaking edge of the coastal bluff line were made for the 10.7-km-long coastline with a survey grade differential global positioning system (DGPS) in mid-August 2003 and in each year between 2006 and 2011 (Fig. 2). Since 2007, DGPS surveys have also been conducted in mid-June to allow for the determination of erosion rates in summer (June–August in the same year) and autumn (August–June of the following year) to be estimated separately. Detailed methods for DGPS data collection and processing are given in Serbin et al. (2003), Aguirre et al. (2008), and Aguirre (2011).

Following differential correction with the GPS base station maintained in Barrow by UNAVCO (http://facility.unavco.org/project_support/polar/barrow/barrow.html), survey data (<10 cm vertical and horizontal error) were imported to ArcGIS as point shapefiles (Fig. 3). Polyline shapefiles were created and the start and end points of each survey standardized for the four coastal sections studied. For each ground survey, the length of the coastal section (A, B, C, and D) was calculated as was the net areal loss/gain within a given survey period. The latter was calculated by building polygons using the modern and historic location of the coastal bluff and the start and end points of the survey as the bounding perimeter of the polygon area. Within the resulting shapefile, the areas of erosion and accretion were tagged as positive and negative, respectively, to allow for the calculation of net areal loss to erosion within a given coastal section and survey period.

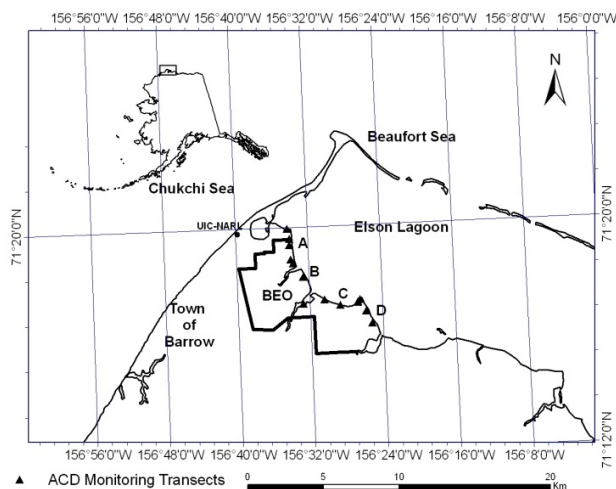


Figure 1. Location of the study site with the four survey sections (A-D) and 14 ACD transects (▲) on the coastline of the BEO near Barrow, Alaska.



Figure 2. Photograph of a DGPS foot survey being conducted along section C.

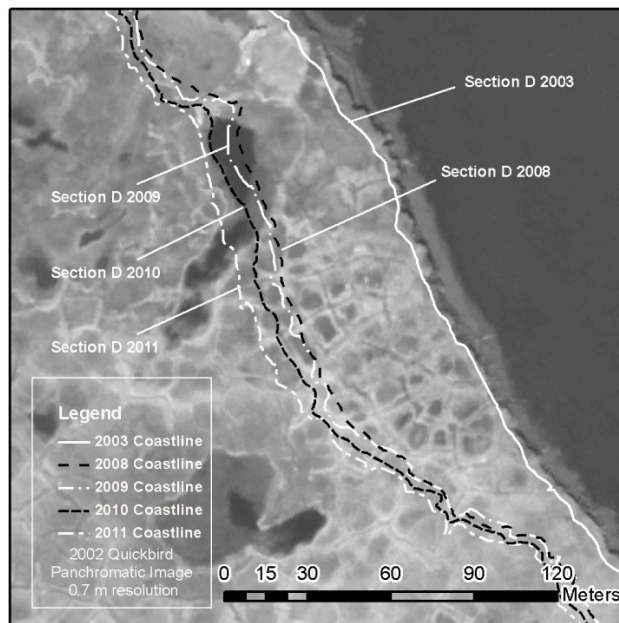


Figure 3. Portion of the section D coastline showing shapefiles of the coastline in August 2003, and for 2008–2011.

Table 1. Length (meters) and cumulative areal loss (hectares) for the four sections and DGPS survey times.

| Section | Length/Cum. Loss | Aug2003 | Aug2006 | Jun2007 | Aug2007 | Jun2008 | Aug2008 | Jun2009 | Aug2009 | Jun2010 | Aug2010 | Jun2011 | Aug2011 |
|---------|----------------------|---------|---------|---------|---------|---------|---------|---------|---------|---------|---------|---------|---------|
| A | Length (m) | 2923 | 2774 | 2683 | 2710 | 2734 | 2509 | 2725 | 2725 | 2724 | 2780 | 2741 | 2798 |
| | Cum. Areal Loss (ha) | 0.00 | 1.41 | 1.55 | 1.61 | 1.84 | 1.96 | 2.03 | 2.23 | 2.44 | 2.58 | 2.85 | 2.93 |
| B | Length (m) | 1666 | 1658 | 1568 | 1633 | 1603 | 1618 | 1642 | 1670 | 1681 | 1718 | 1693 | 1773 |
| | Cum. Areal Loss (ha) | 0.00 | 0.46 | 0.77 | 0.95 | 1.08 | 1.14 | 1.20 | 1.30 | 1.43 | 1.60 | 1.69 | 1.79 |
| C | Length (m) | 3449 | 3464 | 3377 | 3419 | 3426 | 3223 | 3429 | 3446 | 3492 | 3423 | 3605 | 3576 |
| | Cum. Areal Loss (ha) | 0.00 | 1.67 | 1.73 | 1.92 | 2.05 | 2.09 | 2.07 | 2.23 | 2.56 | 2.99 | 2.97 | 3.16 |
| D | Length (m) | 2643 | 2728 | 2651 | 2667 | 2927 | 2722 | 2723 | 2810 | 2643 | 2753 | 2733 | 2820 |
| | Cum. Areal Loss (ha) | 0.00 | 4.66 | 4.95 | 5.31 | 6.22 | 6.64 | 6.68 | 7.00 | 7.49 | 7.95 | 8.44 | 8.84 |
| Total | Length (m) | 10681 | 10624 | 10279 | 10429 | 10690 | 10071 | 10071 | 10651 | 10540 | 10673 | 10771 | 10966 |
| | Cum. Areal Loss (ha) | 0.00 | 8.20 | 9.01 | 9.80 | 11.18 | 11.83 | 11.97 | 12.76 | 13.92 | 15.13 | 15.94 | 16.72 |

Table 2. Linear and logarithmic correlations fit to cumulative erosion rates given in Figure 4.

| Section | Linear | | Logarithmic | |
|---------|---------------|----------------|--------------------|----------------|
| | Equation | r ² | Equation | r ² |
| A | y=0.0034x-129 | 0.97 | 134.85ln(x)-1421 | 0.97 |
| B | y=0.0036x-136 | 0.97 | y=141.15ln(x)-1488 | 0.97 |
| C | y=0.0027x-103 | 0.92 | y=107.99ln(x)-1137 | 0.92 |
| D | y=0.01x-375 | 0.96 | y=394.54ln(x)-4156 | 0.96 |
| Avg. | y=0.005x-187 | 0.96 | y=196.47ln(x)-2070 | 0.97 |

Considerable variability existed between the length of each coastal section and, due to the sinuosity of the coastline, the length of the coastline at different survey times for a given section. Therefore, comparing survey results between sections and surveys is difficult. To compensate for this, areal loss for each study section was normalized to the length of the coastline at the oldest survey within a survey period (i.e., August 2008 in the August 2008–June 2009 survey period) and plotted as the cumulative loss over time (areal loss per meter length of coastline) (Fig. 4). Regression analysis was used to model erosion over time for each study section and for all sections combined.

Sampling protocols for the 14 ACD coastal erosion monitoring transects (Fig. 1) have been described previously (Brown et al. 2003, Aguirre et al. 2008). Since 2002, the distance from fixed markers along these linear transects to the coastal bluff and thaw depths every 10 meters along each transect have been measured. In most years since 2003, these measurements were made on the same day as the August DGPS surveys. While these survey methods do not permit the geospatial elucidation attainable with the repeat DGPS surveys, they are easy to perform, are part of the long-term ACD monitoring protocol, and are excellent for cross-checking the accuracy of the DGPS surveys and for examining patterns of erosion in different land cover units.

Results

Table 1 details the length and cumulative areal loss of each coastal section at each DGPS survey time. Section C is the longest, followed by section A, D, and B. Even though start and end points to the survey were the same between surveys, the length of each section changed from survey to survey. This suggests that the rate of erosion is not constant in different

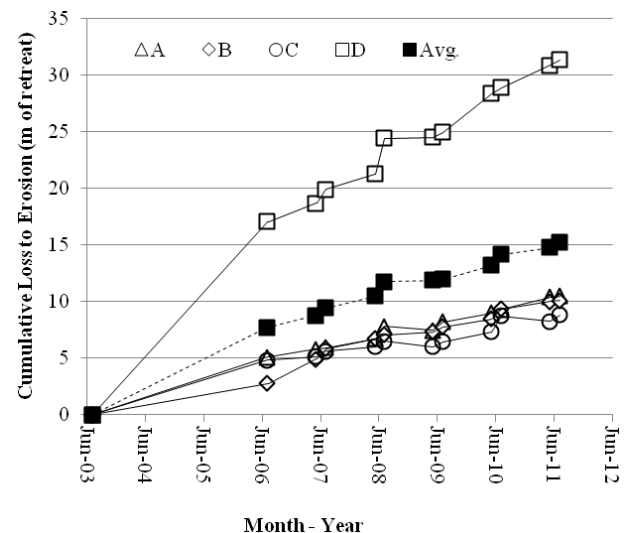


Figure 4. Cumulative loss to erosion over the study period for each section and the average (Avg.) over all sections combined determined from repeat DGPS surveys.

areas of coastline within a section and survey period, and that some sections of coastline are eroding faster or slower than others both within and between survey periods. Cumulative areal loss was greatest in section D, followed by sections C, A, and B (Table 1). Since 2003 (8 years), a total of 16.72 ha of BEO land has been lost to erosion from the ~10.7-km-long study site.

Figure 4 presents the cumulative loss to erosion for each study section derived from the DGPS surveys between 2003 and 2011 (8 years). Cumulative loss in Section D (ca. 4 m/yr) was three times that of sections A, B, or C (ca. 1–1.25 m/yr), which were relatively similar. Although data have not been normalized to the duration of ice-free conditions on Elson Lagoon when erosion occurs, cumulative loss to erosion was greatest between August and June of the following year for all periods between 2007 and 2011, except 2008. Summer loss between June and August 2008 was greater than the preceding or following autumn (August to the following June survey period) (Fig. 4).

Linear and logarithmic regression models fit to data in Figure 4 are presented in Table 2. All regressions were significant ($P < 0.05$) and strongly linear. Logarithmic regressions had a marginally higher fit, suggesting decreased loss to erosion over time, but the difference between linear and logarithmic models was not significant.

Table 3. Loss to erosion measured at the 14 ACD transects. Measurements, at the time of a given survey, refer to the shortest distance between fixed markers and the edge of the coastal bluff.

| Transect | 2002 | 2003 | 2004 | 2005 | 2006 | 2007 | 2008 | 2009 | 2010 | 2011 | total loss | m/yr | |
|----------|-------|-------|------|-------|-------|-------------------|-------------------|-------------------|-------|--------------------|-------------|-------------|-------------|
| A1 | 92.2 | 89.2 | 88.1 | 86.2 | 76.0 | 75.0 | 68.7 | 68.7 | 66.0 | 66.0 | 26.2 | 2.6 | |
| A2 | 45.9 | 44.1 | 41.3 | 40.5 | 36.5 | 35.5 | 32.2 | 31.1 | 30.4 | 29.1 | 16.8 | 1.7 | |
| A3 | 110.4 | 109.1 | | 107.3 | 105.0 | 103.9 | 104 [^] | 103.8 | 103.8 | 102.5 [^] | 7.9 | 0.8 | |
| A4 | 143.0 | 142.4 | | 141.2 | 139.0 | 136.6 | 136.7 | 131.3 | 131.1 | 129.3 | 13.7 | 1.4 | |
| A5 | 56.0 | 55.0 | | 53.6 | 53.2 | 50.8 | 49.5 [^] | 49.3 | 47.1 | 45.3 | 10.7 | 1.1 | |
| B1 | 101.8 | | | 96.5 | 95.7 | 92.7 | 91.4 | 90.3 | 85.0 | 83.3 | 18.5 | 1.9 | |
| C1* | | 72.4 | 70.9 | | 68.8 | 68.2 | 68.3 | 71.2 | | | 1.2 | 0.2 | |
| C2 | | 37.7 | | | 29.3 | 28.6 [^] | 31.0 | 29.5 [^] | 30.1 | 30.0 | 7.7 | 0.9 | |
| C3 | | 34.0 | 31.2 | | 28.2 | 26.4 [^] | 25.8 | 25.1 [^] | 23.1 | 22.8 | 11.2 | 1.2 | |
| C4 | | 97.3 | 95.6 | 91.9 | 88.0 | 80.8 | 79.4 [^] | 78.5 [^] | 77.5 | 75.3 | 22.0 | 2.4 | |
| C5 | 38.0 | 37.0 | 34.6 | 34.8 | | 34.3 | | 33.9 [^] | 33.8 | 33.5 [^] | 4.5 | 0.5 | |
| D1 | 52.0 | 49.0 | 41.6 | 34.5 | 16.7 | 14.3 | 11.2 | 8.6 | 5.4 | Lagoon | 52.0 | 5.8 | |
| D2 | 54.9 | 53.2 | 51.5 | 44.7 | 38.7 | 35.6 | 31.4 | 30.9 | 27.8 | 25.4 | 29.5 | 3.0 | |
| D3 | 64.5 | 59.7 | 57.1 | 49.3 | 34.6 | 26.3 | 11.8 | 7.8 | 3.3 | Lagoon | 64.5 | 7.2 | |
| | | | | | | | | | | | Mean | 21.9 | 2.17 |

[^] Indicates measurements made using the ArcGIS measuring tool due to erroneous field measurements.

*Transect not included in calculation of Mean total loss and m/yr

Lagoon indicates that the initial end-point marker eroded into Elson Lagoon. Blank cells indicate missing data.

Results from measurements of the ACD transects in each section, given in Table 3, generally match rates of loss recorded with the DGPS surveys described above for Figure 4. Rates of loss for the ACD transects are highly variable both between sampling times for the same transect and between transects in a section. The overall loss of 2.17 m/yr (2002–2011) is similar but slightly higher than the cumulative loss averaged over all sections in Figure 4 (ca. 1.87 m/yr 2003–2011).

Discussion

This study further documents substantial spatial and temporal variability in the rates of erosion (Table 1, Fig. 3), similar to other studies focused on erosion of the Elson Lagoon coastline (Brown et al. 2003, Serbin et al. 2004, Aguirre et al. 2008, Aguirre 2011), along other Beaufort Sea coastlines (Arp et al. 2010, Jones et al. 2009b, Jorgenson and Brown 2005), and elsewhere in the Arctic (Lantuit et al. 2011). Rates of erosion derived from the DGPS surveys (1–4 m/yr) are, however, higher than historic erosion rates reported for the study area (0.56–0.86 m/y in Brown et al. 2003), but comparable to other studies in the region that have used linear transect methods and GIS interpolation of remotely sensed imagery (Francis-Chythlook & Brown 2005, Jones et al. 2009b). The Elson Lagoon study site is a much lower energy environment than the coastline studied by Jones et al. (2008, 2009a, 2009b) and Arp et al. (2010) some 130 km to the east, where offshore barrier islands are absent (Mars & Houseknecht 2007). At these latter sites, rates of erosion are up to eight times higher (6–17 m/yr in Arp et al. 2010) than the documented mean rate in this study. Unlike Mars & Houseknecht (2007) and Jones et al. (2009b), who observed increasing erosion rates over the last half century along segments of the Drew Point coastline,

our study documented no significant increase or decrease in the rate of erosion using DGPS surveys during the last decade. A strikingly linear rate of erosion was documented over the study period for all four sections studied (Fig. 4).

For the Elson Lagoon coastline, erosion and removal of frozen slumped ground can commence around July 11, when Elson Lagoon becomes partially ice-free (Craig George, unpublished data). Over the past three decades, Elson Lagoon has begun to freeze around October 8 (Craig George, unpublished data), resulting in the cessation of erosion for the seasonal ice-free period. Although erosion rates were not normalized in this study to the number of ice-free days in a given sampling period, loss to erosion during the autumn (August–June) survey period was almost always greater than losses reported for the summer survey period (June–August). The only exception to this was during 2008, when erosion in the summer survey period was greater than rates recorded during the preceding and following autumn survey periods (Fig. 4). Similar seasonal trends were observed by Arp et al. (2010) for summer versus autumn 2008 erosion rates. This did not appear to correspond with specific differences in regional storm events recorded by Arp et al. (2010) over this timeframe. Interestingly, an analysis performed by Aguirre (2011) used a subset of the seasonal data reported in this study (2007–2009) normalized to ice-free days and concluded that rates of loss were generally greater in the summer than in the autumn for the three years of data analyzed. This difference suggests that normalization of erosion rates to the number of ice-free days in a given survey period is needed to further interpret and understand seasonal variability in rates of erosion along Elson Lagoon and perhaps other arctic coastlines.

Ascertaining and attributing the causes of shoreline retreat is complicated by the gamut of properties and processes that

interact in spatially heterogeneous and temporally dynamic marine, terrestrial, and atmospheric environments. Using a subset of data reported from this study and regression tree analysis, Aguirre (2011) reported that high rates of erosion were positively correlated with water depth at two kilometers offshore, strong winds perpendicular to the coast and from the south-southeast (which appears to propagate long-shore current and removal of eroded material), and where wet and aquatic land cover types prevailed. He also reported that in the absence of strong winds, land cover became relatively more important than other environmental factors in controlling erosion. Although similar analysis of the extended time series presented is beyond the scope of this paper, the study by Aguirre (2011) highlights how DGPS repeat survey data with high spatial and temporal resolution can be used to better understand factors controlling the spatiotemporal variability of coastal erosion.

Conclusions

This study updates erosion rates documented between 2002 and 2011 along the Elson Lagoon coastline of the Barrow Environmental Observatory in northern Alaska. This coastline continues to be monitored as a key contribution to the Arctic Coastal Dynamics Program. Rates of coastal erosion, which ranged between approximately 1 and 4 m/yr, are comparable to those measured elsewhere in the Arctic but are lower than rates reported from the Drew Point section of the Beaufort Sea coastline. Erosion rates were variable between the different sections of the Elson Lagoon coastline and between survey periods. However, cumulative losses to erosion appear to have remained relatively stable over time and do not display a significant increase or decrease over the observational time series. Although this study documented higher erosion rates in the autumn study period, another recent analysis (Aguirre 2011) using a subset of the data suggested that when the erosion rate is normalized to ice-free days, summer erosion rates are higher than those documented for the autumn. The latter study reinforces the value of the DGPS survey method as a logistically feasible means by which high-accuracy locations of this dynamic coastline can be captured. The methodology is also being used to train students in modern sampling technologies.

Acknowledgments

The Barrow Environmental Observatory is owned by the Ukpėagvik Iñupiat Corporation and managed by the Barrow Arctic Science Consortium (BASC). National Science Foundation (NSF) grants ARLS-0454996 and ANS-0856628 provided financial support. BASC, CH2M Hill, and UMIAQ provided logistic support. Numerous volunteers assisted with field data collection. UNAVCO provided DGPS support and training. Any opinions, findings, conclusion, or recommendations expressed in this paper are those of the authors and do not necessarily reflect the views of the NSF.

References

- Aguirre, A. 2011. Patterns and controls of erosion along the Barrow Environmental Observatory coastline, northern Alaska. Master of Science, University of Texas at El Paso. 73 pp.
- Aguirre, A., Tweedie, C.E., Gaylord, A., & Brown, J. 2008. Erosion of The Barrow Environmental Observatory Coastline 2003-2007, Barrow, Alaska. In *NICOP 2008: Proceedings of the Ninth International Conference on Permafrost*. D.L. Kane, K.M. Hinkel (eds.). Institute of Northern Engineering, University of Alaska Fairbanks, 1:7-12.
- Arp, C.D., Jones, B.M., Schmutz, J.A., Urban, F.E., & Jorgenson, M.T. 2010. Two mechanisms of aquatic and terrestrial habitat change along an Alaskan Arctic coastline. *Polar Biology* 33:1629–1640. DOI 10.1007/s00300-010-0800-5.
- Bhatt, U.S., Walker, D.A., Reynolds, M.K., Comiso, J.C., Epstein, H.E., Jia, G., Gens, R., Pinzon, J.E., Tucker, C.J., Tweedie, C.E., & Webber, P.J. 2010. Circumpolar Arctic Tundra vegetation change is linked to sea-ice decline. *Earth Interactions* 14: 1-20.
- Brown, J., Miller, P.C., Tieszen, L., & Bunnell, F.L. 1980. *An Arctic Ecosystem: The Coastal Tundra at Barrow Alaska*. Dowden, Hutchinson and Ross, Inc. Stroudsburg, Pennsylvania. 571 pp.
- Brown, J., Jorgenson, M.T., Smith, O.P., & Lee, W. 2003. Long-term rates of erosion and carbon input, Elson Lagoon, Barrow, Alaska. In *ICOP 2003 Permafrost: Proceedings of the 8th International Conference on Permafrost*. M. Phillips, S.M. Springman, and L.U. Arenson, (Eds.) A.A. Balkema Publishers, Netherlands, pp. 101-106.
- Esteves, L.S., Toldo Jr, E.E., Dillenburg, S.R., & Tomazelli, L.J. 2002. Long- and short-term coastal erosion in southern Brazil. *Journal of Coastal Research*. Special Issue 36: 273–282.
- Forbes, D.L. (ed.). 2011. *State of the Arctic Coast 2010 – Scientific Review and Outlook*. International Arctic Science Committee, Land-Ocean Interactions in the Coastal Zone, Arctic Monitoring and Assessment Programme, International Permafrost Association. Helmholtz- Zentrum, Geesthacht, Germany. 178 pp. <http://arcticcoasts.org>
- Francis-Chythlook, O. & Brown, J. 2005. Additional erosion observations for the Elson Lagoon key site, Barrow, Alaska, ACD-Arctic Coastal Dynamics, 5th International Workshop, October 13-16, 2004, McGill University, Montreal, Canada. *Reports on Polar and Marine Research* 506: 38-41.
- Hoque, M.A. & Pollard, W.H. 2009. Arctic coastal retreat through block failure. *Canadian Geotechnical Journal* 46:1103-1115.
- Jones, B.M., Hinkel, K.M., Arp, C.D., & Eisner, W.R. 2008. Modern erosion rates and loss of coastal features and sites, Beaufort Sea coastline, Alaska. *Arctic* 61(4): 361-372.

- Jones, B.M., Arp, C.D., Jorgenson, M.T., Hinkel, K.M., Schmutz, J.A., & Flint, P.L. 2009a. Increase in the rate and uniformity of coastline erosion in Arctic Alaska. *Geophysical Research Letters* 36: Art. No. L03503.
- Jones, B.M., Hinkel, K.M., Arp, C.D., & Eisner, W.R. 2009b. Modern erosion rates and loss of coastal features and sites, Beaufort Sea coastline, Alaska, Arctic. *Arctic* 61: 361-372.
- Jorgenson, M.T. & Brown, J. 2005. Classification of the Alaskan Beaufort Sea Coast and estimation of carbon and sediment inputs from coastal erosion. *Geo-Marine Letters* 25: 69-80.
- Lantuit, H., Rachold, V., Pollard, W.H., Steenhuisen, F., Ødegård, R., & Hubberten, H.-W. 2009. Towards a calculation of organic carbon release from erosion of Arctic coasts using non-fractal coastline datasets. *Marine Geology* 257: 1-10.
- Lantuit, H., Overduin P.P., Couture, N., Wetterich, S., Aré, F., Atkinson, D., Brown, J., Cherkashov, G., Drozdov, D., Forbes, D.L., Graves-Gaylord, A., Grigoriev, M., Hubberten, H.W., Jordan, J., Jorgenson, T., Ødegård, R.S., Ogorodov, S., Pollard, W.H., Rachold, V., Sedenko, S., Solomon, S., Steenhuisen, F., Streletskaya, I., & Vasiliev, A. 2011. The Arctic Coastal Dynamics Database: A New Classification Scheme and Statistics on Arctic Permafrost Coastlines. *Estuaries and Coasts* DOI 10.1007/s12237-010-9362-6.
- Lestak, L.R., Manley, W.F., Sturtevant, P.M., Maslanik, J.A., Tweedie, C.E., & Brown, J. 2007. High-resolution rectified aerial photography for collaborative research of environmental change at Barrow, Alaska, USA. Boulder, Colorado USA: National Snow and Ice Data Center. DVD.
- MacCarthy, G.R. 1953. Recent changes in the shoreline near Point Barrow, Alaska. *Arctic* 6: 44-51.
- Mars, J.C. & Houseknecht, D.W. 2007. Quantitative remote sensing study indicates doubling of coastal erosion rate in past 50 yr along a segment of the Arctic coast of Alaska. *Geology* 35: 583-586.
- Michaelson, C.J., Ping, C.L., & Lynn, L.A. 2008. Properties of Eroding Coastline Soils Along Elson Lagoon Barrow Alaska. In *NICOP 2008: Proceedings of the Ninth International Conference on Permafrost*. D.L. Kane, K.M. Hinkel (eds.). Institute of Northern Engineering, University of Alaska Fairbanks, 2:1197-1202.
- NSIDC. 2011. Arctic Sea Ice News & Analysis, National Snow and Ice Data Center, Boulder CO. <http://nsidc.org/arcticseaicenews/>. 2nd October 2011.
- Overeem, I., Anderson, R.S., Wobus, C.W., Clow, G.D., Urban, F.E., & Matell, N. 2011. Sea ice loss enhances wave action at the Arctic Coast, *Geophysical Research Letters* DOI:10.1029/2011GL048681, in press.
- Quinn, J.D., Rosser, N.J. Murphy, W., & Lawrence, J.A. 2010. Identifying behavioural characteristics of clay cliffs using intensive monitoring and geotechnical numerical modelling. *Geomorphology* 120: 107-122.
- Rachold, V., Are, F.E., Atkinson, D.E., Cherkashov, G., & Solomon, S.M. 2004. Arctic Coastal Dynamics (ACD): an introduction. *Geo-Marine Letters* 25:63-68.
- Richter-Menge, J. & J.E. Overland (eds.). 2010: Arctic Report Card 2010, <http://www.arctic.noaa.gov/reportcard>.
- Schuur, E.A.G., Bockheim, J., Canadell, J.G., Euskirchen, E., Field, C.B., Goryachkin, S.V., Hagemann, S., Kuhry, P., Laffleur, P.M., Lee, H., Mazhitova, G., Nelson, F.E., Rinke, A., Romanovsky, V.E., Shiklomanov, N., Tarnocai, C., Venevsky, S., Vogel, J.G., & Zimov, S.A. 2008. Vulnerability of permafrost carbon to climate change: implications for the global carbon cycle. *BioScience* 58: 701-714.
- Serbin, S., Graves, A., Zaks, A.D., Brown, J., & Tweedie, C.E. 2004. The utility of survey grade Differential Global Positioning Systems (DGPS) technology for monitoring coastal erosion. Arctic Coastal Dynamics, Report of the 4th International Workshop. St. Petersburg, Russia, 10-13 November 2003. *Reports on Polar and Marine Research* 482: 52-56.
- Smith, S.L., Romanovsky, V.E., Lewkowicz, A.G., Burn, C.R. Allard, M., Clow, G.D., Yoshikawa, K., & Throop, J. 2010. Thermal state of permafrost in North America: A contribution to the International Polar Year. *Permafrost and Periglacial Processes* 21: 117-135.
- U.S. Army Corps of Engineers. 2009. Alaska Baseline Erosion Assessment. USACE Alaska District, Elemendorf Air Force Base, Alaska, USA.
- Wobus, C., Anderson, R., Overeem, I., Matell, N., Clow, G., & Urban, F. 2011. Thermal erosion of a permafrost coastline: Improving process-based models using time-lapse photography. *Arctic, Antarctic, Alpine Research* 43:474-484.

Controls on Patterned Ground Variability at a Continuous Permafrost Site, Central Spitsbergen

Tatsuya Watanabe, Norikazu Matsuoka
University of Tsukuba, Tsukuba, Japan

Hanne H. Christiansen
The University Centre in Svalbard, Longyearbyen, Norway

Abstract

A variety of patterned ground forms dominate arctic tundra surfaces. We examined soil physical and environmental conditions controlling patterned ground variability at a continuous permafrost site in central Spitsbergen, where intensive monitoring of periglacial processes is performed. The distribution of patterned ground depends primarily on soil composition, soil moisture, and winter ground thermal regime associated with snow cover. Mudboils and small polygons occupy well-drained areas composed of clayey fluvial sediments. Compared to mudboils, small polygons are characterized by a clearer contrast in soil texture between barren centers and vegetated margins. Hummocks filled with organic materials develop on poorly drained lowlands associated with a shallow water table and surface flow after rain events. Ice-wedge polygons are dominant on loess-covered areas where local wind regime and micro topography minimize snow cover, resulting in intensive ground cooling that promotes thermal-contraction cracking.

Keywords: active layer; hummock; ice-wedge polygon; mudboil; patterned ground; Svalbard.

Introduction

Patterned ground is one of the most characteristic features in the arctic periglacial landscapes, exhibiting unique surface geometry with various dimensions and shapes. Among a variety of patterns, mudboils, hummocks, and non-sorted polygons are most common on flat tundra surfaces composed of fine-grained soils. A number of mechanisms have been suggested for the formation and development of patterned ground (e.g., Washburn 1956). Differential frost heaving, mass displacement, and/or cryostatic pressure are considered to be responsible for the formation of mudboils and hummocks, whereas desiccation and/or frost cracking contributes to the development of non-sorted polygons (e.g., Lachenbruch 1962, Shilts 1978, Mackay 1980, Ping et al. 2003, Walker et al. 2008). However, it is widely accepted that many patterned ground forms have a polygenetic origin and the same process can produce dissimilar features (Washburn 1956).

Patterned ground distribution, morphology, and activity depend on climate, topography, soil physical properties, hydrology, snow, and vegetation coverage (e.g., Van Vliet-Lanoë 1988, Mackay 1993, Walker et al. 2008). Such environmental variability leads to a transition of patterned ground forms along latitudinal and altitudinal environmental gradients (e.g., Harris 1982, Reynolds et al. 2008). A series of recent studies in Alaska emphasizes the role of longitudinal variation in snow/vegetation cover in controlling the type of non-sorted patterns (e.g., Walker et al. 2008, Reynolds et al. 2008). In Svalbard, the vegetation pattern varies considerably with the type of patterned ground (Cannone et al. 2004). A variety of non-sorted features (e.g., mudboils, hummocks, and polygons) can coexist even within a small area, but little is understood of soil physical and/or environmental factors constraining their distribution. Hence detailed research is

required to identify the factors controlling patterned ground variability.

We studied morphology, structure, and dynamics of non-sorted patterned ground on a fluvial terrace, Adventdalen, Svalbard, to understand soil physical and environmental conditions distinguishing the types of features. Here mudboils, hummocks, composite patterns, and ice-wedge polygons occur on the same terrace, and comprehensive periglacial process monitoring has been undertaken (Matsuoka & Christiansen 2008, Christiansen et al. 2010).

Study Area and Site

Svalbard is an archipelago (74–81°N, 10–35°E) that covers an area of 61,200 km² (Fig. 1a). Adventdalen, located in the central part of the main island (Spitsbergen), is a broad U-shaped valley about 27 km long, 5–6 km wide, and bordered by mountains 800–900 m high. The Adventdalen area is situated in a cold-dry climate with a mean annual air temperature (MAAT) of about -6°C and an annual precipitation of 190 mm, as recorded at Svalbard Airport some 6 km west of the mouth of the valley. However, since 2000, the area has experienced one extraordinarily warm year with MAAT of around -2°C (Førland et al. 2009). Most of the precipitation falls as snow in winter. Nevertheless, the snow cover is generally thin (<30 cm) because strong southeasterly winds redistribute most of the fallen snow.

The monitoring site is located on the outermost part of a large, inactive alluvial fan at the mouth of the Todalen valley, a tributary to Adventdalen (Fig. 1b). The terminus of the inactive fan is continuous with a fluvial terrace eroded by the main stream of the Adventelva River, reflecting long-lasting isostatic uplift of the deglaciated terrain. The surface topography is spatially variable on the terrace. From the upper stream to the

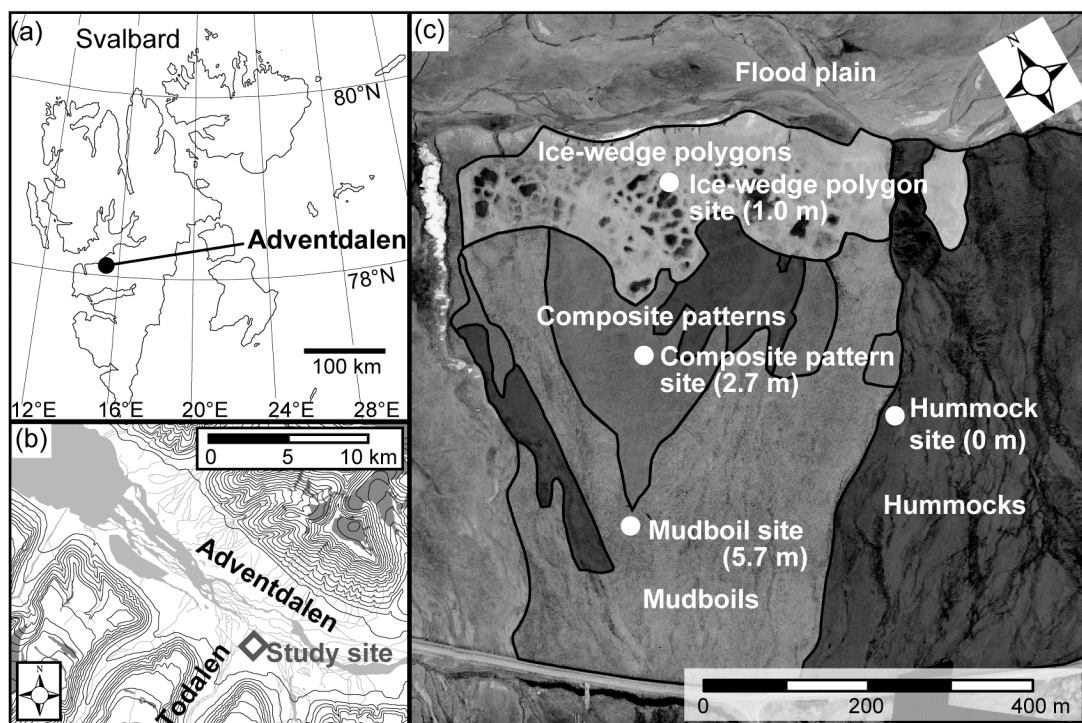


Figure 1. The location of the study site. (a) General map of Svalbard. (b) Topographical map of the lowermost Adventdalen. Contour intervals 50 m. (c) Location of mudboil, composite pattern, hummock and ice-wedge sites, displayed with patterned ground distribution. Numbers in the map show relative elevation with reference to the hummock site. The aerial image was produced by Ulrich Neumann (Kolibri Geo Services).

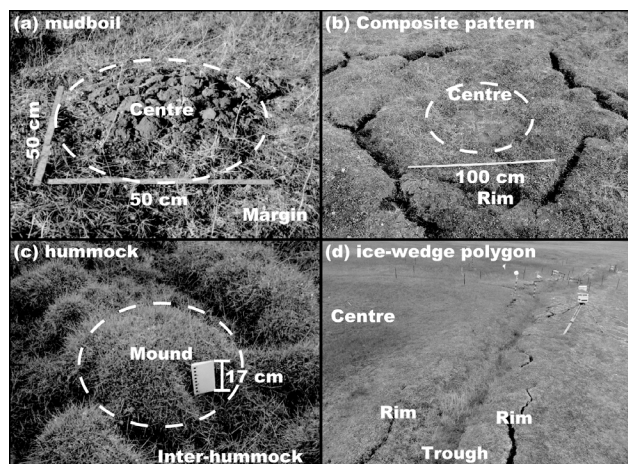


Figure 2. Photographs of patterned ground forms. (a) Mudboil, (b) composite pattern, (c) hummock, and (d) ice-wedge polygon.

central part of the fan, mudboils bordered by a hummocky vegetated surface dominate. The mudboils are typically 40–200 cm in diameter (Fig. 2a). Desiccation cracks occur on the top of the mudboils because of summer evaporation from the bare ground surface. Sporadic vertical stones on the surface indicate intensive frost heaving. In the central part of the fan the surface features change to a composite pattern in which low-centered mudboils are surrounded by small obscured polygons (100–250 cm in diameter) with irregular open cracks (Fig. 2b). In the eastern part of the fan, hummocks typically 15–25 cm

high and 30–60 cm in diameter dominate on the lowland (Fig. 2c). Close to the lowermost part of the fan, where thick fine-grained loess covers the fluvial sediments, large low-centered hexagonal polygons 10–30 m in diameter underlain by ice-wedges are widespread (Fig. 2d). The ice-wedge polygons are typically delineated by shallow troughs maximally 40 cm deep and 20–100 cm wide. The variation in the trough size probably represents different generations of ice wedges constituting the complex polygonal network (Christiansen 2005).

Methods

Data collection

Four automatic monitoring sites in each of the four non-sorted patterns were established to record the timing and magnitude of seasonal soil movement, cracking, and to quantify thresholds for such geomorphic activity. The monitoring systems consist of extensometers, thermistor probes, moisture sensors, and some other instruments (see Matsuoka and Christiansen 2008).

A total of 90 soil samples of 100 ml volume were collected from the upper 20 cm of the mineral horizon at the end of August 2010. We concentrated sampling from the shallow horizons because trial pits showed that (1) large spatial variation in soil properties within a pattern (e.g., center vs. margin) occurs only in the upper active layer, and (2) vertical change in soil water content is insignificant at all sites. At the same time, thermal diffusivity and conductivity at 20 cm depth and the thickness of the organic horizon were measured. Soil thermal properties were measured by a portable thermal

properties analyzer (KD2, Decagon devices, Inc.), which uses the transient lines heat source method and has an accuracy of $\pm 5\%$. Sampling points were divided into nine groups according to the patterned ground type and micro-topography (mudboil center and margin, composite pattern center and rim, hummock mound and inter-hummock and ice-wedge polygon center, rim and trough) (Fig. 2). The bulk density and volumetric soil moisture were calculated by drying soil samples at 110°C for 24 hours. The porosity (n) and degree of saturation (S) were calculated by:

$$n = \left(1 - \frac{d_s}{G_s \cdot \gamma_w}\right) \times 100 (\%) \quad (1)$$

$$S = \frac{V_w}{n} \times 100 (\%) \quad (2)$$

where d_s is the soil bulk density, G_s is the specific gravity of soil particles, γ_w is the density of water, and V_s is the volumetric water content.

Soil pH values were measured using an electronic pH meter (PCSTester35, Eutech Instruments) with an accuracy of 0.01 pH. Grain size distribution was determined with a hydrometer for fine-grained particles (<0.075 mm) and sieves for granular debris (≥ 0.075 mm), and classified by the Wentworth scale into four groups: medium sand to gravel ($<2\phi$), coarse silt to medium sand ($2-5\phi$), fine to medium silt ($5-8\phi$), and clay ($\geq 8\phi$). This classification is useful for identifying the sedimentary origin because loess in Adventdalen is mainly composed of coarse silt to fine sand ($3-5\phi$) (Bryant 1982).

Using a mechanical probe, we measured snow depth at the beginning of May 2011 before the onset of spring melt, and active-layer thickness at the end of August 2011, when thaw depths were nearly at the annual maximum.

Statistical analysis

Principal components analysis (PCA) was applied to determine environmental and soil physical properties responsible for patterned ground variability on the fan. PCA is a widely used multivariable analysis that converts a dataset composed of possibly interrelated variables into a set of values of uncorrelated variables called the principal component. Among the principle components (n : the number of variables), the first component (PC1) explains the maximum amount of variation in a dataset, and successive components explain reducing amounts of the variation, and the last (PC $n-1$) the lowest. The first few components account for most of the variables. The strength of the correlation (r^2 values) between the original variables and each component is used to determine the most significant variables. The analysis was performed using PC-ORD 5 (MjM software). The dataset contains the 90 samples and has 16 variables. Since environmental properties (elevation, snow depth, active-layer thickness, temperature and frost heave amount) were measured at only limited points, representative or mean values were input into the dataset. Before performing PCA, the dataset was relativized by variables because each variable was measured in different units.

Results

Soil and environmental conditions

Soil and environmental conditions varied between the four patterned ground groups and also within a group (e.g., center vs. margin) (Table 1). At the mudboil site, the mudboil center had a slightly higher clay content and bulk density and lower porosity than the margin, although a few soil samples lacked a distinct difference in soil texture. At the composite pattern site, the center and rim showed a clear textural difference. The composite pattern center showed the highest mean clay content (22.4%) and bulk density (1.68 g cm^{-3}) and lowest porosity (37.1%) among the nine sampling groups. In contrast, the rim was mostly dominated by coarse silt to fine sand, which constitutes two-thirds of the soil mass. The spatial variation in the soil texture was insignificant at the hummock and ice-wedge sites; both are dominated by coarse silt to fine sand with homogeneous mean bulk density ($1.08-1.28 \text{ g cm}^{-3}$) and porosity (51.0–57.8%).

Mean volumetric water content in late summer was 34.5–37.3% at the mudboil and small polygon sites, which was about 10% lower than the hummock and ice-wedge sites (43.2–46.0%). Spatial variation in water content was very small within a pattern at all sites. However, despite similar water contents, the mudboil and small polygon centers were often saturated because of the low porosity, while the mudboil margins and small polygon rims were not. The hummock and ice-wedge sites also indicated higher water content but were not saturated due to higher porosity.

Mean thermal diffusivity varied from $0.14 \text{ mm}^2 \text{ s}^{-1}$ at the ice-wedge polygon trough to $0.26 \text{ mm}^2 \text{ s}^{-1}$ at the composite pattern center. Similarly, mean thermal conductivity ranged from $0.68 \text{ W m}^{-1}\text{K}^{-1}$ to $1.21 \text{ W m}^{-1}\text{K}^{-1}$.

Organic soil horizons were generally thinner than 10 cm at all sampling points except at the hummock mound. Since hummock mounds were filled with vegetation roots and humus, the thickness of the organic layer nearly represented the 15–25 cm height of mounds. Mudboil and small polygon centers lacked an organic layer because of the bare surface.

Soil pH was relatively high (5.1–5.5) at the mudboil and composite pattern sites, and low (4.4–4.9) at the hummock and ice-wedge polygon sites. When compared within a pattern, mudboil and composite pattern centers showed slightly higher pH than mudboil margins and composite pattern rims.

Snow depth decreased from the upper to lower alluvial fan. The mudboil and composite pattern sites had a snow depth in excess of 50 cm, whereas the ice-wedge polygon site was covered with thin snow (<30 cm) and well-developed polygon rims were partially exposed at the time of measurement. Snow was deepest at the hummock site, 69 cm on average, where eastward gently inclined lowland allowed snow accumulation. The measured snow depths were slightly underestimated and did not reflect micro-topography, because basal ice layers developed by refreezing of melt snow prevented the snow probe from reaching the ground surface.

Table 1. Mean values of soil physical and environmental conditions.

| | Mudboil | | Composite pattern | | Hummock | | Ice-wedge polygon | | |
|---|---------|--------|-------------------|-------|---------|-------|-------------------|-------|--------|
| | Center | Margin | Center | Rim | Mound | Inter | Center | Rim | Trough |
| <i>Soil properties</i> | | | | | | | | | |
| Grain size (%) | | | | | | | | | |
| Medium sand to gravel (<2φ) | 5.3 | 5.1 | 7.8 | 7.2 | 4.0 | 4.5 | 3.9 | 5.9 | 6.5 |
| Coarse silt to fine sand (2–5φ) | 44.6 | 53.3 | 34.6 | 67.2 | 62.0 | 59.5 | 66.7 | 70.9 | 70.3 |
| Fine to medium silt (5–8φ) | 32.5 | 29.0 | 35.2 | 18.4 | 22.5 | 22.4 | 18.3 | 14.3 | 14.0 |
| Clay (≥8φ) | 17.6 | 12.6 | 22.4 | 7.1 | 11.5 | 13.6 | 11.1 | 9.0 | 9.1 |
| Bulk density (g cm ⁻³) | 1.54 | 1.33 | 1.68 | 1.17 | 1.22 | 1.28 | 1.15 | 1.20 | 1.08 |
| Porosity (%) | 42.1 | 49.6 | 37.1 | 55.2 | 53.2 | 51.0 | 55.6 | 52.5 | 57.8 |
| Water content (vol. %) | 37.1 | 34.5 | 37.3 | 35.5 | 43.2 | 44.1 | 46.1 | 43.6 | 45.4 |
| Degree of saturation (%) | 82.6 | 64.8 | 93.3 | 59.5 | 77.5 | 82.7 | 81.6 | 79.6 | 75.9 |
| Thermal diffusivity (mm ² s ⁻¹) | 0.25 | 0.17 | 0.26 | 0.17 | 0.19 | 0.18 | 0.21 | 0.20 | 0.14 |
| Thermal conductivity (W m ⁻¹ K ⁻¹) | 1.14 | 0.81 | 1.21 | 0.81 | 0.93 | 0.94 | 1.01 | 1.03 | 0.68 |
| O-horizon thickness (cm) | 0.0 | 3.3 | 0.0 | 4.5 | 19.3 | 3.6 | 7.0 | 2.0 | 4.1 |
| Soil pH | 5.4 | 5.2 | 5.5 | 5.1 | 4.6 | 4.5 | 4.4 | 4.8 | 4.9 |
| <i>Environmental properties</i> | | | | | | | | | |
| Snow depth (cm) | 59 | 59 | 53 | 53 | 69 | 69 | 17 | 6 | N/A |
| Active-layer thickness (cm) | 83 | 83 | 67 | 78 | 85 | 71 | 80 | 103 | 78 |
| GSTmin ¹ (°C)* | N/A | -13.7 | -12.5 | -14.7 | -10.1 | -9.8 | N/A | -15.5 | N/A |
| TTOPmin ² (°C)* | N/A | -7.1 | -8.6 | N/A | N/A | -7.0 | N/A | -12.8 | N/A |
| Frost heave amount (cm)* | 8.4 | 2.2 | 9.3 | 2.8 | 8.3 | 8.3 | N/A | 5.2 | N/A |

*Representative values logged at the automatic monitoring stations in the winter of 2010–11. ¹GSTmin: Minimum surface temperature.

²TTOPmin: minimum temperature at the top of permafrost.

Active-layer thickness was affected by micro-topography rather than by insulating vegetation and organic layer. Higher positions (polygon rims and hummock mounds) experienced deeper thaw than low positioned polygon centers and troughs and inter-hummock areas. At the mudboil site, the center and margin showed similar active-layer thickness because of the lack of distinct micro-topographical contrast.

Ground surface temperatures (GST) and temperature at the top of permafrost (TTOP, measured at 100 cm depth) in the winter of 2010–2011 recorded minimum values in mid-February at all sites. At the ice-wedge, the GST minimum was -15.5°C and TTOP -12.8°C, whereas at the hummock site minimum GST was only -9.8°C and TTOP reached only -7.0°C. In general, the mudboil and composite pattern sites recorded lower values than the hummock site, but higher values than the ice-wedge polygon site.

Frost heave amount differed considerably between surface features. Large heave was observed at the centers of mudboil center and composite pattern (8.4 and 9.3 cm, respectively), and hummock mound and inter-hummock (8.3 cm at both positions). In contrast, the mudboil margin and composite pattern rim heaved only by 2.2 and 2.8 cm, respectively, resulting in large differential frost heave between the center and margin of these two features. Differential frost heave was absent (0 cm) at the hummock site, implying the formation of uniform ice layers in the lower part of the active layer.

Principal component analysis

The principal component analysis produced an ordination

space accounting for 83% of the variance using three principal components (Fig. 3). The PC1 explains 46% of the variance, the PC2 20%, and the PC3 17%. These three components have a high contribution ratio as a principal component.

The PC1 is strongly correlated ($r^2 > 0.7$) with bulk density, porosity, and grain size (Table 2). Therefore, the first component represents soil characteristic gradient. Bulk density and fine-grained fraction ($\geq 5\phi$) increase along the PC1, while porosity and coarse-grained fraction (2–5φ) decrease (Fig. 3). The PC2 has r^2 values in excess of 0.5 for volumetric water content, saturation level, and elevation (Table 2). The PC2 is interpreted as a component representing soil moisture gradient. In Figure 3a, elevation increases toward the upper area, and water content and degree of saturation toward the lower area. The PC3 is highly correlated ($r^2 > 0.5$) with snow depth and minimum surface and ground temperature, representing ground thermal regime in winter associated with snow depth. Snow depth increases toward the upper area in Figure 3b, whereas minimum surface and ground temperature decrease toward the lower area. The negative correlation between snow depth and ground thermal regime indicates that ground cooling is tempered by insulating snow cover.

On the ordination space of the PC1 vs. PC2 (Fig. 3a), mudboil and composite pattern centers are grouped in the right area, mudboil margins in the upper area, composite pattern rims in the upper left, hummock mounds and inter-hummock in the lower area, and ice-wedge polygon centers, rims, and troughs are in the lower left. On the ordination space of the PC1 vs. PC3 (Fig. 3b), hummock mounds and inter-

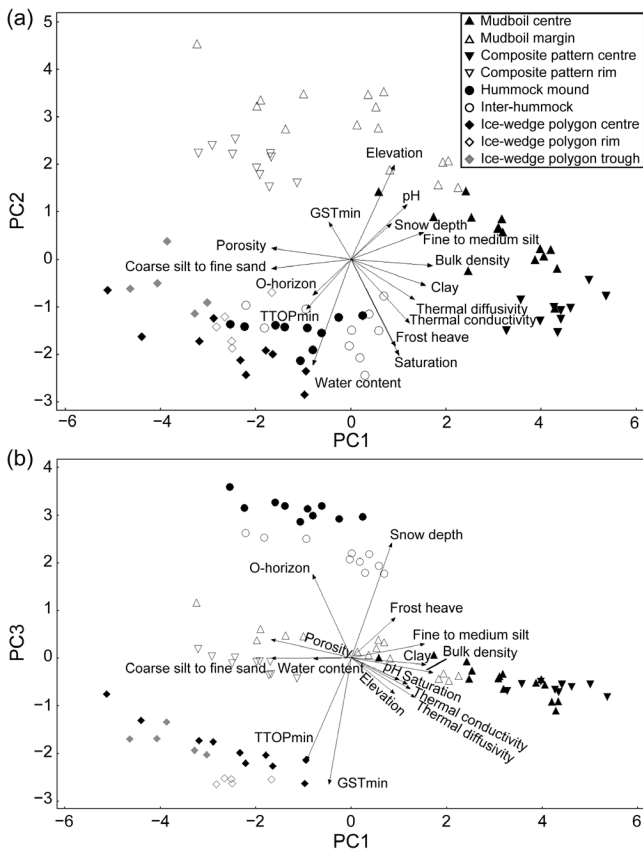


Figure 3. Ordination schemes generated by principal component analysis (PCA). Two schemes are illustrated with reference to (a) PC1 and PC2, and (b) PC1 and PC3. The vectors within the ordination schemes indicate the principal direction and weight of the variables.

hummocks are plotted in the upper side, whereas ice-wedge polygon centers, rims, and troughs are in the lower left.

Discussion

The PCA ordination schemes show that patterned ground distribution is mainly controlled by soil composition, soil moisture, and winter ground thermal regime associated with snow depth.

Soil samples obtained from the mudboil and composite pattern centers have high clay content and bulk density (Table 1, Fig. 3). In terms of the topographical location, clayey fluvial sediments are probably essential in the formation of both patterns. Then the question is what does distinguish between the two patterns? The ordination schemes (Fig. 3) display partial overlap between soil samples from the mudboil center and margin due to the similarity in the composition, whereas the composite pattern centers are completely separated from the rims because of the clear difference in composition. A possible source for the textural contrast is that the repetition of freeze-thaw cycles leading to soil sorting between the barren center and vegetated margin. Loess being trapped by vegetation may have further accentuated the contrast because the soil composition of the polygon rim is similar to that of loess accumulating in the Adventdalen area (Bryant 1982). In

Table 2. Correlation coefficient (r_2) between each variable and component. Bold numbers indicate high correlations for each component.

| | PC 1 | PC 2 | PC 3 |
|----------------------------|--------------|--------------|--------------|
| Bulk density | 0.895 | 0.003 | 0.011 |
| Porosity | 0.859 | 0.007 | 0.017 |
| Coarse silt to medium sand | 0.857 | 0.005 | 0.000 |
| Clay | 0.751 | 0.042 | 0.002 |
| Fine to medium silt | 0.719 | 0.045 | 0.009 |
| Water content | 0.196 | 0.678 | 0.000 |
| Degree of saturation | 0.310 | 0.561 | 0.024 |
| Elevation | 0.253 | 0.543 | 0.065 |
| GSTmin | 0.066 | 0.084 | 0.803 |
| Snow depth | 0.220 | 0.079 | 0.660 |
| TTOPmin | 0.269 | 0.153 | 0.533 |
| Thermal diffusivity | 0.549 | 0.100 | 0.080 |
| Thermal conductivity | 0.466 | 0.250 | 0.049 |
| Soil pH | 0.424 | 0.184 | 0.035 |
| Frost heave amount | 0.262 | 0.459 | 0.079 |
| O-horizon thickness | 0.197 | 0.078 | 0.348 |

addition, the previous terrain condition may contribute to the difference in sedimentation and surface patterns. In fact, aerial photographs show that composite patterns develop in sand bars and mudboils in flow channels on the neighboring floodplain. Although the formative mechanism of the composite pattern has not been fully understood, lateral soil pressure generated by differential frost heave is likely to form the rims associated with irregular open cracks.

The hummock and ice-wedge sites are covered with sandy silt. At the ice-wedge polygon site, the entire active layer consists of horizontally laminated loess, which would restrict the formation of mudboils. In contrast, at the hummock site, a humic silt horizon is confined to the upper 30 cm and underlain by clayey fluvial sediments that favor the development of mudboils or earth (mineral) hummocks. Nevertheless, the active layer did not show any evidence of intensive cryoturbation features, whereas the hummocks are filled with organic materials. The water table is generally shallow at the hummock site, and surface water often flows through the inter-hummock areas after rain events. Such poor drainage may promote the growth of turf hummocks (Raup 1965), but it prevents the development of mudboils or earth hummocks by forming a frozen rigid surface (e.g., Shilts 1978, Van Vliet-Lanoë 1988).

Ice-wedge polygons are widespread in the outermost part of the alluvial fan. Although the active layer at the ice-wedge site has a high water content compared to that at the hummock site, well-developed turf hummocks (15–25 cm high) are uncommon. This means that the ice-wedge site is better drained than the hummock site, as suggested by the absence of a shallow water table and surface flow even after rain events.

The ice-wedge site is characterized by thinner snow cover that promotes intensive ground cooling compared to the other sites (Table 1, Fig. 3b). The interaction between local topography and wind would cause such differential

snow distribution. Snow-free, well-developed polygon rims further contribute to the effective cooling of the active layer (Christiansen 2005). These conditions support active thermal contraction cracking. Ice-wedge polygon networks have also developed in the upper area of the fan where mudboils and composite patterns are found, but their indistinct patterns imply that cracking is unlikely to be active.

Conclusion

Soil composition, moisture, and winter ground thermal regime associated with snow distribution play major roles in controlling the spatial variability of patterned ground at the local scale. Mudboils and composite patterns occur in relatively higher, well-drained areas composed of fluvial sediments. The centers of these patterns lack vegetation and consist of clayey, compact soils. The contrasting soil texture between the barren centers and vegetated margins probably contribute to the formation of composite patterns. Turf hummocks are dominant in low-lying poorly drained areas covered with a thin humic silt layer underlain by fluvial sediments. The poor drainage would promote the formation of turf hummocks and prevent differential frost heave from forming mudboils or mineral hummocks. Ice-wedge polygons develop in downstream areas composed of thick loess deposits. Deflation of snow by local winds and micro-topography permit intensive ground cooling that promotes thermal-contraction cracking.

Acknowledgements

This study was financially supported by the Grants-in-Aid (No. 09J00461 and 20300293) of the Japan Society for the promotion of Science from the Ministry of Education, Science and Culture, Japan, and funding from the Scandinavia-Japan Sasakawa Foundation and the University Center in Svalbard. We appreciate Ulrich Neumann (Kolibri Geo Services) for collecting the aerial images of the study site on which figure 1c is based. We thank Kenneth M. Hinkel and two anonymous reviewers for critical comments on an earlier version of the manuscript.

References

- Bryant, I.D. 1982. Loess deposits in lower Adventdalen, Spitsbergen. *Polar Research* 2: 93–103.
- Cannone, N., Guglielmin, M., & Gerdol, R. 2004. Relationships between vegetation patterns and periglacial landforms in northwestern Svalbard. *Polar Biology* 27: 562–571.
- Christiansen, H.H. 2005. Thermal regime of ice-wedge cracking in Adventdalen, Svalbard. *Permafrost and Periglacial Processes* 16: 87–98.
- Christiansen, H.H., Matsuoka, N., & Watanabe, T. 2010. Ice-wedge process research in Adventdalen. *Fieldguide for excursions EUCOP III Svalbard, Norway 13–18 June 2010*: 44–62.
- Førland, E.J., Benestad, R.E., Flatøy, F., Hanssen-Bauer, I., Haugen, J.E., Isaksen, K., Sorteberg, A., & Ådlandsvik, B. 2009. *Climate development in North Norway and the Svalbard region during 1900–2100*. Tromsø : Norwegian Polar Institute, 44 pp.
- Harris, C. 1982. The distribution and altitudinal zonation of periglacial landforms, Okstindan, Norway. *Zeitschrift für Geomorphologie* 26: 283–304.
- Lachenbruch, A. 1962. Mechanics of thermal-contraction cracks and ice-wedge polygons in permafrost. *Geological Society of America*, special paper 70: 69pp.
- Mackay, J.R., 1980. The origin of hummock, western Arctic coast Canada. *Canadian Journal of Earth Sciences* 17: 996–1006.
- Mackay, J.R. 1983. Air-temperature, snow cover, creep of frozen ground, and the timing of ice-wedge cracking, western Arctic Coast. *Canadian Journal of Earth Sciences* 30: 1720–1729.
- Matsuoka, N. & Christiansen, H.H. 2008. Ice-wedge polygon dynamics in Svalbard: High resolution monitoring by multiple techniques. In *NICOP 2008: Proceedings of the Ninth International Conference on Permafrost*. D.L. Kane, K.M. Hinkel (eds.). Institute of Northern Engineering, University of Alaska Fairbanks, 1149–1154.
- Ping, C.L., Michaelson, G.J., Overduin, P.P., & Stiles, C.A. 2003. Morphogenesis of frost boils in the Galbraith Lake area, Arctic Alaska. *The proceedings of the Eighth International Conference on Permafrost*, Zurich, July 21–25, 2003: 897–900.
- Raup, H.M. 1965. The structure and development of turf hummocks in the Mesters Vig district, Northeast Greenland. *Meddelelser om Grønland* 166: 1–112.
- Raynolds, M.K., Walker, D.A., Munger, C.A., Vonlanthen, C.M., & Kade, A.N., 2008. A map analysis of patterned-ground along a north American Arctic Transect. *Journal of Geophysical Research-Biogeosciences* 113: G03S03.
- Shilts, W.W. 1978. Nature and genesis of mudboils, central Keewatin, Canada. *Canadian Journal of Earth Sciences* 15: 1053–1068.
- Van Vliet-Lanoë, B. 1988. The genesis of cryoturbations and their significance in environmental reconstruction. *Journal of Quaternary Science* 3: 85–96.
- Walker, D.A., Epstein, H.E., Romanovsky, V.E., Ping, C.L., Michaelson, G.J., Daanen, R.P., Shur, Y., Peterson, R.A., Krantz, W.B., Raynolds, M.K., Gould, W.A., Gonzalez, G., Nicosky, D.J., Vonlanthen, C.M., Kade, A.N., Kuss, P., Kelley, A.M., Munger, C.A., Tarnocai, C.T., Matveyeva, N.V., & Daniëls, F.J.A. 2008. Arctic patterned-ground ecosystems: A synthesis of field studies and models along a North American Arctic Transect. *Journal of Geophysical Research* 113: G03S01.
- Washburn, A.L., 1956. Classification of patterned ground and review of suggested origins. *Bulletin Geological Society of America* 67: 823–866.

Design of a Measurement Assembly to Study In Situ Rock Damage Driven by Freezing

Samuel Weber, Stephan Gruber, Lucas Girard

Glaciology, Geomorphodynamics, Geochronology; Geography Department, University of Zurich, Switzerland

Jan Beutel

Computer Engineering and Networks Laboratory, ETH Zurich, Switzerland

Abstract

We describe the design of an acoustic emission (AE) measurement assembly for reliable acquisition of a multi-year time-series in steep alpine rock-walls. The motivation for collection of these data is to enhance understanding of freezing-induced rock damage. Because measurements in natural rock slopes are challenging, this study investigates technical options suitable to capture AE signals from differing depths while incurring minimal signal loss between the rock and the sensor. We first outline the requirements for the measurement assembly and present two generic solutions to be evaluated and refined. We then present candidate materials for building components of the assembly and experimentally estimate their attenuation coefficients and signal loss at the rock-sensor contact. Based on these results, we present the final design chosen for the measurement assembly and briefly report initial experiences from a field deployment site at 3500 m a.s.l. at Jungfrauoch, Switzerland.

Keywords: acoustic emission; measurement assembly; depth; mountain permafrost; rock fracturing; microgelivation.

Introduction

In cold regions, ice formation is known to be an important driver of rock fracturing (Matsuoka & Murton 2008) and is commonly referred to as frost weathering. The formation of ice in rock induces pressure variations in rock pores and cracks, which can cause damage near the surface as well as at a depth of up to several meters (Murton et al. 2006). This process may be crucial for the slow preconditioning of rock fall from warming permafrost areas (Gruber & Haeberli 2007). Most knowledge about the associated processes stems from theoretical studies (Walder & Hallet 1985) or laboratory experiments (Murton et al. 2006). However, the transfer of corresponding insights to natural conditions, involving strong spatial and temporal heterogeneity is nontrivial.

The monitoring of acoustic emissions (AE) is a powerful technique to track the evolution of damage. AE signals are transient elastic waves generated by the release of energy during rapid local changes of inelastic strains in solid materials. These events are accompanied by damage increase, extension, or shearing of existing fractures (Scholz 1968). AE monitoring has been used at the rock sample scale (Lockner 1993) in laboratory studies and under natural conditions to monitor seismicity and rock bursts in mines and tunnels as well as slope instabilities (Amitrano et al. 2005). In a four-day experiment, Amitrano et al. (2011) used AE monitoring to investigate freezing-induced rock damage in a high-elevation rock slope. AE activity was observed to be more intense during freezing periods and in locations subject to diurnal flow of melt water from snow patches.

To better understand rock damage under natural conditions, continuous AE monitoring and the ability to estimate source depths of events are desirable. We expect the investigation of diurnal and seasonal cycles, as well as rock in an advanced

stage of pre-fracturing, to be important for the robust scaling of theoretical insight to field conditions. In this paper, we describe the design of an AE measurement assembly for reliable acquisition of a multi-year time-series in steep alpine rock-walls relying on commercial sensors. Because long-term measurements in natural rock slopes are challenging, this study investigates technical options suitable to capture AE signals from differing depths while incurring minimal signal loss between the rock and the sensor.

We first outline the requirements for the measurement assembly, present two generic solutions that are evaluated and refined and, based on this, identify the problems to be addressed in detail. We then present candidate materials for building parts of the assembly and experimentally estimate their attenuation coefficients and the signal loss at the rock-sensor contact. Based on these results, we present the final design chosen for the measurement assembly and briefly report first experiences from a field deployment site at 3500 m a.s.l. at Jungfrauoch, Switzerland.

Requirements and Problem Statement

In this section, we first present the type of acoustic transducer used in this study and then detail the requirement of the measurement assembly to be designed. By measurement assembly, we refer to the technique used to transmit acoustic signals from a given depth of the rock-wall to an acoustic transducer.

Acoustic signals can be generated by the activation of small flaws such as shearing of a millimeter-long crack, as well as by larger mass movements such as rock falls. In this study, our goal is to monitor the acoustic signals generated by ‘small events.’ There are two reasons for this. First, smaller events are statistically more likely to occur, which allows us to obtain

large catalogs of events and perform robust statistical analysis. Secondly, our goal is to understand the mechanisms that progressively damage rock and pre-condition rock falls. In other words, we are interested in the precursors of rock falls. Therefore, we have chosen to use piezoelectric transducers (R6alpha, Physical Acoustics Limited, UK) that can capture acoustic signals in the frequency range 1–150 kHz. The typical size of the flaws (i.e., defects, cracks, etc.) that are likely to generate AE in this frequency range is on the order of millimeters. Within this frequency range, events where the source is located up to about a meter from the transducer can be detected, while events generated at larger distances are attenuated. We hereafter refer to the acoustic transducers as AE sensors.

The assembly to be designed will enable a reliable, consistent, and repeatable measurement. At the scale of one meter, variations in temperature and ice-induced stress are expected to dominantly occur along the dimension of depth, oriented normal to the rock surface. The use of two sensors, installed at differing depths, could provide a *zonation* of the source depths. While installing more than two sensors may provide more accurate localization, it considerably complicates the installation, increases the disturbance of the rock mass investigated, and increases the cost of a single setup.

Measuring at depth requires a borehole. Two methods are then considered for capturing the AE signal: (1) insertion of the sensor into the borehole, or (2) insertion of a waveguide for transmitting the signal to the rock surface where the sensor is installed. Water flow in the borehole can alter moisture conditions at depth and thus cause spurious AE events related to freezing/thawing (Kaufmann 1999). To avoid such events, the borehole must be sealed after installation. To enable long-term measurements, the ability to exchange sensors in the borehole is desired. Based on these requirements, we propose two generic designs for the measurement assembly to be tested and refined (Fig. 1):

(1) The construction of a **casing**, which accommodates the sensor within the borehole. The rock-sensor contact is made using a thin plate glued to the bottom of the borehole. While the AE signal transmission should be good for this conductive plate, other parts of the casing should exhibit strong attenuation to avoid pollution by acoustic events originating from different depths. The casing has to be made waterproof and extend to the rock surface, where a lid allows signal extraction as well as sensor exchange.

(2) A **waveguide**-based solution uses a thin rod fixed to the bottom of a borehole and a sensor installed on top above the rock surface. The sensor requires mechanical protection to prevent damage from rock fall or icing.

We investigate the feasibility of both solutions, and evaluate their impact on the measured AE signal.

Background

As a basis for investigating suitable materials, we briefly review the propagation of elastic waves in solids, for simplicity only considering compression waves (P-waves). Assuming a

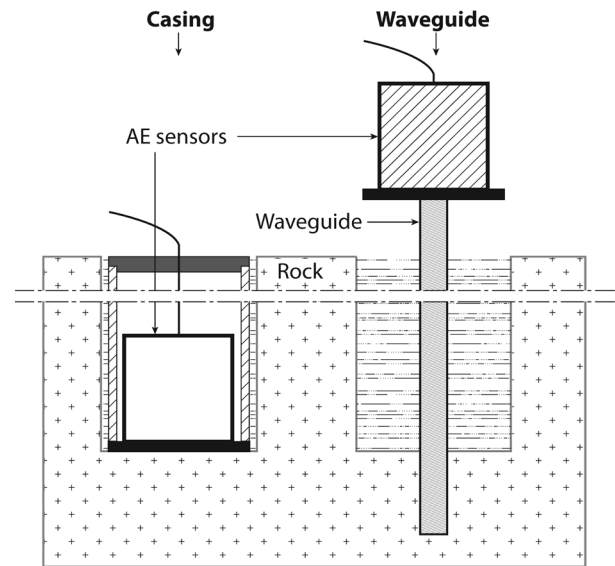


Figure. 1. The two generic measurement assemblies: Casing and waveguide.

homogeneous, isotropic medium, the compressional velocity of elastic waves is given by (e.g., Hardy 2003):

$$C = \sqrt{\frac{E}{\rho} \frac{(1-\nu)}{(1+2\nu)(1+\nu)}} \quad (1)$$

where ρ is the density, E the Young modulus, and ν the Poisson ratio. The acoustic impedance related to P-waves can then be defined as:

$$Z = \rho C \quad (2)$$

The transmission coefficient between two different materials with acoustic impedances Z_a and Z_b can then be calculated as:

$$T = 1 - \left(\frac{Z_a - Z_b}{Z_a + Z_b} \right)^2 \quad (3)$$

The largest transmission of the elastic wave therefore occurs between materials that have similar acoustic impedances. Another property that needs to be accounted for in the choice of the materials is the attenuation coefficient. As an elastic wave propagates from a source through a medium, amplitude decrease due to absorption can be estimated as:

$$A^l = A_0^l e^{-\alpha r} \quad (4)$$

where A_0^l is the linear amplitude at the source, A^l that at a distance r from the source, and α is the frequency-dependent attenuation coefficient.

Candidate Materials and Their Evaluation

Candidate materials for the measurement assembly

Two categories of materials are needed for the assembly: transmitting and attenuating materials. The transmitting

Table 1. Material properties.

| Material | Density (kg/m ³) | Young modulus (GPa) | Poisson's ratio | Speed of sound C (m/s) | Acoustic impedance Z (SI) | Transmission coefficient T | Attenuation coefficient α (dB/m) |
|----------------|------------------------------|---------------------|-----------------|------------------------|---------------------------|----------------------------|---|
| Mild steel | 7900 | 200 | 0.3 | 5838 | 46.1 10 ⁶ | 0.71 | 30 |
| Aluminum | 2700 | 70 | 0.35 | 6451 | 17.4 10 ⁶ | 0.99 | 10 |
| Chromium steel | 7900 | 200 | 0.3 | 5838 | 46.1 10 ⁶ | 0.71 | 60 |
| POM C | 1420 | 3 | 0.35 | 1841 | 2.61 10 ⁶ | 0.53 | 71 |
| Geo-Gel | 1020 | 0.1 | 0.45 | 610 | 0.62 10 ⁶ | 0.16 | 151 |
| Gneiss | 2700 | 56 | 0.28 | 5149 | 13.9 10 ⁶ | 1 | 35 |

materials should have a low impedance mismatch with the rock (i.e., large transmission coefficient) and a small attenuation coefficient, while the damping materials should have the opposite properties: low transmission coefficient and large attenuation.

As transmitting candidate materials we considered ordinary mild steel, chromium steel, and aluminum because metals are typically good acoustic transmitters. For the damping material, we selected a thermoplastic polymer called POM-C (DuPont Delrin). We also examined the physical properties of a two-component polyurethane-resin (Geo-Gel from Kuempel AG, Sarnen, Switzerland). This is a slow-hardening resin with a viscosity of 850 mPa·s (i.e., between olive oil and liquid honey). It could thus be injected in the borehole after the installation of the measurement assembly in order to seal the hole. Finally, the properties of gneiss (from Ticino, Switzerland) were considered as representative of those of the rock at the planned field site.

Table 1 reports the mechanical properties of these materials. The speed of sound, acoustic impedance, and transmission coefficient within gneiss were calculated as detailed above. Considering these results, aluminum appears as the best candidate material to build the rock-sensor contact. In the 'casing-based-solution' this contact is made through a thin metal plate, while in the 'waveguide-based-solution' the contact is made through the waveguide itself. The results also suggest that POM-C is suitable for building the casing since it has a low transmission coefficient with gneiss. Similarly, the Geo-Gel has a low transmission coefficient when applied to gneiss. Its use as a sealing agent would thus provide further reflection and attenuation of spurious AE signals.

Experimental determination of the attenuation coefficient

To facilitate comparison, the attenuation coefficients of candidate materials were determined experimentally (Fig. 2). This was achieved using two AE sensors with a given spacing placed on a sample of each material. An artificial source was applied, and the amplitude of the resulting stress wave monitored with both AE sensors. The source was either a FieldCal pulser (Physical Acoustics Limited, UK) or the breaking of 0.5-mm pencil lead. The frequency of the FieldCal was set to 60 kHz, the resonant frequency of the AE sensors used. The AE sensors and the FieldCal were coupled to the

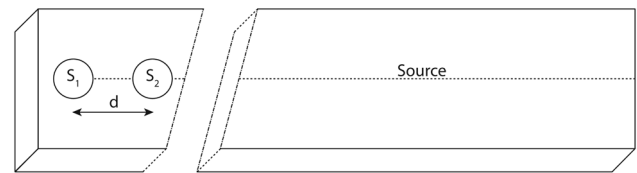


Figure 2. Experimental set-up for determination of the attenuation coefficient.

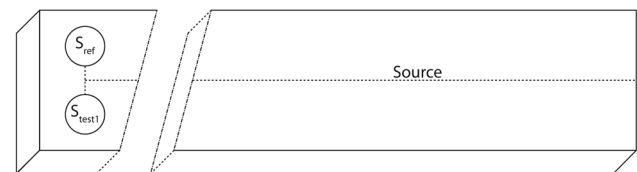


Figure 3. Experimental set-up for determination of attenuation of the rock-sensor contact.

rock using an ultrasonic coupling gel (UCA2 from Sofranel, France). The attenuation coefficient, as defined by equation 4, can then be calculated as $\alpha = \Delta A/d$, where ΔA is the measured amplitude difference (in dB) between the AE sensors separated by distance d . The results, reported in Table 1, suggest that mild steel and aluminum have lower attenuation coefficients than chromium steel. Damping materials indeed demonstrated higher attenuation coefficients, with that of Geo-Gel being about one order of magnitude greater than that of the metals.

Attenuation of the rock-sensor contact

Signal loss at the rock-sensor contact was determined experimentally (Fig. 3) for the two possible solutions. Experiments were performed on a rectangular gneiss block (15 cm x 10 cm x 70 cm) using an artificial source and two receiving AE sensors (using ultrasonic coupling gel): a reference sensor, directly coupled to the rock, and a test 'rock-sensor-contact'. The two sensors are at an equal distance from the source. The rock-sensor contacts tested are:

- (P1) a four-mm thick aluminum plate coupled to the rock with ultrasonic coupling gel;
- (P2) a four-mm-thick aluminum plate glued to the rock;
- (WG1) a steel rod used as waveguide (10 mm diameter, 85 mm long) glued into the rock sample at 5 cm depth;
- (WG2) a steel rod used as waveguide (10 mm diameter,

- 85 mm long) fixed in the rock sample using an expansion anchor at 5 cm depth;
- (WG3) a steel rod used as waveguide (10 mm diameter, 120 mm long) glued into the rock sample at 2.5 cm depth; and
- (WG4) a steel rod used as waveguide (10 mm diameter, 420 mm long) glued into the rock sample at 2.5 cm depth.

Table 2 summarizes the loss in signal amplitude measured between the reference sensor and the different contacts investigated. The smallest attenuation is observed for contacts using a thin aluminum plate. While a simple coupling of the plate on the rock using the gel appears best in this laboratory experiment, this solution does not appear feasible in the field where the rock surface at the bottom of the borehole will be uneven. In this case, the use of glue to affix the metal plate to the borehole bottom is likely a better solution. The waveguide-based contacts generally show larger attenuations. Fixing the waveguide using a glued interface extending over greater depth limits the attenuation, but likely results in less accurate estimation of the source depths. Also, the use of an extension anchor to fix the waveguide should be avoided.

Table 2. Attenuation measured for different rock-sensor contacts.

| | P1 | P2 | WG1 | WG2 | WG3 | WG4 |
|-----------------------|-----|-----|-----|-----|-----|-----|
| Mean attenuation (dB) | 1.1 | 1.9 | 2.7 | 8.3 | 10 | 9.7 |
| Standard deviation | 0.3 | 0.7 | 0.8 | 1.8 | 1.1 | 1.3 |

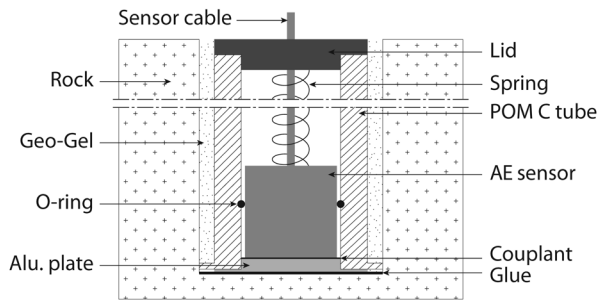


Figure 4. Installed AE-rod measurement assembly.

Design and Test of the Measurement Assembly

Based on the experimental results, we designed the final measurement assembly using the ‘casing-based’ solution (Fig. 4). The casing itself is made of a POM-C tube with an external diameter of 30 mm. It accommodates a piezoelectric sensor (R6alpha, Physical Acoustics Limited, UK) to record AE in the frequency range 1–150 kHz. The sensor (cylinder with 17 mm diameter, 17 mm height and a radial cable exit) is held down on the bottom assembly inside the casing using a spring. The bottom part of the casing is made of a 4-mm-thick aluminum plate. A lid with a waterproof cable port completes the surface end of the casing. The assembly is glued to the bottom of the borehole only, and the remaining space sealed with a 5-mm-thick layer of Geo-Gel injected into the void between the borehole and casing.

A freeze-thaw experiment was performed with the first prototype of this assembly to evaluate the generation of spurious AE events due to the thermal expansion of the casing itself. In this experiment, the casing containing the AE sensor and a reference AE sensor were placed in a freezer and subjected to a temperature cycle from +20°C to -15°C and back to +20°C. The amplitudes of measured AE events are shown in Figure 5. The results are difficult to interpret since the experimental setup was rather crude, and it is likely that a fraction of the measured event was generated by the freezer itself.

Four sensor-casing-assemblies were installed in a rock-wall at Jungfrauoch (3500 m a.s.l.) in Switzerland. This location was chosen for its year-round accessibility by train. The strategy chosen for this deployment was to equip two contrasting sites with measurements at two different depths each. The boreholes were drilled at differing angles, aiming at a final alignment of the sensors normal to the rock surface (Fig. 6). This reduces the disturbance caused by the boreholes in the rock closest to the AE sensors. The sensing parts of the casings are located at 10 and 50 cm depths.

The two sites equipped (Fig. 7) are only ten meters apart and show similar general characteristics: southeasterly slope aspect, 50–70° steep rock wall of granitic gneiss. The main difference between these two sites lies in the availability of liquid water. One site is on a rather dry spur-like feature, and the second site is in a gully-like depression that collects melt water from the surrounding snow patches.

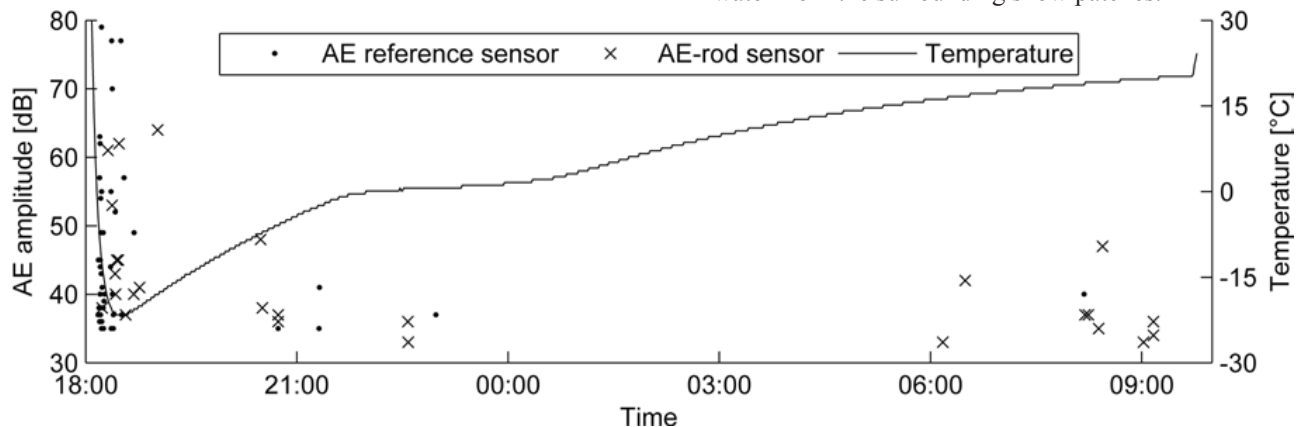


Figure 5. Result of freezer experiment: Temporal AE amplitude and temperature.

The acoustic signals are conditioned and captured by a customized 2-channel, 500 kHz sampling rate data acquisition system, the AE-Node (cf. Hunziker 2011). In addition to the AE sensors, two probes to measure temperature (Th3-s by UMS GmbH, Germany) and relative moisture by capacitance (EnviroSCAN by Sentek Technologies, Australia) at different depth were installed at each site. Data, complemented by a webcam to document surface conditions, are transmitted using a wireless sensor network customized for operation in harsh environments (cf. Beutel et al. 2009, Hasler et al. 2011). The

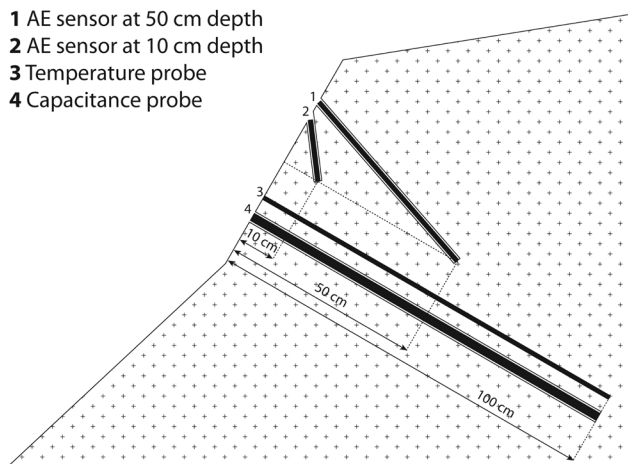


Figure 6. 2D sketch of field installation.

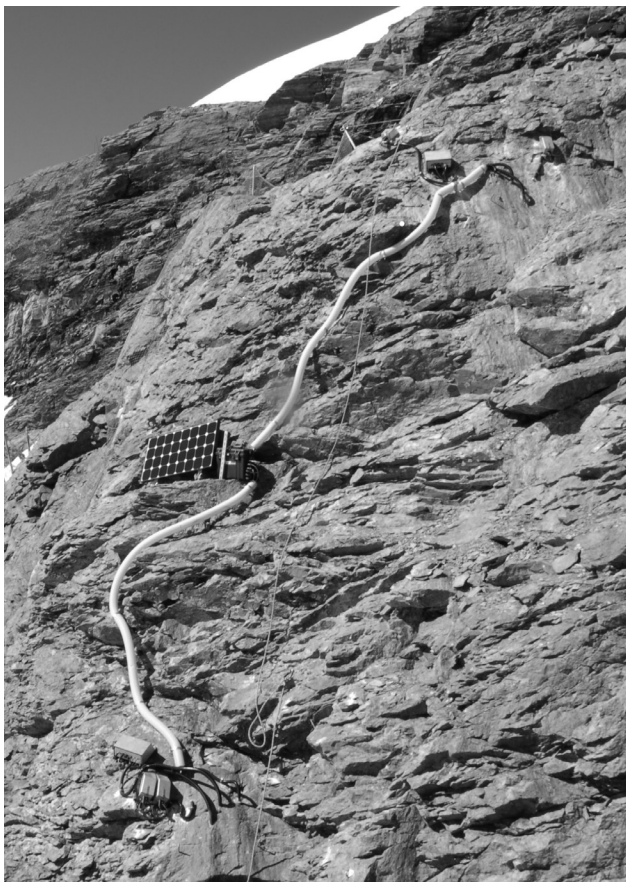


Figure 7. Field site with installed equipment. The distance between the two equipped sites is approximately 10 m.

AE-Node is designed to extract, locally store, and transmit wirelessly the AE signature from the raw acoustic signal once the signal level crosses a configurable threshold. This design and setup of the measurement system is optimized for low-power consumption and unattended operation over long periods of time in harsh environments, while giving the user access to the acquired data with low latency and means for configuration and control of the experiments undertaken.

The work reported on in this paper is the first step of an ongoing research project. The investigation of the continuous time-series of AE events currently being acquired will provide the first direct measurements of rock damage in a permafrost rock-wall. These results should help in transferring laboratory and experimental insights on frost weathering to real conditions.

Acknowledgments

The research presented was supported through the project PermaSense funded by the Swiss National Foundation (SNF) NCCR MICS as well as the International Foundation High Altitude Research Stations Jungfraujoch and Gornergrat. We are grateful for the technical support from the workshop of the Physics Institute, University of Zurich, most specifically for the dedication, patience, and creativity of Reto Maier and the work of numerous helpers from the PermaSense team, Roman Lim, Tonio Gsell, Jeannette Noetzli, and Andreas Hasler.

References

- Amitrano, D., Grasso, J.R., & Senfaute, G. 2005. Seismic precursory patterns before a cliff collapse and critical point phenomena. *Geophysical Research Letters* 32.
- Amitrano, D., Gruber, S., & Girard, L. 2011. Rock damage inferred from acoustic emissions in a partly frozen high-alpine rock-wall. Submitted to *Geophysical Research Letters*.
- Beutel, J. et al. 2009. PermaDAQ: A scientific instrument for precision sensing and data recovery in environmental extremes. *Proc. Int'l Conf. Information Processing in Sensor Networks (IPSN) 2009*. San Francisco, California USA, 265-276.
- Gruber, S. & Haeberli, W. 2007. Permafrost in steep bedrock slopes and its temperature-related destabilization following climate change. *Journal of Geophysical Research-Earth Surface* 112(F2): 10.
- Hardy, H.R. 2003. *Acoustic emission / Microseismic activity*. A. A. Balkema publishers, Tokyo.
- Hasler, A., Gruber, S., & Haeberli, W. 2011. Temperature variability and thermal offset in steep alpine rock and ice faces. *The Cryosphere Discussions* 5: 721-753.
- Hunziker, J. 2011. *Acoustic Emission Sensing in Wireless Sensor Networks*, MA Thesis, ETH Zurich, 2011.
- Kaufmann, J. 1999. Experimental identification of damage mechanisms in cementitious porous materials on phase transition of pore solution under frost deicing salt attack, Ph.D. Thesis, EPFL Lausanne, Switzerland.

- Lockner, D. 1993. The role of acoustic-emission in the study of rock fracture. *International Journal of Rock Mechanics and Mining Science & Geomechanics Abstracts* 30(7): 883-899.
- Matsuoka, N. & Murton, J. 2008. Frost weathering: Recent advances and future directions. *Permafrost and Periglacial Processes* 19(2): 195-210.
- Murton, J.B., Peterson, R., & Ozouf, J.C. 2006. Bedrock fracture by ice segregation in cold regions. *Science* 314(5802): 1127-1129.
- Scholz, C.H. 1968. Microfracturing and inelastic deformation of rock in compression. *Journal of Geophysical Research* 74(4).
- Walder, J. & Hallet, B. 1985. A theoretical model of the fracture of rock during freezing. *Geological Society of America Bulletin* 96: 336-346.

Model Test Study of the Impact of Rainfall on Thermal-Moisture Dynamics of the Active Layer

Zhi Wen, Wei Ma, Yu Sheng, Qingbai Wu, Dayan Wang, Wenjie Feng

State Key Laboratory of Frozen Soils Engineering, Cold and Arid Regions Environmental and Engineering Research Institute, Chinese Academy of Sciences, Lanzhou, Gansu, China

Abstract

The active layer in permafrost regions plays an important role in energy exchange between permafrost and the atmosphere. Rainfall potentially affects the thermal-moisture dynamics of the active layer. To better understand the thermal-moisture dynamics and the interaction between rainfall and the active layer, a model experiment of the active layer was carried out and soil temperature and soil moisture content were measured. The results show that soil temperature and soil moisture content have a close correlation with rainfall, and that rainfall affects the thermal-moisture dynamics of the active layer. Rainfall substantially increases the soil moisture content of the active layer and leads to cooling. Rainfall has a significant effect on the upper active layer and has a slight influence on the deep active layer, and rainfall intensity magnifies the impact. Evaporative cooling of the wet soil and the convective effect of rainfall infiltration both contribute to thermal transfer in the active layer. The influence of summer rainfall on soil temperature can continue until winter, and the lag effect may impact the following year's soil temperature.

Keywords: active layer; soil moisture content; soil temperature; rainfall; Qinghai-Tibetan Plateau.

Introduction

The active layer in permafrost regions is the near-surface layer of ground that experiences seasonal freezing and thawing. It is through this layer that energy exchange between permafrost and atmosphere occurs. The energy from atmosphere will be conducted to the active layer and controls the formation and change of permafrost. On the other hand, permafrost also influences the climate system via the active layer. Many environmental factors contribute to the thermal and moisture dynamics of the active layer. These factors include air temperature, precipitation, surface temperature, vegetation, soil type, physical and thermal properties of the surface cover and subsoil, soil moisture, the duration and thickness of seasonal snow cover, moisture movement, and disturbance by human activities (Zhang et al. 1997, Jorgenson et al. 2001, Brown et al. 2000, Frauenfeld et al. 2004, Zhang 2005, Smith et al. 2009, Wu & Zhang 2010). The active layer plays an essential role in high-latitude environments because most hydrological, biological, and biogeochemical activities take place within it (Hinzman et al. 1998, Kane et al. 1991). Changes of the active layer can lead to many environmental and engineering problems, such as vegetation degradation and infrastructure failure (Esch & Osterkamp 1990, Lunardini 1996). Under conditions of global warming, thickening of the active layer and permafrost degradation may release water and carbon currently sequestered in the upper permafrost, contributing to positive feedback effects in the context of global warming. Thawing of ice-rich permafrost can lead to subsidence and deformation, affecting the hydrological cycle, ecological relationships, and the performance of infrastructure in cold regions (Nelson et al. 2001, Hinkel & Nelson 2003). Therefore, it is important to study the thermal and moisture dynamics of the active layer.

Precipitation potentially affects the thermal and moisture

dynamics of the active layer (Hinzman & Kane 1992). Winter snowfall is thin and melts quickly in most permafrost regions of the Qinghai-Tibetan plateau. Sparse seasonal snow cover has little impact on the active layer due to reduced thickness and short duration. Precipitation infiltration in summer may result not only in the increase in soil moisture, but also in changes in the physical and thermal properties of the subsoil. This results in strong vertical and temporal variability of the heat capacity, thermal conductivity, and thus thermal diffusivity (McGaw et al. 1978, Hinkel et al. 1990). Sparse vegetation and high permeability soil on the Qinghai-Tibetan plateau promotes rainfall penetration into the subsoil, affecting the thermal and moisture dynamics of the active layer. Precipitation on the Tibetan Plateau occurs mainly during May to September, and the distribution of annual precipitation generally has a one-peak pattern, usually in July or August (Yang et al. 2008). The precipitation frequency on the Qinghai-Tibetan plateau is relatively high, and precipitation days account for 95.3% and 84.7% of the total study days during the period June 25 to September 19, 1998, on the southern slope and northern slope of the Tanggula Mountains, respectively (Yang et al. 2007). Evaporation during summer is large, and 50–60% of the total rainfall will re-evaporate into the atmosphere (Tanaka et al. 2003, Yang et al. 2004). Climatic warming of alpine permafrost regions will likely lead to precipitation changes, and the interaction of moisture and thermal processes presents a complex problem. It is vital to understand heat and water movement, and the fluctuations associated with precipitation for heat and mass transport, permafrost distribution, and for determining the response to various disturbances such as climatic warming and engineering activity. However, the influence of rainfall on the active layer has received relatively little attention, and further study is needed.

To better understand the influence of rainfall on the thermal-moisture dynamics of the active layer, a model test was con-

ducted. Based on observational data of soil temperature and soil moisture during testing, the thermal and moisture dynamics of the active layer during rainfall is examined. The effects of rainfall on the active layer are investigated and evaluated.

Sample Preparation and Test

The experimental soil used was sampled from the Beiluhe field site on the Qinghai-Tibet plateau, and the grain size distribution of the experimental soil sample is summarized in Table 1. The soil was classified as a silty clay according to the Chinese standard for soil classification (GBJ-145-90 1991). During sample preparation, the volumetric moisture content of the specimen was 30% and the soil was weighed to maintain a constant density of 2.1g/cm³. Concurrently, SWR sensors (Hongyang Company, China) and thermal resistor temperature probes were embedded along the depth. The SWR sensor obtains the moisture content by measuring the voltage difference resulting from a standing-wave. The SWR method was validated by experiments and a measurement error of 3% was achieved (Zhao & Wang 2002, Zhao et al. 2006). The soil temperature probes are thermal resistors made by the State Key Laboratory of Frozen Soil Engineering, CAREERI, CAS, and their accuracy calibrated in the laboratory is 0.05°C.

The test was conducted in the automatic temperature control model test apparatus of the State Key Laboratory of Frozen Soil Engineering, CAREERI, CAS (Fig. 1). A box with an inside diameter of 70 cm length, 70 cm width, and 35 cm depth was used to simulate the natural active layer. The experiment was designed to simulate a 2.1-m- thick active layer on the Qinghai-Tibetan Plateau. Based on similarity theory, each freezing-thawing cycle lasts 240 hours in the model test and represents one year. The experimental equipment is shown schematically in Figure 2.

To obtain the initial thermal regime, the bottom temperature boundary was set at -0.5°C, and the top temperature boundary was set constant at 10°C and lasted 48 hours. The upper temperature boundary varied according to a sine-cosine periodic change function with the bottom temperature constant -0.5°C. Figure 3 shows the upper soil temperature variation. The average temperature of each cycle was -1°C and the temperature range was 30°C during the test.

An artificial shower was used to simulate natural rainfall. To avoid the influence of water temperature on the soil heat transfer processes, the spray water temperature was controlled to be similar to the soil surface temperature. Each model test was carried out for three consecutive cycles. Simulated rainfall amounts of 10 mm, 20 mm, and 40 mm lasting 2 hours were applied during the first, second, and third test cycles, respectively. The test data were recorded every 30 minutes by a data logger (Datataker 500) and stored on disk.

Table 1. Grain size distribution of the experimental soil sample.

| Soil type | Grain size distribution (%) | | | |
|--------------------------|-----------------------------|----------|------------|--------|
| | >0.1 | 0.1~0.05 | 0.05~0.005 | <0.005 |
| Qinghai-Tibet silty clay | 0.9 | 7.6 | 55.4 | 36.1 |



Figure 1. Photograph of the model test equipment.

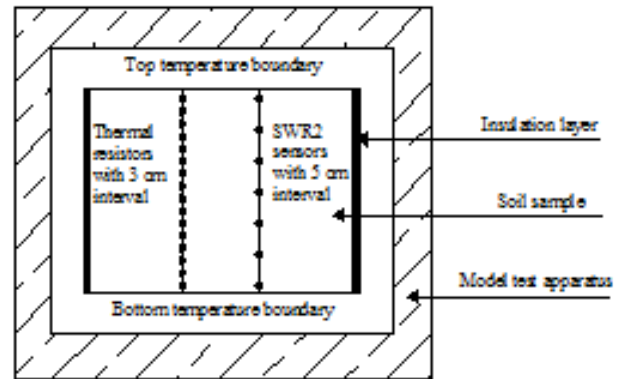


Figure 2. Schematic diagram of experimental equipment.

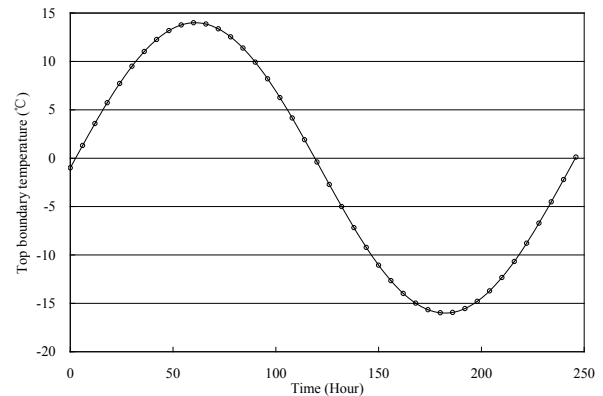


Figure 3. Upper soil temperature variation during the test.

Results and Analysis

The influence of rainfall on soil temperature dynamics

Figure 4 shows soil temperature variations under the conditions of no rainfall and rainfall, respectively. It can be seen that soil temperature responds quickly to the surface temperature boundary and demonstrates periodic variation. Compared with the environmental temperature, soil temperatures have a smaller amplitude and show a slight phase delay (Fig. 4a). After rainfall, the soil surface temperature drops significantly and the heat transfer process is affected by the rainfall event. Compared to the no-rainfall test, soil temperature with rainfall is lower. For example, the 3°C isotherm rose gradually after the first thawing period (Fig. 4b).

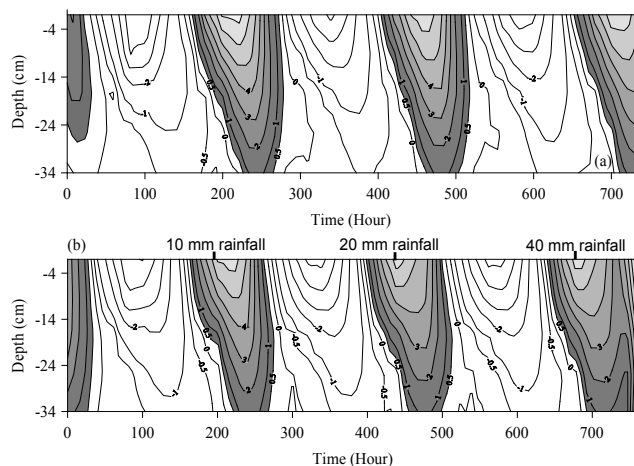


Figure 4. Soil temperature variations ($^{\circ}\text{C}$) during the test (a) without rainfall and (b) with rainfall.

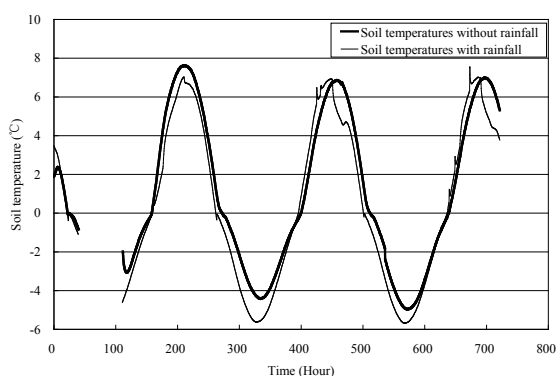


Figure 5. Comparison of soil temperature at the 1 cm depth.

Precipitation increased the soil moisture content considerably and enhanced the evaporation cooling of the wet soil. The convective effect of rainfall infiltration contributes to thermal transfer in the active layer.

Figure 5 shows the comparison of soil temperature at the 1-cm depth during the test. When rainfall occurs, the moisture infiltrates into the subsurface and the soil temperature at a depth of 1 cm quickly declines. Soil temperature has a close correlation with rainfall. Summer rainfall infiltration produces a series of thermal feedbacks in the active layer, causing rapid cooling of the subsurface soil at the depth of 1 cm. Soil temperature with rainfall is lower than that without rainfall, which means that rainfall can affect the thermal regime and the thaw depth of the active layer.

Rainfall can result in long-term effects on the ground thermal regime and the freezing and thawing of the active layer. Soil temperature with rainfall in winter is generally lower than that without rainfall, which means that the cooling effect can last until winter. Reduced soil temperature in winter may lead to a change in the following year's soil temperature and thaw depth.

The influence of rainfall on soil moisture content

Figure 6 shows soil moisture content variation under the conditions of no rainfall and rainfall, respectively. The soil

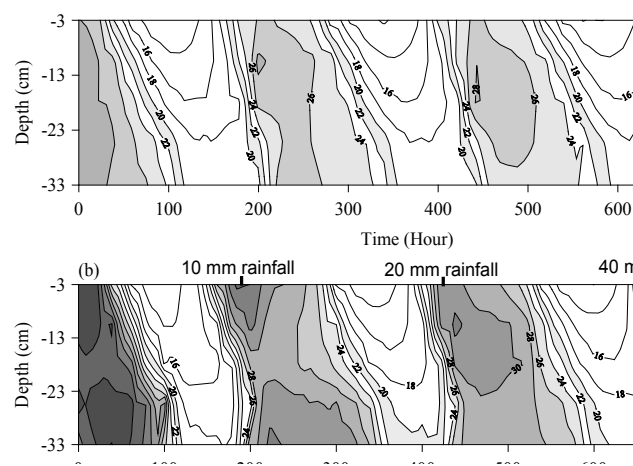


Figure 6. Soil volumetric moisture content (%) variations during the test (a) without rainfall and (b) with rainfall.

moisture content has little variation for the no rainfall test. The isolines of soil moisture content are similar during different test cycles (Fig. 6a). Moisture migration during freezing and thawing is not very significant. The temperature gradient does not have a notable effect on the soil moisture redistribution in the active layer in this experiment. As shown in Figure 6b, the soil moisture content increases significantly with rainfall initiation. The observational data show that rainfall has a remarkable effect on the active layer soil moisture content. The subsurface soil moisture content responds quickly to the rainfall event. The variation in the soil moisture content at a depth of 3 cm can reach about 10% due to the impact of rainfall. The soil moisture content with rainfall during the thawing period is generally higher than that of no rainfall (Fig. 7). Furthermore, evaporative cooling from wetter soils will result in reduced energy conduction into the ground and greatly change the freezing and thawing processes in the subsoil. Therefore, precipitation during summer plays an important role in the thermal-moisture dynamics of the active layer on the Qinghai-Tibetan Plateau.

The test indicates that rainfall can have a significant effect on the thermal-moisture regime of the active layer and tends to thin the active layer on the Qinghai-Tibetan plateau. The impact on the thermal regime can last more than a month and can persist until winter. The lag effect may lead to a change of the following year's soil temperature. Rainfall results in the increase in soil moisture content and will change the surface mass-energy balance. Summer rainfall will ultimately affect the maximum thaw depth of the active layer and permafrost distribution. Therefore, to predict seasonal thaw depth and calculate the permafrost temperature field accurately, summer rainfall should be taken into consideration.

The influence of rainfall intensity

Figure 8 shows soil temperature variations at the 1-cm and 34-cm depths. The results show that high intensity rainfall magnifies the response. As shown in Figure 8, 20-mm and 40-mm rainfall events in the second and third cycles result in greater soil temperature depression than that of a 10-mm

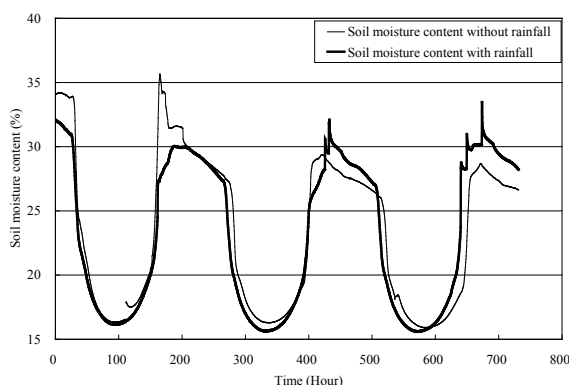


Figure 7. Comparison of soil volumetric water content at the 3-cm depth.

rainfall during the first cycle. The notable effect of rainfall lasts more than 10 hours, after which soil temperatures are mainly affected by the change in ambient temperature. The temperature at the 1-cm level decreases more, and the temperature depression lasts longer as a result of heavier rainfall. Rainfall has a significant impact on the soil temperature at a depth of 1 cm, while the response of soil temperature at a depth of 34 cm decreases greatly and is also delayed. This partly results from the higher soil moisture content. Light rainfall in the first cycle has little impact on the soil temperature at the 34-cm depth. With an increase in rainfall intensity, the deep soil temperature begins to respond to the rainfall event. For example, the 40-mm rainfall in the third cycle leads to a thermal disturbance of the soil at 34-cm depth.

To determine the impact of rainfall intensity on soil volumetric water content, the water content at the 3-cm and 33-cm levels is shown as Figure 9. Soil moisture content disruptions are apparent at the 3-cm level and are clearly associated with the corresponding rainfall event. Rainfall with low intensity has little impact on the soil moisture content at the 3-cm depth. The 20-mm and 40-mm rainfall events tend to affect the soil moisture content at the depth of 3 cm and result in significant soil moisture pulses. However, the soil moisture content at the 33-cm depth remains fairly constant and is nearly free of impact. The experiment indicates that the subsurface soil on the Qinghai-Tibetan Plateau responds quickly to rainfall, and that moisture content increases greatly. The response of the deep active layer is not apparent in this experiment.

Conclusions

The soil temperature and soil moisture content are closely correlated to rainfall. Rainfall infiltration in summer affects the thermal regime of the active layer and results in depression of the soil temperature. Rainfall will notably increase the soil moisture content of the active layer, and rainfall intensity magnifies the response. The significant effect of rainfall lasts more than 10 hours, after which soil temperature is mainly affected by changes in ambient temperature. Rainfall has a measurable effect on the thermal-moisture dynamics of the upper active layer, while the impact of rainfall on the deeper

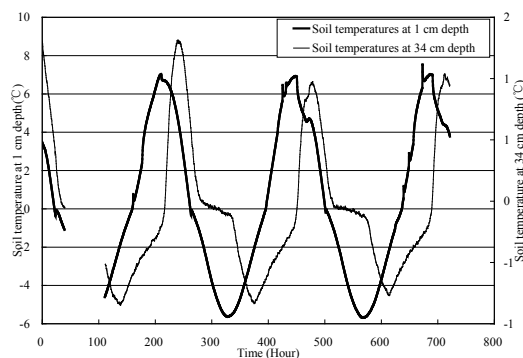


Figure 8. Soil temperature variations at 1-cm and 34-cm depths.

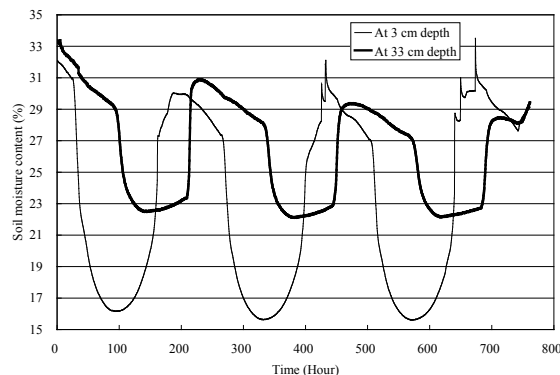


Figure 9. Soil volumetric moisture content variations at the 3-cm and 33-cm depths.

active layer remains fairly constant. Precipitation will increase soil moisture content considerably and enhances evaporative cooling of the wet soil. The convective effect of rainfall infiltration also contributes to thermal transfer in the active layer. The influence of summer rainfall on soil temperature can persist until winter, and the lag may affect the following year's soil temperature. Summer rainfall will ultimately impact the maximum thaw depth of the active layer.

Rainfall infiltration significantly affects the thermal-moisture regime of the subsurface. However, the thermal-moisture characteristic of the active layer has strong spatial and temporal variability, so more experiments should be carried out. This has important implications for permafrost distribution and its variation, hydrogeology in cold regions, and ecosystems. A detailed understanding of the impact of non-conductive heat transfer processes on the soil thermal regime will be necessary for predicting the overall effect on the active layer and permafrost stability on the Qinghai-Tibetan Plateau.

Acknowledgments

The research project was supported by the 100 Talented Young Scientists Project granted to Dr. Zhi Wen, the Program for Innovative Research Group of the National Natural Science Foundation of China (Grant no. 40821001), the CAS Knowledge Innovation Key Directional Project (Grant no. KZCX2-YW-QN307), and Funding of the State Key Laboratory of Frozen Soils Engineering, CAS (Grant no. SKLFSE-ZY-02).

References

- Brown, J., Hinkel, K.M., & Nelson, F.E. 2000. The Circumpolar Active Layer Monitoring (CALM) Program: Research design and initial results. *Polar Geography* 24(3): 165-253.
- Esch, D.C. & Osterkamp, T.E. 1990. Cold regions engineering: climatic concern for Alaska. *Journal of Cold Regions Engineering* 4 (1): 6-4.
- Frauenfeld, O.W., Zhang, T., Barry, R.G., & Gilichinsky, D. 2004. Interdecadal changes in seasonal freeze and thaw depths in Russia. *Journal of Geophysical Research* 109, D05101, doi:10.1029/2003JD004245.
- GBJ-145-90, 1991. Standard for soil classification, Beijing, P.R. China (in Chinese).
- Hinkel, K.M., Outcalt, S.I., & Nelson, F.E. 1990. Temperature variation and apparent thermal diffusivity in the refreezing active layer, Toolik Lake, Alaska. *Permafrost and Periglacial Processes* 1(4): 265-274.
- Hinkel, K.M. & Nelson, F.E. 2003. Spatial and temporal patterns of active layer thickness at Circumpolar Active Layer Monitoring (CALM) sites in northern Alaska, 1975-2000. *Journal of Geophysical Research* 108(D2), 8168 doi:10.1029/2001JD000927.
- Hinzman, L.D. & Kane, D.L. 1992. Potential response of an arctic watershed during a period of global warming. *Journal of Geophysical Research* 97(D3): 2811-2820.
- Hinzman, L.D., Goering, D.J., & Kane, D.L. 1998. A distributed thermal model for calculating soil temperature profiles and depth of thaw in permafrost regions. *Journal of Geophysical Research* 103 (D22): 28975-28991.
- Jorgenson, M.T., Racine, C.H., Walters, J.C., & Osterkamp, T.E. 2001. Permafrost degradation and ecological changes associated with a warming climate in central Alaska. *Climate Change* 48: 551-579.
- Kane, D.L., Hinzman, L.D., & Zarling, J.P. 1991. Thermal response of the active layer to climate warming in a permafrost environment. *Cold Regions Science and Technology* 19: 111-122.
- Lunardini, V.J. 1996. Climatic warming and the degradation of warm permafrost. *Permafrost and Periglacial Processes* 7: 311-320.
- McGaw, R.W., Outcalt, S.I., & Ng, E. 1978. Thermal properties and regime of wet tundra soils at Barrow, Alaska. *Proceedings of the Third International Conference on Permafrost*. National Research Council of Canada, Ottawa, Canada, pp. 47-53.
- Nelson, F.E., Anisimov, O.A., & Shiklomanov, N.I. 2001. Subsidence risk from thawing permafrost. *Nature*, 410: 889-890.
- Smith, S.L., Wolfe, S.A., Risborough, D.W., & Nixon, F.M. 2009. Active layer characteristics and summer climate indices, Mackenzie Valley, Northwest Territories, Canada. *Permafrost and Periglacial Processes* 20: 201-220.
- Tanaka, K., Tamagawa, I., Ishikawa, H., Ma, Y., & Hu, Z. 2003. Surface energy budget and closure of the eastern Tibetan Plateau during the GAME-Tibet IOP 1998. *Journal of Hydrology* 283: 169-183.
- Wu, Q. & Zhang, T. 2010. Changes in active layer thickness over the Qinghai-Tibetan Plateau from 1995 to 2007. *Journal of Geophysical Research* 115, D09107 doi:10.1029/2009JD012974.
- Yang, K., Koike, T., Fujii, H., Tamura, T., Xu, X., Bian, L., & Zhou, M. 2004. The daytime evolution of the atmospheric boundary layer and convection over the Tibetan Plateau: observations and simulations. *Journal of the Meteorological Society of Japan* 82(6): 1777-1792.
- Yang, M.X., Yao, T.D., Gou, X.H., Wang, H.J., & Hao, L.S. 2007. Comparison analysis of the summer monsoon precipitation between northern and southern slopes of Tanggula Mountains, Qinghai-Xizang (Tibetan) Plateau: a case study in summer 1998. *Hydrological Processes* 21: 1841-1847.
- Yang, M.X., Yao, T.D., Gou, X.H., & Wang, H.J. 2008. Precipitation Distribution along the Qinghai-Xizang (Tibetan) Highway, Summer 1998. *Arctic, Antarctic and Alpine Research* 40 (4): 761-769.
- Zhang, T., Osterkamp, T.E., & Starnes, K. 1997. Effect of climate on the Active layer and permafrost on the North Slope of Alaska, U.S.A. *Permafrost and Periglacial Processes* 8 (1): 45-67.
- Zhang, T. 2005. Influence of the seasonal snow cover on the ground thermal regime: An overview. *Reviews of Geophysics* 43, RG4002 doi:10.1029/2004RG000157.
- Zhao, Y.D., Bai, C.X., Kuang, Q.M., Zhang, J., & Wolfgang, P. 2006. Performance of three types of soil moisture sensors: SWR, TDR and FD. *Journal of Beijing Forestry University* 28(3): 158-160 (in Chinese).
- Zhao, Y.D. & Wang, Y.M. 2002. Sensitivity analysis of soil moisture sensor based on the principle of standing wave ratio. *Transactions of the CSAE* 18(2): 5-8 (in Chinese).

Application of the Fill-and-Spill Concept in Permafrost Hydrology

Ming-ko Woo

School of Geography and Earth Sciences, McMaster University, Hamilton, Ontario, Canada

Abstract

The fill-and-spill concept for runoff generation and flow delivery postulates that outflow occurs only when water held in storage exceeds the storage capacity (or rises above the outflow threshold). Each flow production process has its threshold, and in permafrost areas seasonal freeze-thaw and the accumulation-ablation of snow and ice change the storage capacity of the active layer and above ground. Unique to permafrost regions, not only the status of storage (governed by water gains and losses), but also the water-holding capacity (including considerations of the space that can retain water and the outflow threshold elevation) changes during the thaw season. Examples of subsurface, surface, and channel flow production are reviewed in light of the fill-and-spill concept. Permafrost areas are particularly amenable to the realization of this concept as the shallow but uneven active layer allows ready responses to water gains and losses, while seasonal snow and ice in channels create blockages that have to be overcome by spillage before segments of the flow network are hydrologically united for water delivery.

Keywords: fill-and-spill; hydrology; streamflow; subsurface flow; surface flow; variable source area.

Introduction

In the last decade, the idea of fill-and-spill was propounded as a hydrological concept to emulate the processes of runoff generation. This concept formalizes the familiar storage threshold mechanism. Simply stated, fill-and-spill postulates that runoff, be it above ground or in the subsurface, is produced only when water storage exceeds the withholding threshold. Crucially associated with the fill-and-spill mechanism are issues of (1) the storage capacity that is closely related to (2) the size of the aquifer and the outflow threshold below which water cannot spill, (3) the water balance that governs water gained by and lost from storage, and (4) the connectivity or linkage among segments within a hydrological system that delivers the flow. A particular hydrological unit retains water without generating runoff until its storage (S) is filled to capacity (S_{cap}), which is the total space to be filled by water before lateral flow (Q_{out}) commences. For subsurface flow generation and depending on the soil hydraulic properties, filling may be attained without full saturation of the soil, while the hysteresis effect is an added consideration (Spence 2010). Expressed succinctly,

$$\begin{aligned} Q_{out} &> 0, \text{ when } S = [Q_{in} + P - E + S_{ant}] > S_{cap} \\ Q_{out} &= 0, \text{ otherwise} \end{aligned} \quad (1)$$

Here the vertical components are the water gained from direct precipitation that includes snowmelt and rainfall (P), and the water lost to evaporation (E). S_{ant} is the amount of antecedent storage or water previously held in the unit, and Q_{in} is lateral inflow from another unit, which can be zero if there is no inflow from its adjoining areas. If a slope or a channel consists of several segments, Q_{out} from one segment is Q_{in} to the lower segment. The flow pathway can include surface and subsurface routes, and flow connection is severed when one of the segments along the route fails to spill.

The concept was introduced by Spence and Woo (2003)

to explain the initiation of subsurface flow in a Canadian Shield valley. Tromp-van Meerveld and McDonnell (2006) elaborated the principle to depict flow production on a temperate latitude slope, while Wright et al. (2009) applied this principle to subsurface flow generation in the active layer, and Muir et al. (2011) described the retardation of sub-permafrost groundwater flow in coarse morainic materials due to fill-and-spill over uneven bedrock surfaces. The mechanism was also used by Woo and Mielko (2007) to explain the issuance of flow from lakes in a semi-arid Shield environment.

Under cold climates, the presence of seasonal frost and permafrost adds a significant component to the fill-and-spill process that modifies the timing, magnitude, spatial extent, and connectivity of flow on hill slopes and in drainage networks. The present review surveys a number of examples and interprets them in accordance with the fill-and-spill principle to (1) highlight special application of this hydrologic framework in permafrost terrain, and (2) demonstrate the importance of this process in relation to hydrologic connectivity on hill slopes, along river channels, and in drainage basins.

Permafrost, Storage and Flow Threshold

Permafrost and seasonal frost, especially where ice-rich, have very low hydraulic conductivity and may be deemed impervious to bulk water flow. Most frozen soils have very poor capability to accommodate liquid water, and their storage capacity is therefore negligible. With frozen soils and ground freeze-thaw, the fill-and-spill mechanism is affected in several ways:

- 1) Compared with soils in non-permafrost areas, the available storage capacity is restricted mainly to within the active layer in permafrost terrains. With even a small amount of water input, the storage is quickly filled to initiate spilling and rapid rise in flow. However, the limited storage can also be depleted easily and this flow is not sustainable as it would normally be in non-permafrost areas. Such flow characteristics have been well described (e.g., McNamara et al. 1998).

- 2) Storage capacity is not static; it changes as the ground freezes and thaws. Thus storage capacity of the active layer is at a minimum in early spring when snowmelt releases much water that cannot be absorbed, but fills the subsurface and surface storages rapidly and spills over extensive areas to generate flow. Freeze-back also reduces the storage capacity of the active layer, such that groundwater is forced to extrude (spill) to form icing.
- 3) A local sill on the frost table can withhold water behind it, thereby blocking lateral drainage. As the ground thaws, the flow threshold is lowered and the stored water may spill downslope to yield runoff. Thus subsurface thresholds in permafrost are dynamic and are distinguished from static thresholds, such as subsurface bedrock sills that are seasonally invariant (e.g., Spence & Woo 2003, Tromp-van Meerveld & McDonnell 2006).

The sections that follow provide examples of processes that fill or lower the storage, and of various threshold conditions that affect the generation of subsurface, surface, and channel flow in permafrost terrain.

Subsurface Flow

A simple illustration of the fill-and-spill principle is the drainage of porous organic materials. Santeford (1979) found that rainfall on a column of moss does not initiate runoff until a critical level of saturation (threshold) is reached. Drainage then occurs (spills) at a rate approximately equal to that of rainfall but drainage declines exponentially after the rain event. Similar results were obtained by Bello & Arama (1989) for lichen. After drainage has terminated, the stored water continues to be depleted by evaporation. To revive drainage from the lichen, subsequent rain events have to overcome the moisture deficit, which is the difference between the water holding capacity and the water content at a particular time.

Permafrost areas, with thinly thawed active layers that offer limited storage capacity, are particularly responsive to the fill-and-spill mechanism (as noted in the previous section). The threshold for lateral drainage in the active layer also changes during the thaw season as the frost table fluctuates. Slight thaw in the spring requires only small amounts of water input to exceed the storage threshold, and both subsurface and surface flows are common. As the frost table deepens, the storage capacity of the active layer enlarges. The saturated zone would first fall below ground (dropping below the threshold for surface runoff) and then several conditions may arise.

- 1) Wright et al. (2009) noted that differential thaw creates troughs and sills on the frost table. Subsurface flow connection along the slope is interrupted when the supra-permafrost groundwater table falls below the sills; but when sufficient water is accumulated, water spills over the sills and flow connectivity is re-established.
- 2) With uneven microtopography on the frost table, the sills withhold water in isolated pockets in the frost table depressions. Woo & Steer (1983) observed an abrupt rise in the supra-permafrost water table on parts of a high arctic slope during a dry warm spell in

Resolute, Cornwallis Island, Canada. They attributed this phenomenon to subsurface drainage when ground thaw breached a subsurface sill to allow spillage of the stored water, sending a groundwater pulse down the slope. Figure 1 shows that the flow followed preferred pathways as defined by the wells that manifested a steep water table rise, in contrast to other wells on the same slope that lacked such a response.

- 3) Some soils with heterogeneous profiles have more than one flow threshold, as illustrated by the following example. Where soil pipes are present, pipe flow ceases when evaporation and a descending frost table (due to ground thaw) lower the water table below the pipes. However, pipe flow is resumed when rainfall input fills the storage back up to the level of the pipes. Pipe flow is turned on or off quite sharply, as shown by measurements made by Carey and Woo (2000) during snowmelt and rainfall events on a subarctic slope (Fig. 2). Additionally, soils in many permafrost areas have an organic layer overlying clastic materials, the former often with considerably higher hydraulic conductivity than the latter. A two-layer flow system (Carey and Woo 2001) is envisaged in which quick flow can be generated from the organic layer of peat and living plants (mosses and lichens) whereas slow flow is likely in the lower layer. For quick flow to begin, the supra-permafrost water table has to reach the soil matrix of the top (organic) layer, but when drying and descent of the frost table drop the water table into the lower layer, only slow flow is possible. In these situations, the soil has several flow thresholds: for pipe flow, quick flow, and slow flow.

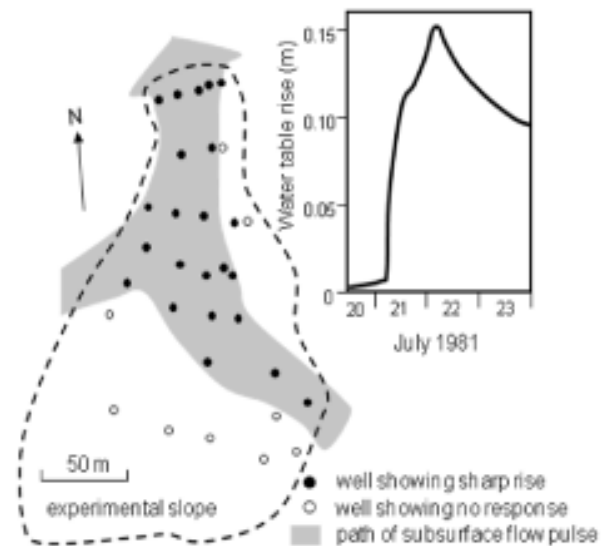


Figure 1. Active layer thaw resulting in the breaching of a sill on the frost table, followed by downslope drainage of groundwater that caused water level rises along a slope in a continuous permafrost area in Resolute, Nunavut. Subsurface flow followed an identifiable path defined by the wells that exhibited a sharp rise in stage (inset provides an example).

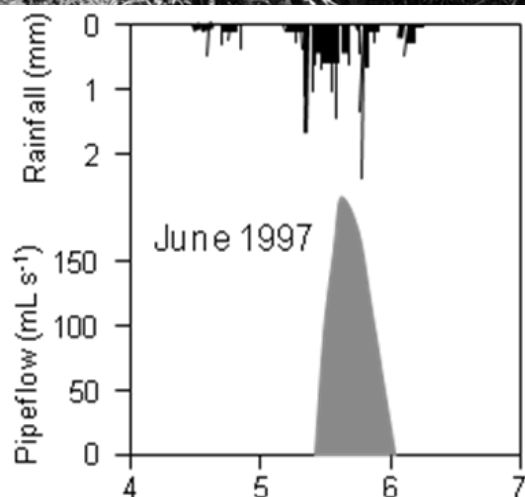
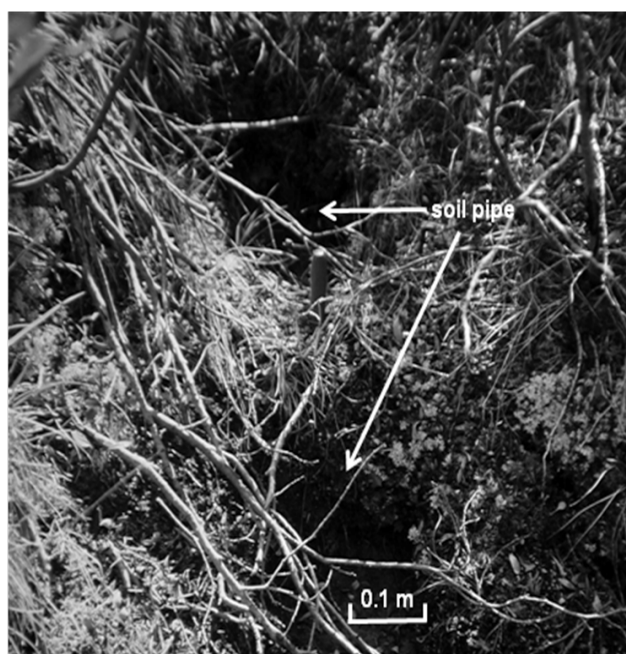


Figure 2. Top shows a soil pipe in a permafrost slope, revealed where its roof has collapsed, Wolf Creek basin, Yukon. Such pipes are often dry in the summer unless rainfall fills the supra-permafrost groundwater storage and raises the water table to spill through the pipes. The bottom hydrograph illustrates that pipe flow rose sharply but also receded steeply when water became insufficient to fill the storage up to the level of the pipes.

These examples echo Spence's (2010) finding that runoff generation is due to several processes, each with its threshold condition. The timing and location that the processes are activated depend on their being triggered by the filling event.

Surface Flow

Surface flow is found where water runs on the ground surface and is mainly produced by two mechanisms:

- 1) Water is supplied at a rate that exceeds infiltration. The resulting surface runoff, known as Hortonian overland flow, is common in the snowmelt period when filling exceeds the water storage capacity of the scarcely thawed active layer.

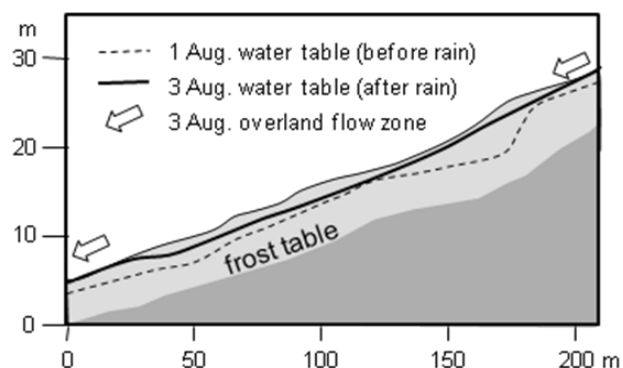


Figure 3. When groundwater storage was increased by a mid-summer rain event in 1978 near Resolute, overland flow was generated at slope concavities, but the overland flow zones were not contiguous and occurred only where groundwater spilled above ground (shown as dark colored patches in the bottom figure). These localized zones where water is frequently spilled promote colonization of the barren polar desert surface by *Nostoc* algae, followed by mosses and lichens.

Hortonian overland flow can also be observed when the soil cannot accept intense summer rain or where rain falls on impermeable bedrock surfaces (Spence & Woo 2002).

- 2) A rise of the water table above ground leads to saturation overland flow, which is a product of exfiltration of groundwater and direct rainfall on the saturated area. In this case, spilling results from excessive filling of the supra-permafrost aquifer. Dingman (1973) made use of this mechanism to explain the generation surface flow in permafrost areas in Fairbanks, Alaska. The same process is invoked by the variable source area concept, which holds that the enlargement and contraction of the source area for surface flow proceed in a continuous fashion and overland flow area extends from the lower to the higher slope and from the lower channel to positions upstream (Dunne 1978). In fill-and-spill, the expansion of surface flow area can be continuous or sudden, and flow can cease in any part of the hydrological system where the amount of water stored fails to overtop the required threshold.

Figure 3 illustrates a saturation overland flow event on a slope near Resolute. Rainfall raised the supra-permafrost water table and where it intercepted the ground surface, such as at local slope concavities, water spilled above ground. Note that overland flow zones were not contiguous along the slope

and when the water table dropped below ground, surface flow terminated abruptly.

It is generally recognized that the source area for runoff is dynamic and variable, expanding when rainfall and snowmelt contribute much water and contracting when the hydrological system is supported by a diminished amount of water. The variable nature of surface flow area is best seen in flat terrain such as extensive wetlands where ground saturation leads to large areal expansion of surface and subsurface flows. Bowling et al. (2003) likened the rapid expansion of surface saturation in an Alaskan coastal wetland to the filling of a surface reservoir. For the 471 km² Putuligayuk watershed, they found that the surface water area varied from 65 to 15% during the thaw season. In the Lone Gull area, Nunavut, Roulet & Woo (1988) found that wetland and hill-slope drainage was abruptly coupled when snowmelt runoff enabled the surface flow area to expand. Meltwater supply quickly filled the storage capacity of the wetlands and the surface runoff contributing area enlarged between June 5 and 15 (Fig. 4). This was accompanied by a rapid rise in discharge of a stream fed by these wetlands. As the melt season waned, meltwater supply declined, evaporation increased, and ground thaw enlarged the water storage capacity of the active layer. Consequently, the surface runoff contributing area decreased (see June 25). Similar expansion and contraction of runoff contributing area to streamflow, due to filling and depletion of storage, were observed in a Canadian Shield basin (Spence et al. 2010).

Many lakes of deltaic and riparian wetlands are surrounded by rims with permafrost cores, and hydrological linkage is almost entirely through overflow. For lakes in the Mackenzie River delta, Marsh & Hey (1989) found that ‘no-closure lakes’ are connected to the river at all times in the thaw season while ‘low-closure lakes’ at higher elevations do so at times of high water stage; but ‘high-closure lakes’ are filled by spring freshets only in exceptional years to effect exchange with the river water. Elevation of the thresholds therefore dictates the frequency and duration of lake water spill. At a smaller scale, a cluster of tundra ponds become separated from or linked with each other depending on the pond level. Woo & Guan (2006) found that a group of ponds in Ellesmere Island overflowed and spilled into one another during the spring freshet but they became progressively isolated as spring flood receded below the lips along the pond margins, with permafrost sealing the ponds against lateral and vertical seepage. Later rainstorms filled the ponds. Subsurface and then surface flow connections resumed when pond levels rose to elevations above their outlets.

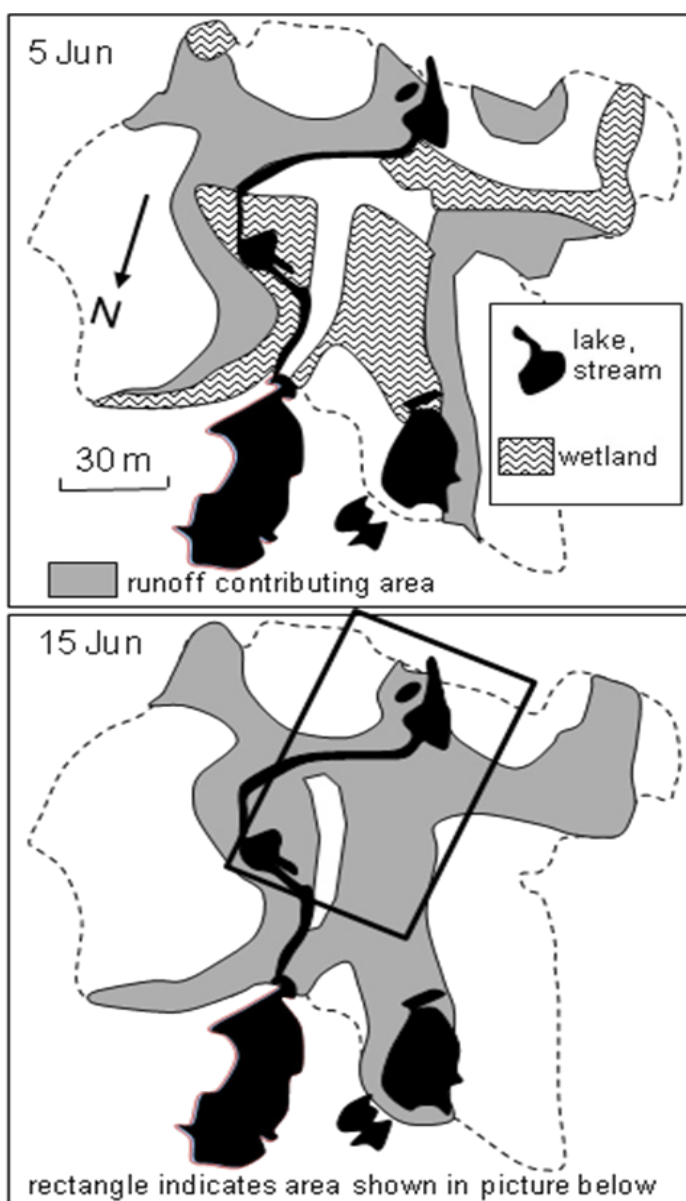


Figure 4. Expansion and contraction of surface runoff in a small catchment, Lone Gull, Nunavut, shown at 10-day intervals in 1981. Snowmelt began in late May and meltwater rapidly filled up the storage capacity to produce much surface runoff. Surface flow area shrank as the melt season advanced, when reduced meltwater input, combined with evaporation losses and increased ground thaw limited the spillage of surface flow.

The filling and spillage of lakes and ponds are clear-cut demonstrations of the fill-and-spill principle (Woo and Mielko 2007). Artificial cutting of a channel in permafrost that drained Lake Illisarvik, Northwest Territories, in 1978 provided a vivid example of rapid and catastrophic outflow as the spillage threshold was drastically and suddenly lowered (Mackay 1981). Such a type of spill may be caused by thermo-erosion through natural processes and is not uncommon in permafrost territories (Walker 1978).

Flow in Channels

Although not restricted to permafrost areas but common to cold regions, the presence of snow and ice in channels plays a major role in creating temporary storage that interrupts river discharge and in magnifying the rate of subsequent flow release. Several situations usually arise:

- 1) Rivers in continuous permafrost areas seldom have winter flow and their dry channels are usually piled with uneven snowdrifts to form troughs and snow ridges. In the snowmelt season, these ridges act as dams that impound water in the troughs to create temporary ponds (Woo and Sauriol 1980). Streamflow development follows filling and spilling of the ponds in the channel network (Fig. 5).
- 2) Where winter flow is maintained by groundwater or by discharge from upstream, as is common in many subarctic and low arctic rivers, river ice develops to considerable thickness (1–2 m). During breakup, ice jams along the channels block the flow. With flood water first filling behind the jams, and then bursting when the jams break, flood waves are produced and propagate downstream (Hicks and Beltaos 2008).
- 3) Sub-permafrost and to some extent, intra- and supra-permafrost groundwater discharge enables the growth of icings in river channels (Kane 1981). These icings present barriers to river flow in the spring, creating local-scale fill-and-spill situations along the channels.

The act of spilling can erode and lead to lowering of the thresholds, thereby sustaining if not prolonging the spill. Outflow that cuts through a snow dam or slices across an icing has a feedback effect that enables the flood water to spill at diminishing threshold elevations as the flow continues.

Flow delivery in the drainage system is significantly affected by channel blockages. Until the flow network is integrated, snowmelt runoff may not reach the basin outlet while discharge varies greatly from segment to segment within the channel network. In the post-melt season, streams may dry up, especially in a semi-arid or arid environment. The result is progressive disconnection of the streamflow network, as noted by Phillips et al. (2011) for several subarctic basins. The revival of streamflow by summer rain requires the much depleted channel storage to be filled before water is spilled sequentially down various segments of the drainage network. Thus the fill-and-spill behavior permeates throughout the basin hydrological system to influence both the generation and the delivery of flow.



Figure 5. Dry valleys in the continuous permafrost area of Resolute are regularly filled with winter snow that forms ridges and troughs; the latter create temporary ponds when infilled with snow meltwater. Outflow occurs when these ponds are filled to the brims and then spill. Spilling enables downcutting of the snow dam, leading to lowering of the threshold for overflow.

Discussion and Conclusions

As an extension of the familiar notion that water overflows when storage threshold is exceeded, ‘fill-and-spill’ is formalized as a concept to account for the processes of runoff generation and flow delivery within a hydrological system. This review emphasizes the unique roles of permafrost, snow, and ice on fill-and-spill. Several generalities emerge from this study:

- 1) Unlike the conventional variable source area concept, which proposes spatially contiguous expansion or contraction of flow contribution area as the water table rises or falls, fill-and-spill represents an on-off switch for flow to occur, being regulated by threshold conditions specific to particular runoff processes.
- 2) Unique to permafrost areas, both the status of storage (which is governed by water gains and losses) and the storage capacity (including considerations of the space that can retain water, and the threshold elevation) change during the thaw season.
- 3) Water retention capacity varies as the active layer deepens or thins, and as snow and ice block off surface depressions of different dimensions on stream channels.
- 4) Spillage thresholds are universally related to surface topography, bedrock configuration and stratigraphic transitions. Special to permafrost regions, most thresholds are not fixed. On hill slopes, they are controlled by the frost table position; in channels, they are regulated by snow and ice conditions. As a feedback, spillage can lower the thresholds through erosion or thaw processes.
- 5) Fill-and-spill events influence the connectivity of flow on slopes, between lakes and ponds, and in channels in cold regions; hence the fill-and-spill process plays a significant role in runoff generation and the maintenance of flow in drainage networks.

References

- Bello, R. & Arama, A. 1989. Rainfall interception in lichen canopies. *Climatological Bulletin (Canada)* 23:74–78.
- Bowling, L.C., Kane, D.L., Gieck, R.E., Hinzman, L.D., & Lettenmaier, D.P. 2003. The role of surface storage in low-gradient Arctic watershed. *Water Resources Research* 39, 1087, doi:10.1029/2002WR001466.
- Carey, S.K. & Woo, M.K. 2000. The role of soil pipes as a slope runoff mechanism, subarctic Yukon, Canada. *Journal of Hydrology* 233:206–222.
- Carey, S.K. & Woo, M.K. 2001. Slope runoff processes and flow generation in a subarctic, subalpine catchment. *Journal of Hydrology* 253:110–129.
- Dingman, S.L. 1973. Effects of permafrost on stream flow characteristics in the discontinuous permafrost zone of Central Alaska. *Proceedings of the Second International Conference on Permafrost, North American Contributions, Yakutsk, USSR. National Academy of Sciences, Washington, DC*: 447–453.
- Dunne, T. 1978. Field studies of hillslope flow processes. In *Hillslope Hydrology*. M.J. Kirkby (ed.). John Wiley, Chichester: 227–293.
- Hicks, F.E. & Beltaos, S. 2008. River ice. In *Cold Region Atmospheric and Hydrologic Studies, the Mackenzie GEWEX Experience, Vol 2: Hydrologic Processes*. M.K. Woo (ed.). Springer, Berlin: 281–305.
- Kane, D.L. 1981. Physical mechanics of aufeis growth. *Canadian Journal of Civil Engineering* 8:186–195.
- Mackay, J.R. 1981. An experiment in lake drainage, Richards Island, Northwest Territories: a progress report. *Current Research, Part A, Geological Survey of Canada Paper* 81-1A:63–68.
- Marsh, P. & Hey, M. 1989. The flooding hydrology of Mackenzie Delta lakes near Inuvik, N.W.T., Canada. *Arctic* 42:41–49.
- McNamara, J.P., Kane, D.L., & Hinzman, L.D. 1998. An analysis of streamflow hydrology in the Kuparuk River Basin, Arctic Alaska: a nested watershed approach. *Journal of Hydrology* 206:39–57.
- Muir, D., Hayashi, M., & McClymont, A.F. 2011. Hydrological storage and transmission characteristics of an alpine talus. *Hydrological Processes* 25:2954–2966.
- Phillips, R.W., Spence, C., & Pomeroy, J.W. 2011. Connectivity and runoff dynamics in heterogeneous basins. *Hydrological Processes* 25, 3061–3075.
- Roulet, N.T. & Woo, M.K. 1988. Runoff generation in a Low Arctic drainage basin. *Journal of Hydrology* 101: 213–226.
- Santeford, H.S. 1979. Toward hydrologic modeling of the black spruce/permafrost ecosystems of Interior Alaska. *Proceedings of the Thirtieth Alaska Science Conference, Fairbanks, Alaska* (unpublished manuscript).
- Spence, C. 2010. A paradigm shift in hydrology: storage thresholds across scales influence catchment runoff generation. *Geography Compass* 4:819–833.
- Spence, C., Guan, X.J., Phillips, R., Hedstrom, N., Granger, R., & Reid, B. 2010. Storage dynamics and streamflow in a catchment with a variable contributing area. *Hydrological Processes* 24: 2209–2221.
- Spence, C. & Woo, M.K. 2002. Hydrology of subarctic Canadian Shield: bedrock upland. *Journal of Hydrology* 262:111–127.
- Spence, C. & Woo, M.K. 2003. Hydrology of subarctic Canadian Shield: soil-filled valleys. *Journal of Hydrology* 279:151–166.
- Tromp-van Meerveld, H.J. & McDonnell, J.J. 2006. Threshold relations in subsurface stormflow: 2. The fill and spill hypothesis. *Water Resources Research* 42:W02411, doi:10.1029/2004WR003800.
- Walker, H.J. 1978. Lake tapping in the Colville River Delta, Alaska. *Proceedings of the Third International Conference on Permafrost, Edmonton, Alberta*: 232–238.
- Woo, M.K. & Guan, X.J. 2006. Hydrological connectivity and seasonal storage change of tundra ponds in a polar oasis environment, Canadian High Arctic. *Permafrost and Periglacial Processes* 17:309–323.
- Woo, M.K. & Mielko, C. 2007. An integrated framework for lake-stream connectivity for a semi-arid, subarctic environment. *Hydrological Processes* 21, 2668–2674.
- Woo, M.K. & Sauriol, J. 1980. Channel development in snow-filled valleys, Resolute, N.W.T., Canada. *Geografiska Annaler* 62A:37–56.
- Woo, M.K. & Steer, P. 1983. Slope hydrology as influenced by thawing of the active layer, Resolute, N.W.T. *Canadian Journal of Earth Sciences* 20: 978–986.
- Wright, N., Hayashi, M., & Quinton, W.L. 2009. Spatial and temporal variations in active layer thawing and their implication on runoff generation in peat-covered permafrost terrain. *Water Resources Research* 45: W05414, doi:10.1029/2008WR006880.

Atmospheric Methane in the High Northern Hemisphere and its Relationship with Permafrost

Xiaozhen Xiong

I.M.Systems Group, Rockville, MD 20852, USA

National Environmental Satellite, Data, and Information Service, NOAA, USA

Tingjun Zhang

Ministry of Education (MOE) Key Laboratory of West China's Environmental System, Lanzhou University, China

National Snow and Ice Data Center, University of Colorado, Boulder, CO, USA

Eric Maddy

Riverside Technology Inc., Colorado, USA

National Environmental Satellite, Data, and Information Service, NOAA, USA

Qianlai Zhuang

Department of Earth and Atmospheric Sciences and Department of Agronomy, Purdue University, Indiana, USA.

Chris Barnet

National Environmental Satellite, Data, and Information Service, NOAA, USA

Abstract

Thawing permafrost as a major source of climate feedback could accelerate climate change by releasing a large amount of methane (CH_4) into the atmosphere. However, due to a lack of measurements, there is much uncertainty about quantification of CH_4 emissions from thawing permafrost. Recent satellite observations using the Atmospheric Infrared Sounder (AIRS) on EOS/AQUA provide valuable data on CH_4 in the mid to upper troposphere. In polar regions, multiple observations are available from the overlap of satellite tracks every day, and some improvements have been made in the retrievals in AIRS version 6. Analysis of the seasonal variation and recent increase of CH_4 over Alaska-Canada and Siberia permafrost regions demonstrated that a significant increase of CH_4 during summer can be linked with the increase of surface emissions, and the higher CH_4 concentration in Siberia suggested a larger emission than Alaska-Canada. Similar to surface observation, an abnormal increase of mid- to upper-tropospheric CH_4 in 2008–2009 was observed successfully, but its association with the change of surface temperature is weak. Long-term observations based on current and future thermal infrared sounders are required.

Keywords: atmospheric CH_4 ; methane emission; thawing permafrost; satellite observation; AIRS.

Introduction

The terrestrial and continental shelf regions of the Arctic contain an immense amount of carbon in shallow reservoirs (Tarnocai et al. 2009), most of which is presently sequestered in permafrost (Zimov et al. 2006). The thawing of subarctic peatland permafrost was found to accelerate over the last 50 years based on observations in the discontinuous permafrost zone of northern Canada (53–58°N) (Payette et al. 2004). Thawing permafrost has the potential to accelerate climate change by releasing a significant quantity of CH_4 into the atmosphere. Sustained release of CH_4 has been found from thawing lakes (Walter 2006) and from the Arctic continental shelf off northeastern Siberia (Laptev and East Siberia seas) (Shakhova et al. 2010). Bloom et al. (2010) estimated that that arctic wetland emissions (>67°N) increased by $30.6 \pm 0.9\%$ over 2003–2007 to approximately 4.2 ± 1.0 Tg of CH_4 /year.

In a study of atmospheric CH_4 growth rate between 1984 and 2003 using an inversion model of atmospheric transport and chemistry, Bousquet et al. (2006) indicated that wetland emissions dominated the inter-annual variability of CH_4

sources. Emission of CH_4 from wetlands is highly sensitive to variations in temperature and water table height (Walter et al. 2001). The most recent abnormal increase of atmospheric CH_4 was found from 2007 to 2008 (Rigby et al. 2008), and this increase is likely driven by more precipitation in the tropics and anomalously high temperatures in the Arctic in 2007 (Dlugokencky et al. 2008).

Great uncertainty exists in the quantification of methane emissions from high northern latitude regions (Zhuang et al. 2009), and the major reason is due to the sparse sampling of ground-based measurements. Recently, space-borne remote sensing has been able to measure atmospheric CH_4 with large spatial and temporal coverage. These measurements use either the near-infrared (NIR) spectrum (Frankenberg et al. 2008) or the thermal infrared (TIR) spectrum (Xiong et al. 2010a). However, the NIR measurements rely on the absorption spectra of solar radiation, so its sensitivity decreases for large solar zenith angles and do not work during the cold-dark winter and over snow/ice surfaces in which the reflectivity at $1.6 \mu\text{m}$ is very small. TIR measurements by AIRS have larger spatial and temporal coverage in all seasons, but sensitivity decreases with colder surface temperature and lower vertical

temperature contrasts (i.e., lower temperature lapse rates). Compared to NIR measurement, the sensitivity of TIR is small near the surface.

This paper uses CH_4 measurements from AIRS, a nadir cross-track scanning infrared spectrometer on EOS/AQUA. Data from 2003 and 2011 were analyzed focusing on two regions, Alaska-Canada and Siberia, which are mostly underlain by wetlands and permafrost.

Data and Method

AIRS was launched in the polar orbit (1:30p.m, ascending node) on EOS/Aqua in May 2002 and has been very stable since its launch (Aumann and Pagano 2008). It has 2378 channels covering $649\text{-}2674\text{ cm}^{-1}$ at high spectral resolution. The spatial resolution of AIRS is 13.5 km at nadir, and in a 24-hour period AIRS nominally observes the complete globe once per day and once per night. Over polar regions there are multiple overlaps of coverage each day. In order to retrieve CH_4 in both clear and partial cloudy scenes, 9 AIRS pixels in the footprint of an Advanced Microwave Sounding Unit (AMSU) are used to derive the cloud cleared radiance in this field of regard (FOR), from which the retrieval is made with the spatial resolution of about 45 km. CH_4 and other trace gases are retrieved under clear and partially cloudy conditions. The atmospheric temperature profile, water profile, surface temperature, and surface emissivity are derived from other AIRS channels before the retrieval of CH_4 . More detail about AIRS CH_4 retrievals (version 5) and its validation can be found in Xiong et al. (2008).

A study based on AIRS V5 CH_4 products shows the CH_4 plume over south Asia during the monsoon season. The study is in good agreement with model simulations (Xiong et al. 2009). Similar results have been obtained from aircraft measurements (Schuck et al. 2010) and satellite observations by IASI (Crevoisier et al. 2009), suggesting that AIRS observations provide valuable information about CH_4 . Another study in the high northern latitude regions, using data from AIRS V5 in conjunction with aircraft measurements and model simulations, illustrated the summer increase of mid- to upper-tropospheric CH_4 . This is nearly opposite of the summer minimum of CH_4 , which occurred in the marine boundary layer in most regions over the globe (Xiong et al. 2010b).

Recent improvements in AIRS retrievals (NOAA version 6) allow a better sensitivity to atmospheric CH_4 in the lower altitude layer of about 600 hPa compared to version 5. Recent validations to NOAA-V6 have been made using aircraft measurements, and the results show a smaller error with the bias of the retrieved CH_4 profiles less than 1.0% and its rms difference less than 1.2%. Using data from AIRS version 6, a further study of CH_4 over regions underlain by permafrost were made in this paper. AIRS V5 data from 2003 to present are used to analyze the trend and seasonal anomalies. Other data used include the MODIS land surface pressure (v005), which is downloaded from GES DISC (Goddard Earth Sciences Data and Information Services Center, <http://disc.gsfc.nasa.gov>), and in situ measurements of the CH_4 mixing

ratio in the marine boundary layer (MBL) in Barrow, Alaska, which are obtained from <ftp://ftp.cmdl.noaa.gov/ccg/ch4/in-situ/brw> (GLOBALVIEW-CH4, 2009).

Results and Discussion

Spatial and vertical distribution of CH_4 and its relationship with permafrost

Most permafrost is located in Alaska-Canada and Eurasia above 50°N (see Figure 1), and some is on the Tibetan Plateau. Compared to the map of AIRS CH_4 at 400 hPa, averaged in July, August, and September 2004 (Figure 2), the AIRS mid- to upper-tropospheric CH_4 mixing ratio over regions underlain by permafrost are higher than their surrounding ocean or lower-latitude regions. This correlation suggests that the release of CH_4 from thawing permafrost in the summer may have a significant impact on the distribution of CH_4 in the atmosphere. However, compared to the map of natural wetland emissions from a land surface model (see Ringeval et al. 2011 and Spahni et al. 2011), the region with high AIRS mid- to upper-tropospheric CH_4 is more likely related with the seasonal wetland emissions since we can discern the emissions from wetland and thawing permafrost. For further analysis of the temporal variation of CH_4 in this paper, two regions marked with the boxes, hereafter referred to as "Alaska-Canada" and "Siberia," were selected.

From the mean profiles in these two regions (marked with boxes in Figure 2), as shown in Figure 3, CH_4 in the mid to upper troposphere (i.e., in layers from 300 to 600 hPa where AIRS has the largest sensitivity) is large in the summer season. Mid- to upper-tropospheric CH_4 , MUT- CH_4 , is small in March and April, and the reason might be the intrusion of air from the upper level. Due to the increase of convection in early

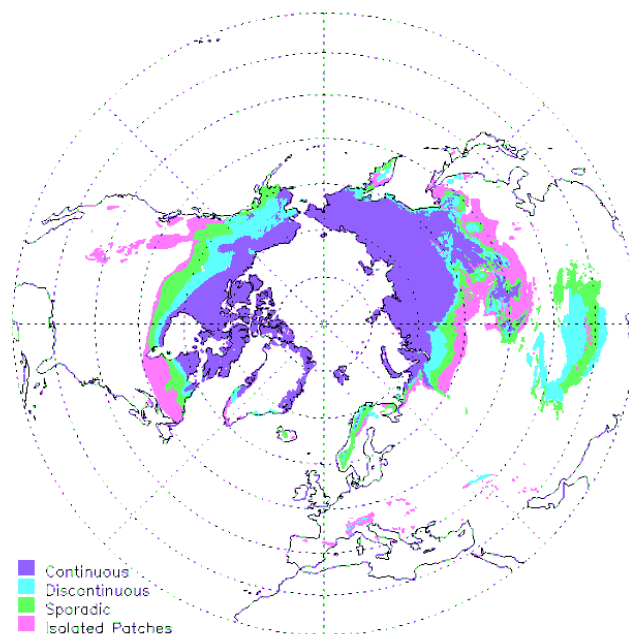


Figure 1. Map of permafrost distribution in the Northern Hemisphere (from Zhang et al. 1999).

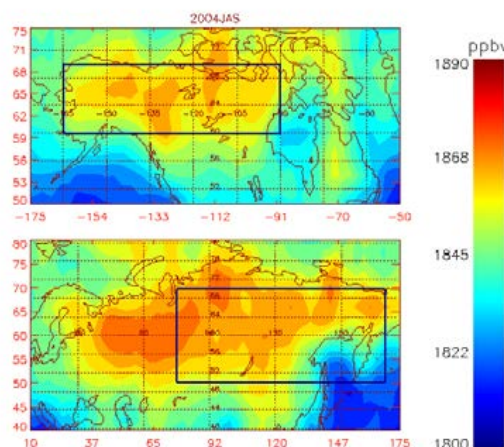


Figure 2. Distribution of AIRS CH_4 at 400 hPa averaged from July to September in 2004. The boxes mark the regions of Alaska-Canada and Siberia for further analysis.

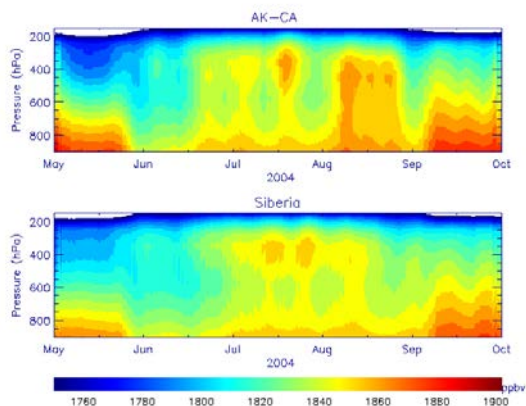


Figure 3. Cross section of CH_4 profiles (using daytime data from ascending node only) for Alaska-Canada and Siberia.

summer, CH_4 in the boundary layer is transported to the mid to upper troposphere, resulting in a nearly uniform vertical distribution of CH_4 in June. The major sink of CH_4 is due to the photochemical reaction with OH. As the emission from wetlands is still limited in June and its loss via photochemical reaction with OH is fairly strong, CH_4 in the MBL (MBL- CH_4) is at its seasonal low. As a result, the increase of MUT- CH_4 is relatively small. Due to the strong wetland emission in July–August, the CH_4 mixing ratio near the surface increases, and thus the CH_4 in the mid to upper troposphere increases in July–August accordingly. After September, with the decrease of vertical convection, the vertical gradient of CH_4 becomes larger, so the MUT- CH_4 begins to decrease. The time of CH_4 increase in Alaska in the summer of 2004 started earlier than in Siberia, which may be associated with the large forest fires in Alaska in June–July 2004. These vertical distributions of CH_4 profiles from version 6 look more reasonable than version 5.

Time series of CH_4 and its seasonal cycle

The seasonal variation of monthly mean CH_4 over Canada-Alaska and Siberia from 2004 to recent (Fig. 4) shows that, overall, CH_4 over Siberia is higher than over Alaska-Canada

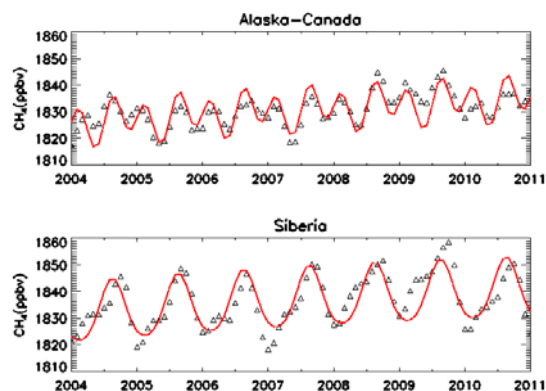


Figure 4. Time series of AIRS CH_4 (from version 5) at 359–460 hPa. Red solid lines are the fitted seasonal cycle.

by ~ 10 ppbv. This suggests a larger surface emission in Siberia as it is covered by a larger area with wetlands/permafrost. A polynomial of six items is used to fit the seasonal cycle as follows:

$$y = C_0 + C_1 t + C_2 t^2 + C_3 \sin(2\pi t) + C_4 \cos(2\pi t) + C_5 \sin(4\pi t) + C_6 \cos(4\pi t)$$

where C_0 , C_1 , C_2 , C_3 , C_4 , C_5 , and C_6 are constants and t is time in days.

From the difference between the fitted seasonal cycle and AIRS retrievals, it is found that the mixing ratios of MUT- CH_4 in late 2008 and the entire year of 2009 are higher than the polynomial fitting. In the fitted season cycles, a trend of recent CH_4 increase has already been included, so the deviation of the fitted seasonal cycle from AIRS observations indicated an abnormal increase of CH_4 in 2008 and 2009, which is about one year later than the abnormal increase in the marine boundary layer in 2007, as reported by Xiong et al. (2010b). More discussion on the recent increase of CH_4 will be given later.

Relationship between CH_4 and surface temperature

To better understand the relationship of CH_4 with surface emission, as well as the recent increase of CH_4 , Figure 5 compares the seasonal cycle and anomaly of AIRS CH_4 with CH_4 in the MBL and the land surface temperature (retrieved from MODIS) from 2006 to 2010. The seasonal cycle was computed after removing the corresponding annual mean in each year, and the anomaly was computed after removing the corresponding monthly mean from 2004 to 2010.

One difference in seasonal cycle between AIRS MUT- CH_4 and MBL- CH_4 (shown in Figure 5a) in Alaska-Canada is that the minima of AIRS MUT- CH_4 usually occurred in May–June, but the minima of MBL- CH_4 in Barrow occurred in June–July. Both are largely controlled by the photochemical reaction with OH, but the minimum in MUT- CH_4 is more closely related to the intrusion of CH_4 from the stratosphere than MBL- CH_4 (Xiong et al. 2010a). With the increase of wetland emission in summer, they both reach the maxima in September. Different from Alaska-Canada is that MUT- CH_4 shows a double seasonal cycle with one peak in late winter and one in late summer (September); in Siberia MUT- CH_4 has

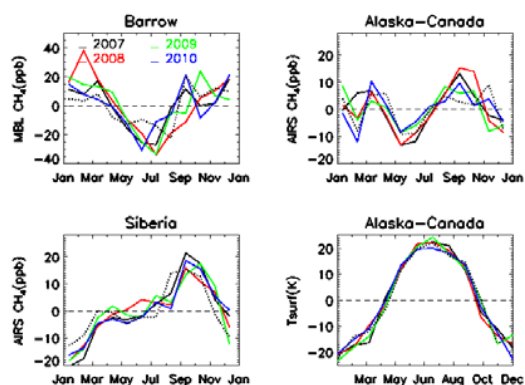


Figure 5a. Seasonal cycle of CH₄ in the marine boundary layer (MBL-CH₄) in Barrow, the mid-upper tropospheric CH₄ in Alaska-Canada and Siberia (from AIRS version 5), and the land surface temperature from MODIS (v005).

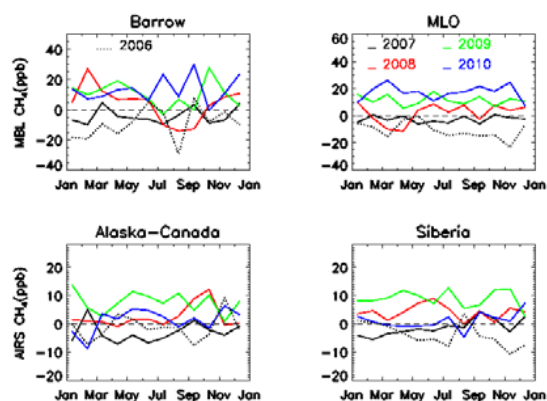


Figure 5b. Anomaly of CH₄ in the marine boundary layer (MBL-CH₄) in Barrow and Mauna Loa, and the anomaly of mid-upper tropospheric CH₄ in Alaska-Canada and Siberia (from AIRS version 5).

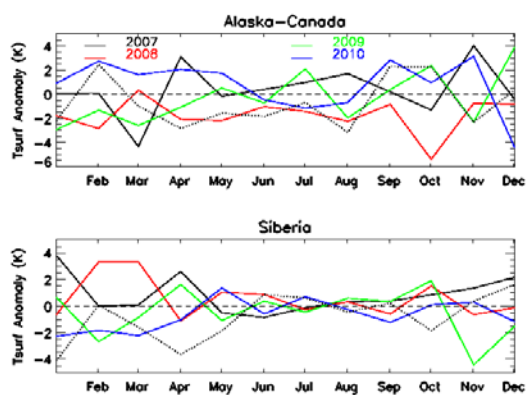


Figure 5c. Anomaly of land surface temperature (Tsurf) from MODIS (v005) during 2006–2010. Dashed line is for 2006.

only one maximum in September–October, and the minimum occurred in the winter season.

Alaska-Canada, West Russia, and Siberia are mostly underlain by wetlands that are frozen and covered by snow in winter and early spring, so the emission of CH₄ from the ground is very low during these periods. After the snow cover starts to melt and the active layer begins to thaw in the late spring, more CH₄ is released from the wetlands into

the atmosphere and this process continues during the entire summer. The maxima of CH₄ emissions from the northern wetlands occur around July (Zhuang et al. 2004). To better understand the recent increase of CH₄ since 2007 and its possible relation with surface emission, Figures 5b and 5c plot the anomaly of CH₄ and surface temperature respectively. For comparison, the anomaly of MBL-CH₄ in the tropics is also included. Compared to the data in 2006, MBL-CH₄ in Barrow significantly increased in 2007 to 2008 (except August and September 2008). However, the increase in 2009 and 2010 is insignificant except in October 2009 and the summer of 2010. The summer low of MBL-CH₄ in 2008 is linked with the cool summer in 2008 (upper panel of Figure 5c), and the increase in the summer of 2010 might be related with the warm winter and spring that year, which resulted in the earlier melting of snow/ice and the growth of plants.

Compared to CH₄ in the MBL, in most months of 2007 AIRS MUT-CH₄ in Alaska-Canada decreased, and significant increases occurred in 2008 and 2009 (Fig. 5b). AIRS MUT-CH₄ started to decrease in 2010. Over Siberia, AIRS MUT-CH₄ started to increase in late 2007, and this increase can be linked with a warm fall-winter in 2007 (lower panel of Figure 5c). The increase in 2008–2009 and decrease in 2010 is similar to that in Alaska-Canada. The anomaly of summer land skin temperature in Siberia is relatively small during these years, so the difference of wetland emissions that resulted from the land surface temperature is hard to discern.

Overall, it is difficult to link the annual change of MUT-CH₄ with the change of surface temperature (or wetland emission). The reason may be due to the following:

- 1) There is uncertainty in the AIRS retrievals in version 5, although this uncertainty is expected to be reduced in version 6, which will be available in about six months. Also, we must recognize that in summer, the most sensitive layer of AIRS measurement is towards higher altitude layers and the information content is larger than other seasons, which makes the interpretation of AIRS CH₄ data more difficult (Xiong et al. 2008).
- 2) In addition to the emission from wetlands, there are other different types of sources in high latitude, which are determined by methane release from destabilizing methane deposits. Rates of methane release from such sources could be determined by factors other than surface temperature. These factors could include, for example, seismic events, tectonic activity, and sediment subsidence. For example, the CH₄ emission could derive from lakes since CH₄ production beneath thaw lakes continues for the entire winter when the lake water does not freeze to the bottom. The methane produced can accumulate at the base of lake ice, and when lake ice is melted, this CH₄ is released to the atmosphere and produces a minor peak in June (Walter et al. 2006). Another source is the contribution of methane emission from the Arctic shelf, which increases in fall (September–October) due to deep fall convection. As a result of water mixing during fall convection, dissolved methane accumulates within the entire water column of the very extensive and shallow

Arctic shelf and is released to the atmosphere during only a few weeks.

- 3) The impact of transport and the sink photochemical reaction with OH must be taken into account. From Figure 5b, it is evident that the tropical MBL-CH₄ in MLO increases almost consistently from 2007 to 2010. This consistent increase in the tropics could impact the global CH₄ distribution, and thus its impact on MUT-CH₄ in the high northern latitude regions cannot be ignored.

Due to the large spatial variation of temperature and emissions from wetlands, to simply link the MUT-CH₄ with wetland emission would be misleading as the emission from other sources, OH photochemistry and transport, have to be taken into account. More work needs to be done to synthesize the model simulated emissions as well as the chemical-transport model results with satellite observations to better understand the impact of CH₄ emission from thawing permafrost.

Conclusion

Improvements to the AIRS retrieval of CH₄ in version V6 make it more promising for studying the spatial and temporal variation of CH₄ in the high northern hemisphere. This paper compared the spatial and temporal variation of CH₄ in Alaska-Canada and Siberia, and the relationship with surface skin temperature. The results suggested that the summer increase of CH₄ can be linked with surface emissions from northern wetlands, which are larger in Siberia than in Alaska-Canada. A significant increase of CH₄ in the mid to upper troposphere was observed in 2008–2009 in the high northern latitude regions. However, this annual variation cannot be explained using the change of surface temperature.

Appropriate use of AIRS CH₄ can provide more information to constrain the model simulation to better estimate source emissions from wetlands in the high northern latitude regions. Similar products from the Infrared Atmospheric Sounding Interferometer (IASI) onboard the METOP satellites at 9:30am/pm are available at NOAA/NESDIS since 2008. NOAA plans to use the same algorithm to retrieve CH₄ from CrIS on the NPP/JPSS satellite. Long-term measurement of CH₄ using these thermal infrared sounders may be used to monitor the trend of CH₄ due to the thawing of permafrost and climate warming.

Acknowledgments

This research was supported by funding from NOAA Office of Application & Research. The views, opinions, and findings contained in this paper are those of the authors and should not be construed as an official National Oceanic and Atmospheric Administration or U.S. Government position, policy, or decision.

References

- Aumann, H.H. & Pagano, T.S. 2008. Using AIRS and IASI data to evaluate absolute radiometric accuracy and stability for climate applications. *Atmospheric and Environmental Remote Sensing Data Processing and Utilization IV: Readiness for GEOSS II*. Edited by Goldberg, Mitchell D.; Bloom, Hal J.; Ardanuy, Philip E.; Huang, Allen H. Proceedings of the SPIE 2008, 7085, 708504-708504-5.
- Bloom, A.A., Palmer, P.I., Fraser, A., Reay, D.S., & Frankenberg, C. 2010. Large-Scale Controls of Methanogenesis Inferred from Methane and Gravity Spaceborne Data. *Science* 327: 322-325.
- Crevoisier, C., Nobileau, D., Fiore, A.M., Armante, R., Chédin, A., & Scott, N.A. 2009. Tropospheric methane in the tropics - first year from IASI hyperspectral infrared observations. *Atmospheric Chemistry and Physics* 9 (17): 6337-6350.
- Frankenberg, C., Bergamaschi, P., Butz, A., Houweling, S., Meirink, J.F., Notholt, J., Petersen, A.K., Schrijver, H., Warneke, T., & Aben, I. 2008. Tropical methane emissions: A revised view from SCIAMACHY onboard ENVISAT. *Geophys. Res. Lett.* 35, L15811, doi:10.1029/2008GL034300.
- MontMontzka, S.A., Dlugokencky, E.J., & Butler, J.H. 2010. Non-CO₂ greenhouse gases and climate change. *Nature* 476: 43–50, doi:10.1038/nature10322.
- Payette, S., Delwaide, A., Caccianiga, M., & Beauchemin, M. 2004. Accelerated thawing of subarctic peatland permafrost over the last 50 years. *Geophys. Res. Lett.* 31, L18028, doi: 10.1029/2004GL020358.
- Rigby, M. et al. 2008. Renewed growth of atmospheric methane. *Geophys. Res. Lett.* 35, L22805, doi:10.1029/2008GL036037.
- Ringeval, B., Friedlingstein, P., Koven, C., Ciais, P., de Noblet-Ducoudré, N., Decharme, B., & Cadule, P. 2011. Climate-CH₄ feedback from wetlands and its interaction with the climate-CO₂ feedback. *Biogeosciences* 8: 2137-2157, doi:10.5194/bg-8-2137-2011.
- Schuck, T.J., Brenninkmeijer, C.A.M., Baker, A.K., Slemr, F., von Velthoven, P.F.J., & Zahn, A. 2010. Greenhouse gas relationships in the Indian summer monsoon plume measured by the CARIBIC passenger aircraft. *Atmos. Chem. Phys.* 2010, 10:3965-3984.
- Shakhova, N., Semiletov, I., Salyuk, A., Yusupov, V., Kosmach, D., & Gustafsson, O. 2010. Extensive methane venting to the atmosphere from sediments of the East Siberia Arctic shelf. *Science* 327: 1246-1250.
- Spahni, R., Wania, R., Neef, L., van Weele, M., Pison, I., Bousquet, P., Frankenberg, C., Foster, P.N., Joos, F., Prentice, I.C., & van Velthoven, P. 2011. Constraining global methane emissions and uptake by ecosystems. *Biogeosciences* 8: 1643-1665, doi:10.5194/bg-8-1643-2011.

- Tarnocai, C., Canadell, J.G., Schuur, E.A.G., Kuhry, P., Mazhitova, G., & Zimov, S. 2009. Soil organic carbon pools in the northern circumpolar permafrost region. *Global Biogeochem. Cycles* 23, GB2023, doi:10.1029/2008GB003327.
- Walter B.P., Heimann, M., & Matthews, E. 2001. Modeling modern methane emissions from natural wetlands. 1. Model description and results. *J. Geophys. Res.* 106, 34,189-34,206.
- Walter, K.M. et al. 2006. Methane bubbling from Siberian thaw lakes as a positive feedback to climate warming. *Nature* 443, doi:10.1038/nature05040.
- Xiong, X., Barnet, C., Maddy, E., Sweeney, C., Liu, X., Zhou, L., Goldberg, M. 2008. Characterization and validation of methane products from the Atmospheric Infrared Sounder (AIRS). *J. Geophys Res.*, 113, G00A01, doi:10.1029/2007JG000500.
- Xiong, X., Houweling, S., Wei, J., Maddy, E., Sun, F., & Barnet, C.D. 2009. Methane Plume over South Asia during the Monsoon Season: Satellite Observation and Model Simulation. *Atmos. Chem. Phys.* 9, 783-794.
- Xiong, X., Barnet, C.D., Maddy, E., Wei, J., Liu, X., & Pagano, T.S. 2010a. Seven Years' Observation of Mid-Upper Tropospheric Methane from Atmospheric Infrared Sounder. *Remote Sensing* 2, 2509-2530, doi:10.3390/rs2112509.
- Xiong, X., Barnet, C.; Zhuang, Q., Machida, T., Sweeney, C., & Patra, P.K. 2010b. Mid-upper Tropospheric Methane in the High Northern Hemisphere: Space-borne Observations by AIRS, Aircraft Measurements and Model Simulations. *J. Geophys. Res.* 115, D19309, doi:10.1029/2009JD013796.
- Zhang, T., Roger, G., Barry, K., Knowles, J., Heginbottom, A., & Brown, J. 1999. Statistics and characteristics of permafrost and ground ice distribution in the Northern Hemisphere. *Polar Geography* 23(2), 147-169.
- Zhuang, Q., Melillo, J.M., Kicklighter, D.W., Prinn, R.G., McGuire, D.A., Steudler, P.A., Felzer, B.S., & Hu, S. 2004. Methane fluxes between terrestrial ecosystems and the atmosphere at northern high latitudes during the past century: A retrospective analysis with a process-based biogeochemistry model. *Global Biogeochemical Cycles* 18, GB3010, doi:10.1029/2004GB002239.
- Zimov, S.A., Schuur, E.A.G., & Chapin, F.S. III. 2006. Permafrost and the global carbon budget. *Science* 312, 1612-1613, DOI: 10.1126/science.1128908.

Stress Path Tests on Artificially Frozen Soil Samples

Yuko Yamamoto, Sarah M. Springman

Institute for Geotechnical Engineering, Swiss Federal Institute of Technology, Zurich, Switzerland

Abstract

Four different stress path tests—Axial Extension (AE), Lateral Extension (LE), Lateral Compression (LC), and Axial Compression (AC)—were conducted on artificially frozen soil samples to investigate the mobilized strength of alpine permafrost under different stress paths representing the stress conditions in rock glaciers. Tests were conducted at temperatures between $T = -2.0^{\circ}\text{C}$ and -0.3°C , which simulate warm alpine permafrost. It was determined that an increase of temperature close to 0°C results in a decrease of mobilized shear strength in all four stress path tests. Moreover, AE stress paths show the weakest response. Acoustic emission responses from the frozen soil specimens during the tests indicate that the deformation behavior may be different, depending on the stress paths followed.

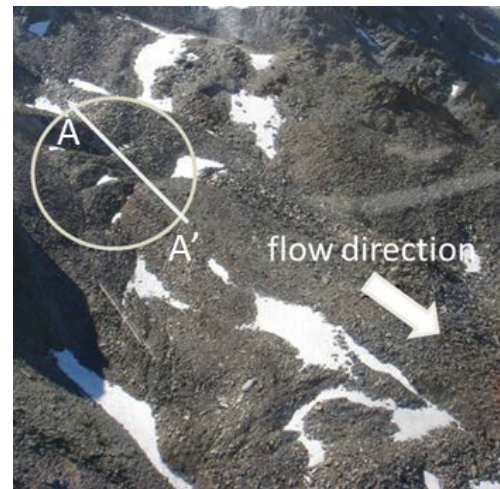
Keywords: compression; extension; frozen soil; permafrost; strength; stress path tests.

Introduction

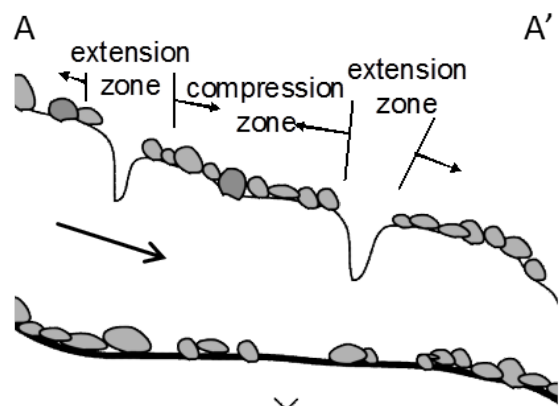
Rising mean annual air temperature and extreme rainfall conditions cause permafrost degradation. Alpine permafrost, which exists at high altitudes at lower latitudes than at the poles and contains ice alone or an ice-water-air-soil mixture, is particularly susceptible to such a climate change. Frauenfelder et al. (2003) report that the rock glacier surface speed seems to increase exponentially with the mean annual air temperature increase, although this can only be valid within limits. Long-term ground temperature monitoring in rock glaciers in the Swiss Alps shows that rock glaciers often contain warm permafrost, i.e., at temperatures close to the thawing point (e.g., Arenson et al. 2010, PERMOS 2010). Warming permafrost causes an accelerated creep motion of the rock glacier due to an increase of unfrozen water content (Williams 1967a, b, Morgenstern et al. 1980). As water fills the interstitial pores, pore water pressure rises and effective stress in the soil matrix decreases, which would reduce the available shear strength and could lead to the initiation of landslide and debris flows impacting the highly populated mountain areas (Springman et al. 2011). Considering a warming thermal regime faced by alpine permafrost, the geotechnical response of warm alpine permafrost needs to be investigated in order to gain better understanding of rock glacier dynamics and stability of permafrost slopes.

Roer et al. (2008) show compression and extension zones, and an existence of crevasses extending downwards in several rock glaciers (Figs. 1a, b). These formations indicate that the instabilities may be triggered within a rock glacier, initiating from these depression zones. Moreover, stress paths experienced by soil elements in the body of the rock glaciers are different from those in the conventional axial compression, which have been mostly studied for frozen soil. Although numerous research projects have been conducted and valuable findings of mechanical properties of frozen soils obtained (e.g., Ting et al. 1983, Jones & Parameswaran 1983, Yuanlin & Carbee 1987, Andersland & Ladanyi 2004, Arenson & Springman 2005), the mobilized strength of alpine permafrost under different stress paths representing the stress conditions in rock glaciers has not been studied as yet.

This paper describes several stress path tests in compression and extension on artificially frozen soil samples conducted at temperatures close to the thawing point. Temperature dependency of the strength was examined between -2 and -0.3°C .



(a)



(b)

Figure 1. (a) Crevasse feature at the Furggwanghorn rock glacier, Canton Valais, CH (photo: Sarah Springman); (b) schematic cross section A-A' through a rock glacier showing zones of extension and compression.

Material and Method

Sample preparation

Cylindrical frozen soil samples, with a diameter of 50 mm and a length of 100 mm, were prepared artificially in the laboratory in a similar way to the artificial soil sampling method described in Arenson (2002). Solid soil grains with maximum diameter of 16 mm were taken from a front slope part of the Murtèl-Corvatsch rock glacier (CH) and sieved. The grain size distribution corresponds to a typical Fuller-distribution (Fig. 2). The maximum grain size for the specimen used for the triaxial test was chosen to be 4 mm, since the grain size should

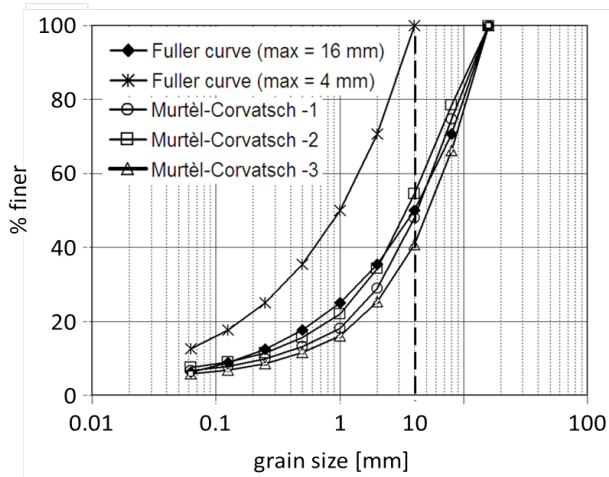


Figure 2. Grain size distribution of the soil taken from Murtèl-Corvatsch rock glacier and Fuller-curves for the maximum grain size of 4 mm and 16 mm.

not be larger than 1/5, preferably less than 1/10 (Sayles et al. 1987) of a diameter of the specimen for triaxial tests. A pre-weighed soil fraction was mixed with crushed ice, according to the planned relative ice-solids volume fractions. The ice-solid mixture was placed in an insulated cylindrical mould and saturated slowly with 0°C de-aired water from the bottom to fill the air voids, with the help of a vacuum applied at the top. The sample was then frozen one-dimensionally from the top in a freezer at a temperature of -18°C, while drainage was permitted from the bottom. The samples had a diameter of 50 mm and an initial length of 130 mm. Both ends of the sample were trimmed to a length of 100 mm with a circular diamond saw to form smooth parallel surfaces before being mounted in a triaxial test apparatus. Relatively high volumetric ice contents of the specimens used in this study modeled the cored sample data from boreholes in Murtèl-Corvatsch (Arenson 2002) with more than 40% ice. It was not possible to saturate the sample fully, and the maximum volumetric air contents of 5% were measured after the tests.

Stress path tests

The stress path method has been established in geotechnical engineering in order to understand and solve stability and deformation problems (Lambe & Marr 1979). A stress path represents what is happening to the stresses in the ground and enables an appropriate laboratory test program to be designed (Holtz et al. 2010). Stress path tests are conducted mostly in a triaxial test apparatus in order to determine soil parameters, notwithstanding the limitation that principal stresses must be axial and radial.

Four typical different stress paths can be assumed, depending

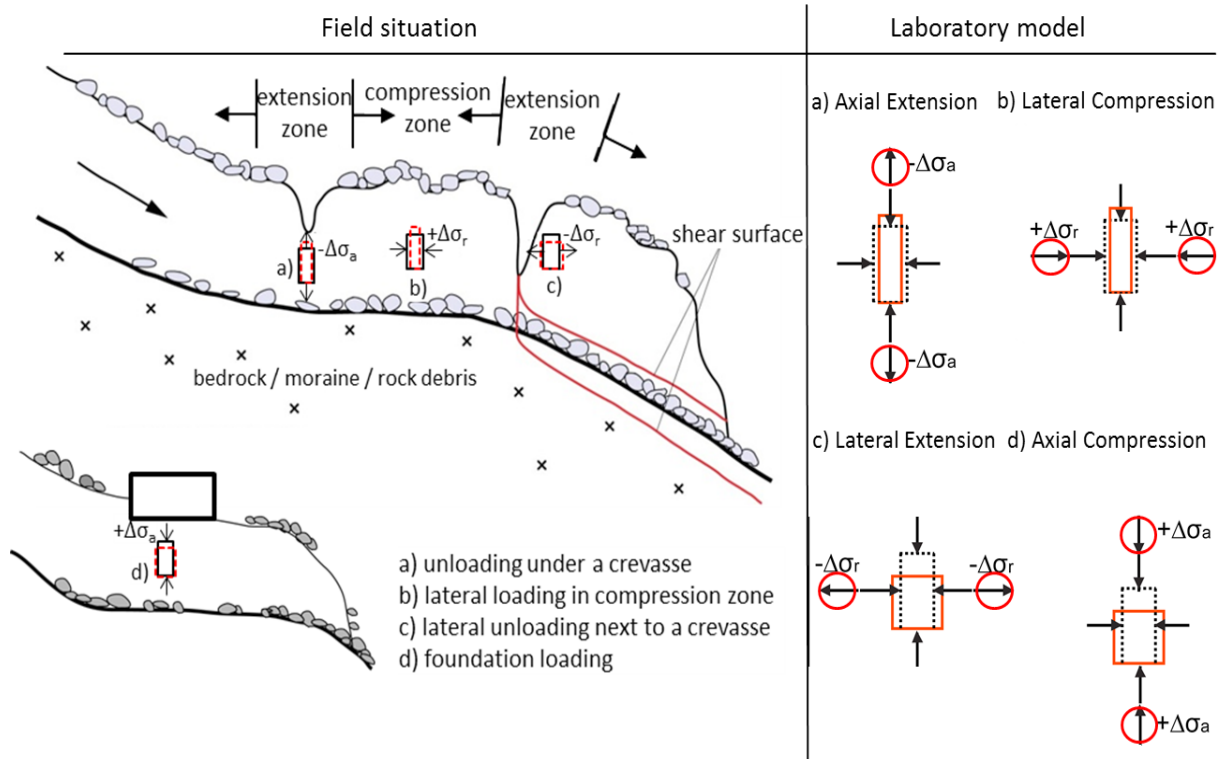


Figure 3. Field stress condition and corresponding laboratory model (after Springman et al. 2011).

on the position of the soil elements in a warming rock glacier with formation of crevasses. Firstly, a soil element under a crevasse will be unloaded axially because the deepening of a crevasse results in a decrease of overburden pressure acting on the soil (Fig. 3a). Secondly, a soil element in the compression zone is loaded laterally because the downslope movement speed of the rock glacier may be slower in a less steep zone (Fig. 3b). Thirdly, a soil element around crevasses may be unloaded laterally because the soil is exposed to an active earth pressure condition (Fig. 3c). Fourthly, a central soil element under a foundation load is axially loaded (Fig. 3d). These four different stress paths can be modeled in stress path tests in a laboratory as Axial Extension (AE), Lateral Compression (LC), Lateral Extension (LE), and Axial Compression (AC), respectively (Fig. 3). Although the AC tests are the most common type of triaxial tests used in engineering practice, it can be said that the stress paths other than AC model some situations in warming rock glaciers.

Test overview

Four different stress path tests (AE, LC, LE, AC) were conducted on cylindrical specimens of 50 mm in diameter and about 100 mm in height. The triaxial test apparatuses were placed in a cold chamber. A new fine temperature control system was developed for the existing IGT triaxial apparatuses, which ensures that the temperatures measured in the top and bottom load platens during the tests can be held constant within $\pm 0.05^\circ\text{C}$.

In addition, acoustic emission signals were detected by the newly installed piezoelectric wide-band sensor type WD, with a frequency spectrum of 100–1000 kHz, in order to gain the knowledge of the microstructural effects on the mobilization of shear strength. The surface of the sensor was attached directly to the bottom of the frozen soil specimen. The signals detected by a piezoelectric sensor were pre-amplified by 60 dB. After pre-amplification, the signal was processed through an oscilloscope to see the wave forms and a burst trigger circuit to count the burst events. One event was recognized when the amplitude of the acoustic emission signal exceeds a trigger level of 400 mV (Fig. 5). A dead time of 1 ms was set to avoid

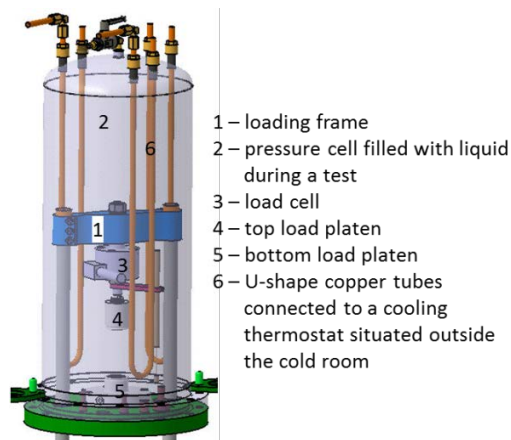


Figure 4. The cell of an IGT triaxial test apparatus (picture: Adrian Zweidler).

counting one event more than once. The cumulative counts were determined by the pulse counter, which analyzes the impulses received from the burst trigger circuit.

Prior to testing, a frozen soil specimen was taken from the storage freezer (-18°C) and placed in the cold room. Triaxial testing requires three phases. Firstly, the specimen was placed between the top and bottom load platens. Secondly, the cell pressure, which is equal to the confining pressure of the test, was applied to the cell liquid to apply an isotropic stress condition in the specimen under undrained conditions. This second phase lasted at least for 24 hours in order to stabilize the cell liquid temperature to the desired test temperature and ensure the temperature in the specimen is uniform throughout the volume. Thirdly, triaxial specimens were exposed to loading conditions that vary the axial and radial total stresses. Confining stress σ_r was held constant ($\Delta\sigma_r=0$) in AE and AC tests, and axial stress σ_a was decreased ($\Delta\sigma_a<0$) in AE tests and increased ($\Delta\sigma_a>0$) in AC tests. A Constant Rate of Strain (CRS) test was conducted for AE and AC tests. Axial stress was held constant ($\Delta\sigma_a=0$) in LE and LC tests, and confining stress was decreased in LE tests ($\Delta\sigma_r<0$) and increased in LC tests ($\Delta\sigma_r>0$). Constant Stress Rate (CSR) tests were conducted for LC and LE tests. The specimens were thawed after each test in order to back calculate the volumetric composition of ice, solid particles, and air. The stress paths achieved can be described using the stress invariants as follows:

$$p = \frac{\sigma_a + 2\sigma_r}{3} \quad (1)$$

$$q = \sigma_a - \sigma_r \quad (2)$$

where p = mean total stress and q = deviatoric stress. Stress gradient of the total stress paths is expressed as equation 3, and should be 3 for AC and AE tests and $-3/2$ for LE and LC tests.

$$\frac{\Delta q}{\Delta p} = \frac{3 * (\Delta\sigma_a - \Delta\sigma_r)}{(\Delta\sigma_a + 2\Delta\sigma_r)} \quad (3)$$

Test Results and Discussion

Tables 1 and 2 summarize test conditions and some key results. The volume change of the specimen during the tests was observed, even though the tests were conducted under nominal undrained conditions. Slower strain rates were used in AE tests in order to ensure a contact between load platens and specimen surfaces during the tests. Initial confining

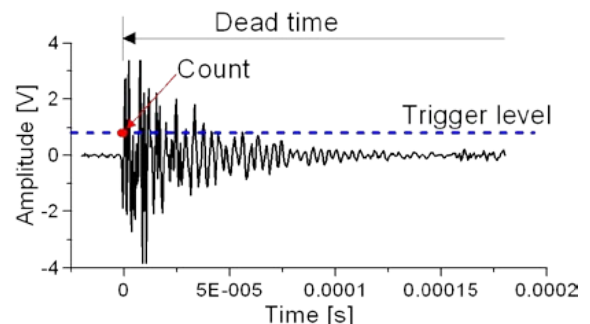


Figure 5. Typical acoustic emission signal.

Table 1. Overview of physical properties of specimens and test conditions of AE and AC Constant Rate of Strain (CRS) tests.

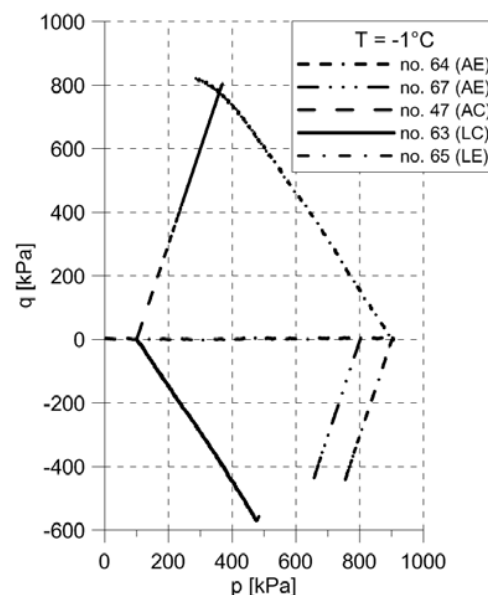
| test | | volumetric composition | | | density | strain rate | σ_r | T | q_{peak} | q_{res} | $M = q_{res}/p$ |
|------|------|------------------------|-------|------|-------------------|-------------|------------|--------------|------------|-----------|-----------------|
| no. | type | ice | solid | air | | axial | | | | | |
| | | % | % | % | Mg/m ³ | /h | kPa | °C | kPa | kPa | - |
| 25 | AE | 92.14 | 3.77 | 4.10 | 0.92 | 0.0001 | 990 | -1.88 ± 0.02 | -422 | -422 | -0.50 |
| 35 | AE | 79.78 | 16.33 | 3.89 | 1.18 | 0.0001 | 990 | -1.94 ± 0.02 | -550 | -550 | -0.68 |
| 64 | AE | 82.80 | 14.51 | 2.69 | 1.15 | 0.00018 | 900 | -1.01 ± 0.03 | -443 | -443 | -0.58 |
| 67 | AE | 81.07 | 15.71 | 3.22 | 1.17 | 0.00018 | 800 | -1.03 ± 0.03 | -435 | -435 | -0.66 |
| 68 | AE | 78.73 | 16.87 | 4.39 | 1.18 | 0.00018 | 800 | -0.56 ± 0.06 | -345 | -345 | -0.50 |
| 29 | AC | 80.97 | 14.59 | 4.43 | 1.14 | 0.0036 | 100 | -0.48 ± 0.03 | 620 | 501 | 1.88 |
| 30 | AC | 78.06 | 17.61 | 4.33 | 1.20 | 0.0036 | 100 | -0.78 ± 0.02 | 592 | 561 | 1.95 |
| 31 | AC | 53.36 | 43.77 | 2.86 | 1.68 | 0.0036 | 100 | -0.47 ± 0.03 | 453 | 453 | 1.80 |
| 47 | AC | 42.71 | 52.75 | 4.54 | 1.83 | 0.0036 | 100 | -1.02 ± 0.03 | 803 | 780 | 2.17 |
| 49 | AC | 78.30 | 17.12 | 4.57 | 1.18 | 0.0036 | 100 | -0.32 ± 0.02 | 524 | 476 | 1.84 |

Table 2. Overview of physical properties of specimens and test conditions of AE and AC Constant Stress Rate (CSR) tests.

| test | | Volume composition | | | density | $\Delta\sigma_r$ | $\sigma_{r, initial}$ | $\sigma_{r, failure}$ | T | q | $M = q/p$ |
|------|------|--------------------|-------|------|-------------------|------------------|-----------------------|-----------------------|--------------|------|-----------|
| no. | type | ice | solid | air | | | | | | | |
| | | % | % | % | Mg/m ³ | kPa/s | kPa | - | °C | kPa | - |
| 23 | LC | 73.42 | 22.63 | 3.95 | 1.29 | 0.01 | 100 | 988 | -2.10 ± 0.05 | -888 | -1.28 |
| 34 | LC | 81.11 | 16.09 | 2.81 | 1.18 | 0.01 | 100 | 672 | -1.92 ± 0.02 | -559 | -1.15 |
| 63 | LC | 78.47 | 17.20 | 4.33 | 1.18 | 0.005 | 100 | 667 | -1.00 ± 0.01 | -571 | -1.20 |
| 66 | LC | 20.77 | 73.31 | 5.91 | 2.18 | 0.005 | 100 | 770 | -1.01 ± 0.03 | -685 | -1.27 |
| 65 | LE | 77.36 | 16.57 | 6.06 | 1.16 | 0.005 | 900 | 9 | -1.04 ± 0.04 | 826 | 2.91 |
| 69 | LE | 79.55 | 15.59 | 4.86 | 1.15 | 0.005 | 900 | 91 | -0.57 ± 0.03 | 739 | 2.19 |
| 70 | LE | 39.91 | 55.41 | 4.68 | 1.87 | 0.005 | 900 | 337 | -0.41 ± 0.03 | 505 | 1.00 |
| 71 | LE | 77.76 | 17.36 | 4.89 | 1.19 | 0.005 | 900 | 183 | -0.40 ± 0.03 | 656 | 1.63 |

stress $\sigma_r = 800\text{--}990$ kPa was chosen to suit maximum load capacity of the apparatus in AE and LE tests. In contrast, an initial confining stress $\sigma_r = 100$ kPa was chosen for AC and LC tests, which corresponds to stress conditions at a depth of 5 to 10 m in the rock glacier. The peak deviatoric stress q_{peak} and residual deviatoric stress q_{res} were distinguished in the AC tests, even though the difference between the q_{peak} and q_{res} is small, i.e., ductile behavior due to the relatively slow strain rate. The failure state was defined by strains over 20% in AC tests, and over 10% in LE tests. The AE and LC tests were finished when the strains reached more than 1.5% after the peak strength was observed. No clear shear band (clear discontinuity) was observed externally in the specimen after the test. The specimen generally exhibited a barrel shape after the AC and LE tests, indicating a ductile failure mode. Since the tests were stopped at an early stage of strain development in the AE tests, only an extension in the axial direction with uniform radial thinning was observed throughout the height. The shape after the tests could not be seen in any of the LC tests because the rubber membrane broke just before the end of them, which resulted in the specimen thawing due to the penetration of the antifreeze liquid in the cell into the frozen soil specimen.

Yasufuku et al. (2003) mention that the use of the critical state concept may be limited for the frozen soil because the measured strength is not at the critical state, which is normally defined as the strength at constant volume of the specimens. Volume change occurs in the specimen during a test due to an initiation of micro-cracks (Yasufuku et al. 2003) and compressibility of the volumetric air content (Arenson

Figure 6. Total stress paths of selected tests in deviatoric (q) versus mean (p) stress.

et al. 2003). In addition, only the total stress is known and considered in this study instead of effective stress. However, a critical state ratio $M = q_{res}/p$ was calculated for every test in order to capture the failure state in the p - q diagram. The critical state ratio in AE, AC, and LC tests seems to be more or less constant. In contrast, the LE tests show a large range of values, which may also reflect the difficulty in using the critical state concept for frozen soils.

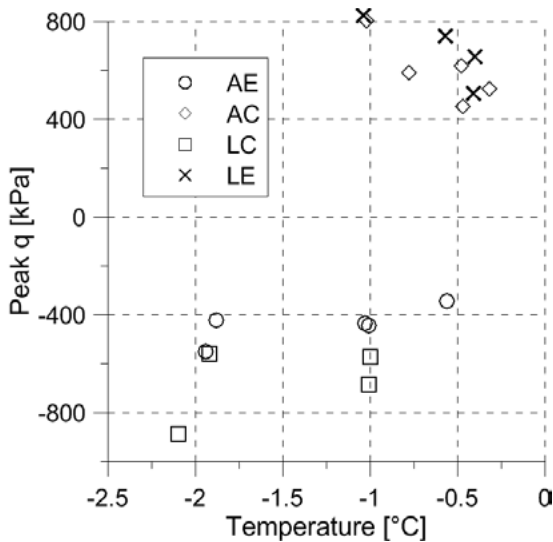


Figure 7. Peak deviatoric stress q versus temperature with different stress paths.

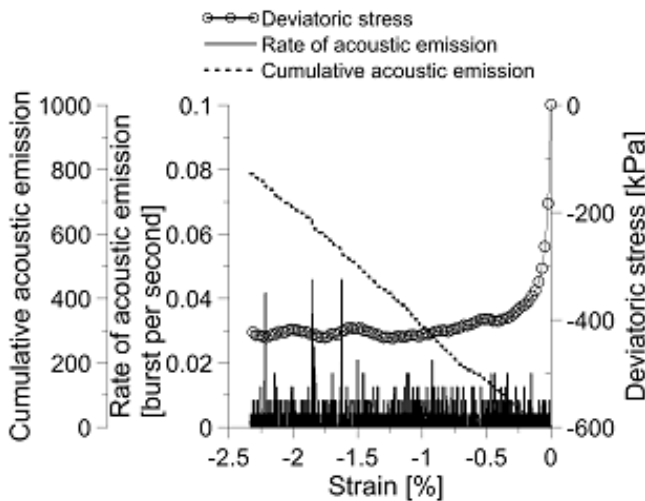


Figure 8. Cumulative acoustic emission, rate of acoustic emission, and deviatoric stress vs. strain of AE test no. 67.

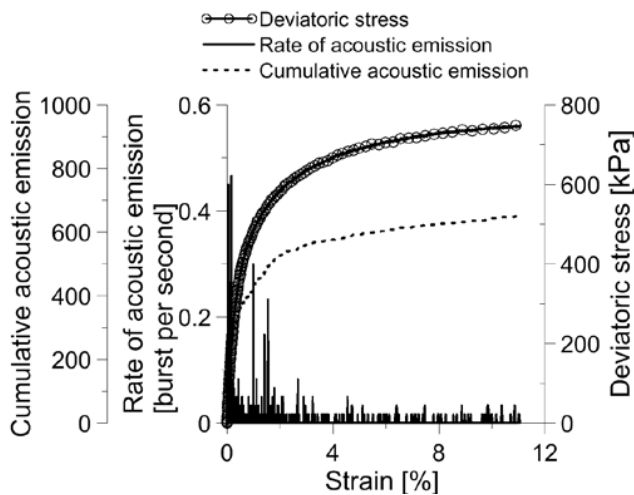


Figure 9. Cumulative acoustic emission, rate of acoustic emission, and deviatoric stress vs. strain of LE test no. 69.

Figure 6 shows total stress paths obtained by the tests conducted at temperatures of about -1°C . Four stress paths closely followed those stress paths predetermined by the loading system in Figure 3. Stress paths following $q < 0$ mobilize less deviatoric stress of failure than those with $q > 0$, which indicates that the axial unloading zone under crevasses and the lateral loading area in the body of the rock glacier (see Figure 3) may have more potential for reaching failure states. Figure 7 shows the effect of temperature on mobilized peak strength. An increase of the temperature close to 0°C results in a decrease of mobilized shear strength for both $q < 0$ and $q > 0$. This behavior can be explained by the greater deformability of the ice particles with temperature increase (e.g., Rist & Murrell 1994) and an increase of the unfrozen water film thickness between ice particles and solid grains, which results in a reduction of suction (Williams 1967a, b). The AE tests seem to indicate the weakest response of all.

Figure 8 shows the acoustic emission measurements obtained during AE test no. 67, together with the stress-strain curve. Cumulative acoustic emission increases almost linearly until the end of the test, which can also be distinguished by the almost constant value of acoustic emission rate throughout. Micro-crack propagation seems to progress gradually in the frozen soil specimen during the AE test. In contrast, test no. 69 (LE test) indicated a different acoustic response. Figure 9 shows the acoustic emission measurements obtained during LE test no. 69. Cumulative acoustic emission increases gradually until the end of the test, following the gradient of the stress-strain curve. There is another peak of the acoustic emission rate after the initial episode, probably due to compliance at the end of the specimens, at around axial strain = 1%. This may correspond to the yield point in the stress-strain relationship. After the second peak, the acoustic emission rate decreases close to zero and shows fluctuations until the end of the test. This indicates that the initiation and propagation of the micro-crack formation is limited at this stage, and more ductile behavior is the dominant physical component of the deformation. Comparison of the acoustic emission response of these stress path tests implies that different deformation processes may be taking place, depending on the stress paths.

Practical Significance of the Test Results

Stress paths to failure must reflect those followed in the field. Three new stress paths were assumed to act on a soil element in different zones of a rock glacier. Comparison of the deformation processes for four stress paths indicates that the development of deep crevasses has more potential to promote slope failure. This is relevant not only for mountain permafrost but also for boundary value problems in permafrost engineering. Many stress paths followed, including stability problems of rock glacier slopes. In reality, they do not coincide with conventional axial compression, which leads to mobilization of the greatest deviatoric stress at failure. Acoustic signals were measured and are expected to play a greater role in monitoring and predicting impending failure in frozen soils.

Conclusions

Stress path tests in Axial Extension (AE), Lateral Extension (LE), Lateral Compression (LC), and Axial Compression (AC) were carried out on artificially frozen soil samples at temperatures between $T = -2.0$ and -0.3°C . Several important findings were recognized:

- The stress paths following $q < 0$ appear to mobilize less strength than those with $q > 0$.
- Results in axial extension are relevant for the zone under the crevasse and indicate the weakest response among the four stress paths.
- Mobilized shear strength in four stress path tests is dependent on the temperature, i.e., an increase of temperature results in a decrease of shear strength.
- Comparison of the acoustic emission behavior of the different stress path tests indicates that the different deformation processes may be taking place, depending on the stress paths.

Further investigations of volumetric behavior of a specimen during stress path tests are necessary.

Acknowledgments

Financial support received from the Swiss National Science Foundation through grant number 200021_125078 is gratefully acknowledged. We thank Ernst Bleiker, Adrian Zweidler, and the workshop and laboratory staff from IGT, ETH Zürich for design, construction, and electrical setup of the triaxial test apparatus upgrades.

References

- Andersland, O.B. & Ladanyi, B. 2004. *An introduction to frozen ground engineering*. Hoboken, New Jersey, John Wiley & Sons, Inc., 363 pp.
- Arenson, L.U. 2002. *Unstable alpine permafrost: a potentially important natural hazard - variations of geotechnical behaviour with time and temperature*. IGT, ETH Zurich. 271 pp.
- Arenson, L.U., Almasi, N., & Springman, S.M. 2003. Shearing response of ice-rich rock glacier material. *Proc. 8th ICOP, Zurich, Switzerland*: 39-44.
- Arenson, L.U. & Springman, S.M. 2005. Triaxial constant stress and constant strain rate tests on ice-rich permafrost samples. *Canadian Geotechnical Journal* 42(2): 412-430.
- Arenson, L.U., Hauck, C., Hilbich, C., Seward, L., Yamamoto, Y., & Springman, S.M. 2010. Sub-surface heterogeneities in the Murtèl-Corvatsch rock glacier, Switzerland. *6th Canadian PC, Calgary*: 1494-1500.
- Frauenfelder, R., Haeberli, W., & Hoelzle, M. 2003. Rockglacier occurrence and related terrain parameters in a study area of the Eastern Swiss Alps. *Proc. 8th ICOP, Zurich, Switzerland*: 253-258.
- Holtz, R.D., Kovacs, W.D., & Sheahan, T.C. 2011. *An Introduction to Geotechnical Engineering, 2nd Ed*, Upp. Saddle River, NJ: Pearson Prentice-Hall, 863 pp.
- Jones, S.J. & Parameswaran, V.R. 1983. Deformation behaviour of frozen sand-ice materials under triaxial compression. *Proc. 4th ICOP, Alaska*: 560-565.
- Lambe, T.W. & Marr, W.A. 1979. Stress path method: second edition. *Journal of the Geotechnical Engineering Division, ASCE*, 105: 727-738.
- Morgenstern, N.R., Roggensack, W.D., & Weaver, J.S. 1980. The behaviour of friction piles in ice and ice-rich soils. *Canadian Geotechnical Journal* 17: 405-415.
- PERMOS. 2010. *Permafrost in Switzerland 2006/2007 and 2007/2008 Series*. Noetzli, J. and Vonder Muehll, D. (eds), Glaciological Report Permafrost No. 8/9 of the Cryospheric Commission of the Swiss Academy of Sciences, 68 pp.
- Rist, M.A. & Murrell, S.A.F. 1994. Ice triaxial deformation and fracture. *Journal of Glaciology* 40(135): 305-318.
- Roer, I., Haeberli, W., Avian, M., Kaufmann, V., Delaloye, R., Lambiel, C., & Kääh, A. 2008. Observations and considerations on destabilizing active rock glaciers in the European Alps. *Proc. 9th ICOP, AK*: 1505-1510.
- Sayles, F.H., Baker, T.H.W., Gallavres, F., Jessberger, H.J., Kinoshita, S., Sadoyskiy, A.V., Sego, D.C., & Vyalov, S.S. 1987. Classification and laboratory testing of artificially frozen ground. *Journal of Cold Regions Engineering* 1(1): 22-48.
- Springman, S.M., Yamamoto, Y., Buchli, T., Hertrich, M., Maurer, H., Merz, K., Gärtner-Roer, I., & Seward, L. 2011. Rock glacier degradation and instabilities in the European Alps: a characterisation and monitoring experiment in Turtmannal. *Proc. 2nd WLF, Rome*.
- Ting, J.M., Martin, R.T., & Ladd, C.C. 1983. Mechanisms of strength for frozen sand. *Journal of the Geotechnical Engineering Division, ASCE* 109(10): 1286-1302.
- Williams, P.J. 1967a. Suction and its effects in unfrozen water of frozen soils. *Pub. Norwegian Geotechnical Institute* 72: 27-35.
- Williams, P.J. 1967b. Unfrozen water in frozen soils. *Pub. Norwegian Geotechnical Institute* 72: 37-48.
- Yasufuku, N., Springman, S.M., Arenson, L.U., & Ramholt, T. 2003. Stress-dilatancy behaviour of frozen sand in direct shear. *Proc. 8th ICOP, Zurich*: 1253-1258.
- Yuanlin, Z. & Carbee, D.L. 1987. Tensile strength of frozen silt. *CRREL Report 87-15. US Army Corps of Engineers*: 29 pp.

The Effect of Freeze-Thaw Action on the Dry Density and Water Content of Soil

Chengsong Yang

State Key Laboratory of Frozen Soils Engineering, Cold and Arid Regions Environmental and Engineering Research Institute, Chinese Academy of Sciences, Lanzhou, Gansu, China

He Ping

Beijing Jiaotong University, Beijing, China

Guodong Cheng

State Key Laboratory of Frozen Soils Engineering, Cold and Arid Regions Environmental and Engineering Research Institute, Chinese Academy of Sciences, Lanzhou, Gansu, China

Abstract

Clayey sand and silty sand are the two most typical soil types along the Qinghai-Tibet Railway (QTR). Under an open system environment, the two types of soils are tested by freeze-thaw cycles. In these experiments, the upper temperature is changed while the confining and bottom temperature is always kept at +1°C. Each of the soil samples was tested with different dry density, water content, and temperature. The results show that the final dry density value is constant after repeated freeze-thaw. The final dry density of clayey sand is 1.55g/cm³, while that for silty sand is 1.78 g/cm³. It can also be concluded that the final dry density of each soil sample depends on the soil granule size distribution but not the original dry density. At the same time, the repeated freeze-thaw cycles can change the water content distribution in the soil. After repeated tests, the water content of soil will increase. The water content at the upper region is greater than that at the bottom, and the greatest water content is on the top due to upward water migration.

Keywords: dry density; freeze-thaw cycles; frost heaving; water content; soil; thaw settlement.

Introduction

The Qinghai-Tibet Railway stretches from Golmud City to Lhasa City, 1180 km in distance, and the extent of the permafrost region of the railway is about 630 km. It is well known that seasonal temperature changes result in frost heave and thaw settlement of the subgrade in frozen soil regions, which will weaken the railway's stability. The railway construction disturbs the balance of water and heat in the natural frozen ground. This imbalance includes changes to the initial thermal field, moisture field, and stress field. The imbalance influences freeze-thaw cycles of subgrade soil, which may cause serious damage to the railway (Wu & Zhu 2002). Studies show that frost heave and thaw settlement are the two main problems in the construction of highways and railways in permafrost regions (Dong & Xu 2000).

Many researchers have studied freeze-thaw mechanisms and the problems of engineering construction. Some valuable measures to prevent frost heave and thaw settlement have been applied to several actual engineering fields (Cheng & He 2001, Sheng et al. 2002, Ma & Xu 1999). Chamberlain and Gow (1979) tested the effect of freezing and thawing on the permeability and structure of four types of fine-grained soils. Their tests showed that freeze-thaw cycles always lead to a reduction in the void ratio and an increase in the vertical permeability. These results have been validated by other studies (Viklander 1998, Kim & Daniel 1992). Further studies show that freeze-thaw creates small cracks in soil samples (Chamberlain et al. 1990, Zimmie & Laplante 1990, Othman & Benson 1993). Zhu (1982, 1983) researched the relationships between the frost coefficient, the thawing settlement coefficient, and some

basic physical parameters based on several experiments. Li & Cheng (1995) and Wang (1992) presented the migration rules of water and heat quantity in an open system. Lai & Wu (2000) analyzed the frost-thaw effect on the tunnel-confining wall by the Computed Tomography (CT) scanning technique. In this paper we examine the changing behavior of dry density and moisture content in soil samples after repeated freeze-thaw cycle tests. The objective of these experiments is to provide a theoretical basis for freezing and thawing theory models and practical engineering design.

Experiment Scheme

Two typical soil types, clayey sand and silty sand, were obtained from two test sites (Beilu River and Anduo) along the Qinghai-Tibet Railway. The soil types show various dry densities, water content, and temperature conditions in repeated freeze-thaw tests. Table 1 shows the physical parameters of the soil samples.

The test samples were mixed with distilled water and dry soil to prevent soluble salt and salinity from affecting the

Table 1. Results of the samples' particles gradation tests.

| Type of soil | Grain size content (%) | | |
|--------------|------------------------|--------------|----------|
| | >0.05mm | 0.05-0.005mm | <0.005mm |
| Silty sand | 65.71 | 23.69 | 10.6 |
| Clayey sand | 54.9 | 12.65 | 32.45 |

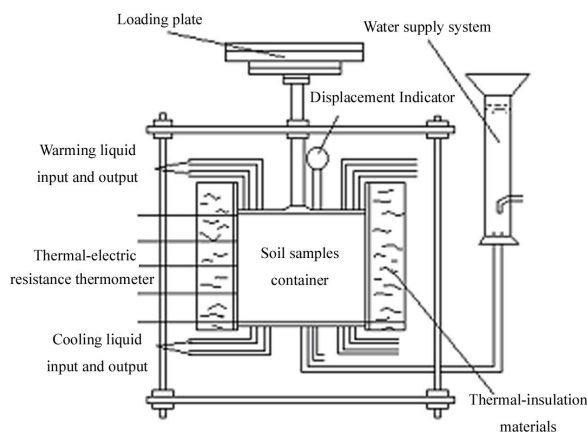


Figure 1. Sketch of freezing and thawing test equipment.

test process of soil freezing and thawing. All samples were made into columns 100 mm high and with a diameter of 100 mm. Thermal resistance sensors to measure temperatures of the different layers were inserted in the soil column every 20 mm from top to bottom, and were read directly into the computer. Test sample molds were wrapped with a sponge, which prevents heat transfer to the interface, so only vertical temperature changes are measured. The height changes of the sample soil surface are observed and recorded by a displacement indicator. Figure 1 shows the design of the freezing and thawing equipment and instrumentation used in these experiments.

The sample mold is put in a control temperature container. In these experiments, the temperature in the container is kept at +1°C in order to minimize lateral heat loss. In all cases, the bottom of the test samples is also kept at +1°C to ensure that there is an unfrozen layer at the bottom. The top temperature of the experimental samples can range between -5°C and +5°C. Freeze-thaw temperature cycling was done in three ways: maintaining -5°C for 3 hours and +5°C for 3 hours; maintaining -5°C for 12 hours and +5°C for 12 hours; and maintaining -5°C for 72 hours and then +5°C for 24 hours. The samples are frozen and thawed from the top down with free access to water at the bottom.

Results and Analysis

The trend analysis of dry density change

Dry density of soil is an important factor for estimating frost heaving quantity and the amount of thawed settlement. Many tests have proved that frost heaving and thaw settlement show a good relationship with dry density of soil (e.g., Zhu 1982, Tong 1988). However, the change rules during repeated freezing and thawing processes were not taken into account.

The process of soil freezing and thawing is a developing process from a non-stationary state to a dynamic balance state. Because repeated freezing and thawing alters the natural characteristics of the experimental soils, the test soil presents a new dynamic equilibrium. Figures 2–4 show that, after a given series of freeze-thaw cycles, the distortion of soil differs

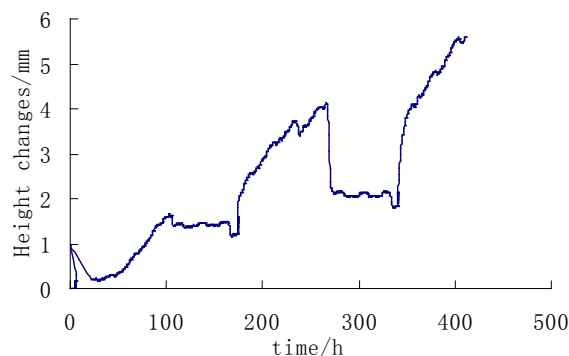


Figure 2. The effect of the freezing and thawing process on the sample's height change in the silty sand sample.

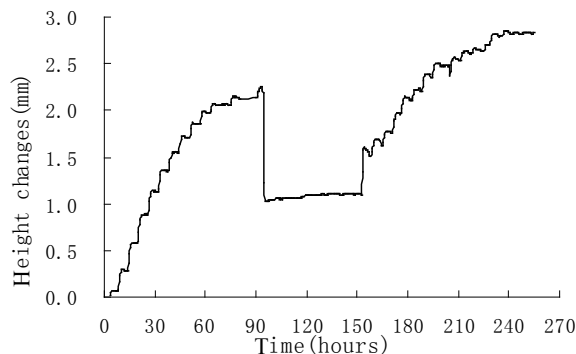


Figure 3. The effect of the freezing and thawing process on the sample's height change in the silty sand sample.

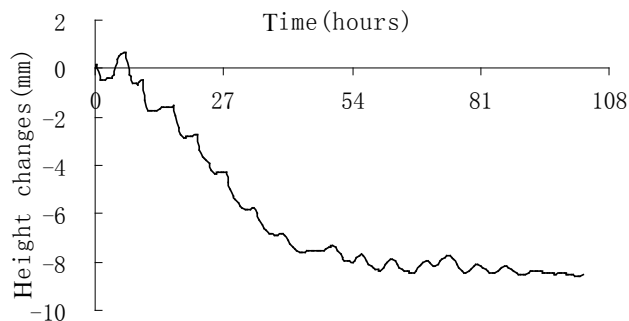


Figure 4. The effect of the freezing and thawing process on the sample's height change in the clayey sand sample.

with different initial dry density and the different temperature cycling.

Figure 2 describes the effect of the freezing and thawing process on the sample's height change in the silty sand sample, which is the sample's height change curve versus time. The beginning dry density of the test sample is 1.9 g/cm³ and the beginning moisture content is 11.84%. In this experiment the upper temperature is alternately freezing and thawing as follows: the temperature is kept at freezing for 96 h; then the temperature controller equipment is closed to keep the sample at a room temperature of 23°C for 96 h.

Figure 3 describes the effect of the freezing and thawing process on the clayey sand sample's height change. This sample

had an initial dry density of 1.7 g/cm³. The top temperature alternated between -5°C and +5°C every 3 hours. Because the temperature controller was stopped, the temperature from 97 h to 153 h was at room temperature during the entire test process shown in the height profile plot of Figure 3. The environmental temperature was 23°C. The result shown in Figure 3 is similar to that in Figure 2. The frost heave quantity is greater than the subsequent thaw settlement that makes the sample expand in the initial cycles. However, after some cycles, the test sample height becomes steady. According to the data analysis of both type of soils, if the dry density of soil is high, the building stress in soil particles is strong enough to repel the thaw settlement of soil particles. So it turns out that the thaw settlement quantity during thaw is smaller than the frost heave during freezing, because the building stress against settlement is greater. After about 30 cycles, the settlement quantity is almost equal to the frost heave quantity.

Figure 4 describes the effect of the freezing and thawing process on the sample's height change in the clayey sand sample. The initial dry density in Figure 4 is 1.4 g/cm³, and the top temperature alternates between -5°C and +5°C every 3 hours. The curve in Figure 4 indicates that the thaw settlement quantity is greater than the earlier frost heave quantity. But after about 17 cycles, the frost heave quantity is nearly equal to the settlement quantity. The explanation is as follows: for low dry density (under 1.55 g/cm³) test soils, repeated freezing and thawing is basically equivalent to the compressed process of the soil samples. Because the dry density is low, accordingly the void ratio of soil will be large. Repeated freezing and thawing makes the water content of the samples increase in an open test system. In a thawing state, ice becoming water reduces the volume, which results in the quick reduction of the supporting stress in the soil and subsidence, making the amount of settlement greater than the frost heave amount in the initial cycles. However, after several cycles, the test soil becomes close-grained and the soil behavior moves toward a

dynamic balance; the amount of heave is approximately equal to that of settlement.

In freezing and thawing tests, the height change quantity Δh is observed by the displacement indicator and recorded in the computer. So the average dry density every minute is computed using the following formula:

$$\gamma'_d = \frac{h * \gamma_d}{h + \Delta h} \tag{1}$$

In the formula, the initial height of the sample h is 100 mm; γ_d represents the initial dry density in g/cm³, and Δh is the amount of height change in mm.

There is a relationship between dry density and height change. The dry density has similar rules with the process of height change in these experiments. For the samples with large initial dry density, the average dry density decreases, and for low dry density, the average dry density increases at the beginning of freeze-thaw action. But after several cycles, the average dry density becomes a constant value

Tables 2 and 3 show results of the average dry density in the experimental samples made of clayey sand from the Beilu River and silty clay from Anduo after repeated freezing and thawing cycles. The test results show that after freezing and thawing cycles, the final dry density of clayey sand is 1.55 g/cm³, while that for silty sand is 1.78 g/cm³, regardless of the initial dry density. If the dry density of the two types of soils reaches the above value, the amount of frost heave during the freezing process amounts to that of settlement during the thaw process observed from the height changing curves, shown in Figures 2–4.

The change of moisture content

After the freezing and thawing tests, the test samples are cut every 10 mm vertically from the top to the bottom in order to measure the moisture content. The plot of water content versus the sample height is shown in Figure 5. The results in

Table 2. Variation of dry density for Beilu River clayey sand after repeated freezing and thawing.

| Sample number | The initial dry density (g/cm ³) | Initial moisture content (%) | Freeze-thaw conditions* | Time (h) | Cycle times (n) | Final dry density(g/cm ³) |
|---------------|--|------------------------------|-------------------------|----------|-----------------|---------------------------------------|
| 1 | 1.4 | 20.9 | 1 | 102.5 | 17 | 1.53 |
| 2 | 1.7 | 20.9 | 1 | 259 | 30 | 1.55 |
| 3 | 1.5 | 20.9 | 1 | 265.9 | 30 | 1.58 |
| 4 | 1.5 | 21.2 | 2 | 99 | 4 | 1.55 |
| 5 | 1.6 | 21.2 | 2 | 430 | 18 | 1.55 |
| 6 | 1.5 | 21.2 | 3 | 639.5 | 5 | 1.53 |

Note*:

Three kinds of freeze-thaw conditions designed for the test samples are as follows:

1. The bottom temperature of the sample and the sample container temperature remain at +1°C; the top temperature of the sample changes from -5°C to +5°C every 3 hours.
2. The bottom temperature of the sample and sample container temperature remain at +1°C; the top temperature of the sample ranges from -5°C to +5°C every 12 hours.
3. The bottom temperature of the sample and sample container temperature remain at +1°C; the top temperature of the sample remains at -5°C for 72 hours and then changes to +5°C for 24 hours.

Table 3. Variation of dry density of Anduo silty sand after repeated freezing and thawing.

| Initial dry density (g/cm ³) | Initial moisture content (%) | Time (hours) | Cycle times (n) | Final dry density (g/cm ³) |
|---|---------------------------------|-----------------|--------------------|---|
| 1.73 | 20.2 | 301 | 3 | 1.78 |
| 1.83 | 16.8 | 307 | 3 | 1.79 |

Note*: the bottom temperature of the sample and sample container remain at +1°C; the top temperature of the sample remains at -5°C for 72 hours and then increases to +5°C for 24 hours.

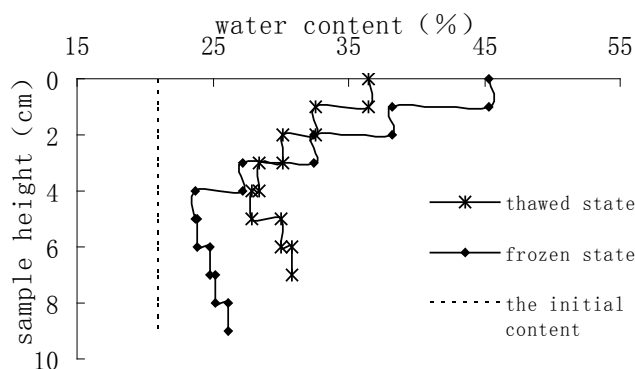


Figure 5. Water content diagram of silty clay in both frozen and thawed states.

Figure 5 show that although the water content gradients in frozen and thawed states differ, after freezing and thawing action, in the upper part of the sample the water content increases significantly while water content in the unfrozen zone increases only slightly. The average water content of the frozen zone is greater than that of the unfrozen zone, and the greatest water content appears in the upper part after several cycles. Contrasting the two curves in Figure 5, we found that in the changed zones, the water content amount in the thawed state is smaller than that in the frozen state. In the unfrozen zone, the water content in the thawed state is greater than that in the frozen state, and near the frost front of the test sample, the water content changes remarkably. The explanation is as follows:

At the beginning of the freezing and thawing action, the water within the soil pores is frozen from the top to the bottom when the two surfaces of test samples are suddenly submitted to a stationary temperature condition that ensures the sample freezes from one surface and keeps thawing at the other surface (in these tests, the temperature condition is always +1°C at the bottom and temporarily -5°C at the top). Because the water potential energy of the frozen zone is far smaller than that of the unfrozen zone, the unfrozen water will flow from the unfrozen zone to the frozen-unfrozen interface (as well as the frozen zone) and then become ice. The flowing water makes ice increase continuously, which fills the soil pores. This causes the thermal conductivity of the soil to rise rapidly, and cool energy is diffused downward more rapidly. The freezing interface moves downward. Segregation ice forming in this way results in the water content increasing in the frozen zone.

During the thawed period, the temperature of the sample upper surface changes to +5°C while the bottom temperature remains at +1°C. The samples begin to thaw from the top and the bottom. The ice changes to water, causing soil pores to instantly become a vacuum. Therefore, the unfrozen water is sucked from the top thawed soil layer to the thawing soil below, which results in water increasing in the thawing soil. For the frozen zone, the bottom part remains frozen and the unfrozen water in the thawed zone can't flow to the top due to the low unfrozen water potential and the small water conductivity. This leads to the water content in the thawed state being smaller compared to that in the frozen state. When the thawing interface approaches the frozen-unfrozen interface, the water is sucked from the top and the thawed zones; that is, the soil thaws from top to bottom as well as from bottom to top. The process described above makes water flow to the interface from the unfrozen zone. Water bi-directional flowing is the result of water content increases in the previous frozen-unfrozen interface, as shown in Figure 5.

Because the unfrozen zone is the route for draining water and sucking water from the bottom, the water content of the unfrozen zone during the thawing period is larger than that in the previous freezing period.

During the subsequent freezing period, the upper temperature is changed to -5°C again and the bottom temperature is maintained at +1°C. The test sample begins to freeze from top to bottom with the unfrozen water being transferred. One result from the repetition test is that the water content of soil increases. In each freeze-thaw action, more water is accumulated, flowing to the frozen zone that forms the frozen fringe faster than during the previous freezing process. In the latter thawing process, water begins to complete the previous process through the action of vacuum suction and permeability. As the test proceeds, water flows to the top continuously, causing greater amounts of water content in the upper part than in the unfrozen zone, peaking approximately at the top of the column. After repeated freezing and thawing, the structure of the test soils changes because moisture is transferred, and rearranged soil particles enhance the soil permeability, inducing water to flow easily.

Practical significance of the test results

According to the test results, the dry density will remain constant after several freeze-thaw cycles. In order to obtain a stable subgrade in frozen soil regions, the subgrade (in

particular, the backfill) should be exposed to several cold and warm seasons before construction. Artificial freezing may be an approach when the period of construction is short.

On the other hand, the freeze-thaw cycles can vertically redistribute the water in soil, which leads to greater water content in upper layers. However, most current models assume the invariable water content within the soil body, or only consider the infiltration. In order to compute the frozen soil heat and water transfer processes, it is necessary to include the frozen soil water potential within the model.

Conclusions

From the experiments and analysis described above, we can make the following conclusions:

- 1) Freeze-thaw processes in an open system are the rearranging processes of density, moisture, and stress within soil body. After freeze-thaw cycles, the soil particles with large initial dry density become loose and the dry density decreases, while the soil with low initial dry density becomes compact and the dry density increases. After several cycles, the amount of thaw settlement is almost equal to the amount of the freezing heave. Therefore, it can also be concluded that the final dry density of each soil sample after repeated freeze-thaw cycles depends on the soil grain-size distribution but not on the original dry density.
- 2) After several freeze-thaw cycles from the top down with free access to water at the base, the water content of soil will increase. The water content in the freeze-thaw section shows a greater increase than that in the unfrozen zone. When comparing the water contents in the frozen and thawed states, the water content in the upper freezing-thawing zone in the frozen state is greater than that in the thawed state, while that in unfrozen zone in the frozen state is smaller than that in the thawed state.

Acknowledgments

This research is supported by the Research Project of Excellent State Key Laboratory (Grant No. 41023003), Independent Foundation of State Key Laboratory of Frozen Soil Engineering (Grant No. SKLFSE-ZY-02-10) and National Natural Science Foundation of China (Grant No. 40701030).

References

- Chamberlain, E.J. & Gow, A.J. 1979. Effect of freezing and thawing on the permeability and structure of soils. *Engineering Geology* 13(1): 73-92.
- Chamberlain, E.J., Iskander, I., & Hunsiker, S.E. 1990. Effect of freeze-thaw on the permeability and macrostructure of soils. *Proceedings of International Symposium on Frozen Soil Impacts on Agriculture, Range and Forest Lands*. U. S. Army Cold Regions Research and Engineering, Hanover, NH, pp. 145-155.
- Cheng, G.D. & He, P. 2001. Linearity engineering in permafrost region. *Journal of Glaciology and Geocryology* 23 (3): 213-217.
- Dong, R.K. & Xu, Z.Y. 2000. Dynamic characteristic of freezing-thawing erosion on Qinghai-Tibet Plateau. *Journal of Soil and Water Conservation* 14 (4): 12-16.
- Kim, W.H. & Daniel, D.E. 1992. Effects of freezing on hydraulic conductivity of compacted clay. *Journal of Geotechnical Engineering* 118(7): 1083-1097.
- Lai, Y.M. & Wu, Z.W. 2000. CT analysis of frost damage of the surrounding rocks of a tunnel in the Daban Mountain. *Journal of Glaciology and Geocryology* 22(3): 206-210.
- Li, S.X. & Cheng, G.D. 1995. *Problem of heat and moisture transfer in freezing and thawing soils*. Lanzhou University Press, Lanzhou.
- Ma, W. & Xu, X.Z. 1999. Influence of freeze-thaw cycles on shear strength of lime silt. *Chinese Journal of Geotechnical Engineering* 21(2): 158-160.
- Othman, M.A. & Benson, C.H. 1993. Effect of freeze-thaw on the hydraulic conductivity and morphology of compacted clay. *Canadian Geotechnical Journal* 30(2): 236-246.
- Sheng, Y., Zhang, L.X., & Yang, C.S. 2002. Application of thermal-insulation treatment to railway engineering in permafrost regions. *Journal of Glaciology and Geocryology* 24(5): 618-622.
- Tong, C.J. 1988. Study on the thawing settlement of frozen soil in China. *Journal of Glaciology and Geocryology* 10(3): 327-331.
- Viklander, P. 1998. Permeability and volume change in till due to cyclic freeze/thaw. *Canadian Geotechnical Journal* 35(3): 471-477.
- Wang, J.C. 1992. Experiment study on the ice formation conditions of saturated silty soil during repeated freezing and thawing. *Journal of Glaciology and Geocryology* 14(2): 101-106.
- Wu, Q.B. & Zhu, Y.L. 2002. Assessment model of permafrost thermal stability under engineering activity. *Journal of Glaciology and Geocryology* 24 (2): 200-204.
- Yu, W.B. & Lai, Y.M. 2002. Laboratory experiment study on the railway ventilated embankment in permafrost regions. *Journal of the China Railway Society* 24(6): 78-83.
- Zhu, Y.L. 1983. Calculation of thawing and compressing settlement in frozen subgrade soils. *Professional Papers on Permafrost Studies of Qinghai-Xizang Tibet Plateau*. Science Press, Beijing: pp. 134-139.
- Zhu, Y.L. 1982. Thaw settlement of frozen ground. *Proceedings of the Symposium on Glaciology and Cryopedology Held by Geographical Society of China (Cryopedology)*. Science Press, Beijing: pp. 145-150.
- Zimmie, T.F. & Laplante, C. 1990. The effect of freeze-thaw cycles on the permeability of a fine-grained soil. *Proceedings of 22nd Mid-Atlantic industrial waste conference*. Drexel University, Philadelphia, PA: pp. 580-593.

Stable Isotope Composition of Ice Cores in Open- and Closed-System Pingos

Kenji Yoshikawa

Water and Environmental Research Center, Institute of Northern Engineering, University of Alaska Fairbanks, USA

Daniel Lawson

Cold Regions Research and Engineering Lab, USA

Sharkhuu Natsagdorj

Institute of Geography, Mongolian Academy of Sciences, Mongolia

Abstract

The first complete record of stable isotopes ($\delta^{18}\text{O}$, δD) in ice within both open- and closed-system pingos indicates a complex history of ice formation and pingo growth. A continuous section of ice was cored through the center of the Mongot Pingo in northwestern Mongolia and through the Weather Pingo in northern Alaska. Ice from each core and the waters from below the open-system pingo were analyzed for stable isotope and chemical composition. Changes in the isotopic signature of the ice core with depth signal several distinct processes by which each pingo grew as permafrost aggradation took place and the groundwater hydrology changed. In the initial stages, in situ water migrating toward the freezing front froze at a relatively rapid rate, as revealed by the complex isotopic record. In the middle and lower sections of each core, the isotopic and chemical compositions revealed unique trends that indicated different processes operated in forming the bulk of the ice within both the open- and closed-system pingos.

Keywords: Alaska; ground ice; ice core; Mongolia; pingo; stable isotope, Alaska.

Introduction

Different types of subsurface ice-cored mounds such as pingo, palsa, and lithalsa are widely known in permafrost regions. These mounds are created by different growth processes and thus exhibit various ice structures (Müller 1959, 1962). However, the details of the physical processes by which each type of mound forms remain poorly understood. One method to establish the mechanics of growth is to analyze the variability in the stable isotopic composition of the ice forming the core of these various mounds. The stable isotopic composition of certain types of ice is relatively well studied, including lake ice (Gibson & Prowse 2002), river ice (Gibson & Prowse 1999), and frost blister ice (Gell 1978, Michel 1986, Pollard 1988, Pollard & French 1985, Yoshikawa 2008, Vasil'chuk & Vasil'chuk 2011). Clark and Fritz (1997) provide a well-documented review of these surface and ground water isotope studies. Michel (1986, 2011) used isotopic signatures to explain the processes of surface water freezing and to understand subsurface ice core growth.

In this paper, we compare the $\delta^{18}\text{O}$ and δD composition of ice within open- and closed-system pingos near Prudhoe Bay, Alaska, and northwestern Mongolia to assess growth conditions. We analyzed a continuous 8–12-cm-diameter core drilled through the center of each pingo (Figs. 1a, 1b). Using the isotope stratigraphy, we reconstruct the growth history of both pingos.

There are few studies of the stable isotope composition of ice forming and freezing processes (Lacelle 2011). For the pingo ice, Mackay (1979, 1990) reported on $\delta^{18}\text{O}$ and δD analyses from one of the closed-system pingos in the Tuktoyaktuk Peninsula, NWT. The isotopic values gradually became lower with depth below the ground surface, indicating a limited supply of water that diminished with time. Yoshikawa (1993)

reported on $\delta^{18}\text{O}$ values from one of the open-system pingos in Svalbard. Here the $\delta^{18}\text{O}$ values remained more or less constant with depth at a value near -13‰, except where dilation cracks had introduced surface water that formed ice within the core after the initial stage of pingo growth was completed.

Open-System Pingo (Mongot Pingo, Mongolia)

Figure 2 shows the $\delta^{18}\text{O}$, δD , D-excess (d), chemical composition (St, Na, K, Ca, Fe, Pb, F, Cl, and sulfate), and temperature profiles in comparison to the 1968 drill log of the Mongot Pingo in northwestern Mongolia. The active layer measured 0.9 m at the top of the pingo on August 7, 2009, during the drilling operation. An ice lens was observed just below the active layer, and a layer enriched in calcium by cryogenic processes was observed at 2.6 m. Pure ice was found at 2.5–2.8 m below the ground surface. Up to 2.5 m of sediments, mainly sand, were not sampled for isotopic analyses. Stable isotope composition of the ice to a depth of 6 m did not exhibit a clear trend, while the core alternated between layers of pure ice (intrusive ice) and ice lens (segregated ice). This structure of alternating segregated and pure ice lenses indicates that the early stage of pingo formation was similar to that of a frost blister. We observed several small mounds (up to 5 m) with craters around Mongot Pingo, suggesting similar early stage growth of Mongot Pingo, perhaps as a result of artesian water lifting weak spots in the upper permafrost layer (Holmes et al. 1968). When it was 2–3 m high, its growth was interrupted by sedimentation of a clay layer at its base in the sub-pingo aquifer.

Mongot Pingo had four major periods of growth. The first event caused pingo growth of about 2 m elevation (ice core section 6–10 m depth). The $\delta^{18}\text{O}$ and δD signals of this ice

indicate that the ice grew in a closed-hydrostatic environment resulting from slow freezing of an isolated water lens under the pingo, akin to frost blister formation. As this sub-pingo groundwater reservoir began to freeze, the first ice to form

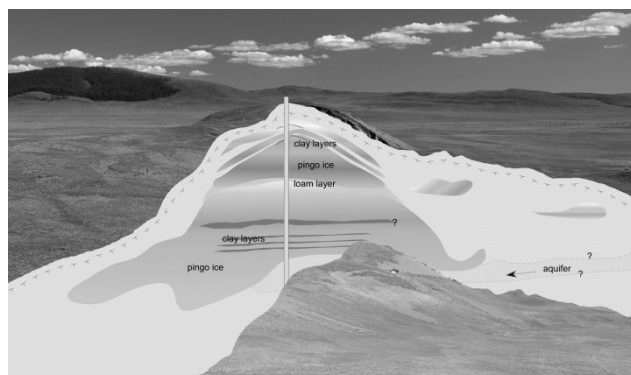


Figure 1a. The open-system pingo, Mongot Pingo, stands approximately 20 m above the valley and is ~200 m in diameter in northwestern Mongolia. Drilling operations took place in 1968 and 2009, with the borehole centered at the top of the pingo. Three sections based on the physical properties of the ice (Fig. 2) are located.

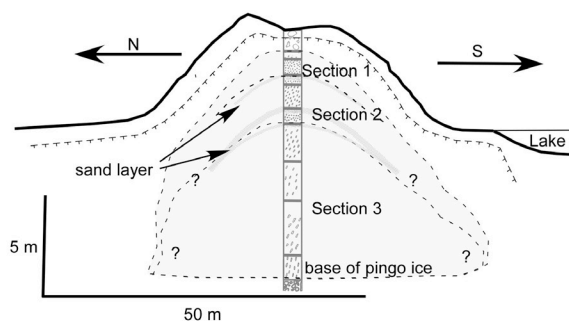
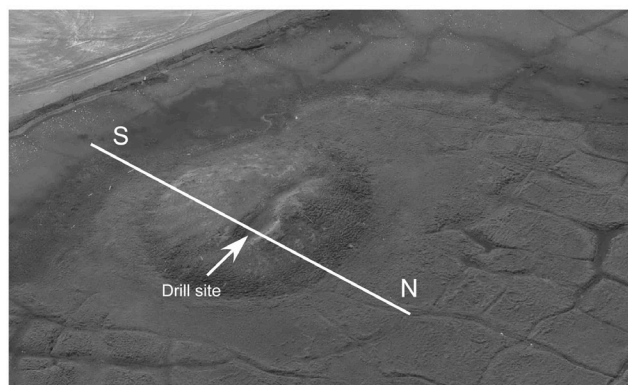


Figure 1b. The closed-system pingo, Weather Pingo, stands approximately 6 m above the drained lake basin and is ~100 m in diameter, North Slope of Alaska. Drilling operations took place in spring 1982, with the borehole centered at the fissure in the pingo surface. Three sections based on the physical properties of the ice (Fig. 3) are located.

would have been enriched by about 3.1‰ for $\delta^{18}\text{O}$ and 19.3‰ for δD (O'Neil 1968). As freezing continued, ice grew from a gradually depleting supply of water, as revealed by increasingly lower isotopic values with depth in the core. These values follow the Rayleigh distillation model for freezing of water in a fixed-volume sub-pingo water lens (Yoshikawa 2008).

Isotopic data from deeper in the core indicate groundwater flow to the base of the pingo was re-initiated and ice growth took place as artesian pressure increased below 10 m depth in the core. More than 5 m of clear, massive ice formed, basically pure except for some plant remnants at a depth of 13.8 m (regression slope of $\delta^{18}\text{O}$ and δD :7.7) (Fig. 2). Both the $\delta^{18}\text{O}$ and δD composition of the ice showed little variation beginning with this core section, indicating freezing under an open-system hydrologic environment, in sharp contrast to the uppermost ice of the pingo. The ^{14}C dating of the plant remnant yielded an age of 8790 ± 50 yr BP (BETA 271760), which suggests that ice formed after the plant fragments entered the groundwater flow or from in situ sediments. To this depth in the core (section 1), the D-excess value is $+5 \pm 15$ ‰, which is heavier than ice at greater depth (section 2) by about -5‰, possibly indicating a dryer environment for the original groundwater. The chemical composition of the ice (e.g., sodium, iron) also supports dryer conditions (Fig. 2).

The ice below 15 m to the sub-pingo water layer reveals a unique stratigraphy with continuous similar isotopic signals with depth. The values of $\delta^{18}\text{O}$ are nearly constant at approximately -13.5‰. Only at a depth of 23–24 m is the continuity interrupted; here a 1-m-thick layer of clay, with almost no visible ice lenses, was apparently deposited over a relatively long period of time, while ice formation above the sub-pingo water lens added nearly 8 m vertically to the central ice core and height of the pingo. Following the deposition of the sediment layer, ice growth increased the central core of the pingo over 8.5 m in thickness. During this growth, several minor interruptions are indicated by ~8 interlaced clay layers. In the lower section of the ice core, the D-excess value is negative (Fig. 2), indicating possibly a wetter or less evaporative environment, compared to the time when the upper part of the pingo ice core formed (section 1). The chemical composition of the lower ice section (e.g., sodium, iron) also supports the likelihood of wetter conditions (Fig. 2). One of the important processes of closed-system freezing is chemical extraction or enrichment. Mackay (1990) reported that several high-ion-concentrate layers were observed in ice of a closed-system pingo.

Ionic segregation or salt precipitation during the freezing process is commonly observed during ice formation (Hallet et al. 1978). We observed high solute concentrations just above each clay layer in the three sections of the core (e.g., 15, 24, and 32 m in depth) (Fig. 2). Isotopic fractionation occurred in concert with this chemical enrichment and thus suggests that ionic segregation occurs within open-system pingos. The sub-pingo water sample has less calcium, iron, and potassium than is found in these enriched layers, but with extremely high sodium (100 mg/L); this significant difference may have occurred relatively recently.

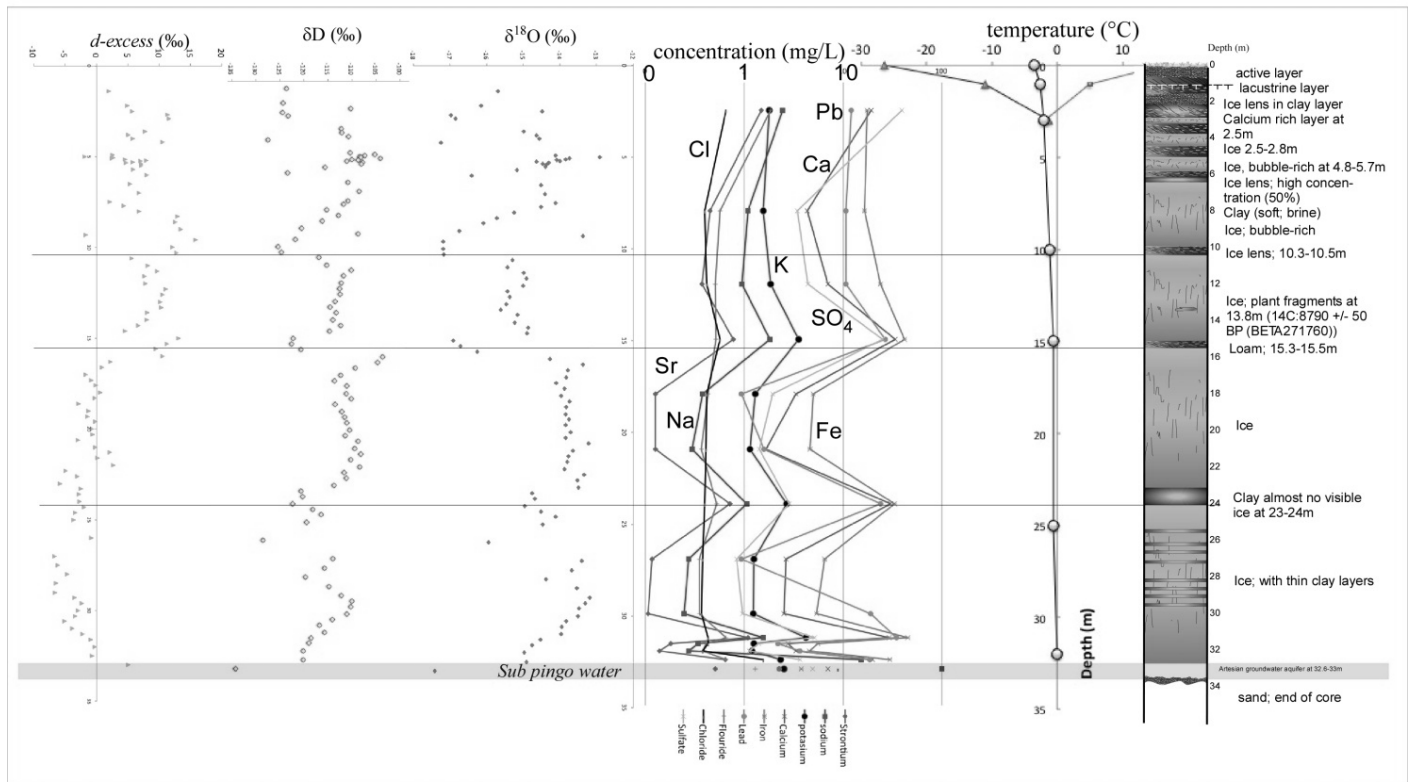


Figure 2. Oxygen and hydrogen stable isotopes, d -excess profiles, and chemical compositions are shown with the pingo ice core drill log, from top (1 m below ground surface) to bottom (32 m; bottom of the pingo ice) from the Mongot open-system pingo.

Closed-System Pingo (Weather Pingo, Prudhoe Bay, Alaska)

Both the physical properties of the ice and the isotope stratigraphy indicate that ice formation and pingo growth of Weather Pingo took place under varying hydrologic conditions. In Figure 3, we compare the physical properties of the ice to the isotopic composition with depth in the central core of the pingo. We subdivide the central core into three sections based on its physical properties and structure (Fig. 3). The uppermost section (1) consists of ice with round air bubbles of 1–2 mm diameter to 2.2 m depth at the uppermost sand horizon. The middle section (2) lies between 2.2 and 4.8 m depth and contains three sand horizons and associated air bubbles that are elongated in a near-vertical position. The bottom section (3) between 4.8 and 13 m has consistently elongated air bubbles at or near vertical orientation in clear debris-free ice, and ice crystals generally larger than those elsewhere in the pingo core. Of note is the increase in air bubble diameter and in crystal size to more than 5 cm at a depth of 8.8 m. These changes indicate a much slower rate of freezing in the latter stages of growth of the pingo's central core of ice, while the much smaller crystals in the upper 4.8 m of the core indicate a more rapid rate of freezing during earlier stages of growth.

The uppermost sample of ice (1 m depth) in contact with the sediment capping the pingo has relatively low δD and

$\delta^{18}O$ values that increase with depth to 1.4 m (Fig. 2). We interpret these values as indicating a progressive, yet rapid, freezing of the waters remaining in the bottom sediments of the lake immediately following its drainage.

Below 1.4 m, the stable isotope data exhibit isotopic differences (trends) that follow the broad physical changes of the ice core (Fig. 4). From ~1.4 to 2.2 m depth (section 1, Fig. 1), the δ -values of the deuterium and oxygen isotopes exhibit a slight increase with depth, but with an apparent repetition of increasing and decreasing values (Fig. 3). These repetitions may indicate short-term changes in the amount of water available or in the rate of freezing or both. This section exhibits a δD - $\delta^{18}O$ trend with a regression slope of 6.1 and δD intercept of -41 (Fig. 4). Between 2.2 and 4.8 m depth (section 2, Fig. 1), the stable isotope values were relatively constant (δD : ~ -140‰, $\delta^{18}O$: ~ -16.5‰) with only slight variations between successive samples.

However, the D -excess values fluctuated within a wide range (-5 to -14‰). We interpret the isotopic range and D -excess values as indicating a mostly continuous migration of water from the surrounding unfrozen basin deposits to the sub-pingo water lens that was temporarily interrupted by several periods of slower and lesser amounts of water available for freezing.

The lowermost ice in the pingo's core is characterized by generally decreasing values for δD and $\delta^{18}O$, except for several short periods of increasing values (Fig. 3). For example from about 5.3 to 6.1 m depth, a well-defined

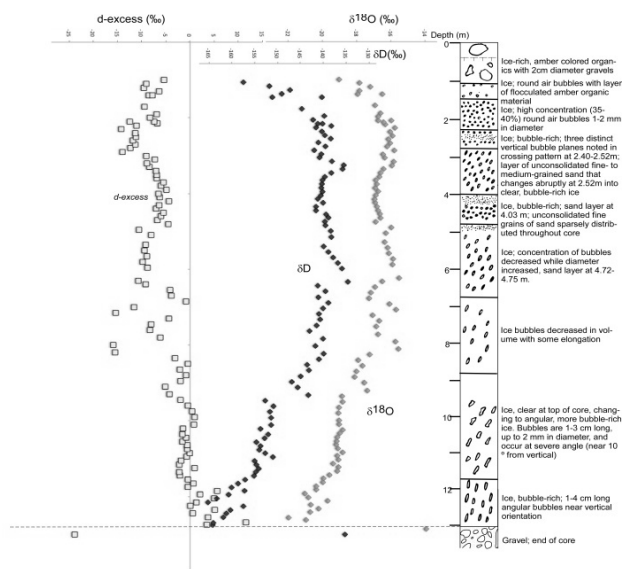


Figure 3. Oxygen and hydrogen stable isotopes and d-excess profiles are shown with the Weather Pingo drill log (by Brocket 1982), from the uppermost sample at 1 m below the ground surface into the sediments just below the pingo's ice core (13 m).

sub-stage of progressively heavier isotopic values suggests perhaps a change in the composition of the migrating water, while from 8.0 to 8.3 m depth, the progressive lightening of the values suggests reduced flow to the freezing front and thus fractionation during freezing of a limited volume and supply of sub-pingo water.

Between 8.3 m and the base of the pingo ice at 13 m, the δD and $\delta^{18}O$ values decrease, becoming progressively lighter to a depth of ~ 11.8 m. Simultaneously, the d-excess value generally increases with depth (Fig. 3). From 11.8 to 13 m, values decrease more rapidly while the D-excess values sharply increase to positive values. Here the bubble-rich ice, elongated air bubbles, and large crystal size indicate slow freezing as the final stages of ice growth took place. The single sample from pore ice within the underlying frozen sediments reverses the trend and sharply increases to the largest values within the core samples (Fig. 3). The overall δD - $\delta^{18}O$ trend in the basal section has a regression slope of 5.3 and δD intercept of -52 (Fig. 4). This slope is much more gradual than that of the expected regional meteoric line (slope: ~ 7 -8). We interpret this trend as indicating that the water within the remaining unfrozen sediments of the lake basin was limited, with no addition possible from the surface or ground water aquifer. The decreasing isotopic values and increase in D-excess are consistent with a Rayleigh distillation process during progressive freezing of a limited volume of water in a hydrostatic environment (Lacelle 2011).

We plot an analysis of changes in δD and $\delta^{18}O$ assuming Rayleigh distillation for progressive freezing of waters having an initial composition equal to that of the water (ice) within the sediments below the pingo. For a residual water volume equal to less than 0.6 total ice volume, the isotopic values track what is expected for Rayleigh distillation (Fig. 5, δD

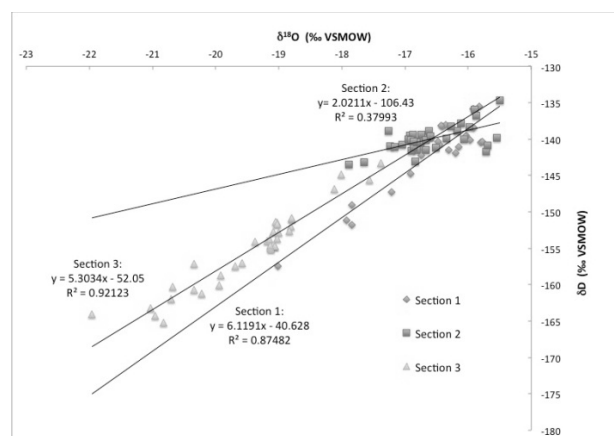


Figure 4. Relationship between oxygen and hydrogen stable isotopes in the closed-system Weather Pingo's ice core. Two trends are identified with depth for the three physical sections shown in Figure 1b.

trend with triangles). The expected simple isotopic fractionation demonstrates this freezing process (Fig. 5). The equilibrium curve (Fig. 5, trends with squares) is calculated using the fractionation factor (α) of 1.0028 for oxygen and 1.0206 for hydrogen (Suzuoki & Kimura 1973). This offset indicates a delay in freezing of the sub-pingo water lens which had limited unfrozen water remaining above permafrost. This equilibrium curve fractionation factor is slightly different ($\alpha=1.03$ for hydrogen). This offset indicates however that the fractionation process did not begin as water initially froze to form the upper part of the pingo's core of ice, but rather at a later stage of ice growth. We interpret this as resulting from a cessation of pore-fluid expulsion from the remaining unfrozen sediments below the former lake. During this latter period of water migration, the volume of ice created caused the primary expansion of the pingo above the local ground surface. Aggrading permafrost in the former lake basin led to a progressive decrease in the volume of thawed sediment (talik). Expulsion of the excess waters created hydrostatic pressures and a more or less continuous supply of water from below the pingo. The complicated isotopic trends that change with depth through the core appear similar to those of previous analyses by Michel (1986) of ice within a frost blister.

Because the pore water from below the pingo core had a much heavier isotopic composition than that of the pingo ice (δD : -135 ‰, $\delta^{18}O$: -14 ‰) (Fig. 3), the change in the isotopic composition with depth to the base of the ice core cannot be accounted for by complete, continuous freezing of all sub-pingo waters when pingo growth ceased, if this value is indeed representative of the last sub-pingo waters to freeze. The gap in isotopic values between this pore ice and basal pingo ice may be explained by several different scenarios, including, for example, that the sub-pingo waters were also freezing within the sediments peripheral to the pingo before the talik at the base of the pingo froze completely. At the very least, we recognize that the ice growth in the pingo stopped before the sub-ice sediments froze completely. Further analyses are required to determine the reasons for the disparity in the isotopic compositions.

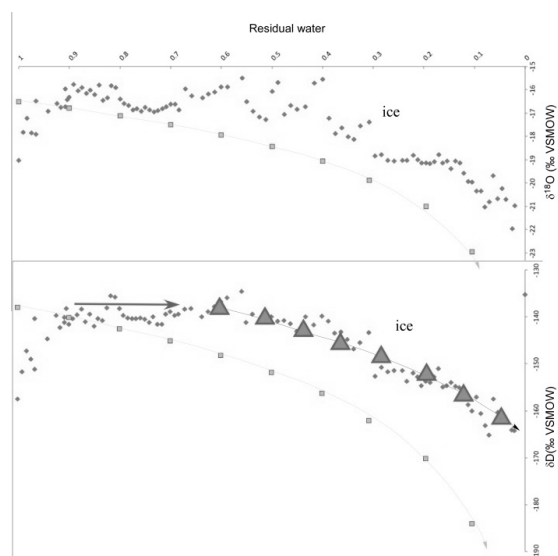


Figure 5. Modeled residual fractions versus oxygen and hydrogen stable isotopes of the ice within the central core of the Weather Pingo. Square dots indicate ideal residual fraction by the Rayleigh distillation model. The equilibrium-type curve used the fractionation factor of 1.0028 for oxygen and 1.0206 for hydrogen (Suzuoki and Kimura 1973) and triangle dots indicate matched equilibrium curve used the fractionation factor of 1.03 for hydrogen.

Conclusion

In 2009, we conducted borehole drilling at Mongot Pingo, a typical open-system pingo in northwestern Mongolia, to obtain a complete series of ice-core samples. Mongot Pingo had been drilled to the bottom of its ice once before, in 1968, by the joint Soviet-Mongolian Scientific-research Geological Expedition, which also had measured discharge of the artesian sub-pingo water. We had the unique opportunity of comparing our ice-core data from 2009 with the data gathered in 1968, which provided insights into open-system pingo formation as well as information on development that might have occurred over a 41-year span. Stable isotope signals and chemical composition from ice samples and adjacent surface water, spring water, sub-pingo water, and ice from the 1968 drilling, indicate that Mongot Pingo has repeatedly experienced a combination of open- and semi-closed-water environments. The major driving mechanism of pingo formation has been groundwater artesian pressure, which has injected water into the permafrost layer. This study identified two different stable isotope patterns in separate ice sections: (1) open-system freezing, and (2) semi-closed-system (or closed-system) freezing. Each of these isotopic trends indicates the critical role played by the growth mechanism in ice formation.

An open-system ice-cored mound, such as an open-system pingo or frost blister, undergoes relatively fast freezing (enrichment of isotope ratio) at the top ice layer in an open hydrologic environment, and this represents the main growth period. The major (60% or more) part of the ice core, however, is still formed by pressurized liquid. At the end of this growth

period or when interrupted, the groundwater reservoir becomes isolated and slowly freezes, forming a closed environment. The D-excess value indicates two major periods of pingo growth in sections 1 and 2. The early stage formation of Mongot Pingo seems to have occurred under more arid conditions.

The upper 3 m of the sediment contain more ice lenses, but not thick intrusive ice. Between depths of 3 and 10 m, at least four periods of intrusive ice formed, each observed to be within 1 m thick. Many open-system pingos indicate a similar trend at the upper part of the main ice body (Yoshikawa 1993). Crystals in the major ice body (section 2) are larger (>2 cm) than crystals in the upper intrusive ice, which suggests that the pingo developed upward relatively quickly by artesian pressure (the intrusive ice layer is thin). Growth of the pingo then slowed, but a large sub-pingo water reservoir provided a continuous water supply (open environment). The water in this dome-shaped area slowly froze downward at the same time that suspended or in situ clay particles were deposited at the bottom. Finally, during a nearly dormant period, weaker artesian pressure and water crystallization occurred occasionally.

The first high-resolution $\delta^{18}\text{O}$ - δD record of ice within a typical closed-system pingo in northern Alaska has revealed a complex history of ice formation and pingo growth. The stable isotope data through the entire thickness of the Weather Pingo including sub-pingo ice (water) reveal that the ice formed during both hydrostatic conditions with a limited supply of water, and as the result of rapid injection freezing from an in situ supply of water, the former being the primary condition during pingo growth. Freezing of the lake waters in the basin sediments initiated ice formation, affecting only the uppermost 1.4 m just below the lake bed. Below this depth, the complex isotopic record indicates in situ waters migrated toward the freezing front and froze at a relatively rapid rate (section 1, Fig. 1b). Subsequently, relatively steady isotopic values indicate a mostly continuous supply of water flowing from the adjacent, unfrozen talik of the lake basin surrounding the pingo (section 2). In the lowermost section above the base of the pingo, isotopic fractionation following Rayleigh distillation and a progressive lightening or decrease in the isotopic values with depth indicate a limited supply of water as most of the remaining talik froze to form permafrost (section 3). The sharp change in values at the ice-sediment interface suggests pingo growth terminated before all of the talik beneath the former lake completely froze. The majority of the ice within the pingo (~6 to 13 m core depth) formed after permafrost aggraded into the drained basin sediments and pore-fluid expulsion created hydrostatic pressures and a mostly continuous supply of water to the freezing front at the base of the pingo. Vertical growth of the pingo to ~6 m above the drained lake basin appears about equivalent to the latter stages (section 3) of ice core formation.

Acknowledgments

The authors thank Dr. Denis Lacelle and an anonymous reviewer of this paper for their helpful comments, suggestions, and revision of English. We thank Bruce Brockett for first

obtaining the undisturbed ice core, Jerry Brown for logistical support of the drilling operation in 1982, and CRREL for support in storing and maintaining the ice in cold rooms at the temperature required to preserve it. The Institute of Northern Engineering, University of Alaska Fairbanks, provided grants for travel by Yoshikawa to CRREL. We also thank Tim Howe, Isao Yuguchi, and Joel Homan for help with field and laboratory analyses and Fran Pedersen for her review of English grammar in this manuscript. Research funding for Lawson was provided by NSF Grant ARC-0949775.

References

- Brockett, B.E. 1982. Modification of and experience with a portable drill, Prudhoe Bay, Alaska, spring, 1982. CRREL, Internal Memorandum, 14 pp.
- Clark, I.D. & Fritz, P. 1997. *Environmental Isotopes in Hydrogeology*. New York: Lewis Publishers, 328 pp.
- Gell, W.A. 1978. Fabrics of icing-mound and pingo ice in permafrost. *Journal of Glaciology* 20, 84: 563-569.
- Gibson, J.J. & Prowse, T.D. 1999. Isotopic characteristics of ice cover in a large northern river basin. *Hydrol. Process.* 13: 2537–2548.
- Gibson, J.J. & Prowse, T.D. 2002. Stable isotopes in river ice: Identifying primary over-winter streamflow signals and their hydrological significance. *Hydrol. Process.* 16: 873–890, doi:10.1002/hyp.366
- Hallett, J., Sax, R.I., Lamb, D., & Ramachandra Murty, A.S. 1978. Aircraft measurements of ice in Florida cumuli. *Quarterly Journal of the Royal Meteorological Society* 104: 631–651.
- Holmes, W.G., Hopkins, M.D., & Foster, L.H. 1968. Pingos in central Alaska. *USGS. Bulletin* 1241-H, 34 pp.
- Lacelle, D. 2011. On the $d^{18}O$, dD and D-excess relations in meteoric precipitation and during equilibrium freezing: theoretical approach and field examples. *Permafrost and Periglacial Processes* 22: 13-25.
- Mackay, J.R. 1979. Pingos of the Tuktoyaktuk Peninsula, Northwest Territories. *Geographie physique et Quaternaire* 33: 3-61.
- Mackay, J.R. 1990. Seasonal growth bands in pingo ice. *Canadian Journal of Earth Sciences* 27:1115-1125.
- Michel, F.A. 1986. Isotope geochemistry of frost-blister ice, North Fork Pass, Yukon, Canada. *Canadian Jour. Earth Sciences* 23: 543-549.
- Michel, F.A. 2011. Isotope characterization of ground ice in Northern Canada. *Permafrost and Periglacial Processes* 22: 3-12.
- Müller, F. 1959. Beobachtungen über Pingos. *Meddelelser om Grønland* 153: 1-127.
- Müller, F. 1962. Analysis of some stratigraphic observations and radiocarbon dates from two pingos in the Mackenzie delta area, N.W.T. *Arctic* 15: 278-288.
- O’Niel, J.R. 1968. Hydrogen and oxygen isotope fractionation between ice and water. *Journal of Physical Chemistry* 72: 3683-3684.
- Pollard, W.H. 1988. *Seasonal frost Mounds*. Advances in periglacial Geomorphology (Clark, M.J. ed.). John Wiley & sons Ltd. Chichester. 201-229.
- Pollard, W.H. & French, H.M. 1985. The internal structure and ice crystallography of seasonal frost mounds. *Journal of Glaciology* 31: 157-162.
- Sharkhuu, N. 1970. *Perennial frozen ground on northern plateau of Bulnai Mountain range*. In Geographic problems of Mongolia. No 9, pp. 86-113 (in Mongolian).
- Sharkhuu, N. & Luvsandagva, D. 1975. *Basic features of permafrost in Mongolia*. MAS press, 108 pp. (in Mongolian).
- Suzuoki, T. & Kimura, T. 1973. D/H and $^{18}O/^{16}O$ fractionation in ice-water systems. *Mass Spectroscopy* 21: 229-233.
- Vasil’chuk, Y.K. & Vasil’chuk, A.C. 2011. *Stable Isotope Geochemistry of Natural Ice*. Lomonosov’s Moscow State University, Moscow University Press. Moscow, 224 pp. (in Russian).
- Yoshikawa, K. 1993. Notes on open-system pingo ice, Adventdalen, Spitsbergen. *Permafrost and Periglacial Processes* 4: 327–334.
- Yoshikawa, K. 2008. Stable-isotope composition of ice-cored mounds. *NICOP 2008: Proceedings of the Ninth International Conference on Permafrost*. D.L. Kane, K.M. Hinkel (eds.). Institute of Northern Engineering, University of Alaska Fairbanks, 2:1997-2002.

Thermal Evidence of Recent Talik Formation in Ritigraben Rock Glacier: Swiss Alps

Evelyn Zenklusen Mutter, Marcia Phillips
WSL-Institute for Snow and Avalanche Research SLF, Switzerland

Abstract

Borehole temperatures from Ritigraben rock glacier in the western Swiss Alps indicate the presence of a seasonal positive thermal anomaly at 12 to 13 m depth from summer 2007 onwards. The thermal characteristics of this talik are investigated and the origins of the water flowing within the permafrost discussed. It is shown that there is a direct link between snow melt and/or precipitation and temperature fluctuations within the talik, suggesting the presence of an open channel system within the rock glacier.

Keywords: borehole temperatures; mountain permafrost; rock glacier; Swiss Alps; talik formation; thermal orbits.

Introduction

Permafrost degradation is becoming an increasingly common state of affairs in alpine mountain permafrost regions (Haerberli et al. 2010), and evidence of thermal changes visible at the ground surface include the occurrence of mass movements such as rock fall and debris flows, accelerating creep rates, the formation of thermokarst depressions or sinkholes, and in some cases damage to mountain infrastructure (Harris et al. 2009). Investigating the subsurface processes leading to such phenomena requires either the use of geophysical methods (Hilbich 2010, Hauck et al. 2011) or, for direct evidence, borehole investigations (Zenklusen Mutter et al. 2010) and ideally a combination of both (Arenson et al. 2010).

Evidence of taliks reported from rock glaciers in alpine permafrost indicates that they are caused by lateral water fluxes within the permafrost (e.g., Vonder Mühl 1992, Arenson et al. 2010, Lugon & Stoffel 2010). Flowing water may cause internal permafrost degradation, sudden deformations, and slumping (Arenson et al. 2010). The origins of the water are difficult to determine due to the complexity of the substrate. The same authors propose two types of intra-permafrost water: melt water run-off and constant ground water flow. Arenson et al. (2002) showed that shear horizons in rock glaciers can coincide with water-bearing layers, and Kääb et al. (2007) underline the importance of investigating shear horizons in order to understand rock glacier dynamics and their response to temperature changes.

This paper focuses on the Ritigraben rock glacier in the western Swiss Alps. Borehole temperature data point towards the seasonal formation of intra-permafrost taliks due to lateral water flow. Here we identify the nature of the thermal anomalies using simple phase-space plots (so-called thermal orbits) (Beltrami 1996) and determine the probable origins of the intra-permafrost water using meteorological data measured on-site.

Site Description and Measurement Method

The active, ice-rich Ritigraben rock glacier is located in the Matter valley (Western Swiss Alps) above Grächen in canton Valais (Fig. 1) and covers approximately 1.4 km².

The borehole site (46°12'N, 7°54'E) is in gently sloping terrain, and the surface cover consists of plurimetric boulders with a maximum size of several cubic meters (Fig. 1). The 30-m tubed borehole was drilled near the rock glacier tongue at 2690 m a.s.l. in 2002 and equipped with 30 YSI 44006 thermistors with a precision of $\pm 0.02^{\circ}\text{C}$ (Herz et al. 2003). The depths of the thermistors are indicated in Figure 2. Drilling logs from other boreholes within a radius of 100 m indicated the presence of water at various depths within the rock glacier



Figure 1. (Top) Map with the location of the rock glacier site Ritigraben (circle) and the IMIS meteorological station Saas Seetal (star). (Bottom) Photograph of the rock glacier Ritigraben (provided by H. Gubler).

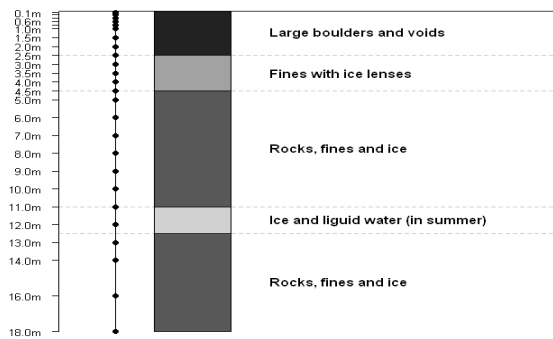


Figure 2. Schematic borehole stratigraphy and depths at which the thermistors are located. Additional thermistors between 0.1 and 1 m, which are not visible on the graph: 0.2, 0.4, and 0.8 m.

(Lugon & Stoffel 2010). The borehole presented here is gradually being sheared off, leading to the loss of thermistors from the base upwards. This is in agreement with borehole deformation data indicating the presence of shearing horizons at 18 to 24 m depth in a nearby borehole (Lugon & Stoffel 2010).

The blocky nature of the ground surface and the approximate borehole stratigraphy showing the most important layers are shown in Figure 2, based on information from Herz et al. (2003) and Lugon & Stoffel (2010).

The borehole site is equipped with a meteorological station. Daily air temperature, snow depth, and precipitation data are used in this study. As the snow depth values have large gaps, we also use snow depth data from the nearby IMIS meteorological station Saas Seetal, which is 2.3 km east of Ritigraben, at 2480 m a.s.l. and on the eastern flank of the mountain (see Fig. 1). Although snow depths are not always comparable, the timing of snow onset and snow melt coincides well with the Ritigraben station (see Fig. 5c).

As Ritigraben rock glacier is located at the head of the steep Ritigraben torrent with a history of debris flows (e.g., Lugon & Stoffel 2010, Stoffel 2010) and above an inhabited area, its activity and the potential risks have been the focus of previous studies (e.g., Stoffel et al. 2005, Stoffel et al. 2008) and they continue to be monitored in detail.

Results and Discussion

Borehole temperatures

Borehole temperature data measured between 2005 and 2011 in the Ritigraben borehole are depicted in the contour plot in Figure 3 (previous data were not available). Active layer depth remains constant at around 4 m. Below, the ground is permanently frozen to a depth of 30 m. However, in summer 2007 an unfrozen zone appeared between 12 and 13 m depth. Subsequently, this talik reformed every summer between June and October with varying duration and thickness.

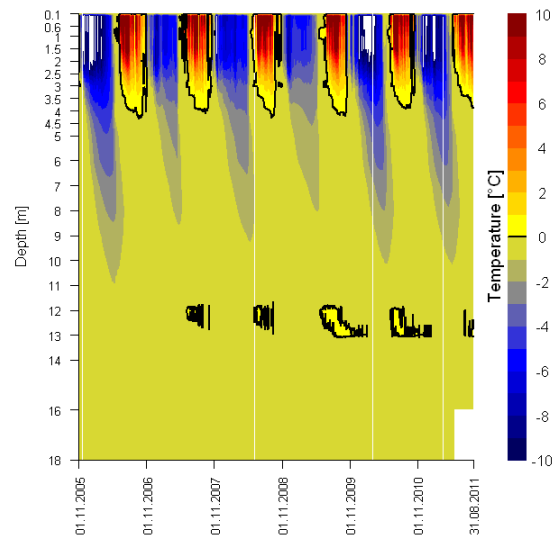


Figure 3. Contour plot showing Ritigraben borehole temperatures measured between 2005 and 2011 between 0.1 and 18 m depth. Thermistor depths are indicated on the y axis. The black line represents the 0°C isotherm. Lack of data below 18 and 16 m is due to thermistor failure caused by borehole shearing from the base upwards.

Types of heat transfer

To determine the type of heat transfer dominating at different depths, we plot the daily ground temperatures measured by neighboring thermistors against each other (Fig. 4 a-d) for each year. This is a semi-quantitative approach to distinguish between conductive and non-conductive heat transfer (Beltrami 1996).

Ground temperatures undergo sinusoidal oscillations with a period of approximately one year. The amplitudes of these temperature series are attenuated and phase shifted with depth. In a purely conductive regime, the superposition of two such temperature series results in a characteristic elliptical pattern (Smerdon et al. 2009). The characteristics of thermal orbits can be distorted by phase changes and daily temperature variability, particularly in near-surface layers (Smerdon et al. 2009).

Four different types of thermal regimes could be identified in the Ritigraben borehole, and one example of each is shown. Thermal orbits from 0.2 to 1.5 m depth (Fig. 4a) show a practically linear relation, indicating a phase lag close to zero. This is due to the fact that the thermistors are located in a very large dry boulder exempt of a phase change surrounded by voids where advection dominates (Herz et al. 2003) and that the spacing between the thermistors is small.

Between 1.5 and 4.5 m, within the active layer, grain sizes are much finer and phase changes occur. This results in 'butterfly' shaped contour plots (e.g., Fig. 4b) with a clearly visible zero-curtain. The irregularities of the plot are typically the result of phase changes (Beltrami 1996), and the biased orientation of the orbits is induced by temperature amplitude damping with depth (Smerdon et al. 2009).

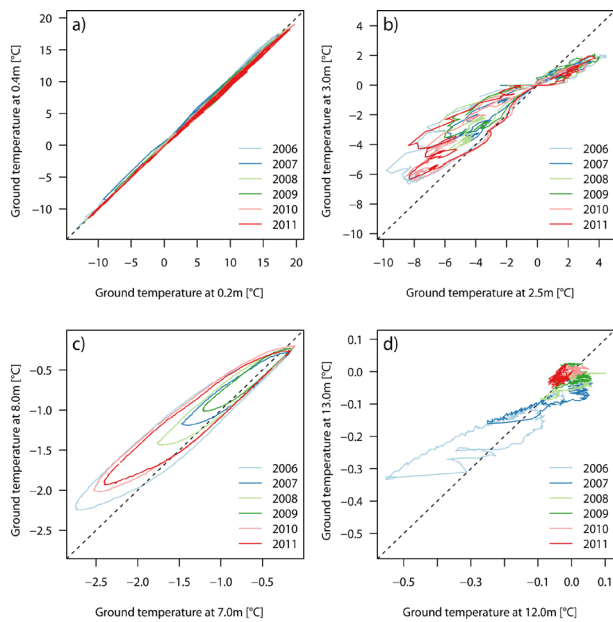


Figure 4. Thermal orbits for daily borehole temperatures measured at 0.2 and 0.4 m (a), 2.5 and 3 m (b), 7 and 8 m (c), and 12 and 13 m depth. Each hydrological year is depicted using a different color (see legend).

Thermal orbits between 4.5 and 10 m are regularly shaped ellipses (Fig. 4c), pointing towards purely conductive heat transfer at these depths. The dimensions of the ellipses and the positions of their centers strongly depend on ground temperature, which is influenced by the insulating effect of the snow cover in winter.

The thermal orbits at 12–13 m have no elliptic geometry, indicating non-conductive heat transfer (Fig. 4d). The orbits decrease in size with time, showing a warming tendency. From 2007 onwards, temperatures just above 0°C are visible, confirming the formation of a talik. Below 13 m (thermal orbits not shown here), the annual temperature variations are very small, but a gradual warming is also visible here (Fig. 5a).

Talik formation

The talik at 12–13 m depth was first registered in 2007, and its subsequent appearance is restricted to the period between June and October. The phenomenon may have occurred prior to the onset of the borehole measurements in 2002 (not available here). There is no mention of a talik between 2002 and 2005 in the existing literature according to Lugin & Stoffel (2010).

During the occurrence of the talik, ground temperatures at 12–13 m depth fluctuate between 0 and 0.08°C. The phenomenon is a lateral thermal disturbance which could be induced by air or water fluxes within the permafrost body. The small range of the temperature fluctuations just above 0°C points towards the presence of water and ice in close proximity. Furthermore, liquid water was observed during drilling of nearby boreholes (Lugin & Stoffel 2010). Air fluxes would likely show larger fluctuations and not necessarily remain so close to and above 0°C (see, e.g., Phillips et al. 2009).

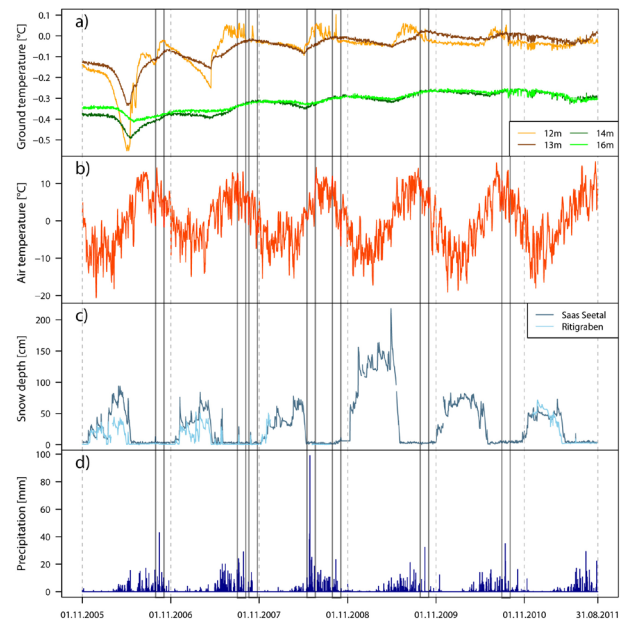


Figure 5. Daily time series plots depicting ground temperature at depths 12–16 m (a), air temperatures (b), snow depth (c), and precipitation (d) for the study site Ritigraben. Grey rectangles encompass precipitation events coinciding with ground temperature increases at 12 m depth.

In order to determine the origin of the thermal anomaly, daily air temperature, snow depth, and precipitation have been analyzed and compared with the ground temperatures (Fig. 5). These show that the establishment of the talik always coincides with the beginning of the main snow melt period in spring, indicating that snow melt is the trigger. In addition there is an evident link between summer precipitation and ground temperatures at 12 m depth. Interestingly, precipitation peaks coincide with positive peaks in temperature at 12 m (see Figure 5, examples highlighted in grey rectangles).

The rapid reaction time (diurnal scale) and distinct temperature peaks at this depth point towards the presence of a well-developed open drainage channel within the rock glacier rather than to the presence of a filled water channel such as that described by Arenson et al. (2010). It is possible that an open drainage channel may not have existed prior to 2007 at this particular location in the rock glacier. If so, it is not clear why the talik did not occur before 2007 yet did so thereafter. One possible explanation is that precipitation in the region (measured at the MeteoSwiss weather station in Grächen, 2.5 km NW of the rock glacier) was particularly high in 2007, following four dry summers, including the hot summer 2003. These circumstances may have paved the way for water infiltration into the rock glacier.

Kääb et al. (2007) note that the presence of water in rock glaciers close to the melting point may play a prominent role in inducing significant rock glacier acceleration. Stoffel et al. (2011) also mention that the destabilization of rock glaciers can result in the delivery of large quantities of sediment into debris flow channels such as the Ritigraben torrent. The presence of a water-bearing talik within Ritigraben rock glacier at 12–13

m depth may indicate the existence of a shear horizon similar to that observed at 18 m depth in a nearby borehole (Lugon & Stoffel 2010). This is corroborated by the successive bottom-up failure of the thermistors discussed here.

Conclusions and Outlook

Seasonal talik formation has been observed at 12–13 m depth in Ritigraben rock glacier since 2007 and results from a laterally induced thermal anomaly. Analysis of phase-space plots indicates that non-conductive heat transfer dominates at this depth, with skewed and chaotic thermal orbits. The nature of the thermal regime points towards the presence of water flowing through the permafrost body. Evidence supporting this exists in nearby boreholes, where water was observed during drilling. Temperature fluctuations at 12–13 m depth in summer coincide with snow melt and/or precipitation events, suggesting the presence of an open channel drainage system.

The results underline the importance of long-term borehole monitoring in combination with in situ meteorological measurements. In view of the presence of water within the warm rock glacier and the potential for rapid acceleration of creep rates, it is advisable to continue monitoring the deformation velocities at this site.

It is not known how long the borehole measurements will continue to be possible due to gradual destruction of the thermistor chain. It is important to note that the combination of creeping permafrost and ground water causes damage to borehole tubing and that thermistors may be exposed to mechanical stress caused by water infiltration or shearing substrates. This may cause sensor drift or other technical problems. It is therefore essential to verify such data very carefully.

In a next step, spectral- and diffusivity analyses will be used to further investigate the types of heat transfer occurring within the rock glacier at different times of year. Numerical modeling would allow us to simulate talik development and to evaluate the importance of positive feedback but would be challenging due to the three-dimensional nature of the phenomenon.

Acknowledgments

The Ritigraben borehole is part of the SLF permafrost network and PERMOS and was drilled by Canton Valais and the University of Giessen, Germany. Canton Valais and, in particular, Charly Wuilloud are thanked for their ongoing support. The authors warmly thank Hansueli Gubler (Alpug) for his valuable technical know-how and for the reliable instrumentation of the site. Christoph Marty and Michael Lehning are thanked for their constructive comments on the manuscript.

References

- Arenson, L., Hoelzle, M., & Springman, S. 2002. Borehole deformation measurements and internal structure of some rock glaciers in Switzerland. *Permafrost and Periglacial Processes* 13: 117-135.
- Arenson, L.U., Hauck, C., Hilbich, C., Seward, L., Yamamoto, Y., & Springman, S. 2010. Sub-surface heterogeneities in the Murtèl-Corvatsch rock glacier, Switzerland. *Proceedings Geo 2010*, Calgary Alberta, 1494-1500.
- Beltrami, H. 1996. Active layer distortion of annual air/soil thermal orbits. *Permafrost and Periglacial Processes* 7: 101-110.
- Delaloye, R., Lambiel, C., Lugon, R., Raetzo, H., & Strozzi, T. 2006. ERS InSAR for detecting slope movement in a periglacial mountain environment (western Valais Alps, Switzerland). *Proceedings 9th International symposium on High Mountain Remote Sensing Cartography (HMRSC-IX)*, Graz, Austria. Sept. 14–15.
- Haeberli, W., Noetzli, J., Arenson, L., Delaloye, R., Gärtner-Roer, I., Gruber, S., Isaksen, K., Kneisel, C., Krautblatter, M., & Phillips, M. 2010. Mountain permafrost: development and challenges of a young research field. *Journal of Glaciology* 56 (200): 1043-1058.
- Harris, C., Arenson, L.U., Christiansen, H.H., Etzelmüller, B., Frauenfelder, R., Gruber, S., Haeberli, W., Hauck, C., Hoelzle, M., Humlum, O., Isaksen, K., Käab, A., Kern-Lütschg, M.A, Lehning, M., Matsuoka, N., Murton, J.B., Nötzli, J., Phillips, M., Ross, N., Seppälä, M., Springman, S.M., & Vonder Mühll, D. 2009. Permafrost and climate in Europe: Monitoring and modelling thermal, geomorphological and geotechnical responses. *Earth-Science Reviews* 92: 117-171.
- Hauck, C., Böttcher, M., & Maurer, H. 2011. A new model for estimating subsurface ice content based on combined electrical and seismic data sets. *The Cryosphere* 5: 453–468.
- Herz, T., King, L., & Gubler, H. 2003. Microclimate within coarse debris of talus slopes in the alpine periglacial belt and its effect on permafrost. *Proceedings of the 8th International Conference on Permafrost*, Zürich 2003. Eds. Phillips, Springman & Arenson, 383-387.
- Hilbich, C. 2010. Time-lapse refraction seismic tomography for the detection of ground ice degradation. *The Cryosphere* 4: 243–259.
- Käab, A., Frauenfelder, R., & Roer, I. 2007. On the response of rockglacier creep to surface temperature increase. *Global and Planetary Change* 56: 172-187.
- Lugon, R. & Stoffel, M. 2010. Rock-glacier dynamics and magnitude-frequency relations of debris flows in a high-elevation watershed: Ritigraben, Swiss Alps. *Global and Planetary Change* 73: 202-210.
- Phillips, M., Zenklusen Mutter, E., Kern-Luetschg, M., & Lehning, M. 2009. Rapid Degradation of Ground Ice in a Ventilated Talus Slope: Flüela Pass, Swiss Alps. *Permafrost and Periglacial Processes* 20: 1-14.

- Stoffel, M., Lièvre I., Conus, D., Grichting, M.A., Raetzo, H., Gärtner, H.W., & Monbaron, M. 2005. 400 Years of Debris-Flow Activity and Triggering Weather Conditions: Ritigraben, Valais, Switzerland. *Arctic, Antarctic, and Alpine Research* 37 (3): 387-395.
- Stoffel, M., Conus, D., Grichting, M.A., Lièvre, I., & Maître G. 2008. Unraveling the patterns of late Holocene debris-flow activity on a cone in the Swiss Alps: Chronology, environment and implications for the future. *Global and Planetary Change* 60: 222-234.
- Stoffel, M. 2010. Magnitude-frequency relationships of debris flows - a case study based on field surveys and tree-ring records. *Geomorphology* 116: 67-76.
- Stoffel, M., Bollschweiler, M., & Beniston, M. 2011. Rainfall characteristics for periglacial debris flows in the Swiss Alps: past incidences-potential future evolutions. *Climatic Change* 105: 263-280.
- Smerdon, J.E., Beltrami, H., Creelman, C., & Stevens, M.B. 2009. Characterizing land surface processes: a quantitative analysis using air-ground thermal orbits. *Journal of Geophysical Research* 114 (D15102), 11p.
- Vonder Mühl, D.S. 1992. Short Communication: Evidence of Intrapermafrost Groundwater Flow beneath an Active Rock Glacier in the Swiss Alps. *Permafrost and Periglacial Processes* 3: 169-173.
- Zenklusen Mutter, E., Blanchet, J., & Phillips, M. 2010. Analysis of ground temperature trends in Alpine permafrost using generalized least squares. *Journal of Geophysical Research* 115 (F04009), 12 pp.

Variability of Soil Organic Carbon Stocks of Different Permafrost-Affected Soils: Initial Results from a North-South Transect in Siberia

Sebastian Zubrzycki, Lars Kutzbach, Eva-Maria Pfeiffer
Institute of Soil Science, KlimaCampus, University of Hamburg, Hamburg, Germany

Polina Vakhrameeva
Arctic and Antarctic Research Institute, St. Petersburg, Russia

Abstract

Twelve sites within a north-south climatological transect in Siberia were investigated to classify the soils and to determine their soil organic carbon stocks in the top 30 cm of the active layer ($S_{\text{SOC-30}}$). There was a distinct arrangement into three groups of increasing $S_{\text{SOC-30}}$ along the transect with decreasing latitude. The greatest $S_{\text{SOC-30}}$ with mean values of $24 \pm 9 \text{ kg m}^{-2}$, were identified for the southern group of forest tundra and taiga sites on the ancient Central Siberian Plateau. The soils of the sand-dominated northwestern part of the Lena River Delta, the second river terrace, had a $S_{\text{SOC-30}}$ of only $4 \pm 2 \text{ kg m}^{-2}$, whereas the delta's third and first river terraces stored on average $12 \pm 3 \text{ kg m}^{-2}$ in the top 30 cm of the active layer. The climatological gradient with changing vegetation productivity and different parent materials result in varying pedogenetic processes and were identified as key controls on the soil organic carbon stocks.

Keywords: climate change; gelisols; permafrost-affected soils; Siberia; soil organic carbon stock.

Introduction

According to climate change projections for the Arctic, organic carbon deposits in permafrost regions are likely to become a future source of atmospheric carbon because of increased active-layer depths. Changed hydrological conditions (Koven et al. 2011) will lead to increased carbon dioxide and methane release from permafrost-affected soils (Dutta et al. 2006, Wagner et al. 2007, Khvorostyanov et al. 2008, Schuur et al. 2009). It is estimated that the carbon pool of permafrost-affected soils accounts for 15 to 50% of the global soil organic carbon pool (Post et al. 1982, Zimov et al. 2006, Ping et al. 2008, Tarnocai et al. 2009, McGuire et al. 2009). These soils—principally Gelisols / Cryosols (with respect to either the US Soil Taxonomy by Soil Survey Staff [2010] or the WRB classification by the Food and Agriculture Organization [2006])—cover 27% of the terrestrial surface in the territories above 50°N (Jones et al. 2010). A significant amount of this carbon is currently frozen and excluded from intensive interactions with the atmospheric biogeochemical cycles.

Quantitative knowledge of the soil organic carbon pool is still poor, with particularly high uncertainties for cold regions of Russia (Tarnocai et al. 2009). During an expedition to Yakutia in August 2009, initial investigations of several soil pedons were carried out along a north-south climatological gradient (Fig. 1). This expedition produced a first description of permafrost-affected soils in this rarely investigated region of Siberia (Klemm & Zubrzycki 2009). The study quantified the soil organic carbon stock in the top 30 cm of the active layer ($S_{\text{SOC-30}}$) within different vegetation zones from arctic tundra in the North to northern taiga in the South. The northernmost site, 10LD1 (Fig. 1), was investigated in 2010. The key objective of this paper is to report the magnitude of top soil organic carbon stocks and to analyze their spatial variability along a transect in a remote Northeast Siberian permafrost-affected region as a basis for more detailed investigations in the future.

Investigation Area

The study sites are located along a north-south transect (73.5° to 69.5°N) on the western side of the Lena River (Fig. 1). These selected sites cover the main geomorphological units of the investigated area along the transect. In the Lena River Delta, investigations were carried out on Arga Island in the northwest (73.5°N) (field IDs 10LD1, Tik01), on Hardang-Sise Island in the west (Tik04), and in the central part of the delta on Samoylov Island (Tik22) and Sardakh Island (Tik21).

One site was on Tit-Ari Island (Tik20), which is located in the main Lena River channel southeast of the delta. It is one of the northernmost places on the tree-limit line in the Russian Arctic.

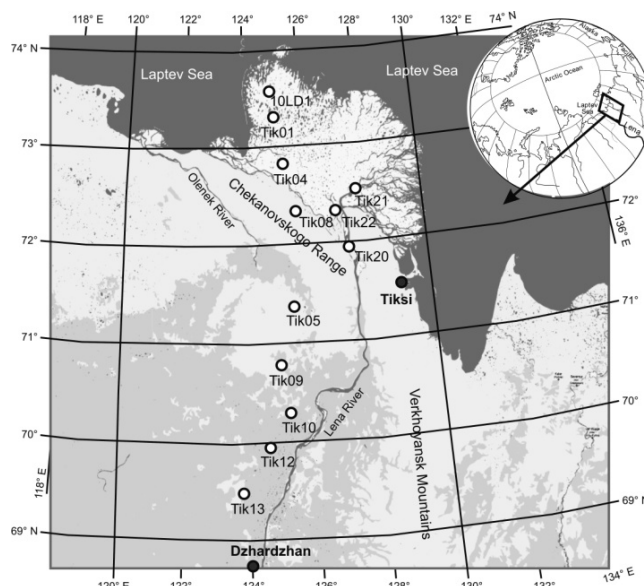


Figure 1. Map of the investigation area in northeast Siberia with locations of study sites. White: delta area (non-forested), light grey: non-forested non-delta area, grey: forested non-delta area. Map based on Google & Geocentre Consulting 2011.

We continued this transect at the north slope of the Chekanovskogo Range, where one site was located near Lake Byluynng-Kyuel' (Tik08). The transect then followed the Lena River to the south (69.5°N), staying on the western side of both the river and the Verkhoyansk Mountains (Tik05, Tik09, Tik10, Tik12, Tik13).

Samoylov Island is a part of the Lena River Delta and consists of a relatively young floodplain (0–4 m a.s.r.l. [above summer river level]) and a higher-elevated river terrace (up to 12 m a.s.r.l.) of Late Holocene age (Akhmadeeva et al. 1999). This higher-elevated part is termed first terrace (Pavlova & Dorozhkina 1999) and has flooded only during extreme high water events (Schwamborn et al. 2002, Kutzbach 2006). Arga Island dominates the northwestern part of the Lena River Delta. Its deep deposits are older than 50 kyr (Schirrmeyer et al. 2011). This island, also referred to as second terrace, is fluvial sand-dominated (10–30 m a.s.r.l.). The areas of Hardang-Sise Island and Sardakh Island belong to the third river terrace complex (up to 55 m a.s.r.l.) of the Lena River Delta. The third terrace is the oldest terrace in the delta (Grigoriev 1993). It was formed in the Middle and Late Pleistocene (Schwamborn et al. 2002, Kuzmina et al. 2003). Generally, this terrace forms autonomous islands along the Olenyokskaya and Bykovskaya channels. Hardang-Sise Island with Lake Mutnoe is located in the eastern part of Olenyokskaya Channel. Sardakh Island represents a relic of the oldest terrace within the recent delta terrace and is located in the southern part of the Trofimovskaya Channel (Grigoriev 1993). The region surrounding the investigated El'gene-Kyuele Lake on the north slope of the Chekanovskogo Range belongs to the Eurasian landmass but represents a transition zone between the Lena River Delta and the mainland. The landscape is characterized by rivers draining the mountain ridge and discharging to the northeast into the Olenyokskaya Channel. The remaining southern sites belong to the eastern part of the ancient plain Central Siberian Plateau and are characterized by a continuous change of vegetation type. Pronounced visible differences in vegetation cover can be observed around 70°N. This transitional zone, classified as forest tundra, contains a continuous gradation from tundra to northern taiga with more and more wooded patches up to densely wooded areas at the southernmost point at Sysy-Kyuele Lake (Tik13).

All investigation sites along the transect are dominated by an arctic-subarctic climate with continental influence and are characterized by low temperatures and low precipitation. The mean annual air temperatures, measured at the climate reference sites in Tiksi (71°41'N, 128°42'E) and Dzhardzhan (68°49'N, 123°59'E) were -13.5°C and -12.4°C, respectively, and the mean annual precipitation was 323 mm and 298 mm, respectively (Fig. 2). The average temperatures of the warmest months in Tiksi (August) and Dzhardzhan (June) were 7.1°C and 14.9°C, respectively (Roshydromet 2011, Russia's Weather Server 2011).

The average temperature and precipitation of both reference climate stations are similar (Fig. 2), but the temperature amplitude is higher at the Dzhardzhan station. The strong continental climate enables longer and warmer summers in the south.

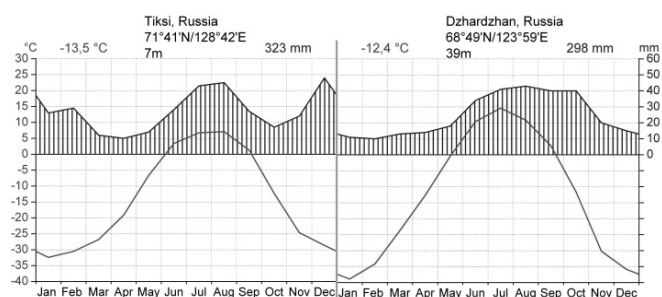


Figure 2. Climate charts for the climate reference sites: Tiksi and Dzhardzhan. Based on data by Roshydromet (Tiksi 1961–1990) and Russia's Weather Server (Dzhardzhan 1998–2011).

This fact, and the different precipitation patterns with more rain during the growing season, favors more intensive development of soils and more productive vegetation in the south.

Materials and Methods

All investigated soil subgroups were classified according to the US Soil Taxonomy (Soil Survey Staff 2010). Based on the classification system for permafrost soils of Yakutia by Yelovskaya (1987), we determined the soil subtypes for a comparison with Russian literature. Disturbed soil samples (in plastic bags) and undisturbed soil samples (in containers with a volume of 100 cm³) were collected from each soil horizon down to the surface of the frozen ground at the date of sampling. Pedological descriptions of the full soil pits including Munsell soil color, fresh weight, texture, fabric, organic substance, roots and hydromorphic features were performed manually in the field. In Germany, these soil samples were analyzed for acidity (pH) and electrical conductivity (CG820, Schott Geraete GmbH, Germany; Cond 330i, WTW, Germany), gravimetric contents of organic carbon (C_{org}) and nitrogen (N) (Vario MAX CNS, Elementar Analysensysteme GmbH, Germany), and texture of the <2 mm fraction (Sedimat 4-12, UGT, Germany). The bulk density (BD) was calculated as the ratio of the dry mass of an undisturbed soil sample and the volume of the soil sample container.

The soil organic carbon stock per horizon and area $S_{\text{SOC-H}}$ (kg m⁻²) was calculated using the formula

$$S_{\text{SOC-H}} = C \times BD \times d \quad (1)$$

where C is the gravimetric organic carbon content, BD is the bulk density, and d is the thickness of the soil horizon.

The top soil organic carbon stock $S_{\text{SOC-30}}$ (kg m⁻²), defined as the organic carbon mass within the top 30 cm from the soil surface per area, was calculated as

$$S_{\text{SOC-30}} = \int_{0\text{cm}}^{30\text{cm}} C \times BD \, dh \quad (2)$$

where h is soil depth. A depth of 30 cm was the average thaw depth of the investigated sites. Thus the $S_{\text{SOC-30}}$ can be considered as approximately representative of the soil organic carbon stock in the present-day active layer.

Table 1. Classification and properties of dominant soil subtypes at investigated sites. Site identifier with the number of soil pits in parentheses, Soil Subgroup (Soil Survey Staff 2010), Soil Subtype (Yelovskaya 1987), Soil Organic Carbon content for the top soil down to 30 cm ($S_{\text{SOC-30}}$), C/N-ratio, Bulk Density (BD), Active Layer depth and the respective standard deviations.

| Site ID (n) | Soil Subgroup | Soil Subtype | $S_{\text{SOC-30}}$ kg m ⁻² | C/N ratio | BD g cm ⁻³ | Active Layer depth cm |
|-------------|--------------------------|-------------------------------------|--|-------------|-----------------------|-----------------------|
| 10LD1 (1) | Psammentic Aquiturbel | Permafrost alluvial turfy typical | 5.4 | 15.4 ± 1.7 | 1.19 ± 0.27 | 52.0 |
| Tik01 (6) | Typic Psammenturbel | Permafrost alluvial primitive sandy | 2.9 | 19.1 ± 4.1 | 1.03 ± 0.56 | 35.0 ± 13.6 |
| Tik04 (1) | Folistic Haplorthel | Permafrost turfness-gley | 12.1 | 13.5 ± 1.5 | 1.06 ± 0.20 | 39.0 |
| Tik21 (1) | Typic Aquorthel | Permafrost silty-peat-gley | 12.4 | 16.5 ± 0.1 | 1.11 ± 0.67 | 24.0 |
| Tik22 (2) | Glacic Aquiturbel | Permafrost peatish-gley | 10.9 | 26.4 ± 11.0 | 1.07 ± 0.42 | 37.0 ± 7.1 |
| Tik08 (2) | Ruptic Historthel | Permafrost peatish | 17.2 | 18.0 ± 1.4 | 0.64 ± 0.49 | 21.5 ± 5.0 |
| Tik20 (1) | Typic Aquiturbel | Permafrost peatish-gley typical | 9.3 | 18.0 ± 3.9 | 1.33 ± 0.72 | 30.0 |
| Tik05 (2) | Ruptic Historthel | Permafrost peat | 32.7 | 22.5 ± 0.2 | 1.03 ± 0.10 | 26.5 ± 3.5 |
| Tik09 (2) | Ruptic-Histic Aquiturbel | Permafrost peat-gley | 27.5 | 25.8 ± 11.5 | 0.32 ± 0.42 | 22.5 ± 3.5 |
| Tik10 (1) | Typic Histoturbels | Permafrost peatish-gleyic | 23.2 | 22.7 ± 8.5 | 0.34 ± 0.33 | 19.0 |
| Tik12 (1) | Fluvaquentic Historthel | Permafrost peat | 27.3 | 26.2 ± 4.4 | 0.18 ± 0.11 | 30.0 |
| Tik13 (1) | Typic Haplorthel | Cryogenic soil | 10.3 | 24.4 ± 5.8 | 1.01 ± 0.63 | 49.0 |

We analyzed the $S_{\text{SOC-H}}$ of all single horizon types (equation 1) and then calculated their contribution to the $S_{\text{SOC-30}}$ for each pedon (cS_{H}) with

$$cS_{\text{H}} = \frac{\sum_{i=0}^{n_{\text{H}}} S_{\text{SOC-H},i}}{S_{\text{SOC-30}}} \quad (3)$$

where the index H indicates the horizon type: A, B, Oi, or Oe, and n_{H} is the number of horizons of a specific type per pedon up to the 30 cm depth. Then the cS_{H} for each horizon type was averaged over all investigated pedons. An additional calculation following equation 3 was conducted where a specific horizon type was not considered, but instead the group of all cryoturbated horizons. Correlation analyses on latitude and $S_{\text{SOC-30}}$ were done using SPSS Package, version 16.0.1.

Results

We classified all soils along the transect as Gelisols (Soil Survey Staff 2010). With respect to the soil classification by Yelovskaya (1987), the investigated soils belong to the Permafrost type (see also Desyatkin et al. 1991, Pfeiffer et al. 2000) with the exception of the southernmost one. The soil at Tik13 is a Cryogenic soil. The results of the classification and the physical and chemical soil analyses are summarized by only one representative soil subgroup per site (Table 1). The representative soils dominating the twelve transect sites were six Turbels and six Orthels; no Histels were identified. The maximum depth to frozen ground was found to be 57 cm from the surface (min. 18 cm, mean 30 cm, standard deviation 10 cm).

The main landscape unit of Arga Island is covered by sparse vegetation, mainly lichens, mosses and *Carex*-species and is dominated by Psammenturbels and Psammorthels without any rock fragments and with sandy texture within the particle-size control section.

The genesis of these permafrost-affected soils is dominated by the accumulation of fluvial sediments and their dislocation and retransportation by wind. Very often they are cryoturbated

The main landscape units of the Holocene first as well as the Pleistocene third terrace are covered mainly by vegetation with species like *Carex aquatilis*, *Dryas punctata*, *Astragalus umbellatus*. These soils developed as soil complexes which consist of cryoturbated and ice-rich Aquiturbels, and very wet and organic-rich Historthels (Pfeiffer et al. 2002, Fiedler et al. 2004, Kutzbach et al. 2004, Sanders et al. 2010). The Historthels formed in the centers of low-centered polygons, which are depressed, water-saturated, and characterized by high accumulation of organic matter due to anaerobic soil conditions. Aquiturbels, which formed at the elevated borders, have gleyic properties and prominent cryoturbation (see Pfeiffer et al. 2002, Fiedler et al. 2004, Kutzbach et al. 2004, Sanders et al. 2010).

Going southward to the continental hinterland of the Lena River Delta, the soils are still dominated by polygonal patterned ground and contain soil complexes of organic-rich Orthels within the polygon centers and Turbels on the borders. Generally, these soils are drier than those from the delta region due to a different cover of densely rooted vegetation (e.g., *Larix sibirica* L). The soil at the southernmost site differs in profile composition (cambic horizon) and soil structure from the other soils of the Central Siberian Plateau investigated in this study.

The mean BD, C/N ratios, and $S_{\text{SOC-30}}$ (0–30 cm depth) calculated for the investigated sites along the north-south transect are given in Table 1.

Disregarding the southernmost site, which is different in genesis, we found a distinct increase in $S_{\text{SOC-30}}$ following the transect from north to south. The Pearson product-moment correlation coefficient for the relationship between latitude and $S_{\text{SOC-30}}$ was $R = 0.85$.

The highest calculated $S_{\text{SOC-30}}$ was found at the site Tik05 at the El'gene-Kyuele Lake at 71.3°N and amounted to 32.65 kg m⁻².

The lowest stock of 2.85 kg m⁻² was found on Arga Island at the second northernmost site (Tik01). The mean S_{SOC-30} of the sites amounted to 15.9 kg m⁻² ± 9.6 kg m⁻². The C/N ratios, which are regarded as indicators of the decomposability of soil organic matter (van Cleve 1974), varied from 10.4 to 51.4 when every single horizon was considered. Averaged over the soil pedons, they ranged from 13.5 to 26.4 (Table 1). Low ratios were found mainly for A (Ø: 18.1±5.2) and sandy B horizons (Ø: 18.7±6.4), whereas water-saturated O horizons were characterized by higher ratios (Oe Ø: 21.8±5.4, Oi Ø 27.3±9.9).

Considering the S_{SOC-H} and taking into account the high variability of C_{org} contents and BD of the different horizons in the same soil pedon, a closer inspection of single horizon types appears interesting. The highest C_{org} contents are found in the Oi and Oe horizons with 35 to 50% and 6 to 45%, respectively (Table 2). Generally, an Oi horizon is characterized by a high fiber content and low SOM decomposition. The Oe horizons show intermediate SOM decomposition with fiber contents of 17 to 40% after rubbing (Soil Survey Staff 2010). Conversely, due to the high fiber content, these O horizons had low BD values of 0.03 g cm⁻³ to 0.27 g cm⁻³ and 0.12 g cm⁻³ to 0.92 g cm⁻³ for Oi and Oe, respectively (table 2).

The A horizons formed at the surface or beneath an O horizon and consisted of organic matter and sandy sediments (mean sand content 77%). The high sand content led to relatively high average BD values of 0.79 g cm⁻³. These horizons showed moderate C_{org} contents of on average 9.5% with a maximum of 17.7%. The investigated B horizons had the lowest C_{org} contents (on average 4.1%) varying from 0.2% to 17%, and had a relatively high mean BD of 1.33 g cm⁻³. The moderate C_{org} content of 7.1% and the high bulk density of horizons showing cryoturbation result in high S_{SOC-H}, which ranges between those of the Oe and A horizons.

Regarding the number of analyzed horizons, their mean S_{SOC-H} and their mean thickness, it became clear that the Oe horizons had the highest overall contribution to the summed S_{SOC-30} of all investigated soils within the transect (50% ± 6.41%), followed by the organic matter-poor B horizons (36% ± 5.29%). The Oi horizons showed a low overall contribution of 9% ± 3.29% and were undercut only by the A horizons (5% ± 1.90%).

Discussion and Conclusions

The point data of the preliminary exploration presented in this paper give a first impression of the high stocks of organic carbon in the permafrost-affected soils of northern Yakutia. Disregarding the low number of investigated pedons and the uncertainty involved, the results are in the range of comparable studies on permafrost-affected soils recently published (Kuhry et al. 2002, Ping et al. 2008, Hugelius & Kuhry 2009). Due to our limited database, as well as the high natural soil heterogeneity and variability, we decided neither to prescribe any spatial distribution to our data nor to upscale to any large soil map unit.

Nevertheless, the presented data indicate that the North-Siberian permafrost-affected regions are rich in soil organic

Table 2. Average properties of different horizons in sampled permafrost-affected soils. Horizon identifier with sample numbers in parentheses, mean C_{org} content, mean BD, mean S_{SOC-H} per horizon thickness d, mean horizon thickness, and the respective standard deviations. **turb* = cryoturbated horizons.

| Horizon (n) | C _{org} % | BD g cm ⁻³ | S _{SOC-H} / d kg m ⁻² cm ⁻¹ | Thickness cm |
|--------------------|--------------------|-----------------------|--|--------------|
| Oi (6) | 43.9±5.9 | 0.11±0.08 | 0.48±0.31 | 6.2±2.93 |
| Oe (13) | 26.7±15.5 | 0.39±0.21 | 0.86±0.51 | 9.3±4.05 |
| A (3) | 9.5±7.7 | 0.79±0.44 | 0.52±0.25 | 6.7±0.58 |
| B (13) | 4.1±5.1 | 1.33±0.38 | 0.39±0.31 | 14.6±5.72 |
| <i>turb</i> * (10) | 7.1±5.9 | 1.08±0.43 | 0.58±0.31 | 11.5±8.3 |

carbon. The results show a distinct arrangement into three groups of comparable stocks. The soils of the northernmost sites on Arga Island are characterized by the lowest amounts of S_{SOC-30} and the soils of the permafrost-affected part of the Central Siberian Plateau by the highest amounts of S_{SOC-30}. The soils of the southcentral Lena River Delta (i.e., without Arga Island) range between these bounds. Due to its transitioning appearance, the Tik08 site was included into the “delta group” although it actually belongs with the Siberian main landmass. On the one hand, the large differences between the groups are caused by the varying sources of the parent material and the resulting pedogenetic processes. On the other hand, the climatologic gradient within the N-S transect likely has an additional strong effect on the S_{SOC-30} of the groups. Arga Island, probably formed by coarse fluvial sediments (Schirrmeister et al. 2011), is covered with sparse vegetation only. The pedogenic processes are strongly related to physical weathering of the sediment and light accumulation of the organic matter provided by the sparse vegetation. The pronounced cryoturbation reworks the sediment and transports small portions of the organic matter to deeper horizons. The other sediments forming the Lena River Delta are of different age and include, in our case, the first Holocene and third Pleistocene terraces (Schwamborn et al. 2002, Wetterich et al. 2008). These two terraces, despite the differing overall geomorphology, provide comparable conditions for soil genesis. The moderately organic soils of the third terrace developed on top of ice complexes and have mineral sediments of aeolian origin. The vegetation cover is dense and results in a higher accumulation of organic matter than on the Arga Island site. The first terrace, especially the rarely flooded elevated part, is also dominated by high accumulation of organic matter and is composed primarily of fine fluvial sands and silts with additions of aeolian sands. The soil organic matter of the O horizons in the delta region is only slightly decomposed. In contrast, the soil organic matter on the Central Siberian Plateau is more decomposed and shows a higher density. Here the different vegetation, which includes trees, produces higher amounts of biomass that can be reworked into the soils; it accumulates there and is preserved over long timescales.

Regarding the accumulation of organic matter due to the dif-

ferent vegetation covers, we consider the climatologic gradient as an important factor that impacts soil carbon stocks. The pronounced increase of $S_{\text{SOC-30}}$ in the active layer of the soils from north to south is probably caused by the increase in summer length and summer temperature with decreasing latitude. Although higher temperatures cause accelerated decomposition of the organic matter, the accumulation rates are still high. Additionally, the distribution of precipitation in the south with major summer rains supports more productive plant growth than in the north, where a similar total annual amount is shared between two maxima, one in the summer and one in winter.

The degree of transformation of soil organic material can be described by the ratio of the C and N contents of the organic matter. The C/N ratios in the studied pedons were relatively high and comparable to values reported from other polar regions (Bardgett et al. 2007, Knoblauch et al. 2008, Sanders et al. 2010). The knowledge of the initial botanical composition at the investigated sites is essential for the discussion of C/N ratio (Kuhry & Vitt 1996, Vardy et al. 2000). Based on the fact that all sites were dominated by *Carex* species, mosses and lichens (in the south *Larix*), we assume that low ratios indicate stronger alteration of the organic material, whereas high ratios indicate recalcitrant or only slightly decomposed material. The high C/N ratios observed in our investigation area likely result from the lack of oxygen caused by persistent water saturation and therefore low SOM decomposition. Better aeration of some A and sandy B horizons allows higher decomposition rates, which results in lower C/N ratios.

Comparing our results with the most current carbon stock estimation for northern permafrost soils by Tarnocai et al. (2009), which includes our investigation area, we want to emphasize the importance of further intensive fieldwork within the heterogenic permafrost-affected area, particularly in the rarely researched permafrost regions of Siberia. The calculations by Tarnocai et al. (2009) with the best data available overestimated the soil organic carbon stock of the sandy Arga Island by classifying it as a carbon-rich area with stocks of more than 50 kg SOC m^{-2} , whereas the stock in the area south to the Lena River Delta with values of 10.01 to 50 kg SOC m^{-2} (both to 1 m depth) was underestimated (Tarnocai et al. 2009) (Fig. 3).

Calculating the $S_{\text{SOC-H}}$ of single soil horizons resulted in interesting insights that should be included in future studies in order to quantify and generalize these observations. Taking into account their low C_{org} contents, high BD, and additionally their abundance, it turned out that the inconspicuous B horizons make a large contribution to the overall $S_{\text{SOC-30}}$ at our sites. These mineral horizons are widespread throughout most of the pedons (Tik04, Tik08, Tik13, Tik20, Tik21) and are often cryoturbated with gleyic features. The cryoturbation mixes considerable amounts of organic material into the fine-grained layer (averaged clay content = 19.4%). Anaerobic conditions in these zones hinder decomposition and preserve organic matter.

Evaluating the existing data and consulting our preliminary results with all their weaknesses, we encourage more intensive soil sampling in the Russian Arctic to improve the soil database

of this region. This sampling should not be limited to the active layer but should include investigations of deep, currently still permanently frozen soil horizons.

Acknowledgments

This study was supported through the Cluster of Excellence ‘‘CliSAP’’ (EXC177), University of Hamburg, funded through the German Research Foundation (DFG) and a dissertation fellowship funded through the University of Hamburg (HmbNFG).

References

- Akhmadeeva, I., Becker, H., Friedrich, K., Wagner, D., Pfeiffer, E.-M., Quass, W., Zhurbenko, M., & Zöller, E. 1999. Investigation site ‘Samoylov’. *Reports on Polar and Marine Research* 315: 19-21.
- Bardgett, R.D., van der Wal, R., Jónsdóttir, I.S., Quirk, H., & Dutton, S. 2007. Temporal variability in plant and soil nitrogen pools in a high-Arctic ecosystem. *Soil Biol. Biochem.* 39: 2120-2137.
- Desyatkin, R. & Teterina, L. 1991. The soils of Lena River Delta. *Genesis and melioration of Yakutian soils* 55-66 (in Russian).
- Dutta, K., Schuur, E.A.G., Neff, J.C., & Zimov, S.A. 2006. Potential carbon release from permafrost soils of Northeastern Siberia. *Glob. Change Biol.* 12: 2336-2351.
- Fiedler, S., Wagner, D., Kutzbach, L., & Pfeiffer, E.-M. 2004. Element redistribution along hydraulic and redox gradients of low-centered-polygons, Lena Delta, Northern Siberia. *Soil Science Society of America Journal* 68: 1002-1011.
- Food and Agriculture Organization. 2006. *World reference base for soil resources 2006*. Rom: FAO, 128 pp.
- Grigoriev, M.N. 1993. *Criomorphogenesis in the Lena Delta*. Yakutsk: Permafrost Institute Press, 176 pp. (in Russian).
- Hugelius, G. & Kuhry, P. 2009. Landscape partitioning and environmental gradient analyses of soil organic carbon in a permafrost environment. *Global Biogeochem Cycles* 23: GB3006.
- Jones, A., Stolbovov, V., Tarnocai, C., Broll, G., Spaargaren, O., & Montanarella, L. (eds.). 2010. *Soil Atlas of the Northern Circumpolar Region*. Luxembourg: European Commission, Publications Office of the European Union, 144 pp.
- Khvorostyanov, D.V., Krinner, G., & Ciais, P. 2008. Vulnerability of permafrost carbon to global warming. Part I. Model description and role of heat generated by organic matter decomposition. *Tellus* 60B: 343-358.
- Klemm, J. & Zubrzycki, S. 2009. Investigation on soil and vegetation units along a North-South transect in Northeast Siberia & central part of Lena Delta, Yakutia. *Reports on Polar and Marine Research* 600: 28-29.
- Knoblauch, C., Zimmermann, U., Blumenber, M., Michaelis, W., & Pfeiffer, E.M. 2008. Methane turnover and temperature response of methaneoxidizing bacteria in permafrost-affected soils of northern Siberia. *Soil Biol. Biochem.* 40: 3004-3013.

- Kuhry, P. & Vitt, D.H. 1996. Fossil carbon/nitrogen ratios as a measure of peat decomposition. *ECOLOGY* 77, 1: 271–275.
- Kuhry, P., Mazhitova, G.G., Forest, P.-A., Deneva, S.V., Virtanen, T., & Kultti, S. 2002. Upscaling soil organic carbon estimates for the Usa Basin (northeast European Russia) using GIS-based landcover and soil classification schemes. *Dan. J. Geogr.* 102: 11–25.
- Kutzbach, L., Wagner, D., & Pfeiffer, E.-M. 2004. Effect of microrelief and vegetation on methane emission from wet polygonal tundra, Lena Delta, Northern Siberia. *Biogeochemistry* 69: 341–362.
- Kutzbach, L. 2006. *The exchange of energy, water and carbon dioxide between wet arctic tundra and the atmosphere at the Lena River Delta, Northern Siberia*. Bremerhaven: Reports on Polar and Marine Research, 141 pp.
- Kuzmina, S., Wetterich, S., & Meyer, H. 2003. Paleoecological and sedimentological studies of Permafrost deposits in the Central Lena Delta (Kurungnakh and Samoylov Islands). *Reports on Polar and Marine Research* 466: 71–81.
- Pavlova, E. & Dorozhkina, M. 1999. Geological-geomorphological studies in the northern Lena river delta. *Reports on Polar and Marine Research* 315: 112–126.
- Pfeiffer, E.-M., Wagner, D., Becker, H., Vlasenko, A., Kutzbach, L., Boike, J., Quass, W., Kloss, W., Schulz, B., Kurchatova, A., Pozdnyakov, V., & Akhmadeeva, I. 2000. Modern processes in permafrost affected soils. *Reports on Polar and marine Research* 354: 22–54.
- Pfeiffer, E.-M., Wagner, D., Kobabe, S., Kutzbach, L., Kurchatova, A., Stoof, G., & Wille, C. 2002. Modern processes in permafrost affected soils. *Reports on Polar and Marine Research* 426: 21–41.
- Ping, C.L., Michaelson, G.J., Jorgenson, M.T., Kimble, J.M., Epstein, H., Romanovsky, V.E., & Walker, D.A. 2008. High stocks of soil organic carbon in the North American Arctic region. *Nature Geoscience* 1: 615–619.
- Post, W.M., Emanuel, W.R., Zinke, P.J., & Stangenberger, A.G. 1982. Soil carbon pools and world life zones. *Nature* 298: 156–159.
- Roshydromet. 2011. *Russian Federal Service for Hydrometeorology and Environmental Monitoring*. <http://www.worldweather.org>. (Aug. 8, 2011.)
- Russia's Weather Server. 2011. *Weather Archive for Sakha*. <http://meteo.infospace.ru>. (Aug. 8, 2011.)
- Sanders, T., Fiencke, C., & Pfeiffer, E.-M. 2010. Small-scale variability of dissolved inorganic nitrogen (DIN), C/N ratios and ammonia oxidizing capacities in various permafrost affected soils of Samoylov Island, Lena River Delta, Northeast Siberia. *Polarforschung* 80(1): 23–35.
- Schirmermeister, L., Grosse, G., Schnelle, M., Fuchs, M., Krbetschek, M., Ulrich, M., Kunitsky, V., Grigoriev, M., Andreev, A., Kiensat, F., Meyer, H., Babiy, O., Klimova, I., Bobrov, A., Wetterich, S., & Schwamborg, G. 2011. Late Quaternary paleoenvironmental records from the western Lena Delta, Arctic Siberia. *Paleogeography, Paleoclimatology, Paleoecology* 299: 175–196.
- Schuur, E., Vogel, J., Crummer, K., Lee, H., Sickman, J., & Osterkamp, T. 2009. The effect of permafrost thaw on old carbon release and net carbon exchange from tundra. *Nature* 459: 556–559.
- Schwamborn, G., Rachold, V., & Grigoriev, M.N. 2002. Late quaternary sedimentation history of the Lena Delta. *Quaternary International* 89: 119–134.
- Soil Survey Staff. 2010. *Keys to Soil Taxonomy*. Washington, D.C.: United States Department of Agriculture & Natural Resources Conservation Service, 329 pp.
- Tarnocai, C., Canadell, J.G., Schuur, E.A.G., Kuhry, P., Mazhitova, G., & Zimov, S. 2009. Soil organic carbon pools in the northern circumpolar permafrost region. *Global Biogeochemical Cycles* 23, GB2023: 11 pp.
- van Cleve, K. 1974. Organic matter quality in relation to decomposition. *Proceedings of the Microbiology, Decomposition and Invertebrate Working Groups Meeting (IBP)*, Fairbanks 1973: 311–324.
- Vardy, S.R., Warner, B.G., Turunen, J., & Aravena, R. 2000. Carbon accumulation in permafrost peatlands in the Northwest Territories and Nunavut, Canada. *The Holocene* 10, 2: 273–280.
- Wagner, D., Gattinger, A., Embacher, A., Pfeiffer, E.-M., Schloter, M., & Lipski, A. 2007. Methanogenic activity and biomass in Holocene permafrost deposits of the Lena Delta, Siberian Arctic and its implication for the global methane budget. *Global Change Biology* 13: 1089–1099.
- Wetterich, S., Kuzmina, S., Kuznetsova, T., Andreev, A.A., Kienast, F., Meyer, H., Schirmermeister, L., & Sierralta, M. 2008. Paleoenvironmental dynamics inferred from late Quaternary permafrost deposits on Kurungnakh Island, Lena Delta, Northeast Siberia, Russia. *Quaternary Science Reviews* 27: 1523–1540.
- Yelovskaya, L.G. 1987. *Klassifikaciya i diagnostika merzlotnyh pochv Yakutii. (Classification and diagnosis of permafrost soils of Yakutia)*. Yakutsk, Russia: 172 pp. (in Russian).
- Zimov, S.A., Schuur, E.A.G., & Chapin, F.S. III. 2006. Permafrost and the Global Carbon Budget. *Science* 312: 1612–1613.

Author Index

- Abbott, B.W., 61
Abermann, J., 49
Abraham, J.D., 15
Abramov, A., 203
Adams, B., 221
Aguirre, A., 425
Akagawa, S., 21, 197
Aksenov, V., 67
Anarmaa, S., 371
Andersen, D., 305
Anderson, L., 15
Angelopoulos, M., 27
- Ball, L.B., 15
Balsar, A.W., 101
Barnet, C., 455
Baron, A.F., 61
Barrett, J., 221
Bartsch, A., 33, 85, 413
Bashaw, E., 45
Beutel, J., 437
Bjella, K., 39, 73
Black, W., 45
Blade, M., 353
Boike, J., 85
Bollmann, E., 49, 215
Bommer, C., 55
Bowden, W.B., 61, 101
Bray, M., 383
Brown, J., 1, 425
Burger, D., 329
- Cannia, J.C., 15
Castro, M., 419
Cater, T., 179
Cavanagh, P., 67
Cheng, G., 467
Christensen, J.H., 401
Christiansen, H.H., 431
Christoffersen, P., 271
Chuvilin, E.M., 21
Cody, R., 425
Connor, B., 191
Consonni, A., 271
Coutts, R., 301
Crosby, B.T., 61
Cysewski, M., 73
- Daanen, R.P., 79, 401
Davaa, G., 173
Davila, A.F., 305
- Davydov, S., 203
Delangle, E., 359
Dillon, M., 107, 191, 383
Doré, G., 261
Dowdeswell, J.A., 271
Drage, J., 45
Duchesne, C., 335
Duguay, C., 85
- Elger, K., 33, 85
Endrizzi, S., 91
Epstein, H.E., 119
Ermokhina, K., 119
- Falorni, G., 113
Fedorov, A.N., 161
Feng, W., 227
Feng, W., 443
Finseth, J., 97
Flinn, M.B., 61, 101
Fortier, D., 107, 125, 179, 261, 383
Fortier, R., 113
Fountain, A., 221
Fox, D., 27
Friedt, J-M., 359
Frost, G.V., 119
- Gabriela Lenzano, M., 419
Gieck, R.E., 185
Gilichinsky, D., 203
Girard, L., 437
Godin, E., 125
Godsey, S.E., 61
Gooseff, M.N., 61, 101, 221
Grenier, C., 359
Grigoriev, M.N., 137
Griselin, M., 359
Grosse, G., 137
Gruber, S., 91, 131, 437
Günther, F., 137
Günzel, F.K., 143
- Hachem, S., 85
Harris, S.A., 149
Hatleberg, E., 407
Heim, B., 33, 85
Heldmann, J., 305
Hinkel, K.M., 155
Hinzman, L.D., 231
Horne, B., 353
Hurd Jr., J.K., 155
- Iijima, Y., 161
Instanes, A., 97, 167, 341
Ishikawa, M., 173
Istomin, V.A., 21
Iwahana, G., 21
- Jambaljav, Y., 173
Jin, H., 149, 243
Jin, R., 317
Jones, J.B., 61, 101
Jorgenson, M.T., 61, 107, 179, 383
- Kääb, A., 215
Kampman, J., 61
Kane, D.L., 185
Kanevskiy, M., 107, 179
Kanevskiy, M., 191, 383
Kanie, S., 197
Kholodov, A., 203
Kitover, D.C., 209
Klene, A.E., 295
Kling, G.W., 61
Klug, C., 49, 215
Kmack, R., 45
Kotani, A., 161
Kraimer, K., 215
Krieger, K., 61
Kutzbach, L., 485
- Lacelle, D., 305
Lantuit, H., 85
Larouche, J.R., 61
Lawson, D., 473
LeBlanc, A-M., 113
Levy, J., 221
Li, G., 227
Li, X., 227, 317
Liljedahl, A.K., 231
Lin, L., 243
Lin, Z., 289
Liu, S., 237
Liu, H., 289
Liu, Z., 289
Lu, J., 289
Luo, D., 243
Lyons, W.B., 221
- Ma, W., 227, 249, 443
Mack, M., 61
Maddy, E., 455
Marchenko, S., 401

- Marinova, M., 305
Marlin, C., 359
Matsuoka, N., 431
Matyshak, G., 119
Maximov, T.C., 161
McCuaig, S., 353
McGraw, M., 255
McKay, C.P., 305
Melzer, T., 33
Miller, P., 179
Minsley, B.J., 15
M-Lepage, J., 262
Mori, J., 267
Mu, Y., 227
Mugford, R.I., 271
Murchison, P., 261
Muskett, R.R., 277
- Natsagdorj, S., 473
Nelson, F.E., 283, 295, 377
Nielson, U., 221
Niu, F., 289
Nyland, K.E., 295
- O'Donnell, J., 191
Ohata, T., 173
Ohta, T., 161
Osterkamp, T., 179
Ostroumov, V., 203
Oswell, J.M., 301
Overduin, P.P., 137
- Paulik, C., 85
Pearce, A.R., 61
Pfeiffer, E-M., 485
Phillips, M., 479
Ping, H., 467
Pollard, W.H., 27, 305, 389
- Qi, J., 311
- Ran, Y., 317
Rastetter, E.B., 61
Rees, W.G., 413
Regular, M., 353
Renssen, H., 209
Riddle, C.H., 323, 347
Rieg, L., 329
Riseborough, D., 335
Romanovsky, V.E., 203, 277, 401
Rongved, J.L., 341
Rooney, J.W., 323, 347
Roujanski, V.E., 353
Roux, N., 359
Ruiz, L., 365
- Sabel, D., 413
- Sailer, R., 49, 215, 329
Saintenoy, A., 359
Sandakov, A.V., 137
Schlaffer, S., 413
Schulla, J., 231
Schuur, E.A.G., 61
Seifert, F-M., 85
Sharkhuu, N., 173, 371
Sheng, Y., 443
Shiklomanov, N.I., 295, 377, 407
Shur, Y., 107, 179, 191, 383
Sloan, H.A., 389
Smith, B.D., 15
Soliman, A., 85
Sone, T., 267
Sorokovikov, V., 203
Sparrow, E., 395
Spencer, K., 67
Springman, S.M., 461
Stancliffe, R., 301
Stendel, M., 401
Stephani, E., 107, 191, 383
Stötter, J., 49, 215, 329
Streletskiy, D.A., 295, 377, 407
Sturm, M., 39, 73
- Tchekhovski, A., 67
Therrien, R., 113
Trofaier, A.M., 413
Trombotto Liaudat, D., 365, 419
Tweedie, C.E., 425
- Vakhrameeva, P., 485
Van Balen, R.T., 209
Vandenberghe, J., 209
Vargas, S., 425
Voss, C.I., 15
- Walker, D.A., 119
Walker, H.J., 255
Wall, D., 221
Walvoord, M.A., 15
Wang, D., 249, 443
Wang, S., 311
Watanabe, K., 21
Watanabe, T., 431
Weber, S., 437
Wen, Z., 249, 443
Wolfe, S., 335
Woo, M., 449
Wu, Q., 443
Wylie, B.K., 15
- Xiong, X., 455
- Yamamoto, Y., 461
Yang, C., 467
- Yoshikawa, K., 173, 371, 395, 473
Youcha, E.K., 185
Yu, F., 311
- Zenklusen Mutter, E., 479
Zhang, J., 237
Zhang, H., 237
Zhang, G., 353
Zhang, T., 455
Zheng, H., 197
Zheng, B., 237
Zhuang, Q., 455
Zubrzycki, S., 485